

Tom Proulx *Editor*

Modal Analysis Topics, Volume 3

Proceedings of the 29th IMAC,
A Conference on Structural Dynamics, 2011



Conference Proceedings of the Society for Experimental Mechanics Series

For other titles published in this series, go to
www.springer.com/series/8922

Tom Proulx
Editor

Modal Analysis Topics, Volume 3

Proceedings of the 29th IMAC, A Conference
on Structural Dynamics, 2011

Editor

Tom Proulx
Society for Experimental Mechanics, Inc.
7 School Street
Bethel, CT 06801-1405
USA
tom@sem1.com

ISSN 2191-5644 e-ISSN 2191-5652
ISBN 978-1-4419-9298-7 e-ISBN 978-1-4419-9299-4
DOI 10.1007/978-1-4419-9299-4
Springer New York Dordrecht Heidelberg London

Library of Congress Control Number: 2011922538

© The Society for Experimental Mechanics, Inc. 2011

All rights reserved. This work may not be translated or copied in whole or in part without the written permission of the publisher (Springer Science+Business Media, LLC, 233 Spring Street, New York, NY 10013, USA), except for brief excerpts in connection with reviews or scholarly analysis. Use in connection with any form of information storage and retrieval, electronic adaptation, computer software, or by similar or dissimilar methodology now known or hereafter developed is forbidden.

The use in this publication of trade names, trademarks, service marks, and similar terms, even if they are not identified as such, is not to be taken as an expression of opinion as to whether or not they are subject to proprietary rights.

Printed on acid-free paper

Springer is part of Springer Science+Business Media (www.springer.com)

Preface

Modal Analysis Topics represents one of six clusters of technical papers presented at the 29th IMAC, A Conference and Exposition on Structural Dynamics, 2011 organized by the Society for Experimental Mechanics, and held in Jacksonville, Florida, January 31 - February 3, 2011. The full proceedings also include volumes on: Advanced Aerospace Applications; Linking Models and Experiments; Civil Engineering, Rotating Machinery, Structural Health Monitoring, and Shock and Vibration, and Sensors, Instrumentation, and Special Topics.

Each collection presents early findings from experimental and computational investigations on an important area within Structural Dynamics. The current volume on *Modal Analysis Techniques* includes studies on Modal Analysis, Modal Parameter Identification, Modal Parameter Estimation, Modal Testing Methods, Processing Modal Data, Experimental Techniques, Active Control, Nonlinear Systems, and Vibration Damping

IMAC covers the wide variety of subjects that are related to the broad field of Structural Dynamics. It is SEM's mission to disseminate information on a broad selection of subjects. To this end, research and application papers in this volume relate to the broad field of Structural Dynamics. Modal Analysis is a major enabling technology in this area and consequently is a significant component of this volume.

The organizers would like to thank the authors, presenters, session organizers and session chairs for their participation in this track.

Bethel, Connecticut

Dr. Thomas Proulx
Society for Experimental Mechanics, Inc

Contents

| | | |
|-----------|---|------------|
| 1 | Selecting Appropriate Analytical Mode Basis for SEREP-expansion of Experimental Modes | 1 |
| | A.T. Johansson, T.J.S. Abrahamsson, Chalmers University of Technology | |
| 2 | Tutorial Guideline VDI 3830: Damping of Materials and Members | 17 |
| | L. Gaul, University of Stuttgart | |
| 3 | Optimal Second Order Reduction Basis Selection for Nonlinear Transient Analysis | 27 |
| | P. Tiso, Delft University of Technology | |
| 4 | Operating Vibration Measurements of Test Fuel Assembly in Reactor Thermo-hydraulic Test Condition | 41 |
| | K.-H. Lee, C.-H. Shin, H.-S. Kang, D.-S. Oh, N.-K. Park, Korea Atomic Energy Research Institute | |
| 5 | Output-only Modal Analysis Using Continuous-scan Laser Doppler Vibrometry and Application to a 20kW Wind Turbine | 47 |
| | S. Yang, M.S. Allen, University of Wisconsin-Madison | |
| 6 | Coupling a Compliant Structure With a Hand – arm System Using FBS | 65 |
| | S. Perrier, Y. Champoux, J.-M. Drouet, Université de Sherbrooke | |
| 7 | A Comparison of Accelerometer Selection Methods for Modal Pretest Analysis | 79 |
| | D. Linehan, K. Napolitano, ATA Engineering, Inc. | |
| 8 | Modal Impact Testing of Ground Vehicle Enabling Mechanical Condition Assessment | 93 |
| | A. Meyer, B. Wang, S. Britt, R. Kazi, D.E. Adams, Purdue University | |
| 9 | Identifying Parameters of Nonlinear Structural Dynamic Systems Using Linear Time-periodic Approximations | 103 |
| | M.W. Sracic, M.S. Allen, University of Wisconsin-Madison | |
| 10 | B-spline Laminate Shell Finite Element Updating by Means of FRF Measurements | 127 |
| | A. Carminelli, G. Catania, The University of Bologna | |
| 11 | Measurement of 2D Dynamic Stress Distributions With a 3D-Scanning Laser Doppler Vibrometer | 141 |
| | M. Schüssler, M. Mitrofanova, Polytec GmbH; U. Retze, MTU Aero Engines GmbH | |

| | | |
|-----------|--|-----|
| 12 | A Particle Damper for Transient Oscillations S.E. Semercigil, Ö.F. Turan, Victoria University; G.A. Kopp, University of Western Ontario | 153 |
| 13 | Tool Chatter in Turning With a Two-link Robotic Arm A. Özer, Gyeongsang National University; S.E. Semercigil, Victoria University | 161 |
| 14 | An Identification Method for the Elastic Characterization of Materials D. Yang, Day Software Systems, Inc. | 169 |
| 15 | An Alternating Least Squares (ALS) based Blind Source Separation Algorithm for Operational Modal Analysis J. Antoni, University of Technology of Compiegne; S. Chauhan, Bruel and Kjaer Sound and Vibration Measurement A/S | 179 |
| 16 | Automated Interpretation of Stabilization Diagrams E. Reynders, J. Houbrechts, G. De Roeck, Katholieke Universiteit Leuven | 189 |
| 17 | The Optimization and Autonomous Identification of Modal Parameters J.M. Liu, Tsinghua University/China Orient Institute of Noise & Vibration; S. Sheng, M. Ying, S.W. Dong, Tsinghua University | 203 |
| 18 | Independent Modal Space Control Technique for Mitigation of Human-Induced Vibrations in Floors D.S. Nyawako, P. Reynolds, M. Hudson, University of Sheffield | 215 |
| 19 | Nonlinear Normal Modes of a Full-scale Aircraft M. Peeters, G. Kerschen, J.C. Golinval, University of Liège; C. Stéphan, P. Lubrina, Office National d'Etudes et de Recherches Aérospatiales (ONERA) | 223 |
| 20 | FRF Measurements and Mode Shapes Determined Using Image-based 3D Point-tracking C. Warren, C. Niezrecki, P. Avitabile, University of Massachusetts Lowell | 243 |
| 21 | Experimental Modal Analsis (EMA) Using Ibrahim Time Domain (ITD) Method and Winer Filter J. Lee, S. Kim, D. Kim, S. Wang, Gwangju Institute of Science and Technology | 253 |
| 22 | A New Broadband Modal Identification Technique With Applications L. Zhang, Nanjing University of Aeronautics and Astronautics; Y. Tamura, Wind Engineering Research Center; T. Wang, X. Sun, Tokyo Polytechnic University | 261 |
| 23 | Advanced Dynamic Absorber Design Method for Practical Application J.W. Lee, Ajou University | 273 |
| 24 | Use of Operational Modal Analysis in Solving Ship Vibration Issues A. Boorsma, E.P. Carden, Lloyd's Register EMEA | 281 |
| 25 | The Use of Layered Composites for Passive Vibration Damping C.E. Lord, J.A. Rongong, A. Hodzic, University of Sheffield | 289 |
| 26 | Unbiased Estimation of Frequency Response in the Presence of Input and Output Noise A. Brandt, University of Southern Denmark | 299 |

| | | |
|-----------|---|-----|
| 27 | Vibration Control Using the Non-model Based Algorithm | 307 |
| | H. Rhee, G. Hamm, G.H. Kim, S.J. Park, S.Y. Lee, Suncheon National University | |
| 28 | Active Suspension Systems for Passenger Cars: Operational Modal Analysis as a Tool for the Performance Assessment | 313 |
| | L. Soria, Politecnico di Bari; A. delli Carri, Università degli Studi di Brescia; B. Peeters, J. Anthonis, H. Van der Auweraer, LMS International | |
| 29 | Structural Dynamics With Coincident Eigenvalues: Modelling and Testing | 325 |
| | E. Bonisoli, C. Delprete, M. Esposito, Politecnico di Torino; J.E. Mottershead, University of Liverpool | |
| 30 | Nonlinear Dynamics of an Electro-mechanical Energy Scavenger | 339 |
| | S. Tornincasa, E. Bonisoli, F. Di Monaco, S. Moos, M. Repetto, F. Freschi, Politecnico di Torino | |
| 31 | Practical Trouble Shooting Test Methodologies | 351 |
| | D.L. Brown, A.W. Phillips, M.C. Witter, University of Cincinnati | |
| 32 | Autonomous Modal Parameter Estimation: Methodology | 363 |
| | A.W. Phillips, R.J. Allemang, D.L. Brown, University of Cincinnati | |
| 33 | Autonomous Modal Parameter Estimation: Statistical Considerations | 385 |
| | R.J. Allemang, A.W. Phillips, D.L. Brown, University of Cincinnati | |
| 34 | Autonomous Modal Parameter Estimation: Application Examples | 403 |
| | D.L. Brown, R.J. Allemang, A.W. Phillips, University of Cincinnati | |
| 35 | Combined State Order and Model Order Formulations in the Unified Matrix Polynomial Method (UMPA) | 429 |
| | R.J. Allemang, A.W. Phillips, D.L. Brown, University of Cincinnati | |
| 36 | Interaction Between Structures and Their Occupants | 445 |
| | L. Pedersen, Aalborg University | |
| 37 | Evaluation of Site Periods in the Metro Vancouver Region Using Microtremor Testing | 451 |
| | J. Traber, K. Kutyn, C.E. Ventura, W.D. Liam Finn, University of British Columbia | |
| 38 | Experimental Study of the Nonlinear Hybrid Energy Harvesting System | 461 |
| | M.A. Karami, Virginia Polytechnic Institute and State University; P.S. Varoto, University of São Paulo; D.J. Inman, Virginia Polytechnic Institute and State University | |
| 39 | Using Transmissibility Measurements for Nonlinear Identification | 479 |
| | A. Carrella, D.J. Ewins, University of Bristol; L. Harper, AugustaWestland | |
| 40 | Steer Control of Motorcycle by Power Steering | 491 |
| | T. Koizumi, N. Tsujichi, T. Takemura, Doshisha University | |
| 41 | Estimating Low-bias Frequency Response Using Random Decrement | 497 |
| | R. Brincker, Aarhus University; A. Brandt, University of Southern Denmark | |

- 42 A Study of Mechanical Impedance in Mechanical Test Rigs Performing Endurance Testing Using Electromagnetic Shakers** 503
D. Di Maio, D.J. Ewins, University of Bristol
- 43 A Global-local Approach to Nonlinear System Identification** 513
Y.S. Lee, New Mexico State University; A. Vakakis, D.M. McFarland, L. Bergman, University of Illinois at Urbana-Champaign
- 44 Characterization of Rotating Structures in Coast-down by Means of Continuous Tracking Laser Doppler Vibrometer** 525
M. Martarelli, Università degli Studi e-Campus; C. Santolini, P. Castellini, Università Politecnica delle Marche
- 45 Pyroshock Loaded MISO Response** 533
J.C. Wolfson, J.R. Foley, Air Force Reserach Laboratory; A.L. Beliveau, Applied Research Associates, Inc.; G. Falbo, J. Van Karsen, LMS Americas
- 46 Development of a Long Term Viable Dynamic Data Archive Format** 541
A.W. Phillips, R.J. Allemang, University of Cincinnati
- 47 Data Analysis Strategies for Characterizing Helmet-head Performance** 557
T. Robbins, D. Adams, Purdue University; S. Walsh, U.S. Army Research Laboratory
- 48 Understanding the Effect of Preload on the Measurement of Forces Transmitted Across a Bolted Interface** 567
C. Butner, D.E. Adams, Purdue University; J. Foley, Air Force Research Laboratory

Selecting Appropriate Analytical Mode Basis for SEREP-Expansion of Experimental Modes

Anders T. Johansson, Thomas J.S. Abrahamsson

Abstract Since being introduced in 1986, the System Equivalent Reduction Expansion Process (SEREP) has been used to expand experimental eigenvector elements to the number of degrees-of-freedom of an associated FE-model. In fact, expansion for interpolation and extrapolation was its original purpose. Since then, studies of SEREP and other reduction/expansion methods have been abundant. A remarkable number of these have concentrated on the selection of master degrees of freedom for model reduction. Few have however considered the modal basis best used when SEREP is used for expansion.

Expanded experimental modes are expected to correlate well with their analytical siblings. However, we argue that the degree of global correlation should only be in parity with the local correlation between the analytical and experimental modes at locations where measurements are made. Since SEREP is a method which basically approximates a measured mode by a linear combination of analytical modes, perfect agreement between the expanded experimental and analytical modes is easily achieved, e.g. by simply using only one single mode for expansion. Of course, in this way the expanded mode normally has very little in common with the measured mode. On the other hand, using too many modes may result in something similar to the well known problem of fitting a high-order polynomial to noisy data: Perfect agreement at measurement locations is achieved at the expense of unrealistic deviations and large curvatures between these. To make sure that the experimental mode has been expanded in a manner faithful to the actual measurements, it is therefore reasonable to use a correlation based criterion in the selection of the expansion basis. Such a criterion is presented in the present paper.

Anders T. Johansson

Chalmers University of Technology, Department of Applied Mechanics, SE-412 96 Göteborg, Sweden e-mail: anders.t.johansson@chalmers.se

Thomas J.S. Abrahamsson

Chalmers University of Technology, Department of Applied Mechanics, SE-412 96 Göteborg, Sweden e-mail: thomas.abrahamsson@chalmers.se

1 Introduction

The System Equivalent Reduction Expansion Process (SEREP) was introduced in the late eighties by O’Callahan *et al.* [16, 17] and, slightly altered, by Kammer [9]. Its use as an expansion method for experimental modes will be discussed here. Assume that the i :th experimental eigenvector $\phi_{L,i}^X$ exists on some local level L defined as a subset of the degrees of freedom (DOFs) of an FE model, where the full set of FE DOFs is denoted the global level, G . Using a set of analytical modes in the modal matrix Φ_G^A , the SEREP expansion of $\phi_{L,i}^X$ is

$$\phi_{G,i}^X = \Phi_G^A (\Phi_L^A)^+ \phi_{L,i}^X \quad (1)$$

Where superscript $(\cdot)^+$ denotes the Moore-Penrose pseudoinverse.

The method has been used and discussed vividly within the structural dynamics community. To mention a few examples of its use, Yun *et al.* [20] used SEREP reduction in a damage detection application, Mitra *et al.* [14] applied it to fit a piezoelectric beam into a control algorithm, and Das and Datt [7] presented a modified version of SEREP adapted to rotating machinery applications.

SEREP, both by construction and name, is an expansion as well as a reduction method, and much work has been directed at reduction, with an emphasis on the choice of master nodes, *i.e.* the nodes to be retained in a reduction process, see for instance [3, 6]. The latter article, by Bonisoli *et al.*, touches the subject of modal incompleteness, which by extension, or perhaps rather reversion, leads to the choice of basis for expansion.

In fact, quite a few authors have noted the importance of the reduction/expansion basis. Noor [15] wrote:

The effectiveness of reduction methods depends, to a great extent, on the appropriate choice of the global approximation vectors (or reduced-basis subspace).

Which is to say that the choice of modal basis is highly important (also when using SEREP as a reduction method). Sastry *et al.* [19] considered this in devising a method for an efficient choice of modal basis when using a reduced model to try and reproduce time-domain system responses with a high frequency band-limited content.

In studying expansion methods for experimental modes, Balmès ([4, 5]) also pinpointed the main drawback of SEREP as being the sensitivity to the selection of FE modes that should form the expansion basis (the term used is "modal methods" - Balmès distinguishes between the work presented by O’Callahan, know as SEREP, [16, 17] and that by Kammer, known as Modal [9] - the difference being that Modal keeps the eigenvector elements at local DOF:s from measurements as is, while SEREP filters them by the FE-modes). Kammer [10, 11] also noted that the

accuracy of modal methods is dependent on the accurate correlation between analytical and experimental modes, that is; the goodness of the analytical modal basis used for expansion.

Balmès therefore discards modal methods in favor of a Least Squares framework minimizing the difference between the expanded model response and the measurements at local level, a methodology also advocated by Levine-West *et al.* [13]. Kammer went on to devise a Hybrid method which combines static expansion with Modal [10]. In contrast, we try to select an optimal basis of FE modes to achieve a good expansion.

Pascual *et al.* [18] discussed such a selection of expansion basis for the specific purpose of damage detection. In their article, a metric defined by the maximum residual energy of a particular expansion is evaluated to verify that the expansion basis is large enough.

When comparing experimental eigenvectors to analytical ditto, it is commonplace to use a correlation metric such as the Modal Assurance Criterion (MAC, [1]). In particular, and in constraining the discussion to the modal expansion methods, such a metric is most likely to be used in practice to select the set of analytical modes to be used for expansion. Realizing this, it is but a small step to include this information into a discrete optimization scheme aimed at selecting the best modal base for SEREP-expansion.

2 Selection through optimization

This article aims to improve the performance of the SEREP modal expansion method by approaching the selection of FE modes forming the basis of the expansion as a discrete optimization problem. Let the analytical modes be sorted in ascending frequency order. If there are n analytical modes available such that the full set of analytical modes can be defined by the numbers:

$$S := \{k \in \mathbb{N}^* | k \leq n\} \quad (2)$$

The problem is to find $I \subset S$, a set of indices defining a subset of the analytical modes such that the i :th experimental mode $\phi_{L,i}^X$, is expanded as well as possible (using $\Phi_{G,I}^A$ in (1)). The problem of finding the optimal set of analytical modes I^* for SEREP expansion of $\phi_{L,i}^X$ is:

$$I^* = \arg \min_{I \subset S} \mathcal{J}(I) \quad (3)$$

Where \mathcal{J} is the cost function defined below. Note that the optimization procedure hence needs to be rerun for each mode i to be expanded. The number of optimiza-

tion problems which needs to be solved is hence equal to the number of measured modes. Below, the steps for expanding a mode i are described; letting i run over all measured modes, the entire set is expanded. Note that all entities including i or j , which includes all correlations and candidate sets, hence both I :s and \mathcal{J} , will vary for each experimental mode $\phi_{L,i}^X$ to be expanded.

While the optimization perspective comes with standard performance aids such as the use of constraints, the key to successful optimization is the cost function, the quantity to be minimized by the optimization routine. For the purpose of this article, the cost function is created from a correlation metric which quantifies the agreement between local and global levels. The cost function's purpose is to assess the quality of the mode expansion, and so ideally, it should compare the actual measured mode at the full set of FE DOFs with the expanded mode. Since by its nature, the measured mode is defined at measured DOFs only, this metric is not available, and so the more indirect approach of including correlation comparisons using different sets of DOFs is needed.

2.1 Cost function

Above, we state that an expanded experimental mode should correlate with its analytical counterpart only as well as to the degree of correlation between analytical and experimental modes at the DOFs where measurements were made. Upon defining the full FE model DOFs as the global level and the subset where measurements have been taken the local level, this can be concisely expressed in the following proposition:

Proposition 1. *The correlation between a measured mode and its analytical counterpart at the global level should be similar to their correlation at the local level.*

Several things combine to complicate this, however. Foremost is the fact that correlation between two modes may be defined in several ways. An interesting article by Allemang, [2], provides an overview of correlation metrics in use in modal analysis. We performed the comparisons of this article with several of the metrics described, achieving best results using the most well known of them, **the Modal Assurance Criterion, MAC**, introduced by Allemang and Brown 1982 [1] and deduced originally in a linear regression setting. It is calculated as

$$MAC(\phi_a, \phi_b) = \frac{|\phi_a^H \phi_b|^2}{(\phi_a^H \phi_a)(\phi_b^H \phi_b)} \quad (4)$$

Where ϕ_a and ϕ_b are two modal vectors and $(\cdot)^H$ denotes Hermitian transpose.

At face value, the construction of a cost function from a correlation metric is straightforward. Recall that we try to find the optimal basis for expanding mode

i , $\phi_{L,i}^X$. Let $\phi_{L,j}^A$ be the analytical mode which correlates best with it at local level, and define the scalar correlations at local and global level as

$$m_L = \text{MAC}(\phi_{L,i}^X, \phi_{L,j}^A) \quad (5a)$$

$$m_G = \text{MAC}(\phi_{G,i}^X, \phi_{G,j}^A) \quad (5b)$$

A cost function in keeping with proposition 1 is:

$$\mathcal{J} = \|m_G - m_L\| \quad (6)$$

Where $\|\cdot\|$ is a user-defined norm.

But what if $\phi_{L,i}^X$ does not correlate well with any one of the analytical modes? If the FE model is poor, this is a likely situation. But even if the analytical model is of high quality, this can occur when modes are present that correspond to closely spaced eigenvalues. To incorporate as much valuable information as possible into the cost function it may be beneficial to include other MAC values, *i.e.* degrees of correlation between the measured mode and analytical modes other than the one which correlates best with $\phi_{L,i}^X$.

Recall that the experimental mode to be expanded, $\phi_{L,i}^X$, correlates best with analytical mode j . The index set of all modes except j becomes:

$$S_{\setminus j} := S \setminus \{j\} \quad (7)$$

At this point, we can define the two correlation arrays:

$$M_L = \text{MAC}(\phi_{L,i}^X, \Phi_{L,S_{\setminus j}}^A) \quad (8a)$$

$$M_G = \text{MAC}(\phi_{G,i}^X, \Phi_{G,S_{\setminus j}}^A) \quad (8b)$$

And a cost function similar to that of equation (6) can be written as:

$$\mathcal{J} = W_1 \|m_G - m_L\| + W_2 \|M_G - M_L\| \quad (9)$$

Most of the analytical modes will however have very low correlation with a given experimental mode. Furthermore, in increasing the number of degrees of freedom, we expect the correlation between two separate eigenvectors to drop because of the orthogonality properties of the eigenvectors. The second term in (9) may then force the correlation to be higher than desirable. To prevent this, it can be beneficial to include only analytical modes whose correlation with the experimental mode to be expanded, at the local level, is above a certain limit. Thus, the set $S_{\setminus j}$ modifies to:

$$\bar{S}_{\setminus j} := \{k \in S_{\setminus j} | \text{MAC}(\phi_{L,i}^X, \phi_{L,k}^A) > \sigma\} \quad (10)$$

Where $0 < \sigma < 1$ is a user-defined limit value. The user must also set the relative weights W_1 and W_2 , and define which norm to use. If taking the ℓ^2 -norm, (9) can be generalized further to the quadratic form $\mathcal{J} = \boldsymbol{\varepsilon}^T W \boldsymbol{\varepsilon}$ popular in engineering sciences, where $\boldsymbol{\varepsilon}^T = [(m_G - m_L) (M_G^T - M_L^T)]$ and W is a positive definite weighting matrix.

2.2 Reduction of candidate sets

The number of index sets I satisfying $I \subset S$ is vast. If a brute-force method is to be used for the solution of this problem, with n analytical modes under consideration, the number of combinations N to be compared is

$$N = \sum_{k=1}^n \frac{n!}{(n-k)!k!} \quad (11)$$

Even for a relatively moderate number of FE modes, this becomes prohibitive computational-wise. For instance to include up to 30 FE modes as basis would require considering just over one billion combinations. To examine the entire solution space must therefore be considered impractical, if not outright impossible.

We propose to circumvent this through considering only combinations of analytical eigenvectors such that the corresponding eigenvalue indices make up an interval $I := [j_{min}, j_{max}]$ (such that $I \subset S$). This reduces the number of combinations needed, and yet it still requires the evaluation of a great many uninteresting sets, such as ones that do not contain the analytical eigenvector which correlates best with the mode to be expanded. Thus, the concept of an iterative method of candidate set construction arose.¹

2.2.1 Constructing candidate sets

The candidate set construction algorithm proposed here is based on closed frequency intervals; that is, to include all analytical modes in a frequency range. The optimization problem of (3) is then reduced to finding the limits of that frequency band. The algorithm consists of two steps; the first step *expands* the candidate set, while the second *translates* the frequency band in the frequency domain.

¹ An idea inspired by Kammer's method of Effective Independence [12] for sensor placement. A candidate set construction algorithm based on a methodology more closely resembling the EFI, in which the analytical eigenvector making the largest impact on the cost function was added without restricting the candidate sets to be intervals, was also tested. In this context, it did not perform as good as the algorithm in the subsequent section, however, and was left out.

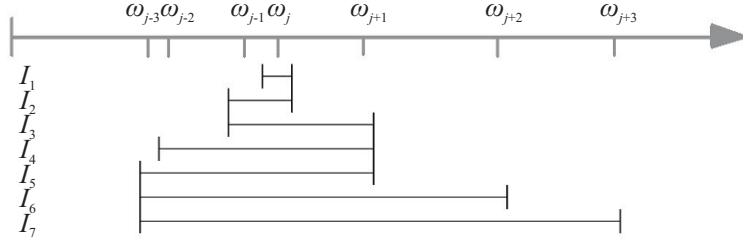


Fig. 1 Concept of sequential construction of candidate sets consisting of frequency intervals.

Step 1: Expanding the candidate set In step 1, the candidate sets are created through sequential expansion, starting at a set including only the mode with the highest correlation with mode i and iteratively increasing the interval through adding that of the two modes adjacent to the set which affects the cost function the most: Let the initial set consist only of j , the analytical eigenvector with the highest correlation to experimental mode i , so that $I_1 := \{j\}$. This will result in a global diagonal MAC 1, see (5b). Next, add the mode adjacent to j which together with j gives the lowest cost function value to create set number two. Hence,

$$I_2 := \{j-1, j\}, \text{ or } I_2 := \{j, j+1\} \quad (12)$$

Assume $I_2 := \{j-1, j\}$. To form I_3 , consider the modes adjacent to I_2 ; denote the set of these two modes I_2 , where in this example

$$I_2 := \{j-2, j+1\} \quad (13)$$

Include the mode in I_2 which together with I_2 gives the lowest cost function. Continue the process until $a = N_{DOF}$. See [Figure 1](#).

Step 2: Translating the candidate set When the number of analytical modes exceeds the number of measured DOFs, SEREP (1) corresponds to an over-determined least-squares problem. To avoid the problems associated, the size of each candidate set I_a must be less than or equal to the number of DOFs at local level, N_{DOF} . If there are still analytical modes to be tried when $a = N_{DOF}$, the mode adjacent to $I_{N_{DOF}}$ which gives the lowest cost function value can be added, compensated by through removing the last index at the other end of the set to render the next candidate set. In effect, this means sweeping the frequency window up or down the frequency axis.

Concisely, the candidate set construction algorithm can be written as:

Step 1

1.1) $I_1 := \{j\}$

1.2) $k^* = \arg \min_k \mathcal{J}_i(I_a \cup \{k\})$, $k \in \Gamma_a$

$$\Gamma_a := \{s \in \mathbb{C}_S(I_a) \mid \exists t \in I_a \text{ s.t. } s = \arg \min_{u \in \mathbb{C}_S(I_a)} \|t - u\|\}$$

1.3) $I_{a+1} := I_a \cup \{k^*\}$

1.4) Repeat 1.2) and 1.3) until:

$$a = N_{DOF}$$

Step 2

2.1) $k^* = \arg \min_k \mathcal{J}_i(I_a \cup \{k\})$, $k \in \Gamma_a \setminus \bigcup_{r=1}^a I_r$

2.2) $\bar{I}_{a+1} := I_a \cup \{k^*\}$

$$I_{a+1} := \bar{I}_{a+1} \setminus \{s \in I_a \mid s = \text{extremum}^*(\bar{I}_{a+1})\}$$

2.3) Repeat 2.1) and 2.2) until:

$$\Gamma_a \setminus \bigcup_{r=1}^a I_r = \emptyset$$

* Extremum is here defined as the largest and smallest value of the set, *i.e.* maximum and minimum.

Each candidate set calculated is stored, as an array of indices, along with the corresponding cost function values. The set with the lowest cost function value is denoted I^* ; the expansion of $\phi_{L,i}^X$ is then $\phi_{G,I^*,i}^X$.

Unfortunately, the algorithm described above does not yield monotonically decreasing cost function values, wherefore this cumbersome approach is necessary. Whether (3) is actually fulfilled, that is, whether I^* is the optimal solution in the solution space of all sets $I \subset S$, is not further investigated.

2.2.2 Constraints

Constraints on the feasible domain is standard in optimization. In (3), the feasible domain is defined by $I \subset S$. Constraining I further, the feasible domain becomes:

$$I \subset \hat{S} \subset S \quad (14)$$

Where \hat{S} is a proper subset of S . In effect, this means excluding certain analytical eigenvectors from the full eigensolution. On what grounds can such an exclusion be justified? We have come up with two potential scenarios:

First, if an analytical eigenvector is not observable at the local (measurement) level, its contribution to system motion cannot be identified from the measurements, and it should be excluded. Using the observability metric proposed by Hamdan and Nayfeh [8], the subset \hat{S} becomes:

$$\hat{S} := \{s \in S \mid o_s > \sigma\} \quad (15a)$$

where

$$o_s = \max_k \frac{|c_k \phi_{G,s}^A|}{\|c_k\| \|\phi_{G,s}^A\|} = \frac{|\{\phi_{G,s}^A\}_k|}{\|\phi_{G,s}^A\|} \quad (15b)$$

Where σ is a user-defined limit value and c_k is the k :th row of the observation matrix relating the local and global levels. Hence, c_k is a row vector with unit value at the position of the DOF corresponding to measurement DOF k and zeros otherwise, which makes the observability metric simply the normalized local-level high-value of the analytical mode under scrutiny; the second identity in (15b).

Second, if for some reason an analytical eigenvector correlates extremely little with the measured mode to be expanded at the local level, its use as one of the basis vectors is likely to be limited. Using MAC exclusion, the subset \hat{S} becomes:

$$\hat{S} := \{s \in S \mid \max_k \text{MAC}(\phi_{L,s}^A, \phi_{L,k}^X) > \sigma\} \quad (16)$$

Where again σ is user-defined. In using these excluding constraints, simply replace S with \hat{S} in the candidate set construction algorithm above (making the I_a :s intervals only in transferred sense, *i.e.* such that $I_a := [j_{min}, j_{max}] \cap \hat{S}$).

Apart from excluding modes from the potential set, we also have the option of adding proper constraints, such that the optimization problem of equation (3) modifies to:

$$\begin{aligned} I_i^* &= \arg \min_{I \subset \hat{S}} \mathcal{J}_i(I) \\ \text{s.t. } &g_i(I) \leq 0 \end{aligned} \quad (17)$$

Two constraints of this type have been considered. One verifies the numerical soundness of SEREP: When the expansion has been successful, the expanded mode should

resemble the original mode very closely at the local level (this is not applicable when using the Modal version of SEREP, see the discussion regarding differences between SEREP and Modal in the introduction):

$$MAC(\phi_{i,L,i}^X, \phi_{L,i}^X) > \sigma \quad (18)$$

Where σ is a user-defined limit value somewhat smaller than unity.

As for the other one, recall that in equation 10, we created a modified set $\bar{S}_{\setminus j}$ which excluded modes with low local level correlation from the cost function, since we expected the correlation to drop as the number of DOFs increased. These can instead be kept below their initial value (with some slack):

$$MAC(\phi_{G,k}^A, \phi_{i,i}^X) - MAC(\phi_{L,k}^A, \phi_{L,i}^X) \leq \sigma, \forall k \in S \setminus (\bar{S}_{\setminus j} \cup \{j\}) \quad (19)$$

Again, σ is a small user-defined limit value.

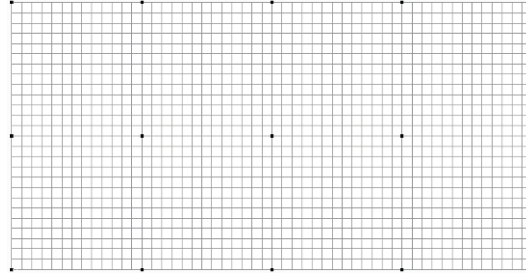
Sets which do not comply with these constraints are deemed infeasible and discarded, provided that a feasible set can be found. If a feasible set cannot be found, the constraints are disregarded and the mode set with the lowest cost function value is used for expanding mode i .

3 Numerical validation

The procedure described in the previous section has been evaluated on two simple numerical examples. In both cases, results are compared to "SEREP classic", interpreted as using the same set of analytical modes in the expansion of every experimental mode, letting the set of analytical modes included in the expansion basis start at the first mode and be a proper interval up to a given mode, such that the highest number of modes is accurately expanded. This is ensured in the following examples.

The first example (see [Figure 2](#)) consists of a single flat 153x299.5mm titanium plate ($E = 108GPa$, $\nu = 0.22$), which was modeled using 1352 plate elements with FEMAP[®] and MD NASTRANTM. The analytical model represents a 10mm thick plate, while a 12mm plate model emulates measurements. Emulated sensing is taken perpendicular to the plate at the 15 locations shown in figure 2, with added normal distribution eigenvector errors of a magnitude of 2% of the maximum magnitude vector element of each mode. In-plane modes are not included in the measured set. Using the method described above with $W_1 \neq 0$ and $W_2 = 0$, exclusion based on observability with a limit value corresponding to 0.5% of the maximum observability value and the constraint ensuring a MAC-value when comparing the expanded mode with its original no lower than 0.99, all 36 observable eigenvectors below 19000Hz are accurately expanded, see [Table 1](#). When increasing eigenvector element error levels to 5%, all experimental modes except for eigenvector number 25 are accu-

Fig. 2 Basic FE-model of planar plate used for validation, numerical example one. The bold dots indicate measurement locations.



rately expanded. Eigenvector 25 is not accurately expanded due to the fact that, at the local level, it has MAC correlation of 0.99 with the second eigenvector of the analytical mode shape basis. When noise levels increase, a mode mismatch occurs. In comparison, the original SEREP algorithm accurately expands only at most 15 modes (several choices gave 15 accurate modes), see [Table 2](#). The poor results of SEREP classic in this example are due to the fact that the analytical modal basis includes modes that are not observable at the local level - modes perpendicular to the measurement direction. Since these are zero vectors at the local level, bar numerical errors, SEREP is unable to calculate their contribution to the solution.

Table 1 MAC values of SEREP-expanded modes and the modes used to emulate measurements. Results for example 1 with 2% white gaussian noise. First 38 modes used in SEREP classic.

| Mode | optim | classic 38 | Mode | optim | classic 38 |
|------|-------|------------|------|-------|------------|
| 1 | 1.00 | 0.00 | 19 | 1.00 | 1.00 |
| 2 | 1.00 | 0.01 | 20 | 1.00 | 1.00 |
| 3 | 1.00 | 0.00 | 21 | 1.00 | 1.00 |
| 4 | 1.00 | 0.00 | 22 | 1.00 | 0.00 |
| 5 | 1.00 | 1.00 | 23 | 1.00 | 1.00 |
| 6 | 1.00 | 0.00 | 24 | 1.00 | 1.00 |
| 7 | 1.00 | 0.02 | 25 | 1.00 | 0.00 |
| 8 | 1.00 | 1.00 | 26 | 1.00 | 1.00 |
| 9 | 1.00 | 0.00 | 27 | 1.00 | 1.00 |
| 10 | 1.00 | 0.01 | 28 | 1.00 | 0.01 |
| 11 | 1.00 | 0.00 | 29 | 1.00 | 1.00 |
| 12 | 1.00 | 0.01 | 30 | 1.00 | 0.00 |
| 13 | 1.00 | 0.00 | 31 | 1.00 | 1.00 |
| 14 | 1.00 | 1.00 | 32 | 1.00 | 1.00 |
| 15 | 1.00 | 1.00 | 33 | 1.00 | 0.00 |
| 16 | 1.00 | 1.00 | 34 | 1.00 | 0.01 |
| 17 | 1.00 | 0.00 | 35 | 1.00 | 0.00 |
| 18 | 1.00 | 0.00 | 36 | 1.00 | 0.00 |

The second example is an assembly consisting of three titanium plates rigidly connected at their intersections. The resulting model, seen in figure 3, was made up of

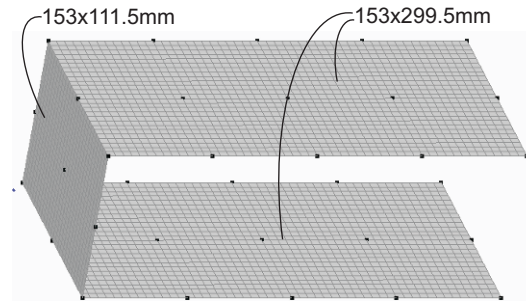
Table 2 MAC values comparing expanded modes and the modes used to emulate measurements. Results for example 1 with 5% white gaussian noise. First 38 modes used in SEREP classic.

| Mode | optim | classic 38 | Mode | optim | classic 38 |
|------|-------|------------|------|-------|------------|
| 1 | 1.00 | 0.01 | 19 | 1.00 | 0.99 |
| 2 | 0.99 | 0.01 | 20 | 1.00 | 1.00 |
| 3 | 1.00 | 0.01 | 21 | 1.00 | 0.99 |
| 4 | 1.00 | 0.00 | 22 | 1.00 | 0.00 |
| 5 | 1.00 | 0.99 | 23 | 1.00 | 0.99 |
| 6 | 1.00 | 0.00 | 24 | 1.00 | 0.98 |
| 7 | 0.99 | 0.01 | 25 | 0.01 | 0.00 |
| 8 | 1.00 | 1.00 | 26 | 1.00 | 1.00 |
| 9 | 0.99 | 0.00 | 27 | 1.00 | 0.99 |
| 10 | 1.00 | 0.01 | 28 | 1.00 | 0.01 |
| 11 | 0.99 | 0.00 | 29 | 1.00 | 0.99 |
| 12 | 0.99 | 0.01 | 20 | 1.00 | 0.00 |
| 13 | 1.00 | 0.00 | 31 | 1.00 | 0.99 |
| 14 | 1.00 | 1.00 | 32 | 0.96 | 0.98 |
| 15 | 0.99 | 0.99 | 33 | 1.00 | 0.00 |
| 16 | 1.00 | 1.00 | 34 | 1.00 | 0.01 |
| 17 | 1.00 | 0.00 | 35 | 1.00 | 0.00 |
| 18 | 1.00 | 0.00 | 36 | 1.00 | 0.00 |

3380 plate elements at a grand total of 21222 DOFs. The model emulating measurements is such that the left plate in [Figure 3](#) has 12mm thickness, while the other two plates are 10mm thick. By contrast, all of the plates in the analytical model are 10mm thick. This means in effect that we are using a symmetric model as a basis for expanding non-symmetric modes. The experimental mode set consists of the first 34 elastic modes (the first 40 from FEM minus 6 rigid body modes). For the analytical solution, ten more modes were included, making the number of analytical candidate modes 44.

In this case, all 44 elastic analytical candidate modes are observable, so no exclusion was used. The weighting parameters were set to $W_1 = W_2$ to account for the problem of finding a best fit symmetric or anti-symmetric counterpart to the non-symmetric mode to be expanded. No analytical modes were left out of the cost function. Furthermore, the constraint was again used with the local-level correlation after expansion no lower than 0.99, and the constraint with keeping off-diagonal MAC-values low was used for all modes with a local-level correlation below 0.7 and a slack variable of $\sigma = 0.05$. The measurements are taken in a symmetric pattern at 33 nodes measuring in the direction normal to the plates; in total three measurements are perpendicular to the smaller plate. Again, 2% normal distribution eigenvector element error was added. At most, the classical SEREP routine managed to accurately expand 22 modes out of the first 34 flexible. Using the proposed method, 31 out of 34 were accurately expanded. The three modes that were not expanded properly, modes 24, 25 and 27, were such that the main deformation in the two larger plates was in-plane, *i.e.* largely unobservable. See [Table 3](#). [Figure 4](#) shows mode 23 as an example of a mode where the proposed method clearly outperforms SEREP classic.

Fig. 3 Basic FE-model used for validation, numerical example two. The bold dots indicate measurement locations.



It should be noted that the results in this section are somewhat sensitive to the

Table 3 MAC values comparing expanded modes and the modes used to emulate measurements. Results for example 2. First 24 modes used in SEREP classic.

| Mode | optim | classic 24 | Mode | optim | classic 24 |
|------|-------|------------|------|-------|------------|
| 1 | 0.99 | 0.97 | 18 | 0.97 | 1.00 |
| 2 | 0.99 | 0.99 | 19 | 0.99 | 0.99 |
| 3 | 0.99 | 0.99 | 20 | 0.99 | 0.99 |
| 4 | 0.99 | 0.99 | 21 | 0.98 | 0.98 |
| 5 | 1.00 | 1.00 | 22 | 0.99 | 0.99 |
| 6 | 0.99 | 0.99 | 23 | 1.00 | 0.30 |
| 7 | 1.00 | 1.00 | 24 | 0.88 | 0.82 |
| 8 | 1.00 | 1.00 | 25 | 0.67 | 0.02 |
| 9 | 1.00 | 1.00 | 26 | 1.00 | 0.01 |
| 10 | 0.99 | 0.99 | 27 | 0.59 | 0.02 |
| 11 | 0.99 | 0.99 | 28 | 1.00 | 0.09 |
| 12 | 1.00 | 0.99 | 29 | 0.98 | 0.03 |
| 13 | 1.00 | 1.00 | 30 | 0.97 | 0.00 |
| 14 | 0.99 | 0.99 | 31 | 0.96 | 0.01 |
| 15 | 1.00 | 0.99 | 32 | 0.99 | 0.00 |
| 16 | 0.98 | 0.99 | 33 | 1.00 | 0.01 |
| 17 | 1.00 | 0.99 | 34 | 0.95 | 0.00 |

noise realization. For different realizations of the first example with 5% error, for instance, there were cases where both mode 2 and mode 25 were inaccurately expanded, and there were cases where they were both expanded correctly. Other times, other modes could not be properly expanded at this error level.

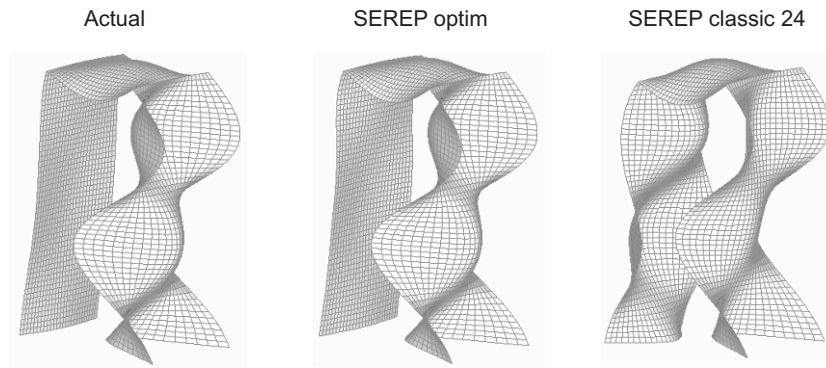


Fig. 4 Comparison of mode number 23, numerical example 2. First 24 modes used in SEREP classic.

4 Conclusions and further work

The most important contribution of this work is the focus on the basis selection in modal expansion methods. A first example highlights the importance of excluding analytical modes that are not observable at measurement locations from the expansion set. A second example illustrates that even an FE model whose normal modes correlate quite poorly with the measured modes can be successfully used as an expansion basis. The original SEREP method also works quite well for this example in the lower end of the frequency range.

The method proposed in this paper clearly outperformed the classical SEREP expansion method in the comparisons performed. Its drawbacks are however its computational inefficiency as an abundance of candidate expansions are to be tested for each mode and the extensive input needed to set the user-defined limit values of the various constraints.

In the future, we hope to compare this methodology with other methods such as those proposed by Balmès [4, 5] and Kammer [10, 11]. As the latter method also uses a modal basis, it would also be interesting to investigate the effects of basis selection on it as well.

References

1. Allemang, R.J., Brown, D.L., A Correlation Coefficient for Modal Vector Analysis, in *Proceedings of the first International Modal Analysis Conference, Orlando, Florida, November 1982.*

2. Allemang, R.J., The Modal Assurance Criterion - Twenty Years of Use and Abuse, *Journal of Sound and Vibration*, 2003.
3. Avitabile, P., Pechinsky, F., O'Callahan, J., Study of Modal Vector Correlation Using Various Techniques for Model Reduction, in *Proceedings of the Ninth International Modal Analysis Conference, Florence, Italy*, April 1991.
4. Balmès, E., Review and Evaluation of Shape Expansion Methods, in *Proceedings of the 18:th International Modal Analysis Conference, San Antonio, Texas*, February 2000.
5. Balmès, E., Sensors, Degrees of Freedom, and Generalized Modeshape Expansion Methods, in *Proceedings of the 17:th International Modal Analysis Conference, Kissimmee, Florida*, February 1999.
6. Bonisoli, E., Delprete, C., Rosso, C., Proposal of a modal-geometrical-based master nodes selection criterion in modal analysis, *Mechanical Systems and Signal Processing* 23, 606-620, 2009.
7. Das, A.S., Dutt, J.K., Reduced model of a rotor-shaft system using modified SEREP, *Mechanics Research Communications* 35, 398-407, 2008.
8. Hamdan, A. M. A. and Nayfeh, A. H., *Measures of Modal Controllability and Observability for First- and Second-Order Linear Systems*, Journal of guidance, control, and dynamics, Vol. 12, No. 3 (1989), pp. 421-428
9. Kammer, D.C., Test-analysis-model development using exact model reduction, *The International Journal of Analytical and Experimental Modal Analysis* 2 (4), 174-179, (1987).
10. Kammer, D.C., A Hybrid Approach to Test-Analysis-Model Development for Large Space Structures, *Journal of Vibration and Acoustics* 113, 325-332, 1991.
11. Kammer, D.C., Correlation considerations - Part 2, Model reduction using modal SEREP and Hybrid, in *Proceedings of 16th International Modal Analysis Conference, Santa Barbara, California*, February 1998.
12. Kammer, D., Sensor set expansion for modal vibration testing, *Mechanical Systems and Signal Processing*, 2005.
13. Levine-West, M., Kissil, A., Milman, M., Evaluation of Mode Shape Expansion Techniques on the Micro-Precision Interferometer Truss, in *Proceedings of the 12:th International Modal Analysis Conference, Honolulu, Hawaii*, Jan-Feb 1994.
14. Mitra, M., Gopalakrishnan, S. and Seetharama Bhat. M, Vibration control in a composite box beam with piezoelectric actuators, *Smart Materials and Structures* 13, 676-690, 2004.
15. Noor, A.K., Recent advances and applications of reduction methods, *Applied Mechanics Reviews* 47 (5), 125-145, 1994.
16. O'Callahan, J.C., Avitabile, P., Madden, R., Lieu, I.W., An Efficient Method of Determining Rotational Degrees of Freedom From Analytical and Experimental Modal Data, in *Proceedings of the Fourth International Modal Analysis Conference, Los Angeles, California*, February 1986.
17. O'Callahan, J.C., Avitabile, P., Riemer, R., System Equivalent Reduction Expansion Process (SEREP), in *Proceedings of the Seventh International Modal Analysis Conference, Las Vegas, Nevada*, February 1989.
18. Pascual, R., Schälchli, Razeto, M., Improvement of damage-assessment results using high-spatial density measurements, *Mechanical Systems and Signal Processing* 19, 123-138, 2005.
19. Sastry, C.V.S., Roy Mahapatra, D., Gopalakrishnan, S., Ramamurthy, T.S., An iterative system equivalent reduction expansion process for extraction of high frequency response from reduced order finite element model, *Computer Methods in Applied Mechanics and Engineering* 192, 1821-1840, 2003.
20. Yun, G.J., Ogorzalek, K.A., Dyke, S.J., Song, W., A parameter subset selection method using residual force vector for detecting multiple damage locations, *Structural Control and Health Monitoring*, 1987.

Tutorial Guideline VDI 3830: Damping of Materials and Members

Lothar Gaul

Committee Background

It was Nov 10, 1982 when Prof. Federn, Prof. Gaul, Prof. Mahrenholtz, and Dr. Pieper VDI decided to work out a guideline on damping in the VDI/FANAK C13 Committee “Material Damping”. They were joined by Prof. Ottl, Prof. Kraemer, Prof. Pfeiffer, Prof. Markert, Prof. Wallaschek, and Mr. Hilpert VDI lateron in their names order. The idea was to comprise distributed theoretical and experimental knowledge and to homogenize the nomenclature of this subject.

At the very beginning, important knowledge was provided by the books

J.D. Ferry: *Viscoelastic Properties of Polymers*

John Wiley & Sons, New York, 1960

B.J. Lazan: *Damping of Matrials and Members in Structural Mechanics*

Pergamon Press, Oxford, 1968

Important contributions to the subject were made at conferences in the USA, such as

- Damping
Lynn Rogers
- The Role of Damping in Vibration and Noise Control, ASME Boston
Lynn Rogers, Lothar Gaul
- Damping Sessions at IMAC
Lothar Gaul et al

and in Germany by the colloquium

Lothar Gaul

Institute of Applied and Experimental Mechanics, University of Stuttgart, Pfaffenwaldring 9, 70569 Stuttgart, Germany e-mail: gaul@iam.uni-stuttgart.de

- Daempfnungsverhalten von Werkstoffen und Bauteilen
Kolloquium, TU Berlin, 1975 VDI-GKE
H. Fuhrke, K. Federn, R. Gasch

Results of five guidelines worked out by the named committee

VDI-Richtlinie 3830, Blatt 1-5

have been presented at the conference

Schwingungsdaempfung (Vibration Damping)
October 16 and 17, 2007, Wiesloch near Heidelberg

providing information about

- modelling
- numerical methods (Finite Elements, Boundary Elements, Modal Analysis)
- experimental techniques for determining material damping properties from measured components or system characteristics

along with

- passive and adaptive practical applications.

The guideline VDI 3830 “Damping of Materials and Members”

The guideline VDI 3830 consists of the following parts:

Part 1 Classification and survey

Part 2 Damping of solids

Preliminary note

- 1 Physical phenomena
- 2 Linear models
- 3 Nonlinear models

Part 3 Damping of assemblies

Preliminary note

- 1 From the material to the homogeneous member
- 2 Laminated members
- 3 Damping in joints
- 4 Damping due to fluids
- 5 Damping by squeezing
- 6 Assemblies

Part 4 Models for damped structures

Preliminary note

- 1 Basic model
- 2 Structures with finite number of degrees of freedom
- 3 Calculation of viscoelastic components using the boundary element method

Part 5 Experimental techniques for the determination of damping characteristics

Preliminary note

- 1 Remarks on experimental techniques
- 2 Experimental techniques and possible instrumentation
- 3 Special experimental techniques for determining damping characteristics under aggravated conditions
- 4 Experimental Modal Analysis (EMA)
- 5 Experimental techniques for the damping measurement of subsoil

Introduction

All dynamic processes in mechanical systems are more or less damped. Consequently, damping is highly relevant in those fields of technology and applied physics which deal with dynamics and vibrations. These include

- machine-, building-, and structural dynamics,
- system dynamics,
- control engineering, and
- technical acoustics,

because damping in these cases often has a considerable effect on the time history, intensity, or even the existence of vibrations. Important applications are:

- transient vibrations (transient effects associated with the onset or decay of vibrations, shock-induced vibrations, reverberation effects)
- resonance vibrations (unavoidable with random excitation)
- wave propagation
- dynamic-stability problems

Accordingly, a multitude of scientific publications dealing with damping, or taking it into account at least, are found in technical literature. Due to different theory approaches, objects, and task definitions in the applications listed above, the designations, the characterisation of damping, the experimental techniques, and the analytical and numerical methods are not harmonised.

The dynamic behaviour of damped structures can, in special cases, be calculated using generally valid material laws for inelastic materials based on continuum mechanics taking into account boundary effects (e.g. joints). In general, this approach is too elaborate or expensive, or not at all practicable. In most cases, therefore, phenomenological equivalent systems or mathematical models tailored to the task definition are used which are only valid assuming a special state of stresses and/or a special time history. Harmonic (sinusoidal) time histories are a preferred special case where complex quantities describe the elastic and damping properties. These depend on a number of parameters: material data, rate of deformation, frequency, temperature, number of load cycles, etc. In the case of nonlinear behaviour there is also a dependence on the amplitude.

For certain problems, it is sufficient to state, for one deformation cycle, the energy dissipated in a unit volume or within the system, or the energy released into the environment at the system boundaries, often related to a conveniently chosen elastic energy in a unit volume or in the system as a whole. In structural dynamics, the use of modal damping ratios has proven useful, which do no longer contain detailed information about the damping.

This guideline is not a textbook; it cannot be a compilation of generally mandatory rules. It is intended

- to contribute to a better understanding of the physical causes of damping,
- to facilitate interdisciplinary cooperation by defining harmonised terms and pointing out the relations between different approaches to the modelling of damping, and
- to allow an overview of the state of knowledge and experience gathered in various fields of application and research,

in order to promote the application of existing knowledge.

This guideline is structured in accordance with its objective. It starts off with the notion of damping and the causes of damping before dealing with different modelling approaches for the linear and nonlinear behaviour of solids, and establishing cross-references between these approaches. Linear viscoelastic materials being the best investigated. Their behaviour is discussed in great detail. They are followed by the damping of assemblies, relevant to the user, by its mathematical characterisation and its relation to material damping. Models for damped structures are discussed next, and the application of the boundary element method (BEM) is explained. Finally, as statements on damping rely on experiments, Part 5 describes established experimental techniques, possible instrumentation for the determination of damping characteristics, and analytical methods.

The notion of damping

Damping in mechanical systems is understood to be the irreversible transition of mechanical energy into other forms of energy as found in time-dependent processes. Damping is mostly associated with the change of mechanical energy into thermal energy. Damping can also be caused by releasing energy into a surrounding medium. Electromagnetic and piezoelectric energy conversion can also give rise to damping if the energy converted is not returned to the mechanical system.

Classification of damping phenomena

The physical causes of damping are multifarious. In addition to friction, wave propagation or flow effects, other possible causes are phase transitions in materials or energy conversion by piezoelectric, magnetostrictive, or electromechanical processes.

Forces associated with damping are non-conservative. They can be internal or external forces. If both action and reaction forces in a free body diagram the damping force, are effective within the system boundaries, the effect is said to be an internal damping effect. Where the reaction force is effective outside the system boundaries, the effect is an external damping effect.

Examples of internal damping are:

- material damping due to nonelastic material behaviour
- friction between components, e.g. in slide ways, gears, etc.
- conversion of mechanical vibration energy into electrical energy by means of the piezoelectric effect and dissipation due to dielectric losses

Examples of external damping are:

- friction against the surrounding medium
- air-borne-sound radiation into the environment
- structure-borne-sound radiation into the ground

Phenomenologically, the damping in a mechanical system can be composed of the following contributions:

- *Material damping*

The energy dissipation within a material, due to deformation and/or displacement, is called material damping. Its physical causes are, in essence:

- in solids
 - heat flows induced by deformation (thermomechanical coupling)
 - slip effects
 - microplastic deformations
 - diffusion processes
- in fluids
 - viscous flow losses

- *Contact-surface damping*

Relative motion, friction

Contact-surface damping is caused by relative motions in the contact surfaces of joined components such as screwed, riveted, and clamped joints. The physical causes are:

- friction due to relative motions in the contact surface
- pumping losses in the enclosed medium due to relative motion in a direction normal to the contact surface (e.g. gas pumping)

The term “structural damping” includes:

- Damping in guides
This includes energy dissipation in longitudinal guides (e.g. slides) and circular guides (e.g. journal bearings).
- Electromechanical damping
Electromechanical damping can be caused by piezoelectric, magnetostrictive, or electromagnetic effects.
- Energy release to the surrounding medium
This includes:
 - air damping
 - fluid damping
 - bedding damping

Notes on modern, computer-based analytical and measurement programs

Whereas the mass and stiffness matrices of relatively complex structures can be readily determined nowadays using three-dimensional CAD drawings, automatic grid generation, and subsequent FEM analysis, an appropriate calculation model cannot usually be established which sufficiently precise information on damping. More precise damping parameters contains can be determined experimentally.

“Experimental Modal Analysis” (EMA) has become established as the suitable tool worldwide. It uses measured frequency-response curves between appropriately chosen excitation points and measuring points, and modern curve-fitting techniques for identifying the modal parameters: natural frequencies, eigenmodes, and modal damping ratios. In the case of simple structures, the system can be excited by means of a hammer impact. In the case of complex components and considerable damping, excitation using one or several exciters has proven convenient, allowing to control exciter amplitudes and energy distribution for selected frequency ranges. The system response is often measured by means of piezoelectric accelerometers or laser-optical sensors.

Modern measurement and analytical systems offer the possibility to identify discrete damping couplings provided that the substructures have been separately investigated beforehand.

Link modules allow to establish the connection between the results of experimental modal analysis and the calculated FEM analysis (e.g. matching of nodal points and coordinate axes through interpolation). Quality criteria such as MAC (Modal Assurance Criterion) compare the relations (such as orthogonality) between the eigenmodes found in terms of the scalar product of the eigenvectors. Additional normalisation using the mass or stiffness matrix allows a quantitative assessment.

After model updating on the modal level, including damping ratios determined by experiment, operation vibrations can be calculated for any load function. The

simulation model which was developed step by step can thus be verified under practical conditions.

Content of tutorial

The content of the guideline VDI 3830 is explained in the tutorial along with physics, theory, numerical approaches, and practical applications taken from review articles and archival publications of the tutor and his coworkers focussed on damping topics.

1. L. Gaul: The Influence of Damping on Waves and Vibrations

Mechanical Systems and Signal Processing (1999) 13(1), 1-30

Wave propagations and vibrations are associated with the removal of energy by dissipation or radiation. In mechanical systems damping forces causing dissipation are often small compared to restoring and inertia forces, However, their influence can be great and is discussed in the present survey paper together with the transmission of energy away from the system by radiation. Viscoelastic constitutive equations with integer and fractional time derivatives for the description of stress relaxation and creep of strain as well as for the description of stress-strain damping hysteresis under cyclic oscillations are compared. Semi-analytical solutions of wave propagation and transient vibration problems are obtained by integral transformation and elastic-viscoelastic correspondence principle. The numerical solution of boundary value problems requires discretization methods. Generalized damping descriptions are incorporated in frequency and time domain formulations for the boundary element method and the finite element method.

2. L. Gaul and R. Nitsche: The Role of Friction in Mechanical Joints

Appl Mech Rev vol 54, no 2, March 2001, 93-109

Vibration properties of most assembled mechanical systems depend on frictional damping in joints. The nonlinear transfer behavior of the frictional interfaces often provides the dominant damping mechanism in a built-up structure and plays an important role in the vibratory response of the structure. For improving the performance of systems, many studies have been carried out to predict, measure, and/or enhance the energy dissipation of friction. This article reviews approaches for describing the nonlinear transfer behavior of bolted joint connections. It gives an overview of modeling issues. The models include classical and practical engineering models. Constitutive and phenomenological friction models describing the nonlinear transfer behavior of joints are discussed. The models deal with the inherent nonlinearity of contact forces (e. g. Hertzian contact), and the nonlinear relationship between friction and relative velocity in the friction interface. The research activities in this area are a combination of theoretical, numerical, and experimental investigations. Various solution techniques, commonly applied to friction- damped systems, are presented and discussed. Recent applications are outlined with regard to the use of joints as semi-active damping devices for

vibration control. Several application areas for friction damped systems due to mechanical joints and connections like shells and beams with friction boundaries are presented. This review article includes 134 references.

3. A. Schmidt and L. Gaul: Finite Element Formulation of Viscoelastic Constitutive Equations Using Fractional Time Derivatives

Nonlinear Dynamics 29, 37-55, 2002

Fractional time derivatives are used to deduce a generalization of viscoelastic constitutive equations of differential operator type. These so-called fractional constitutive equations result in improved curve-fitting properties, especially when experimental data from long time intervals or spanning several frequency decades need to be fitted. Compared to integer-order time derivative concepts less parameters are required. In addition, fractional constitutive equations lead to causal behavior and the concept of fractional derivatives can be physically justified providing a foundation of fractional constitutive equations. First, three-dimensional fractional constitutive equations based on the Grünwaldian formulation are derived and their implementation into an elastic FE code is demonstrated. Then, parameter identifications for the fractional 3-parameter model in the time domain as well as in the frequency domain are carried out and compared to integer-order derivative constitutive equations. As a result the improved performance of fractional constitutive equations becomes obvious. Finally, the identified material model is used to perform an FE time stepping analysis of a viscoelastic structure.

4. L. Gaul and M. Schanz: A comparative study of three boundary element approaches to calculate the transient response of viscoelastic solids with unbounded domains

Comput. Methods Appl. Mech. Engrg. 179 (1999), 111-123

As an alternative to domain discretization methods, the boundary element method (BEM) provides a powerful tool for the calculation of dynamic structural response in frequency and time domain. Field equations of motion and boundary conditions are cast into boundary integral equations (BIE), which are discretized only on the boundary. Fundamental solutions are used as weighting functions in the BIE which fulfil the Sommerfeld radiation condition, i.e., the energy radiation into a surrounding medium is modelled correctly. Therefore, infinite and semi-infinite domains can be effectively treated by the method. The soil represents such a semi-infinite domain in soil-structure-interaction problems. The response to vibratory loads superimposed to static pre-loads can often be calculated by linear viscoelastic constitutive equations. Conventional viscoelastic constitutive equations can be generalized by taking fractional order time derivatives into account. In the present paper two time domain BEM approaches including generalized viscoelastic behaviour are compared with the Laplace domain BEM approach and subsequent numerical inverse transformation. One of the presented time domain approaches uses an analytical integration of the elastodynamic BIE in a time step. Viscoelastic constitutive properties are introduced after Laplace transformation by means of an elastic-viscoelastic correspondence principle. The transient response is obtained by inverse transformation in each

time step. The other time domain approach is based on the so-called ‘convolution quadrature method’. In this formulation, the convolution integral in the BIE is numerically approximated by a quadrature formula whose weights are determined by the same Laplace transformed fundamental solutions used in the first method and a linear multistep method. A numerical study of wave propagation problems in 3-d viscoelastic continuum is performed for comparing the three BEM formulations.

5. L. Gaul, H. Albrecht and J. Wirtzner: Semi-active friction damping of large space truss structures

Shock and Vibration 11 (2004), 173-186

The authors dedicate this paper to the memory of Professor Bruno Piombo. We commemorate him as a vital contributor to our science. From the experience of sharing conferences and workshops with Bruno since many years, learning from his expertise and appreciating his advice, the first author mourns the loss of a good friend whose works and words will be kept in our minds and hearts.

The present approach for vibration suppression of flexible structures is based on friction damping in semi-active joints. At optimal locations conventional rigid connections of a large truss structure are replaced by semi-active friction joints. Two different concepts for the control of the normal forces in the friction interfaces are implemented. In the first approach each semi-active joint has its own local feedback controller, whereas the second concept uses a global, clipped-optimal controller. Simulation results of a 10-bay truss structure show the potential of the proposed semi-active concept.

Optimal second order reduction basis selection for nonlinear transient analysis

Paolo Tiso

Abstract Effective Model Order Reduction (MOR) for geometrically nonlinear structural dynamics problems can be achieved by projecting the Finite Element (FE) equations on a basis constituted by a set of vibration modes and associated second order modal derivatives. However, the number of modal derivatives generated by such approach is quadratic with respect to the number of chosen vibration modes, thus quickly making the dimension of the reduction basis large. We show that the selection of the most important second order modes can be based on the convergence of the underlying linear modal truncation approximation. Given a certain time dependency of the load, this method allows to select the most significant modal derivatives set before computing it.

1 Introduction

Several advanced structural systems often exploit nonlinear geometrical effects rather than avoiding them. Large displacements are unavoidable for aeronautics and aerospace structures for which the minimum weight is a key design factor. It is therefore important to consider nonlinearity even in the early design stage by appropriate modeling practice. However, the nonlinear dynamic analysis of large finite element (FE) models is an onerous task, and effective Model Order Reduction (MOR) techniques are widely welcomed.

The vibration mode superposition has become a standard practice for linear dynamics problems. However, its straightforward extension to geometrical nonlinear dynamic analysis poses some problems. In principle, to reduce the number of degrees of freedom, several vibration modes can be extracted at certain dynamic equilibrium states and used to project the dynamic set of equations on. This approach

Paolo Tiso

Delft University of Technology, Mekelweg 2, 2628CD, Delft, The Netherlands, e-mail: p.tiso@tudelft.nl

bears the drawback of recomputing the modal basis too frequently to preserve accuracy, and the effectiveness of the method is often lost [6].

A major issue in nonlinear structural applications is the bending-stretching coupling arising from the finite out-of-plane displacements a slender or thin-walled structure exhibits during operation. Typically, low frequency vibration modes are bending dominated and they do not contain the proper membrane displacement contribution that is necessary to accurately represent the effect of the nonlinearity. Various workarounds have been proposed. A selection of modes, dual or companion modes, has been proposed, relying on membrane static displacements induced by specified transverse displacements directly related to the bending modes used. These modes, representing the membrane behavior resulting from bending are considered in the implicit condensation strategy (using companion modes) presented by [3] and the full modeling approach using dual modes introduced by [7]. Both methods use bending modes in the basis. The implicit condensation method uses only bending modes in the basis and extracts membrane modes through an assumed quadratic functional form, while the full modeling method using dual modes adds modes to the basis that directly describe the membrane response. A different procedure using dynamic analysis to calculate companion modes is proposed by [8]. They found that very good results are obtained using a basis formed by a combination of bending vibration modes and membrane vibration modes. Forming the optimal basis could require the extraction of many modes, and also the selection of the most significant ones is an issue. Moreover, for more complicated structures, a categorization in bending modes and membrane modes might not be possible.

Past contributions [4, 5] have outlined the potential of including higher order modes to enrich the modal basis and avoid expensive recomputing of the modal basis during the time integration. Essentially, the modal derivatives are calculated by differentiating the eigenvalue problem or alternatively by using finite differences [10]. An interesting application of modal derivatives can be found in the computer-graphics world, [1] although the attention is more focused on a realistic representation of the deformation rather than on the actual accuracy of the reduced solution. Methods based on higher order modes are a natural extension of linear modal superposition analysis. Once a good modal basis has been formed for the underlying linear system, the corresponding second order modes are directly generated from this basis and provide the displacement contributions that are essential to represent the effects of the nonlinearity.

The number of modal derivatives is quadratic with respect to the size of the size of the generating set of vibration modes. However, not all the modal derivatives are relevant to the accuracy of the reduced response. We present in this contribution a simple and effective selection criterion that allows to choose the most significant modal derivatives before computing the actual shapes. The criterion is based on the convergence of the modal truncation of the underlying linearized problem.

2 Reduced equations of motion

We consider here the discretized N FE nonlinear dynamic equations of motion of a general tridimensional structure. For this study, we do not consider damping and we assume that the external force term can be expressed as a constant shape scaled by a time dependent function. The governing FE system of equations, together with the boundary conditions, writes:

$$\begin{cases} \mathbf{M}\ddot{\mathbf{u}} + \mathbf{g}(\mathbf{u}) = \mathbf{f}\varphi(t) \\ \mathbf{u}(0) = \mathbf{u}_0 \\ \dot{\mathbf{u}}(0) = \dot{\mathbf{u}}_0 \end{cases} \quad (1)$$

where \mathbf{u} is the generalized displacement vector, \mathbf{M} is the mass matrix, $\mathbf{g}(\mathbf{u})$ is the nonlinear force vector and \mathbf{f} is the applied load shape multiplied by the time function $\varphi(t)$. The initial conditions for the displacement and the velocity vector are indicated with \mathbf{u}_0 and $\dot{\mathbf{u}}_0$, respectively. We further assume that the nonlinearity of $\mathbf{g}(\mathbf{u})$ is caused by geometrical effects only, i.e. when the displacements are so large that a linear kinematic model does not hold. This is typically the case of thin-walled structures, which can undergo large displacements while staying in the elastic range of the material.

In practical applications, the system of N equations 1 is usually large. The number of unknowns can be reduced to M , with $M \ll N$, by projecting the displacement field \mathbf{u} on a suitable basis Ψ of time-independent vectors, as:

$$\mathbf{u} = \Psi \mathbf{q} \quad (2)$$

where $\mathbf{q}(t)$ is the $M \times 1$ vector of modal amplitudes. The governing equations can then be projected on the chosen basis Ψ in order to make the residual orthogonal to the subspace in which the solution \mathbf{q} is sought. This results in a reduced system of M non-linear equations:

$$\Psi^T \mathbf{M} \Psi \ddot{\mathbf{q}}(t) + \Psi^T \mathbf{g}(\Psi \mathbf{q}) = \Psi^T \mathbf{f} \varphi(t) \quad (3)$$

or, equivalently,

$$\hat{\mathbf{M}} \ddot{\mathbf{q}}(t) + \hat{\mathbf{g}}(\Psi \mathbf{q}) = \hat{\mathbf{f}} \varphi(t) \quad (4)$$

We refer to the numerical solution of the full model as the *full* solution, while the solution of the reduced model will be called *reduced* solution. The key of a good reduction method is to find a suitable basis Ψ that is able to reproduce the full solution with a good, hopefully controlled, accuracy.

3 Reduction basis

We discuss in this section how to form the reduction basis Ψ . We propose a basis of vibration modes calculated around a given equilibrium position \mathbf{u}_{eq} enriched by the so-called modal derivatives (MD). The two contributions will be separately discussed.

3.1 Vibration modes

Let us consider a static equilibrium position \mathbf{u}_{eq} when the applied load is constant and given by $\mathbf{f}\varphi_{eq}$. We can then linearize the system of equations 1 around such configuration assuming that the motion $\tilde{\mathbf{u}}$ around \mathbf{u}_{eq} is small, i.e. $\mathbf{u} = \mathbf{u}_{eq} + \tilde{\mathbf{u}}$, $\ddot{\mathbf{u}} = \ddot{\tilde{\mathbf{u}}}$. The linearized dynamic equilibrium equations become:

$$\mathbf{M}\ddot{\tilde{\mathbf{u}}} + \mathbf{K}_{eq}\tilde{\mathbf{u}} = \mathbf{f}\tilde{\varphi}(t) \quad (5)$$

where $\tilde{\varphi}(t)$ is a small load variation from φ_{eq} . The tangent stiffness matrix \mathbf{K}_{eq} is defined as:

$$\mathbf{K}_{eq} = \left. \frac{\partial \mathbf{g}}{\partial \mathbf{u}} \right|_{\mathbf{u}=\mathbf{u}_{eq}} \quad (6)$$

the associated eigenvalue problem to equation 5 writes:

$$(\mathbf{K}_{eq} - \omega_i^2 \mathbf{M}) \Phi_i = \mathbf{0}, \quad i = 1, 2, \dots, N \quad (7)$$

and its solution provides N vibration modes (VMs) Φ_i and associated vibration frequencies ω_i^2 .

3.2 Modal derivatives

The projection of the governing equations on a reduction basis formed by a reduced set of VMs is a well-known technique for linear structural dynamics. The main advantage of this technique is that the resulting reduced model consists of a system of uncoupled equations that can therefore be solved separately. As discussed in the introduction, several attempts have been made to extend the vibration modes projection for nonlinear analysis. The main limitation of such approach lies in the fact that the vibration basis changes as the configuration of the system changes. It is therefore required to upgrade the basis during the numerical time integration to account for the effect of the nonlinearity.

For thin-walled structural applications as the one considered in this contribution, the system is usually characterized by significant nonlinear bending-stretching cou-

pling effects that are usually not captured by a reduction basis formed by linear vibration modes only.

Since the VMs change with respect to the configuration, a natural way of accounting for the main effect of nonlinearity is to compute their derivatives with respect to the configuration around the reference state $(\mathbf{u}_{eq}, \varphi_{eq})$ at which the modes are calculated. The direction for the derivatives are provided by the VMs chosen for the linear analysis. We want to compute the modal derivatives (MDs) Φ_{ij} :

$$\Phi_{ij} = \frac{\partial \Phi_i}{\partial q_j} \quad (8)$$

where q_j is the amplitude associated to Φ_j . In other words, we would like to know how a certain mode Φ_i changes if the structure is displaced according to the shape described by mode Φ_j .

A way to proceed is to differentiate the eigenvalue problem 7 with respect to the modal amplitudes.

$$[\mathbf{K}_{eq} - \omega_i^2 \mathbf{M}] \frac{\partial \Phi_i}{\partial q_j} + \left[\frac{\partial \mathbf{K}_{eq}}{\partial q_j} - \frac{\partial \omega_i^2}{\partial q_j} \mathbf{M} \right] \Phi_i = \mathbf{0} \quad (9)$$

It has been shown by [10] and [5] that the terms associated to the mass can be neglected. The derivative $\frac{\partial \omega_i^2}{\partial q_j}$ is zero since the frequency variation should not be an odd function of the modal amplitude. The term $\omega_i^2 \mathbf{M} \frac{\partial \Phi_i}{\partial q_j}$ is related to the inertial forces associated to the second order mode Φ_{ij} . Since these terms are typically featuring in-plane deformations (at least for thin-walled structures), their contribution is negligible. Numerical experiments have shown that the neglecting of mass related terms does not change the results appreciatively. By doing so, the problem 9 becomes:

$$\mathbf{K}_{eq} \frac{\partial \Phi_i}{\partial q_j} = - \frac{\partial \mathbf{K}_{eq}}{\partial q_j} \Phi_i \quad (10)$$

The right-hand side pseudo-force can be calculated at element level and then assembled. It can be shown that the modal derivatives are symmetric, i.e. $\Phi_{ij} = \Phi_{ji}$. Therefore, given M vibration modes, $R = M(M+1)/2$ MD can be calculated. Note that the matrix of coefficients can be factorized once for all and only the right-hand sides need to be computed. This can be done at element level and subsequently assembled, see for details [11].

3.3 Projection basis

Once a set of M VMs Φ_i are calculated by solving the eigenvalue problem 7, the MDs Φ_{ij} can be generated by solving the linear problems 10. A reduction basis including both VMs and MDs can be formed, as:

$$\Psi = [\Phi_i \Phi_{ij}] , i, j = 1, \dots, M, \Phi_{ij} = \Phi_{ji} \quad (11)$$

This complete reduction basis provides a very accurate reduced model, as shown in the numerical example. However, the number of MDs that can be generated from a subset of M VMs is quadratic with respect to M . For complex problems when a rather large VMs basis is required, the number of MDs quickly becomes large. We would like to find a simple selection criterion that allows to form the best reduced MDs set for a given problem. Specifically, we would like to answer the following questions:

1. Given a certain time dependent load, is it possible to find the best P MDs, where $P < R$?
2. Can the selection be based on the convergence of the underlying linear dynamics problem, i.e. the convergence of the modal truncation based on the chosen M VMs?
3. Can the most significant MDs be selected before computing them?
4. Given a reduction basis, can an error bound be devised?

We show in this contribution that the first three questions can be answered. The selection criterion is discussed in the following section.

4 Selection criterion

Suppose we extracted a set of VMs $\Phi_i, i = 1, 2, \dots, M$ with $M \ll N$, together with the associated frequencies ω_i . The approximation of the response $\mathbf{u}(t)$ of the linear system 5 is given by [2]:

$$\mathbf{u}(t) = \sum_{i=1}^M \frac{\Phi_i \Phi_i^T \mathbf{f}}{\mu_i} \int_0^t \frac{\sin(t-\tau)}{\omega_i} \varphi(\tau) d\tau = \sum_{i=1}^k \alpha_i \theta_i(t) \quad (12)$$

where $\mu_i = \Phi_i^T \mathbf{M} \Phi_i$ is the modal mass associated to the i^{th} VM. We dropped the \sim for clarity. The convergence of the modal truncation approximation thus depend on two distinct contributions, namely a *quasi-static* contribution and a *spectral* contribution. The first, associated to the spatial factors α_i :

$$\alpha_i = \frac{\Phi_i \Phi_i^T \mathbf{f}}{\mu_i} \quad (13)$$

implies that the load shape \mathbf{f} has to be nearly orthogonal to the $N - M$ modes left out of the approximation. The spectral type is determined by the convergence to zero of the convolution products 12 when progressing in the eigenspectrum of the system. The temporal factors $\theta_i(t)$ depend in general on the frequency content of the system and of the applied load. Let us consider here two relevant cases:

- for a step load $\varphi(t) = 1$ for $t \geq 0$:

$$\theta_i(t) = \frac{1 - \cos(\omega_i t)}{\omega_i^2} \quad (14)$$

- for a harmonic load $\varphi(t) = \cos(\Omega t)$:

$$\theta_i(t) = \frac{\omega_i \sin(\Omega t) - \Omega \sin(\omega_i t)}{\omega_i(\omega_i^2 - \Omega^2)} \quad (15)$$

We can now assume that the M VMs selected for a good accuracy for the linear problem 5 will interact when the nonlinearity is considered. However, if the nonlinearity is mild, they will still roughly contribute to the solution as indicated by 12. We can then further assume that the contribution of the MDs is of second order, and their mutual relevance could be indicated by:

- : for step load:

$$b_{step}^{ij} = \frac{|\alpha_i| |\alpha_j|}{\omega_i^2 \omega_j^2} \quad (16)$$

- for harmonic load:

$$b_{harm}^{ij} = |\alpha_i| |\alpha_j| \beta_i \beta_j \quad (17)$$

where the generic term $\beta_k(\Omega)$ is:

$$\beta_k(\Omega) = \left| \frac{1}{(\omega_k^2 - \Omega^2)} \right| + \left| \frac{\Omega}{\omega_k(\omega_k^2 - \Omega^2)} \right|$$

The factors b_{step}^{ij} and $b_{harm}^{ij}(\Omega)$ indicate the relative amplitude of the MD mode Φ_{ij} given the contribution of Φ_i and Φ_j to the linear solution. Note that $b_{harm}^{ij}(0) = b_{step}$. The selection of the best MDs subset can be based on the magnitude of the b_{ij} coefficients: the most relevant MD will be the ones with the highest values of the corresponding b_{ij} coefficients. This simple criterion is heavily based on the convergence properties of the linear reduced problem. This implicitly assumes that the nonlinearity effect is, in a mathematical sense, a second order effect. How far this concept can be stretched is a problem-dependent issue. Moreover, the actual interaction between the modes is not investigated: we are simply assuming that two VMs that bear a relevant part of the reduced solution are likely to interact a lot. The big advantage of this method lies in the fact that the most important contributions can be estimated prior the actual calculation of the MDs. In the following section we show the potential of this method by mean of a numerical example.

5 Numerical Example

We consider here a short cantilever plate modeled with triangular shell elements. The geometrical nonlinearity is due to the von-Karman kinematic model adopted [11]. The full model consists of 546 degrees of freedom. The load is applied at one corner of the free edge in order to induce both bending and twisting modes in the response. The geometric and material properties are reported in Figure 1 together with the tip displacement component when the load is applied statically. The markedly nonlinear behavior is evident. The nonlinear static FE equations are solved with the normal flow algorithm as proposed by [9].

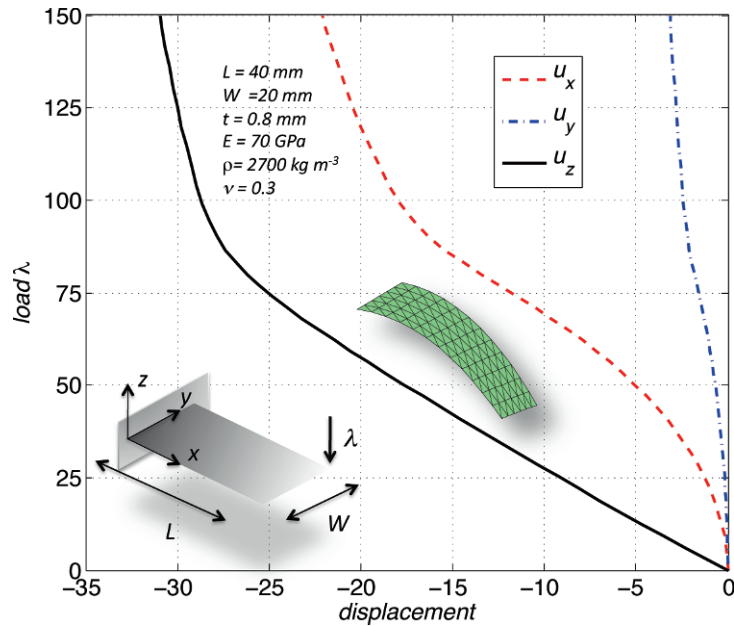


Fig. 1 Static nonlinear response of the short cantilever. The three components of the displacement at the point where the load is applied are shown. The load is applied in the vertical direction throughout the entire analysis. The stiffening is due to the axial stretching caused by the bending deflection.

We first consider the case of a dynamic step load of a magnitude of 30 N. For all the reduced analysis, a basis formed with the first 10 VMs is considered. The VMs are calculated around the initial undeformed configuration, i.e. $\mathbf{u}_{eq} = \mathbf{0}$. This generates $R = 55$ second order MDs Φ_{ij} . To better illustrate the concept of MDs, the first three VMs and the corresponding MDs are shown in 5. The results of the selection criterion for the step load are shown in the bar plot on Figure 3. The b_{step} value has been raised to 0.25 power in order to better show the smaller contributions on the

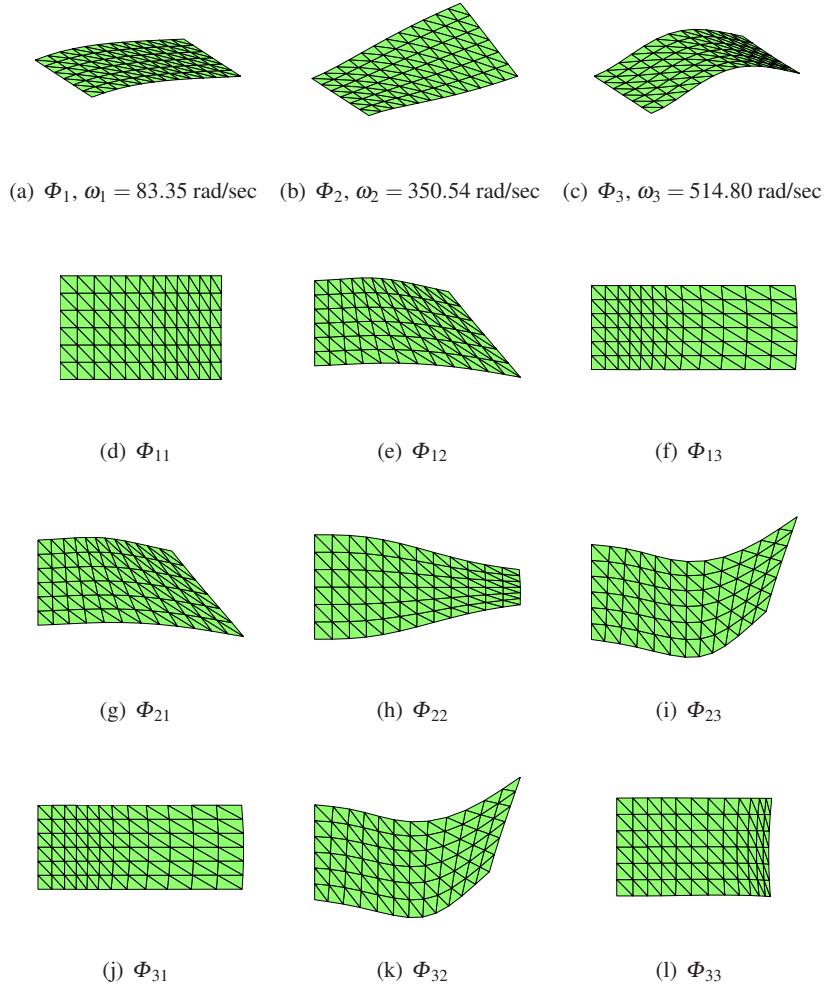


Fig. 2 The first three vibration modes (VMs) and the corresponding modal derivatives (MDs). The VMs are out-of-plane modes, featuring bending and torsion. For this specific application, the MDs are in-plane only, and they are represented top-view to better show the non-uniform in-plane deformation.

bar plot. Rather intuitively, the MD Φ_{11} is the more important. The cross terms relating the first two VMs to all the other VMs are comparable to the diagonal entries, indicating the importance of the interaction between the retained VMs. Mode 6 does not give any contribution since it consists of a bending motion in the plane of the plate.

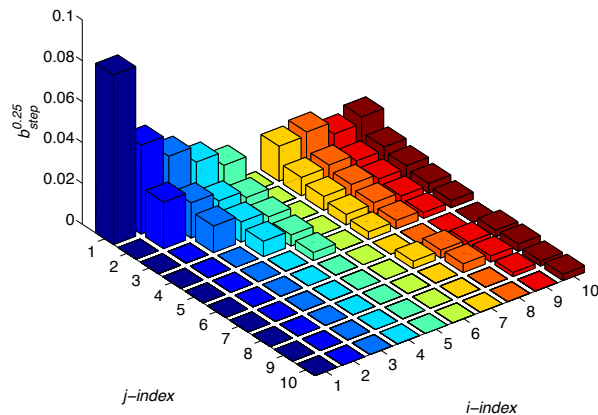


Fig. 3 Values of b_{step} relative to the first $M = 10$ vibration modes. The emphasis is put on the first mode and its interaction with all the other modes. The values for b_{step} are raised to 0.25 power to better highlight the relative contribution of all the terms. Mode 6 does not participate since it features in-plane lateral bending. (The lower diagonal part of the symmetric b_{ij} is set to zero for display purposes)

The nonlinear FE dynamic equations are solved with the Implicit Newmark time integration scheme. The results for the dynamic analysis are shown in [Figure 4](#) for the vertical component of the displacement at the loaded point. The nonlinear reduced model with a basis formed by the first 10 vibration modes and all the possible second order MDs ($M = 10, R = 55$) yields a very good approximation of the full nonlinear response. Also, a reduced analysis with the basis formed by VMs only ($M = 10$) is shown (case (c)). The result is overly stiff and clearly wrong, and apparently much worse than the linear analysis. This might be deceiving, since only the vertical displacement is monitored here. In fact, unlike the nonlinear model, the linear analysis will not reproduce any axial contribution. A stiffening axial force is generated by the bending-only vibration modes through the nonlinear bending-stretching coupling. Since no axially dominated second order modes are included in the basis, there is no way to alleviate the resulting membrane tension. The outcome is the shown overly stiff response. Several reduced responses generated by randomly choosing a set of $P = 20$ second order MDs to enrich the $M = 10$ VMs basis are also plotted. None of these responses provide the same accuracy as the one resulting from the proposed selection criterion.

Similar results are shown for the case of harmonic load, see [Figure 6](#). The frequency of the applied load Ω is set as 450 rad/sec, an intermediate value between the first and the second eigenfrequency of the system. The outcome of the selection criterion b_{harm} as per equation 17 is shown in [Figure 5](#), while the load amplitude is 60 N. In this case, the criterion places more emphasis on the second and the third VM and their interaction. Also the interaction of the first VMs with all the other modes is rather important. The slight discrepancy between the full nonlinear

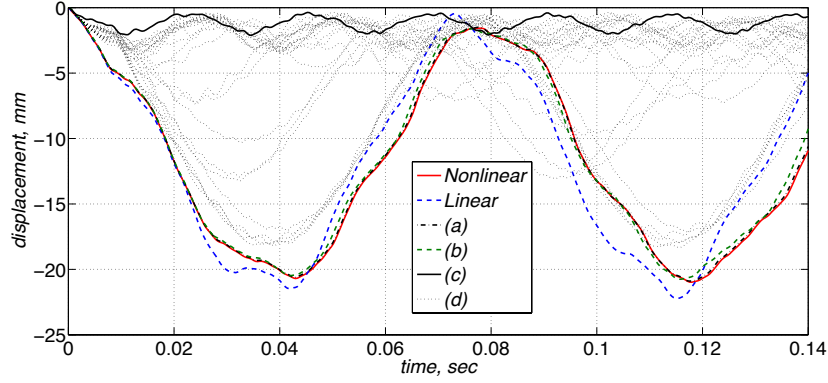


Fig. 4 Dynamic response at the loaded tip for a step load of magnitude $\phi(t) = 30$ N. The u_z component is shown. (a) : basis formed with all the possible second order modes $M = 10$, $R = 55$; (b) : basis formed with the best 20 second order fields, $M = 10$, $P = 20$; (c) : basis formed with vibration modes only, $M = 10$, $P = 0$; (d) : basis formed with several random choices of $P = 20$ second order modes.

response and the complete reduced basis ($M = 10$ and $R = 55$) might be due to a too reduced underlying basis of VMs. The response of the reduced system with the proposed selection is rather close to the full response and much more accurate than the responses generated with a random choice of the second order fields. The reason for the overly stiff response of the nonlinear reduced system when using vibration modes only is the same as explained for the case of step load.

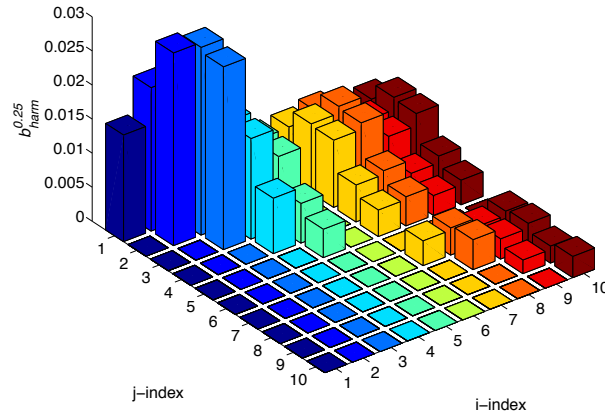


Fig. 5 Values of b_{harm} relative to the first $M = 10$ vibration modes and a forcing frequency Ω of 450 rad/sec. The emphasis is in this case on the second and the third mode, and their interaction with all the other modes. (The lower diagonal part of the symmetric b_{ij} is set to zero for display purposes)

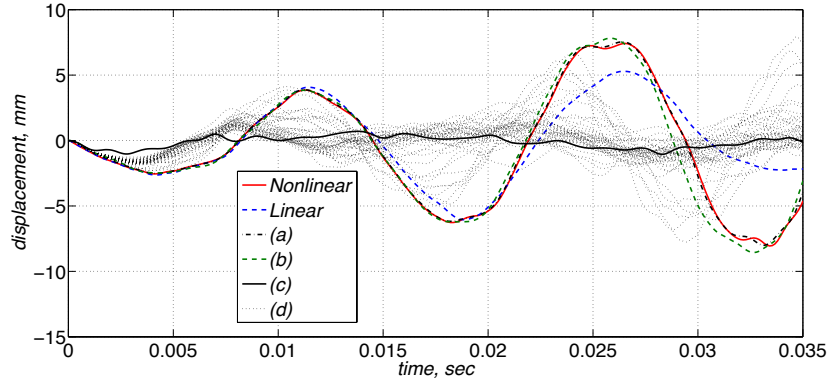


Fig. 6 Dynamic response at the loaded tip for a harmonic load $\varphi(t) = 60\cos(450t)$ N. The u_z component is shown. (a) : basis formed with all the possible second order modes $M = 10, R = 55$; (b) : basis formed with the best 20 second order fields, $M = 10, P = 20$; (c) : basis formed with vibration modes only, $M = 10, P = 0$; (d) : basis formed with several random choices of $P = 20$ second order modes.

6 Conclusions and Discussion

We presented a simple and effective criterion to select the most significant second order modal derivatives for the MOR of geometrically nonlinear structural analysis. The criterion is based on the convergence of the vibration modes truncation for the underlying linearized dynamic problem. Given a certain first order modal basis which is converged in a linear sense, the selection criterion looks at the spatial and spectral properties of the eigenspectrum and the applied load. In this way, the most relevant second order modes can be selected before their actual calculation. Numerical results confirmed the effectiveness of the proposed approach.

The power of this simple yet effective method lies on the fact that the second order modes enrichment can be seen as higher order expansion of the solution. Therefore, the convergence properties of the base linearized problem should naturally provide a guideline also for the higher order expansion.

Yet, the number of second (most significant) order modes required for a given accuracy is in general not known. Future work will focus on the derivation of an error bound as function of the selected second order modes as well as the spectral properties of the linearized system.

References

1. Jernej Barbič and Doug L. James. Real-time subspace integration for st. venant-kirchhoff deformable models. *ACM Trans. Graph.*, 24(3):982–990, 2005.
2. M. Gradin and D.J. Rixen. *Mechanical vibrations. Theory and Application to Structural Dynamics*. Wiley, 1997.
3. Joseph J. Hollkamp, Robert W. Gordon, and S. Michael Spottswood. Nonlinear modal models for sonic fatigue response prediction: a comparison of methods. *Journal of Sound and Vibration*, 284(3-5):1145 – 1163, 2005.
4. S. R. Idelsohn and A. Cardona. A load-dependent basis for reduced nonlinear structural dynamics. *Computer & Structures*, 20:203–210, 1985.
5. S. R. Idelsohn and A. Cardona. A reduction method for nonlinear structural dynamic analysis. *Computer Methods in Applied Mechanics and Engineering*, 49:253–279, 1985.
6. B. P. Jacob and N. F. F. Ebecken. Adaptive reduced integration method for nonlinear structural dynamic analysis. *Computers Structures*, 45(2):333 – 347, 1992.
7. M. Mignolet, A. Radu, and X. Gao. Validation of reduced order modeling for the prediction of the response and fatigue life of panels subjected to thermo-acoustic effects. In *Proceedings of the 8th International Conference on Recent Advances in Structural Dynamics, Southampton, United Kingdom*, 2003.
8. Adam Przekop and Stephen A. Rizzi. A reduced order method for predicting high cycle fatigue of nonlinear structures. *Computers & Structures*, 84(24-25):1606 – 1618, 2006. Non-linear Dynamics of Structures and Mechanical Systems.
9. S.A. Ragon, Z. Gürdal, and L.T. Watson. A comparison of three algorithms for tracing nonlinear equilibrium paths of structural systems. *International Journal of Solids Structures*, 139:689–698, 2002.
10. P. M. A. Slaats, J. de Jong, and A. A. H. J. Sauren. Model reduction tools for nonlinear structural dynamics. *Computer & Structures*, 54:1155–1171, 1995.
11. P. Tiso, E. Jansen, and M.M.Abdalla. A reduction method for finite element nonlinear dynamic analysis of shells. In *47th AIAA/ASME/ASCE/AHS/ASC Structures, Structural Dynamics, and Materials Conference*, 2006.

Operating Vibration Measurements of Test Fuel Assembly in Reactor Thermo-hydraulic Test Condition

Kang-Hee Lee, Chang-Hwan Shin, Heung-Seok Kang, Dong-Seok Oh, Nam-Kyu Park*

Korea Atomic Energy Research Institute, Innovative Nuclear Fuel Division

* KEPCO Nuclear Fuel, Nuclear Fuel Design Group

1045 Daedeok-daero, Yuseong-gu, Daejeon, Korea(Ref. of), 305-353

leekh@kaeri.re.kr

ABSTRACT

The design verification of a newly-developed nuclear fuel assembly requires a long-term endurance test under thermo-hydraulic test condition simulating power reactor core. For this verification test, vibration of the test fuel assembly inside the simulated test core should be measured under high system temperature (over 200 °C), high system pressure (over 2.5 MPa) and fast moving coolant flow (over 5 m/s). To measure the vibration, we use specially fabricated accelerometers, various sealing techniques and conduit channel design for signal cable protection. The effects of the flow rate, coolant temperature, pre-sized support clearance on the test fuel vibration response and orbit motion were discussed. The measured data is used for fuel compatibility evaluation and a basis for endurance verification, as well as the validation tool for theoretical response prediction model.

1. Introduction

Nuclear fuel assembly is a mechanical cluster of fuel rods grouped by the series of intermediate spacer grids. Fig. 1 shows a nuclear power plant with a reactor cross-cut and a typical fuel assembly. Fuel assembly absorbs the energy from the axial upward coolant flow in the power reactor core and vibrates with relatively small amplitude. Even small vibration can lead to fatal mechanical damage on the fuel cladding tube at the support point [1]. Not only does the flow-induced vibration of a fuel assembly engaged in complex fluid-structure interaction and inter-rod physical coupling through medium, the vibration responses can become more complex due to the change of support condition and the flow disturbances by intermediate spacer grids with flow mixer. Although the averaged response can be estimated with the aid of stochastic finite element analysis method combined with experimental measurement for hydrodynamic forces, results of theoretical prediction which is limited to the simple problem have large scatter [2]. Thus, experimental validation for theoretical model is essential and functional verification tests are required for each fuel assembly design.

The design verification of a newly-developed nuclear fuel assembly requires a long-term endurance test under thermo-hydraulic test condition simulating power reactor core using a real scale fuel test model. Design compatibility to the neighboring fuel assembly and wear resistance capability of cladding tube can be assured by measuring a vibration response in transient test flow condition and an accumulated wear of the test rods in long-term steady-state test flow condition [3]. For this verification test, vibration of the test fuel assembly in the simulated test core has to be measured under high system temperature (over 200 °C), high system pressure (over 2.5 MPa) and fast moving coolant flow (over 5 m/s). The proper selection of the sensors based on the measurement requirements, gauge installation, signal cable protection had a key role in a successful data measurement for final test purposes.

The paper deals with the flow-induced vibration measurement of test fuel assemblies in the power reactor

simulating test condition and discuss spectral response characteristics and orbit motion of the interconnected test rod in an assembly according to the test flow rate, the amount of pre-sized support clearance of the grid support and coolant temperature.

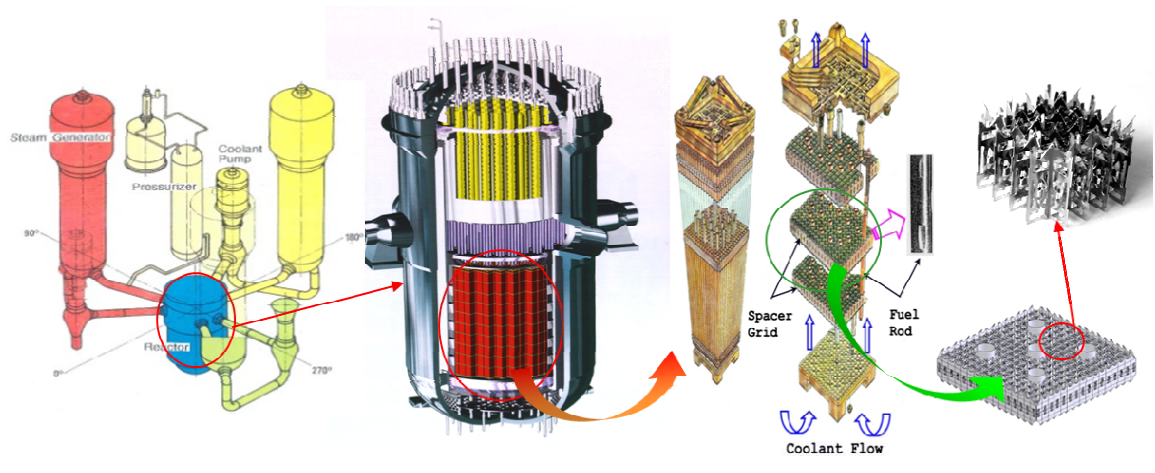


Fig. 1 Nuclear power plant, reactor vessel cross-cut, and nuclear fuel assembly

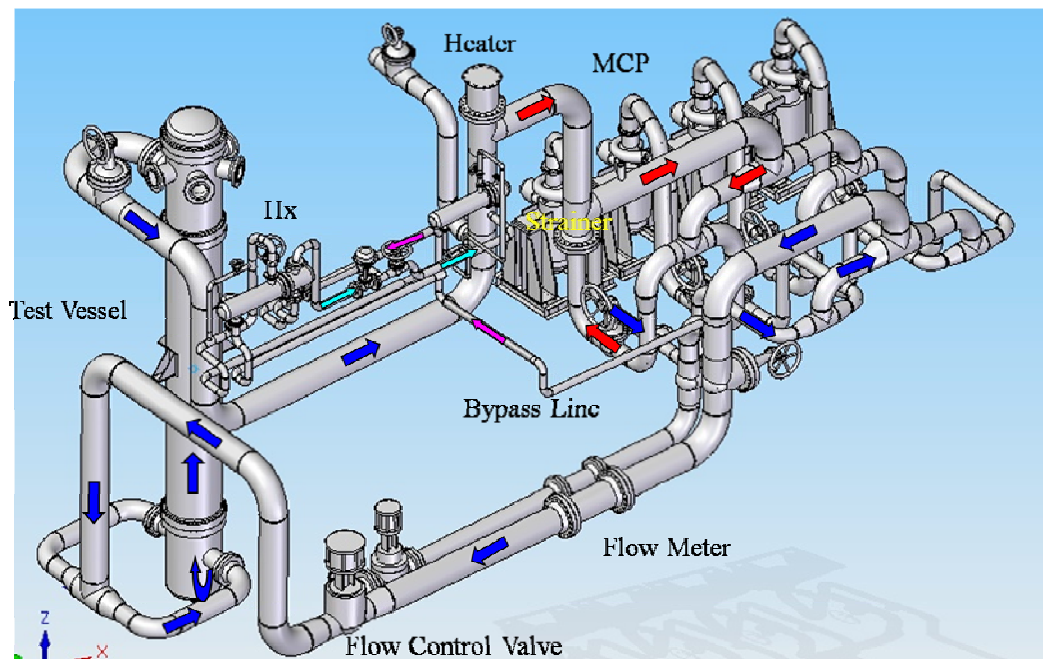


Fig. 2 Hydraulic test facility (PLUTO); Hx: Heat Exchanger, MCP: Main Coolant Pump

2. Test and measurement overview

The hydraulic test facility consists of a test housing, pressure vessel, pumps, heat exchanger, loop heater and expansion tank. Working fluid is de-ionized water with a typical chemistry and purity requirements. Fig. 2 shows a schematic diagram of the test facility. Four centrifugal pumps circulate the working fluid with vertical upward flow while passing through the flow housing. The flow rate is controlled by variable frequency pump drives. The heat sources of working fluid are the pump blade's frictional work and complementary loop heater. The maximum operating temperature and pressure are 210 °C and 3 MPa, respectively. The maximum system flow rate is about 1400 m³/hr. All components within pressure boundary were designed in accordance with Section VIII of the ASME Boiler and Pressure Vessel Code and ANSI/ASME Standard B31.1 for power piping. The flow housing is mounted inside the test vessel. Two neighboring test fuel assemblies can be placed inside the flow housing.

Test fuel assembly consisted of the most non-instrumented dummy rods and some instrumented rods embedded with special accelerometer to measure lateral vibration. Instrument rod has a small cylindrical shape, high temperature biaxial accelerometer with built-in metal cables. Fig. 3 represents the photo of biaxial accelerometer insertion, a schematic drawing of the instrument rod and vibration sensor installation. Pre-clearance (deformation) from 0.025 mm to 0.25 mm at the rod-support points can simulate the fuel's and grid's degradation from corrosion, irradiation deformation, and thermal relaxation in the power reactor core. The measurement locations of the two test assemblies were selected as 8 points along assembly length and across the cross-sectional loading pattern based on the reference data to be compared.

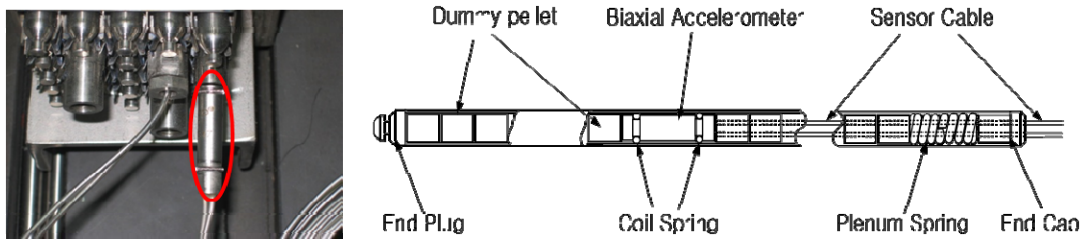


Fig. 3 Instrument rod embedded with accelerometer

Initial preparation to protect signal cable and to reduce cable movement noise by clamping cables to the bar frame inside the vessel was failed. Excessive vibration and large strain leads to fatigue-induced and wear-induced failure of the signal cable as shown in Figure 4 (the lower left). Final remedy for this problem was to divide flow channel into two separate regions (flow channel and conduit channel) so that the signal cable inside shield pipe was located at the inner face of the vessel and do not to meet the main coolant flow. Fig. 4 shows the broken signal cable, the initial and final measures to protect signal cables.

The test will be performed to obtain fuel rod vibration characteristics. The loop setup and operation temperature will remain the same for both the transient vibration test and the long-term wear test. The loop was operated at a coolant temperature of 193 °C. The loop pressure should be maintained at a value to avoid vaporization. Before the test begins, the working fluid should be heated up to test temperature for 12 hours.

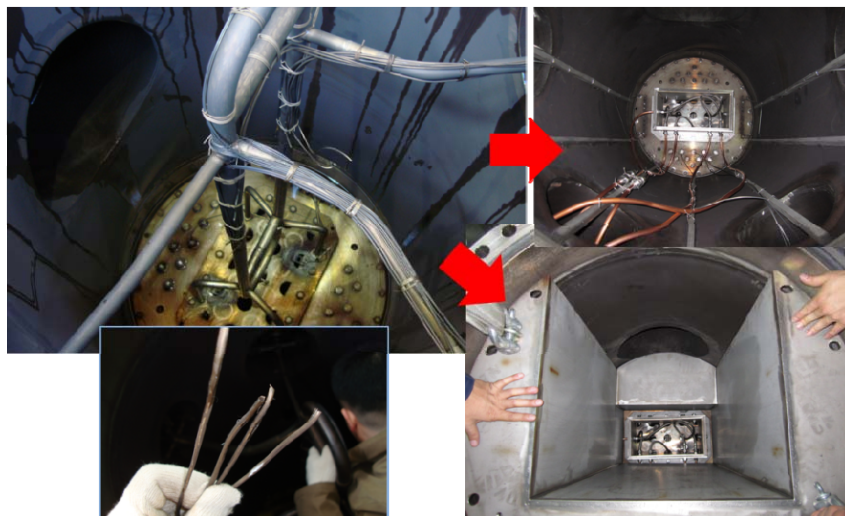


Fig. 4 Initial and final measures for signal cable protection

3. Results and Discussion

Figure 5 shows typical frequency response spectrums of a test rod during the upward flow sweep at hot test condition. As the system flow rate increases, the average power level is gradually growing due to the increase of

flow (turbulence) excitation energy and the frequency bandwidth of dominant response components become slowly wider. Frequency separation among dominant response component groups in the low flow rate becomes weaker with the increase of flow; this can be interpreted that the test assembly's and rod's damping increase with the flow rate. While detail damping mechanisms and their respective contribution to the response cannot be identified from the test results, it can be said that viscous damping between rod and fluid, squeeze film damping in the clearance at the support and frictional damping at the rod-support determine the fuel rod damping[4, 5]. Periodic response components corresponding to motor-induced frequency and pump blade passing frequency appeared with relatively small amplitude.

Dominant power components in the measured response spectrum can be classified into two distinguished groups; components with sharp spike and components with distributed side band. Generally, the flow periodics from far and near field excitation sources such as motor rotation, pump blade passing frequency, and their harmonics generates clear response peaks, of which frequency varied with flow rate, in the response spectrum. It can be said that distributed response comes from fluid coupling and dissipation of the fluid-coupled-system damping. Interesting things was that the dominant power components in the response spectrum were concentrated on the frequency ranges associated with test assembly's and test rod's modal frequencies. Test fuel assemblies act as band pass filter and vibrate near or at their own natural frequencies. This implies that the pressure fluctuation, which was known as a primary excitation mechanism of the axial flow-induced vibration, in the turbulent boundary layer of the flow channel has relatively uniform excitation power distribution over the frequency range of interest.

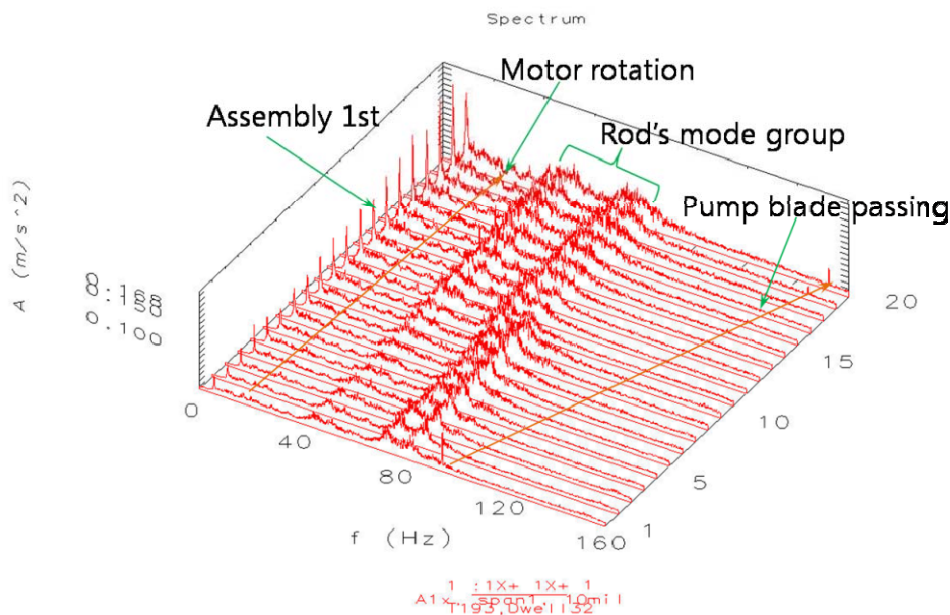


Fig. 5 Typical sweep vibration response of a test rod according to the flow rate

Figure 6 represents the normalized vibration displacement of various instrument rods measured at different locations according to the flow rate. Normalized displacement was calculated from measured acceleration by double integration of optional sampling filter. The vibration of the test rod gradually increases with the flow rate and has a location-dependent nature. Averaged time domain responses measured at mid region show relatively higher amplitude. Variation of coolant temperature did not make noticeable differences in the measured response for the same measurement target while the fluid viscosity experiences considerable changes (decrease) according to the coolant temperature.

Pre-sized support clearance applied to all mid-grids spring support along the target instrument rod had the frequency of the dominant power components moved to the lower frequency region in the response spectrum. This is because of the reduction of fuel rod's modal frequency due to the decrease of support stiffness from the support gap. Figure 7 shows the time-domain orbit locus (for 120 seconds) of test rods according to the different

pre-sized support gap at the same operational flow condition. Orbit displacement was transformed from measured acceleration by double integration of optional sampling filter. They gave motion traces and range of the test rod vibration. The accumulated orbit shape was close to elliptic, but the orbit shape changed with the amount of pre-sized support gap and measurement locations of the test rod.

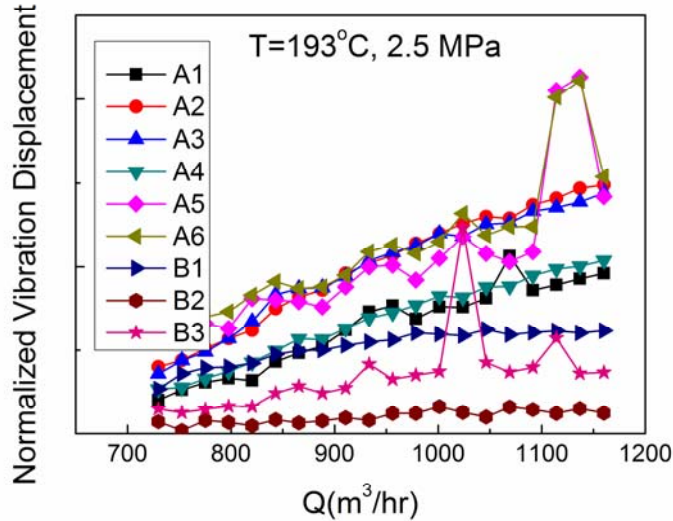


Fig. 6 Vibration amplitude of instrument rod in the test assembly

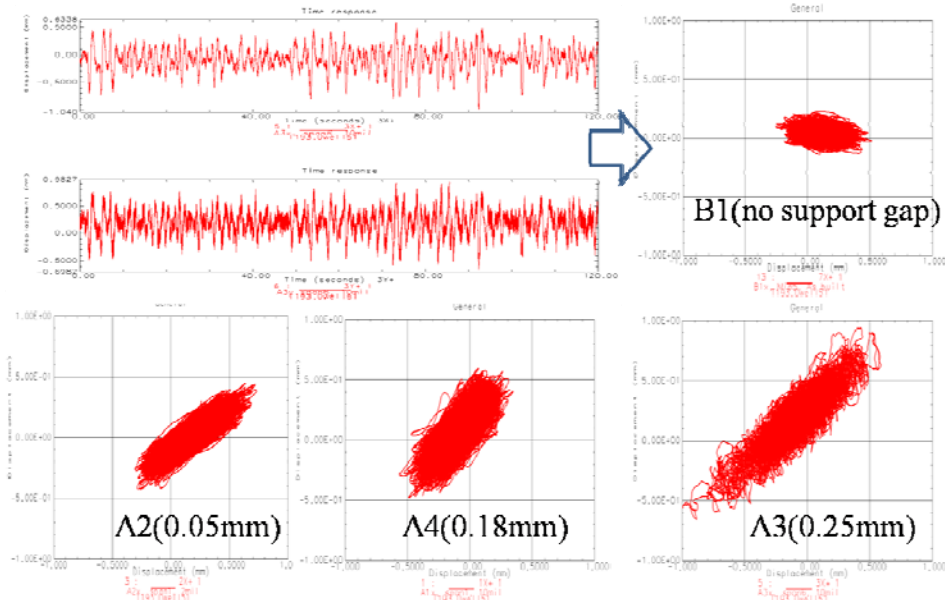


Fig. 7 Vibration orbit of the test rod according to the pre-sized support clearance

The reason for an elliptic pattern of the orbital motion must be due to the 1st mode cross sectional modal pattern of the test bundle assembly and pre-sized support gap. Most figures leaned toward a certain direction except the zero clearance. It can be seen that the orbital motion of the test rod in the assembly will take an orientation according to the position of active grid support or pre-sized inactive support with clearance and its support direction. If the orbital trace of the fuel rod has a dependency on a specific direction, it might increase the possibility of a fuel fretting at a location with a larger sliding distance according to the support configuration and the neighboring flow condition.

4. Conclusion

As a design verification test, vibration of the test fuel assembly inside the simulated test core was measured under high system temperature (over 200 °C), high system pressure (over 2.5 MPa) and fast moving coolant flow (over 5 m/s). Specially fabricated accelerometers, various sealing techniques and conduit channel design for signal cable protection were used to measure the vibration. The effects of the flow rate, coolant temperature, pre-sized support clearance on the test fuel vibration response and orbit motion were discussed.

As the system flow rate increases, the average vibration level was gradually growing due to the increase of flow (turbulence) excitation energy and the frequency bandwidth of dominant response components became slowly wider because of the increase of flow-dependant damping. The dominant power components in the response spectrum were concentrated on the frequency ranges associated with test assembly's and test rod's modal frequencies. Test fuel assemblies acted as band pass filter and vibrated near or at their own natural frequencies. Variation of coolant temperature did not make noticeable differences in the measured response for the same measurement target. Pre-sized support clearance had the frequency of the dominant power components moved to the lower frequency region in the response spectrum. The accumulated vibration orbit had nearly elliptical shape; its size increased with the amount of pre-sized support gap and measurement locations of the test rod. The measured data is used for fuel compatibility evaluation and a basis for endurance verification, as well as the validation tool for theoretical response prediction model. In the future, theoretical model development to estimate steady-state fuel response is needed based on the acquired test results.

Reference

- [1] Kim, K. T., The effect of fuel rod supporting conditions on fuel rod vibration characteristics and grid-to-rod fretting wear, *Nuclear Engineering and Design*, Vol. 240, pp. 1386-1391, 2010.
- [2] Paidoussis, M. K., *Fluid-structure Interactions; Slender Structure and Axial Flow*, Elsevier Academic Press, Vol. 2, pp. 787~1220, 2004.
- [3] Shin, C. H., et al, Fuel assembly endurance test facility development and verification, *Proceedings of KSME autumn meeting*, Paper number We18F048, 2010(In Korean).
- [4] Pettigrew M. J., Goyder, H. G. D., Qiao, Z. L., Axisa, F., Damping of multispan heat exchanger tubes; Part 1 : in gases, *Proceedings of ASME PVP*, Vol. 104, p. 81-88, 1986.
- [5] Pettigrew M. J., Rogers, R. J., Axisa, F., Damping of multispan heat exchanger tubes ; Part 2 : in liquids, *Proceedings of ASME PVP*, Vol. 104, p. 89-98, 1986.

Acknowledgement

This work was supported by Nuclear Research & Development Program of National Research Foundation of Korea (NRF) grant funded by the Korean government (MEST). (Grant code: M20706020005-08M0602-00510)

Output-Only Modal Analysis Using Continuous-Scan Laser Doppler Vibrometry and Application to a 20kW Wind Turbine

Shifei Yang

Graduate Research Assistant, Ph.D. Candidate

syang66@wisc.edu

&

Matthew S. Allen,

Assistant Professor

msallen@engr.wisc.edu

Department of Engineering Physics

University of Wisconsin-Madison

535 Engineering Research Building

1500 Engineering Drive

Madison, WI 53706

Abstract:

Continuous-scan laser Doppler vibrometry (CSLDV) is a method whereby one continuously sweeps the laser measurement point over a structure while measuring, in contrast to the conventional scanning LDV approach where the laser spot remains stationary while the response is collected at each point. The continuous-scan approach can greatly accelerate measurements, allowing one to capture spatially detailed mode shapes along a scan path in the same amount of time that is typically required to measure the response at a single point. The method is especially beneficial when testing large structures, such as wind turbines, whose natural frequencies are very low and hence require very long time records. Several CSLDV methods have been presented that employ harmonic excitation or impulse excitation, but no prior work has performed CSLDV with an unmeasured, broadband random input. This work extends CSLDV to that class of input, developing an output-only CSLDV method (OMA-CSLDV). This is accomplished by adapting a recently developed algorithm for linear time-periodic systems to the CSLDV measurements, which makes use of harmonic power spectra and the harmonic transfer function concept developed by Wereley. The proposed method is validated on a randomly excited free-free beam, where one-dimensional mode shapes are captured by scanning the laser along the length of the beam. The natural frequencies and mode shapes are extracted from the harmonic power spectrum of the vibrometer signal and show good agreement with the first seven analytically-derived modes of the beam. The method is then applied to identify the shapes of several modes of a 20kW wind turbine using a ground based laser and with only a light breeze providing excitation.

1 Introduction

Continuous-Scan Laser Doppler Vibrometry (CSLDV) is a novel method of employing a laser vibrometer in which the laser spot sweeps over the structure continuously while measuring, capturing the response of the structure from a moving measurement point. Various methods have been devised to determine the mode shapes of the structure everywhere along the scan path from as few as one such measurement. Hence, the method can greatly accelerate measurements from structures with low frequency modes, which require long time records at each measurement point when the conventional point-by-point scanning method is used. Indeed, CSLDV may be the only viable method for obtaining mode shape measurements from structures that change with time or which are subjected to inputs that are difficult to replicate. One may also obtain measurements with greatly increased spatial detail, leading to insights into the dynamics of a structure that may be helpful when performing model correlation and updating [1].

Although Sriram et al. were the first to publish regarding CSLDV in early 1990's [2-4], the research group at Imperial College in London (Stanbridge, Martarelli, Ewins and Di Maio) had been working with moving sensors

some time previously and are responsible for most of the advancements in this area.. Stanbridge, Martarelli and Ewins coined the name “CSLDV” and developed a number of algorithms that extract one and two-dimensional operating deflection shapes from CSLDV measurements under sinusoidal and impact excitation [5-9]. Other notable contributions include the work by Vanlanduit et al. [10], who presented a CSLDV method that uses multi-sine excitation (periodic broadband excitation). Allen & Sracic explored the use of higher scan frequencies together with impact excitation, presenting the lifting technique that allows conventional modal analysis curve fitting methods and tools such as the CMIF to be applied to CSLDV measurements [11-13]. They also presented a method for mass-normalizing the mode vectors obtained by CSLDV when the input force has been measured [13, 14]. All of the existing CSLDV methods are valid only for the case where the input is either zero (free response) or else it follows a specific form and is carefully controlled. In practice one cannot always apply an input of one of these forms to a structure, but unmeasured random input forces may be present. For example, wind turbines are difficult to adequately excite due to their large size and mass, yet each day the wind provides a convenient, broadband source of ambient excitation.

This work extends CSLDV to Output-only Modal Analysis (OMA), identifying modes from responses under an unmeasured, broadband random input. Since the mode shapes of a linear system are functions of position, the CSLDV measurement appears to be from a time-periodic system when the laser spot moves in a periodic, closed scan path. A few system identification strategies have been proposed for linear time-periodic systems, as discussed in [11]. This work utilizes a method recently presented by Allen et al. in [15, 16] that is based on the spectra of the output of a linear time periodic system when it is excited by a broadband random input. The method utilizes the harmonic transfer function concept by Wereley and Hall, which is an extension to the concept of a frequency response function (FRF) to linear time-periodic systems [17-19]. This method can be thought of as an extension of Output-only Modal Analysis [20-25] or the Natural Excitation Technique (NExT) [26] to time-periodic systems.

The rest of this paper is organized as follows. Section 2 reviews the proposed output-only identification technique with particular emphasis on how to interpret the response spectra of an LTP system. In Section 3 the proposed technique is demonstrated by identifying the mode shapes of a free-free beam under random excitation, and the performance of the method and effect of the chosen scan frequency are discussed. The method is then applied to a CSLDV measurement of a wind turbine blade in Section 4, and Section 5 summarizes the conclusions.

2 Theoretical Basis

A Linear Time Invariant (LTI) structure can be modeled with the following well known equation of motion,

$$M\ddot{y} + C\dot{y} + Ky = F(t) \quad (1)$$

which can be written in an equivalent state space form as follows with $x = [y^T, \dot{y}^T]^T$

$$\begin{aligned} \dot{x} &= Ax + Bu \\ y &= Cx + Du \end{aligned} \quad (2)$$

When a laser vibrometer is used so that the velocity is measured, $D = 0$. One can diagonalize the modal equations for the system using $x = Pq$ where,

$$P = \begin{bmatrix} \Psi \\ \Psi\Lambda \end{bmatrix} \quad (3)$$

with Ψ a matrix of the complex modes of the system $\Psi = [\psi_1 \ \cdots \ \psi_N]$ and Λ a diagonal matrix containing the eigenvalues of the system $\Lambda = \text{diag}(\lambda_1 \ \cdots \ \lambda_N)$, with $\lambda_r = -\zeta_r \omega_r + j\omega_r \sqrt{1 - \zeta_r^2}$ in terms of the r th natural frequency ω_r and damping ratio ζ_r of the system. The equations of motion become

$$\begin{aligned} \dot{q} &= \Lambda q + P^{-1}Bu \\ y &= CPq \end{aligned} \quad (4)$$

The output matrix C can be taken to be a matrix with all zeros and a one at the location of the nodal point that the laser is measuring. If the k th measurement point is being measured, then CP is a $1 \times N$ matrix

$CP = [\psi_{k1} \ \cdots \ \psi_{kN}] \Lambda$. On the other hand, when the continuous-scan approach is employed with a periodic scan pattern, the laser position changes periodically with time so CP becomes a periodic $1 \times N$ matrix of mode shapes that seem to change with time since the measurement point is moving. This can be written as $C(t)P = [\psi_1(t) \ \cdots \ \psi_N(t)] \Lambda$ with the condition that $\psi_r(t + T_A) = \psi_r(t)$, and where it is understood that the mode shapes are written as time periodic functions only because the measurement point is changing with time. Hence, a system under CSLDV measurement can be modeled with a set of linear time periodic (LTP) equations of motion. The CSLDV system has A , B and D constant and C time varying. In the most general case, the response of a linear time periodic system can be written as follows in terms of its state transition matrix.

$$y(t) = C(t)\Phi(t, t_0)x(t_0) + \int_{t_0}^t C(t)\Phi(t, \tau)B(\tau)u(\tau)d\tau + D(t)u(t) \quad (5)$$

Since the state matrix A is constant and considering the modal form of the equations of motion in Eq. (4), the state transition matrix is simply.

$$\Phi(t, t_0) = e^{\Lambda(t-t_0)} \quad (6)$$

This reveals that the eigenvalues of the structure measured using CSLDV are equal to the Floquet exponents of the LTP model. Hence, both the mode shapes and natural frequencies of the structure can be determined once the Floquet Exponents and time periodic mode shapes of the LTP system have been identified.

Werely [17] used Eq. (5) to extend the concept of a transfer function to linear time periodic systems. He derived the concept of a harmonic transfer function (HTF) that relates the input and output of a time-periodic system in a transfer function type manner. The primary difference is that, whereas a transfer function relates the output at a single frequency to the input at the same frequency, the HTF relates the input at a collection of frequencies to the output at that same comb of frequencies. Specifically, consider the Fourier transform of the response $y(t)$ shifted by $n\omega_A$,

$$y_n(\omega) = \int_{-\infty}^{\infty} y(t)e^{(-j\omega - jn\omega_A)t} dt \quad (7)$$

An EMP signal, denoted with bold uppercase in the following, is the collection of frequency shifted copies of the response. In the case of CSLDV measurements, there is only one measurement point so $y(t)$ is a scalar. Hence, the EMP representation is,

$$\mathbf{Y}(\omega) = [\cdots \ y_{-1} \ y_0 \ y_1 \ \cdots]^T \quad (8)$$

The autospectrum of the EMP signal is found in the usual way,

$$S_{yy}(\omega) = E(\mathbf{Y}(\omega)\mathbf{Y}(\omega)^H) \quad (9)$$

where $E()$ denotes the expectation and $()^H$ denotes the Hermitian. Allen et al. showed in [15, 16] that the output autospectrum can be written as follows in terms of the modes of the state transition matrix,

$$[S_{yy}(\omega)] \approx \sum_{r=1}^N \sum_{l=-\infty}^{\infty} \frac{\bar{\mathbf{C}}_{r,l} \mathbf{W}(\omega)_{r,l} \bar{\mathbf{C}}_{r,l}^H}{[i\omega - (\lambda_r - il\omega_A)][i\omega - (\lambda_r - il\omega_A)]^H} \quad (10)$$

This has the same mathematical form as the output autospectrum of a multi-output linear time invariant system. Each denominator is multiplied by its complex conjugate, so the response is a sum of modal contributions squared. As with an LTI system, each numerator contains $\mathbf{W}(\omega)_{r,l}$, which can be shown to be the autospectrum of the net force exciting the r th mode.

There are also two notable differences between Eq. (10) and the equivalent expression for an LTI system. First, the expression contains a summation over both the modes, whose eigenvalues are λ_r , and also a summation over the harmonics of ω_A using the integer index l . Hence, the autospectrum of the LTP system will have peaks near each natural frequency, ω_r , and also at the frequencies $\omega_r \pm l\omega_A$ for any integer l . Second, the mode vectors $\bar{C}_{r,l}$ are not the usual collections of the mode shape at different points, but have a different definition. As discussed in [15, 16], the mode vectors $\bar{C}_{r,l}$ are a collection of the Fourier coefficients of the r th observed mode vector $C(t)\psi_r$ shifted by l . Specifically, $C(t)\psi_r$ is expanded in a Fourier series as follows

$$C(t)\psi_r = \sum_{n=-\infty}^{\infty} C_{r,n} e^{jn\omega_A t} \quad (11)$$

and then the Fourier coefficients are collected into $\bar{C}_{r,l}$ after shifting by l .

$$\bar{C}_{r,l} = [\dots \ C_{r,-1-l} \ C_{r,-l} \ C_{r,1-l} \ \dots]^T \quad (12)$$

Here we shall refer to the autospectrum of the EMP signal as the harmonic power spectral density or HPSD. Since the HPSD has the same form as the PSD of a linear system, OMA techniques for LTI system scan be used to identify the modes of the system. However, one will obtain multiple estimates for each mode since each mode is present at a comb of frequencies $\omega_r \pm l\omega_A$. This can be addressed in a post processing step, but care must be taken since the mode vectors identified at each harmonic will not generally be of equal quality. Some of them will be strong and stand out above the noise while others might be weaker or contaminated by neighboring modes. A weighted average method can be employed to decrease the effect of the less reliable estimates. In addition, each of the estimates of $\bar{C}_{r,l}$ can differ by a complex scale factor, so their phases should be aligned before averaging.

Theoretically, one must consider an infinite number of harmonics to characterize an LTP system, yet one would expect that most systems can be well approximated with a finite, perhaps even small number. When a range of harmonics, $n = -p \dots p$, are used to describe the CSLDV output signal in eq. (7) and (8), the resulting auto spectrum matrix $S_{yy}(\omega)$ has the dimension of $[N_p \times N_p \times N_f]$, where $N_p = 2*p + 1$ and N_f is the number of frequency lines. One is free to use any of the rows (or columns) in the power spectrum matrix to identify the $[N_p \times 1]$ vector $\bar{C}_{r,l}$. In this work, only the power spectra along the primary column $S_{yy}(\omega)_{n,0} = E(\mathbf{Y}(\omega)y_0(\omega)^H)$, are used. Once a vector $\bar{C}_{r,l}$ is found, one can reconstruct the time periodic mode shape of the system according to eq. (11) and then plot it against the laser path to generate the mode shape of the LTI system.

3 Experimental Validation

3.1 Experimental Setup

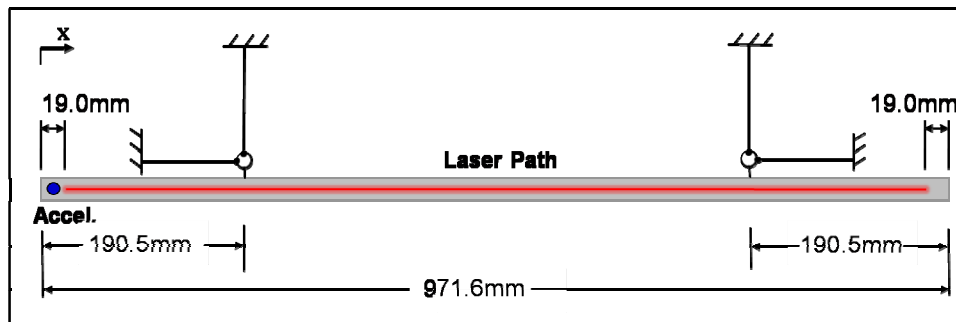


Figure 1: Schematic of test setup

In order to validate the new OMA-CSLDV methodology, CSLDV was used to measure the modes of a free-free aluminum beam, as shown schematically in Figure 1. The beam was suspended by soft bungee cables so the laser scan path would remain on the beam as it was excited. The supports were made as soft as possible and placed at the nodes of the first analytical bending mode to minimize the effect of the support stiffness on the beam's modes. A 5.2g accelerometer (PCB J351B11) was attached at the left end of the beam ($x = 6.3\text{mm}$), the same configuration as in [13], so that the identified modes can be compared to the analytical model used in that previous work. The signal from the accelerometer was not used in any of the following.

Continuous-Scan Laser Doppler Vibrometry was employed to measure the beam's transient response using a Polytec® PSV-400 scanning laser vibrometer with the customized mirror system described in [27]. To improve the laser signal strength and reduce noise, the front surface of the beam was covered with light weight retro-reflective tape (3M Scotchlite™ High Gain Reflective Sheeting 7610). The mirror system was used to scan the laser along the length of the beam sinusoidally at 1.5Hz and 3Hz. The mirror driving voltage was manually adjusted until the laser traversed all but 19mm from the ends of beam; this ensured that the laser remained on the beam throughout the tests. The beam was excited at random times and at random locations for 10mins with an instrumented hammer (PCB 086C01), although the force signal from the hammer was not measured. A sampling frequency of 2560Hz was selected to record the vibrometer signal, mirror driving signal and mirror output signal using a National Instruments PXI data acquisition system. To further reduce the noise, the vibrometer signal was filtered with a low-pass filter and down sampled to 1280Hz before processing the measurements. This sampling frequency appeared to be sufficient to capture all of the frequency content that stood out above the noise floor.

3.2 Validation

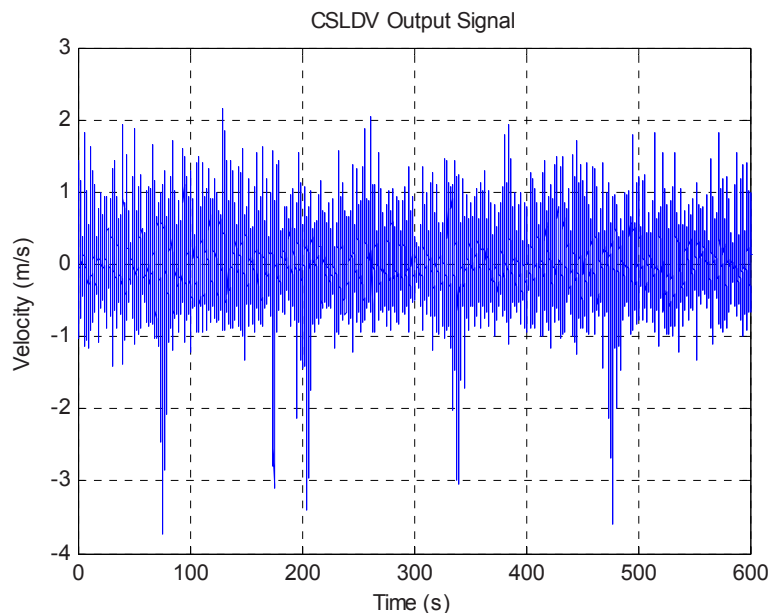


Figure 2: CSLDV output signal under random excitation (1.5Hz scan frequency)

Figure 2 shows the 10 minute long CSLDV output signal that was acquired at a scan frequency of 1.5Hz. The vibration signal appears to be random, although it drops to -3 m/s periodically during the measurement (the same phenomenon was noted when a 3Hz scan frequency). This phenomenon seems to have been caused by the VD-03 velocity decoder used in the Polytec system, although its cause is not well understood. Measurements with the VD-08 decoder did not show this feature, but the largest range setting for that decoder was inadequate for this system. The output signal including these dropouts was used in the following analysis without any special treatment and fortunately, reasonable results were still obtained in spite of that contamination.

To form the EMP output signal $Y(\omega)$ in eq. (8), the CSLDV output signal was exponentially modulated with harmonics $n=-5\dots 5$ according to eq. (7). The number of harmonics required to accurately describe each mode shape was not known, but when low scan frequencies such as these are used, choosing a large number of harmonics may cause the harmonics from neighboring modes to overlap so that the mode shape cannot be accurately determined. Hence, one must choose the scan frequency carefully to avoid this difficulty. The authors

have typically chosen the scan frequency to be large relative to the natural frequencies of interest in order to simplify matters [12, 28], although in this work smaller scan frequencies are explored since they make the spectra easier to interpret and reduce laser speckle noise [29, 30]. Other researchers, such as Stanbridge et al. typically use relatively small scan frequencies in their work, see [5-8] for examples.

The modulated CSLDV output signal was then decomposed into 20 s long blocks to calculate $S_{yy}(\omega)$. A Hanning window was applied to each of the blocks with 75% overlap, resulting in 104 blocks for each modulated output signal. The auto and power spectra of the modulated output signal are then calculated on each block and averaged over all 104 blocks, resulting in a $[11 \times 11 \times 16385]$ harmonic power spectrum matrix. Recall that a single CSLDV signal was measured, but it was expanded into 11 signals so the Power Spectral Density (PSD) for this system is an 11 by 11 matrix at each frequency.

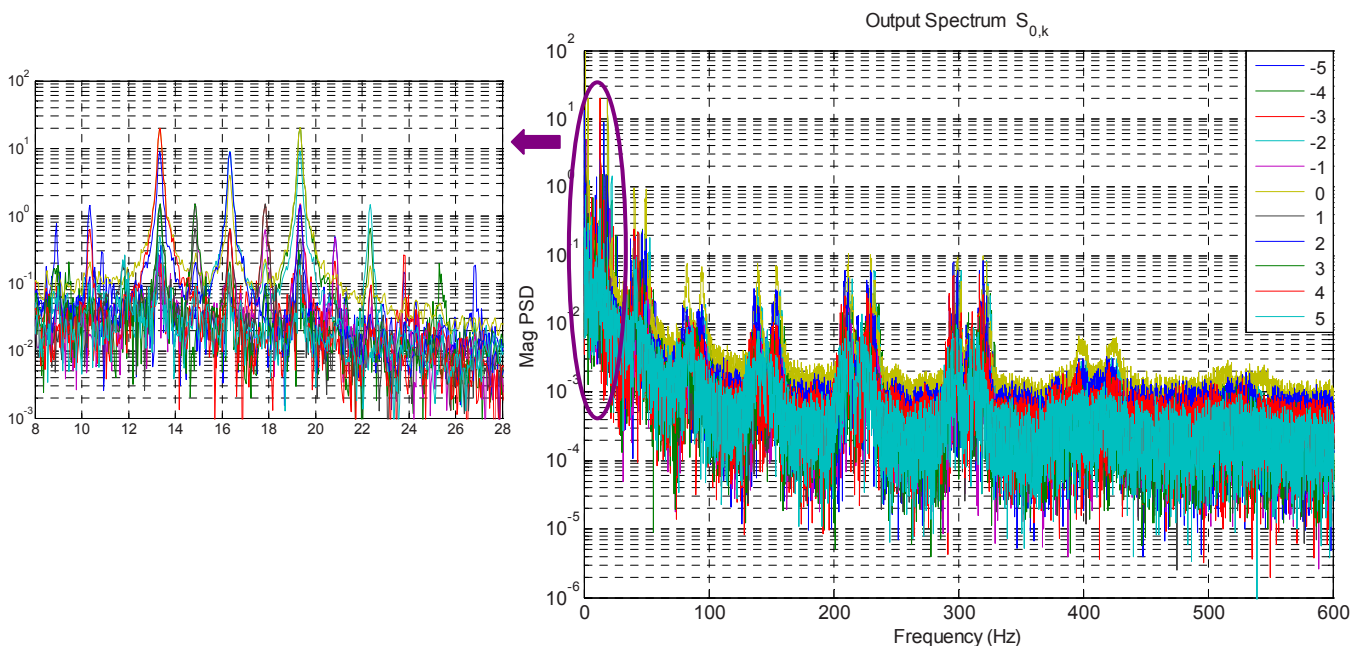


Figure 3: Harmonic PSD of CSLDV measurement at 1.5Hz scan frequency. The pane on the left shows an expanded view of the measurement near 16 Hz.

Figure 3 shows the power spectrum along the primary row of $S_{yy}(\omega)$. The eleven curves shown correspond to each of the n, k th elements of S_{yy} for $n = 0$ and $k = -5 \dots 5$. The spectra show clusters of strong harmonics around each of the natural frequencies. The view on the left focuses on the 1st mode, whose natural frequency is 16.34Hz. Besides the peak at 16.34Hz, the 1st mode is also responsible for the harmonics in the spectrum at 13.34Hz, 14.85Hz, 17.85Hz, 19.34Hz, etc, all separated by multiples of 1.5Hz, which is the fundamental frequency $\omega_n/(2\pi)$. The peak picking method can be used to identify the Fourier coefficients $\bar{C}_{r,l}$ from the power spectra in Figure 3, and this approach was found to provide good accuracy in most cases. However, better results were obtained by fitting the measurements to single DOF modes using the Algorithm of Mode Isolation (AMI) [31]. This algorithm was modified from the version in [31] to fit squared modes to the power spectrum near each mode. The AMI algorithm identified the natural frequencies, damping ratios and mode shapes $\bar{C}_{r,l}$ of the mode manifest at each of the peaks in the spectrum.

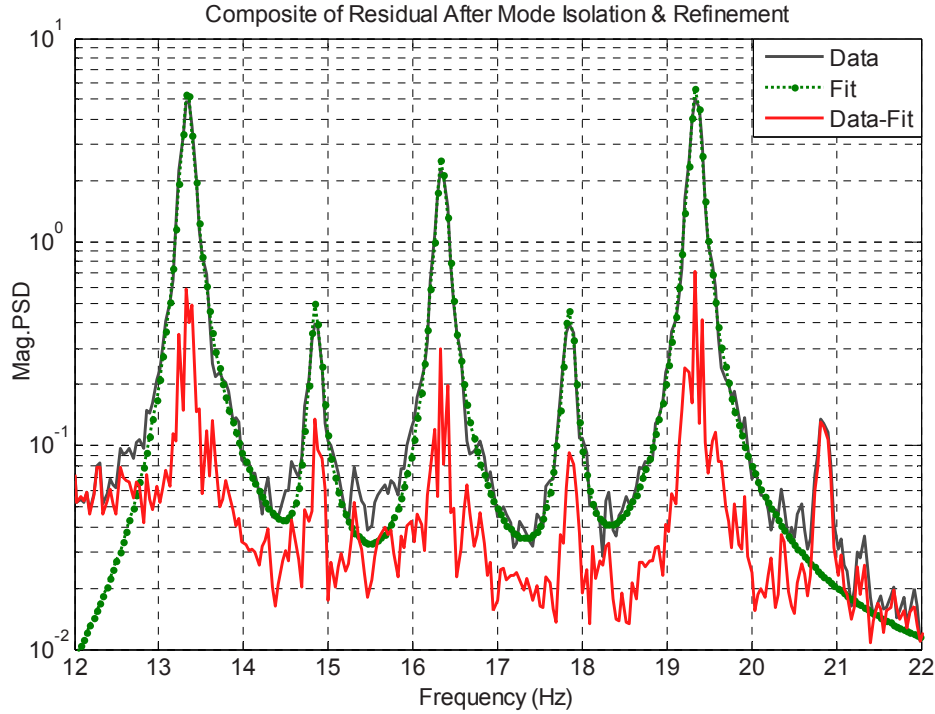


Figure 4: AMI fit of the 1st mode using a 1.5Hz scanning frequency

Figure 4 shows an AMI fit to several of the peaks arising from the 1st mode, again for the 1.5Hz scanning frequency. The gray solid line indicates the composite FRF, which is the average of the 11 FRFs in 3, and the green dash-dot line is the AMI fit curve. The 5 dominant harmonics of this mode are well approximated by the reconstructed spectrum. A third curve shows the composite of the difference between the measurement and the reconstruction, revealing that the fit is superior at the three dominant peaks. The response stands out above the noise (due to imperfection in the LDV and to the non-flatness of the input spectrum) by about one order of magnitude. Table 1 shows the normalized Fourier coefficient vectors identified from the 5 harmonics shown in Figure 4. Each of the identified coefficient vectors should contain the same Fourier coefficients $C_{r,n}$, but those coefficients are shifted by l in each of the identified vectors $\bar{C}_{r,l}$ and each of those vectors may have a different complex scale factor. The scale differences are addressed by normalizing the vector by dividing by the largest value and then rotating the vector to the same phase so that they can be averaged. To minimize the noise, the largest value in each identified Fourier coefficient vector $\bar{C}_{r,l}$ is used as the weight during the averaging. Some higher order Fourier coefficients have large discrepancy because of the noise (see $C_{1,5}$, $C_{1,6}$ and $C_{1,7}$ in Table 1), but those terms are from weakly represented peaks in the spectrum and so they become much smaller applying the weighted average.

Table 1 Shifted Fourier coefficient vectors of the 1st mode under 1.5Hz scanning frequency

| | Averaged | Harmonics of 1 st mode | | | | |
|------------|-------------------|-----------------------------------|-------------------|------------------|------------------|------------------|
| Frequency | 16.3391 | 13.3372 | 14.8429 | 16.3349 | 17.8412 | 19.3392 |
| Weight | 1 | 0.3629 | 0.0275 | 0.159 | 0.0296 | 0.3536 |
| r/l | $\bar{C}_{1,0}$ | $\bar{C}_{1,2}$ | $\bar{C}_{1,1}$ | $\bar{C}_{1,0}$ | $\bar{C}_{1,-1}$ | $\bar{C}_{1,-2}$ |
| $C_{1,-7}$ | -0.0058 - 0.0013i | 0.0080 - 0.0004i | 0 | 0 | 0 | 0 |
| $C_{1,-6}$ | -0.0259 + 0.0087i | -0.0083 + 0.0055i | -0.0490 - 0.0095i | 0 | 0 | 0 |
| $C_{1,-5}$ | -0.0030 + 0.0121i | 0.0104 - 0.0119i | -0.0000 - 0.0027i | 0.0104 - 0.0061i | 0 | 0 |

| | | | | | | |
|------------|-------------------|-------------------|-------------------|-------------------|-------------------|-------------------|
| $C_{1,-4}$ | -0.0779 + 0.0123i | 0.0536 - 0.0032i | 0.0301 + 0.0034i | 0.0664 - 0.0029i | 0.0163 - 0.0639i | 0 |
| $C_{1,-3}$ | 0.0049 - 0.0050i | -0.0055 + 0.0087i | 0.1186 + 0.0559i | -0.0011 + 0.0067i | -0.0043 + 0.0200i | -0.0065 + 0.0134i |
| $C_{1,-2}$ | 1 | -0.9946 - 0.1034i | -0.9358 - 0.0859i | -0.9943 - 0.1063i | -0.9944 - 0.1059i | -0.9945 - 0.1051i |
| $C_{1,-1}$ | -0.0729 - 0.0034i | 0.0689 + 0.0082i | 0.1461 + 0.0457i | 0.0709 + 0.0069i | 0.0421 - 0.0036i | 0.0759 + 0.0083i |
| $C_{1,0}$ | 0.4464 + 0.0771i | -0.4211 - 0.1139i | -0.4045 - 0.1223i | -0.4267 - 0.1196i | -0.3882 - 0.1069i | -0.4232 - 0.1175i |
| $C_{1,1}$ | -0.0769 - 0.0185i | 0.0735 + 0.0217i | 0.1239 + 0.0214i | 0.0723 + 0.0228i | 0.1089 + 0.0242i | 0.0727 + 0.0196i |
| $C_{1,2}$ | 0.9354 + 0.3048i | -0.8994 - 0.3967i | -0.9121 - 0.4099i | -0.9077 - 0.3987i | -0.8801 - 0.3941i | -0.9120 - 0.4074i |
| $C_{1,3}$ | 0.0114 + 0.0180i | -0.0058 - 0.0178i | -0.0707 - 0.0498i | -0.0107 - 0.0149i | -0.0337 - 0.0465i | -0.0082 - 0.0174i |
| $C_{1,4}$ | -0.0346 - 0.0188i | 0 | -0.0186 + 0.0253i | 0.0533 + 0.0378i | 0.0645 + 0.0436i | 0.0519 + 0.0333i |
| $C_{1,5}$ | -0.0038 - 0.0009i | 0 | 0 | 0.0074 + 0.0037i | 0.0054 - 0.0027i | 0.0040 + 0.0023i |
| $C_{1,6}$ | 0.0006 + 0.0016i | 0 | 0 | 0 | -0.0248 + 0.0059i | 0.0000 - 0.0073i |
| $C_{1,7}$ | -0.0009 - 0.0001i | 0 | 0 | 0 | 0 | 0.0023 - 0.0019i |

The mode shapes reconstructed from these Fourier coefficient vectors are plotted in Figure 5, as well as the averaged mode shape from the weighted average of all of the Fourier coefficients. It can be seen that the mode shapes from the -1 and 1 harmonics have some discrepancy from the ones from the -2 , 0 and 2 harmonics. This is to be expected since the -1 and 1 harmonics have about 10 times smaller amplitude in Figure 4, so they are much more strongly influenced by noise. Any of the other harmonics gives a reasonable estimate of this mode's shape.

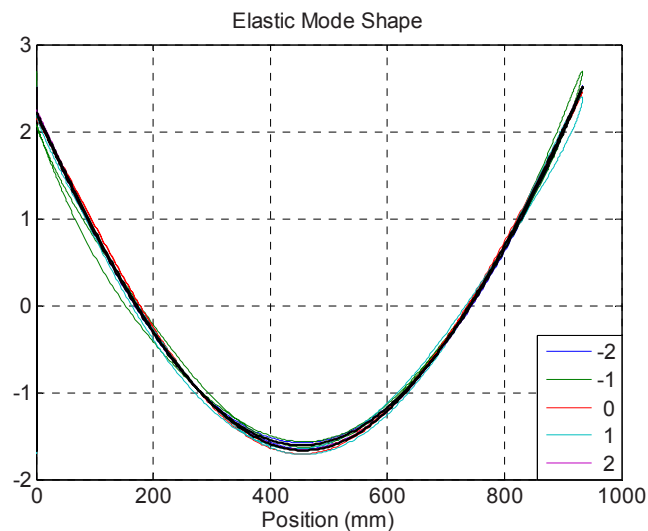


Figure 5: Mode shapes reconstructed from each of the five groups of harmonics in Table 1. The solid black line shows the mode shape computed from the weighted average of the harmonics.

All of the other modes were identified in a similar manner. Table 2 shows the natural frequencies of each of the modes that were identified from the harmonic spectra in Figure 6. The 1.5Hz scan frequency was used for the first two modes, while the rest were extracted from the measurements with the 3Hz scan frequency. With the higher modes it was possible to compute the harmonic autospectrum for $n=-8:8$, so that was used for modes 3 through 7. The value in the column labeled "OMA" is the average of the natural frequency estimated at each of the harmonics, after shifting each by an integer multiple of ω_1 . The standard deviation of the natural frequency estimates is also shown, which is very small in all cases, revealing that each of the harmonics gives a very similar estimate of the natural frequency. The values in the column "Analytical" are the natural frequencies of a tuned analytical model, which is an Euler-Bernoulli beam model that was tuned to account for the mass of the accelerometer as described in [13]. All of the OMA identified natural frequencies agree well with the analytical values, the largest difference is a few Hz for the higher modes, but the analytical model was found to be somewhat inaccurate for these modes so the OMA result is still within the margin of error for the analytical model.

Table 2 Comparison of analytical and experimental modes

| No. | Analytical Freq. (Hz) | OMA Freq. (Hz) | Std | n | Scan Frequency | MAC |
|-----|-----------------------|----------------|------|------|----------------|------|
| 1 | 16.38 | 16.34 | 0.01 | -5:5 | 1.5 | 1.00 |
| 2 | 45.35 | 45.15 | 0.03 | -5:5 | 1.5 | 0.98 |
| 3 | 89.23 | 88.73 | 0.10 | -8:8 | 3 | 0.95 |
| 4 | 147.99 | 146.99 | 0.02 | -8:8 | 3 | 0.98 |
| 5 | 221.71 | 221.07 | 0.01 | -8:8 | 3 | 0.95 |
| 6 | 310.49 | 309.53 | 0.01 | -8:8 | 3 | 0.92 |
| 7 | 414.37 | 411.57 | 0.10 | -8:8 | 3 | 0.92 |

Figure 6 shows the mode shapes of each of the identified modes, as well as the shapes from the tuned analytical model from [13]. The mode shapes agree very well with the analytical model, except for the 3rd and 7th modes which show significant discrepancies. The 3rd mode was heavily damped and the harmonics overlapped with each other even when using a 3Hz scanning frequency, so it was difficult to identify. The 7th mode was weakly excited since the hammer force had rolled off significantly near its natural frequency, so it did not stand out sufficiently above the noise. This mode was also difficult to identify using the authors original CSLDV approach, as described in [12]. The MAC values between the analytical mode shapes and the CSLDV mode shapes are listed in Table 2; the worst MAC values occur for the 6th and 7th modes, but those values are still above 0.92.

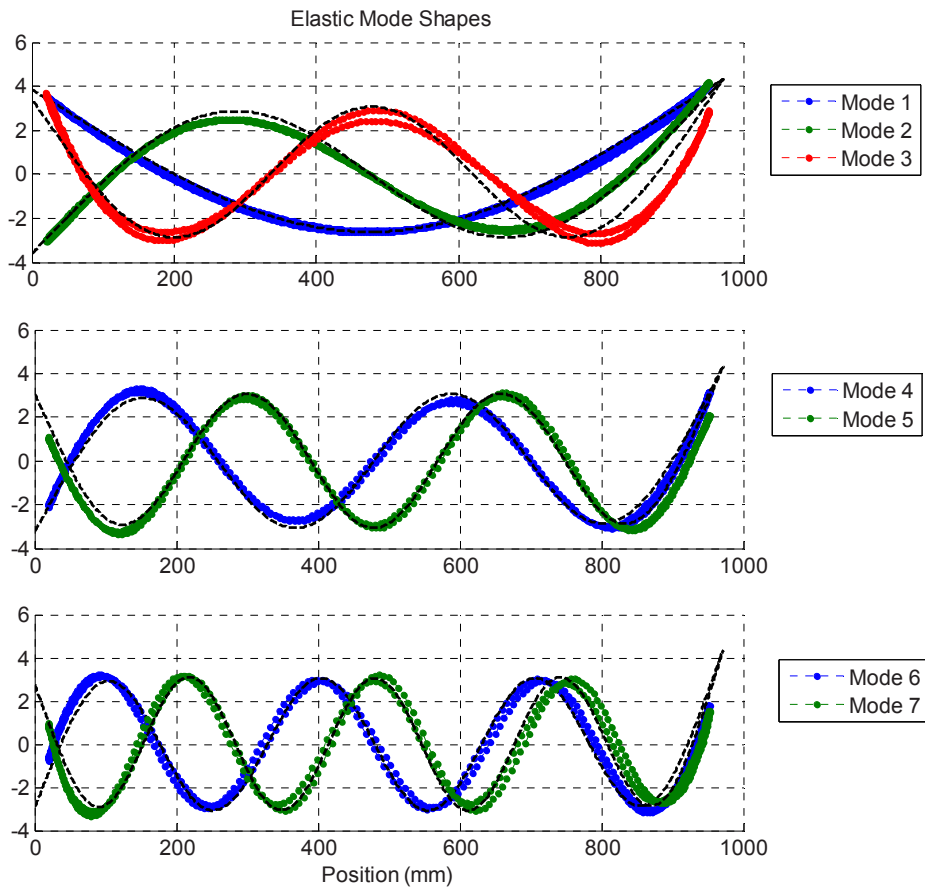


Figure 6 Mode shapes identified by CSLDV at 1.5Hz and 3Hz scanning frequencies. Solid black lines denote the analytical shapes; dots show the shapes from OMA

3.3 Effect of Scan Frequency

As these results illustrate, one must take some care to choose an acceptable scan frequency. As mentioned previously, low scan frequencies were chosen in this work so that the harmonics of each mode would occur in a cluster, as illustrated in Figure 3. However, this may lead to difficulty if many harmonics are needed to describe a mode, since the harmonics from one mode may overlap with those from the neighboring modes, especially when the modes are close to each other. In addition, if one mode is heavily damped, the scanning frequency must be large to distinguish the harmonics belonging to this mode. Figure 7 demonstrates this issue by comparing the spectrum near the heavily damped 3rd mode for 1.5Hz and 3Hz scanning frequencies. The harmonics of this mode overlap significantly when a 1.5Hz scanning frequency was used. Though one can still identify the natural frequency and mode shape from the strongest harmonics, the mode shape is somewhat contaminated by the other nearby harmonics. A better estimate of the mode shape is obtained with a 3Hz scanning frequency. Its harmonics are better separated so the Fourier coefficients estimated from each peak are not as strongly affected by the neighboring peaks.

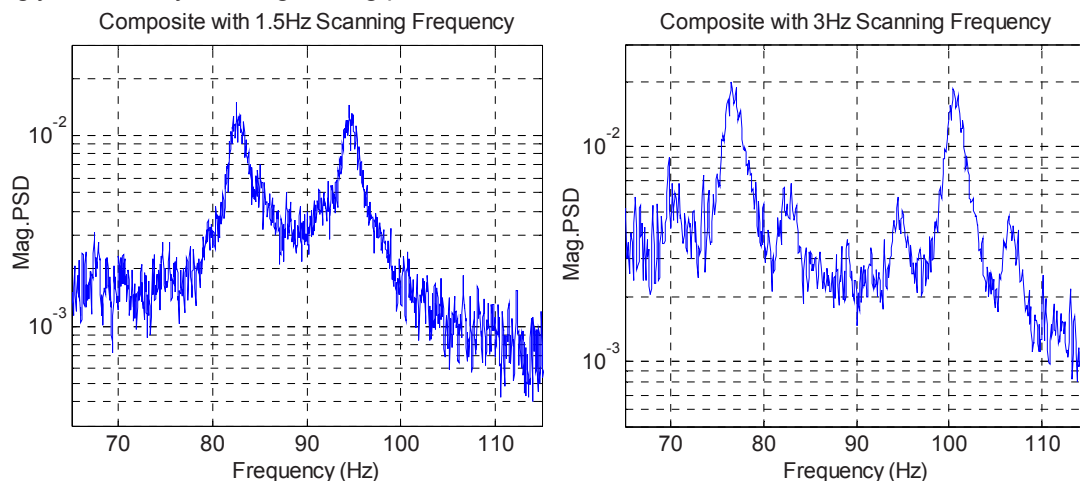


Figure 7: Composites of the harmonic PSD near the 3rd mode with 1.5Hz (left) and 3Hz (right) scanning frequencies.

The most straight forward approach for selecting the scan frequency is to choose one that is higher than the highest mode that is excited. This assures that all of the harmonics in eq. (10) occur at distinct frequencies. Unfortunately, this may result in excessive noise with current lasers and for some systems the scan frequency needed may even exceed the capabilities of the mirror system. On the other hand, CSLDV is most advantageous for systems that have low natural frequencies and hence require long time records, so limitations of the laser and mirror system may not be a significant concern. A high scan frequency produces a spectrum that is a little more complicated than those shown above, since each of the mode peaks may be present in each frequency band for which $n\omega_\Lambda < \omega < (n+1)\omega_\Lambda$. This makes the spectra more difficult to interpret visually. In previous works the authors circumvented this difficulty by lifting the measurements, which effectively aliases the CSLDV signal producing a collection of signals that are limited to $0 < \omega < \omega_\Lambda/2$ [12]. An analog of this method has not yet been developed for autospectra, so in this work we have worked with the spectra directly.

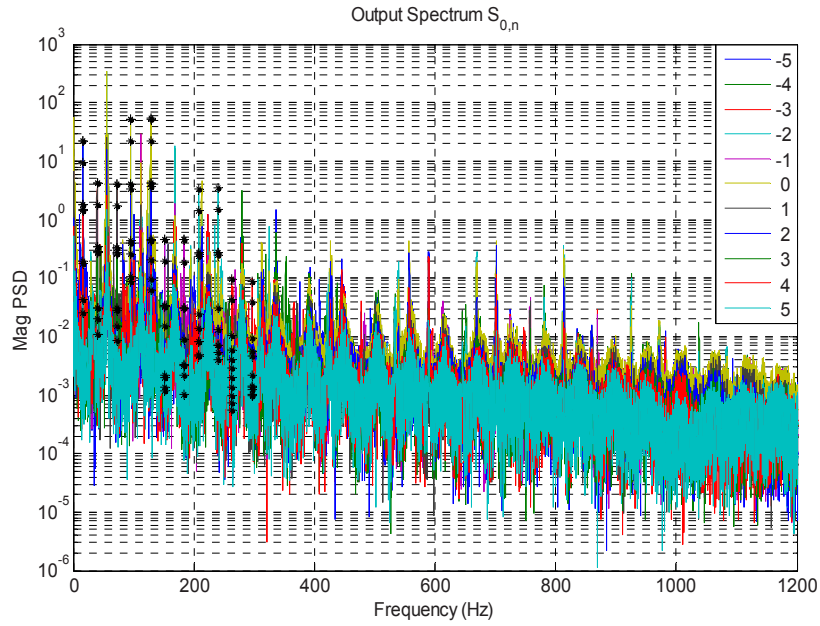


Figure 8: Harmonic PSD of CSLDV measurement at 56 Hz scan frequency

Figure 8 gives an example of the measurement under 56Hz scanning frequency, where the black stars indicate the harmonics of the first mode ($f_n = 16.34$ Hz). The harmonics of this mode no longer appear in a cluster as in Figure 3 but throughout the band for $16.34\text{Hz} \pm n56\text{Hz}$. Some of the harmonics for negative n fold about zero frequency occurring at positive frequencies $|16.34\text{Hz} - n56\text{Hz}|$, complicating matters further. Nevertheless, the same identification procedure can still be applied as long as the harmonics of each mode can be located. When reconstructing the mode shapes, one should note that the folded harmonics actually correspond to positive harmonics of the complex conjugate eigenvalue, so the identified vectors $\bar{C}_{r,l}$ will be complex conjugates and have the Fourier coefficients in opposite order of those identified from the positive harmonics.

Figure 9 shows the mode shapes that were identified from the power spectrum in Figure 8. The peak picking method was used to obtain the Fourier coefficient vector at each harmonic instead of AMI in this case. The reconstructed mode shapes still show great agreement with the analytical ones. However, the grid on which the mode shapes is plotted is coarser to reflect the fact that the 2560 Hz sampling rate only produces 46 samples per period at a 56Hz scan frequency measurement. A higher scan frequency could have been used to obtain a finer measurement grid, or if one is certain that all of the important Fourier Coefficients have been obtained then one could reconstruct the mode shapes with any desired spatial resolution [6].

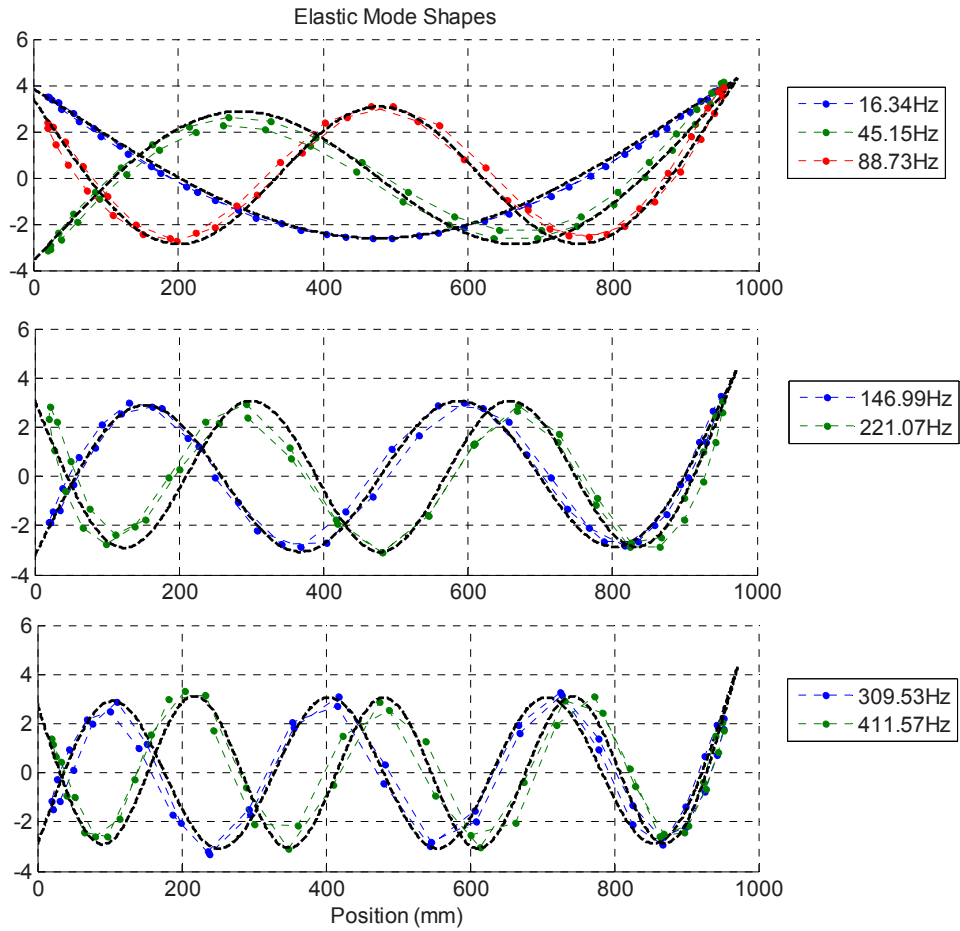


Figure 9: Mode shapes identified by CSLDV at 56Hz scanning frequency. Solid black lines denote the analytical shapes; dots show the shapes identified by OMA-CSLDV.

4 Application to Wind Turbine Blade

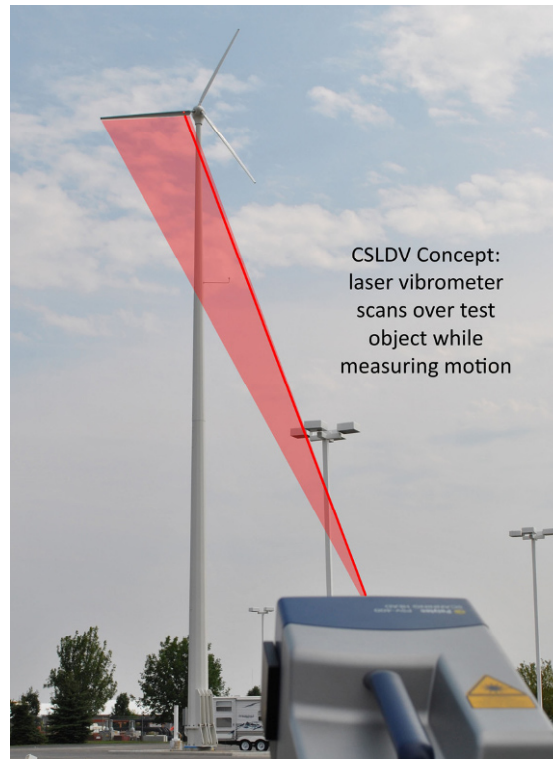


Figure 10: Photograph from CSLDV test of a wind turbine blade with a graphic illustrating the scan pattern.

The proposed method was applied to identify the natural frequencies and mode shapes of a wind turbine blade as depicted in Figure 10. The blade is one of three that comprise the turbine rotor. For all of the tests described here, the turbine rotor was locked by applying the brake and the blade of interest was pitched so that the laser was nominally perpendicular to the chord of the blade (i.e. measuring in the flapwise direction). The laser scanned over as much as possible of the 4.3m long blade. For the results shown here the laser was 66m from the base of the tower and the tower height is 30m, so the total distance from the laser head to the blade is approximately 72.5m. The same retro-reflective tape was applied on the blade to increase the signal strength. This tape was necessary to obtain any signal at all from the vibrometer, and the increased reflectivity made the laser spot easy to locate when it was on the tape. The blade was excited purely by the wind, whose maximum speed was measured to be 3.5-3.75m/s at the conclusion of testing, by a sensor mounted on the tower and which can be seen in the figure about two-blade lengths down from the top of the tower.

Before acquiring CSLDV measurements, the laser spot was fixed near the tip of the blade and the power spectrum was estimated using the LDV software to compute the PSD over about a 10 minute period. The power spectrum is shown in Figure 11. At least seven peaks are seen in the spectrum, each of which is presumed to correspond to a natural frequency of the system. The frequencies of each of these peaks are listed in Table 3. Beyond about 25 Hz the wind apparently does not excite the system significantly as the measurement seems to reduce to noise above that frequency. One should note that the seven modes seen in Figure 11 are not expected to be seven bending modes of a simple beam. The turbine is comprised of three nominally identical blades so each blade bending mode occurs three times, at two or three distinct frequencies depending on the stiffness properties of the tower and nacelle.

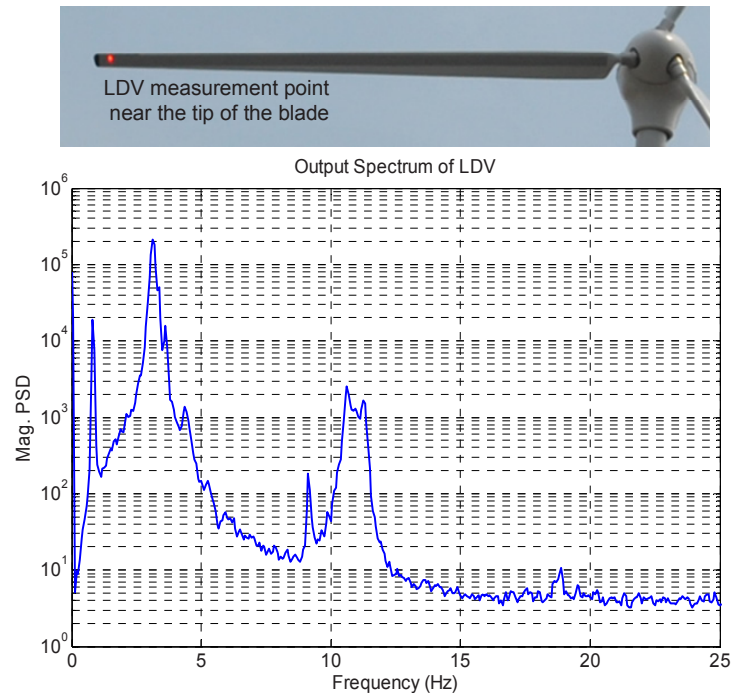


Figure 11: PSD of LDV output signal with the laser measuring at a fixed point near the tip of the blade

The LDV was then set to continuously scan the blade for 10min at a time at several different scan frequencies ranging from 0.8Hz to 9.3Hz. Both low and relatively high frequencies were investigated. The sampling frequency for these tests was 2560Hz, which was sufficient to capture the highest mode excited by the wind even at the 9.3 Hz scanning frequency.

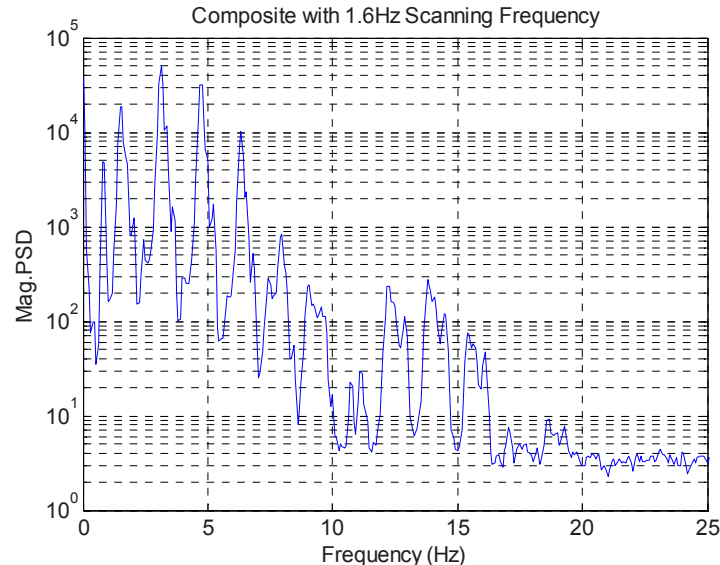


Figure 12: Composite of harmonic PSD of the CSLDV measurement with 1.6Hz scanning frequency

Figure 12 shows the power spectra of the modulated CSLDV output signal using a 1.6Hz scanning frequency. The harmonics $n=-3 \dots 3$ were used to create the harmonic PSD. As was also the case in the signal from the fixed test, the spectra seems to reduce to noise above about 25 Hz. The harmonics of several modes are visible in the spectrum, but it is difficult to determine which harmonics go with each natural frequency since they are all so closely spaced. Therefore, the point measurement in Figure 11 was used to determine which frequencies to search for each of the system's modes. The natural frequencies thus identified in the harmonic spectra are listed in Table 3, along with the seven frequencies identified from the tip spectrum in Figure 11. Also

listed are the first 2 bending modes obtained by a conventional hammer-accelerometer test on a similar blade when it was mounted in a stiff fixture on the ground.

The mode shapes constructed from the harmonic power spectra are shown in [Figure 13](#), found by computing the weighted average of the Fourier coefficients identified by the peak picking method at each of the significant harmonics. The mode shapes reveal that the mode at 0.81Hz is predominantly a tower bending mode, where the tower bends and the blade moves as a rigid body. As reported in the table, the first bending mode of a single blade in a stiff fixture was 3.36Hz, which is close to the frequency of the next three modes identified by OMA at 3.13, 3.36 and 3.62Hz. Each of these modes shows the blade bending with the familiar shape reminiscent of the first mode of a cantilever beam. However, the mode shape of the 3.62Hz mode seems to show some displacement at the root of the blade. This would seem reasonable since the symmetric flapwise mode of a horizontal axis wind turbine such as this tends to occur at higher frequency than the yaw and tilt flapwise modes (see, e.g. [32, 33]). The mode seen at 4.38Hz in the tip measurement was not identifiable in the harmonic autospectrum, so its mode shape could not be determined. The first edgewise mode of this blade occurred at 5.24 Hz when the blade was mounted in the stiff fixture, so this peak in the tip spectrum may come about due to edgewise motion of the blade and the fact that the blade twists from root to tip. A 9.13Hz mode is also seen in the fixed point LDV test and not in the CSLDV test. It may have been buried in the harmonics of the other modes or may simply be poorly excited in the CSLDV test. The last three modes that are identified have shapes that agree very well with the second bending mode of a cantilevered beam, and their frequencies at 10.63Hz, 10.86Hz and 11.29Hz are similar to that of the blade in the fixture. All of these results were obtained from the CSLDV measurements at the 1.6 Hz scan frequency. Similar results were obtained at some of the other scan frequencies.

Table 3: Natural frequencies of wind turbine blade

| Mode | Conventional test in stiff fixture | Fixed point OMA on tower | CSLDV OMA on tower |
|--------------------------------|---------------------------------------|-----------------------------|-----------------------|
| - | - | 0.81Hz | 0.78Hz |
| Flap Wise Bending 1 | 3.36Hz | 3.13Hz | 3.13Hz |
| | | 3.37Hz | 3.36Hz |
| Edge Wise Bending 1 | 5.24Hz | 3.63Hz | 3.62Hz |
| | | 4.38Hz | - |
| - | - | 9.13Hz | - |
| Flap Wise Bending 2 | 11.40Hz | 10.63Hz | 10.62Hz |
| | | 10.94Hz | 10.86Hz |
| | | 11.25Hz | 11.29Hz |

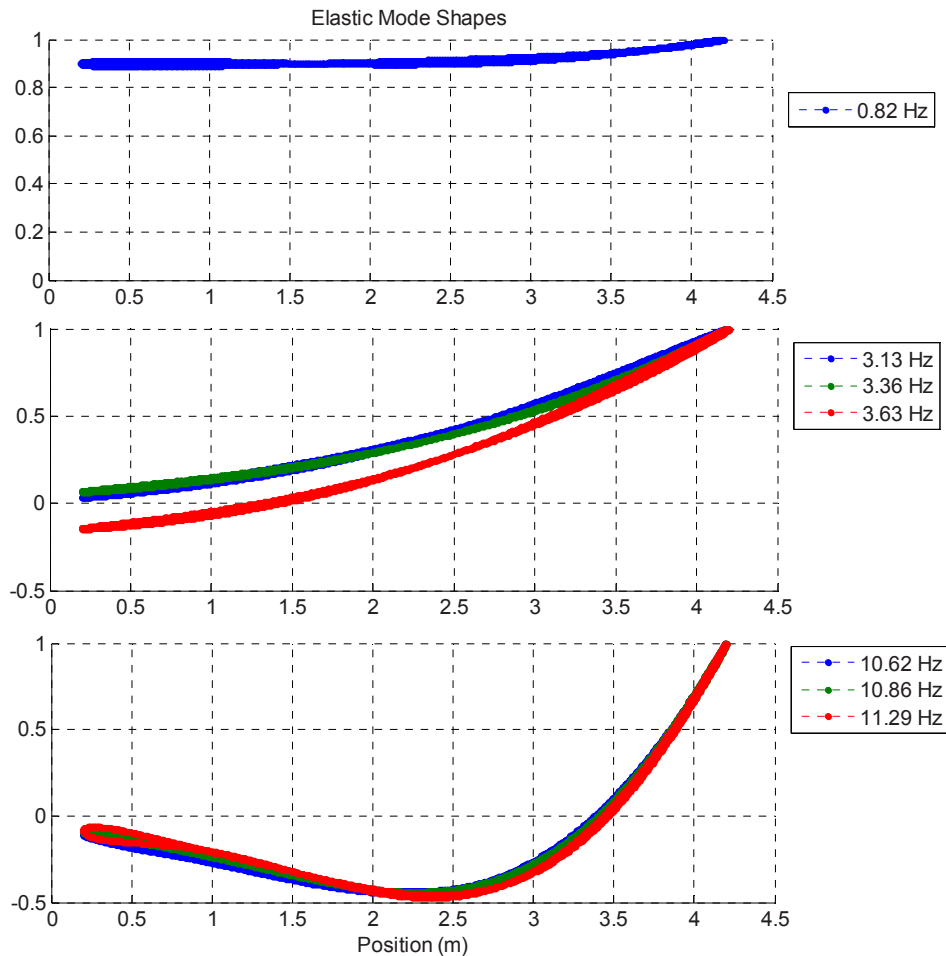


Figure 13: Mode shapes of wind turbine blade identified by CSLDV at 1.6Hz scanning frequency

5 Conclusions

This paper has extended Continuous Scanning Laser Doppler Vibrometry to output only measurements (OMA-CSLDV) by capitalizing on a recently developed system identification methodology for linear time-periodic systems. As with conventional OMA, the method assumes that the forces exciting the system are random, white and that they sufficiently excite all of the modes of interest. The theoretical development reveals that when CSLDV is used, each mode appears at several peaks in the power spectrum. The measured CSLDV signal is exponentially modulated to create what is called a harmonic power spectrum, and then a standard OMA algorithm such as peak-picking can be used to identify the modes of the system. Each identified mode is comprised of a set of Fourier coefficients that describe the variation of the mode shape as a function of time as the laser scans periodically. In this work, the harmonic power spectra were processed both by peak-picking and by curve fitting using a least squares algorithm (the Algorithm of Mode Isolation). Both methods gave good results for the systems studied here.

The new OMA-CSLDV methodology was first validated on a free-free beam in a laboratory setting. OMA-CSLDV was found to give results that were very similar to those obtained by the authors' hammer excited CSLDV method, identifying spatially detailed mode shapes of the first seven modes of the beam from one time record. Various scan frequencies were investigated and the associated issues were discussed. The output spectra shown here seemed to be considerably noisier than the spectra of the free-response that was processed in the previous work [13], but the same has been observed when comparing conventional OMA with EMA methods where the input forces are measured and controlled.

The methodology presented here was further studied by using it to measure the modes of a parked wind turbine. The vibrometer was used to measure the spectrum of the response at the tip of the blade (conventional

fixed-point OMA) and CSLDV measurements were also acquired along the length of one blade to identify the mode shapes of the turbine on that blade. Qualitatively reasonable results were obtained for seven modes of the turbine, which were found to correspond to a tower bending mode and the first two bending modes of the blades. It would have been preferable to have also measured the modes of the turbine by some other means so that the shapes obtained in that test could be validated, but that was not possible, so here they were only evaluated qualitatively.

It is informative to consider the effort and expense that would have been required to estimate the mode shapes of the turbine using conventional methods. In order to perform an OMA test using accelerometers, one would have to install sensors along the length of the blade and then run cables to a central data acquisition system (more than 30 meters if that was located on the ground). The sensors and cabling would mass load the blade to some extent, and all of the instrumentation would have to be removed after the test was complete. If conventional LDV were used to obtain the mode shapes, one would need at least one additional laser to serve as a reference. The other laser could then be roved to obtain the power spectrum at various points along the length of the blade. The laser must observe each point for at least 10 minutes to obtain a reasonable power spectrum, so a long test would be required to obtain even a few point measurements using that approach. Furthermore, the point measurements could be contaminated if the wind conditions and hence the excitation changed significantly as the test progressed from one point to the next. In contrast, the OMA-CSLDV method acquired reasonable mode shapes for several modes of the turbine from only two 10-minute time records (one fixed-point measurement at the tip and one 1.6 Hz CSLDV measurement).

6 Acknowledgements

This material is based on work supported by the National Science Foundation under Grant No. CMMI-0969224. The authors also wish to thank Renewegy LLC, www.renewegy.com, for making their facilities available for the testing described here and for their help and support in this regard.

7 References

- [1] M. S. Allen and D. M. Aguilar, "Model Validation of a Bolted Beam Using Spatially Detailed Mode Shapes Measured by Continuous-Scan Laser Doppler Vibrometry," in *50th AIAA/ASME/ASCE/AHS/ASC Structures, Structural Dynamics, and Materials Conference* Palm Springs, California, 2009.
- [2] P. Sriram, J. I. Craig, and S. Hanagud, "Scanning laser Doppler vibrometer for modal testing," *International Journal of Analytical and Experimental Modal Analysis*, vol. 5, pp. 155-167, 1990.
- [3] P. Sriram, S. Hanagud, and J. I. Craig, "Mode shape measurement using a scanning laser doppler vibrometer." vol. 1 Florence, Italy: Publ by Union Coll, Schenectady, NY, USA, 1991, pp. 176-181.
- [4] P. Sriram, S. Hanagud, and J. I. Craig, "Mode shape measurement using a scanning laser doppler vibrometer," *International Journal of Analytical and Experimental Modal Analysis*, vol. 7, pp. 169-178, 1992.
- [5] C. W. Schwingshackl, A. B. Stanbridge, C. Zang, and D. J. Ewins, "Full-Field Vibration Measurement of Cylindrical Structures using a Continuous Scanning LDV Technique," in *25th International Modal Analysis Conference (IMAC XXV)* Orlando, Florida, 2007.
- [6] A. B. Stanbridge and D. J. Ewins, "Modal testing using a scanning laser Doppler vibrometer," *Mechanical Systems and Signal Processing*, vol. 13, pp. 255-70, 1999.
- [7] A. B. Stanbridge, M. Martarelli, and D. J. Ewins, "Measuring area vibration mode shapes with a continuous-scan LDV," *Measurement*, vol. 35, pp. 181-9, 2004.
- [8] M. Martarelli, "Exploiting the Laser Scanning Facility for Vibration Measurements," Ph.D. Thesis, *Imperial College of Science, Technology & Medicine*, London: Imperial College, 2001.
- [9] A. B. Stanbridge, A. Z. Khan, and D. J. Ewins, "Modal testing using impact excitation and a scanning LDV," *Shock and Vibration*, vol. 7, pp. 91-100, 2000.
- [10] S. Vanlanduit, P. Guillaume, and J. Schoukens, "Broadband vibration measurements using a continuously scanning laser vibrometer," *Measurement Science & Technology*, vol. 13, pp. 1574-82, 2002.
- [11] M. S. Allen, "Frequency-Domain Identification of Linear Time-Periodic Systems using LTI Techniques," *Journal of Computational and Nonlinear Dynamics*, vol. 4, 24 Aug. 2009.

- [12] M. S. Allen and M. W. Sracic, "A New Method for Processing Impact Excited Continuous-Scan Laser Doppler Vibrometer Measurements," *Mechanical Systems and Signal Processing*, vol. 24, pp. 721–735, 2010.
- [13] S. Yang, M. W. Sracic, and M. S. Allen, "Two algorithms for mass normalizing mode shapes from impact excited continuous-scan laser Doppler vibrometry," *Journal of Vibration and Acoustics*, submitted, 2010.
- [14] M. S. Allen and M. W. Sracic, "Mass Normalized Mode Shapes Using Impact Excitation and Continuous-Scan Laser Doppler Vibrometry," in *8th International Conference on Vibration Measurements by Laser Techniques* Ancona, Italy, 2008, pp. 7098-3.
- [15] M. S. Allen, M. W. Sracic, S. Chauhan, and M. H. Hansen, "Output-Only Modal Analysis of Linear Time Periodic Systems with Application to Wind Turbine Simulation Data," in *28th International Modal Analysis Conference (IMAC XXVIII)* Jacksonville, Florida, 2010.
- [16] M. S. Allen, M. W. Sracic, S. Chauhan, and M. H. Hansen, "Output-Only Modal Analysis of Linear Time Periodic Systems with Application to Wind Turbine Simulation Data," *Mechanical Systems and Signal Processing*, vol. submitted Oct. 2010, 2010.
- [17] N. M. Wereley, "Analysis and Control of Linear Periodically Time Varying Systems," PhD Thesis, *Department of Aeronautics and Astronautics*, Cambridge: Massachusetts Institute of Technology, 1991.
- [18] N. M. Wereley and S. R. Hall, "Linear time periodic systems: transfer functions, poles, transmission zeroes and directional properties," in *Proceedings of the 1991 American Control Conference* Boston, MA, USA: American Autom. Control Council, 1991, pp. 1179-84.
- [19] N. M. Wereley and S. R. Hall, "Frequency response of linear time periodic systems," Honolulu, HI, USA, 1990, pp. 3650-3655.
- [20] L. Hermans and H. Van Der Auweraer, "Modal Testing and Analysis of Structures Under Operational Conditions: Industrial Applications," *Mechanical Systems and Signal Processing*, vol. 13, pp. 193-216, 1999.
- [21] E. Parloo, B. Cauberghe, F. Benedettini, R. Alaggio, and P. Guillaume, "Sensitivity-Based Operational Mode Shape Normalization: Application to A Bridge," in *22nd International Modal Analysis Conference (IMAC XXII)* Dearborn, Michigan, 2004.
- [22] B. Peeters and G. D. Roeck, "Stochastic System Identification for Operational Modal Analysis: A Review," *Journal of Dynamic Systems, Measurement, and Control*, vol. 123, December 2001.
- [23] A. Fasana, L. Garibaldi, E. Giorelli, and D. Sabia, "Z24 Bridge Dynamic Data Analysis by Time Domain Methods," in *International Modal Analysis Conference (IMAC XIX)* Kissimmee, Florida, 2001.
- [24] A. Guyader and L. Mevel, "Covariance driven subspace methods : input/output vs output-only," in *International Modal Analysis Conference (IMAC XXII)* Dearborn, Michigan, 2004.
- [25] M. Richardson and B. Schwarz, "Modal Parameter Estimation from Operating Data," in *Sound and Vibration*, 2003, pp. 28-36.
- [26] G. H. James and T. G. Carne, "Damping measurements on operating wind turbines using the natural excitation technique (NExT)," in *11th ASME Wind Energy Symposium presented at the Energy Sources Technology Conference and Exhibition*. vol. 12 Houston, TX, USA: Publ by ASME, New York, NY, USA, 1992, pp. 75-81.
- [27] A. Gasparoni, M. S. Allen, S. Yang, M. W. Sracic, P. Castellini, and E. P. Tomasini, "Experimental Modal Analysis on a Rotating Fan Using Tracking-CSLDV," in *9th International Conference on Vibration Measurements by Laser and Noncontact Techniques* Ancona, Italy, 2010.
- [28] S. Yang, M. W. Sracic, and M. S. Allen, "Two algorithms for mass normalizing mode shapes from impact excited continuous-scan laser Doppler vibrometry," *Journal of Vibration and Acoustics*, vol. Submitted Aug 2010, 2010.
- [29] S. Rothberg, "Numerical simulation of speckle noise in laser vibrometry," *Applied Optics*, vol. 45, pp. 4523-33, 2006.
- [30] S. J. Rothberg, "Laser vibrometry. Pseudo-vibrations," *Journal of Sound and Vibration*, vol. 135, pp. 516-522, 1989.
- [31] M. S. Allen and J. H. Ginsberg, "A Global, Single-Input-Multi-Output (SIMO) Implementation of The Algorithm of Mode Isolation and Applications to Analytical and Experimental Data," *Mechanical Systems and Signal Processing*, vol. 20, pp. 1090–1111, 2006.
- [32] S. Chauhan, M. H. Hansen, and D. Tcherniak, "Application of Operational Modal Analysis and Blind Source Separation / Independent Component Analysis Techniques to Wind Turbines," in *27th International Modal Analysis Conference (IMAC XXVII)* Orlando, Florida: SPIE, 2009.
- [33] J. Jonkman, "NREL 5 MW Baseline Wind Turbine," Technical report, NREL/NWTC, 1617 Cole Boulevard; Golden, CO 80401-3393, USA 2005.

Coupling a compliant structure with a Hand – arm system using FBS

Sébastien Perrier, PhD student
Dr. Yvan Champoux, Professor
Dr. Jean-Marc Drouet, Associate Professor

VélUS, Université de Sherbrooke,
Department of mechanical engineering,
2500 boul. de l'Université, Sherbrooke (Québec),
CANADA, J1K 2R1

ABSTRACT

The vibrational behavior of a lightweight compliant structure with low damping is strongly influenced by contact with parts of the human body. In this work, a close look is taken at the influence of the hand-arm system in the context of cycling sports. Force transmitted to the hand, along with hand-arm vibration, generates discomfort and sometimes results in injury. Designing structural changes in a given road bike component with the goal of reducing discomfort requires a clear understanding, in this case, of the interaction mechanisms between the hand-arm system and the handlebar (the coupled structure).

This paper describes an experimental investigation of this type of interaction between the hands and a handlebar using an FRF Based Substructuring method (FBS) to calculate the resulting dynamic behavior of the coupled structure. The equations supporting the FBS method for this particular application are presented. The compliant structure and the hand-arm system are individually characterized by mechanical mobility Frequency Response Functions (FRF) in the frequency range of 20-400 Hz. Hand mobility is obtained by using the FBS method in a reverse manner. The influence of the hands and the upper body position on hand-arm mechanical mobility is considered. The merits and limitations of using FBS are discussed.

INTRODUCTION

In a recent trend, the cycling sports market has witnessed the emergence of rider comfort as the most desirable characteristic in a bike along with performance. Rider comfort is a subjective human experience, and although traditional evaluations have been carried out by expert panels, most notably in the automotive industry, no similar studies have been done in the cycling field. As a consequence, objective evaluation indicators and universal design guidelines have not yet been developed. Quantification of human sensitivity in evaluating rider comfort using measured physical values thus emerges as an interesting avenue for research [1]. Recent evaluation methods focusing on vibration sensitivity characteristics and human vibration characteristics have attracted intense scrutiny. For future developments and designs, there is a need to establish a clear understanding of the dynamic involved, and a method to evaluate rider comfort that focuses on the improvement of specific bike components.

In the context of functioning as a system in tandem with the human body, the dynamic behavior of a lightweight structure changes radically from its original uncoupled condition. The dynamic behavior of the human body has to be taken into account in order to evaluate how the system is modified and to evaluate the response in terms of transmitted force or measured velocity at the interface points. Furthermore, vibrations transmitted to the human body through the structure generate discomfort, can also reduce performance or even cause injury.

The purpose of this study is to establish the basic mechanical knowledge of the coupling between a structure and a unit or dynamic system of the human body. Rider comfort would thus take into account human sensitivity as well as the dynamic behavior of an entire system composed of various units.

In this work, the FBS technique (Frequency Response Function Based Substructuring) is used in an investigational manner to couple a structure assembled from both mechanical components and human body parts. This technique was chosen because it enables us to couple various components from an overall structure using their individual dynamic behaviors. It also allows us to classify these elements in terms of vibration isolation capacity. An original element in this paper is that this technique has been used with the human hand-arm system, which is known to be nonlinear. Moreover, this method can be used when only mobility data at the connecting points are known, which is the case with the human body where only the interface points are of interest. Since this approach is an investigational one, the merits and limitations of using the technique with human involvement will be discussed.

There are only three contact points between the cyclist and the bike: hand-transmitted vibration is thus one of the major concerns for road bike comfort. In this paper, the coupling between the cyclist and the bike at the points of the handlebar has been examined. Road excitation is predominant along the vertical Z-axis, therefore the excitation considered in this paper will be limited to this direction.

Hand position and direction, along with other factors, have a strong influence on the dynamic behavior of the hand-arm system [2; 3]. For the sake of accuracy when using the FBS method, hand mobility data that represent real operating conditions must be used. However, this data does not exist in the literature. A technique employing the FBS method in a reverse manner has therefore been selected to obtain hand-arm input mechanical mobility.

A bike's dynamic behavior is also strongly influenced by the cyclist's position and posture [4]. A typical cycling position was used and posture was controlled for by measuring the cyclist's leaning vertical DC force applied to the stem.

The merits and limitations of this approach will be examined by comparing experimental values obtained with the assembled structure to the data calculated using the FBS method. Results show solid agreement which confirms that this method is promising.

COUPLING METHODOLOGY USING THE FBS INTERFACE EQUATIONS

To obtain the dynamic behavior of a complete structure using the dynamic contribution of its components, a generalized frequency domain substructure synthesis was used. This well known technique, also referred to as FBS (Frequency Based Substructuring), combines the response FRF data of each component to analyze the dynamics of an assembled structure. The dynamic behavior of the assembled structure can be synthesized through the method presented here. This method is based on an implicit statement of the force and velocity continuity considerations at the connection nodes and enables substructures to be coupled by considering interface characteristics only [5; 6]. The two substructures involved in this paper (the hands and the handlebar) can be effectively characterized separately by measuring their respective input mobilities. The methodology is thus ideally suited to the analysis of hands-on-handlebar coupling.

Let's consider two substructures as shown in [Fig. 1](#).

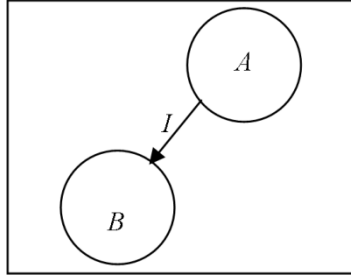


Figure 1. Diagram of two coupled substructures A and B with interface coupling interface I

The known mathematical expression of the mobility FRF coupling method is:

$$\begin{bmatrix} Y_{AA}^{ab} & Y_{AI}^{ab} & Y_{AB}^{ab} \\ Y_{IA}^{ab} & Y_{II}^{ab} & Y_{IB}^{ab} \\ Y_{BA}^{ab} & Y_{BI}^{ab} & Y_{BB}^{ab} \end{bmatrix} = \begin{bmatrix} Y_{AA}^a & Y_{AI}^a & 0 \\ Y_{IA}^a & Y_{II}^a & 0 \\ 0 & 0 & Y_{BB}^b \end{bmatrix} - \begin{Bmatrix} Y_{AI}^a \\ Y_{II}^a \\ -Y_{BI}^b \end{Bmatrix} \left[Y_{II}^a + Y_{II}^b \right]^{-1} \begin{Bmatrix} Y_{IA}^a \\ Y_{II}^a \\ -Y_{IB}^b \end{Bmatrix}^T \quad (1)$$

where superscripts a and b identify the two substructures involved.. For the subscripts:

A is the set of internal degrees of freedom of structure a ,

I is the set of interface contact points degrees of freedom between the substructures a and b and

B is the set of internal degrees of freedom in structure b .

In this paper, substructure a represents a handlebar connected to a stem which is clamped to a rigid steel table. The stem handlebar end is identified as point $A1$. This point will be used to apply an external force and is part of the internal set of the degrees of freedom A of structure a . Substructure b is the hand-arm system. The contact points between the two structures (hands and handlebar) are designated $I1$ and $I2$. They represent the set of interface contact point degrees of freedom I , as illustrated in Fig. 2.

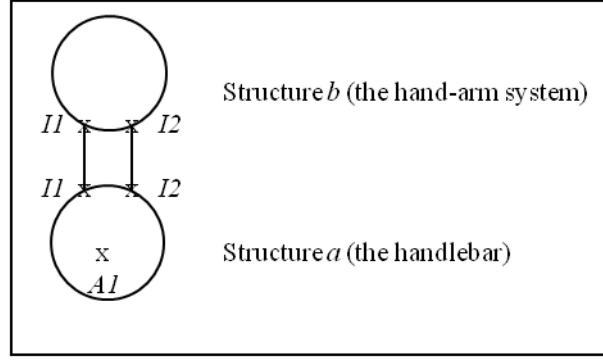


Figure 2. Symbolic coupling of the two substructures with the points of interest

The context of this study is the transmission of vibration to the cyclist. Only the contact points between the hand and the handlebar are of interest and consequently only one specific term from Eq. (1) is relevant:

$$Y_{IA}^{ab} = Y_{IA}^a - Y_{II}^a [Y_{II}^a + Y_{II}^b]^{-1} Y_{IA}^a \quad (2)$$

where Y_{IA}^{ab} corresponds to an excitation force applied in A and a velocity response in I for the assembled structure ab . Considering that set A contains point $A1$, and set I points $I1$ and $I2$, Eq. 2 becomes:

$$\begin{bmatrix} Y_{I1A1}^{ab} \\ Y_{I2A1}^{ab} \end{bmatrix} = \begin{bmatrix} Y_{I1A1}^a \\ Y_{I2A1}^a \end{bmatrix} - \begin{bmatrix} Y_{I1I1}^a & Y_{I1I2}^a \\ Y_{I2I1}^a & Y_{I2I2}^a \end{bmatrix} \left[\begin{bmatrix} Y_{I1I1}^a & Y_{I1I2}^a \\ Y_{I2I1}^a & Y_{I2I2}^a \end{bmatrix} + \begin{bmatrix} Y_{I1I1}^b & Y_{I1I2}^b \\ Y_{I2I1}^b & Y_{I2I2}^b \end{bmatrix} \right]^{-1} \begin{bmatrix} Y_{I1A1}^a \\ Y_{I2A1}^a \end{bmatrix} \quad (3)$$

Assumptions

- Hands are uncoupled ($Y_{I1I2}^b = 0$; $Y_{I2I1}^b = 0$).
- Only vertical axis Z is considered for the excitations or the responses
- There are no couplings between the three directional axes (X , Y , and Z) for each substructure. All measurements are along the vertical Z axis.
- Left and right hand measurements are identical because $Y_{I1zI1z}^b = Y_{I2zI2z}^b$.

Formulation

Using the assumptions, the following expression is obtained:

$$\begin{bmatrix} Y_{1zAz}^{ab} \\ Y_{2zAz}^{ab} \end{bmatrix} = \begin{bmatrix} Y_{1zAz}^a \\ Y_{2zAz}^a \end{bmatrix} - \begin{bmatrix} Y_{1z1z}^a & Y_{1z2z}^a \\ Y_{2z1z}^a & Y_{2z2z}^a \end{bmatrix} \left[\begin{bmatrix} Y_{1z1z}^a & Y_{1z2z}^a \\ Y_{2z1z}^a & Y_{2z2z}^a \end{bmatrix} + \begin{bmatrix} Y_{1z1z}^b & 0 \\ 0 & Y_{1z1z}^b \end{bmatrix} \right]^{-1} \begin{bmatrix} Y_{1zAz}^a \\ Y_{2zAz}^a \end{bmatrix} \quad (4)$$

Specific method to obtain the dynamic characteristics of the hands

In Eq. 4, the only term related to the hands is Y_{1z1z}^b . In practice, this term cannot be measured directly [7]. Hand mobility is influenced by several factors such as the direction the hands are facing, grip, and the push forces. A specific technique to evaluate this term was developed so that measurements using a typical and realistic posture could be taken. Using the same setup as described previously, the handlebar was replaced by a stiff, short hollow tube long enough for the placement of both hands. This new structure, a short tube connected to a stem clamped to a stiff table, is called structure *c*. This structure does not have any mode in the frequency range of interest. Using Eq. 4 and replacing structure *a* by structure *c*, Eq. 5 can be obtained.

$$\begin{bmatrix} Y_{1z1z}^b & 0 \\ 0 & Y_{1z1z}^b \end{bmatrix} \left[\begin{bmatrix} Y_{1z1z}^c & Y_{1z2z}^c \\ Y_{2z1z}^c & Y_{2z2z}^c \end{bmatrix} \right]^{-1} \left[\begin{bmatrix} Y_{1zC1z}^c \\ Y_{2zC1z}^c \end{bmatrix} - \begin{bmatrix} Y_{1zC1z}^{cb} \\ Y_{2zC1z}^{cb} \end{bmatrix} \right] = \begin{bmatrix} Y_{1zC1z}^{cb} \\ Y_{2zC1z}^{cb} \end{bmatrix} \quad (5)$$

All the terms from this equation can be measured and Y_{1z1z}^b can be computed. This is a sort of reverse way of using the FBS method. Instead of using the dynamic behavior of two substructures *b* and *c* to calculate the dynamic behavior of the assembled structure *cb*, measurements from structures *cb* and *c* are used to calculate the dynamic behavior of substructure *b*.

EXPERIMENTATION

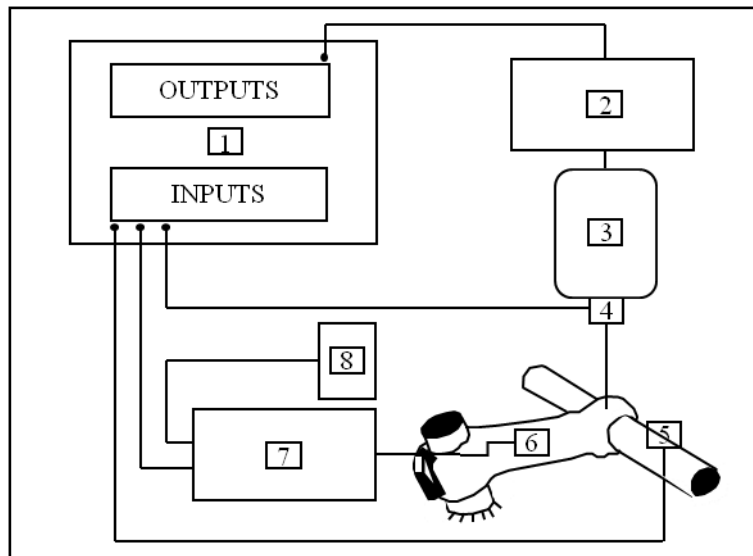


Figure 3. Diagram of the measurement system

- 1) LMS Test.Lab software Rev 10A (Spectral Testing, Random Excitation, Hanning Windowing, 0.5 Hz resolution)
- 2) Power amplifier type 2706 from Brüel & Kjaer for the shaker
- 3) Vibration exciter type 4809 from Brüel & Kjaer (shaker)
- 4) Force sensor 208C03 type ICP from PCB Piezotronics
- 5) Accelerometer 356B11 type ICP from PCB Piezotronics
- 6) Instrumented stem with strain gauges to obtain the static vertical push force from the hands
- 7) Signal conditioning amplifier type 2310 from Vishay for the stem
- 8) Fluke 112 True RMS multimeter to allow the subject to control his posture

Dynamic characterization of the hands

This section of the paper describes the materials and the procedure used to get the term $Y_{11z/1z}^b$ which represents the dynamic characteristic of the hand (structure b).

The intrinsic dynamic characteristics of the hands were obtained using the measurement system. The handlebar was replaced by a hollow aluminum tube long

enough for both hands. The tube has a circular section with a diameter of 2.54 cm; it is 20 cm long with a wall thickness of 3.18 mm.

Figure 4 shows the diagram of the measurement showing the stiff hollow tube and the measurement location $C1$, $I1$ and $I2$. The accelerometer was placed under the tube but it was assumed that the acceleration levels at the top and bottom of the tube are the same.

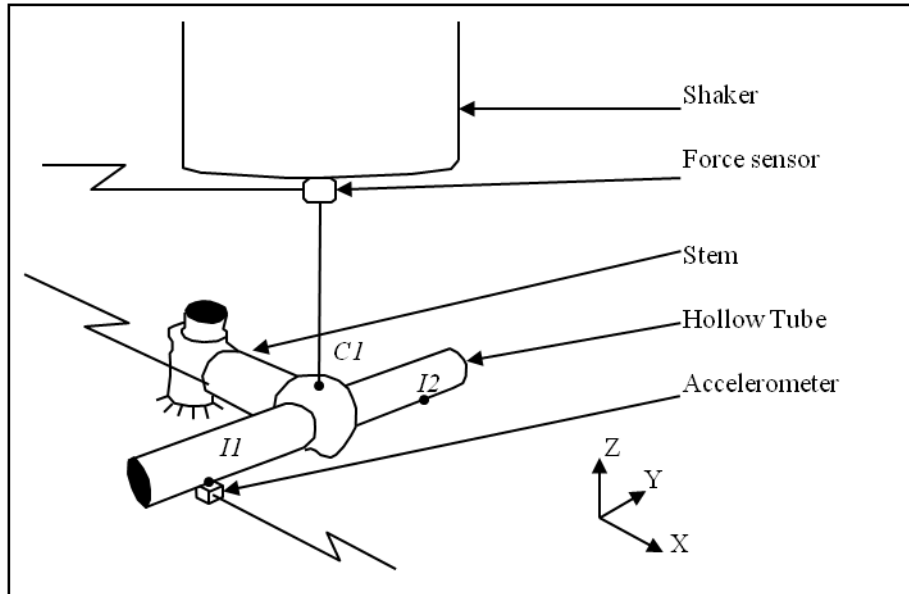


Figure 4. Experimental setup to measure the dynamic behavior of the hands $Y_{I1z/I1z}^b$

Typical cyclist position was used and the posture was controlled by measuring the cyclist's leaning vertical DC force applied to the instrumented stem. Looking at the monitored DC force value, the cyclist was asked to keep the force constant at a level of 110 N. The data was obtained in 2 steps with 2 configurations:

- Tests on structure c , meaning that no hands are touching the tube to measure $Y_{I1z/C1z}^c, Y_{I2z/C1z}^c, Y_{I1z/I1z}^c, Y_{I1z/I2z}^c, Y_{I2z/I1z}^c, Y_{I2z/I2z}^c$
- Tests with the hands on the tube, corresponding to structure cb to get $Y_{I1z/C1z}^{cb}, Y_{I2z/C1z}^{cb}$

Dynamic characterization of structure *a* and measurement on structure *ab*

The objective of this paper is to investigate the FBS method (Eq. 4) to determine if it can provide accurate results when a compliant low damped mechanical structure and a human body segment are involved.

This section presents the method used to obtain the dynamic characteristics of the other structure (structure *a* stem-handlebar) and to obtain this measurement when both structures are coupled (*a* and *b*).

For the sake of simplicity in this investigational work, a simple homemade handlebar was manufactured. As shown in Figure 5, we used a hollow aluminum tube with a circular section of 2.54 cm in diameter, a wall thickness of 1.59 mm and a total length of 55 cm. The modal behavior of a real road handlebar was tested to measure its first natural frequency. This information was used to select the mass (0.68 kg) of two steel cylinders fixed at both ends of the tube. The objective was to obtain a similar first natural frequency for the custom-made handlebar. The same measuring system is used and an input force is applied on *A1*. Fig. 5 shows the custom-made handlebar along with the measurement points *A1*, *I1*, *I2*.

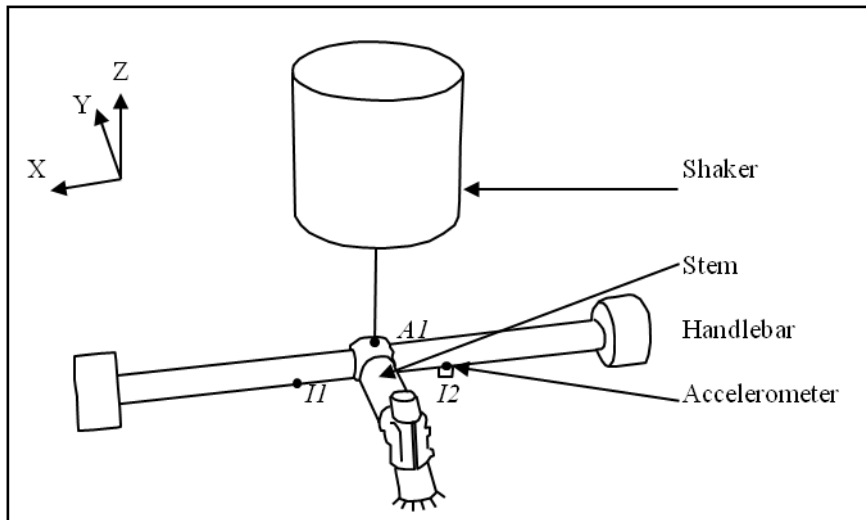


Figure 5. Experimental setup for measurement on structure *a* (handlebar- clamped stem)

Two sets of measurements were also done using the structure shown in Fig.5

- Tests on structure *a* to measure $Y_{I1zA1z}^a, Y_{I2zA1z}^a, Y_{I1zI1z}^a, Y_{I1zI2z}^a, Y_{I2zI1z}^a, Y_{I2zI2z}^a$
- Tests on the structure shown in Fig.5 with the hands on the handlebar which corresponds to structure *ab* to get $(Y_{I1zA1z}^{ab}, Y_{I2zA1z}^{ab})$

The same position and posture as described previously were used in this test.

RESULTS

- Dynamic characterization of the hands

The Fig. 6 shows the mobility obtained at point *II* for the structure b (the hands) using the FBS technique in a reverse way. Results show various damped peaks mainly in the frequency range of 50 - 200 Hz. They reveal the dynamic behavior of the hand-arm system for a specific cyclist position and push force. There is no data available for comparison in the published scientific literature.

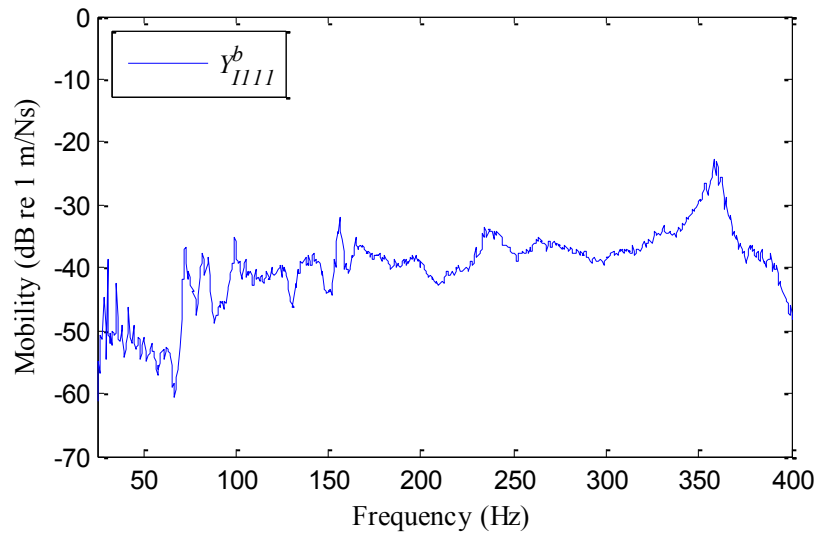


Fig. 6. Mobility of Y_{IIII}^b

- Dynamic characterization of structure a

The Fig. 7 shows the mobility between points $A1$ and $I1$ which was measured on structure a (handlebar-clamped stem). This result along all the other measured mobilities Y_{I1zA1z}^a , Y_{I2zA1z}^a , Y_{I1zI1z}^a , Y_{I1zI2z}^a , Y_{I2zI1z}^a , Y_{I2zI2z}^a provide the intrinsic dynamic characteristic of structure a . This undamped structure has 2 modes as shown in Fig.7 by the two peaks at 56 Hz and 280 Hz. On Fig. 7, the mobility Y_{I1zA1z}^{ab} measured with the hands in contact to handlebar is provided. This shows the influence of the hands on the structure a . The hands essentially add damping to the 2 modes.

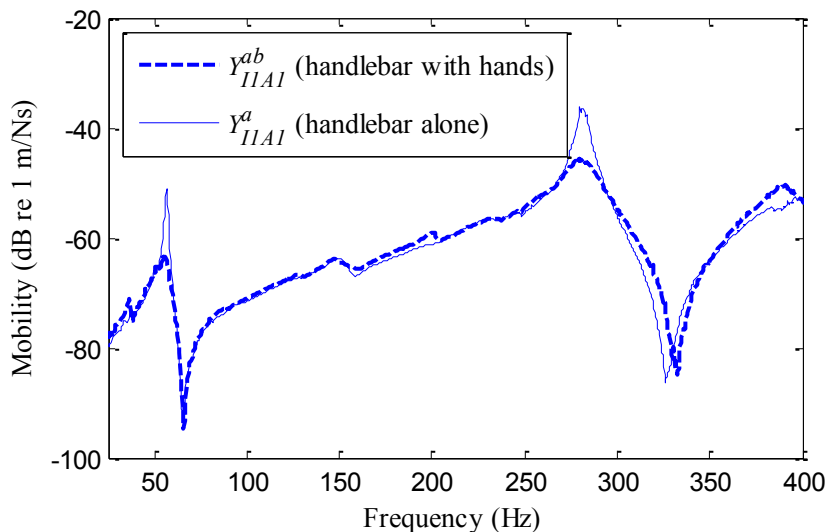


Fig. 7. Mobility measured between point $A1$ and $I1$.
 Solid line: structure a (handlebar-clamped stem)
 Dashed line: structure ab : hands grip the handlebar

- Measured and calculated results

The Figs. 8 and 9 show results in relation to the main objective of this paper. Two mobility curves are presented. The solid line represents the calculated results for the assembled structure ab obtained by using the intrinsic characteristics of both structures a and b using Eq. 4. The dashed line represents the measured curve when the hands were grasping the handlebar. The agreement between the curves is satisfactory at this stage of development in the ongoing project.

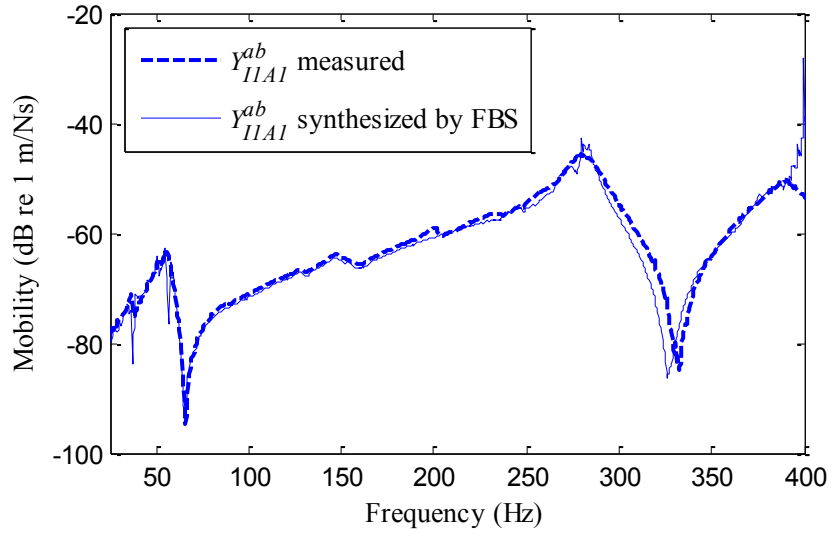


Fig. 8. Mobility measured between points $A1$ and $I1$ on structure ab . Solid line: calculated results; Dashed line: measure where hands are on the handlebar

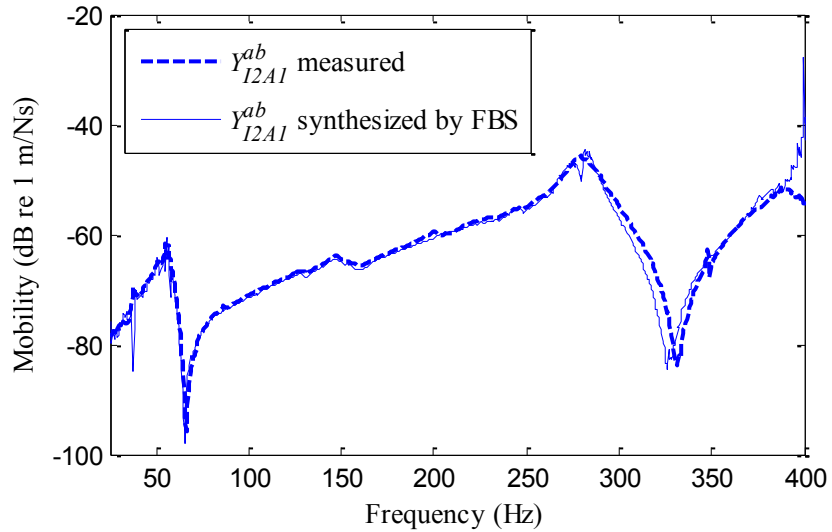


Fig. 9. Mobility measured between points $A1$ and $I2$ on structure ab . Solid line: calculated results; Dashed line: measure where hands are on the handlebar

DISCUSSION

Figures 8 and 9 show that the FBS method succeeds in providing reliable results which gives a strong indication that coupling between a human body part and a compliant structure is possible using this method. These results cannot invalidate the assumptions that the hands are well uncoupled; that for a vertical excitation, only Z axis results need to be considered and finally, that the left and right hand have similar intrinsic characteristics and the same influence on structure a .

This work highlights the following characteristics of the FBS method

- Merits:
 - Direct use of shaker test data
 - Combination of substructures when only interface data is known
 - Direct and relatively simple calculation
- Limitation

One important disadvantage of the technique is the requirement of measuring a full matrix of FRFs for all the points and degrees of freedom involved. According to the results in some specific cases such as the one described in this paper, only degrees of freedom of interest would be needed to be considered to get appropriate results.

The hand-arm systems input mobilities are sensitive to several factors such as position, orientation, etc. Also, the human body input mobility depicts some non-linear behavior. The technique used in this paper to measure the hand-arm dynamic characteristics allows us to obtain data while taking into account the specific real life posture, attitude and hand preload of the cyclist. It is believed that this minimizes the non-linear effect and enables measurements under real operating conditions. Another interesting feature of this approach is that it does not require any complex setups or instrumentation using large electromagnetic shakers, instrumented handles, etc. because in this case, the same basic structure studied (stem) is also used to get the hand-arm characteristics. However, a legitimate question is: are these results fundamentally intrinsic to the hand-arm segment. Answering this question will require further investigation.

Despite its limitation and the need to process a large amount of data when several structures are coupled through several contact points, the preliminary results disclosed in this work indicate that the FBS method is a promising solution to study vibration interaction mechanisms between a structure and a human body part.

REFERENCES

- [1] Richard S., Champoux Y., “Development of a metric related to the dynamic comfort of a road bike”, Proc. IMAC XXIV, St. Louis, 2006
- [2] Aldien Y., Marcotte P., Rakheja S., Boileau P-E., “Mechanical Impedance and Asorbed Power of Hand-Arm under x_h -axis Vibration and Role of Hand Forces and Posture”, Industrial Health, 43 : 495 – 508, 2005
- [3] Burström L., “The influence of biodynamic factors on the mechanical impedance of the hand and arm”, International Archives of Occupational and Environmental Health, 69 : 437 – 446, 1997
- [4] Richard S., « Etude du comportement dynamique d’un vélo de route en lien avec le confort du cycliste », Université de Sherbrooke, MScA Thesis, 2005
- [5] Ewins D. J., “Modal Testing: theory, practice and application”, 2nd edition Research Studies Press, 2000
- [6] Jetmundsen B., “On frequency domain methodologies for prescribed structural modification and subsystem synthesis, Rensselaer Polytechnic Institute”, New York, PhD Thesis 1986
- [7] Burström L., “Measurement of the impedance of the hand and arm”, International Archives of Occupational and Environmental Health, 62 : 431 – 439, 1990

A Comparison of Accelerometer Selection Methods for Modal Pretest Analysis

Daniel Linehan
Kevin Napolitano
ATA Engineering, Inc.
11995 El Camino Real, Suite 200
San Diego, California 92130

ABSTRACT

Prior to performing a modal survey test, pretest analysis is typically performed to determine the optimal number and location of response measurements (usually acceleration) and reference measurements (dynamic loads). This pretest analysis begins with the preparation of an accurate finite element model (FEM). Typically, the test measurement set cannot practically contain more than several hundred degrees of freedom (DOF) (although some recent tests have used as many as a thousand), so any method of pretest analysis should extract the best possible candidate locations from the initial FEM. Automated sensor selection algorithms first up-select to a candidate set of potential degrees of freedom that are several times larger than the final set of sensors. The methods then down-select from this candidate set to an optimal set of sensors. This paper presents the methods used to arrive at an initial candidate set for measurements, from the perspective of a practicing test engineer. Specifically, the iterative residual kinetic energy (IRKE) method is compared to manual DOF selection, noting the advantages and drawbacks of each. While some test articles may lend themselves to simple manual DOF selection (i.e., symmetric structures such as aircraft), others are far more asymmetric and may require more rigorous analytic methods to complement or entirely replace any manual selection of a candidate set. This paper utilizes an "iron bird" demonstration test article as a tool to compare and contrast these candidate DOF selection methods.

INTRODUCTION

To increase the chances of a successful test, modal survey tests should often be prefaced with an accurate pretest analysis of the test article. A variety of tools and methods are available to select an optimized set of acceleration response measurements. Pretest analyses begin with a cursory examination of the dynamic FEM to determine the target modes that must be extracted to complete a successful test program. Once these target modes are identified, a mass-reduced test-analysis model (TAM) is generated by determining an accelerometer set (ASET) that uniquely describes the target modes. The number of accelerometers that can be used may be limited by resources such as available test time, budget, and data acquisition channels. Generally, no more than ten accelerometers per target mode will be necessary to adequately capture all target modes.

While purely analytical methods exist to generate a TAM and a highly efficient ASET that minimizes the ASET and maximizes the quality of extracted modes, practical considerations influence the final ASET development. Analytically generated TAMs may select measurement DOF that are not physically realizable on the test article. For example, selected measurement DOF may include inaccessible locations such as internal components, locations that are unreachable on large test articles, or locations that cannot physically accommodate the dimensions of available accelerometers. Manual effort can be spent to remove these inaccessible locations from consideration in the automated selection of the candidate set.

Often, analytically selected measurement DOF are accessible but accelerometer installation may still be difficult or cause unnecessary delays in the test program. Examples of such measurement DOF may include:

1. Locations requiring the removal of paneling to access internal components.
2. Locations requiring technical support personnel to operate a manlift.
3. Locations that are not easily referenced to identifiable features of the test article such as rivet lines, edges or corners; with additional time and effort, such locations may still be identified by a template or laser tracker.

This paper discusses the compromises that can be made when developing the TAM in order to successfully extract all target modes while minimizing the difficulty of installing the sensors. The ultimate figure of merit for a successful pretest is the pseudo-orthogonality, defined in the following section. Holding the number of accelerometers constant, a purely analytically derived TAM will produce the best possible pretest pseudo-orthogonality. A TAM that has been adjusted to allow for an easily installed and maintained ASET may have a slightly degraded, but still sufficient, pseudo-orthogonality. The following sections describe the pretest analysis process, including the iterative residual kinetic energy (IRKE) method to select the candidate accelerometer locations, the genetic algorithm for down-selecting to an optimal set of accelerometers, and how these relate to the construction of the test display model (TDM). The specific test article studied in this paper is the “iron bird,” which was fabricated by ATA Engineering, Inc., (ATA) as an internal development and training tool that simulates the dynamics and form factor of a fighter jet. While only the FEM of the iron bird is studied in this paper, the physical test article is depicted in [Figure 1](#) undergoing a modal test.

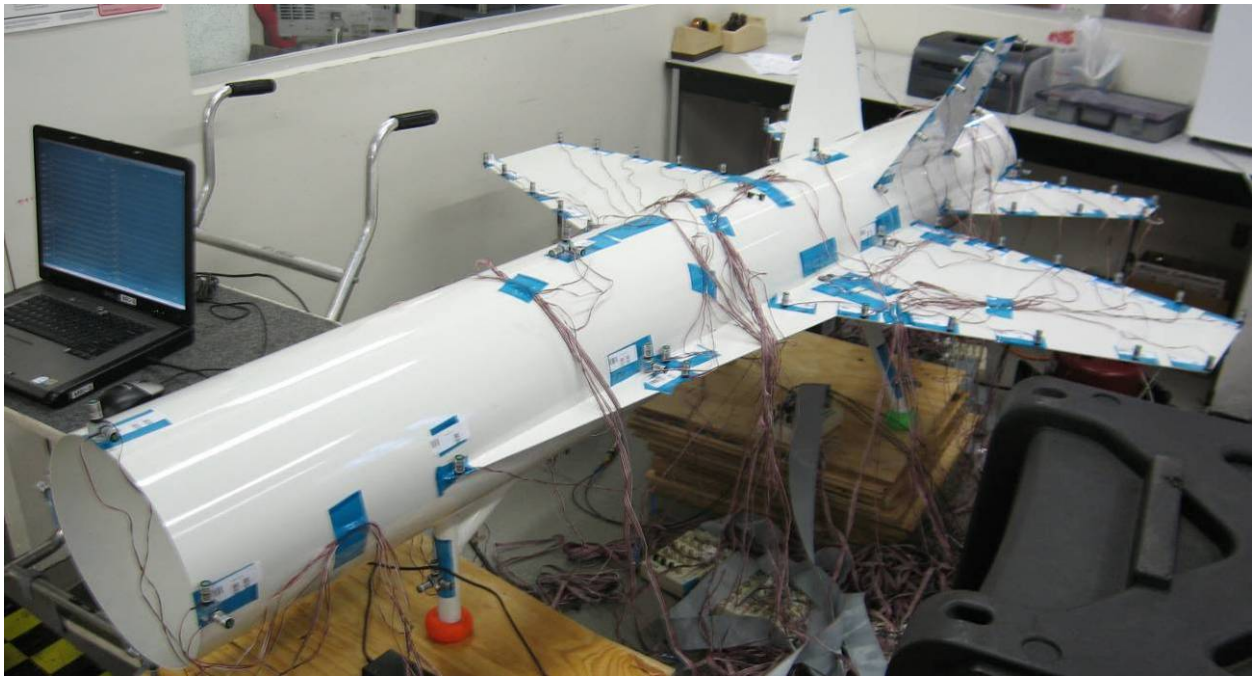


Figure 1. ATA “iron bird” test article.

DESCRIPTION OF ANALYTIC PRETEST PROCESS

A successful pretest analysis results in an optimized ASET that captures all pretest target modes, as evidenced by the pseudo-orthogonality:

$$[O_{12}] = [\Phi_1]^T [M_{AA}] [\Phi_2] \quad \text{Equation 1}$$

where $[\Phi_1]$ and $[\Phi_2]$ are full FEM mode shape matrices parsed to the ASET DOF, and $[M_{AA}]$ is the TAM analytical mass matrix. Ideally, the on-diagonal terms of this matrix should be 0.95 or greater, and the off-diagonal terms should be less than 0.10.

The ASET is derived from the test article's dynamic FEM, which may contain several hundred thousand DOF. Once the target modes are defined, the IRKE method can be used to generate an initial candidate ASET from the full FEM. The IRKE method is particularly useful for test articles with complex form factors and multiple mass simulators, such as large satellites. The IRKE method functions by assessing the modal kinetic energy of all translational DOF in the test article FEM, and iteratively determining which DOF are most important with respect to the supplied target modes [1]. The user inputs an initial DOF set (this is generally very small—it need only be a single DOF) and requests a final number for the candidate ASET DOF. Additional DOF are selected that are not included in the initial DOF set, and the process is repeated until the final user-requested DOF set is completed. All IRKE analyses presented in this paper were completed using NX Nastran™.

Once the IRKE method is completed, the pseudo-orthogonality of the candidate ASET must be checked. If the pseudo-orthogonality does not meet the aforementioned numeric quality, this is likely due to an insufficient number of requested DOF for the candidate ASET; the user must regenerate the candidate ASET, requesting a larger number until a satisfactory pseudo-orthogonality is achieved.

Once the initial candidate ASET is established, additional analytic methods exist to reduce the ASET to the final measurement ASET, if the candidate set is purposely too large. The genetic algorithm (GA) is used frequently to establish a final ASET that is within the available accelerometer budget [2]. As with the initial IRKE analysis, the pseudo-orthogonality of the final TAM must be checked to verify that all target modes will be attainable during testing.

The use of the IRKE up-selection and GA down-selection methods generates an efficient ASET for a pre-determined accelerometer budget. To prepare for an efficient test program, a more heuristic approach is needed, and both of these methods can provide guidance in arriving at a practical TAM. The following section discusses the complete pretest process on the iron bird test article, highlighting this heuristic approach from the viewpoint of a practicing test engineer.

PRETEST ANALYSIS OF THE IRON BIRD TEST ARTICLE

The iron bird FEM is comprised of 6194 nodes and 6057 elements (mostly quadrilateral plate elements—CQUAD4). Only translational DOF were considered in the development of the TAM, bringing the maximum possible candidate set to $6194 * 3 = 18582$. The prior modal test on the physical test article required 105 test DOF, so this number is used as the target ASET size for this current pretest study. All modes up to 55 Hz were considered target modes (including the six rigid body modes), resulting in a total of 26 target modes based on an analysis of the full dynamic FEM.

The IRKE method was run on the dynamic FEM, with six initial seed DOF located at the wingtips, tail tips, and fuselage. The IRKE method was run with a requested 1000 ASET DOF. The pseudo-orthogonality of this result was checked, verifying that this 1000-DOF TAM is nearly identical to the full FEM. GA was applied to this TAM with ASET requests of 105, 95, 85, 75, and 65 measurement DOF. Based on the pseudo-orthogonality results, the 75-DOF TAM yielded a quality ASET; the result is displayed in [Figure 2](#). The pseudo-orthogonality is displayed at the top of the figure and the FEM at the bottom. Values less than 0.01 are not displayed in the pseudo-orthogonality. The arrows plotted on the FEM represent selected accelerometer locations. While the pseudo-orthogonality verifies whether the TAM quality is good, the ASET—generalizing the result displayed in [Figure 2](#) to many different types of test articles encountered by ATA—has the following practical disadvantages.

1. The accelerometer spacing is uneven and irregular. This will require individual measurements for locating and marking each accelerometer in the ASET, requiring an excessive amount of test set-up time.

2. The selected accelerometer locations may not correspond to easily identifiable hardware features such as rivet lines, edges, or mass simulator edges or corners. Additionally, these locations may not reference convenient local displacement coordinate systems, which would otherwise allow accelerometer installations that are normal or parallel to test article surfaces.
3. The selected accelerometer locations may be difficult or impossible to access. Inaccessible locations may include internal components or unreachable surfaces. Other difficult locations may include locations on tall structures requiring technical support (e.g., the use of a manlift and accompanying operator support).

Instead of the fully automated IRKE and GA selection method, the ASET can be selected manually based on test engineering experience. The TDM, ASET, and TAM were generated manually for the initial modal test of the iron bird. The 105-DOF ASET and pseudo-orthogonality are presented in [Figure 3](#). The accelerometers are deliberately located on the edges of the test article and are spaced evenly for a convenient and simple test setup. However, the pseudo-orthogonality indicates that the TAM is not sufficient—and that the ASET may not adequately capture all target modes. To verify that the manual TDM ASET selection is insufficient, the pseudo-orthogonality was checked by including all three DOF for every node in the TDM. The 243-DOF result is displayed in [Figure 4](#). Since this represents the best-case scenario for the manual TDM selection, a GA reduction is irrelevant until the initial TAM is improved.

Modes 15, 16, 25, and 26, which are plotted in [Figure 5](#), are the modes requiring additional instrumentation. These four modes are wing modes. Both the plotted mode shapes in [Figure 5](#) and the IRKE/GA result provide guidance for the next step in the pretest process. Specifically, accelerometers placed manually in the center of the wings and tails should sufficiently strengthen the TAM. If the accelerometer budget must be held constant at 105, the TAM may be improved by adding 126 additional candidate DOF at 42 regularly spaced locations on the centers of the wings and tails, and running a GA reduction. The TAM is checked again with this new 369-DOF candidate set, and the result is shown in [Figure 6](#). The pseudo-orthogonality now demonstrates that the TAM is sufficient to proceed with a GA reduction to 105 DOF.

| FEM Pseudo Orthogonality Table | | | | | | | | | | | | | | | | | | | | | | | | | | | | |
|--------------------------------|------|------------|------|------|------|------|------|------|------|------|------|------|------|------|------|------|------|------|------|------|------|------|------|------|------|------|------|------|
| | | FEM shapes | | | | | | | | | | | | | | | | | | | | | | | | | | |
| | | 1 | 2 | 3 | 4 | 5 | 6 | 7 | 8 | 9 | 10 | 11 | 12 | 13 | 14 | 15 | 16 | 17 | 18 | 19 | 20 | 21 | 22 | 23 | 24 | 25 | 26 | |
| FEM shapes | POgg | 0.4 | 0.4 | 0.4 | 1.1 | 1.2 | 1.4 | 5.4 | 7.8 | 12.8 | 12.8 | 14.5 | 15.6 | 20.3 | 20.4 | 27.9 | 28.6 | 32.5 | 42.6 | 42.8 | 42.9 | 43.8 | 45.3 | 45.9 | 50.4 | 54.0 | 54.5 | |
| | 1 | 0.4 | 1.00 | | | | | | | | | | | | | | | | | | | | | | | | | |
| | 2 | 0.4 | | 1.00 | | | | | | | | | | | | | | | | | | | | | | | | |
| | 3 | 0.4 | | | 1.00 | | | | | | | | | | | | | | | | | | | | | | | |
| | 4 | 1.1 | | | | 1.00 | | | | | | | | | | | | | | | | | | | | | | |
| | 5 | 1.2 | | | | | 1.00 | | | | | | | | | | | | | | | | | | | | | |
| | 6 | 1.4 | | | | | | 1.00 | | | | | | | | | | | | | | | | | | | | |
| | 7 | 5.4 | | | | | | | 1.00 | | | | | | | | | | | | | | | | | | | |
| | 8 | 7.8 | | | | | | | | 1.00 | | | | | | | | | | | | | | | | | | |
| | 9 | 12.8 | | | | | | | | | 1.00 | | | | | | | | | | | | | | | | | |
| | 10 | 12.8 | | | | | | | | | | 1.00 | | | | | | | | | | | | | | | | |
| | 11 | 14.5 | | | | | | | | | | | 0.99 | | | | | | | | | | | | | | | |
| | 12 | 15.6 | | | | | | | | | | | | 0.99 | | | | | | | | | | | | | | |
| | 13 | 20.3 | | | | | | | | | | | | | 0.99 | | | | | | | | | | | | | |
| | 14 | 20.4 | | | | | | | | | | | | | | 0.99 | | | | | | | | | | | | |
| | 15 | 27.9 | | | | | | | | | | | | | | | 0.98 | | | | | | | | | | | |
| | 16 | 28.6 | | | | | | | | | | | | | | | | 0.98 | | | | | | | | | | |
| | 17 | 32.5 | | | | | | | | | | | | | | | | | 0.99 | | | | | | | | | |
| | 18 | 42.6 | | | | | | | | | | | | | | | | | | 0.98 | | | | | | | | |
| | 19 | 42.8 | | | | | | | | | | | | | | | | | | | 0.98 | | | | | | | |
| | 20 | 42.9 | | | | | | | | | | | | | | | | | | | | 0.98 | | | | | | |
| | 21 | 43.8 | | | | | | | | | | | | | | | | | | | | | 0.97 | | | | | |
| | 22 | 45.3 | | | | | | | | | | | | | | | | | | | | | | 0.98 | | | | |
| | 23 | 45.9 | | | | | | | | | | | | | | | | | | | | | | | 0.96 | | | |
| | 24 | 50.4 | | | | | | | | | | | | | | | | | | | | | | | | 0.95 | | |
| | 25 | 54.0 | | | | | | | | | | | | | | | | | | | | | | | | | 0.96 | |
| | 26 | 54.5 | | | | | | | | | | | | | | | | | | | | | | | | | | 0.97 |

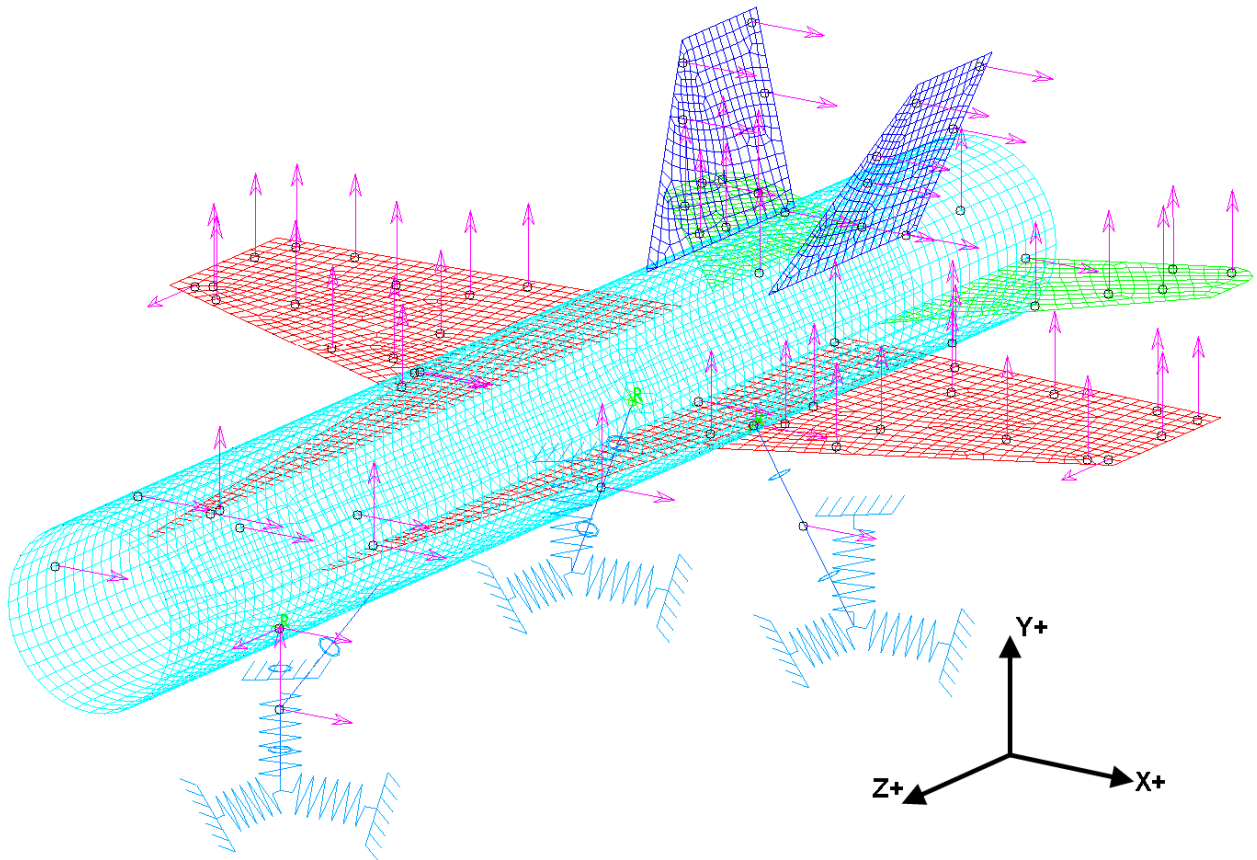


Figure 2. IRKE-selected and GA-reduced 75-DOF ASET. The pseudo-orthogonality and FEM are displayed.

| FEM Pseudo Orthogonality Table | | | | | | | | | | | | | | | | | | | | | | | | | | | | |
|--------------------------------|----|------|------|------|------|------|------|------|------|------|------|------|------|------|------|------|------|------|------|------|------|------|------|------|------|------|------|------|
| FEM shapes | | | | | | | | | | | | | | | | | | | | | | | | | | | | |
| POgg | | 1 | 2 | 3 | 4 | 5 | 6 | 7 | 8 | 9 | 10 | 11 | 12 | 13 | 14 | 15 | 16 | 17 | 18 | 19 | 20 | 21 | 22 | 23 | 24 | 25 | 26 | |
| FEM shapes | 1 | 0.4 | 1.00 | | | | | | | | | | | | | | | | | | | | | | | | | |
| | 2 | 0.4 | | 1.00 | | | | | | | | | | | | | | | | | | | | | | | | |
| | 3 | 0.4 | | | 1.00 | | | | | | | | | | | | | | | | | | | | | | | |
| | 4 | 1.1 | | | | 1.00 | | | | | | | | | | | | | | | | | | | | | | |
| | 5 | 1.2 | | | | | 1.00 | | | | | | | | | | | | | | | | | | | | | |
| | 6 | 1.4 | | | | | | 1.00 | | | | | | | | | | | | | | | | | | | | |
| | 7 | 5.4 | | | | | | | 0.99 | | | | | | | | | | | | | | | | | | | |
| | 8 | 7.8 | | | | | | | | 0.99 | | | | | | | | | | | | | | | | | | |
| | 9 | 12.8 | | | | | | | | | 0.99 | | | | | | | | | | | | | | | | | |
| | 10 | 12.8 | | | | | | | | | | 0.98 | | | | | | | | | | | | | | | | |
| | 11 | 14.5 | | | | | | | | | | | 0.96 | | | | | | | | | | | | | | | |
| | 12 | 15.6 | | | | | | | | | | | | 0.96 | | | | | | | | | | | | | | |
| | 13 | 20.3 | | | | | | | | | | | | | 0.96 | | | | | | | | | | | | | |
| | 14 | 20.4 | | | | | | | | | | | | | | 0.97 | | | | | | | | | | | | |
| | 15 | 27.9 | | | | | | | | | | | | | | | 0.77 | | | | | | | | | | | |
| | 16 | 28.6 | | | | | | | | | | | | | | | | 0.78 | | | | | | | | | | |
| | 17 | 32.5 | | | | | | | | | | | | | | | | | 0.97 | | | | | | | | | |
| | 18 | 42.6 | | | | | | | | | | | | | | | | | | 0.94 | | | | | | | | |
| | 19 | 42.8 | | | | | | | | | | | | | | | | | | | 0.93 | | | | | | | |
| | 20 | 42.9 | | | | | | | | | | | | | | | | | | | | 0.93 | | | | | | |
| | 21 | 43.8 | | | | | | | | | | | | | | | | | | | | | 0.92 | | | | | |
| | 22 | 45.3 | | | | | | | | | | | | | | | | | | | | | | 0.98 | | | | |
| | 23 | 45.9 | | | | | | | | | | | | | | | | | | | | | | | 0.94 | | | |
| | 24 | 50.4 | | | | | | | | | | | | | | | | | | | | | | | | 0.97 | 0.03 | |
| | 25 | 54.0 | | | | | | | | | | | | | | | | | | | | | | | | | 0.03 | 0.85 |
| | 26 | 54.5 | | | | | | | | | | | | | | | | | | | | | | | | | | 0.81 |

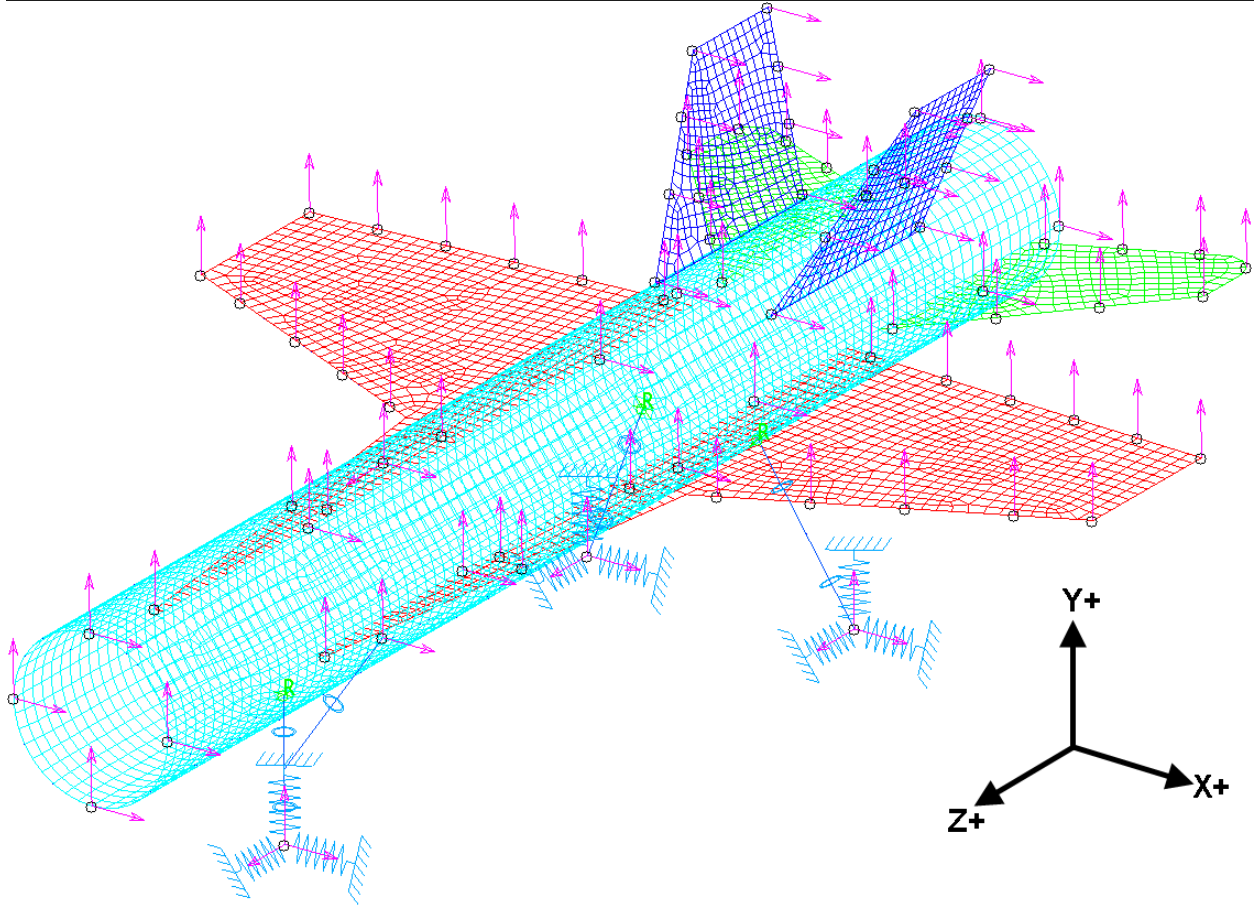


Figure 3. Manually selected ASET. The pseudo-orthogonality and FEM are displayed.

| FEM Pseudo Orthogonality Table | | | | | | | | | | | | | | | | | | | | | | | | | | | |
|--------------------------------|------|------|------|------|------|------|------|------|------|------|------|------|------|------|------|------|------|------|------|------|------|------|------|------|------|------|------|
| FEM shapes | | | | | | | | | | | | | | | | | | | | | | | | | | | |
| FEM shapes | | 1 | 2 | 3 | 4 | 5 | 6 | 7 | 8 | 9 | 10 | 11 | 12 | 13 | 14 | 15 | 16 | 17 | 18 | 19 | 20 | 21 | 22 | 23 | 24 | 25 | 26 |
| POgg | | 0.4 | 0.4 | 0.4 | 1.1 | 1.2 | 1.4 | 5.4 | 7.8 | 12.8 | 12.8 | 14.5 | 15.6 | 20.3 | 20.4 | 27.9 | 28.6 | 32.5 | 42.6 | 42.8 | 42.9 | 43.8 | 45.3 | 45.9 | 50.4 | 54.0 | 54.5 |
| 1 | 0.4 | 1.00 | | | | | | | | | | | | | | | | | | | | | | | | | |
| 2 | 0.4 | | 1.00 | | | | | | | | | | | | | | | | | | | | | | | | |
| 3 | 0.4 | | | 1.00 | | | | | | | | | | | | | | | | | | | | | | | |
| 4 | 1.1 | | | | 1.00 | | | | | | | | | | | | | | | | | | | | | | |
| 5 | 1.2 | | | | | 1.00 | | | | | | | | | | | | | | | | | | | | | |
| 6 | 1.4 | | | | | | 1.00 | | | | | | | | | | | | | | | | | | | | |
| 7 | 5.4 | | | | | | | 0.99 | | | | | | | | | | | | | | | | | | | |
| 8 | 7.8 | | | | | | | | 0.99 | | | | | | | | | | | | | | | | | | |
| 9 | 12.8 | | | | | | | | | 0.99 | | | | | | | | | | | | | | | | | |
| 10 | 12.8 | | | | | | | | | | 0.98 | | | | | | | | | | | | | | | | |
| 11 | 14.5 | | | | | | | | | | | 0.96 | | | | | | | | | | | | | | | |
| 12 | 15.6 | | | | | | | | | | | | 0.96 | | | | | | | | | | | | | | |
| 13 | 20.3 | | | | | | | | | | | | | 0.96 | | | | | | | | | | | | | |
| 14 | 20.4 | | | | | | | | | | | | | | 0.97 | | | | | | | | | | | | |
| 15 | 27.9 | | | | | | | | | | | | | | | 0.77 | | | | | | | | | | | |
| 16 | 28.6 | | | | | | | | | | | | | | | | 0.78 | | | | | | | | | | |
| 17 | 32.5 | | | | | | | | | | | | | | | | | 0.99 | | | | | | | | | |
| 18 | 42.6 | | | | | | | | | | | | | | | | | | 0.94 | | | | | | | | |
| 19 | 42.8 | | | | | | | | | | | | | | | | | | | 0.93 | | | | | | | |
| 20 | 42.9 | | | | | | | | | | | | | | | | | | | | 0.93 | | | | | | |
| 21 | 43.8 | | | | | | | | | | | | | | | | | | | | | 0.92 | | | | | |
| 22 | 45.3 | | | | | | | | | | | | | | | | | | | | | | 0.98 | | | | |
| 23 | 45.9 | | | | | | | | | | | | | | | | | | | | | | | 0.97 | | | |
| 24 | 50.4 | | | | | | | | | | | | | | | | | | | | | | | | 0.97 | 0.04 | |
| 25 | 54.0 | | | | | | | | | | | | | | | | | | | | | | | | | 0.04 | 0.85 |
| 26 | 54.5 | | | | | | | | | | | | | | | | | | | | | | | | | | 0.81 |

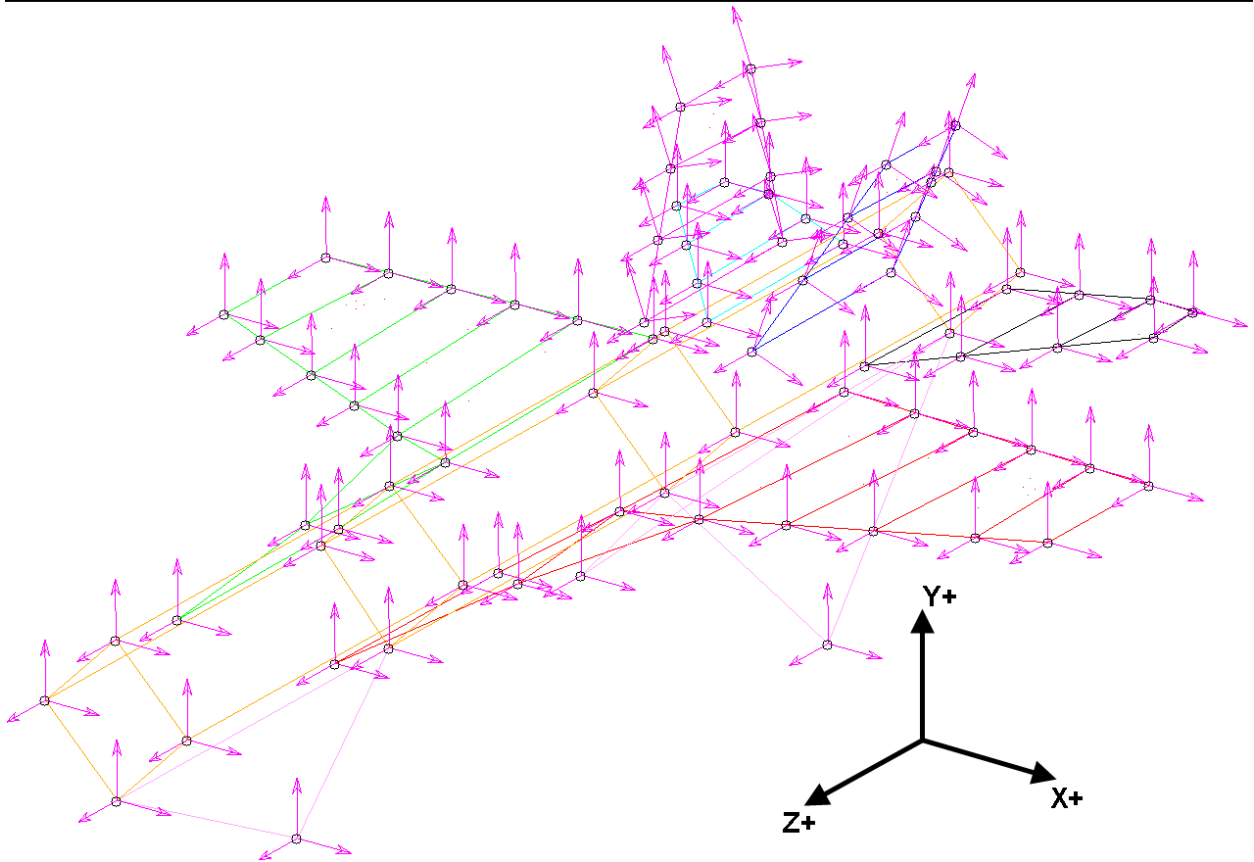


Figure 4. Manually selected ASET, including all three DOF. The pseudo-orthogonality still indicates an insufficient TAM, so a GA reduction will not be productive.

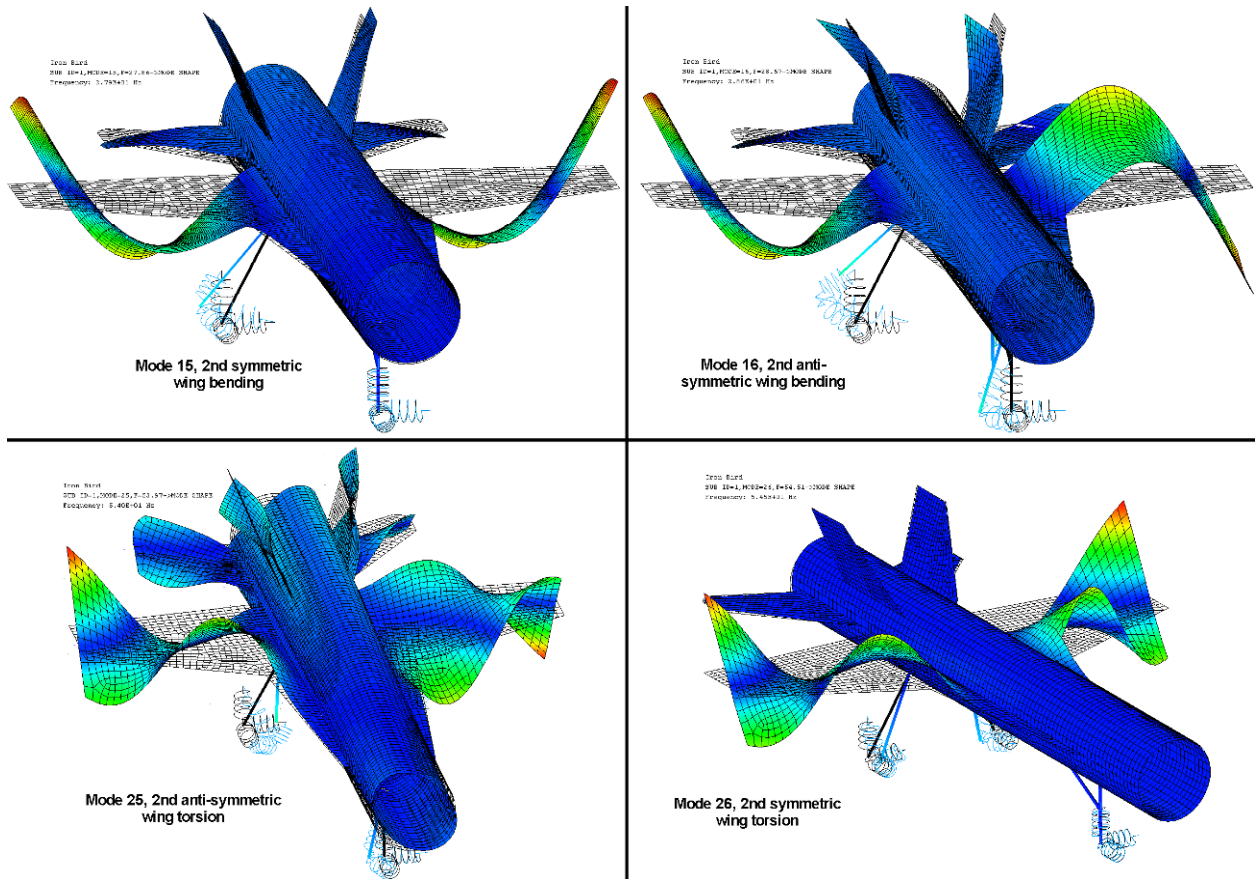


Figure 5. The pseudo-orthogonality of the manual ASET selection indicates that modes 15, 16, 25, and 26 are not sufficiently represented in the TAM. All four modes are wing modes.

After adding 126 candidate DOF to locations in the wing and tail centers, the GA reduced the ASET to the 105-measurement DOF budget. A final pretest iteration is displayed in [Figure 7](#). Predictably, the GA selected DOF that corresponded closely with the original manual selection, consisting of mostly accelerometers perpendicular to the various iron bird surfaces. The pseudo-orthogonality demonstrates that this TAM is sufficient to capture all target modes. The IRKE/GA result provided guidance in arriving at this final TAM, but since the ASET was still manually selected, none of the drawbacks of irregularity and inaccessibility will be encountered in the test setup. While the final TAM includes thirty more accelerometers than the IRKE/GA-derived TAM, this is a small cost to bear for a convenient, practical, and easily maintained test setup.

The four TAMs are summarized in the following list as well as in [Table 1](#).

1. IRKE/GA-selected ASET, 75 DOF ([Figure 2](#)).
2. Manually selected ASET, 105 DOF ([Figure 3](#)).
3. Manually selected ASET, 243 DOF. All three translational DOF from every TDM node were included to check the viability of any possible manual TDM-derived ASET ([Figure 4](#)).
4. Manually selected ASET, 369 DOF. Additional candidate DOF were added to the wings and tail sections, and all three translational DOF from every TDM node were included ([Figure 6](#)).
5. Manually selected ASET, reduced via GA to 105 DOF ([Figure 7](#)).

[Table 1](#) condenses the four results studied above by displaying only the on-diagonal pseudo-orthogonality results and the FEM/TAM frequency comparisons. The IRKE/GA result clearly produced the best TAM, as evidenced by the pseudo-orthogonality. Additionally, a fully manual ASET selection resulted in an insufficient TAM. Studying the IRKE/GA result was useful to augment the manual and heuristic development of an ASET that would be sufficient to capture all target modes. While TAM 5 ([Figure 7](#)) requires thirty additional accelerometers, it has a comparable pseudo-orthogonality to the IRKE/GA result and is both sufficient and practical for a successful test program.

Further manual iterations on the TAM were not completed for this paper, but the IRKE/GA result suggests two additional modifications to bolster the pseudo-orthogonality and perhaps even lower the channel count. First, accelerometers may not be needed along the most inboard locations on the wings. Second, the mid-section of the fuselage could possibly be de-emphasized, though additional accelerometers may be placed towards the forward and aft areas of the fuselage.

| FEM Pseudo Orthogonality Table | | | | | | | | | | | | | | | | | | | | | | | | | | | | |
|--------------------------------|------|------------|------|------|------|------|------|------|------|------|------|------|------|------|------|------|------|------|------|------|------|------|------|------|------|------|------|------|
| | | FEM shapes | | | | | | | | | | | | | | | | | | | | | | | | | | |
| | | 1 | 2 | 3 | 4 | 5 | 6 | 7 | 8 | 9 | 10 | 11 | 12 | 13 | 14 | 15 | 16 | 17 | 18 | 19 | 20 | 21 | 22 | 23 | 24 | 25 | 26 | |
| FEM shapes | POgg | 0.4 | 0.4 | 0.4 | 1.1 | 1.2 | 1.4 | 5.4 | 7.8 | 12.8 | 12.8 | 14.5 | 15.6 | 20.3 | 20.4 | 27.9 | 28.6 | 32.5 | 42.6 | 42.8 | 42.9 | 43.8 | 45.3 | 45.9 | 50.4 | 54.0 | 54.5 | |
| | 1 | 0.4 | 1.00 | | | | | | | | | | | | | | | | | | | | | | | | | |
| | 2 | 0.4 | | 1.00 | | | | | | | | | | | | | | | | | | | | | | | | |
| | 3 | 0.4 | | | 1.00 | | | | | | | | | | | | | | | | | | | | | | | |
| | 4 | 1.1 | | | | 1.00 | | | | | | | | | | | | | | | | | | | | | | |
| | 5 | 1.2 | | | | | 1.00 | | | | | | | | | | | | | | | | | | | | | |
| | 6 | 1.4 | | | | | | 1.00 | | | | | | | | | | | | | | | | | | | | |
| | 7 | 5.4 | | | | | | | 1.00 | | | | | | | | | | | | | | | | | | | |
| | 8 | 7.8 | | | | | | | | 1.00 | | | | | | | | | | | | | | | | | | |
| | 9 | 12.8 | | | | | | | | | 1.00 | | | | | | | | | | | | | | | | | |
| | 10 | 12.8 | | | | | | | | | | 1.00 | | | | | | | | | | | | | | | | |
| | 11 | 14.5 | | | | | | | | | | | 1.00 | | | | | | | | | | | | | | | |
| | 12 | 15.6 | | | | | | | | | | | | 1.00 | | | | | | | | | | | | | | |
| | 13 | 20.3 | | | | | | | | | | | | | 1.00 | | | | | | | | | | | | | |
| | 14 | 20.4 | | | | | | | | | | | | | | 1.00 | | | | | | | | | | | | |
| | 15 | 27.9 | | | | | | | | | | | | | | | 0.99 | | | | | | | | | | | |
| | 16 | 28.6 | | | | | | | | | | | | | | | | 0.99 | | | | | | | | | | |
| | 17 | 32.5 | | | | | | | | | | | | | | | | | 1.00 | | | | | | | | | |
| | 18 | 42.6 | | | | | | | | | | | | | | | | | | 0.97 | | | | | | | | |
| | 19 | 42.8 | | | | | | | | | | | | | | | | | | | 0.97 | | | | | | | |
| | 20 | 42.9 | | | | | | | | | | | | | | | | | | | | 0.96 | | | | | | |
| | 21 | 43.8 | | | | | | | | | | | | | | | | | | | | | 0.97 | | | | | |
| | 22 | 45.3 | | | | | | | | | | | | | | | | | | | | | | 0.99 | | | | |
| | 23 | 45.9 | | | | | | | | | | | | | | | | | | | | | | | 0.97 | | | |
| | 24 | 50.4 | | | | | | | | | | | | | | | | | | | | | | | | 0.98 | | |
| | 25 | 54.0 | | | | | | | | | | | | | | | | | | | | | | | | | 0.98 | |
| | 26 | 54.5 | | | | | | | | | | | | | | | | | | | | | | | | | | 0.97 |

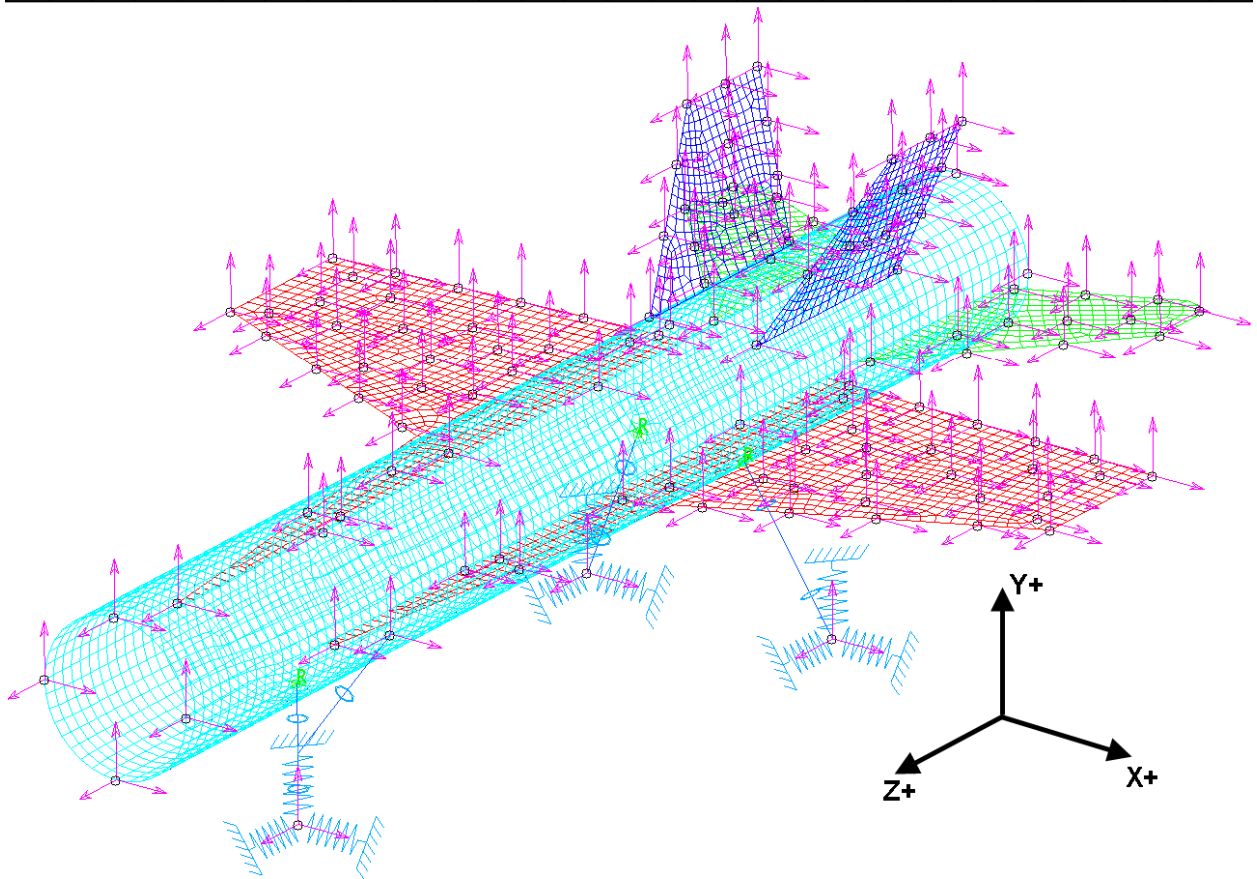


Figure 6. Manually selected ASET, including all three DOF. Additional DOF were added to the wings and tails, and the pseudo-orthogonality indicates a sufficient TAM.

| FEM Pseudo Orthogonality Table | | | | | | | | | | | | | | | | | | | | | | | | | | | | |
|--------------------------------|------|------------|------|------|------|------|------|------|------|------|------|------|------|------|------|------|------|------|------|------|------|------|------|------|------|------|------|------|
| | | FEM shapes | | | | | | | | | | | | | | | | | | | | | | | | | | |
| | | 1 | 2 | 3 | 4 | 5 | 6 | 7 | 8 | 9 | 10 | 11 | 12 | 13 | 14 | 15 | 16 | 17 | 18 | 19 | 20 | 21 | 22 | 23 | 24 | 25 | 26 | |
| FEM shapes | POgg | 0.4 | 0.4 | 0.4 | 1.1 | 1.2 | 1.4 | 5.4 | 7.8 | 12.8 | 12.8 | 14.5 | 15.6 | 20.3 | 20.4 | 27.9 | 28.6 | 32.5 | 42.6 | 42.8 | 42.9 | 43.8 | 45.3 | 45.9 | 50.4 | 54.0 | 54.5 | |
| | 1 | 0.4 | 1.00 | | | | | | | | | | | | | | | | | | | | | | | | | |
| | 2 | 0.4 | | 1.00 | | | | | | | | | | | | | | | | | | | | | | | | |
| | 3 | 0.4 | | | 1.00 | | | | | | | | | | | | | | | | | | | | | | | |
| | 4 | 1.1 | | | | 1.00 | | | | | | | | | | | | | | | | | | | | | | |
| | 5 | 1.2 | | | | | 1.00 | | | | | | | | | | | | | | | | | | | | | |
| | 6 | 1.4 | | | | | | 1.00 | | | | | | | | | | | | | | | | | | | | |
| | 7 | 5.4 | | | | | | | 1.00 | | | | | | | | | | | | | | | | | | | |
| | 8 | 7.8 | | | | | | | | 1.00 | | | | | | | | | | | | | | | | | | |
| | 9 | 12.8 | | | | | | | | | 1.00 | | | | | | | | | | | | | | | | | |
| | 10 | 12.8 | | | | | | | | | | 1.00 | | | | | | | | | | | | | | | | |
| | 11 | 14.5 | | | | | | | | | | | 1.00 | | | | | | | | | | | | | | | |
| | 12 | 15.6 | | | | | | | | | | | | 1.00 | | | | | | | | | | | | | | |
| | 13 | 20.3 | | | | | | | | | | | | | 0.99 | | | | | | | | | | | | | |
| | 14 | 20.4 | | | | | | | | | | | | | | 0.99 | | | | | | | | | | | | |
| | 15 | 27.9 | | | | | | | | | | | | | | | 0.98 | | | | | | | | | | | |
| | 16 | 28.6 | | | | | | | | | | | | | | | | 0.99 | | | | | | | | | | |
| | 17 | 32.5 | | | | | | | | | | | | | | | | | 0.99 | | | | | | | | | |
| | 18 | 42.6 | | | | | | | | | | | | | | | | | | 0.97 | | | | | | | | |
| | 19 | 42.8 | | | | | | | | | | | | | | | | | | | 0.97 | | | | | | | |
| | 20 | 42.9 | | | | | | | | | | | | | | | | | | | | 0.96 | | | | | | |
| | 21 | 43.8 | | | | | | | | | | | | | | | | | | | | | 0.97 | | | | | |
| | 22 | 45.3 | | | | | | | | | | | | | | | | | | | | | | 0.99 | | | | |
| | 23 | 45.9 | | | | | | | | | | | | | | | | | | | | | | | 0.96 | | | |
| | 24 | 50.4 | | | | | | | | | | | | | | | | | | | | | | | | 0.98 | | |
| | 25 | 54.0 | | | | | | | | | | | | | | | | | | | | | | | | | 0.97 | |
| | 26 | 54.5 | | | | | | | | | | | | | | | | | | | | | | | | | | 0.97 |

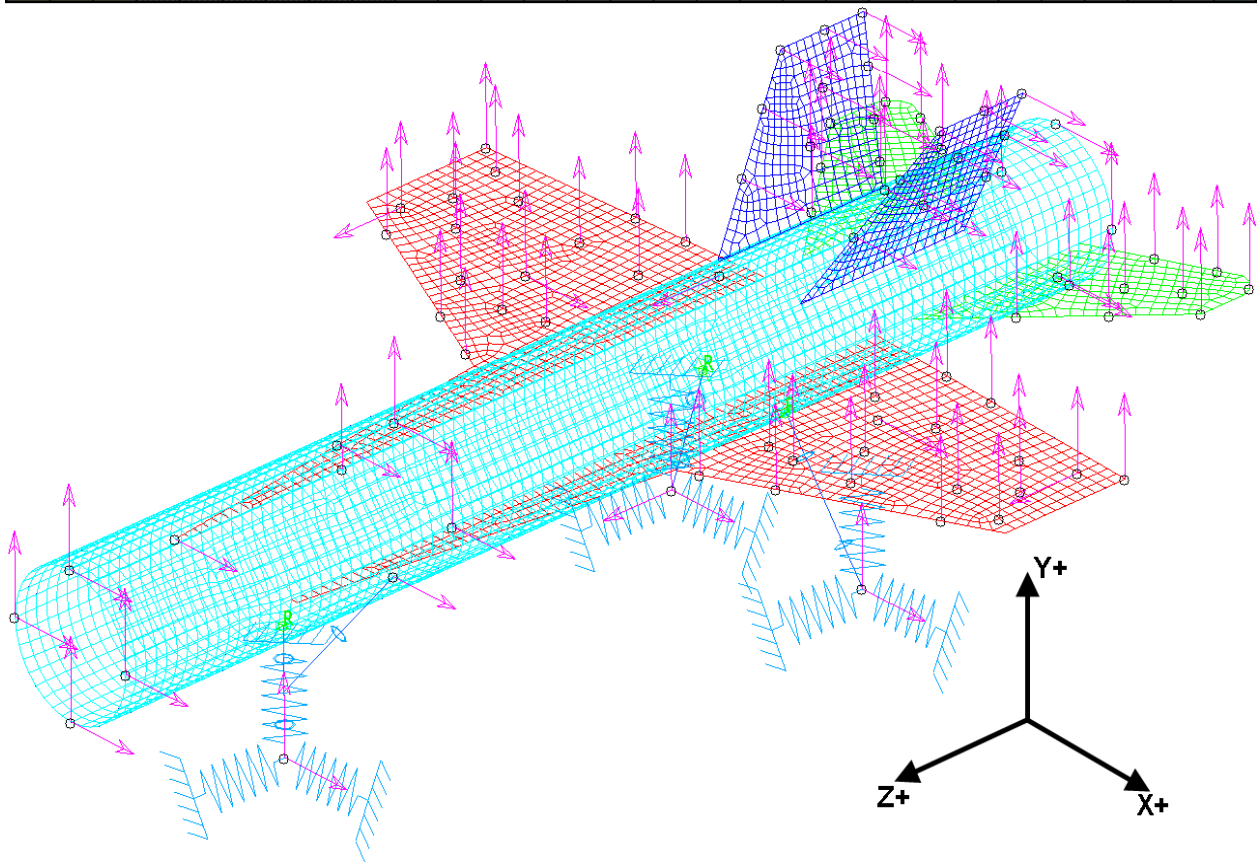


Figure 7. Final ASET, derived from the manual 369-DOF TDM, with accelerometers added to the wings and tails and then reduced via GA.

Table 1. Condensed TAM results.

| FEM | | TAM 1 | TAM 2 | TAM 3 | TAM 4 | TAM 5 | FEM | | TAM 1 | TAM 2 | TAM 3 | TAM 4 | TAM 5 | | | | |
|--------|-----------|--------|--------|--------|--------|--------|----------|-----------|-----------|--------------|-----------|--------------|-----------|--------------|------|--------|-----|
| Mode # | Freq (Hz) | PORTHO | PORTHO | PORTHO | PORTHO | PORTHO | FEM Mode | Freq (Hz) | Freq (Hz) | % Difference | Freq (Hz) | % Difference | Freq (Hz) | % Difference | | | |
| 1 | 0.36 | 1.00 | 1.00 | 1.00 | 1.00 | 1.00 | 1 | 0.36 | 0.361 | 0.0 | 0.361 | 0.0 | 0.4 | 0.361 | 0.0 | | |
| 2 | 0.40 | 1.00 | 1.00 | 1.00 | 1.00 | 1.00 | 2 | 0.40 | 0.400 | 0.0 | 0.400 | 0.0 | 0.4 | 0.400 | 0.0 | | |
| 3 | 0.43 | 1.00 | 1.00 | 1.00 | 1.00 | 1.00 | 3 | 0.43 | 0.432 | 0.0 | 0.432 | 0.0 | 0.4 | 0.432 | 0.0 | | |
| 4 | 1.15 | 1.00 | 1.00 | 1.00 | 1.00 | 1.00 | 4 | 1.15 | 1.147 | 0.0 | 1.147 | 0.0 | 1.1 | 1.147 | 0.0 | | |
| 5 | 1.23 | 1.00 | 1.00 | 1.00 | 1.00 | 1.00 | 5 | 1.23 | 1.235 | 0.0 | 1.235 | 0.0 | 1.2 | 1.235 | 0.0 | | |
| 6 | 1.43 | 1.00 | 1.00 | 1.00 | 1.00 | 1.00 | 6 | 1.43 | 1.429 | 0.0 | 1.429 | 0.0 | 1.4 | 1.429 | 0.0 | | |
| 7 | 5.38 | 1.00 | 0.99 | 0.99 | 1.00 | 1.00 | 7 | 5.38 | 5.380 | 0.0 | 5.397 | 0.3 | 5.4 | 5.380 | 0.0 | | |
| 8 | 7.82 | 1.00 | 0.99 | 0.99 | 1.00 | 1.00 | 8 | 7.82 | 7.820 | 0.0 | 7.841 | 0.3 | 7.8 | 7.819 | 0.0 | | |
| 9 | 12.80 | 1.00 | 0.99 | 0.99 | 1.00 | 1.00 | 9 | 12.80 | 12.807 | 0.1 | 12.837 | 0.3 | 12.8 | 12.802 | 0.1 | | |
| 10 | 12.80 | 1.00 | 0.98 | 0.98 | 1.00 | 1.00 | 10 | 12.80 | 12.813 | 0.1 | 12.849 | 0.4 | 12.8 | 12.814 | 0.1 | | |
| 11 | 14.49 | 0.99 | 0.96 | 0.96 | 1.00 | 1.00 | 11 | 14.49 | 14.541 | 0.4 | 14.639 | 1.0 | 14.5 | 14.500 | 0.1 | | |
| 12 | 15.64 | 0.99 | 0.96 | 0.96 | 1.00 | 1.00 | 12 | 15.64 | 15.694 | 0.4 | 15.804 | 1.1 | 15.7 | 15.653 | 0.1 | | |
| 13 | 20.28 | 0.99 | 0.96 | 0.96 | 1.00 | 0.99 | 13 | 20.28 | 20.352 | 0.3 | 20.464 | 0.9 | 20.3 | 20.324 | 0.2 | | |
| 14 | 20.44 | 0.99 | 0.97 | 0.97 | 1.00 | 0.99 | 14 | 20.44 | 20.511 | 0.3 | 20.590 | 0.7 | 20.5 | 20.485 | 0.2 | | |
| 15 | 27.86 | 0.98 | 0.77 | 0.77 | 0.99 | 0.98 | 15 | 27.86 | 27.989 | 0.5 | 29.812 | 7.0 | 29.799 | 7.0 | 27.9 | 27.966 | 0.4 |
| 16 | 28.57 | 0.98 | 0.78 | 0.78 | 0.99 | 0.99 | 16 | 28.57 | 28.699 | 0.4 | 30.460 | 6.6 | 30.455 | 6.6 | 28.6 | 28.673 | 0.4 |
| 17 | 32.48 | 0.99 | 0.97 | 0.99 | 1.00 | 0.99 | 17 | 32.48 | 32.598 | 0.3 | 32.735 | 0.8 | 32.602 | 0.4 | 32.5 | 32.561 | 0.3 |
| 18 | 42.62 | 0.98 | 0.94 | 0.94 | 0.97 | 0.97 | 18 | 42.62 | 42.874 | 0.6 | 43.301 | 1.6 | 43.272 | 1.5 | 42.9 | 42.940 | 0.8 |
| 19 | 42.82 | 0.98 | 0.93 | 0.93 | 0.97 | 0.97 | 19 | 42.82 | 43.066 | 0.6 | 43.560 | 1.7 | 43.558 | 1.7 | 43.2 | 43.213 | 0.9 |
| 20 | 42.87 | 0.98 | 0.93 | 0.93 | 0.96 | 0.96 | 20 | 42.87 | 43.104 | 0.5 | 43.643 | 1.8 | 43.640 | 1.8 | 43.3 | 43.296 | 1.0 |
| 21 | 43.81 | 0.97 | 0.92 | 0.92 | 0.97 | 0.97 | 21 | 43.81 | 44.086 | 0.6 | 44.672 | 2.0 | 44.670 | 2.0 | 44.1 | 44.151 | 0.8 |
| 22 | 45.30 | 0.98 | 0.98 | 0.98 | 0.99 | 0.99 | 22 | 45.30 | 45.524 | 0.5 | 45.555 | 0.6 | 45.538 | 0.5 | 45.4 | 45.450 | 0.3 |
| 23 | 45.90 | 0.96 | 0.94 | 0.97 | 0.97 | 0.96 | 23 | 45.90 | 46.381 | 1.0 | 46.605 | 1.5 | 46.216 | 0.7 | 46.2 | 46.341 | 1.0 |
| 24 | 50.43 | 0.95 | 0.97 | 0.97 | 0.98 | 0.98 | 24 | 50.43 | 51.067 | 1.2 | 50.827 | 0.8 | 50.784 | 0.7 | 50.6 | 50.671 | 0.5 |
| 25 | 53.97 | 0.96 | 0.85 | 0.85 | 0.98 | 0.97 | 25 | 53.97 | 54.552 | 1.1 | 56.145 | 4.0 | 56.029 | 3.8 | 54.3 | 54.407 | 0.8 |
| 26 | 54.51 | 0.97 | 0.81 | 0.81 | 0.97 | 0.97 | 26 | 54.51 | 54.987 | 0.9 | 57.436 | 5.4 | 57.434 | 5.4 | 54.9 | 54.921 | 0.8 |

DISCUSSION

The analytic tools for pretest, such as IRKE and GA, can guide a manual pretest process. A flowchart depicting the complete analytical and manual TAM development process is shown in Figure 8. The pretest analysis can take either an analytic path, with later adjustments influenced by practical test program considerations, or a manual path that is influenced as necessary by the analytic results.

This paper has focused on the iron bird test article, but actual pretest analyses require collaboration with the customer—the owner of the test article. In the iron bird study, all 26 modes below 55 Hz were accepted as target modes of equal importance. Other test articles may have modes of variable importance, which can affect the manual ASET selection. For example, if the iron bird fuselage breathing modes were determined to be of low value (due to future correlation efforts or relatively high modal frequencies), additional DOF may have been subtracted from the ASET. This hypothetical determination, which would be made with customer and analyst concurrence, has the advantage of reducing the size of the ASET.

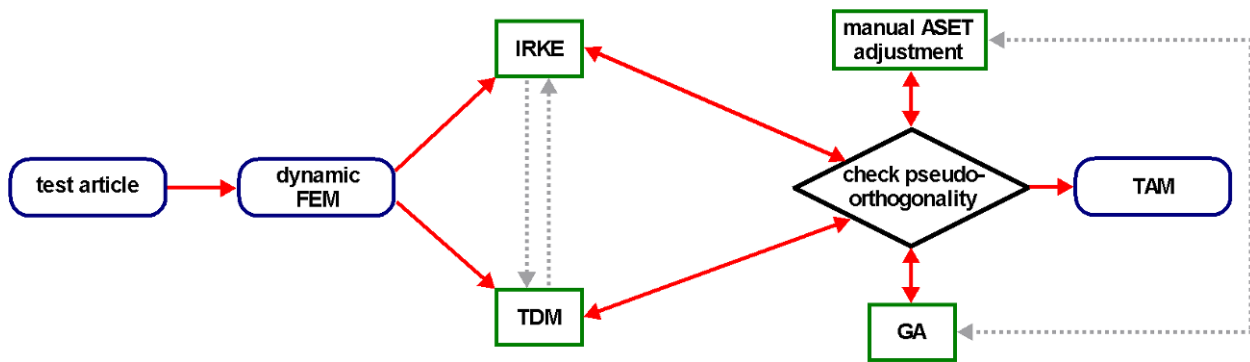


Figure 8. Flowchart depicting the pretest process. The dashed grey lines indicate that analysis results can influence a manual TAM development, and vice versa.

Additionally, should such a determination be made, the selected ASET may still be sufficient to visualize the target mode shapes. This is checked initially through observation of the analysis modes. TAM 2 has sufficient measurement DOF to visualize the second wing torsion modes, but if TAM 2 was used in an actual test, test engineers could not expect the final test-extracted mode list to pass rigorous orthogonality checks. The importance of such a data-quality check (successful visualization of all target modes and perhaps a high-quality modal assurance criteria check) is again subject to negotiation between the customer and analysis engineers, with the goal of having a successful yet practical test program.

Measurement DOF that may be difficult or time-consuming to install, such as those requiring manlifts or test article disassembly (and the accompanying customer technical support), should also be considered for exclusion from the ASET if the TAM results allow for such a compromise. The customer should work with the test engineers prior to the test program to provide as much information, including drawings and pictures, about the test article as possible. Test engineers and the customer should be cognizant of the additional time and resources required by both parties for accelerometers that are difficult to install and maintain.

In the iron bird study, the GA was used to reduce the manual TDM set. Additional manual DOF rearrangements and pseudo-orthogonality checks may be performed to further improve the ASET. Like with the IRKE method, the GA may produce a highly efficient, but irregular, ASET, and manual adjustments should be made to regularize and simplify the final ASET—within the constraints of a sufficient TAM.

REFERENCES

- [1] Tuttle, R., T. Cole, and J. Lollock, "An Automated Method for Identification of Efficient Measurement Degrees-of-Freedom For Mode Survey Testing," 46th AIAA/ASME/ASCE/AHS/ASC Structures, Structural Dynamics & Materials Conference, Austin, Texas, 2005.
- [2] Stabb, M., and P. Biełloch, "A Genetic Algorithm For Optimally Selecting Accelerometer Locations," 13th International Modal Analysis Conference, Nashville, Tennessee, 1995.

Modal Impact Testing of Ground Vehicle Enabling Mechanical Condition Assessment

Alan Meyer, Bryan Wang, Sean Britt, Ridwan Kazi, Dr. Douglas E. Adams
Purdue Center for Systems Integrity (PCSI)
Purdue University
1500 Kepner Drive
Lafayette, IN 47905

ABSTRACT

Military tactical wheeled vehicles must operate on wide ranging terrains under varying payload driving conditions, which lead to high dynamic loads in the wheels and suspension. High loads can, in turn, lead to mechanical and structural failures. The ability to quickly detect damage in a vehicle in the field can be extremely advantageous for condition-based maintenance. In this paper, the use of modal impact testing to characterize the modal properties of an H1 chassis in its healthy and faulty conditions was studied. The results show that five modes of vibration – bounce, pitch, roll and two flexible body modes of the frame – can be identified using the Complex Mode Indicator Function. Frequency response functions are measured by applying modal impacts to the chassis and measuring the response using a roving set of accelerometers on the wheel, body, and chassis. The frame of the vehicle was impacted at three locations and response accelerations were measured at 19 points on the chassis, vehicle body, suspension and wheels. The sprung mass vibrations in roll, bounce, pitch, beaming and torsional shake were estimated to have modal frequencies of 2.0 Hz, 3.5 Hz, 4.1 Hz, 9.8 Hz and 13 Hz, respectively. The experiments also indicated that modal impact testing has the ability to detect faults in the vehicle, such as low tire pressure. The results suggest that modal impact testing on ground vehicles is a feasible means of identifying the operational deflection shapes and certain types of mechanical damage. Furthermore, this knowledge could be used by onboard structural health monitoring systems to effectively analyze operational data to identify damage in operation.

INTRODUCTION

The ability to accurately characterize the free dynamic response characteristics of a vehicle is invaluable in the development of a ground vehicle or the modification of a vehicle suspension system. Modal hammer impact testing is often thought to be limited in its ability to provide accurate results for large, heavily damped structures, such as an H1 military vehicle. However, this study shows that good estimates of the modal properties can be gleaned from impact testing of a large vehicle in a relatively quick and inexpensive fashion. Modal impact testing was conducted on a military, Hummer H1 vehicle. Faults were induced in the Hummer H1 to determine if the FRFs would suggest that there was some sort of fault within the vehicle. These tests indicated that faults could be observed by analyzing the discrepancies in the faulted and un-faulted vehicle frequency response functions. To obtain the baseline frequency response, modal impact testing was employed using an impact sledge hammer at three specific points on the H1. This work will be useful long term in the creation of a vehicle health monitoring system, which has the potential to reduce the maintenance costs of the vehicle and increase asset readiness.

Operating Deflection Shapes

In the article by Schwarz and Richardson on operating deflection shapes [1], an operating deflection shape (ODS) is defined as any forced motion of two or more points on a structure. In other words, the specification of the motion of two or more points defines a shape; more generally, a shape is the motion of one point relative to all other points. Operating deflection shapes are measured to identify the modes of vibration, which superimpose to produce the operating shapes when a structure is driven by various forcing functions. Mode shapes are inherent properties of a system, whereas ODSs depend on the forces or loads applied to a system. The ODSs are measured in the time domain using a multi-channel data acquisition system to simultaneously acquire the responses at certain degrees of freedom, including reference (fixed) responses across all of the measurements.

Complex Mode Indicator Function

The Complex Mode Indicator Function (CMIF) is a simple algorithm based on singular value decomposition (SVD) methods applied to multiple reference frequency response measurements [2]. CMIF properly identifies the existence of real normal or complex modes and the relative magnitude of each mode, particularly when there are closely spaced or repeated modal frequencies by maximizing the use of spatial data. The SVD approach does not require multiplication of the FRF matrix by the Hermitian as in $[H(\omega)] \cdot [H(\omega)]^H$. By taking the SVD of the FRF matrix at each frequency, the following expression is obtained [2]:

$$[H(\omega)] = [U(\omega)] [\Sigma(\omega)] [V(\omega)]^H \quad (1)$$

where:

$[H(\omega)]$ is the FRF matrix of size N_o (number of response points) by N_i (number of excitation points)

$[U(\omega)]$ is the left singular value matrix (unitary)

$[\Sigma(\omega)]$ is the singular value matrix (diagonal)

$[V(\omega)]$ is the right singular vector matrix (diagonal)

Vehicle Vibrations

Common low frequency vibrations of the sprung mass of a vehicle as a rigid body consist of pitch, bounce, and roll. Pitch is the angular component of vibration of the sprung mass, or vehicle body, about the vehicle y-axis [3]. Bounce is the translational component of ride vibrations of the sprung mass in the direction of the vehicle z-axis, while roll is the angular component of ride vibrations of the sprung mass about the vehicle x-axis. Vibrations of the sprung mass as a flexible body include torsional shake and beaming. Beaming is a mode of vibration involving predominantly bending deformations of the sprung mass about the y-axis. Torsional shake is a mode of vibration involving twisting deformations of the sprung mass about the x-axis.

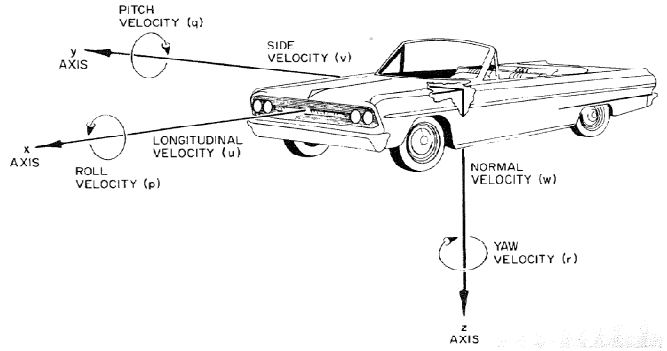


Fig. 1 Local pitch, bounce, and roll angles [3]

THEORY

The quarter-car model provides an excellent basis to analyze and estimate the body bounce and wheel hop; it consists of a quarter of the vehicle body, m_s (sprung mass) and one wheel of the vehicle, m_u (unsprung mass), where each mass is permitted to undergo vertical motion only. The spring stiffness k_s and shock absorber with damping coefficient c_s represent the stiffness and damping of the independent suspension system. The unsprung mass, m_t , k_t and c_t represent the stiffness and damping of the tire. The theoretical model is different from typical quarter car models due to a unique experimental setup. The governing equations of motion and transfer functions when modal-impacting a quarter-car are:

$$m_s \ddot{x}_s + c_s \dot{x}_s + k_s x_s - c_s \dot{x}_u - k_s x_u = f_{hammer} \quad (2)$$

$$m_u \ddot{x}_u + (c_s + c_t) \dot{x}_u + (k_s + k_t) x_u - c_s \dot{x}_s - k_s x_s = 0 \quad (3)$$

$$\frac{X_s}{F_{hammer}} = \frac{m_u s^2 + (c_s + c_t) s + k_s + k_t}{m_u m_s s^4 + m_s (c_s + c_t) s^3 + m_u c_s s^3 + m_s (k_s + k_t) s^2 + m_u k_s s^2 + c_s c_t s^2 + (c_t k_s + c_s k_t) s + k_s k_t} \quad (4)$$

$$\frac{X_u}{F_{hammer}} = \frac{c_s s + k_s}{m_u m_s s^4 + m_s (c_s + c_t) s^3 + m_u c_s s^3 + m_s (k_s + k_t) s^2 + m_u k_s s^2 + c_s c_t s^2 + (c_t k_s + c_s k_t) s + k_s k_t} \quad (5)$$

For this set of equations, the road input z_{in} is zero, since the external excitation only occurs on the body of the HMMWV. However, it should be noted that this model does not accurately represent the real operating conditions of the vehicle.

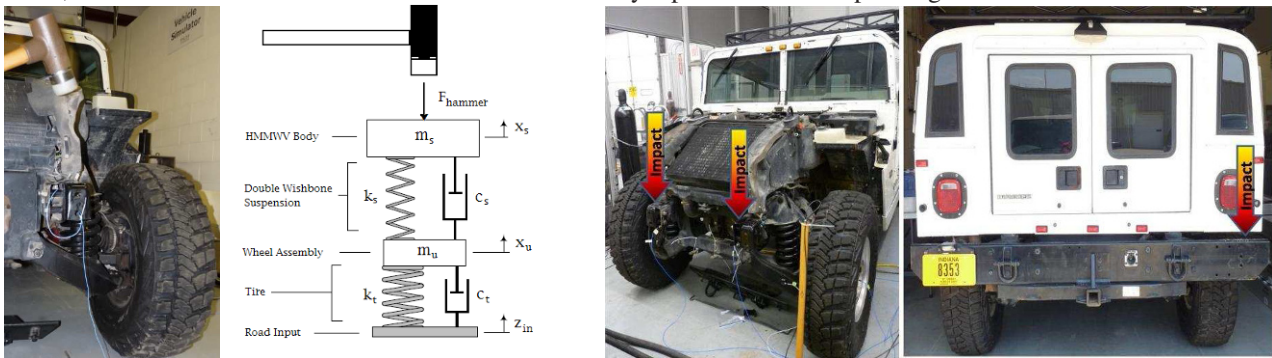


Fig. 2 Theoretical quarter-car model of vehicle and impact locations

Since it was deemed too difficult to excite the wheels directly using the equipment on hand, it was decided to use a modal sledge hammer to excite the vehicle frame instead. Methods using the road simulator to apply initial conditions to the vehicle wheels are also being explored for possible use in impulse testing. The wheels were kept in contact with the floor. Assuming reciprocity, three impact points were identified on the vehicle frame: left and right front frame rails and the rear bumper. The hood of the vehicle was removed to expose the front frame rails so they could be impacted with the hammer in Fig. 2.

EXPERIMENTAL APPLICATION

Six DC accelerometers were placed at various locations on the vehicle because the expected vehicle vibration modes were low in frequency ($< 20\text{Hz}$). Super glue was used to attach the sensors. The vehicle frame was then impacted at each of the three locations described above and the responses were recorded. The ODS measurement method was applied and the accelerometers were moved to different positions on the vehicle and the impacts were repeated to obtain more spatial data. Overall, three sets of data were collected. There was also one unique point from the fault testing portion of the experiment, yielding a total of 19 spatial response points. The locations of the accelerometers in each set are listed in Table 1 and Fig. 3.

TABLE 1 Sensor locations and descriptions for each measurement set

| Location Number | Description | Coordinates | | |
|-----------------|-------------|-------------|--------|-------|
| | | X | Y | Z |
| Data Set 1 | 1 | 0 | -27.25 | 0 |
| | 2 | -50 | 0 | 0 |
| | 3 | -9.5 | 7 | -10.5 |
| | 4 | -180 | 0 | 0 |
| | 5 | -16 | 25 | -12 |
| | 6 | 0 | 0 | 0 |
| Data Set 2 | 7 | -14.5 | 0 | 0 |
| | 8 | -14.5 | -27.25 | 0 |
| | 9 | -72.75 | 0 | -6 |
| | 10 | -154 | -27.25 | 0 |
| | 11 | -16 | -50 | -12 |
| | 12 | -154 | 0 | 0 |
| Data Set 3 | 13 | -20 | 11 | 3 |
| | 14 | -88 | -17 | -5 |
| | 15 | -159 | -40 | -11 |
| | 16 | -176 | -39 | 2 |
| | 17 | -149 | -56 | -12 |
| | 18 | -102 | -27.25 | -6 |
| Fault Analysis | 19 | -12 | 9 | 5 |

- The origin for all coordinates listed above is at response point 6, which is the left front frame rail (Impact Point 1)
- Positive x points towards forward vehicle driving direction, y points towards driver side, z points up toward ceiling
- Right hand coordinate system and all measurements in INCHES



Fig. 3 Sensor locations for each measurement set

To excite the vehicle suspension, the modal sledge hammer was used to impact the frame. After experimenting with different hammer tips, a soft rubber tip was used to obtain the most uniform low frequency energy input [4]. A force threshold of 5 lbs was also applied to the input force. This threshold caused the data acquisition system to ignore any forces that are less than 5 lbs resulting in a smoothed input power spectrum, as shown in Fig. 4. The figure also shows the desired shape of a typical hammer impact. The roll off in the frequency domain should be smooth and consistent to indicate a clean impact. An effort was also made to impact with a consistent amplitude. The data acquisition software was programmed to screen for double hits and to only accept impacts that fell within a specified range. All impacts fell between 1,850 and 2,150 lbs. A total of five impacts were averaged at each location. Since only the vertical motion of the vehicle was measured, care was taken to ensure that each hit was as “square” as possible to avoid exciting modes in other degrees of freedom (other than vertical).

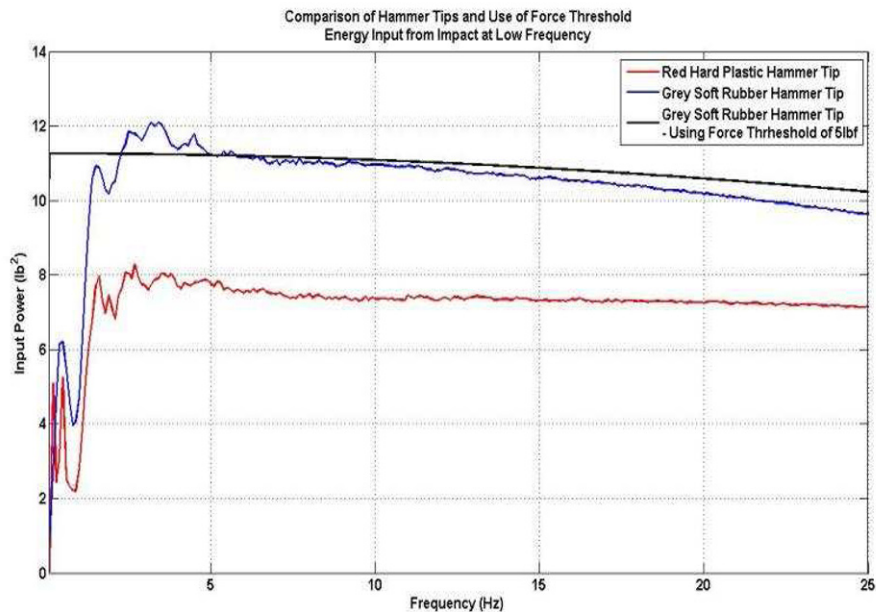


Fig. 4 Hammer tips and force threshold comparison

The CMIF was used to analyze the closely spaced and heavily damped modes of vibration of the vehicle as shown in Figure 5. The function also provided an estimate of the mode shapes contained in the left singular matrix in Eq.(1). The estimated modal vectors were obtained from the left singular matrix at each corresponding frequency and input (reference) location. The mode shapes were then animated using the modal vectors to more easily interpret the motion at each frequency. The modes listed in Table 2 were animated and still images of the deflection shapes were plotted in Figure 7 for the pitch mode at 4.125 Hz. Figure 6 is the un-deformed shape of the vehicle based on the response points collected for each measurement set.

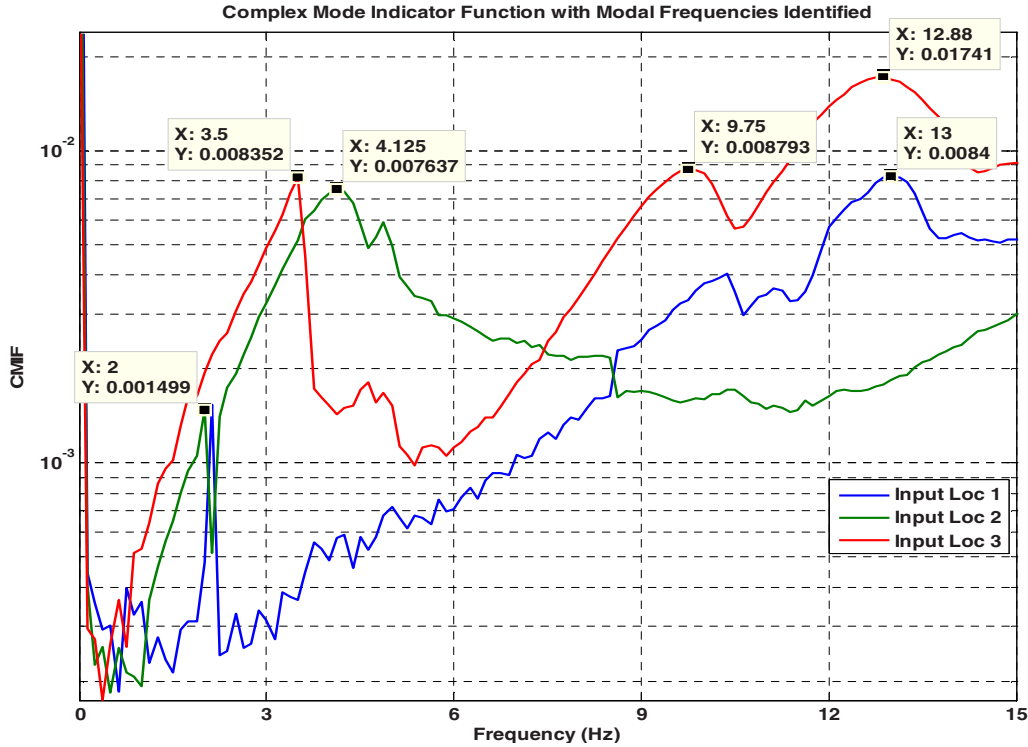


Fig. 5 CMIF plot for three reference points and identified modal frequencies

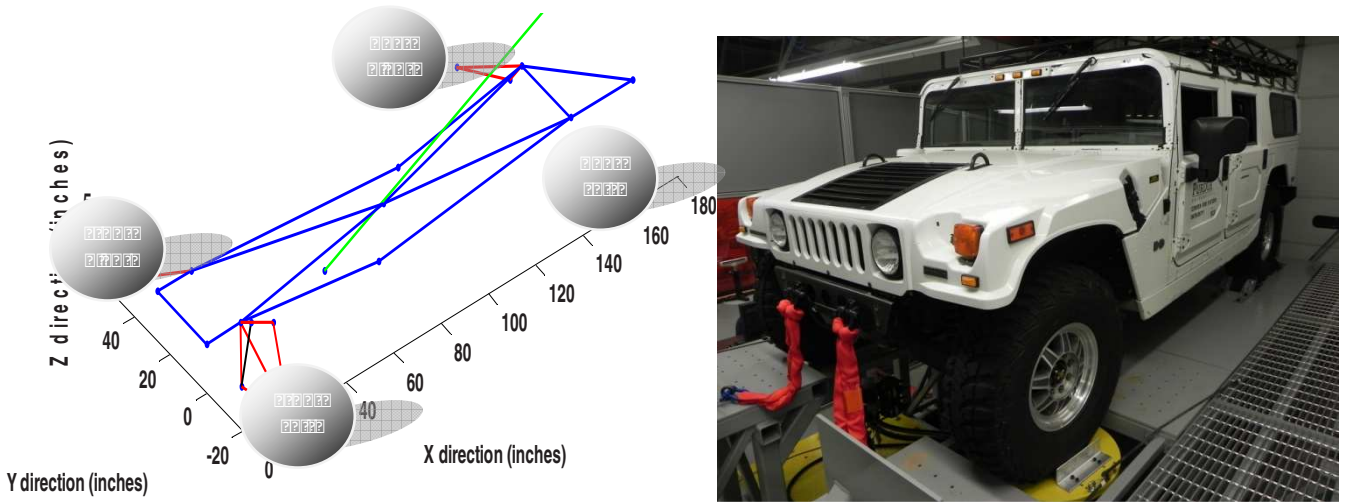


Fig. 6 Representation of un-deformed geometry of the vehicle

In Figure 6, the blue lines represent the vehicle frame or chassis. The red lines represent the suspension, the black line represents the left front shock absorber and the green line represents the vehicle body or cab structure.

ODS at 4.125 Hz - MV from Input 2

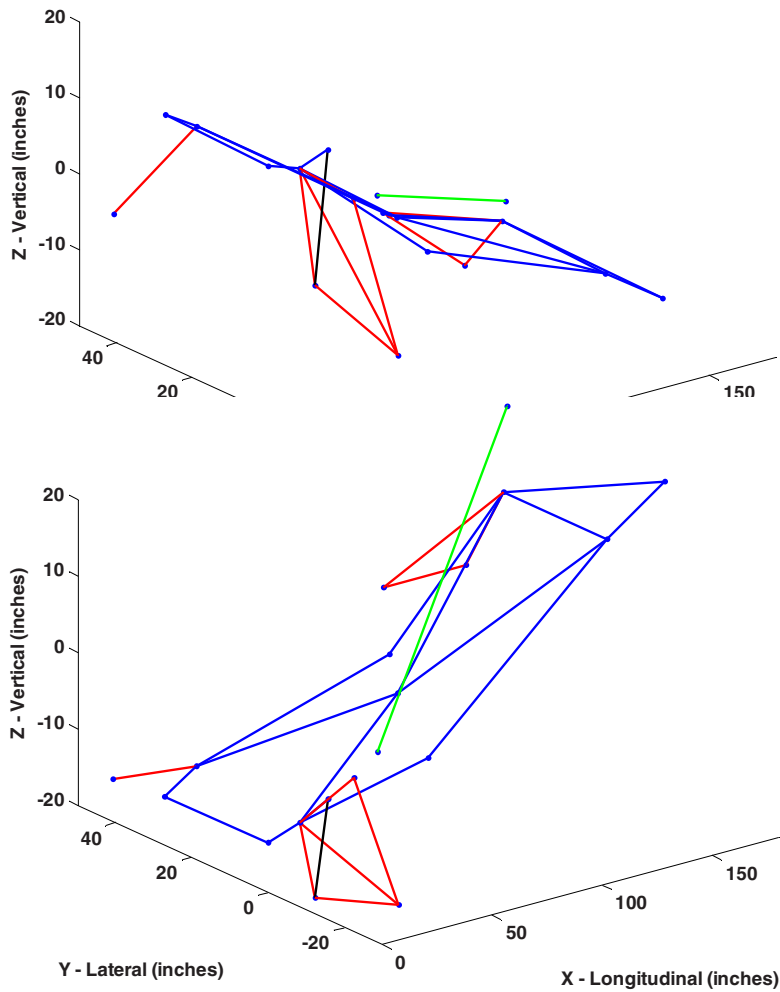


Fig. 7 Pitch mode at 4.125 Hz

Five modes of vibration of the vehicle sprung mass were identified in Table 2. These five modes determine the ride and shake characteristics of the vehicle as defined by SAE J670e [3].

TABLE 2 Identified vehicle modes of vibration

| Mode No. | Frequency (Hz) | Mode Description |
|----------|----------------|------------------|
| 1 | 1.5 | Roll mode |
| 2 | 2.5 | Pitch mode |
| 3 | 3.5 | Yaw mode |
| 4 | 4.125 | Pitch mode |
| 5 | 5.5 | Roll mode |

Due to the location of the modal impact excitation on the vehicle frame, the theoretical model was analyzed using typical vehicle parameters to determine whether or not differences existed for the impact location and road input location. For comparison, Figure 9 revealed that the second peak of the green line, which corresponded to the tire degree of freedom (wheel hop), was non-existent in the FRF of the modal impact location (X_{sprung}/F_{hammer}). These observations indicated that the wheel hop mode of vibration would also not be evident in the experimental data.

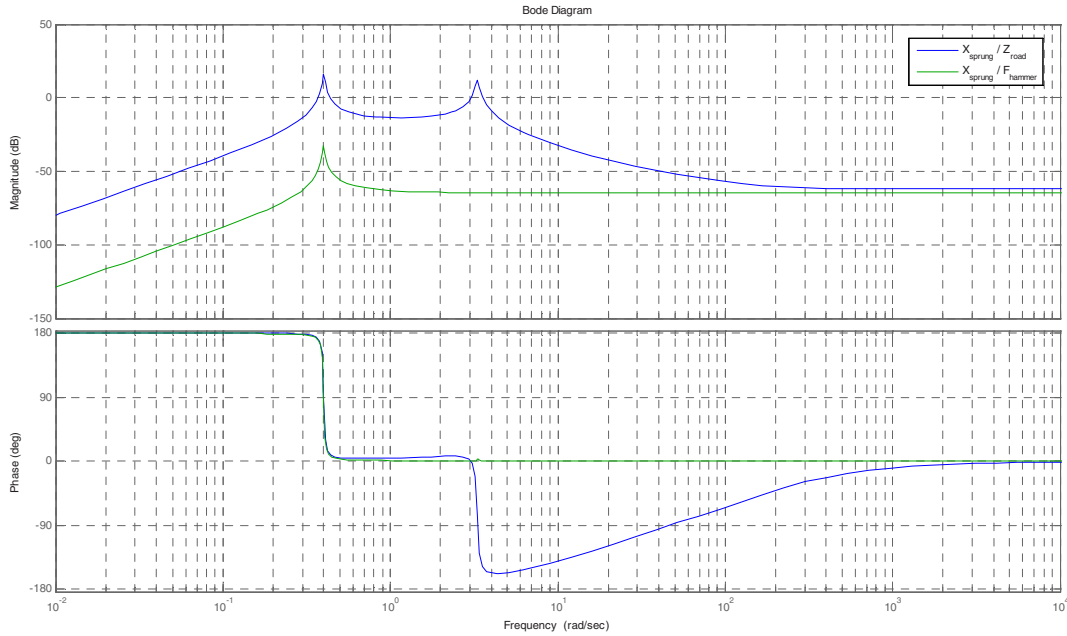


Fig. 8 Theoretical model comparing modal impact and road input locations

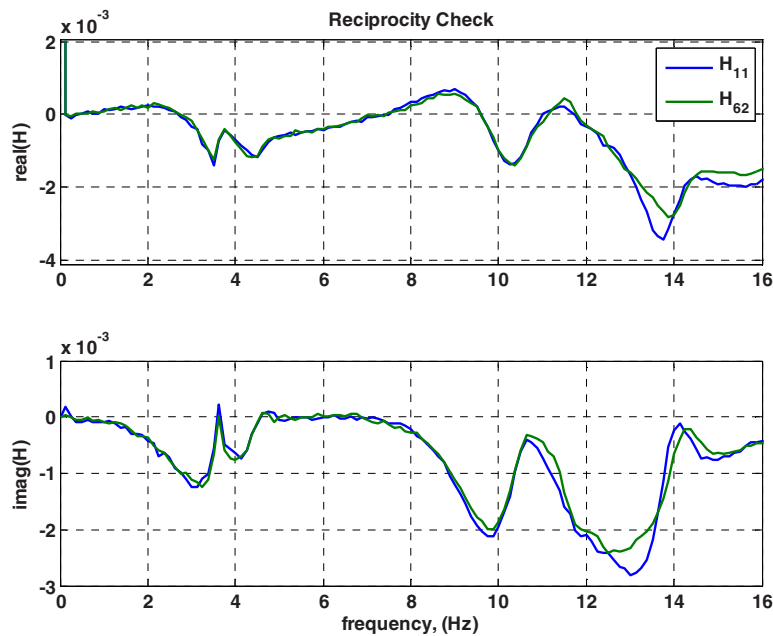


Fig. 9 Verification of reciprocity assumption for vehicle chassis

Figure 10 shows the FRF for the input at location 1 and response at input location 2 as well as the FRF for the input at location 2 and response at input location 1. The fact that these plots lay on top of one another verifies the assumption of reciprocity across the vehicle chassis.

FAULT IDENTIFICATION

In the second half of the experiment, a fault was induced on the vehicle and the change in its response to a frame excitation was measured. All the accelerometers were mounted at points around the front driver side wheel and suspension as shown in Table 3 and Figure 11. The modal hammer was used to impact the frame in the manner described previously. Again, all three impact points were used. However, in this case the tire pressure was reduced from 30 psi to 10 psi in both front tires. Since the two front tires are connected to a central air pressure system, it was not possible to reduce the pressure on one tire only. The rear tires were left unchanged. The vehicle was impacted again to study the effect of low tire pressure on the response.

Table 3 Fault analysis sensor locations

| Location Number | Description | Coordinates | | | |
|-----------------------|-------------|---|-------|-----|-------|
| | | X | Y | Z | |
| Fault Analysis | 13 | Left front upper control arm | -18 | 9.5 | 4 |
| | 7 | Left front frame near shock tower | -14.5 | 0 | 0 |
| | 3 | Left front lower control arm (near shock connection pt) | -9.5 | 7 | -10.5 |
| | 6 | Left front frame - Impact pt 1 | 0 | 0 | 0 |
| | 5 | Left front Wheel Spindle | -16 | 25 | -12 |
| | 19 | Left front shock tower (outside top of spring) | -12 | 9 | 5 |

- The origin for all coordinates listed above is at response point 6, which is the left front frame rail (Impact Point 1)
- Positive x points towards forward vehicle driving direction
- Positive y points towards the driver side of vehicle
- Positive z points up toward the ceiling
- Right hand coordinate system and all measurements in INCHES

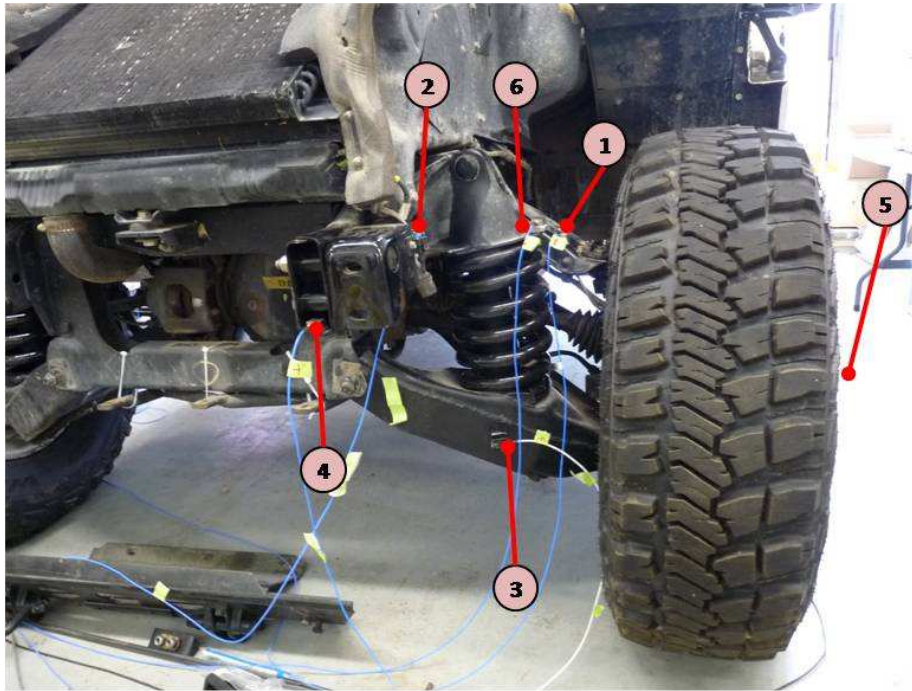


Fig. 10 Sensor locations for low tire pressure fault analysis

Figure 12 illustrates a comparison between estimates of modal frequencies with the front tires at the standard 30 psi pressure in contrast to the 10 psi faulted pressure. This plot indicates that several modes especially the vehicle bounce mode were sensitive to changes in tire pressure because the bounce mode shifted from 3.5 to 3.0 Hz.

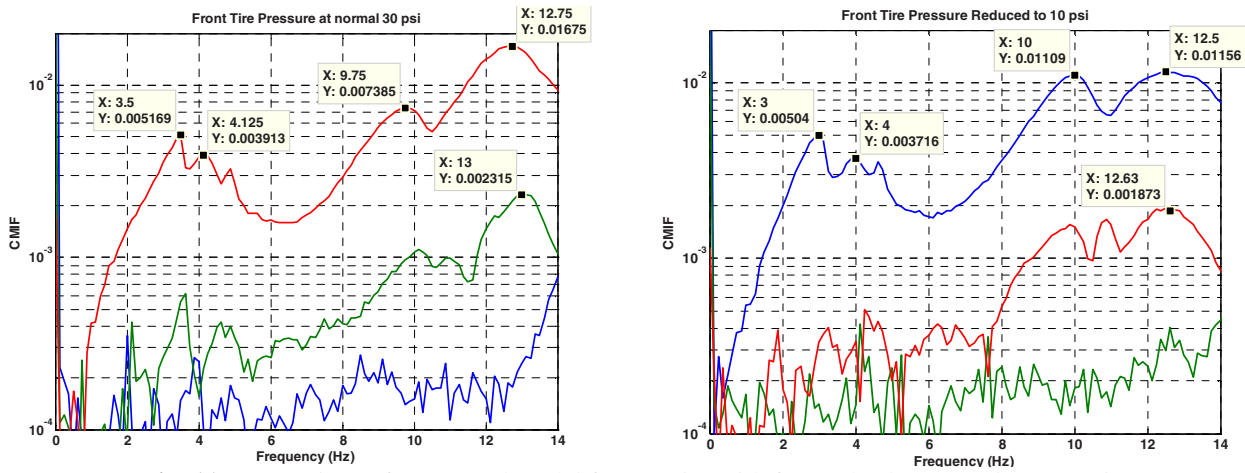


Fig. 11 Comparison of CMIF and modal frequencies with front wheels at 30 psi vs. 10 psi

CONCLUSION

One of the fundamental assumptions that was made at the beginning of the experiment was that inputs on the tire footprint would produce the same dynamic response characteristics as inputs on the frame. However, the experimental data and the model showed that this assumption does not hold across the suspension system. The fact that the wheel hop mode was not seen in the mode shapes indicates that the vehicle suspension may be isolating the un-sprung mass and preventing enough energy from reaching the tire to excite wheel hop.

This experiment showed that although the first choice would probably have been to use a shaker test, the modal impact method still produced meaningful results. The data collected revealed bounce, pitch, roll, and two flexible body modes of the frame. Modal impact testing can be used on a vehicle to quickly investigate the modal properties of the suspension and frame.

The data indicates that modal testing may also have the ability to detect faults in the vehicle suspension. When the front tire pressure was reduced, the frequency of the bounce mode dropped from 3.5 Hz to 3 Hz. This result is logical because a reduction in the tire pressure should reduce the overall stiffness of the suspension. This reduction in stiffness, in turn, would lower the natural frequency as was observed experimentally in this study.

REFERENCES

- [1] B. Schwarz, M.H. Richardson, "Measuring Operating Deflection Shapes Under Non-Stationary Conditions" Proceedings of IMAC XVIII, February 7-10, 2000.
- [2] Allemang, Randall J. "Vibrations: Experimental Modal Analysis." A Complete Review of the Complex Mode Indicator Function (CMIF) with Applications. University of Cincinnati, Cincinnati. 12 Apr. 2010. Lecture.
- [3] Gillespie, T. D. *Fundamentals of Vehicle Dynamics*. Warrendale, PA: Society of Automotive Engineers, 1992. Print.
- [4] Adams, Douglas E. *Health Monitoring of Structural Materials and Components Methods with Applications*. Chichester: Wiley, 2007. Print.

Identifying parameters of nonlinear structural dynamic systems using linear time-periodic approximations

Michael W. Sracic
Graduate Research Assistant, Ph.D Candidate
mwsracic@wisc.edu

&

Matthew S. Allen
Assistant Professor
msallen@engr.wisc.edu
Department of Engineering Physics
University of Wisconsin-Madison
534 Engineering Research Building
1500 Engineering Drive
Madison, WI 53706

ABSTRACT

While numerous mature parametric identification methods are available for linear systems, there are only a few methods capable of identifying parametric models for multiple degree of freedom nonlinear systems. In a previous work, the authors proposed a new identification routine for nonlinear systems based on harmonically forcing a system in a periodic orbit and then recording deviations from that orbit. Under mild assumptions one can model the response about the periodic orbit using a linear time-periodic system model that is relatively easy to identify from the measurements using a variety of techniques. The method provides an estimate of the time periodic state coefficient matrix of the system which gives direct information on the order of the system and the nonlinear-parameters. A prior work explored the method in detail for a single degree-of-freedom system, but it has only been applied to an MDOF system with a limited set of excitation conditions. This work explores a range of possible excitation signals using an analytical model of a cantilever beam with a cubic spring at its tip. Numerical continuation techniques are used to find the stable and unstable periodic responses of the beam and different excitation strategies are explored. Additionally, the method is validated on the analytical model with a conventional approach for nonlinear system identification. The most promising strategies are then applied to a real beam with a significant geometric nonlinearity.

1. Introduction

Most dynamical systems behave nonlinearly in the most general scenario. This can be observed in various structural dynamic systems such as an airplane wing that flutters wildly near a stall point bifurcation [1], in rotor dynamic systems with bearing contact nonlinearities [2], in biomechanics systems such as the human body which has muscles that produce nonlinear forces that move joints through large angles [3-5], or in social science systems such as psychology [6] and economics [7]. While many techniques are available to extract linear time-invariant mathematical models from experimental measurements of these systems, the linear models cannot correctly characterize some of the complex nonlinear phenomena exhibited. Therefore, nonlinear models are needed and nonlinear identification methods are required to extract the nonlinear models from measurements.

A few methods for experimental identification are currently available. Some notable time domain techniques have been successfully applied experimentally such as the restoring force surface method [8], the Hilbert and Huang-Hilbert transforms [9], and the NARMAX method [10]. The former three methods cannot be easily applied to higher order systems while the latter method requires one to assume a form for the nonlinearity in the system prior to the identification. The notable frequency domain techniques consist of the Volterra and Wiener series techniques, the Conditioned Reverse Path method, and the Nonlinear Identification through Feedback of the Output method, all of which were reviewed in [10]. The Volterra and Wiener series techniques require very large amounts of data for even low order nonlinearities. The other two methods

require one to first assume a form of the nonlinearity. A nonlinear normal-modal based technique has also been proposed and is currently being investigated [10, 11].

The authors recently proposed an alternative to these approaches that may overcome some of these limitations. It is a frequency domain technique [12] based on spectra that are similar to linear frequency response functions. Because of this similarity, it allows many concepts from linear system identification to be applied to nonlinear systems and the analyst can distinguish the features in the spectra that are due to the nonlinear response rather than measurement noise. The method provides direct information on the order of the system, the nonlinear parameters, and does not require an a priori assumption regarding the form of the nonlinearities. The basic idea is to drive the nonlinear system so that it responds in a stable periodic orbit and then to perturb the system slightly from the periodic orbit. If the nonlinearities are sufficiently smooth and the deviations from the periodic orbit are sufficiently small, the resulting response can be well approximated with a linear time-periodic model. A number of techniques are then available for identifying a linear time-periodic model for the system. This work utilizes the *Lifting* and *Fourier Series Expansion* (FSE) methods, which were both proposed by Allen in [13]. These techniques are appealing because the linear time-periodic response can be shown to be mathematically equivalent to the response of an augmented linear time invariant system. Therefore, a linear time-invariant parameter extraction method can be used to estimate the linear time-periodic system model, making this parameter estimation step quite convenient. The linear time-periodic model is used to construct the state transition matrix and state coefficient matrix for each state along the original periodic orbit. Finally, the constructed state coefficient matrix can be used to calculate an estimate of the nonlinear system parameters.

The original work by the authors [14] verified the method on simulated measurements of a second order analytical Duffing oscillator, and some original efforts were made to apply the method to a fourth order analytical nonlinear cantilever beam [12]. This work more thoroughly explores the performance of the method for systems with multiple degrees of freedom, and also applies the method to real experimental measurements of a high order system. The experimental system consists of a cantilever beam with a strip of spring steel connected between its free end and a fixture. The spring steel provides a geometric stiffening nonlinearity. The measurements are probed and found to contain clear evidence of time-periodic effects that are distinguishable from noise. A few different harmonic forcing conditions are considered and the state coefficient matrix is estimated, revealing the level of accuracy that is required to obtain meaningful results. Furthermore, in all of the preceding works the authors identified the periodic limit cycle but then used it only to define the state of the system. However, the limit cycle itself is strongly dependent on the nonlinear dynamic model for the system and could be used to perform nonlinear identification with a conventional algorithm. This work explores this possibility, using a variant on the restoring force surface method to compute the net nonlinear restoring force on each mass. That restoring force is then used to validate the results of the more detailed model that is found using the proposed linear time-periodic approximation. The following section provides the background theory that supports the technique. Then Section 3 introduces the nonlinear beam for the experimental setup and the analytical model and applies the identification to simulated and experimental measurements of the beam. The results are presented and discussed, and finally some conclusions are provided.

2. Theory

2.1 Linear Time-Periodic Approximations of Nonlinear Systems

Generally, a forced nonlinear system can be represented in state space with the following equation

$$\begin{aligned}\dot{x} &= f(x, u) \\ y &= h(x, u)\end{aligned}\tag{1}$$

where f and h are functions that describe how the time-dependent state of the system, $x(t)$, and the time-dependent inputs applied to the system, $u(t)$, influence the dynamics of the system. Assuming that the system has a periodic solution $\bar{x}(t+T) = \bar{x}(t)$, then one can define a periodic orbit γ , which is a trajectory in the state space that contains the state \bar{x} for every time t . If a small input is applied to perturb the system from γ , then the state and input of the system can be described as small deviations from the periodic orbit, $x = \bar{x} + \tilde{x}$ and $u = \bar{u} + \tilde{u}$. If the nonlinearities are C^1 (at least one time continuously differentiable), then eq. 1 can be expanded in a Taylor series, and if the perturbation is sufficiently small the higher order terms can be neglected to obtain the following.

$$\begin{aligned}\dot{\tilde{x}} &= \left[\frac{\partial f_i}{\partial x_j} \right]_{\bar{x} \in \gamma} \tilde{x} + \left[\frac{\partial f_i}{\partial u_j} \right]_{\bar{u}} \tilde{u} \\ \tilde{y} &= \left[\frac{\partial h_i}{\partial x_j} \right]_{\bar{x} \in \gamma} \tilde{x} + \left[\frac{\partial h_i}{\partial u_j} \right]_{\bar{u}} \tilde{u}\end{aligned}\quad (2)$$

The shorthand notation $\left[\frac{\partial f_i}{\partial x_j} \right]$ is used for the partial derivative matrices meaning that the component in the i^{th} -row and j^{th} -column is the partial derivative of the i^{th} component of f with respect to the j^{th} component of x . Generally, these matrices may depend on both x and u and would need to be evaluated at both \bar{x} and \bar{u} , but typical structural dynamic systems do not contain this type of cross coupling. The approximate model given by the previous equation is that of a linear time-periodic state space system with $A(t) = \left[\frac{\partial f_i}{\partial x_j} \right]$, $B(t) = \left[\frac{\partial f_i}{\partial u_j} \right]$, $C(t) = \left[\frac{\partial h_i}{\partial x_j} \right]$, and $D(t) = \left[\frac{\partial h_i}{\partial u_j} \right]$. The solution of such a system is governed by the state transition matrix $\Phi(t, t_0)$, which transfers the state of the system from an initial time t_0 to time t . For this work, the disturbance force is impulsive such that $\tilde{u} = 0$ after the impulse. Then, the solution to eq. (2) is given by the following equation.

$$\begin{aligned}\tilde{x} &= \Phi(t, t_0) \tilde{x}_0 \\ \tilde{y} &= C(t) \Phi(t, t_0) \tilde{x}_0\end{aligned}\quad (3)$$

2.2 Review of System Identification Methods for Linear Time-Periodic Systems

When a system is well approximated as linear time-periodic without any degenerate modes, its state transition matrix can be represented using Floquet theory [13, 15-17] in summation form as

$$\begin{aligned}\Phi(t, t_0) &= \sum_{r=1}^n [R(t)]_r e^{\lambda_r(t-t_0)} \\ [R(t)]_r &= \{\phi(t)\}_r \{\eta(t_0)\}_r^T\end{aligned}\quad (4)$$

where n is the order of the system and $[R(t)]_r$ is the r^{th} residue matrix corresponding to the r^{th} Floquet exponent, λ_r , and is composed of the product of the r^{th} time-periodic right Floquet eigenvector $\{\phi(t)\}_r$ and r^{th} constant left Floquet eigenvector $\{\eta(t_0)\}_r$ of the state transition matrix. Allen has suggested two techniques for extracting a model from such a system. The first is called the Fourier Series Expansion technique and the second is called the Lifting technique, and both result in a representation of the response that is linear time-invariant. The methods are summarized briefly here and are provided with further details in [13].

2.2.1 Fourier Series Expansion Technique

The residue matrix $[R(t)]_r$ in the previous equation is periodic because of the periodic Floquet eigenvectors $\{\phi(t)\}_r$ and can therefore be expanded in a Fourier series. After exchanging the order of summation and simplifying terms, the result is

$$\Phi(t, t_0) = \sum_{r=1}^n \sum_{m=-N_B}^{N_B} [B_m]_r e^{(\lambda_r + im\omega_T)(t-t_0)}\quad (5)$$

where $[B_m]_r$ is the m^{th} Fourier coefficient matrix of the r^{th} mode and $\omega_T = 2\pi/T$ is the period frequency. To be exact, the Fourier expansion must include an infinite number of terms, but in practice a finite number of Fourier terms, $m = -N_B, \dots, N_B$, will sufficiently approximate the expansion [12, 13]. The Fourier Series Expansion representation of the response is equivalent to a linear modal model with $n^*(2*N_B+1)$ eigenvalues $\lambda_r + im\omega_T$.

2.2.2 Lifting technique

If the measured response of a time-periodic system is resampled at an integer number of points per period T , then an analysis can be performed based on ‘‘lifting’’ augmented signals from the full linear time-periodic response. Suppose that the response $y(t)$ has been sampled M times per period for an integer N_c cycles of the fundamental period. The lifted response y_m^l is the vector such that

$$y_m^l = [y_0^T, y_1^T, \dots, y_{M-1}^T]^T \quad (6)$$

where y_k for $k=0, \dots, M-1$ is the response vector at t_j with $j=k+mM$ and m ranges from 0 to N_c-1 [13]. In the absence of an input force the lifted response can be arranged as

$$y_m^l = \sum_{r=1}^n \{R^{ld}\}_r e^{\lambda_r m T} \quad (7)$$

where $\{R^{ld}\}_r$ is the residue vector of size M times the number of outputs of the response. One should note that $\{R^{ld}\}_r$ must account for the delay between the initial time and the k^{th} time instant as discussed in [13]. The advantage of this approach is that the lifted response retains the order of the original linear time-periodic system. The eigenvalues may be aliased, but the aliased eigenvalues still provide a valid representation for the linear time-periodic system.

2.2.3 Constructing the System Model from Experimental Measurements

In [13], Allen discusses how the state transition matrix can be constructed from either of the models above assuming that one has measured the displacement of the system. The state vector of such a system consists of the measured displacement states as well as the corresponding velocity states, but the velocities are not typically measured, so Allen differentiated the Fourier Series Expansion model of the system to find the velocity states needed to form the state vector of the system. In this work, acceleration measurements are considered. When this is the case, the Fourier series expansion model for the free acceleration response is written as

$$x_a = \sum_{r=1}^N \sum_{m=-N_B}^{N_B} \{B_m\}_r e^{(\lambda_r + im\omega_T)(t-t_0)} \quad (8)$$

where N is the number of degrees of freedom and $\{B_m\}_r$ is the residue vector. In order to create a full state vector that consists of N position states x_d and N velocity states x_v , one can integrate the previous equation two times successively to calculate the velocity and position states.

$$\begin{aligned} x_v &= \sum_{r=1}^N \sum_{m=-N_B}^{N_B} \{B_m\}_r (\lambda_r + im\omega_T)^{-1} e^{(\lambda_r + im\omega_T)(t-t_0)} \\ x_d &= \sum_{r=1}^N \sum_{m=-N_B}^{N_B} \{B_m\}_r (\lambda_r + im\omega_T)^{-2} e^{(\lambda_r + im\omega_T)(t-t_0)} \end{aligned} \quad (9)$$

Then, the state transition matrix and state coefficient matrix can be calculated as in [13].

2.2.4 Calculating the equation of motion from $A(t)$

In eq. (2), the original nonlinear system model was differentiated to obtain the time-varying coefficient matrices of the linear time-periodic model, which resulted in a total derivative form for the system.

$$df = \frac{\partial f}{\partial x} dx + \frac{\partial f}{\partial u} du \quad (10)$$

In this work, only the linearized model $A(t) = [\partial f_i / \partial x_j]$ has been identified, so a model for the first term in the previous equation can be used to estimate that terms contribution to the nonlinear equations of motion. It was assumed that the coefficient matrix $[\partial f_i / \partial x_j]$ depended only on x and $[\partial f_i / \partial u_j]$ only on u . Using this assumption, the periodic orbit state vector and input components, which are known, can be used to integrate the linear time-periodic system and define the following,

$$a_{i,j}(x_j) = \int_{\bar{x}_j(t=0)}^{\bar{x}_j(t=T)} A_{(i,j)} dx_j, \quad i, j = 1, \dots, n, \quad n = 2N \quad (11)$$

where $a_{i,j}(x_j)$ is the integral of the component in the i^{th} row and j^{th} column of $A(t)$ and is taken with respect to the j^{th} component of the state vector for all the states within the original periodic orbits. The terms in the first N rows of the $[a_{i,j}]$ matrix define the identity relationships of the state vector components, but those in the lower N rows define the force relationship of the i^{th} degree of freedom with respect to the j^{th} state vector component. So this method allows these dynamic forces to be individually calculated from the identified time-periodic model. The total dynamic force that acts on a degree of freedom of the system is then equal to the sum of a single row of the matrix $[a_{ij}]$, and is a function of the position and velocity states of the system.

$$a(x_d, x_v) = \sum_{j=1}^n a_j(x_j) \quad (12)$$

In the previous equation, a_j is the j^{th} column of the matrix, $[a_{ij}]$. This function is directly related to the total restoring force of the system, since the following equation

$$\hat{f}(x, u) = a(x_d, x_v) + \int \frac{\partial f}{\partial u} du \quad (13)$$

Fully defines the reconstructed nonlinear equations of motion.

2.2.5 Modified Restoring Force Surface Method for Periodic Response

In this section a method is developed based on the restoring force surface approach [8] for solving for the net restoring forces over the periodic orbit from the measured periodic response. The restoring force surface method is based on the following equation of motion, which is valid for a broad range of structural systems.

$$Mx_a + g_{RF}(x_d, x_v) = F(t) \quad (14)$$

Assuming that the acceleration of each of the nodes of the system has been measured as well as the applied force $F(t)$, the restoring forces can be found as follows if one has an estimate for the mass matrix M .

$$g_{RF}(x_d, x_v) = F(t) - Mx_a \quad (15)$$

The restoring forces are functions of the displacement and velocity, and since x_a is known, x_d and x_v can be found by integrating x_a . Since x_a is the periodic response, it can be readily described by a Fourier series. As long as the constant term in the series is zero, then the Fourier series model can be integrated as in eq. (9) and then the restoring force can be plotted versus x_d and x_v or versus time over the periodic orbit.

3. Nonlinear cantilever beam system

The proposed identification method was evaluated by applying it to measurements from a nonlinear beam. [Figure 1](#) below shows a top view photograph of the actual experimental setup. An aluminum 6061 beam is bolted to a steel mounting block, shown on the left side of the image. A small strip of spring steel is bolted to the free end of the cantilever and clamped to another steel mounting block. Both of the mounting blocks are bolted to a massive steel tube. The steel tube and mounting blocks approximate the fixed support of an ideal cantilever. The whole setup rests on a foam pad on a massive table top. The beam is oriented such that the bending axis is parallel to the plane of the table top. [Figure 2](#) shows a close top and front view of the spring steel between the tip of the beam and the right hand side support. [Table 1](#) below provides the physical dimensions of the beam and the spring steel in millimeters.

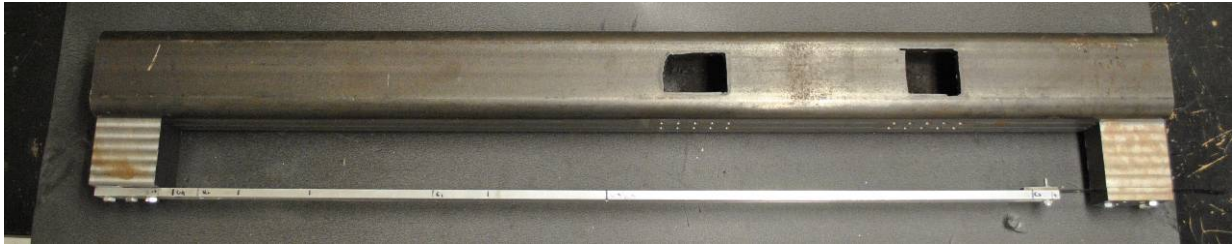
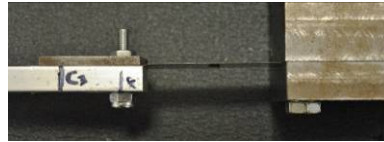
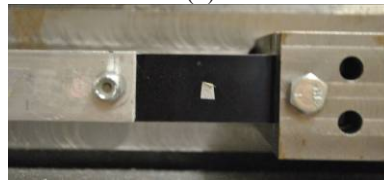


Fig. 1 Top view of the experimental nonlinear beam setup



(a)



(b)

Fig. 2 Top view (a) and front view (b) of the spring steel connected to free end of the cantilever beam

Table 1 Aluminum 6061 beam and blue-finished and polished 1095 spring steel dimensions in millimeters

| Dimension | Al 6061 Beam | 1095 Spring Steel |
|-----------|--------------|-------------------|
| Length | 1016 | 53.2 |
| Width | 25.4 | 25.4 |
| Thickness | 9.5 | 0.0762 |

The spring steel on the tip of the beam adds stiffness at that point that is geometrically nonlinear. This setup was originally proposed in [18] and other researchers have studied similar beam setups [10, 19, 20].

Figure 3 below shows a schematic of the system, which is modeled as a uniform, prismatic cantilever beam with material density ρ , elastic modulus E , cross sectional area A_b , bending area moment of inertia I , and length L . The position along the length of the beam is given by the variable 'x'. The deflection of the beam is designated with the variable y . The beam has a nonlinear tip spring with stiffness k_{nl} that is assumed to be a function of the tip displacement.

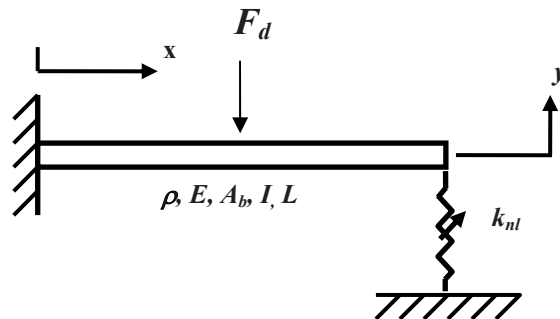


Fig. 3 Schematic of the nonlinear beam

3.1 Ritz-Galerkin Discrete Model

A Galerkin approach was used to create a finite-order model for the beam that exhibits similar properties of the experimental system. Assuming that the beam behaves linear-elastically, mode shapes corresponding to transverse bending motion were used as shape functions to construct the Ritz-Galerkin representation [21]. The displacement of the beam at a position x was approximated as

$$y(x, t) = \sum_{r=1}^{N_m} \psi_r(x) q_r(t) \quad (16)$$

where $\psi_r(x)$ is the r^{th} Euler-Bernoulli beam mode shape for a cantilever, $q_r(t)$ is the r^{th} generalized coordinate, and N_m is the number of modes used. The system's undamped equations of motion are provided in Eq. (17), where the coordinates are the amplitudes of the basis functions.

$$\rho A_b L [M] \ddot{q} + \frac{EI}{L^3} [K] q = Q = \sum f_{ext} \psi_r(x_f) \quad (17)$$

Modal damping was added to the equation by performing an eigenvector analysis on the linear system and then using,

$$[C] = (\rho A_b L)^2 [M] [\phi_b] [diag(2\zeta_r \omega_r)] [\phi_b]^T [M] \quad (18)$$

where $[\phi_b]$ is a matrix containing the eigenvectors in the columns, ω_r is the r^{th} circular natural frequency, and ζ_r is the r^{th} desired damping ratio. The generalized force vector Q is a sum of the product between all external forces and the value of the shape functions at the point where the force is applied, x_f . Therefore, Q includes Ritz series formulated contributions from F_d in Figure 3 as well as the restoring force due to the spring [21]. The beam provides linear stiffness at the tip due to its flexural rigidity, so the spring stiffness was chosen to be purely nonlinear as given below.

$$k_{nl} = k_3 y(L)^2 \quad (19)$$

The physical restoring force due to the spring is then equal to

$$f_{sp} = k_3 y(L)^3. \quad (20)$$

The generalized force vector then has components corresponding to the nonlinear spring $\{Q_{sp}\}$ located at $x=L$ and the externally applied force $\{Q_{ext}\}$ located at $x=x_f$.

$$\{Q\} = \{Q_{sp}\} + \{Q_{ext}\} = k_3 y(L)^3 \begin{Bmatrix} \psi_1(L) \\ \vdots \\ \psi_N(L) \end{Bmatrix} + F_D \begin{Bmatrix} \psi_1(x_f) \\ \vdots \\ \psi_N(x_f) \end{Bmatrix} \quad (21)$$

The external force is given by the following.

$$F_D(t) = A \sin(2\pi ft) + A_{impulse} \sin\left(\frac{\pi}{\bar{\tau}}(t - t_p)\right) \quad (22)$$

where A is the amplitude and f is the frequency of the periodic forcing term, and $A_{impulse}$ is the amplitude of the impulsive forcing term, which is used to perturb the system from the periodic orbit. The impulsive force has duration $\bar{\tau}$ and is initiated at t_p .

After using the Ritz-Galerkin method to form the discrete beam model and to account for the nonlinear applied force of the spring, the equations of motion were transformed back into physical coordinates using the relationship in eq. (16). The differential equations of motion can then be arranged in state space format.

$$\begin{Bmatrix} \{\dot{y}\} \\ \{y\} \end{Bmatrix} = \begin{Bmatrix} \{y\} \\ -[M_p]^{-1} \left([C_p] \dot{y} + [K_p] y + \{F\} \right) \end{Bmatrix} \quad (23)$$

$$[M_p] = \rho A_b L [\Psi]^T [M] [\Psi]^{-1}, \quad [C_p] = [\Psi]^T [C] [\Psi]^{-1},$$

$$[K_p] = \frac{EI}{L^3} [\Psi]^T [K] [\Psi]^{-1}, \quad \{F\} = [\Psi]^T \{Q\}$$

The matrix $[\Psi]$ has the numerical values of the mode vectors for specific position coordinates on the beam. Since this matrix must be square in order to form an inverse, it is convenient to choose the number of degrees of freedom in the system to be equal to the number of modes used in the Galerkin expansion. Then, $[\Psi]$ can contain shape functions evaluated at the nodal degrees of freedom on the beam. In this study the number of mode shapes used in the expansion and the number of degrees of freedom used to model the beam was $N_m=N=2$. The degrees of freedom were located at the center and tip of the beam.

In order to mimic the experimental system, the following parameters were used in the model, which are based on the nominal properties of the experimental hardware: $\rho=2700 \text{ kg/m}^3$, $E=68\text{e}9 \text{ N/m}^2$, $A_b=3.23\text{e-}4 \text{ m}^2$, $I=4.34\text{e-}9 \text{ m}^4$, $L=1.016 \text{ m}$. Using these properties with the Ritz-Galerkin method, the two linear natural frequencies of the system are $\omega_1/(2\pi)=9.97 \text{ Hz}$ and $\omega_2/(2\pi)=62.51 \text{ Hz}$. The transverse stiffness contribution of the spring steel on the experimental beam is approximated in the model as $k_3=1.4764\text{e}9 \text{ N/m}^3$. A derivation of this approximation can be found in the appendix.

3.2 Simulated Measurements

In order to apply the proposed nonlinear identification, the nonlinear beam must first be driven to respond in a periodic orbit. However, there are many possible periodic orbits that this system may be driven in so it is desirable to consider all of the possible periodic orbits for different forcing configurations. In a companion paper [22], the authors used a numerical continuation technique to calculate the periodic solutions of the beam model for forcing amplitude of $A=1$ Newton and for forcing frequencies in the band 6-70 Hz. The results of the computation are shown in Figure 4. In (a) and (b), the response curve near the first linear natural frequency is plotted. The red and blue curves in (a) correspond to the displacement initial conditions of the first and second degree of freedom, respectively. The green and black curves in (b) are the analogous velocity initial conditions. This color format is repeated in (c) and (d) for the frequency band near the second linear natural frequency. The curves quantify the resonant responses of the first and second modes of the nonlinear beam (referenced to zero phase of the force), but they also provide the initial state vector for a specific frequency that one can integrate in time to achieve a periodic orbit. A detailed discussion of the dynamics of the frequency response curves is provided in [22]. The important implications of these nonlinear frequency response curves is that the resonance peaks tend to bend towards higher frequencies for this system, which causes regions where multiple periodic orbits are possible for a single forcing frequency, and for this system one of those possible solutions is unstable (unstable solutions are designated in the plots with the dashed lines). The forcing configuration needs to be carefully selected in order to achieve a successful identification of the nonlinear parameters. Guidelines for selecting forcing configurations for the system identification method used here are discussed in detail in [14] for a single degree of freedom system, and those guidelines apply equally well here.

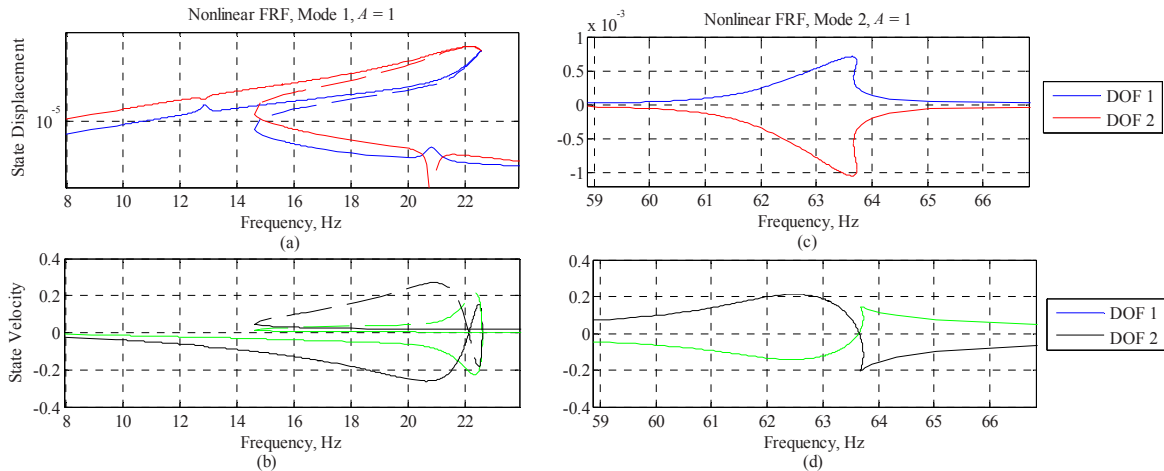


Fig. 4 Initial conditions that result in periodic responses for $A=1$ plotted versus forcing frequency

The nonlinear frequency response curves were used to understand what types of periodic orbits were possible, and a few of the different alternatives were selected for study. It is desirable to drive the system in a stable periodic orbit that is sufficiently nonlinear and isolated from other nearby stable periodic orbits. Sracic and Allen [14] showed that periodic orbits on the larger amplitude branch of the bent resonance peak tend to provide suitable periodic orbit conditions to use for the identification procedure for a hardening resonance such as that of the peak in Figure 4(a). Therefore, a forcing frequency of $f_1=15.4 \text{ Hz}$ was chosen on the first resonance peak of Figure 4(a). Since the beam model has two modes that produce resonance responses, a second forcing frequency of $f_3=60.9 \text{ Hz}$, which is just below the second resonance peak of Figure 4(c),

was chosen to explore the results of the identification when the periodic orbits from different modes are used. For each case, the procedure that was employed in [14] is also used here to simulate the response and perform the identification. First, the acceleration periodic and periodic plus perturbation responses are simulated using MATLAB's 4-5th order Runge-Kutta integrator function 'ode45'. (Although the discrete system is derived for a state vector consisting of all the displacement and velocity states, 'ode45' allows one to extract the acceleration states of the system from the calculation as well.) For each response, the amplitude of the harmonic forcing was $A=1$ N and the amplitude, duration, and time of initiation of the impulsive force were $A_{impulse}=10$ N, $\bar{\tau}=0.02$ seconds, and $t_p=0$ seconds (the impulsive force was set to zero when computing the periodic response). The response was calculated for a time history that was long enough for the perturbation to decay such that only the underlying periodic orbit response remained.

Case 1:

The responses were calculated from initial conditions $[y \dot{y}] = [-3.517e-5; -1.223e-4; 3.639e-2; 0.1160]$, which define the periodic orbit at 15.4 Hz relative to zero phase on the forcing function, and the solution was sampled at a 616.4 Hz, which gave 40 samples per period of the periodic orbit. Figure 5 shows the time history of the tip degree of freedom both early (a) and late (b) in the response. The periodic response is plotted with the dashed blue curve and the periodic plus perturbed response is plotted with the solid red line. The difference between the periodic and perturbation responses is plotted in (c) with the solid black line, and this plot shows that the perturbation is small compared to the periodic response and that it eventually decays to approximately zero, meaning the response has returned to the periodic orbit. The responses of the beam midpoint degree of freedom are not shown, but they were in phase with the tip responses shown here and have similar characteristics but smaller extreme amplitudes.

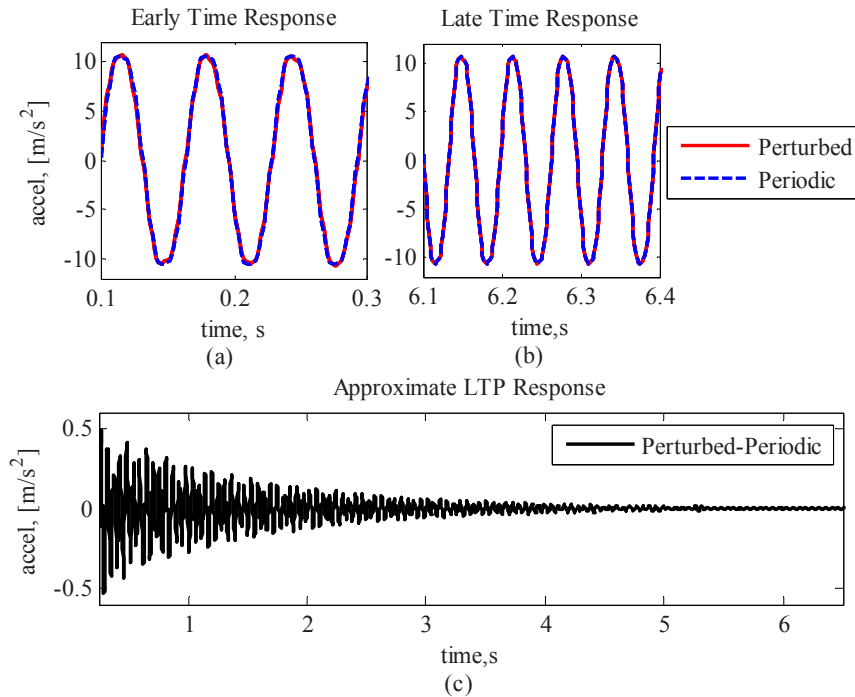


Fig. 5 Tip responses of the beam model for forcing frequency $f_1=15.4$ Hz

The spectra of the perturbed responses and those of the difference between the perturbed and the periodic response were calculated with the Fast Fourier Transform (FFT) algorithm in MATLAB and are plotted in Figure 6(a) and (b) for the midspan and tip degrees of freedom, respectively. The perturbed responses are plotted with the solid red lines and the perturbed minus the periodic responses are plotted with the dashed black curves. The red curves contain a number of sharp peaks at the frequencies 15.4, 46.2, 77, 107.8, and 138.6, and the magnitudes of these peaks diminish with increasing frequency. These frequencies correspond to the forcing frequency and a few of its odd harmonics (e.g. 3×15.4 Hz = 46.2 Hz). The spectra of the red and black curves also contain a number of broad peaks near 12.6, 18.2, 43.4, 49, 65.8, 74.2, 79.8, 96.6, 110.6, and 127.4 Hz in both degrees of freedom, at 35 Hz in the first degree of freedom, and at 105 Hz in the second degree of freedom.

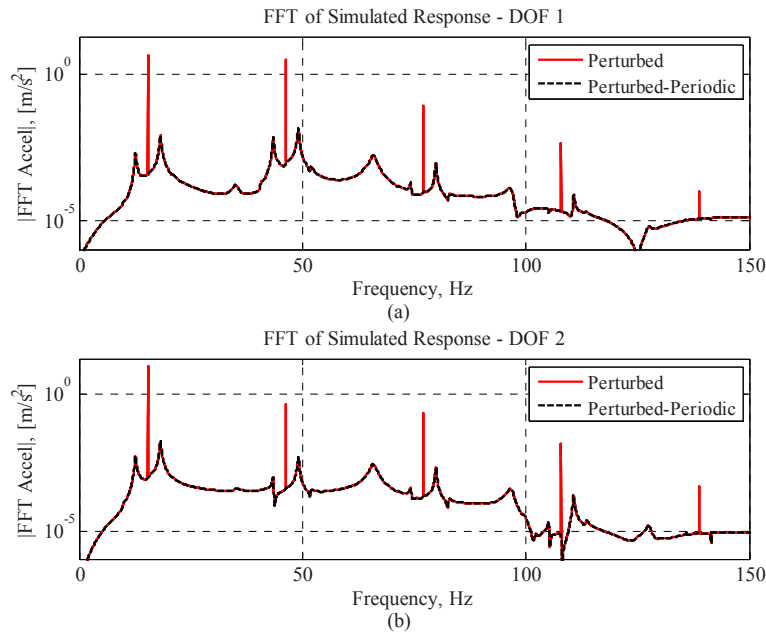


Fig. 6 Response spectra of the nonlinear beam simulation for forcing frequency $f_1=15.4$ Hz

The response of the beam is strongly nonlinear, since a single harmonic input was applied at 15.4 Hz, and the system responded at that frequency as well as at a number of its harmonics. The broad peaks in the response all seem to have the characteristics of linear mode peaks; Eqs. (5) and (8) can be used to understand that many of these peaks are due to time-periodic effects of the perturbation about the periodic orbit. For example, the peaks at 12.6 and 18.2 Hz have similar characteristics to the peaks at 43.4 and 49, and the two peak clusters are separated by 30.8 Hz, which is twice the fundamental frequency of the periodic orbit. These two peak clusters seem to be repeated at intervals of 30.8 Hz, although the magnitudes of the peaks change. The peaks at 35, 65.8, and 96.6, and 127.4 Hz are also increasing in frequency by 30.8 Hz and have similar characteristics albeit different magnitudes. The fact that many of these peaks seem to be related and occur at frequencies that can be linked by the fundamental periodic orbit frequency is strong evidence that the system is behaving time-periodically about the orbit. Noise or some other artifact in the response is not likely to have the characteristic shape of a mode nor to occur at frequencies that are related by the periodic orbit frequency.

In order to fit a time-periodic model to the perturbed minus the periodic responses, the lifting technique [13] was used to resample the responses into a set of ‘lifted responses’ that are exemplary of the responses exhibited by a lower-order linear time-invariant system. The composite spectra (or average) of the lifted responses is plotted in Figure 7 with the solid black line, and it contains one prominent peak near 2.8 Hz and a much weaker, broader peak near 4.2 Hz. The Algorithm of Mode Isolation (AMI) [23] identified two modes in the composite response spectra. A reconstruction of the two mode fit is plotted in the figure with the dashed line. The difference between the response curve and the fit is plotted with the dashed-dot gray curve, and it shows that the two-mode fit approximates the response very well. AMI identified two eigenvalues $\lambda_1 = -0.7310 + 17.6158i$ and $\lambda_2 = -3.9901 + 26.2590i$, natural frequencies $|\lambda_1|/(2\pi) = 2.806$ Hz and $|\lambda_2|/(2\pi) = 4.227$ Hz, and damping ratios 0.0415 and 0.1502, respectively.

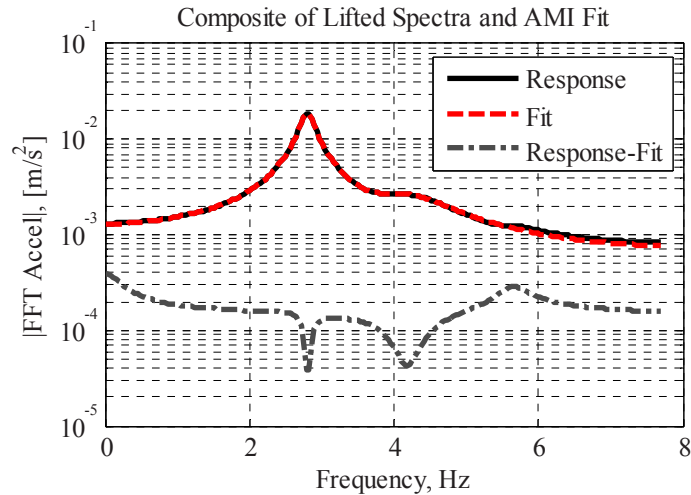


Fig. 7 Composite spectrum and AMI fit of the lifted responses for forcing frequency $f_1=15.4$ Hz

The lifting technique is advantageous because any peaks in a response that are due to time-periodic mode effects are collected to a single peak, so the underlying order of the system is more easily determined; even though the spectra in Figure 6 contain many peaks, the composite spectrum of the lifted responses shows clearly that the system has only two dominant modes. The modal fit obtained by AMI provides the time-periodic mode shapes of the system for one full period of the underlying periodic orbit. The next step towards constructing the state transition matrix and state coefficient matrix of the linear time-periodic system is to expand the identified mode shapes in a Fourier series and to determine which Fourier coefficients contribute meaningful information to the response. This process is clearer if the identified time periodic modes are first unaliased (a discussion of aliasing due to lifting can be found in [13, 24]).

After the identified modes were unaliased, they were expanded in a Fourier series. Figure 8 shows a plot of the amplitudes of each of the coefficients in the Fourier series expansion of Mode 1 (a) and Mode 2 (b). The open blue circles designate all of the coefficients calculated in the expansion. The red dots designate the Fourier coefficients that will be retained in the linear time-periodic model when computing $A(t)$.

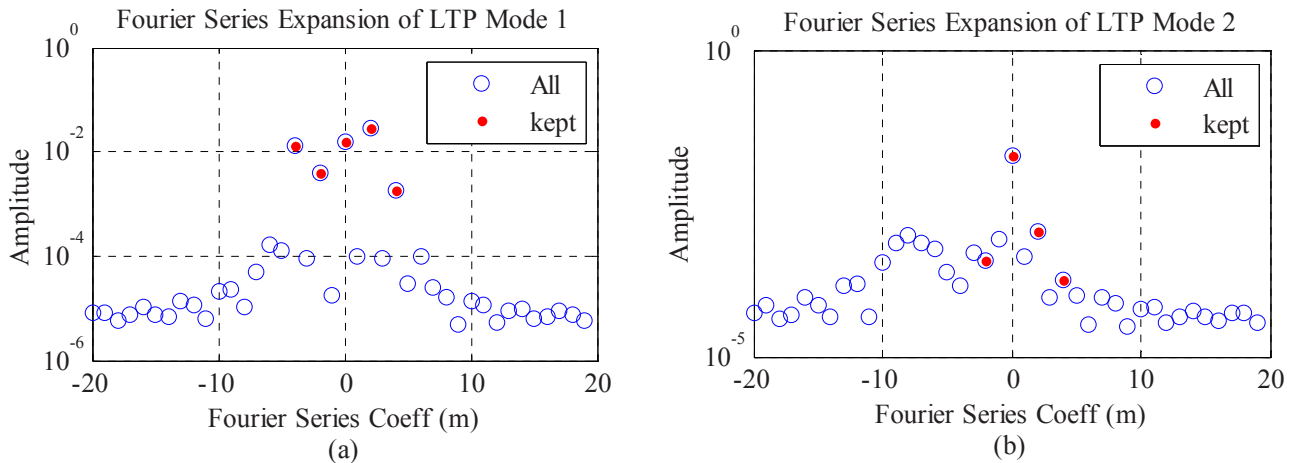


Fig. 8 Fourier series expansions of the identified modes for forcing frequency $f_1=15.4$ Hz

For the first mode, the dominant coefficients were easily determined because of their large amplitude relative to the others. One can verify that these coefficients are important to the response by interrogating the spectra in Figure 6(a) and (b) for the corresponding peaks. It was determined that the unaliased Floquet exponent was attributed to the peak at 18.2 Hz, so this is the $m=0$ harmonic in the Fourier series expansion. The peaks at 49, 79.8, and 110.6 Hz can be attributed to the $m = +2, +4,$ and $+6$ harmonics (i.e. $18.2+2*15.4= 49$, $18.2+4*15.4 = 79.8$, and etc.). The peaks at 12.6, 43.4, 74.2, 105 Hz can be attributed to the $m=-2, -4,$ and -6 harmonics since for example, $18.2-2*15.4= -12.6$ and negative frequencies reflect back to positive frequencies. The Fourier series expansion in Figure 8 reveals that the harmonics $m=-4,-2,0,+2,$ and $+4$, have larger amplitude than the baseline noise, so only those are retained when forming $A(t)$.

The dominant coefficients of the second mode (b) are more ambiguous. One might presume from Figure 8(b) that only the $m=0$ term is significant. However, the spectra from Figure 6(a) and (b) show that there are significant time-periodic peaks at 35, 96.6, and 127.4 Hz that can be resolved from the noise. Since the Floquet exponent of this mode is 65.8 Hz, these peaks correspond to the $m=-2, +2$, and $+4$ harmonics of the expansion, and because the peaks in the spectra can be resolved from noise they are physically meaningful and should be retained in the Fourier series expansion of the mode.

After the Fourier series models of the identified modes have been formed, they were integrated twice according to Eq. (9) in order to obtain a description of the modes in terms of displacement. Then, the state transition matrix and state coefficient matrix were constructed based on the method in [13]. An analytical model for the state coefficient matrix was also constructed using the same method as in [14]. The system is fourth order, so the state coefficient matrix is a 4×4 time dependent matrix. The lower left 2×2 block corresponds to scaled stiffness components of the model. The (3, 2) and (4, 2) components of the state coefficient matrix, which are the stiffness coefficients that multiply the beam tip degree of freedom are plotted versus time in Figure 9. The components that were estimated using the proposed identification method are plotted with open circles, and the analytical coefficient values are plotted with a solid line. The analytical (3, 2) component of the matrix (black line) varies over the periodic orbit by approximately 30% of its initial value of $3.46e4$ [N/(kg-m)], and the analytical (4, 2) component varies by approximately 51% of its initial value of $-5.26e-4$ [N/(kg-m)], so the system is quite time periodic based on the analytical model. The estimated coefficients for the (3, 2) and (4, 2) terms of the state coefficient matrix agree fairly well with the analytical values. The (3, 2) term differs from the analytical term by at most about 8.5% and the (4, 2) term differs by at most about 12.5%.

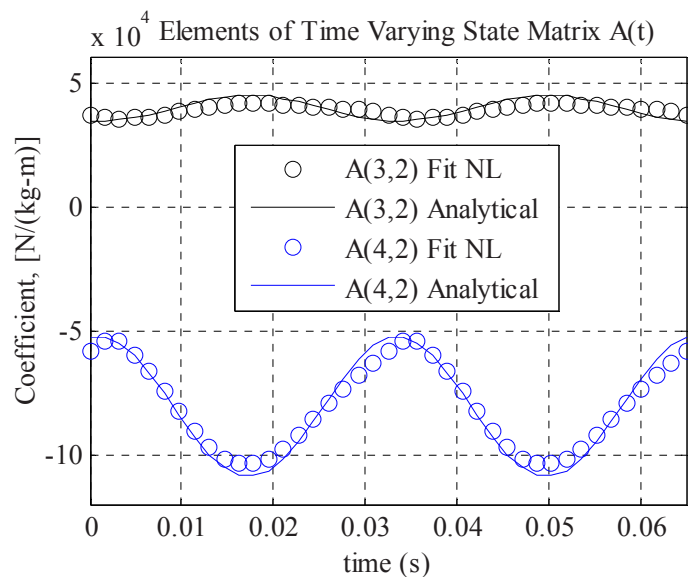


Fig. 9 Time-periodic state coefficient matrix components for forcing frequency $f_1=15.4$ Hz

The (3, 1) and (4, 1) terms of the state coefficient matrix are also related to the stiffness of the system, but for brevity they are not shown. The analytical (3, 1) and (4, 1) terms are constant, but their estimates showed between 8% and 14% variation with time, although they were relatively accurate in an average sense.

Because the damping in the system is linear, the lower right 2×2 block of the true analytical state coefficient matrix is also composed of terms that are constant with time. The estimates of these damping terms from the identification method vary significantly with time. Each of the four terms varies by an amount that is at least an order of magnitude larger than the constant value predicted by the analytical model, and they did not tend to agree very well in an average sense either. However, the identified STM matched the decay of the actual response well, so the error seems to arise when estimating $A(t)$ from the STM.

The identified state coefficient matrix can now be used to calculate its force contributions to the equations of motion of the nonlinear system according to eq. (11). This was done using MATLAB's 'cumtrapz' function, which is an approximation of the cumulative integral using the trapezoidal method. The lower left- 2×2 block of the matrix in eq. (11) is plotted in Figure 10 versus the corresponding displacement term. Since these terms were integrated with respect to the displacement components of the state vector, they are the scaled force-displacement functions of the system. The top row of plots relates

to the first degree of freedom (DOF) and the bottom row the second DOF. The identified scaled force-displacement curves are plotted with the open blue circles. The analytical state coefficient matrix was also integrated according to eq. (11). The scaled force-displacement curves for the analytical system are plotted with the blue lines. The underlying periodic orbit defines the displacement of the DOFs, and the first DOF displaces between about $\pm 0.5\text{mm}$ ((a) and (c)), while the second DOF displaces farther, between about $\pm 1.2\text{mm}$ ((b) and (d)). The restoring force on the first DOF ($a_{1,1}$) has a negative correlation with y_1 displacement. This is also seen for the $a_{2,2}$ versus y_2 relationship, while both the cross terms ($a_{1,2}$ and $a_{2,1}$) are positively correlated. The magnitudes of the $[a_{1,1}, a_{1,2}]$ and $[a_{2,1}, a_{2,2}]$ force components oscillate between about $\pm 50\text{ N/kg}$ and $\pm 90\text{ N/kg}$, respectively. All the force-displacement curves are predominantly linear, except for the $a_{2,2}$ component in (d). The identified force-displacement relationships agree exceptionally well with the analytical relationships.

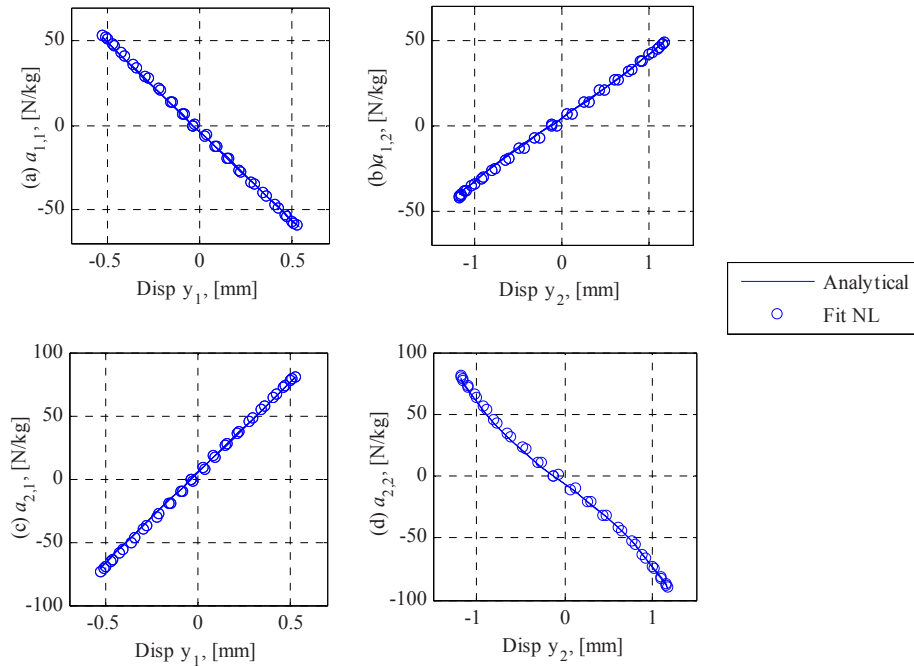


Fig. 10 Scaled force-displacement relationships acting on the beam DOFs for forcing frequency $f_1=15.4\text{ Hz}$

The forced-displacement curves can be directly linked to the dynamics of the system and how the DOFs interact. These functions completely characterize the nonlinear equation of motion of the system. According to these results, only the beam tip is subjected to nonlinearity, and this is consistent with the location of the nonlinear spring. It is significant that these results were obtained without any a priori assumption regarding the shape of the force-displacement relationships.

The force displacement relationships that have been identified for the system can be validated to some degree by using them to compute the total restoring force in the system at each point within the periodic limit cycle. This sum of the restoring forces can also be computed using the method described in Section 2.2.5, and the two can be compared to validate the results. To do this, each block of terms must be premultiplied by the analytical mass matrix to achieve the same scaling. This puts the terms into units of force rather than units of acceleration. The restoring forces have components due to the stiffness of the beam and due to the dissipative effects of damping. The total restoring force acting on a degree of freedom is the sum of these, but it has already been noted that the damping estimates are questionable, so the restoring forces were computed both with and without the damping terms. Figure 10 shows the restoring forces versus time for one cycle of the periodic orbit. The total restoring force estimate ($\text{RF}_{\text{LTP Total}}$) is plotted with the open blue circles. The estimate that excludes the velocity related forces is labeled ($\text{RF}_{\text{LTP Disp}}$) and plotted with open black squares. The total restoring forces computed using the RFS method outlined in Section 2.2.5 are also shown with the solid blue line. In the first half of the orbit, the restoring force on the beam tip leads the restoring force on the beam center, which initially remains near zero, but both forces are in phase and increase to a maximum near 0.017 seconds. The maximum value of the analytical restoring force is near 5 N for the beam center and 2 Newton for the beam tip. After the maximum, both restoring forces decrease towards zero, and the force on the beam center reaches the near zero around 0.03 seconds, while the force of the beam tip goes through zero near the half period time of 0.033 seconds. The restoring forces during the second half of the period are antisymmetric to the first half. In

general, the estimated total restoring force that acts on the beam center agrees very well with the force computed using the RFS method. However the estimate at the beam tip shows significant discrepancies when the damping terms are included. This reveals that the damping in the linear time-periodic model has not been accurately identified, but the actual damping is small so we can verify that the displacement dependent terms have been properly identified.

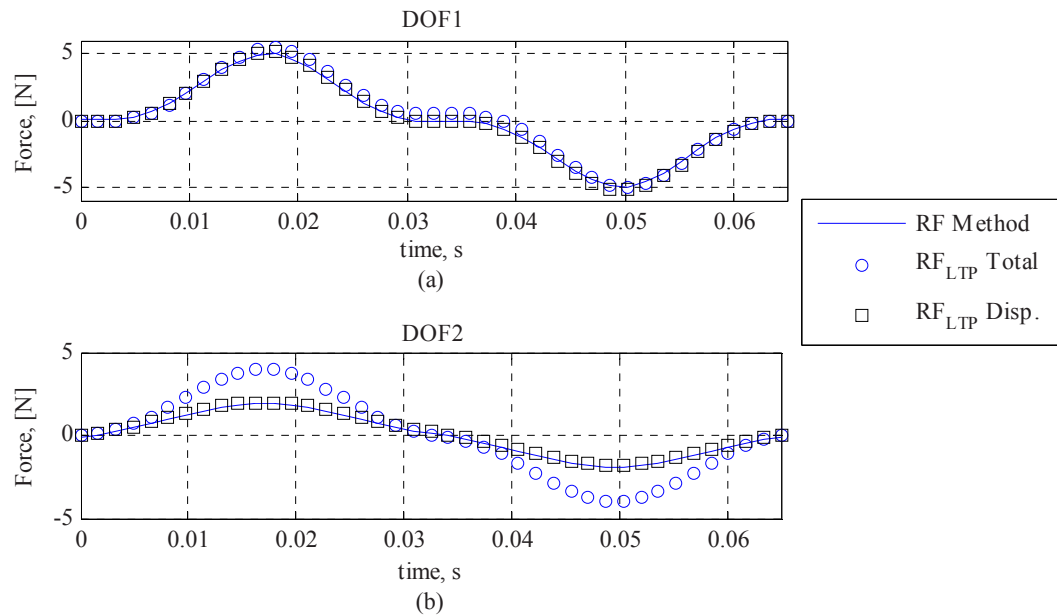


Fig. 11 Time-periodic restoring forces acting on the beam degrees of freedom for forcing frequency $f_1=15.4$ Hz

Discussion

Using the proposed identification method, a functional form of the force-displacement and force-velocity (not shown) relationships was directly calculated. Each term of the state coefficient matrix that was directly related to a parameter of the system was integrated individually to produce a force relationship. This approach also allows one to separate the effects of stiffness and damping, thereby using only the trustworthy identified parameters. For example, the components of the estimated state coefficient matrix that related to damping contained a measurable amount of error, so those terms could be approximated with some other method to achieve a more trustworthy model. Additionally, this method allows one to evaluate how errors in each identified state coefficient component are transferred to the force relationships. Even though the estimated (4,2) term of $A(t)$ was different than the analytical term by up to 12.5%, the estimated $a_{2,2}$ force-displacement curve compares remarkably well to the analytical model. Finally, the method provides important information on the interaction of the multiple-degrees of freedom. The $a_{2,2}$ curve provided evidence that DOF y_2 was subjected nonlinear effects, and it could be used to extract the functional form of the nonlinearity.

Case 2:

The system may also be driven in a periodic orbit near the second resonance condition, which will also produce a large amplitude response that maps a large portion of the state space. In order to assess the results of the identification when using different resonance conditions, a second simulation case was considered with forcing at $f_2=60.9$ Hz. The system was simulated from initial conditions $[y \dot{y}] = [-8.631e-5; 1.217e-4; 9.103e-2; -1.345e-1]$, and the same procedure as Case 1 was used to calculate the periodic and perturbed responses for the same harmonic forcing amplitude and impulsive forcing configuration. The time histories in this case were similar to those shown for the previous case, only now the two measurement points are out of phase since the second mode dominates the response.

The spectra of the perturbed responses and those of the difference between the perturbed and the periodic response responses were calculated with the FFT function, and those curves are plotted in Figure 12(a) and (b). The periodic response at the drive frequency 60.9 Hz and at the third harmonic of the drive frequency, 187.2 Hz, are both clearly visible, as well as several peaks due to the time-periodic effects caused by the nonlinearity. The lifting technique was applied as before, and the

composite spectrum of the lifted responses is plotted in Figure 12(c) with the solid black line. The lifting technique again results in a much simpler spectrum, and there are two prominent peaks at 1.85 Hz and 11.6 Hz and a very weak peak at 23.2 Hz in the composite of the lifted responses. There also seems to be some high amplitude response near the zero frequency line. AMI identified two modes in the responses with eigenvalues $\lambda_1 = -3.9850 + 11.5712i$ and $\lambda_2 = -0.6290 + 72.8480i$, natural frequencies $|\lambda_1|/(2\pi) = 1.9478$ Hz and $|\lambda_2|/(2\pi) = 11.5945$ Hz, and damping ratios 0.3256 and 0.0086, respectively, and a composite of the reconstruction of the responses from the two mode fit is plotted with the dashed red curve. The subtraction residual is substantially reduced by the two mode fit, but some artifacts remain near the zero frequency line and near 23.1 Hz.

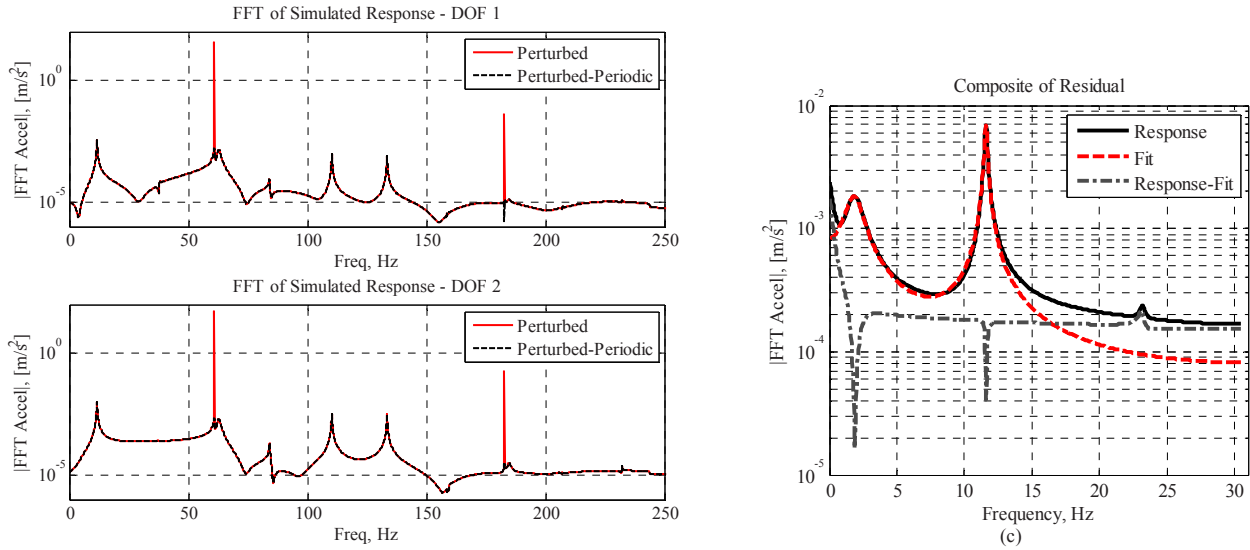


Fig. 12 Response spectra for forcing frequency $f_2=60.9$ Hz

The spectra from the perturbed response contain far fewer peaks than with the Case 1 forcing. The peak near 11.6 Hz in (a) and (b) directly corresponds to the 11.6 Hz peak in the composite of the lifted responses, so AMI identified an unaliased eigenvalue for this mode in this case. The peaks at 110.2 and 133.4 Hz in (a) and (b) can be attributed to the $m=-2$ and $+2$ harmonics of the time periodic mode at 11.6 Hz, since $11.6 \cdot 2 \cdot 60.9 \text{ Hz} = -110.2 \text{ Hz}$, which reflects back to a positive value, and $11.6 + 2 \cdot 60.9 \text{ Hz} = 133.4 \text{ Hz}$. The broad peak at 62.8 Hz becomes aliased in the composite spectrum of the lifted responses and corresponds to the peak at 1.85 Hz in (c). This eigenvalue can be unaliased by adding $2\pi \cdot 60.9$ rad/s to the imaginary part of the eigenvalue for this peak, which results in the natural frequency $|-3.985 + 394.4i|/(2\pi) = 62.77$ Hz that matches the peak in (a) and (b). The other notable peaks at 37.8 Hz in (b) and 84 Hz in (a) and (b) cannot be attributed to time-periodic effects of the identified modes. These peaks differ from the drive frequency by -23.1 Hz and $+23.1$ Hz for the 37.8 and 84 Hz peaks, respectively, so they both alias to 23.1 Hz in the composite of the lifted responses. Those peaks may be [14] caused by the domain of attraction [25] of a nearby (in state space), strong, and stable periodic orbit (e.g. the perturbation about the limit cycle may not be sufficiently small). The cause of such artifacts and their quantitative effect on the identification results will be a focus of future works.

The responses for this forcing case contain fewer time periodic effects than in the previous case, and thus the Fourier series expansion models of the mode shapes are quite straightforward to construct. The Fourier series were formed for each mode shape, and the $m=-2$, 0, and $+2$ terms were retained for the 11.6 Hz mode (λ_2 from AMI) and only the $m=0$ term was retained for the 62.8 Hz mode (λ_1 from AMI before unaliasing). Then, the Fourier series expansions of the modes were integrated twice to get displacement models and used to construct the state transition matrix and state coefficient matrix of the time-periodic model. The estimated values of the (3, 2) and (4, 2) terms of the identified state coefficient matrix are plotted in Figure 13 with the open circles. The analytical state coefficient model was also calculated for this forcing case, and the values of the analytical coefficients are plotted with solid lines. The analytical (3, 2) coefficient varies throughout the period by about 3% of its minimum magnitude, and the analytical (4, 2) coefficient varies by about 11%, so this model is not as strongly time-periodic as the model from forcing Case 1. The terms from the estimated state coefficient matrix agree well with the analytical model, differing by about 2% and 7% over the course of the periodic orbit, respectively. The (3, 1) and (4, 1) terms from the estimated state coefficient matrix vary by relatively small amounts over the course of the period, but their mean values over time agree very well with the constant analytical values for those matrix terms. Like forcing Case 1, the estimates for the state coefficient terms that are related to damping (in the lower right 2x2 block) tend to vary over the course of the period with large errors. However, fluctuations in these terms are not as large as those of forcing Case 1.

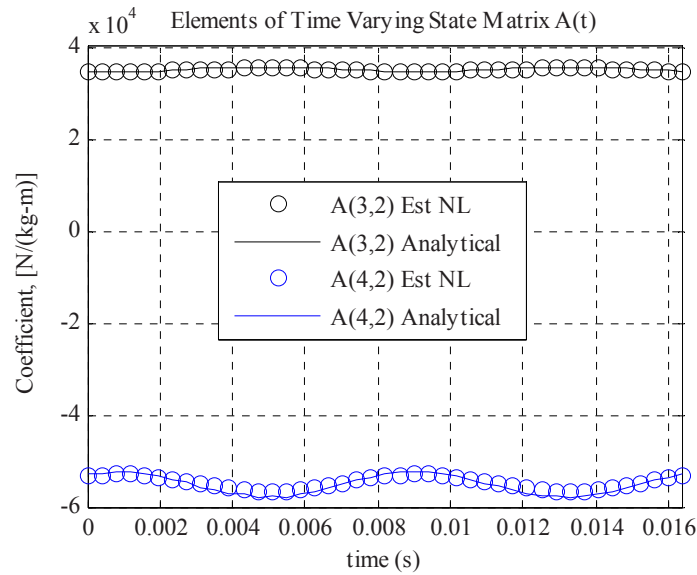


Fig. 13 Time-periodic state coefficient matrix components for forcing frequency $f_2=60.9$ Hz

The estimated state coefficient matrix was used to calculate the restoring forces using the same method as for forcing Case 1. The left-2x2 block of the resulting function g is plotted in Fig. 14 for the estimated and analytical force-displacement relationships using open black squares and solid black lines, respectively. The force-displacement results from the Case 1 identification are also shown with open blue circles and solid blue lines for the estimated and analytical results. The displacements of the DOFs for this periodic orbit are much smaller than the previous case, and correspondingly the magnitudes of the restoring forces are also smaller. The force-displacement curves for Case 2 have the same correlation with the DOFs as Case 1, with the diagonal terms that are plotted correlated negatively and the off diagonal terms correlated positively. Although the Case 2 estimated force-displacement values agree very well with the Case 2 analytical values, there appears to be some offset between curves from Case 1 and Case 2. However, the slopes of the curves between the displacements that are shared for both cases agree very well

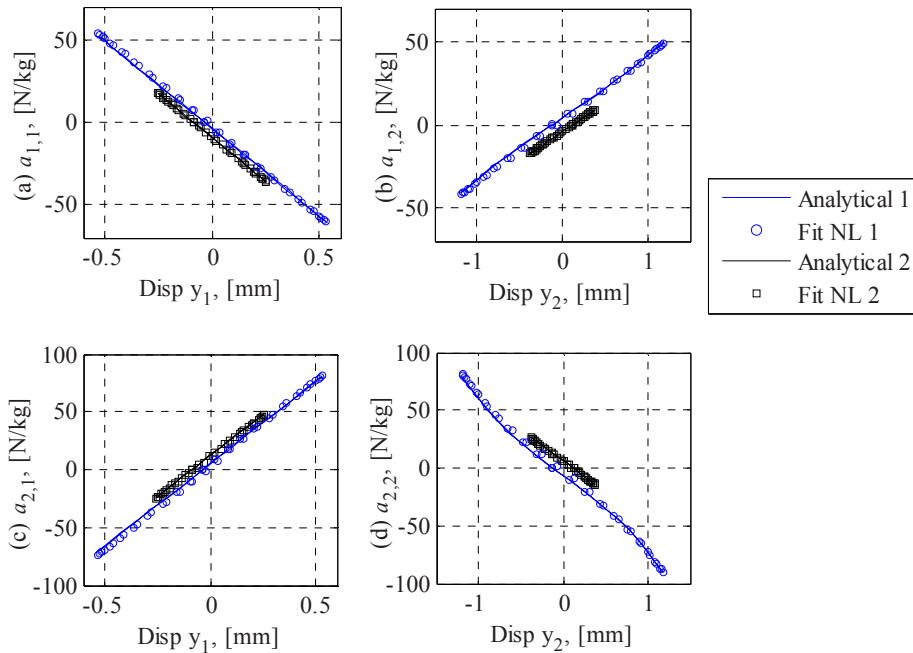


Fig. 14 Time-periodic restoring forces acting on the beam degrees of freedom for forcing frequency $f_2=60.9$ Hz (the Case 1 results are shown for comparison)

Discussion

When the system was excited with a frequency near the second nonlinear resonance, a very different periodic orbit was produced. The DOF responses were out of phase, and the magnitudes of the displacements were smaller. Despite the differences of the periodic orbit and interaction of the DOF, the procedure was still very straightforward to apply, and a trustworthy time-periodic model was identified. Due to the smaller amplitudes of the DOFs, the model contained less time-periodic effects, and the force-displacement relationships that were constructed were only weakly nonlinear. Nevertheless, these curves did match the linear slope of the Case 1 force displacement model providing good evidence that the two models are in agreement. It is clear from the results that the Case 1 forcing configuration provides better opportunity to identify a nonlinear model of the system. The higher frequency can be used, but the system must then be forced at higher amplitude in order to better excite the nonlinearity.

3.3 Experimental Measurements

The identification method was next applied to the experimental system. Harmonic excitation was applied to the beam with a model 2100E11-100 lb Modal Shaker from The Modal Shop, Inc. The beam was approximated as having a fixed support, so the shaker was freely hung from a lateral excitation stand, as recommended in [26] for shaker excitation. A thin steel stinger was used to transmit the excitation from the shaker to the beam. One end of the stinger was clamped inside the shaker armature and the other end was fixed to a force transducer, model 208C04 from PCB Piezotronics, Inc. (PCB), which was bolted to the beam at a location $x = 508$ mm from the fixed end of the beam. Harmonic forcing was provided by a Tectronix model 3022 arbitrary function generator, amplified by a model 2050E05 power amplifier from The Modal Shop, Inc., and input to the modal shaker. The amplitude and frequency of the excitation were varied to find forcing conditions that drove the beam to respond in a desirable stable periodic orbit. A modally tuned impulse hammer, model 086C01 from PCB was used to impact the beam at various locations to disturb the response from its periodic orbit. The response was measured with an Edeveco model 66A12 triaxial accelerometer (z-channel was used) located at $x = 508$ mm (beam center) and with an Edeveco model 256-100 isotron accelerometer located near the free end of the beam at $x = 984$ mm (beam tip). All the accelerometers were secured to the beam with wax. The measurements were acquired using a Photon II portable dynamic signal analyzer by LDS Dactron. This system was also used to apply sine-sweep forcing signals.

An initial sine sweep test was performed to evaluate the frequency response of the beam from 1-150 Hz. The Photon II output voltage was set to 0.2 Volts for this test (the gain on the amplifier was held at a constant level for all tests). The frequency was swept from 1-150Hz in a period of 699 seconds, and the acceleration responses of the beam and the applied force response were measured during this sweep. The Hilbert Transform was applied to these signals to determine the instantaneous amplitude and frequency for all time instants during the sweep. Then, a moving average with a ten sample bandwidth was applied to the results of the transformed signals and the ratio of the response to the force was calculated at each frequency line. [Figure 15](#) shows the nonlinear frequency response computed in this way, with the beam center degree of freedom plotted with the blue curve and the beam tip plotted with the red curve. There are a number of peaks in the spectra below 150 Hz, including two broad peaks near 17 and 43 Hz, two very weak peaks near 30 and 60 Hz, and a prominent sharp peak near 120 Hz. Both of the broad peaks are very noisy despite the smoothing that was applied to the signals. The lowest frequency peak in particular is very irregular below 17 Hz in both degrees of freedom. Near 37 Hz, there appears to be a large discrete jump in the amplitude of degree of freedom one and a small jump in the amplitude of the tip.

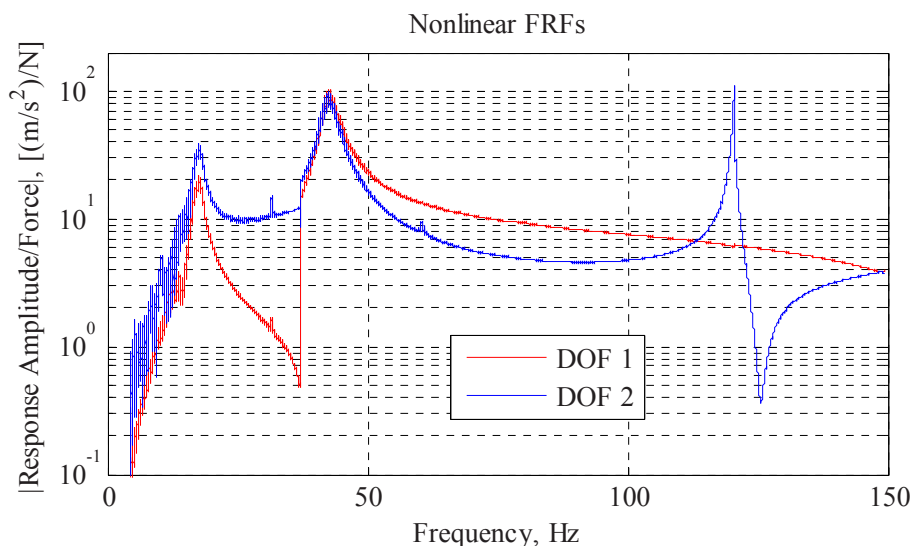


Fig. 15 Nonlinear frequency response of the experimental nonlinear beam for DOF 1(midspan) and DOF 2(tip)

The peaks in the nonlinear frequency response can be deciphered using knowledge of the underlying linear system. The third linear bending mode of a cantilever will tend to have significant tip response but minimal beam center response (due to a nearby node), so the peak near 120 Hz could be related to the third linear bending mode and appears to be predominantly linear. The peaks at 17 and 43 Hz could then be related to the first and second linear bending modes, respectively. All the remaining artifacts in the responses must be attributed either to noise or the nonlinearity of the system. The jump in the amplitude of the responses is a typical characteristic of nonlinear systems, so it can be assumed that the system responds nonlinearly when forced near these frequencies. The jaggedness of the curve below 17 Hz seems to be caused both by super harmonic resonances in that region and by limitations of the shaker and setup at these low frequencies. Therefore, a forcing frequency of 20 Hz was selected to drive the system and apply the proposed identification, since it is near the 17 Hz peak and both degrees of freedom are adequately excited at this frequency.

The function generator was used to drive the system at 20 Hz with amplitude of 0.2 Volts. The impact hammer was used to apply an impulsive force at the free end of the beam (at $x = 990$ mm), and the force transducer signal and two accelerometer signals were sampled at a frequency of 2.56 kHz over a window of approximately 12.8 seconds. The sampling frequency provided measurements at 128 samples per cycle of the periodic orbit, and the time window allowed enough time for the perturbed response to decay until only the underlying periodic orbit remained. In order to determine the underlying periodic orbit and match its phase to that of the perturbed responses, the second half of the time histories, which consisted of only the periodic orbit, were used to find the true frequency of the periodic orbit based on a minimization search with MATLAB's 'fminsearch' function. This frequency was found to be 20.0000 Hz, and it was used to fit a multi-harmonic sinusoid to the periodic orbit (i.e. over the second half of the time histories). This fit can be used to recreate the periodic orbit over the entire time series (assuming that it is stationary). This process produces the underlying periodic orbit and assures that its phase is aligned with that of the underlying periodic orbit. The reconstructed periodic orbit, the perturbed response, and the difference between the two are plotted for the tip degree of freedom in Figure 16 with the same format that was used previously. The perturbation about the periodic orbit can clearly be seen in the early time response, since its relative magnitude is somewhat large compared to the periodic orbit magnitude. At late times the perturbed signal is almost indistinguishable from the periodic orbit. Note also that the periodic orbit is far from a pure sinusoid (as one would expect for a linear system). Several high frequency oscillations are present.

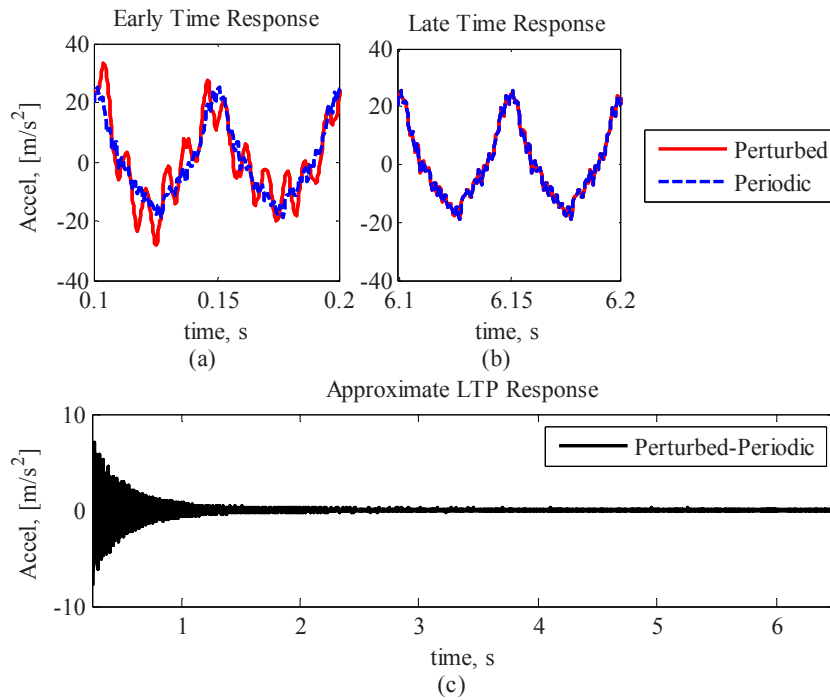


Fig. 16 Tip responses of the experimental beam for forcing frequency $f_{exp}=20$ Hz

The FFTs of the perturbed response and the perturbed minus the periodic responses were calculated, and those spectra are plotted in Figure 17 using the same format that was used previously. A number of sharp peaks occur in the perturbed response at 20 Hz and all of the harmonics of that frequency (i.e. 40, 60, 80 Hz, etc.) that are shown in the plots. Although the 20 Hz peak is the largest, the remaining peaks do not appear to diminish with increasing frequency. Since a single 20 Hz frequency sinusoid was used to force the system, this suggests that the system is highly nonlinear. There are many other artifacts that occur in the spectra, but a few coherent peaks can be seen at 28.2 and 188.2 Hz in (a) and (b) as well as 48.2 and 68.2 Hz in (b). A prominent peak occurs in both plots at 122.1 Hz, and two peaks of similar characteristics but much smaller magnitudes occur at 102.1 Hz and 162.2 Hz in plot (b). In each group of peaks previously listed, the peaks are separated by integer multiples of the scan frequency, and therefore are likely due to time-periodic effects.

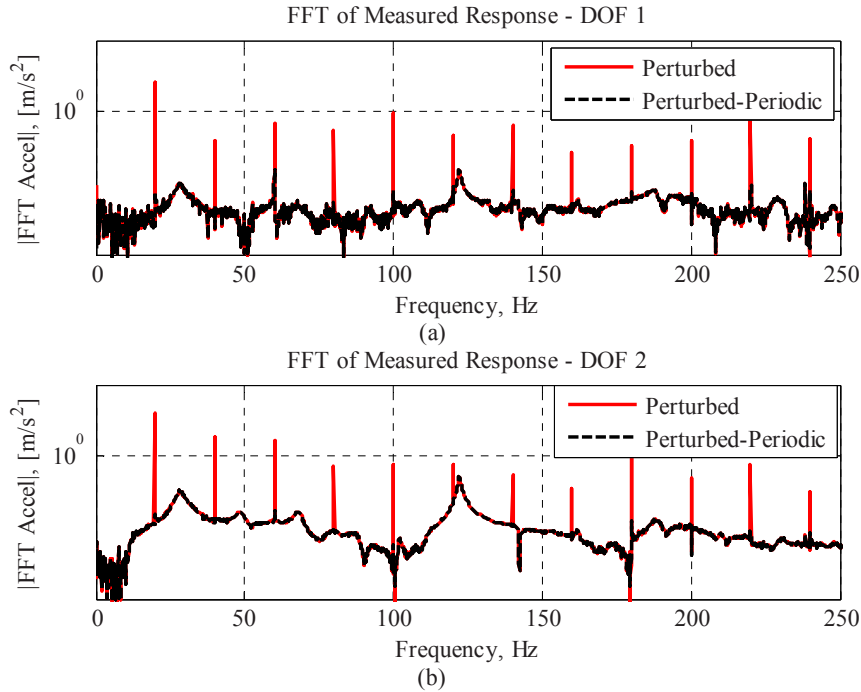


Fig. 17 Response spectra of the nonlinear beam measurements for forcing frequency $f_{exp}=20$ Hz

The peaks at 28.2 Hz and 122.2 Hz can be attributed to the $m=0$ harmonics of the two time-periodic modes of this system. The peaks at 48.2, 68.2, and 188.2 Hz can be attributed to $m=+1$, $+2$, and $+8$ harmonics of the former, and the peaks at 102.2 and 162.2 Hz can be seen as the $m=-1$ and $+2$ harmonics of the latter. The lifting method was applied to the perturbed minus periodic responses, and the FFT of the lifted responses was calculated. The composite spectrum of the lifted responses is plotted in Figure 18 with the solid black line. AMI identified two modes in the responses with eigenvalues $\lambda_1 = -2.777 + 13.491i$ and $\lambda_2 = -6.966 + 51.553i$, natural frequencies $|\lambda_1|/(2\pi) = 2.192$ Hz and $|\lambda_2|/(2\pi) = 8.280$ Hz, and damping ratios 0.2016 and 0.1339, respectively. The plot also shows the reconstruction of the composite spectrum based on the fit and the subtraction residual, which is significantly reduced by the two mode fit. This reveals that a linear-time periodic model fits the response of this highly nonlinear system very well about the limit cycle.

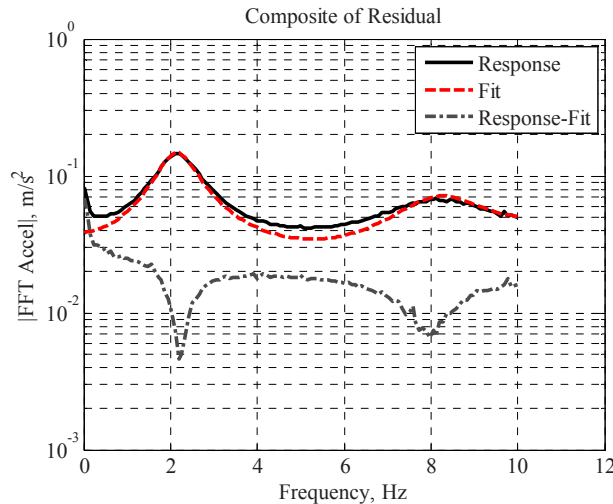


Fig. 18 Composite spectrum of lifted responses and AMI fit of the lifted responses for the nonlinear beam simulation for forcing frequency $f_{exp}=20$ Hz

The first eigenvalue can be deciphered to be an aliased version of the mode at 122.1, since $2.192 + 6 \cdot 20 = 122.192$, and the second eigenvalue is the aliased version of the mode at 28.2 Hz, since $8.280 + 1 \cdot 20 = 28.280$. The time-periodic modes that

AMI extracted from the measurements were very noisy, so when they were expanded in a Fourier series, the previous information was used to retain only those harmonics that were clearly represented in the measurements. Different time varying state matrices would be obtained depending on which terms were retained in the model for the state transition matrix. To illustrate this, the state transition matrix and state coefficient matrix were constructed based on using one, two, and three Fourier terms for this system. The Fourier coefficients that were used to construct these models are defined in the legend for modes 1 (denoted m_1) and 2 (denoted m_2). The (3, 2) and (4, 2) coefficients of the resulting estimated state coefficient matrices are plotted in Figure 19. The estimated models with a single $m=0$ Fourier term have linear time-invariant coefficients, and as more terms are included in the expansion, the coefficients show increasing variation with time. With the three Fourier term model, the (3, 2) term of the state coefficient matrix varies by 85% of its minimum magnitude and the (4, 2) term varies by 30%.

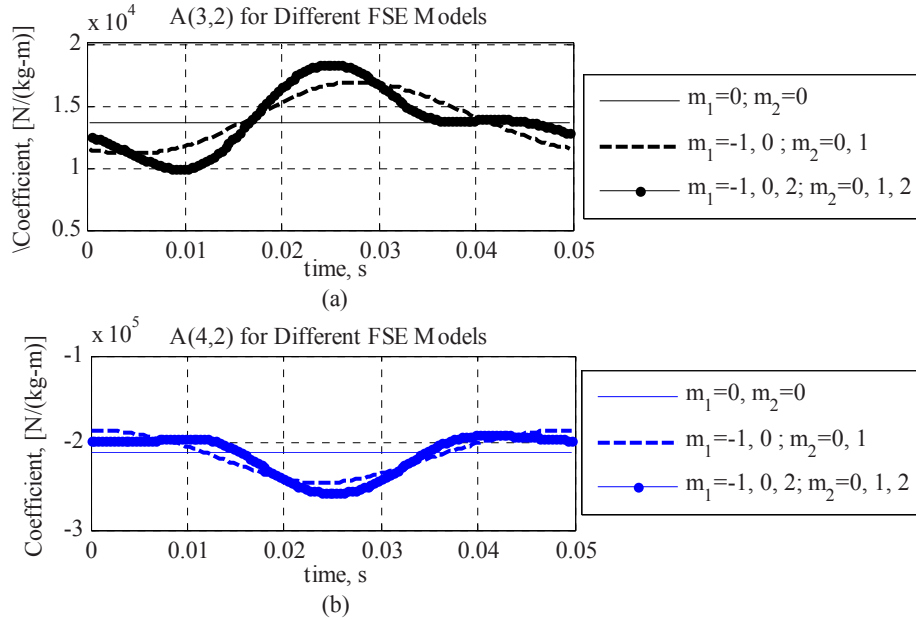


Fig. 19 Estimated time-periodic state coefficient matrix components for forcing frequency $f_{exp}=20$ Hz

The proposed identification method assumes that the system is oscillating in a stable periodic limit cycle. As mentioned previously, the limit cycle is measured by capturing the response of the system after the perturbation has decayed. The Fourier coefficients of the periodic limit cycle are then obtained and used in the analysis. Those Fourier coefficients are used to calculate the restoring forces using eq. (13), and also to compute the total restoring forces using eq. (15) as part of the validation step described in Section 2.2.5. The two measured acceleration signals and the measured force signal are plotted with blue dots in Figure 20. Each cycle of the assumed periodic response is overlaid, so the time window shown corresponds to only one period of the steady state force and response. The Fourier series fit to each signal is also plotted with a solid red line. The acceleration of the beam's midspan (Accel 1) and tip (Accel 2) DOFs ranges between about $\pm 10\text{m/s}^2$ and $\pm 40\text{m/s}^2$, respectively. The input force ranges between about ± 5 N. There is significant uncertainty due to noise in all three signals, yet each signal also seems to contain some high frequency fluctuations that are quite repeatable as well. These fluctuations are responsible for the high frequency harmonics seen in Figure 17. The harmonics describing the periodic orbit do not seem to diminish substantially in magnitude as frequency increases. Although it is not shown, these peaks are present at the integer multiples of the forcing frequency for the entire sampling bandwidth.

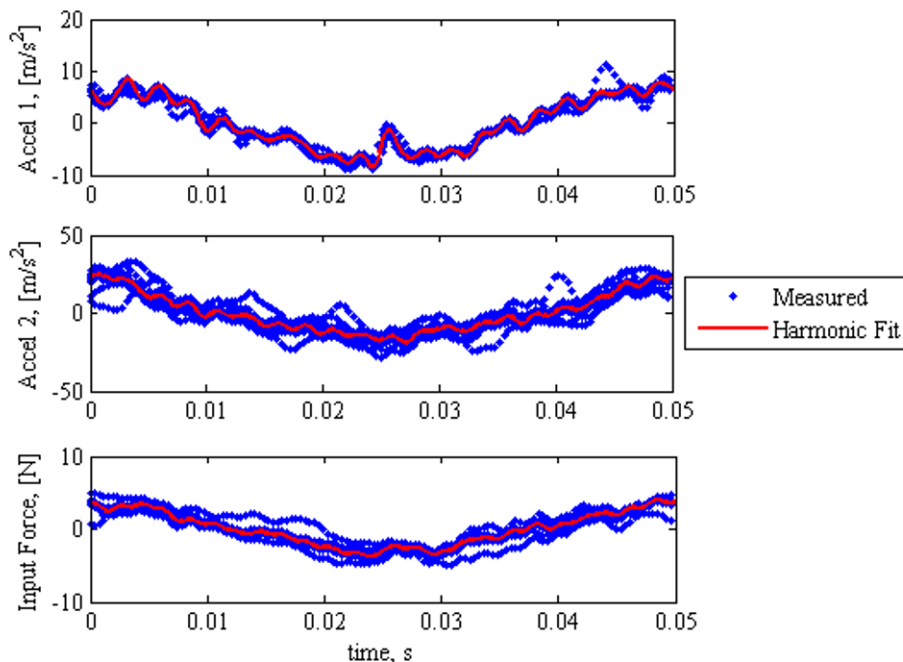


Fig. 20 Measured periodic signals and harmonic fits plotted period and overlaid for $f_{exp}=20$ Hz

Discussion

The signals plotted in the figure seem to indicate that the accelerations in this system fluctuate wildly over the limit cycle, especially at the midspan of the beam. Hence, many harmonics are needed to define the periodic limit cycle, and so one would expect that the linear time-periodic model of the system about this limit cycle must also contain many harmonic terms. Although linear time-periodic behavior was clearly visible in the experimental measurements, only a few harmonics were discernible from the noise, so a trustworthy estimate of the $A(t)$ matrix could not be obtained. In any event, the accuracy with which the limit cycle is known seems questionable, so any measure of the dynamics about that limit cycle would have limited value. It seems that more care must be taken to obtain a valid limit cycle before the proposed system identification technique can be applied to this system. It would also be preferable to have a limit cycle that is described by a smaller number of harmonics. Furthermore, in this work we have proposed to validate the nonlinear model identified by linear time-periodic identification using the restoring force surface method, but that method was also found to give meaningless results due to the fluctuations in the measured accelerations and input force. Future works will seek to refine the test methodology to produce more reliable measurements in order to address these issues. Even then, it is also interesting to note that very clear linear time-periodic behavior was visible in this system's response (e.g. Figures 17 and 18), even though the measurements were not of sufficient quality to allow that behavior to be related to the system's nonlinear equation of motion.

4. Conclusions

This work explores a new system identification strategy for nonlinear systems that is based on approximating the system's dynamics as linear time-periodic about a stable limit cycle. A variant of the restoring force surface method was proposed that estimates the total restoring forces in the system over the periodic orbit, which can be helpful in validating the nonlinear model found by the linear time-periodic identification approach. The approach was applied to simulated measurements from a two DOF cantilever beam and found to be capable of identifying the force-displacement relationships in the system from simulated measurements. However, the damping forces were not accurately estimated and the method was sensitive to the number of terms used in the state transition matrix of the linear time-periodic model. Even then, it is significant that the method identifies the nonlinear force displacement relationships in the system without any a priori assumption regarding the form of the nonlinearity or the order of the system. Two different excitation strategies were explored, which illustrated that it is important to choose an excitation that strongly activates the nonlinear parameters over a large range of motion in order to observe the nonlinearity. Additionally, the simulations revealed that it was important to assure that the perturbation from the underlying periodic orbit was small enough so that it could be modeled as linear time-periodic.

The methods were also applied to experimental measurements from a nonlinear beam with a geometric nonlinearity at its tip. Measurements from this system showed clear signs of time-periodic behavior. However, the system was found to deviate significantly from the periodic limit cycle and that cycle itself was not very repeatable, so neither the proposed linear time-periodic identification method nor the restoring force surface method gave reasonable results. The authors are presently studying this issue and mapping the periodic orbits that are possible (see [22]) to better understand how to best apply the proposed identification methodology to experimental measurements from high order systems.

5. References

- [1] G. Dimitriadis and J. Li, "Bifurcation of Airfoil Undergoing Stall Flutter Oscillations in Low-Speed Wind Tunnel," *AIAA Journal*, vol. 47, pp. 2577-2596, 2009.
- [2] G. T. Flowers, *et al.*, "The Application of Floquet Methods in the Analyses of Rotordynamic Systems," *Journal of Sound and Vibration*, vol. 218, pp. 249-259, 1998.
- [3] C. Basdogan and F. M. L. Amirouche, "Nonlinear Dynamics of Human Locomotion: From the Perspective of Dynamical Systems Theory.," in *Engineering Systems Design and Analysis Conference*, 1996.
- [4] J. B. Dingwell and J. P. Cusumano, "Nonlinear time series analysis of normal and pathological human walking," *Chaos*, vol. 10, pp. 848-63, 2000.
- [5] R. F. Ker, *et al.*, "The Spring in the Arch of the Human Foot," *Nature*, vol. 325, pp. 147-149, 1987.
- [6] R. A. Heath, *et al.*, "Detecting Nonlinearity in Psychological Data: Techniques and Applications," *Behavior Research Methods, Instruments, & Computers*, vol. 32, pp. 280-289, 2000.
- [7] C. Georges and J. C. Wallace, "Learning Dynamics and Nonlinear Misspecification in an Artificial Financial Market," *Macroeconomic Dynamics*, vol. 13, pp. 625-655, 2009.
- [8] S. F. Masri and T. K. Caughey, "A Nonparametric Identification Technique for Nonlinear Dynamic Problems," *Journal of Applied Mechanics*, vol. 46, pp. 433-447, 1979.
- [9] D. Donnelly and E. Rogers, "Time Series Analysis with the Hilbert-Huang Transform," *American Journal of Physics*, vol. 77, pp. 1154-1161, 2009.
- [10] G. Kerschen, *et al.*, "Past, Present and Future of Nonlinear System Identification in Structural Dynamics," *Mechanical Systems and Signal Processing*, vol. 20, pp. 505-592, 2006.
- [11] G. Kerschen, Kowtko, J., McFarland, D.M., Bergman, L., Vakakis, A., "Theoretical and Experimental Study of Multimodal Targeted Energy Transfer in a System of Coupled Oscillators," *Nonlinear Dynamics*, vol. 47, pp. 285-309, 2007.
- [12] M. S. Allen and M. W. Sracic, "System Identification of Dynamic Systems with Cubic Nonlinearities Using Linear Time-Periodic Approximations," presented at the ASME International Design Engineering Technical Conferences & Computers and Information in Engineering Conference, San Diego, California, USA, 2009.
- [13] M. S. Allen, "Frequency-Domain Identification of Linear Time-Periodic Systems Using LTI Techniques," *Journal of Computational and Nonlinear Dynamics*, vol. 4, pp. 041004.1-041004.6, 2009.
- [14] M. W. Sracic and M. S. Allen, "Method for Identifying Models of Nonlinear Systems Using Linear Time Periodic Approximations," *Mechanical Systems and Signal Processing*, vol. Submitted, 2010.
- [15] G. Floquet, "Sur Les Equations Lineaires a Coefficients Periodiques," *Ann. Sci. Ecole Norm. Sup.*, vol. 12, pp. 47-88, 1883.
- [16] P. Arambel and G. Tadmor, "Robust H_{∞} Identification of Linear Periodic Discrete-Time Systems," *International Journal of Robust and Nonlinear Control*, vol. 4, pp. 595-612, 1994.
- [17] P. Friedmann and C. E. Hammond, "Efficient Numerical Treatment of Periodic Systems with Application to Stability Problems," *International Journal for Numerical Methods in Engineering*, vol. 11, pp. 1117-1136, 1977.
- [18] F. Thouverez, "Presentation of the ECL Benchmark," *Mechanical Systems and Signal Processing*, vol. 17, pp. 195-202, 2003.
- [19] G. Kerschen, Lenaerts, V., Golinval, J.C., "Identification of a Continuous Structure with a Geometrical Non-Linearity. Part I: Conditioned Reverse Path Method," *Journal of Sound and Vibration*, vol. 262, pp. 889-906, 2003.
- [20] K. Worden and G. R. Tomlinson, "A Review of Nonlinear Dynamics Applications to Structural Health Monitoring," *Structural Control and Health Monitoring*, vol. 15, pp. 540-567, 2007.
- [21] J. H. Ginsberg, *Mechanical and Structural Vibrations Theory and Applications*, 1 ed. New York: John Wiley & Sons, Inc., 2001.
- [22] M. W. Sracic and M. S. Allen, "Numerical Continuation of Periodic Orbits for Harmonically Forced Nonlinear Systems," presented at the 29th International Modal Analysis Conference (IMAC XXVI), Jacksonville, Florida, USA, 2011.

- [23] M. S. Allen and J. H. Ginsberg, "A Global, Single-Input-Multi-Output (SIMO) Implementation of The Algorithm of Mode Isolation and Applications to Analytical and Experimental Data," *Mechanical Systems and Signal Processing*, vol. 20, pp. 1090–1111, 2006.
- [24] M. S. Allen and M. W. Sracic, "A New Method for Processing Impact Excited Continuous-Scan Laser Doppler Vibrometer Measurements," *Mechanical Systems and Signal Processing*, vol. 24, pp. 721-735, 2010.
- [25] A. H. Nayfeh and D. T. Mook, *Nonlinear Oscillations*. New York: John Wiley and Sons, 1979.
- [26] R. L. Mayes and A. J. Gomez. (2006) What's Shakin', Dude? Effective Use of Modal Shakers. *Experimental Techniques*. 51-61.

Appendix

The spring steel on the tip of the beam acts as a tension on element, and transfers force by its line of action which is assumed to always be straight. When the beam tip is deflected by a small amount δ , then so is the spring steel element, and it forms a small angle with the right support, θ . A diagram of this geometry is shown in Figure 21. The spring steel which had original length l_s is assumed to strain by an amount Δl_s due the tension force F in the element. By the force displacement relationship of a tensile element, $\Delta l_s = Fl_s / (E_s A_s)$ where E_s is the elastic modulus of the spring steel and A_s is the cross section area of the strip. Therefore, the tensile force is $F = E_s A_s / l_s * \Delta l_s$. Next, the strain can be related to the geometry of the tip deflection.

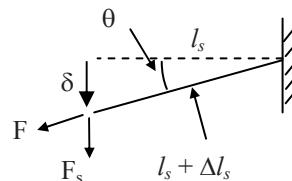


Fig. 21 Geometry for beam tip deflection and interaction of the strip of spring steel

The tip of the beam has a deflection of δ , which can be used to write the strain in the spring steel as a function of the undeformed length.

$$\Delta l_s = \sqrt{l_s^2 + \delta^2} - l_s \quad (24)$$

The vertical contribution of the tensile force is $F_v = F \sin(\theta)$, or using the geometry of the figure and the previous relationship,

$$F_v = \frac{E_s A_s}{l_s} \left(\sqrt{l_s^2 + \delta^2} - l_s \right) \left(\frac{\delta}{l_s + \sqrt{l_s^2 + \delta^2} - l_s} \right) = \frac{E_s A_s}{l_s} \left(\delta - l_s \delta \left(l_s^2 + \delta^2 \right)^{1/2} \right) \quad (25)$$

In order approximate the vertical force displacement relationship about small tip deflections of the beam, the previous equation was expanded in a Taylor series about $\delta=0$ for terms to $O(\delta^3)$, and the higher order terms were neglected. This results in the following expression for the vertical force contribution of the spring steel.

$$F_v \cong \frac{E_s A_s}{2l_s^3} \delta^3 \quad (26)$$

The nonlinear spring constant can therefore be approximated as $k_3 = E_s A_s / (2l_s^3)$.

B-spline laminate shell finite element updating by means of FRF measurements

Antonio Carminelli, Giuseppe Catania

DIEM, Dept. of Mechanical Design, University of Bologna,
viale Risorgimento 2, 40136 Bologna, Italy

ABSTRACT

A B-spline based FE model updating procedure is proposed. The approach is based on the least squares minimization of an objective function dealing with residues, defined as the difference between the model based response and the experimental measured response, at the same frequency. The B-spline FE model can make it possible to limit the number of dofs. A constraint model and a damping model are proposed, being parameterized by means of B-spline functions. The incompatibility between the measurement dofs and the model dofs is also taken into consideration. An example dealing with a composite car front spoiler is reported, considering the presence of random noise. Results are critically discussed.

1. Introduction

Finite Element (FE) models are commonly used to predict the system response of mechanical systems, but theoretically derived mathematical models may often be inaccurate, in particular when dealing with complex structures. Several papers on FE models based on B-spline shape functions have been published in recent years [1-5].

Estimated data from measurements on a real system, such as frequency response functions (FRFs), can be used to improve FE model response. Although there are many papers in the literature dealing with FE updating [6-10], several open problems still exist. Some issues concerning the use of FRF residues are the selection of frequency data [11-12], the ill-conditioning of the resulting system of equations [13] and the choice of measurement degrees of freedom (dofs) [7]. Although many frequency data in measured FRFs are available to set an over-determined system of equations, a limited number of frequency points are usually adopted for practical reasons. However, it should be pointed out that a sufficient number of data are required in order to avoid an ill-defined system of equations and the consequent adoption of regularization methods. The parametrization of the finite element model is a critical issue to cover to avoid an ill-conditioned system of equations. It is important that the updating parameters should be able to model the expected system response while avoiding a non-physical solution. The modeling of boundary conditions [8] and the damping of structures [14] is sometimes difficult to effectively parameterize, and such issues are not covered to a great extent in the literature to the authors' knowledge.

Furthermore, the incompatibility between the measurement dofs and the model dofs is an issue common to many FRF updating techniques. Reduction or expansion techniques are a common way to treat this kind of incompatibility [7]. A more general approach should also take into account the adoption of different dofs in the two models [15]. In this paper a composite shell B-spline based FE model updating procedure is proposed. The approach is based on the least squares minimization of an objective function dealing with residues, defined as the difference between the model based response and the experimental measured response, at the same frequency. The boundary conditions and the system damping are modeled by employing B-spline functions. A B-spline FE model is adopted to limit the number of dofs. The incompatibility between the measured dofs and the model dofs is also dealt with.

An example dealing with a composite car front spoiler is reported, considering the presence of random noise. Results are critically discussed.

2. B-spline laminate shell finite element model

A shell geometry can be efficiently described by means of B-spline functions mapping the parametric domain (ξ, η, τ) (with $0 \leq \xi, \eta, \tau \leq 1$) into the tridimensional Euclidean space (x, y, z) . The position vector of a single B-spline surface patch, with respect to a Cartesian fixed, global reference frame \mathbf{O} , $\{x, y, z\}$, is usually defined by a tensor product of B-spline functions [16]:

$$\mathbf{r}(\xi, \eta) = \begin{Bmatrix} r_x \\ r_y \\ r_z \end{Bmatrix} = \sum_{i=1}^m \sum_{j=1}^n B_i^p(\xi) \cdot B_j^q(\eta) \cdot \mathbf{P}_{ij}, \quad (1)$$

involving the following parameters:

- a control net of $m \times n$ Control Points (CPs) \mathbf{P}_{ij} ;
- the uni-variate normalized B-spline functions $B_i^p(\xi)$ of degree p , defined with respect to the curvilinear coordinates ξ by means of the knot vector $\mathbf{U} = \{\xi_1, \dots, \xi_r\} = \left\{ \underbrace{0, \dots, 0}_{p+1}, \xi_{p+1}, \dots, \xi_{r-p-1}, \underbrace{1, \dots, 1}_{p+1} \right\}$;
- the uni-variate normalized B-spline functions $B_j^q(\eta)$ of degree q , defined with respect to the curvilinear coordinates η by means of the knot vector $\mathbf{V} = \{\eta_1, \dots, \eta_r\} = \left\{ \underbrace{0, \dots, 0}_{q+1}, \eta_{q+1}, \dots, \eta_{r-q-1}, \underbrace{1, \dots, 1}_{q+1} \right\}$.

The degenerate shell model is a standard in FE commercial software because of its simple formulation [17]. The position vector of the degenerate shell can be expressed as:

$$\mathbf{s}(\xi, \eta, \tau) = \sum_{i=1}^m \sum_{j=1}^n B_i^p(\xi) \cdot B_j^q(\eta) \cdot \left[\mathbf{P}_{ij} + t_{ij} \left(\tau - \frac{1}{2} \right) \mathbf{v}_{ij}^3 \right], \quad (2)$$

where the versors \mathbf{v}_{ij}^3 and the thickness values t_{ij} can be calculated from the interpolation process proposed in [18].

The displacement field can be defined by following the isoparametric approach [17]:

$$\mathbf{d}(\xi, \eta, \tau) = \sum_{i=1}^m \sum_{j=1}^n B_i^p(\xi) \cdot B_j^q(\eta) \cdot \begin{bmatrix} 1 & 0 & 0 \\ 0 & 1 & 0 \\ 0 & 0 & 1 \end{bmatrix} t_{ij} \left(\tau - \frac{1}{2} \right) \begin{bmatrix} -\mathbf{v}_{ij}^2 & \mathbf{v}_{ij}^1 \end{bmatrix} \cdot \begin{Bmatrix} \mathbf{u}_{ij} \\ \mathbf{v}_{ij} \\ w_{ij} \\ \alpha_{ij} \\ \beta_{ij} \end{Bmatrix} = \begin{bmatrix} \mathbf{N}_u \\ \mathbf{N}_v \\ \mathbf{N}_w \end{bmatrix} \cdot \boldsymbol{\delta} = \mathbf{N} \cdot \boldsymbol{\delta}, \quad (3)$$

where $\boldsymbol{\delta}$ is the vector collecting the $N = 5 \cdot m \cdot n$ generalized dofs:

$$\boldsymbol{\delta}^T = \{u_{11} \quad v_{11} \quad w_{11} \quad \alpha_{11} \quad \beta_{11} \quad \dots \quad u_{mn} \quad v_{mn} \quad w_{mn} \quad \alpha_{mn} \quad \beta_{mn}\}, \quad (4)$$

$(\mathbf{v}_{ij}^1, \mathbf{v}_{ij}^2, \mathbf{v}_{ij}^3)$ refer to orthonormal sets defined on \mathbf{P}_{ij} starting from the vector \mathbf{v}_{ij}^3 [19], u_{ij} , v_{ij} and w_{ij} are translational dofs, α_{ij} and β_{ij} are rotational dofs.

The equation of motion can be obtained by means of the principle of minimum total potential energy as shown in [15]:

$$\mathbf{M} \cdot \ddot{\boldsymbol{\delta}} + (\mathbf{K}_f + \Delta \mathbf{K}) \cdot \boldsymbol{\delta} = \mathbf{F}, \quad (5)$$

the only difference being the derivation of the elasticity matrix for the laminate shell model:

$$\mathbf{K}_f = \sum_k \mathbf{K}_k, \quad (6)$$

where \mathbf{K}_k is the contribution of the k -th lamina:

$$\mathbf{K}_k = \int_{\Omega_k} \mathbf{B}^T \mathbf{E}_k \mathbf{B} \cdot \det J \cdot d\Omega, \quad (7)$$

Ω_k being the restriction to the k -th lamina of solid geometry Ω under analysis and \mathbf{E}_k is the plane stress constitutive matrix in the global reference frame:

$$\mathbf{E}_k = \mathbf{T}_k^T \cdot \mathbf{E}'_k \cdot \mathbf{T}_k, \quad (8)$$

\mathbf{T}_k is the transformation matrix from the k -th lamina local material reference frame (1,2,3) to the global reference frame (x,y,z) [17]. The plane stress constitutive matrix \mathbf{E}'_k in the local material reference frame is obtained according to the Mindlin theory [20]:

$$\mathbf{E}'_k = \begin{bmatrix} \frac{E_1}{(1-\nu_{12}\nu_{21})} & \frac{\nu_{12}E_2}{(1-\nu_{12}\nu_{21})} & 0 & 0 & 0 & 0 \\ \frac{\nu_{12}E_2}{(1-\nu_{12}\nu_{21})} & \frac{E_2}{(1-\nu_{12}\nu_{21})} & 0 & 0 & 0 & 0 \\ 0 & 0 & 0 & 0 & 0 & 0 \\ 0 & 0 & 0 & G_{12} & 0 & 0 \\ 0 & 0 & 0 & 0 & G_{23} & 0 \\ 0 & 0 & 0 & 0 & 0 & G_{13} \end{bmatrix}, \quad (9)$$

where E represents the Young moduli and G the shear moduli.

2.1 Modeling of boundary conditions

Distributed elastic constraints are taken into account by including, in the functional of the total potential energy, the potential energy ΔW of the constraint force per unit surface area Φ_c , assumed as being applied on the external surface of the shell model:

$$\Phi_c = -\mathbf{R} \cdot \mathbf{d}, \quad (10)$$

where \mathbf{R} is the matrix containing the stiffness coefficients r_a of a distributed elastic constraint, modeled by means of B-spline functions:

$$r_a = \sum_{i=1}^{m^a} \sum_{j=1}^{n^a} B_i^{p^a} \cdot B_j^{q^a} \cdot \kappa_{ij}^a, \quad (11)$$

where $B_i^{p^a}$ and $B_j^{q^a}$ are the uni-variate normalized B-spline functions defined by means of the knot vectors, respectively, \mathbf{U}^a and \mathbf{V}^a :

$$\Delta W = -\frac{1}{2} \int_S (\mathbf{d}^T \cdot \Phi_c) dS = \frac{1}{2} \delta^T \cdot \int_S (\mathbf{N}^T \cdot \mathbf{R} \cdot \mathbf{N}) dS \cdot \delta. \quad (12)$$

The stiffness matrix due to the constraint forces is:

$$\Delta \mathbf{K} = \int_S (\mathbf{N}^T \cdot \mathbf{R} \cdot \mathbf{N}) dS. \quad (13)$$

The introduction of this last term in the equation of motion yields:

$$\mathbf{M} \cdot \ddot{\delta} + (\mathbf{K}_r + \Delta \mathbf{K}) \cdot \delta = \mathbf{F}. \quad (14)$$

2.2 Modelling of system damping

For lightly damped structures, appropriate results may be obtained by imposing the real damping assumption (real mode-shapes). The real damping assumption is imposed by adding a viscous term in the equation of motion:

$$\mathbf{M} \cdot \ddot{\boldsymbol{\delta}} + \mathbf{C} \cdot \dot{\boldsymbol{\delta}} + (\mathbf{K}_r + \Delta \mathbf{K}) \cdot \boldsymbol{\delta} = \mathbf{F}, \quad (15)$$

where the damping matrix \mathbf{C} is:

$$\mathbf{C} = \boldsymbol{\Phi}^{-T} \cdot \mathbf{diag}(2\zeta\omega) \cdot \boldsymbol{\Phi}^{-1}, \quad (16)$$

and

$$\mathbf{diag}(2\zeta\omega) = \begin{bmatrix} 2\zeta_1\omega_1 & 0 & \dots & 0 \\ 0 & 2\zeta_2\omega_2 & & \vdots \\ \vdots & & \ddots & 0 \\ 0 & \dots & 0 & 2\zeta_N\omega_N \end{bmatrix}, \quad (17)$$

where $\boldsymbol{\Phi}$ is the matrix of the eigen-modes $\boldsymbol{\Phi}_i$ obtained by solving the eigen-problem:

$$(\mathbf{K} - \omega_i^2 \mathbf{M}) \boldsymbol{\Phi}_i = \mathbf{0}, \quad (18)$$

and ω_i^2 is the i -th eigen-value of Eq.(18). Modal damping ratios ζ_i can be evaluated from:

$$\zeta_i = \zeta(f_i) = \zeta(2\pi \cdot \omega_i), \quad (19)$$

where the damping $\zeta(f)$ is defined by means of control coefficients γ_z and B-spline functions B_z defined on a uniformly spaced knot vector:

$$\zeta(f) = \zeta(f(u)) = \sum_{z=1}^{n^2} B_z(u) \cdot \gamma_z; \quad f = f_{ST} + u \cdot (f_{FI} - f_{ST}); \quad u \in [0,1], \quad (20)$$

where f_{ST} and f_{FI} are, respectively, the lower and upper bound of the frequency interval in which the spline based damping model is defined. In order to take into account the contribution to the FRF of modes outside the input data frequency interval, $f_{ST} = (1.2 \cdot f_{MAX})$ is considered, where f_{MAX} is the maximum frequency adopted in the input data.

3. Updating

The parametrization adopted for the elastic constraints and for the damping model is employed in an updating procedure based on Frequency Response Functions experimental measurements.

The ℓ measured FRFs $H_b^X(\omega)$, with $b=1, \dots, \ell$, are collected in a vector $\mathbf{h}_X(\omega)$:

$$\mathbf{h}_X(\omega) = \begin{Bmatrix} H_1^X(\omega) \\ \vdots \\ H_\ell^X(\omega) \end{Bmatrix}. \quad (21)$$

The dynamic equilibrium equation in the frequency domain, for the spline-based finite element model, can be defined by Fourier transforming Eq.(15), where $(\tilde{\cdot}) = (\cdot)$:

$$(-\omega^2 \mathbf{M} + j\omega \mathbf{C} + \mathbf{K}_r + \Delta \mathbf{K}) \cdot \tilde{\boldsymbol{\delta}} = \mathbf{Z}(\omega) \cdot \tilde{\boldsymbol{\delta}} = \mathbf{H}^{-1}(\omega) \cdot \tilde{\boldsymbol{\delta}} = \tilde{\mathbf{F}}, \quad (22)$$

where $\mathbf{Z}(\omega)$ is the dynamic impedance matrix and $\mathbf{H}(\omega) = (\mathbf{Z}(\omega))^{-1}$ is the receptance matrix.

Since the vector $\tilde{\boldsymbol{\delta}}$ contains non-physical displacements and rotations, the elements of the matrix $\mathbf{H}(\omega)$ cannot be directly

compared with the measured FRFs $H_q^X(\omega)$. The analytical FRFs related to physical dofs of the model can be obtained by means of the FE shape functions. Starting from the input force applied and measured on the point $\mathbf{P}^i = \mathbf{s}(\xi_i, \eta_i, \tau_i)$ along a direction $\boldsymbol{\varphi}$ and the response measured on the point $\mathbf{P}^r = \mathbf{s}(\xi_r, \eta_r, \tau_r)$ along the direction $\boldsymbol{\psi}$, the corresponding analytical FRF is:

$$H_{\boldsymbol{\psi}, \boldsymbol{\varphi}}^{r,i}(\omega) = \mathbf{N}_{\boldsymbol{\psi}}(\xi_r, \eta_r, \tau_r) \cdot \mathbf{H}(\omega) \cdot \mathbf{N}_{\boldsymbol{\varphi}}^T(\xi_i, \eta_i, \tau_i), \quad (23)$$

where $\boldsymbol{\varphi}$ and $\boldsymbol{\psi}$ can assume a value among \mathbf{u} , \mathbf{v} or \mathbf{w} (Eq.3).

The sensitivity of the FRF $H_{\boldsymbol{\psi}, \boldsymbol{\varphi}}^{r,i}$ with respect to a generic parameter p_k is:

$$\begin{aligned} \frac{\partial H_{\boldsymbol{\psi}, \boldsymbol{\varphi}}^{i,s}(\omega, \mathbf{p})}{\partial p_k} &= \mathbf{N}_{\boldsymbol{\psi}}(\xi_r, \eta_r, \tau_r) \cdot \frac{\partial \mathbf{H}(\omega, \mathbf{p})}{\partial p_k} \cdot \mathbf{N}_{\boldsymbol{\varphi}}^T(\xi_i, \eta_i, \tau_i) = \\ &= -\mathbf{N}_{\boldsymbol{\psi}}(\xi_r, \eta_r, \tau_r) \cdot \mathbf{H}(\omega, \mathbf{p}) \cdot \frac{\partial \mathbf{Z}(\omega, \mathbf{p})}{\partial p_k} \cdot \mathbf{H}(\omega, \mathbf{p}) \cdot \mathbf{N}_{\boldsymbol{\varphi}}^T(\xi_i, \eta_i, \tau_i), \end{aligned} \quad (24)$$

where $\mathbf{p} = \{p_1 \dots p_{n^p}\}^T$ is the vector containing the updating parameters p_k .

Since each measured FRF $H_b^X(\omega)$ corresponds to a well-defined set $\{i, r, \boldsymbol{\varphi}, \boldsymbol{\psi}\}$, it is possible to collect, with respect to each measured FRF, the corresponding analytical FRFs in the vector:

$$\mathbf{h}_a(\omega, \mathbf{p}) = \begin{Bmatrix} H_{\boldsymbol{\varphi}, \boldsymbol{\psi}}^{i,s}(\omega, \mathbf{p}) \\ \vdots \\ H_{\boldsymbol{\theta}, \boldsymbol{\sigma}}^{t,t}(\omega, \mathbf{p}) \end{Bmatrix}. \quad (25)$$

The elements of $\mathbf{h}_a(\omega, \mathbf{p})$ are generally nonlinear functions of \mathbf{p} . The problem can be linearized, for a given angular frequency ω_i , by expanding $\mathbf{h}_a(\omega, \mathbf{p})$ in a truncated Taylor series around $\mathbf{p} = \mathbf{p}_0$:

$$\mathbf{h}_a(\omega_i, \mathbf{p}_0) + \sum_{k=1}^{n^p} \frac{\partial \mathbf{h}_a(\omega_i, \mathbf{p}_0)}{\partial p_k} \Delta p_k = \mathbf{h}_x(\omega_i), \quad (26)$$

in matrix form:

$$\left[\frac{\partial \mathbf{h}_a(\omega_i, \mathbf{p}_0)}{\partial p_1}, \dots, \frac{\partial \mathbf{h}_a(\omega_i, \mathbf{p}_0)}{\partial p_k}, \dots, \frac{\partial \mathbf{h}_a(\omega_i, \mathbf{p}_0)}{\partial p_{n^p}} \right] \begin{bmatrix} \Delta p_1 \\ \vdots \\ \Delta p_k \\ \vdots \\ \Delta p_{n^p} \end{bmatrix} = \mathbf{h}_x(\omega_i) - \mathbf{h}_a(\omega_i, \mathbf{p}_0), \quad (27)$$

or:

$$\mathbf{S}_i \cdot \Delta \mathbf{p} = \Delta \mathbf{h}_i, \quad (28)$$

where \mathbf{S}_i is the sensitivity matrix for the i -th angular frequency value ω_i .

It is possible to obtain a least squares estimation of the n^p parameters p_k , by defining the error function \mathbf{e} :

$$\mathbf{e} = \sum_{i=1}^{n^f} \mathbf{S}_i \cdot \Delta \mathbf{p} - \Delta \mathbf{h}_i, \quad n^f \gg n^p, \quad (29)$$

and by minimizing the objective function g :

$$\mathbf{g} = (\mathbf{e}^T \cdot \mathbf{e}) \rightarrow \min . \quad (30)$$

Since the updating parameters p_k can have very different sensitivities, ill-conditioned updating equations may result. A normalization of the variables was employed to prevent ill-conditioning of the sensitivity matrix and, in order to avoid updating parameters assuming non-physical values during the iterative procedure, a proper variable transformation is adopted to constrain the parameters in a compact domain without using additional variables [15].

Since FRF data available from measurement are usually large in quantity, a least squares estimation of the parameters can be obtained by adopting various FRF data at different frequencies. The proposed technique is iterative because a first order approximation was made during derivation of Eq.(26).

4. Applications

The numerical example concerns a front car spoiler. It is an E-glass fiber reinforced plastic component modeled with a single B-spline surface employing third degree B-spline functions and 21×10 CPs (blue dot in Fig.2) for which the adopted material properties are: $E_1 = 53.78 \cdot 10^9 \text{ Pa}$, $E_2 = 17.93 \cdot 10^9 \text{ Pa}$, $G_{12} = G_{13} = G_{23} = 4.3 \cdot 10^8 \text{ Pa}$, $\rho = 1470 \text{ Kg} / \text{m}^3$ and $\nu_{12} = 0.25$.

Because of FRF experimental measurement unavailability, a set of experimental measurements was obtained by numerical simulation, in the frequency range $[0, 800]$ Hz, assuming the input force applied on point 1 along z direction and four response dofs (along z direction, red squares in Fig.2)

The simply supported constraint was modelled as a distributed stiffness acting on a portion of the bottom surface of the shell ($\tau = 0$):

$$\Delta \mathbf{K} = \int_S (\mathbf{N}^T \cdot \mathbf{R} \cdot \mathbf{N}) \cdot dS , \quad (31)$$

where \mathbf{R} is the matrix containing the stiffness of distributed spring acting only in vertical direction z :

$$\mathbf{R} = \begin{bmatrix} 0 & 0 & 0 \\ 0 & 0 & 0 \\ 0 & 0 & r(\xi, \eta) \end{bmatrix} . \quad (32)$$

The distributed stiffness r is modelled by means of B-spline functions:

$$r = \sum_{i=1}^1 \sum_{j=1}^4 B_i^0(\xi) \cdot B_j^2(\eta) \cdot \kappa_{ij} , \quad (33)$$

where $\boldsymbol{\kappa} = 10^{11} \cdot [1.1 \cdot 10^2 \quad 2.8 \cdot 10^2 \quad 5 \quad 5]$, and the associated B-spline functions are defined on the knot vectors $\mathbf{U}^{\kappa} = \{0, 0.03\}$ and $\mathbf{V}^{\kappa} = \{0, 0, 0, 0.5, 1, 1, 1\}$. The distribution of the spring stiffness is plotted in Fig.3. The modal damping ratio values reported in Fig.4 were employed for the first 8 eigen-modes.

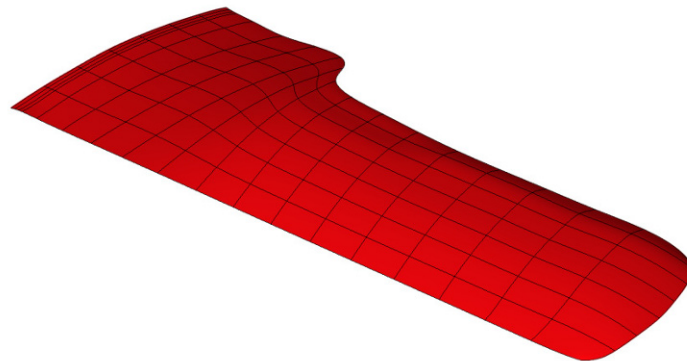


Fig. 1 Fiberglass composite front car spoiler model.

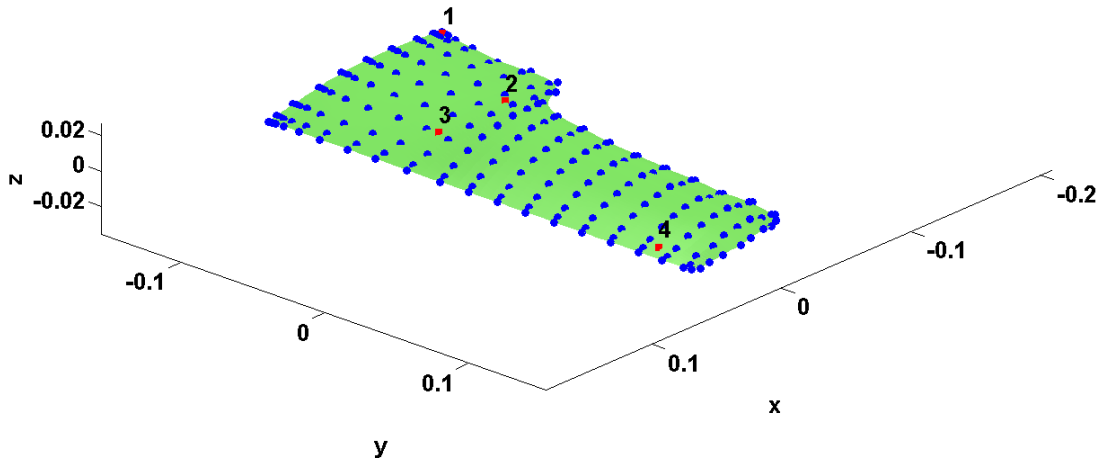


Fig. 2 The B-spline FE model with the 21x10 CPs (blue dot) and the 4 measurement response dofs (red squares).

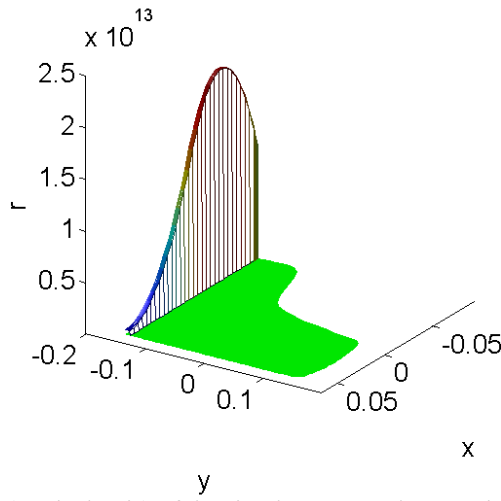


Fig. 3 Distributed stiffness values (vertical-axis) of the simply supported constraint employed to generate the measurements.

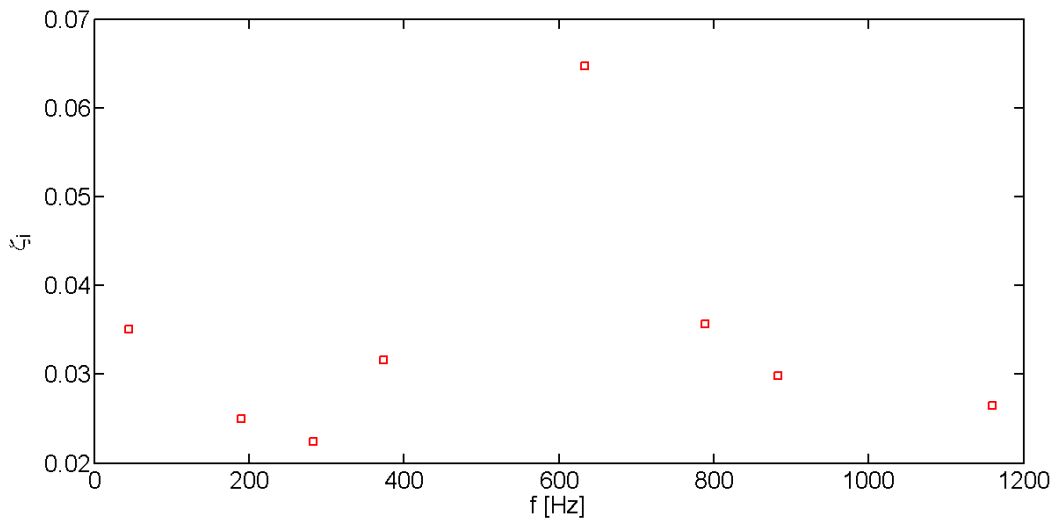


Fig. 4 Modal damping ratio values adopted to simulate the measurements. The values refer to the first 8 modes.

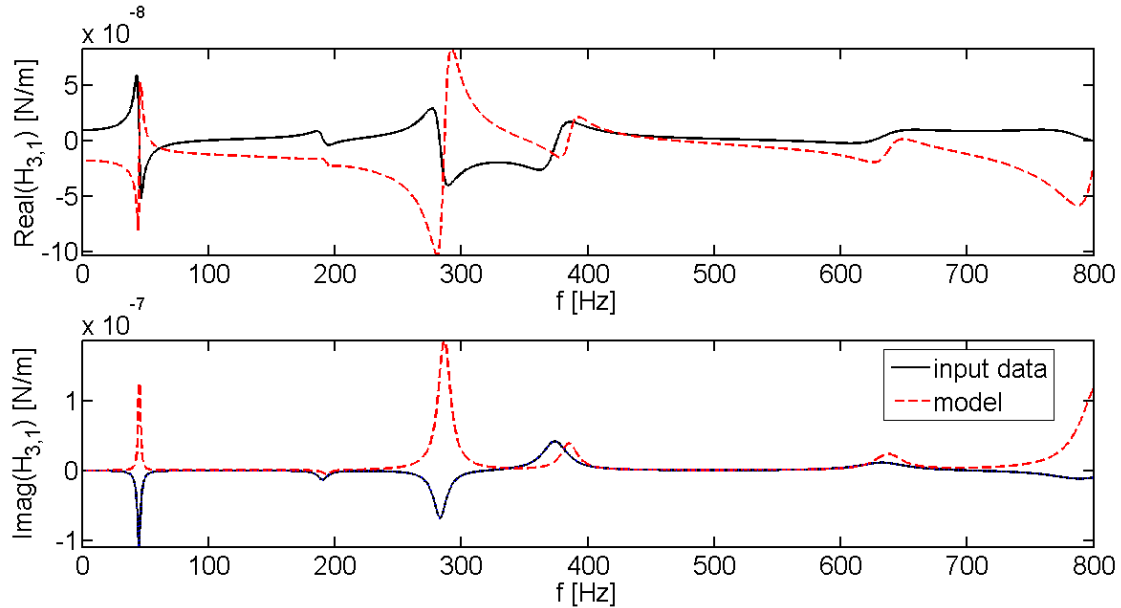


Fig. 5 Comparison of (input in dof 1; output in dof 3) FRF before updating: the input data (black continuous line) and the model (red dotted line).

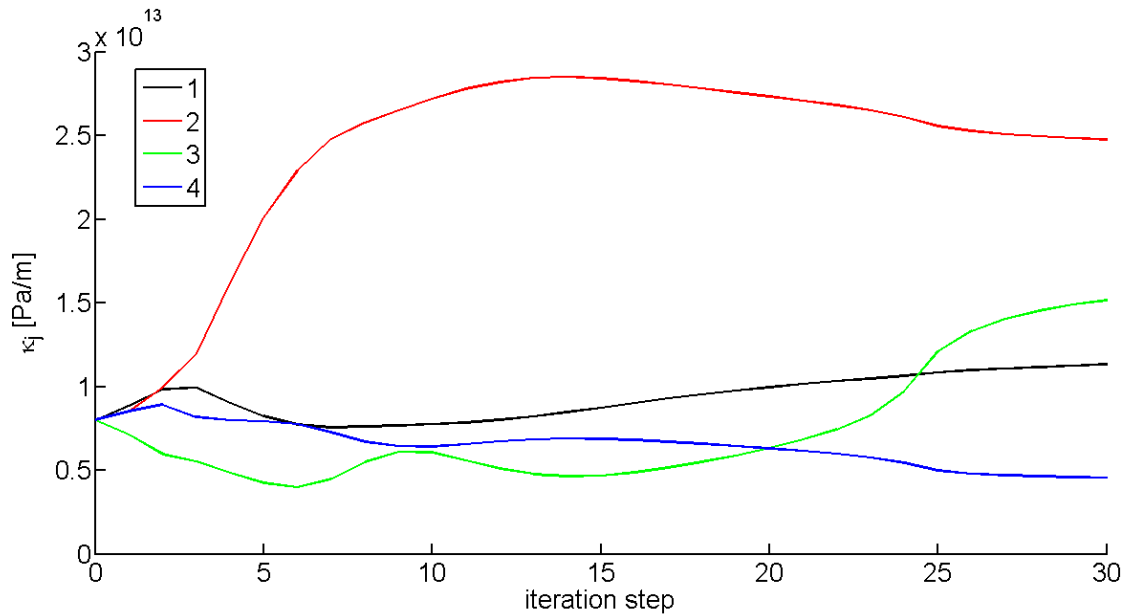


Fig. 6 Evolution of the stiffness parameters κ_j ($j=1, \dots, 4$ in the legend) during iterations by adopting the proposed updating procedure. Example without considering noise.

4.1 Measurement simulation: noise not included

Coefficients in vector κ and damping coefficients γ_z (quadratic B-spline functions, $n^z=5$, $f_{ST}=0\text{ Hz}$ and $f_{FI}=(1.2 \cdot 800)\text{ Hz}$ in Eq.20) are assumed as the updating identification variables. The updating procedure is started by putting all of the coefficients in κ equal to $8 \cdot 10^{12}\text{ Pa}$ and all of the damping coefficients equal to 0.02. The comparison of the resulting FRFs is reported in Fig.5. The gradient of \mathbf{C} with respect to the stiffness parameters is disregarded, i.e. $\frac{\partial \mathbf{C}}{\partial p_k} = 0$ if

$p_k \neq \gamma_z$. All four measurement dofs (Fig. 2) are considered as input. The value of the identification parameters at each step, adopting the proposed procedure, is reported in Fig.6 for the stiffness coefficients, and in Fig.7 for the γ_z coefficients; Fig.8

4.2 Measurement simulation: noise contribution

In this simulation, the same updating parameters of the previous examples are considered with the same starting values. A random noise is added in FRFs, by considering a normal distribution with a standard deviation equal to 10% of the signal RMS value. Four FRFs data (dofs from 1 to 4, Fig.2) are employed in the updating process.

When 10% noise is added, the value of the identification parameters at each step, adopting the proposed procedure, is reported in Fig.10 for the stiffness coefficients, and in Fig.11 for the γ_z damping coefficients; Fig.12 refers to the comparison of the modal damping ratio used to simulate the measurements (red squares) and the identified curve (black line) where the green filled squares are the B-spline control coefficient γ_z . Fig.13 refers to the comparison of the input and updated FRFs.

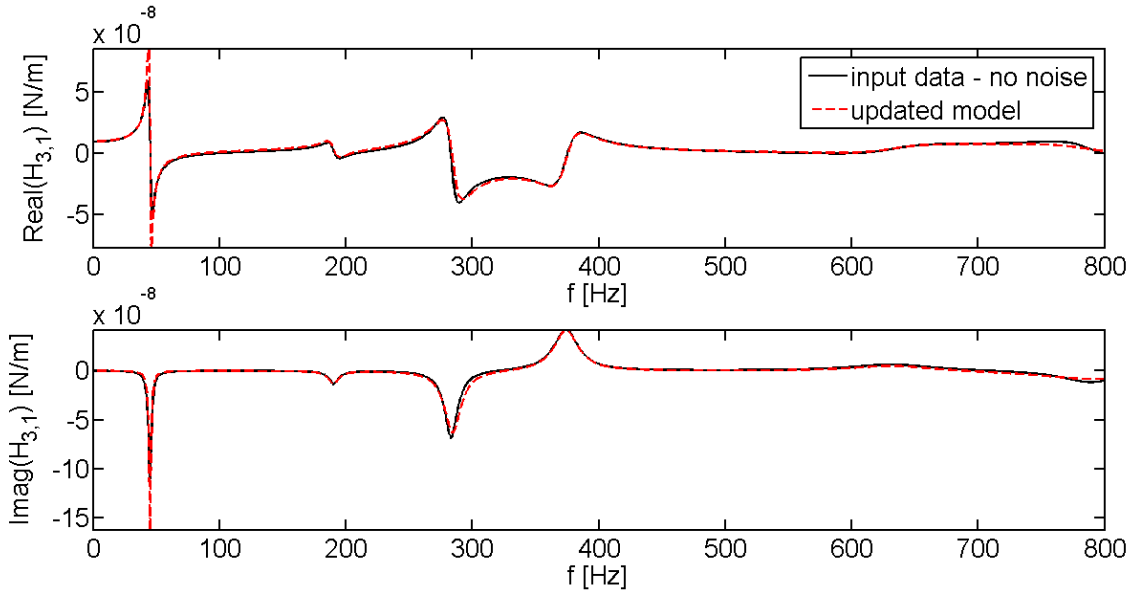


Fig. 9 Comparison of (input dof 1; output dof 3) FRF after updating (example with 4 measurement response dofs without noise): the input data (black continuous line) and the updated model (red dotted line).

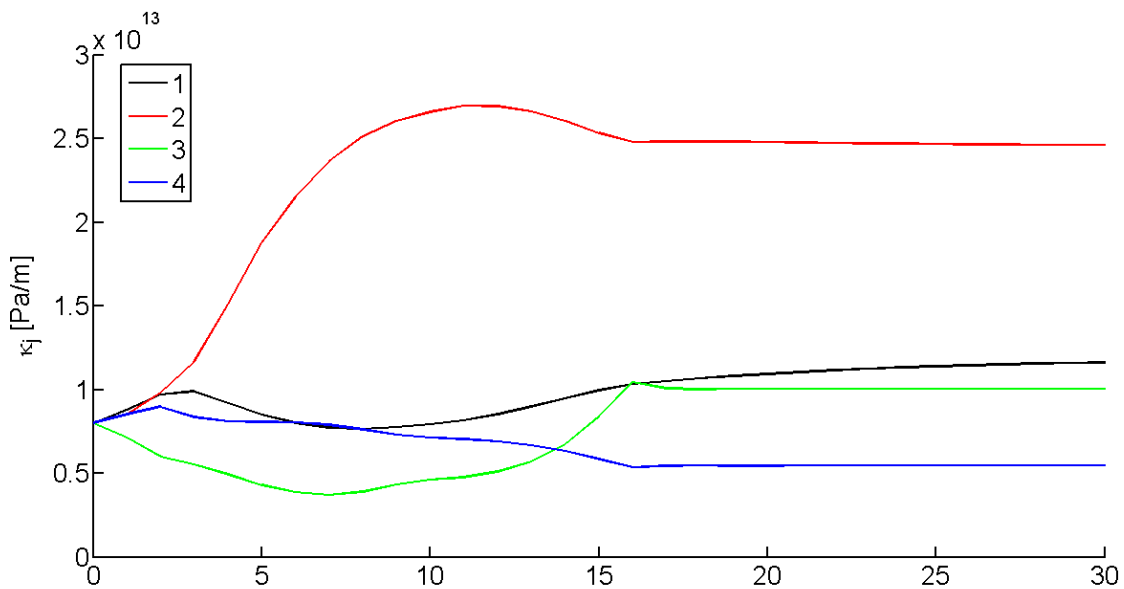


Fig. 10 Evolution of stiffness parameters κ_j ($j=1,\dots,4$ in the legend) during iterations by adopting the proposed updating procedure. Example with 10% noise.

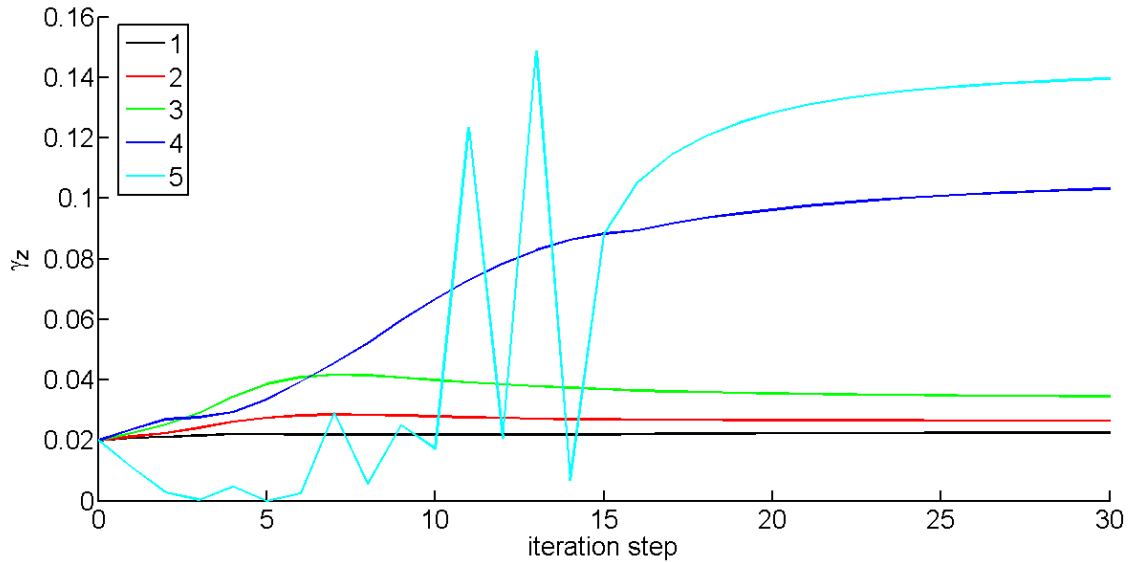


Fig. 11 Evolution of the damping parameters γ_z ($z=1, \dots, 5$ in the legend) during iterations by adopting the proposed updating procedure. Example with 10% noise.

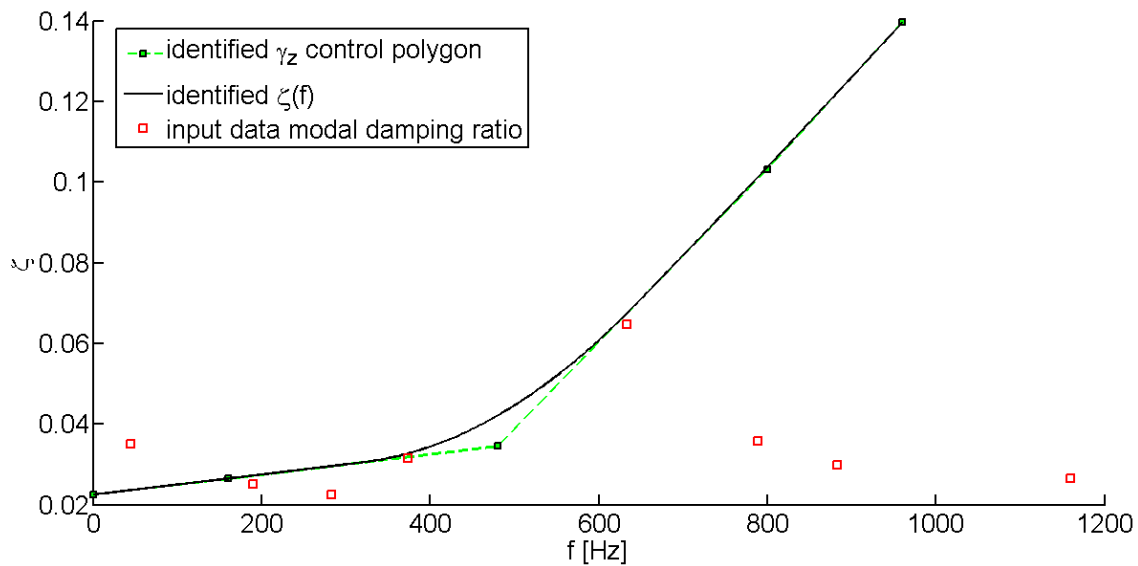


Fig. 12 Comparison of the modal damping ratio used to simulate the measurements (red squares) and the identified $\zeta(f)$ (black line; green filled squares refer to B-spline curve control coefficients). Example with 10% noise.

5. Critical discussion and conclusions

An updating procedure of a B-spline FE model of a car front spoiler was proposed, the updating parameters being the coefficients of a distributed constraint stiffness model and the damping ratios, both modeled by means of B-spline functions. The optimization objective function was defined by considering the difference between the measured (numerically synthesised) FRFs and the linearized analytical FRFs. The incompatibility between the measured dofs and the non-physical B-spline FE model dofs was overcome by employing the same B-spline shape functions, thus adding a small computational cost. A test case was investigated by simulating the experimental measurements by model based numerical simulations considering random noise as well. Experimental measurement data were simulated by adopting the same B-spline analytical model

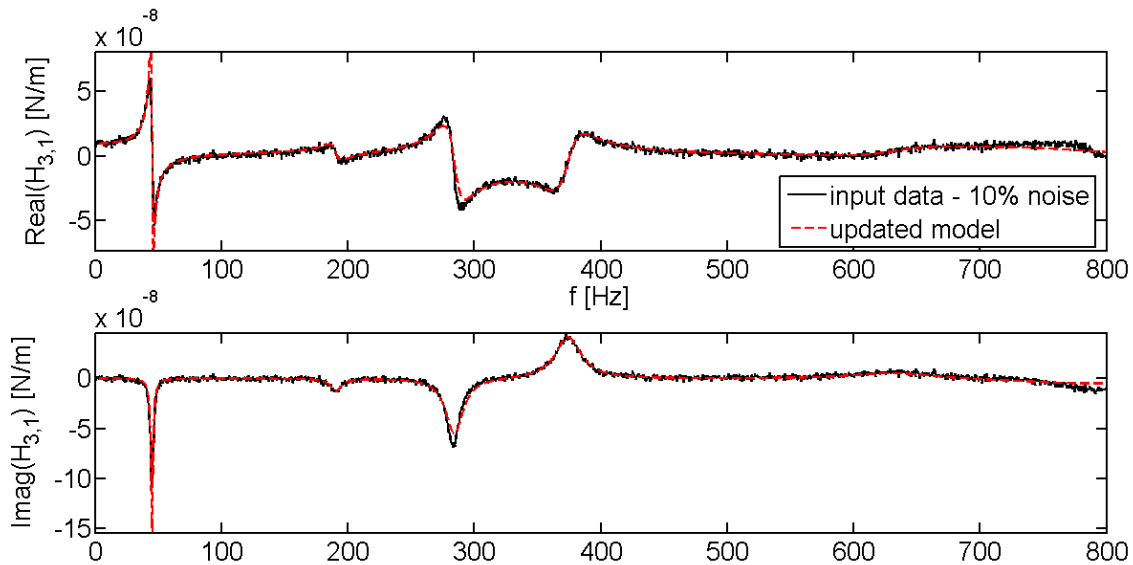


Fig. 13 Comparison of (input dof 1; output dof 3) FRF considering noise (10% case) after updating (4 measurement response dofs): the input data (black line) and the updated model (red line).

used as the updating model. Numerical results showed good matching of the FRFs after the updating process with only four measurement dofs, when noise is not considered. The updated FRFs showed a good matching with the input FRFs even with the adoption of four measurement dofs and noisy data as input in the updating procedure. The parameterization proposed for boundary condition and damping model can be efficiently adapted to the modeled structures regardless of the number of FE dofs. The proposed procedure requires that the structural system to be updated is lightly damped.

The approach needs to be tested by adopting true measurement data as input, in order to assess the effect of model errors, measurement dofs spatial distribution and measurement estimate. Future applications will be addressed towards both the adoption of real measurement data and the optimal selection of the frequency measurement data.

6. Acknowledgments

The present study was developed within the LAV-INTERMECH laboratory, with the contribution of the Regione Emilia-Romagna, PRRITT, misura 3.4, Azione A, obiettivo 2. Support from the Italian Ministero dell'Università e della Ricerca (MIUR), under the "Progetti di Interesse Nazionale" (PRIN07) framework is also gratefully acknowledged.

7. References

- [1] Kagan, P. & Fischer, A. (2000). Integrated mechanically based CAE system using B-spline finite elements. *Computer Aided Design*, 32, pp. 539-552.
- [2] Hughes, T.J.R.; Cottrell, J.A. & Bazilevs, Y. (2005). Isogeometric analysis: CAD, finite elements, NURBS, exact geometry, and mesh refinement. *Computer Methods in Applied Mechanics and Engineering*, 194, pp. 4135-4195, 2005.
- [3] Hughes, T.J.R.; Reali, A. & Sangalli, G. (2009). Isogeometric methods in structural dynamics and wave propagation, *Proceedings of COMPDYN 2009 - Computational Methods in Structural Dynamics and Earthquake Engineering*, Rhodes, Greece, 22-24 June 2009.
- [4] A. Carminelli, G. Catania, *B-spline finite element formulation for laminated composite shells*. Proceedings of ASME IMECE 2008, pp.1-7, October 31-November 6, 2008, Boston, Massachusetts, USA.
- [5] A. Carminelli, G. Catania, *PB-spline finite element shell modeling and refinement technique*. Proceedings of ASME IDETC/CIE 2009, pp.1-8, August 30-September 2, 2009, San Diego, California, USA.
- [6] Esfandiari, A.; Bakhtiari-Nejad, F.; Rahai, A. & Sanayei, M. (2009). Structural model updating using frequency response function and quasi-linear sensitivity equation. *Journal of Sound and Vibration*, Vol. 326, 3-5, pp. 557-573, ISSN 0022-460X.
- [7] Friswell, M. I. & Mottershead, J. E. (1995) *Finite element modal updating in structural dynamics*, Kluwer Academic Publisher, ISBN 0-7923-3431-0, Dordrecht, Netherlands.
- [8] Friswell, M.I.; Mottershead, J.E. & Ahmadian, H. (2001). Finite-Element Model Updating Using Experimental Test Data:

- Parametrization and Regularization. *Philosophical Transactions: Mathematical, Physical and Engineering Sciences*, 359, 1778, Experimental Modal Analysis (Jan. 2001), pp. 169-186.
- [9] Gabriele S.; Valente, C. & Brancaleoni, F. (2009). Model calibration by interval analysis. *Proceedings of XIX AIMETA CONFERENCE*, Ancona, Italy, September 14-17, 2009.
- [10] Garibaldi, L.; Catania, G.; Brancaleoni, F.; Valente, C. & Bregant, L. (2005). Railway Bridges Identification Techniques. *Proceedings of IDETC2005: The 20th ASME Biennial Conference on Mechanical Vibration and Noise*, Long Beach, CA, USA, September 24-28, 2005.
- [11] D'ambrogio W. & Fregolent A. (2000). Robust dynamic model updating using point antiresonances. *Proceedings of the 18th International Modal Analysis Conference*, pp. 1503-1512, San Antonio, Texas.
- [12] Kye-Si Kwon, Rong-Ming Lin, Frequency selection method for FRF-based model updating, *Journal of Sound and Vibration* 278 (2004) 285–306
- [13] H AHMADIAN, J.E. MOTTERSHEAD, M. I. FRISWELL. REGULARISATION METHODS FOR FINITE ELEMENT MODEL UPDATING *Mechanical Systems and Signal Processing* (1998), 12(1), pp47-64
- [14] Lin, R.M. & Zhu, J. (2006). Model updating of damped structures using FRF data. *Mechanical Systems and Signal Processing*, **20**, pp. 2200-2218.
- [15] A. Carminelli, G. Catania, *B-Spline Shell Finite Element Updating By Means Of Vibration Measurements*. Participation in the book *Vibration Analysis*, 2010, INTECH, ISBN: 978-953-7619-X-X (In press).
- [16] Piegl L. & Tiller, W. (1997). *The NURBS Book, 2nd Edition*. Springer-Verlag, ISBN 3-540-61545-8, New York, NY, USA.
- [17] Cook, R.D.; Malkus, D.S.; Plesha, M.E. & Witt, R.J. (1989). *Concepts and applications of finite element analysis*, J. Wiley & Sons, ISBN 0-471-35605-0, New York, NY, USA.
- [18] Carminelli, A. & Catania, G. (2009). PB-spline hybrid surface fitting technique. *Proceedings of ASME IDETC/CIE 2009*, pp.1-7, San Diego, California, USA, August 30-September 2, 2009.
- [19] Carminelli, A. & Catania, G. (2007). Free vibration analysis of double curvature thin walled structures by a B-spline finite element approach. *Proceedings of ASME IMECE 2007*, pp. 1-7, Seattle (Washington), USA, 11-15 November 2007.
- [20] Reddy, J.N (2004). *Mechanics of laminated composite plates and shells: theory and analysis*, CRC Press, ISBN 9780849315923.

Measurement of 2D dynamic stress distributions with a 3D-Scanning Laser Doppler Vibrometer

Matthias Schüssler^a, Dr. Maria Mitrofanova^a, Dr. Ulrich Retze^b

^aPolytec GmbH, R&D, Polytec Platz 1-7, 76337 Waldbronn, Germany

^bMTU Aero Engines GmbH, Component testing, Dachauer Str. 665, 80995 Muenchen, Germany

ABSTRACT

Recently a method has been developed to measure surface dynamic strain and stress fields by using a contactless 3D scanning laser Doppler vibrometer. Assuming a free visible surface of the test specimen this method, a combination of advanced measurement technique and a post-processing algorithm, enables the assessment of high resolution dynamic surface loadings including quantity and direction of strain/stress distributions.

The first part of the article describes the basic principles of the method. The second part informs about the validation work of the measurement results. Different steps were performed in order to measure real structures. A numerical model was the base for correlation with measured deflection-shapes, strain- and stress-fields. During this analysis, the different influencing parameters for measuring the strain information could be analyzed systematically. The third part presents a comparison of vibrometer measurements to strain gauge values.

The validation of the method shows a high level of agreement between measured values compared to numerical strain and stress results. The correctness of the absolute strain values could be validated by the comparison with strain gauges. Further research will be done to close the gap between simulation and measurement.

1. INTRODUCTION

For a safe and reliable design of structures the knowledge of mechanical stresses under structural usage is inevitable. Especially for dynamically loaded structures precise information about maximum stresses is important in order to design robust components.

A newly developed technique based on a 3D-Scanning Laser Doppler Vibrometer (3D-SLDV) enables the contactless measurement of surface stresses of a vibrating structure. The primarily measured information is the 3D deflections at all surface grid points of the measured structure. The 3D deflection components are used to calculate strain and stress distributions in a post-processing routine. This procedure has first been proposed by Mitchell et al. [1]. The basic principles of the method and details on the post-processing routine have been published by Meitzner [2] and Cazzolato et al. [3].

In this work, the focus is on the validation of the method.

2. THEORETICAL BASICS

The 3D-SLDV (see [fig. 1](#)) measures the three-dimensional vibration vectors at all specified surface points. It consists of three 1D-SLDVs. For the measurement three lasers are directed simultaneously to one point. Each vibrometer measures the vibration vector in the direction of its laser beam. The three vibration vectors are then transformed into a global orthogonal coordinate system. All points are measured sequentially; therefore, the object vibration must be repeated for the measurement of each point. The method has been described by Bendel et al. [4].



Fig. 1: Test setup comprising the three scanning heads and a digital camera (left) and a test specimen, mounted on an electromagnetic shaker (right)

[Fig. 2](#) shows the basic principle of the strain measurement with the 3D-SLDV. To position the lasers, the geometry data of the object is imported from the FE-model. For the measurement a routine called VideoTriangulation has been developed; this routine uses image processing of a high resolution video camera to ensure that the three lasers are on the same spot. From the updated laser angles, the geometry data of the real object can be obtained.

Once the three lasers are on the same spot, the three vibrometers acquire data simultaneously. The raw data is transformed into the global coordinate system of the object.

The next step is an optional smoothing. As the following strain calculation requires a spatial differentiation of the data, it is very sensitive to noise. Sophisticated smoothing algorithms reduce the noise prior to strain calculation.

The raw data for the strain calculation is the 3D displacement vectors. These vectors are transformed into a local coordinate system which is aligned with the local geometry of the object's surface. From the local in-plane displacement and the geometry, strain is calculated for each surface triangle.

The final step is the transformation of the strain data into the object's global coordinate system, this allows for displaying and analyzing the data. The results can be directly compared to the results of the FE calculation.

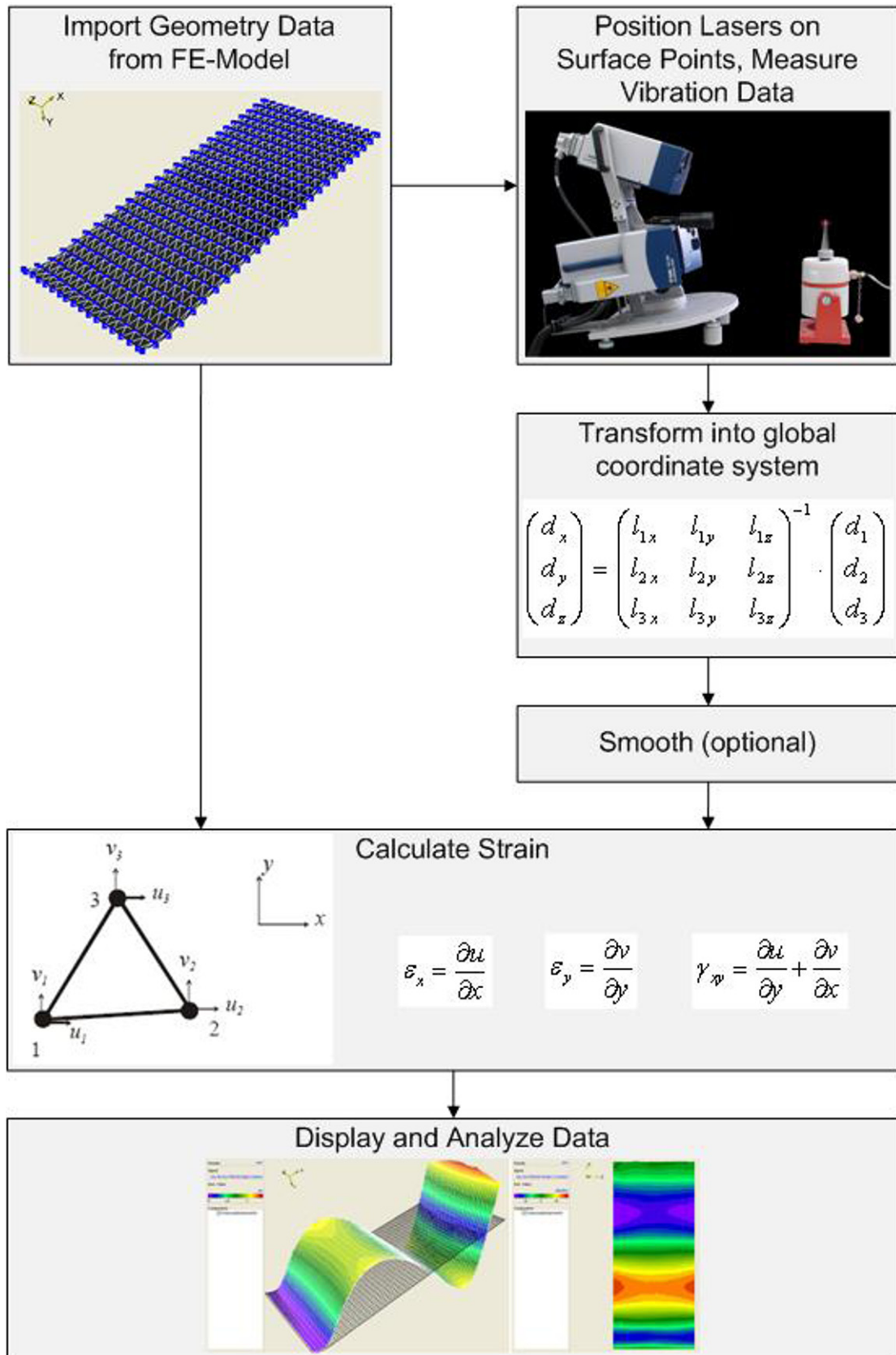


Fig. 2: Basic principle of the strain measurement with a 3D-SLDV

An example for the measurement is shown in [fig 3](#). It shows the third bending mode (mode 6) of the hereafter described test specimen at 7.8 kHz.

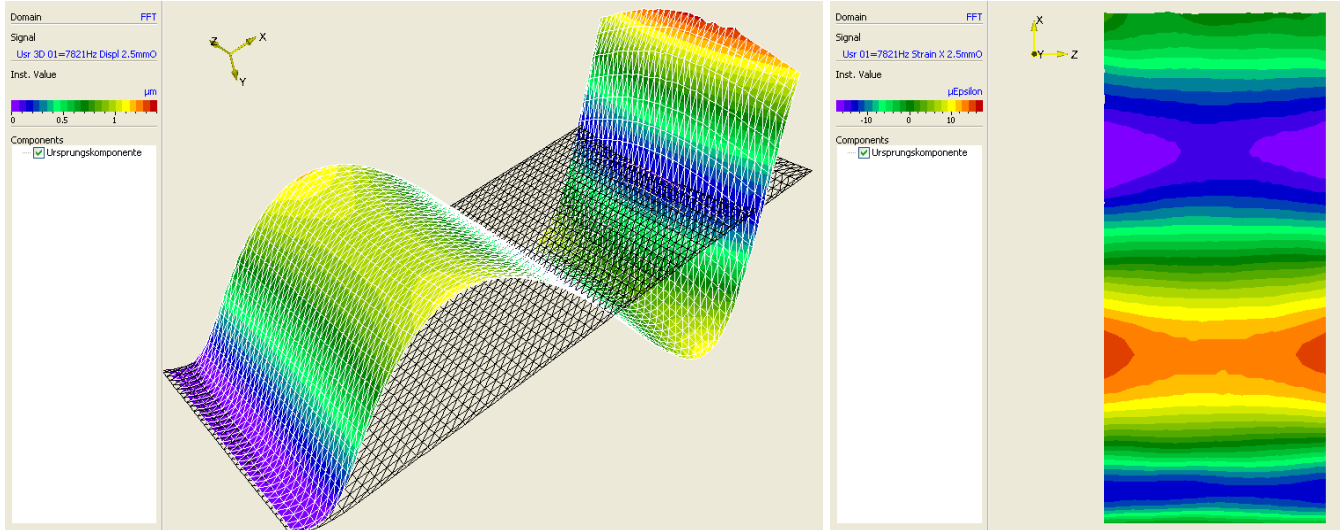


Fig. 3: Deflection shape and strain distribution of test specimen at 7.8 kHz

3. VALIDATION OF THE STRAIN AND STRESS MEASUREMENT

In order to determine the validity and the limits of the method for structural measurements, extensive validation work has been performed.

The validation work has been performed in three main steps:

1. Validation of the post-processing routine
2. Correlation of the Vibrometer measurement with FE-simulation
3. Correlation of the Vibrometer measurement with a strain gauge

The validation has been performed on a symmetric cantilever test structure ([fig. 4](#)). A 3 mm thin rectangular plate was used to identify and validate modal strain distributions. To achieve well defined boundary conditions the test specimen contains a 15 mm thick base. A fillet radius of 9.4 mm helps pushing the maximum strains away from the fixed base.

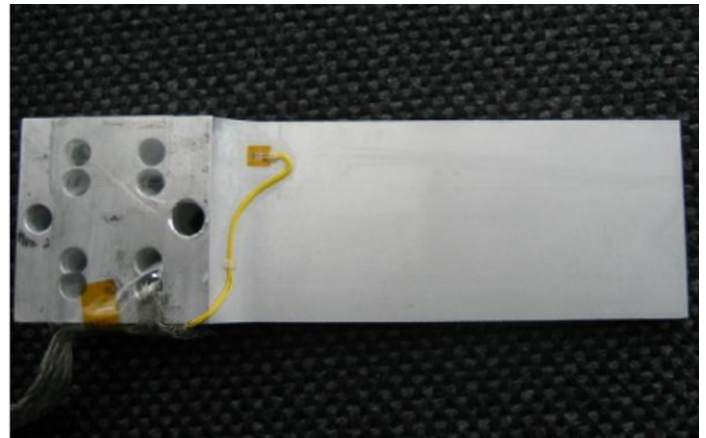
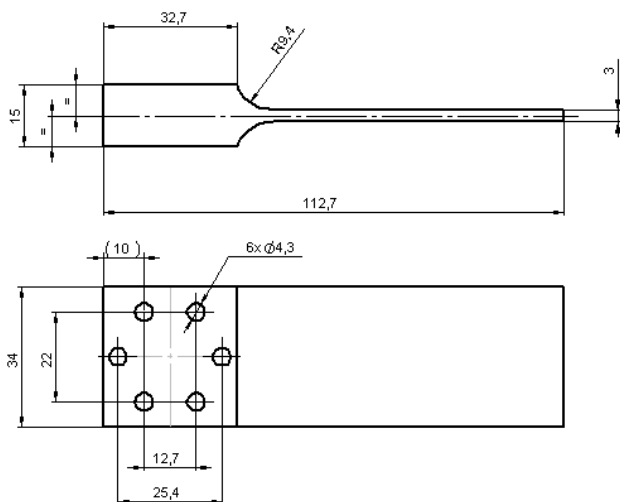


Fig. 4: Drawing and photograph of the test specimen, the applied strain gauge can be seen in the photograph

3.1 Validation of the post-processing routine

The first step in validation work was to validate the strain calculation post-processing routine. For this purpose a 3D numerical simulation model of the test specimen has been build, using the FE-Software CalculiX [6] (fig. 5).

After performing a numerical modal analysis [5], the calculated mode shapes and the strain and stress distributions have been available directly from Calculix. Those calculated mode shapes have been used to validate the post-processing routine which calculates surface strains from the measured surface displacement values (fig. 6).

The post-processing routine has been validated by a calculation of the Modal Assurance Criterion (MAC) with the strain values calculated by CalculiX.

The obtained MAC-values are shown in fig. 7. All linear strain values are 0.999 which proves the post-processing routine to be correctly implemented. Some shear strain values are below 0.99, this fact can be attributed to very high gradients at the edges of the structure which can be better resolved by the FE simulation due to a higher point density.

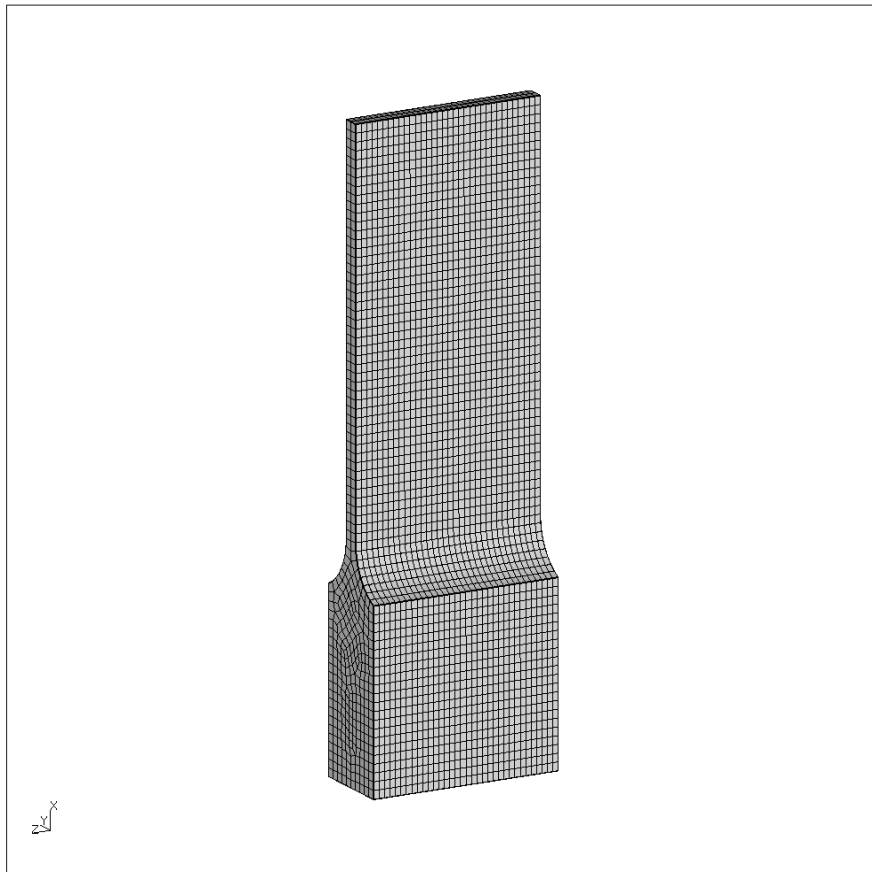


Fig. 5: Simulation model of the test specimen

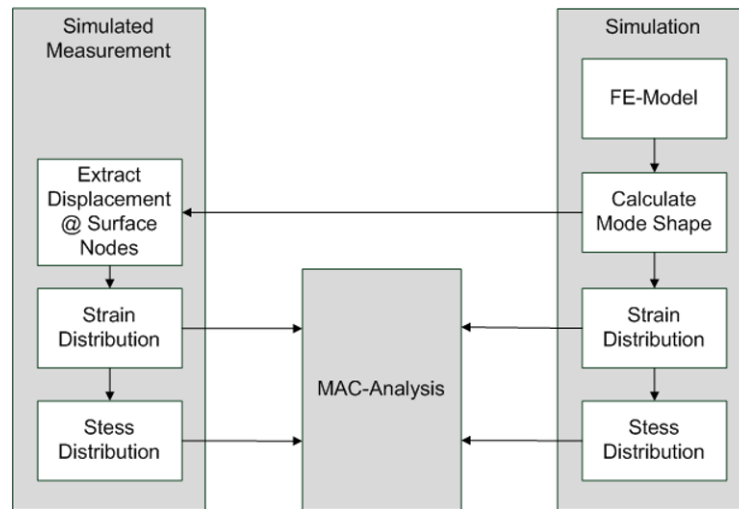


Fig. 6: Validation of the post-processing routine

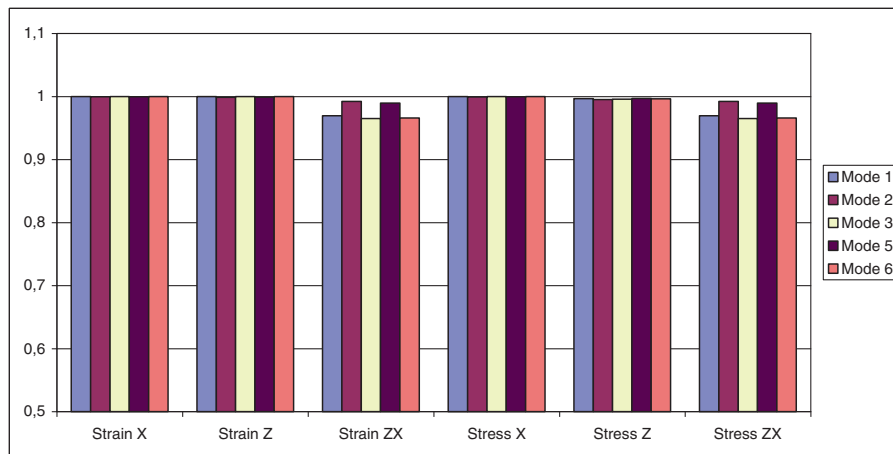


Fig. 7: MAC values between the post-processing routine and CalculiX

3.2 Correlation of the Vibrometer measurement with FE-simulation

In order to perform a measurement, the specimen has been mounted on an electromagnetic shaker (see [fig. 1](#)). A measurement with broad-band excitation has been performed at a single point to find the exact resonance frequencies. At each resonance frequency, the deflection shape has been measured with sine excitation.

As described above, the deflection shapes have been post-processed to calculate strain and stress distributions. In the following, those post processed measurement values are referred to as measured strain and stress distributions.

The measured strain and stress distributions have been compared to those from simulation. The procedure of this validation step is shown in [fig. 8](#). The results of the MAC analysis are shown in [fig. 9](#). The results of the visual comparison for one mode are displayed in [Table 1](#).

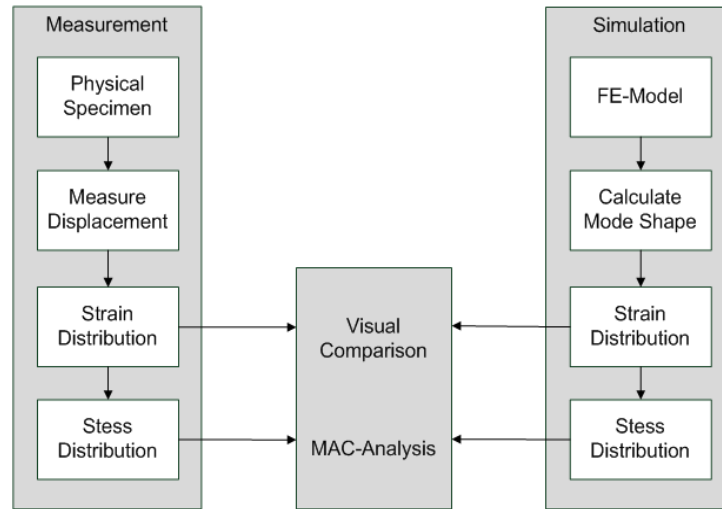


Fig. 8: Validation of the strain and stress measurement

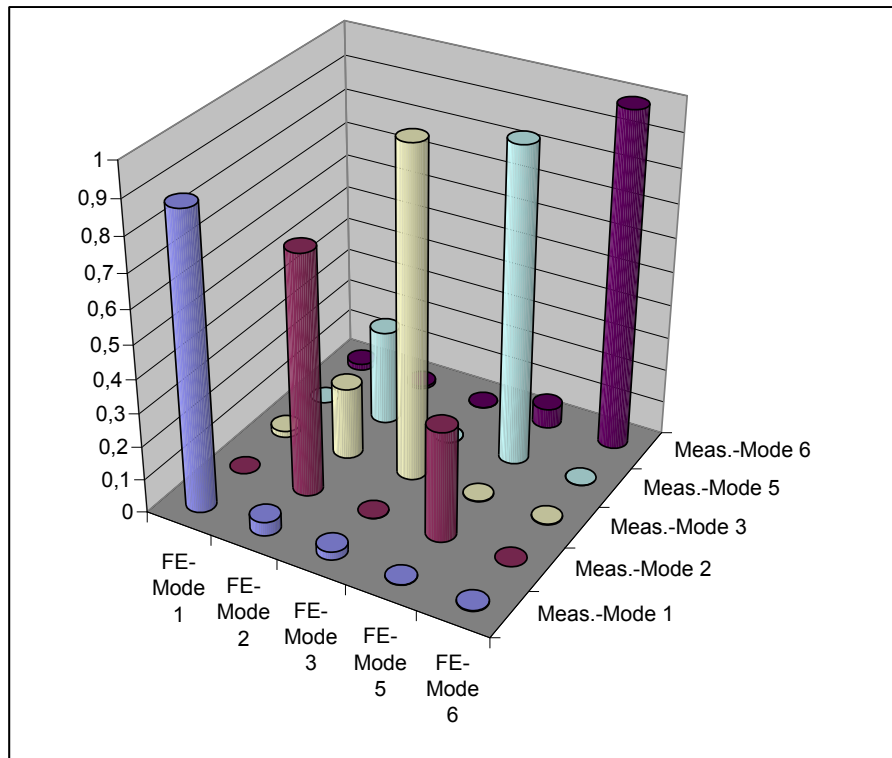


Fig. 9: MAC values between simulation and measurement

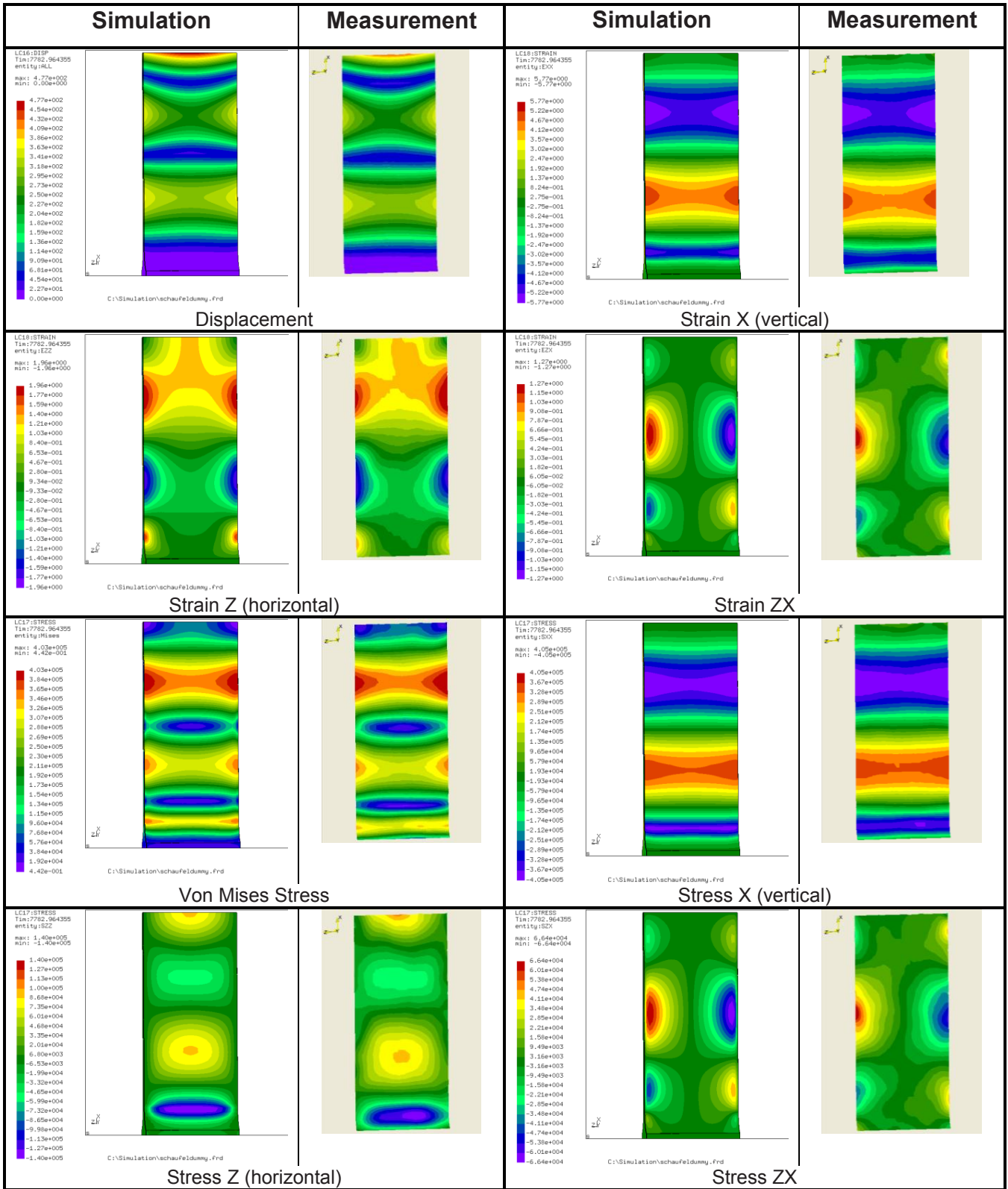


Table 1: Visual comparison between measurement and simulation for the third bending mode at 7.8 kHz

3.3 Comparison of the Vibrometer measurement with strain gauges

Strain gauge measurements are well established in durability testing. However, determining the absolute strain value with strain gauges means to get an integral value from the gauge's sensitive area. A single strain gauge provides furthermore only information in its spatial validity. The newly developed technique based on 3D-deflection measurements provides the complete information about directions and quantitative strains.

To confirm the validity of the absolute strain values, measured with the 3D-SLDV, a strain gauge has been applied on the back of the double symmetric test specimen (see [fig. 3](#), left). The strain values have been measured simultaneously with the 3D-SLDV on the front of the test specimen. For the comparison, the point, opposite to the strain gauge has been analyzed together with the values from the strain gauge. [Fig. 10](#) shows the measured values for the modes up to 10 kHz.

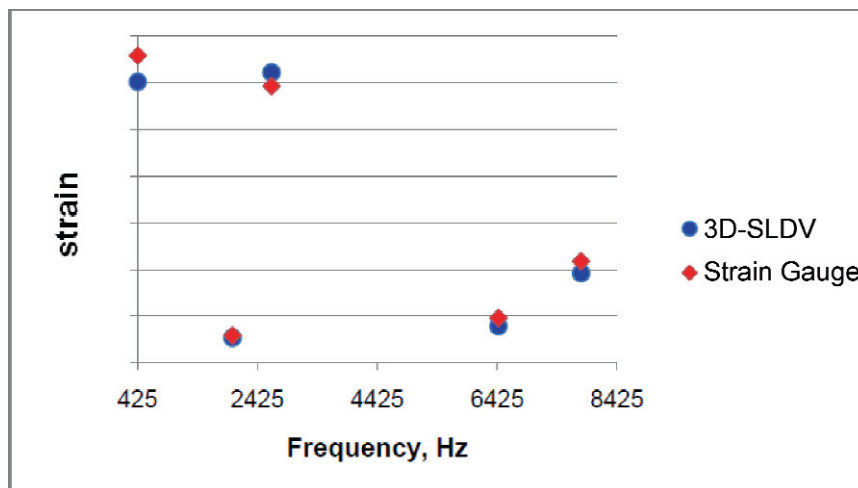


Fig. 10: Measured values from the strain gauge and the 3D-SLDV

Both methods show a very good agreement, it could not be analyzed if the differences stem from the measurement or from asymmetries of the test specimen.

4. INFLUENCE OF DATA SMOOTHING

As shown in [fig. 2](#), an optional smoothing of the measured vibration data is in the process of calculating strain and stress distributions from the measured vibration data. The purpose of smoothing is to minimize measurement noise which becomes apparent in the strain data, as the post-processing routine is a numerical differentiation.

The smoothing has a great influence on the quality of the results. To adjust the strength of smoothing a radius parameter must be specified in millimeters. [Table 2](#) shows strain values with different filter settings for a sample measurement. It can be seen that for the chosen example, a filter radius of 2.5 mm is optimum. For a filter radius of 5 mm, the smoothing effects are better, but it can be seen that the maximum strain values are significantly reduced by the smoothing.

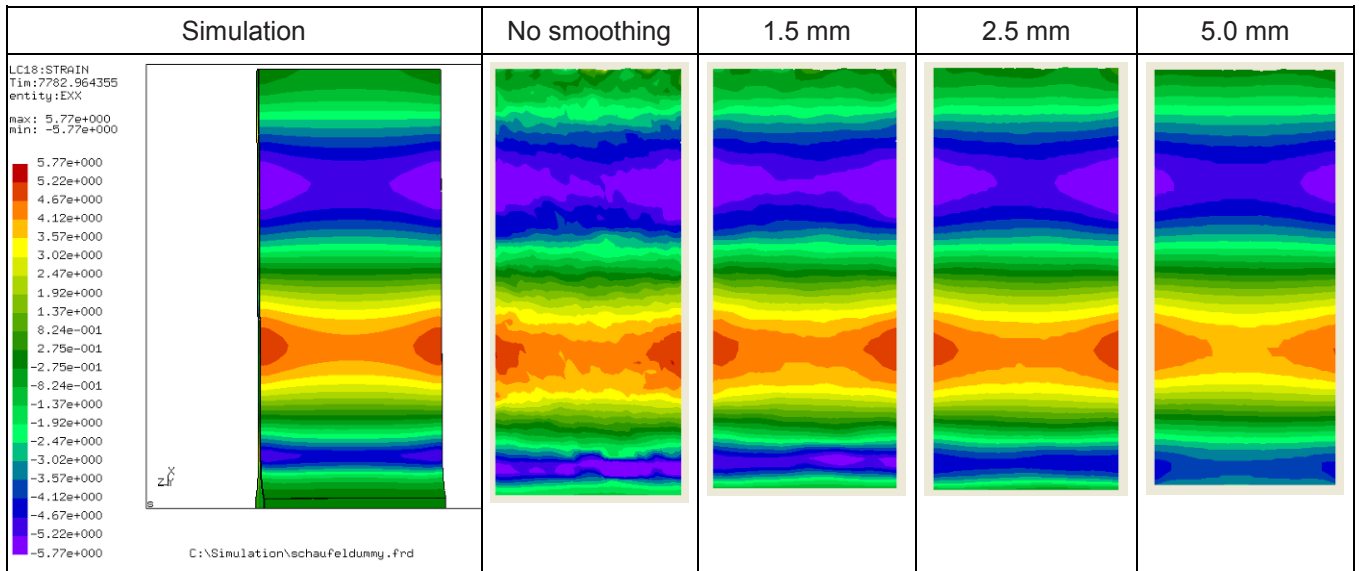


Table 2: Influence of the smoothing filter radius for Strain_X of the third bending mode at 7.8 kHz

A qualitative research of the influence of the smoothing filter radius has been performed by MAC-analysis. After calculating the strain values by post-processing, the MAC-values with the simulated strain distributions have been calculated. For the chosen example, the optimum filter setting is at 2.5 mm (fig. 11), which confirms the visual analysis above.

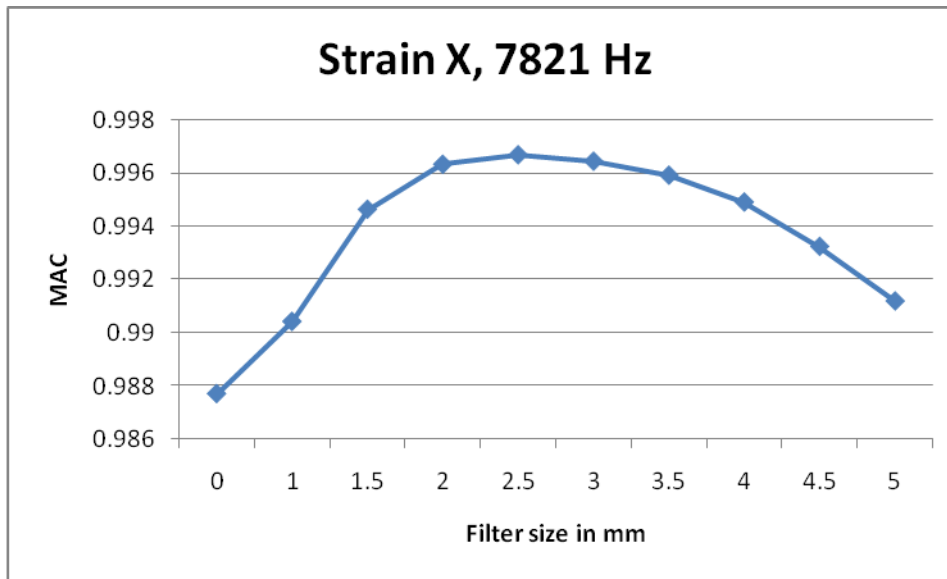


Fig. 11: Influence of the filter size on the MAC values for Strain_X of the third bending mode at 7.8 kHz

5. CONCLUSIONS

A method to optically measure strain and stress values has been presented. The validation of this method showed a high level of agreement between the measured values and the simulation results and the measured strain gauges. Based on the high sensitivity of the 3D-SLDV, high resolution surface dynamic strain measurements can be performed. An accurate structural validation between numerical simulations and high resolution measurement results is possible. This contactless measurement device helps to reduce costs concerning instrumentation work and leads to reliable data even under rough measurement conditions. The complete measurement can be performed within a few hours.

REFERENCES

- [1] Mitchell, L.D., West, R.L. and Wicks, A.L. (1998), "An emerging trend in experimental dynamics: Merging of laser-based three-dimensional structural imaging and modal analysis", *Journal of Sound and Vibration*, 211(3),323-333.
- [2] Meitzner, R.; MTU Aero Engines (2005); *patent applications DE 102005042820A1 and US20080249722A1*.
- [3] Ben Cazzolato, Stuart Wildy, John Codrington, Andrei Kotousov and Matthias Schuessler (2008), "Scanning laser vibrometer for non-contact three-dimensional displacement and strain measurements", *Proceedings of the Australian Acoustical Society Conference, Geelong, Australia, Nov 24-26*.
- [4] K. Bendel, M. Fischer, M. Schüssler (2004), "Vibrational analysis of power tools using a novel three dimensional scanning vibrometer", *6th International Conference on Vibration Measurements by Laser Techniques: Advances and Applications*, ed. E. P. Tomasini, *Proc. of SPIE Vol. 5503 pp. 177-184*.
- [5] Dhondt, G. (2004), "The Finite Element Method for Three-Dimensional Thermomechanical Applications", *Wiley*
- [6] www.calculix.de

A Particle Damper for Transient Oscillations

S. Eren Semercigil¹, Özden F. Turan¹ and Gregory A. Kopp²

¹Victoria University, School of Engineering and Science, PO BOX 14428, MCMC
Melbourne, Victoria 8001 AUSTRALIA

²Boundary Layer Wind Tunnel Laboratory, University of Western Ontario
London, Ontario CANADA

ABSTRACT

Tuned vibration absorbers, in various disguises, still form the basis of vibration suppression for light and flexible structures. These simple auxiliary components may be tuned at critical frequencies of the structure to be controlled. Tuning frequencies may be constant (in case of passive absorbers) or varied (in case of semi-active and active absorbers). Tuning ensures a strong interaction, and facilitates the transfer of the harmful energy from the problem structure to the absorber. The task then becomes to dissipate the transferred energy rapidly in the absorber, before it has a chance to return the energy back to the structure.

Returning the energy back to the structure, when the rate of dissipation in the absorber is not fast enough, manifests itself as a beat, significantly deteriorating the control performance. The obvious solution to avoid the undesirable beat is to include dissipative components in the design of the tuned absorber. However, such an inclusion has two consequences. First, the effectiveness at the tuning frequency is sacrificed, at a level proportional to the amount of damping in the absorber. Second, and more critically, dissipative components are high maintenance components by nature, rendering the damped tuned absorber to be less practical.

A particle damper is presented in this paper which can dissipate energy rapidly while maintaining the tuning of the absorber effectively. Simple experiments are detailed to demonstrate the tuning, and the level of dissipation.

1. INTRODUCTION

Tall and flexible structures (such as high-rise buildings, long-span bridges, communication/transmission towers and even monuments) are susceptible to large oscillations caused by wind and ground disturbances. Due to the physical dimensions of these structures, the critical frequencies of concern may be below 1 Hz.

Tuned vibration absorbers in various configurations have been used for suppression of excessive oscillations of tall and flexible structures. The primary principle of design of this popular remedy, is to add an auxiliary oscillator to the structure of concern, and tune the critical frequency of the auxiliary oscillator to the critical frequency of the structure. Such tuning ensures strong interaction and rapid extraction of harmful energy from the structure to the sacrificial oscillator. This harmful energy then needs to be dissipated rapidly, as tuning also ensures the flow of the harmful energy back to the structure if it is not dissipated in the absorber.

An undamped tuned vibration absorber is a simple, and therefore practical, structure in its passive form. Its deficiency is to periodically return the extracted harmful energy back to the structure to be controlled. Hence, the oscillation envelopes of the absorber and the structure “beat” out-of-phase from each other, resulting in poor control. Generally, the beat period depends upon the ratio of the mass of the absorber and that of the structure, resulting in longer periods for larger mass ratios.

Effectiveness of a tuned absorber can be enhanced significantly by including dissipative elements in it. Historically, studies suggested procedures to determine the optimum damping from the classical reference of DenHartog in 1940's [1], in the comprehensive treatments of Hunt [2] and Snowdon [3], to just about any textbook on the study of structural vibrations. Contributions in this academically intriguing area still continue to trickle even in the last decade [4]. In all of these studies, a damping level in the order of about 20% of the equivalent critical

damping is demonstrated to be quite effective. This level, however, is quite high, difficult to achieve in a practically small size and, once achieved, to maintain it at the desired level. The difficulty is the nature of dissipative elements by design. Dissipative elements mostly work on the general principle of generating large pressure differentials in different fluid chambers. Energy is dissipated by moving the fluid agents back-and-forth between these chambers. Such a process induces mechanical wear and need frequent maintenance. Active components which can be programmed to act like dampers, are excluded in this argument, due to their inherent requirements of sensing and computing.

An experimental investigation is presented in this paper dealing with a rolling tuned vibration absorber, as an alternative to the more conventional classical tuned absorbers. Rolling dampers have been reported earlier in Pirner [5] and Legeza [6] where a solid ball inside a spherical hollow chamber was used as an alternative to pendulum type of tuned vibration absorbers. The primary advantage of these rolling balls was their compact design, whereas a classical pendulum absorber would require impractically long arms, to achieve tuning at low frequencies. Both References 5 and 6 report effective suppression during forced vibrations where a phase opposition between the structure and the rolling ball is responsible for the control action. Dissipation in such a geometry is due to contact friction, and it is quite marginal. In contrast, the rolling element in this study includes dissipative agents in the form of granular particles placed inside a hollow cylindrical container. Experiments are detailed in the next section. Then experimental observations are reported.

2. EXPERIMENTS

The structure in [Figure 1\(a\)](#) consists of long flexible strips (1) cantilevered from the floor. A platform (2) is formed at the free tip, to accommodate a curved track (3). The rolling element is a simple hollow cylinder (4) with granular particles inside. The curvature of the track is the critical design parameter to tune the rolling cylinder's natural frequency, whereas the granules inside the cylinder are primarily responsible for energy dissipation. A sheet of 200-grit sandpaper is used to line the contact surfaces of the track to limit slip. Lentils are used as dissipative granular agents. A photograph of the curved track is given in [Figure 1\(b\)](#). The relevant parameters are listed in [Table 1](#).

The experiments consisted of displacing the cantilevered structure by 56 ± 0.5 mm and observing the resulting free decay of oscillations. A stop block (item 5 in [Figure 1\(a\)](#)) ensured repeatable initial displacements. A non-contact displacement gage (6) enabled capturing the history of structural displacements with a digitizing board and a personal computer. The output of the displacement gage was sampled at 100 Hz, for 4096 points. [Figure 2](#) is a close-up photograph of a cylindrical container and the lentils used in the experiments. The lentils have a geometry of circular disks with a nominal diameter of about 6 mm and thickness of about 2mm in their center.

Table 1. Relevant geometric and structural parameters.

| | |
|--|--|
| Diameter of the cylinder | : 56 mm |
| Diameter of the track | : 475 mm |
| Cantilevered beams | : 2mm thick, 35 mm deep (perforated with 10 mm holes), and 710 mm tall, mild steel |
| Mass of beams | : 397 g each (~ 100 g equivalent mass, in the first mode) |
| Mass of track with platform and connectors | : 2.157 kg (± 0.1 g) |
| Mass of hollow cylinder | : 83.2 ± 0.1 g |
| Mass of 140-count lentils | : 15.4 ± 0.1 g |
| Mass ratio of the hollow cylinder with structure | : $0.0832/2.357 \cong 0.03$ |
| Mass ratio of the lentils with structure | : $0.0154/2.357 \cong 0.006$ |
| Structural natural frequency | : 0.95 ± 0.01 Hz - measured |
| Structural equivalent stiffness | : 83.6 N/m - calculated |
| Structural equiv. viscous critical damping ratio | : 0.011 ± 0.003 - measured |

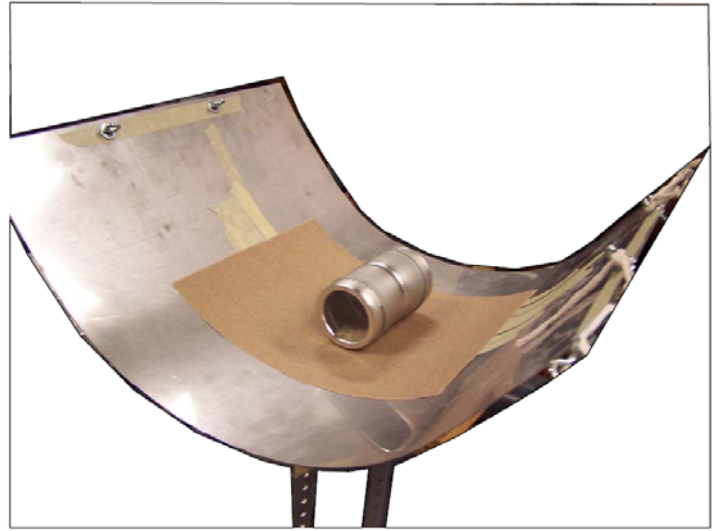
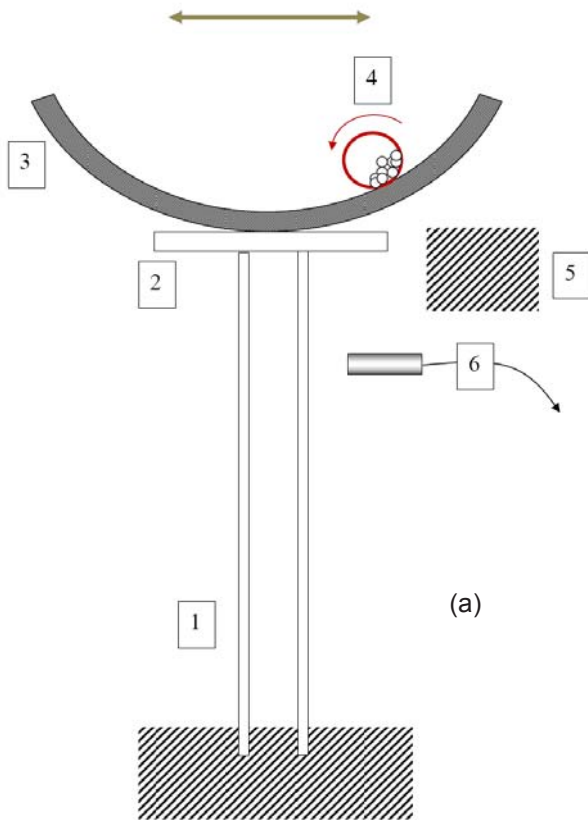


Figure 1. Showing (a) the experimental setup and (b) a close-up photograph of the curved track and the rolling container at rest.



Figure 2. Photograph of the container and 140-count lentils.

3. EXPERIMENTAL OBSERVATIONS

The history of transient oscillations of the uncontrolled structure is given in [Figure 3\(a\)](#). The uncontrolled structure has relatively poor inherent damping (approximately 1 % of the equivalent critical viscous damping), and the resulting transient oscillations persist even at the end of the 40-second sampling period. The natural frequency of the structure is 0.95 Hz, as clearly indicated in its frequency spectrum in [Figure 4\(a\)](#).

[Figure 3\(b\)](#) corresponds to the case where the empty cylindrical container is introduced in the curved track. The container's mass is approximately 3% of that of the structure. With the rolling container, the envelope of oscillations changes quite drastically from the slow exponential decay of the uncontrolled case in [Figure 3\(a\)](#). The container is able to extract the kinetic energy of the structure effectively, but unable to dissipate this energy rapidly enough. As a result, the kinetic energy is returned back to the structure periodically causing a beat, and a relatively poor performance.

At the start, container rests at the bottom of the track, at the position of least potential energy. After the structure is released from rest, container starts to roll back-and-forth in its track energetically, while structure's displacements are attenuated quite drastically. By the third cycle, the container starts to lose its energy, returning it back to the structure, resulting in the beat. The beat period in [Figure 3\(b\)](#) is approximately 5 s, as may be confirmed by the 0.2 Hz difference in the two spectral peaks shown in [Figure 4\(b\)](#).

At the end of the sampling period, the displacement magnitudes of the case in [Figure 3\(b\)](#), are only marginally smaller than those of the uncontrolled case in [Figure 3\(a\)](#). The decay is due to energy dissipation by some slip between the container and the track. Including a sheet 200-grit sandpaper limited this slip, but not eliminated it entirely. Sandpaper is shown in [Figure 1\(b\)](#).

The displacement history with a 140-count lentil in the container, is given in [Figure 3\(d\)](#). The lentils occupy just under 5% of the available volume inside the container, with a mass of $1/5^{\text{th}}$ of that of the container. The relevant dimensions are given in [Table 1](#).

Similar to the case in [Figure 3\(b\)](#), the container eagerly receives the kinetic energy from the structure, after its release. However, dissipation due to the "flow" of granular material is so effective that the oscillations practically stop by the 4th cycle. The equivalent damping ratio of the structure with the granular material is about 8%, an 8-fold increase from the uncontrolled case. The drastic increase in structural damping is also apparent in the frequency spectrum given in [Figure 4\(d\)](#).

The motion of the granular particle bed is similar to that of the oscillations of a pendulum, much like the rolling oscillations of the container on its track. As the container tumbles many times on its track for each period of the structure, the particle bed simply oscillates inside the container displacing by no more than 30° at its peak. The predominant motion of the particle bed, is sliding relative to the inside walls of the container. No particle is airborne at any time.

It should be mentioned that the most effective control corresponds to the case in [Figure 3\(d\)](#). With different size containers, it is possible to achieved tuning similar to that given in [Figure 3\(b\)](#). However, there seems to be a clear preference to the container used for this case. The dimensions given in [Table 1](#) result in approximately 8 full tumbles of the container for each period of the structure. During the same period, there is approximately three full cycles of oscillation of the particle bed inside the container. Hence, with the inclusion of the particle bed, there is a configuration of a two-tier pendulum. There is also a two-tier of tuning between the two pendulums and the structure. This intriguing point requires more attention to receive the most control benefit.

By increasing the number of particles, or volume fraction of fill, it is possible to significantly increase the capacity to increase the rate of energy dissipation. The best case in [Figure 3\(d\)](#) corresponds to a small fraction of this full capacity of dissipation. A typical case is shown in [Figure 3\(e\)](#) where the amount of lentil is doubled to a 280-count. The increased rate of dissipation is clearly detrimental to the control action. As the container starts to roll from its rest position, the rate of dissipation is so fast that it can only climb a fraction of the full height on its track, before it rolls back to the rest position to stay. Hence, the container simply rests on the track, unable to receive the harmful energy from the structure. This case is quite similar to any overly damped tuned absorber where the

absorber is simply an added mass to the structure to be controlled. In [Figure 4\(e\)](#), the spectral distribution of the displacement confirms this assertion, with a comparably large spectral peak to the uncontrolled case, at a lower frequency.

Amplitude distribution of the four cases is given in [Figure 5](#), in same order as in [Figures 3 and 4](#). The uncontrolled case, [Figure 5\(a\)](#), and the over-damped case, [5\(e\)](#), have very similar broad distributions. The empty cylinder case in [Figure 5 \(b\)](#) is somewhat distorted, due to its strong beat. The most effectively controlled case of 140-count lentils, has approximately three times larger frequency count at the rest position, with significantly narrower spread than those of the other three cases.

4. CONCLUSIONS

Simple experiments are described in this paper to explore the potential of granular flow as an energy sink for structural control applications. A tuned absorber, in the form of a cylindrical rolling container, is first designed. Then, the granular flow is introduced in the container to provide the required energy dissipation. With an approximately 3.5% addition to the mass of the structure, it is possible to increase the structural damping by an 8-fold. Hence, these preliminary experiments are encouraging and certainly warrant continued investigation.

Although not presented, experiments also involved using a (2 orders of magnitude) larger structure than the one presented here, with similar control effect. The objective was to scale and to predict performance for practical implementation. Scaling is one of the current design challenges.

REFERENCES

1. DenHartog, J. P., *Mechanical Vibrations*, 2nd. ed., McGraw-Hill, New York, 1940.
2. Hunt, J. B., *Dynamic Vibration Absorbers*, Mechanical Engineering Publications Ltd., London, 1979.
3. Snowdon, J.C., *Vibration and Shock in Damped Mechanical Systems*, John Wiley and Sons Inc., New York, 1968.
4. Liu, K. and Liu, J., The damped dynamic vibration absorbers: revisited and new result, *Journal of Sound and Vibration*, 284, 1181-89, 2005.
5. Pirner, M., Actual Behavior of a Ball Vibration Absorber, *Journal of Wind Engineering and Industrial Aerodynamics*, 90, 987–1005, 2002.
6. Legeza, V. P., Dynamics of Vibroprotective Systems with Roller Dampers of Low-Frequency Vibrations, *Strength of Materials*, 36(2), 185-194, 2004.

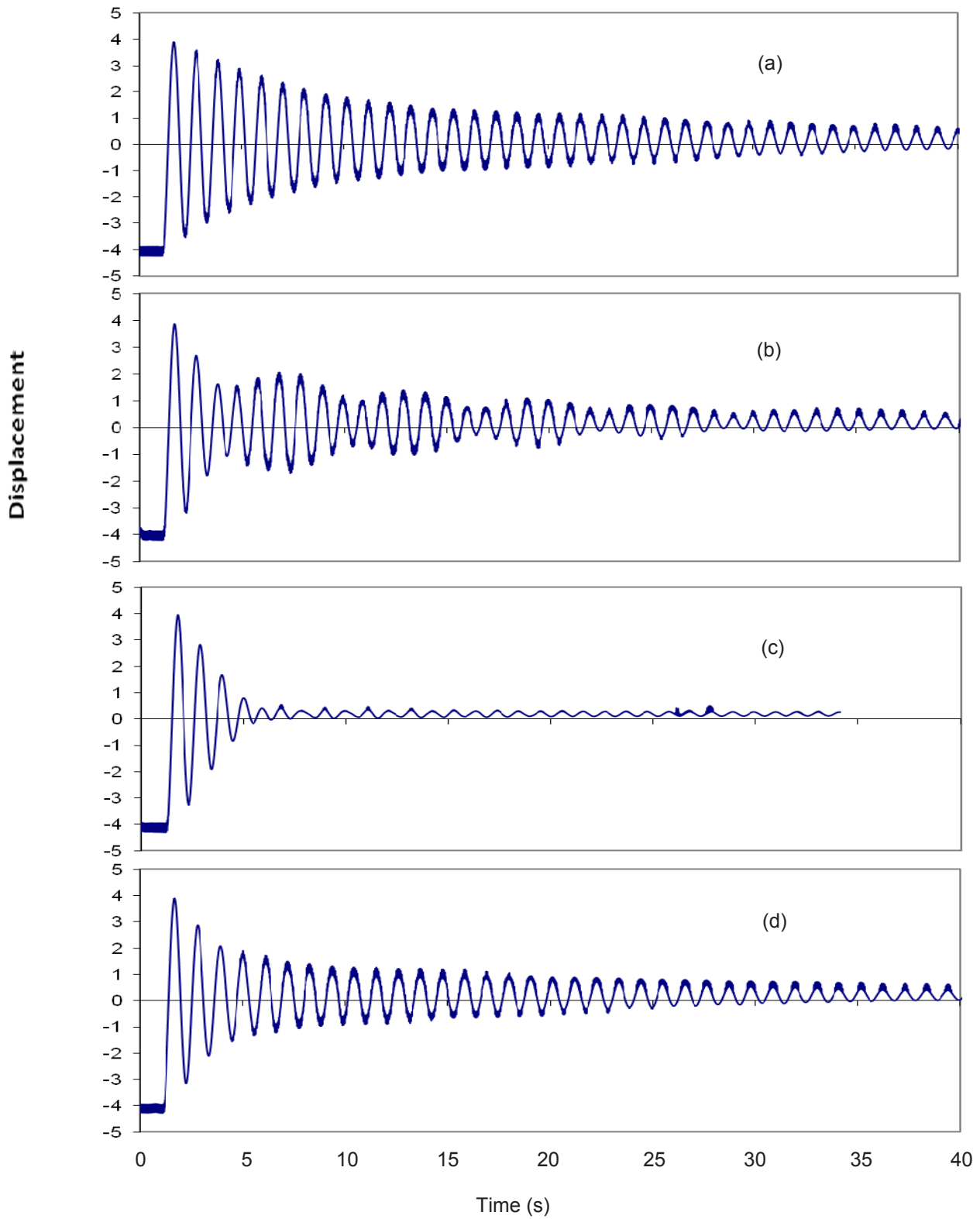


Figure 3. Displacement histories of the structure (a) uncontrolled, (b) with the empty container, (c) with 140-count lentils and (d) 280-count lentils. Vertical axis units are arbitrary, but all correspond to a 56 mm initial displacement.

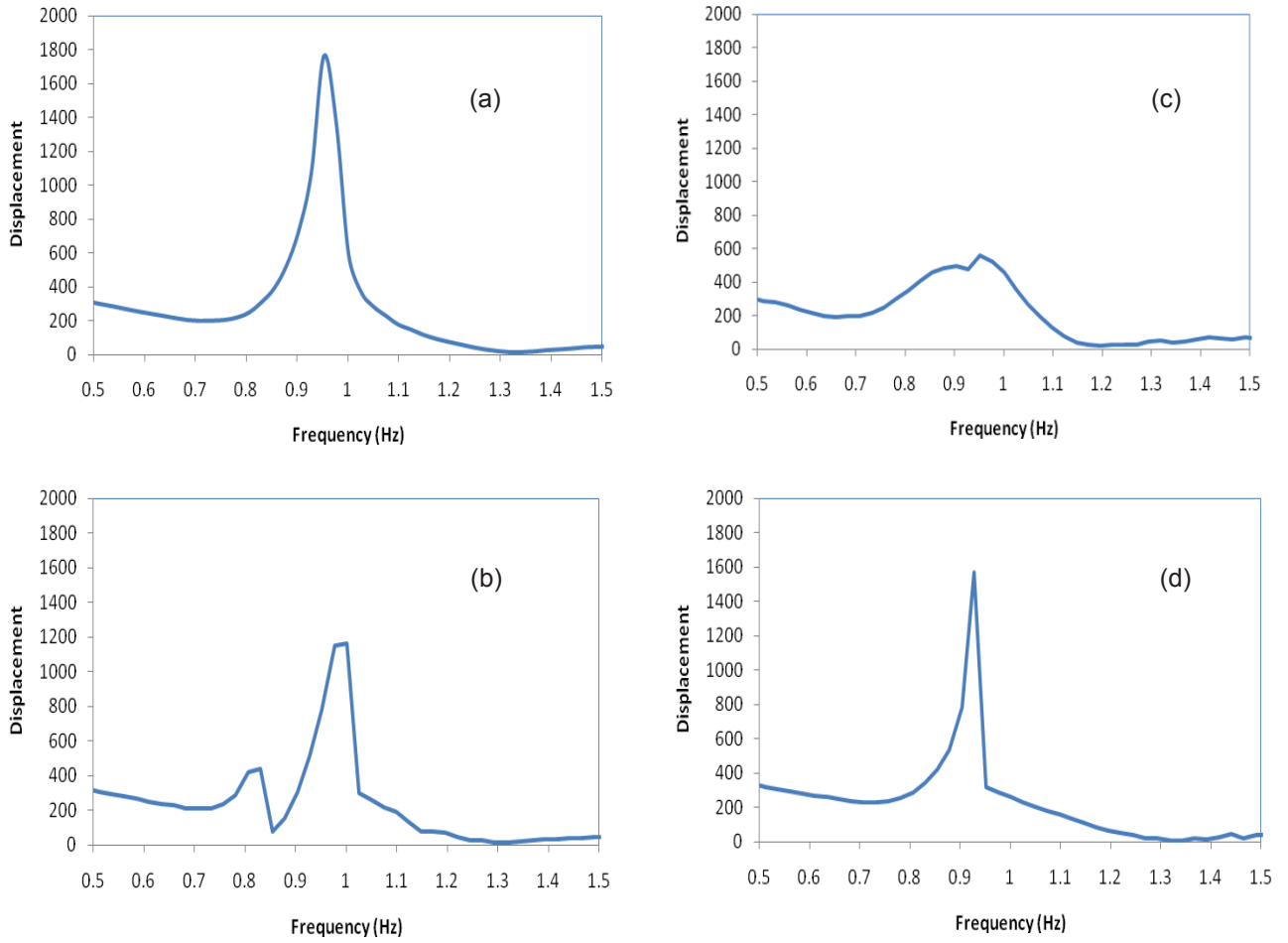


Figure 4. Same as in [Figure 3](#), but for the frequency spectra.

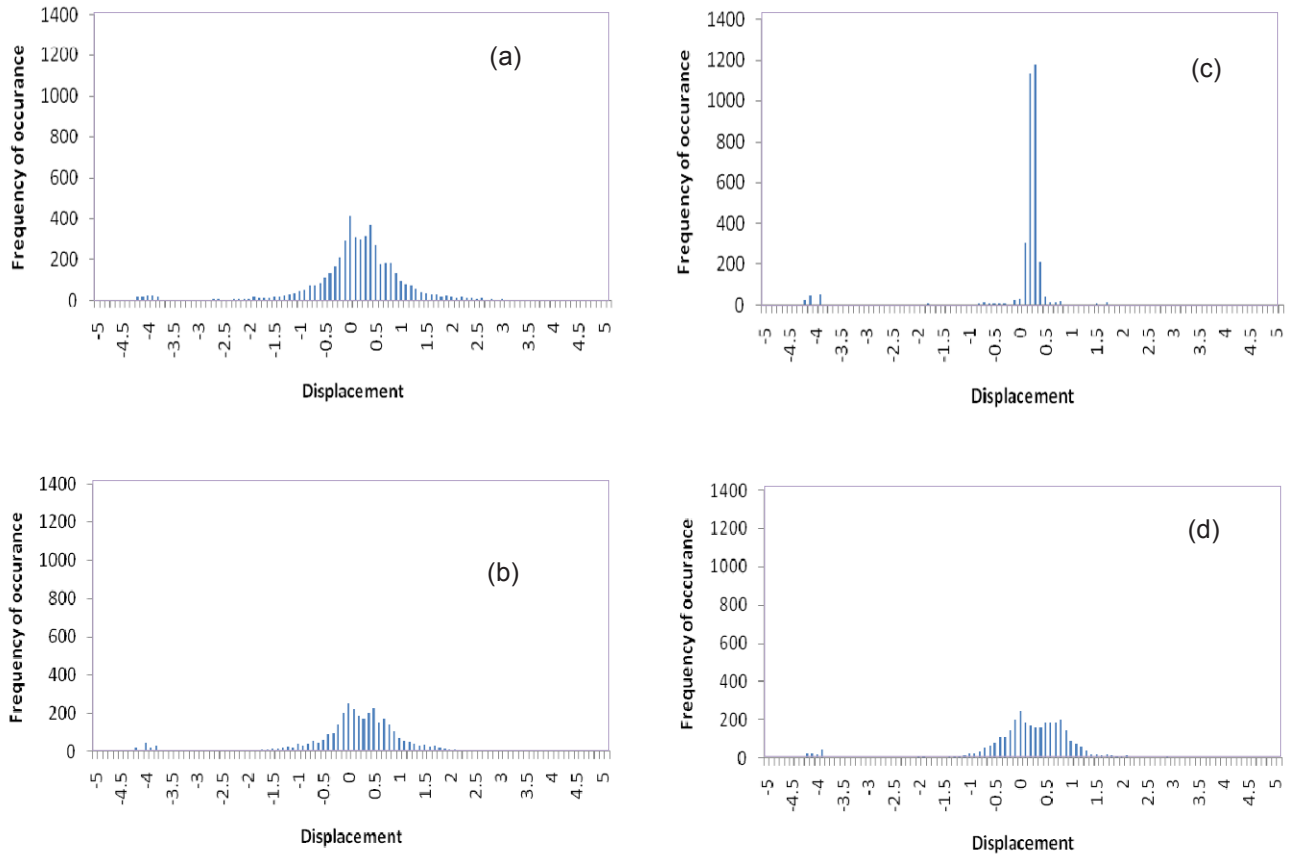


Figure 5. Same as in [Figure 3](#), but for the frequency of occurrence. Displacement units are the same as those in [Figure 3](#).

Tool Chatter in Turning with a Two-Link Robotic Arm

Abdullah Özer^{1,2} and S. Eren Semercigil²

¹Gyeongsang National University, School of Mechanical and Aerospace Engineering,
Jinju, Gyeongnam 660-701, KOREA

²Victoria University, School of Engineering and Science
Footscray Park Campus, PO Box 14428 MC Melbourne, Victoria 8001 AUSTRALIA

ABSTRACT

Robotic operations have undeniable advantages of speed and precision in machining. However, such operations are generally limited by the self-excited tool chatter problem. When uncontrolled, chatter leaves a rough machined surface, accelerates wear of the cutter and creates unacceptably loud noise levels. A conventional approach to suppress chatter is to slow the waste removal rate. Such an action is usually successful to avoid chatter, but causes increased production time and cost. Therefore, it is desirable to maintain a reasonably fast rate of production and employ a chatter control measure. A simple semi-active parameter control technique is investigated numerically in this study. The proposed method is effective and requires no additional hardware to implement at the actuated joints such as those in robotic structures.

1. INTRODUCTION

Currently, manufacturing robots are generally used for simple, repetitive tasks of low added value, which substitute for unskilled operations. There is growing interest in robotic applications in machining. On the other hand, in such tasks, robotic structures may have to endure excessive oscillations in the form of machine-tool chatter. Motivation for the present work is to provide stimulus to effectively deal with the problem of chatter in such structures.

Tool chatter is an undesirable dynamic instability. It is usually the result of aggressive machining conditions where rapidly removed waste material leads to excessive vibrations of the tool relative to the workpiece. Tool chatter causes accelerated wear of the cutting tool, irritating noise levels and leaves a rough surface which requires additional machining to provide the dimensional accuracy and acceptable surface finish.

A common solution to the tool chatter problem is to lower the cutting speed, to take advantage of the enhanced frictional interaction between the workpiece and the cutter. However, low speeds decrease production rate, and consequently, increase production costs. Selection of cutting conditions with respect to surface finish, tool life and rate of production, is a compromise at best. Therefore, effective control to delay the onset of chatter still represents a well-justified contribution to applied science.

The analysis, prediction and control aspects of the chatter phenomenon have received considerable attention in the literature, and only a brief summary will be given here for completeness. One approach for chatter control is to monitor the cutting process on-line, and to change cutting parameters upon detection of chatter. Improvements are reported when the detection parameters are "tuned empirically" to the particular cutting parameters [1]. An effective control can be achieved by varying the parameters of the otherwise passive system, rather than imposing control with force actuators. Therefore, control effort can be quite minimal and the problem of instability can be avoided. In a recent research, Cardi et al. report experiments to investigate the mechanism responsible for the transition between a stable cut to unstable chatter [2]. By experimentally measuring the variation in chip thickness history, they demonstrate that the phase difference (between the workpiece velocity and the variation in uncut chip thickness) is a reliable indicator of the presence of chatter. They also observe that it is possible to implement control within the first revolution of the workpiece. Mei [3] has analytically studied active regenerative chatter phenomenon and its suppression in boring. Through simulations, a wave controller is designed to cause discontinuity of reflected vibration waves, and control robustness is demonstrated for broad spectrum of conditions.

Although very limited, several studies have considered robotic machining processes. Fields et al. [4] have presented the design of a flexible robotic drilling system for aircraft sheet metal parts. Requiring active end point recalibration, the system has been shown to be very flexible, allowing drilling in three dimensions while maintaining good positioning accuracy and repeatability. Pan et al. [5] have investigated chatter in robotic machining processes both analytically experimentally, giving guidelines to avoid “mode coupling” as the dominant source of vibrations. Olgac and Sipahi [6] have recently studied variable-pitch cutters in milling process and provided guidelines to combine tool design features (pitch angle) and operational selections (the spindle speed and the axial depth of cut) to optimize productivity without sacrificing machining quality. Anderson et al. [7] have proposed a new design procedure to enhance the chatter stability of an end mill cutter. In this research, the principle objective is to incorporate an adaptor to enhance chatter stability of a cantilevered cutter. Altintas and Weck [8] provide a comprehensive review of chatter vibrations in cutting and grinding processes and its control in industry.

Simple semi-active control technique is reported in this paper to delay the onset of chatter when turning with a two-link robotic arm. For control, it is proposed to manipulate the joint stiffness of a two-link robotic arm using a simple on-off type strategy. The control is implemented at pre-determined instances. The two primary advantages of the proposed control are robustness and requiring no additional hardware (by applying the control by using already existing joint actuators). In the following, the modeling and control methods are discussed briefly. Then representative numerical predictions are discussed to demonstrate the level of suppression.

2. A SIMPLIFIED NONLINEAR FEEDBACK CUTTING MODEL

The cutting forces in turning a rigid disk are illustrated in Figure 1. Waste is removed, while the workpiece rotates in the counter-clockwise direction. The resulting cutting force F makes an angle β from the Y direction which is normal to the cut surface. Although this angle is expected to be (a rather weak) function of the cutting tool geometry, it is assumed to be constant. Here, the useful component of the force, to shear the chip from the workpiece, is the tangential component in X direction.

After each pass, the tool feeds in the radial direction by h_{av} , and leaves behind an undulated surface due to the oscillations of the structure holding the tool. Hence, h_{av} is the intended constant chip thickness, and Y_n and Y_{n-1} represent the surface left behind the cutter as a result of the current pass ‘n’, and the preceding pass ‘n-1’, respectively. The magnitude of the resulting cutting force $F(t)$ is proportional to the instantaneous chip thickness $h(t)$

$$F = C \cdot b \cdot h(t) \quad (1)$$

where C is specific resistance of the workpiece [18]. C is a function of the tool geometry and the material of the workpiece. It is normally provided empirically and has a unit of force per unit cross sectional area of the chip. Cross sectional area, $b \cdot h(t)$, is a time variant where b is the width of cut in a normal direction to the view shown in Figure 1.

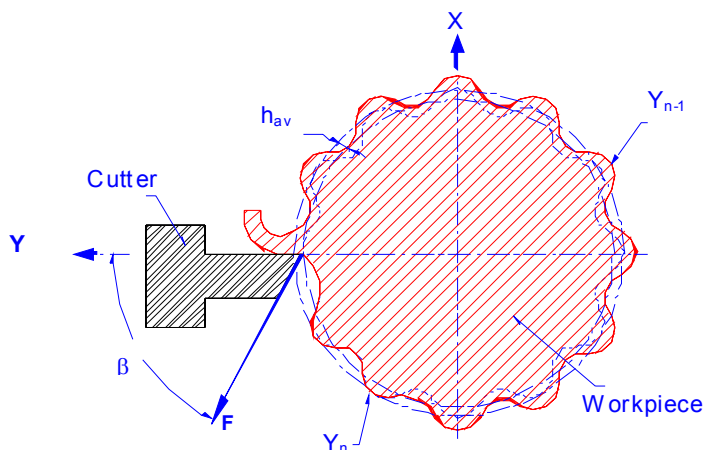


Figure 1. Cutting model used in the simulations.

Equation 1 represents the primary feedback between the cutting force and the oscillations of the cutting tip relative to the cut surface. As the cut progresses in the radial direction, a secondary feedback mechanism emerges through the most critical parameter, the instantaneous chip thickness $h(t)$. This chip thickness is a function of h_{av} and the surface undulations

$$h(t) = h_{av} - Y_n + Y_{n-1} \quad (2)$$

where Y_{n-1} and Y_n represent the topography of the cut surface at the same angular position in the last two passes. However, as the cut progresses, more than one preceding cut may be involved to determine $h(t)$. Thus, equation (2) is modified for such cases as

$$h(t) = Y_{\min} - Y_n \quad (3)$$

where Y_{\min} is the smallest of $(h_{av} + Y_{n-1})$, during the second pass; $(2h_{av} + Y_{n-2})$, during the third pass; $(3h_{av} + Y_{n-3})$, during the fourth pass; etc.

In Equation (3), there is a possibility that Y_{\min} is smaller than Y_n , and consequently $(Y_{\min} - Y_n)$ is negative. This condition indicates that the cutter runs out of material, as it oscillates in the direction away from the workpiece. A negative $(Y_{\min} - Y_n)$ requires that the cutting force be set to zero, to represent free vibrations, until contact is reestablished. This intermittency is the primary non-linearity included in the cutting model.

The undulations of the wavy cut surface contain the natural frequency of the structure, as they are generated during the transients. It may be worthwhile to remember that the frequency of the undulations is 'read' by the cutting force during the next pass of the cutter. Hence, the frequency content of the surface undulations plays a critical role in the secondary feedback, to lead to the occurrence of chatter. This particular aspect of the secondary feedback forms the rationale of the proposed control described in Section 4.

3 NUMERICAL MODEL

Robots are powered by electric motors in series with harmonic drives, couplings and belt drives. Inherent flexibility in these components can produce undesired oscillations, even when the linkages are designed to be rigid. Control of these undesired oscillations can be challenging in the presence of changing structural dynamics, measurement inaccuracies and complex modeling requirements.

The model of the arm investigated in this paper is shown in [Figure 2](#). It consists of two rigid beams, connected by revolute joints at the elbow and at the base. Torsional springs at elbow, K_{elbow} , and at base, K_{base} , represent the joint resilience of the arm. Torsional viscous dampers are also included to model frictional dissipation at the joints (not shown for clarity). In addition, a 0.5% critical viscous damping for the first two modes is incorporated in the structural model to represent the inherent dissipation [19]. The arm is assumed to move in the horizontal plane to avoid the effect of gravity. Lumped masses M_{tip} and M_{motor} model the cutter mass and elbow motor mass, respectively. Driver components at the base joint are assumed to be a part of a rigid base, and are not modeled. Relevant parameters are summarized in [Table 1](#).

A structural model has been developed using standard finite-element method as [20]

$$[M]\{\ddot{U}\} + [C]\{\dot{U}\} + [K]\{U\} = \{P(t)\} \quad (4)$$

where $[M]$, $[C]$ and $[K]$ are the global mass, damping and stiffness matrices; $\{U\}$ represents the generalized coordinate vector; and $\{P(t)\}$ represents the generalized force vector. Overdot indicates time derivative.

Matrix equations of motion are numerically integrated by using the Newmark- β scheme [22], in MATLAB [21] environment with a custom-coded program. Feedback of the cutting process is implemented according to Equations 1 to 3. Starting with zero initial conditions, a perfectly smooth surface is assumed during the first pass. An unstable state of cut is identified when the envelope of cutter oscillations is divergent. Chatter stability is determined over a period of 8 full passes (turns) of the workpiece which has been observed to be sufficient to indicate stability.

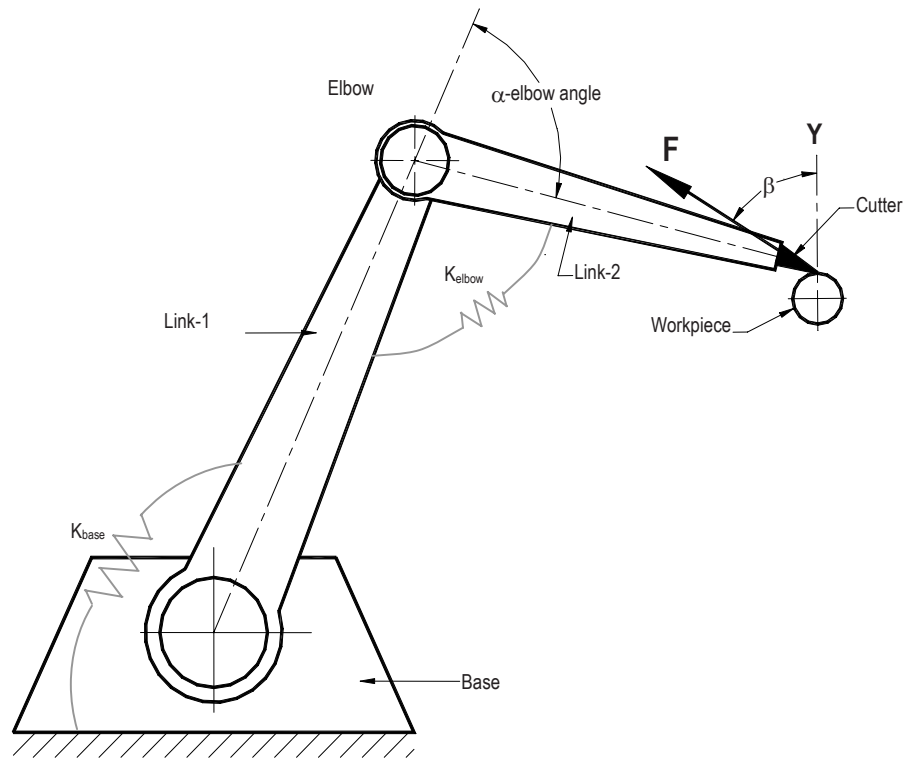


Figure 2. Two-link arm model.

Table 1. Structural and cutting parameters.

| | |
|--|---------------------------------|
| Length of each arm, L | 0.25 m |
| Width of each arm, b | 0.05 m |
| Mass/length, m | 0.85 kg/m |
| Number of finite elements for each arm | 10 |
| Cutter Mass, M_{tip} | 0.5 kg |
| Actuator mass, M_{motor} | 0.5 kg |
| Elbow stiffness, K_{elbow} | $400 \cdot 10^3$ Nm/rad |
| Base stiffness, K_{base} | $200 \cdot 10^9$ Nm/rad (rigid) |
| Equiv. viscous damping ratio- structural | 0.005 |
| Elbow viscous damping | 1 Nm/rad/s |
| Chip thickness, h_{av} | 0.015 mm |
| Cutting stiffness, C | 2000 N/mm ² [18] |
| Cutting angle, β | 70° [18] |
| Workpiece speed, n | 600 rpm (0.1 s/pass) |

One of the features of a two-link manipulator arm is its varying elbow angle. With the elbow angle, the orientation of the resultant cutting force changes, affecting the relative magnitudes of the transverse and axial components. Numerical trials have indicated that the elbow angle of 15° is significantly more stable than the open arm case (which was initially employed as a comparison base). Hence, all predictions are reported for the 15° elbow angle.

4. A SIMPLE ON-OFF CONTROL

Tool chatter is a self-excited vibration problem where the excitation is the cutting force which is necessary to perform the turning operation. The magnitude of the cutting force is a function of the instantaneous thickness of the chip to be removed from the workpiece. In turn, the thickness of the chip is determined by the relative oscillations between the cutter and the workpiece, caused by the cutting force. This circular reference, termed the primary feedback, is clearly significant.

As discussed in relation to [Figure 1](#), the undulations left behind from previous passes, also play an important role as a secondary feedback, to impose an additional variation of the instantaneous chip thickness. These undulations invariably correspond to the natural frequency of the structure, as they are initiated by the transient response of the structure.

If the cutting parameters are light, the transient oscillations of the cutter would decay due to the presence of damping of the system. The result is a stable cut. When the cutting parameters are severe, however, the transient response of the structure is large, and the inherent damping is insufficient to dissipate it quickly enough. As a result, cutting force eagerly acquires the natural frequency of the structure from the surface undulations of the previous passes, and excites the structure with growing magnitudes at its resonance. The result is an unstable cut.

If the dominant structural natural frequencies are varied in time, it may be possible to avoid the secondary feedback, before the cutting force is able to acquire the (now varying) natural frequency of the structure. A semi-active vibration controller to modulate the structural natural frequencies, is used in this paper to delay chatter. This modulation is accomplished by varying the elbow stiffness at each pass in a step-wise fashion. The objective of the control technique is to avoid the secondary feedback.

The proposed concept is similar to that of varying the speed of the workpiece. Variable speed cutting has been reported to increase the stability of cutting process by changing the wavelength of the surface undulations [18]. The drawback of this technique is the need for excessive reserve power to impose large enough fluctuations of the cutting speed to be effective. On the other hand, changing the stiffness properties of the structure can be a much simpler proposition to implement, with no additional hardware for a robotic arm. Since source of structural flexibility is the elbow joint, and since the effective stiffness of the elbow joint can be manipulated with the torque resistance of the actuator, the stiffness variation can simply be programmed to the joint actuator. In addition, no sensing is required to decide on the instant of actuation, as the stiffness change is required at known intervals, for each pass of the tool.

5. NUMERICAL PREDICTIONS

Numerical predictions are presented in [Figure 3](#) for the uncontrolled case. The relevant structural and cutting parameters are given in [Table 1](#). The elbow stiffness is kept constant at its highest value in [Table 1](#), to be $400 \cdot 10^3$ Nm/rad. Chip width, b , is varied from 0.5 mm to 0.75 mm in [Figures 3\(a\)](#) and [3\(b\)](#) to search for the limit of stability.

In [Figure 3\(a\)](#), with chip width of 0.5 mm, the envelope of oscillations gradually decay, representing a stable cut. The divergence is well established for the chip width of 0.75 mm, in [Figure 3\(b\)](#). Transition from a stable to an unstable cut is quite abrupt. Simulations performed with 0.05 mm increments determined the uncontrolled limit of stability to be 0.70 mm. It may be of interest to remember that the simulations presented in [Figure 3](#) correspond to the 15° elbow angle of the arm. The limit of stability is around 0.1 mm for the open arm configuration (0° elbow angle).

The next series of investigations refer to the controlled cases where the elbow stiffness is modulated between its uncontrolled $400 \cdot 10^3$ Nm/rad and lower values. As mentioned earlier, the semi-active control strategy is based on modulating the structural stiffness in a stepwise fashion for each pass of the cutter. The rationale of such modulation is to avoid the structural resonance through the undulations left on the cut surface due to transient response of the cutter's structure. It should be emphasized that practical implementation of such a stiffness change, is simply a result of modulating the torque resistance of the elbow joint from its controller. Hence, implementation of the control should only be a software issue rather than requiring additional hardware.

The uncontrolled and controlled displacement histories of the cutter are shown in [Figure 4](#) for $b = 1.75$ mm, the largest stable controlled width of cut. This width of cut is clearly into the unstable region for the uncontrolled arm in [Figure 4\(a\)](#), with a severely divergent envelope. The cutter starts jumping off the surface of the workpiece during the third pass. Then the cutter starts spending increasingly longer portion of its time off-contact with the workpiece. When the cutter is off contact, there is opportunity to dissipate energy through inherent damping which eventually leads to some decay of the oscillation envelope after the 5th pass.

In [Figure 4\(b\)](#), the displacement history of the cutter is presented for the controlled case in which the elbow stiffness is reduced from its largest $400 \cdot 10^3$ Nm/rad to $250 \cdot 10^3$ Nm/rad at 0.1 s, and then back to $400 \cdot 10^3$ Nm/rad at 0.2 s, and continued changing between these two stiffnesses periodically at the end of each pass. As a result, the tip displacements of the controlled case has a convergent envelope with significantly smaller magnitudes than those of [Figure 4\(a\)](#). The 1.75 mm chip width represents an improvement of approximately 2.5 times, over the uncontrolled limit of 0.7 mm.

Considering that the changing stiffness is simply accomplished by programming appropriate torque resistance of the elbow actuator, there is no reason why the control should be limited to only two stiffnesses. In fact, any number of stiffness changes should be just as practical to implement as two. Numerical experiments with three stiffnesses, has not yet shown much enhancement of the 1.75 mm, the limiting width of cut with the dual control. However, significant other advantages could be observed as demonstrated in [Fig. 4\(c\)](#).

In [Figure 4\(c\)](#), the variation described for [Figure 4\(b\)](#), is supplemented with a third value of $200 \cdot 10^3$ Nm/rad, following the first two passes of $400 \cdot 10^3$ Nm/rad and $250 \cdot 10^3$ Nm/rad. Hence, the elbow stiffness is now varied in periodic blocks of three. This new sequence of stiffness changes, brings a beat whenever two close stiffness values follow each other (every third pass when $250 \cdot 10^3$ Nm/rad is followed by $200 \cdot 10^3$ Nm/rad). The response with triple stiffness, is suppressed more effectively than that of the dual stiffness leading to a smoother surface.

The cutting force has a critical role on the dynamics of cutting process. Tip force histories of [Figure 4](#) are plotted in [Figure 5](#) for completeness. The mean force and its standard deviation of the uncontrolled and two controlled cases are 55.9 N and 62.5 N, 52 N and 3.1 N (dual stiffness), and 51.9 N and 2.4 N (triple stiffness), respectively. It is worth noting that the standard deviation of the uncontrolled case in [Figure 5\(a\)](#) is larger than its mean, very frequently fluctuating down to zero magnitude, indicating jumping off contact, starting from the third pass. In contrast, both controlled cases suppress the force fluctuations very effectively, with the triple stiffness doing a better job than that of the dual stiffness. (It is further worth noting that the cutting force for a perfectly rigid structure would be 52.5 N.)

6. CONCLUSIONS

A novel semi-active controller is presented to delay chatter oscillations to improve the cutting performance and the tool life when turning with a two-link robotic arm. The results show that considerable improvements are possible. The proposed method may facilitate the use of robots in machining industry more extensively.

Current predictions in this paper suggest a performance improvement of about 2.5 times over an uncontrolled case. In addition, the implementation of the suggested control is an ideal add-on item, requiring no additional hardware when programmable joint actuators are already available. Control actuation requires no detection effort. It is implemented at pre-determined regular intervals, synchronised with the speed of the workpiece. These findings are encouraging and certainly warrant continued investigation and experimental verification.

REFERENCES

1. Lin, S.C. and Hu, M.R., Low vibration control system in turning, *International Journal of Machine Tools and Manufacture*, 32(5), 629-640, 1992.
2. Cardi, A.A., Firpi, H.A., Bement, M.T. and Liang, S.Y., Workpiece dynamic analysis and prediction during chatter of turning process, *Mechanical Systems and Signal Processing* 22, 1481–1494, 2008.
3. Mei, C., Active regenerative chatter suppression during boring manufacturing process, *Robotics & Computer-Integrated Manufacturing*, 21, 153–158, 2005.

4. Fields, A., Toumi, K.Y. and Asada, H., Flexible fixturing and automatic drilling of sheet metal parts using a robot manipulator, *Robotics & Computer-Integrated Manufacturing*, 5(4), 371-380, 1989.
5. Pan, Z., Zhang, H., Zhu Z. and Wang, J., Chatter analysis of robotic machining process, *Journal of Materials Processing Technology*, 173, 301-309, 2006.
6. Olgac, N. and Sipahi, R., Dynamics and stability of variable-pitch milling, *Journal of Vibration and Control*, 13-7, 1031-1043, 2007.
7. Anderson, C.S., Semercigil, S.E. and Turan, Ö.F., A passive adaptor to enhance chatter stability for end mills, *International Journal of Machine Tools & Manufacture* 47, 1777–1785, 2007.

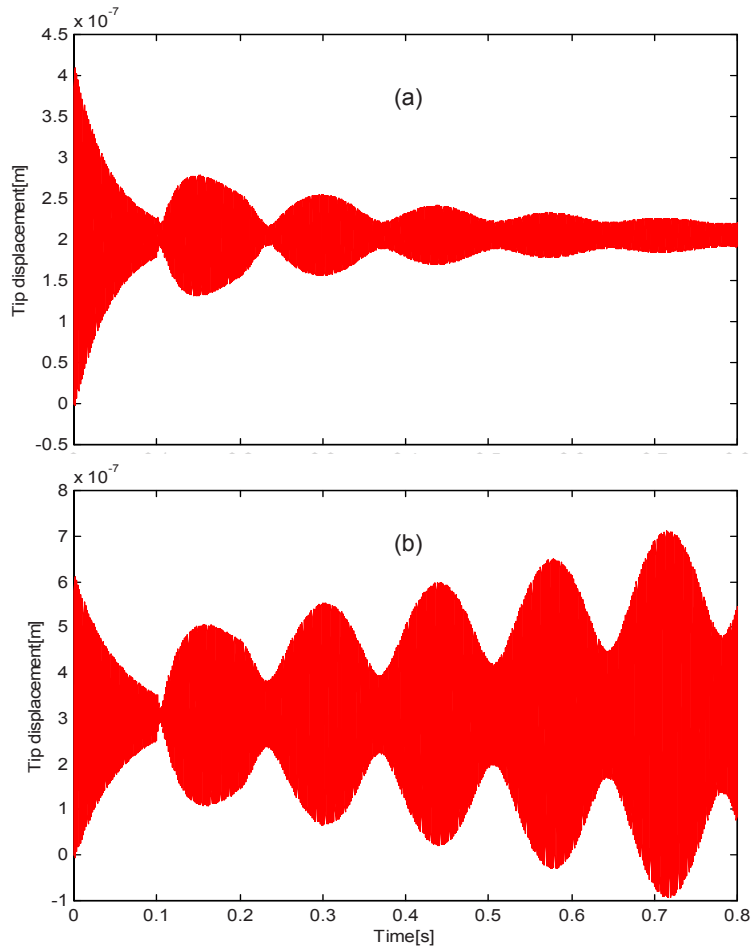


Figure 3. History of tip displacement for (a) 0.5 mm and (b) 0.75 mm chip width.

8. Altintas, Y. and Weck, M., Chatter stability of metal cutting and grinding, *CIRP Annals - Manufacturing Technology Volume 53-2*, 619-642 2004.
9. Yang, F., Zhang, B. And Yu, J., Chatter suppression via an oscillating cutter, *Journal of Manufacturing Science and Engineering*, 55-60, 1999.
10. Soliman, E. and Ziaei, R., Chatter suppression in five-axis machining of flexible parts, *International Journal of Machine Tools and Manufacture*, 42, 115-122, 2002.
11. Tarn, Y.S., Kao, J.Y. and Lee, E.C., Chatter suppression in turning operations with a tuned vibration absorber, *Journal of Materials Processing Technology*, 105, 55–60, 2000.
12. Book, W.J., Controlled motion in an elastic world, *ASME Journal of Dynamic Systems, Measurement and Control* 113, 252–261, 1993.
13. Andeen, G.B., editor in chief, *Robot design handbook*, McGraw-Hill Book Company, New York, 1988.
14. Wang, D. and Vidyasagar, M., Passive control of a stiff flexible link, *The International Journal of Robotics Research* 11 (12), 572–578, 1992.
15. Hong, S. and Park, Y., Vibration reduction for flexible manipulators using torque wheel mechanism, *Proceedings of the Third International Conference on Motion and Vibration Control*, Chiba, Japan, 364–369, 1996.
16. Matsuoka, S., Shimizu, K., Yamazaki, N. and Oki, Y., High-speed end milling of an articulated robot and its characteristics, *Journal of Materials Processing Technology*. 95. 83-89. 1999.

16. Tobias, S.A., *Machine-Tool Vibration*, Blackie & Son Ltd, Glasgow, 1965.
17. Tlustý, J., *Handbook of High-Speed Machining Technology*, R. I. King, Chapman & Hall Ltd, New York, 1985.
18. Bathe, K.J., *Finite Element Procedures in Engineering Analysis*, Prentice-Hall, Englewood Cliffs, NJ, 1982.
19. Thomson, W.T., *Theory of Vibrations with Applications*, fourth ed, Prentice-Hall, Englewood Cliffs, NJ, 1993.
20. Matlab, MATLAB, *The Language of Technical Computing, Using MATLAB Version 5*, The MathWorks, Inc, MA, 1997.
21. Craig, R.R., *Structural Dynamics, An Introduction to Computer Methods*, Wiley, USA, 1981.

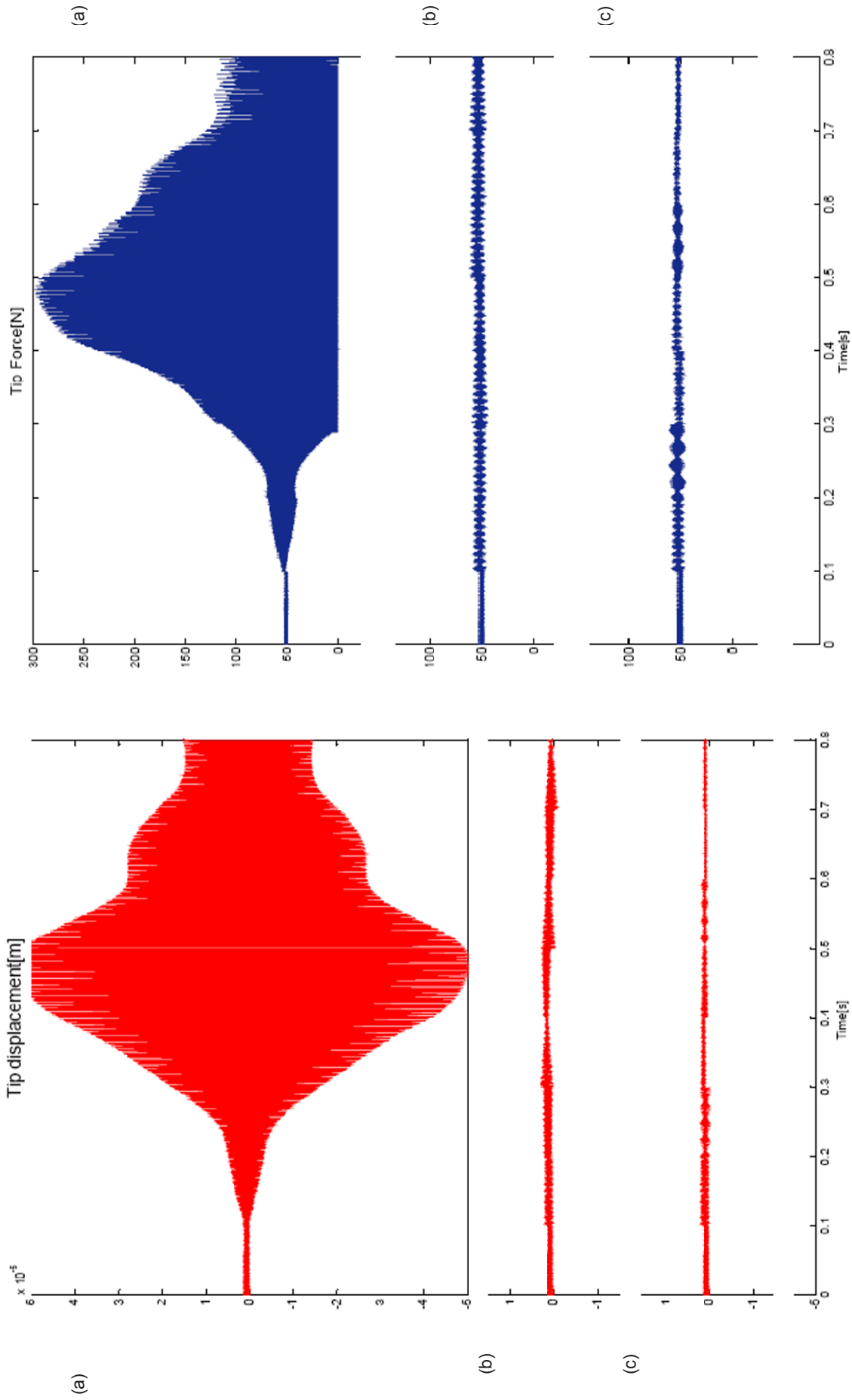


Figure 5. Same as in Figure 4 but the cutting force.

Figure 4. Histories of tip displacement with $b= 1.75$ mm for (a) the uncontrolled case, and controlled cases (b) with dual stiffness of $400/250 \times 10^3$ Nm/rad and (c) with triple stiffness of $400/250/200 \times 10^3$ Nm/rad.

An Identification Method for the Elastic Characterization of Materials

David Yang
Research Associate
Day Software Systems, Inc.
209 Shelter Rock Rd
Stamford, CT 06903

ABSTRACT

A driving point dynamic load non destructive test can be used to determine a structure's first modal stiffness and indirectly the material's coefficient of elasticity. Such a dynamic test will be shown to be theoretically equivalent to a static load destructive test that directly determines the coefficient of elasticity. Assuming linear, elastic dynamic analysis is appropriate then knowing the first modal stiffness from experimental modal data and a numerical model of the structure with known geometric dimensions, an exact solution for the coefficient of elasticity can be determined when the frequency equations are available and depends on one elastic constant. The solutions for the coefficient of elasticity for uniform beams in axial deformation, torsion and bending as a function of the first modal stiffness will be given.

INTRODUCTION

There are several methods to determine the coefficient of elasticity of a pavement's sub grade soil from dynamic load non destructive tests. The frequency sweep method [8] uses the driving point frequency response to correlate to the static response of a pavement from a plate load test. The frequency sweep method uses a weighted average of the driving point frequency response to determine the equivalent static response. This paper uses the concept of correlating the response from a dynamic test to the static response from a conventional test but uses the zero frequency response of the dynamic test to compare to the static response of a conventional test. Results are shown for uniform beams but in the future will be extended to composite materials and in particular multiple elastic layered pavement systems.

DYNAMIC MODAL MODEL

The response of a multiple degree of freedom system under forced harmonic vibration ([1],[2],[6]), given by the general dynamic modal model is

$$x_s(t) = \sum_{n=1}^N \frac{\phi_{sn} \sum_{d=1}^N \phi_{dn} F_d}{K_n - \omega^2 M_n + i\omega C_n} e^{i\omega t} \quad (1)$$

For the special case when there is only one harmonic load at the s^{th} degree of freedom and the mode shapes are normalized with respect to that location of the load, then $\phi_{sn} = 1$ for $n = 1, 2, \dots, N$ and $F_d = 0$ for all $d \neq s$ and $F_d = F$ when $d=s$. The driving point response is

$$x(t) = H(i\omega) F e^{i\omega t} \quad (2)$$

$$H(i\omega) = \sum_{n=1}^N H_n(i\omega) \quad (3)$$

$$H_n(i\omega) = \frac{1}{K_n - \omega^2 M_n + i\omega C_n} \quad (4)$$

The driving point response can be written as the sum of the magnitudes and phases of the individual modes

$$x(t) = \sum_{n=1}^N |H_n(i\omega)| e^{i(\omega t + \theta_n)} \quad (5)$$

$$|H_n(i\omega)|^2 = \frac{1}{(K_n - \omega^2 M_n)^2 + (\omega C_n)^2} \quad (6)$$

$$\theta_n = -\tan^{-1} \left(\frac{\omega C_n}{K_n - \omega^2 M_n} \right) \quad (7)$$

The driving point response can also be written directly as the total system magnitude and phase

$$x(t) = |H(i\omega)| F e^{i(\omega t + \theta)} \quad (8)$$

$$|H(i\omega)|^2 = \text{real}(H(i\omega))^2 + \text{imaginary}(H(i\omega))^2 \quad (9)$$

$$\theta = \tan^{-1} \left(\frac{\text{imaginary}(H(i\omega))}{\text{real}(H(i\omega))} \right) \quad (10)$$

$$\text{real}(H(i\omega)) = \sum_{n=1}^N \frac{K_n - \omega^2 M_n}{(K_n - \omega^2 M_n)^2 + (\omega C_n)^2} \quad (11)$$

$$\text{imaginary}(H(i\omega)) = -\sum_{n=1}^N \frac{\omega C_n}{(K_n - \omega^2 M_n)^2 + (\omega C_n)^2} \quad (12)$$

When the load is harmonic, the response is harmonic and the magnitude and phase of the response has contributions from the individual modes. In theory, the magnitude of the frequency response at a frequency of zero corresponds to the static deflection due to a unit force. The zero frequency response [7] is defined as

$$H(0) = |H(0)| = \sum_{n=1}^N \frac{1}{K_n} \quad (13)$$

The zero frequency response is equivalent to the static deflection (flexibility) under a unit load of N springs in series where the spring constants, K_n , $n = 1, 2, \dots, N$, are the modal spring constants. The system stiffness is simply the inverse of the zero frequency response.

STATIC RESPONSE OF UNIFORM BEAM

The basic mechanical tension, compression, torsion and bending tests of uniform beams to determine the coefficient of elasticity are based on the following equations of static equilibrium [4].

Axial Tension/Compression

$$w = \frac{FL}{EA} \quad (14)$$

Torsion

$$\vartheta = \frac{TL}{GJ} \quad (15)$$

3 Point Bending at mid span

$$w = \frac{FL^3}{48EI} \quad (16)$$

Poisson's Ratio can be determined by the relation

$$\nu = \frac{E}{2G} - 1 \quad (17)$$

DYNAMIC RESPONSE OF UNIFORM BEAM IN BENDING

From the available frequency equation of a simply supported uniform beam bending at mid span ([1],[2],[6])

$$\omega_n^2 = \frac{K_n}{M_n} = \frac{n^4 \pi^4 EI}{L^4 m} \quad (18)$$

$$M_n = \frac{mL}{2} \quad (19)$$

$$K_n = \frac{n^4 \pi^4 EI}{2L^3} \quad (20)$$

$$\phi_n = \sin\left(\frac{n\pi x}{L}\right) \quad (21)$$

$$H(0) = \sum_{n=1}^{\infty} \frac{\phi_n^2}{K_n} \quad (22)$$

If the static response for a simply supported uniform beam bending under a static force at mid span is equal to the zero frequency response for a simply supported uniform beam bending under a dynamic force at mid span then

$$\frac{L^3}{48EI} = \sum_{n=1}^{\infty} \frac{\sin\left(\frac{n\pi}{2}\right)^2}{\frac{n^4 \pi^4 EI}{2L^3}} \quad (23)$$

If the above equation is to be valid then must show that

$$\frac{\pi^4}{96} = \sum_{n=1}^{\infty} \frac{1}{n^4} \quad n \text{ is odd since } \sin\left(\frac{n\pi}{2}\right)^2 \text{ is 0 when } n \text{ is even and 1 when } n \text{ is odd.}$$

With the aid of Fourier series, it can be shown that the above is true.

Let $f(x) = x^4$ and expressed as an infinite series of the form

$$f(x) = \frac{a_0}{2} + \sum_{n=1}^{\infty} a_n \cos(nx) + b_n \sin(nx) \quad (24)$$

$$\pi a_n = \int_{-\pi}^{\pi} f(x) \cos(nx) dx \quad (25)$$

$$\pi b_n = \int_{-\pi}^{\pi} f(x) \sin(nx) dx \quad (26)$$

$$\pi a_0 = \int_{-\pi}^{\pi} f(x) dx \quad (27)$$

$$a_0 = \frac{2\pi^4}{5} \quad (28)$$

Since x^4 is an even function then none of the sine terms can be present and after integrating (25) by parts

$$a_n = \frac{48(-1)^n}{n^4} \quad (29)$$

Substituting $x = 0$ and $x = \pi$ into $f(x)$ gives two equations

$$0 = \frac{\pi^4}{5} + \sum_{n=1}^{\infty} \frac{48(-1)^n}{n^4} \quad (30)$$

$$\pi^4 = \frac{\pi^4}{5} + \sum_{n=1}^{\infty} \frac{48(-1)^n (-1)^n}{n^4} \quad (31)$$

Subtracting the (30) from the (31) has only values when n is odd

$$\pi^4 = 2 \sum_{n=1}^{\infty} \frac{48}{n^4} \quad (32)$$

The static response is equal to the zero frequency response of the simply supported uniform beam in bending at mid span and can be expressed as a function of the first modal stiffness

$$\frac{L^3}{48EI} = \frac{\pi^4}{96K_1} \quad (33)$$

And finally the coefficient of elasticity as a function of the first modal stiffness is

$$E = \frac{2L^3 K_1}{\pi^4 I} \quad (34)$$

DYNAMIC RESPONSE OF UNIFORM BEAM IN AXIAL DEFORMATION

For axial deformation the available frequency equation ([1],[2],[6]) for a beam fixed at $x=0$ and free at $x=L$ is

$$\omega_n^2 = \frac{K_n}{M_n} = \frac{\pi^2 (2n-1)^2 EA}{4mL^2} \quad (35)$$

$$M_n = \frac{mL}{2} \quad (36)$$

$$K_n = \frac{\pi^2 (2n-1)^2 EA}{8L} \quad (37)$$

$$\phi_n = \sin\left((2n-1)\frac{\pi x}{2L}\right) \quad (38)$$

Setting the static response equal to the zero frequency response at $x=L$

$$\frac{L}{EA} = \frac{8L}{\pi^2 EA} \sum_{n=1}^{\infty} \frac{\sin\left((2n-1)\frac{\pi}{2}\right)^2}{(2n-1)^2} \quad (39)$$

The following can also be shown to be true by using Fourier series.

$$\frac{\pi^2}{8} = \sum_{n=1}^{\infty} \frac{1}{(2n-1)^2} \quad (40)$$

The static response is equal to the zero frequency response of the beam and can be expressed as a function of the first modal stiffness

$$\frac{L}{EA} = \frac{\pi^2}{8K_1} \quad (41)$$

And finally the coefficient of elasticity as a function of the first modal stiffness is

$$E = \frac{8LK_1}{\pi^2 A} \quad (42)$$

DYNAMIC RESPONSE OF UNIFORM BEAM IN TORSION

For torsion the frequency equation ([1],[2],[6]) for a cylindrical beam fixed at $x=0$ and free at $x=L$ is similar to the axial frequency equation

$$\omega_n^2 = \frac{K_n}{M_n} = \frac{\pi^2 (2n-1)^2 GJ}{4mL^2} \quad (43)$$

$$G = \frac{8LK_1}{\pi^2 J} \quad (44)$$

Knowing E and G , Poisson's ratio can be determined as

$$\nu = \frac{JK_{\text{axial}}}{2AK_{\text{torsion}}} - 1 \quad (45)$$

DAMPING

After introducing viscous damping into the axial equations of motion [6], the coefficient of elasticity is independent of the rate of loading as determined by the dynamic test. The damping coefficient determines the response due to the rate of loading.

$$\sigma_x = E \left(\epsilon_x + a_1 \frac{\partial \epsilon_x}{\partial t} \right) \quad \text{where } \epsilon_x = \frac{\partial u}{\partial x} \quad (46)$$

$$F = EA \left(\frac{\partial u}{\partial x} + a_1 \frac{\partial^2 u}{\partial x \partial t} \right) \text{ stiffness proportional damping} \quad (47)$$

$$\frac{\partial F}{\partial x} = m \left(\frac{\partial^2 u}{\partial t^2} - a_0 \frac{\partial u}{\partial t} \right) + q(x,t) \text{ mass proportional damping} \quad (48)$$

$$EA \frac{\partial^2 u}{\partial x^2} + EA a_1 \frac{\partial^3 u}{\partial x^2 \partial t} - m \frac{\partial^2 u}{\partial t^2} + m a_0 \frac{\partial u}{\partial t} = q(x,t) \quad (49)$$

$$\text{Let } u(x,t) = \sum_{n=1}^{\infty} \phi_n(x) U_n(t) \quad (50)$$

$$M_n \frac{d^2 U_n}{dt^2} + (a_0 M_n + a_1 K_n) \frac{dU_n}{dt} + K_n U_n = \int_0^L \phi_n(x) q(x,t) dx \quad (51)$$

So the modal damping coefficient is

$$C_n = a_0 M_n + a_1 K_n \quad (52)$$

a_0 and a_1 should be constant for all modes if the above model is valid. a_1 is a property of the material and a_0 is a property of the system.

For hysteretic damping, the coefficient of elasticity is also independent of the rate of loading. Once again the damping coefficient determines the response due to the rate of loading.

$$\sigma_x = E \left(\varepsilon_x + \frac{a_3}{\omega} \frac{\partial \varepsilon_x}{\partial t} \right) \text{ where } \omega \text{ is the excitation frequency} \quad (53)$$

SQUARE PLATE IN BENDING

A simply supported uniform plate bending due to a center load [5]

$$K_{ij} = \frac{D\pi^4}{4L^2} (i^2 + j^2)^2 \quad (54)$$

$$M_{ij} = \frac{\rho HL^2}{4} \quad (55)$$

At the center of the plate

$$D = \frac{EH^3}{12(1-\nu^2)} = \frac{4L^2 K_{11}}{\pi^4} \quad (56)$$

UNIFORM BEAM IN BENDING QUARTER SPAN

Previously the zero frequency response was not determined by the mode shapes being normalized with respect to the load point. For the uniform beam when the mode shapes are normalized with respect to the load point the following are the expected measured K_n for the experimental modal data for mid span and quarter span.

The general mode shape is

$$\phi_{sn} = \sin\left(\frac{n\pi x_s}{L}\right) \quad (57)$$

Normalized when the load is at $x_d = \frac{L}{2}$

$$\text{Normalized } \phi_{sn} = \frac{\sin\left(\frac{n\pi x_s}{L}\right)}{\sin\left(\frac{n\pi}{2}\right)} \text{ which is 1 when } x_s = \frac{L}{2} \quad (58)$$

The zero frequency response when $x_d = x_s = \frac{L}{2}$

$$\sum_{n=1}^{\infty} \left(\frac{1}{\frac{K_n}{\sin\left(\frac{n\pi}{2}\right)^2}} \right) \quad (59)$$

$$\text{So measured } K_n = \frac{K_n}{\sin\left(\frac{n\pi}{2}\right)^2} \quad (60)$$

When $x_d = \frac{L}{2}$ and $x_s = \frac{L}{4}$ then the zero frequency response is

$$\sum_{n=1}^{\infty} \left(\frac{\frac{\sin\left(\frac{n\pi}{4}\right)}{\sin\left(\frac{n\pi}{2}\right)}}{\frac{K_n}{\sin\left(\frac{n\pi}{2}\right)^2}} \right) \quad (61)$$

and includes modes where $\sin\left(\frac{n\pi}{4}\right) \neq 0$

When $x_d = x_s = \frac{L}{4}$ then the zero frequency response is

$$\sum_{n=1}^{\infty} \left(\frac{1}{\frac{K_n}{\sin\left(\frac{n\pi}{4}\right)^2}} \right) \quad (62)$$

$$\text{So measured } K_n = \frac{K_n}{\sin\left(\frac{n\pi}{4}\right)^2} \quad (63)$$

$$K_n \left(x_d = x_s = \frac{L}{4} \right) = \frac{K_n \left(x_d = x_s = \frac{L}{2} \right)}{\sin \left(\frac{n\pi}{4} \right)^2} \quad (64)$$

From statics [4], the quarter span elastic deformation is related to the mid span elastic deformation

$$w \left(x_d = x_s = \frac{L}{4} \right) = \frac{9}{16} w \left(x_d = x_s = \frac{L}{2} \right) \quad (65)$$

So

$$\sum_{n=1}^{\infty} \frac{\sin \left(\frac{n\pi}{4} \right)^2}{n^4} = \frac{\pi^4}{96} \frac{9}{16} \quad (66)$$

Reciprocity is valid because the zero frequency response when $x_d = \frac{L}{4}$ and $x_s = \frac{L}{2}$ is equal to the zero frequency response

when $x_d = \frac{L}{2}$ and $x_s = \frac{L}{4}$

The zero frequency response is

$$\sum_{n=1}^{\infty} \left(\frac{\sin \left(\frac{n\pi}{2} \right)}{\sin \left(\frac{n\pi}{4} \right)} \right) \left(\frac{K_n}{\sin \left(\frac{n\pi}{4} \right)^2} \right) = \sum_{n=1}^{\infty} \left(\frac{\sin \left(\frac{n\pi}{4} \right)}{\sin \left(\frac{n\pi}{2} \right)} \right) \left(\frac{K_n}{\sin \left(\frac{n\pi}{2} \right)^2} \right) \quad (67)$$

From statics [4], the quarter span deformation due to the load at the mid span is related to the mid span elastic deformation.

$$w \left(x_d = \frac{L}{2}, x_s = \frac{L}{4} \right) = \frac{11}{16} w \left(x_d = x_s = \frac{L}{2} \right) \quad (68)$$

So

$$\sum_{n=1}^{\infty} \frac{\sin \left(\frac{n\pi}{2} \right) \sin \left(\frac{n\pi}{4} \right)}{n^4} = \frac{\pi^4}{96} \frac{11}{16} \quad (69)$$

SUMMARY

The solutions for the coefficient of elasticity for uniform beams in axial deformation, torsion and bending as a function of the first modal stiffness were presented. This enables the determination of the elastic properties of uniform beams from knowledge of the first modal stiffness. The first modal stiffness is assumed to be derived from parameter estimation using experimental modal data [3]. The experimental modal data can be from any dynamic test using a time domain or frequency domain parameter estimation technique. After introducing viscous damping into the equations of motion, the coefficient of elasticity remains constant but the dynamic response is dependent on two additional constants, a stiffness proportional constant and a mass proportional constant. The stiffness proportional constant is dependent on the material and the mass proportional constant is dependent on the system.

REFERENCES

- [1] Biggs, J. M., Introduction to Structural Dynamics, McGraw-Hill, Inc., 1964
- [2] Clough, R. W., Penzien J., Dynamics of Structures, McGraw-Hill, Inc., 1993
- [3] Richardson, M. H., Formenti, D. L., "Parameter Estimation from Frequency Response Measurements using Rational Fraction Polynomials", Proceedings of the 1st International Modal Analysis Conference, Orlando, FL, November 8-10, 1982.
- [4] Roark, R. J., Formulas for Stress and Strain, McGraw-Hill, Inc., 1954
- [5] Timoshenko, S., Woinowsky-Krieger, S., Theory of Plates and Shells, McGraw-Hill, Inc., 1959
- [6] Warburton, G. B., The Dynamical Behaviour of Structures, Pergamon Press, 1976
- [7] Yang, D., Response of Multi-Frequency Pavement Systems, Masters' Thesis, MIT, 1978
- [8] Yang, N. C., Design of Functional Pavements, McGraw-Hill, Inc., 1972

?

?

?

An Alternating Least Squares (ALS) based Blind Source Separation Algorithm for Operational Modal Analysis

J. Antoni+, S. Chauhan*

+Department of Mechanics, University of Technology of Compiègne,
Centre de Recherche de Royallieu, BP 20529 – 60205, Compiègne, France

*Brüel & Kjær Sound and Vibration Measurement A/S
Skodsborgvej 307, DK 2850, Naerum, Denmark

Email: jerome.antoni@utc.fr, schauhan@bksv.com

Nomenclature

| | |
|------------------------------|---|
| \mathbf{x} | State vector |
| \mathbf{A}_d | State matrix |
| \mathbf{y} | Measurement vector |
| \mathbf{f} | Unknown force vector |
| \mathbf{v} | Measurement noise vector |
| λ_i | i^{th} pole of the system |
| T_s | Sampling Period |
| Φ | Mode shapes of the system |
| \mathbf{R}_{yy} | Correlation matrix of the measurements |
| τ | Time lag |
| \mathbf{R}_{yy}^a | Augmented correlation matrix |
| $\mathbf{L}^a, \mathbf{R}^a$ | Left and Right factors of augmented correlation matrix, containing information about mode shape. |
| \mathbf{D} | Diagonal matrix such that $\mathbf{R}_{yy}^a = \mathbf{L}^a \mathbf{D}[\tau] \mathbf{R}^a$, contains information about system poles. |

ABSTRACT

In a former paper (“Second Order Blind Identification (SOBI) and its relation to Stochastic Subspace Identification (SSI) algorithm”, 28th IMAC, 2010), the authors established the link between the popular SSI algorithm used in output-only modal analysis and the Second Order Blind Identification (SOBI) algorithm developed for blind source separation in the field of signal processing. It was concluded that the two algorithms, although seemingly very different, are actually jointly diagonalizing the same covariance matrix over a range of time-lags. This is explicit in SOBI and implicit in SSI. One main difference, however, is that SOBI focuses on estimating the (real) modal matrix as a joint diagonalizer, but without taking advantage of the specific structure of the covariance matrix formed by the Markov coefficients and by incorrectly assuming no-damping or very low damping. On the other hand, SSI specifically exploits the covariance matrix structure so as to estimate complex modes, but puts less emphasis on the “joint diagonalizing” property of the modal matrix. The aim of this communication is to introduce a new algorithm based on Alternating Least Squares (ALS) approach that combines advantages of both SOBI and SSI in order to return improved estimates of modal parameters. It is shown in this work that this algorithm is capable of identifying complex modes, closely spaced modes and heavily damped and can also be expanded

to deal with the cases where there are less number of sensors available than the number modes to be estimated. The suggested approach therefore is a step towards expanding the applicability of BSS based approaches to Operational Modal Analysis applications.

1. Introduction

Several recent works have shown how second order blind source separation (SO-BSS) techniques, such as Second Order Blind Identification (SOBI) [1, 2], can be utilized for the purpose of output-only modal analysis [3-7]. However, in spite of encouraging results shown by these algorithms, applicability of BSS based algorithms for OMA purposes has been quite limited. This can be attributed to certain limitations associated with BSS based algorithms for OMA. Mathematical formulation of SO-BSS based OMA algorithms suggest that they are more suitable for lightly damped systems having real normal modal vectors. The fact that SO-BSS algorithms only estimate real modal vectors is a serious issue as this is seldom a case in real life. A methodology based on Hilbert transform is suggested in [8] to estimate complex mode shapes. However, the robustness of the method is yet to be ascertained. Yet another issue which restricts applicability of these algorithms is that they can only estimate as many modes as the number of output responses being measured.

Despite these limitations SO-BSS techniques present an interesting outlook with regards to operational modal analysis, as they differ from traditional OMA algorithms in terms of estimating the modal parameters of a system. In [9], the authors showed how SO-BSS algorithms, such as SOBI, are related to well known Stochastic Subspace Identification (SSI) algorithm [10, 11]. In this work it was shown that whereas SSI estimate the modes of a system by putting a constraint on the poles of the system, SO-BSS based algorithms use a joint diagonalization procedure to obtain the modal parameters by estimating orthogonal vectors that diagonalize the correlation matrices of observed responses. These orthogonal vectors are estimates of the modal vectors which are then used to obtain modal frequencies and damping by means of modal expansion theorem [12]. Since the two algorithms, SSI and SO-BSS, that share similar mathematical foundations, estimate modal parameters using different approaches, it is intriguing to pursue an algorithm that can combine the advantages of both the algorithms.

In this paper, an Alternative Least Squares (ALS) [13] based algorithm is proposed that combines the advantages of SO-BSS and SSI algorithms in order to overcome the limitations SO-BSS algorithms suffer from in terms of their application for OMA purposes. This algorithm can be explained within the framework of Parallel Factor (PARAFAC) theory [14]. Mathematical development of this algorithm is presented in the next section and preliminary results of this algorithm are shown in Section 3 by means of studies conducted on an analytical system. Finally, conclusions are made, in light of the results obtained and performance of the algorithm in general, with regards to its further development and suitability for OMA applications.

2. A PARAFAC based BSS Algorithm for OMA

2.1 General Background

This section recalls the main results and notations used in [8] as these results serve as the background and main motivation for the ALS based PARAFAC algorithm suggested in this paper.

Consider the following n degree of freedom (DOF) discrete-time state-space system,

$$\begin{cases} \mathbf{x}[k+1] = \mathbf{A}_d \mathbf{x}[k] + \mathbf{B}_d \mathbf{f}[k] \\ \mathbf{y}[k] = \mathbf{C}_d \mathbf{x}[k] + \mathbf{D}_d \mathbf{f}[k] + \mathbf{v}[k] \end{cases} \quad (1)$$

where $\mathbf{x}[k]$ is the $2n \times 1$ state vector, $\mathbf{y}[k]$ the $m \times 1$ measurement vector, $\mathbf{f}[k]$ the unknown force vector, $\mathbf{v}[k]$ the measurement noise vector, and \mathbf{A}_d the $2n \times 2n$ state matrix. Let

$$\mathbf{A}_d = \mathbf{\Psi} \mathbf{\Sigma}_d \mathbf{\Psi}^{-1} \quad (2)$$

be the eigenvalue decomposition of the state-matrix where the $2n \times 2n$ diagonal matrix, where

$$\mathbf{\Sigma}_d = \begin{bmatrix} \exp\{\mathbf{\Lambda} T_s\} & \mathbf{0}_{p \times n} \\ \mathbf{0}_{n \times n} & \exp\{\mathbf{\Lambda}^* T_s\} \end{bmatrix} \quad (3)$$

(T_s = sampling period and $*$ = conjugate operator) contains the modal parameters of interest, $\mathbf{\Lambda} = \text{diag}(\lambda_1, \dots, \lambda_n)$ with λ_i the i -th pole of the system, and

$$\Psi = \begin{bmatrix} \Phi \Lambda & \Phi^* \Lambda^* \\ \Phi & \Phi^* \end{bmatrix} \quad (4)$$

contains the mode shapes of the structure in the columns of Φ .

It has been shown in [8] that the correlation matrix of the measurements $\mathbf{y}[k]$ takes the following simple form under the assumption of white noise excitation.

$$\mathbf{R}_{yy}[\tau] = \mathbf{L} \Sigma_d^\tau \mathbf{R}, \quad \tau > 0 \quad (5)$$

where the left and right factors read

$$\mathbf{L} = \mathbf{C}_d \Psi \in C^{m \times 2n}, \quad \mathbf{R} = \mathbf{R}_{qq}[0] \mathbf{L}^t \in C^{2n \times m} \quad (6)$$

respectively, with $\mathbf{R}_{qq}[0]$ the (unknown) correlation matrix of the modal coordinate $\mathbf{q}[k] = \Psi^{-1} \mathbf{x}[k]$. Such factorization of the correlation matrix, if it can be performed, returns all information about global parameters (modal frequency and damping) in the diagonal entries of Σ_d^τ , and the information about (unscaled) mode shapes through the left factor \mathbf{L} .

Since only m modes are recoverable in theory, one obvious shortcoming of the above approach is in cases where the number of measurements is less than twice the number of dof's of the system, i.e. $m < 2n$. This can however be dealt by considering the augmented correlation matrix as shown below

$$\mathbf{R}_{yy}^a[\tau] = \begin{bmatrix} \mathbf{R}_{yy}[\tau] & \cdots & \mathbf{R}_{yy}[\tau + K_2] \\ \vdots & & \vdots \\ \mathbf{R}_{yy}[\tau + K_1] & \cdots & \mathbf{R}_{yy}[\tau + K_1 + K_2] \end{bmatrix} \in IR^{mK_1 \times mK_2} \quad (7)$$

This augmented correlation matrix can be factorized as

$$\mathbf{R}_{yy}^a[\tau] = \begin{bmatrix} \mathbf{L} \\ \mathbf{L} \Sigma_d \\ \vdots \\ \mathbf{L} \Sigma_d^{K_1} \end{bmatrix} \Sigma_d^\tau \begin{bmatrix} \mathbf{R} & \Sigma_d \mathbf{R} & \cdots & \Sigma_d^{K_2} \mathbf{R} \end{bmatrix} = \mathbf{L}^a \Sigma_d^\tau \mathbf{R}^a \quad (8)$$

where \mathbf{L}^a and \mathbf{R}^a are now $mK_1 \times 2n$ and $2n \times mK_2$ matrices which contain all information about the m modes of the system provided that $mK_1 \geq 2n$ and $mK_2 \geq 2n$, with K_1 and K_2 set arbitrarily large by the user.

The next subsection describes an Alternating Least Squares (ALS) based PARAFAC algorithm that can achieve the proposed factorization on the empirical correlation matrix (or the augmented correlation matrix (Eqn. 7)) estimated from the measured data.

2.2 PARAFAC factorization

Let $\hat{\mathbf{R}}_{yy}^a[\tau]$ be the empirical correlation matrix estimated from the (finite-length) measurement vector $\mathbf{y}[k]$. The objective is then to find three matrices \mathbf{L}^a , \mathbf{R}^a and $\mathbf{D}[\tau] = \Sigma_d^\tau$ such that the product $\mathbf{L}^a \mathbf{D}[\tau] \mathbf{R}^a$ is as close as possible to $\hat{\mathbf{R}}_{yy}^a[\tau]$ for a set of time-lags $\tau \in T = \{\tau_0, \dots, \tau_K\}$, $\tau_K > \dots > \tau_0 > 0$. Note that matrix $\mathbf{D}[\tau]$ is diagonal, but not semi-positive definite in general because its diagonal elements will contain an imaginary part as soon as damping is present in the system. For the same reason, the right factor \mathbf{R}^a is in general different from the transpose of the left factor \mathbf{L}^a and allowed to be complex-valued. This precludes the factorization to be solved by a joint diagonalization procedure, as done in SO-BSS and revisited in Ref. [9]. Clearly, this is a difficult non-linear problem, yet hopefully with a unique solution, provided that the set of considered time-lags T is large enough.

This type of problem has been studied in the statistical literature as parallel factor analysis or PARAFAC. In short, PARAFAC generalizes the eigenvalue decomposition of a matrix to a similar decomposition of a cube. The three dimensions of concern in operational modal analysis are the two spatial directions of the correlation matrix $\hat{\mathbf{R}}_{yy}^a[\tau]$ (column and row indices corresponding to sensor labels) and the time-lag direction.

The investigation of efficient algorithms to solve the PARAFAC problem is a current and active topic of research [15][16]. For the sake of simplicity, the simplest algorithm is described here, based on alternative least squares (ALS) [13]. ALS consists in iteratively estimating one of the three matrices entering in the factorization assuming that the other two are fixed. This way, the minimization problem turns out linear in the parameters and is easily solved by least-squares. The algorithm is described in a step-by-step manner as follows:

1) Step $I = 0$: initialize $\mathbf{L}_{(i)}^a$, $\mathbf{R}_{(i)}^a$ and $\mathbf{D}[\tau]_{(i)}$

2) Step $i+1$: update $\mathbf{L}_{(i)}^a$, $\mathbf{R}_{(i)}^a$ and $\mathbf{D}[\tau]_{(i)}$ as

$$\text{a) } \mathbf{L}_{(i+1)}^a = \arg \min_{\mathbf{L}^a} \sum_{\tau \in T} \left\| \hat{\mathbf{R}}_{yy}^a[\tau] - \mathbf{L}^a \mathbf{D}[\tau]_{(i)} \mathbf{R}_{(i)}^a \right\|^2 = \sum_{\tau \in T} \hat{\mathbf{R}}_{yy}^a[\tau] \mathbf{R}_{(i)}^{aH} \mathbf{D}[\tau]^H \left(\sum_{\tau \in T} \mathbf{D}[\tau] \mathbf{R}_{(i)}^a \mathbf{R}_{(i)}^{aH} \mathbf{D}[\tau]^H \right)^{-1} \quad (9)$$

$$\text{b) } \mathbf{R}_{(i+1)}^a = \arg \min_{\mathbf{R}^a} \sum_{\tau \in T} \left\| \hat{\mathbf{R}}_{yy}^a[\tau] - \mathbf{L}_{(i)}^a \mathbf{D}[\tau]_{(i)} \mathbf{R}^a \right\|^2 = \left(\sum_{\tau \in T} \mathbf{D}[\tau]^H \mathbf{L}_{(i)}^{aH} \mathbf{L}_{(i)}^a \mathbf{D}[\tau] \right)^{-1} \sum_{\tau \in T} \mathbf{D}[\tau]^H \mathbf{L}_{(i)}^{aH} \hat{\mathbf{R}}_{yy}^a[\tau] \quad (10)$$

$$\text{c) } \mathbf{D}_{(i+1)}^a = \arg \min_{\mathbf{D}^a} \sum_{j=1}^{mK_2} \left\| \tilde{\mathbf{R}}_{yy}^a[j] - \mathbf{D} \tilde{\mathbf{R}}[j] \mathbf{L}_{(i)}^a \right\|^2 = \sum_{j=1}^{mK_2} \tilde{\mathbf{R}}_{yy}^a[j] \mathbf{L}_{(i)}^{a*} \tilde{\mathbf{R}}[j]^H \left(\sum_{j=1}^{mK_2} \tilde{\mathbf{R}}[j] \mathbf{L}_{(i)}^a \mathbf{L}_{(i)}^{a*} \tilde{\mathbf{R}}[j]^H \right)^{-1} \quad (11)$$

where, in the last line,

$$\tilde{\mathbf{R}}_{yy}^a[j] = \begin{bmatrix} \mathbf{R}_{yy}^a[\tau_0]_{1,j} & \cdots & \mathbf{R}_{yy}^a[\tau_0]_{mK_1,j} \\ \vdots & & \vdots \\ \mathbf{R}_{yy}^a[\tau_K]_{1,j} & \cdots & \mathbf{R}_{yy}^a[\tau_K]_{mK_1,j} \end{bmatrix} \in \mathbb{R}^{K \times mK_1},$$

$$\tilde{\mathbf{R}}[j] = \begin{bmatrix} \mathbf{R}_{1,j} & & \mathbf{0} \\ & \ddots & \\ \mathbf{0} & & \mathbf{R}_{2n,j} \end{bmatrix} \in \mathbb{C}^{2n \times 2n}, \quad j = 1, \dots, mK_2, \quad \text{and} \quad \mathbf{D}^a = \begin{bmatrix} \Sigma_1^{\tau_0} & \cdots & \Sigma_{2n}^{\tau_0} \\ \vdots & & \vdots \\ \Sigma_1^{\tau_K} & \cdots & \Sigma_{2n}^{\tau_K} \end{bmatrix} \in \mathbb{C}^{K \times 2n_1}$$

3) Stop iterating if the relative errors $\left\| \mathbf{L}_{(i+1)}^a - \mathbf{L}_{(i)}^a \right\|$, $\left\| \mathbf{R}_{(i+1)}^a - \mathbf{R}_{(i)}^a \right\|$ and $\left\| \mathbf{D}_{(i+1)}^a - \mathbf{D}_{(i)}^a \right\|$ are all smaller than a predefined value.

At this point, it is important to mention a few remarks about the convergence of the ALS algorithm, which also happens to be one the limitations of the suggested approach.

- First it is clear that there is no guarantee of convergence to a global minimum. Hence, the final estimates will strongly depend on the quality of the starting values. It has been observed by the authors that reasonable estimates are returned after initializing matrix \mathbf{D} with the resonance frequencies obtained from a simple peak-picking method, with assumed zero damping ratios. Matrices \mathbf{L}^a and \mathbf{R}^a have been initialized randomly, although better strategies could perhaps be investigated such as using results from SO-BSS.

- Second, ALS is known to exhibit a low convergence speed, which is the price to pay for its simplicity. Accelerating strategies have recently been proposed in the literature, but this is outside the scope of this paper. Indeed, it is underlined that ALS is only one possible technique to solve the PARAFAC problem, and that more efficient algorithms are expected to come in the near future. Hence, this should not lower the interest of the proposed approach.

One apparent weakness of the proposed PARAFAC approach, however, is that it places no constraint on the estimated **D** matrix to be an actual correlation matrix, i.e. with elements in the form $\exp\{\lambda_i \tau T_s\}$ or conjugate of. But this is also where the limit lays between a fully BSS approach and an *ad hoc* approach such as SSI purposely designed for operational modal analysis. Based on this work, the authors are of the opinion that involving further efforts into forcing such a constraint would quickly drive the analysis into the realm of SSI algorithms, where the simplicity of BSS approaches would be lost.

3. Results and Discussions

A simple 3 degree of freedom (DOF) system with following [M], [C] and [K] matrices is used in this study. It should be noted that the damping matrix [C] is chosen randomly.

$$M = \begin{bmatrix} 1 & 0 & 0 \\ 0 & 1 & 0 \\ 0 & 0 & 1 \end{bmatrix} \quad K = \begin{bmatrix} 100 & -50 & 0 \\ -50 & 100 & -50 \\ 0 & -50 & 50 \end{bmatrix} \quad C = \begin{bmatrix} 1.1334 & 0.2764 & 0.1217 \\ 0.1846 & 1.2215 & 0.2806 \\ 0.2376 & 0.0529 & 1.2751 \end{bmatrix}$$

Table 1 shows the theoretical eigen frequencies and corresponding modal shapes of the system. Note that the mode shapes are normalized with respect to the first DOF.

Table 1: Theoretical System Parameters (Frequency, Damping and Mode Shapes)

| Eigen Freq | Freq (Hz) | Damping (%) | DOF 1 | DOF 2 | DOF 3 |
|--------------------------|-----------|-------------|--------|-------------------|------------------|
| -0.1244 + 0.4852i | 0.4852 | 24.83 | 1 + 0i | 1.7959 + 0.0205i | 2.2325 + 0.0488i |
| -0.0861 + 1.4005i | 1.4005 | 6.14 | 1 + 0i | 0.4438 + 0.0133i | -0.8033 + 0.0096 |
| -0.0784 + 2.0265i | 2.0265 | 3.86 | 1 + 0i | -1.2454 - 0.0327i | 0.5512 + 0.0521i |

The system is excited by means of a random uncorrelated set of input at all 3 degrees of freedom. The response time history and corresponding auto spectra is shown in Figure 1.

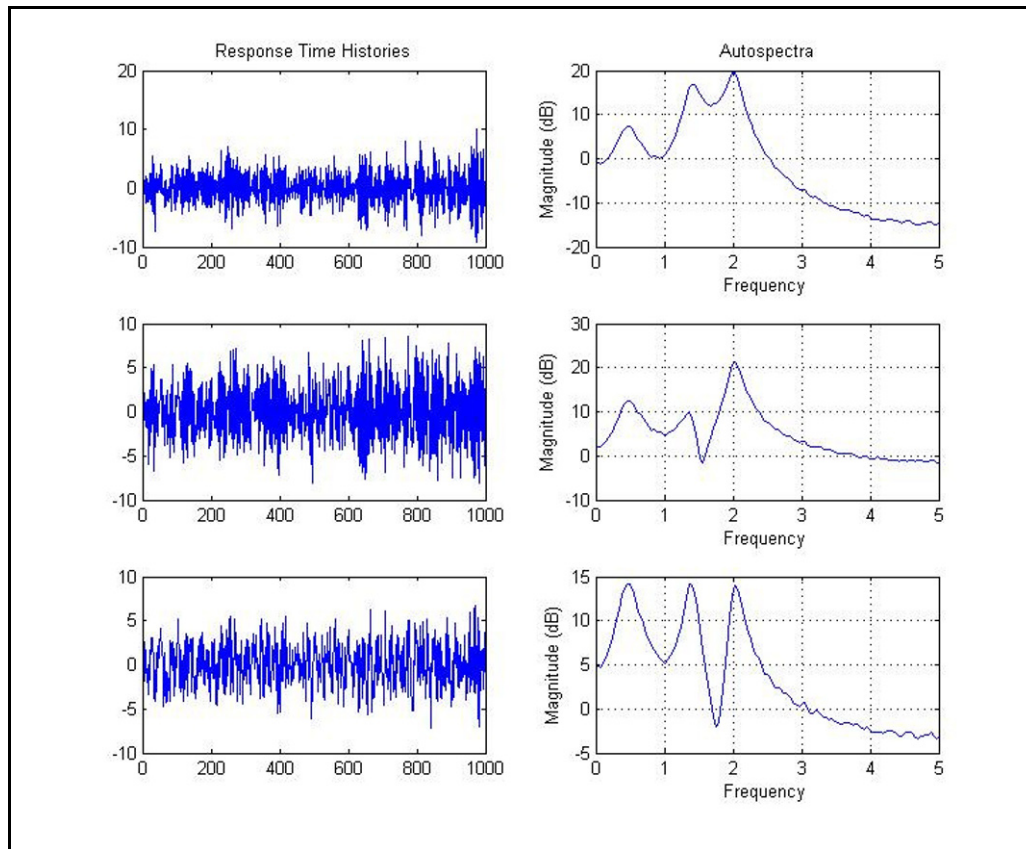


Figure 1: Response time histories and corresponding autospectra

As mentioned in Section 2.2, ALS based PARAFAC algorithm requires initial estimates of L , D and R matrices. For this study L and R are initialized by means of random complex matrices and D is initialized by means of peak picking the frequencies from the summation of the three autospectra. It should be noted that regular joint diagonalization as in SOBI can be used as a preprocessing step to get the initial estimates of D , however this step is not performed in present study.

Table 2 compares results obtained from ALS algorithm with theoretical values of modal parameters.

Table 2: Comparison of Estimated (A) and Theoretical (T) Modal Parameters (Frequency, Damping, Mode Shapes)

| Mode # | | Freq (Hz) | Damping (%) | DOF 1 | DOF 2 | DOF 3 |
|--------|---|-----------|-------------|--------|-------------------|-------------------|
| Mode 1 | T | 0.4852 | 24.83 | 1 + 0i | 1.7959 + 0.0205i | 2.2325 + 0.0488i |
| | A | 0.4883 | 25.50 | 1 + 0i | 1.7955 + 0.0226i | 2.2231 + 0.0499i |
| Mode 2 | T | 1.4005 | 6.14 | 1 + 0i | 0.4438 + 0.0133i | -0.8033 + 0.0096i |
| | A | 1.4060 | 6.28 | 1 + 0i | 0.4443 + 0.0257i | -0.8041 + 0.0192i |
| Mode 3 | T | 2.0265 | 3.86 | 1 + 0i | -1.2454 - 0.0327i | 0.5512 + 0.0521i |
| | A | 2.0310 | 4.01 | 1 + 0i | -1.2392 - 0.0312i | 0.5505 + 0.0414i |

Mode shape comparison is also shown by means of Figure 2, which shows very good agreement with theoretical mode shapes.

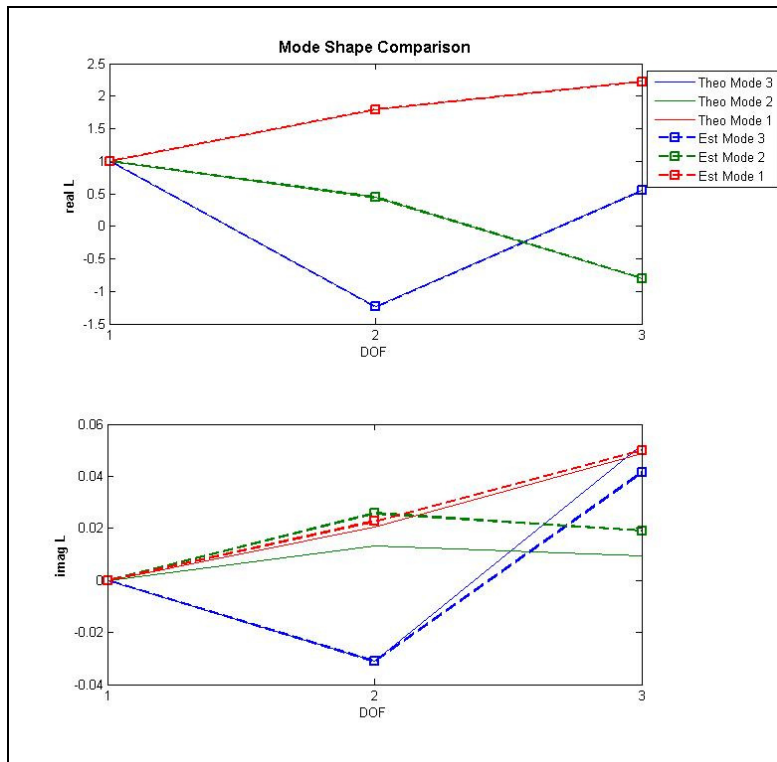


Figure 2: Mode Shape Comparison

The performance of ALS algorithm with regards to estimation of modal frequency and damping can also be evaluated by comparing the estimated D matrix with theoretical solution. This is shown in Figure 3.

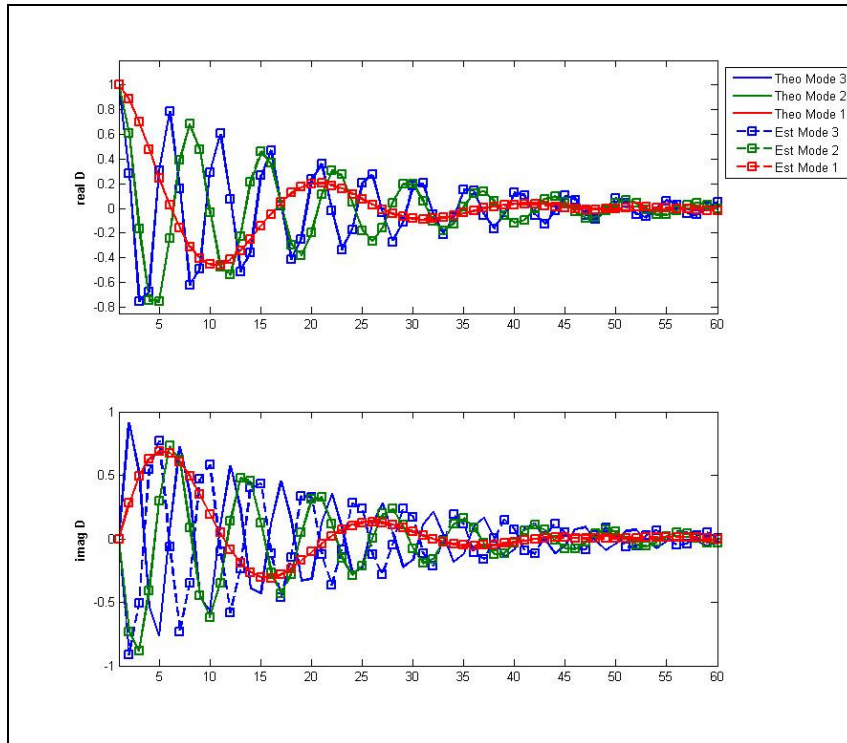


Figure 3: Comparison of D matrices

Modal parameters estimated using the proposed algorithm are in very good agreement with the theoretical modal parameters. These simulations show that the algorithm handles the heavily damped modes very well and is also able to estimate complex mode shapes. This is a definite improvement over SO-BSS algorithms such as SOBI whose performance is not satisfactory while dealing with cases of heavy damping or complex mode shapes. Based on these results it can be said that the performance of the suggested algorithm is very encouraging and augurs well for further development of the algorithm. Further development of this algorithm needs to address the limitations which this algorithm suffers in its current formulation. These limitations are on account of the simple ALS based approach used for factorizing the covariance matrices using PARAFAC framework. First major concern is convergence of this algorithm. The fact that since the ALS algorithm requires initial estimates of L , D and R , it is possible that if these initial estimates are not chosen carefully, the algorithm might not converge or converge to a local minimum. To avoid this scenario, it is suggested that SOBI can be performed as a pre-processing step and its results can be used as initial estimates of L , D and R . In the current simulation, even when only D is initialized with intelligent estimates based on peak-picking the frequencies (L and R are initialized randomly), the results are very satisfactory. However, it needs to be verified if this procedure can be generalized to work for all kind of systems and situations. The performance of the algorithm is also required to be evaluated in presence of noisy data and for some real world cases, to have a more definite word regarding its suitability for OMA. As mentioned before, ALS is a very simple algorithm for performing PARAFAC based factorization. A more robust algorithm with better convergence properties might be another step in this research.

4. Conclusions

This paper proposes a Parallel Factor based Alternating Least Squares Blind Source Separation algorithm for Operational Modal Analysis applications. Development of this algorithm follows from the previous work by the authors that establishes and explores the fundamental relationship between second order BSS algorithms and Stochastic Subspace Iteration algorithm. It is shown by means of a simulated system that this algorithm is capable of estimating heavily damped modes and complex mode shapes. These results are very encouraging and serve as great motivation to further improve and optimize the proposed algorithm and test it on more realistic scenarios in order to use it for OMA purposes.

REFERENCES

- [1] Cichocki, A., Amari, S., *Adaptive blind signal and image processing*, John Wiley and Sons, New York, 2002.
- [2] Belouchrani, A., Abed-Meraim, K.K., Cardoso, J.F., Moulines, E., *Second order blind separation of correlated sources*, Proceedings of International Conference on Digital Signal Processing, pp. 346-351, 1993.
- [3] *Special Issue: Blind source separation*, Mechanical Systems and Signal Processing, Vol. 19 (6), pp. 1163-1380, November, 2005.
- [4] Kerschen, G., Poncelet, F., Golinval, J.C., *Physical Interpretation of Independent Component Analysis in Structural Dynamics*, Mechanical Systems and Signal Processing (21), pp. 1561-1575, 2007.
- [5] Poncelet, F., Kerschen, G., Golinval, J.C., *Experimental Modal Analysis Using Blind Source Separation Techniques*, Proceedings of ISMA International Conference on Noise and Vibration Engineering, Katholieke Universiteit Leuven, Belgium, 2006.
- [6] Chauhan, S., Martell, R., Allemang, R. J. and Brown, D. L., *Application of Independent Component Analysis and Blind Source Separation Techniques to Operational Modal Analysis*, Proceedings of the 25th IMAC, Orlando (FL), USA, 2007.
- [7] McNiell, S.I., Zimmerman, D.C., *A Framework for Blind Modal Identification Using Joint Approximate Diagonalization*, Mechanical Systems and Signal Processing (22), pp. 1526-1548, 2008.
- [8] McNiell, S.I., Zimmerman, D.C., *Blind Modal Identification Applied to Output-only Building Vibration*, Proceedings of the 28th IMAC, Jacksonville (FL), USA, 2010.
- [9] Antoni, J., Chauhan, S., *Second Order Blind Source Separation Techniques (SO-BSS) and Their Relation to Stochastic Subspace Identification (SSI) Algorithm*, Proceedings of the 28th IMAC, Jacksonville (FL), USA, 2010.
- [10] Van Overschee, P., De Moor, B., *Subspace Identification for Linear Systems: Theory-Implementations-Applications*, Kluwer Academic Publishers, Dordrecht, Netherlands, 1996.

- [11] Brincker, R., Andersen, P., *Understanding Stochastic Subspace Identification*, Proceedings of the 24th IMAC, St. Louis, Missouri, 2006.
- [12] Allemang, R.J.; *Vibrations: Experimental modal analysis*, Structural Dynamics Research Laboratory, Department of Mechanical, Industrial and Nuclear Engineering, University of Cincinnati, 1999, http://www.sdr.luc.edu/sdr_l_jscript_homepage.html
- [13] Ten Berge, J.M.F, *Least Squares Optimization in Multivariate Analysis*, DSWO Press, Leiden, The Netherlands, 1993.
- [14] Tucker, L.R., *Some mathematical notes on three-mode factor analysis*, Psychometrika, 31, 279-311, 1966.
- [15] Vega-Montoto, L. & Wentzell, P.D., *Maximum likelihood parallel factor analysis (MLPARAFAC)*, Journal of Chemometrics, 17, 237-253, 2003.
- [16] Tomasi, G. & Bro, R., *A comparison of algorithms for fitting the Parafac model*, Computational Statistics & Data Analysis, 50, 1700-1734, 2006.

Automated interpretation of stabilization diagrams

E. Reynders, J. Houbrechts and G. De Roeck

K.U.Leuven, Dept. of Civil Engineering, Kasteelpark Arenberg 40, B-3001 Leuven, Belgium

Abstract Modal parameter estimation requires a lot of user interaction, especially when parametric system identification methods are used and the modes are selected in a stabilization diagram. In this paper, a fully automated, three-stage clustering approach is developed for interpreting such a diagram, that does not require any user-specified parameter or threshold value. The three stages correspond to the three stages in a manual analysis: setting stabilization thresholds for clearing out the diagram, detecting columns of stable modes, and selecting a representative mode from each column. A validation study, where nine real-life noisy operational modal bridge data sets are both automatically and manually analyzed, illustrates the accuracy and robustness of the proposed automatization strategy.

1 Introduction

The estimation of modal parameters from measured vibration data involves a substantial amount of user interaction. This prevents the further spread of modal testing to applications such as fault detection at mechanical production lines, or health monitoring of crucial infrastructure, where lots of data need to be processed in a short amount of time. Automating the modal parameter estimation process is therefore an important research objective, and it is the subject of this paper.

In most of the literature on automated modal testing, no clear distinction is made between *modal parameter estimation* (MPE), which is the estimation of modal parameters from (a single record of) measured data, and *modal tracking*, i.e., tracking the evolution of the modal parameters of a structure or a group of similar structures through repeated MPE. Automated modal tracking algorithms often need baseline modal parameters to start from, in which case they can not be used for modal parameter estimation based on a single data record. This work is concerned with automated MPE and as such it is assumed that only a single data record is available.

Based on the type of excitation, a distinction can be made between experimental, operational, and combined modal analysis. In *experimental modal analysis* (EMA), all forces acting on a structure are recorded, and unmeasured forces are regarded as an unwanted noise source that needs to be removed. For in-situ measurements, *operational modal analysis* (OMA) is often more appropriate. In such test, the response of the structure to the unknown operational loading is recorded, and the modal parameters are extracted from these output-only data, based on additional assumptions on the nature of the unknown forces. A combined approach, where in the identification process, both measured and unmeasured forces are accounted for, yields optimal results, and contains EMA and OMA as special cases [16]. This approach is often called *operational modal analysis with exogenous inputs* (OMAX). For each analysis type, a wide range of modal parameter identification algorithms is available. A distinction can be made between *parametric* and *nonparametric* methods. Nonparametric methods are in general straightforward and physically intuitive, but simulation studies have confirmed that parametric models yield far more accurate modal parameter estimates [15, 16]. In this work, a general automatization strategy is set up for parametric modal parameter estimation, that is independent from the type of test and the identification algorithm used.

All parametric modal parameter estimation techniques require at least one user-defined integer: the *model order* n , which equals the number of eigenvalues present in the model, hence, in theory, twice the number of positive eigenfrequencies. In control theory, several model validation techniques are available that allow choosing n in an automated way, so that the prediction capacity of the identified model is maximized. However, in modal testing applications, one is not primarily interested in the prediction capacity of an identified model as such, but rather in the physical relevance of the individual modes that constitute the model. An alternative approach has therefore been developed, based on the empirical observation that in a very large number of modal identification problems, the physical modes of the structure appear at nearly the same eigenfrequency when the model order is over-specified, while the other, spurious modes, do not [21]. Parametric models are then identified for a wide range of model orders, most of which are larger than the number of modes in the considered frequency band, and the modes of all these models are plotted in a model order vs. eigenfrequency diagram, called a *stabilization diagram*. The physical modes should then show up as vertical lines in this diagram. Although the stabilization diagram has become a key tool in modal test-

ing, see, e.g., the textbooks [1, 10], its interpretation, i.e., the selection of physical modes as columns in the diagram, is often not straightforward, the results may depend on the judgement of the analyst and possible additional validation criteria may be needed.

The automated interpretation of a stabilization diagram constitutes the goal of this work. In particular, the developed approach should obey the following five criteria:

1. not rely on more than one data record or on a priori estimates for any of the modal parameters;
2. be as physically intuitive as possible and follow the course of a manual analysis;
3. produce similar results as in a manual analysis;
4. be of use in an EMA, OMA and OMAX framework;
5. not contain parameters that need to be specified or tuned by the user.

All automated MPE methods known to the authors breach at least one of these five targets. In particular, they all need user-specified parameter or threshold values. The only exception is the partitioning approach of Verboven et al. [24] and Vanlanduit et al. [23] for splitting the modes, estimated with frequency-domain Maximum Likelihood Estimation (MLE) for a *single* model order n , into two categories: physical and spurious. However, it is not directly clear whether this approach can be extended to the process of picking modes from a stabilization diagram.

In this paper, we present a fully automated approach for the interpretation of stabilization diagrams, involving clustering in three stages:

1. All modes in the stabilization diagram are classified into two categories: probably physical and spurious modes. Hereto, a partitioning method is employed that makes use of as many relevant single-mode validation criteria as possible. The modes that are classified as spurious are removed from the diagram. This first stage automates the setting of the stabilization thresholds, performed by the user to obtain a clear diagram.
2. Similar modes in the cleared stabilization diagram are grouped together. Hereto, hierarchical clustering is used, where the cut-off distance is not a user-defined quantity, but based on the result of stage 1. This stage corresponds to the visual inspection of the stabilization diagram by the user, in order to detect vertical lines of stable modes.
3. The clusters are grouped into two categories, those containing physical and those containing spurious modes, and a single mode is chosen from each physical cluster. Cluster validation criteria such as the number of modes in a cluster are employed. This stage corresponds to the selection by the user of a representative mode from columns of stable modes in the diagram.

The text is organized as follows. The validation criteria that are used in stage one of the automated approach are presented in section 2. The three stages of the automated approach are detailed in section 3. Section 4 contains a validation study, where nine real-life noisy operational modal bridge data sets are both automatically and manually analyzed. Finally, section 5 concludes the paper.

2 Single-mode validation criteria

This section provides an overview of validation criteria that may be used in stage 1 of the proposed automated approach. They are termed *single-mode* validation criteria since they are used here to determine whether a particular mode from a stabilization diagram is physical or spurious, rather than to assess the completeness or accuracy of a modal model, i.e., a set of identified modal parameters for the considered frequency range. Some of these single-mode criteria are *hard criteria*, yielding a binary answer (such as stability), while other are *soft criteria*, yielding a range of values (such as relative frequency difference).

2.1 Eigenfrequency, damping ratio and mode shape distance measures

Let f_{uj} , ξ_j and ϕ_j denote the undamped eigenfrequency (in Hz), damping ratio (dimensionless), and unscaled mode shape (in any suitable output quantity), respectively, belonging to a particular mode j . Obvious dimensionless distance measures between two modes j and l are the relative eigenfrequency and damping ratio differences:

$$d(f_{uj}, f_{ul}) = \frac{|f_{uj} - f_{ul}|}{\max(|f_{uj}|, |f_{ul}|)} \quad \text{and} \quad d(\xi_j, \xi_l) = \frac{|\xi_j - \xi_l|}{\max(|\xi_j|, |\xi_l|)}. \quad (1)$$

Alternatively, a distance between the continuous-time eigenvalues λ_{cj} and λ_{cl} of modes j and l , respectively, could be used:

$$d(\lambda_{cj}, \lambda_{cl}) = \frac{|\lambda_{cj} - \lambda_{cl}|}{\max(|\lambda_{cj}|, |\lambda_{cl}|)}. \quad (2)$$

This distance incorporates both eigenfrequency and damping ratio information, since [16]

$$\lambda_{cj} = -|2\pi f_{uj}| \xi_j + 2i\pi f_{uj} \sqrt{1 - \xi_j^2}. \quad (3)$$

For comparing the unscaled mode shapes, the *modal assurance criterion* (MAC) [2], which is the (dimensionless) correlation coefficient between both mode shapes, is a commonly used tool:

$$\text{MAC}(\phi_j, \phi_l) \triangleq \frac{|\phi_j^* \phi_l|^2}{\|\phi_j\|_2^2 \|\phi_l\|_2^2}. \quad (4)$$

When the mass is approximately equally distributed and the damping is proportional, one has that, when ϕ_j and ϕ_l are mode shapes belonging to different modes, their MAC value should be close to zero. The MAC is commonly used for measuring the distance between eigenvectors in a stabilization diagram, for comparing identified and calculated modes, and for validating the identified set of modal parameters. Note that $0 \leq \text{MAC}(\phi_j, \phi_l) \leq 1$.

The classic stabilization criteria are the distance in eigenfrequency, damping ratio, and mode shape of a mode at a certain model order to the closest mode at the closest lower model order. As a combined, dimensionless measure of the *distance between two modes*, we propose to use

$$d(j, l) = d(\lambda_{cj}, \lambda_{cl}) + 1 - \text{MAC}(\phi_j, \phi_l). \quad (5)$$

2.2 Measuring mode shape complexity

When a structure is proportionally damped, the mode shape components of a single mode lie on a straight line in the complex plane. For double modes, i.e., two modes with exactly the same eigenfrequency, this is not the case, but such modes occur very rarely in practice, except for double symmetric structures; for nearly axisymmetric structures, valid mode shapes that tend to form a circle in the complex plane have been identified [6]. Mode shape collinearity is a very powerful single-mode validation criterion, but it should be used with care.

The complexity of a mode shape can be measured with the *modal phase collinearity* (MPC):

$$\text{MPC}(\phi_j) = \frac{\|\text{Re}(\tilde{\phi}_j)\|_2^2 + \frac{1}{\varepsilon_{MPC}} \text{Re}(\tilde{\phi}_j^T) \text{Im}(\tilde{\phi}_j) (2(\varepsilon_{MPC}^2 + 1) \sin^2(\theta_{MPC}) - 1)}{\|\text{Re}(\tilde{\phi}_j)\|_2^2 + \|\text{Im}(\tilde{\phi}_j)\|_2^2} \quad (6)$$

where

$$\tilde{\phi}_{jo} = \phi_{jo} - \frac{\sum_{o=1}^{n_y} \phi_{jo}}{n_y}, \quad \varepsilon_{MPC} = \frac{\|\text{Im}(\tilde{\phi}_j)\|_2^2 - \|\text{Re}(\tilde{\phi}_j)\|_2^2}{2\text{Re}(\tilde{\phi}_j^T) \text{Im}(\tilde{\phi}_j)}, \quad \text{and}$$

$$\theta_{MPC} = \arctan \left(|\varepsilon_{MPC}| + \text{sign}(\varepsilon_{MPC}) \sqrt{1 + \varepsilon_{MPC}^2} \right).$$

A detailed motivation of this expression can be found in [13]. MPC values are dimensionless; they lie between 0 (not collinear at all) and 1 (perfect collinearity).

Alternatively, the *mean phase* (MP) of the mode shape components can be computed, and the *mean phase deviation* (MPD), i.e., the mean (weighted) deviation of these components from the mean phase. Approximate expressions for these are provided in [10], but they fail when a mode shape component has a large imaginary and a small real part, which may occur for instance when a mode shape is well identified in an EMA or OMAX test, but its mass-normalization is of poor quality. Therefore, we derive new expressions. The mean phase can be computed as the angle of the best straight line fit through the mode shape in the complex plane, in the sense that the *orthogonal regression* is minimal (see [fig. 1](#)). This boils down to the following total least squares problem [22]

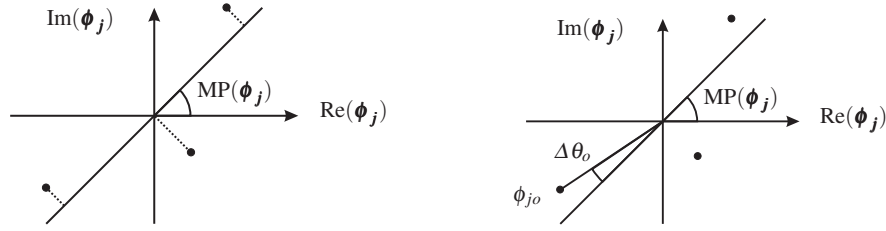


Fig. 1 The mean phase is determined such that the orthogonal distance of the mode shape components to the corresponding straight line fit, is minimized (left). The mean phase deviation is determined as a weighted mean of the phase deviations $\Delta\theta_o$ of the individual mode shape components ϕ_{jo} from the mean phase $\text{MP}(\phi_j)$.

$$\text{MP}(\phi_j) = \arg \min_{\theta} \frac{\|\text{Im}(\phi_j) - \tan(\theta)\text{Re}(\phi_j)\|_2^2}{1 + \tan^2(\theta)}, \quad (7)$$

that can be solved as [9]

$$\text{MP}(\phi_j) = \arctan\left(\frac{-V_{12}}{V_{22}}\right), \quad \mathbf{USV}^T = [\text{Re}(\phi_j) \text{Im}(\phi_j)], \quad (8)$$

where $\mathbf{U} \in \mathbb{C}^{n_y \times 2}$, $\mathbf{S} \in \mathbb{R}^{2 \times 2}$ and $\mathbf{V} \in \mathbb{C}^{2 \times 2}$ constitute a singular value decomposition, i.e., \mathbf{S} is a diagonal matrix with decreasing entries along the diagonal, and \mathbf{U} and \mathbf{V} have orthonormal columns. V_{12} and V_{22} denote the elements (1,2) and (2,2) of \mathbf{V} . The deviation of the phase of ϕ_{jo} from the mean phase can be easily computed from the scalar product between $[\text{Re}(\phi_{jo}) \text{Im}(\phi_{jo})]^T$ and $[1 \tan(\text{MP}(\phi_j))]^T$. The mean phase deviation is then obtained as:

$$\text{MPD}(\phi_j) = \frac{\sum_{o=1}^{n_y} w_o \arccos \left| \frac{\text{Re}(\phi_{jo}) + \tan(\text{MP}(\phi_j))\text{Im}(\phi_{jo})}{\sqrt{1 + \tan^2(\text{MP}(\phi_j))} |\phi_{jo}|} \right|}{\sum_{o=1}^{n_y} w_o}, \quad (9)$$

where w_o are weighting factors, that may be chosen equal to $|\phi_{jo}|$ in order to give mode shape components with a larger amplitude a higher weight.

2.3 Modes appearing in complex conjugate pairs

It is well known that, for every physical mode of a structure with continuous-time eigenvalue λ_{cj} , mode shape ϕ_j , and continuous-time modal participation vector \mathbf{l}_{cj} , the structure has a second mode with parameters $\overline{\lambda_{cj}}$, $\overline{\phi_j}$, and $\overline{\mathbf{l}_{cj}}$, where $\overline{}$ denotes the complex conjugate [1, 7, 10, 12]. The presence of such a complex conjugate mode can be used as a hard single-mode validation criterion. Also the discrete-time eigenvalues λ_{dj} and modal participation vectors \mathbf{l}_{dj} appear in complex conjugate pairs.

2.4 Measuring the contribution of a mode to the total response

The term *modal transfer norm* (MTN) was introduced in [17] to denote a scalar measure for the contribution of a particular identified mode to the total response. Two variants of the MTN may be discriminated: they are denoted as MTN_{∞} and MTN_2 , respectively. MTN_2 equals the root mean square value of the autocorrelations of the response of mode j to white loading [8]; it is not used in this paper. MTN_{∞} equals the peak gain of a transfer function containing mode j only. In an EMA context, this may be the mobility of mode j , so that, when the measured outputs are velocities, one has:

$$\text{MTN}_{\infty}^d = \max_{\omega} \sigma(\mathbf{H}_{\text{mob},j}(\omega)) = \max \sigma \left(\frac{\phi_j \mathbf{l}_{dj}^T}{z - \lambda_{dj}} \Big|_{z=e^{i\omega_j T}} \right),$$

where $\sigma(\square)$ denotes the set of singular values, T the sampling period, and ω_j the *damped* circular eigenfrequency of mode j . When some measured outputs are not velocities, the corresponding components of the mode shape ϕ_j should be divided by (in case of accelerations) or multiplied by (in case of displacements) the continuous-time eigenvalues λ_{cj} . In an OMA context, the modal contribution to the *positive power spectral density* (PSD⁺), in physical units of velocity, can be measured:

$$\text{MTN}_{\infty j}^s = \max_{\omega} \sigma \left(\mathbf{S}_{y^s y^s, j}^+(\omega) \right) = \max_{\omega} \sigma \left(\left. \frac{\phi_j \mathbf{g}_{dj}^T}{z - \lambda_{dj}} \right|_{z=e^{i\omega_j T}} + \frac{\phi_j \mathbf{g}_{dj}^T}{\lambda_{dj}} \right), \quad (10)$$

where \mathbf{g}_{dj} is the discrete stochastic participation vector of mode j . When some measured outputs are not velocities, the corresponding components of the mode shape ϕ_j and the stochastic participation vector \mathbf{g}_{dj} should be divided by (in case of accelerations) or multiplied by (in case of displacements) the continuous-time eigenvalues λ_{cj} . In an OMAX context, both $\text{MTN}_{\infty j}^d$ and $\text{MTN}_{\infty j}^s$ can be used; a combined criterion has also been defined [17], but it might perform less well in some cases since $\mathbf{H}_j(\omega)$ and $\mathbf{S}_{y^s y^s, j}^+(\omega)$ have different physical units and may therefore be of completely different orders of magnitude. Several well-established algorithms are available for computing the maxima in the MTN_{∞} definitions, see, e.g., [3, 4].

A stabilization diagram in which only the modes with the highest values of a modal transfer norm are plotted, is usually very clear, as illustrated with simulated and experimental examples in [5, 8, 17, 19]. Since a modal transfer norm is a positive definite quantity belonging to a particular mode, a relative difference in modal transfer norm between modes,

$$d(\text{MTN}_j, \text{MTN}_l) = \frac{|\text{MTN}_j - \text{MTN}_l|}{\max(\text{MTN}_j, |\text{MTN}_l|)}, \quad (11)$$

can be used as a stabilization criterion, or to distinguish modes from each other.

In [8], it is shown that, when for a certain mode, the poles and the zeros at all outputs coincide, the corresponding modal transfer norm is zero. Since pole-zero cancelation is a typical symptom of spurious modes, this provides another explanation of why modal transfer norms of spurious modes tend to have a low value. However, modal contribution criteria should be applied with care, since weakly excited or highly damped physical modes may exhibit low values.

2.5 Stability

In normal operating conditions, structures are strictly stable, hence the damping ratios of the physical modes should be positive. Stability is therefore a very useful hard single-mode validation criterion. On the other side, modes that are nearly critically damped are rarely encountered in practice. In nearly all modal testing applications, damping ratios larger than 20% are not physically realistic.

2.6 Other criteria

Several other validation criteria have been proposed, some of which can only be used when measured forces are available, or only in conjunction with a particular system identification algorithm. Although only the criteria that have been discussed in the previous section will be used further on in this text, the proposed strategy is general enough to include additional or alternative single-mode validation criteria.

3 Automated interpretation of a stabilization diagram in 3 clustering stages

3.1 Automated clearing of a stabilization diagram

When all identified modes would be plotted in a stabilization diagram, it would look very busy and complex, and it would be very difficult to select a set of physical modes from the diagram, cfr. [figs 2\(a,c,e\)](#), [3\(a,c,e\)](#) and [4\(a,c,e\)](#). In a manual analysis, the user therefore chooses a set of threshold values for the stabilization criteria and possibly other single-mode validation criteria discussed in section 2, and modes that do not pass the thresholds are classified as spurious and removed from the

diagram. Setting these threshold values judiciously is a task that is hard to automate, especially when many validation criteria are considered, because different sets of data require different sets of threshold values in order to obtain a clear diagram in which all relevant modes are present.

For clearing out the stabilization diagram, we therefore propose a different approach, which consists of the following steps:

1. Selection of as many relevant single-mode validation criteria as possible.
2. Automated classification of the modes as certainly spurious or possibly physical, using the soft validation criteria and a clustering algorithm.
3. Application of the hard validation criteria to the set of possibly physical modes.

Suppose that n_{vs} soft and n_{vh} hard validation criteria have been selected and computed for each mode in step 1. In step 2, each mode is represented by an n_{vs} -dimensional vector containing its soft validation criteria, i.e., mode j is represented by a point in $\mathbb{R}^{n_{vs}}$, in which the clustering will take place. Table 1 shows the soft validation criteria that are used in this paper. In order to give each criterion equal weight, the variables VS3, VS4, VS5 and VS6 are subtracted by their minimum and divided by their range, so that they produce values in the interval $[0, 1]$. A partitioning method is then employed for classifying the modes into two clusters: one of them containing the certainly spurious modes and the other one containing the possibly physical modes. In this work, a k -means clustering algorithm with $k = 2$ clusters is employed, but alternative partitioning methods may be employed as well.

| criterion | value | ideal physical | ideal spurious |
|-----------|------------------------------|----------------|----------------|
| VS1 | $d(\lambda_j, \lambda_l)$ | 0 | 1 |
| VS2 | $\text{MAC}(\phi_j, \phi_l)$ | 1 | 0 |
| VS3 | $\text{MTN}_{\infty j}^d$ | large (1) | 0 |
| VS4 | $\text{MTN}_{\infty j}^s$ | large (1) | 0 |
| VS5 | MTN_{2j}^d | large (1) | 0 |
| VS6 | MTN_{2j}^s | large (1) | 0 |
| VS7 | $\text{MPC}(\phi_j)$ | 1 | 0 |
| VS8 | $\text{MPD}(\phi_j)/90$ | 0 | 1 |

Table 1 List of soft validation criteria that are used in this paper, and the values they take for an ideal physical and an ideal spurious mode. The values between brackets are the ideal values after re-scaling, i.e., subtracting the parameters VS3 till VS6 by their minimum value and dividing them by their range.

The 2-means clustering algorithm minimizes the sum of the squared Euclidian distances between each mode j , represented by a point $\mathbf{p}_j \in \mathbb{R}^{n_{vs}}$, and the nearest cluster centroid \mathbf{p}_{ck} , i.e., the centroid of the cluster to which the mode belongs. In other words, the centroid of the cluster of possibly physical modes, denoted as \mathbf{p}_{c1} , and the centroid of the cluster of certainly spurious modes, denoted as \mathbf{p}_{c2} , are computed as

$$\{\mathbf{p}_{c1}, \mathbf{p}_{c2}\} = \underset{\mathbf{p}_{ck}}{\text{args min}} \sum_{k=1}^2 \sum_{j=1}^{n_m(k)} \|\mathbf{p}_{j,c} - \mathbf{p}_{ck}\|_2^2, \quad (12)$$

where the number of modes in each cluster k is denoted as $n_m(k)$, the modes belonging to the cluster of possibly physical modes are members of the set $\{\mathbf{p}_{j,1}\} = \{\mathbf{p}_j | \|\mathbf{p}_j - \mathbf{p}_{c1}\| \leq \|\mathbf{p}_j - \mathbf{p}_{c2}\|\}$, and the modes belonging to the cluster of certainly spurious modes are members of the set $\{\mathbf{p}_{j,2}\} = \{\mathbf{p}_j | \mathbf{p}_j \notin \{\mathbf{p}_{j,1}\}\}$. The objective function in (12) is minimized locally in an iterative minimization process, where the starting points for \mathbf{p}_{c1} and \mathbf{p}_{c2} are chosen according to their ideal values listed in table 1. Each iteration consists of two stages:

1. The Euclidian distance between each point \mathbf{p}_j and each cluster center \mathbf{p}_{ck} is computed, and point \mathbf{p}_j is assigned to the set $\{\mathbf{p}_{j,1}\}$ or $\{\mathbf{p}_{j,2}\}$.
2. The centroids are computed so as to minimize the total squared Euclidian distance within each cluster, i.e., they are computed as in (12), but for fixed sets $\{\mathbf{p}_{j,1}\}$ and $\{\mathbf{p}_{j,2}\}$.

The modes that belong to $\{\mathbf{p}_{j,2}\}$ after convergence of the partitioning method are classified as certainly spurious, and they are removed from the stabilization diagram.

In the third and final step, the stabilization diagram is cleared out further by applying the n_{vh} hard validation criteria. Only the modes that meet all hard criteria are retained in the diagram as possibly physical modes. It is important to perform steps 2 and 3 in the correct order, since the application of the hard validation criteria (step 3) may remove all of the spurious modes,

and as a result physical modes may be lost in the partitioning (step 2). [Table 2](#) lists the hard validation criteria that are used in this paper.

| critierion | value | possibly physical | certainly spurious |
|------------|---------------------------------|-------------------|--------------------|
| VH1 | $\xi_j > 0$ | 1 | 0 |
| VH2 | $\xi_j < 20\%$ | 1 | 0 |
| VH3 | complex conjugate mode present? | 1 | 0 |

Table 2 List of hard validation criteria that are used in this paper, and the boolean values they take for a possibly physical and a certainly spurious mode.

3.2 Grouping similar modes in a cleared stabilization diagram

After a stabilization diagram has been cleared out as described in the previous section, similar modes in the diagram are grouped together with a hierarchical clustering approach. Hierarchical clustering of stabilization diagrams is not a new idea, but the main difference with previously reported approaches is that the current approach does not contain any parameter that needs to be specified by the user. The different steps of the proposed approach are:

1. All modes from the cleared stabilization diagram are put in separate clusters, and the mutual distance between all clusters is computed according to (5).
2. The two clusters that are closest together are collected in a single cluster, and the mutual distance between all clusters is recomputed as the average distance between their elements.
3. Step 2 is continuously repeated until the distance between the closest clusters exceeds

$$3(p_{c1}(1) + 1 - p_{c1}(2)), \quad (13)$$

where $p_{c1}(1)$ and $p_{c1}(2)$ are the first and second elements of \mathbf{p}_{c1} , the centroid of possibly physical modes obtained in the previous clustering stage, according to [table 1](#). Note that the term between brackets in (13) corresponds to the distance between a typical physical mode in the analyzed data set, and the closest mode at a lower model order, according to the distance measure (5).

As a result, the hierarchical clustering stage yields a set of similar mode sets from the cleared stabilization diagram.

3.3 Selecting a final set of physical modes

The sets of modes obtained in stage 2 are split into two clusters: one containing the sets of physical modes, and one containing the sets of spurious modes. Since in contrast to spurious modes, physical modes are ideally identified at each model order from a certain model order on, it can be expected that the sets of physical modes contain many elements, while the sets of spurious modes do not. In order to avoid that a threshold number of elements needs to be specified by the user, again a partitioning method, e.g., k -means clustering with $k = 2$, is employed for performing the clustering. Since stage 2 may yield physical mode sets only, an additional number of empty sets is added, equal to the number of mode sets containing more than one fifth of the maximum number of modes in any set. As a result, there are n_h mode sets in total, some of which are empty.

If the number of modes in set j is denoted as n_{hj} , $j = 1, \dots, n_h$, the 2-means algorithm computes the centroid of the cluster of physical mode sets $n_{hc,1}$, and the cluster of spurious mode sets $n_{hc,2}$, as

$$\{n_{hc,1}, n_{hc,2}\} = \operatorname{args\,min}_{n_{hc,k}} \sum_{k=1}^2 \sum_{j=1}^{n_S(k)} (n_{hj,c} - n_{hc,k})^2, \quad (14)$$

where the number of mode sets in each cluster k is denoted as $n_S(k)$, the modes belonging to the cluster of possibly physical modes are members of the set $\{n_{hj,1}\} = \{n_{hj} \mid (n_{hj} - n_{hc,1})^2 \leq (n_{hj} - n_{hc,2})^2\}$, and the mode sets belonging to the cluster of spurious modes are members of the set $\{n_{hj,2}\} = \{n_{hj} \mid n_{hj} \notin \{n_{hc,1}\}\}$. The objective function in (14) is minimized in an iterative local minimization process, as explained in section 3.1, and the starting points are chosen to be $n_{hc,1} = \max_j(n_{hj})$ and $n_{hc,2} = 0$.

Finally, a representative element is chosen from each set of similar physical modes that results from the partitioning. In this work, the mode with the median damping value is chosen. When real normal modes are expected, the mode with the highest MPC or MPD value can be alternatively chosen as the representative element.

4 Validation example: the Z24 bridge

4.1 The structure

The Z24 bridge was part of the road connection between the villages of Koppigen and Utzenstorf, Switzerland, over-passing the A1 highway between Bern and Zürich. It was a classical post-tensioned concrete two-cell box-girder bridge with a main span of 30 m and two side spans of 14 m. The bridge, that dated from 1963, was demolished at the end of 1998, because a new railway adjacent to the highway required a new bridge with a larger side span. Before complete demolition, the bridge was subjected to a short-term progressive damage test, and after each applied damage scenario, a full forced and ambient operational vibration test were performed.

The data from one of these scenarios (no. 8) were presented as benchmark data for assessing the performance of system identification methods for (operational) modal analysis; here, we will analyze the benchmark data from the ambient vibration test. In this test, 291 degrees of freedom have been measured in total: three acceleration components on the pillars, and mainly vertical and lateral accelerations on the bridge deck. The data were collected in 9 different setups using 5 channels that were common to all setups. In each setup, 65536 data samples were collected at a sampling rate of 100 Hz, using an analog anti-aliasing filter with cut-off frequency of 30 Hz.

More information on the structure, the experimental setup, the short-term progressive damage tests and a long-term vibration monitoring test that was performed as well, and reported benchmark results, can be found in [18].

4.2 Identification results

The data from each of the 9 setups have been processed with the reference-based covariance-driven stochastic subspace identification (SSI-cov/ref) algorithm [14]. The 5 channels that were common to each setup were chosen as reference channels, $\iota = 50$ was chosen as half the number of block rows in the data Hankel matrix, and a model order range from 2 to 160 in steps of 2 was chosen for the construction of the stabilization diagrams. These diagrams were then interpreted with the fully automatic three-stage approach proposed in section 3, for which no user-defined parameters are needed.

Figures 2, 3 and 4 show the full stabilization diagrams before and after clearing them out according to step 1 of the automated approach. The automatically selected eigenfrequencies are plotted as vertical lines on top of the cleared out stabilization diagrams. It can be noticed that they coincide with columns of stabilized modes, as in a manual analysis.

In the automated analysis, 6 modes are found in all 9 setups. They all have eigenfrequencies below 14 Hz. It appears that the higher modes are not always well excited by the ambient forces. This is in agreement with benchmark results reported in the literature, where, based on a manual stabilization diagram analysis, only the first 5 modes are used for damage assessment [11, 20]. Figure 5 shows the global mode shapes, obtained after merging the partial mode shapes obtained in all setups in a least-squares sense. The corresponding eigenfrequency and damping ratio values, obtained through averaging over all setups, are also listed.

In order to assess the performance of the automated analysis, a manual analysis, where the stabilization diagrams are cleared out by means of user-defined thresholding, and stable modes are picked from the diagram, was performed as well. It should be noted that, since the manual interpretation of a stabilization diagram depends on the experience and engineering judgement of the analyst, the result of such analysis is user-dependent; only one such result is reported here, but it agrees very well with results reported by other expert users that have analyzed the same benchmark data, cfr. [18] and the references therein. In the manual analysis, only 6 modes were found in all 9 setups, so the automated analysis was able to retrieve all relevant modes. Table 3 offers a quantitative comparison between the results obtained from the automated and manual analyses. The quality of the identified eigenfrequency and damping ratio values, measured in terms of the sample standard deviation over all 9 setups, is very similar, except for mode 6, where the eigenfrequency estimate is more accurate in the manual analysis, while the damping ratio estimate is more accurate in the automated analysis; this is probably due to the fact that, in the last step of each automated analysis, the mode with the median damping value is chosen as the representative from each set of similar physical modes. The MPC values for the merged mode shapes are also plotted; they are again very similar except for mode 6, where the manual

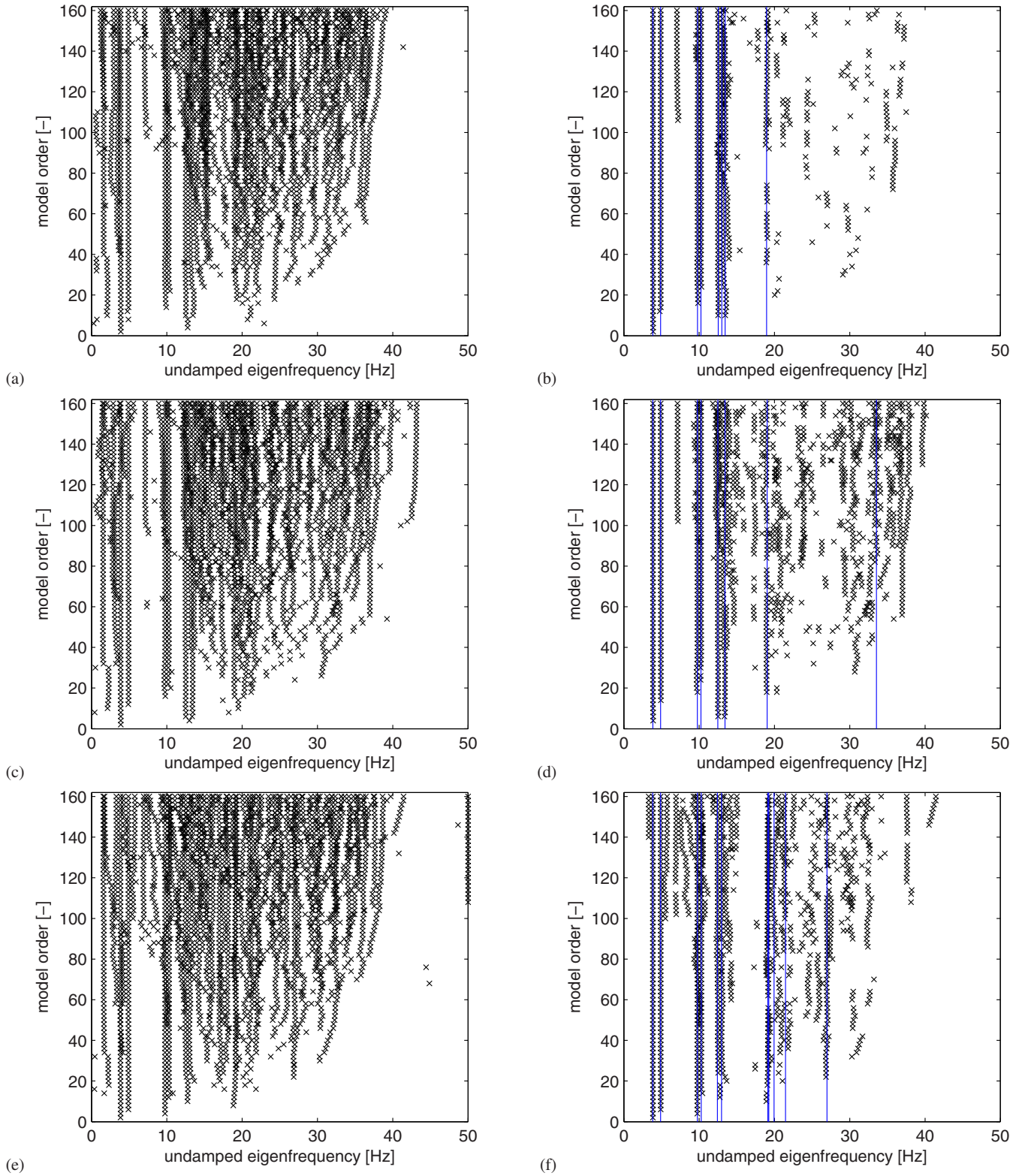


Fig. 2 Z24 bridge: (a-c-e) full stabilization diagrams and (b-d-f) automatically cleared stabilization diagrams for (a-b) setup 1, (c-d) setup 2 and (e-f) setup 3. The automatically selected eigenfrequencies are plotted as vertical lines on top of the cleared diagrams.

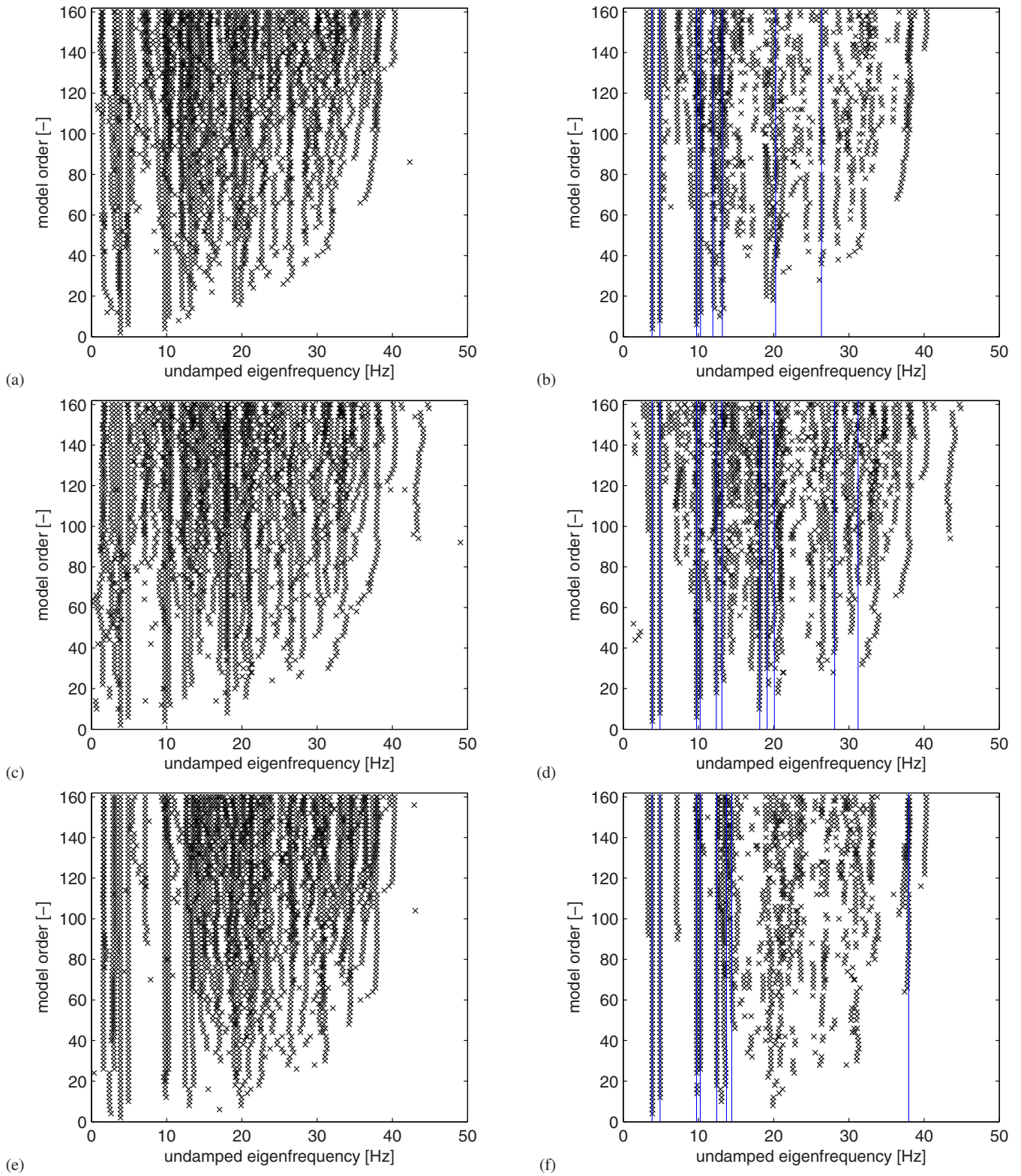


Fig. 3 Z24 bridge: (a-c-e) full stabilization diagrams and (b-d-f) automatically cleared stabilization diagrams for (a-b) setup 4, (c-d) setup 5 and (e-f) setup 6. The automatically selected eigenfrequencies are plotted as vertical lines on top of the cleared diagrams.

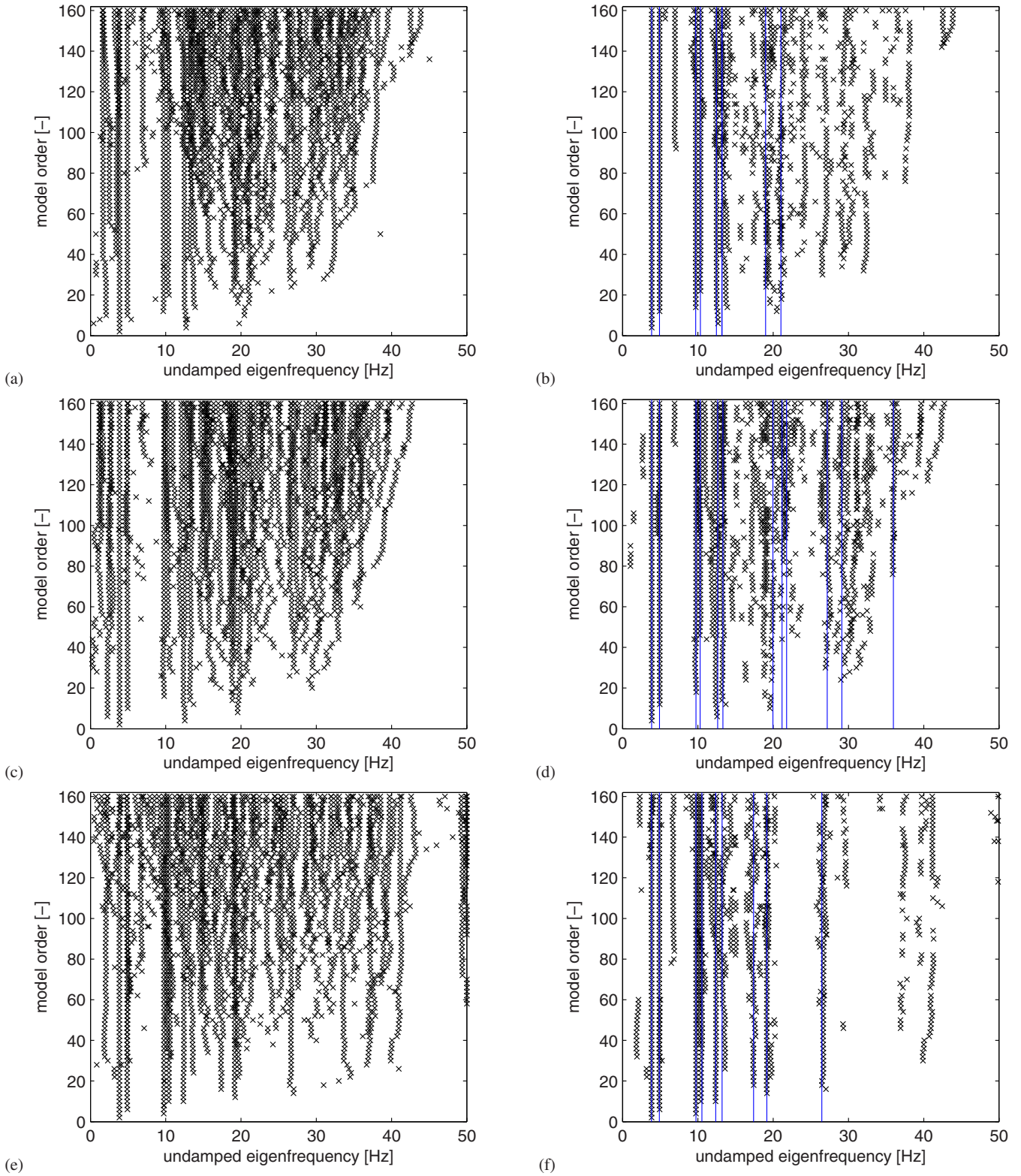


Fig. 4 Z24 bridge: (a-c-e) full stabilization diagrams and (b-d-f) automatically cleared stabilization diagrams for (a-b) setup 7, (c-d) setup 8 and (e-f) setup 9. The automatically selected eigenfrequencies are plotted as vertical lines on top of the cleared diagrams.

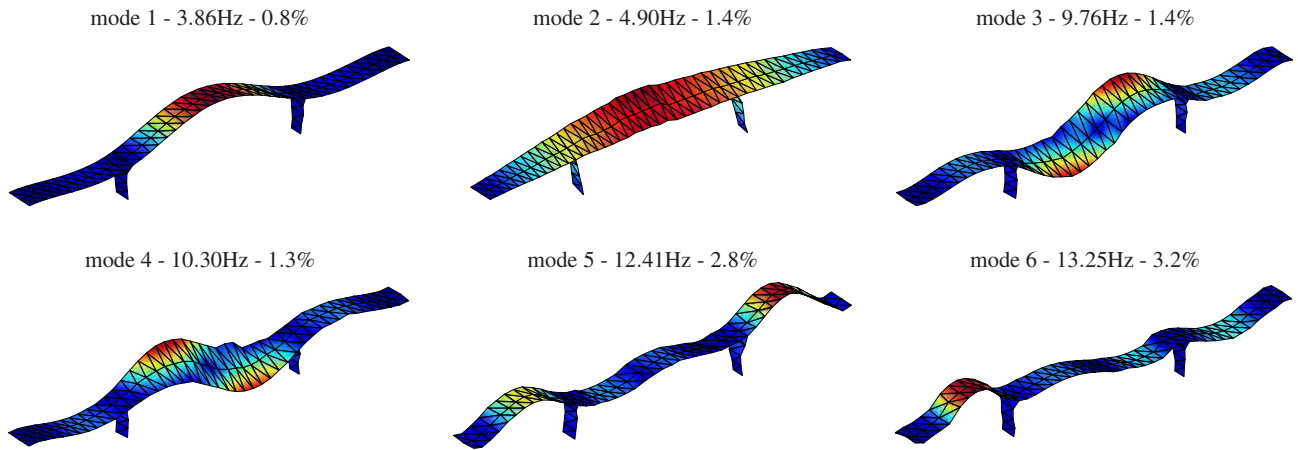


Fig. 5 Z24 bridge: eigenfrequency, damping ratio, and mode shape estimates, obtained through an automated stabilization diagram analysis.

analysis yields a higher value. Finally, the merged mode shapes are compared by means of the MAC; it can be concluded that mode shapes 1 tot 5 are identical while mode shape 6 is almost identical.

| mode | $\mu(f_{uj,a})$ [Hz] | $\sigma(f_{uj,a})$ [Hz] | $\mu(f_{uj,m})$ [Hz] | $\sigma(f_{uj,m})$ [Hz] | $\mu(\xi_{j,a})$ [%] | $\sigma(\xi_{j,a})$ [%] | $\mu(\xi_{j,m})$ [%] | $\sigma(\xi_{j,m})$ [%] | MPC _a [-] | MPC _m [-] | MAC [-] |
|------|-------------------------|----------------------------|-------------------------|----------------------------|-------------------------|----------------------------|-------------------------|----------------------------|-------------------------|-------------------------|------------|
| 1 | 3.86 | 0.006 | 3.86 | 0.006 | 0.8 | 0.1 | 0.8 | 0.1 | 1.000 | 1.000 | 1.00 |
| 2 | 4.90 | 0.013 | 4.89 | 0.012 | 1.4 | 0.2 | 1.4 | 0.1 | 0.991 | 0.996 | 0.99 |
| 3 | 9.76 | 0.020 | 9.76 | 0.022 | 1.4 | 0.2 | 1.4 | 0.2 | 0.966 | 0.967 | 1.00 |
| 4 | 10.30 | 0.095 | 10.30 | 0.080 | 1.3 | 0.3 | 1.3 | 0.2 | 0.934 | 0.942 | 1.00 |
| 5 | 12.41 | 0.200 | 12.39 | 0.182 | 2.8 | 0.4 | 2.9 | 0.4 | 0.951 | 0.950 | 0.99 |
| 6 | 13.25 | 0.230 | 13.35 | 0.145 | 3.2 | 1.4 | 3.6 | 1.7 | 0.877 | 0.960 | 0.94 |

Table 3 Z24 bridge: mean values (μ) and standard deviations (σ) of the undamped eigenfrequencies (f_{uj}) and damping ratios (ξ_j), computed from the values obtained for each setup with a manual (m) or automated (a) analysis of the stabilization diagrams. The MPC values of the merged mode shapes are also tabulated, as well as the MAC values between the mode shapes obtained in the manual and the automated analysis.

5 Conclusions

In this paper, a fully automated, three-stage clustering approach is developed for interpreting stabilization diagrams, that obeys the following five target criteria:

1. not rely on more than one data record or on a priori estimates for any of the modal parameters;
2. be as physically intuitive as possible and follow the course of a manual analysis;
3. produce similar results as in a manual analysis;
4. be of use in an EMA, OMA and OMAX framework;
5. not contain parameters that need to be specified or tuned by the user.

As a nice side result, improved formulae for computing the mean phase and mean phase deviation of a mode shape were derived (8-9). A validation study was performed, where nine real-life benchmark operational modal bridge data sets were analyzed, and the resulting modal parameters were compared with those obtained from a manual analysis by an expert user. With the automated approach, all relevant modal parameters were recovered with an accuracy that is almost identical as in the manual analysis. Additional validation studies on other structures are required, however, in order to confirm the accuracy and robustness of the proposed automatization strategy.

Acknowledgements

This research was partially supported by the Ministerio de Fomento, Spain (research project *Low cost bridge health monitoring system by ambient vibrations using wireless sensors*), the Fund for Special Research of K.U.Leuven, Belgium (Postdoctoral Research Fellowship provided to the first author), and the Research Foundation - Flanders, Belgium (Postdoctoral Research Fellowship provided to the first author). The authors gratefully acknowledge the financial support from these institutes.

References

1. R.J. Allemang. *Vibrations: experimental modal analysis*. University of Cincinnati, Cincinnati, OH, seventh edition, 1999.
2. R.J. Allemang and D.L. Brown. A correlation coefficient for modal vector analysis. In *Proceedings of the 1st International Modal Analysis Conference*, pages 110–116, Orlando, FL, 1982.
3. S. Boyd and V. Balakrishnan. A regularity result for the singular values of a transfer matrix and a quadratically convergent algorithm for computing its L_∞ -norm. *Systems and Control Letters*, 15(1):1–7, 1990.
4. N. A. Bruinsma and M. Steinbuch. A fast algorithm to compute the H_∞ -norm of a transfer function matrix. *Systems and Control Letters*, 14(4):287–293, 1990.
5. A. Deraemaeker, E. Reynders, G. De Roeck, and J. Kullaa. Vibration based Structural Health Monitoring using output-only measurements under changing environment. *Mechanical Systems and Signal Processing*, 22(1):34–56, 2008.
6. D. Dooms, G. Degrande, G. De Roeck, and E. Reynders. Finite element modelling of a silo based on experimental modal analysis. *Engineering Structures*, 28(4):532–542, 2006.
7. D. J. Ewins. *Modal testing*. Research Studies Press, Baldock, U.K., second edition, 2000.
8. I. Goethals and B. De Moor. Model reduction and energy analysis as a tool to detect spurious modes. In P. Sas and B. van Hal, editors, *Proceedings of ISMA2002 International Conference on Noise and Vibration Engineering*, pages 1307–1314, Leuven, Belgium, September 2002.
9. G.H. Golub and C.F. Van Loan. *Matrix computations*. John Hopkins University Press, Baltimore, MD, 3d edition, 1996.
10. W. Heylen, S. Lammens, and P. Sas. *Modal analysis theory and testing*. Department of Mechanical Engineering, Katholieke Universiteit Leuven, Leuven, Belgium, 1997.
11. J. Maeck, B. Peeters, and G. De Roeck. Damage identification on the Z24-bridge using vibration monitoring. *Smart Materials and Structures*, 10(3):512–517, 2001.
12. N.M.M. Maia and J.M.M. Silva. *Theoretical and experimental modal analysis*. Research Studies Press, Taunton, U.K., 1997.
13. R. S. Pappa, K. B. Elliott, and A. Schenk. A consistent-mode indicator for the eigensystem realization algorithm. Report NASA TM-107607, National Aeronautics and Space Administration, April 1992.
14. B. Peeters and G. De Roeck. Reference-based stochastic subspace identification for output-only modal analysis. *Mechanical Systems and Signal Processing*, 13(6):855–878, 1999.
15. B. Peeters and G. De Roeck. Stochastic system identification for operational modal analysis: A review. *ASME Journal of Dynamic Systems, Measurement, and Control*, 123(4):659–667, 2001.
16. E. Reynders. *System identification and modal analysis in structural mechanics*. PhD thesis, Department of Civil Engineering, K.U.Leuven, 2009.
17. E. Reynders and G. De Roeck. Reference-based combined deterministic-stochastic subspace identification for experimental and operational modal analysis. *Mechanical Systems and Signal Processing*, 22(3):617–637, 2008.
18. E. Reynders and G. De Roeck. Continuous vibration monitoring and progressive damage testing on the Z24 bridge. In C. Boller, F.K. Chang, and Y. Fujino, editors, *Encyclopedia of Structural Health Monitoring*, pages 2149–2158. John Wiley & Sons, New York, NY, 2009.
19. E. Reynders, R. Pintelon, and G. De Roeck. Uncertainty bounds obtained from Stochastic Subspace Identification. *Mechanical Systems and Signal Processing*, 22(4):948–969, 2008.
20. A. Teughels and G. De Roeck. Structural damage identification of the highway bridge Z24 by FE model updating. *Journal of Sound and Vibration*, 278(3):589–610, 2004.
21. H. Van der Auweraer and B. Peeters. Discriminating physical poles from mathematical poles in high order systems: use and automation of the stabilization diagram. In *Proceedings of the 2004 IEEE Instrumentation and Measurement Technology Conference*, pages 2193–2198, Como, Italy, May 2004.
22. S. Van Huffel and J. Vandewalle. *The total least squares problem*. SIAM, Philadelphia, PA, 1991.
23. S. Vanlanduit, P. Verboven, P. Guillaume, and J. Schoukens. An automatic frequency domain modal parameter estimation algorithm. *Journal of Sound and Vibration*, 265(3):647–661, 2003.
24. P. Verboven, E. Parloo, P. Guillaume, and M. Van Overmeire. Autonomous structural health monitoring - part 1: modal parameter estimation and tracking. *Mechanical Systems and Signal Processing*, 16(4):637–657, 2002.

The Optimization and Autonomous Identification of Modal Parameters

J. M. Liu^(1,2), S. Shen⁽¹⁾, M. Ying⁽¹⁾, S. W. Dong⁽¹⁾

⁽¹⁾Dept. of Engineering Mechanics, Tsinghua University, Beijing 100084, China

⁽²⁾China orient institute of noise and vibration, Beijing 100085, China

<http://www.coinv.com.cn>

ABSTRACT

For modal analysis (including SISO, MIMO, OMA), the accuracy of modal parameters depends mainly on the estimators used. Different parameters will be extracted even by the same user with the same method at different time. Here a criterion is presented which can compare the accuracy of the identification results. An optimization method is put forward by which all identification results of different methods can be approximately unified. The difficult problem for the optimization of MIMO test, to calculate modal participation factors by the modal frequency and damping independently, is solved in the paper. An optimization mechanism is put forward by which the mathematical poles can be deleted automatically during the optimization process. By this way, the autonomous identification of modal parameter for SISO, MIMO, OMA test can be realized, the best identification result can be obtained which only depends on the frequency bands of interest without relation to analysis methods and user. Two examples, a car brake disk of MIMO test and a real bridge of OMA test, are used to testify the optimization and autonomous analysis method and are proven successful.

1 INTRODUCTION

The main methods for multi-input-multi-output(MIMO) modal analysis are ERA[1] (Eigensystem Realization Algorithm), PolyMAX[2] (Poly-reference Least Square Complex Frequency Domain method), PRCE[3] (Poly-reference Complex Exponential method). The stabilization diagram will be used for all these methods, the dimension of characteristic matrix will be chosen first, when choosing different poles at stabilization diagram different modal parameters will be obtained. To get the correct modal parameters the user with high academic level and plenty measuring experience is required. In a word, different analysis method will cause different modal parameters. Different modal parameters will be identified even by the same user with the same analysis method at different time.

Given a reasonable and practical criterion of optimization for modal parameters, through optimization, the modal parameters identified by different methods can be optimized to an almost unified result.

In MIMO modal analysis, the modal participation factors are identified at the same time with modal frequency and damping, and the vibration shape is identified at last. The different poles in stabilization diagram correspond to different modal frequency, damping and participation factor. Only the user with high academic level and plenty measuring experience can choose the correct poles and get reliable modal parameters.

The optimization method suitable for SIMO and MISO which optimized characteristic roots and vibration shapes has been put forward recently [4]. This method cannot be extended to MIMO directly because in MIMO there is modal participation factor which is correlated to modal shape, the optimization method for MIMO need to be adjusted.

The different modal parameters identified by different method can be unified by optimization theoretically. After the optimization, the identified modal parameters have no relation with initial analysis method. But in practice, the situation is

not always in this way. For example, by the limitation of user's academic level and measuring experience, some important modes is lost in analysis, this error cannot be corrected by optimization.

To ensure the identified modal parameters have no relation with analysis method and user, the only way is autonomous analysis. Based on the optimization method, optimization mechanism by which pseudo modes will be deleted automatically is put forward. As long as an initial solution is given including all the physical poles, through the optimization mechanism, all the mathematical poles will be deleted automatically, only the physical poles are left, and the optimal modal parameters will be identified and the MIMO autonomous analysis is realized.

2 OPTIMIZATION OF MIMO MODAL PARAMETERS

For MIMO analysis, assuming the number of responding points is q and the number of exciting points is p . There are pq FRFs or half spectrum [5]. When characteristic roots S_r ($r=1, 2, \dots, n$) are known, the FRF or half spectrum can be written as:

$$[H(s)] = \sum_{r=1}^n \left(\frac{\{v_r\} \{w_r\}^T}{s - S_r} + \frac{\{v_r^*\} \{w_r\}^H}{s - S_r^*} \right) + \frac{[LR]}{s} + [UR] \quad (1)$$

where $s = j\omega$, \bullet^H denotes complex conjugate transpose of a matrix; $\{v_r\} \in C^{q \times 1}$ are the mode shapes, $\{w_r\} \in C^p$ the modal participation factors. $[LR], [UR] \in R^{q \times p}$ respectively lower and upper residues modeling the influence of the out-of-band modes in the considered frequency band.

Equation (1) can be written as

$$[H(s)] = \sum_{r=1}^{2n} \left(\frac{\{v_r\} \{w_r\}^T}{s - S_r} \right) + \frac{[LR]}{s} + [UR] \quad (2)$$

Only considering the optimization of S_r , we get

$$[dH(s)] = \sum_{r=1}^{2n} \frac{\{v_r\} \{w_r\}^T}{(s - S_r)^2} dS_r \quad (3)$$

$[E(s)] = [\hat{H}(s)] - [H(s)]$ represents the error between measured and synthesized FRFs or half spectrum, where $\hat{H}(s)$ are measured FRFs or half spectrum; $H(s)$ are synthesized FRFs or half spectrum and with

$$[E(s)] = \sum_{r=1}^{2n} \frac{\{v_r\} \{w_r\}^T}{(s - S_r)^2} dS_r \quad (4)$$

Considering all spectral lines at the same time, the dS_r ($r=1, 2, \dots, n$) will be solved by the least-squares (LS) method.

With $S_r + dS_r$ the new characteristic roots, modal participation factors $\{w_r\}$ can be solved by a new algorithm introduced below, modal vibration shapes $\{v_r\}$ be solved by equation (1) with LS method, as well as lower and upper

residues $[LR],[UR]$ modeling the influence of the out-of-band modes in the considered frequency band.

Modal shapes and modal participation factors are related with each other, so for MIMO modal analysis, the characteristic roots, modal shape and modal participation factor cannot be optimized at the same time.

The optimization method of only considering S_r ($r=1, 2, \dots, n$), keeping modal shapes and modal participation factors unchanged, can be used for optimization of MIMO modal parameters. The number of terms need to optimized is decreased greatly.

Define a frequency fitting coefficient as

$$Fit_f = \sqrt{E^H E / H^H H} \quad (5)$$

where E and H including all spectral lines in the considered frequency band, and the matrices E, H is arranged in only one column. The value of the frequency fitting coefficient is the smaller the better. This coefficient can be used as the object of optimization, or to compare the accuracy of modal parameters estimated by different methods.

According to Parseval's theorem, if all spectrum lines are taken into account, the frequency fitting coefficient can be looked as a time fitting coefficient.

In equation (4) and (5), each lines in E and H can be weighted according to frequency. There are $\omega^2, \omega, 1, \omega^{-1}, \omega^{-2}$ five types, which are decided by the measurements and the FRFS or half-spectrum used. For example, if the measurements are accelerations, the FRFs or half spectrums for fitting are displacement, the weighting mode should be ω^{-2} .

The modal parameters identified by different methods are looked as the initial solution of the optimization method. The frequency fitting coefficient can be used to compare the accuracy of different methods. The method with the smaller frequency fitting coefficient is the better, and the optimization process is fast.

The whole optimization procedure is as follows:

While modal frequencies and dampings are known, we get characteristic roots S_r ($r=1, 2, \dots, n$)

$$s_r = -(2\pi f_r)\xi_r + j\sqrt{1 - \xi_r^2} (2\pi f_r) \quad (6)$$

where f_r, ξ_r is the frequency and damping of mode r .

If FRFs or half-spectrum are calculated by applying the exponential window [6], which is defined as

$$ExpW_i = e^{-Exp(j/SF)} \quad (7)$$

with $i = 0, 1, 2, \dots, N - 1$, SF the sampling frequency, N the points number of the impulse response function corresponding to FRF or cross correlation function corresponding to half spectrum, Exp is the exponential window coefficient.

Therefore, the characteristic roots S_r are

$$s_r = -(2\pi f_r)\xi_r - Exp + j\sqrt{1 - \xi_r^2} (2\pi f_r) \quad (8)$$

Thereafter the modal participation factors can be calculated. When modal participation factor is known, the modal shapes

$\{v_r\}$ ($r=1, 2, \dots, n$) as well as lower and upper influencing residues $[LR], [UR]$ can be calculated by the LS method with equation (1). The frequency fitting coefficient can be calculated with equation (5). ds_r and ds_r^* can be calculated by the LS method with equation (4).

$s_r + ds_r$ is used as the new characteristic roots for the next iteration.

The optimization will stop when the frequency fitting coefficient doesn't decrease any more.

The difficulty of MIMO optimization is to get participation factors with modal frequency and damping known. There are algorithms based on PolyMAX, PRCE or ERA.

The PolyMAX method needs FRFs or half spectrum as primary data and identifies a right matrix-fraction model:

$$[H(z)] = \left[\sum_{k=0}^L z^k \langle \beta_{ok} \rangle \right] \left[\sum_{k=0}^L z^k [\alpha_k] \right]^{-1} \quad (9)$$

With z transform, $z = e^{s\Delta t}$, Δt is the sampling interval. Where $[H(z)] \in C^{q \times p}$ is FRF or half spectrum matrix containing the FRFs or half spectrums between all p inputs and q outputs, $\langle \beta_{ok} \rangle \in R^{1 \times p}$ the numerator row-vector polynomial of output o , and $[\alpha_k] \in R^{p \times p}$ the denominator matrix polynomial.

By the PolyMAX algorithm, $L+1$ matrices $[\alpha_k] \in R^{p \times p}$ ($k=0, 1, 2, \dots, L$) can be extracted. L must satisfy $Lq \geq 2n$. To ensure optimization quality, L should be large enough.

Let $\lambda_r = e^{s_r \Delta t}$, there is

$$\left[\sum_{k=0}^L [\alpha_k]^T \lambda_r^k \right] \{w_r\} = \{0\}, \quad r = 1, 2, \dots, 2n \quad (10)$$

Let $A = \left[\sum_{k=0}^L [\alpha_k]^T \lambda_r^k \right]$, $A \in C^{q \times q}$, using singular value decomposition, we get $A = [U][S][V]^H$, $[U] \in C^{q \times q}$, $[V] \in C^{q \times q}$, $[S] \in R^{q \times q}$ is a diagnostic matrix. The vector corresponding to the smallest singular value $\{V_r\}$ is the modal participation factor $\{w_r\}$.

By PRCE algorithm, $L+1$ ($Lq \geq 2n$) real coefficient square matrices $[\beta_0], [\beta_1], \dots, [\beta_L]$ with dimension q can be solved, there is

$$\left[\sum_{k=0}^L [\beta_k] \lambda_r^k \right] \{w_r\} = \{0\}, \quad r = 1, 2, \dots, 2n \quad (11)$$

By singular value decomposition, the modal participation factor $\{w_r\}$ can be solved.

For complete double roots situation, i.e. there are two identical roots λ_r , using two vectors $\{V_r\}$ responding the two

smallest singular values as modal participation factors $\{w_r\}$.

If all characteristic roots λ_r ($r=1, 2, \dots, n$) are known, how to get the participation factor by ERA algorithm is shown below:

1st step: Choose r, s , with $pr > 2n$ and $qs > 2n$, According to

$$H(k) = \begin{bmatrix} h(k) & h(k+1) & \cdots & h(k+s-1) \\ h(k+1) & h(k+2) & \cdots & h(k+s) \\ \vdots & \vdots & \ddots & \vdots \\ h(k+r-1) & h(k+r) & \cdots & h(k+r+s-2) \end{bmatrix}_{pr \times qs} \quad (12)$$

We construct the Hankel matrix $H(0), H(1)$.

where

$$h(k) = \begin{bmatrix} h_{11}(k) & h_{12}(k) & \cdots & h_{1q}(k) \\ h_{21}(k) & h_{22}(k) & \cdots & h_{2q}(k) \\ \vdots & \vdots & \ddots & \vdots \\ h_{p1}(k) & h_{p2}(k) & \cdots & h_{pq}(k) \end{bmatrix}_{p \times q} \quad (13)$$

with $h_{ij}(k)$ the impulse response function or cross correlation function between input j and output i for time k .

2nd step: By singular value decomposition, choose $2n$ as order, we get matrices A, B and C .

$$H(0) = USV^T \quad (14)$$

Where $U \in R^{pr \times pr}$, $S \in R^{pr \times qs}$ is diagnostic matrix, $V \in R^{qs \times qs}$.

According to the diagnostic element value of S , choose largest $2n$ orders, we get

$$H(0) \approx U_{2n} S_{2n} V_{2n}^T \quad (15)$$

$$U_{2n} \in R^{pr \times 2n}, \quad S_{2n} \in R^{2n \times 2n}, \quad V_{2n} \in R^{qs \times 2n}$$

The smallest eigensystem realization is

$$A = S_{2n}^{-1/2} U_{2n}^T H(1) V_{2n} S_{2n}^{1/2}, \quad B = S_{2n}^{1/2} V_{2n}^T E_q, \quad C = E_p^T U_{2n} S_{2n}^{1/2} \quad (16)$$

$$\text{Where } E_q = \begin{bmatrix} [I] \\ [0] \\ \vdots \\ [0] \end{bmatrix}_{qs \times q}, \quad E_p^T = \begin{bmatrix} [I] & [0] & \cdots & [0] \end{bmatrix}_{p \times pr}$$

3rd step: According to

$$A[\phi] = [\lambda][\phi] \quad (17)$$

We get eigenvector $[\phi]$ by LS method. Modal participation matrix is

$$[W]_{2n \times q} = [\phi]^{-1} B \quad (18)$$

3 AUTONOMOUS MODAL ANALYSIS

By tracking all poles' changing tendency as the model order increases, an effective optimization mechanism can be designed to make the distinction between the physical and mathematical modes, to realize the automated modal analysis.

The poles which are near physical poles move to physical poles quickly and stabilize soon in the optimization process.

The tendency of mathematical poles is unstable. There are 3 probabilities for mathematical poles, can be distinguished with physical poles and deleted during the optimization process.

1st possibility: Move to a physical pole, cause one real mode with two physical poles, these two poles is very close and the vibration shape very similar. In modal test, if measured points are enough, the vibration shapes of different modes are nearly orthogonal. By the value of MAC of two closely poles this situation can be found. Set a threshold value of MAC, such as 0.5, when the MAC value of two closely poles is greater than this threshold, delete the pole with less modal energy.

2nd possibility: The damping ratio becomes greater step by step. Set a maximum damping value, such as 10%, if a pole's damping is greater than this value, delete this pole.

3rd possibility: The energy corresponding to a pole becomes smaller step by step. According to modal important index MII[7], $MII_r = E_r / E_{\max}$, the value ranges from 0 to 1, E_r is the vibration mean energy of mode r, E_{\max} is the maximum one among all poles. After physical poles stabilized, the energy of mathematical poles will become less and less, so set an energy threshold, such as 0.001, when MII_r is smaller than this, delete this pole.

The principle for initial poles is preferable superabundance than shortage. We can get the initial poles from the stability chart. First we set a threshold value, if the number of stable poles in a very closely frequency band is greater than that value, we set one of the stable poles as an initial pole. Decreasing the threshold will produce more mathematical poles but the physical poles will not be lost. The mathematical poles will be deleted during optimization process.

MIMO autonomous analysis process is summarized as bellow:

1st step: Calculate FRFs or half spectrum for all measurements.

2nd: Choose the frequency band of interest for analysis. In the band, we get the initial poles from the stabilization diagram. To prevent too many mathematical poles exist or physical poles to be lost, the Multivariate Mode Indicator Function (MIF) can be plotted on the stability chart for reference [8, 9]. Only when value of MIF is less than a threshold, such as 0.5, the poles will be reserved as initial poles. Check the local minima of all MIF lines, if there is no initial pole near a local minimum, add one pole from the stabilization diagram which is closest to the local minimum point in frequency domain.

3rd step: Optimize as the method introduced in part 1. During optimization, delete mathematical poles as introduced above.

4th step: When frequency fitting coefficient does not decrease any more, stop the optimization process, and the autonomous analysis is completed.

4 ENGINEERING EXAMPLE

MIMO example:

To testify the algorithm, MIMO test for a brake disk with closed modes is analyzed with autonomous analysis and the modal parameters optimization.

The brake disk is shown in [figure 1](#), its size is:

Outer diameter $R=15\text{cm}$, inner diameter $R=9\text{cm}$, hole diameter $R=4\text{cm}$, height= 6cm , thickness of bottom= 1cm , thickness of wall= 0.7cm , thickness of top= 0.5cm .

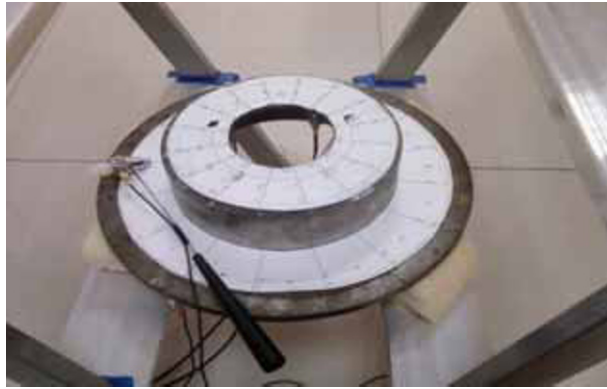


Figure 1: the brake disk for MIMO test

There are total 160 measurement points. By roving a hammer to impact at each point and keeping 4 reference accelerometers fixed, 4 sets of FRF for MIMO modal analysis are obtained.

The frequency band of interest is up to 5000Hz.

[Table 1](#) is the modal parameters comparing with ERA and PolyMAX methods, before and after optimization, as well as autonomous analysis.

From [table 1](#), we can find two methods is very accurate, the left space for optimization is small. After optimization, the frequency fitting coefficient is improved from 18.59% to 17.27% and from 17.66% to 17.06% respectively, both improved. After optimization, the accuracy of frequency fitting coefficient is very close, modal frequency and damping ration is much more in accordance(except 1 pole). If poles in two methods are not chosen suitable, the initial frequency fitting coefficient will be greater obviously, but after optimization, it can still reach the level in [table 1](#). Furthermore, if there are mathematical poles at the beginning, the mathematical poles can be deleted during the optimization process.

In autonomous analysis the initial poles is obtained by ERA stabilization diagram, which including many mathematical poles, these mathematical poles are deleted automatically during the optimization process. The identified parameters are listed in [table 1](#) ERA (optimized). In autonomous analysis, PolyMAX algorithm is used for calculating modal participation factors, L is set 50, MAC threshold value is 0.5, the maximum damping is 10%, energy coefficient value is 0.0001. The MIF threshold value is 0.4 which will affect the initial poles.

Table 1: Modal parameters identified using ERA /PolyMAX before and after optimization as well as autonomous analysis

| modes | Modal freq.(Hz) and damping ratio(%) | | | | | | | | | |
|--------|--------------------------------------|-------|-----------------|-------|----------|-------|---------------------|-------|---------------------|-------|
| | ERA | | ERA (Optimized) | | PolyMAX | | PolyMAX (Optimized) | | Autonomous Analysis | |
| 1 | 899.608 | 0.753 | 900.236 | 0.760 | 900.143 | 0.680 | 900.278 | 0.733 | 900.331 | 0.752 |
| 2 | 918.114 | 0.255 | 918.890 | 0.278 | 918.878 | 0.297 | 919.042 | 0.275 | 919.089 | 0.275 |
| 3 | 1112.055 | 0.643 | 1113.031 | 0.568 | 1112.600 | 0.540 | 1113.015 | 0.553 | 1113.172 | 0.556 |
| 4 | 1370.353 | 0.715 | 1371.023 | 0.713 | 1371.977 | 0.729 | 1371.356 | 0.717 | 1371.126 | 0.709 |
| 5 | 1388.493 | 0.526 | 1388.854 | 0.526 | 1390.588 | 0.495 | 1389.271 | 0.520 | 1388.857 | 0.523 |
| 6 | 1439.577 | 0.378 | 1440.377 | 0.389 | 1439.913 | 0.393 | 1440.364 | 0.393 | 1440.488 | 0.391 |
| 7 | 1446.522 | 0.263 | 1447.307 | 0.251 | 1446.465 | 0.219 | 1447.093 | 0.246 | 1447.354 | 0.245 |
| 8 | 2005.728 | 0.271 | 2007.233 | 0.213 | 2005.645 | 0.268 | 2006.891 | 0.226 | 2008.724 | 0.155 |
| 9 | 2016.708 | 0.607 | 2016.274 | 0.536 | 2016.154 | 1.431 | 2009.274 | 1.082 | 2014.714 | 0.425 |
| 10 | 2025.363 | 0.483 | 2025.696 | 0.491 | 2025.571 | 0.495 | 2025.752 | 0.488 | 2025.193 | 0.467 |
| 11 | 2034.539 | 0.391 | 2035.119 | 0.389 | 2035.716 | 0.437 | 2036.097 | 0.425 | 2036.212 | 0.424 |
| 12 | 2113.402 | 0.183 | 2115.304 | 0.151 | 2114.112 | 0.202 | 2115.231 | 0.159 | 2115.653 | 0.137 |
| 13 | 2555.327 | 0.223 | 2557.386 | 0.180 | 2556.622 | 0.152 | 2557.257 | 0.155 | 2557.805 | 0.153 |
| 14 | 2571.578 | 0.224 | 2573.699 | 0.178 | 2574.428 | 0.152 | 2574.370 | 0.152 | 2574.244 | 0.158 |
| 15 | 2899.162 | 0.659 | 2900.761 | 0.599 | 2901.171 | 0.572 | 2900.935 | 0.586 | 2900.921 | 0.591 |
| 16 | 2905.860 | 0.410 | 2906.501 | 0.417 | 2906.803 | 0.403 | 2906.730 | 0.412 | 2906.657 | 0.415 |
| 17 | 3708.427 | 0.134 | 3708.554 | 0.148 | 3706.795 | 0.179 | 3708.006 | 0.164 | 3708.601 | 0.151 |
| 18 | 3726.574 | 0.170 | 3725.947 | 0.158 | 3725.467 | 0.156 | 3725.798 | 0.156 | 3725.945 | 0.155 |
| 19 | 3948.062 | 0.405 | 3949.087 | 0.431 | 3949.236 | 0.459 | 3949.136 | 0.442 | 3950.312 | 0.425 |
| 20 | 3987.571 | 0.507 | 3986.147 | 0.510 | 3989.689 | 0.458 | 3988.616 | 0.505 | 3986.409 | 0.491 |
| 21 | 4003.776 | 0.280 | 4004.340 | 0.264 | 4008.950 | 0.313 | 4005.559 | 0.263 | 4004.072 | 0.251 |
| 22 | 4043.685 | 0.346 | 4039.308 | 0.290 | 4043.716 | 0.453 | 4037.911 | 0.444 | 4042.064 | 0.177 |
| Fit(f) | 18.59% | | 17.27% | | 17.66% | | 17.06% | | 17.09% | |
| Fit(t) | 56.40% | | 56.10% | | 56.18% | | 56.05% | | 56.06% | |

If the MIF threshold is set to be lower, there is less mathematical poles among the initial poles, and the optimization be completed sooner. However if MIF threshold is set small enough, physical poles may be lost. So observing the MIF curve and averaged power spectrum of FRF or half spectrum is of importance. In this case, averaged FRF power, MIF and frequency band of interest is shown in [figure 2](#). Some modal shapes are shown in [figure 3](#).

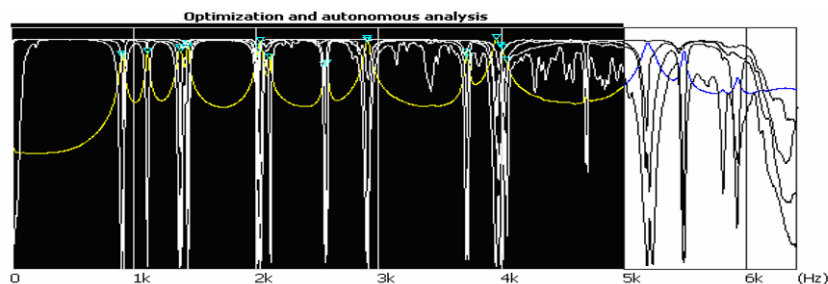


Figure 2: Averaged FRF power, MIF and frequency band of interest

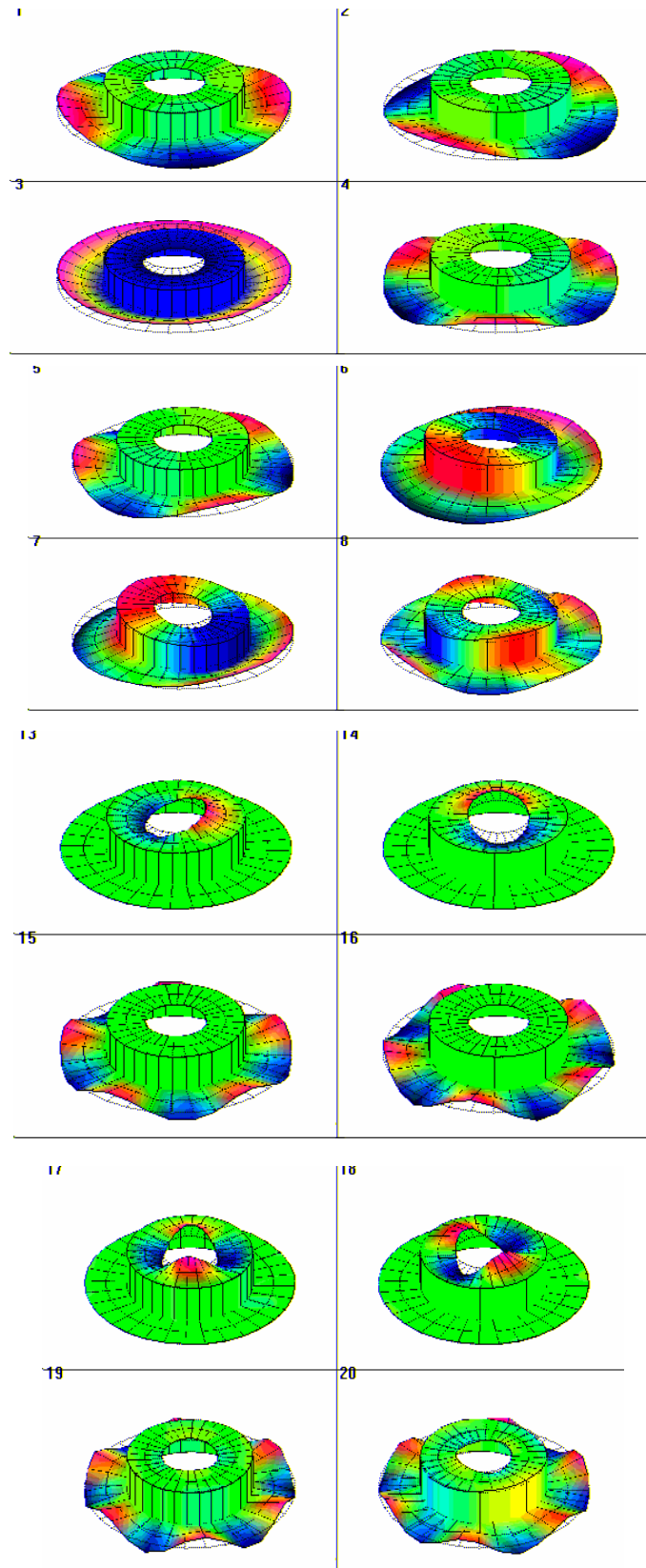


Figure 3: Modal shapes

OMA Example:

The Lupu bridge, located in Shanghai, China, illustrated as [Figure 4](#), is the longest span concrete-filled steel tubular arch bridge in the world now. The bridge is composed of a central span of 500m, two lateral spans of 100m and transition span of 41m, resulting in a total length of 750m. Measuring the acceleration along the 3 orthogonal directions in all the points represented in [Figure 5](#), two reference points permanently located at points 15/34, other accelerometers are roved to obtain four datasets. 5 methods are used for analysis, they are SSI[10], PolyMAX, EFDD[11], PZM[12] and PPM[13]. The most important 12 modes are obtained in the frequency range up to 2Hz.



Figure 4: Lupu Bridge

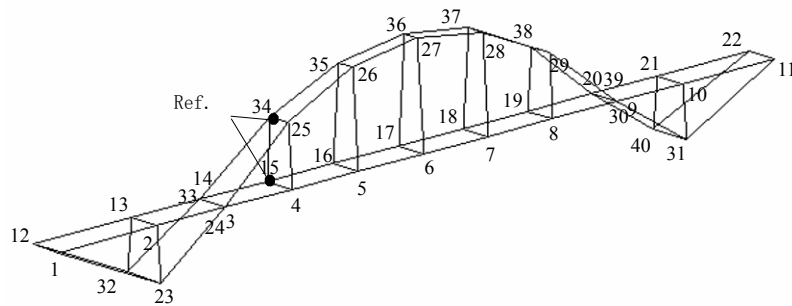


Figure 5: Layout of measuring points and reference points

The comparison of optimized method and 5 algorithms for Lupu Bridge OMA test are listed in [Table 2](#). The identified modal frequencies are very close for different algorithms, and damping ratios are different slightly. Using the modal parameters by the different algorithm as initial solution, after optimization, all the algorithms produced the same optimized parameters. After optimization, the vibration shapes are more harmonized.

Table 2: The comparison of Optimized method and 5 algorithms for Lupu Bridge OMA test

| modes | | Modal frequency(Hz) and Damping(%) | | | | | Optimized |
|--------|-------|------------------------------------|---------|--------|--------|--------|-----------|
| | | SSI | PolyMAX | EFDD | PZM | PPM | |
| 1 | f | 0.362 | 0.362 | 0.362 | 0.362 | 0.361 | 0.362 |
| | ξ | 0.264 | 0.171 | 0.364 | 0.153 | 0.220 | 0.131 |
| 2 | f | 0.401 | 0.401 | 0.402 | 0.402 | 0.402 | 0.401 |
| | ξ | 0.497 | 0.288 | 0.360 | 0.347 | 0.309 | 0.206 |
| 3 | f | 0.600 | 0.600 | 0.591 | 0.598 | 0.599 | 0.600 |
| | ξ | 0.639 | 0.489 | 1.906 | 0.579 | 0.831 | 0.543 |
| 4 | f | 0.704 | 0.700 | 0.698 | 0.699 | 0.699 | 0.701 |
| | ξ | 1.183 | 1.330 | 0.585 | 0.550 | 0.565 | 1.300 |
| 5 | f | 0.894 | 0.892 | 0.892 | 0.892 | 0.895 | 0.893 |
| | ξ | 1.530 | 1.310 | 1.749 | 0.990 | 1.349 | 1.617 |
| 6 | f | 0.989 | 0.991 | 0.990 | 0.992 | 0.990 | 0.989 |
| | ξ | 0.848 | 0.850 | 0.857 | 0.800 | 1.037 | 0.883 |
| 7 | f | 1.111 | 1.114 | 1.118 | 1.108 | 1.117 | 1.126 |
| | ξ | 1.415 | 1.307 | 2.168 | 1.767 | 2.559 | 2.644 |
| 8 | f | 1.174 | 1.173 | 1.175 | 1.174 | 1.175 | 1.175 |
| | ξ | 0.422 | 0.214 | 0.649 | 0.237 | 0.227 | 0.165 |
| 9 | f | 1.339 | 1.336 | 1.338 | 1.337 | 1.338 | 1.338 |
| | ξ | 0.323 | 0.253 | 0.316 | 0.294 | 0.317 | 0.239 |
| 10 | f | 1.483 | 1.477 | 1.467 | 1.479 | 1.481 | 1.474 |
| | ξ | 1.041 | 1.051 | 1.466 | 1.488 | 1.356 | 1.393 |
| 11 | f | 1.616 | 1.627 | 1.625 | 1.617 | 1.622 | 1.616 |
| | ξ | 1.317 | 0.853 | 0.973 | 0.786 | 1.211 | 1.791 |
| 12 | f | 1.815 | 1.819 | 1.812 | 1.822 | 1.812 | 1.819 |
| | ξ | 0.673 | 0.176 | 0.353 | 0.391 | 0.594 | 0.880 |
| Fit(f) | | 21.11% | 22.25% | 24.99% | 22.10% | 20.71 | 16.90% |
| Fit(t) | | 68.49% | 71.59% | 69.43% | 70.92% | 67.31% | 65.70% |

5 CONCLUSIONS

The autonomous modal analysis in the past is based on stabilization diagram [14], the mathematical poles are difficult to distinguish automatically, and the identified parameters can't be optimized further. By using the methods introduced bellow, these two problems are solved.

1. Put forward a frequency fitting coefficient. By which the accuracy of the identified parameters can be compared. It is the mathematical base for the modal parameters optimization.
2. Put forward a MIMO optimization method. By keeping participation factors and vibration shapes unchanged, optimize the modal frequency and damping. The difficulty of this method is to calculate the participation factors with known modal frequency and damping. By using PolyMAX, PRCE or ERA algorithms, this problem is solved. Through optimization, the

identified parameters by different methods are almost the same.

3. Put forward an optimization mechanism of deleting mathematical poles automatically. Helped by modal important index (MII) and multivariate mode indicator function (MvMIF), the autonomous modal analysis can be realized. The modal parameters identified by autonomous method are free from mathematical poles.

REFERENCES

- [1] Juang, J.-N., and Pappa, R.S. An Eigensystem Realization Algorithm for Modal Parameter Identification and Mode Reduction, *Journal of Guidance, Control, and Dynamics*, Vol 8, No. 1, 1985, pp 620-627
- [2] Bart Peeters, Patrick Guillaume, Herman Van der Auweraer, etc, Automotive and aerospace applications of the PolyMAX modal parameter estimation method. Proc. of 22th IMAC, 2004
- [3] Vold H., Rocklin, G. T., The Numerical Implementation of A Multi-Input Modal Estimation Method for Mimi-Computers, Proc. of 1st IMAC, 1982
- [4] D.B.Li, Q.H.Lu, Test modal analysis and application, Science Press, 2001, Beijing, P.R.C, pg 171-173.
- [5] E. Pierro, E. Mucchi, L. Soria and A. Vecchio, On the vibro-acoustical operational modal analysis of a helicopter cabin, *Mechanical Systems and Signal (2008)*, doi:10.1016/j.ymssp.2008.10.00
- [6] W.Fladung and R.Rost, Application and Correction of the Exponential Window for Frequency Response Functions, *Mechanical Systems and Signal Processing*, vol. 11, issue 1, pp. 23-36, 1997
- [7] J.M.Liu, H.Q.Ying, S.Shen, S.W.Dong, the Function of Modal Important Index in Autonomous Modal Analysis, Proc. of 25th IMAC 2007
- [8] William R. the Multivariate Mode Indicator Function in Modal Analysis, Proc. of 3th IMAC, 1985
- [9] Nash M. Use of the Multivariate Mode Indicator Function for Normal Mode Determination. Proc. of 6th IMAC, 1988
- [10] Hermans L, Vander Auweraer H. Modal testing and analysis of structures under operational conditions; industrial applications. *Mechanical Systems and Signal Processing*, 1999;13(2):193-216
- [11] J.M.Liu, H.Q.Ying, S.Shen, M.Ying, A fast frequency domain modal parameter identification algorithm, Proc., 24th IMAC 2006
- [12] Brincker, R., C. Ventura and P. Andersen: "Damping Estimation by Frequency Domain Decomposition", Proc. 19th IMAC, 2001.
- [13] H.Q.Ying, J.M.Liu, S.Shen, etc. Precise output-only modal parameter identification from power spectrum. Proc., 24th IMAC 2006
- [14] Richard Pappa. George H. James III and Davicid C. Zimmerman, Autonomous Modal Identification of the Space Shuttle Tail Rudder. NASA Technical Memorandum 112866, June 1997

Independent Modal Space Control Technique for Mitigation of Human-Induced Vibrations in Floors

D.S. Nyawako, P. Reynolds, M. Hudson

Vibration Engineering Section

Department of Civil and Structural Engineering, The University of Sheffield

Sir Frederick Mappin Building, Mappin Street, Sheffield, S1 3JD, UK

ABSTRACT

Significant levels of vibration in civil engineering floors under human-induced excitations often cause annoyance to their occupants. Various Active Vibration Control (AVC) strategies have been investigated in the past for mitigating the effect of such vibrations in some problematic floors; for example, control laws making use of acceleration feedback and velocity feedback schemes. The research presented in this paper aims to demonstrate that the use of the Independent Modal Space Control (IMSC) approach, previously tried and implemented in marine applications, can be invaluable to isolating and controlling specific modes of vibration in civil engineering floors.

This approach may prove attractive particularly in floors with very close modes of vibrations where only certain modes prove to be problematic under human-induced excitations. The IMSC technique is implemented in a reduced order model (ROM) of a laboratory structure and two sets of studies with this technique are presented here. In the first study, only the first mode of vibration of the laboratory structure is targeted, while in the second study, both the first and second vibration modes of the laboratory structure are targeted.

1 INTRODUCTION

Civil engineering structures, particularly floors, have become prone to human-induced vibrations as a result of advancements in structural technology enabling design of light and slender structures often spanning long distances. Many contemporary floor structures also comprise more open-plan layouts with less inherent damping thereby increasing their susceptibility to such vibrations (Bachmann 1992, Nyawako and Reynolds 2007).

There has been significant research in recent years into passive, semi-active and active control of vibrations in civil engineering structures (Bachman and Weber 1995, Setareh 2002, Koo et al 2004, Hanagan et al 2003a, Diaz and Reynolds 2009). As pertains to active vibration control of these structures, there have been rigorous studies aimed at trying to derive suitable control laws for different scenarios, ranging from controlling wind/earthquake induced vibrations in civil engineering structures to controlling human-induced vibrations. Some of the control laws that have been investigated and implemented in the past for mitigating human induced vibrations in floors include direct velocity feedback (DVF), direct acceleration feedback (DAF), Compensated Acceleration Feedback (CAF), and Response Dependent Velocity Feedback schemes (Hanagan et al 2003b, Hanagan et al 2000, Diaz and Reynolds 2010, Nyawako and Reynolds 2009).

Notwithstanding the above mentioned active vibration control laws, the potential benefits of other categories of active control approaches widely used in the mechanical and aerospace sectors are being investigated for mitigation of human induced vibrations in civil engineering structures. Among these categories is the Independent Modal Space Control technique (IMSC), a modal control approach. This technique has been extensively used in the marine industry for developing isolation systems that improve the crew and passenger comfort (Daley et al 2004). Its attractiveness stems from the fact that it can be invaluable for isolating and controlling target modes of vibration in civil engineering structures.

The basic idea of the IMSC approach is that by looking at frequency response functions of structural systems, for example of floors, designers can detect troublesome modes or groups of modes. Desired structural behaviours in terms of modal damping

ratios and frequencies can be defined and a modal control strategy can then be designed to adjust the closed-loop behaviour in some suitable way (Inman 2001, Daley et al 2004, Fang et al 2003). Performances that can be realised are dependent on the number of sensor and actuators available as well as their dynamics. It has widely been observed that an IMSC implementation typically requires the number of actuators to be equal to that of modelled modes (Nguyen 1991).

The work presented here explores the possibility of realising an IMSC controller for mitigating human induced vibrations in floors. A structural model and input forces used in analytical simulations is introduced. A brief overview of the IMSC strategy used in this analytical work is shown and some results of analytical simulations for two different IMSC controllers setting are presented. IMSC controller 1 aims to target only the first mode of vibration of the reduced order model (ROM) of the laboratory structure while IMSC controller 2 aims to target both the first and second modes of vibration of the ROM. Some results and conclusions are finally presented.

2 STRUCTURAL MODEL AND INPUT FORCES

2.1 Structural Model

The laboratory structure is a simply-supported in-situ cast post-tensioned slab strip of span 10.8m. Its total length is 11.2m, which includes 200mm overhangs over the knife-edge supports. It has a width of 2.0m, depth of 275mm, and weighs approximately 15 tonnes. The first and second modes of vibration have natural frequencies of 4.55 Hz and 17.02 Hz with modal damping ratios of 0.4 % and 0.2 %, respectively. The first mode is particularly prone to excitation by the second and third harmonics of walking excitation (Reynolds 2000).

The IMSC controller design presented in these studies is formulated from a ROM of the laboratory structure. This ROM is developed based on uncontrollability and unobservability at node points of vibration modes of the laboratory structure (Seto and Mitsuta 1992). The mode order is chosen as two here and the node points of the third bending mode have been chosen as the locations of the masses for the lumped parameter system as shown in Fig. 1.

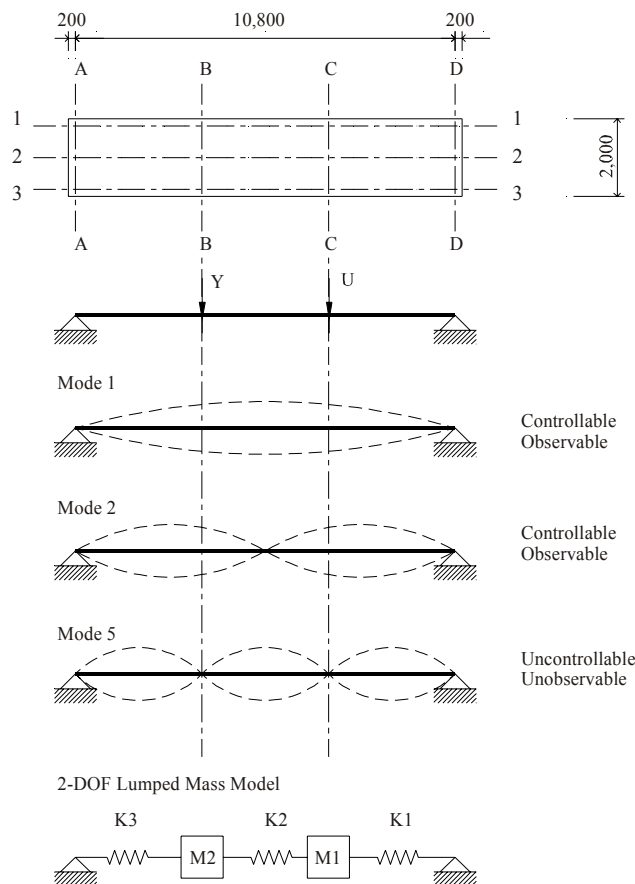


Fig. 1 Laboratory structure grid, mode shapes and 2-DOF lumped mass model

By making use of a mass normalised scaling for the mode shapes at the chosen locations of the third bending mode, i.e. $[\Phi]^T [M][\Phi] = [I]$, the mass and stiffness matrices of the physical co-ordinates can be derived from Eqs. (1) and (2). Equation 3 is often used to obtain convergence i.e. diagonalisation of the mass and stiffness matrices of the physical co-ordinates.

$$M = (\Phi^T)^{-1} \Phi^{-1} = (\Phi \Phi^T)^{-1} \quad M^{-1} = (\Phi \Phi^T) \quad (1)$$

$$K = (\Phi^T)^{-1} \Omega^2 \Phi^{-1} \quad (2)$$

$$[\delta\phi_{11} \quad \delta\phi_{21} \quad \delta\phi_{12} \quad \delta\phi_{22}]^T = \left[\frac{\partial \varepsilon_r}{\partial \phi} \right]^T \left[\left[\frac{\partial \varepsilon_r}{\partial \phi} \right] \left[\frac{\partial \varepsilon_r}{\partial \phi} \right]^T \right]^{-1} (-\varepsilon_r) \quad (3)$$

By applying Eqs. (1), (2) and (3) to the mass-normalised mode shapes of the laboratory structure derived from a Finite Element model, the following physical parameters of the 2-DOF lumped mass model in Eqs. (4) and (5) are obtained. $M_1 = M_2 = 5596.3 \text{ Kg}$; $K_1 = K_3 = 0.4565e+7 \text{ N/m}$; $K_2 = 2.9876e+7 \text{ N/m}$. The assumed Rayleigh damping matrix is as shown in Eq. (6).

$$\text{Mass matrix (Kg)} \quad M = \begin{bmatrix} 5596.3 & 0 \\ 0 & 5596.3 \end{bmatrix} \quad (4)$$

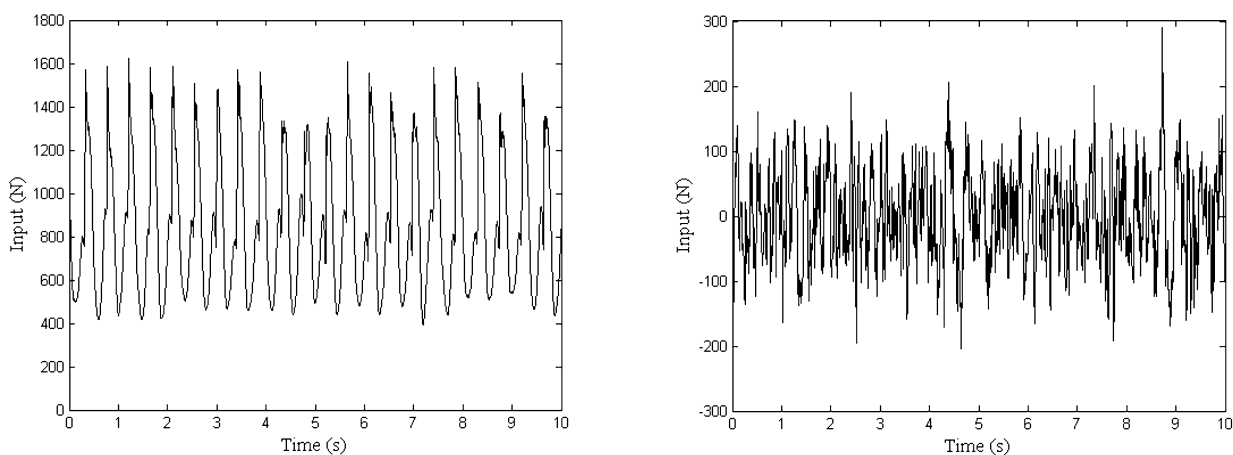
$$\text{Stiffness matrix (N/m)} \quad K = \begin{bmatrix} 3.4441e+7 & -2.9876e+7 \\ -2.9876e+7 & 3.4441e+7 \end{bmatrix} \quad (5)$$

$$\text{Damping matrix (Ns/m)} \quad C = \begin{bmatrix} 1896.5 & -616.7 \\ -616.7 & 1896.5 \end{bmatrix} \quad (6)$$

2.2 Input Forces for Analytical Studies

Human movement is often characterised by rhythmical body motions such as walking and running. Such motions induce dynamic loads into the structures they occupy and may result in significant resonant, transient, steady-state or impulsive responses (Bachmann et al 1995).

The disturbance forces considered here are walking force time histories obtained from treadmill walking tests and a random excitation signal with a frequency span of 0 – 40 Hz. These are shown in Figs. 2a and 2b for 10s durations.



a) Walking force time history (2.25 Hz)

(b) Random excitation force (0 – 40 Hz)

Fig. 2 Walking force time history and random excitation force time history for analytical simulations

3 INDEPENDENT MODAL SPACE CONTROL (IMSC) STRATEGY

For a discrete set of measurements, \underline{x} , the equation of motion for the 2-DOF lumped mass model of the laboratory structure shown in Fig. 1 can be determined as shown in Eq. 7. The parameters M, C, K are as shown in Eqs. 4 and 5. f denotes the vector of applied forces. For the IMSC approach, a decoupled independent modal description of a structure is often necessary. The decoupled independent modal space description outlined in Eq. 8, which is derived from Eq. 7 can be obtained from the transformation shown in Eq. 9 (Daley 2004, Inman 2001). ϕ is an orthonormal matrix of the eigenvectors of $M^{-1/2}KM^{-1/2}$.

$$[M]\{\ddot{x}(t)\} + [C]\{\dot{x}(t)\} + [K]\{x(t)\} = f \quad (7)$$

$$\ddot{\eta} + \Lambda\dot{\eta} + \Omega\eta = \underline{f}^m \quad (8)$$

$$\underline{\eta} = \phi^T M^{1/2} \underline{x} \quad (9)$$

Where:

$$\Lambda = \begin{bmatrix} 2\zeta_1\omega_1 & & & \\ & \ddots & & \\ & & 2\zeta_i\omega_i & \\ & & & \ddots \end{bmatrix}, \Omega = \begin{bmatrix} \omega_1^2 & & & \\ & \ddots & & \\ & & \omega_i^2 & \\ & & & \ddots \end{bmatrix}, \underline{f}^m - \text{modal force,}$$

Λ - damping ratios, Ω - spectral matrix

Thus, the problem is transformed from a MIMO (multiple-input multiple-output) control design problem in Eq. (7) into a series of multiple independent SISO (single-input single-output) control problem in Eq. (8). A general independent modal controller can now be defined as shown in Eq. (10). The closed loop description of each mode takes the form of Eq. (11), which enables the damping and frequency of each mode to be manipulated independently. The configuration of the vector of modal forces, \underline{f}^m can be set depending on the number of modes to be controlled whilst taking into account the number of sensors and actuators available as well. In the work presented here, two IMSC controllers are designed as explained in section 1.4.

$$\underline{f}^m(s) = \underline{r}_m(s) - G_m(s)\underline{\eta}(s) \quad (10)$$

Where:

$$G_m(s) = \begin{bmatrix} g_1(s) & 0 & \dots & 0 \\ 0 & g_2(s) & \dots & 0 \\ \vdots & \vdots & \ddots & 0 \\ 0 & 0 & 0 & g_m(s) \end{bmatrix}$$

$$\eta_i(s) = \frac{1}{s^2 + 2\zeta_i\omega_i s + \omega_i^2 + g_i(s)} r_{m,i}(s) \quad (11)$$

Since the controller in Eq. (10) is defined in the modal space, it cannot be implemented directly and a transformation is necessary from the measured input signals. The matrix transformation required for extracting the first two bending modes of the laboratory structure at the locations pre-determined can be determined by making use of the rows of the matrix $\phi^T M^{1/2}$. This enables Eq. (10) to be re-arranged in the physical domain as shown in Eq. (12) and this can now be implemented directly. A vector $y(s)$ contains the sensor measurements and vector $f(s)$ is the local demand force.

$$f(s) = M^{1/2} \phi r_m(s) - M^{1/2} \phi G_m(s) \phi^T M^{1/2} y(s) \quad (12)$$

The local demand forces can now be determined from the linear displacements, velocities and accelerations at each actuator location as noted in Eq. (12). For the work presented in this paper, once the local demand forces are evaluated, an inverse actuator model (i.e. an inverse model for the APS Dynamics Model 400 Electrodynamic Shakers) is used to calculate the desired control voltage signal which is then transmitted to the actuators. A typical global processing stage is demonstrated in Fig. 3.

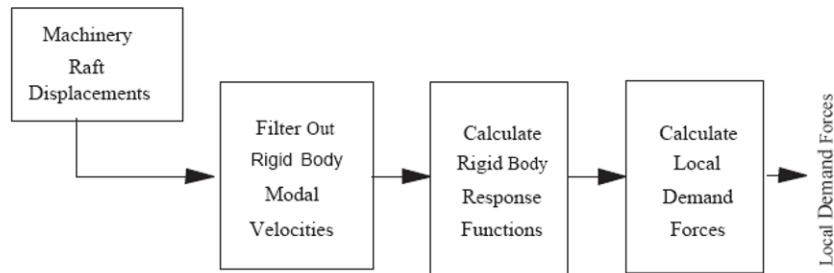


Fig. 3. Typical global control processor (after Daley et al. 2004)

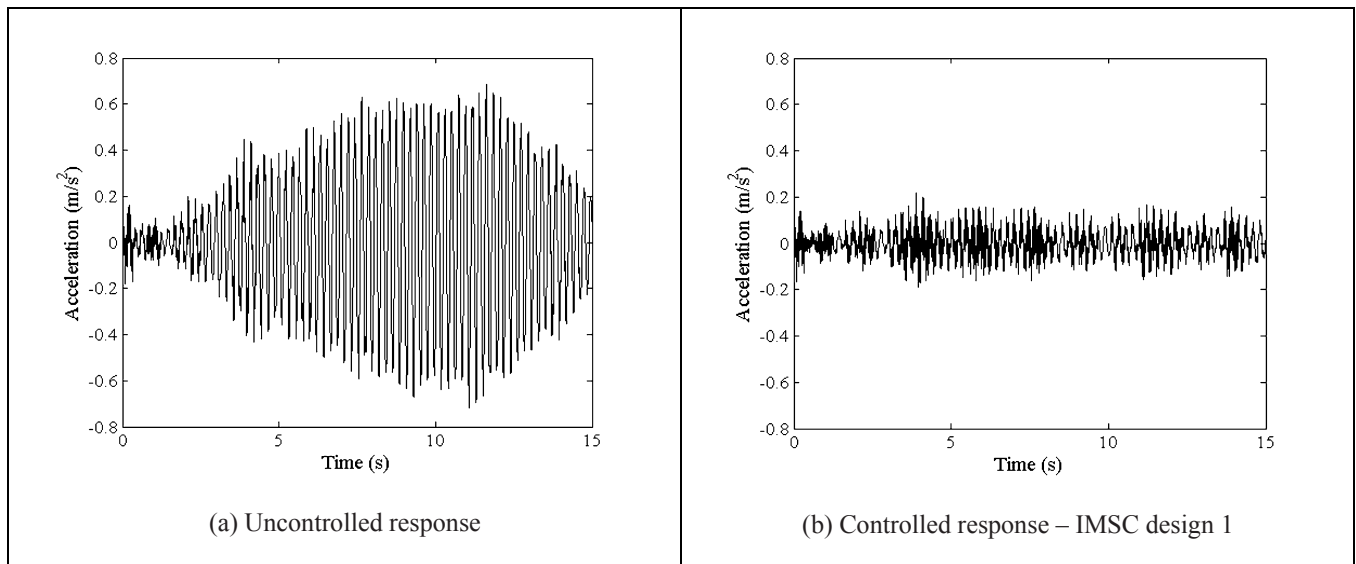
4 ANALYTICAL SIMULATIONS

The analytical simulations presented in this work cover two IMSC controller designs

- IMSC Controller 1 – This controller aims to increase the damping in the first mode of vibration of the ROM of the laboratory structure by up to 20 times while not engaging the second mode of vibration.
- IMSC Controller 2 – This controller aims to increase the damping in both the first and second modes of vibration of ROM of the laboratory structure by up to 20 times.

4.1 IMSC Controller 1

The settings of this controller are set so as to target an increase in damping of the 1st mode only by up to 20 times whilst not engaging the second mode of vibration. Figs. 4a and 4b show the uncontrolled and controlled acceleration responses of the laboratory structure model to a walking excitation force noted in section 1.2. Fig. 4c illustrates the control force whilst Fig. 4d shows the point mobility frequency response function for the uncontrolled and controlled structural model. The peak 1s running RMS acceleration responses for the uncontrolled and controlled ROM are 0.44 m/s^2 and 0.088 m/s^2 , respectively. This follows the recommendation of ISO 2631:1997, for which the peak 1s running RMS is defined as the Maximum Transient Vibration Value (MTVV).



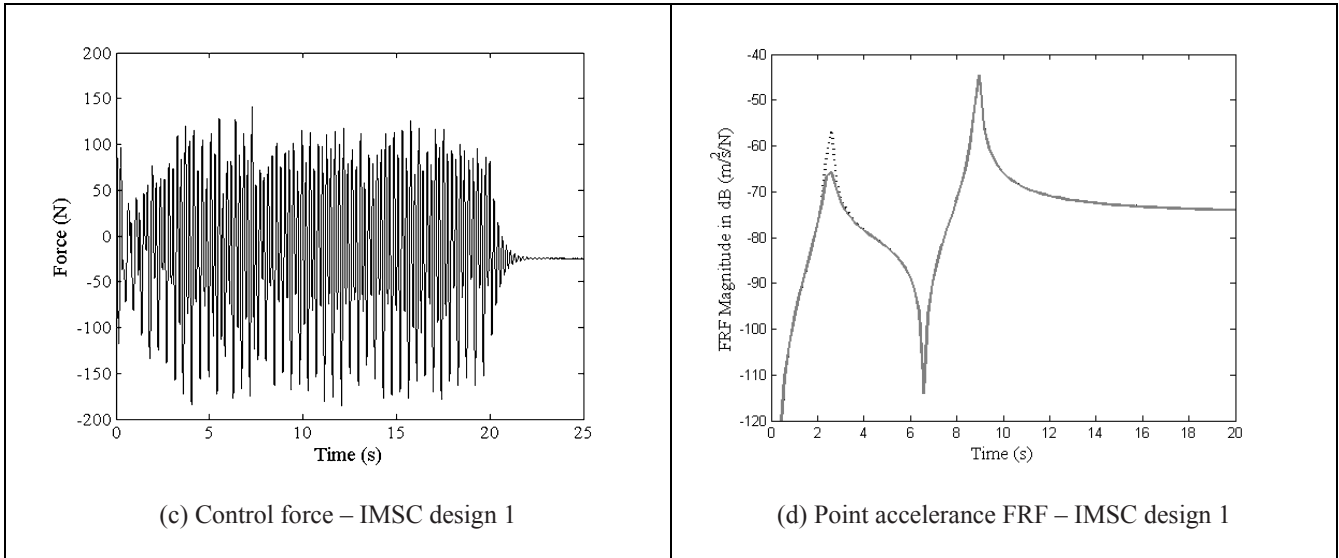
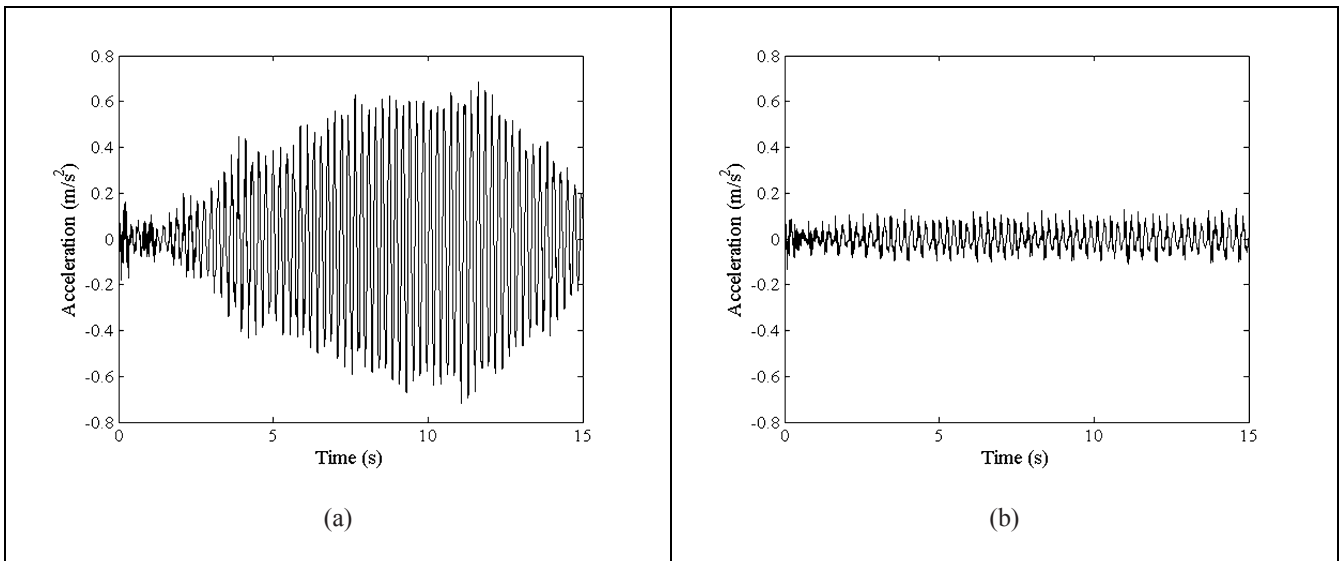
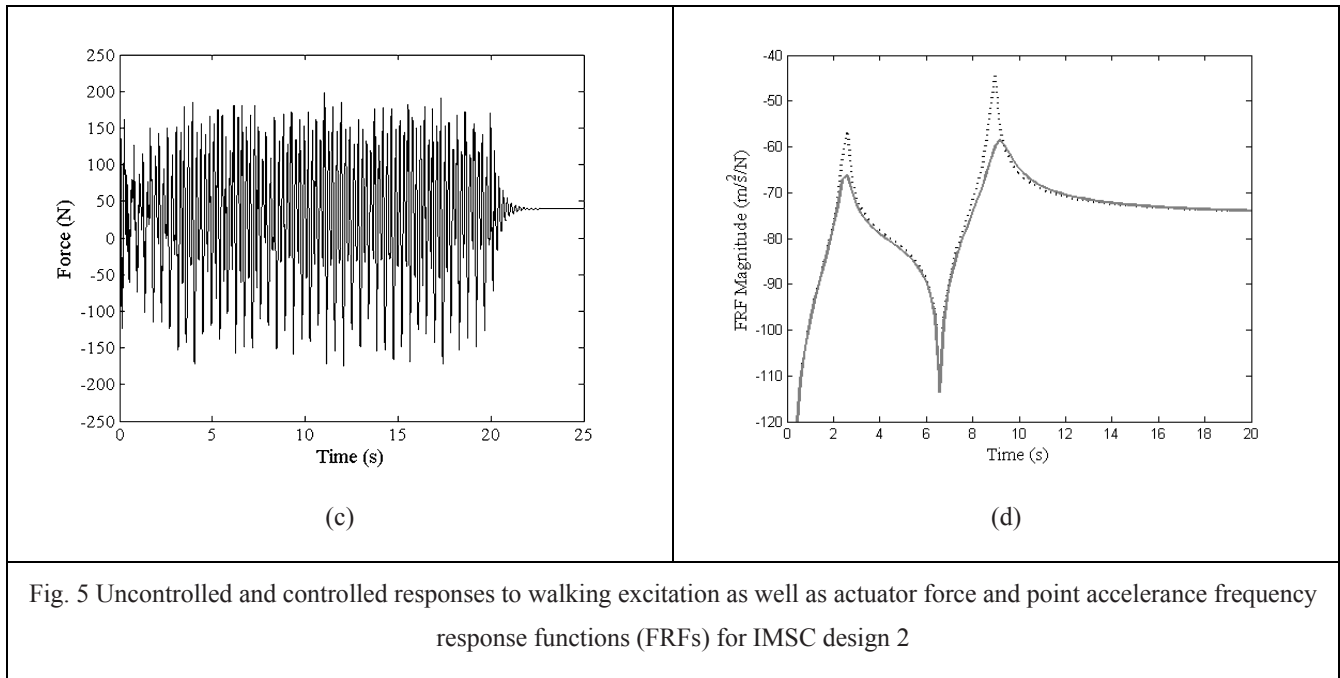


Fig. 4 Uncontrolled and controller responses to walking excitation as well as actuator force and point acceleration frequency response functions (FRFs) for IMSC design 1

4.2 IMSC Controller 2

In this second controller design, the settings are tuned to achieve an increase in damping of both the 1st and 2nd modes of the ROM structural model by up to 20 times. Figs. 5a and 5d show the uncontrolled and controlled acceleration responses of the laboratory structure model to a walking excitation force noted in section 1.2. Fig. 5c illustrates the control force and Fig. 5d shows the point mobility frequency response function for the uncontrolled and controlled structural model. The peak 1s running RMS acceleration responses for the uncontrolled and controlled ROM are 0.44 m/s² and 0.054m/s², respectively.





5 RESULTS AND CONCLUSIONS

Tables 1 and 2 demonstrate the vibration mitigation performances of the two IMSC controller structures outlined in section 1.4. The benefits of the IMSC controller design technique in meeting the desired vibration mitigation performances can clearly be seen from these results.

Table 1. Peak 1s running RMS acceleration for uncontrolled and controlled laboratory structure model under walking excitation for IMSC Controllers 1 and 2

| Case | Uncontrolled (ms^{-2}) | Controlled (ms^{-2}) | % red. |
|-------------------|--------------------------------------|------------------------------------|--------|
| IMSC Controller 1 | 0.44 | 0.088 | 80.0 % |
| IMSC Controller 2 | 0.44 | 0.054 | 87.7 % |

Table 2. Attenuations in vibration at target modes of vibration (4.55 Hz and 17.02 Hz) for IMSC Controllers 1 and 2

| Case | Attenuation Mode 1 (dB) | Attenuation Mode 2 (dB) |
|-------------------|----------------------------|----------------------------|
| IMSC Controller 1 | 10.0 | 0.0 |
| IMSC Controller 2 | 10.0 | 13.0 |

Based on this work, the modal control technique is seen as a potential and attractive method for controlling human induced vibrations in civil engineering floor structures. As previously noted by some researchers, its benefit is that civil engineering designers can now evaluate frequency response functions of floors, detect a troublesome mode or groups of modes and design a modal control strategy to adjust the closed loop behaviour in some suitable way. The effects of the controller designer on other modes can also be evaluated to determine its robustness.

6 ACKNOWLEDGEMENT

The authors would like to acknowledge the financial assistance provided by the UK Engineering and Physical Sciences Research Council (EPSRC) through a responsive mode grant entitled “Active Control of Human-Induced Vibration” (Ref: EP/H009825/1).

REFERENCES

- Bachmann, H. (1992) Case Studies of Structures with Man-Induced Vibrations, *Journal of Structural Engineering*, **118**(3).
- Bachmann, H. and Weber, B. (1995) Tuned Vibration Absorbers for Lively Structures, *Structural Engineering International* 1/95, Science and Technology, 31–36.
- Daley, S., Johnson, F.A., Pearson, J.B. and Dixon, R. (2004) Active Vibration Control for Marine Applications, *Control Engineering Practice* 12, 465 – 474.
- Diaz, I.M., and Reynolds, P. (2009) Robust Saturated Control of Human-Induced Floor Vibrations via a Proof-Mass Actuator, *Smart Materials and Structures* 18, 1 – 10.
- Diaz, I.M., and Reynolds, P. (2010) Acceleration Feedback Control of Human-Induced Floor Vibrations, *Engineering Structures* 32, 163-173.
- Fang, J Q , Li, Q S and Jeary A P (2003) Modified independent modal space control of m.d.o.f systems, *Journal of Sound and Vibration* 261, pp 421 – 441.
- Hanagan, L.M., Kulasekere, E.C., Walgama, K.S., and Premaratne, K. (2000) Optimal Placement of Actuators and Sensors for Floor Vibration Control, *Journal of Structural Engineering*, **126**(12), 1380–1387.
- Hanagan, L.M., Murray, T.M., and Premaratne, K. (2003a) Controlling Floor Vibration with Active and Passive Devices, *The Shock and Vibration Digest*, **35**(5), 347–365.
- Hanagan, L.M., Raebel, C.H., and Trethewey, M.W. (2003b) Dynamic Measurements of In-Place Steel Floors to Assess Vibration Performance, *Journal of Performance of Constructed Facilities*, **17**(3), 126–135.
- Inman, D.J. (2001) Active Modal Control for Smart Structures, *Phil. Trans. Royal Society London A* 359, 205 – 219.
- ISO 2631:1997 Mechanical vibration and shock evaluation of human exposure to whole body vibration.
- Koo, J.H., Ahmadian, M., Setareh, M., and Murray, T.M. (2004) In Search of Suitable Control Methods for Semi-Active Tuned Vibration Absorbers, *Journal of Vibration and Control*, **10**(2), 163–174.
- Nguyen, C C (1991) Implementation of Actuators for the Independent Modal Space Control Scheme, *Computers Elec. Engng* Vol. 17, No. 2, pp. 75-90.
- Nyawako D. and Reynolds P. (2007) Technologies for mitigation of human-induced vibrations in civil engineering structures, *The Shock and Vibration Digest*, 39 (6), 465-493.
- Nyawako, D. and Reynolds, P. (2009) Response-dependent velocity feedback control for mitigation of human-induced floor vibrations, *Smart Materials and Structures* 18, 1 – 14.
- Reynolds P. (2000) The effects of raised access flooring on the vibrational performance of long-span concrete floors PhD Thesis, University of Sheffield, UK, February 2000.
- Setareh, M. (2002) Floor Vibration Control using Semi-Active Tuned Mass Dampers, *Canadian Journal of Civil Engineering*, **29**, 76–84.
- Seto, K. and Mitsuta, S. (1992) A new method for making a reduced order model flexible structures using unobservability and uncontrollability and its application in vibration control, In: *Proc. 1st Int. Conf. Motion and Vibration Control (MOVIC)*, 152–158.

Nonlinear Normal Modes of a Full-Scale Aircraft

M. Peeters, G. Kerschen, J.C. Golinval

Structural Dynamics Research Group
Department of Aerospace and Mechanical Engineering
University of Liège, Liège, Belgium
E-mail: m.peeters, g.kerschen, jc.golinval@ulg.ac.be

C. Stéphan, P. Lubrina

Office National d'Etudes et de Recherches Aérospatiales (ONERA)
DADS-ADSE
Châtillon, France
E-mail: cyrille.stephan, pascal.lubrina@onera.fr

ABSTRACT

The objective of this paper is to demonstrate that the numerical computation of the nonlinear normal modes (NNMs) of complex real-world structures is now within reach. The application considered in this study is the airframe of the Morane-Saulnier Paris aircraft, whose ground vibration tests have exhibited some nonlinear structural behaviors. The finite element model of this aircraft, elaborated from drawings, has more than 80000 degrees of freedom, and softening nonlinearities exist in the connection between the external fuel tanks and the wing tips. From this model, a reduced-order model, which is accurate in the [0-100Hz] range, is constructed using the Craig-Bampton technique. The NNMs of the reduced model are then computed using a numerical algorithm combining shooting and pseudo-arclength continuation. The results show that the NNMs of this full-scale structure can be computed accurately even in strongly nonlinear regimes and with a reasonable computational burden. Nonlinear modal interactions are also highlighted by the algorithm and are discussed.

1 INTRODUCTION

Nonlinear normal modes (NNMs) offer a solid theoretical and mathematical tool for interpreting a wide class of nonlinear dynamical phenomena, yet they have a clear and simple conceptual relation to the LNMs^[1–3]. However, most structural engineers still view NNMs as a concept that is foreign to them, and they do not yet consider NNMs as a useful concept for structural dynamics. One reason supporting this statement is that most existing constructive techniques for computing NNMs are based on asymptotic approaches and rely on fairly involved mathematical developments.

There have been very few attempts to compute NNMs using numerical methods^[4–7]. Algorithms for the continuation of periodic solutions are really quite sophisticated and advanced (see, e.g.,^[8–10]), and they have been extensively used for computing the forced response and limit cycles of nonlinear dynamical systems (see, e.g.,^[11]). Interestingly, they have not been fully exploited for the computation of nonlinear modes.

In this paper, we support that these numerical algorithms pave the way for an effective and practical computation of NNMs. The proposed algorithm, implemented in MATLAB, relies on two main techniques, namely a shooting procedure and a method for the

continuation of NNM motions. The objective is to demonstrate that the numerical computation of the NNMs of complex real-world structures is then within reach. The application considered in this study is the airframe of the Morane-Saulnier Paris aircraft, whose ground vibration tests have exhibited some nonlinear structural behaviors.

2 NONLINEAR NORMAL MODES (NNMS)

A detailed description of NNMs and their fundamental properties (e.g., frequency-energy dependence, bifurcations and stability) is given in ^[1–3]. For completeness, the two main definitions of an NNM are briefly reviewed in this section.

The free response of discrete conservative mechanical systems with n degrees of freedom (DOFs) is considered, assuming that continuous systems (e.g., beams, shells or plates) have been spatially discretized using the finite element method. The equations of motion are

$$\mathbf{M} \ddot{\mathbf{x}}(t) + \mathbf{K} \mathbf{x}(t) + \mathbf{f}_{nl} \{\mathbf{x}(t), \dot{\mathbf{x}}(t)\} = 0 \quad (1)$$

where \mathbf{M} is the mass matrix; \mathbf{K} is the stiffness matrix; \mathbf{x} , $\dot{\mathbf{x}}$ and $\ddot{\mathbf{x}}$ are the displacement, velocity and acceleration vectors, respectively; \mathbf{f}_{nl} is the nonlinear restoring force vector.

There exist two main definitions of an NNM in the literature due to Rosenberg and Shaw and Pierre:

1. Targeting a straightforward nonlinear extension of the linear normal mode (LNM) concept, Rosenberg defined an NNM motion as a *vibration in unison* of the system (i.e., a synchronous periodic oscillation).
2. To provide an extension of the NNM concept to damped systems, Shaw and Pierre defined an NNM as a two-dimensional invariant manifold in phase space. Such a manifold is invariant under the flow (i.e., orbits that start out in the manifold remain in it for all time), which generalizes the invariance property of LNM to nonlinear systems.

At first glance, Rosenberg's definition may appear restrictive in two cases. Firstly, it cannot be easily extended to nonconservative systems. However, the damped dynamics can often be interpreted based on the topological structure of the NNMs of the underlying conservative system ^[3]. Secondly, in the presence of internal resonances, the NNM motion is no longer synchronous, but it is still periodic.

In the present study, an NNM motion is therefore defined as a (*non-necessarily synchronous*) *periodic motion* of the conservative mechanical system (1). As we will show, this extended definition is particularly attractive when targeting a numerical computation of the NNMs. It enables the nonlinear modes to be effectively computed using algorithms for the continuation of periodic solutions.

3 NUMERICAL COMPUTATION OF NNMS

The numerical method proposed here for the NNM computation relies on two main techniques, namely a shooting technique and the pseudo-arclength continuation method. A detailed description of the algorithm is given in ^[12].

3.1 Shooting Method

The equations of motion of system (1) can be recast into state space form

$$\dot{\mathbf{z}} = \mathbf{g}(\mathbf{z}) \quad (2)$$

where $\mathbf{z} = [\mathbf{x}^* \quad \dot{\mathbf{x}}^*]^*$ is the $2n$ -dimensional state vector, and star denotes the transpose operation, and

$$\mathbf{g}(\mathbf{z}) = \begin{pmatrix} \dot{\mathbf{x}} \\ -\mathbf{M}^{-1} [\mathbf{K}\mathbf{x} + \mathbf{f}_{nl}(\mathbf{x}, \dot{\mathbf{x}})] \end{pmatrix} \quad (3)$$

is the vector field. The solution of this dynamical system for initial conditions $\mathbf{z}(0) = \mathbf{z}_0 = [\mathbf{x}_0^* \quad \dot{\mathbf{x}}_0^*]^*$ is written as $\mathbf{z}(t) = \mathbf{z}(t, \mathbf{z}_0)$ in order to exhibit the dependence on the initial conditions, $\mathbf{z}(0, \mathbf{z}_0) = \mathbf{z}_0$. A solution $\mathbf{z}_p(t, \mathbf{z}_{p0})$ is a periodic solution of the autonomous system (2) if $\mathbf{z}_p(t, \mathbf{z}_{p0}) = \mathbf{z}_p(t + T, \mathbf{z}_{p0})$, where T is the minimal period.

The NNM computation is carried out by finding the periodic solutions of the governing nonlinear equations of motion (2). In this context, the *shooting method* is probably the most popular numerical technique. It solves numerically the two-point boundary-value problem defined by the periodicity condition

$$\mathbf{H}(\mathbf{z}_{p0}, T) \equiv \mathbf{z}_p(T, \mathbf{z}_{p0}) - \mathbf{z}_{p0} = \mathbf{0} \quad (4)$$

$\mathbf{H}(\mathbf{z}_0, T) = \mathbf{z}(T, \mathbf{z}_0) - \mathbf{z}_0$ is called the *shooting function* and represents the difference between the initial conditions and the system response at time T . Unlike forced motion, the period T of the free response is not known a priori.

The shooting method consists in finding, in an iterative way, the initial conditions \mathbf{z}_{p0} and the period T that realize a periodic motion. To this end, the method relies on direct numerical time integration and on the Newton-Raphson algorithm.

Starting from some assumed initial conditions $\mathbf{z}_{p0}^{(0)}$, the motion $\mathbf{z}_p^{(0)}(t, \mathbf{z}_{p0}^{(0)})$ at the assumed period $T^{(0)}$ can be obtained by numerical time integration methods (e.g., Runge-Kutta or Newmark schemes). In general, the initial guess $(\mathbf{z}_{p0}^{(0)}, T^{(0)})$ does not satisfy the periodicity condition (4). A Newton-Raphson iteration scheme is therefore to be used to correct an initial guess and to converge to the actual solution. The corrections $\Delta\mathbf{z}_{p0}^{(k)}$ and $\Delta T^{(k)}$ at iteration k are found by expanding the nonlinear function

$$\mathbf{H}\left(\mathbf{z}_{p0}^{(k)} + \Delta\mathbf{z}_{p0}^{(k)}, T^{(k)} + \Delta T^{(k)}\right) = 0 \quad (5)$$

in Taylor series and neglecting higher-order terms (H.O.T.).

The phase of the periodic solutions is not fixed. If $\mathbf{z}(t)$ is a solution of the autonomous system (2), then $\mathbf{z}(t + \Delta t)$ is geometrically the same solution in state space for any Δt . Hence, an additional condition, termed the *phase condition*, has to be specified in order to remove the arbitrariness of the initial conditions. This is discussed in detail in [12].

In summary, an isolated NNM is computed by solving the augmented two-point boundary-value problem defined by

$$\mathbf{F}(\mathbf{z}_{p0}, T) \equiv \begin{cases} \mathbf{H}(\mathbf{z}_{p0}, T) & = 0 \\ h(\mathbf{z}_{p0}) & = 0 \end{cases} \quad (6)$$

where $h(\mathbf{z}_{p0}) = 0$ is the phase condition.

3.2 Continuation of Periodic Solutions

Due to the frequency-energy dependence, the modal parameters of an NNM vary with the total energy. An NNM family, governed by equations (6), therefore traces a curve, termed an NNM branch, in the $(2n + 1)$ -dimensional space of initial conditions and period (\mathbf{z}_{p0}, T) . Starting from the corresponding LNM at low energy, the computation is carried out by finding successive points (\mathbf{z}_{p0}, T) of the NNM branch using methods for the *numerical continuation of periodic motions* (also called *path-following methods*) [8, 9]. The space (\mathbf{z}_{p0}, T) is termed the continuation space.

Different methods for numerical continuation have been proposed in the literature. The so-called pseudo-arclength continuation method is used herein.

Starting from a known solution $(\mathbf{z}_{p0,(j)}, T_{(j)})$, the next periodic solution $(\mathbf{z}_{p0,(j+1)}, T_{(j+1)})$ on the branch is computed using a *predictor step* and a *corrector step*.

Predictor step

At step j , a prediction $(\tilde{\mathbf{z}}_{p0,(j+1)}, \tilde{T}_{(j+1)})$ of the next solution $(\mathbf{z}_{p0,(j+1)}, T_{(j+1)})$ is generated along the tangent vector to the branch at the current point $\mathbf{z}_{p0,(j)}$

$$\begin{bmatrix} \tilde{\mathbf{z}}_{p0,(j+1)} \\ \tilde{T}_{(j+1)} \end{bmatrix} = \begin{bmatrix} \mathbf{z}_{p0,(j)} \\ T_{(j)} \end{bmatrix} + s_{(j)} \begin{bmatrix} \mathbf{p}_z,(j) \\ p_T,(j) \end{bmatrix} \quad (7)$$

where $s_{(j)}$ is the predictor stepsize. The tangent vector $\mathbf{p}_{(j)} = [\mathbf{p}_{z,(j)}^* \ p_{T,(j)}]^*$ to the branch defined by (6) is solution of the system

$$\begin{bmatrix} \frac{\partial \mathbf{H}}{\partial \mathbf{z}_{p0}} \Big|_{(\mathbf{z}_{p0,(j)}, T_{(j)})} & \frac{\partial \mathbf{H}}{\partial T} \Big|_{(\mathbf{z}_{p0,(j)}, T_{(j)})} \\ \frac{\partial h}{\partial \mathbf{z}_{p0}}^* \Big|_{(\mathbf{z}_{p0,(j)})} & 0 \end{bmatrix} \begin{bmatrix} \mathbf{p}_{z,(j)} \\ p_{T,(j)} \end{bmatrix} = \begin{bmatrix} \mathbf{0} \\ 0 \end{bmatrix} \quad (8)$$

with the condition $\|\mathbf{p}_{(j)}\| = 1$. The star denotes the transpose operator. This normalization can be taken into account by fixing one component of the tangent vector and solving the resulting overdetermined system using the Moore-Penrose matrix inverse; the tangent vector is then normalized to 1.

Corrector step

The prediction is corrected by a shooting procedure in order to solve (6) in which the variations of the initial conditions and the period are forced to be orthogonal to the predictor step. At iteration k , the corrections

$$\begin{aligned} \mathbf{z}_{p0,(j+1)}^{(k+1)} &= \mathbf{z}_{p0,(j+1)}^{(k)} + \Delta \mathbf{z}_{p0,(j+1)}^{(k)} \\ T_{(j+1)}^{(k+1)} &= T_{(j+1)}^{(k)} + \Delta T_{(j+1)}^{(k)} \end{aligned} \quad (9)$$

are computed by solving the overdetermined linear system using the Moore-Penrose matrix inverse

$$\begin{bmatrix} \frac{\partial \mathbf{H}}{\partial \mathbf{z}_{p0}} \Big|_{(\mathbf{z}_{p0,(j+1)}^{(k)}, T_{(j+1)}^{(k)})} & \frac{\partial \mathbf{H}}{\partial T} \Big|_{(\mathbf{z}_{p0,(j+1)}^{(k)}, T_{(j+1)}^{(k)})} \\ \frac{\partial h}{\partial \mathbf{z}_{p0}}^* \Big|_{(\mathbf{z}_{p0,(j+1)}^{(k)})} & 0 \\ \mathbf{p}_{z,(j)}^* & p_{T,(j)} \end{bmatrix} \begin{bmatrix} \Delta \mathbf{z}_{p0,(j+1)}^{(k)} \\ \Delta T_{(j+1)}^{(k)} \end{bmatrix} = \begin{bmatrix} -\mathbf{H}(\mathbf{z}_{p0,(j+1)}^{(k)}, T_{(j+1)}^{(k)}) \\ -h(\mathbf{z}_{p0,(j+1)}^{(k)}) \\ 0 \end{bmatrix} \quad (10)$$

where the prediction is used as initial guess, i.e., $\mathbf{z}_{p0,(j+1)}^{(0)} = \tilde{\mathbf{z}}_{p0,(j+1)}$ and $T_{(j+1)}^{(0)} = \tilde{T}_{(j+1)}$. The last equation in (10) corresponds to the orthogonality condition for the corrector step.

This iterative process is carried out until convergence is achieved. The convergence test is based on the relative error of the periodicity condition:

$$\frac{\|\mathbf{H}(\mathbf{z}_{p0}, T)\|}{\|\mathbf{z}_{p0}\|} = \frac{\|\mathbf{z}_p(T, \mathbf{z}_{p0}) - \mathbf{z}_{p0}\|}{\|\mathbf{z}_{p0}\|} < \epsilon \quad (11)$$

where ϵ is the prescribed relative precision.

3.3 Sensitivity Analysis

Each shooting iteration involves the time integration of the equations of motion to evaluate the current shooting residue $\mathbf{H}(\mathbf{z}_{p0}^{(k)}, T^{(k)}) = \mathbf{z}_p^{(k)}(T^{(k)}, \mathbf{z}_{p0}^{(k)}) - \mathbf{z}_{p0}^{(k)}$. As evidenced by equation (10), the method also requires the evaluation of the $2n \times 2n$ Jacobian matrix

$$\frac{\partial \mathbf{H}}{\partial \mathbf{z}_0}(\mathbf{z}_0, T) = \frac{\partial \mathbf{z}(t, \mathbf{z}_0)}{\partial \mathbf{z}_0} \Big|_{t=T} - \mathbf{I} \quad (12)$$

where \mathbf{I} is the $2n \times 2n$ identity matrix.

The classical finite-difference approach requires to perturb successively each of the $2n$ initial conditions and integrate the *non-linear* governing equations of motion. This approximate method therefore relies on extensive numerical simulations and may be computationally intensive for large-scale finite element models.

Targeting a reduction of the computational cost, a significant improvement is to use sensitivity analysis for determining $\partial \mathbf{z}(t, \mathbf{z}_0) / \partial \mathbf{z}_0$ instead of a numerical finite-difference procedure. The sensitivity analysis consists in differentiating the equations of motion (2) with respect to the initial conditions \mathbf{z}_0 which leads to

$$\frac{d}{dt} \left[\frac{\partial \mathbf{z}(t, \mathbf{z}_0)}{\partial \mathbf{z}_0} \right] = \frac{\partial \mathbf{g}(\mathbf{z})}{\partial \mathbf{z}} \Big|_{\mathbf{z}(t, \mathbf{z}_0)} \left[\frac{\partial \mathbf{z}(t, \mathbf{z}_0)}{\partial \mathbf{z}_0} \right] \quad (13)$$

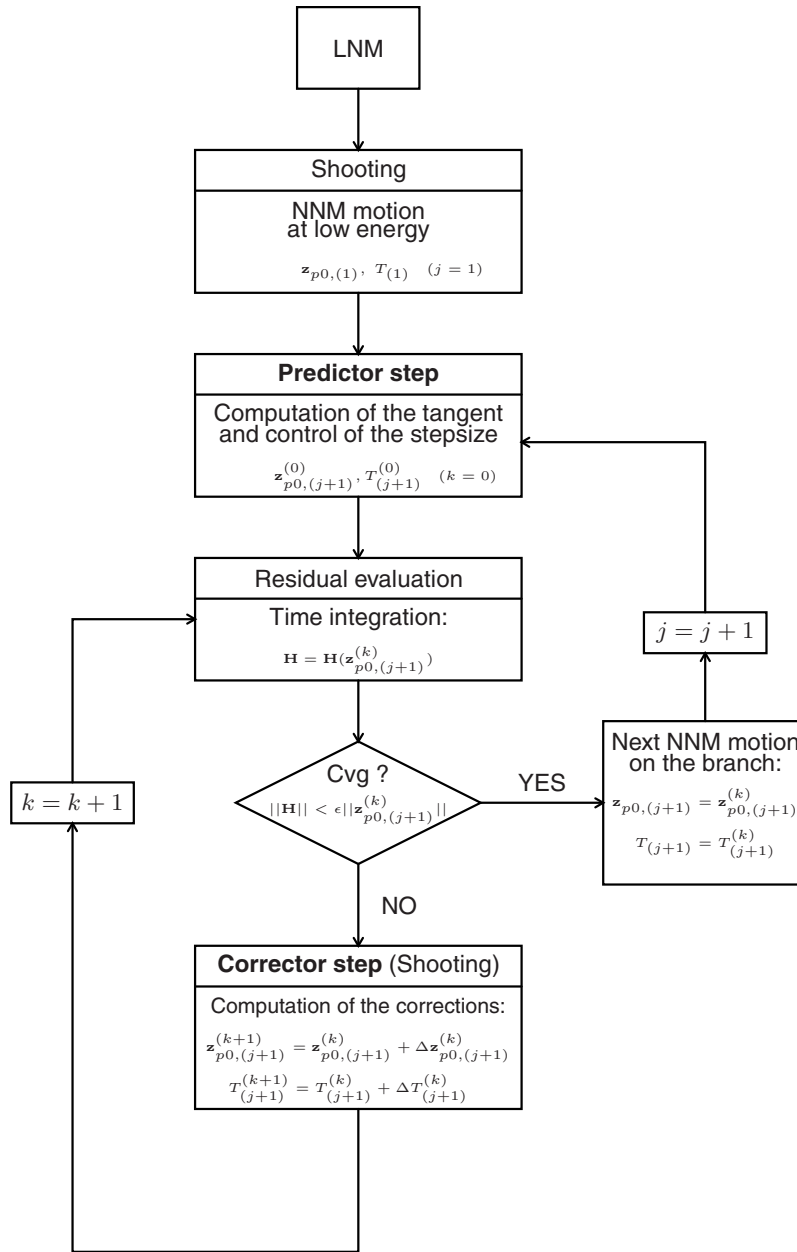


Figure 1: Algorithm for NNM computation.

with

$$\frac{\partial \mathbf{z}(0, \mathbf{z}_0)}{\partial \mathbf{z}_0} = \mathbf{I} \quad (14)$$

since $\mathbf{z}(0, \mathbf{z}_0) = \mathbf{z}_0$. Hence, the matrix $\partial \mathbf{z}(t, \mathbf{z}_0)/\partial \mathbf{z}_0$ at $t = T$ can be obtained by numerically integrating over T the initial-value problem defined by the *linear* ordinary differential equations (ODEs) (13) with the initial conditions (14).

In addition to the integration of the current solution $\mathbf{z}(t, \mathbf{x}_0)$ of (2), these two methods for computing $\partial \mathbf{z}(t, \mathbf{z}_0)/\partial \mathbf{z}_0$ require $2n$ numerical integrations of $2n$ -dimensional dynamical systems, which may be computationally intensive for large systems. However, equations (13) are linear ODEs and their numerical integration is thus less expensive. The numerical cost can be further reduced if the solution of equations (13) is computed together with the solution of the nonlinear equations of motion in a single numerical simulation ^[13].

The sensitivity analysis requires only one additional iteration at each time step of the numerical time integration of the current motion to provide the Jacobian matrix. The reduction of the computational cost is therefore significant for large-scale finite element models. In addition, the Jacobian computation by means of the sensitivity analysis is exact. The convergence troubles regarding the chosen perturbations of the finite-difference method are then avoided. Hence, the use of sensitivity analysis to perform the shooting procedure represents a meaningful improvement from a computational point of view.

As the monodromy matrix $\partial \mathbf{z}_p(T, \mathbf{z}_{p0})/\partial \mathbf{z}_{p0}$ is computed, its eigenvalues, the Floquet multipliers, are obtained as a by-product, and the stability analysis of the NNM motions can be performed in a straightforward manner.

3.4 Algorithm for NNM Computation

The algorithm proposed for the computation of NNM motions is a combination of shooting and pseudo-arclength continuation methods, as shown in [Figure 1](#). It has been implemented in the MATLAB environment. Other features of the algorithm such as the step control, the reduction of the computational burden and the method used for numerical integration of the equations of motion are discussed in ^[12].

So far, the NNMs have been considered as branches in the continuation space (\mathbf{z}_{p0}, T) . An appropriate graphical depiction of the NNMs is to represent them in a frequency-energy plot (FEP). This FEP can be computed in a straightforward manner: (i) the conserved total energy is computed from the initial conditions realizing the NNM motion; and (ii) the frequency of the NNM motion is calculated directly from the period.

4 NUMERICAL EXPERIMENT - FULL-SCALE AIRCRAFT

The numerical computation of the NNMs of a complex real-world structure is addressed. This structure is the airframe of the Morane-Saulnier Paris aircraft, which is represented in [Figure 2](#). This French jet aircraft was built during the 1950s and was used as a trainer and liaison aircraft. The structural configuration under consideration corresponds to the aircraft without its jet engines and standing on the ground through its three landing gears with deflated tires. For information, general characteristics are listed in [Table 1](#). A specimen of this plane is present in ONERA's laboratory, and ground vibration tests have exhibited nonlinear behavior in the connection between the wings and external fuel tanks located at the wing tip. As illustrated in [Figure 3](#), this connection consists of bolted attachments.

4.1 Structural Model of the Paris Aircraft

4.1.1 FINITE ELEMENT MODEL OF THE UNDERLYING LINEAR STRUCTURE

The linear finite element model of the full-scale aircraft, illustrated in [Figure 4](#), was elaborated from drawings by ONERA ^[14]. The wings, vertical stabilizer, horizontal tail and fuselage are modeled by means of 2-dimensional elements such as beams and shells. The complete finite element model has more than 80000 DOFs. Three-dimensional spring elements, which take into account the structural flexibility of the tires and landing gears, are used as boundary conditions of the aircraft. At each wing tip, the external fuel tank is connected with front and rear attachments (see [Figure 3](#)). In this linear model, these connections between the wings and the fuel tanks are modeled using beam elements. The linear model, originally created in the Nastran



Figure 2: Morane-Saulnier Paris aircraft.

TABLE 1: Properties of the Morane-Saulnier Paris aircraft

| Length (m) | Wingspan (m) | Height (m) | Wing area (m ²) | Weight (kg) |
|------------|--------------|------------|-----------------------------|-------------|
| 10.4 | 10.1 | 2.6 | 18 | 1945 |

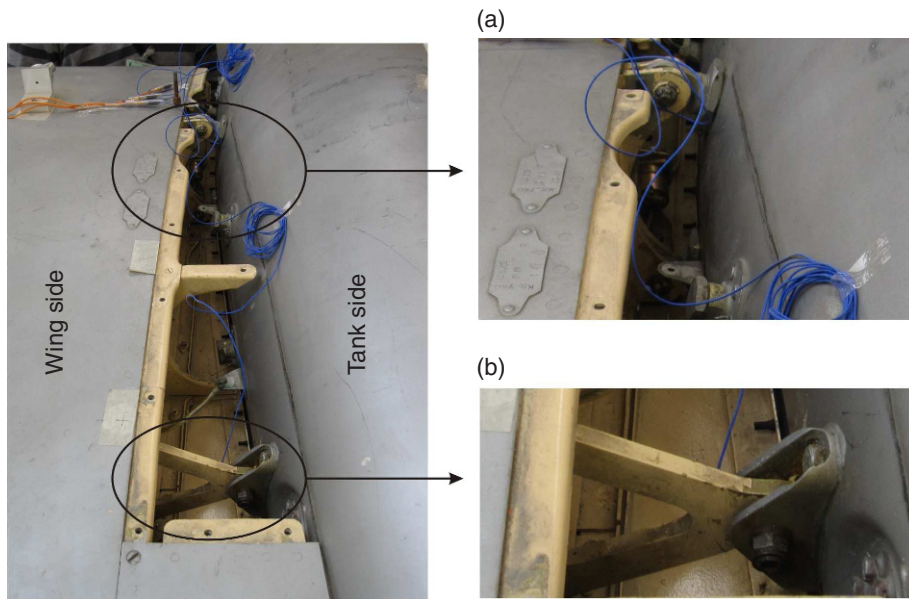


Figure 3: Connection between external fuel tank and wing tip (top view). Close-up of (a) front and (b) rear bolted attachments.

software, was converted and exploited in the Samcef finite element environment for this study.

The natural frequencies of the underlying linear system in the [0-50Hz] frequency range are given in Table 2. The first nine modes correspond to aircraft rigid-body modes: six modes are modes of suspensions of the landing gear while the three others are associated to rigid-body motions of the control surfaces (i.e., the ailerons, elevator and rudder). The frequency range of the rigid-body modes is comprised between 0.09 and 3.57 Hz, i.e., noticeably lower than the first flexible mode located at 8.19 Hz. The modal shapes of different elastic normal modes of vibrations are depicted in Figure 5. Figure 5(a) represents the first wing bending mode. The first and second wing torsional modes are depicted in Figures 5(b) and 5(c). These two torsional modes correspond to symmetric and anti-symmetric wing motions, respectively. As shown thereafter, these modes are of particular interest in nonlinear regime since there is a significant deformation of the connections between the wings and fuel tanks. Indeed, the other modes mainly concern the aircraft tail and are consequently almost unaffected by these nonlinear connections.

4.1.2 REDUCED-ORDER MODEL

The proposed algorithm for the numerical computation of NNMs is computationally intensive for the large-scale original model possessing more than 80000 DOFs. Since the nonlinearities are spatially localized, condensation of the linear components of the model is an appealing approach for a computationally tractable and efficient calculation.

A reduced-order model of the linear finite element system is constructed using the Craig-Bampton (also called component mode) reduction technique^[15]. This method consists in describing the system in terms of some retained DOFs and internal vibration modes. By partitioning the complete system in terms of n_R remaining \mathbf{x}_R and $n_C = n - n_R$ condensed \mathbf{x}_C DOFs, the n governing equations of motion of the global finite element model are written as

$$\begin{bmatrix} \mathbf{M}_{RR} & \mathbf{M}_{RC} \\ \mathbf{M}_{CR} & \mathbf{M}_{CC} \end{bmatrix} \begin{bmatrix} \ddot{\mathbf{x}}_R \\ \ddot{\mathbf{x}}_C \end{bmatrix} + \begin{bmatrix} \mathbf{K}_{RR} & \mathbf{K}_{RC} \\ \mathbf{K}_{CR} & \mathbf{K}_{CC} \end{bmatrix} \begin{bmatrix} \mathbf{x}_R \\ \mathbf{x}_C \end{bmatrix} = \begin{bmatrix} \mathbf{g}_R \\ \mathbf{0} \end{bmatrix} \quad (15)$$

The Craig-Bampton method expresses the complete set of initial DOFs in terms of: (i) the remaining DOFs through the static modes (resulting from unit displacements on the remaining DOFs) and (ii) a certain number $m < n_C$ of internal vibration modes (relating to the primary structure fixed on the remaining nodes). Mathematically, the reduction is described by relation

$$\begin{bmatrix} \mathbf{x}_R \\ \mathbf{x}_C \end{bmatrix} = \begin{bmatrix} \mathbf{I} & \mathbf{0} \\ -\mathbf{K}_{CC}^{-1}\mathbf{K}_{CR} & \Phi_m \end{bmatrix} \begin{bmatrix} \mathbf{x}_R \\ \mathbf{y} \end{bmatrix} = \mathbf{R} \begin{bmatrix} \mathbf{x}_R \\ \mathbf{y} \end{bmatrix} \quad (16)$$

which defines the $n \times (n_R + m)$ reduction matrix \mathbf{R} . \mathbf{y} are the modal coordinates of the m internal linear normal modes collected in the $n_C \times m$ matrix $\Phi_m = [\phi_{(1)} \dots \phi_{(m)}]$. These modes are solutions of the linear eigenvalue problem corresponding to the system fixed on the remaining nodes

$$(\mathbf{K}_{CC} - \omega_{(j)}^2 \mathbf{M}_{CC}) \phi_{(j)} = \mathbf{0} \quad (17)$$

The reduced model is thus defined by the $(n_R + m) \times (n_R + m)$ reduced stiffness and mass matrices given by

$$\begin{aligned} \overline{\mathbf{M}} &= \mathbf{R}^* \mathbf{M} \mathbf{R} \\ \overline{\mathbf{K}} &= \mathbf{R}^* \mathbf{K} \mathbf{R} \end{aligned} \quad (18)$$

where star denotes the transpose operation. After reduction, the system configuration is expressed in terms of the reduced coordinates (i.e., the remaining DOFs and the modal coordinates). The initial DOFs of the complete model are then determined by means of the reduction matrix using relation 16.

In order to introduce the nonlinear behavior of the connections between the wings and the tanks, the reduced-order linear model of the aircraft is constructed by keeping one node on both sides of the attachments. For each wing, four nodes are retained: two nodes for the front attachment and two nodes for the rear attachment. In total, only eight nodes of the finite element model are kept to build the reduced model. It is completed by holding the first 500 internal modes of vibrations. Finally, the model is thus reduced to 548 DOFs: 6 DOFs per node (3 translations and 3 rotations) and 1 DOF per internal mode. The reduction is performed using the Samcef software. The generated reduced-order model is next exported in the MATLAB environment.

Before proceeding to nonlinear analysis, the accuracy of the reduced-order linear model is assessed. To this end, the linear normal modes of the initial complete finite element model are compared to those predicted by the reduced model. The deviation

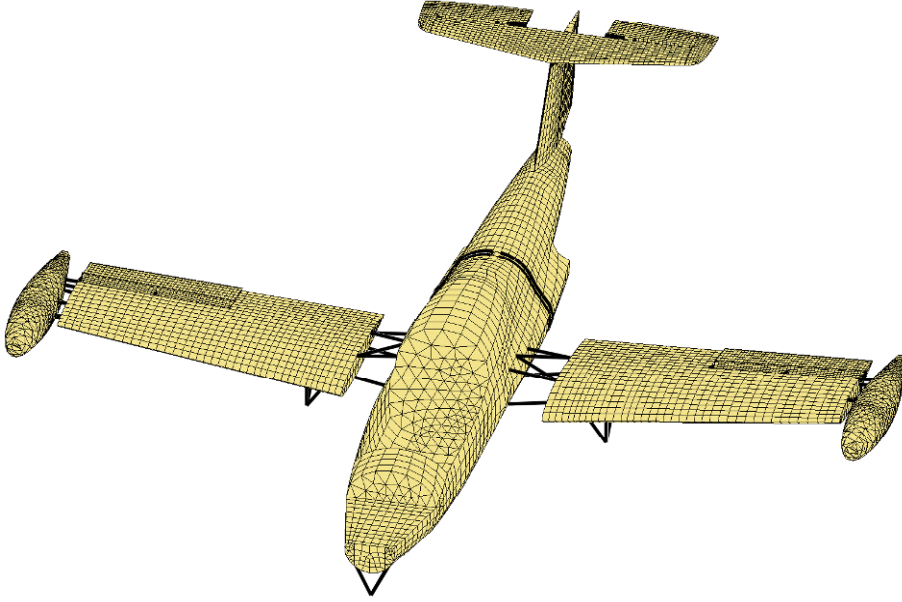


Figure 4: Finite element model of the Morane-Saulnier Paris aircraft.

| Mode | Freq. (Hz) | Mode | Freq. (Hz) |
|------|------------|------|------------|
| 1 | 0.0936 | 13 | 21.2193 |
| 2 | 0.7260 | 14 | 22.7619 |
| 3 | 0.9606 | 15 | 23.6525 |
| 4 | 1.2118 | 16 | 25.8667 |
| 5 | 1.2153 | 17 | 28.2679 |
| 6 | 1.7951 | 18 | 29.3309 |
| 7 | 2.1072 | 19 | 31.0847 |
| 8 | 2.5157 | 20 | 34.9151 |
| 9 | 3.5736 | 21 | 39.5169 |
| 10 | 8.1913 | 22 | 40.8516 |
| 11 | 9.8644 | 23 | 47.3547 |
| 12 | 16.1790 | 24 | 52.1404 |

TABLE 2: Natural frequencies of the linear finite element model of the Paris aircraft.

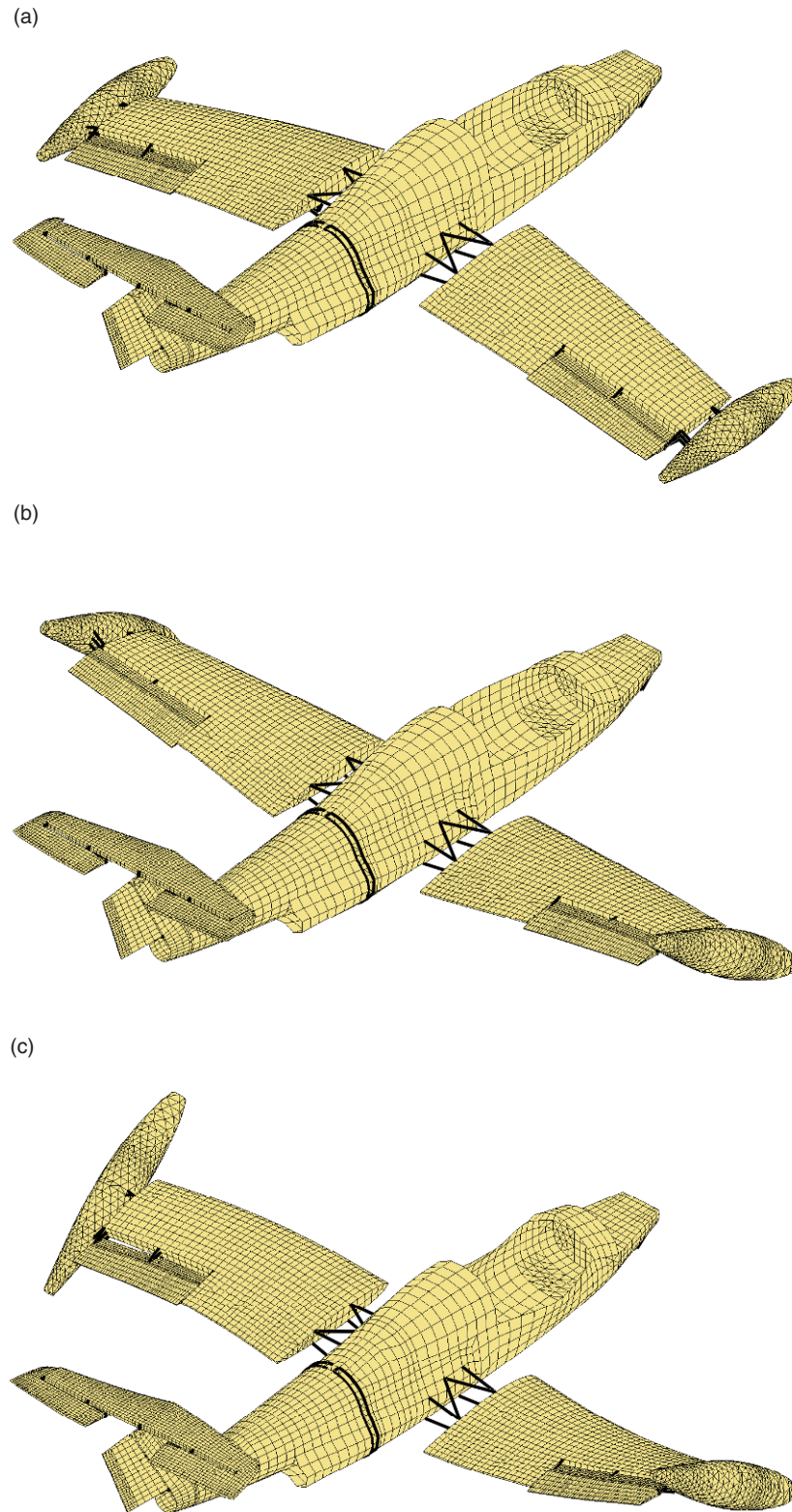


Figure 5: Normal modes of the linear finite element model of the Morane-Saulnier Paris aircraft. (a) First wing bending mode (8.19 Hz), (b) first (symmetric) wing torsional mode (31.08 Hz) and (b) second (anti-symmetric) wing torsional mode (34.92 Hz).

between the mode shapes of the original model $\mathbf{x}_{(o)}$ and of the reduced model $\mathbf{x}_{(r)}$ is determined using the Modal Assurance Criterion (MAC)

$$\text{MAC} = \frac{|\mathbf{x}_{(o)}^* \mathbf{x}_{(r)}|^2}{|\mathbf{x}_{(o)}^* \mathbf{x}_{(o)}| |\mathbf{x}_{(r)}^* \mathbf{x}_{(r)}|} \quad (19)$$

MAC values range from 0 in case of no correlation to 1 for a complete coincidence. In the [0-100Hz] range, MAC values between modes shapes are all greater than 0.999 and the maximum relative error on the natural frequencies is 0.2%. It therefore validates the excellent accuracy of the reduced linear model in this frequency range. It is worth noticing that less internal modes are sufficient to ensure such a correlation in the [0-100Hz] frequency range, which is typically the range of interest for aircrafts. However, a larger number of modes was deliberately chosen for two main reasons. On the one side, it serves to illustrate the ability of the numerical algorithm to deal with the NNM computation of higher-dimensional systems. On the other hand, due to nonlinearity, modes of higher frequencies may interact with lower modes of interest. In nonlinear regimes, higher internal modes should then be necessary to guarantee the accuracy of the model.

4.1.3 NONLINEAR MODEL

The existence of a softening nonlinear behavior was evidenced during different vibration tests conducted by ONERA. In particular, FRF measurements reveal the decrease of resonant frequencies with the level of excitation. The connections between the wings and fuel tanks are assumed to cause this observed nonlinear effect.

To confirm this hypothesis, both (front and rear) connections of each wing were instrumented and experimental measurements were carried out. Specifically, accelerometers were positioned on both (wing and tank) sides of the connections and two shakers were located at the tanks. This is illustrated in [Figure 6](#) for rear connection.

The dynamic behavior of these connections in the vertical direction is investigated using the restoring force surface (RFS) method ^[16]. By writing Newton's second law at the wing side of each connection, it follows

$$m_c \ddot{x}_c(t) + f_{r,c} = 0 \quad (20)$$

where $f_{r,c}$ is the restoring force applied to this point. The index c is related to the connection under consideration (i.e., either the rear or front attachment of the left or right wing). From Equation (20), the restoring force is obtained by

$$f_{r,c} = -m_c \ddot{x}_c(t) \quad (21)$$

Except the multiplicative mass factor m_c , the restoring force is then given by the acceleration $\ddot{x}_c(t)$. Nevertheless, this total restoring force does not consist only of the internal force related to the connection of interest, but also includes contributions from the linking forces associated to the wing elastic deformation. Provided that these latter do not play a prominent role, the measurement of the acceleration signal may still provide a qualitative insight into the nonlinear part of the restoring force in the connection between the tank and the wing.

The aircraft is excited close to the second torsional mode (see [Figure 5\(c\)](#)) using a band-limited swept sine excitation in the vicinity of its corresponding resonant frequency. In [Figure 7](#), the measured acceleration at the wing side is represented in terms of the relative displacement x_{rel} and velocity \dot{x}_{rel} of the connection obtained by integrating the accelerations on both sides of the attachment. It is given for the rear connections of the right and left wings. A nonlinear softening elastic effect is observed from the evolution of these estimated restoring force surfaces. In particular, the detected behavior has a piecewise characteristic. This is more clearly evidenced by the corresponding stiffness curves also depicted in [Figure 7](#). Softening nonlinearity is typical of bolted connections ^[17, 18]. Similar nonlinear effect occurs for the front connections, but they participate much less in the considered response. Finally, the deviation between the right and left connections seems to show asymmetry of the connections.

Although purely qualitative, the RFS results therefore indicate that the tank connections present a softening stiffness in the vertical direction. As previously mentioned, a model with piecewise characteristic might be consistent with the experimental observations. However, the NNM algorithm, in its present form, cannot handle nonsmooth nonlinearities. Alternatively, linear and negative cubic stiffness terms are one possible manner of describing the observed nonlinear behavior. Indeed, the reconstructed stiffness curve obtained by fitting to the data the mathematical model

$$f_{r,c} = kx_{rel} + k_{nl}^- x_{rel}^3 \quad (k_{nl}^- < 0) \quad (22)$$

is in relatively good agreement.



Figure 6: Instrumentation of the rear attachment of the right wing.

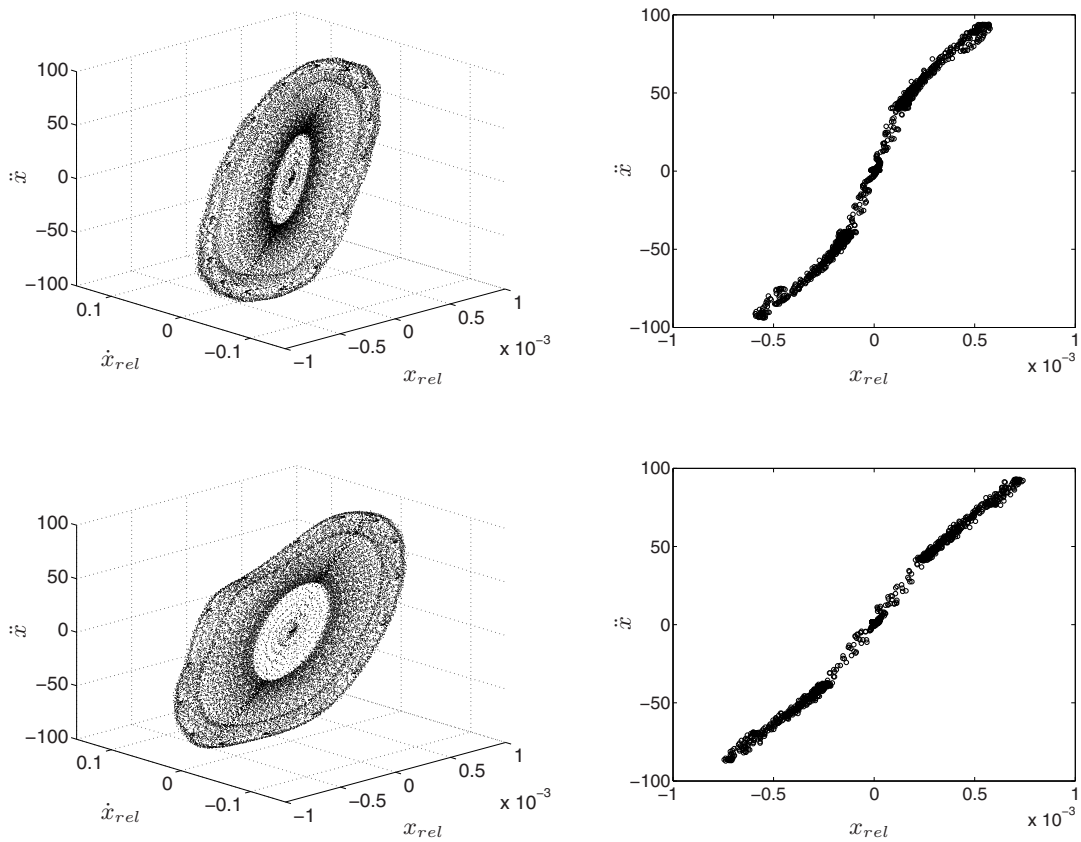


Figure 7: Estimated restoring force in the connections between tanks and wings. Left plots: measured acceleration in terms of the relative displacement (m) and velocity (m/s). Right plots: stiffness curve given by the measured acceleration for zero velocity. Top plots: rear tank connection of the left wing. Bottom plots: rear tank connection of the right wing.

In view of the qualitative value of this approach, we note that the objective followed here is to derive a simplified realistic model in order to illustrate the numerical computation procedure of NNMs. Accordingly, in the present study, the nonlinear behavior is modeled by adding negative cubic stiffness nonlinearities into the linear part of the connections. An indicative value of -10^{13}N/m^3 is adopted for each connection. Finally, the nonlinear system is then constructed from the reduced-order model by means of cubic springs positioned vertically between both corresponding nodes retained on either side of connections.

4.2 Nonlinear Normal Modes

From the nonlinear reduced-order model, the numerical computation of NNMs is realized in the MATLAB environment using the previously developed algorithm. The goal followed here is to show that the proposed method can deal with complex structures such as this real-aircraft model. In this context, this section focuses on some specific modes.

4.2.1 FUNDAMENTAL NNMS

The modes of the aircraft can be classified into two categories, depending on whether they correspond to wing motions or not. The modes localized mainly on other structural parts (such as the vertical stabilizer, the horizontal tail or the fuselage) are almost unaffected by the nonlinear connections located at the wing tips. Only the modes involving wing deformations are perceptibly affected by nonlinearity. According to the relative motion of the fuel tanks, these modes are more or less altered for increasing energy levels.

An unaffected mode is first examined in [Figure 8](#). It corresponds to the nonlinear extension of the first tail bending LNM (mode 13 in [Table 2](#)). In this figure, the computed backbone and related NNM motions are depicted in the FEP. The modal shapes are given in terms of the initial displacements (with zero initial velocities assumed) that realize the NNM motion. It clearly confirms that the modal shape and the oscillation frequency remain practically unchanged with the energy in the system.

Modes involving wing deformations are now investigated. The first wing bending mode (i.e., the nonlinear extension of mode 10 in [Table 2](#)) is illustrated in [Figure 9](#). The FEP reveals that this mode is weakly affected by the nonlinearities. The frequency of the NNM motions on the backbone slightly decreases with increasing energy levels, which results from the softening characteristic of the nonlinearity. Regarding the modal shapes, they are almost similar over the energy range and resemble the corresponding LNM. MAC value between the NNM shapes at low and high energy levels (see [\(a\)](#) and [\(b\)](#) in [Figure 9](#)) is 0.99.

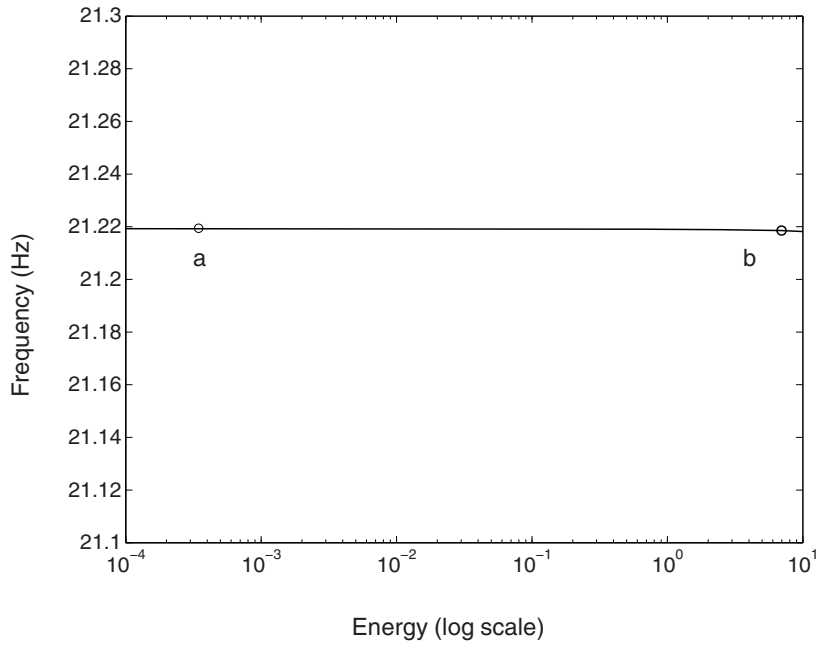
[Figure 10](#) represents the FEP of the first (symmetric) wing torsional mode (i.e., mode 19 in [Table 2](#)). For this mode, the relative motion of the fuel tanks is more important, which enhances the nonlinear effect of the connections. As a result, the oscillation frequency have a more marked energy dependence along the backbone branch. On the other hand, the modal shapes are still weakly altered. MAC value between the NNM shapes on the backbone at low and high energy levels (see [\(a\)](#) and [\(b\)](#) in [Figure 10](#)) is equal to 0.98. In addition, the FEP highlights the presence of three tongues, revealing the existence of internal resonances between this symmetric torsional mode and other modes. These observed modal interactions are discussed in the next section.

Finally, the second (anti-symmetric) wing torsional mode (i.e., mode 20 in [Table 2](#)) is plotted in the FEP of [Figure 11](#). While the oscillation frequency is noticeably altered by nonlinearity, modal shapes are again slightly changed. Over the energy range of interest, the decrease in frequency is around 5% along the backbone branch. MAC value between the modal shapes at low and high energy levels (see [\(a\)](#) and [\(b\)](#) in [Figure 11](#)) is 0.97. It shows that the nonlinearities spatially localized between the wing tips and the tanks weakly influence the NNM spatial shapes. Besides the NNM backbone, one tongue is present at higher energy. For information, the computation of the backbone branch up to the tongue needs 20 min with 100 time steps over the half period (using Intel i7 920 2.67GHz processor). Due to the presence of turning points, the computation of the tongue is more expensive and demands about one hour.

Similar dynamics were observed for the higher modes and are not further described herein.

4.2.2 INTERNALLY RESONANT NNMS

Besides the backbone branches, the previous FEPs show the presence of tongues of internally resonant NNMs. Following a resonance scenario similar to that described in ^[3], these additional branches emanate from the backbone of a specific NNM



(a)

(b)

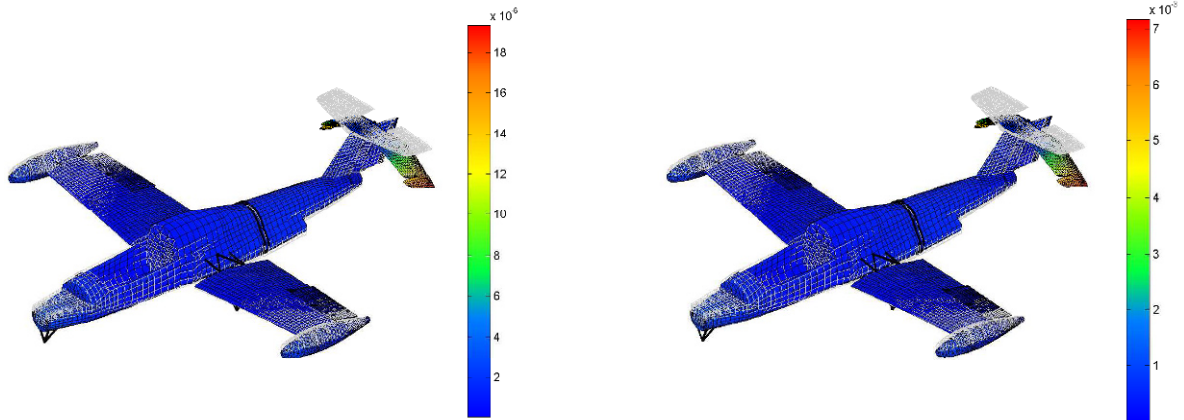
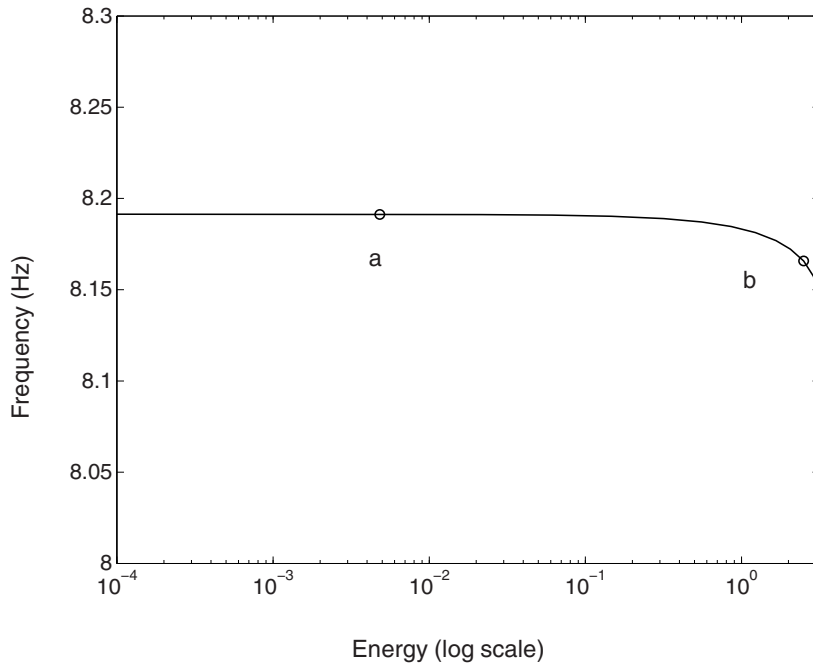


Figure 8: FEP of the first tail bending NNM of the Paris aircraft. NNM shapes at energy levels marked in the FEP are inset; they are given in terms of the initial displacements (m) that realize the periodic motion (with zero initial velocities assumed).



(a)

(b)

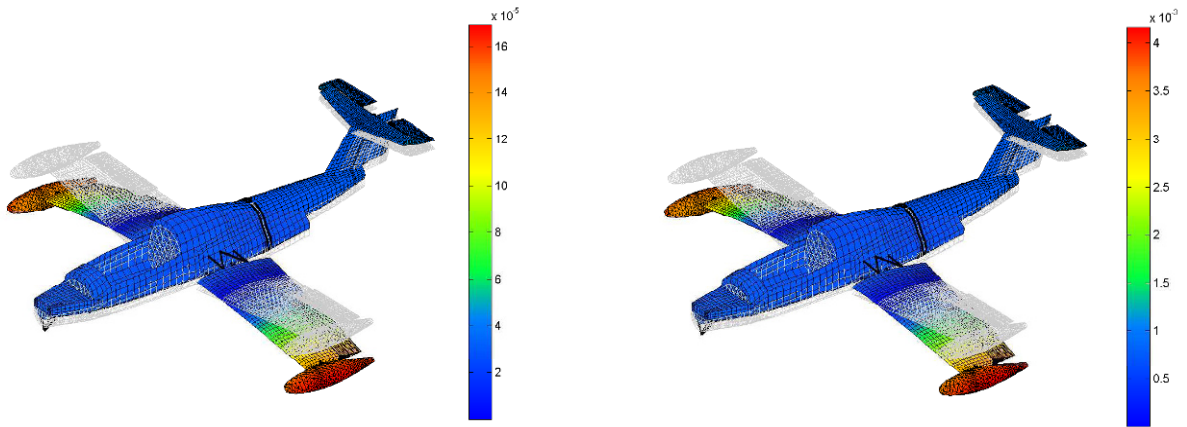
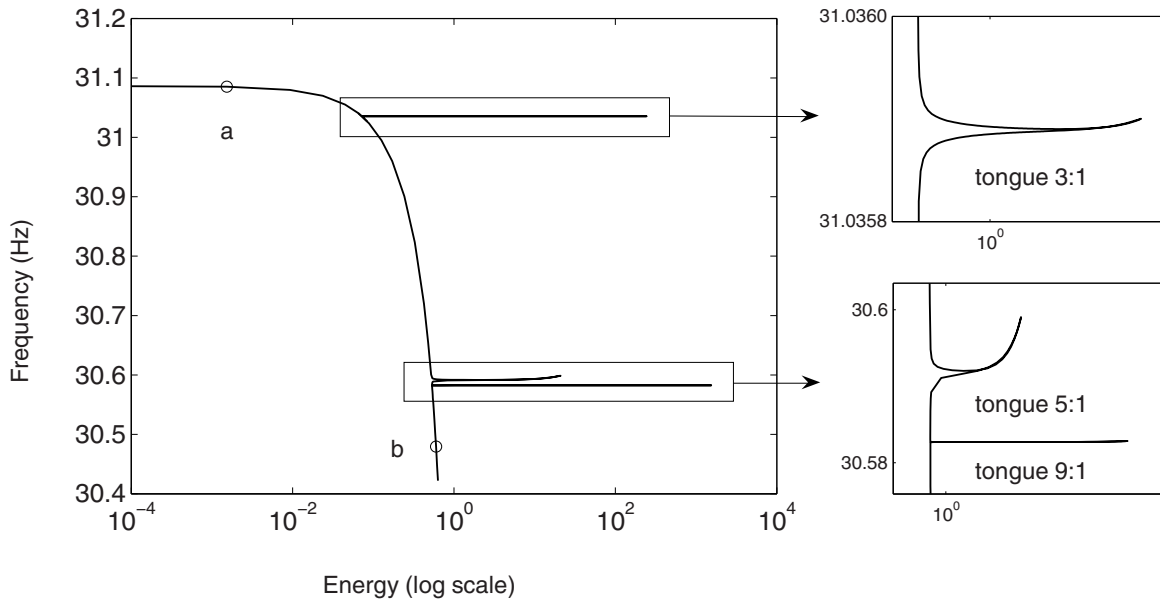


Figure 9: FEP of the first wing bending NNM of the Paris aircraft. NNM shapes at energy levels marked in the FEP are inset; they are given in terms of the initial displacements (m) that realize the periodic motion (with zero initial velocities assumed).



(a)

(b)

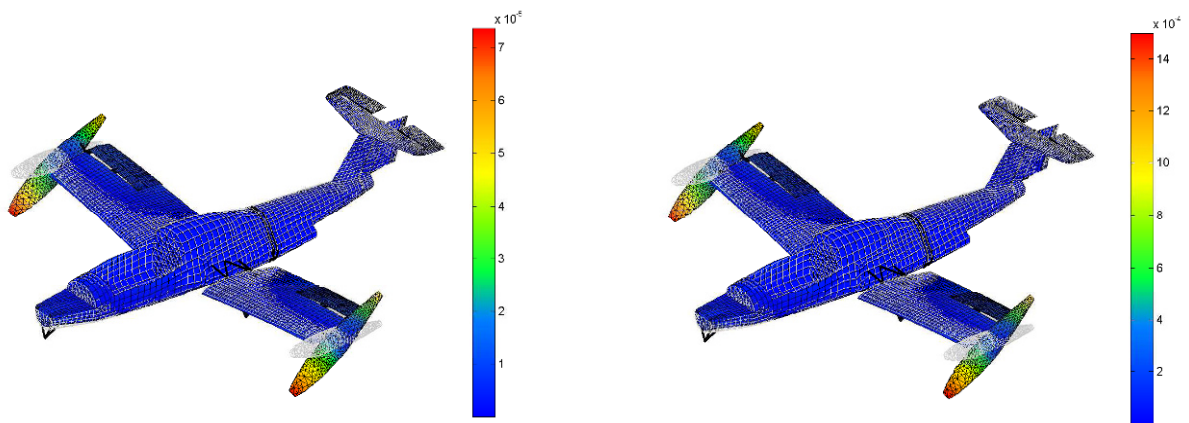
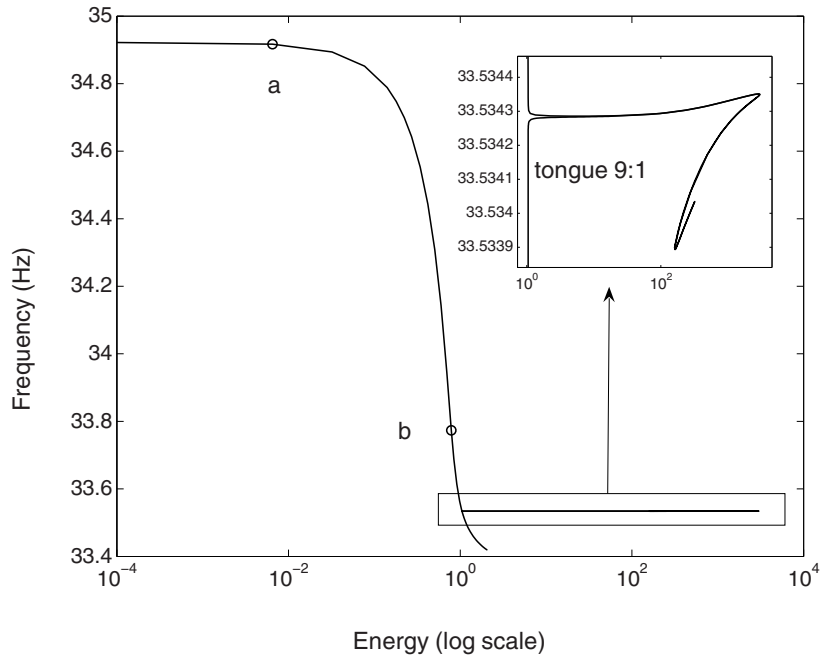


Figure 10: FEP of the first (symmetric) wing torsional NNM of the Paris aircraft. NNM shapes at energy levels marked in the FEP are inset; they are given in terms of the initial displacements (m) that realize the periodic motion (with zero initial velocities assumed).



(a)

(b)

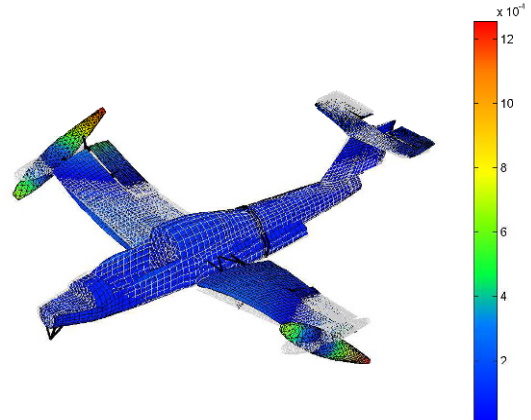


Figure 11: FEP of the second (anti-symmetric) wing torsional NNM of the Paris aircraft. NNM shapes at energy levels marked in the FEP are inset; they are given in terms of the initial displacements (m) that realize the periodic motion (with zero initial velocities assumed).

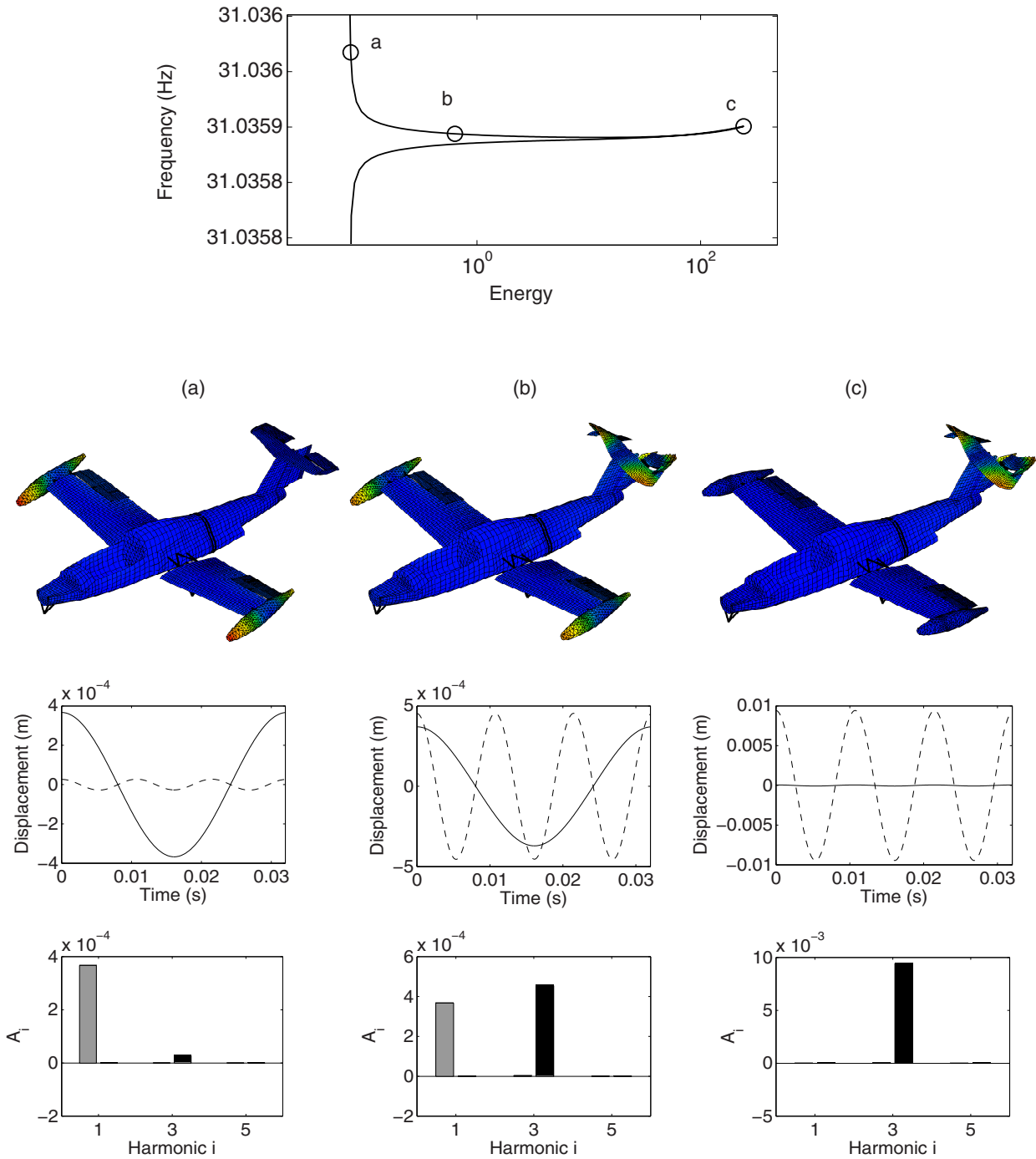


Figure 12: 3:1 internal resonance between the first wing torsional mode and a higher tail mode of the Paris aircraft. Top plot: close-up in the FEP of the 3:1 tongue of Figure 10. Bottom plots: NNM motions at (a) beginning of the tongue (in the vicinity of the backbone of the the first wing torsional mode); (b) middle of the tongue; and (c) extremity of the tongue. From top to bottom: NNM shapes; time series of the vertical displacements at the rear tip of the right tank (—) and at the right side of the horizontal tail (---); Fourier coefficients of both displacements (in grey and black, respectively).

and coalesce into the backbone branch of another NNM, thereby realizing an internal resonance between the two modes.

This is briefly illustrated in [Figure 12](#) regarding the 3:1 tongue emanating from the backbone of the first wing torsional mode (see [Figure 10](#)). Modal shapes are given at three different locations on the tongue (see (a), (b) and (c) in [Figure 12](#)). When the energy gradually increases along the tongue, a smooth transition from the first wing torsional mode to a higher tail torsional mode clearly occurs. Interestingly, [Figure 12\(b\)](#) shows an inherently nonlinear mode with no counterpart in the underlying linear system. It corresponds to a 3:1 internal resonance as evidenced by the evolution of the time series and the frequency content, also represented in [Figure 12](#), of the periodic motions along the tongue. A third harmonic progressively appears, and the structure vibrates according to a subharmonic motion characterized by two dominant frequency components. The relative importance of the third harmonic grows along the tongue, until the mode transition is realized.

Similarly, two other tongues corresponding to a 5:1 and a 9:1 internal resonance between this first wing torsional mode and higher modes are observed in the FEP of [Figure 10](#). Moreover, the FEP of [Figure 11](#) reveals the presence of a 9:1 internal resonance between the second wing torsional mode and another higher mode of the aircraft. We note that the practical realization of these internal resonances is questionable in view of the low frequency changes.

5 CONCLUSION

In this paper, a numerical method for the computation of NNMs of mechanical structures was introduced. The approach targets the computation of the undamped modes of structures discretized by finite elements and relies on the continuation of periodic solutions.

This computational approach turns out to be capable of dealing with complex real-world structures, such as the full-scale aircraft studied herein. Through a reduced-order model accurate in the [0-100Hz] range, the NNMs were indeed computed accurately even in strongly nonlinear regimes and with a reasonable computational burden. Internal resonances were also computed by the algorithm and were briefly discussed.

REFERENCES

- [1] A.F. Vakakis, L.I. Manevitch, Y.V. Mikhlin, V.N. Pilipchuk, A.A. Zevin, *Normal Modes and Localization in Nonlinear Systems*, John Wiley & Sons, New York (1996).
- [2] A.F. Vakakis, *Non-linear normal modes (NNMs) and their applications in vibration theory: An overview*, Mechanical Systems and Signal Processing, Vol. 11, No. 1 (1997), pp. 3-22.
- [3] G. Kerschen, M. Peeters, J.C. Golinval, A.F. Vakakis, *Nonlinear normal modes, Part I: A useful framework for the structural dynamicist*, Mechanical Systems and Signal Processing, Vol. 23, No. 1 (2009), pp. 170-194.
- [4] J.C. Slater, *A numerical method for determining nonlinear normal modes*, Nonlinear Dynamics, Vol. 10, No. 1 (1996), pp. 19-30.
- [5] E. Pesheck, *Reduced-order modeling of nonlinear structural systems using nonlinear normal modes and invariant manifolds*, PhD Thesis, University of Michigan, Ann Arbor (2000).
- [6] Y.S. Lee, G. Kerschen, A.F. Vakakis, P.N. Panagopoulos, L.A. Bergman, D.M. McFarland, *Complicated dynamics of a linear oscillator with a light, essentially nonlinear attachment*, Physica D-Nonlinear Phenomena, Vol. 204, No. 1-2 (2005), pp. 41-69.
- [7] R. Arquier, S. Bellizzi, R. Bouc, B. Cochelin, *Two methods for the computation of nonlinear modes of vibrating systems at large amplitudes*, Computers & Structures, Vol. 84, No. 24-25 (2006), pp. 1565-1576.
- [8] R. Seydel, *Practical Bifurcation and Stability Analysis, from Equilibrium to Chaos*, Springer-Verlag, 2nd Edition (1994).
- [9] A.H. Nayfeh, B. Balachandran, *Applied Nonlinear Dynamics: Analytical, Computational, and Experimental Methods*, Wiley-Interscience, New York (1995).
- [10] E. Doedel, *AUTO, Software for Continuation and Bifurcation Problems in Ordinary Differential Equations*, (2007).

- [11] C. Touzé, A. Amabili, O. Thomas, *Reduced-order models for large-amplitude vibrations of shells including in-plane inertia*, In *Proceedings of the EUROMECH Colloquium on Geometrically Nonlinear Vibrations, Porto, Portugal, July 2007*, Porto (2007).
- [12] M. Peeters, R. Viguié, G. Sérandour, G. Kerschen, J.C. Golinval, *Nonlinear normal modes, Part II: Toward a practical computation using numerical continuation techniques*, *Mechanical Systems and Signal Processing*, Vol. 23, No. 1 (2009), pp. 195-216.
- [13] O. Brüls, P. Eberhard, *Sensitivity analysis for dynamic mechanical systems with finite rotations*, *International Journal for Numerical Methods in Engineering*, Vol. 1 (2006), pp. 1-29.
- [14] A. Remy, *Updating of the finite element model of the MS 760 Paris aircraft*, Training period report at ONERA (2006).
- [15] R. Craig, M. Bampton, *Coupling of substructures for dynamic analysis*, *AIAA Journal*, Vol. 6 (1968), pp. 1313–1319.
- [16] S.F. Masri, T.K. Caughey, *A nonparametric identification technique for nonlinear dynamic problems*, *Journal of Applied Mechanics*, Vol. 46 (1979), pp. 433-447.
- [17] L. Gaul, J. Lenz, *Nonlinear dynamics of structures assembled by bolted joints*, *Acta Mechanica*, Vol. 125 (1997), pp. 169-181.
- [18] C.J. Hartwigsen, Y. Song, D.M. McFarland, L.A. Bergman, A.F. Vakakis, *Experimental study of non-linear effects in a typical shear lap joint configuration*, *Journal of Sound and Vibration*, Vol. 277 (2004), pp. 327-351.

FRF Measurements and Mode Shapes Determined Using Image-based 3D Point-tracking

Chris Warren, Chris Niezrecki, Peter Avitabile
Structural Dynamics and Acoustic Systems Laboratory
University of Massachusetts Lowell
One University Avenue
Lowell, Massachusetts 01854

ABSTRACT

Today, accelerometers and laser Doppler vibrometers are widely accepted as valid measurement tools for structural dynamic measurements. However, limitations of these transducers prevent the accurate measurement of some phenomena. For example, accelerometers typically measure motion at a limited number of discrete points and can mass load a structure. Scanning laser vibrometers have a very wide frequency range and can measure many points without mass-loading, but are sensitive to large displacements and can have lengthy acquisition times due to sequential measurements. Image-based stereophotogrammetry techniques provide additional measurement capabilities that compliment the current array of measurement systems by providing an alternative that favors high-displacement and low-frequency vibrations typically difficult to measure with accelerometers and laser vibrometers. Within this paper, displacements determined using 3D point-tracking are used to calculate frequency response functions, from which mode shapes are extracted. The image-based frequency response functions (FRFs) are compared to those obtained at collocated accelerometers. Mode shapes are then compared to a previously validated finite element model (FEM) and are shown to have excellent agreement between the FEM and the conventional measurement approaches when compared using the Modal Assurance Criterion (MAC) and Pseudo-Orthogonality Check (POC).

INTRODUCTION

With the advent of digital cameras, image-based point-tracking is becoming a more common method to track the motion of optical targets that are attached to a rigid or flexible body. To date, 3D point-tracking (3DPT) has not been validated within the field of structural dynamics as a non-contacting vibration measurement tool. When evaluating the performance of any new system or technique, one must compare the new approach to existing measurement methods or to analytical solutions. To accomplish this end, a well documented and understood test article was chosen to compare the image-based approach to established measurement techniques. A structure known as the “Base-Upright” (BU) has been used in a number of studies and was chosen for its well-known dynamic characteristics [1-4]. Several test setups were needed to study the BU, depending on the measurement system and transducers used. A summary of past work using accelerometers, laser Doppler vibrometers, and slow-speed cameras is presented, followed by a thorough discussion of the setup and results of tests run with high-speed cameras. Finally, conclusions are drawn to highlight the strengths and weaknesses of 3D point-tracking using high-speed cameras relative to the other measurement techniques.

Description of the Test Article and Finite Element Model

The BU was designed to be a structure with well-spaced, directional modes that could be identified easily. [Figure 1a](#) shows the BU with the primary dimensions labeled. The base plate is 24 x 24 inches in dimension and rigidly bolted to the concrete laboratory floor at four locations, while the upright is 24 x 30 inches in dimension. Both plates are made from 3/4” thick aluminum and are bolted together by two steel angle brackets. A finite element model (FEM) is available and has been shown to be very well correlated to other measured test data from previous studies [1-4]. The FEM was assembled with solid elements and has approximately 58,000 degrees of freedom (DOF). For reference, the analytical frequencies and mode shapes for the first 8 modes are shown in [Figure 1b](#).

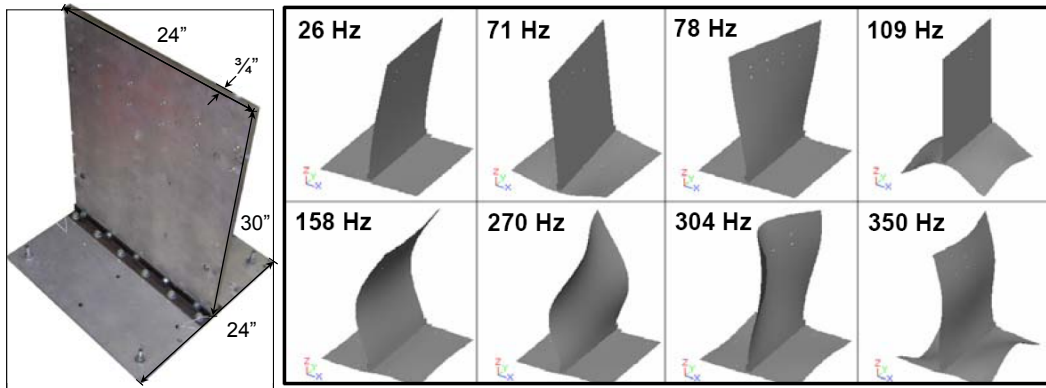


Figure 1: (a) Photo of the Base-Upright (BU) with dimensions. (b) First 8 analytical frequencies and mode shapes of the BU.

Results of Previous Studies

Prior work using slow-speed cameras with phase-stepped sampling and forced normal-mode testing (FNMT) yielded highly-accurate measurements of the BU mode shapes at many points [5]. The results of the study showed that DIC and 3DPT can be used to measure mode shapes that correlate very well to those obtained using accelerometers and a scanning laser Doppler vibrometer. When the accelerometer and laser data was acquired, shaker excitation was provided at an angle 45 degrees relative to all three principal axes so that all modes would be excited. Figure 2a depicts shaker mounted to the BU with the laser and accelerometer measurement points indicated by red dots and their corresponding numbers. At these measurement locations optical targets were placed on the structure that are measured and tracked by the dynamic photogrammetry system Pontos™ [6]. An overlay of FRFs in the z-direction measured by an accelerometer and the laser Doppler vibrometer at point 3 is shown in Figure 2b. A frequency domain, polynomial curvefitter was then used to extract the modal parameters and mode shapes.

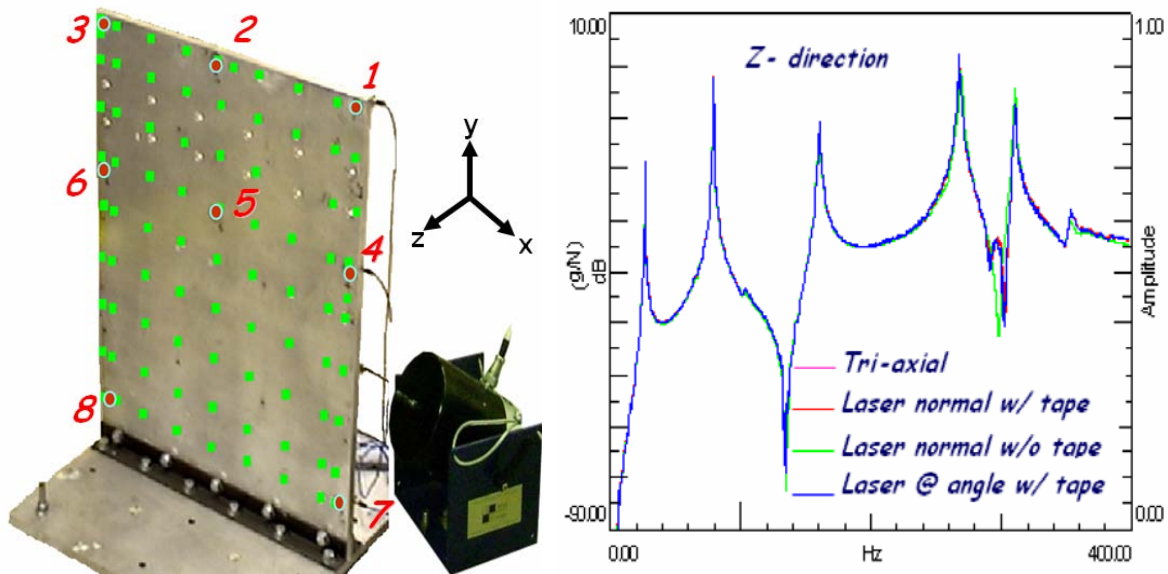


Figure 2: (a) Shaker orientation and measurement points. Red dots correspond to accelerometer measurement points. Green squares represent SLDV points from a previous study. (b) Sample FRF from previous study [4].

All four measurement approaches were used to acquire the first and third modes of the structure studied and then were correlated to each other as well as a highly accurate finite element model. Excellent correlation between the measurements and the FEM was obtained; each MAC value was above 97.8. When the experimental results were compared, all MAC values were above 95.6. Figure 3 presents a comparison between the FEM analytical mode shape and the accelerometer, laser Doppler vibrometer (LDV), DIC, and 3D point-tracking based mode shapes for modes 1 and 3 of the BU.

The greatest advantage of the FNMT phase-stepping approach is that the mode shapes are measured directly, so no post-processing is necessary (beyond the stereophotogrammetry calculations required to determine displacements of course). Unfortunately, time- and frequency-domain results cannot be obtained. To address this deficiency, tests were conducted using high-speed cameras which satisfy Shannon's sampling criteria.

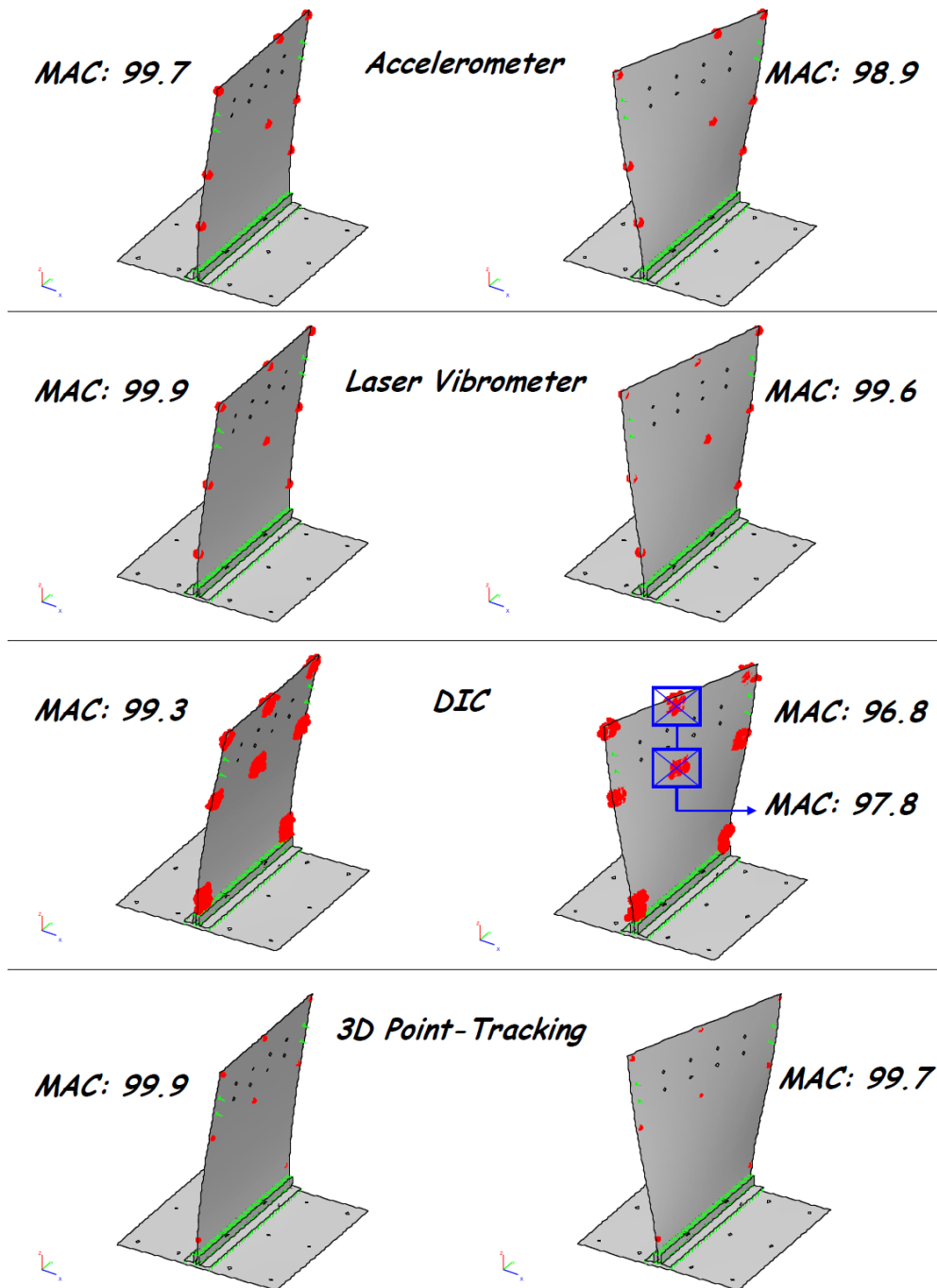


Figure 3: Previously Obtained Experimental Mode Shapes Compared to the BU FEM [5].

HIGH-SPEED CAMERA TESTING: EQUIPMENT AND EXPERIMENTAL SETUP

Two impact tests were performed on the BU that were designed to target different modes of the structure. In both cases, the cameras were positioned approximately 2 meters from the BU so the entire upright could be seen in the field of view. A 3 lb modal hammer was used to impact the structure. Time data for the hammer was captured using separate, synchronized data acquisition systems. Digital signal processing was carried out in MATLAB and curvefitting was performed using LMS PolyMAX [7,8].

In the first test, a pair of 1.3 Mega-pixel cameras measured the response of the BU due to a perpendicular 1500 lbf impact near Point 1 (see Figure 2a), at one of the top corners of the upright. In this case, only the out-of-plane modes of the upright were excited. The frame rate was set to 500 fps, corresponding to a Nyquist frequency of 250Hz. Three-dimensional point-tracking data was calculated at 30 points evenly distributed on the upright of the BU, including the 8 measurement points common to the other tests. Two averages were taken.

For the second impact modal test, the BU was impacted with approximately 4000 lbf at the same point where the shaker input was located for the accelerometer and LDV tests, to excite both the in-plane and out-of-plane modes. Images were taken at a rate of 250 fps with a pair of 3.6 Mega-pixel cameras. The goal was to acquire the first two in-plane modes of the BU which were not measurable from the previous impact test. For this test the Nyquist frequency was 125 Hz and therefore sufficient to capture the modes of interest. A total of 4 averages were taken and the response was tracked with 40 evenly-distributed photogrammetric targets distributed on the structure.

EXPERIMENTAL CONSIDERATIONS

The experimental considerations in the two impact tests were very similar to those of any other impact modal survey, but with a few additional things requiring attention. As with any impact test, the consistency of the input was a concern because of the variations in the force input due to the human excitation. While the level of amplitude varied somewhat, the input spectra were monitored to ensure a fairly uniform amount of energy was distributed across the frequency ranges of interest. Also, force/exponential windows were applied as needed to reduce the effects of leakage.

Beyond these standard concerns, the main issue was the synchronous triggering of the cameras with the other data acquisition systems. Typically, a DAQ system is triggered from the force signal generated by the impact hammer with a pre-trigger delay that captures the beginning part of the transient that would have otherwise been lost. Modern high-end, high-speed cameras have pre-trigger capabilities, but these were not available during the first round of testing. Both systems were triggered via an external source prior to impact, so the timing of the impact was not consistent. Due to the timing variation, different windows had to be applied for each average.

In the second impact test, the use of a different timing scheme and trigger synchronization mechanism was investigated. Due to a time delay between the two systems, the phase of the input and output spectra were misaligned. As a result, the poles of the frequency response functions were not stable and the FRFs could not be curvefit. Therefore, the linear spectra calculated from the displacements measured by the imaging systems were used to approximate mode shapes. This procedure provided useful data that were used in correlation studies and for comparisons with the results from the finite element model and with tri-axial accelerometers.

EXPERIMENTAL RESULTS AND CORRELATION TO THE FEM

The initial results obtained from the first impact test (out-of-plane impact, 500 fps) showed a very high level of correlation to the reference finite element model when compared using the Modal Assurance Criterion (MAC) [9,10] and Pseudo-Orthogonality Check (POC) [11,12]. Tables 1 through 3 summarize the correlation results for the first impact test. For modes 1 (26 Hz), 3 (78 Hz), and 5 (158 Hz), the diagonal MAC values are 99.9⁺, 99.8, and 98.1 percent, respectively. The average frequency difference is -0.14%. The diagonal POC terms are all within 3.2% of correlation to the FEA and the off-diagonal terms are all less than 2%.

Table 1: Mode Shape Pairs for the FEM and the First (500 fps) Impact Test

| Pair | FEA Mode # | FEA Freq. (Hz) | 3DPT Mode # | 3DPT Freq. (Hz) | Diff. (%) | MAC |
|------|------------|----------------|-------------|-----------------|-----------|-------------------|
| 1 | 1 | 26.03 | 1 | 25.79 | 0.94 | 99.9 ⁺ |
| 2 | 3 | 77.68 | 2 | 78.03 | -0.44 | 99.8 |
| 3 | 5 | 158.01 | 3 | 158.16 | -0.09 | 98.1 |

Table 2: MAC Matrix comparing the FEM and the First (500 fps) Impact Test

| <i>Modal Assurance Criteria</i> | | | | | |
|---------------------------------|------------------|--------------------------|-----------------|------------------|--|
| | | 3D Point-Tracking | | | |
| | | <i>25.79 Hz</i> | <i>78.03 Hz</i> | <i>158.16 Hz</i> | |
| FEM | <i>26.03 Hz</i> | 99.99⁺ | 0.10 | 11.30 | |
| | <i>77.68 Hz</i> | 0.10 | 99.80 | 0.20 | |
| | <i>158.01 Hz</i> | 10.30 | 0.00 | 98.10 | |

Table 3: POC matrix comparing the FEM and the First (500 fps) Impact Test

| <i>Pseudo-Orthogonality Check</i> | | | | | |
|-----------------------------------|------------------|--------------------------|-----------------|------------------|--|
| | | 3D Point-Tracking | | | |
| | | <i>25.79 Hz</i> | <i>78.03 Hz</i> | <i>158.16 Hz</i> | |
| FEM | <i>26.03 Hz</i> | 1.0143 | -.0105 | .0045 | |
| | <i>77.68 Hz</i> | -.0104 | 1.0200 | -.0198 | |
| | <i>158.01 Hz</i> | -.0089 | .0128 | .9681 | |

Despite the phase-lag between the input and outputs, the results of the oblique impact modal test are excellent. Tables 4 through 6 summarize the mode shape pairs and MAC and POC matrices, respectively. Though the 5th mode was not measured, the 2 additional in-plane modes were measured very clearly. When comparing the 3D point-tracking mode shapes with the FEM, the diagonal MAC values through the first 4 consecutive modes are at least 98.9% with a maximum off-diagonal value of 0.4%. The POC matrix also indicates a very high level of correlation to the FEM. At most, the diagonal terms deviate from 1 by 0.16% and the maximum off-diagonal term is 6.69%.

Table 4: Mode Shape Pairs for the FEM and the 250 fps Oblique Impact Test

| Pair | FEA Mode # | FEA Freq. (Hz) | 3DPT Mode # | 3DPT Freq. (Hz) | Diff. (%) | MAC |
|------|------------|----------------|-------------|-----------------|-----------|------|
| 1 | 1 | 26.03 | 1 | 25.94 | 0.35 | 99.8 |
| 2 | 2 | 70.69 | 2 | 63.94 | 9.55 | 99.6 |
| 3 | 3 | 77.68 | 3 | 78.19 | -0.65 | 98.9 |
| 4 | 4 | 108.8 | 4 | 98.69 | 9.29 | 99.6 |

Table 5: MAC Matrix for the FEM and the 250 fps Oblique Impact Test

| <i>Modal Assurance Criteria</i> | | | | | |
|---------------------------------|--------------|--------------------------|--------------|--------------|--------------|
| | | 3D Point-Tracking | | | |
| | | <i>25.94</i> | <i>63.94</i> | <i>78.19</i> | <i>98.69</i> |
| FEM | <i>26.03</i> | 99.8 | 0 | 0.2 | 0 |
| | <i>70.69</i> | 0.1 | 99.6 | 0 | 0 |
| | <i>77.68</i> | 0.2 | 0 | 98.9 | 0 |
| | <i>108.8</i> | 0.1 | 0.4 | 0 | 99.6 |

Table 6: POC Matrix for the FEM and the 250 fps Oblique Impact Test

| <i>Pseudo-Orthogonality Check</i> | | | | | |
|-----------------------------------|--------------|--------------------------|--------------|---------------|---------------|
| | | 3D Point-Tracking | | | |
| | | <i>25.94</i> | <i>63.94</i> | <i>78.19</i> | <i>98.69</i> |
| FEM | <i>26.03</i> | .9999 | .0000 | .0392 | .0000 |
| | <i>70.69</i> | .0240 | .9984 | .0000 | .0010 |
| | <i>77.68</i> | .0221 | .0000 | 1.0008 | .0000 |
| | <i>108.8</i> | .0339 | .0669 | .0000 | 1.0000 |

In all correlation studies, including accelerometer and laser Doppler vibrometer test results, there is at least a 5% difference between the finite element model and the experimental results for the in-plane modes. The stereophotogrammetry oblique impact data show even more deviation – the differences for modes 2 and 4 are 9.55% and 9.29%, respectively.

To confirm that these natural frequencies are consistent with another reference, the 3D point-tracking frequency response functions and poles were compared to the results obtained from collocated tri-axial accelerometers that measured data simultaneously during the oblique testing. The out-of-plane motion measured at points 1 and 3 are compared in [Figures 4](#) and [5](#), respectively. At the peaks, the two measurement types agree very well. The curves for the stereophotogrammetry FRFs are not as smooth as those from the accelerometers, indicating a lower signal to noise ratio. This is even more apparent for the in-plane measurements shown in [Figures 6](#) and [7](#).

In addition to visually inspecting the FRFs, the poles for the 3DPT and accelerometers were compared. [Table 7](#) compares the poles from the average 3D point-tracking linear input spectra and those from the FRFs from the tri-axial accelerometers at points 1 and 3 (top corners). The maximum difference between any two corresponding poles is 1.45%, so the 3DPT and accelerometer results are consistent. Furthermore, the accelerometer and LDV results were obtained as part of a previous study over the course of 2008 and 2009, while the 3DPT experiments were run in March, 2010. Though there are differences, the results are acceptable when considering the amount of time between the tests; small variations such as these are reasonable considering the length of time between tests and the nature of the bolted configuration used for these tests.

Table 7: Comparison of 3DPT and Accelerometer Poles for the Oblique Impact Test

| 3D Point-Tracking Poles (Hz) | Tri-axial Accelerometer Poles (Hz) | Diff. (%) |
|------------------------------|------------------------------------|-----------|
| 25.94 | 25.65 | 1.11 |
| 63.94 | 64.44 | -0.78 |
| 78.19 | 77.78 | 0.52 |
| 98.69 | 97.26 | 1.45 |

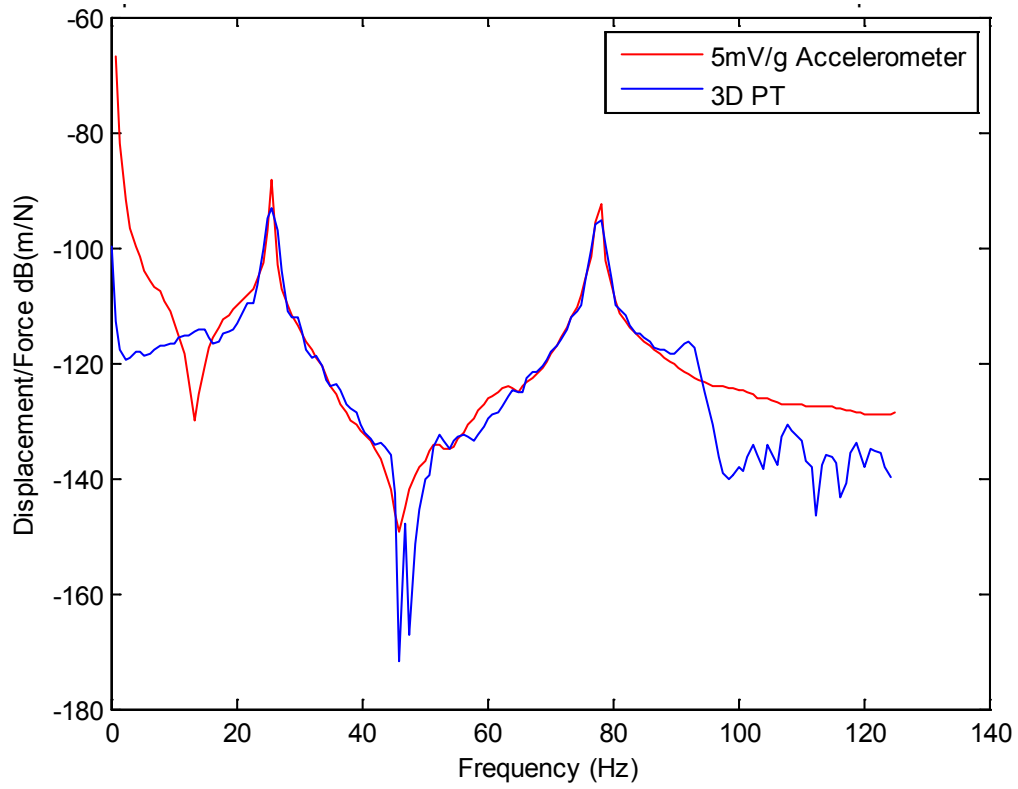


Figure 4: FRF comparison of 3DPT to a collocated accelerometer – Pt 1 out-of-plane.

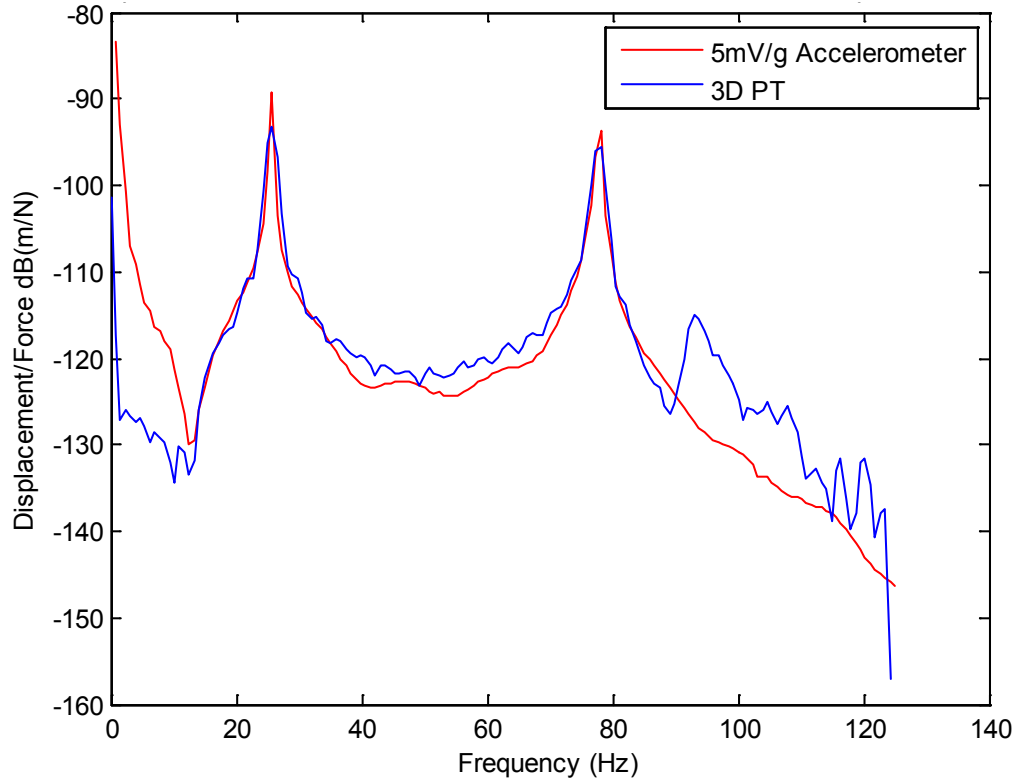


Figure 5: FRF comparison of 3DPT to a collocated accelerometer – Pt 3 out-of-plane.

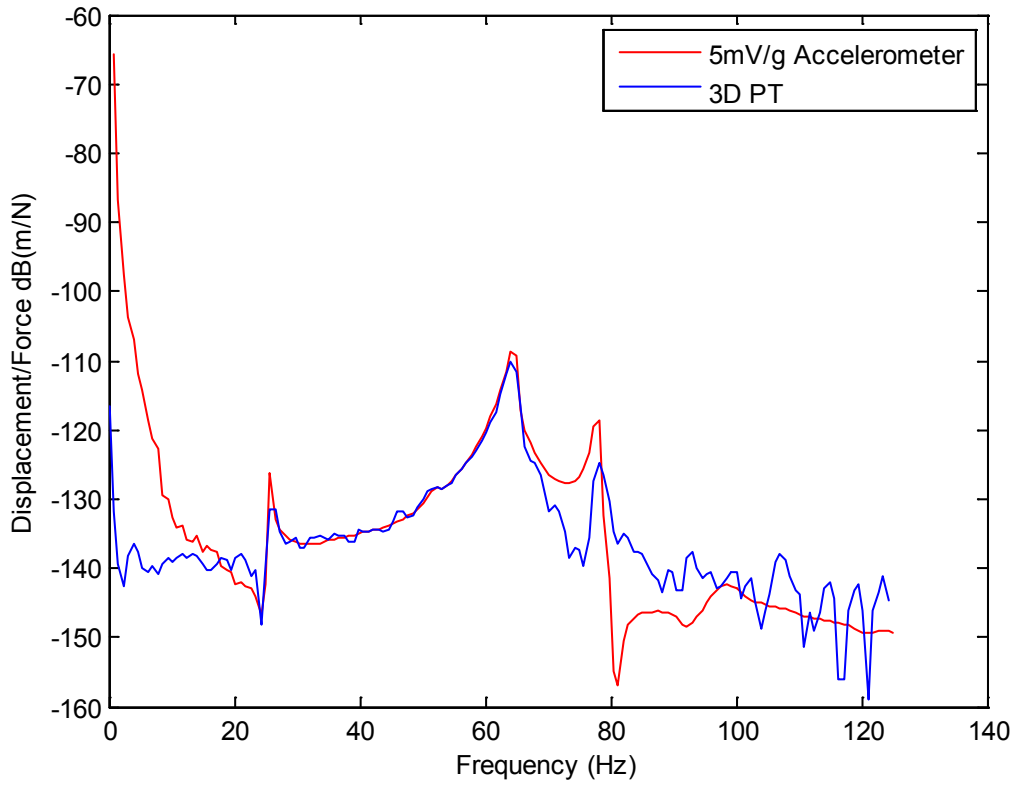


Figure 6: FRF comparison of 3DPT to a collocated accelerometer – Pt 1 horizontal.

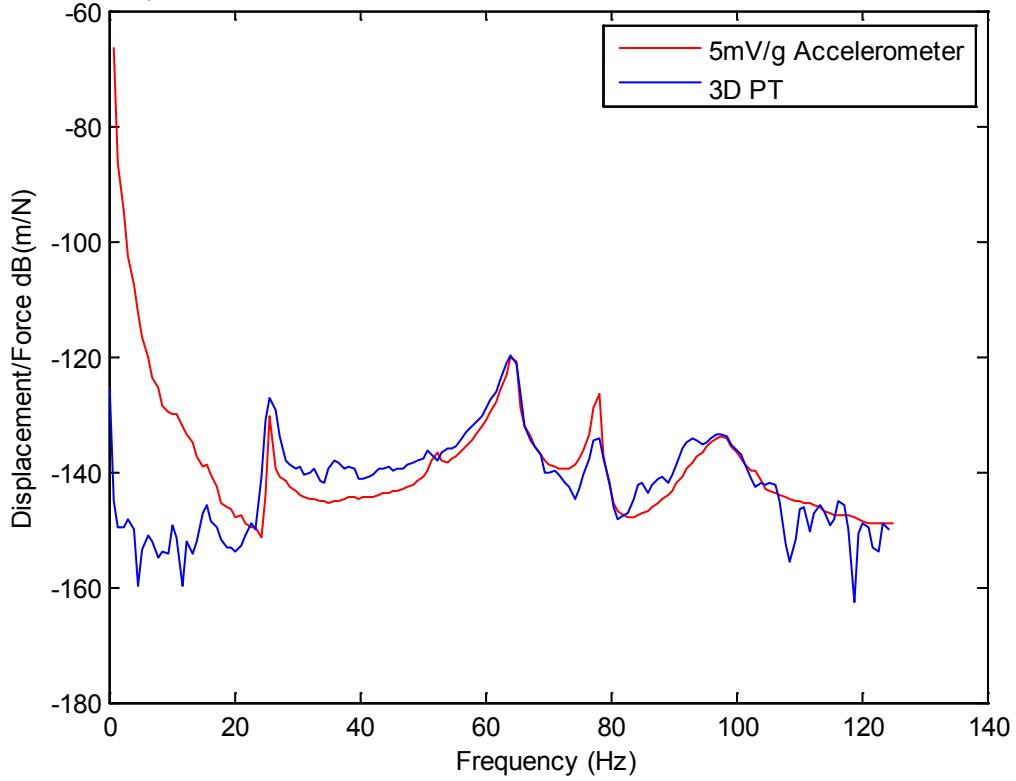


Figure 7: FRF comparison of 3DPT to a collocated accelerometer – Pt 1 vertical.

OBSERVATIONS AND CONCLUSIONS

Stereophotogrammetry techniques provide additional measurement capabilities that compliment the current array of traditional measurements by providing an alternative that favors high-displacement and low-frequency vibrations typically difficult to measure with accelerometers and laser vibrometers. The techniques presented here generated results that showed a very high level of correlation to the reference finite element model of the Base-Upright. Therefore, the application of the image-based systems for vibrations and modal analysis is a viable technique for the development of structural dynamic models.

Previous studies showed that when low-speed cameras are used in conjunction with forced-normal-mode-testing, both digital image correlation and 3D point-tracking can accurately capture mode shapes as long as measurable displacements are present. The biggest difference between the traditional and the FNMT-based techniques is the approach taken to measure multiple modes. Accelerometers and scanning laser Doppler vibrometers measure multiple modes over a broad frequency range point by point. Conversely, the two image-based approaches measure all points simultaneously. If FNMT is used, all approaches measure the response of one mode at a time. DIC can provide an incredibly fine spatial resolution that would be unobtainable with accelerometers or would take a significant amount of time with a scanning LDV. Had the entire surface of the upright been patterned and the same facet settings used, roughly 40,000 effective data points could have been measured.

Combining DIC and 3DPT with high-speed cameras enables simultaneous measurement of multiple modes over a wide frequency range. The high-speed 3DPT results were the best obtained in these studies through the first 5 modes of the Base-Upright. Nearly all MAC values were higher than 99%. Though not presented here, time traces from DIC could theoretically be exported and used to calculate mode shapes just as was done with the 3D point-tracking. A higher point-density may be obtained with DIC, but larger amounts of data recording needs to be considered. For a given measurement, unless local strain data is desired, the use of 3DPT is recommended.

Another possible use for DIC or 3D point-tracking is the measurement of rigid body motion of a test article suspended in a free-free condition. Measuring structures that exhibit large displacements or rigid body motion is difficult for LDVs, because the specific position on the structure at which the laser is pointing will change. Accelerometers provide an inertial reference frame, but their useful ranges usually begin at frequencies above those where rigid body motion occurs. The use of the optically-based displacement measurements presented in this work (DIC and 3DPT) provides an alternative measurement technique that increases the envelope over which engineers can now make vibration measurements.

ACKNOWLEDGEMENTS

The authors gratefully appreciate the financial support for this work provided by the U.S. Army Research Office Nanomanufacturing of Multifunctional Sensors Ref. Award Number: W911NF-07-2-0081 and the National Science Foundation under Grant No. 0900534, entitled “Dynamic Stress-Strain Prediction of Vibrating Structures in Operation”. Any opinions, findings, and conclusions or recommendations expressed in this material are those of the authors and do not necessarily reflect the views of the National Science Foundation or Army Research Office. The authors would also like to thank Tim Schmidt of Trillion Quality Systems for providing insight and equipment necessary to conduct the measurements.

REFERENCES

- [1] Butland, Adam, “A Reduced Order, Test Verified Component Mode Synthesis Approach for System Modeling Applications,” Master’s Thesis, University of Massachusetts Lowell, January 2008.
- [2] Nicgorski, Dana, “Investigation on Experimental Issues Related to Frequency Response Function Measurements for Frequency Based Substructuring,” Master’s Thesis, University of Massachusetts Lowell, January 2008.
- [3] Wirkkala, N.A., “Development of Impedance Based Reduced Order Models for Multi-Body Dynamic Simulations of Helicopter Wing Missile Configurations,” Master’s Thesis, University of Massachusetts Lowell, April 2007.
- [4] Pingle, P., J. Sailhamer, & P. Avitabile, “Comparison of 3D Laser Vibrometer and Accelerometer Frequency Measurements,” Proceedings of the IMAC-XXVII, February 9-12, 2009 Orlando, Florida USA.
- [5] Warren, Chris, Pawan Pingle, Chris Niezrecki, & Peter Avitabile, “Comparison of Image Based, Laser, and Accelerometer Measurements,” Proceedings of the IMAC-XXVIII, February 1-4, 2010, Jacksonville, Florida USA.
- [6] PONTOS – GOM mbH, Mittelweg 7-8, 38106 Braunschweig, Germany.

- [7] MATLAB. The Mathworks, Inc. 3 Apple Hill Drive, Natick, MA 01760-2098.
- [8] PolyMAX, Leuven Measurement Systems, Leuven, Belgium.
- [9] Allemang, R.J. and Brown,D.L., "A Correlation Coefficient for Modal Vector Analysis," First International Modal Analysis Conference, Orlando, Florida, November 1982, 110-116.
- [10] Allemang, Randall J. "The Modal Assurance Criterion – Twenty Years of Use and Abuse." Sound and Vibration Magazine. August 2003. 14-21.
- [11] Avitabile, Peter, John C. O'Callahan, and J. Milani. "Model Correlation and Orthogonality Criteria," Sixth International Modal Analysis Conference, Orlando, Florida, February 1988, 1039-1047.
- [12] Avitabile, Peter. "Modal Model Correlation Techniques," Doctoral Dissertation Thesis, University of Massachusetts Lowell, 1998.

Experimental Modal Analysis (EMA) Using Ibrahim Time Domain (ITD) Method and Wiener Filter

Jongsuh Lee, Sunghwan Kim, Daesung Kim, and Semyung Wang

Abstract it is important to know the dynamic characteristics of a system such as natural frequency, mode shape and damping ratio. In order to obtain the dynamic characteristics of the system, experimental modal analysis (EMA) is carried out for analyzing such a system. Frequency domain approaches are generally used in EMA, those are based on estimation of frequency response function (FRF). In this paper, the EMA is performed in time domain with Ibrahim Time Domain (ITD) method, it is advantageous in analyzing a highly damped system compared with frequency domain approaches. In order to estimate such a system accurately, we adopted Wiener filter in ITD method.

1 Introduction

An unwanted vibration is produced by rotation, unbalance force of reciprocation, dynamic effect of friction, and contact between accessories. When the applied frequency is closed to the natural frequency of the system, resonance would be happened and cause a serious problems. Therefore it is important to find out the modal

Jongsuh Lee

Gwangju Institute of Science and Technology (GIST), 261 Cheomdan-gwagiro (Oryong-dong), Buk-gu, Gwangju, 500-712, Republic of Korea, e-mail: leejongsuh@gist.ac.kr

Sunghwan Kim

Gwangju Institute of Science and Technology (GIST), 261 Cheomdan-gwagiro (Oryong-dong), Buk-gu, Gwangju, 500-712, Republic of Korea e-mail: shkim@gist.ac.kr

Daesung Kim

Gwangju Institute of Science and Technology (GIST), 261 Cheomdan-gwagiro (Oryong-dong), Buk-gu, Gwangju, 500-712, Republic of Korea e-mail: dskim@gist.ac.kr

Semyung Wang

Gwangju Institute of Science and Technology (GIST), 261 Cheomdan-gwagiro (Oryong-dong), Buk-gu, Gwangju, 500-712, Republic of Korea e-mail: smwang@gist.ac.kr

parameters (the natural frequencies, damping ratios, and mode shapes) to cope with problems in vibration. Determination of modal parameters of a structure using response and excitation measurements is a primary interest in structural dynamics. The methods for identifying modal parameters can be categorized into two groups: frequency domain methods and time domain methods. The frequency domain analysis [1] has been widely used and has been proved to be efficient in many cases. However, there are limits with these methods in dealing with heavy damping, closed natural frequencies because of spectral leakages occurred in transforming the time domain to frequency domain. If a structure has very closed natural frequencies, very heavy damping, the frequency domain methods would not identify accurate modal parameters. The reason for the limitation is essentially modal interference and hence some individual modes and natural frequencies cannot be observed separately. To avoid limitation of frequency domain analysis, time domain methods have been developed. In this paper, a time domain approach which is called as Ibrahim time domain (ITD) method [2] [3] [4] is used. It has been shown that the identification of structural modal parameters from experimental data can be placed in the form of a complex eigenvalue problem. Furthermore, the method can identify multi modal (highly coupled) systems and modes that have very small contribution in the responses. Also, the rapid measurement not influencing dynamic characteristics of the structure is required for ITD. More accurate modal estimation can be achieved because of canceling out the output noise by using Wiener Filter [5]. Because of this reason, Wiener ITD method that is called Modified Ibrahim time domain method is proposed.

2 Theory of the Ibrahim Time Domain Method

The governing equations of motion for an n-degree-of-freedom free vibration system can be written as

$$[M]\{\ddot{x}\} + [C]\{\dot{x}\} + [K]\{x\} = 0 \quad (1)$$

where M, C, and K are mass, damping, and stiffness matrices, x represent n-dimensional displacement vectors. The solution of this equation can be expressed in the form of

$$x_i(t_j) = \sum_{r=1}^{2N} (\psi_{ir}) e^{s_r t_j} \quad (2)$$

where i represents the coordinate and j the specific time increment at which the response is measured, s_r is the r th root or complex eigenvalue of the system's characteristic equation and ψ_{ir} is the i th component of the complex eigenvector ψ_r . The eigenvectors are unscaled. Also, total number of degrees of freedom are assumed to be N . For m response locations and q time instants, it leads to an expression of the type

$$\begin{matrix} [x(t)] = [\Psi] \cdot [\Lambda(t)] \\ (m \times q) \quad (m \times 2N) \quad (2N \times q) \end{matrix} \quad (3)$$

where $[x(t)]$ is an m by q matrix of free response measurements from the structure. $[\Psi]$ is an m by $2N$ matrix of unknown eigenvector, and $[\Lambda(t)]$ is an $2N$ by q matrix depending on the complex eigenvalues (as yet unknown) and the response measurement times. Let us consider now a second set of responses delayed by an interval Δt with respect to the first set now a second set of responses delayed by an interval with respect to the first set

$$x_i(t_j + \Delta t) = \sum_{r=1}^{2N} (\psi_{ir}) e^{s_r(t_j + \Delta t)} \text{ or } \hat{x}_i(t_j) = \sum_{r=1}^{2N} (\hat{\psi}_{ir}) e^{s_r(t_j)} ; \quad (\hat{\psi}_{ir}) = (\psi_{ir}) e^{s_r \Delta t} \quad (4)$$

Following a third set delayed by an interval $2\Delta t$ with respect to the first set is

$$x_i(t_j + 2\Delta t) = \sum_{r=1}^{2N} (\psi_{ir}) e^{s_r(t_j + 2\Delta t)} \text{ or } \hat{\hat{x}}_i(t_j) = \sum_{r=1}^{2N} (\hat{\hat{\psi}}_{ir}) e^{s_r(t_j)} \quad (5)$$

where $(\hat{\hat{\psi}}_{ir}) = (\psi_{ir}) e^{s_r 2\Delta t}$

combining eqs. (3) and (4) lead following equation

$$\begin{bmatrix} x(t) \\ \hat{x}(t) \end{bmatrix} = \begin{bmatrix} \Psi \\ \hat{\Psi} \end{bmatrix} [\Lambda(t)] \text{ or } [Y(t)] = [P] [\Lambda(t)] \quad (6)$$

Also, combining eqs. (4) and (5) lead to following equation

$$\begin{bmatrix} \hat{x}(t) \\ \hat{\hat{x}}(t) \end{bmatrix} = \begin{bmatrix} \hat{\Psi} \\ \hat{\hat{\Psi}} \end{bmatrix} [\Lambda(t)] \text{ or } [\hat{Y}(t)] = [\hat{P}] [\Lambda(t)] \quad (7)$$

where $[Y(t)]$, $[\hat{Y}(t)]$, $[P]$ and $[\hat{P}]$ are non-singular matrices. the number of assumed modes N is a variable, we can arrange as $m = N$, so that the matrices $[P]$ and $[\hat{P}]$ are squared. If the number of time samples q is identical to $2N$, from Eqs. (6) and (7), the following equation is obtained

$$[\hat{Y}(t)][Y(t)]^{-1}[P] = [\hat{P}] \quad (8)$$

In eq. 8 shows the system matrix

$$[A] = [\hat{Y}(t)][Y(t)]^{-1} \quad (9)$$

However, it is customary to use more data than the minimum required by setting q to a value greater than $2N$. In this case, use of Eq. 8 to determine $[A]$ will be via the pseudo-inverse process which yields a least squares solution for the matrix. In this case, an expression for $[A]$ is

$$[A] = [\hat{Y}(t)][Y(t)]^T \left([Y(t)][Y(t)]^T \right)^{-1} \quad (10)$$

when Eq. (8) is opened out into $2N$ identical sets of equations, each one relates column $\{P\}_r$ of $[P]$ to column $\{\hat{P}\}_r$ of $[\hat{P}]$

$$[A]\{P\}_r = \{\hat{P}\}_r, \quad r = 1, 2, \dots, 2N \quad (11)$$

Eqs. (6) and (7) allow a relation between $\{P\}_i$ and $[\hat{P}]$ to be written in the form

$$\{\hat{P}\}_r = e^{s_r \Delta t} \{P\}_r \quad (12)$$

Eq. (10) can be written in the form

$$[A]\{P\}_r = e^{s_r \Delta t} \{P\}_r \quad (13)$$

Eq. (13) represents a set of $2N$ linear non-homogeneous equations in $2N$ unknown eigenvalues. This set is therefore solvable and one is able to determine the $2N$ eigenvalues and their corresponding $2N$ eigenvectors. It must be noted that these eigenvalues are not the same as those of the original equations of motion but they are closely related and we shall see that it is a straightforward process to extract the system's natural frequencies, damping factors and mode shapes from eq. (13)

$$e^{s_r \Delta t} = a_r + ib_r = e^{-\omega_r \zeta_r \Delta t} e^{i\omega'_r \Delta t} \quad (14)$$

From the above equation the undamped natural frequency (ω_r) and viscous damping factor (ζ_r) can be derived.

$$\begin{aligned} \omega_r \zeta_r &= \frac{-\ln(a_r^2 + b_r^2)}{2\Delta t} \\ \omega'_r &= \omega_r \sqrt{1 - \zeta_r^2} = \frac{\tan^{-1}(b_r/a_r)}{\Delta t} \end{aligned} \quad (15)$$

2.1 Experiment

An experimental modal analysis algorithm, ITD method is done by Laser Scanning Vibrometer (LSV). Fig. 1 shows the experimental configuration and LSV. A Random signal is used to apply force to the system. In order to obtain modal parameters, generally frequency response function (FRF) is used. From the measured response and applied force, the Frequency Response Function (FRF) is calculated. The modal parameters are estimated by Peak in Magnitude, Half-Power Bandwidth and Quadrature Peak Method from each node FRFs. In this paper, the applied force signal and measured each node responses are involved being applied to both methods (FRF and ITD). Fig. 2 is FRF obtained by experiment, the circles on the figure indicates each modes composing of the structural dynamic characteristics, modal

parameter estimation can be achieved by the result values of FRF at those circle locations.

3 Modified Ibrahim Time Domain of Experimental Modal Analysis

In previous, it looked into the Ibrahim Time Domain (ITD) algorithms. This part will introduce the different approach which is process to get the Impulse Response Function (IRF) using Wiener Filter that makes to be able to calculate accurate IRF. In addition more accurate modal estimation can be possible because of output noise canceling. System identification on the basis of measurement can be express block diagram the [fig. 3](#) when the input noise can be ignored. Wiener filter is used to minimize the mean square error estimation, $\hat{x}(t)$ of $x(t)$. With $d(t)$ is input of the system as well as FIR filter, $h(t)$. $\hat{x}(t)$ is output of the FIR filter which can be expressed by convolution sum of $d(t)$ and $h(t)$.

$$\sum_{l=0}^{p-1} h(l)d(t-l) = \hat{x}(t) \quad (16)$$



Fig. 1 Configuration of experiment.

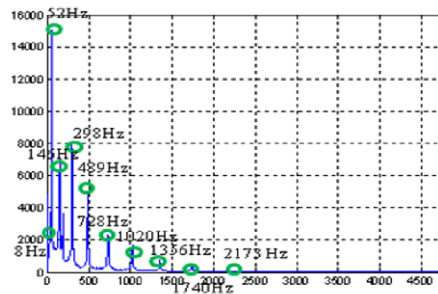


Fig. 2 Frequency Response Function (FRF) of the structure.

Design of the Wiener filter requires finding filter coefficients, $h(t)$, that minimize the mean-square error. In order for a set of filter coefficients to minimize ξ , it is necessary and sufficient that derivatives of ξ with respect to $h^*(k)$ are equal to zero for $k = 0, 1, \dots, p - 1$.

$$\frac{\partial \xi}{\partial h^*(k)} = \frac{\partial E \{e(t)e^*(t)\}}{\partial h^*(k)} = -E \{e(t)d^*(t-k)\} = 0 \tag{17}$$

$$e(t) = x(t) - \hat{x}(t) = x(t) - \sum_{l=0}^{p-1} h(l)d(t-l) \tag{18}$$

from eqs. (17) and (18), eliminating $e(t)$, the following equation is obtained.

$$E \{x(t)d^*(t-k)\} - \sum_{l=0}^{p-1} h(l)E \{d(t-l)d^*(t-k)\} = E \left\{ \left[x(t) - \sum_{l=0}^{p-1} h(l)d(t-l) \right] d^*(t-k) \right\} = 0 \tag{19}$$

The impulse response of the optimal filter $h(t)$, minimizing coefficient ξ , can be obtained from the Wiener-Hopf equation. The Wiener-Hopf equation is given by

$$\sum_{l=0}^{p-1} h(l)R_d(k-l) = r_{dx}(k) ; k = 0, 1, \dots, p - 1 \tag{20}$$

Eq. (20) may be written concisely as below.

$$R_d \mathbf{h} = \mathbf{r}_{dx} \tag{21}$$

Where R_d is $k \times k$ Hermitian Toeplitz matrix of input autocorrelations, \mathbf{r}_{dx} is the vector of cross-correlations between the input and output and \mathbf{h} is the vector of impulse response of the optimal filter. Finally, impulse response of the optimal filter can be obtained from eq. (21) to

$$\mathbf{h} = R_d^{-1} \mathbf{r}_{dx} \tag{22}$$

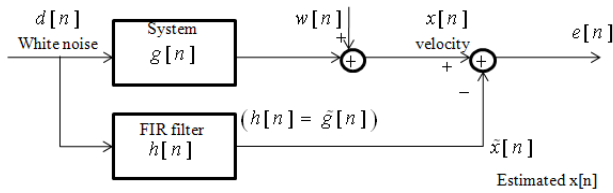


Fig. 3 Block diagram for Winer Filter.

Impulse response of the optimal filter is used instead of Inverse Fourier Transform of FRF that is applied to the ITD algorithm. All experimental results, LSV (obtained by FRF), The ITD method and the Wiener-ITD method, are compared in next chapter.

4 Comparison the experimental results with each algorithm

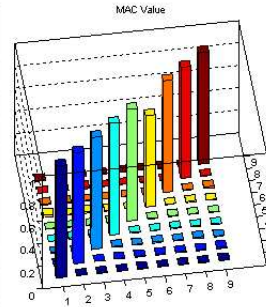
Table 1 is shown the natural frequencies and damping ratio of LSV results, ITD algorithm results and Wiener ITD algorithm results, all algorithms are used with same experimental measured time data. From the Table 1, there are no difference between both natural frequencies except of 9th and 10th. However there are large differences between both damping ratios, which are the Wiener ITD results is the smallest among the others results. The Modal Assurance Criterion (MAC) is used to confirm closeness of mode shape between got from LSV and from Wiener ITD method.

Table 4 is shown the Modal Assurance Criterion (MAC) of the measured structure with the LSV results and Wiener ITD results. From these the diagonal elements are closed unity and other off diagonal elements are close to zero. Therefore, the mode shape vectors are relation of independence is validated. And the fact that the estimated mode shape vectors of Wiener-ITD results are really close to LSV results are confirmed.

| Natural Frequency (Hz) | | | | Dampingratio (%) | | | |
|------------------------|------|---------|------------|------------------|--------|---------|------------|
| | LSV | LSV_ITD | Wiener ITD | | LSV | LSV_ITD | Wiener ITD |
| 2 nd | 52 | 53.234 | 52.9508 | 2 nd | 1.7432 | 12.5 | 8.9 |
| 3 rd | 146 | 143.514 | 142.491 | 3 rd | 2.9761 | 4.9 | 3.5 |
| 4 th | 298 | 298.789 | 299.756 | 4 th | 0.7501 | 1.4 | 1.7 |
| 5 th | 489 | 490.159 | 491.171 | 5 th | 0.5141 | 0.5 | 0.5 |
| 6 th | 728 | 728.886 | 730.607 | 6 th | 0.6008 | 0.5 | 0.3 |
| 7 th | 1020 | 1014.79 | 1018.32 | 7 th | 0.314 | 0.4 | 0.2 |
| 8 th | 1356 | 1336.28 | 1348.7 | 8 th | 0.3245 | 0.9 | 0.3 |
| 9 th | 1740 | 1613.99 | 1710.07 | 9 th | 0.2733 | 6.1 | 0.8 |
| 10 th | 2173 | | 1958.18 | 10 th | 0.2733 | | 5.8 |

Table 1 Natural frequency and damping ratio results obtained by each algorithm (LSV, ITD and Wiener-ITD).

| Wiener_ITD \ LSV | $\{\psi\}_2$ | $\{\psi\}_3$ | $\{\psi\}_4$ | $\{\psi\}_5$ | $\{\psi\}_6$ | $\{\psi\}_7$ | $\{\psi\}_8$ | $\{\psi\}_9$ | $\{\psi\}_{10}$ |
|------------------|--------------|--------------|--------------|--------------|--------------|--------------|--------------|--------------|-----------------|
| $\{\psi\}_2$ | 0.997 | 0.005 | 0.006 | 0.002 | 0.006 | 0.020 | 0.009 | 0.002 | 0.006 |
| $\{\psi\}_3$ | 0.003 | 0.987 | 0.000 | 0.015 | 0.002 | 0.005 | 0.006 | 0.004 | 0.008 |
| $\{\psi\}_4$ | 0.006 | 0.001 | 0.998 | 0.012 | 0.003 | 0.014 | 0.004 | 0.011 | 0.003 |
| $\{\psi\}_5$ | 0.003 | 0.006 | 0.007 | 0.996 | 0.010 | 0.005 | 0.005 | 0.002 | 0.008 |
| $\{\psi\}_6$ | 0.008 | 0.007 | 0.004 | 0.004 | 0.994 | 0.001 | 0.005 | 0.006 | 0.005 |
| $\{\psi\}_7$ | 0.005 | 0.006 | 0.009 | 0.005 | 0.005 | 0.812 | 0.005 | 0.002 | 0.006 |
| $\{\psi\}_8$ | 0.008 | 0.008 | 0.005 | 0.008 | 0.008 | 0.003 | 0.997 | 0.000 | 0.007 |
| $\{\psi\}_9$ | 0.005 | 0.006 | 0.010 | 0.004 | 0.005 | 0.011 | 0.007 | 0.990 | 0.002 |
| $\{\psi\}_{10}$ | 0.008 | 0.013 | 0.006 | 0.007 | 0.004 | 0.006 | 0.014 | 0.008 | 0.995 |



LSV Wiener ITD.

Table 2 Modal Assurance Criterion (MAC) between LSV Wiener ITD.

5 Conclusion

Ibrahim time domain (ITD) method has been shown that the identification of structural modal parameters from experimental data can be expressed as the form of a complex eigenvalue problem when the viscous damping system has free vibration condition. This method is useful in estimation of the modal parameters when the system has heavy damping. However, ITD method is only dealing with response of system, it does not guarantee to give good approximation of modal parameters compared with general other methods which use applied force to the system as well as response of system. In order to overcome disadvantage of ITD method, this paper suggest additional procedure that gives more accurate IRF by adopting Wiener-filter in which both force and response are included. A simple beam is used to verify the results of Wiener-ITD method and those are compared with LSV results and original ITD method.

References

1. D.J. Ewins, 1995, (Taunton : Research Studies Press)
2. Ibrahim, S.R. Mikulcik, E.C., 1973, (Shock and Vibration Bulletin), Vol. 43, pp. 21-37.
3. Ibrahim, S.R. Pappa. R.S., 1981, (Shock and Vibration Bulletin), Vol. 51, pp. 43-72.
4. Ibrahim, S.R., 1978, (Journal of Spacecraft and Rockets), Vol. 15, pp. 313-316.
5. Simon Haykin, 2001, (Prentice Hall), Forth Edition

A New Broadband Modal Identification Technique with Applications

Lingmi Zhang¹, Yukio Tamura², Tong Wang¹, Xinghui Sun¹

¹Institute of Vibration Engineering

Nanjing University of Aeronautics and Astronautics, Nanjing 210016, China P.R.

²Wind Engineering Research Center, Dept. of Architectural Engineering

Tokyo Polytechnic University, 1583 Iiyama, Atsuge, Kanagawa 243-0297, Japan

ABSTRACT Frequency domain polyreference (FDPR) and frequency domain direct parameter identification (FDDPI) methods developed in the middle of 1980 s has superior performance in selected frequency band, and become major MIMO modal identification techniques in frequency domain. However, the methods, as well as rational fraction polynomial (RFP) algorithm developed in late 1980 s, are not suitable for broadband application compared to their time domain counterparts, i.e. extended Ibrahim time domain (EITD) or eigensystem realization algorithm (ERA), and polyreference complex exponential (PRCE) methods, due to numerical issues. But all time domain modal identification algorithms have a serious drawback in discrimination structural (physical) modes from spurious (noise) ones. In this paper, a new frequency domain modal identification technique is presented based on left or right matrix fraction description (LMFD or RMFD) of MIMO FRF or half PSD matrix. Theoretical background of the two broadband modal identification procedures is discussed with relevant numerical issues. It is revealed that the RMFD-based procedure is actually z-domain implementation of the RFP algorithm. FDPR and FDDPI are actually special cases, i.e. first and second order of LMFD-based broadband modal identification procedure implementing in discrete z-domain, instead of continuous s-domain. It is also shown that both RMFD-based and LMFD-based broadband modal identification procedures are parallel to their time domain counterparts, i.e. PRCE and EITD algorithm. However, much easier and reliable structural mode discrimination can be obtained with much clearer stability diagram. Engineering applications of the two procedures, which make use of FRF measurements for EMA of an aircraft model and h-PSD measurements for OMA of a middle-raised office building, are presented with comparison with its counterparts in time and continuous frequency domain.

1 Introduction

Experimental modal analysis becomes a new research direction for dynamic testing and analysis of mechanical structures since 1970 s. Parametric modal identification procedures, e.g. least squares complex exponential (LSCE) and Ibrahim time domain (ITD) were developed and applied in mechanical and aerospace engineering. A breakthrough of the experimental modal analysis (EMA) took place in 1980 s, featured in the development of multiple-input multiple-out (MIMO) modal identification algorithms. MIMO modal identification algorithms in time domain were developed, e.g. polyreference complex exponential (PRCE), extended ITD (EITD) and eigensystem realization algorithm (ERA), in early 1980 s. Frequency domain MIMO modal identification procedures were also proposed afterwards, such as frequency domain polyreference (FDPR), direct frequency domain parameter identification (FDDPI), as well as MIMO version of rational fraction polynomial (RFP) implemented with orthogonal polynomial. PRFD/ DPI and RFP work pretty well in selected frequency band. A complex

modal indication function (CMIF) procedure was proposed as a mode indicator, and applied for modal identification in 1990 s afterwards. CMIF extracts one mode at a time with the ability to deal with closely-spaced and repeated modes as a MIMO approach in narrow band. EMA in both TD and FD have the ability in dealing with large account of I/O measurement and obtained widely applications in aerospace and automotive engineering. ^[1].

Since early 1990 s, operational modal analysis (OMA) has been proposed and drawn great attention in civil engineering community with applications for off-shore platforms, buildings, towers, bridges, etc. Operational modal analysis (OMA), named also as ambient or output-only modal analysis, utilizes only response measurements of the structures in operational condition subjected to ambient or natural excitation to identify modal characteristics. Advance from traditional experimental modal analysis (EMA) to the operational modal analysis (OMA) was the other major breakthrough in modal analysis. The key idea of implementing OMA was proposed in early 1990 s as Natural Excitation Technique (NExT), in which correlation function of the random response of a structure is utilized for modal identification ^[2]. NExT has shown that the correlation function can be expressed as a summation of decaying sinusoids. Each decaying sinusoid has a damped natural frequency, damping ratio and mode shape coefficient that is identical to the one of the corresponding structural mode. Correlation function can therefore be employed as impulse response function (IRF) in EMA to estimate modal parameters for OMA. Hence, major MIMO TD modal identification procedures developed in traditional EMA can directly be adopted for OMA.

Modal identification has been thought of a branch of general system identification. However, instead of directly making use of input/output data or output-only based on time series or state space model, in the modal community frequency response function (FRF), or impulse response function (IRF) are preferred, which takes advantage of the development of dynamic signal analyzer based on fast Fourier transformation (FFT). Driven by the OMA applications where IRF and FRF can not be obtained, modal community seeks new tools developed in general system identification. One is stochastic subspace identification (SSI) based on innovative state-space equation with Kalman filter, and the other is time series identification based on autoregressive moving averaging (ARMA) model with prediction-error method (PEM). Both of them are adopted from system identification community, and can make direct use of output-only data for modal identification. Compared to NExT as two-stage approach, conducting correlation estimation as first stage followed by modal parameter extraction as the second stage, the data-driven SSI and PEM-ARMA are one-stage approaches ^[3].

Modal identification has been dominated by the TD procedures for the industry applications with advantage in that all the modes in the frequency band can be identified simultaneously. However, the TD modal identification procedures, no matter advanced and sophisticated math models are based, have a serious drawback as described below. All modal identification procedure consists of two sequent steps, i.e. to determine structural modes at first, and then to estimate modal parameters for structural mode. Unfortunately, spurious or noise modes are always generated when extracting structural or physical modes. These spurious (noise) modes are even necessary to account for unwanted effects, such as measurement noise, leakage in signal processing, residuals and non-linearity s in the parametric model, etc. The spurious (noise) modes fulfill an important role in that they permit more accurate modal parameter estimation by supplying statistical DOFs to absorb these effects. For effective differentiation of physical (structural) from spurious (noise) modes, a variety of modal indicators have been developed but without preferred success ^[4]. In stead, a graphical approach making use of stability diagram is a much more effective measure. However, difficulties are often encountered to discrimination of structural modes with TD modal identification when dealing with real-world complex structure.

The major development and breakthrough of modal identification in 2000 s is to find solution in better determination of structural modes and extraction of modal parameters for all the structural modes in frequency domain. The new procedure in

FD is based on matrix fraction description of the FRF matrix linking with MIMO measurements and system parameters. There are two potential models, i.e. right matrix fraction description (RFMD) and left matrix fraction description (LMFD). The new FD modal identification procedures have the superiority in determination of structural modes over the TD counterparts and, at meantime, keep the advantage in extracting modal parameters of all modes in broadband, instead of selected or narrow band for other MIMO FD procedures [5].

2 Broadband Modal Identification based on Right Matrix Fraction Description (RMFD)

2.1 Theoretical Background of RMFD-based broadband modal identification

In the RFMD, a row of the FRF matrix can be described as

$$H_o(\omega) = B_o(\omega)A^{-1}(\omega) \quad (1)$$

Where $H_o(\omega) \in C^{1 \times N_i}$ is o^{th} row of the FRF matrix, corresponding to o^{th} response and $o = 1 \dots N_o$. $B_o(\omega) \in C^{1 \times N_i}$ and $A(\omega) \in C^{N_i \times N_i}$ denote the numerator and denominator matrix polynomials, respectively, which can be expressed as:

$$B_o(\omega) = \sum_{r=0}^n B_{o,r} \Omega_r(\omega) \quad A(\omega) = \sum_{r=0}^n A_r \Omega_r(\omega) \quad (2)$$

Where n is the order of the matrix polynomials, $\Omega_r(\omega)$ is the base function. Coefficient matrices $A_j \in C^{N_i \times N_i}$ and

$B_{o,j} \in C^{N_i \times N_i}$ contain parameters to be estimated.

A linearized error matrix for single output can be defined as

$$E_o(\omega_k) = B_o(\omega_k) - \tilde{H}_o(\omega_k)A(\omega_k) \quad k = 1, 2, \dots, N_f \quad (3)$$

Where $\tilde{H}_o(\omega_k)$ denotes the measured FRF, N_f is the spectral lines in the FRF.

A linear least squares solution can be derived when the following objective function is assumed

$$l(\theta) = \sum_{o=1}^{N_o} \sum_{k=1}^{N_f} E_o(\omega_k) E_o^H(\omega_k) \quad (4)$$

To minimize the objective function, a least squares solution can then be obtained by solving the following linear equations. :

$$J\theta = \begin{bmatrix} X_1 & 0 & \dots & 0 & Y_1 \\ 0 & X_2 & \dots & 0 & Y_2 \\ \vdots & \vdots & \ddots & \vdots & \vdots \\ 0 & 0 & \dots & X_{N_o} & Y_{N_o} \end{bmatrix} \theta = 0 \quad (5)$$

Where

$$\theta = \begin{Bmatrix} \beta_1 \\ \vdots \\ \beta_1 \\ \alpha \end{Bmatrix} \beta_o = \begin{Bmatrix} B_{o,0} \\ B_{o,1} \\ \vdots \\ B_{o,n} \end{Bmatrix} \alpha = \begin{Bmatrix} A_0 \\ A_1 \\ \vdots \\ A_n \end{Bmatrix} \quad o = 1, 2, \dots, N_o \quad (6)$$

$$X_o = \begin{bmatrix} [\Omega_0(\omega_1) & \Omega_1(\omega_1) & \dots & \Omega_n(\omega_1)] \\ [\Omega_0(\omega_2) & \Omega_1(\omega_2) & \dots & \Omega_n(\omega_2)] \\ \vdots \\ [\Omega_0(\omega_{N_f}) & \Omega_1(\omega_{N_f}) & \dots & \Omega_n(\omega_{N_f})] \end{bmatrix} \in C^{N_f \times (n+1)} \quad (7)$$

$$Y_o = - \begin{bmatrix} [\Omega_0(\omega_1) & \Omega_1(\omega_1) & \cdots & \Omega_n(\omega_1)] \otimes \tilde{H}_o(\omega_1) \\ [\Omega_0(\omega_2) & \Omega_1(\omega_2) & \cdots & \Omega_n(\omega_2)] \otimes \tilde{H}_o(\omega_2) \\ \vdots & \vdots & \ddots & \vdots \\ [\Omega_0(\omega_{N_f}) & \Omega_1(\omega_{N_f}) & \cdots & \Omega_n(\omega_{N_f})] \otimes \tilde{H}_o(\omega_{N_f}) \end{bmatrix} \in \mathbb{C}^{N_f \times N_f(n+1)} \quad (8)$$

Where symbol \otimes represents the Kronecker product.

After solving the denominator coefficient matrices, calculation of the poles is turned to be an eigenvalue problem of the companion matrix.

$$A_c V = \begin{bmatrix} 0 & I & \cdots & \cdots & 0 & 0 \\ 0 & 0 & \cdots & \cdots & 0 & 0 \\ \vdots & \vdots & \cdots & \cdots & 0 & I_{N_f} \\ -A_0^T & -A_1^T & \cdots & -A_{n-2}^T & -A_{n-1}^T & 0 \end{bmatrix} V = V \Lambda \quad (9)$$

All the poles can be found as the diagonal terms in the diagonal eigenvalue matrix. And the modal frequencies and damping ratios can then easily be obtained with following formula.

$$\omega_r = |\ln(\Lambda_r)| / T_s$$

$$\xi_r = \text{Re}(\ln(\Lambda_r)) / |\ln(\Lambda_r)| \quad (10)$$

The modal participating function (MPF) matrices can be located from the last N_f lines of the eigenvector matrix. Modal vectors, i.e. mode shapes can then be estimated by solving the following linear matrix equations under knowing the poles λ_r and MPF γ_r :

$$H(\omega) = \sum_{r=1}^{N_m} \left(\frac{\Phi_r \gamma_r^T}{j\omega - \lambda_r} + \frac{\Phi_r^* \gamma_r^H}{j\omega - \lambda_r^*} \right) - \frac{LR}{\omega^2} + UR \quad (11)$$

The RMFD-based broadband modal identification algorithm is a typical two-stage method. It can be observed that its implementation procedure is parallel to its two-stage TD counterpart PRCE [6].

2.2 Implementations and numerical issues of RMFD-based broadband modal identification

There are a few different implementations for modal identification when matrix fraction description of FRF is adopted depending on the form of the base function $\Omega_r(\omega)$ in the Eq. (2). The simplest way is to implement the base function in continuous domain letting $\Omega_r(\omega) = (i\omega)^r$. However, serious numerical problem will be encountered, i.e. the normal equation for solving coefficients of the denominator and numerator matrices will be ill-conditioned. The better way of implementation is making use of orthogonal base function, e.g. Forsythe orthogonal polynomial, which leads to MIMO version of orthogonal rational fraction polynomial (RFP) procedure. The best way, from numerical point of view, is to implement the base function in discrete domain, i.e. z-domain, by simply assuming $\Omega_r(\omega) = e^{i\omega T_s r}$, which leads to polyreference version of the least squares complex frequency domain (p-LSCF) algorithm [7]. RMFD-based p-LSCF procedure can determine structural modes in the broadband much more easily and reliably via very clean stability diagram, compared to its both counterparts in frequency domain (RFP), as well as in time domain (PRCE).

The other numerical issue encountered in FD broadband modal identification is the computational efficiency. Considering tremendous computational load, especially when large number of modes should be extracted in the broadband, computational efficiency become another numerical issue. The FFT is utilized to calculate the submatrices in the normal equation, which is used for coefficient matrices. Fig. (1) shows a comparison of computing time with FFT to replace direct computation via multiplication

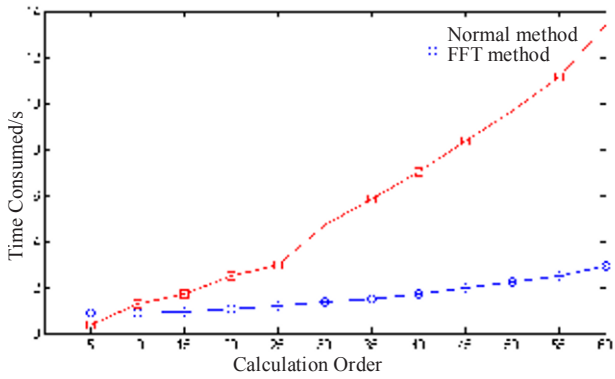


Fig. 1 Comparison of computing time with & without FFT

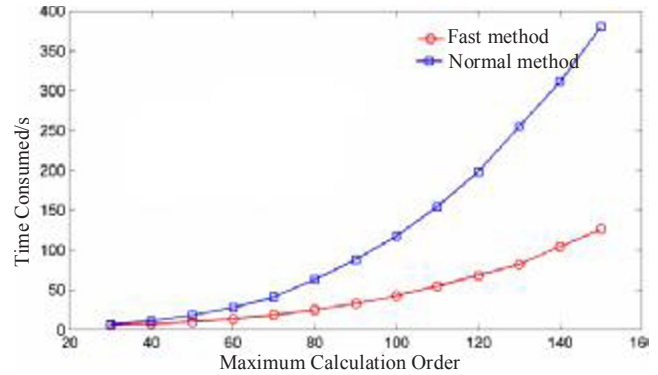


Fig. 2 Reduction of computing time over p-LSCF algorithm

The computation can further be speed up during calculation of coefficient matrix of the normal equation. The comparison between new fast algorithm in **BroBand** and p-LSCE is depicted in Fig. (2)^[8].

3 Broadband Modal Identification based on Left Matrix Fraction Description (LMFD)

3.1. Theoretical Background of LMFD-based Broadband modal identification

MIMO broadband modal identification procedure can also be developed based on left matrix fraction description (LMFD).

The FRF matrix of a linear system with N_o output and N_i input can be described as

$$H(\omega) = A^{-1}(\omega)B(\omega) \tag{12}$$

Where the denominator and the numerator matrix polynomials $A(\omega) \in C^{N_o \times N_o}$ and $B(\omega) \in C^{N_o \times N_i}$ are defined as follows,

$$\begin{cases} A(\omega) = \sum_{r=0}^n A_r \Omega_r(\omega) \in C^{N_o \times N_o} \\ B(\omega) = \sum_{r=0}^n B_r \Omega_r(\omega) \in C^{N_o \times N_i} \end{cases} \tag{13}$$

The coefficient matrices $A_j \in C^{N_o \times N_o}$ and $B_j \in C^{N_o \times N_i}$ contain parameters to be estimated, $\Omega_r(\omega)$ is the base function and n is the order of the matrix polynomial. It is noticed that the dimension of the coefficient matrices is different compare to the ones in the model with RMFD.

The linearized error matrix can be written as

$$E(\omega) = B(\omega) - A(\omega)H(\omega) \tag{14}$$

Substituting the expressions of $A(\omega), B(\omega)$ in Eq. (13) into Eq. (14) yields error function in matrix form

$$E^T(\omega) = \begin{bmatrix} \Omega_0(\omega) & \dots & \Omega_n(\omega) \end{bmatrix} \otimes I_{N_i} \begin{Bmatrix} B_0^T \\ B_1^T \\ \vdots \\ B_n^T \end{Bmatrix} - \begin{bmatrix} \Omega_0(\omega) & \dots & \Omega_n(\omega) \end{bmatrix} \otimes \tilde{H}^T(\omega) \begin{Bmatrix} A_0^T \\ A_1^T \\ \vdots \\ A_n^T \end{Bmatrix} \tag{15}$$

For a least squares solution, the objective function can be expressed as follows

$$l = \sum_{k=1}^{N_f} tr(E^H(\omega_k)E(\omega_k)) \tag{16}$$

Minimization of the objective function leads to linear equations

$$J\theta = [Y \quad X] \begin{Bmatrix} \beta \\ \alpha \end{Bmatrix} = 0 \quad (17)$$

Where

$$Y = \begin{bmatrix} [\Omega_0(\omega_1) \quad \cdots \quad \Omega_n(\omega_1)] \otimes I_{N_i} \\ [\Omega_0(\omega_2) \quad \cdots \quad \Omega_n(\omega_2)] \otimes I_{N_i} \\ \vdots \\ [\Omega_0(\omega_{N_f}) \quad \cdots \quad \Omega_n(\omega_{N_f})] \otimes I_{N_i} \end{bmatrix} = \begin{bmatrix} [\Omega_0(\omega_1) \quad \cdots \quad \Omega_n(\omega_1)] \otimes \tilde{H}^T(\omega_1) \\ [\Omega_0(\omega_2) \quad \cdots \quad \Omega_n(\omega_2)] \otimes \tilde{H}^T(\omega_2) \\ \vdots \\ [\Omega_0(\omega_{N_f}) \quad \cdots \quad \Omega_n(\omega_{N_f})] \otimes \tilde{H}^T(\omega_{N_f}) \end{bmatrix} \quad (18)$$

$$\beta = \begin{Bmatrix} B_0^T \\ B_1^T \\ \vdots \\ B_n^T \end{Bmatrix} \quad \alpha = \begin{Bmatrix} A_0^T \\ A_1^T \\ \vdots \\ A_n^T \end{Bmatrix} \quad (19)$$

Similar to RMFD case, instead of solving directly the normal equation, the coefficient matrices of the denominator matrix polynomial can be obtained from eigenvalue problem of the following companion matrix:

$$A_c = \begin{bmatrix} 0 & I_{N_o} & \cdots & 0 & 0 \\ 0 & 0 & \cdots & 0 & 0 \\ \vdots & \vdots & \ddots & \vdots & \vdots \\ 0 & 0 & \cdots & 0 & I_{N_o} \\ -A_0 & -A_1 & \cdots & -A_{n-2} & -A_{n-1} \end{bmatrix} \in \mathbb{C}^{N_o n \times N_o n} \quad (20)$$

All the poles can be found as the diagonal terms in the diagonal eigenvalue matrix. And the modal frequencies and damping ratios can then easily be obtained as in the previous procedure. Instead of modal participating factors, mode shapes can be located in the eigenvector matrix of the solution. With known poles and mode shapes, the modal participation factors (MPF) can then be obtained via linear least squares solution of the following equation

$$H(\omega) = \sum_{r=1}^{N_m} \left(\frac{\Phi_r \gamma_r^T}{j\omega - \lambda_r} + \frac{\Phi_r^* \gamma_r^H}{j\omega - \lambda_r^*} \right) - \frac{LR}{\omega^2} + UR \quad (21)$$

The LMFD-based broadband modal identification algorithm is also a typical two-stage method. It can be seen that its implementation procedure is parallel to its two-stage TD counterpart EITD [7].

3.2 LMFD-based broadband modal identification as extension and improvement of RPF

FDPR is the first MIMO modal identification procedure in frequency domain [9], together with its sister algorithm FDDPI [10], is widely applied in modal community. With FDPR, the system matrix A can be solved from the following equation :

$$[A \quad K \quad h(0) - AK] \begin{bmatrix} \tilde{H}(\omega_1) & \tilde{H}(\omega_2) & \cdots & \tilde{H}(\omega_L) \\ j\omega_1 I_{N_i} & j\omega_2 I_{N_i} & \cdots & j\omega_L I_{N_i} \\ I_{N_i} & I_{N_i} & \cdots & I_{N_i} \end{bmatrix} = [j\omega_1 \tilde{H}(\omega_1) \quad j\omega_2 \tilde{H}(\omega_2) \quad \cdots \quad j\omega_L \tilde{H}(\omega_L)] \quad (22)$$

Where A is the system matrix, K is the residue represents the inferences of complex conjugate part of FRF and out-of-band modes, $h(0)$ is the initial condition term, and L is the number of spectrum lines in the frequency band of interest.

In the algorithm based on LMFD, when the base function is simply chosen in continuous domain, the same as in PRFD, $\Omega_r(\omega_k) = (i\omega_k)^r$, and $n=1, A_1 = I_{N_o}$, the linear equation Eq. (5) for the parameters in the matrix polynomials can be simplified as,

$$\begin{bmatrix} I_{N_i} & j\omega_1 I_{N_i} \\ I_{N_i} & j\omega_2 I_{N_i} \\ \vdots & \vdots \\ I_{N_i} & j\omega_{N_f} I_{N_i} \end{bmatrix} \begin{Bmatrix} B_0^T \\ B_1^T \end{Bmatrix} - \begin{bmatrix} \tilde{H}^T(\omega_1) \\ \tilde{H}^T(\omega_2) \\ \vdots \\ \tilde{H}^T(\omega_{N_f}) \end{bmatrix} \{A_0^T\} = \begin{bmatrix} j\omega_1 \tilde{H}^T(\omega_1) \\ j\omega_2 \tilde{H}^T(\omega_2) \\ \vdots \\ j\omega_{N_f} \tilde{H}^T(\omega_{N_f}) \end{bmatrix} \quad (23)$$

Re-writing the above equation yields

$$\begin{bmatrix} -A_0 & B_1 & B_0 \end{bmatrix} \begin{bmatrix} \tilde{H}(\omega_1) & \tilde{H}(\omega_2) & \cdots & \tilde{H}(\omega_{N_f}) \\ j\omega_1 I_{N_i} & j\omega_2 I_{N_i} & \cdots & j\omega_{N_f} I_{N_i} \\ I_{N_i} & I_{N_i} & \cdots & I_{N_i} \end{bmatrix} = [j\omega_1 \tilde{H}(\omega_1) \quad j\omega_2 \tilde{H}(\omega_2) \quad \cdots \quad j\omega_{N_f} \tilde{H}(\omega_{N_f})] \quad (24)$$

Compare between Eqs. (24) and (22), it is seen, when noticing $A = -A_0$, $K = B_1$, $h(0) - AK = B_0$, that the PRFD is actually a special case of new broadband modal identification procedure based on LMFD! Since FDPR is implemented in continuous domain (s-domain), and the numerical condition of the normal equation is unfavorable, and can be applied in selected band. However, with dramatic improvement of numerical condition in discrete domain (z-domain), new procedure based on LMFD performs excellently for broadband modal identification with reliable determination of structural mode based on clear stability diagram and accurate modal parameter extraction of all modes in broadband.

4 Applications of new broadband modal identification procedures

All the FD modal identification procedures are making use of FRF measurement data. However, in operational or output-only modal analysis, only output data are available. Power spectrum density (PSD), instead of FRF, can then be estimated. It is interested to aware that so-called positive or half PSD (h-PSD), which contains values corresponding to only positive frequencies, has similar modal decomposition expression,

$$G_{yy}^+(\omega) = \sum_{r=1}^{N_m} \frac{\Phi_r Q_r^T}{j\omega - \lambda_r} + \frac{\Phi_r^* Q_r^H}{j\omega - \lambda_r^*} \quad (25)$$

Therefore, FD modal identification algorithm can be adopted for OMA with h-PSD data instead of FRF data for EMA. It should be noticed that the only difference of broadband modal identification in OMA making use of h-PSD is that modal participation factors are missing due to absence of input force measurement. Therefore, only modal frequencies, damping ratios and un-scaled mode shaped can be obtained.

The new broadband modal identification algorithms based on RMFD and LMFD have been implemented in a new-generation modal software named as N-Modal and applied for traditional experimental modal analysis (EMA) and operational modal analysis (OMA) in aerospace, mechanical and civil engineering.

4.1 OMA Application of RMFD-based *BroBand* Algorithm to a middle-raised building

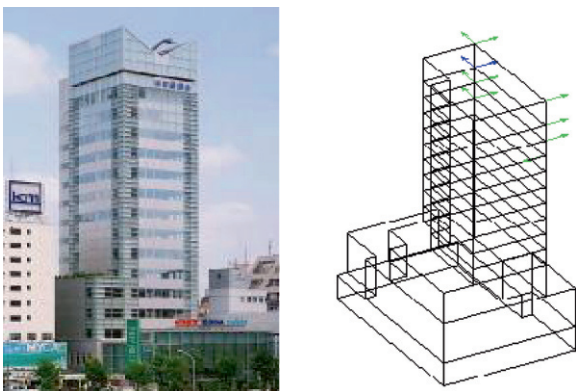


Fig. 3 CFT building with geometric model

Table 1 Identified modal frequencies & damping ratios

| Mode # | Freq. (Hz) | Std. Div. Freq. (Hz) | Damp. (%) | Std.Div. Damp. |
|--------|------------|----------------------|-----------|----------------|
| 1 | 0.760 | 0.0025 | 1.60 | 0.11 |
| 2 | 0.855 | 0.0018 | 1.58 | 0.09 |
| 3 | 1.11 | 0.0010 | 1.29 | 0.14 |
| 4 | 2.23 | 0.0032 | 1.24 | 0.15 |
| 5 | 2.47 | 0.0061 | 1.64 | 0.28 |
| 6 | 2.94 | 0.0072 | 1.73 | 0.37 |
| 7 | 3.85 | 0.018 | 2.23 | 0.15 |
| 8 | 4.26 | 0.037 | 1.60 | 0.38 |
| 9 | 4.47 | 0.037 | 1.92 | 0.38 |

The RMFD-based *BroBand* algorithm was applied to a 15-story office building with concrete -filled-tube (CFT) columns

located in Tokyo. In order to have sufficient spatial domain resolution and to correlate with finite element analysis, an experimental model with 200 DOFs in two lateral directions was established (see Fig. 3). Field ambient response measurements were conducted in four (4) setups with 53 acceleration measurements in horizontal direction with two sensors as references, and 14 channels for one setup. With a reasonable assumption that the floor subjects to lateral rigid body motion, 147 "virtual measurements#" are added from constrain equations. Half power spectrum density (h-PSD) matrix is then calculated from ambient response measurements via FFT of correlation function with only positive time lags. Unbiased correlation estimation is adopted based on periodogram approach. Data length is $N=2048$, and exponential window is applied to reduce variance error. RMFD-based **BroBand** procedure is applied for modal identification. Within interested frequency range of 0 to 4.5 Hz, altogether 9 modes were accurately located in the stability diagram (Fig. 4), and modal parameters are then identified. The identified modal frequencies and damping ratios are shown in Table 1. Mode shapes are depicted in Fig. 6. Perfect curve fittings of almost all measured h-PSD have been obtained showing the performance of the **BroBand** algorithm (Fig. 7). The identified modal frequencies and mode shapes were utilized for FE model correlation and calibration. As a comparison, advanced OMA algorithm stochastic subspace identification (SSI) is also applied to the same measured data. Fig.5 is the stability diagram obtained for SSI. It is seen that **BroBand** offer much clearer stability diagram, and .shows promise in autonomous modal identification.

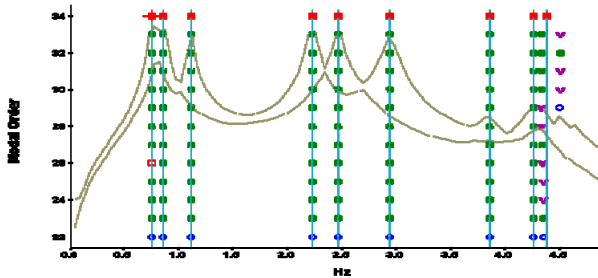


Fig. 4 Stability diagram of CFT Building with **BroBand** Algorithm

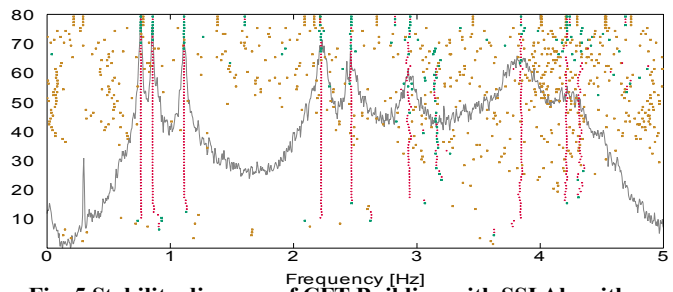


Fig. 5 Stability diagram of CFT Building with SSI Algorithm

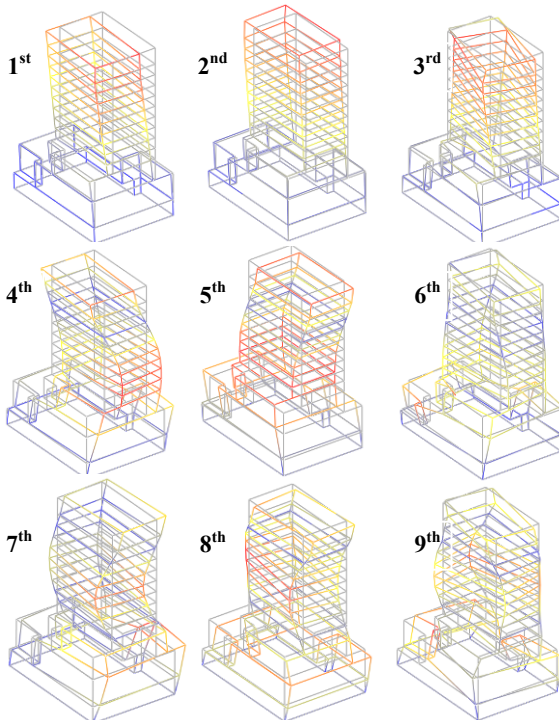


Fig. 6 identified nine (9) mode shapes

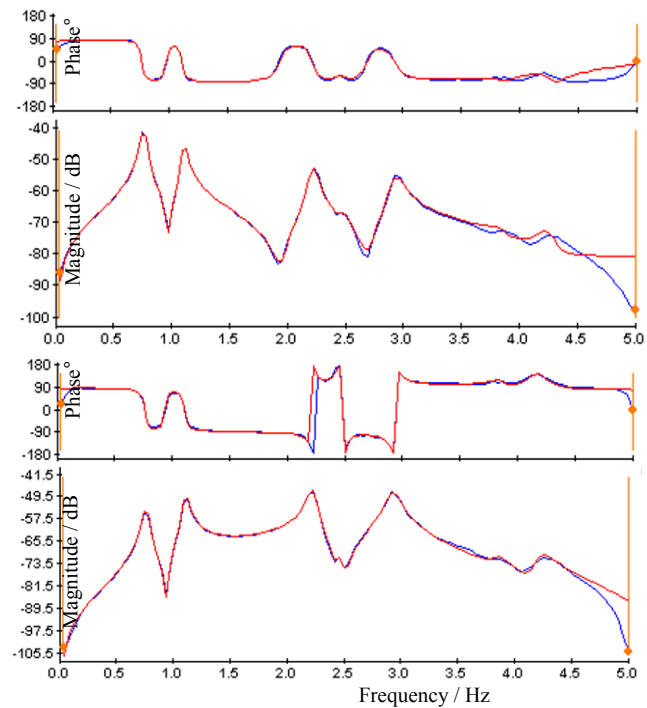


Fig. 7 Curve fittings of h-PSD

4.2 Applications of LMFD-based BroBand algorithm to an Aircraft Model

A delta-wing aircraft model is utilized as an EMA application example for LMFD-based *BroBand* modal identification and comparison study between LMFD-based and FDPR procedures. The delta-wing model is made of aluminum with dimension of 1240mm in length and 1100mm in wing span. Two accelerometers are utilized as references, and an instrumented hammer is applied for force input in all 41 coordinates in vertical direction sequentially (See Fig. 8). MIMO FRF matrix with 800 spectrum line for each FRF is estimated in the signal processing modular of the N-Modal software.

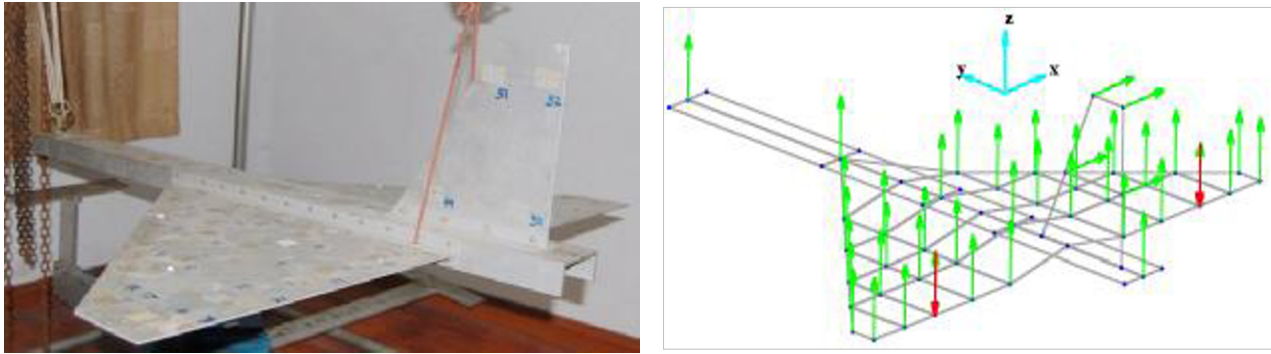


Fig. 8 Delta Wing Aircraft Model with I/O Coordinates

Stability diagrams, derived from both FDPR and LMFD algorithms are depicted in the Fig. 9 and Fig. 10, respectively.

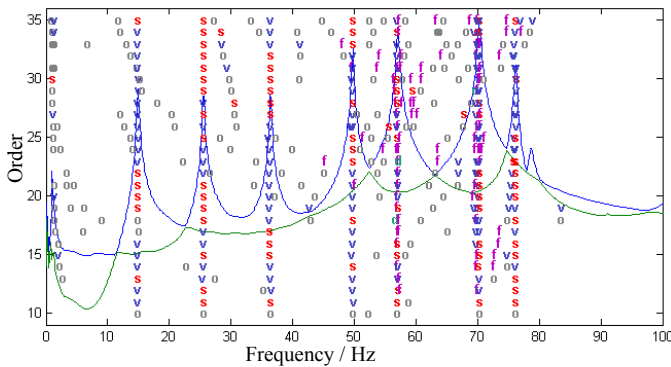


Fig. 9 Stability diagram of the aircraft model with FDPR algorithm

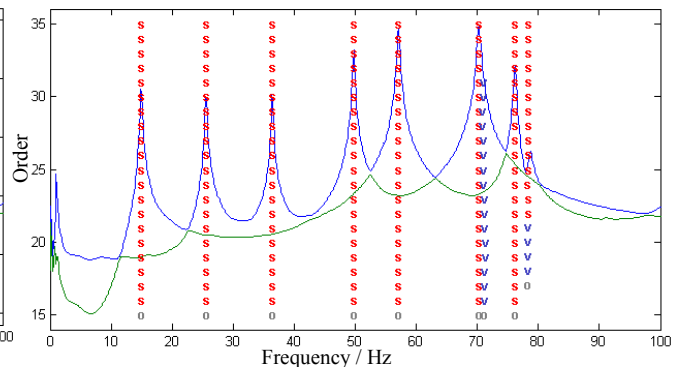


Fig. 10 Stability diagram of the aircraft model with LMFD-base *BroBand* algorithm

It is observed that LMFD-based *BroBand* algorithm shows much clearer stability diagram compared to the one from FDPR as expected. Modal parameters of the modes are then estimated as shown in Table 2. Mode shapes are presented in Fig. 11.

Table 2 Identified modal frequencies and damping ratios of the aircraft model

| No. | Modal Freq./Hz | Damping ration/% | Mode Shapes |
|-----|----------------|------------------|--|
| 1 | 14.93 | 0.31 | 1 st symmetric bending of wing |
| 2 | 25.57 | 0.31 | 1 st anti-symmetric bending of wing |
| 3 | 36.41 | 0.17 | 1 st torsion of wing |
| 4 | 49.75 | 0.13 | 1 st symmetric torsion of wing |
| 5 | 57.08 | 0.16 | 2 nd anti-symmetric torsion of wing |
| 6 | 70.24 | 0.21 | 2 nd symmetric bending of wing |
| 7 | 76.17 | 0.14 | 2 nd anti-symmetric bending of wing |
| 8 | 78.48 | 0.24 | Anti-symmetric bending & torsion of wing |

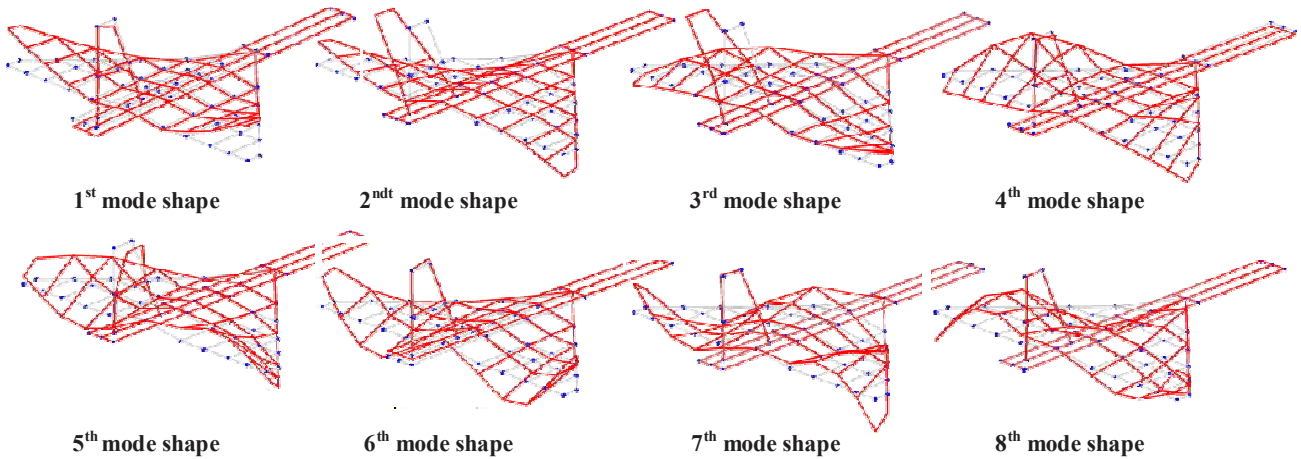


Fig. 11 Mode shapes of the aircraft model identified with LMFD-based *BroBand* algorithm

Fig. (12a) and (12b) show the synthesized driving-point FRF and cross-point FRF, respectively. It can be seen that perfect curve fittings are reached.

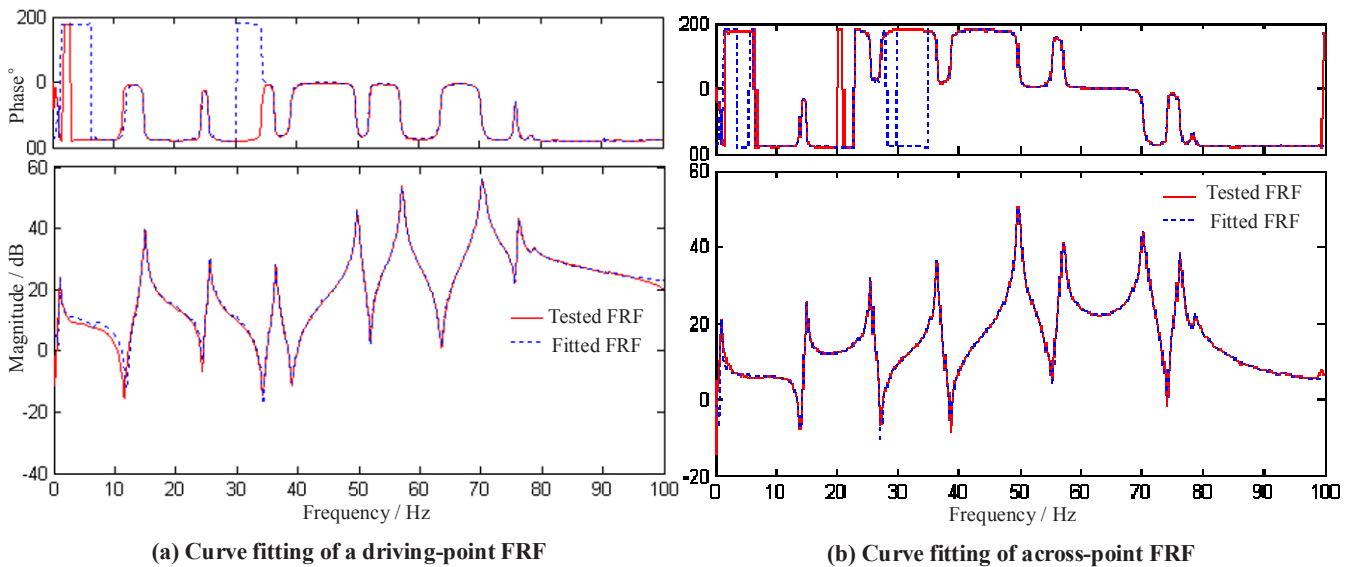


Fig. 12 Synthesized FRFs of the aircraft model with LMFD-based *BroBand* algorithm

4. Concluding remarks

- ✧ The development of model identification in time and frequency domain and for experimental and operational modal analysis with major issues is briefly overviewed.
- ✧ Theoretical background of the two broadband modal identification procedures is presented with relevant issues with numerical implementations.
- ✧ It is revealed that the procedure based on right matrix fraction description (RMFD) is actually the z-domain implementation of rational fraction polynomial algorithm (RFP) in s-domain but with significant improvement in numerical condition.

- ✧ The procedure based on left matrix fraction description (LMFD) is an extension of s-domain frequency domain polyreference (FDPR) and frequency domain direct parameter identification (FDDPI) algorithms, with much better performance in broadband modal identification.
- ✧ It is also shown that both RMFD-based and LMFD-based broadband modal identification procedures are parallel to their time domain counterparts, i.e. PRCE and EITD algorithm, in numerical implementation. However, much easier and reliable structural mode discrimination can be obtained with much clearer stability diagram.
- ✧ Engineering application of the broadband modal identification technique making use of FRF measurements for EMA of an aircraft model is presented. It shows advantage compared to the advanced time domain modal identification algorithm, e.g. stochastic subspace identification (SSI), in determination of structural modes with much clearer stability diagram, and promise in autonomous modal identification.
- ✧ Engineering application making use of h-PSD measurements for OMA of a middle-raised office building is given with comparison with frequency domain polyreference (FDPR). Superiority is shown over its FD counterpart as special case and implemented in continuous s-domain.

Acknowledgement

The first two authors, as a Guest Professor and the Director of the 21st Century Global Center of Excellence (G-COE) program, respectively, gratefully acknowledge the support from the G-COE Program at the Tokyo Polytechnic University under the Ministry of Education, Culture, Sports, Science and Technology (MEXT), Japan..

References

- [1]. Zhang L-M, An Overview of Major Development and Issues in Modal Identification, Proc. of the IMAC-XXII, A Conf. on Structural Dynamics, Dearborn, Michigan, USA, Jan.,2004
- [2]. James, G. H., Carne, T.G., Lauffer, J.P. Nard, A. R., Modal Testing Using Natural Excitation, Proc. of the 10-th IMAC, San Diego, CA, USA, Feb. 3-7, 1992
- [3]. Zhang, L.-M, Brincker, R. And Andersen, P., An Overview of Operational Modal Analysis: Major Developments and Issues, Proc. Of the International Operational Modal Analysis Conference, Copenhagen, Denmark, 26-27, April, 2005
- [4]. Zhang, L.-M., Brincker, R. and Andersen, P., Modal Indicators for Operational Modal Identification, IMAC XIX, Kissimmee, USA, Feb.5-8, 2001
- [5]. Zhang L.-M, Sun X.-H, Wang T., Tamura Y., Narrow-band, Select-band vs Broadband Modal Identification: their Features and Comparisons, Proc. Of the IMAC XXVII, Orlando, USA, Feb. 9-12, 2009
- [6]. Zhang, L.-M., On the Two-Stage Time Domain Modal Identification, Proc. Of the IMAC XX, Orlando, Florida, Feb. 2003
- [7]. Guillaume P., Peter Verboven, S. Vanlanduit, H. Van der Auweraer, and B. Peeters. A poly-reference implementation of the least-squares complex frequency domain-estimator. Proc. of the 21th International Modal Analysis Conference, Kissimmee (Florida), February 2003.
- [8]. Sun X.-H, A study on Frequency Domain Modal Parameter Identification with Software Implementation, PhD Thesis, Nanjing University of Aeronautics and Astronautics, April 2010
- [9]. Zhang, L.-M., Kanda, H., Brown, D. L. and Allemang, R.J, A frequency domain polyreference method for modal analysis, ASME Paper 85-Det-106, 1985
- [10]. Lembrets, F., Leuridan, J., Zhang, L.-M., Kanda, H., Multiple Input Modal Analysis of Frequency Response Functions based on Direct Parameter Identification, Proc. Of the IMAC, 1986

Advanced dynamic absorber design method for practical application

Jin Woo Lee

Division of Mechanical Engineering, Ajou University, San 5 Woncheon-Dong, YeongTong-Gu, Suwon 443-749, Republic of Korea

ABSTRACT A close investigation is made on dynamic absorber design using simplified vibration models. Dynamic absorbers have been widely used to reduce excessive vibration of engineering equipment at resonance frequencies. From the practical point of view, however, the conventional theory on the dynamic absorber design should carefully be applied because it is formulated under ideal assumptions. In this work, we point out errors that researchers may make when dynamic absorbers are designed in industry and suggest alternatives to conventional dynamic absorber design scheme.

Introduction

Dynamic absorber design is a very old topic and has been widely used to reduce excessive vibration level of mechanical equipments due to resonance. The basic theory for the dynamic absorber design is easily found in vibration textbooks and has been advanced depending on its applications. Sun *et al.* [1] applied dynamic vibration absorbers to floating raft system. Al-Bedoor and Moustafa [2] designed a dual dynamic absorber to reduce the torsional vibrations exhibited during start-up of systems driven by synchronous motors. Williams *et al.* [3] used shape memory alloy adaptive tuned vibration absorbers for adaptive passive vibration control. Huang and Fuller [4] attached multiple dynamic absorbers to the shell to reduce the vibration and the consequent interior acoustic sound pressure. Al-Hulwah *et al.* [5] used three-degree-of-freedom tuned mass dampers to control floor vibration.

A linear compressor, which was recently commercialized for refrigerators, requires a properly designed dynamic absorber to reduce high level vibration re-

sponse because the compressor operates most efficiently at its resonant frequency [6-10]. A linear compressor consists of moving parts compressing refrigerant and a shell with a grommet. The moving part is mounted on plastic springs of the shell, which is placed on the floor through the grommet made of rubber. To maximize the efficiency of the compressor, the natural frequency of the moving part driven by a motor should be tuned to the motor current frequency. Therefore, the operation condition results in extremely high vibration displacement at the shell of the linear compressor.

This work discusses errors that researchers may easily make for linear compressor vibration reduction and points out the key ideas in dynamic absorber design. To the end, the basic theory of dynamic absorber will be presented for one and two degree-of-freedom mass-spring-damper systems. Practical dynamic absorber design scheme will be discussed.

Basic Theory of Dynamic Absorbers

In this section, basic equations are developed to make a close investigation on design technique of dynamics absorbers. Although dynamic absorber design scheme is well explained in vibration textbooks, the key ideas based on equations are required for the close investigation. Frequency response functions are derived for four simple models in Fig. 1, which consist of mass, spring and damping elements using a linear vibration theory. The 1st model is one-degree-of freedom mass-spring-damper system, the 2nd and 3rd models are two-degree-of freedom mass-spring-damper system and the 4th model is a three-degree-of freedom mass-spring-damper system. The difference between the 2nd model and the 3rd model is the location of an excitation force.

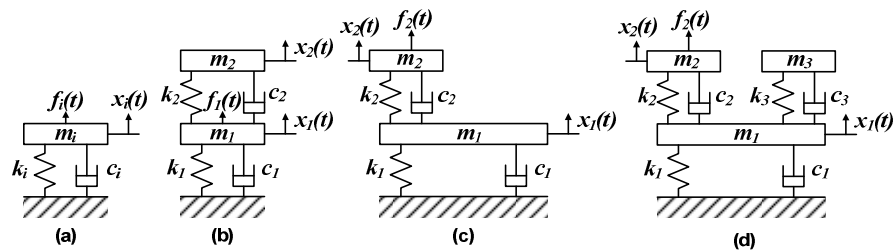


Fig. 1 Theoretical models for close investigation on dynamic absorber design technique: (a) 1st model; (b) 2nd model; (c) 3rd model; and (d) 4th model.

Conceptual Design Strategy of Dynamic Absorber

The dynamic elements denoted by subscripts '2' in Fig. 1b consist of an additional harmonic mechanical system connected to the 1st model in Fig. 1a to reduce the extremely high response displacement when the excitation force frequency coincides with natural frequency of the 1st model. For the two simple models in Fig. 1a and 1b, frequency response functions are derived with basic equations of motion to explain the concept of dynamic absorber design

The vibration displacement $x_i(t)$ of the 1st model excited by an external force $f_i(t)$ in Fig. 1a is governed by

$$m_i \cdot \ddot{x}_i(t) + c_i \cdot \dot{x}_i(t) + k_i \cdot x_i(t) = f_i(t), \quad (1)$$

where m_i , c_i , and k_i are mass, damping coefficient and spring constant. Assuming the harmonic motion of the external force and the displacement ($f_i(t) = F_i \cdot e^{j\omega t}$, $x_i(t) = X_i \cdot e^{j\omega t}$), Eq. (1) is converted to the following equation:

$$\{k_i - m_i \cdot \omega^2 + j\omega \cdot c_i\} X_i = F_i, \quad (2)$$

where ω is an angular frequency. The frequency response function of the 1st model is

$$\frac{X_i}{F_i} = \frac{1}{k_i [1 - (\omega/\omega_i)^2 + j2\omega/\omega_i \cdot \zeta_i]}, \quad (3)$$

where $\omega_i = \sqrt{k_i/m_i}$ and $\zeta_i = 1/2 \cdot \omega_i \cdot c_i/k_i$ are the natural frequency and the damping ratio of the 1st model, respectively.

Assuming the harmonic motions of vibration displacements and the external force ($x_1(t) = X_1 \cdot e^{j\omega t}$, $x_2(t) = X_2 \cdot e^{j\omega t}$, $f_1(t) = F_1 \cdot e^{j\omega t}$) in Fig. 1b, the vibration equation for the 2nd model is expressed in a matrix form:

$$\begin{bmatrix} k_1 + k_2 - m_1\omega^2 + j\omega(c_1 + c_2) & -k_2 - j\omega c_2 \\ -k_2 - j\omega c_2 & k_2 - m_2\omega^2 + j\omega c_2 \end{bmatrix} \begin{Bmatrix} X_1 \\ X_2 \end{Bmatrix} = \begin{Bmatrix} F_1 \\ 0 \end{Bmatrix}. \quad (4)$$

In this system, one can obtain the following two frequency response functions:

$$\frac{X_1}{F_1} = \frac{1}{k_1} \cdot \frac{H(\Omega_2, \zeta_2)}{H(\Omega_1, \zeta_1) \cdot H(\Omega_2, \zeta_2) - K_{21} \cdot \Omega_2^2 \cdot G(\Omega_2, \zeta_2)}, \quad (5a)$$

$$\frac{X_2}{F_1} = \frac{1}{k_1} \cdot \frac{G(\Omega_2, \zeta_2)}{H(\Omega_1, \zeta_1) \cdot H(\Omega_2, \zeta_2) - K_{21} \cdot \Omega_2^2 \cdot G(\Omega_2, \zeta_2)}, \quad (5b)$$

where $K_{21} (= k_2 / k_1)$ is the stiffness ratio and $\Omega_i (= \omega / \omega_i, i = 1, 2)$ is a normalized angular frequency. The symbols $H(\Omega_i, \zeta_i)$ and $G(\Omega_i, \zeta_i)$ are functions of the normalized angular frequency and the damping ratio:

$$G(\Omega_i, \zeta_i) = 1 + j2\zeta_i\Omega_i \quad (6a)$$

$$H(\Omega_i, \zeta_i) = 1 - \Omega_i^2 + j2\zeta_i\Omega_i \quad (6b)$$

where $i = 1, 2$.

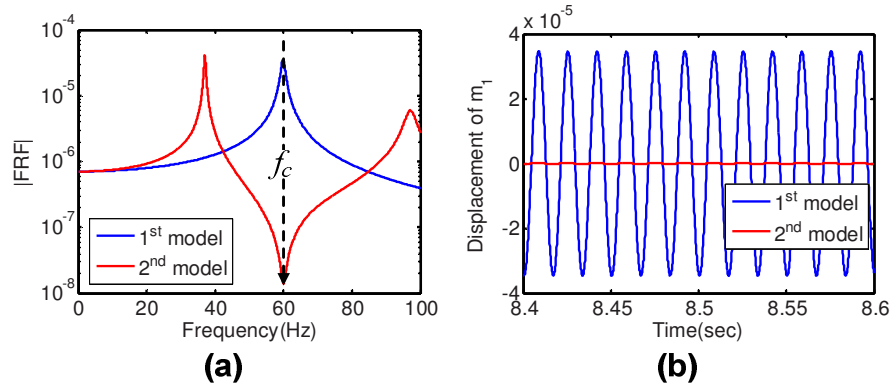


Fig. 2 Comparison of the 1st model and the 2nd model: (a) Frequency response functions at m_1 ; and (b) time responses at m_1 . f_c is an excitation force frequency.

If the damping ratios ζ_i are much less than one, the response in Fig. 2a is extremely high when the excitation force frequency (ω_c) coincides with the natural

frequency (ω) of the 1st model: $\Omega_1 = \Omega_c (= \omega / \omega_c)$. This phenomenon is called ‘resonance’. To avoid the resonance, an additional one-degree-of freedom mass-spring-damper system is attached to the original system as shown in Fig. 1b, and the natural frequency Ω_2 of the additional system is adjusted to that of the original system: $\Omega_1 = \Omega_c = \Omega_2$. The reason why the physical treatment can reduce the vibration magnitude is that the additional system modifies the frequency response function of X_1 / F_1 as shown in Eq. (5a): an anti-resonance frequency is created at the excitation force frequency due to natural frequency adjustment for the additional system as shown in Fig. 2.

In many engineering environments, however, a forced vibration response is disregarded as resonance phenomenon or incorrectly simplified models are used for theoretical vibration analysis and reduction. That is, the natural frequency adjustment always does not yield an anti-resonance frequency at an excitation frequency resulting in response reduction at the excitation frequency. To point out these errors, in the following subsection, some equations are developed for two-degree-of-freedom mass-spring-damper system.

Dynamic Absorber Design for Two-degree-of-freedom Systems

The 3rd model is a simplified vibration model representing low-frequency vibration characteristics of linear compressors, and the 4th model is considered to reduce high level vibration response due to resonance phenomenon. As a similar way in the previous subsection, two frequency response functions for the 3rd and 4th models are derived respectively as follows:

$$\frac{X_1}{F_2} = \frac{1}{k_2} \cdot \frac{K_{21} \cdot G(\Omega_2, \zeta_2)}{H(\Omega_1, \zeta_1) \cdot H(\Omega_2, \zeta_2) - K_{21} \cdot \Omega_2^2 \cdot G(\Omega_2, \zeta_2)} \quad (7a)$$

$$\frac{X_1}{F_2} = \frac{1}{k_2} \cdot \frac{K_{21} \cdot G(\Omega_2, \zeta_2) \cdot H(\Omega_3, \zeta_3)}{H(\Omega_1, \zeta_1) \cdot H(\Omega_2, \zeta_2) \cdot H(\Omega_3, \zeta_3)} \quad (7b)$$

$$\frac{-K_{21} \cdot \Omega_2^2 \cdot G(\Omega_2, \zeta_2) \cdot H(\Omega_3, \zeta_3) - K_{31} \cdot \Omega_3^2 \cdot G(\Omega_3, \zeta_3) \cdot H(\Omega_2, \zeta_2)}{H(\Omega_1, \zeta_1) \cdot H(\Omega_2, \zeta_2) \cdot H(\Omega_3, \zeta_3)}$$

If an extremely high response happens due to $\omega_c = \omega_2^*$, only frequency adjustment ($\Omega_c = \Omega_2^* = \Omega_3$) can yield vibration reduction as shown in Fig. 3a. How-

ever, the frequency adjustment may increase the vibration level of an original system if the high level vibration response is just a forced vibration phenomenon, not resonance as shown in Fig. 3b. In the next section, reasons causing these errors are discussed and a right dynamic absorber design scheme is suggested.

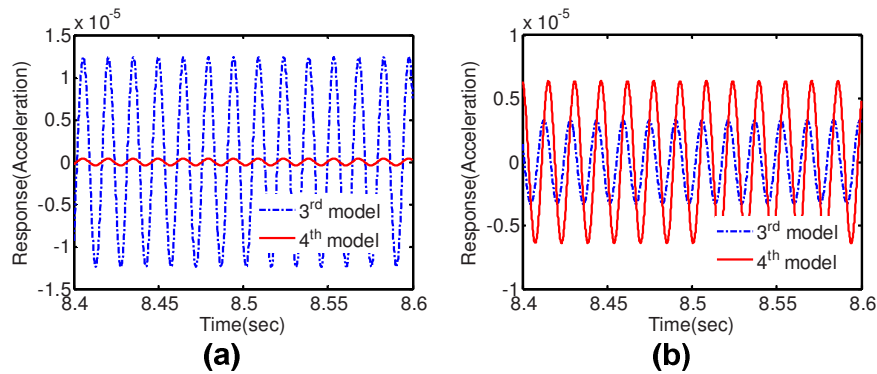


Fig. 3 Level change in time responses of the 3rd and 4th models depending on excitation force frequency: (a) $\Omega_c = \Omega_2^* = \Omega_3$ (b) $\Omega_c \neq \Omega_2^* = \Omega_3$.

Practical Scheme for Dynamic Absorber Design

As summarized above, the natural frequency of an additional system must properly be tuned so that an anti-resonance frequency should coincide with an excitation force frequency. To the end, one must check two things: the first one is to check if the high level response is due to resonance or just a forced vibration response; and the second one is to check if a used theoretical well represents vibration characteristics of a real mechanical device.

Fig. 4 compares response change in a main system when an additional system is attached for two cases: resonance and just a forced vibration response. As shown in the Fig. 4b, the system has a high level response due to a single excitation frequency force, which does not coincide with its natural frequency. This case corresponds to just a forced vibration phenomenon, not resonance. Nevertheless, if an additional mass-spring-damper system is designed on the basis of dynamic absorber design theory and is attached to an original system, the response at the excitation frequency may increase as shown in Fig. 3b.

An improper theoretical model may result in vibration increase in a main system. A general way to operate a linear compressor most efficiently is to tune the natural frequency of a pump in a linear compressor to the motor current frequency ω_m using the following equation [10]:

$$\omega_m = \sqrt{\frac{K_t}{M_t}} \quad (8)$$

where M_t is the total moving mass and K_t is the total equivalent spring stiffness. This approach is based on one degree-of-freedom system in Fig. 1a. Strictly speaking, however, this theoretical model is improper because the moving mass part is not directly connected to ground, but it is mounted on the shell through snubbers and the shell is placed on the hard floor through the grommet. That is, a linear compressor operating at a motor current frequency can be characterized by the 3rd model in Fig. 1c. Therefore, to reduce high level vibration response, one must use the 4th model in Fig. 1d, not the 2nd model in Fig. 1b.

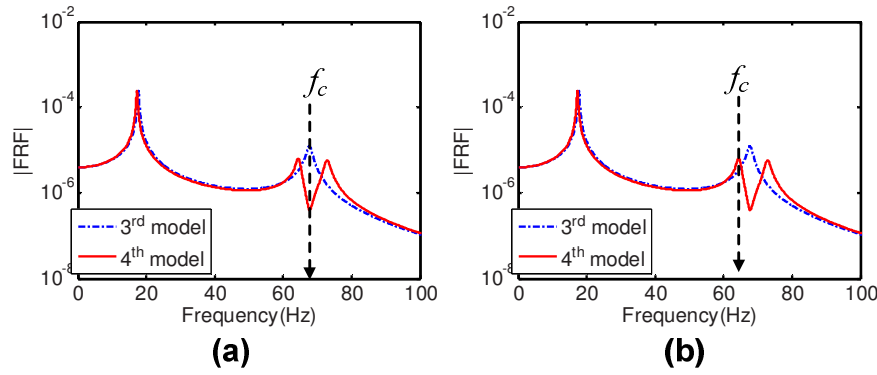


Fig. 4 Level change in frequency response functions of the 3rd and 4th models depending on excitation force frequency: (a) $\Omega_c = \Omega_2^* = \Omega_3$ (b) $\Omega_c \neq \Omega_2^* = \Omega_3$.

Conclusions

In this work, dynamic absorber design scheme was investigated in terms of industrial application. The key idea in dynamic absorber design theory is to adjust the natural frequency of an additional system to excitation force frequency. However, the reason that the vibration response of the original system is reduced is that an anti-resonance frequency in a frequency response function is tuned to the excitation force frequency. Sometimes, the natural frequency adjustment of the additional system may not result in exact shift in the anti-resonance frequency. From the practical point of view, therefore, the anti-resonance frequency tuning is much more important than the natural frequency adjustment.

Acknowledgement

This work was supported by the new faculty research fund of Ajou University and Ajou university research fellowship of 2010.

Reference

- [1] H. L. Sun, K. Zhang, P. Q. Zhang and H. B. Chen, Application of dynamic vibration absorbers in floating raft system, *Applied Acoustics*, 71, pp. 250-257, 2010.
- [2] B. O. Al-Bedoor and K. A. Moustafa, Dual dynamic absorber for the torsional vibrations of synchronous motor-driven compressors, *Journal of Sound and Vibration*, 220(4), pp. 729-748, 1999.
- [3] K. A. Williams, G. T. -C. Chen and R. J. Bernhard, Dynamic modeling of a shape memory alloy adaptive tuned vibration absorber, *Journal of Sound and Vibration*, 280, pp. 211-234, 2005.
- [4] Y. M. Huang, C. R. Fuller, The effects of dynamic absorbers on the forced vibration of a cylindrical shell and its coupled interior sound field, *Journal of Sound and Vibration*, 200(4), pp. 401-418, 1997.
- [5] K. I. Al-Hulwah, Floor vibration control using three-degree-of-freedom tuned mass dampers, *Proceedings of ASME International Mechanical Engineering Congress and Exposition*, CD-Rom, 2004.
- [6] N. Chen, Y. J. Tang, Y. N. Wu, X. Chen and L. Xu, Study on static and dynamic characteristics of moving magnet linear compressors, *Cryogenics*, 47, pp. 457-467, 2007.
- [7] Y. Choi, J. Lee, W. Jeong and I. Kim, Dynamic behavior of valve system in linear compressor based on fluid-structure interaction, *Journal of Mechanical Science and Technology*, 24(7), pp. 1371-1377, 2010.
- [8] H. Kim, C. Roh, J. Kim, J. Shin, Y. Hwang and J. Lee, An experimental and numerical study on dynamic characteristic of linear compressor in refrigeration system, *International Journal of Refrigeration*, 32, pp. 1536-1543, 2009.
- [9] B. J. Huang and Y. C. Chen, System dynamics and control of a linear compressor for stroke and frequency adjustment, *Transactions of ASME-Journal of Dynamic System, Measurement, and Control*, 124, pp. 176-182, 2002.
- [10] Z. Lin, J. Wang and D. Howe, A resonant frequency tracking technique for linear vapor compressors, *Proceedings of Electric Machines and Drives Conference*, pp. 370-275, 2007.

Use of Operational Modal Analysis in Solving Ship Vibration Issues

Anne Boorsma*, E. Peter Carden
Lloyd's Register EMEA, 71 Fenchurch St. London EC3M 4BS, UK

*Corresponding Author: anne.boorsma@lr.org

Abstract

Vibration in ships can cause crew and passenger discomfort and induce structural cracking. The mitigation of excessive vibration requires knowledge of both excitation and response. Observation techniques and advanced Computational Fluid Dynamics have been applied successfully to investigate and characterise propeller excitation. Operational modal analysis (OMA) has proven to be a useful practical technique for investigating and solving vibration issues on ships. The use of these techniques is discussed in the context of two case studies:

1. The investigation of cracking in freshwater tanks due to vibration, and the use of OMA in tracing the transfer of energy from the propeller to the tank panels, are described. Observations of propeller cavitation and measurements of the pressure caused by its development are presented. Solutions to reduce the excitation energy and to shift the natural frequencies of the tank panels are discussed.
2. An example of vibration of a navigation bridge and accommodation block causing crew discomfort is presented. The use of OMA identified several modes that were excited by the main engine and the propeller during normal service conditions. This improved the understanding of vibration of the accommodation whilst reducing the risks associated with the uncertainty of implementing solutions.

Introduction

Vibration of ship structures is unavoidable because of design constraints such as the relative close proximity of the excitation sources and working and living quarters, the operating environment, construction and strength requirements and the desire to reduce the weight of the vessels and increase the payload. Vibration can cause crew and passenger discomfort and the assessment of vibration for these purposes is described for instance in the ISO6954-2000 standard [1] and in the Lloyd's Register's Passenger and Crew Accommodation Comfort notation [2]. Higher, and sometimes localized levels of vibration can lead to failure of structural components through fatigue. Vibration levels above which fatigue is likely to occur are given for instance in the Lloyd's Register Ship Vibration and Noise Guidance Notes [3].

Primary sources of vibration excitation on board ships are the propeller, the main engine and auxiliary machinery. In many cases the main and auxiliary engines are reciprocating machines and acceptable levels of vibration for such machinery are set out for example in ISO10816-6 [4]. Levels of acceptable propeller excitation for different ship types are given in [4]

Notwithstanding the identification of acceptable levels of excitation and vibration and the computational tools available to predict these in the design stages, ships with unacceptable vibration levels are still being built. This is in part a result of the very nature of shipbuilding, where only a very limited number of ships of one particular design are built, for instance due to different requirements from different owners. This makes it expensive to assess the vibration characteristics of each ship in detail.

The prediction of vibration excitation, and in particular the propeller, is sometimes inaccurate. Engine builders in general make relatively large numbers of engines without significant modifications and have detailed guides on expected external engine forces and moments. The same can not be said for propellers that are usually designed specifically for each ship owing to the different hull shapes, shaft speeds, ship speeds, ship powers and operation profiles. Although propeller designers do take into account all these different factors, not all physical phenomena are accurately predicted by state of the art computational tools. This can make it difficult to design propellers with an acceptable pressure signature.

The use of specialist experimental techniques, such as OMA, can aid problem resolution after a ship has entered service and validate computational techniques. An illustration of this is given with two case studies that the authors dealt with recently.

Case Study 1 – Cracking of tank bulkheads as a result of propeller excitation

Cracking of water tank bulkheads of an LNG carrier occurred 1 year after delivery of the vessel. Despite continuous repairs and modifications to these bulkheads, cracking persisted for several years in service. The tanks were located directly above the propeller, as shown in [Figure 1](#), and contained distilled water, for use in a steam turbine, and fresh water, for human consumption. Hence contamination could have serious consequences for staff and machinery.

Panel vibration was measured at the centre of the affected panels and midway between stiffeners. Typical overall velocity amplitudes of two tank bulkheads are shown in [Figure 2](#). Vibration levels had typical maximum amplitudes of around 200 mm/s and thus exceeded 30 mm/s, the upper limit for safe panel vibration in [Reference 3](#), from relatively low speeds and powers. It was therefore likely that cracking had occurred as a result of vibration and in order to assess how much excitation and response contributed to the issue both were investigated.

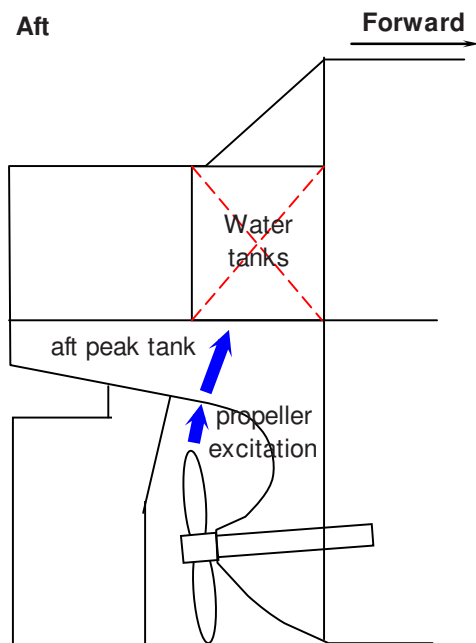


Fig. 1 Tanker aft body showing the location of water tanks and the propeller

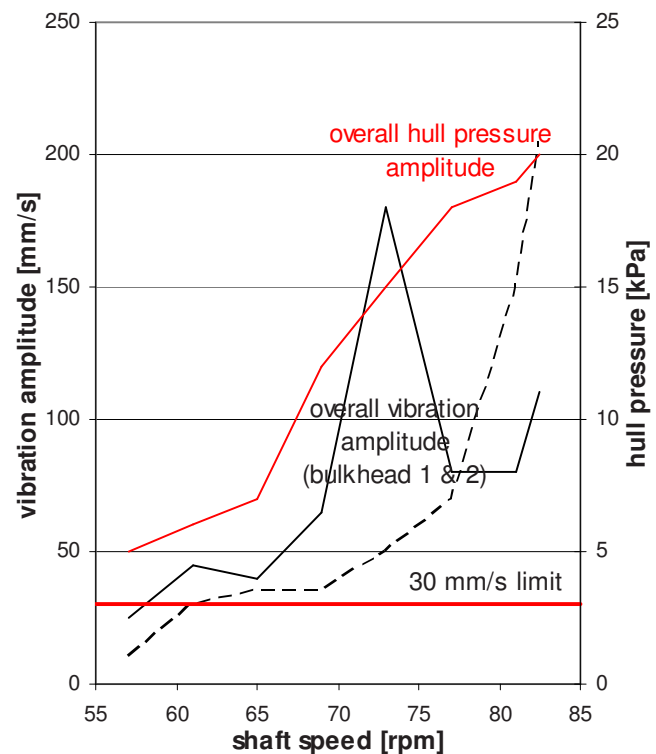


Fig. 2 Hull pressure amplitudes and vibration amplitudes of two tank bulkheads

As discussed previously, machinery is usually the principle source of vibration excitation on board a vessel. The main engine of this ship was a steam turbine which, in general, does not cause a lot of vibration excitation and, therefore, the propeller was the most likely source of excitation. Propeller radiated hull pressures were measured and considered high, with overall pressure amplitudes exceeding 15 kPa ([Figure 2](#)).

A typical time series of hull pressure excitation during one blade passage is shown in [Figure 3](#). There is an underlying blade rate pressure fluctuation resulting from the non-cavitating pressure field around the blade. Superimposed on this is the contribution of the pressure caused by cavitation. This pressure consists of a cavitation growth phase as the blade enters the wake peak, possibly causing a gradual reduction in pressure, which is followed by a high pressure peak resulting from the sudden collapse of the main body of sheet cavitation. The three secondary pressure pulses have been observed on other vessels and could be related to tip vortex activity.

Hull pressure energy is generally contained in harmonics of the blade passing frequency (Figure 4) and, in this case, the amplitudes of the pressure pulse at the second and third harmonic of the blade passing frequency were of a similar value as the blade rate component. This is relevant because natural frequencies of local structures can be typically found at these frequencies. This distribution of pressure energy suggests a violent cavitation collapse and is not uncommon for vessels where propeller excitation is high.

Observations of propeller cavitation were performed through a borescope that was passed through an M20 hole in the ship's shell plating just forward of the propeller. These holes were drilled while the ship was underway and did not disrupt the ship's schedule. Two images of a propeller blade passing through the twelve o'clock position, Figure 5, showed cavitation phenomena which normally lead to significant pressure pulses and which are indicative of a severely retarded propeller inflow. It is likely that the severely retarded propeller inflow was a result of the large amount of stagnant flow that was injected into the ship's boundary layer just upstream of the propeller by the steam turbine cooling water outlet.

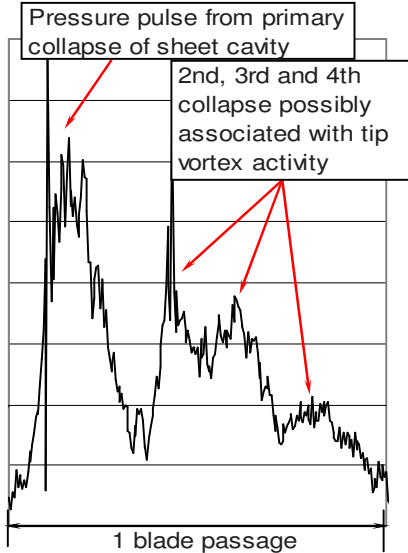


Fig. 3 Hull pressure measured during one blade passage

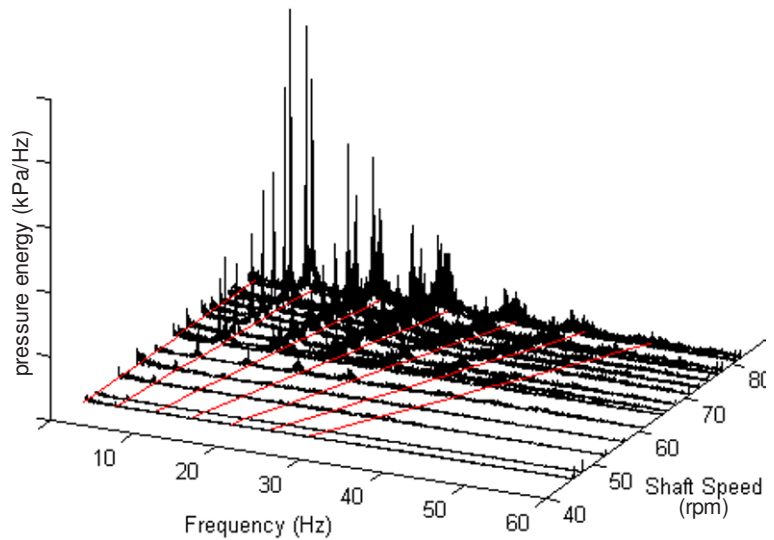


Fig. 4 Frequency distribution of pressure energy

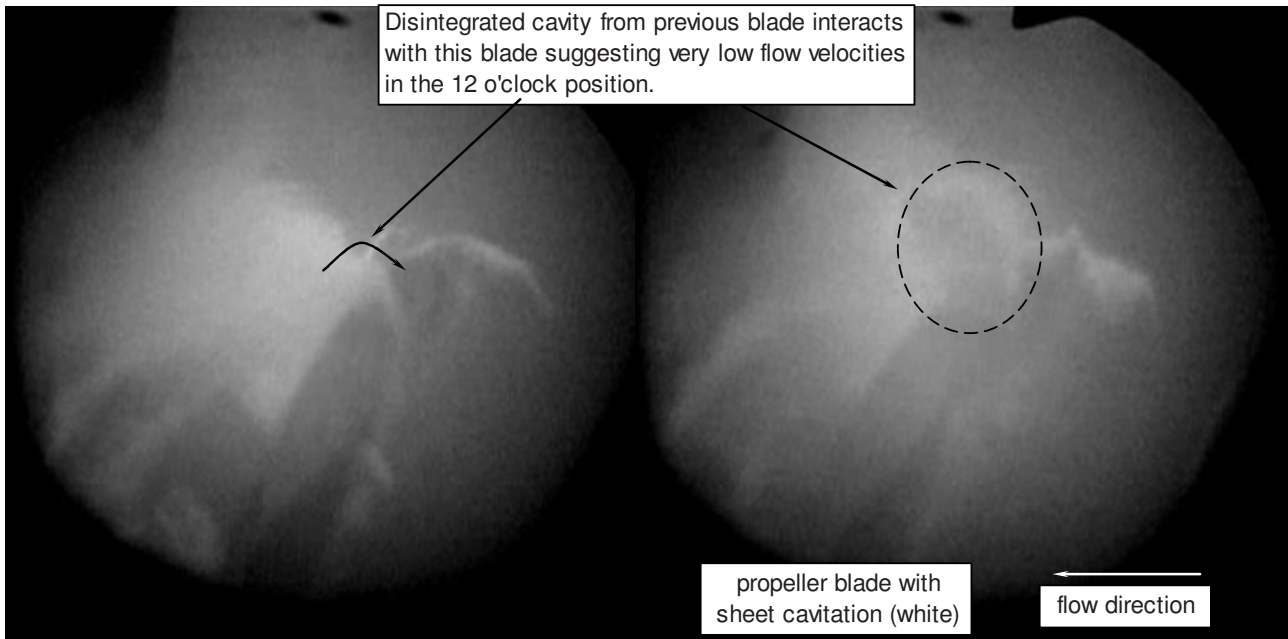


Fig 5 Two images of a propeller blade passing through the wake peak showing various cavitation phenomena

The transmission of vibration energy from the location of excitation, i.e. the shell plating above the propeller, to the tank bulkheads was investigated by performing an operational modal analysis of the aft peak tank structure using Stochastic Subspace Identification [5, 6, 7].

A stability diagram of the aft peak tank structure, produced with OMA, is shown in **Figure 6**. There are a number of natural frequencies located between 28 Hz and 85 Hz and these represent modes of the aft peak tank and local modes of the stiffener to which the sensors were attached. These modes will resonate when energy is input at and close to the frequencies at which they are present. This phenomenon is seen in **Figure 7** which shows the waterfall plot related to a sensor in the aft peak tank. There are two distinct areas of high energy: below 10 Hz and between 28 Hz and 60 Hz. Vibration energy is present at twice and three times propeller blade passing frequencies, between approximately 11 Hz and 26 Hz, but this is less than the energy measured between 28 Hz and 60 Hz. This is despite the fact that **Figure 4** shows that the second and third blade rates have higher amplitudes of input pressure than the higher blade rates. The greater vibration energy in the 28 Hz to 60 Hz band is due to the modal properties of this stiffener. The largest peaks in the 28 Hz to 60 Hz spectrum are located at the stiffener's natural frequencies. Vibration energy from propeller excitation must pass through the aft peak tank structure on its way to the water tank bulkheads. It may therefore be concluded that pressure energy input between 28 Hz and 85 Hz will be passed through the aft peak tank to the connecting tank bulkhead above it with little loss in energy.

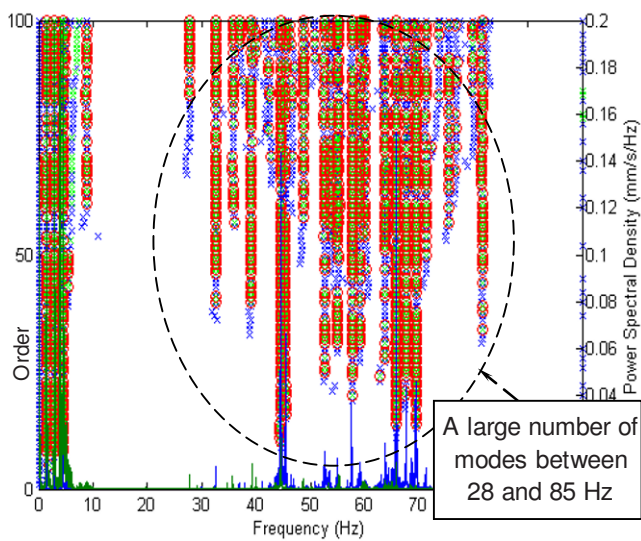


Fig. 6 Stability diagram of the aft peak tank structure. Red circles indicate stable poles while green and blue crosses indicate unstable pole

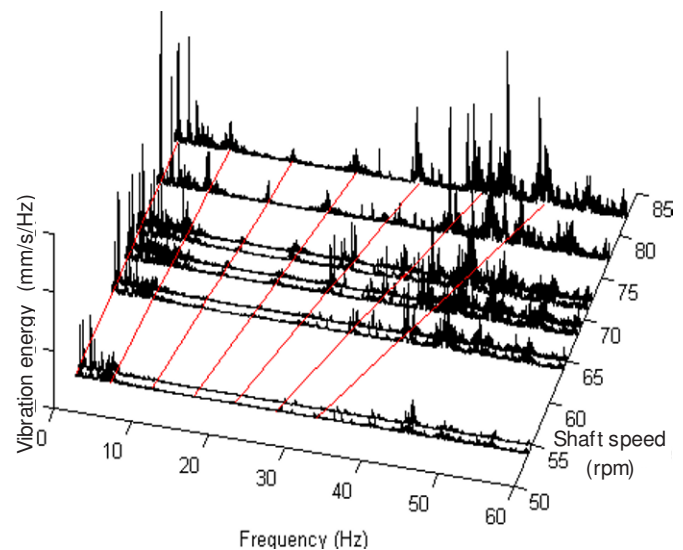


Fig. 7 Frequency distribution of vibration energy of the aft peak tank structure during normal operating.

The modal analysis of a bulkhead of an empty and a filled water tank is shown in **Figure 8**. For the empty tank a large number of modes were present between 40 Hz and 80 Hz. During the test there was machinery running with shaft speeds of 1170 rpm and 1800 rpm and hence, the modes identified at 20 Hz and 30 Hz are attributed to harmonic excitation.

For the bulkhead of the filled tank a large number of modes were present between 25 Hz and 80 Hz. The reduction of frequencies when compared to the empty tank was due to the added effective mass of the water. The added mass lowers the natural frequencies of the tank bulkhead. The effect tends to be greater for lower modes as higher modes engage less of the structural mass.

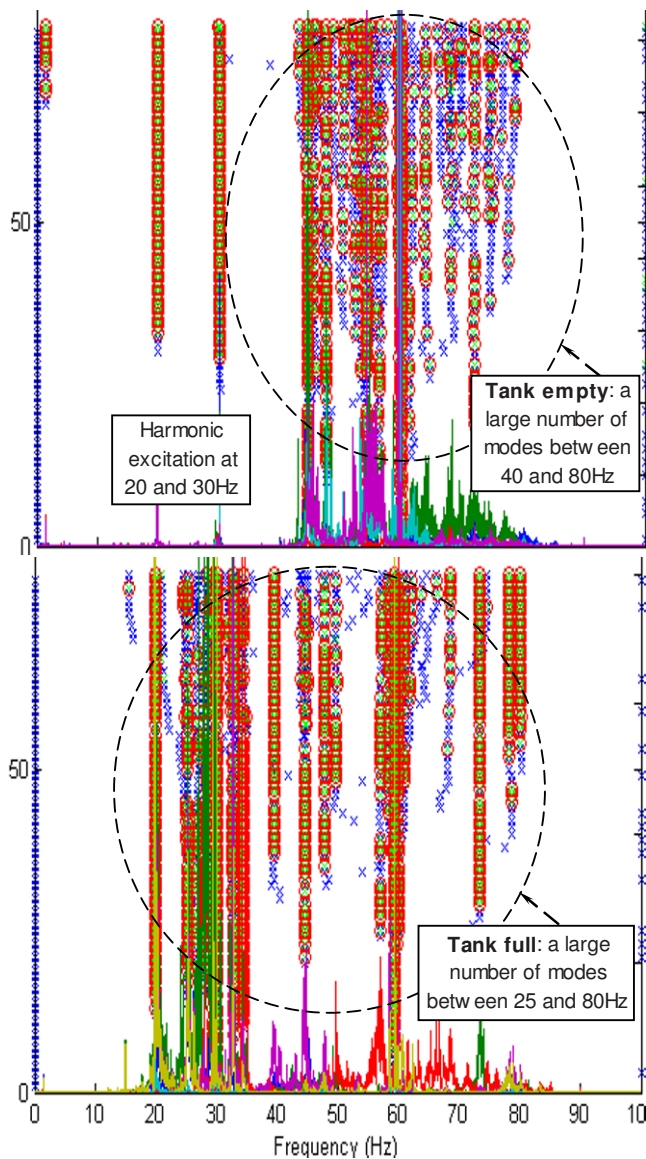


Fig. 8 Stability diagram of a tank bulkhead. The analysis results shown are for an empty and a full tank

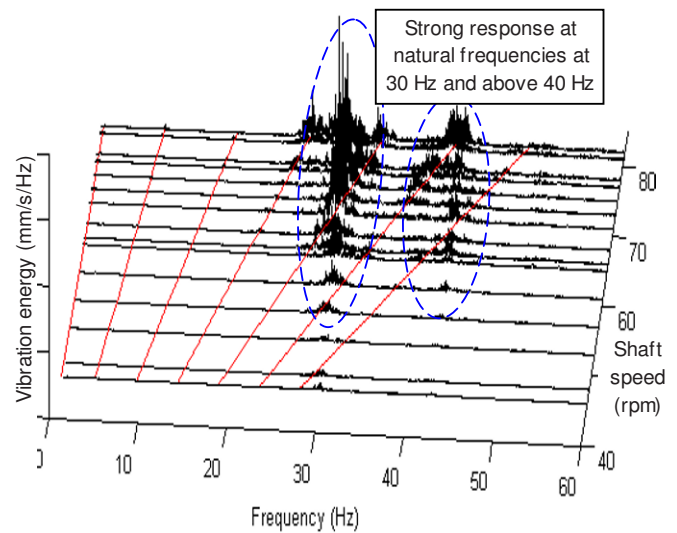


Fig. 9 Frequency distribution of vibration energy of a tank bulkhead during normal operating.

A waterfall plot showing the frequency distribution of vibration energy of a bulkhead of a filled tank is shown in [Figure 9](#) with the shaft rate and propeller blade rates shown as red lines. There is no substantial vibration of the bulkhead up to about 25 Hz and two areas of high energy are seen around 30 Hz and 40 Hz. These areas correspond to frequencies that the aft peak is passing energy through as shown in [Figure 6](#).

The highest peak in the waterfall plot of the tank bulkhead ([Figure 9](#)) is present at 73 RPM at 29 Hz. At this frequency the hull is excited by the fourth blade order and the aft peak tank has a mode as shown by both the modal analysis ([Figure 6](#)) and the waterfall plot ([Figure 7](#)). Therefore, a large amount of energy is passed from the hull to the water tanks at this frequency. This explains why the largest vibration level of tank bulkhead 1 in [Figure 2](#) occurs at 73 RPM rather than at the maximum shaft speed when propeller excitation is most energetic

Analysis of further measurements confirmed that the largest excitation at a particular frequency in the tank bulkheads occurs when the third, fourth or fifth order of the blade rate coincides with a local natural frequency of the aft peak tank and a local natural frequency of the tank bulkhead. Lower, but non-negligible, excitation will occur when these nearly coincide. Negligible excitation energy from the hull pressure will pass through to the tank when they do not coincide

Three principle measures of reducing the vibration levels of the tank bulkheads were identified.

1. High propeller excitation, a result of poor flow around the aft ship, could be reduced by fitting vortex generators upstream of the propeller. These vortex generators will mix the high energy flow, away from the ship, with the low energy boundary layer flow. As such, it will increase propeller inflow velocities and reduce the cavitation and consequently the radiated hull pressures. An added significant benefit of this strategy would be the reduction of vibration levels in other parts of the ship. The optimum location, shape and size of vortex generator can be determined with Computational Fluid Dynamics. An example of such an optimization is shown in [Figure 10](#) where the stagnant flow from a cooling water outlet is forced to outside the propeller inflow by an appropriately placed vortex generator.

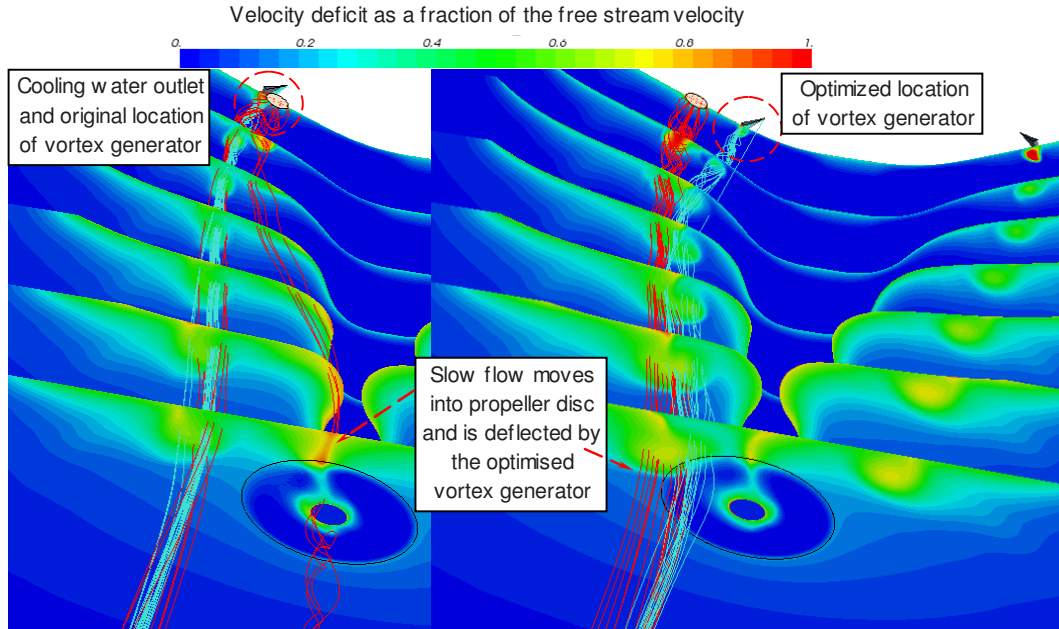


Fig. 10 The cooling water outlet causes slow (poor) inflow into the propeller plane and results in high pressure pulses. Optimization of the vortex generator location improves inflow conditions and reduces propeller excitation

2. The transmission of energy from the propeller through the aft peak tank could be reduced by increasing the local natural frequencies of the aft peak tank structure beyond the fourth and possibly the fifth blade rate; an increase in frequency of the order of 50%. It is expected that this would require a significant amount of steelwork.
3. The response of the bulkheads could be reduced by increasing the local natural frequencies of the water tank beyond the fourth and possibly fifth blade rates and or reduce the mobility. This also would require a significant amount of steelwork. Alternatively the amplitude of excitation could be reduced by fitting dampers to the tanks. These could possibly be mounted internally, spanning between the walls.

Case Study 2 – Navigation bridge vibration

A tanker, such as shown in [Figure 11](#), suffered from high vibrations of the navigation bridge and in particular the bridge wings. At several shaft speeds vibration levels exceeded the ISO6954 - 2000 standard [1] and it was understood that the ship's officers found it difficult to make chart corrections at these speeds. In addition, concerns existed that electronic components on the bridge deck might fail as a result of excessive vibration.

The distribution of vibration energy of the navigation bridge wing during a shaft speed run up is shown in [Figure 12](#). Vibration energy is confined to harmonics of shaft rate, in particular 6x and 8x shaft rate. The 6x shaft rate vibration coincided with the principal excitation frequency of the 6 cylinder diesel main engine whereas the 8x shaft rate coincided with the twice blade frequency of the four bladed propeller. Levels of engine vibration were within acceptable limits of [3] and accordingly, excitation from the main engine was not considered excessive. The maximum measured hull pressure excitation from the propeller was also within acceptable limits.



Fig. 11 A typical tanker deck house of a vessel unrelated to the work described in this paper

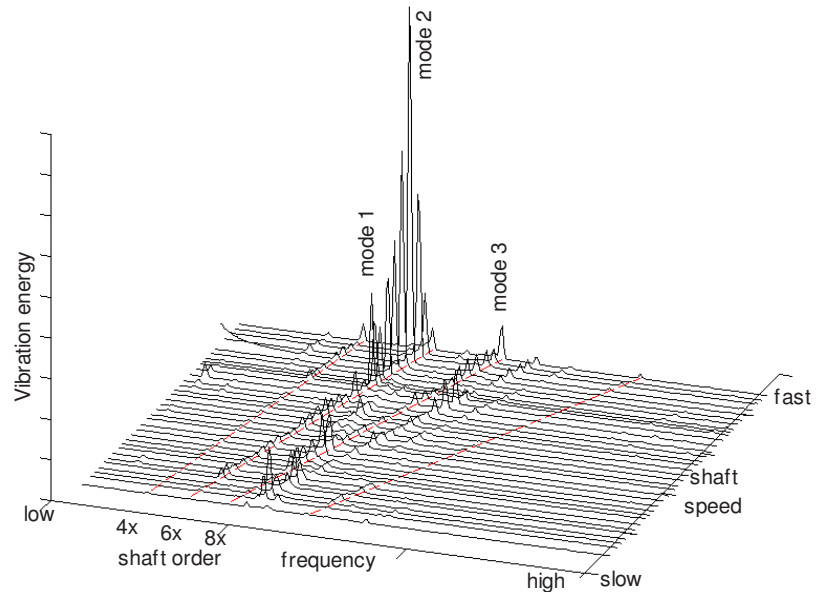


Fig. 12 Frequency distribution of vibration energy of the navigation bridge during a shaft speed run up

The peaks of energy at certain frequencies during the run up were the results of resonance of different modes of vibration with the diesel engine and propeller excitation. An operational modal analysis was performed and the resulting mode shapes, designated mode 1, 2 and 3, are shown in **Figure 13**. Mode 1 involved the accommodation moving as a cantilever with the bridge wings in phase with the navigation bridge. Mode 2 was a torsional mode of the accommodation with the bridge wings out of phase with the navigation bridge whereas mode 3 involved the accommodation moving as a cantilever with the bridge wings out of phase with the navigation bridge.

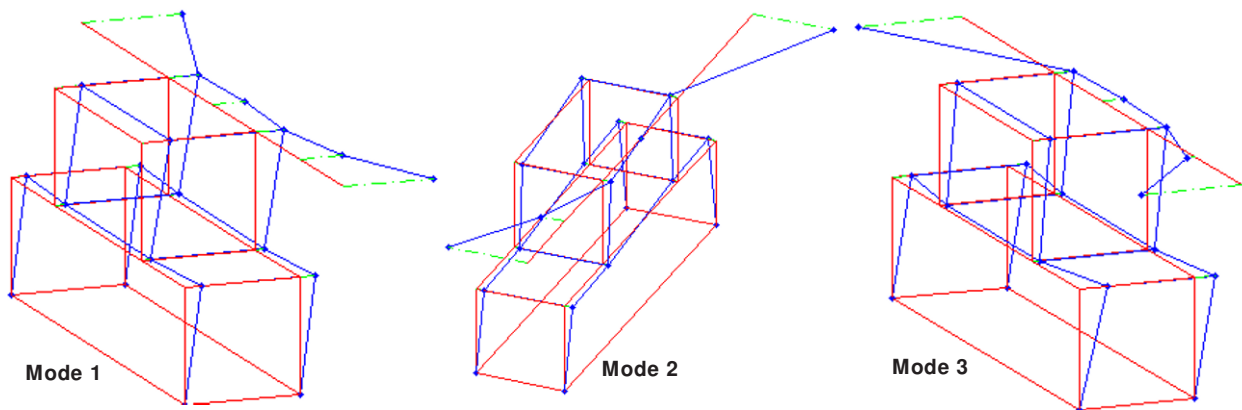


Fig. 13 Mode shapes of the accommodation

Mode 1 and Mode 2 were identified to be within 0.3Hz of each other, however, their character was very different which was seen through examination of their mode shapes. Mode 1 and mode 3 could be described as global modes in that modal ordinates of the accommodation block were of the similar magnitude to those of the bridge wings. In contrast, mode 2 was significantly more localized to the bridge wings. This explained why, during the run up (**Figure 12**), the maximum response was seen at the frequency corresponding to mode 2 compared to the lower responses seen at the frequencies corresponding to modes 1 and 3. In this case the excitation was not excessive and so possible solutions focused on making structural modifications and to this end an FE model was constructed. It is notable that the closeness of mode 1 and mode 2 would have meant that an operational deflection shape would have been misleading in estimating a mode shape and using it to validate the FE model. The

identification of the mode shapes and their characterizations which was provided by OMA was extremely valuable in developing palliative measures. The identified mode shapes were useful in deciding the extent of the ship structure to include in the FE model.

Conclusions

Despite advances in computational techniques vibration problems still occur on board ships. For some problems it is possible to reduce the excitation energy as was shown for an LNG carrier (case study 1) where the location of a vortex generator could be optimized using Computational Fluid Dynamics.

In cases where it is more difficult to alter the excitation (case study 2), operational modal analysis has proven to be useful for the detailed characterization of modes (natural frequencies and mode shapes), giving a better understanding of the problem and helping to reduce the risks associated with the implementation of structural modifications.

Vibration problems onboard ships are most easily solved by modifying the excitation characteristics. However, if this is not possible, structural solutions are favored.

References

1. Mechanical vibration - Guidelines for the measurement, reporting and evaluation of vibration with regard to habitability on passenger and merchant ships, ISO 6954:2000(E)
2. Passenger Crew and Accommodation Comfort Notation, 2007, Lloyd's Register
3. Lloyd's Register Ship Vibration and Noise Guidance Notes, 2006, Lloyd's Register
4. Mechanical vibration – Evaluations of machine vibration by measurement on non-rotating parts – part 6: Reciprocating machines with power ratings above 100kW, ISO 10816-6:1995
5. Van Overschee P, De Moor B, Subspace Identification for Linear Systems, 1996 Kluwer Academic Publishers, USA, pp254
6. Peeters B, De Roeck G, Reference-Based Stochastic Subspace Identification For Output-Only Modal Analysis, Mechanical Systems and Signal Processing (1999) 13(6), 855-878
7. Van der Auweraer H, Peeters B, Discriminating Physical Poles in High Order Systems: Use and Automation of the Stabilization Diagram, Instrumentation and Measurement Technology Conference, Como, Italy, 18-20 May 2004

The Use of Layered Composites for Passive Vibration Damping

C.E. Lord, J.A. Rongong, A. Hodzic

Department of Mechanical Engineering, University of Sheffield, Mappin Street
Sheffield S1 3JD, United Kingdom

NOMENCLATURE

| | | | |
|----------------|---|--------------|--|
| A | contact area, amplitude | n | number of layers |
| c | viscous damping | P_r | average contact pressure |
| c_{eq} | equivalent Coulombic damping | r | relative motion |
| E_{eff} | effective elastic modulus | x | displacement, node location |
| E_N | energy | \dot{x} | velocity |
| F | tip force | \ddot{x} | acceleration |
| \bar{F} | average force | y | distance from neutral axis |
| F' | breakaway force | β | distributed force coefficient |
| F'' | tip force during sliding | γ | sub-coefficient |
| F_C | compressive force | δx | x position, deflection |
| \bar{F}_{fr} | average frictional force | δy | y position, deflection |
| F_N | normal force | $\delta^* y$ | adjusted y deflection |
| F_T | total vertical force | η | number of discretized nodes |
| F_v | vertical nodal force | μ_d | dynamic friction coefficient |
| G_d | dynamic artificial interfacial shear stress | μ_s | static friction coefficient |
| G_s | static artificial interfacial shear stress | τ | shear stress |
| I_{eff} | effective second area moment of inertia | φ | angle |
| k | stiffness | Φ | phase angle |
| k^* | complex stiffness | ψ | system artificial interfacial shear stress |
| L | length | ω | natural angular frequency |
| m | mass | ω_e | forcing angular frequency |

ABSTRACT

With the advent of increasingly severe vibration environments, comes the need for better vibration damping control and alternate vibration damping methods. As a response to this, these methods need to be able to be accurately predicted through the use of analytical and numerical models. In this paper, an analytical model is proposed to analyze and predict the passive damping macro-slip behavior of multiple debonded layered composites. The aim of the paper is to develop a multi-layered model that is accurate yet easy to be analyzed so that it can be used efficiently in the design of layered composite dry friction dampers. The proposed analytical model allows for calculating an equivalent viscous damping coefficient from the kinematic tracking of the layer interfaces where Coulombic damping occurs. The equivalent viscous damping coefficient can be used in conjunction with a bilinear material model to represent the multiple layered composite as an Equivalent Single Layer (ESL) for linearizing the non-linear interfacial contact. The validation of the method is demonstrated by comparing the analytical results obtained in this study with those from numerical results.

1. INTRODUCTION

One of the most common sources of nonlinearity originates in frictional contact. When relative interfacial motion occurs this is in the form of micro-slip, macro-slip, or both. This is highly dependent on the friction coefficients at the interface as well as the normal forces that are present. With these frictional interfaces significant amounts of energy dissipation can be accomplished [1]. The use of friction for vibration damping is a relatively inexpensive method to provide damping to a system and can be used effectively for a broad range of amplitudes and frequencies. Layered composites have many benefits. One ideal benefit is that they are highly tunable and can be tailored for very specific environments

and structures as a result of the multiple parameters that are available to change their damping characteristics. Another benefit to this type of damping is that it does not exhibit the level of temperature dependence as compared to viscoelastic materials, which are commonly used for vibration damping applications due to their high loss factors. With metallic debonded layered systems, as the materials begin to increase in temperature from the frictional and thermoelastic heating, the material properties remain nearly unchanged. This is an extreme benefit as these materials will behave in a consistent way over a wide range of temperatures. In addition, these dampers can be used as primary structural elements without the undesired added mass of typical dampers and could be used along the primary load paths to provide system damping.

2. ANALYTICAL MODEL DEVELOPMENT

For this work, the analytical models are developed on the basis of using simplified geometries. A slender cantilever beam of rectangular cross-section and uniform thickness with linear elastic material properties will be used to model each layer of the naturally debonded composite. It is assumed that the cantilever beams are inextensible and axial displacements are negligible since these will be relatively small with respect to the bending displacements. A further assumption will be that the stiction of all nodes at a single interface are overcome simultaneously since the beams are assumed to be inextensible. It is also assumed that the cross-sections of the beams remain constant along their length, ignoring the effect of Poisson's ratio and any geometric nonlinearities. The beams are based on Bernoulli-Euler beam theories and assume that the curvature of the beams is proportional to the bending moment. During dynamic motion, since friction is present in the system, there are oscillating intervals of time in which stiction occurs and intervals of time in which relative sliding at the interfaces occurs. This can be represented by the following two equations of motion in Equations 1 (stiction) and 2 (sliding) and in Figure 1.

$$m\ddot{x} + k^*x = 0 \quad (1)$$

$$m\ddot{x} + kx = F_{fr} \quad (2)$$

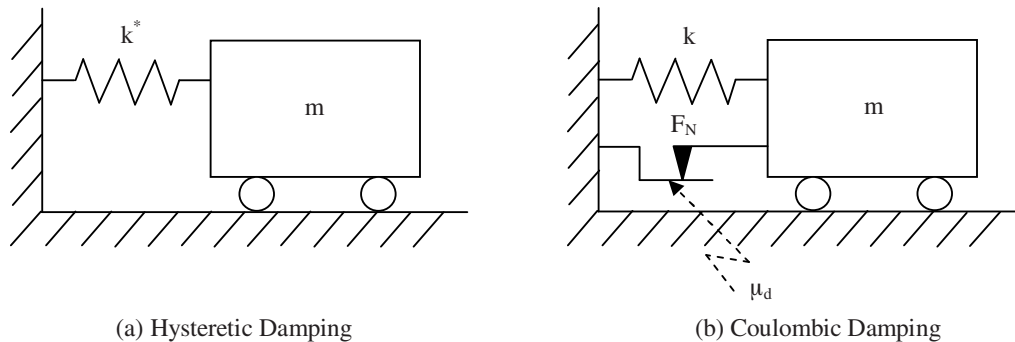


Fig. 1. Single degree of freedom (SDOF) system with (a) hysteretic damping and (b) Coulombic damping

When stiction occurs, the damping is solely hysteretic from the material and is denoted as a complex stiffness in the system. On the other hand, when sliding occurs, the damping is a combination of Coulombic damping and hysteretic damping. Damping that occurs in debonded layered systems is primarily Coulombic for metallics and for other materials that have small magnitude loss factors. In this paper, focus will only be on the Coulombic portion of the total damping and the model will neglect any material damping that is present. It must be noted that the frictional force in Equation 2, opposes the motion always. Therefore, as the body is displaced in the opposing direction, the sign convention changes polarity. In the case of the Coulombic damping system in Figure 1, the normal force and dynamic friction occurs at the layer interfaces and the hysteretic damping is ignored.

2.1 STIFFNESS MODEL

Since this model is based on only macro-slip friction, there is no decay between the static and dynamic friction coefficients. This would indicate that velocity has no influence on the overall coefficients during interfacial sliding. Much like the Classic Coulomb, Regularized Coulomb, and Karnopp friction models, the presliding is not characterized

and is ignored [2]. This presliding results in a hysteretic damping from elastic deformations, but is different from that due to bending deformations. The presliding hysteretic damping is purely due to shear strains and accounts for even a smaller percentage of the total damping as compared to that from the bending hysteresis. With the presence of macro-slip friction, in debonded layered composites, the system behaves bilinearly [3,4]. This can be characterized by a single point discontinuous softening load-deflection curve comprised of an initial modulus and a secant modulus as shown in Figure 2.

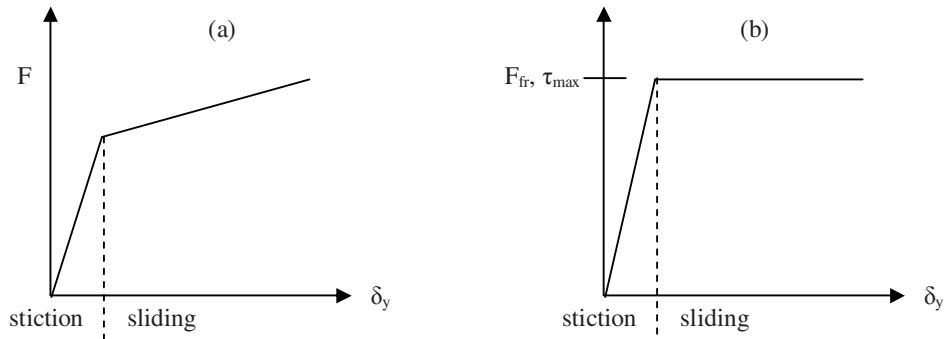


Fig. 2. Layer behaviour for (a) stiction and sliding bilinear representation and (b) frictional and shear stresses

To define the moduli of the bilinear behaviour, the system needs to be separated into two categories: stiction and sliding. When stiction occurs at the interfaces, the layers are locked together and act as one. The layered system can then be treated as a single layer following Equivalent Single Layer (ESL) theories. When sliding occurs, the layers act as separate individual layers and motion for each layer must be resolved with respect to the adjacent layer.

To calculate the force-deflections for the bilinear curve, the stiction portion will first be calculated. To initiate this, the interfacial forces along the beam will need to be known. If no compression is present on the beams, then small load steps will need to be made to determine if the nodal forces are great enough to overcome the stiction or not. When a cantilever beam has a concentrated tip force, the moment along the length of the beam is linear. The maximum moment is at the fixed-end and the moment approaches zero where the force is applied at the free-end. When a cantilever beam has a uniformly distributed load, or a triangularly distributed load, the moment along the length of the beam is nonlinear from the fixed-end to the free-end. This nonlinear moment would indicate that the tip force could be replaced with a parabolic distributed load to represent the same behaviour as the concentrated tip force [4]. To find this parabolic function, the parabolic load can be discretized into a multilinear curve comprised of multiple triangular loads. If the first triangular load is considered, the force along the length of the beam can be deduced by evaluating the constant distributed force coefficient for a given length of the beam through the use of proportionality since there is a constant slope. The nodal forces can then be expressed as

$$F_v = \frac{\beta}{2L} x^2 \quad (3)$$

To calculate the distributed force coefficient β , each sub-coefficient must first be considered for each node. These sub-coefficients are then summed and the product of their inverse, and the tip deflection from Equation 3, are used to arrive at

$$\gamma_n = \frac{x^4(3L - x_n)}{6E_{eff}Ie_{ff}} \quad (4)$$

$$\beta = 2L\delta_{y(L)}\Sigma\gamma_n^{-1} \quad (5)$$

Once the vertical nodal forces are calculated, they must be resolved into vector components. Each node within the beam will have a different temporal x and y coordinate that will behave nonlinearly. Ascertaining the force vectors is accomplished through kinematically tracking each of the nodes to estimate their final position. Assuming that the interface between each layer remains frictionless, for the time being, the elastic curve, for the system can be tracked

using a variant of Bernoulli's elastic curve equation by substituting the effective flexural rigidity of the system. The temporal y displacements are expressed as

$$\delta_{yn} = \frac{(F_{vn}x^2)(3L - x_n)}{6E_{eff}I_{eff}} \quad (6)$$

Tracking the nodal x position relies on a back looking approach. The temporal x displacements of the previous node are used for information to track the following node.

$$\delta_{xn} = (d\delta_x^2 - d\delta_y^2)^{1/2} + \delta_{xn\ i-1} \quad (7)$$

Once the x and y nodal positions are known, the rotation referenced from the un-deformed shape, for the beam, for each of the nodes, can be calculated using

$$\varphi = \tan^{-1}(d\delta_y - d\delta_x) \quad (8)$$

Once the nodes are tracked, with their respective angles, the nodal normal forces can be calculated through recalling Equation 8. The normal nodal forces become

$$F_{Nn} = \cos(\varphi_n)(F_{vn}) \quad (9)$$

These nodal forces are used to initiate the looped convergence process of determine the actual nodal normal forces that stiffen the system when accounting for the presence of the frictional interactions. These normal forces will require an adjustment when an out-of-plane compressive force is present in the system. This is taken into account by linearly decomposing the compressive forces. Once these are decomposed these are added directly to the nodal normal forces in Equation 9 and the nodal normal forces are then expressed as

$$F_{Tn} = F_{Nn} + \frac{F_c}{n-1} \quad (10)$$

It is assumed that the compression remains constant when the composite experiences bending. For calculating the decreased displacements from the nodal normal forces, the nodal normal forces can be averaged since all the nodes are assumed to move simultaneously along their respective interface. This is done by

$$\bar{F} = \left(\frac{(F_{Tn} - F_{Tn\ i-1})(x_n - x_{n\ i-1})(\eta - 1)}{2} \right) + ((x_{n3} - x_{n\ i-1})F_{T_2}) + \dots + ((x_{n\eta} - x_{n\ i-1})F_{T\eta\ i-1}) \quad (11)$$

Using the average nodal normal force, the averaged frictional stress is found by

$$G_s = \frac{\bar{F}\mu_s}{A} \quad (12)$$

Once G_s has been calculated, the displacements of the composite can be calculated with the inclusion of the frictional stiffness. G_s can be used to represent an artificial shear strength at the layer interfaces. The shear stress for a solid beam with the same geometry as the composite must first be calculated. Timoshenko and Goodier [5] express this as

$$\tau_{xynl} = \frac{F}{2I} \left(\frac{t^2}{4} - y_{nl}^2 \right) \quad (13)$$

τ_{xy} must be calculated for each of the interface locations, with respect to the solid beam neutral axis and then summed. If the artificial shear stress is less than the shear stress for the solid beam, then the load step chosen was too large and a smaller load step is necessary. Convergence is achieved once the ratio of the artificial shear stress and the shear stress of the beam approach 1. Using the sum of τ_{xy} and interfacial stiffness of the entire composite can be calculated using

$$\psi_{nl} = \Sigma G_{sni} \quad (14)$$

From Equation 13 the breakaway force and displacement can be calculated. The breakaway force is the ratio of the tip force that was used to get convergence of the artificial shear stress and the sum of the shear stress of the interfaces of the layers. The corresponding deflection comes from the tip displacement using the effective modulus of elasticity and the effective second area moment of inertia using a Volume Fraction (VF) approach to arrive at an ESL.

To calculate the secant modulus, the coordinate system for the elastic modulus must be replaced with the secant modulus ($F=0, \delta=0$). Once τ_{xy} is equal to ψ , the layers will slip relative to one another. The secant modulus is simply the remaining balance of the load while accounting for the opposing friction once slipping begins. To calculate the secant modulus deflection, the remaining tip force must be calculated. This is done by

$$F'' = (F - \bar{F}) - \left[\left(\frac{8I_{eff} \bar{F} (\mu_s - \mu_d)}{A(t^2 - y_{nl}^2)} \right) \right] (F - \bar{F}) \quad (15)$$

Once the remaining force has been calculated, the displacement for the secant modulus of the bilinear curve can be resolved. Since the layers are now at the point of sliding, and μ_d has been removed from the remaining force as an opposing force, the layers will behave as though they are frictionless. Therefore the solution for solving this is relatively straightforward and is described as

$$\delta y = \left(\frac{F'' L^3}{3E_{eff} I_{eff}} \right) (2^n) \quad (16)$$

It should be noted that although the secant modulus should be a factor of 2^n , as indicated in Equation 16, it is not, as the shift in the opposing frictional force and has been removed. If this is added back into F'' then the secant modulus does follow this behaviour. As the ratio between static and dynamic friction coefficients changes, so does the secant modulus. The comparison between the analytical model and the numerical model can be seen in [Figure 3](#).

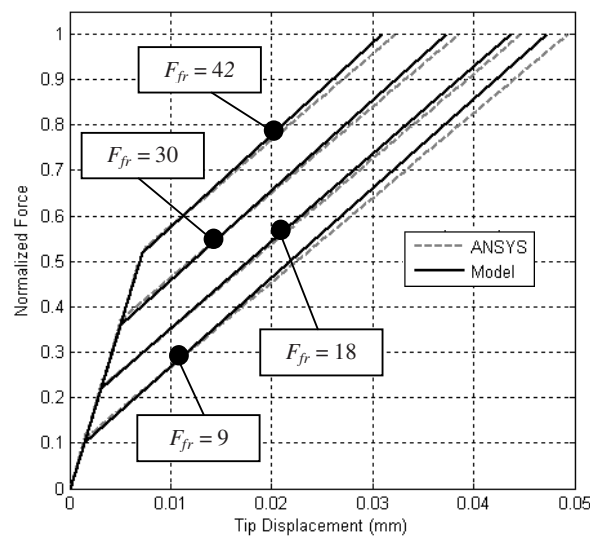


Fig. 3. Numerical and analytical bilinear behavioural comparison

2.2 DAMPING MODEL

In most nonlinear systems, only the frequency response functions (FRFs) can be linearized, at best, for frequencies close to a single resonance of a system [6]. The parameters that are linearized are usually for short frequency ranges. This often leads to difficulties when assessing the energy dissipation and the damping in nonlinear systems. Because

nonlinear stiffness and damping effects are usually inseparable, it is generally considered to be an advantage to also consider the energy dissipation in nonlinear systems rather than the damping alone [7].

In the proposed damping model, the interfacial forces from the stiffness model are used in conjunction with the known dynamic friction coefficients to arrive at an equivalent viscous damping. Each node, in each layer, is tracked to determine the relative motion while the F_N is modeled as a linear motion sliding tangential joint much like that in Figure 1. One method that can be used to evaluate the effectiveness of the F_{fr} , with respect to the steady state excitation, is through energy dissipation. Consider the debonded layered composite being excited at the tip by a force of $F \sin \omega t$. As the beams pass from zero amplitude to maxima and minima amplitudes, and assuming that they are into the macro-slip region, that is $F \sin \omega t \geq F_{fr}$, then Coulombic damping will occur. Since the exciting force is sinusoidal, it is reasonable to assume that

$$x = X \sin(\omega t - \phi) \quad (17)$$

which leads to

$$F \sin \omega t - F_{fr} = kx - m\omega^2 x = kx \left(1 - \left(\frac{\omega_e}{\omega} \right)^2 \right) \quad (18)$$

The energy dissipated per cycle is then represented as

$$E_N = 4Ffr \left[\frac{F - F_{fr}}{k \left(1 - \left(\frac{\omega_e}{\omega} \right)^2 \right)} \right] \quad (19)$$

It is quite easy to see that the ratio of F/F_{fr} is important for maximizing the energy (damping) dissipated.

For debonded layered composites, the damping within each layer is non-uniform for two reasons. Firstly, the interfacial forces from bending are nonlinear along the length of each layer. The highest interfacial forces, due to bending, are located at the free end of the layer and represented by a low order polynomial. This becomes less significant if there is a presence of an externally applied compression. Secondly, the highest rotations are also located at the free end of each layer. This results in the highest relative motion between layers being at the tip. To determine the damping in each of the layers, the average nodal F_N and the average relative motion can be determined by Equations 20 and 21, respectively.

$$\overline{F_N} = \frac{\int F_N dx}{L} \quad (20)$$

$$|\overline{r}| = \frac{\int r dx}{L} \quad (21)$$

It is important to understand that the relative motion between layers will be greater than for just a single layer at the interface. As a result, both layers of the interface need to be summed together. As one face of the layer is moving in a positive direction, the adjacent face, of the adjacent layer, is moving in the opposing direction due to tensile and compressive stresses. The amount of relative motion is dependent on the thickness of the layer and where the neutral axis of that layer is located. For layers of the same thickness, the motion for the interface is simply twice that of the individual beam surface at the interface. The proposed model is slightly flawed by not accounting for when the layers overlap each other at the tips and some of the tip of the interface is no longer in contact. However, this will result in a very small overall percentage of the damping in the system and will decrease as the length of the layers increase.

Once F_N and r are solved for each individual layer, the summation of F_N and r for all layers can be used, with a single interface, in a Coulombic free vibration decay for a SDOF model. This takes the form of

$$x(t) = A_1 \cos \omega t + A_2 \sin \omega t \pm \frac{F_N \mu_d}{k} \quad (22)$$

where the sign convention alternates between positive and negative directions. For the first half-cycle ($0 \leq \omega t \leq \pi$), the displacement is less than the previous displacement amplitude by

$$\frac{2\mu_d F_N}{k} \quad (23)$$

This trend continues until the displacement reaches the “dead zone”, which is equal to

$$\frac{\mu_d F_N}{k} \quad (24)$$

To find the damping of the system we can view it as being equivalent viscous damping. The energy dissipated per cycle by the viscous damping force in a single degree of freedom vibrating system is approximated by

$$4 \int_0^x c \dot{x} dx \quad (25)$$

If it is assumed that $x = X \sin \omega t$ occurs for each complete cycle. The energy dissipated is therefore

$$4 \int_0^{\pi/2} c X^2 \omega^2 \cos^2 \omega t dt = \pi c \omega X^2 \quad (26)$$

Since it is known that the energy dissipated per cycle by Coulomb damping is $4F_N \mu X$, approximately, an equivalent viscous damping coefficient for Coulomb damping can be solved for and can be expressed as

$$c_{eq} = \frac{4F_N \mu}{\omega \pi X} \quad (27)$$

3. FINITE ELEMENT MODEL

Multiple Finite Element Models (FEM's) have been used to investigate and validate the analytical models. Each of the models are full 3-D models using hexahedron 20 node higher-order elements. For this work, three primary different FEM's, with multiple simulations, were used for the validation process.

The first FEM was a nonlinear static model, with frictional contact elements and without nonlinear materials or geometry, was used to represent the layered beams for the stiffness model. The contact elements employed a Coulomb friction model without the friction decay.

The second FEM was the same as the static model but was used for flexible dynamic analyses in the form of free vibrations. Solving these types of problems numerically is computationally costly, especially when there are contact nonlinearities. These contact nonlinearities are riddled with complexities that can often lead to unconverged results for implicit analyses. Various simulations were performed with and without the application of external compression loads. For transient models, the time steps are extremely important in order to capture the true dynamics of the system. The time steps in this case were based on the first natural frequency (bending mode) when stiction is present between the layers. This produces a higher natural frequency and in turn will create a smaller time step for the following criteria. For the maximum time step $1/30^{\text{th}}$ of the period of the natural frequency was used, while for the minimum time step $1/300^{\text{th}}$ of the period was used. The results seemed to indicate reasonable capture of the physics of the layers when they were used as having frictional interfaces.

For representation of the ESL model, for the stiffness and damping models, a third FEM was used. This consisted of a single geometric layer using an elastic-plastic isotropic hardening material model initially. When using this material model for free vibrations, hysteretic damping from the Bauschinger Effect [8] was present since the material was used to go into the plastic region of the material model. This is an artificial hysteresis and does not really occur as the material model is for an elastic-plastic material and in this work it is being exploited for the use of accounting for macro-slip. An

alternative to this is to use a bilinear spring in which the damping is ignored. Each layer of the composite was modeled using nearly 2 000 elements (Figure 4) using ANSYS commercial implicit code.

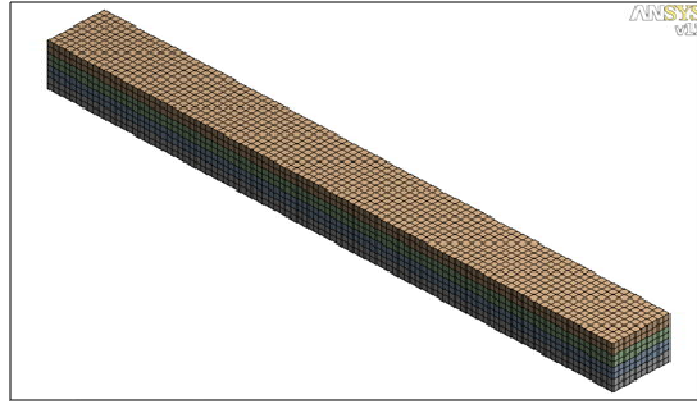


Fig. 4. Structural FEM ANSYS mesh

4. RESULTS AND DISCUSSION

As mentioned above, the premise of this paper is to provide an ESL model that can be used to represent the stiffness and damping properties of multilayer debonded composites. Once these two properties are solved for analytically, the adjusted properties can be input directly into finite element code and solved at a fraction of the computational cost with still maintaining reasonable accuracy. By exploiting the two proposed models this representation can be accomplished with reasonable accuracy and at a significant decrease in solve time.

Figure 5 shows that, for a rigid mass, once the displacement is equal to Equation 24 then stiction occurs and the motion is halted resulting in a relaxation position in which for this case is approximately 2mm. This is however not necessarily true for flexible bodies, such as the multilayered debonded composites. This is dependent on the stiffness of the system when stiction occurs. This behaviour of a secondary motion, in the form of oscillations, is analogous to presliding motion [9] as it is for a flexible body and can be seen in Figure 6.

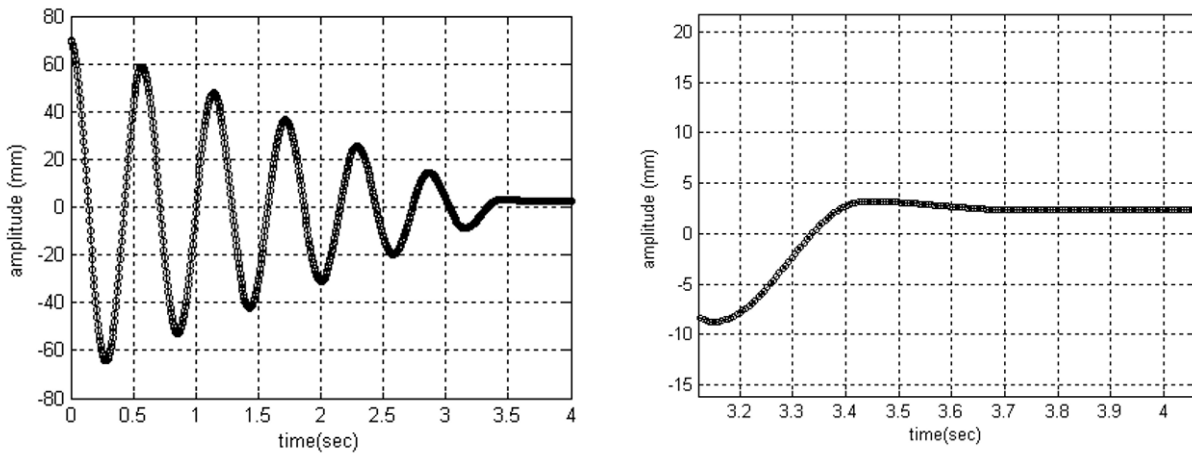


Fig. 5. Analytical Coulombic free vibration decay of a rigid body

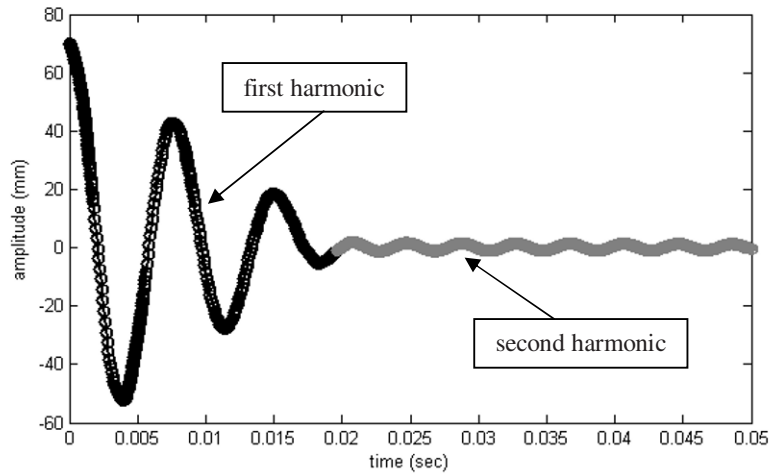


Fig. 6. Numerical Coulombic free vibration decay of a flexible body

Figure 6 is the numerical nonlinear transient response waveform for two beams that are damped by friction. The decay is linear as would be expected. However this waveform consists of two separated harmonics. The first harmonic is that of the beams during sliding, acting near frictionless, and with the friction component acting as predominantly damping and not as a stiffness shift. The second harmonic is that of when the layers are in stiction from when the system has damped out and now the layers act as a single beam. For the first harmonic the natural frequency is around 135.69Hz while the second harmonic is approximately 256.40Hz. This is expected and predicted as there were only two beams which results in the stiffness between stiction and frictionless is to be nearly 4X (2^n) and since $\omega_n = (k/m)^{0.5}$. It should also be noted that there is little decay in the second harmonic as this is purely hysteretic and the defined material damping was extremely low.

It has been shown that the bilinear nature has little effect on the shape of the overall waveform. Figure 7 is a comparison between an ESL representation of three layers with a bilinear material property derived from the analytical stiffness model and a steady-state sine wave in the form of $x(t)=Xsin\omega t$. In the zoomed view (on the right-hand side), there are some noticeable nonlinearities seen but do not have much of an effect on the actual waveform profile. It should be noted that from $\pi/2$ to π , of the first cycle, the waveform corrects itself and is not a permanent alteration that is cumulative. Attention should also be directed at the waveform comparison when $t=0.03s$. The waveforms begin to diverge in their profiles. This is a result of the second harmonic, similar to that in Figure 6.

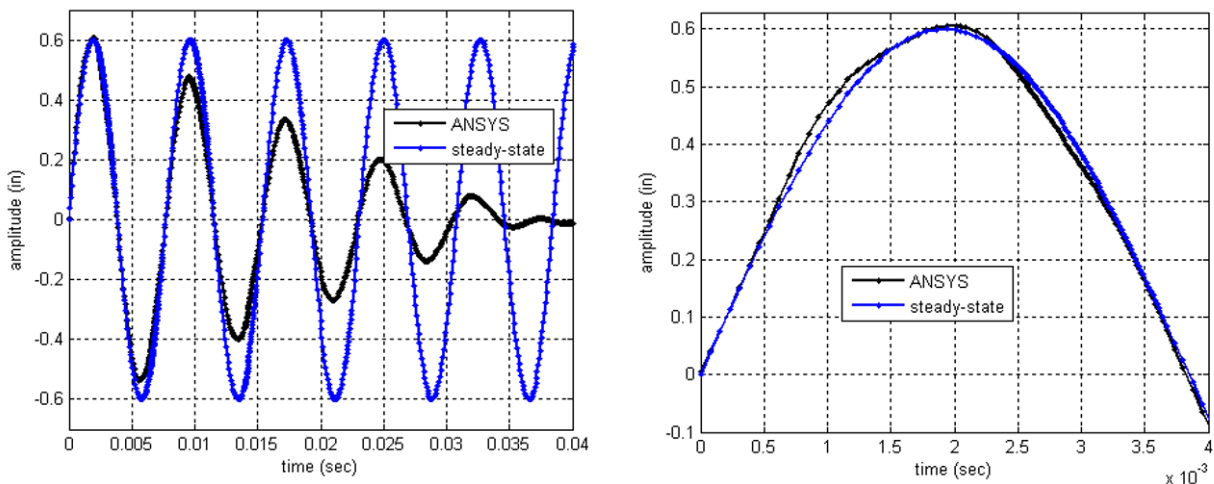


Fig. 7. Waveform comparison for ANSYS bilinear Coulombic free vibration decay and steady-state sinusoidal excitation

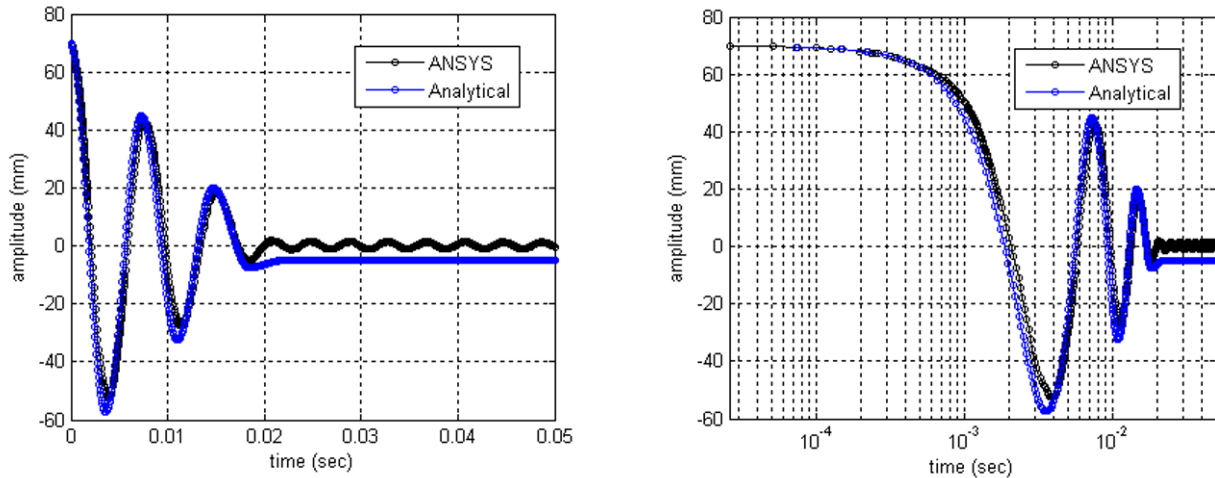


Fig. 8. Linear-linear and logarithmic-linear comparisons for Coulombic free vibration decay between ANSYS and for the analytical model

5. CONCLUSION

Naturally debonded composites can accurately be analysed, and the behaviour predicted, using finite element methods, however these methods are computationally expensive, especially for transient analyses, and require large DOF models to include every layer and their nonlinear interfaces. In this work, an analytical validity model has been developed in the context of a debonded multilayer composite in the form of a cantilever beam bending behavioural model. The validity is emphasised for a model reduction technique that can be used for numerical analyses and/or as a straightforward analytical approach. Comparisons between the analytical models and numerical models have been made and indicate acceptable accuracy. The numerical model is in good agreement with both the stiffness model and the damping model. Current experiments are being conducted to validate the analytical and numerical models in addition to the inclusion of presliding behaviour is being investigated to extend the accuracy of the models and to help determine localized damping effects.

REFERENCES

- [1] Beards, C. F., *Structural Vibration Analysis and Damping*, Wiley, New York, 1996
- [2] Karnopp, D., *Computer Simulations of Stick-slip Friction in Mechanical Dynamic Systems*, ASME J. of Dynamic Systems, Measurement and Control, 107(1),100-103,1985.
- [3] Prime, M. B., Shevitz, D. W., *Linear and Nonlinear Methods for Detecting Cracks in Beams*, 14th International Modal Analysis Conference, 1437-1443, 1996.
- [4] Lord, C. E., Rongong, J. A., Hodzic, A., *Linearized Material Properties of Nonlinear Interfacial Contact for Layered Composites*, International Conference on Interfaces & Interphases in Multicomponent Materials, 2010.
- [5] Timoshenko, S. P., Goodier, J.N., *Theory of Elasticity*, McGraw-Hill, New York, 1970.
- [6] Rivin, E. I., *Handbook on Stiffness & Damping*, ASME, New York, 2010.
- [7] Liang, J., Feeny, B. F., *Balancing Energy to Estimate Damping Parameters in Forced Oscillators*, 2005.
- [8] Chawla, N., Jester, B., Vonk, D. T., *Bauschinger effect in porous sintered steels*, Material Science and Engineering, A346, 266-272, 2002.
- [9] Dupont, P., Armstrong, B., Hayward, V., *Elasto-Plastic Friction Model: Contact Compliance and Stiction*, AACC, 2000.

Unbiased Estimation of Frequency Response in the Presence of Input and Output Noise

Anders Brandt, Associate Professor

Dept. of Industrial and Civil Engineering, University of Southern Denmark

Niels Bohrs Allé 1, DK-5230, Odense M, Denmark

ABSTRACT

Many attempts have been made on finding a frequency response estimator which minimizes the bias error in cases where both the input and output signals of a linear system are contaminated by extraneous noise, for example, H_v and H_s . It is well-known that these estimators only minimize the bias error if the input and output extraneous noise spectra are known, which they are normally not. This paper describes how time domain averaging (cyclic averaging) of periodic excitation signals can be used to eliminate the bias due to both input and output extraneous noise. It is demonstrated by simulation results that asymptotically unbiased estimates of frequency response functions can be obtained by using time domain averaging and periodic random noise. Examples are given of both single-input/single-output (SISO) and of multiple-input/multiple-output (MIMO) systems. The fact that periodic excitation signals in this way can be used to eliminate the bias error in FRF estimates does not seem to have been recognized previously.

INTRODUCTION

Estimating frequency response functions (FRFs) in mechanical measurements is an important tool. The main established theory for estimators commonly used was established in early editions of [1], most notably the H_l estimator which minimizes contaminating noise on the output. It is well-known that the H_l estimator is biased if contaminating noise exists in the measured input signal. This situation is not uncommon when using shaker excitation on weak structures. The H_2 estimator, which minimizes noise on the input, on the other hand, is biased if contaminating noise exists in the measured output signal. The H_2 estimator, furthermore, is only available for multiple-input/multiple-output system identification in the special case where the number of inputs equals the number of outputs, which is rarely the case.

Early attempts to minimize noise on both input and output simultaneously led to the H_s estimator and the special case of this estimator called H_v , [2, 3], but these estimators have the limitation that knowledge of at least the ratio of the input and output contaminating noise is required to produce optimum estimates, which is rarely available in practice. Recently, [4], the H_v estimator has been shown to be a special case of a maximum likelihood estimator, but the requirement of knowing the relation between input and output contaminating noise remains.

In [5], an unbiased estimator, the H_α estimator, based on special, cyclostationary excitation signals was presented. This is a promising estimator, particularly since the commonly used burst random excitation signal was shown to be useable as a cyclostationary excitation signal.

Recently time domain averaging, referred to as “cyclic averaging”, was investigated in [6], where it was shown that time domain averaging in the frequency domain can be viewed as equivalent to a comb filter being applied to data (FRFs). However, the paper did not analyze the effect of time domain averaging on the noise suppression of input and output noise, as the focus of the paper was on the bias error due to the limited frequency resolution.

In [7] it was demonstrated that using time domain averaging, the bias due to contaminating noise on both input and output signals can be suppressed when using periodic excitation signals in both single-input/single-output (SISO) and multiple-input/multiple-output (MIMO) cases. The present paper aims at developing some more fundamental understanding of this method. It will be shown that asymptotically unbiased estimates can be obtained by using the well-known pseudo random or periodic chirp excitation signal for SISO measurements, and periodic random excitation for MIMO measurements.

SISO ESTIMATOR

Using time domain averaging in the case of a single input is relatively straight-forward. The excitation signal can be any broadband periodic signal, typically pseudorandom or periodic chirp [7]. The procedure is to turn the excitation signal on, and then wait a number of periods until the linear system is achieving its steady-state response. For moderately damped systems 5 to 7 periods is often considered sufficient, whereas for very low damping, it can be necessary to wait much longer. After this waiting time, a number of periods are acquired for further processing.

In Fig. 1 a model is shown with contaminating noise on both input and output. It is well known that in the case of input noise $m(t)$ existing when using an H_1 estimator, a biased estimate will result. The H_1 estimator is

$${}^1\hat{H}_{yx}(f) = \frac{\hat{G}_{yx}(f)}{\hat{G}_{xx}(f)} \quad (1)$$

where G_{yx} and G_{xx} are the cross- and autospectral densities, respectively, between the measured input signal, $x(t)$, and the measured output signal, $y(t)$.

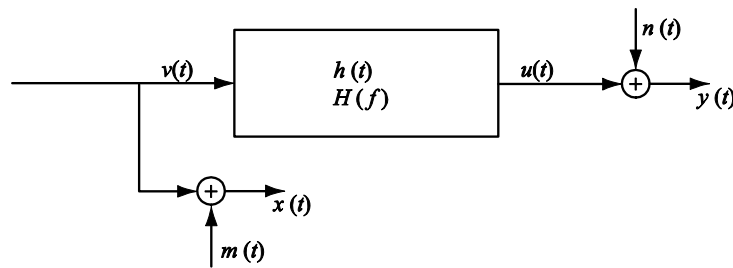


Fig 1 Illustration of linear system $H(f)$ with the input and output signals contaminated by extraneous noise.

The normalized bias error in the magnitude of ${}^1H_{yx}$, when input noise is present [1], is

$$\varepsilon_b \left[\hat{H}_{yx} \right] = -\frac{G_{mm}}{G_{vv} + G_{mm}} \quad (2)$$

where $v(t)$ is the “true” input signal going through the linear system, see Fig. 1.

The principle of time domain averaging is that we make the excitation signal periodic in the time window of the DFT. We thus let the input signal $x(t)$ be N -periodic, i.e. $x_N(t+N) = x_N(t)$, which means the measured input signal can be written as

$$x(t) = x_N(t) + m(t) \quad (3)$$

where $x_N(t)$ is the “pure” excitation signal with variance

$$\text{Var}[x_N(t)] = \sigma_{x_N}^2 \quad (4)$$

and $m(t)$ is a zero-mean random signal with variance

$$\text{Var}[m(t)] = \sigma_m^2. \quad (5)$$

Assuming K time averages are used to produce the time-averaged input signal, $x_a(t)$, the ensemble average of $x(t)$ is

$$x_a(t) = \text{E}[x(t)] = x_N(t) + \bar{m}(t) \quad (6)$$

where the variance of the average signal $\bar{m}(t)$ approaches zero at the rate $1/K$. The spectral density of x_a , G_{aa} , is then

$$G_{aa}(f) = G_{x_N x_N} + \frac{1}{K} G_{mm}. \quad (7)$$

The bias error of the FRF estimate in Eq. (2) is thus reduced by the time domain averaging using K averages to

$$\varepsilon_b \left[\hat{H}_{yx} \right] = - \frac{G_{mm}/K}{G_{yy} + G_{mm}/K} \quad (8)$$

which means that the bias error due to the input noise $m(t)$ is asymptotically eliminated by the averaging process. A similar treatment can be applied to the output signal in the case of output noise, $n(t)$, see Fig. 1.

To achieve maximum suppression of both input and output noise, all time data should be used for time domain averaging. In that case the FRF can be estimated as the simple ratio of the two spectra of the time averaged signals. We can denote this estimator ${}^t \hat{H}(f)$, or the H_t estimator, and it is computed by

$${}^t \hat{H}(f) = \frac{\hat{Y}_a}{\hat{X}_a} \quad (9)$$

where $\hat{Y}_a(f) = \text{DFT}[y_a(t)]$ and $\hat{X}_a(f) = \text{DFT}[x_a(t)]$.

When time domain averaging as proposed here is applied, the interpretation of the coherence function becomes somewhat more complicated than in the frequency domain averaging case. First of all, the coherence function has to be computed by using frequency domain averaging, on the raw data. In principle, the coherence function is a measure of the amount of contaminating noise, if we assume that the system is linear and no time delays exist. For measurements on linear mechanical systems, we can assume that around resonances and antiresonances, the dominating contaminating noise will be in the “small” signal (force signal at resonance, and response signal at antiresonance). At each of these frequencies, the coherence function then

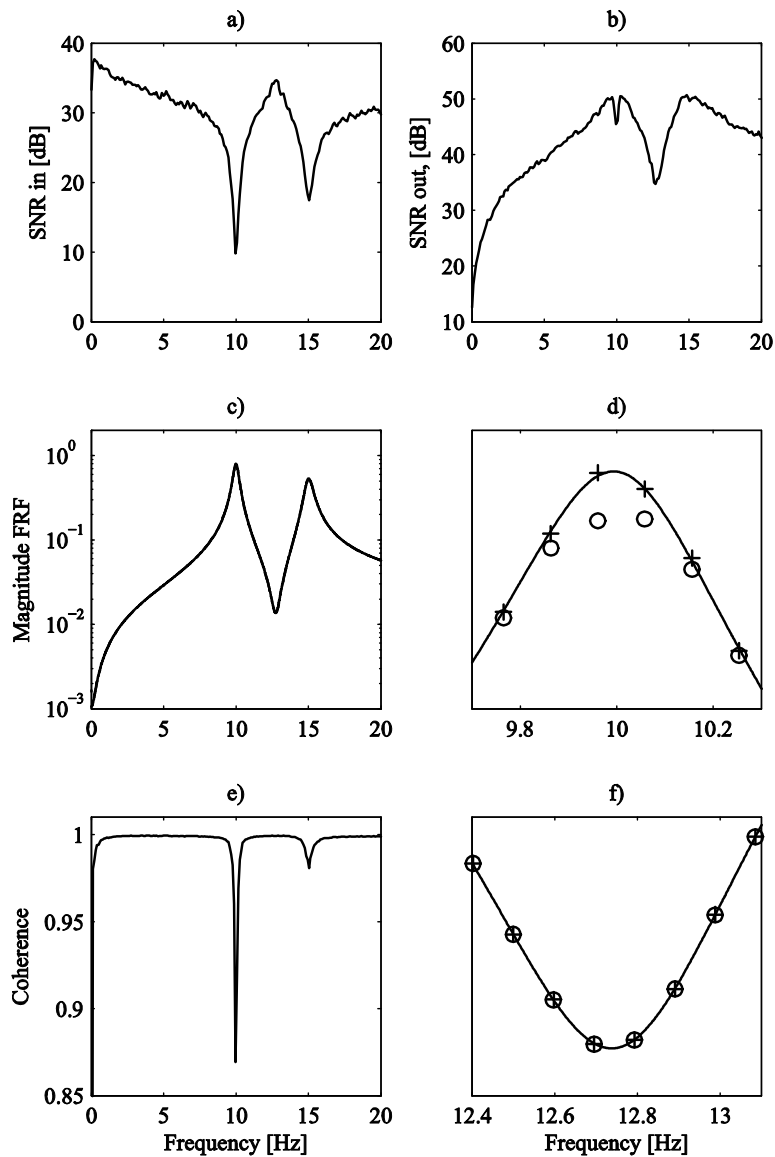


Fig. 2 Simulation results using frequency domain and time domain averaging, respectively. In a) and b) the signal-to-noise ratios of the input and output signals and the contamination noise are shown in dB scale. In c) the true FRF is overlaid by the estimates using frequency domain and time domain averaging, respectively. In d) the plot in c) is zoomed in around the first resonance, where the frequency domain estimate is plotted with rings, and time domain with plus signs overlaid on the true FRF in solid. In e) the ordinary coherence is shown and in f) a the FRF is zoomed in around the antiresonance. The latter plot shows that time domain averaging is as efficient as the H_1 estimator to remove the effect of the output noise.

is a measure of how much contaminating noise is present. The effect of the time domain averaging can then be estimated by using the following relation to compute an “efficient coherence function” estimate for the time domain averaged process

$$\hat{\gamma}_a^2(f) = \frac{K}{K-1 + \frac{1}{\hat{\gamma}_{yx}^2(f)}}. \quad (10)$$

For example, applying Eq. (10) on the coherence estimate in Fig. 2 e) which has a dip of approximately 0.87, would give an efficient coherence value of $\hat{\gamma}_a^2(10) \approx 0.999$ indicating that the bias is almost entirely eliminated. This coherence function is giving the amount of contaminating noise remaining to bias the FRF estimate. It can also be used to calculate how many averages are needed for sufficient suppression of the input noise.

MIMO ESTIMATOR

In the case of MIMO estimation, the principle of periodic excitation is more complicated because the input cross-spectral matrix needs to be invertible [7]. The so-called “periodic random” excitation signal is the most common solution to this problem. In effect, this method is based on producing independent random signals with N samples for each shaker, and repeating these signals until the system is achieving a periodic steady-state response. After this waiting time, single records of all input and output signals are acquired and auto and cross-spectra accumulated. New independent excitation signals are then produced, which are repeated until steady-state conditions occur, after which a record is acquired and spectra accumulated, etc. Theoretically, at least as many realizations of the input signals as there are shakers need to be used, but in practice many more averages have to be used to produce suppression of output noise.

For the time domain averaging procedure suggested in the present paper, a slight modification to the frequency domain approach has to be made. The difference is that for each realization of the random input signals, a number of blocks are acquired from the steady-state response. These blocks are time averaged before spectra are computed and accumulated in the standard frequency domain averaging process to produce the input cross-spectral matrix $[G_{xx}]$ and the input-output cross-spectral matrix $[G_{yx}]$. Since in this case frequency domain averages exist, the coherence (in this case, of course, multiple coherence) can be computed using standard procedures [7], although due to the few averages used, the estimate will be poorly defined.

SIMULATIONS

To illustrate the effect of time domain averaging, a 2DOF system with natural frequencies of 10 and 15 Hz and relative damping of 2 % was used. The output displacement of DOF 1 was computed by the time domain forced response technique described in [8], which can also be found in [7], and contaminating noise added to the input and output signals. To obtain a realistic case with low SNR around the resonances, the input pseudorandom noise was created with PSD approximately equal to the inverse of the frequency response and the contaminating noise with flat PSD. The SNR of the input and output signals are shown in Fig. 2 a) and b).

In the first simulation, pseudo random noise was generated and 100 averages used, after waiting 10 periods for steady state conditions. The driving point FRF in DOF 1 was computed using both “traditional” frequency domain averaging, and using the procedure described in the present paper. The results are shown in Fig. 2. As can be seen in the figure, the time domain averaging decreases the bias error around the resonance, whereas both methods work well to remove the bias at the antiresonance. Thus time domain averaging is a powerful tool to decrease bias in the FRF estimate in cases where there is poor SNR around the resonance frequencies, which sometimes happens on weak structures which are difficult to excite near the resonances.

In the second simulation, both DOFs were excited by periodic random noise. First, frequency domain periodic random was simulated with 10 idle periods followed by an acquired record, and in all 40 such records were averaged, thus comprising a total of 40 times 11 blocks of data. After this, new simulation data were generated for time domain averaging. The difference with this method is that after the idle blocks, 100 averages were acquired for each generated random block, and five such sequences were accumulated to compute the input and output cross-spectral matrices. In total, thus 110 times 5 blocks were used in the simulation. The results of this simulation are shown in Fig. 3, where the FRFs zoomed in around the first resonance and around the antiresonance are shown. As can be seen in the figure, the time domain method decreases the bias error due to the input noise at the resonance, whereas both methods perform well to suppress the effect of output noise at the antiresonance.

It should be mentioned that the large number of averages used for each realization in the MIMO case was made to obtain a low random error in the FRF estimate, to clearly see the difference in the time domain averaging based estimate compared to the frequency domain based estimate. In practice fewer averages may be able to be used if a larger random error can be tolerated. The necessary number of averages in the time domain averaging is dependent on the SNR around the resonances and antiresonances, which can be evaluated by observing the multiple coherence.

CONCLUSIONS

In this paper we have investigated the effects of suppressing contaminating noise on both the input and output signal in FRF estimation, by using periodic excitation signals and time domain averaging. It was shown that estimators for SISO as well as MIMO cases are asymptotically unbiased. A formula was also given in the SISO case for an “efficient coherence function” which is well-defined at frequencies where only one of the contaminating noise sources is present, such as around resonances and antiresonances.

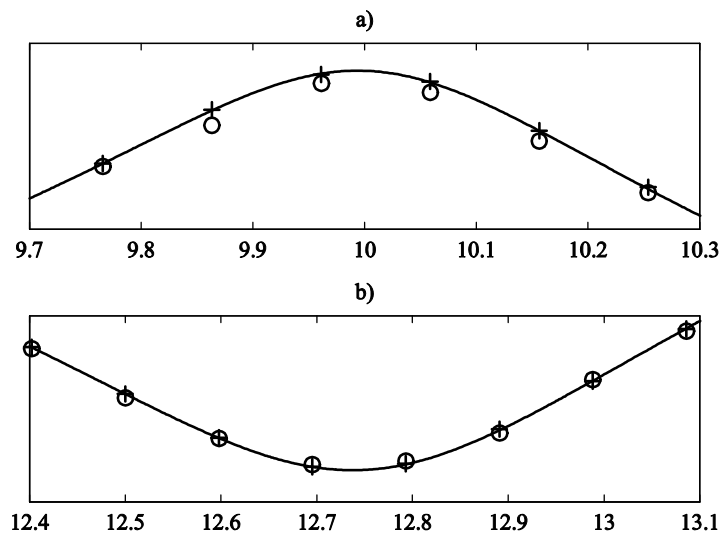


Fig. 3 FRF estimates from a simulation of a 2-input-1-output model excited by periodic random with frequency domain averaging (rings), and with time domain averaging (plus signs). In solid, the true FRF is shown. The FRF is zoomed in around the resonance in a) and around the antiresonance in b), similar to Fig. 2 d) and f). See text for details.

REFERENCES

- [1] Bendat, J. & Piersol, A. G. *Random Data: Analysis and Measurement Procedures* Wiley Interscience, 2010.
- [2] Wicks, A. & Vold, H. The H_s Frequency Response Estimator. Proc. 4th International Modal Analysis Conference, Los Angeles, CA, 1986.
- [3] Rocklin, G. T.; Crowley, J. & Vold, H. A Comparison of H_1 , H_2 , and H_v Frequency Response Functions. Proc. 3rd International Modal Analysis Conference, Orlando, FL, 1985.
- [4] White, P. R.; Tan, M. H. & Hammond, J. K. Analysis of the maximum likelihood, total least squares and principal component approaches for frequency response function estimation. *Journal of Sound and Vibration*, 290, pp. 676-689, 2006.
- [5] Antoni, J.; Wagstaff, P. & Henrio, J. C. H_α – A consistent estimator for frequency response functions with input and output noise. *IEEE Transactions On Instrumentation And Measurement*, 53, pp. 457-465, 2004.

- [6] Phillips, A. W. & Allemang, R. J. An overview of MIMO-FRF excitation/averaging/processing techniques *Journal of Sound and Vibration*, 262, pp. 651-675, 2003.
- [7] Brandt, A. *Noise and Vibration analysis: Signal Analysis and Measurement Procedures*, Wiley, 2011.
- [8] Ahlin, K.; Magnevall, M. & Josefsson, A. Simulation of forced response in linear and nonlinear mechanical systems using digital filters. Proc. ISMA2006, International Conference on Noise and Vibration Engineering, Catholic University, Leuven, Belgium, 2006.

Vibration Control Using the Non-Model Based Algorithm

Huinam Rhee

Professor, Sunchon National University, 150 Maegok-dong Sunchon Chonnam 540-742 S. Korea

Gil Hamm, Gee Hee Kim, Sang Jin Park, Sang Yoon Lee

Graduate and Undergraduate students, Sunchon National University, 150 Maegok-dong Sunchon Chonnam 540-742 S. Korea

ABSTRACT

A study on the vibration control of a steel beam and plate using electromagnetic actuator has been performed. The system is assumed time-varying so that the system model is considered unknown, therefore the mathematical model of the control structure is not used in the control algorithm. The algorithm only needs the vibration displacement data in real-time. The control algorithm is based on PID with an adaptive function to the change of dynamic characteristics of the structure. The vibration suppression or excitation was successfully achieved by using a test setup including a cantilever beam, a laser displacement sensor, electromagnet and microcomputer loaded with the developed control program.

1. Introduction

This paper deals with the active vibration control of a cantilever beam structure using electromagnetic force. Active vibration control is the active application of force in an equal and opposite manner to the forces imposed by external vibration. With this application, a precision industrial process can be maintained on a platform essentially vibration-free. Over many years numerous studies [1] have been performed for this kind of subjects. Most of the previous studies for the vibration control of mechanical structures are based on the mathematical models of the system. However, in many cases especially in the industrial field rather than a laboratory, the mathematical model of the vibrating structure is hard to obtain. Even though the model is once known, it may be varying with time as the machine is being aged, therefore, its natural frequencies and mode shapes do not remain the same which the model is based on. Although many great ideas for this situation such as robust control algorithms [2] with complicated mathematical procedures have been developed, this paper introduces a very simple method to suppress or amplify the vibration level, which reads the vibration displacement data in real-time and then generates out-of-phase signals to activate electromagnets.

2. Vibration Control of a Cantilever Beam

Fig. 1 shows the experimental set-up which is consisted of a cantilever, laser displacement sensor, electromagnet and the microcomputer loaded with the control program. The length of the beam can be varied. The mass property of the beam can

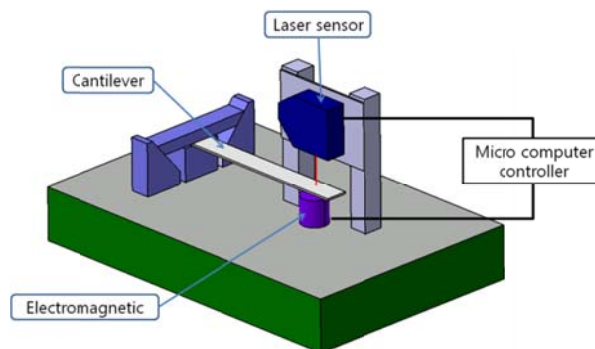
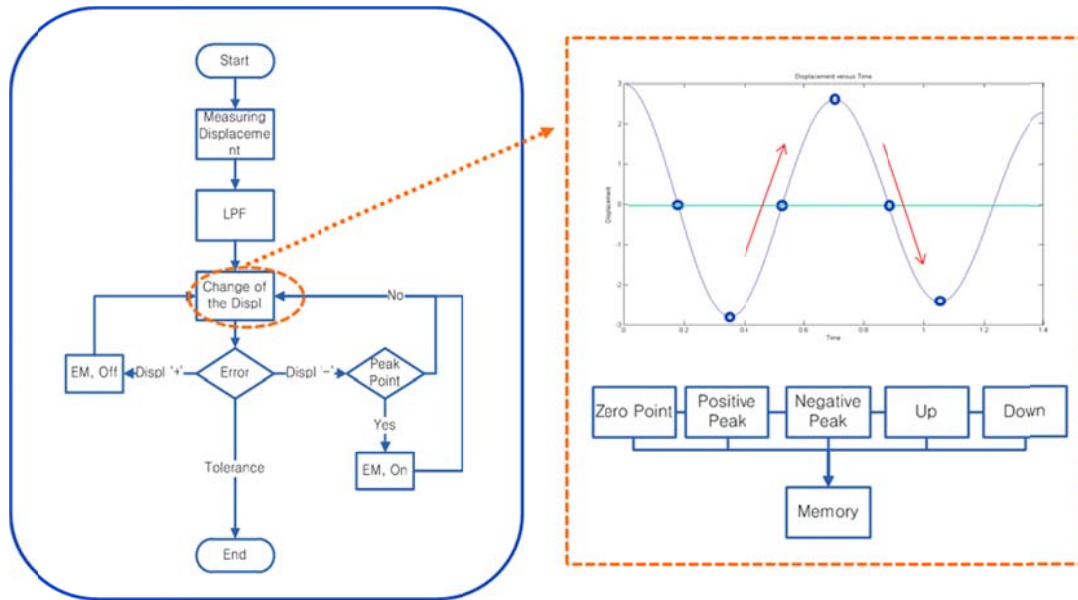
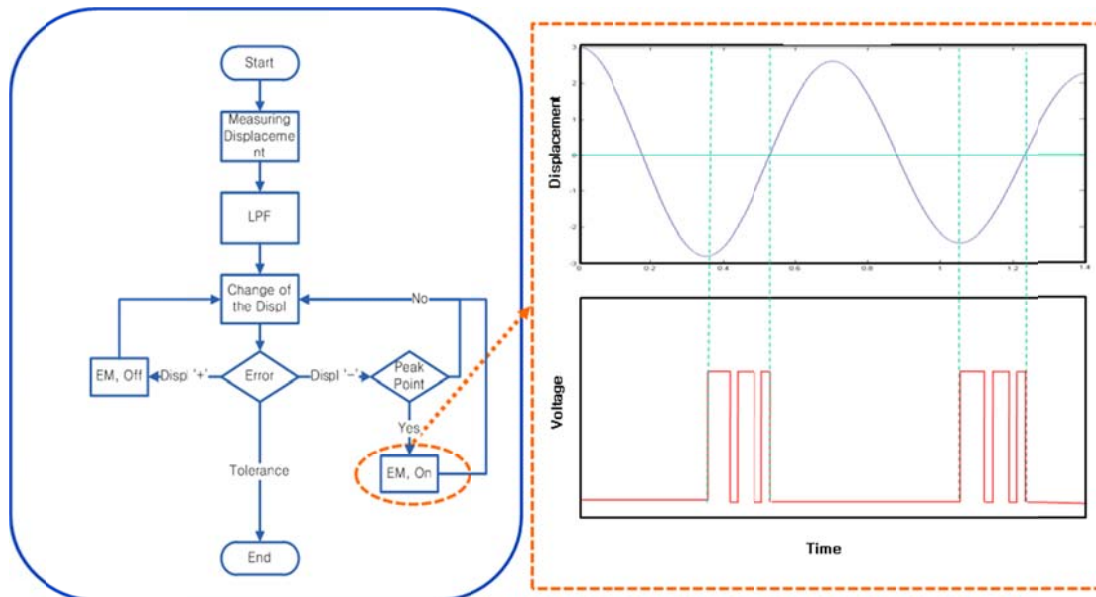


Fig. 1 Experimental Test Set-up

also be modified by adding some additional masses, e.g., by attaching magnets so that the dynamic characteristics of the beam be varied. The laser sensor measures the displacement at a point of the beam and on the other side an electromagnet is placed to suppress or amplify the vibration level of the beam in real-time.



(a) Determination of the position and the velocity of the beam



(b) Electromagnet driving PWM signals

Fig. 2 Overview of the Control Procedure

While the displacement data is measured and stored in the memory of the microcomputer the control program determines which of the following categories the present status is : equilibrium (zero) point, positive peak, negative peak, going up or down as shown in Fig. 2(a). Then the pulse width modulation signals are appropriately generated to control the vibration level using the proportional-integral-derivative control concept. That is, the electromagnet is actuated while the beam is going away from the magnet to suppress the vibration. On the other hand the electromagnet is actuated while the beam is approaching the magnet to activate the vibration.

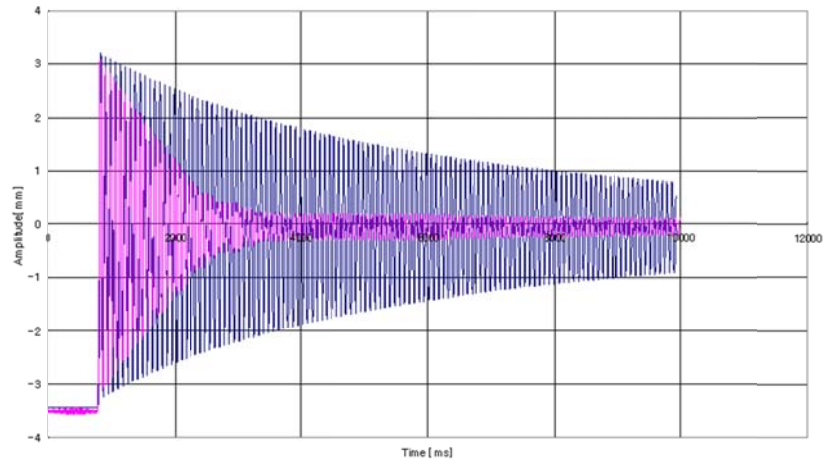


Fig. 3 Vibration suppression

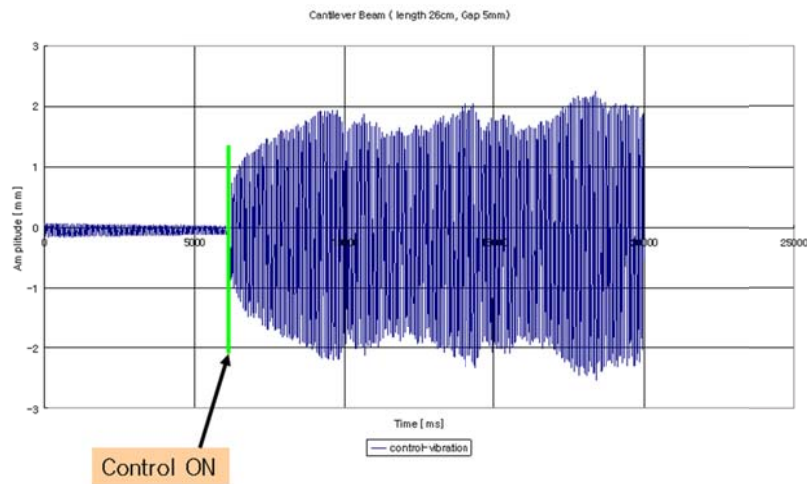


Fig. 4 Vibration activation

Figs. 3 and 4 show the experimental results of the free vibration suppression and amplification, respectively. The advantage of the present method is that the vibration control can be achieved even when the dynamic characteristics of the beam is varied relatively a lot. The range of the allowable variation depends on the detailed design of the control system such as the performance of the microcomputer, and other auxiliary electronic parts and circuits designs. In order to verify this feature,

in Fig. 5 the control program was made targeting the beam having 15 Hz first mode natural frequency and verified that the vibration is suppressed satisfactorily. Then the same control program without any parameter or gain modification was applied to the 12 Hz and 18 Hz systems. Right column of Fig. 5 shows that the control performance is not affected much by the variation of the system natural frequency. On the contrary the conventional PID control algorithm was revealed to be unstable as the natural frequency deviation increased as shown in the left column of Fig. 5. The proposed method was successfully applied even for 37 Hz system in Fig. 6 while the conventional algorithm was very unstable.

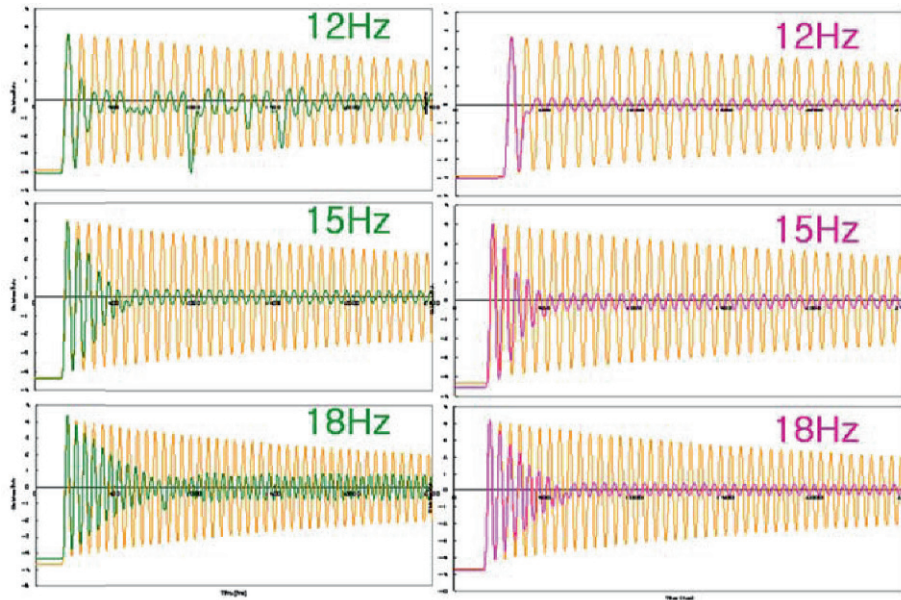


Fig. 5 Comparison of vibration control between the conventional (left column) and the proposed method (right column)

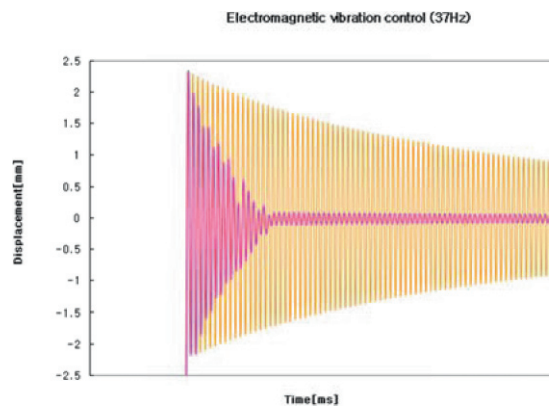


Fig. 6 Control Performance for Large Variation of the Beam Dynamic Characteristics

3. Conclusions

In this study a simple algorithm to control the vibration of a beam structure using electromagnetic force has been introduced. The proposed method uses the real-time vibration displacement data and does not require the mathematical model of the structure, therefore, it shows robust performance against a fairly large variation of the target structure. The proposed method was applied for the free vibration suppression or the amplification of the vibration of a variable cantilever beam, but the method can be extended for the suppression of the vibration due to the intermittent impact forces and/or continuous driving forces.

References

- [1] Ver , Istan L. and Beranek, L. L. , “Noise and Vibration Control Engineering: Principles and Applications”, 2nd ed., John Wiley & Sons, 2006.
- [2] Dellured, G.E. and Paganini, F., “A Course in Robust Control Theory: A Convex Approach”, Springer, 2010.

Active Suspension Systems for Passenger Cars: Operational Modal Analysis as a Tool for the Performance Assessment

Leonardo Soria^{1,a}, Arnaldo delli Carri^{2,b}, Bart Peeters^{3,c}, Jan Anthonis^{3,d} and
Herman Van der Auweraer^{3,e}

¹Politecnico di Bari, Viale Japigia, 182, 70126 Bari, Italy

²Università degli Studi di Brescia, Via Branze, 38, 25123 Brescia, Italy

³LMS International, Interleuvenlaan 68, B-3001 Leuven, Belgium

^asoria@poliba.it, ^barnaldo.dellicarri@unibs.it, ^cbart.peeters@lmsintl.com,
^djan.anthonis@lmsintl.com, ^eherman.vanderauweraer@lmsintl.com

ABSTRACT

Comfort, road holding and safety of passenger cars are mainly influenced by an appropriate design of suspension systems. Improvements of the dynamic behaviour can be achieved by implementing semi-active or active suspension systems. In these cases, the correct design of a well-performing suspension control strategy is fundamental for obtaining satisfying results.

In-Operation Modal Analysis allows the experimental structural identification in real operating conditions: moving from output-only data, leading to modal models linearised around the more interesting working points and, in the case of controlled systems, providing the needed information for the optimal design and verification of the controller performance. All these characters are needed for the experimental assessment of vehicle suspension systems.

In the paper, two suspension architectures are considered equipping the same car type. The former is a semi-active commercial system, the latter a novel prototypic active system. For the assessment of suspension performance, two different kind of tests have been considered, proving ground tests on different road profiles and laboratory four poster rig tests.

By OMA-processing the signals acquired in the different testing conditions and by comparing the results, it is shown how this tool can be effectively utilised to verify the operation and the performance of those systems, by only carrying out a simple, cost-effective road test.

1 INTRODUCTION

Passenger car comfort, road holding, handling and safety are strongly related to an appropriate design of suspensions. In particular, once the sprung body is given, the correct choice of damping values is related to the spring stiffness ones. Improvements of the dynamic behaviour of the whole system can be achieved by implementing semi-active or active suspension systems instead of the simply passive ones, commonly utilised. In these cases, the correct design of a well performing suspension control strategy is of fundamental importance for obtaining satisfying results, and, in the case of active systems, also from energy consumption point of view. The not so high overall efficiency of active systems still remains, indeed, one of their main drawbacks.

Operational or Output-only Modal Analysis [1-4] allows the experimental identification of structural dynamics models in the real operating conditions. The strength is that, frequently, (i) only the response data are measurable and not the actual loadings. Hence, the system identification has to be based on output-only data. More over, since all the real systems are to a certain extent non-linear and often also subjected to non-linear constraining conditions, (ii) the modal models obtained under real loadings give a picture of the system, once linearised around the more interesting and representative working points. In the case of control systems, at last, (iii) the identification of the real in-operation behaviour is essential in the areas of the optimal design and verification of the controller performance.

All these characters are needed for the experimental assessment of an active suspension system equipping a passenger car. In this paper two Ford S-MAX, two instances of the same type of vehicle, equipped with two different suspension architectures are considered. The former is a commercial vehicle equipped with a sky-hook semi-active suspension system having three different parameter arrangements that the driver is able to select, actually modifying the amount of damping in the system: A normal one which is useful in the most common situations and two other ones corresponding the first to a more comfortable

behaviour and the second to a stiffer one. These settings are generally referred to as normal, comfort and sport. The latter is a prototypic vehicle, equipped with a novel sky-hook active suspension system, designed in the framework of a specific research project [15] and implemented on the vehicle by removing some components and replacing others, in a word modifying the mass, but also the stiffness distribution of the car, besides the damping one. The suspension behaviour is effectively governed by a controller which logic depends on several parameters as the car body heave, pitch and roll velocities and the wheel-body relative velocities. The car speed and the steering wheel angular position and velocity are other parameters that the control strategy can be influenced by, during operation.

On these two cars, two different in-operation type of tests have been performed, (i) proving ground tests on two different road profiles, running at different car speeds and (ii) laboratory tests performed by using a four poster test rig. A four poster test rig basically consists of four actuators, one for each wheel, able to reproduce a running condition on a certain road profile on a car that actually stands still on them at null speed. On the test rig, the excitation signals sent to the four shakers have been firstly the ones needed to simulate the same roughness profiles considered in the road test campaigns. Secondly four uncorrelated random signals have been utilised, to have a useful reference condition in which the basic OMA assumption was verified.

By OMA-processing the acquired signals in the different testing conditions and by comparing the obtained results, it is shown in what follows how this tool can be effectively utilised to verify the operation and the performance of the two suspension systems. OMA, indeed, becomes a useful designing tool in this field, since it can be utilised to check the actual behaviour of a prototype at an intermediate or final stage of its optimisation.

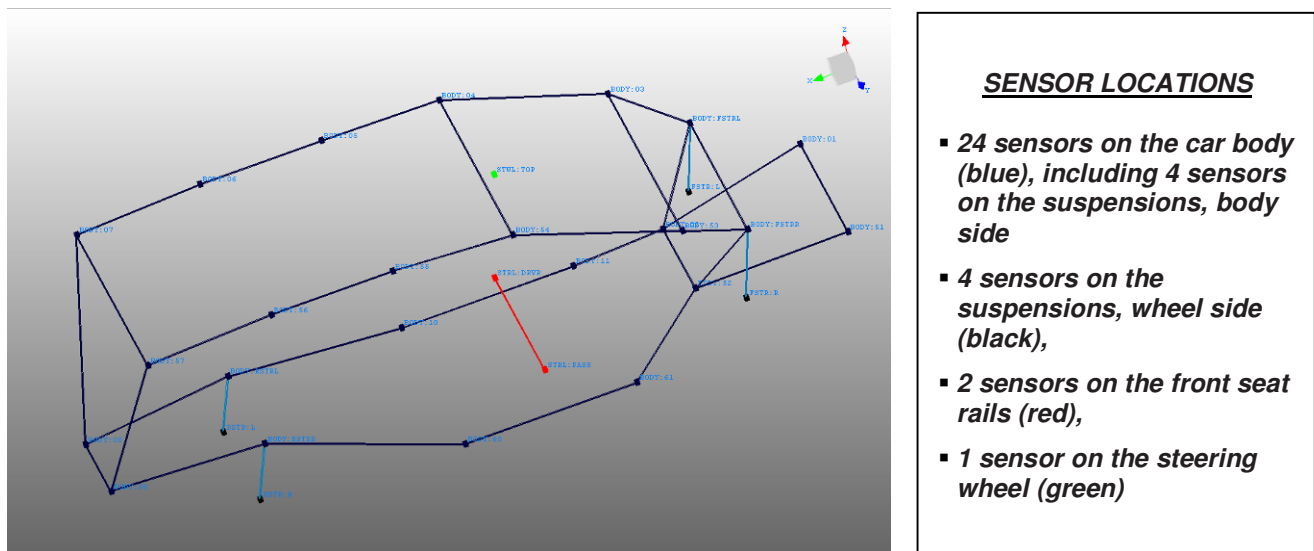


Fig.1 The geometry of the analysed system with the sensor locations represented

2 TEST CAMPAIGN DESCRIPTION

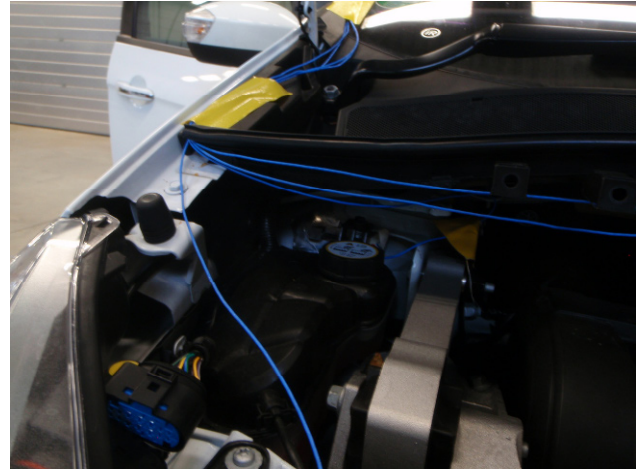
For both the cars considered, the semi-active suspension equipped car and the active suspension equipped one, four poster and proving ground tests have been performed, as anticipated. The test campaign on each car lasted about three days. Two different road profiles have been considered for both the test typologies, namely (i) the Blue-kay track and (ii) the Florida one. The car velocity on the former profile was 60 km/h, on the latter 80 km/h. In the case of four poster tests, also random excitation has been considered, as said. In this case four uncorrelated white sequences have been sent to the four hydraulic actuators. Different maximum amplitudes, in terms of shaker displacement have been considered, in particular 1, 3, 5 mm in the frequency range from 0 to 30 Hz and 10 mm in that from 0 to 15 Hz.

The complete accelerometer layout consisted of 31 sensor locations. In each location the three components of the point acceleration have been measured, by using tri-axial piezoelectric ICP accelerometers. The output signals have been acquired and recorded by using LMS SCADAS front-ends, connected in master-slave configuration to achieve the needed number of channels and to a laptop PC, running the LMS Test.Lab analysis suite.

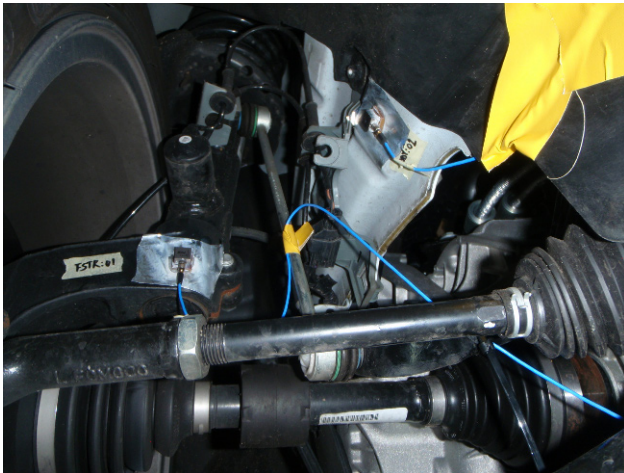
In Fig.1, the geometry of the sensor layout is reported. The different colours identify the sensors placed on (i) the car body (containing also that on the suspension dampers, body side), (ii) the suspension dampers, wheel side, (iii) the front (driver and passenger) seat rails and (iv) the steering wheel. In Fig.2, several images of the tests campaign performed on one of the two cars are reported, showing the acquisition set-up. In particular some of the sensor locations listed above are depicted and the two front-ends utilised.



(a)



(b)



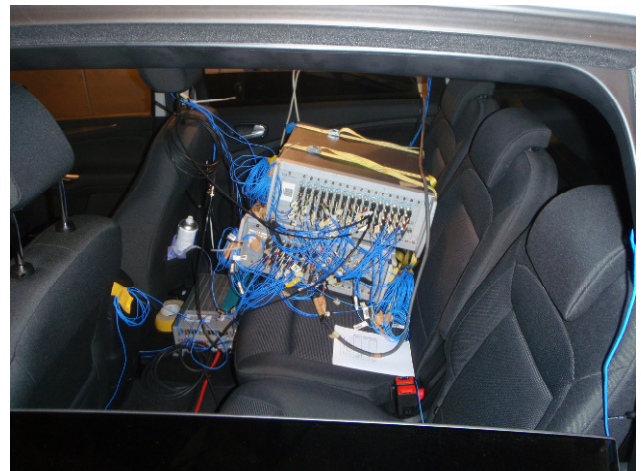
(c)



(d)



(e)



(f)

Fig.2 The acquisition set-up, (i) some sensor locations: On the car body (a), on the front-right suspension, body side (b), on the front-left suspension, wheel side (c), on the rear-right suspension, wheel side (d) and on the driver seat rail (e), and (ii) the two LMS SCADAS 316 front-ends employed in master-slave configuration (f)

3 VEHICLE OMA: THEORETICAL BACKGROUND

3.1 The road profile roughness excitation

It is well known that the power spectral density (PSD) of the roughness of a road profile as a function of the spatial frequency, the wavenumber k , has the general decreasing behaviour reported in Fig.3a. In particular, in the figure one can actually see the trend of several possible analytical approximations of the PSD function, basically obtained by fitting the experimental data, that have been proposed and can be found in the technical literature. Those analytical expressions are reported in Fig.3b [5,6].

Since the wavenumber k is the inverse of the wavelength λ , the time frequency $f = uk$, where u is the car velocity.

In Figures 4a and 4b the PSDs of the two road roughness profiles, Blue-kay and Florida, considered in the road tests are shown as functions of the time frequency f .

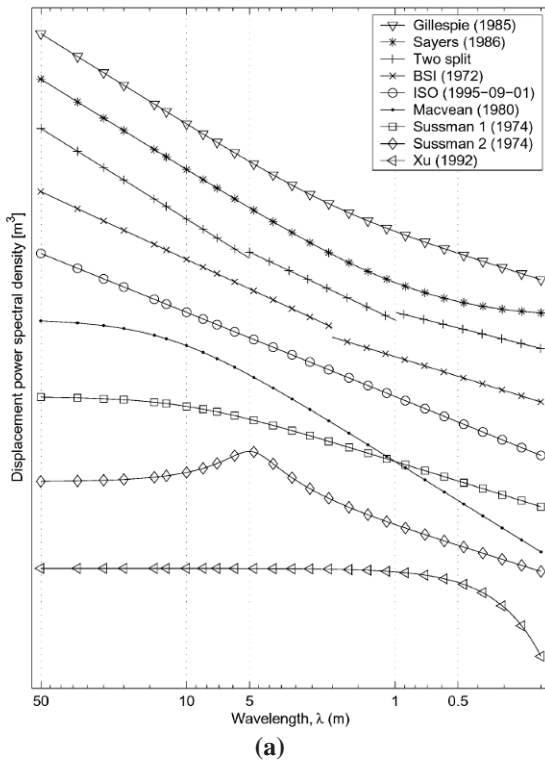
Simple calculations lead to the conclusion that the wavelength range from 100 to 1 m, corresponds to a time frequency range from 0.2 to 20 Hz, which is that normally considered in vehicle dynamics for comfort, safety and road holding analyses and that is usually referred to as *ride* [7].

As it is possible to see, it is actually the range in which the PSD function of a road profile decreases. For time frequencies smaller than 0.2 Hz and, hence, for wavelengths higher than 100 m the PSD function is quite flat.

From these considerations one can conclude that the road input excitation, on each wheel, is not actually a white noise sequence, as requested to be the basic OMA assumption strictly respected, but something more similar to a *Brownian* or *red* noise, whose PSD is inversely proportional to f^2 . This is still a suitable type of excitation for OMA, since it does not contain peaks in the spectrum that could lead to extra-peaks in the output responses, not related to structural modes.

What needs to be more over said is that the input excitation on the front wheels is in a certain way correlated with that on the rear wheels, as a correlation could also exist between inputs belonging to the two different sides of the vehicle. This means that the input power spectral density matrix will have some of the off-diagonal terms not null.

Even this second violation of the basic OMA assumption is considered weak in this paper. Aim of the analysis reported in the following sections is, indeed, to show that although the overall input excitation does not strictly respect the basic OMA hypotheses, it is still possible to obtain reliable modal models by processing the raw time output data recorded during a simple, cost-effective road test, with a classical operational modal parameter estimation algorithm.



| Name | PSD approximation | Wavenumber |
|----------------------------|---|--|
| ISO (1995-09-01) | $G_d(n) = Cn^{-w}$ | $0 \leq n \leq \infty$ |
| BSI (1972) | $G_d(n) = \begin{cases} Cn^{-w_1} & 0 \leq n \leq n_0 \\ Cn^{-w_2} & n_0 \leq n \leq \infty \end{cases}$ | $0 \leq n \leq n_0$ $n_0 \leq n \leq \infty$ |
| Two Split | $G_d(n) = \begin{cases} Cn^{-w_1} & 0 \leq n \leq n_1 \\ Cn^{-w_2} & n_1 \leq n \leq n_2 \\ Cn^{-w_3} & n_2 \leq n \leq \infty \end{cases}$ | $0 \leq n \leq n_1$ $n_1 \leq n \leq n_2$ $n_2 \leq n \leq \infty$ |
| Sayers (1986) | $G_d(n) = C_1/n^4 + C_2/n^2 + C_3$ | $0 \leq n \leq \infty$ |
| Gillespie (1985) | $G_d(n) = C(1 + (0.066/n)^2)/n^2$ | $0 \leq n \leq \infty$ |
| Marcondes et al. (1991) | $G_d(n) = \begin{cases} C_1 \exp(-kn^p) & 0 \leq n \leq n_0 \\ C_2(n - n_0)^q & n_0 \leq n \leq \infty \end{cases}$ | $0 \leq n \leq n_0$ $n_0 \leq n \leq \infty$ |
| Sussman (1974) | $G_d(n) = \frac{C}{\alpha^2 + n^2}$ | $0 \leq n \leq \infty$ |
| Macvean (1980) | $G_d(n) = \frac{C}{(\alpha^2 + n^2)^2}$ | $0 \leq n \leq \infty$ |
| Sussman (1974) | $G_d(n) = \frac{C(n^2 + \alpha^2 + \beta^2)}{(n^2 + \alpha^2 + \beta^2)^2 + 4n^2\alpha^2}$ | $0 \leq n \leq \infty$ |
| Xu et al. (1992) | $G_d(n) = A/2a \exp(-n^2/(2a^2))$ | $0 \leq n \leq \infty$ |
| Kozin and Bogdanoff (1961) | $G_d(n) = A/a \exp(-n^2/a^2)$ | $0 \leq n \leq \infty$ |

Note: $C, C_1, C_2, C_3, p, k, q, \alpha$ and β are real positive constants

Fig.3 General behaviour of the road profile roughness PSD approximations (a) and their analytical expressions (b) (adapted from [5])

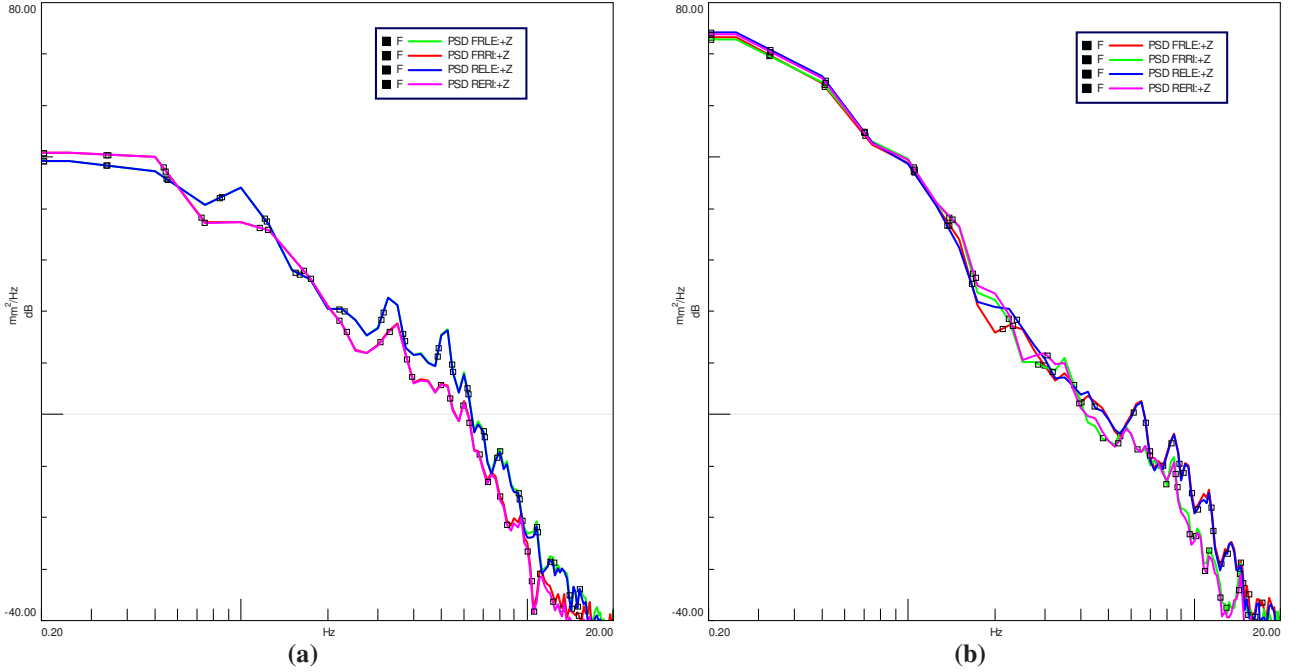


Fig.4 The road profile roughness PSD of (a) the Blue-key track (60 km/h) and of (b) the Florida track (80 km/h)

3.2 Pre-processing of the operational data

In [Fig.5a](#) the vertical acceleration response signal at the driver seat rail location is shown in the time domain. Since most of the modal parameter estimation methods do not directly use the raw acceleration measurements, but rely on reduced data such as cross-correlations and cross-spectra between signals measured simultaneously at different locations, the correlation or covariance matrix $R_i \in \mathbb{R}^{l \times l}$ between the measured output signals $y_m \in \mathbb{R}^l$, with l the number of outputs and m the sample index, has to be firstly estimated as

$$R_i = \frac{1}{N} \sum_{m=0}^{N-1} y_{m+i} y_m^T \quad (1)$$

where N is the total number of samples and i the correlation sample index (also called time lag). A typical cross-correlation sequence is shown in [Fig.5b](#). The fact that the correlations of a structure excited by white noise are similar to impulse responses is the basis for correlation-driven Stochastic Subspace Identification [8].

Frequency-domain methods require cross-spectra as primary data. As non-parametric spectrum estimate, the so-called weighted correlogram can be used. It is computed as the DFT of the weighted estimated correlation matrix (1):

$$S_{yy}(j\omega) = \sum_{m=-L}^L w_m R_m e^{-j\omega m \Delta t} \quad (2)$$

where L is the maximum number of time lags at which the correlations are estimated and w_m denotes the time window. This number is typically much smaller than the number of data samples to avoid the greater statistical variance associated with the higher lags of the correlation estimates. As the correlation samples at negative time lags ($m < 0$) contain redundant information, it suffices to consider only the positive time lags when computing the spectra. This lead to so-called half spectra of which even the auto spectra have a phase different from zero:

$$S_{yy}^+(j\omega) = \frac{w_0 R_0}{2} + \sum_{m=1}^L w_m R_m e^{-j\omega m \Delta t} \quad (3)$$

A more traditional non-parametric spectrum estimate is the so-called weighted averaged periodogram (also known as modified Welch's periodogram). The advantage of the described correlogram approach (3) is that the use of a Hanning window can be avoided. A Hanning window introduces a bias on the damping estimates. Instead, just like in impact testing, an exponential window can be applied to the correlation functions before computing the DFT.

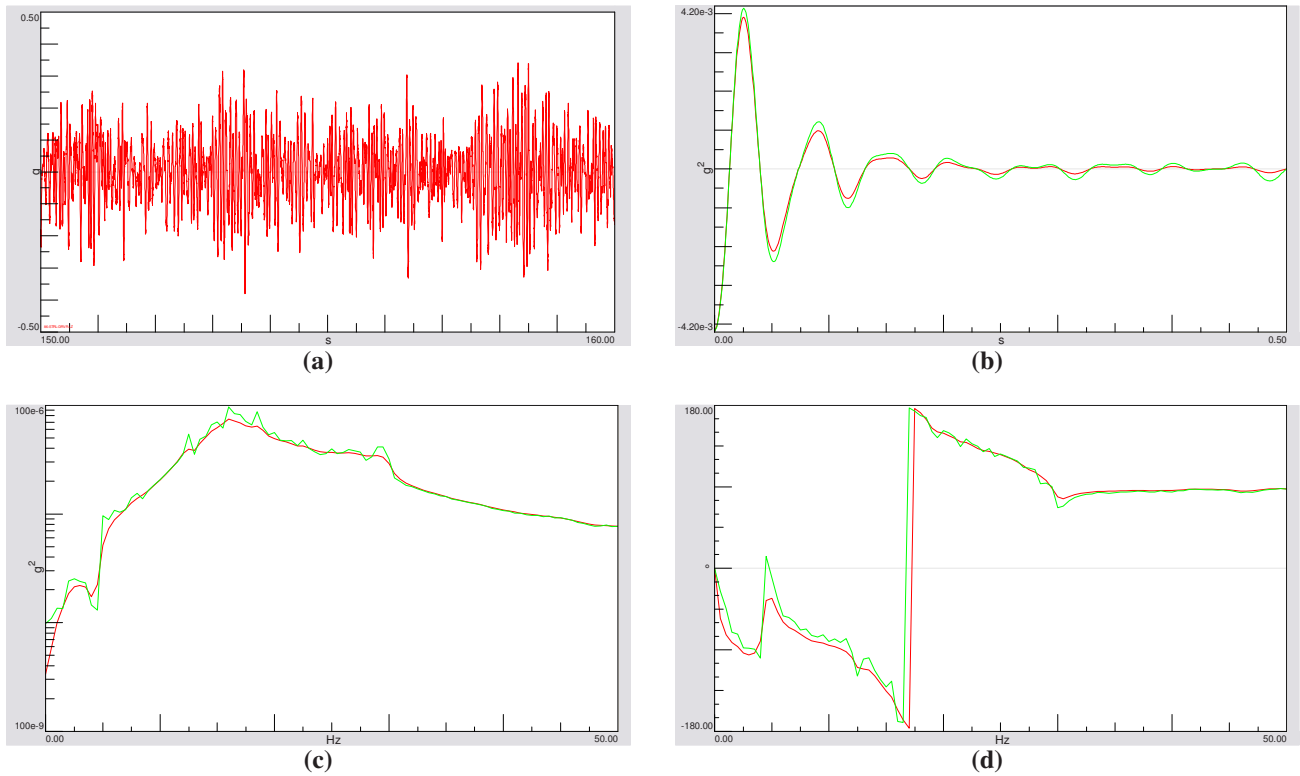


Fig.5 A time record (a), (b) a typical cross-correlation function (in green the unwinded one), calculated with respect to a certain reference output signal with its cross-power spectrum, amplitude (c) and phase (d)

An exponential window reduces the effect of leakage and the influence of the higher time lags, which have a larger variance. Moreover, the application of an exponential window to correlations is compatible with the modal model and the pole estimates can be corrected.

A thorough discussion and a comparison between the correlogram and periodogram estimates can be found in [9-10].

The weighted correlogram approach to estimate half spectra is illustrated in Fig.5. An exponential window of 10% has been used and its effect on the correlation (Fig.5b) and spectrum (Figures 5c and 5d) data is clearly visible.

3.3 Operational modal parameter estimation

It can be shown that the $l \times l$ half spectrum matrix can be modally decomposed as [9,10]

$$S_{yy}^+(j\omega) = \sum_{i=1}^n \frac{\{v_i\}\langle g_i \rangle}{j\omega - \lambda_i} + \frac{\{v_i^*\}\langle g_i^* \rangle}{j\omega - \lambda_i^*} \quad (4)$$

where n is the number of modes, $\{v_i\} \in \mathbb{C}^l$ are the mode shapes, $\langle g_i \rangle \in \mathbb{C}^l$ are the so-called operational reference factors, which replace the modal participation factors in the case of output-only data and λ_i are the poles, occurring in complex-conjugated pairs and related to the eigenfrequencies ω_i and damping ratios ξ_i by the relation

$$\lambda_i, \lambda_i^* = -\xi_i \omega_i \pm j \omega_i \sqrt{1 - \xi_i^2} . \quad (5)$$

By using an operational modal identification technique, as the recalled output-only data version of the Stochastic Subspace Identification in the time or frequency domain [11] or of the Polyreference Least Square Complex Exponential in the time domain or PolyMAX (Polyreference Least Square Complex Frequency Domain) in the frequency domain [12,13], it is possible to build up a stabilization diagram (Fig.6a), assuming subsequently an increasing number of poles.

The stabilization diagram gives a strong indication of the number of present physical modes and allows the selection of the best estimates for physical poles and, hence, for eigenfrequencies and damping ratios and for the said operational reference factors.

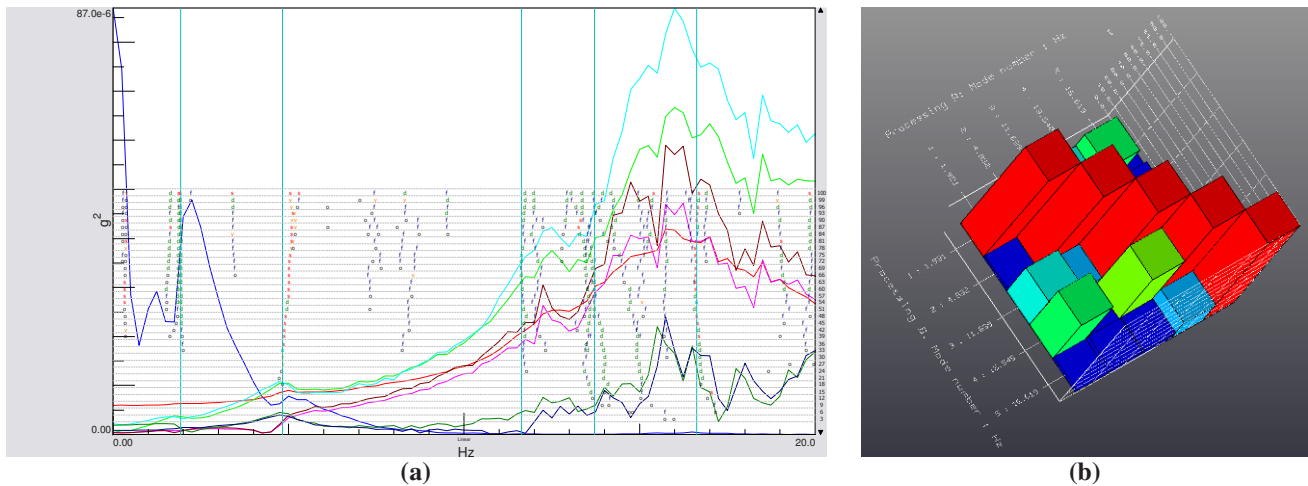


Fig.6 An example of stabilization diagram (a), obtained by using the LMS operational PolyMAX algorithm, and of the Modal Assurance Criterion applied to the corresponding set of modes (b)

The interpretation of the stabilization diagram yields a set of poles and corresponding operational reference factors. The mode shapes can then be found from

$$S_{yy}^+(j\omega) = \frac{LR}{j\omega} + \sum_{i=1}^n \frac{\{v_i\}\langle g_i \rangle}{j\omega - \lambda_i} + \frac{\{v_i^*\}\langle g_i^* \rangle}{j\omega - \lambda_i^*} + j\omega UR \quad (6)$$

in which all the present terms are now $l \times m$ matrices, with m the number of outputs selected as references and, in particular, LR, UR, respectively the lower and upper residuals, have been introduced to model the influence of the out-of-band modes in the considered frequency range [14].

A validation phase has then to follow, of course, to evaluate the quality of the estimated modal model, by using tools as the Modal Assurance Criterion (Fig.6b).

4 ANALYSIS OF THE RESULTS

In the *ride* time frequency range from 0.2 to 20 Hz, recalled above, it is possible to identify a first sub-range, up to 3 Hz, where the heave, pitch and roll modes have to be found. It is well known that those modes and their eigenfrequencies are mainly related to the stiffness of suspension elastic elements and to the car body geometry and mass distribution. The damping ratios depend of course on damper coefficients.

In the following sections, hence, the suspension operation will be analysed by OMA-estimating the modal parameters in the said 0 to 3 Hz frequency range. OMA leads, of course, also to the identification of higher-frequency deformation modes, that, for simplicity, are not considered and discussed in this paper.

It is useful to stress from the beginning that during the random tests performed on the four poster test rig, not enough energy was delivered in the frequency range of interest (0 to 3 Hz) with the result that the said searched modes were not excited enough. In Fig. 7, for both the considered vehicles, a comparison is proposed of the auto-power spectrum of the vertical output signal at the driver seat rail location, during the different four poster tests. As one can clearly see the curves related to random excitation achieve lower values at the lower frequencies. In the case of road input, instead, the lower is the frequency, the higher is the energy delivered in the band of interest and, consequently, the better excited are the lower modes. More over, the higher is the car velocity, the higher is the excitation level, of course.

4.1 The semi-active suspension equipped car

In this section the results obtained in the case of the vehicle equipped with the commercial semi-active suspension system are reported. In Tab.1 are, in particular, collected the modal parameters estimated by OMA-processing the data acquired and recorded during the four poster tests performed on this car. As it is possible to see, besides what anticipated regarding random excitation, the results got in the case of the two tracks, reproduced on the test rig, are in good agreement, as also confirmed by the modal validation reported in Fig.8. The modes identified in the case of the Florida track are represented in Fig. 9.

In tab.2 are, then, collected the modal parameters estimated by OMA-processing the data coming from the proving ground tests, performed on the same car.

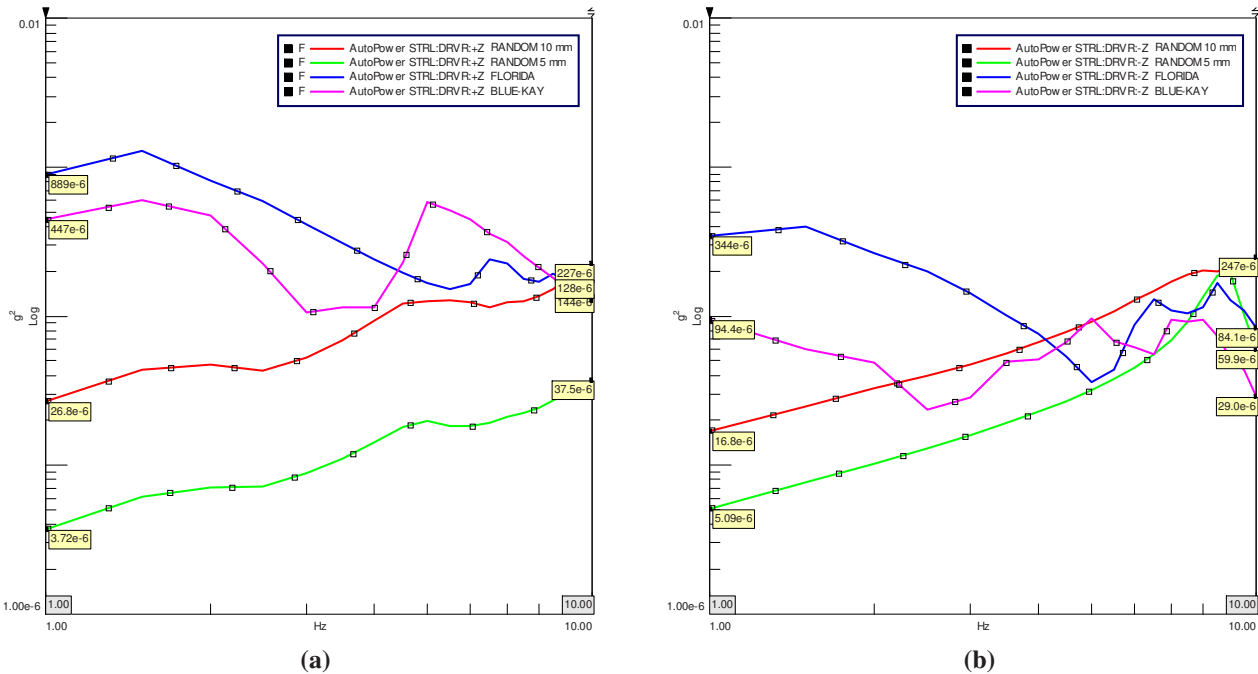


Fig.7 Comparison of the driver seat rail output auto-power spectrum in the four poster test cases reported in the legend and for (a) the semi-active suspension equipped car and (b) the active suspension equipped one

Again a good agreement has been reached, not only between proving ground tests performed on the two different roads, as shown in Fig.10a, but also between proving ground and four poster tests, as shown in Figures 10b and 10c. In all the cases there are small discrepancies between the eigenfrequencies, with quite well correlated modes. Higher discrepancies are achieved on damping ratios, even because dissipation is more difficult to be estimated.

| 4P mode | Eigenfrequency [Hz] | | | Damping ratio [%] | | |
|-------------------------|---------------------|----------|---------|-------------------|----------|---------|
| | 5 mm random | Blue-kay | Florida | 5 mm random | Blue-kay | Florida |
| 1 st (heave) | - | 1.10 | 1.27 | - | 13.42 | 13.73 |
| 2 nd (roll) | 1.86 | 1.58 | 1.80 | 14.83 | 7.86 | 7.45 |
| 3 rd (pitch) | - | 2.30 | 2.14 | - | 10.68 | 17.40 |

Tab.1 Semi-active suspension equipped car: Comparison of the modal parameters estimated in different four poster tests (random excitation proved to be not reliable in the frequency range from 0 to 3 Hz)

| PG mode | Eigenfrequency [Hz] | | Damping ratio [%] | |
|-------------------------|---------------------|---------|-------------------|---------|
| | Blue-kay | Florida | Blue-kay | Florida |
| 1 st (heave) | 1.08 | 1.19 | 7.05 | 15.52 |
| 2 nd (roll) | 1.46 | 1.55 | 14.92 | 19.67 |
| 3 rd (pitch) | 1.77 | 2.19 | 9.07 | 12.82 |

Tab.2 Semi-active suspension equipped car: Comparison of the modal parameters estimated in different proving ground tests

4.2 The active suspension equipped car

In the case of the vehicle equipped with the novel, prototypic suspension system, higher damping values are expected, due to the active operation and performance of the system itself.

As it is possible to see from the recalled comparison proposed in Fig.7, indeed, in the case of this second vehicle, the active system operation reduces the output energy levels in the frequency range of interest (0 to 3 Hz) for all the tests performed. As a consequence it becomes more difficult to extract the information from corresponding sets of data, with respect to the semi-active system equipped car.

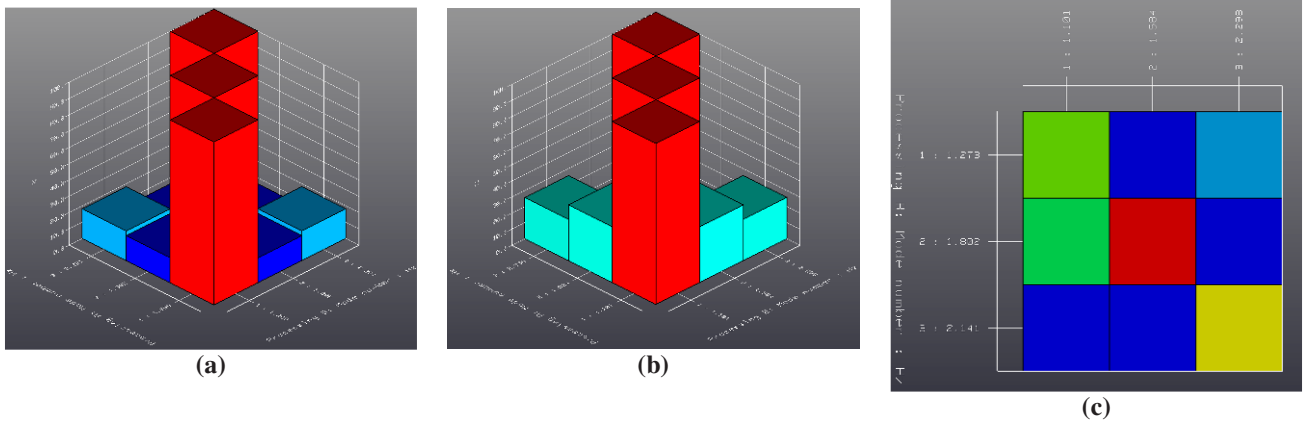


Fig.8 Semi-active suspension equipped car, four poster tests: AutoMAC matrix in the cases (a) Florida and (b) Bluekay, MAC matrix between them (c)

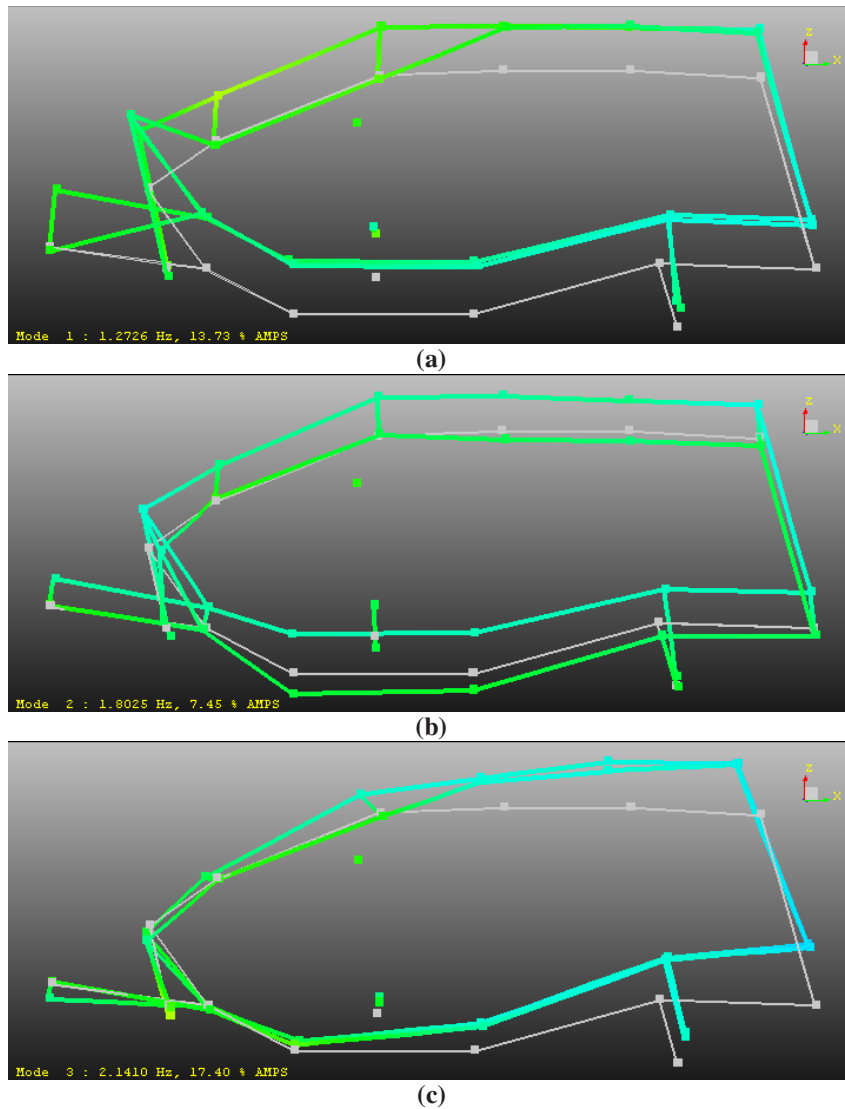


Fig.9 Semi-active suspension equipped car, four poster tests, Florida track: representation of the modes identified in the range from 0 to 3 Hz (a) heave (b) roll, pitch (c)

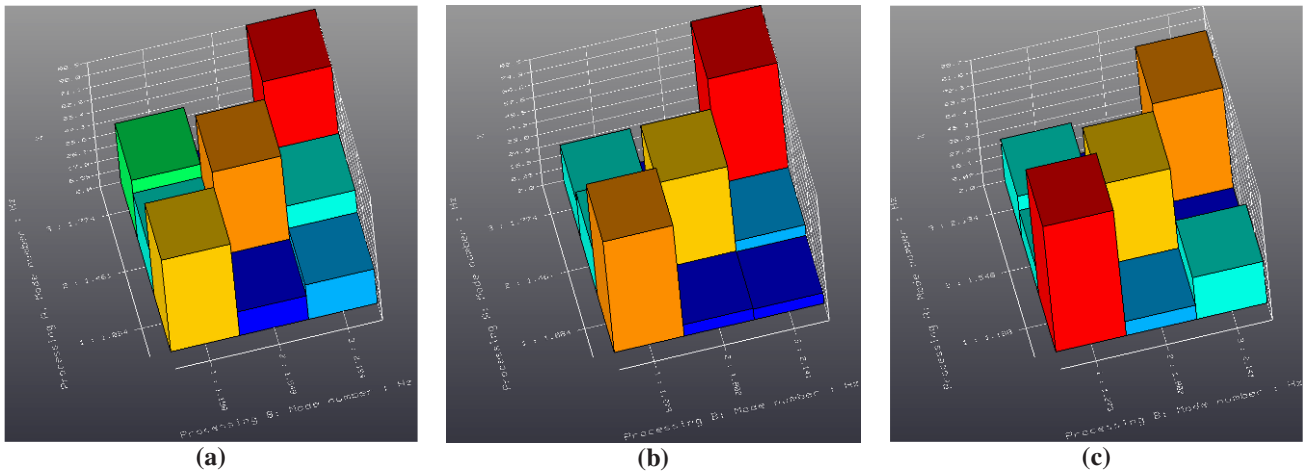


Fig.10 Semi-active suspension equipped car: MAC matrix in the cases (a) Blue-key and Florida, proving ground, (b) Blue-key, proving ground and Florida, four poster and (c) Florida, proving ground and Florida, four poster

| PG mode | Eigenfrequency [Hz] | | Damping ratio [%] | |
|-------------------------|---------------------|---------|-------------------|---------|
| | Blue-key | Florida | Blue-key | Florida |
| 1 st (heave) | - | 1.22 | - | 31.20 |
| 2 nd (roll) | - | 1.46 | - | 15.30 |
| 3 rd (pitch) | 2.33 | 2.27 | 10.02 | 9.00 |

Tab.3 Active suspension equipped car: Comparison of the modal parameters estimated in different proving ground tests

Nevertheless, a still satisfying agreement is obtained between four poster and proving ground tests, at least for the identified modes. For the sake of simplicity, in this section only the results of the latter test typology are reported (Tab.3, Fig.11a).

Two aspects have to be stressed: (i) the estimated damping ratio of the heave mode is for this vehicle twice higher than in the previous case and (ii) the second mode shape (roll) seems to behave in a different way with respect to the other car. The correlation among them is indeed low. This can be explained recalling that on the active suspension equipped car the anti-roll bar has been removed since the active system has itself the goal of counteracting the vehicle roll.

An overall comparison can be finally proposed: In Fig.11b the MAC evaluated between the set of modes identified on the active suspension equipped vehicle during the Florida proving ground test and that identified on the semi-active suspension equipped one during the Blue-key proving ground test is reported. More over in Fig.11c one can see the MAC evaluated between again the set of modes identified on the active suspension equipped vehicle during the Florida proving ground test and that identified on the semi-active suspension equipped one during the Florida four poster test. As it is shown the heave and the pitch mode are clearly identified and fine correlated, although the data set analysed come from different vehicles during different types of test.

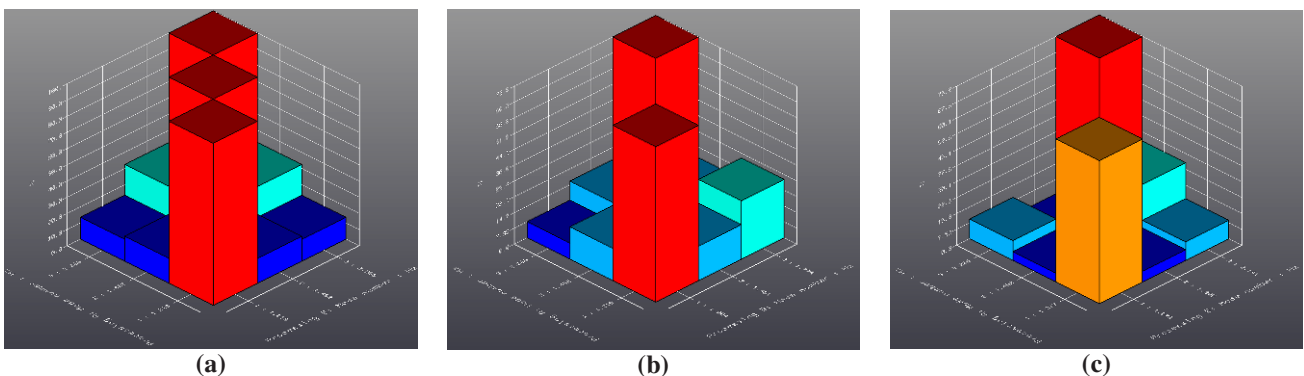


Fig.11 MAC matrix in the cases (a) Active suspension, Florida, proving ground (AutoMAC), (b) Active, Florida, proving ground vs. semi-active, Blue-key, proving ground and (c) Active, Florida, proving ground vs. semi-active, Florida, four poster.

5 CONCLUDING REMARKS

In this paper, Operational Modal Analysis is proposed as a tool for the performance assessment of different type of suspension systems for passenger cars. Of course the idea can be extended to other classes of vehicles.

Two different suspension architectures have been, in particular, considered equipping the same model of car, a Ford S-MAX. The former is a semi-active commercial suspension system, the latter is a novel prototypic active one.

Two different in-operation types of test have been then performed on both the vehicles: Proving ground tests on different road profiles and laboratory tests carried out on a four poster test rig. In the latter case, not only the same road profiles considered in the former one have been reproduced on the test rig, but also four uncorrelated white noise sequences have been utilised as input excitations, sent to the four actuators.

By OMA-processing the output responses acquired in the different testing conditions and by comparing the results, it is shown how this tool can be effectively utilised to verify the operation and the performance of those systems, by only carrying out a simple, cost-effective road test. In particular, the suspension operation has been analysed by OMA-estimating the modal parameters in the frequency range from 0 to 3 Hz, which the heave, roll and pitch modes are expected to belong to. These modes have been actually identified for both the vehicles considered. Regarding the heave mode, in particular, the damping ratio estimated in the case of the active system equipped vehicle, has been found to be quite higher than that obtained in the other vehicle case, due to the operation of the active suspension system.

From excitation point of view, it is useful to stress that in the case of road input, the lower are the considered frequencies, the higher is the energy level in the band and, consequently, the better excited are the included modes, with respect to random input, that can be, instead, effectively utilised to identify only higher-frequency structural deformation modes. Road tests are in conclusion suggested for the performance assessment of suspension operation.

ACKNOWLEDGEMENTS

The presented research is conducted in the frame of the Flanders' Drive project InAST (Integrated Active Safety Technology) and the European Commission FP7 project MoDe ("Maintenance on Demand") coordinated by Volvo Trucks (grant agreement nr. 233890). The financial contribution from the EC is gratefully acknowledged.

REFERENCES

- [1] BRINCKER R., HENNING KIRKEGAARD P., Editors, Special Issue: Operational Modal Analysis, Mechanical Systems and Signal Processing, Vol. 24 (5), pp 1209-1323, 2010.
- [2] SHEN F., ZHENG M., FENG SHI D., XU F., Using the cross-correlation technique to extract modal parameters on response-only data, Journal of Sound and Vibration, 259(5), 1163-1179, 2003.
- [3] HERMANS L., VAN DER AUWERAER H., Modal testing and analysis of structures under operational conditions: industrial applications, Mechanical Systems and Signal Processing, 13(2), 193-216, 1999.
- [4] PEETERS B., VAN DER AUWERAER H., PAUWELS S., DEBILLE J., Industrial relevance of Operational Modal Analysis – Civil, Aerospace and Automotive case histories. In Proc. of 1st IOMAC, Copenhagen, Denmark, 2005.
- [5] ANDRÉN P., Power spectral density approximations of longitudinal road profiles, International Journal of Vehicle Design, Vol. 40, Nos. 1/2/3, 2006.
- [6] TURKAY S., AKCAY H., A study of random vibration characteristics of the quarter-car model, Journal of Sound and Vibration, 282, 111-124, 2005.
- [7] GUIGGIANI M., Dinamica del veicolo. Città Studi Edizioni, 2006.
- [8] PEETERS B., System identification and damage detection in civil engineering. PhD thesis, Department of Civil Engineering, K.U.Leuven, Belgium, 2000.
- [9] CAUBERGHE B., Applied frequency-domain system identification in the field of experimental and operational modal analysis. PhD thesis, Department of Mechanical Engineering, Vrije Universiteit Brussel, Belgium, 2004.
- [10] PARLOO E., Application of frequency-domain system identification techniques in the field of operational modal analysis. PhD thesis, Department of Mechanical Engineering, Vrije Universiteit Brussel, Belgium, 2003.
- [11] PEETERS B., DE ROECK G., Stochastic system identification for operational modal analysis: a review, ASME Journal of Dynamic Systems, Measurement, and Control, 123(4), 659-667, 2001.
- [12] HERMANS L., VAN DER AUWERAER H., GUILLAUME P., A frequency-domain maximum likelihood approach for the extraction of modal parameters from output-only data. In Proc. of ISMA23, 367-376, Leuven, Belgium, 1998.
- [13] PEETERS B., VAN DER AUWERAER H., GUILLAUME P., LEURIDAN J., The PolyMAX frequency-domain method: a new standard for modal parameter estimation? Shock and Vibration, Special Issue dedicated to Professor Bruno Piombo, 11, 395-409, 2004.
- [14] HEYLEN W., LAMMENS S., SAS P., Modal Analysis Theory and Testing. K.U.Leuven, Belgium, 1997.
- [15] ANTHONIS J., GUBITOSA M., DONDEERS S., GALLO M., MAS P., VAN DER AUWERAER H., Multi-Disciplinary Optimization of an Active Suspension System in the Vehicle Concept Design Stage. In M. Diehl et al. (Eds.), Recent Advances in Optimization and its Applications in Engineering 2010, Part 7, 441-450.

Structural Dynamics with Coincident Eigenvalues: Modelling and Testing

Elvio Bonisoli, Cristiana Delprete and Marco Esposito
Politecnico di Torino, Corso Duca degli Abruzzi, 24 - 10129, Torino, Italy

John E. Mottershead
Department of Engineering, University of Liverpool,
1.19 Harrison-Hughes Building, The Quadrangle, Liverpool L69 3GH, United Kingdom

ABSTRACT

Theory of curve crossing and curve veering phenomena is well known in structural dynamics, but only few papers have used test bench to demonstrate and validate this eigenvalues behaviour. The aim of this paper is to present a theoretical and experimental analysis on a nonsymmetric experimental structure with eigenvalues curve veering and crossing phenomena. Starting from literature examples, detailed numerical models on lumped parameters systems and continuous systems with coincident and/or close eigenvalues are examined in order to develop a numerical FE model suitable to describe a tunable and simple test rig with coincident eigenvalues and curve veering phenomena without symmetric properties or completely uncoupled dynamic systems. The test bench is made of simple beams and masses properly linked together. The angle of an intermediate beam is used as tunable physical parameter to vary the eigenvalues of the system and to couple two bending modes or bending and torsional modes. Numerical and experimental results are compared, and sensitivity of mode shapes to variation of system parameters is discussed.

INTRODUCTION

There have been extensive research works on veering and crossing phenomena in dynamic systems. The behaviour is generally well understood. In the former, as the eigenvalues change under a parameter variation, converging roots loci get closer and then suddenly veer away. During this process all the properties of the involved modes are swapped, leading to a curious behaviour in the so called "transition zone". In the latter eigenvalues loci do not veer away but intersect without any swap of modal properties. Therefore, when two eigenvalues loci approach each other, they can cross or abruptly diverge.

Theoretical studies of this behaviour have been reported for half a century but despite this heritage, explicit references to experimental results are scarce. Moreover, literature presents mainly symmetric or uncoupled lumped systems with coincident eigenvalues properties and eigenvalues curve veering and crossing are not deeply analysed with experimental viewpoint.

One of the earlier observer of these phenomena, in structural dynamics, was Leissa [1], that cited further examples to draw attention to the possibility of fallacious artefacts in numerical models, and demonstrated that veering could be artificially induced through inadequate approximations and discretizations. Furthermore, to explain that in the veering away region mode shapes and nodal patterns must undergo sudden changes, Leissa used this sentence: "figuratively speaking, a dragonfly one instant, a butterfly the next, and something indescribable in between". The rapid change in the eigenfunctions during the veering has raised doubt on the validity of many approximate solutions.

Later, Kuttler and Sigillito [2] used an example of fixed membrane problem on rectangle to confirm the existence of curve veering in accurate mathematical models.

Perkins and Mote [3] presented an exact mathematical solution of elementary eigenvalue problem to confirm the existence of curve veering physical phenomena. Thus, the purpose of their study was to validate the existence of curve veering in continuous models by presenting an exact eigensolution, which veers, and to derive simple

criteria for predicting veerings and crossings in both continuous and discretized models. They showed that the key point to differentiate crossing and veering phenomena is the coupling factor, and they suggested a simple example: coupled oscillator. To summarize, Perkins and Mote [3] used perturbation theory to derive “coupling factors” to quantify the eigenfunctions coupling.

Pierre [4] explained how localization and veering are related to two kind of “coupling”: the physical coupling between component structures, and the modal coupling seen between mode shapes through parameter perturbations. He asserted localization and veering occur when modal coupling is of the same order or greater than physical coupling. His studies showed that, in structures with close eigenvalues, small structural irregularities result in both strong localization of mode shapes and abrupt veering away of the loci of the eigenvalues when these are plotted against a parameter representing the system disorder.

Regarding coupling factors in curve veering and curve crossing, there are some fields in which these phenomena are studied. For example, modal analysis of bridges with aeroelastic effects [5] and vibration analysis of rotating cantilever beams [6] are strongly influenced by coupling problems.

Balmès [7] analysed the eigenvector transformations of a three degree of freedom lumped-mass system. The simplest cyclic symmetric spring-mass system predicts a double mode and it shows the effect of a parameter variation on the variables of the parameterization. Balmès pointed out that only very particular conservative structures present eigenvalues veer and the exchange of mode shape properties happens as a rotation in a fixed subspace, similar to that of the example [7]. Only three types of conservative structure have been identified as allowing truly multiple modes (allowing the eigenvalues to be equal and therefore modal crossing with instantaneous rotation on mode shapes):

1. symmetric or cyclic structures, where it is allowed through algebraic properties of the group of symmetric properties,
2. multi-dimensional substructures for which motions in different dimensions uncouple, such as plates having a bending and a torsional mode at the same frequency,
3. structures with fully uncoupled substructures.

Mode localization and curve veering phenomena have been studied in the frequency domain by Mugan [8]. The singular-value decomposition (SVD) was employed to study the effects of localization phenomena on input-output relationships, and power and energy transmission ratios of structures.

The problem of measuring the phenomena of eigenvalue curve veering and mode localization has been studied also by Liu [9]. He suggested to define a critical value for the derivative of the eigenvectors or for the second derivative of the eigenvalues, above which the modes would be deemed to be veering.

Adhikari [10] cited examples where veering is influenced, and sometimes even suppressed, by the effect of damping. The use of expression for derivative of undamped modes can give rise to erroneous results even when the modal damping is quite low.

Young [11] dealt with the problem using two simple examples, concerning with the theory of continuous bodies. The inadequacy of approximate methods has been shown to be one source of couplings, while recently it has been found that there exist two different kinds of coupling responsible for the occurrence: implicit and explicit couplings. The former is generated by the incompleteness of the admissible function used in the approximate approach, while the latter is induced by the interaction between the main component and sub-component of structure. Curve veering can be observed in systems with explicit coupling where exact solutions are available.

More recently Du Bois, Adhikari and Lieven [12] presented a detailed experimental and numerical investigation on veering and crossing phenomena. Despite the widespread acceptance of veering theory, supported by poor experimental data, they developed an experimental structure made up of redundant truss. The transverse stiffness of the beams is influenced by the applied axial load. This structural stiffness modulation is used to provide the parametric variation for the experiment. Also a FE model have been developed to compare experimental and numerical data. In particular the counterintuitive variations of the mode shapes in these regions have been confirmed. The investigation has highlighted the impact of veering on model updating and modal correlation algorithms, as well as any discipline concerned with the analysis of closely spaced modes.

The analysis of mode shape transformations in terms of eigenvector rotations is found to be a valuable tool in quantifying the dynamic behaviour, and this is expected to find application in a wide range of parametric modal analyses.

In literature there are many articles that talk about repeated eigenvalues, but in term of algorithms for computing the derivatives of eigenvalues and eigenvectors. For example in [13] it is shown an algorithms for computing the derivatives of eigenvalues and eigenvectors for real symmetric matrices in the case of repeated eigenvalues.

Finally, in [14] D'Ambrogio and Fregolent proposed an extension of Modal Assurance Criterion (MAC) for coincident or close eigenvalues problems. They consider the correlation between a modal vector and subspace spanned by several modal vectors, instead of the usual correlation between two modal vectors.

At the end of this introduction it is possible to say that literature are very full of articles that deal with close eigenvalues, double eigenvalues, curve veering and crossing phenomena and mode localization, and a lot of fields use this concept to study physical phenomena. But, on the other end, there are not very experimental studies, except [12], that focus on this issues. This is the reason that have switched on idea to identify tunable and simple test bench with two coincident and/or close eigenvalues without symmetric properties or completely uncoupled dynamic systems. After a review about theory of curve veering and crossing phenomena in lumped parameters systems and continuous systems, this paper presents a simple test rig for experimentally testing coincident or close eigenvalues with crossing or veering phenomena.

The main aims of the test rig design are:

- to obtain a simple and tunable test rig for experimental validation of its dynamic behaviour;
- to understand curve crossing and curve veering taking into account uncertainty and variability of the structure, concerning natural frequencies and mode shapes with an experimental viewpoint;
- to comprehend possible energy paths with close or coincident systems, also to analyse possible dissipation strategies locally far from sources (application as damping systems).

OVERVIEW OF CURVE CROSSING AND CURVE VEERING PHENOMENA

Eigenvalues are often plotted versus a system parameter creating a family of root loci. Two converging loci either do or do not intersect. It is necessary to distinguish between curve crossing (coincident eigenvalues) and curve veering (close eigenvalues) phenomena. The former occurs when one eigenvalue curve intersects another curve and the dynamics behaviour is characterized by coincident eigenfrequencies: modes order changes, whereas the eigenfunctions (or eigenvectors in lumped systems) remain associate to the corresponding eigenvalues. In the latter two loci approach each other and abruptly diverge without meeting. Moreover an important characteristic of curve veering is that the eigenfunctions associated with the eigenvalues on each locus are interchanged during veering in a rapid but continuous way.

In order to identify curve crossing and curve veering the MAC index has been used [15], applying it before and after the occurrence of phenomena. With MAC is possible to evaluate the modes correlation in the transition area. To better understand curve crossing and curve veering phenomena and to explain the utility of MAC to distinguish one of other, two different cases of crossing and veering phenomena are taken into account:

- a monodimensional lumped system (see Balmès's system in [7]);
- a two-dimensional system concerning an axial-symmetric system, such as a bell.

Figure 1 shows the cyclic and symmetric system of Balmès [7]. Without losing generality, unitary masses and springs are assumed.

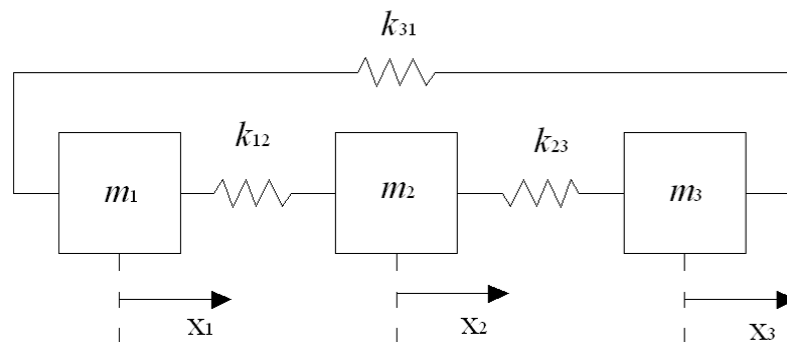


Figure 1 – Lumped cyclic and symmetric monodimensional system.

To obtain curve crossing and curve veering k_{23} e k_{31} have been used as parameters. This allows the system to lose symmetry property, and desired phenomena to set up. The different behaviour is described through the following two cases:

- $k_{23} = 1 \text{ N/m}$ \Rightarrow curve crossing (coincident eigenvalues),
- $k_{23} = 1.02 \text{ N/m}$ \Rightarrow curve veering (close eigenvalues).

It is straightforward that crossing and veering phenomena are tightly linked with certain physical parameters of the system. This last concept is used to design the test rig.

Solving the eigenvalue problem for each value of k_{31} and plotting eigenvalues curves of mode 2 and mode 3 versus this parameter, leads to the results displayed in Figure 2.

In the first case of perfect cyclic and symmetric system ($k_{23} = 1 \text{ N/m}$), applying MAC between eigenvectors close to the crossing point ($k_{31} = 0.99 \text{ N/m}$ and $k_{31} = 1.01 \text{ N/m}$) it is possible to easily depict the mode reversal (Figure 3 on the left). During curve crossing phenomena, involved modes maintain their peculiarities, but they do swap: mode 2 become mode 3 and viceversa. Orthogonality of eigenvectors is guaranteed, due to mass matrix proportional to identity. This change is only a marginal effect because order is only linked with frequency value and not with substantial mode characteristics. This is confirmed by observing eigenvectors before and after occurrence of crossing phenomena in Figure 4 on the left: every mode maintains its property and changes only the identification number. In the exact configuration of crossing, system shows two coincident eigenvalues and the associated eigenspace has size two, while in all other cases, where eigenvalues are very close but not coincident, each eigenspace has size one.

In the second case of non perfect symmetric system ($k_{23} = 1.02 \text{ N/m}$), solving the eigenvalue problem for each value of k_{31} and plotting eigenvalues curves of mode 2 and mode 3 versus this parameter, leads to the results displayed in Figure 2 on the right. Starting from $k_{31} = 0.9 \text{ N/m}$ and by increasing this stiffness value, eigenvalues curves get closer but they abruptly veer away. In this case there are not coincident eigenvalues, not even for $k_{31} = 1$.

Applying MAC for two different values of k_{31} ($k_{31} = 0.99 \text{ N/m}$) and after ($k_{31} = 1.01 \text{ N/m}$), where the distance between the two eigenvalues is minimum, it is possible to obtain the result reported on the right of Figure 3. It is straightforward to understand that the modes undergo a modal properties change, maintaining the initial rank. The modal assurance criterion confirms the alteration of mode shape by varying one of the parameter of the system.

This result agrees to the Leissa's sentence [1], in fact the modes shapes across the curve veering mix their dynamic properties in a continuous manner.

The strange and sudden variation of the 2nd and 3rd mode shapes can be seen in Figure 4 on the right. Presence of symmetry could be justify because results come from physical system with symmetry and cyclic properties, despite of the abrupt change is very clear. Leissa said that was very difficult to identify a continuity between modes shapes [1], as confirmed in Figure 4. In fact, despite the step of k_{31} has been refined, modes shapes suddenly change.

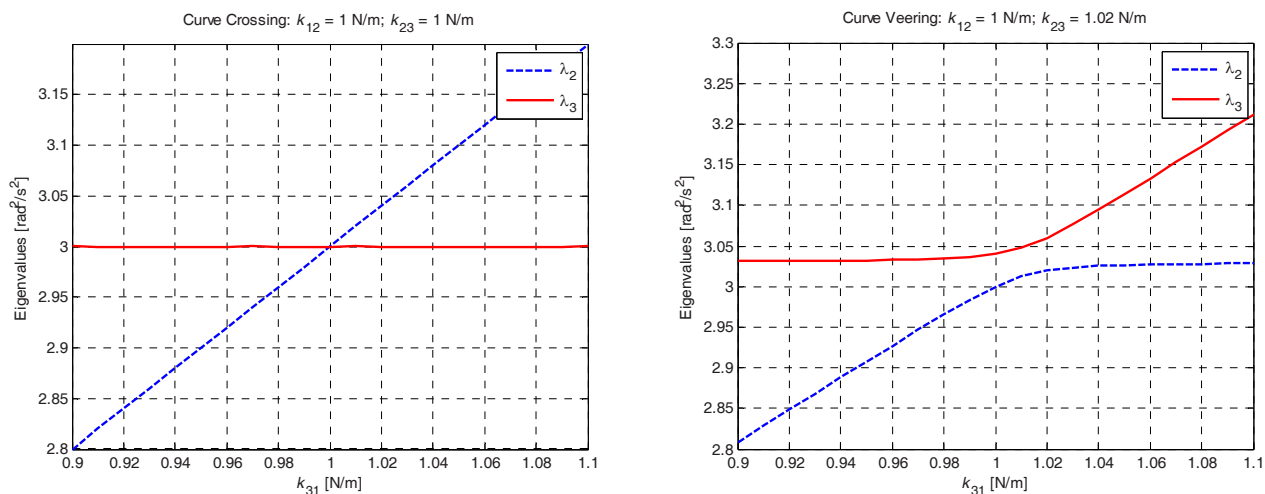


Figure 2 – Natural frequencies of the lumped system versus k_{31} parameter: curve crossing with $k_{23} = 1 \text{ N/m}$ (left), curve veering with $k_{23} = 1.02 \text{ N/m}$ (right).

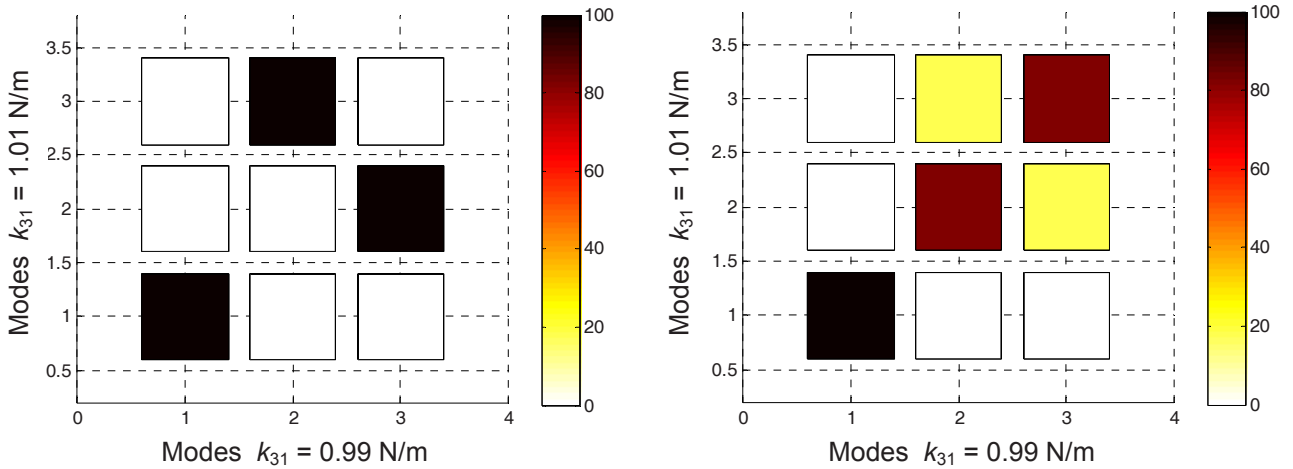


Figure 3 – MAC index between mode-shapes of different k_{31} parameter: curve crossing with $k_{23} = 1 \text{ N/m}$ (left), curve veering with $k_{23} = 1.02 \text{ N/m}$ (right) involving the 2nd and 3rd modes.

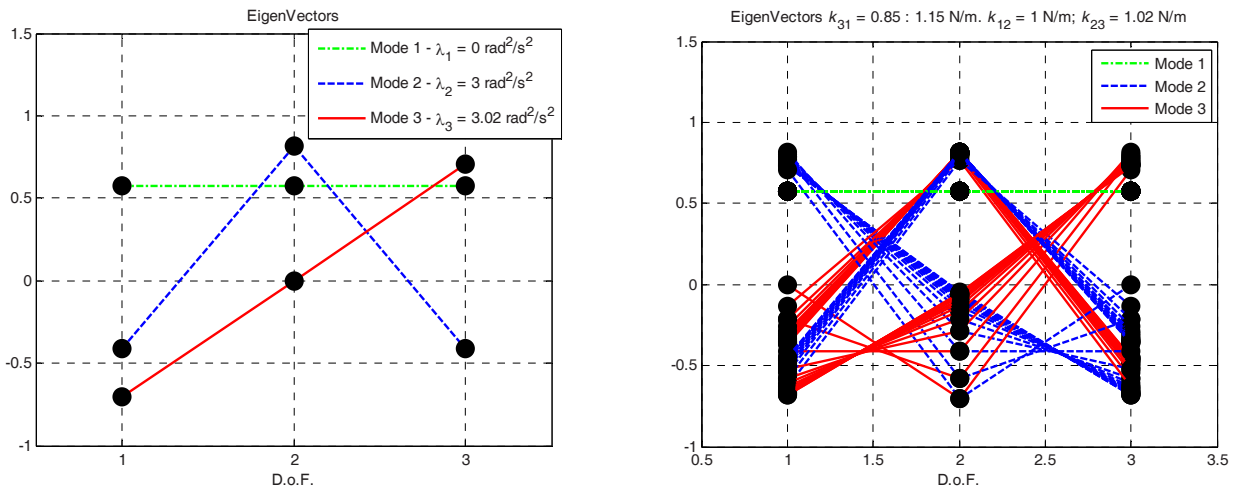


Figure 4 – Mode-shapes of the lumped system: curve crossing with perfect symmetric system (left), curve veering with non-perfect symmetric system (right).

In order to study a symmetric mono-axial system and to simulate its dynamics behaviour, a simple FE model of a bell has been developed. **Figure 5** shows the CAD model and the corresponding FE model, made of bar elements. This system has been implemented in Matlab to easily obtain frequencies and modes shapes.

In **Figure 6** are displayed the first four mode shapes: couples of two coincident eigenvalues with rotated eigenvectors come out, due to axial-symmetric properties.

To obtain crossing and veering phenomena it has been defined to alter stiffness parameters of one or more bar elements. In particular, **Figure 5** shows the corresponding nodes of constant and variable stiffness parameters. Lumped mass matrix is taken into account.

Like in the example of Balmès, it is necessary to set up a variable parameter and use another parameter as a discriminant between crossing and veering phenomena. k_{Bar} represents constant stiffness value that should have a perfect axial-symmetric model.

Figure 7 shows the first 16 eigenfrequencies curves varying the circumferential stiffness k_{2-3} parameter. The different behaviour is described through the following two cases:

- $k_{2-3} = k_{Bar}$ \Rightarrow curve crossing (coincident eigenvalues),
- $k_{2-3} = 1.3 k_{Bar}$ \Rightarrow curve veering (close eigenvalues).

Crossing phenomena is present for $k_{2-3} = 100\% k_{Bar}$ (Figure 7 on the left), in fact this value allows the model to possess axial-symmetric property and then to have coincident eigenvalues. In case of different stiffness, i.e. $k_{2-3} \neq 100\% k_{Bar}$, curve veering appears in some couples of modes (Figure 7 on the right).

When it is imposed a stiffness parameter variation, different by a circumferential variable parameter like k_{2-3} , it will be obtained a curve veering phenomena. When symmetric characteristics are not present, most of crossing phenomena involving mode-shapes of Figure 6 became veering, but some curve crossing between bending and torsional modes are still evident. In Figure 7 letter “C” and ellipse specify curve crossing point, whilst letter “V” and rectangle specify curve veering point. Similarly, to order eigenfrequencies a swap matrix obtained from MAC across every point of veering and/or crossing phenomena is adopted.

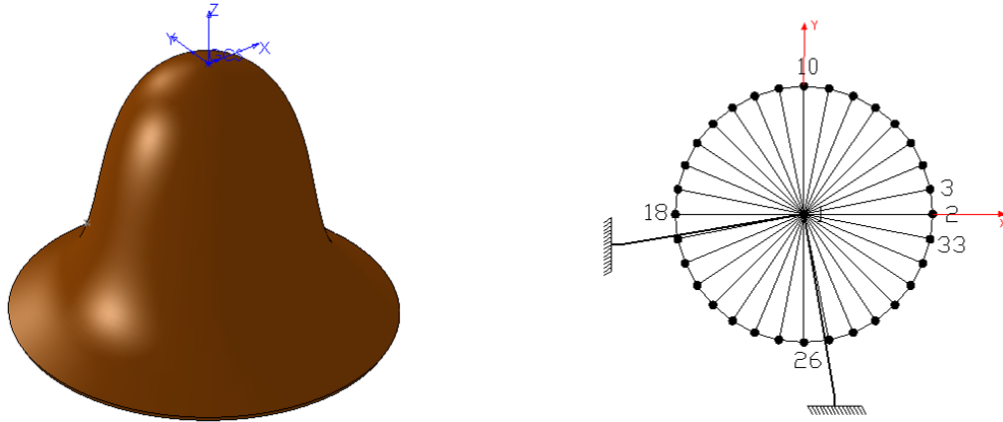


Figure 5 – Bell and corresponding FE model.

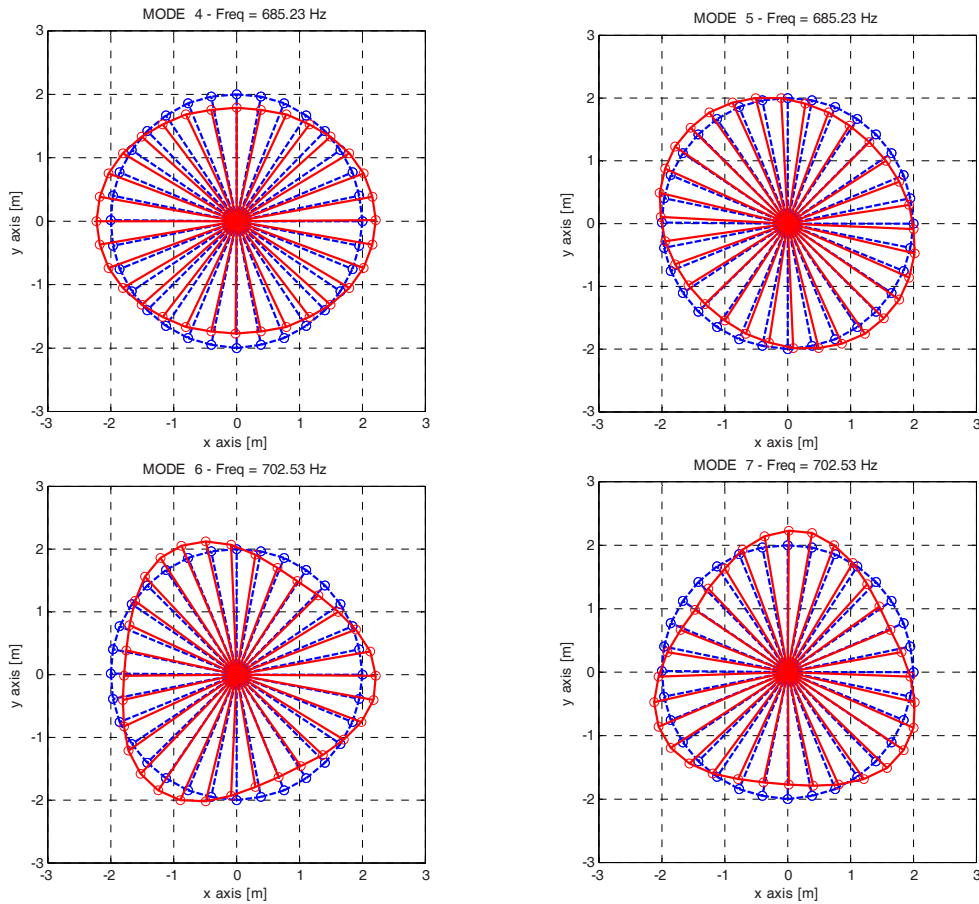


Figure 6 – First mode-shapes of the bell system (red lines) superimposed on the underformed shapes(blue lines).

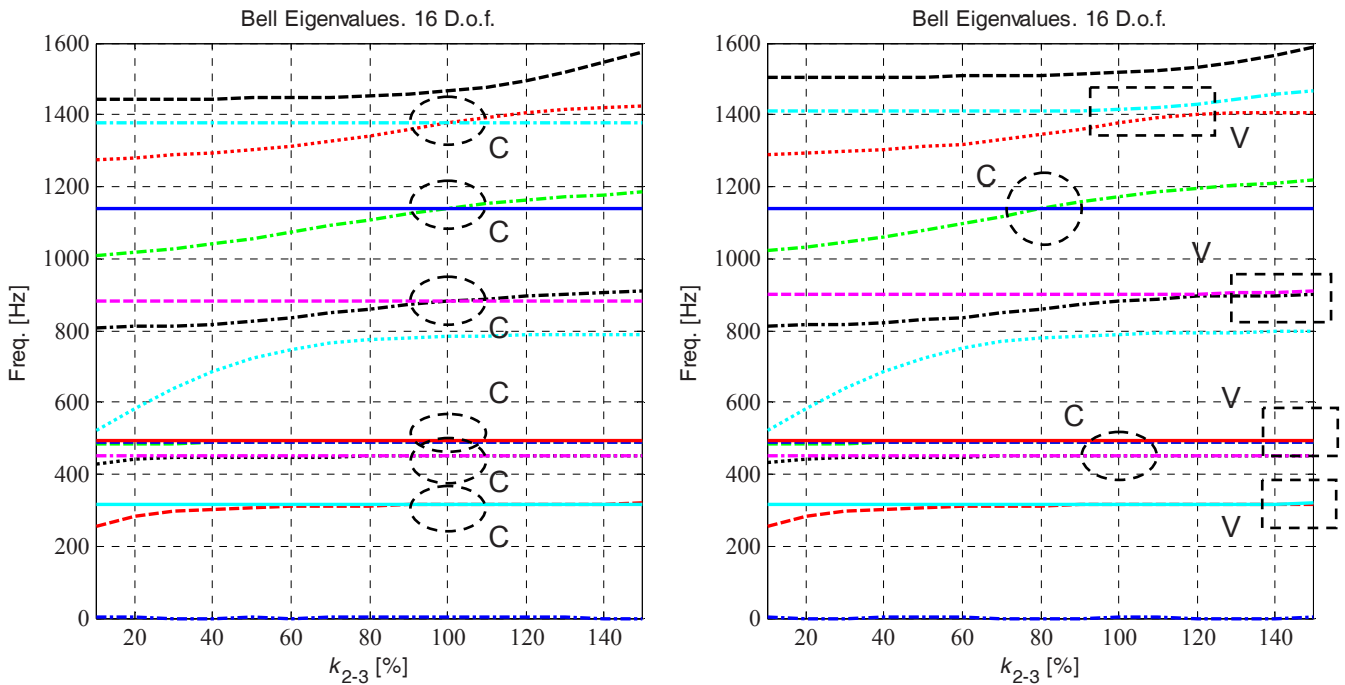


Figure 7 – Natural frequencies of the structure versus angle configuration α .

At the end of this paragraph it is possible to assert that curve crossing and curve veering are phenomena tightly linked with physical parameters and their occurrence depends on symmetric or nonsymmetric properties. In particular, a slight loss of symmetry allows to obtain curve veering in a system with only curve crossing phenomena. Also in these last systems, crossing phenomena may be again present, if different eigenspaces with independent eigenvalues are interacting. The properties of symmetry is not, therefore, a fundamental requirement to have a system with coincident or very closed modes. Finally, MAC is an efficient tool to discriminate crossing and veering phenomena.

TEST RIG DESCRIPTION

Main ideas of the test bench are to obtain a structure without symmetric and cyclic properties but with dynamics behaviour characterised by coincident eigenvalues (curve crossing) and/or close eigenvalues (curve veering). Observing the dynamic instability of flutter phenomena, the structure shown in [Figure 8](#) has a very simplified wing shape, where a sensitive geometrical parameter is chosen to change its dynamic properties.

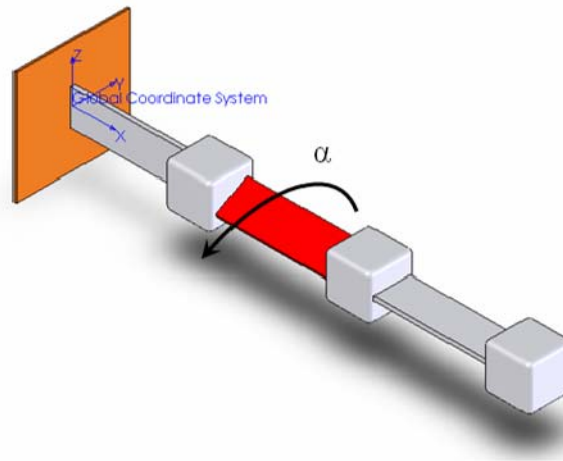


Figure 8 – Sketch of the test rig.

The sketch of the system is composed by three beam elements and three lumped masses. The test bench uses the angle of the intermediate beam as a tunable physical parameter to modify the system eigenvalues, in order to couple two bending modes or a bending with a torsional mode. In particular, a coupling between torsional and bending modes is expected at a particular configuration.

According to the boundary configurations with the intermediate beam horizontal or vertical, the eigenproblem for different α values predicts sensitive changes in the bending modes. Drawing eigenvalues curves versus this physical parameter demonstrates the dynamic properties of the test bench.

Neglecting structural damping in the FE model, the system equations for a n-dofs structure result:

$$[\mathbf{M}]\{\ddot{\mathbf{x}}\} + [\mathbf{K}]\{\mathbf{x}\} = \{\mathbf{0}\} \tag{1}$$

where the mass matrix $[\mathbf{M}]$ and the stiffness matrix $[\mathbf{K}]$ are real, symmetric and positive definite. Therefore, the eigenproblem results:

$$([\mathbf{K}] - \omega^2[\mathbf{M}])\{\boldsymbol{\varphi}\} = 0 \tag{2}$$

where the n eigenvalues ω^2 and eigenvectors $\{\boldsymbol{\varphi}\}$ are evaluated through determining no trivial solutions, therefore:

$$\det([\mathbf{K}] - \omega^2[\mathbf{M}]) = 0 \tag{3}$$

In order to evaluate curve crossing or veering phenomena, the evaluation of $[\mathbf{M}]$ and $[\mathbf{K}]$ matrices are obtained through a FE model developed in Matlab. Beam finite elements with six degree of freedom for each node are adopted as shown in Figure 9. This choice is suitable to evaluate the dynamic properties of three-dimensional structures that may be approximated with truss schemes.

These beam elements are used to discretize the physical structure as shown in Figure 9. Beam finite elements in 2D and 3D representation are sketched with cyan boxes, while lumped masses are identified by red balls.

A very flexible FE model toolbox has been developed to represent different configurations and to simulate the sensitivity of different structural parameters, such as lumped masses, beam sections and lengths.

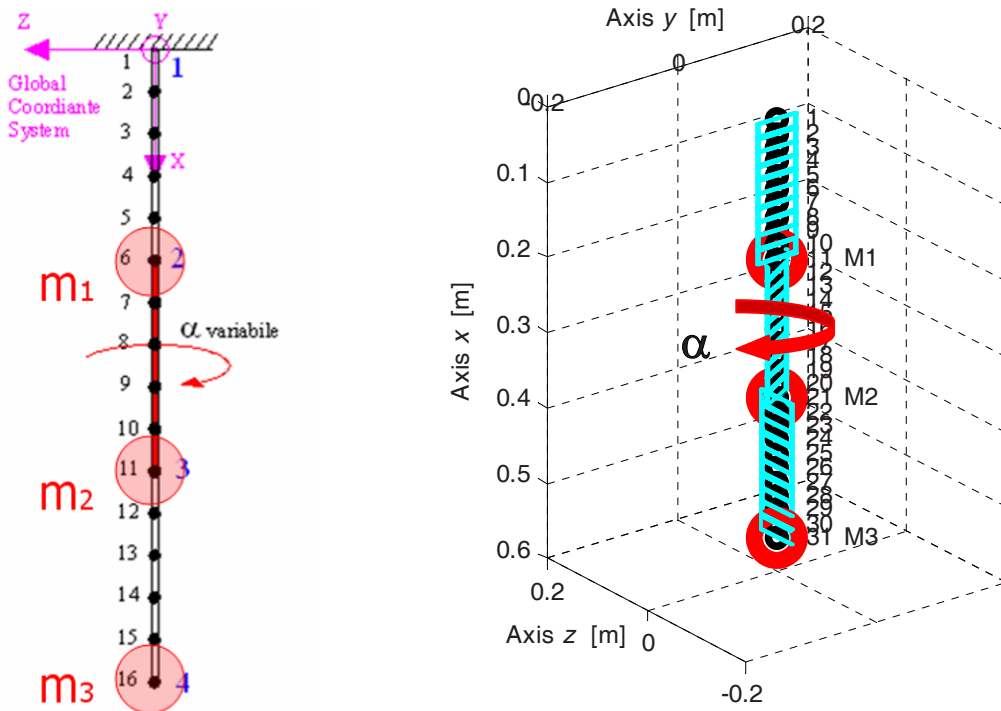


Figure 9 – FE model of the structure.

The design aim is to define suitable configurations where it is possible to see a high number of curve veering and curve crossing phenomena with respect to the angle parameter. The eigenvalues graph shown in Figure 10 represents the expected dynamic behaviour in the frequency range up to 220 Hz. The mode-shapes related to the configuration $\alpha = 0$ are used for labelling the curves and for following the eigenfrequencies modifications; different colours are adopted for distinguishing crossing (“C” symbols) and veering phenomena (“V” symbols).

MAC index is adopted to follow the mode-shapes and to distinguish crossing from veering.

Another result that can be obtained by the FE model is the analysis of modes shapes, especially across the curve veering or curve crossing points.

In Figure 11 MAC index between eigenvectors with $\alpha = 44^\circ$ and 45° are plotted on the left. They involve the 6th mode (2nd torsional) and the 7th mode (bending); a typical crossing phenomena is evinced. Therefore this case produces a order change of modes, the modes shapes remain the same and the corresponding curves intersect each other.

The same approach is used between eigenvectors with $\alpha = 68^\circ$ and 69° on the right of Figure 11, where two bending modes are involved in a curve veering phenomena. The 5th and 6th bending modes are very similar first and after occurrence of veering phenomena, in fact the MAC index is not suitable to distinguish two different modes. Increasing the angular resolution between the eigenvector comparison produces always diagonal MAC index, corresponding to not crossing phenomena.

Non zeros values of off-diagonal MAC terms are due to non perfect orthogonal properties of eigenvectors. The mass matrix is not proportional to identity because, although beam elements are equal, translational and rotational inertial terms are different and lumped masses are taken into account.

Finally, even for the test bench curve crossing and curve veering present the same peculiarity described in the last paragraph. Therefore the design of the test bench allows to validate the theoretical results about crossing and veering and to study, in the future, energy transfer paths.

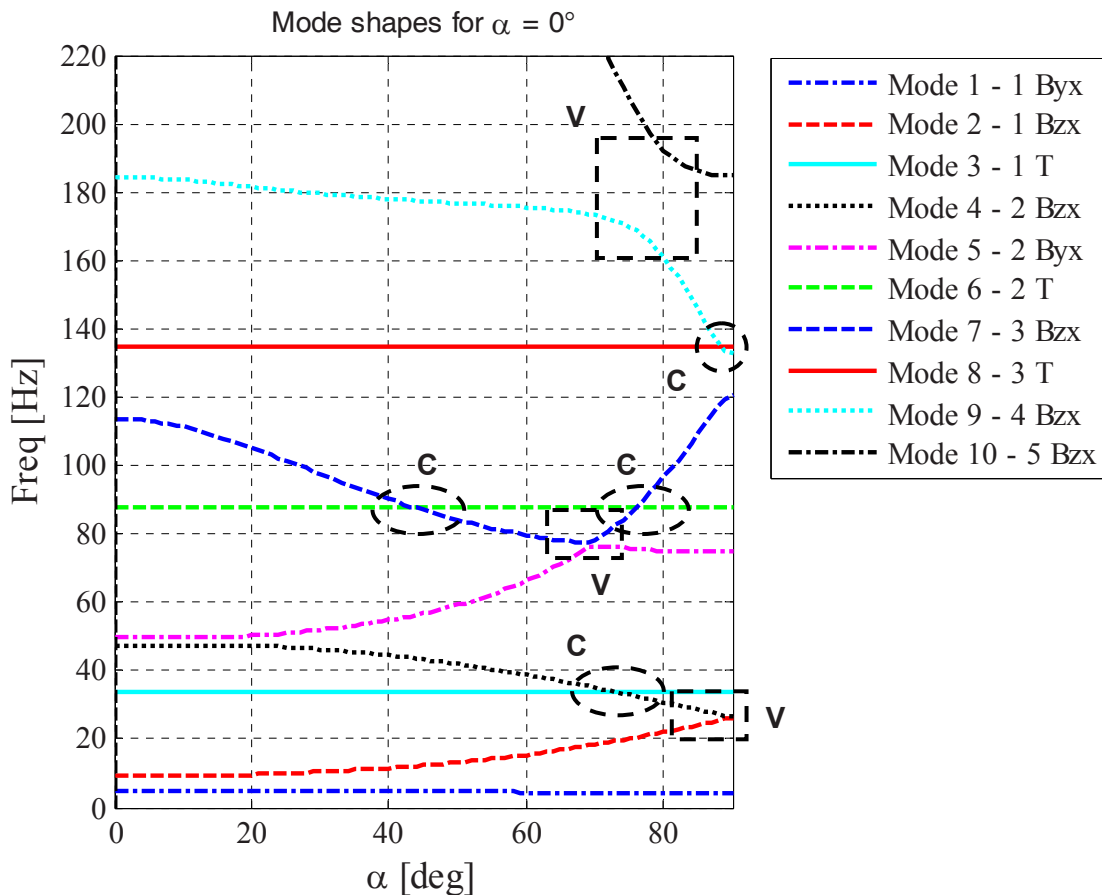


Figure 10 – Natural frequencies of the structure versus angle configuration α .

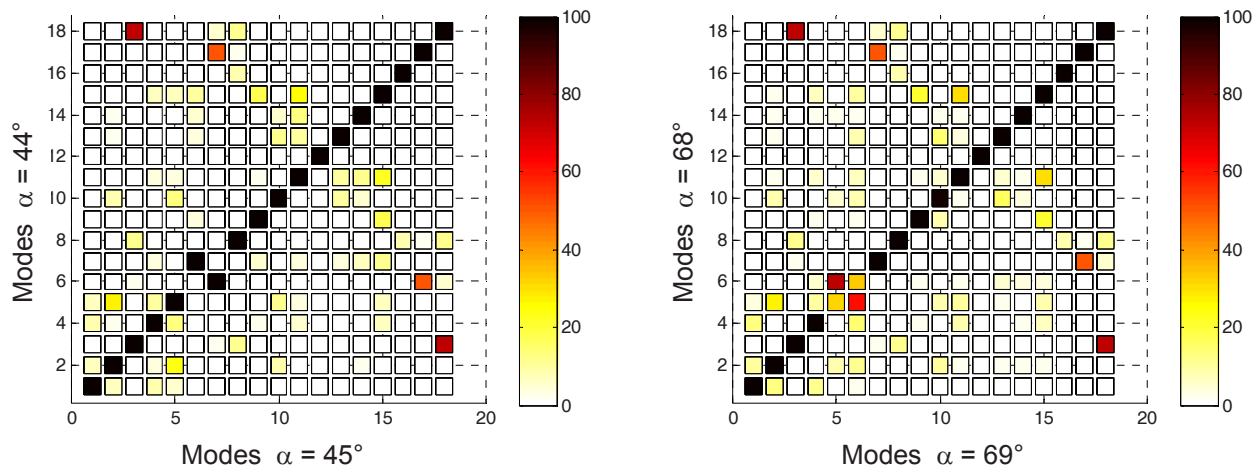


Figure 11 – MAC index between mode-shapes of different angle configuration: curve crossing involving the 6th and 7th modes (left), curve veering involving the 5th and 6th modes (right).

TEST RIG DESIGN AND EXPERIMENTAL RESULTS

Some practical approximations and physical dimensions are neglected or not simulated in the FE model, therefore to design and build the test rig some engineering choices are adopted to reproduce the numerical behaviour in physical reality. The most important characteristic is to have a tunable parameter in the structure to vary and tune the angle α of the middle beam.

A manual rotary table is chosen in the first lumped mass. It guarantees the rotation of the middle beam and controls the orthogonality of the third beam by means of a clamp with a device integrated in the second lumped mass. One main peculiarity of the test bench is the flexibility, in fact the structure allows different lumped masses and beam element dimensions in a simple way.

Figure 12 shows 3D drawings and photographs of the lumped masses in which is possible to see the rotary table and other parts of the group. An exploded view of the group shows rotational pins, jaws and twice parts necessary to obtain the tunable angular parameter. Beam elements used to join the lumped masses and to obtain correct stiffness properties are chosen in order to reproduce the dynamic properties predicted in Figure 10. These elements are interchanging with others that have rectangular section but with different dimensions and length. This is a further flexibility characteristic of the test bench.

To obtain the reciprocal position (parallel or orthogonal) between the first and the third beam of the test bench during variation of the angular parameter α , an alignment profile is developed (transparent light blue profile of Figure 12). This profile must be used only during the tuning of test bench, to guarantee alignment, but it must be removed during the experimental test.

To constrain the test bench, a bracket that joins the main structure with a seismic mass is designed. This bracket has its first bending mode over 250 Hz, in order to not interact in the frequency range of experimental testes.

After the assembly of the test bench, a preliminary experimental campaign has been conducted to validate theoretical results. Three three-axial accelerometers are set on every lumped mass (Figure 13), and subsequently rowing hammer technique is implemented for data acquisition. A mean of 10 impact tests are used for the measurement of FRF for each testing configuration. In particular 19 different configurations are taken into account, from $\alpha = 0^\circ$ to $\alpha = 90^\circ$ with a step of 5° . An updating procedure is now necessary to validate the numerical result of Figure 10.

By means of experimental data two main results are obtained for the FE model: the calibration of equivalent length of beam elements, considering lumped masses and the updated stiffness parameter for the analytical FE data with respect to the experimental modes. To calibrate beam elements in the model, torsional modes are used because they are not influenced by length of actual masses, but only by section and length of beams.

To be more confident with respect to the numerical model, the following step is to use a commercial FE model integrated in a CAD software, like SolidWorks-Cosmos, to predict more accurately the dynamic behaviour with respect to the angle parameter α .

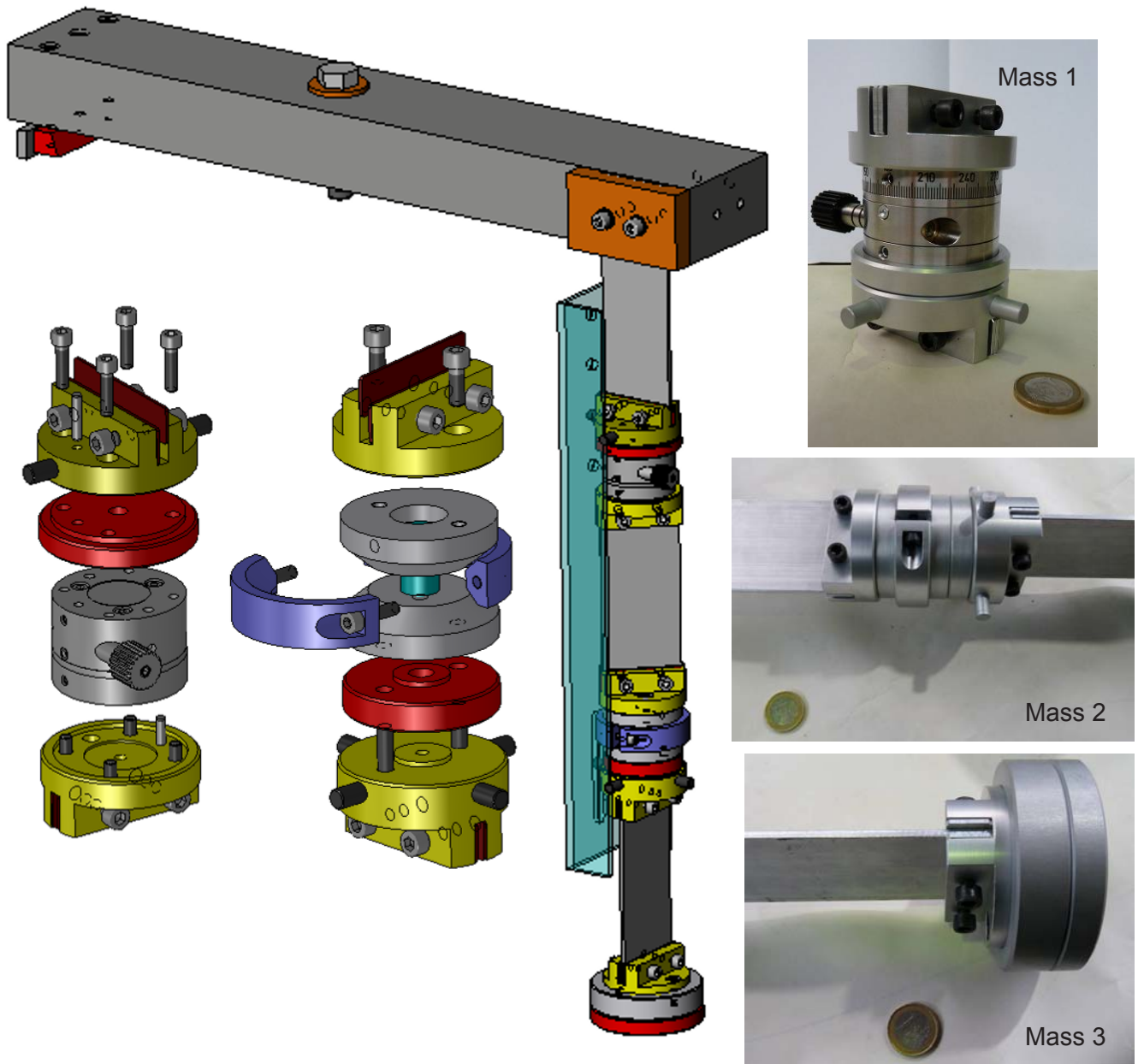


Figure 12 – 3D drawings and photographs of the test rig.

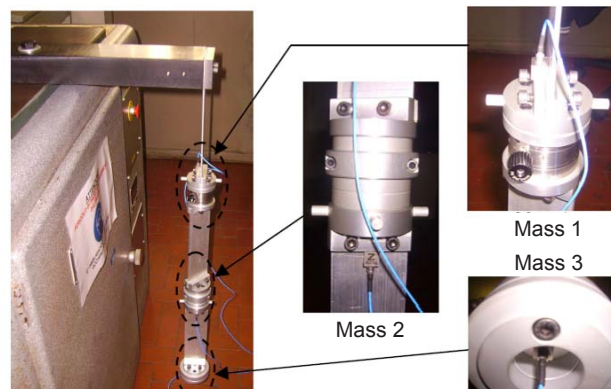


Figure 13 – Experimental setup of the test rig.

CONCLUSIONS

The paper presents a theoretical analysis and an experimental test rig on a nonsymmetric structure with eigenvalues curve veering and crossing phenomena. Detailed numerical models on lumped parameters systems and continuous systems with coincident and/or close eigenvalues are examined to develop a numerical FE model suitable to describe the tunable and simple test rig with coincident eigenvalues and curve veering phenomena without symmetric properties or completely uncoupled dynamic systems.

A consistent numerical FE model has been developed to design the structure. The initial comparison between the experimental data obtained through the test rig and the numerical results seems to be suitable for validate the methodology.

The test bench is useful to investigate curve veering phenomena with an experimental overview. It allows to completely control the dynamic behaviour through a physical system parameters, and it could also be a consistent tool, due to its form similar to a wing, to understand flutter dynamic instability through coupling bending wing mode with torsional one.

BIBLIOGRAPHY

- [1] Leissa W., "On a curve veering aberration", *Journal of Applied Mathematics and Physics (ZAMP)*, **25**, 1974, pp. 99-111.
- [2] Kutter J.R., Sigillito V.G., "On curve veering", *Journal of Sound and Vibration*, **75**, 1981, pp. 585-588.
- [3] Perkins N.C., Mote C.D.Jr., "Comments on curve veering in eigenvalue problems", *Journal of Sound and Vibration*, **106**(3), 1986, pp. 451-463.
- [4] Pierre C., "Mode localization and eigenvalue loci veering phenomena in disordered structures", *Journal of Sound and Vibration*, **126**(3), 1988, pp. 485-502.
- [5] Chen X., Kareem A., "Curve Veering of Eigenvalue Loci of Bridges with Aeroelastic Effects", *Journal of Engineering Mechanics*, **129**(2), 2003, pp. 146-159.
- [6] Yoo H.H., Shin S.H., "Vibration analysis of rotating cantilever beams", *Journal of Sound and Vibration*, **212**(5), 1998, pp. 807-828.
- [7] Balmès E., "High modal density, curve veering, localization: a different perspective on the structural response", *Journal of Sound and Vibration*, **161**(2), 1993, pp. 358-363.
- [8] Mugan A., "Effect of mode localization on INPUT-OUTPUT directional properties of structures", *Journal of Sound and Vibration*, **258**(1), 2002, pp. 45-63.
- [9] Liu X.L., "Behaviour of derivatives of eigenvalues and eigenvectors in curve veering and mode localization and their relation to close eigenvalues", *Journal of Sound and Vibration*, **256**(3), 2002, pp. 551-564.
- [10] Adhikari S., "Rates of change of eigenvalues and eigenvectors in damped dynamic system", *AIAA Journal*, **39**(11), 1999, pp. 1452-1457.
- [11] Young L.J., Hwang M. C., "Curve Veering Phenomena One-Dimensional Eigenvalue Problems", *Proceedings of the Eighteenth National Conference of the Chinese Society of Mechanical Engineers*, **12**, 2001, Taipei, Taiwan, R.O.C., pp. 239-246.
- [12] Du Bois J.L., Adhikari S., Lieven N.A.J., "Eigenvalue curve veering in stressed structures: An experimental study", *Journal of Sound and Vibration*, **322**, 2009, pp. 1117-1124.

- [13] Lane D.R., "Eigenvector Derivatives with Repeated Eigenvalues", *AIAA Journal*, **27**(4), 1989, pp. 486-491.
- [14] D'Ambrogio W., Fregolent A., "Higer-order MAC for the correlation of close and multiple mode", *Mechanical Systems and Signal Processing*, **17**(3), 2003, pp. 559-610.
- [15] Allemang R.J., Brown D.L., "A correlation coefficient for modal vector analysis", *Proceedings of 1st IMAC*, Orlando, Florida, USA, 1982, pp. 110-116.

Nonlinear Dynamics of an Electro-Mechanical Energy Scavenger

Stefano Tornincasa*, Elvio Bonisoli*, Francesco Di Monaco*, Sandro Moos*,
Maurizio Repetto**, Fabio Freschi**

*Department of Production Systems and Business Economics - Politecnico di Torino, Italy

**Department of Electrical Engineering - Politecnico di Torino, Italy

Abstract

This paper presents a very compact electro-mechanical wideband energy harvester optimized for tire applications. The energy conversion process of the device takes into account the simulation of different phenomena like: non linear dynamic and adaptive resonant behavior of the seismic mass, electromagnetic and magneto-static coupling between floating magnetic mass and coils, transfer of the generated power to an external load by means of a nonlinear circuit interface.

The paper is focused on the pneumatic effects of the floating magnet sliding into a calibrated guide. A convenient choice of clearance between moving and fixed parts can be used to create an effective air brake preventing or softening shocks with end stops and to modify system dynamic.

A block-oriented Simulink®, experimentally validated, model has been realized to predict scavenger device performance and to optimize design parameters. Equivalent linearized stiffness and damping factors due to pneumatic effects have been modeled in the lumped parameters system to get a simplified model and to formalize relations with the geometrical characteristics. Analysis of the effect of several nonlinearities at different vehicle speed have been performed.

Keywords: energy scavenger, electro-mechanical device, adaptive resonance

Introduction

To power remote sensor nodes, if the batteries substitution is unadvisable, unsafe, onerous or even impossible, a possible solution is the use of energy scavenger (or energy harvester) devices. These devices are designed to recover energy from a specific source available in the destination environment. It is possible to scavenge energy from a wide set of sources as: ambient-radiation, temperature deltas, motion and vibrations. To scavenge energy from vibrations are typically used resonant spring mass systems linked to piezoelectric, magneto-mechanic or electrostatic generators [1-2].

A sensor node installed inside a tire, where it is obviously impossible to bring power through wires, is a suitable application for an energy scavenger device, if a battery enough capacious to power the sensor for its whole lifetime is too big or too heavy. In fact during the wheel rotation, variation in acceleration components can induce vibrations in properly designed parts and it is possible to exploit these vibrations to scavenge and accumulate energy. Due to the very high stresses that a component installed in a tire has to resist, in this work it has been chosen to design a magneto-mechanic (instead of electrostatic or piezoelectric) energy scavenger device.

Since the tire can be subjected to an extended range of revolving speed, a challenge to overcome is to properly design an energy scavenger device able to exploit a wide range of frequencies so to obtain an acceptable power output in many different working conditions.

Working principle

Fig. 1 shows all the components of the device [3]. The scavenger is composed by a floating magnet running into a guide around which are wound in opposite direction two series connected coils so that their electromotive force is summed when the floating permanent magnet is moving. A preload magnet, inserted in the lower lid, push the floating magnet toward the upper lid. Two rubber bumpers prevent excessively rough shocks between floating magnet and lid. When the floating magnet moves along the guide the variation of the magnetic flux linked to the coils produce an electromotive force that can be used as power supply for an electrical load.

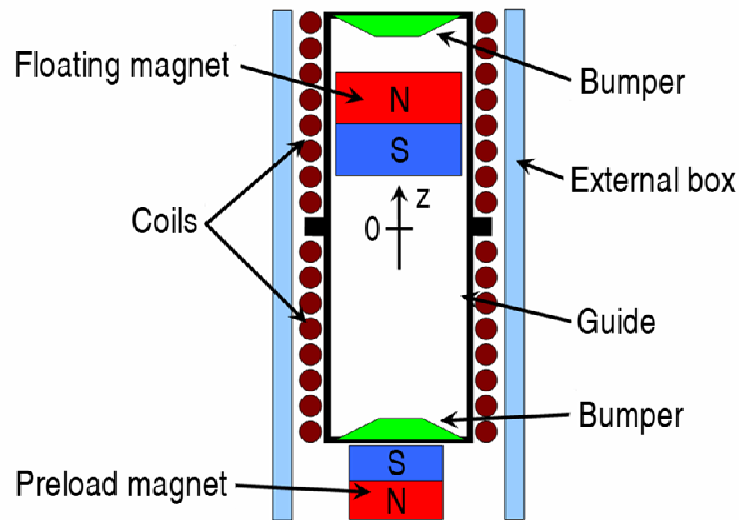


Fig. 1 Energy scavenger device components

When revolving around its axis, the external surface of the tire is subjected to high deformation gradients when contacting ground. This deformations lead to large variation on the radial acceleration acting on the device. Fig. 2 (a) shows a typical acceleration profile for a point on the tire inner-liner during a wheel round: acceleration is about constant (v^2/R) during the larger part of the round and has a peak entering and exiting the contact zone. In the contact zone the radial acceleration is close to zero because the point is actually translating and not rotating.

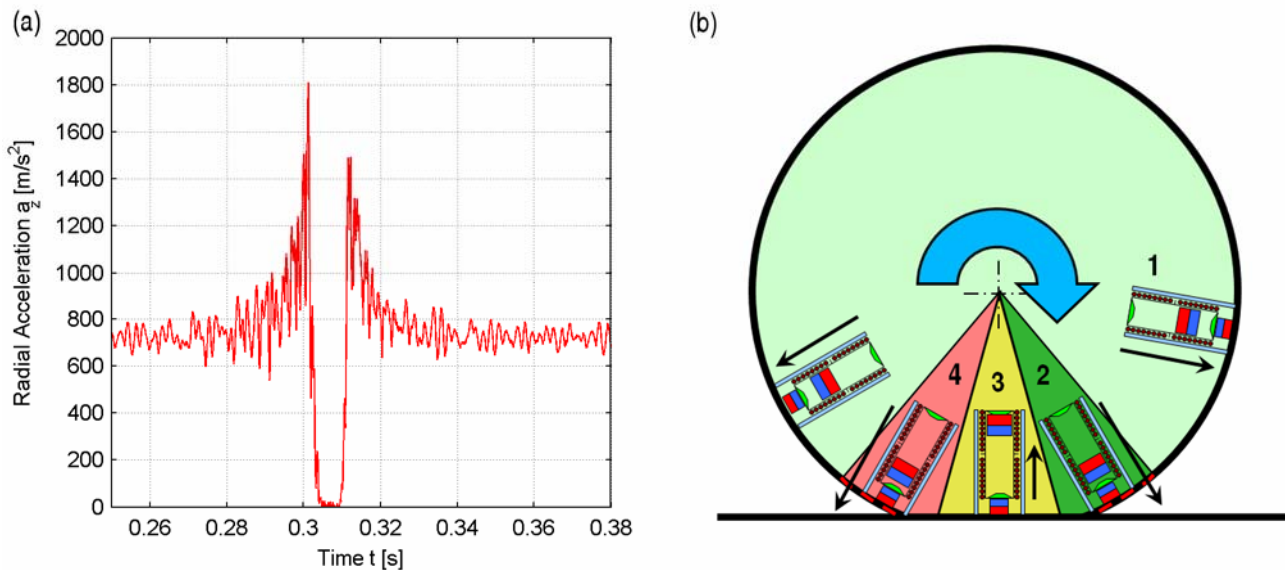


Fig. 2 Typical radial acceleration profile (a) and energy scavenger behavior during wheel rotation (b)

Fig. 2 (b) shows the main phases of the process:

1. the tire is not touching the ground, so the scavenger is subjected to radial (centripetal) acceleration, therefore a centrifugal force acts on the device,
2. the tire is arriving on the ground and is deforming, so the scavenger is subjected to an acceleration peak,
3. the tire is on the ground (contact patch, footprint) and it is moving with a straight motion, the radial acceleration quickly drops to zero,
4. the tire leaves the ground contact and the scavenger is again subjected to another acceleration peak.

Mechanical model

An accurate model of the energy scavenger requires the study of different phenomena, in particular:

- magnetic circuit and interaction with magnet movement, taking into account nonlinearities of materials,
- interaction with external electric load and definition of a scavenger equivalent circuit,
- dynamic simulation of the floating magnet as a response from external acceleration,
- evaluation of the wasted energy due to dry friction and pneumatic forces arising from mass motion.

The design phase of the energy scavenger requires the definition of a simulation tool that is able to couple the different physical phenomena involved. The complete block diagram is shown in Fig. 3. The block-oriented sub-structuring technique has the following properties [4]:

- starting from analytical or experimental component behavior, to predict system performance in time domain, for several operating conditions;
- to underline correspondences between model blocks and physical system, input/output relations between components and their interactions on system behavior;
- to allow a high level of flexibility in pre-development and development phases, through the use of a multi-sharing component library and the adoption of a user-friendly graphical interface;
- to develop and compare performance and limitations of different electric/electronic or mechanical layouts, in particular focusing on power absorption and efficiency of the whole system.

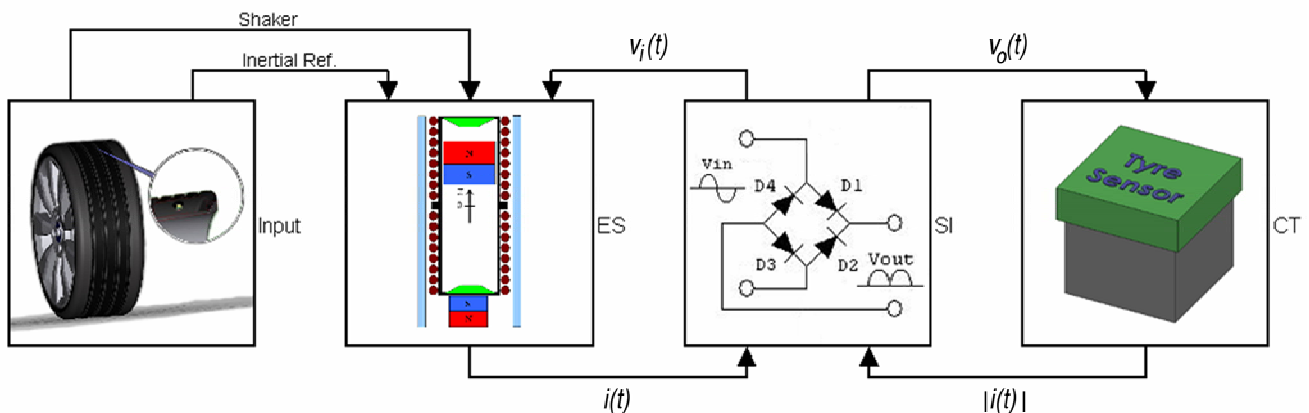


Fig. 3 Block diagram of the energy scavenger simulator

Each substructure is connected to the others through a direct link (e.g., in Fig. 4 the coil and the preload magnet interact on the floating magnet with forces) and a feedback link (the evaluated forces are dependent on the state of the floating magnet) that produces the corresponding reaction to the acting state.

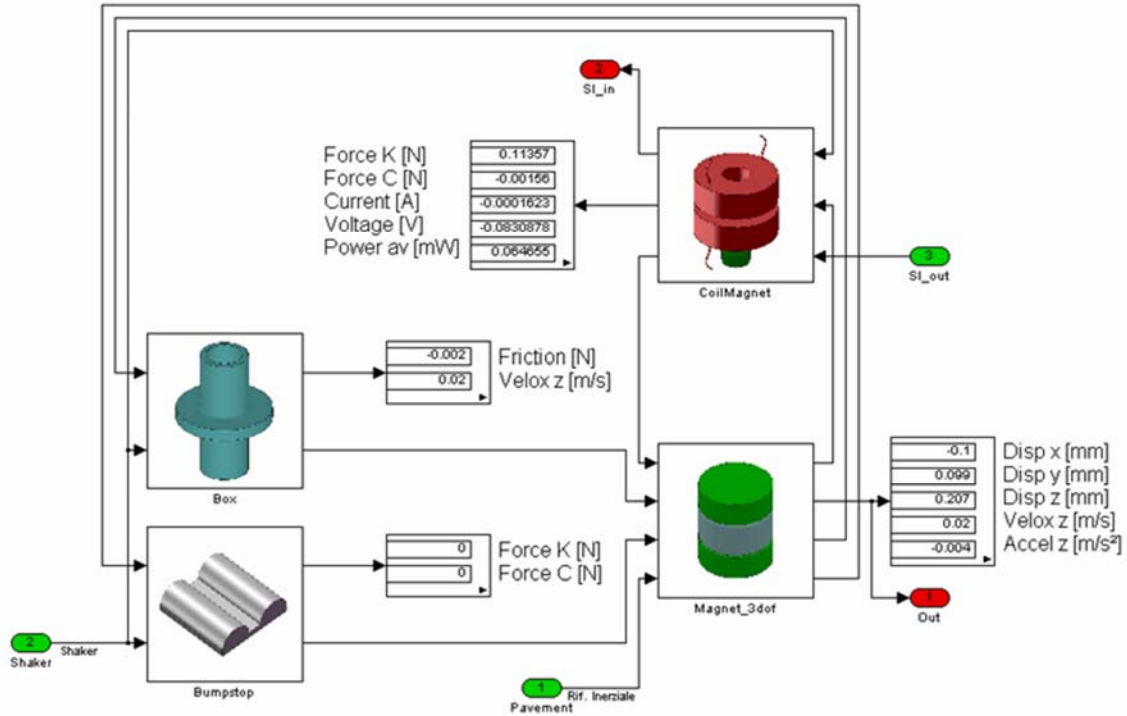


Fig. 4 Mechanical Sub-block

The mechanical model takes into account the movement of the floating magnet along three coordinate axes. After a preliminary investigation, the rotation around the axes has been considered negligible. The resultant 3-dof model is

$$\begin{cases} m\ddot{x} = F_x^C \\ m\ddot{y} = F_y^C \\ m\ddot{z} = F_z^C + F^{fric} + F^{bump} + F^{em} + F^{air} \end{cases} \quad (1)$$

where F_i^C is the input force along the i^{th} direction, F^{fric} is the force due to dry friction, F^{bump} is the Kelvin–Voigt elasto-dissipative force due to the bumpers, F^{em} is the magnetic force, F^{air} is the force due to pneumatic effect. The mechanical dynamic sub-block is shown in Fig. 4.

Parametric analysis of non-linear elements

Magneto-elastic effect

From the mechanical point of view, the electromagnetic simulation provides two force contributions: elastic and dissipative. The elastic component is due to the position of the floating magnet during its movement along the guide with respect to the preload magnet and it is dependent only on the z coordinate. The force values are estimated by a finite element model or from experimental measurements and can fit a negative exponential function in the empirical form:

$$F_{elastic}^{em}(z) = Ae^{-\left(\frac{z}{B}\right)^n} \quad (2)$$

where coefficient A , B and n can be estimated in a least-mean-square algorithm. A comparison between FEM force values and the negative exponential characteristic is shown in Fig. 5 (a).

It has been demonstrated for other empirical formula that this kind of system with a pure magnetic suspension has a nonlinear softening behavior [5]. Similar results can be evaluated with force in form of Eq. (2) with $0 < n \leq 1$.

The dissipative effect is due to the power supplied to the electric circuit:

$$F_{diss}^{em} = \frac{(e_1 - e_2) i}{\dot{z} - \dot{z}_{input}} \quad (3)$$

where e_1 and e_2 are the electromotive-forces induced in the coils. Their coupled contributions can be described as a function of z and \dot{z} :

$$e(z - z_{input}, \dot{z} - \dot{z}_{input}) = (e_1 - e_2) = -\frac{d\lambda_1}{dt} + \frac{d\lambda_2}{dt} = \left(-\frac{d\lambda_1}{d(z - z_{input})} + \frac{d\lambda_2}{d(z - z_{input})} \right) (\dot{z} - \dot{z}_{input}) \quad (4)$$

Coulomb friction

The friction between moving magnet and guide is calculated by an exponential model of the coefficient of friction depending on the relative velocity between the two components:

$$\mu_f(\dot{z} - \dot{z}_{inp}) = \mu_s e^{-\alpha(\dot{z} - \dot{z}_{inp})} + \mu_k (1 - e^{-\beta(\dot{z} - \dot{z}_{inp})}) \quad (5)$$

where constant μ_s and μ_k are respectively the adhesion and friction coefficient, while α and β are two parameters controlling the transition between static and kinematic behavior. An example of the trend of the friction model is shown in Fig. 5 (b).

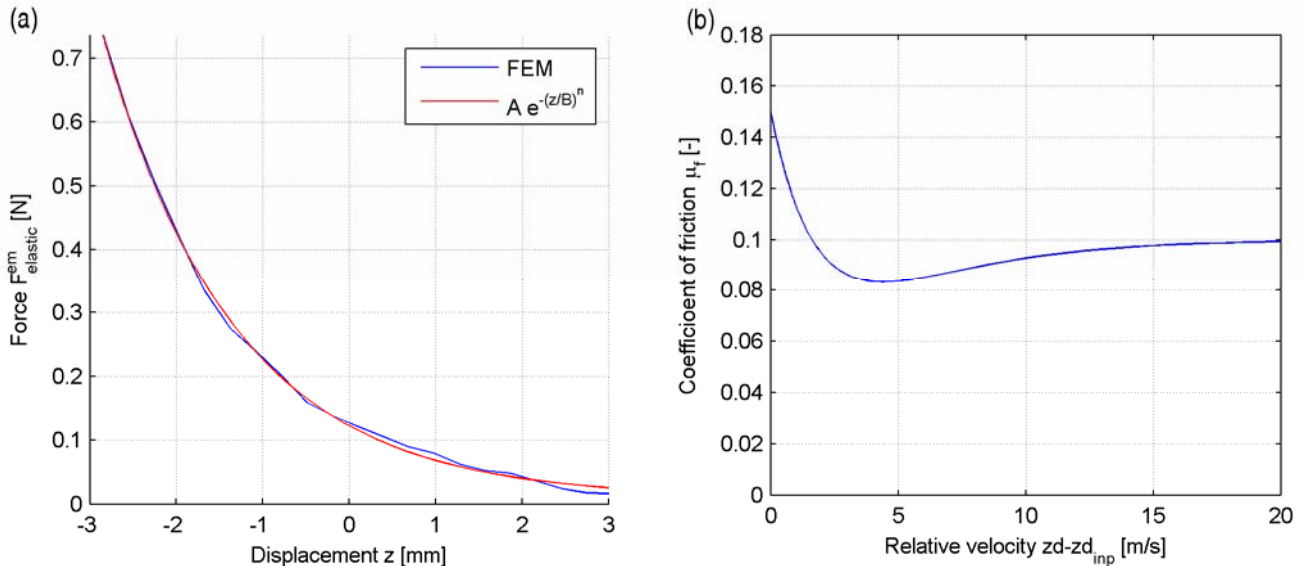


Fig. 5 Magneto-elastic force due to the interaction between moving magnet and preload magnet (a) and coefficient of friction vs. relative velocity (b)

End stroke bumpers

End stroke elastic bumpers are represented through a Kelvin-Voigt model [6] with a bi-linear spring. The resulting elasto-dissipative force F^{bump} is shown in equation (6):

$$F^{bump} = \begin{cases} -k_1(z - z_{inp} - z_{lim1}) - k_2(z - z_{inp} - z_{lim2}) - c(\dot{z} - \dot{z}_{inp}) & \text{if } z - z_{inp} > z_{lim2}, F^{bump} < 0 \\ -k_1(z - z_{inp} - z_{lim1}) - c(\dot{z} - \dot{z}_{inp}) & \text{if } z - z_{inp} > z_{lim1}, F^{bump} < 0 \\ 0 & \text{otherwise} \\ -k_1(z - z_{inp} + z_{lim1}) - c(\dot{z} - \dot{z}_{inp}) & \text{if } z - z_{inp} < -z_{lim1}, F^{bump} > 0 \\ -k_1(z - z_{inp} + z_{lim1}) - k_2(z - z_{inp} + z_{lim2}) - c(\dot{z} - \dot{z}_{inp}) & \text{if } z - z_{inp} < -z_{lim2}, F^{bump} > 0 \end{cases} \quad (6)$$

where $\pm z_{lim1}$ are the values of the relative coordinate $z - z_{inp}$ in which the moving magnet hits the bumpers and starts acting the first linear spring and $\pm z_{lim2}$ are the values beyond which acts the second linear spring. The force is equal to zero within $\pm z_{lim1}$ and when the magnet is moving away from the bumpers.

Pneumatic effect

When sliding into the guide the moving magnet acts as a piston into a pneumatic cylinder dividing it in two chambers. A displacement of the magnet creates a pressure delta that reacts to the movement. The two chambers are connected by the clearance between the magnet and the guide and the airflow in the clearance reduces the pressure delta. Moreover another reaction to the movement is due by the viscous friction:

$$F^{air} = F_{\Delta p}^{air} + F_{vis}^{air} \quad (7)$$

The main pneumatic contribute is the force due to pressure delta:

$$F_{\Delta p}^{air} = \frac{\pi d^2}{4} (p_2 - p_1) \quad (8)$$

where p_1 and p_2 are the pressure in the chambers and d is the diameter of the moving magnet.

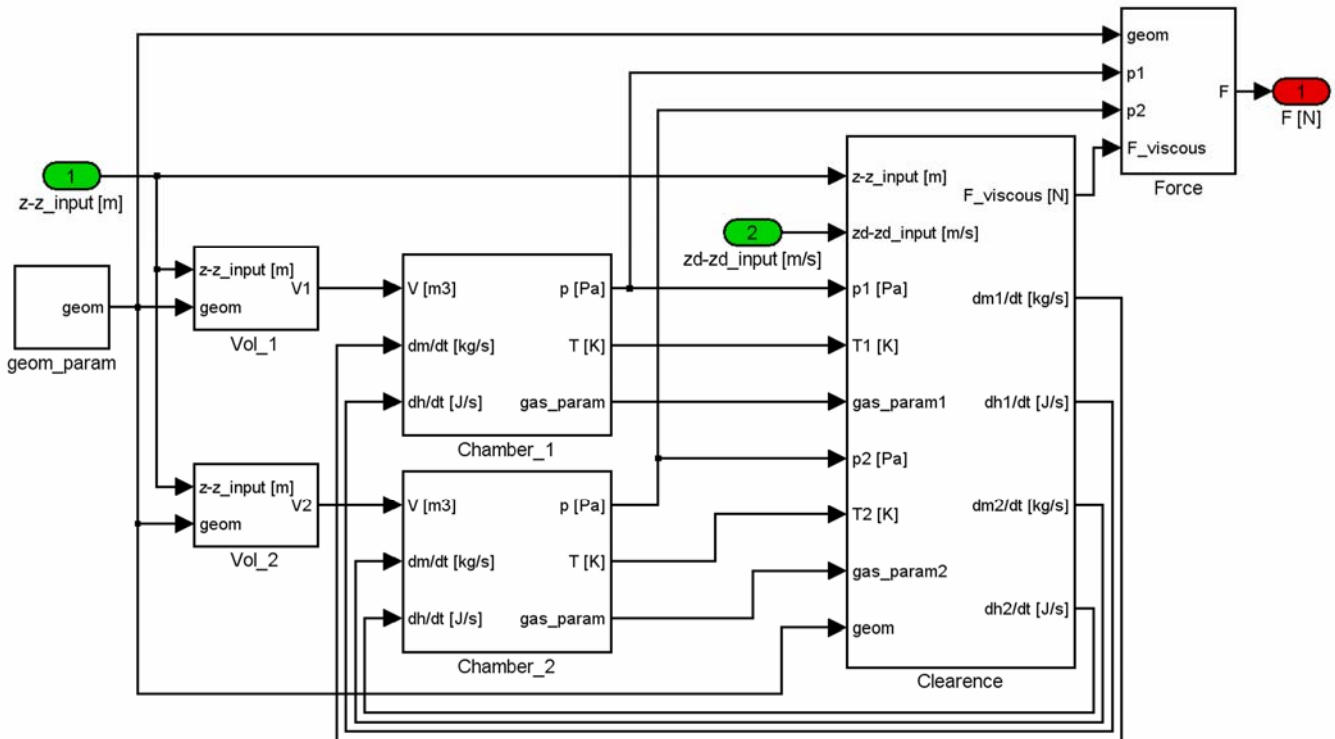


Fig. 6 Pneumatic sub-model

To calculate the force due to the pressure delta it is necessary to know the pressure in both chambers. To obtain these values a whole model of the pneumatic piston has been made (Fig. 6). In the chamber blocks are calculated the values of pressure and temperature depending on volume of the chamber and mass flow by first law of thermodynamics and ideal gas law. The value of mass flow is provided by the clearance block based on the equation [7]:

$$\dot{m}_{1 \rightarrow 2} = \frac{\rho \pi d c_r^3}{12 \mu h} (p_1 - p_2) \quad (9)$$

where ρ is the air density, c_r is the radial clearance, μ is the dynamic viscosity and h the height of the moving magnet.

All the temperature dependant parameters (constant pressure specific heat, constant volume specific heat, density and dynamic viscosity) are recalculated at any integration step. The model in Fig. 6 also calculates the force due to viscous friction proportional to the relative velocity between guide and magnet:

$$F_{vis}^{air} = -\beta_{vis} (\dot{z} - \dot{z}_{inp}) = -\frac{\pi \mu d h}{c_r} (\dot{z} - \dot{z}_{inp}) \quad (10)$$

Since the considered fluid is air the viscous force calculated above is smaller of several orders of magnitude if compared to the force due to pressure delta and can be neglected.

In order to simplify the model is possible to calculate the effect of the force due to pressure delta through a Maxwell model [8] where the spring represents the air elasticity and the dashpot the effect of the airflow in the clearance (Fig. 7).

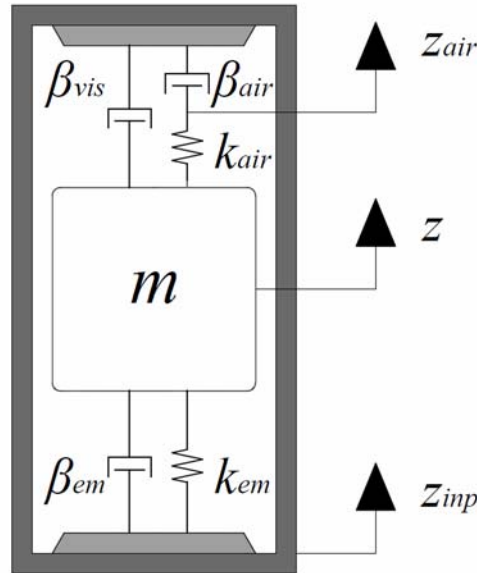


Fig. 7 The simplified Maxwell model of the pressure delta effect

The dashpot is connected to the guide and the spring to the moving magnet. To the point between spring and dashpot is assigned the coordinate z_{air} . The force equilibrium gives:

$$\begin{cases} F_{\Delta p}^{air} = -k_{air} (z - z_{air}) \\ F_{\Delta p}^{air} = -\beta_{air} (\dot{z}_{air} - \dot{z}_{inp}) \end{cases} \quad (11)$$

$$F_{\Delta p}^{air} + \frac{\beta_{air}}{k_{air}} \dot{F}_{\Delta p}^{air} = -\beta_{air} (\dot{z} - \dot{z}_{inp}) \quad (12)$$

The linearized model proposed above is effective only for small displacement. To extend the validity of the model is possible to introduce a nonlinear spring in place of the linear one. As an example in equation (13) the model is proposed with a cubic polynomial expansion.

$$\begin{cases} F_{\Delta p}^{air} = -k_{air,1}(z - z_{air}) - k_{air,2}(z - z_{air})^2 - k_{air,3}(z - z_{air})^3 \\ F_{\Delta p}^{air} = -\beta_{air}(\dot{z}_{air} - \dot{z}_{inp}) \end{cases} \quad (13)$$

To estimate the parameters $k_{air,i}$ is necessary to hypothesize that there is no clearance between magnet and guide. Thus $\beta_{air} = \infty$ and $z_{air} = z_{inp}$ and so the force due to the pressure delta can be calculated by the hypothesis of a generic polytropic transformation in the chambers:

$$F_{\Delta p}^{air} = -\frac{\pi d^2}{4} \left[p_{10} \left(\frac{l_{1C}}{l_{1C} + (z - z_{air})} \right)^\gamma - p_{20} \left(\frac{l_{2C}}{l_{2C} - (z - z_{air})} \right)^\gamma \right] \quad (14)$$

where l_{1C} and l_{2C} are the initial length of the chambers modified to take into account the dead volume of each chamber, p_{10} and p_{20} are the initial pressures and γ is an appropriate polytropic index. From equation (14) is possible to get the power series:

$$F_{\Delta p}^{air} = \frac{\pi d^2}{4} \left\{ \sum_{i=0}^{\infty} \left[\frac{1}{i!} \prod_{j=1}^i (\gamma + j - 1) \frac{l_{1C}^i p_{20} + (-1)^{i+1} l_{2C}^i p_{10}}{l_{1C}^i \cdot l_{2C}^i} (z - z_{air})^i \right] \right\} \quad (15)$$

and obtain the generic $k_{air,i}$ coefficient:

$$k_{air,i} = -\frac{\pi d^2}{4} \frac{1}{i!} \prod_{j=1}^i (\gamma + j - 1) \frac{l_{1C}^i p_{20} + (-1)^{i+1} l_{2C}^i p_{10}}{l_{1C}^i \cdot l_{2C}^i} \quad (16)$$

In Fig. 8 (a) is shown the comparison of the ideal gas law and its linear and cubic forms in the hypothesis of no clearance between the two chambers. The characteristic depends on the initial position of the moving magnet. If the magnet is not centered, as in Fig. 8 (a), the characteristic is asymmetric and the cubic gas law has a second order term.

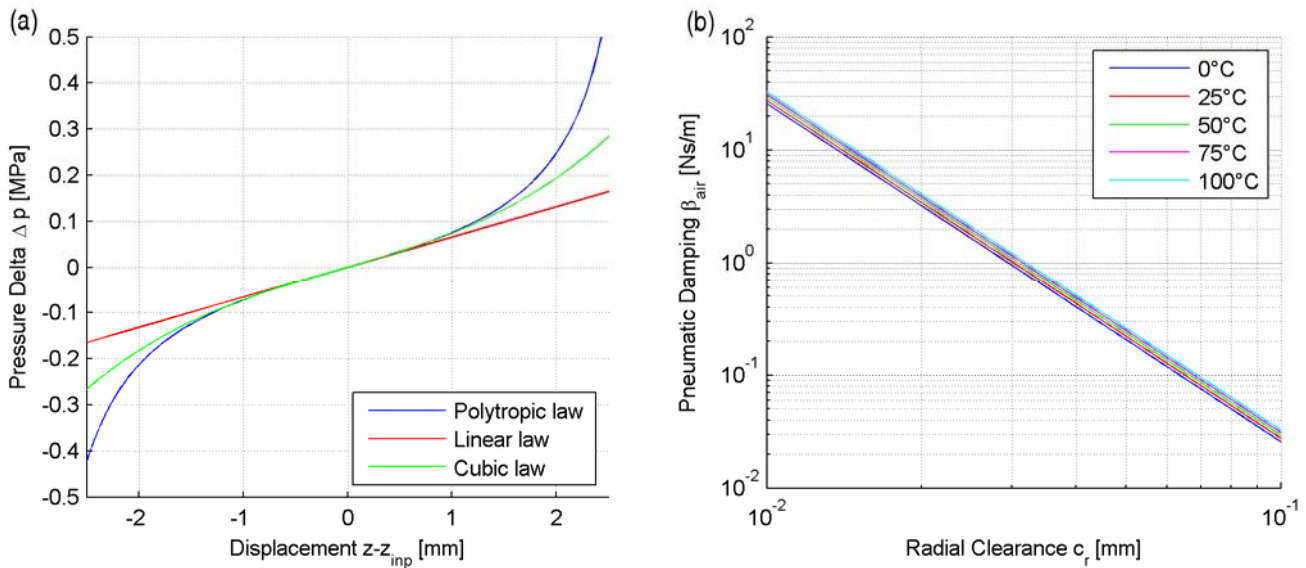


Fig. 8 Pressure delta vs. displacement in the hypothesis of no airflow in the clearance between magnet and guide (a) and pneumatic damping vs. radial clearance (b)

For small pressure delta values both linear and cubic forms can fit the polytropic law.

The parameter β_{air} can be estimated by extracting the pressure delta from the equation (9) through few simple steps obtaining:

$$\beta_{air} = \frac{\pi \mu h d}{c_r} \left(\frac{3 d^2}{4 c_r^2} + 1 \right) \quad (17)$$

Fig. 8 (b) shows the values of β_{air} for radial clearance from 0.01 to 0.1 mm at different temperatures for a moving magnet of 5 mm diameter and 5 mm height.

Comparison of different non-linear effects

In Fig. 9 are shown the effects of the different non-linear components on the moving magnet behavior at different vehicle speed. Two black dashed lines indicate the position of end-stroke bumpers. Starting from a system with only electromagnetic forces and bumpers have been added the effects of friction and air initially separated and then coupled.

Fig. 9 (a) shows the behaviors of the moving magnet at 30 km/h. At low speed it takes several oscillations to dissipate its energy and the equilibrium point of magnetic and radial forces is at about half of the stroke. Fig. 9 (b) shows that at 60 km/h there is only one relevant oscillation of the moving magnet. The small oscillations outside the footprint are not useful in energy recovering. The equilibrium point is noticeably lower in respect to the previous case. In Fig. 9 (c) at 100 km/h there is only one oscillation of the magnet and the moving magnet have to deform the bumper to reach an equilibrium point.

Shown results can vary a lot modifying choices about friction and clearance between magnet and guide. With a clearance of several tenth of millimeter on the diameter the pneumatic effect is almost negligible.

In order to improve the energy scavenger performance in a wide range of vehicle velocities, two complementary dynamic behaviors are taken into account:

- for low velocities, the non-linear elastic magnetic force is used for tuning the adaptive mechanical resonance of the energy scavenger and for increasing the oscillations of the floating magnet around the stationary state;
- for intermediate and high velocities, the resonant contribution is progressively less important and the typical one-stroke behavior is adequate for the power recovery, as a consequence to the increasing number of revolutions in time of the wheel.

Experimental validation of the model

In Fig. 10 the block-oriented model and the experimental outcomes are compared. The test is conducted on a shaker and reproducing the wheel profile without the mean centrifugal acceleration at 40 km/h. Due to the absence of a mean value of force, the prototype has been modified with symmetric preload obtained adding a second fixed magnet with repulsive force with respect to the floating magnet. A good agreement is found in the comparison between theoretical model and experiments.

Conclusions

This paper analyses through an integrated block oriented methodology the dynamic behavior of the moving magnet of an electro-magnetic energy scavenger. The effects of the different non-linearities on the system have been compared.

The paper underlines the separated and integrated effects of magnetic, friction, dead-zone end-stops and pneumatic effects of the floating magnet sliding into a calibrated guide. A convenient choice of clearance between moving and fixed parts can be used to create an effective air brake preventing or softening shocks with end stops and to modify system dynamic.

The equivalent parameters for a simplified Maxwell model with a polynomial spring and a linear dashpot of the pneumatic effect have been calculated as function of the device geometry.

The optimization design of these parameters demonstrates effective performance of the energy scavenger. Simulations and some numerical comparisons try to empathize these results.

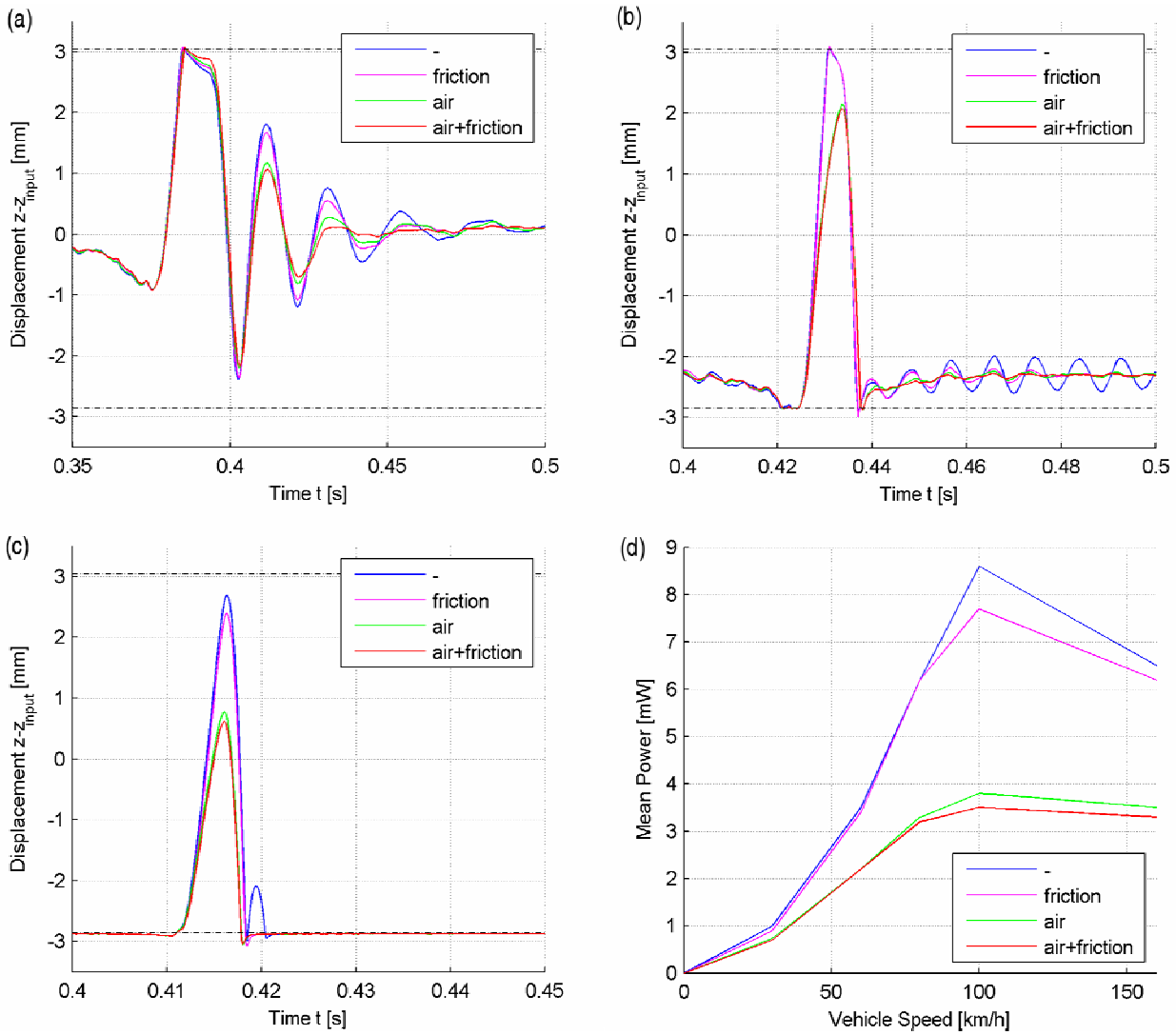


Fig. 9 Moving magnet displacement at 30 (a), 60 (b) and 100 (c) km/h in a wheel round and mean power output at different vehicle speed (d)

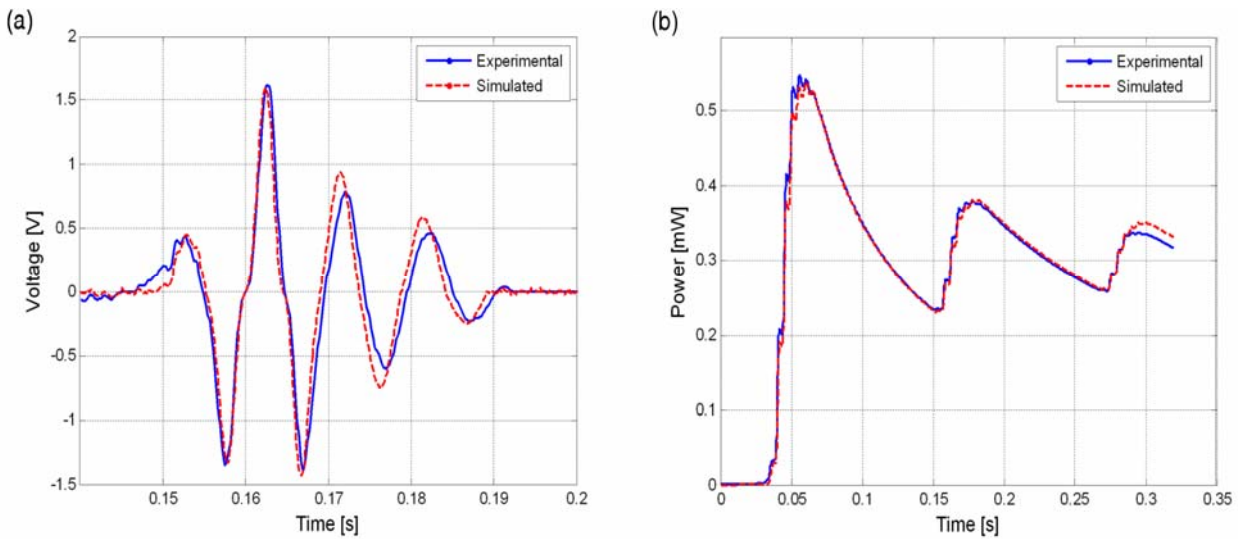


Fig. 10 Comparison between experimental and simulated results for voltage (a) and power (b) output

Acknowledgments

The work has been performed under a research project with Pirelli Tyre S.p.A. The authors would like to thank Dr. Giorgio Audisio, Dr. Federico Mancosu, and Dr. Massimo Brusarosco from Pirelli Tyre S.p.A. for their enthusiasm and driving force in the project.

References

1. Paradiso, J.A., Starner, T., “Energy scavenging for mobile and wireless electronics”, *IEEE Pervasive Computing*, vol. 4(1), pp. 18-27, 2005, doi:10.1109/MPRV.2005.9.
2. Mann, B.P., Sims, N.D., “Energy harvesting from the nonlinear oscillations of magnetic levitation”, *Journal of Sound and Vibration*, vol. 319(1-2), pp. 515-530, 2009, doi:10.1016/J.JSV.2008.06.011.
3. Bonisoli, E., Canova, A., Freschi, F., Moos, S., Repetto, M., Tornincasa, S., “Dynamic Simulation of an Electromechanical Energy Scavenging Device”, *IEEE Transactions on Magnetics*, vol. 46(8), pp. 2856-2859, 2010, doi:10.1109/TMAG.2010.2044156.
4. Velardocchia, M., D’Alfio, N., Bonisoli, E., Galvagno, E., Amisano, F., Sorniotti, A., “Block-oriented models of torque gap filler devices for AMT transmissions”, SAE Technical Paper 2008-01-0631, 2008, doi:10.4271/2008-01-0631.
5. Bonisoli, E., Vigliani, A., “Passive elasto-magnetic suspensions: nonlinear models and experimental outcomes”, *Mechanics Research Communications* vol. 34(6), pp. 385-394, 2007, doi:10.1016/j.mechrescom.2007.02.005.
6. Maia, N., Silva, J., “Theoretical and Experimental Modal Analysis”, Research Studies Press Ltd., New York, ISBN 978-0863802089, 1997.
7. Fox, R.W., McDonald, A.T., Pritchard, P.J., “Introduction to Fluid Mechanics”, John Wiley & Sons, Hoboken, ISBN 0470234504, 2008.
8. Li, Z. Q., Xu, Y. L., Zhou, L. M., “Adjustable fluid damper with SMA actuators”, *Smart Material and Structures*, vol. 15(5), pp. 1483-1492, 2006, doi:10.1088/0964-1726/15/5/038.

Practical Trouble Shooting Test Methodologies

D.L. Brown A.W. Phillips M.C. Witter
University of Cincinnati Structural Dynamic Research Laboratory
Cincinnati Ohio 45221

Abstract:

Trouble shooting acoustic, vibration and controls problems has been a historical application where modal analysis has been employed to characterize the troubled system or systems. For many of the troubled systems no existing analytical models or previous test results are available. Many problems involve systems which have very high overhead or loss production cost, therefore the time required to obtain a solution is important. This paper will examine test methods and characterization techniques which are well suited to trouble shooting applications including the use of semi-autonomous and autonomous modal parameter estimation and modal modeling methods which can be used to simplify and speed up the process.

Acronyms

| | | | |
|------|---|------|---|
| 3D | Three Dimensional | HP | Hewlett Packard |
| ADC | Analog Digital Converter | IRF | Impulse Response Function |
| ARMA | Auto Regressive Moving Average | LSCE | Least Squares Complex Exponential |
| CMIF | Complex Mode Indicator Function | MAC | Modal Assurance Criteria |
| EFRF | Enhanced Frequency Response Function | MDOF | Multiple Degree-of-Freedom |
| EMIF | Enhanced Mode Indicator Function | MIMO | Multiple-Input Multiple-Output |
| ESSV | Extended State Space Vector | MRIT | Multiple Reference Impact Testing |
| DFRF | Directional Frequency Response Function | NASA | National Aeronautics and Space Administration |
| DOF | Degree-of-Freedom | PTD | Poly Reference Time Domain |
| DOT | Department of Transportation | SDA | System Dynamic Analysis |
| DSIT | Digital System Interface Transmitter | SDOF | Single Degree-of-Freedom |
| DSP | Digital Signal Processing | SDRL | Structural Dynamics Research Laboratory |
| DSS | Digital Sensor System | SDRC | Structural Dynamics Research Corporation |
| ERA | Eigenvalue Realization Algorithm | SDOF | Single Degree of Freedom |
| GVT | Ground Vibration Test | SST | Spatial Sine Testing |
| GUI | Graphical User Interface | SVD | Singular Value Decomposition |
| FEM | Finite Element Model | UC | University of Cincinnati |
| FRF | Frequency Response Function | UMPA | Unified Matrix Polynomial Algorithm |
| FFT | Fast Fourier Transform | UIF | Unit Impulse Function |

Introduction

Speeding up and simplifying the measurement process for Frequency Response Functions was the stimulus for the development of digital Fourier analysis in the late sixties. The main application at the time was troubleshooting machine tool chatter problems but in the mid sixties in the University of Cincinnati Structural Dynamic Laboratory (UCSDRL) a large number of industrial and government projects were being run through the lab. Some were used as Masters and PhD thesis topic but many were simple industrial troubleshooting problems. The volume of simple trouble shooting work was interfering with the educational process at the university so in the late sixties several spin-off commercial companies were formed by the university staff and students. The most successful was the Structural Dynamic Research Corporation (SDRC) which had a large structural testing operation but whose product development was directed towards computer aided design. A number of

smaller companies spun-off the university or SDRC into specialized testing areas or in developing products for testing.

As mentioned, above Fourier Analysis was one of the developments in the late sixties and early seventies which had immediate impact on the structural dynamics and controls measurement area. The problem of interest was solving machine tool chatter which is a self excitation vibration problem. It is modeled as a close loop feedback problem that becomes unstable under certain cutting conditions. It is necessary to measure the open loop characteristics of the machine tool structure which is done by measuring the Directional Frequency Response Function (DFRF) between the cutting force and the relative motion between the tool and the work piece of the machine tool. In the seventies Cincinnati was the machine tool manufacturing center of the world with over thirty companies in the Cincinnati area. The University of Cincinnati is a mandatory Cooperative Engineering School a number of the students at the undergraduate and graduate worked in or was supported by the machine tool industry. As a result, it was common practice to get both undergraduate and master level students involved in some of the trouble shooting projects. Master thesis projects were often defined to investigate improved methodology for trouble shooting. One of these projects was to investigate impact testing as alternate testing method for measuring Frequency Response Functions (FRF).

Fortunately, in the 1965 the Fast Fourier Transform was developed and this was implemented on a large hybrid computer in the Electrical Engineering Department at the University of Cincinnati and impact testing was demonstrated to be practical by testing a small milling machine base and comparing the results from impacting testing and sine testing.

In 1971 using an HP 5451A impact testing and measuring the Directional Frequency Response Function and mode shapes of a small milling machine with impact testing became practical. The results, of this work were reported and demonstrated at an International conference in 1972 [1,2,3,4]. As a result of this exposure, applications of Fourier Analysis spread into many other industries. Initially, ninety percent of these applications were trouble shooting applications. It should be noted that currently, probably less than ten percent of the applications are trouble shooting and the majority are for verifying or updating Finite Element or Boundary Element analytical models.

In this paper, the practical methodologies used in trouble shooting application will be reviewed. It should be noted that there are two general classes of trouble shooters available. The first are the companies and/or individual consultants that specialize in trouble shooting special types of vibrations, controls of acoustic problems. The second group consists of individual consultants who freelance. These groups often work together with the freelancer working as a consultant or as an extra hand on specific trouble shooting or model verification projects.

Trouble Shooting

Most modal testing is planned with a pretest analysis and a clear set of test objectives whereas trouble shooting is very often a spontaneous action based upon a serious vibration or acoustic event that has suddenly become a problem. In the worst case scenario, there is very often no vibration historical data or pretest information available plus no one at the agency requesting the test that is familiar with vibration testing procedures or with a method of characterizing the excitation forcing function acting on the system. In the best case scenario, the problem is just the current episode in a recurring problem. As result, the troubleshooter's toolbox has to be large in order to cover the general areas of vibration, acoustic and controls. There are tools that are used in the field and tools for post processing the data back at the office. In this paper the on-site testing will be reviewed since the post processing tools are similar to the tools used in processing laboratory test data. The on-site tools data reduction tools are simple and designed to get a quick look at the data and then to gather and record sufficient data which can be processed in much more detail in the post processing phase. The biggest difference between on-site testing and laboratory testing is that a great deal of operating response data is required to identify and characterize the nature and/or source of the problem. Modal data is also collected on site to characterize the structural dynamics of the system under test. A quick analysis of the modal data is performed to determine good locations to add structural tuning devices (Mass Dampers, stiffeners, etc) and to determine if large forced responses are possibly due to structural resonances. Based upon the results of this initial effort, the modal database is expanded so that a more complete modal analysis can be performed as part of the post processing phase.

If the pretest analysis indicates that structural tuning device is a possible solution then a set of driving point and cross impedance measurements are taken at points where the vibration levels need to be controlled and at the locations where the tuning device and/or devices are installed.

On-site Testing

On-site testing is the most critical phase of most trouble shooting projects. The 1st stage requires understanding the forcing functions which are the primary contributors to vibration and acoustic problems. These forcing functions can be due to the operation of the device with the problem or can be environmental forcing functions due to other devices. This testing phase can require a wide range of sensors to monitor the vibration, noise levels, rotational speeds of various rotating, etc. (for example typical sensors are accelerometers non-contacting displacement sensors, load cells, strain gages, tachometers, shaft encoders, etc). The time histories of these sensor array need to be recorded for post processing and portion of it needs to be processed in real time to monitor the test and to make decisions about the direction of the test. Special signal processing software packages are useful for the real time processing. {Spectrums (maps, narrow band, octave, order tracking etc)}.

The 2nd stage very often involves performing a modal test to determine how the system responds to external forcing functions. Most modal tests are performed by exciting the system with measured forces and measuring the responses with accelerometers or some other displacement measuring sensor. This data is used to compute a set of Frequency Response Functions (FRF) which can be used to estimate the systems modal parameters (eigenvalues, eigenvectors and modal scale factors). One of the most common testing method used during trouble shooting is conducting a Multiple Reference Impact Testing (MRIT) since it requires minimum fixturing, instrumentation and test set up. This method is well documented in the literature with hundreds of references since it's development in the late sixties. A complete review of MRIT was presented in the IMAC 2010 conference[15] which includes a number of historical references.

Electro-mechanical and hydraulic exciter have been used historically for a number of cases where the forcing function cannot be applied conveniently with transient testing method. Historically, very small but powerful hydraulic have been used on machine tools and on rolling mills to measured directly the Directional Frequency Response Function which was used to predict regenerative self excited vibration problems (machine tool chatter or wash boarding of rolls in rolling mills, etc). Large hydraulic actuators have been used on large infrastructure or pieces of equipment. Arrays of smaller electro-mechanical exciters have be used on machine tools, equipment racks, etc.

In the seventies there was a significant effort to development multiple input excitation techniques which would minimize "leakage" and the influence of non-linearity's on the measurement of FRFs. These methods have proven to be very good for conducting laboratory tests where signal processing requirements are well defined. For trouble shooting case it is not clear in many cases exactly what you are looking for in the data. Many of the important discoveries are made in the post processing of the data. Therefore, all of the time data taken during the on-site test should be recorded in a manner so that it can be reprocessed using different signal process in the post processing phase. As a result, if exciters are used, the best excitation signal is uncorrelated pure random data excitation signals. With uncorrelated random, in the post processing it is possible to zoom the data to increase the frequency resolution within the Nyquist frequency. The inputs are randomized so signal processing can reduces non-linear distortion errors and cyclic averaging can be used to control leakage. In fact, in the early seventies, one of the fantasies was to be able to ADC throughput time data so that the data could be reprocessed with different signal processing but it was not until the nineties when inexpensive data storage became available that the fantasy became a reality.

The 3rd stage of the onsite processing is to extract the modal parameters from the measured FRF's. The modal parameter estimation techniques that are used onsite for trouble shooting have been simple one DOF quadrature peak picking methods in the seventies and eighties. In the early 90's, the method of choice became the CMIF parameter estimation using the imaginary part of the Multiple Input Multiple Output(MIMO) FRF matrix measured with either the MRIT or MIMO testing methods. This method uses the Singular Value Decomposition (SVD) to obtain an excellent approximation of the best least square estimate of the quadrature mode shapes from multiple reference Frequency Response Function data. It was used with good success on infrastructure testing in the early to mid nineties.

It requires moderate experience to interpreting a CMIF plot and subsequently selecting the peaks in the SVD plot which correspond to the eigenvalues of the system being tested. The singular value vector at the selected peak is an estimate of the systems eigenvector. This vector is used to generate a Enhanced Frequency Response Function (EFRF) which can be used to

estimate the systems eigenvalues and modal scale factors. The eigenvalues, eigenvectors and modal scale factor define a modal model of the system being tested. A more detailed description of this method can be found in the following references[8,9,10,11].

In the post processing phase a narrow band frequency domain model has been used to improve the estimate of the modal parameters in frequency bands where the modal density makes it difficult to separate the modes using the CMIF method. The process is referred to as the Enhanced Mode Indicator Function (EMIF) method and its description in the following reference [12].

In the past 10 years a simple method which was originally developed as part of the SDA II course has become a method which is almost a purely autonomous procedure. In the SDA II the students have to program a UMPA model which can simulate nearly all of the commercial modal parameter algorithms in a period of just a few weeks. In order to write the programs in a few weeks the students are instructed to not waste their time on developing a Graphical User Interface (GUI) or any other graphical aids such as stability diagrams to aid in filtering out computational modes but to just concentrate solving for the coefficients of the basic UMPA algorithm. The UMPA was formulated to emulate an ERA algorithm which could be used to emulate all the standard time domain methods. CAE and PTD were emulated by using a state space expansion to reduce their high order to a 1st order ERA formulation. Instead of referring to input and output Degree-of-Freedom, the dimension of UMPA model is referred to in terms of a long or short dimension where the long dimension could be a reference to either the inputs or the outputs depending upon the testing method used to gather the data (roving inputs or fixed inputs).

Test Log

A very important part of any test is to keep a very good and detail test log. This is particularly true for trouble shooting applications. Over the years one of the required test items is a good camera which can be used to document every exciter and sensor location. Pictures of test article should be taken from every angle and labels and bar codes should be used to identify each component, etc.

In the sixties and seventies Polaroid cameras were used for instant photos and 35 mm slide cameras for high quality photos. Today digital cameras have become inexpensive and very powerful and for less than 300 dollars a relatively small digital camera with a 12 mega pixel sensor, 26x zoom lens, HD movie with audio. An audio tag can be attached to each picture and thousands of pictures can be stored on a small Secure Device (SD) memory chip. Programs like Photomodeler can take the photos and automatically digitize points on the test object using photo reflective circular bar code targets. In [Figure 1](#) a photo taken recently of a sensor located on test object from a distance of fifteen feet is shown. It is possible to read the serial number of the sensor and the point on structure.

Case History

Two stations used to machine transmission housing were experiencing chatter problem where on one station the problem was intermittent and on the second station the chatter problem was totally unacceptable. Only one machining station was required for production and the second was a backup in case the first needed servicing. This transfer line was in the processing of replacing an older line which was currently running production.

The problem was to determine a fix for the inoperable station and to



Figure 1 Picture of a typical transducer location



Figure 2 -- Spindle

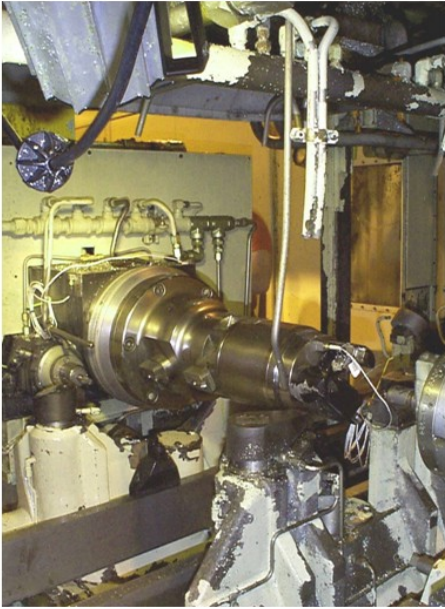


Figure 3 Alternate View Spindle

the cutting spindle is shown and alternate view of the spindle is shown in Figure(3). It is designed to fit inside the housing of automatic transmission case and machine 13 internal surfaces.

The machine cycle for machining consisted of 10 sec cutting cycle with 13 cuts being made simultaneously on the interior surface of the automatic transmission case. The chatter was occurring on only one surface which was sealing surface for the

improve the performance of the underperforming station. The test was to be conducted during a two to three hours test window per night on the third shift since the first two shifts were in the process of bringing the new transfer line on-line. It was to take several months to bring the transfer line on-line and the trouble shooting would be worked into that schedule. The problem on both stations was a machine tool chatter problem. It was anticipated that the on-site testing could take 10 to 20 hours. The fix might involve modifying the test stands by adding a mass damper or by making structural changes.

The test crew consisted of two UCSDRL graduate students which were hired as consultants by The Modalshop in Cincinnati who was under contract with the auto company to solve the chatter problem. The initial test was to measure vibration data at accessible points as close to the cutting zone as possible.

The test equipment was supplied by the The Modalshop and consisted of a 48 channel HP VXI data acquisition system data acquisition system. The sensors consisted of two pound impact hammer, 10 - 1 volt per g tri-axial accelerometers, 2 tear drop, 10 mv per g, and 5 single axis 100mv per g. Several pictures of the test site are shown for general reference. In figure (2) a picture of



Figure 4 -- Impacting Point 10

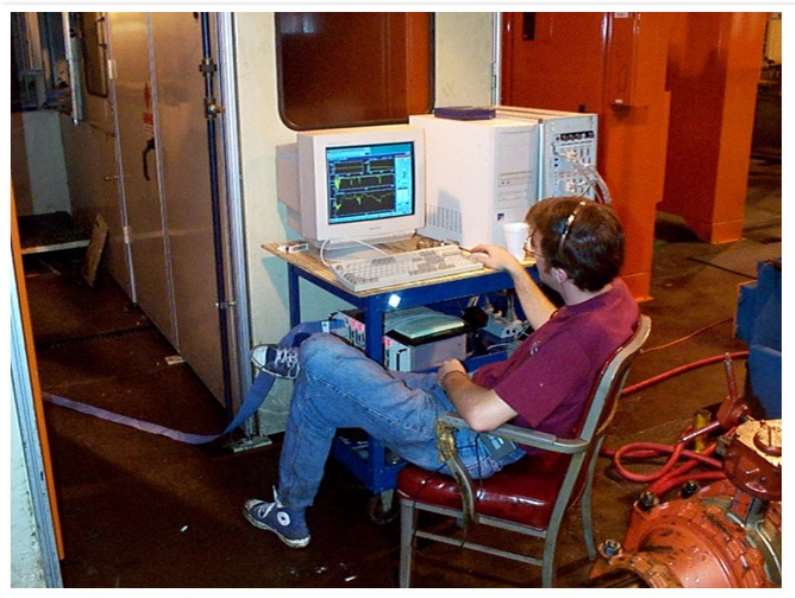


Figure 5 VXI System

drive shaft. This was an important surface where the surface finish and accuracy were critical. Unfortunately, this surface could not be cleaned up by a subsequent machine process and the complete transmission housing had to be discarded if chatter occurred. The 1st test was to measure the vibration due to the chatter and check this frequency against the chatter marks on the

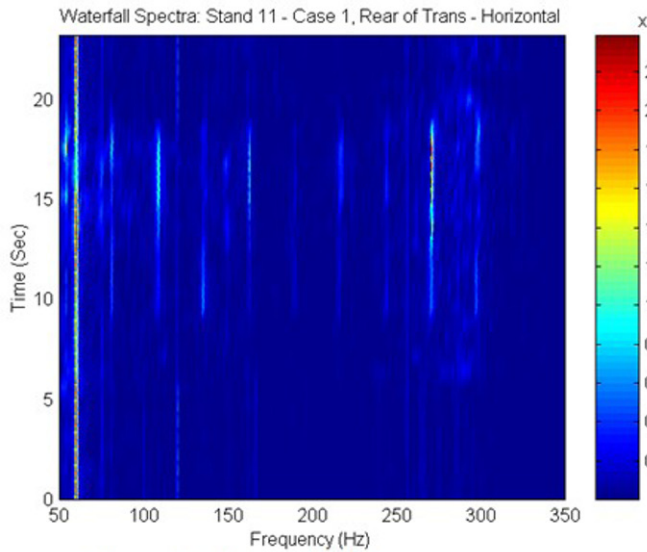


Figure 6 Water fall Spectrum

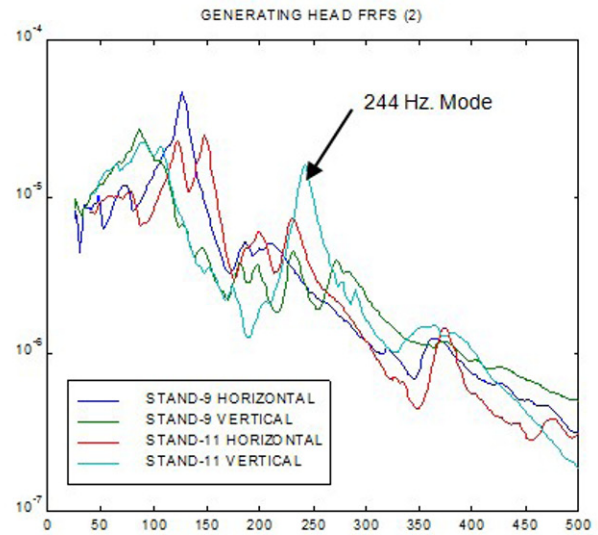


Figure 7 – Generating Head FRFs

transmission housing. A small accelerometer was mounted on the exterior surface of the transmission during the cutting process and the waterfall spectrum was measured during the cutting process. The chatter frequency shows up clearly in the waterfall spectrum (See Figure 6) and this frequency corresponds with the observed chatter marks on the transmission housing.

The next step was to measure the Directional Frequency Response Function (DFRF) which is the relative motion between the cutting tool and work piece due the cutting force. This measurement was made using impact testing. It was not possible to impact of the cutting spindle without removing the housing since the spindle was completely inside of the transmission housing. The only possibility of impacting on the spindle was to drill a hole through the transmission housing and use the modal punch to impact through the hole. The modal punch is PCB product which can be used to impact hard to reach points during an impact test. An examination of mechanical design of the machine tool suggested that the work piece support and the cutting spindle support were basically uncoupled. This was verified in the subsequent modal test. As a result, the DFRF could be measured by impacting on the transmission housing; then removing the housing and then impacting on the spindle and then estimating the relative motion to the relative forcing function.

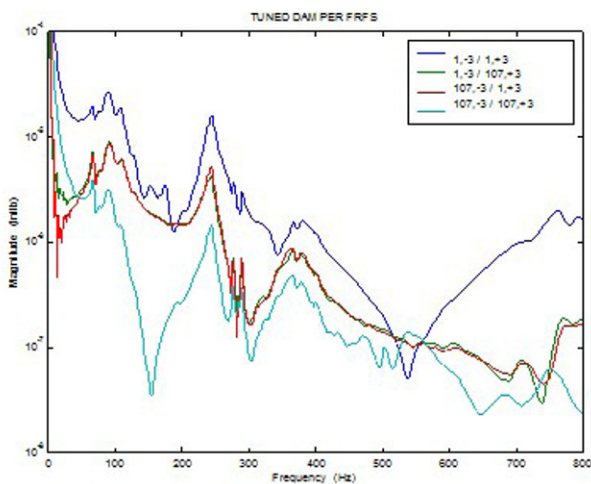


Figure 8 – FRFs Impedance Model

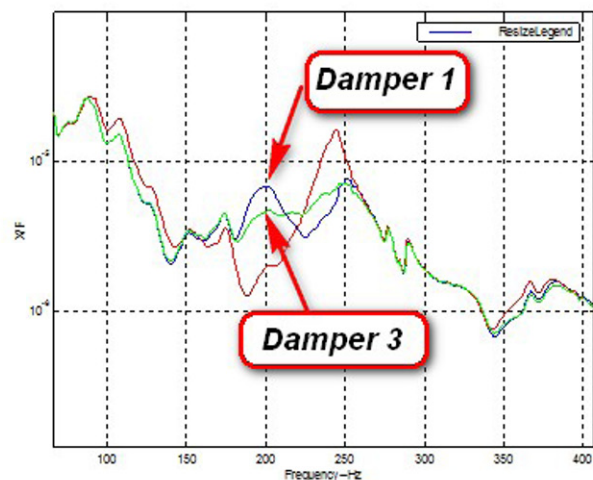


Figure 9 – Damper Design

This testing process was repeated upon both machining stations and the results are shown in Figure 7. There is a significant

resonance at 244 Hz on the machine which is responsible for the significant chatter that is observed in the waterfall spectrum data. The chatter is not at the frequency of the mode but normally at a slightly higher frequency. This phenomenon is consistent with the close loop response of the single point machine tool chatter feedback loop.

The next step was the make measurements that could be used to predict the influence a mass damper mounted on the machine tool. The mass damper could not easily be build into the spindle but it could be mounted on the head stock. Driving point FRF measurement at the spindle end and the point on the head stock and the cross measurement between the two locations were made. This data is shown in [Figure 8](#). Using this data a simple impedance model was built and used to predict the effect of several mass damper designs mounted on the head stock. The results are shown in [Figure 9](#). This damper would improve the bad machine to be comparable with good machine. However, the good machine was marginal.

The next phase was to perform a complete modal test on the two machines to develop a better understanding of their dynamics. There were two questions that needed to be answer why did one machine have a strong resonance at 144 HZ and the identical second machine had a much smaller response in the same frequency band and secondly what could be done to improve the performance of the good machine.

Two complete MRIT tests were performed on the two machines. Five points were selected as impact points and reference accelerometers were mounted at the impact points and 10 tri-axial accelerometers were roved over the structure. This is one of standard testing protocols for MRIT testing.

The modal data was processed with The CMIF and EMIF parameter estimation procedures using the X-Modal program developed in the UCSDRL. These methods have been the methods of choice for many of the MRIT trouble shooting cases and performed well on the data taken during this trouble shooting project.

The initial prognosis was that the most likely reason for the difference was due to some problem within the spindle but the modal test indicated that there was abnormal deformation of the headstock on the bad machine. See [Figure 10](#). The head stock was subsequently removed and examine and it was discovered that one of the internal stiffeners in the head stock weldment was missing.

The modal analysis also indicated that modes which contributed to intermitted chatter problems problem around 100 and 150 Hz had modes with significant motion between the machine tool foundation and machine tool. In other words, the machine was not properly mounted to the foundation. This was a fixed by a machine repairman by simply bolting the machine properly to the foundation. The headstock was replaced on the bad machine and it was fasten to foundation. Correcting these two

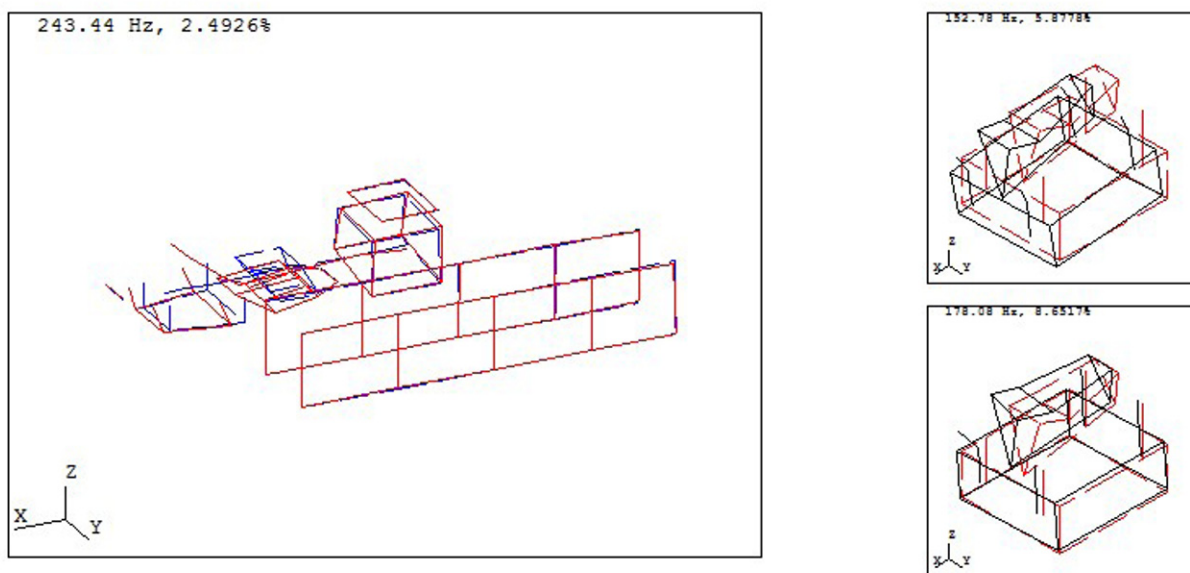


Figure 10 – Mode Shapes

problems corrected the chatter problems on the two machining stations which machined the internal surfaces of the automatic transmission case.

This trouble shooting case is typical of many of the machine test that had been performed historically.

Case 2

The second case is not a case history of solving a trouble shooting problem but a review of the development of a fairly autonomous testing method that will have impact on future trouble shooting application because it will simplify the process of extracting modal parameters. The technique is a methodology that evolved from the System Dynamic Course at the University of Cincinnati. In this course the students have to develop their own MATLAB programs to process raw time data into Frequency Response Functions (FRF). Then take their FRF data and extract the modal parameters with their own MATLAB programs and then develop both a modal modeling and an impedance modeling program to predict modifications to a system in the laboratory based upon a model they built from their own modal database. This sound impossible considering that at any one step in this parameter estimation process was a Masters of PhD thesis project. However, for the past 15 years students have been quite successful at fulfilling the course requirements.

With the development of the UMPA modeling concepts, the programming of the various parameter estimation has been simplified to the point where in a matter a three to four weeks the students develop MATLAB code which can emulate most of the current commercial parameter estimation algorithms. They could program the algorithms but they had to come up with a simple method of sorting out the computational modes. Sorting out computational modes has been a historical problem and in the last 5 to 10 years and it has become one of the main selling points for commercial software.

The student discovered a fairly simple method. One of the techniques they tried was to use the spatial information as a filtering agent. This was done in the early days by NASA which used main frame computers and the ERA algorithm to estimate their modal parameters. They ran two solutions based upon different starting times through the ERA algorithm and checked the correlation between the estimate eigenvectors and found that this correlation was a fairly effective filter for eliminating computational modes. The students modified this method by using the 1st order UMPA model and instead of different starting values for the two solutions they used two different objective functions to minimize the noise. They normalized the model with respect to the A0 term and the A1 term. They correlated the state space eigenvectors between the two solutions using the Modal Assurance Criteria and found that in general this was a very effective filtering method. The computational modes were not well correlated relative to each other while the system modes showed a fairly high degree of correlation. The eigenvalues were not used in the filtering process but could be used as an indication of the variance on the eigenvalue estimates. If there was little variance then there was some confidence that the eigenvalues were fairly well estimated. With no other data but the two estimates, the average value, the eigenvalues for a given mode was used as the best estimate of the eigenvalues.

Once the eigenvalues and eigenvectors are estimated then it is necessary to get estimate for the modal scale factors for each mode. There are a number of methods for doing this but the student's could take advantage of the fact that they had to estimate the modal scale factor in the course when they were programming the CMIF method. The EFRF for a given mode could be computed using the estimated eigenvector. Since they already had a estimate of the eigenvalues they only had to fit for the residue of the EFRF for the modal scale factor. Once they had this estimate of the modal scale factor, they had a truncated modal model of the system.

One way of checking whether the modal model was good was to compare the CMIF plot from the measured data with a CMIF plot of the synthesized data. If they got a good comparison then they could have some confidence in the modal model. To get a better comparison, they would need to fit the measured data for residuals and included these terms when they synthesized the data.

In order to demonstrate this method, three input shaker data for the C-plate was processed using a simple student MATLAB UMPA program. The UMPA model was a long dimension model with 13 states. The number of states is the only parameter that needs to be set in this method for the computation and the MAC value can be set to filtering level for the eigenvectors. In this example only eigenvectors with a MAC values above 0.98 were saved.

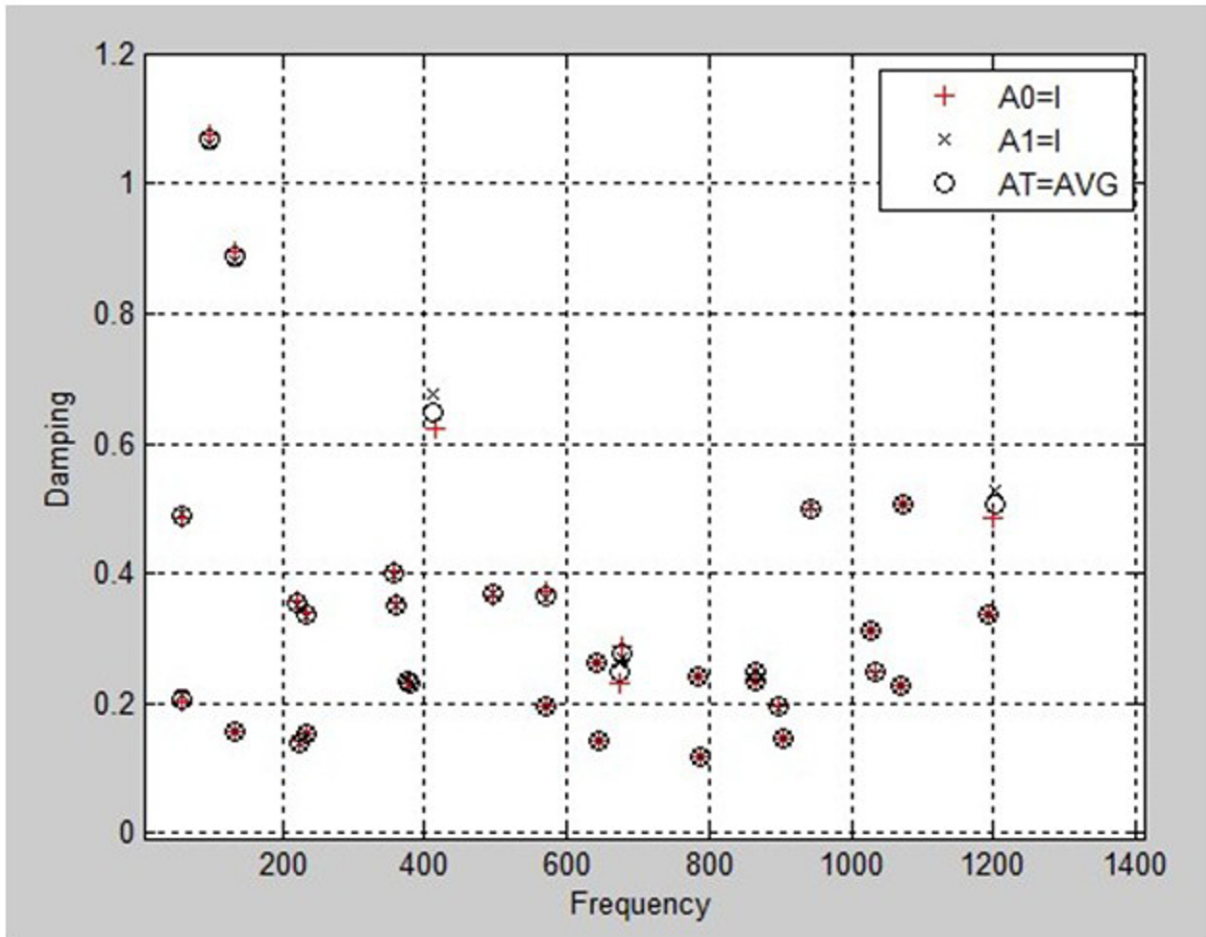


Figure 11 – Plot of pole location for C-Plate

The number of states times the length of the long vector is equal to the number of estimated eigenvalues. For example, in this case the number of responses is equal to 30 so the number of estimated eigenvalues is 13 time 30 or 390 eigenvalues. It takes approximately 1 minute to solve for the eigenvalues and eigenvectors of the system and filter the results using a fairly ordinary current generation notebook computer running windows. The resulting poles are display plotted in the complex plane; See [Figure \(11\)](#) and the filtered eigenvalues and eigenvectors are saved in a MAT files which acts as input to a MATLAB program which calculates the EFRFs . These EFRFs are curve fits to determine their residue which is equal to modal scale factor. The eigenvalues, eigenvectors and modal factors are then stored in a file along with the geometry of the plate. This is a complete modal model for the system. This process is almost completely autonomous the only parameters were the number of states and MAC filter set at the beginning of the parameter estimation process.

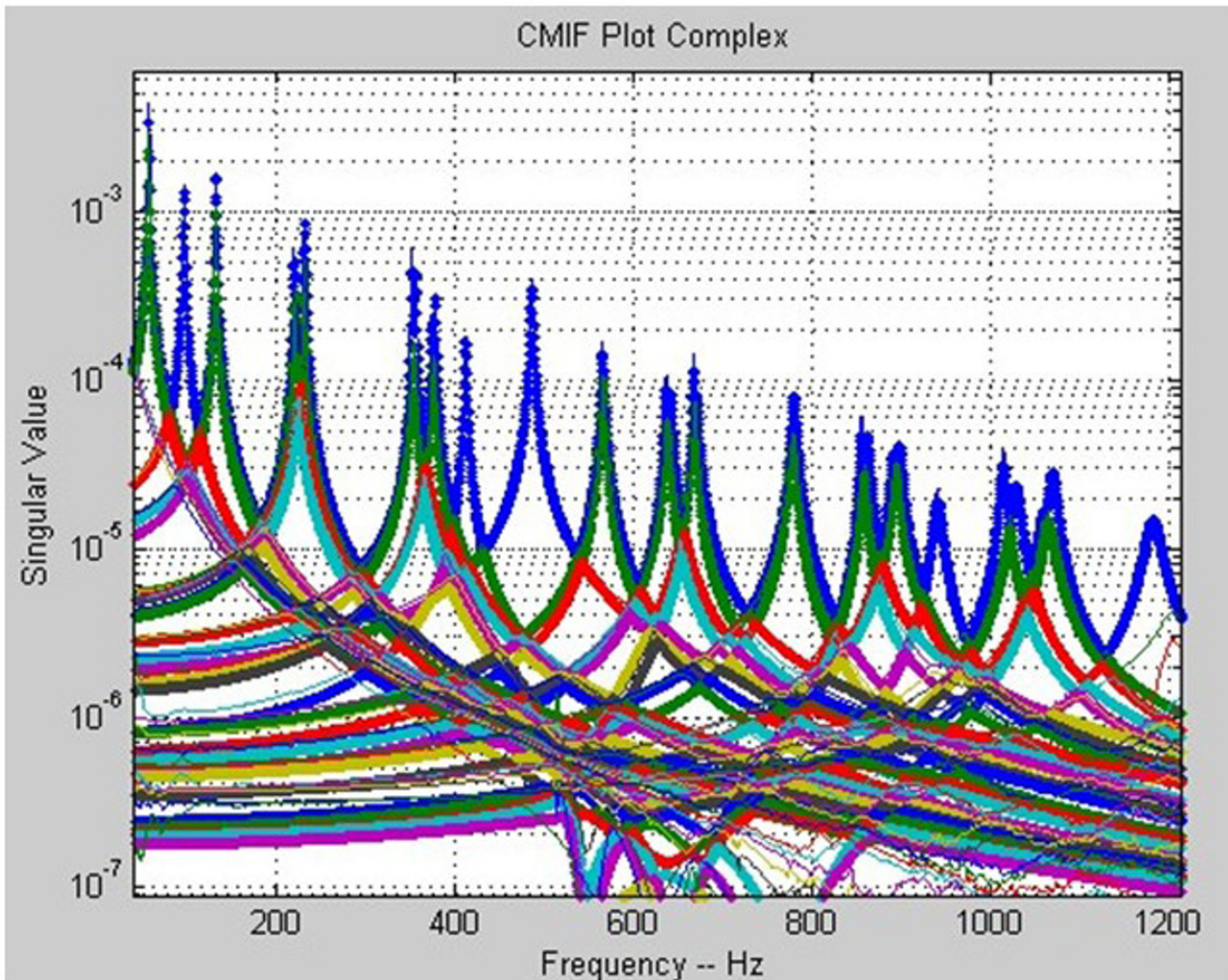


Figure 12 – Comparison of CMIF plot of measured data vs synthesized data from modal model

The next step is to synthesize the measurement and compare the synthesized measurements to measured data. A CMIF plot of the synthesized data is plotted on a CMIF plot of the measured data; See [Figure\(12\)](#). This is a quick way to get a overview of all the data.

For this example, there does not appear to be any missing modes in the 0-1000 Hz frequency band. The frequencies seem to match well but there are small differences in the amplitudes of some of the modes. In the reconstruction of the data in [figure \(12\)](#), no residual terms were included and there are variation in the estimates of the damping on some of the poles as indicated in [figure \(11\)](#) which shows the pole locations in the complex plane.

This method has been described in detail in a paper that was just presented at the latest ISMA conference [16] along with a much more powerful method that is also almost completely autonomous. This newer method is being incorporated into X-Modal III which is the latest version of the MATLAB modal program developed in UCSDRL. This newer method will be described in a paper being presented in the upcoming IMAC conference. It should be noted that the method described in this paper can easily be run directly in X-modal and the students used it as another means of checking their results.

Summary

Trouble shooting vibration, acoustic and control problems has a long application history. It was probably ninety percent of the vibration testing applications in the seventies and probably only ten percent today. There is significantly more people doing testing today relative to the seventies and they are doing more model verification testing.

In terms of the testing practices:

- On-site
 - Need lots of tools
 - Large variety of sensors
 - Run Log important
 - Simple but quick real time data analysis tools
 - Need to record all time histories for post processing
 - Make sure recorded time history data is not compromised relative to post-processing in order to get optimum on-site processing
 - Whenever possible used tri-axial sensors to improve on site visualization of mode shapes. Very often a visual distortion when looking at on-site mode shapes may confuse the diagnostic of a vibration problem.
- Post Processing
 - More sophisticated modal data processing similar to techniques used for laboratory testing applications.

References

1. "Dynamic Testing of Mechanical Systems Using Impulse Testing Techniques", Application Note 140-3, Hewlett Packard Corporation, 1972
2. Morse, I. E., Shapton W. R., Brown, D. L., Kuljanic, E. "Application of Pulse Testing For Determining Dynamic Characteristics of Machine Tools", 13th International Machine Tool Design and Research Conference, University of Birmingham, England, 1972
3. Brown D. L, "Grinding Dynamics", PhD Thesis, Department of Engineering, University of Cincinnati, 1976
4. Brown, D.L., Halvorsen, W.G., "Impulse Techniques for Structural Frequency Response Testing", Sound and Vibration, pp. 8-21, Nov. 1977.
5. Ibrahim, S. R., Mikulcik, E. C., "A Method for the Direct Identification of Vibration Parameters from the Free Response," Shock and Vibration Bulletin, Vol. 47, Part 4, 1977, pp. 183-198.
6. Allemang, R.J., Zimmerman, R.D., Mergeay, M., "Parameter Estimation Techniques for Modal Analysis", Brown, D.L., SAE Paper Number 790221, SAE Transactions, Volume 88, pp. 828-846, 1979.
7. Juang, J.N., Pappa, R.S., "An Eigensystem Realization Algorithm for Modal Parameter Identification and Model Reduction", AIAA Journal of Guidance, Control, and Dynamics, Vol. 8, No. 4, 1985, pp. 620-627.
8. Fladung, W.F., "Multiple Reference Impact Testing", MS Thesis, University of Cincinnati, 1994.
9. Catbas, F.N., Lenett, M., Brown, D.L., Doebling, C.R., Farrar, C.R., Tuner, A., "Modal Analysis of Multi-reference Impact Test Data for Steel Stringer Bridges", Proceedings IMAC, 1997
10. Lenett, M., Catbas, F.N., Hunt, V., Aktan, A.E., Helmick, A., Brown, D.L., "Issues in Multi-Reference Impact Testing of Steel Stringer Bridges, Proceedings, IMAC Conference, 1997

11. Catbas, F.N., "Investigation of Global Condition Assessment and Structural Damage Identification of Bridges with Dynamic Testing and Modal Analysis", PhD. Dissertation University of Cincinnati, Civil and Env. Engineering Department, 1997
12. Fladung, W.F., "A Generalized Residuals Model for the Unified Matrix Polynomial Approach to Frequency Domain Modal Parameter Estimation", PhD Dissertation, University of Cincinnati, 146 pp., 2001.
13. Brown D. L., "Review of Spatial Domain Parameter Estimation procedures and Testing Methods", Proceedings, International Modal Analysis Conference, 23pp., 2009
14. "A First Order, Extended State Vector Expansion Approach to Experimental Modal Parameter Estimation", Brown, D.L., Phillips, A.W., Allemang, R.J., Proceedings, International Modal Analysis Conference, 11 pp., 2005.
15. Brown, D.L., Witter, M.C., "Review of Recent Developments in Multiple Reference Impact Testing (MRIT)", Proceedings, IMAC Conference, 17pp., 2010
16. Allemang, R.J., Brown, D.L., Phillips, A.W., "Survey of Modal Techniques Applicable to Autonomous/Semi-Autonomous Parameter Identification", ISMA Conference, 43pp., 2010

Autonomous Modal Parameter Estimation: Methodology

A.W.Phillips, R.J. Allemang, D.L. Brown
Structural Dynamics Research Laboratory
School of Dynamic Systems
College of Engineering and Applied Science
University of Cincinnati
Cincinnati, OH 45221-0072 USA
Email: Allyn.Phillips@UC.EDU

ABSTRACT

Traditionally, the estimation of modal parameters from a set of measured data has required significant experience. However, as the technology has matured, increasingly, analysis is being performed by less experienced engineers or technicians. To address this development, frequently software solutions are focusing upon either wizard-based or autonomous/semi-autonomous approaches. A number of autonomic approaches to estimating modal parameters from experimental data have been proposed in the past. In this paper, this history is reviewed and a technique suitable for either approach is presented. By combining traditional modal parameter estimation algorithms with a-priori decision information, the process of identifying the modal parameters (frequency, damping, mode shape, and modal scaling) can be relatively simple and automated. Examples of the efficacy of this technique are shown for both laboratory and real-world applications in a related paper.

Nomenclature

| | |
|--|---|
| N_i = Number of inputs. | t_i = Discrete time (sec). |
| N_o = Number of outputs. | ω_i = Discrete frequency (rad/sec). |
| N_S = Short dimension size. | s_i = Generalized frequency variable. |
| N_L = Long dimension size | $x(t_i)$ = Response function vector ($N_o \times 1$)). |
| N = Number of modal frequencies. | $X(\omega_i)$ = Response function vector ($N_o \times 1$)). |
| λ_r = S domain polynomial root. | $f(t_i)$ = Input function vector ($N_i \times 1$) |
| λ_r = Complex modal frequency (rad/sec). | $F(\omega_i)$ = Input function vector ($N_i \times 1$)). |
| $\lambda_r = \sigma_r + j \omega_r$ | $[h(t_i)]$ = IRF matrix ($N_o \times N_i$)). |
| σ_r = Modal damping. | $[H(\omega_i)]$ = FRF matrix ($N_o \times N_i$)). |
| ω_r = Damped natural frequency. | $[\alpha]$ = Denominator polynomial matrix coefficient. |
| z_r = Z domain polynomial root. | $[\beta]$ = Numerator polynomial matrix coefficient. |
| $\{\psi_r\}$ = Base vector (modal vector). | m = Model order for denominator polynomial. |
| $\{\phi_r\}$ = Pole weighted base vector (state vector). | n = Model order for numerator polynomial. |
| $[A_r]$ = Residue matrix, mode r . | v = Model order for base vector. |
| $[I]$ = Identity matrix. | r = Mode number. |

1. Introduction

The desire to estimate modal parameters automatically, once a set or multiple sets of test data are acquired, has been a subject of great interest for more than 40 years. In the 1960s, when modal testing was limited to analog test methods, several researchers were exploring the idea of an automated test procedure for determining modal parameters ^[1-3]. Today, with the increased memory and compute power of current computers used to process test data, an automated or autonomous, modal parameter estimation procedure is entirely possible and is being attempted by numerous researchers.

Before proceeding with a discussion of autonomous modal parameter estimation, some philosophy and definitions regarding

what is considered autonomous is required. In general, autonomous modal parameter estimation refers to an automated procedure that is applied to a modal parameter estimation algorithm so that no user interaction is required once the process is initiated. This typically involves setting a number of parameters or thresholds that are used to guide the process in order to exclude solutions that are not acceptable to the user. When the procedure finishes, a set of modal parameters is identified that can then be reduced or expanded if necessary. The goal is that no further reduction, expansion or interaction with the process will be required.

The larger question concerning autonomous modal parameter estimation is the intended user. Is the autonomous modal parameter estimation procedure expected to give results sufficiently robust for the novice user? This implies that the user could have no experience with modal analysis and, therefore, have no experiential judgement to use in assessing the quality of the results. The use of the term *wizard* implies that this is the desired situation. In contrast, the user could be very knowledgeable in the theory and experienced. For this case, the autonomous modal parameter estimation procedure is simply an efficient mechanism for sorting a very large number of solutions into a final set of solutions that satisfies a set of criteria and thresholds that are acceptable to the user. This user is the assumed reader for the purposes of this discussion.

In order to discuss autonomous modal parameter estimation, some background is needed to clarify terminology and methodology. First, a brief history and overview of documented autonomous modal parameter estimation methods is presented. Second, an overview of some of the tools or semi-autonomous methods that are useful as part of the autonomous modal parameter estimation procedure are reviewed. Finally, the general procedure for an autonomous modal parameter estimation methods that is based upon consistent state vectors, referred to as **Common Statistical Subspace Autonomous Mode Identification (CSSAMI)**, is presented followed by a number of examples. Note that much of the background of the following discussion will be based upon the Unified Matrix Polynomial Algorithm (UMPA) developed by the authors and described in a number of other papers^[4-8].

2. Background: Autonomous Modal Parameter Estimation

The interest in automatic modal parameter estimation methods has been documented in the literature since at least the mid 1960s when the primary modal method was the analog, force appropriation method^[1-3]. Following that early work, there has been a continuing interest in autonomous methods^[9-28] that, in most cases, have been procedures that are formulated based upon a specific modal parameter estimation algorithm like the Eigensystem Realization Algorithm (ERA), the Polyreference Time Domain (PTD) algorithm or more recently the Polyreference Least Squares Complex Frequency (PLSCF) algorithm or the commercial version of the PLSCF, the PolyMAX[®] method.

Each of these past procedures have shown some promise but have not yet been widely adopted. In many cases, the procedure focussed on a single modal parameter estimation algorithm and did not develop a general procedure. Most of the past procedural methods focussed on pole density but depended on limited modal vector data to identify correlated solutions. Currently, due to increased computational speed and larger availability of memory, procedural methods can be developed that were beyond the computational scope of available hardware only a few years ago. These methods do not require any initial thresholding of the solution sets and rely upon correlation of the vector space of thousands of potential solutions as the primary identification tool. With the addition to any modal parameter estimation algorithm of the concept of pole weighted vector, the length, and therefore the sensitivity, of the these extended vectors provides an additional tool that appears to be very useful in autonomous modal parameter estimation.

3. Numerical Tools - Autonomous Modal Parameter Estimation

The development of many of the past procedures and any new proposed procedure depends heavily on a number of numerical tools that have been developed over the last twenty years or so^[29-55]. These tools are currently used by many algorithms as a user interaction tool or semi-autonomous tool to assist the user in picking an appropriate set of modal parameters. These tools are described in great detail in the literature and are summarized briefly in the next several sections.

3.1 Consistency Diagrams

For the last thirty years, modal parameter estimation based upon experimental data, primarily frequency response functions (FRFs), has utilized some form of error chart and/or stabilization diagram to visualize and assist in the determination of the correct modal frequencies^[46-49,53-54]. The conceptual basis of the stabilization diagram is that distinct and unique modal frequencies can be identified by comparing the roots of a characteristic polynomial when the model order of the characteristic polynomial is increased or the subspace is altered in a systematic manner. The stabilization or consistency diagram is based upon successive solutions of Equation (1) or Equation (2) for different values of the maximum model order m . If the roots are consistent as the model order is increased, these roots are identified as modal frequencies. If the roots are inconsistent,

these roots are associated with noise on the data and are discarded. Since there is generally much more FRF data available than is needed to solve for the number of modal parameters of interest, the characteristic polynomial is normally estimated in a least squares sense and can be reformulated from the measured data for each model order ^[4-5].

Frequency Domain Algorithms:

$$\left| [\alpha_m] s^m + [\alpha_{m-1}] s^{m-1} + [\alpha_{m-2}] s^{m-2} + \dots + [\alpha_0] \right| = 0 \quad (1)$$

where:

$$s_r = \lambda_r \quad \lambda_r = \sigma_r + j \omega_r$$

Time Domain Algorithms:

$$\left| [\alpha_m] z^m + [\alpha_{m-1}] z^{m-1} + [\alpha_{m-2}] z^{m-2} + \dots + [\alpha_0] \right| = 0 \quad (2)$$

where:

$$z_r = e^{\lambda_r \Delta t} \quad \lambda_r = \sigma_r + j \omega_r$$

$$\sigma_r = \operatorname{Re} \left[\frac{\ln z_r}{\Delta t} \right] \quad \omega_r = \operatorname{Im} \left[\frac{\ln z_r}{\Delta t} \right]$$

In most implementations, the **stabilization diagram** or **consistency diagram** is presented as a two dimensional plot with frequency on the abscissa and characteristic polynomial model order on the ordinate. A plot of the summed magnitude of all of the FRFs, or a plot of one of the mode indicator functions (complex mode indicator function (CMIF) or multivariate mode indicator function (MvMIF)), is placed in the background for reference. For each model order, symbols are plotted along the frequency axis wherever a root of the characteristic polynomial has been estimated. Historically, the characteristic polynomial had scalar coefficients (single reference data) so the roots are complex valued and have both frequency and damping information. The original symbols were used to indicate, in increasing importance, Level 1: a pole was found, Level 2: a pole was found with an associated complex conjugate, Level 3: Level 2 plus the damping was realistic (negative real part of pole), Level 4: Level 3 plus a damped natural frequency (imaginary part of pole) consistency within a specified percentage (normally 1 percent) and Level 5: Level 4 plus a damping consistency with a specified percentage (normally 5 percent).

As multiple reference parameter estimation was developed, this led to matrix coefficient, characteristic polynomial equations which created further evaluation criteria, Level 6: Level 5 plus a vector consistency within a specified modal assurance criterion (MAC) value (normally 0.95). Since the vector that is associated with the matrix coefficient, characteristic polynomial may be different sizes (function of N_S or N_L), a variation of Level 6 involves an additional solution for the vector at the largest dimension N_L so that a more statistically significant comparison of vectors can be utilized. Finally, numerical conditioning can be evaluated for each solution and if the numerical conditioning is approaching a limit based upon the accuracy of the data or the numerical limitations of the computer algorithm or word size, Level 7 can be added to indicate a possible numerical problem. In general, all of the specified values that indicate consistency at each level can be user defined and are referred to as the stability or consistency tolerances.

This information generates a consistency diagram, for a simple circular plate structure, that looks like [Figure 1](#). With all of the symbols presented, the consistency diagram for even this simple structure can be very complicated. [Figures 1](#) and [2](#) demonstrate two different presentations of consistency diagrams based upon different presentations of the characteristic matrix coefficient polynomial information. In both figures, an average autopower of the measured data is plotted on the consistency diagram in the background for reference.

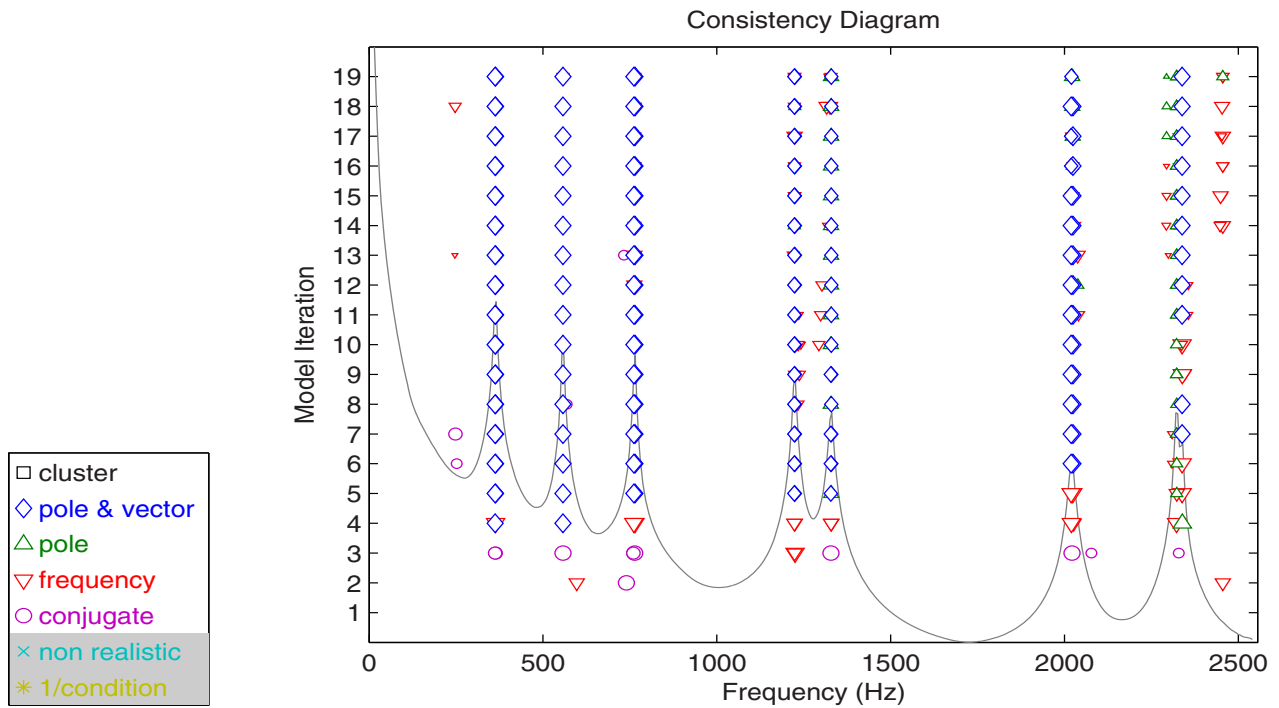


Figure 1. Typical Consistency Diagram

Figure 2 presents the consistency diagram using an entirely different method that involves using the modal assurance criterion (MAC) to compare vectors from successive solutions of the characteristic polynomial equation. Rather than comparing the unscaled modal vectors (base vectors) directly, a pole weighted vector of v -th order is constructed for each solution and compared to similarly constructed pole weighted vectors for the previous solution. Further explanation of the pole weighted vector is provided in Section 3.3 and can also be found in the literature ^[46-47].

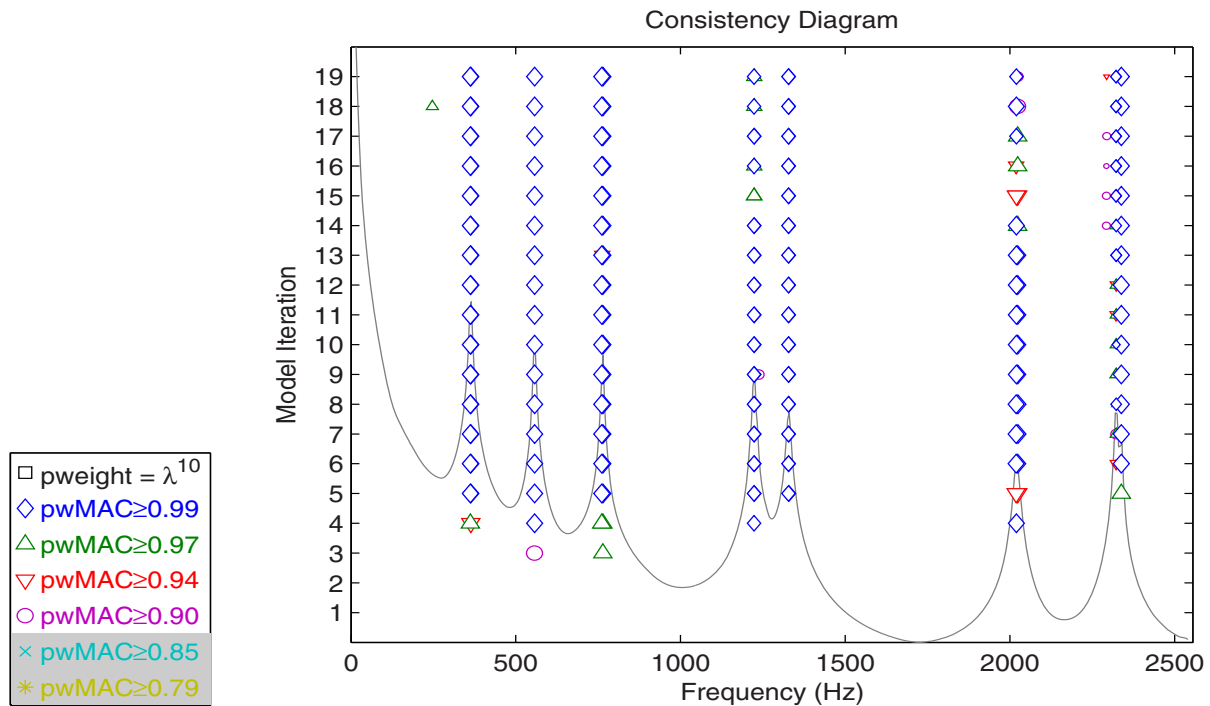


Figure 2. Alternate Consistency Diagram - Pole Weighted MAC

3.1.1 Clear Consistency Diagrams

A number of different methods can be used to generate the consistency diagram that will impact the clarity of the consistency diagram. A number of recent papers [46-47,53-54] have identified the effects of changing the consistency tolerances on the resultant consistency diagrams, yielding a clearer presentation of symbols that indicate the presence of a structural mode of vibration. These methods can be combined with the coefficient normalization and consistency tolerances to generate a very clear diagram in most cases where the measured data has a reasonable match to linear, reciprocal system assumptions, observability issues and reasonable data noise levels. These methods have been used on a wide range of data cases in the automotive and aerospace application areas with good success. The methods include:

- Symbol Sizing Based Upon Normal Mode Criteria
- Complete or Incomplete Vector Comparisons
- Using Both Coefficient Normalization Methods
- Numerator and Denominator Model Order Variation
- Fixed Denominator and Numerator Order Variation
- Frequency Normalization Variation

3.2 Long Dimension Vector Solution

While many high order, matrix coefficient modal parameter estimation methods estimate unscaled modal vectors as part of the estimation of the poles, there is no reason to limit the length of the unscaled modal vector to the short dimension. Each short dimension vector can be used to estimate the unscaled vector for the long dimension as a part of the solution. This requires an extra solution step but, for each model order, requires very little additional computational effort. In this case, regardless of the method employed to estimate the modal frequencies, all unscaled modal vectors will be of length equal to the long dimension. No attempt to restrict the set of modal frequencies is used at this point in the procedure; all possible poles are included in this calculation. This set of unscaled vectors will include structural modal vectors and computational vectors. Sorting these vectors is left to a correlation procedure such as the modal assurance criterion (MAC) with a threshold (minimum MAC value). Note that this extra step can include the estimation of modal scaling so that scaled modal vectors and modal scaling values can be used as part of the evaluation process.

3.3 Pole Weighted Modal Vectors

When comparing base vectors, at either the short or the long dimension, a pole weighted base vector can be constructed independent of the original UMPA(m,n,v) procedure used to estimate the poles and base vectors. For a given order v of the pole weighted vector, the base vector and the associated pole can be used to formulate the pole weighted vector as follows:

$$\{\phi\}_r = \begin{Bmatrix} \lambda_r^v \{\psi\}_r \\ \cdot \\ \cdot \\ \lambda_r^2 \{\psi\}_r \\ \cdot \\ \lambda_r^1 \{\psi\}_r \\ \lambda_r^0 \{\psi\}_r \end{Bmatrix}_r \quad (3)$$

The above formulation will be dominated by the high order terms if actual frequency units are utilized. Generalized frequency concepts (frequency normalization or z domain transform) are normally used to minimize this problem as follows:

$$\{\phi\}_r = \begin{Bmatrix} z_r^v \{\psi\}_r \\ \cdot \\ \cdot \\ z_r^2 \{\psi\}_r \\ \cdot \\ z_r^1 \{\psi\}_r \\ z_r^0 \{\psi\}_r \end{Bmatrix}_r \quad (4)$$

$$z_r = e^{j^* \pi^* (\omega_r / \omega_{\max})} = e^{j^* \omega_r^* \Delta t} \quad (5)$$

$$z_r^m = e^{j^* \pi^* m^* (\omega_r / \omega_{\max})} \quad (6)$$

In the above equations, Δt and ω_{\max} can be chosen as needed to cause the positive and negative roots to wrap around the unit circle in the z domain without overlapping (aliasing). Normally, ω_{\max} is taken to be five percent larger than the largest frequency identified in the roots of the matrix coefficient polynomial.

3.4 Pole Surface Consistency and Density

A number of other pole presentation diagrams, related to the consistency diagram, such as pole surface consistency and pole surface density diagrams have proven useful for identifying modal parameters [43-44,56-57] and may be more powerful than the consistency diagram alone. Generally, pole surface density diagrams are more powerful than consistency or stability diagrams at locating similar pole vector estimates from all of the possible solutions represented in the consistency diagram. All of the poles from all solutions involved in the consistency diagram are plotted in the second quadrant of the s plane. Pole estimates that are located within a two dimensional threshold from each other are defined as participating in a pole cluster or a dense region of estimated poles in the s plane. The poles that are compared on these pole surface diagrams are generally limited to the poles identified on the consistency diagram (if some symbols are omitted from the consistency diagram, these poles will not be included on the pole surface diagram. The distribution of the poles that participate in a pole cluster can be used to find a single pole-vector estimate and the distribution can be used to estimate statistics related to the variance in the pole estimate. An example of a pole surface consistency diagram is given in [Figure 3](#) and the companion pole surface density diagram in [Figure 4](#).

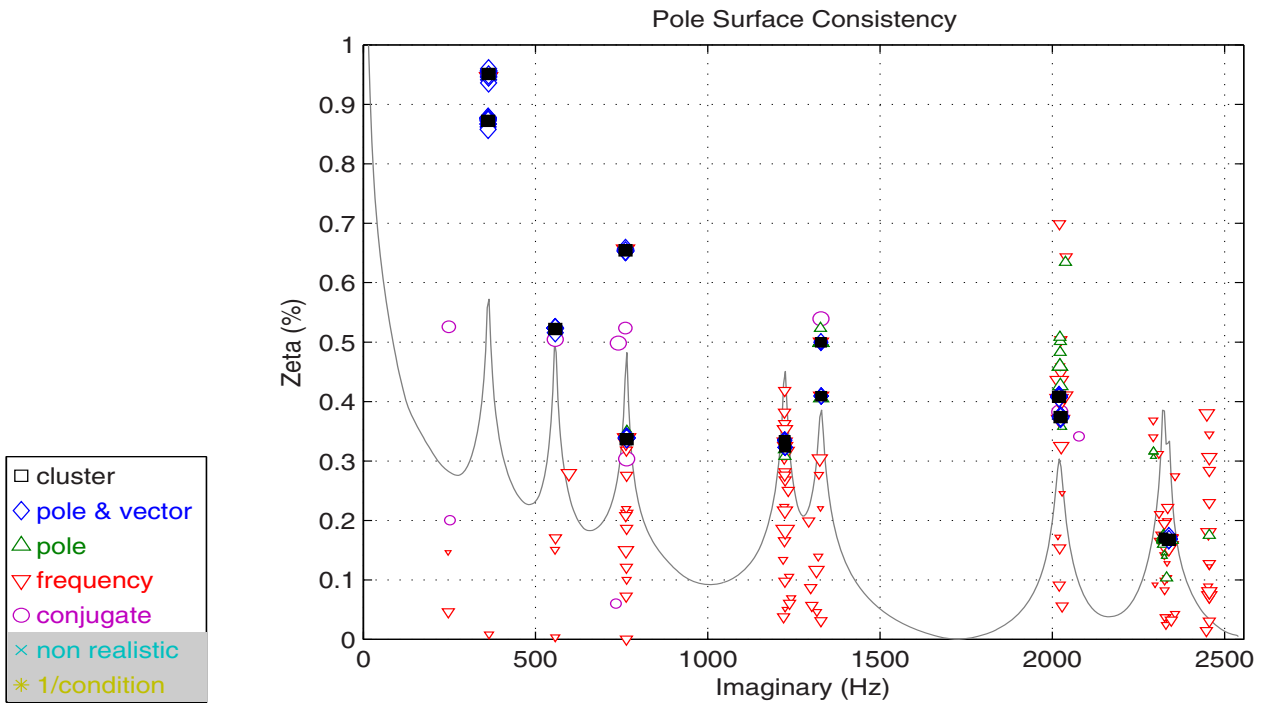


Figure 3. Pole Surface Consistency Diagram with Final Autonomous Estimates

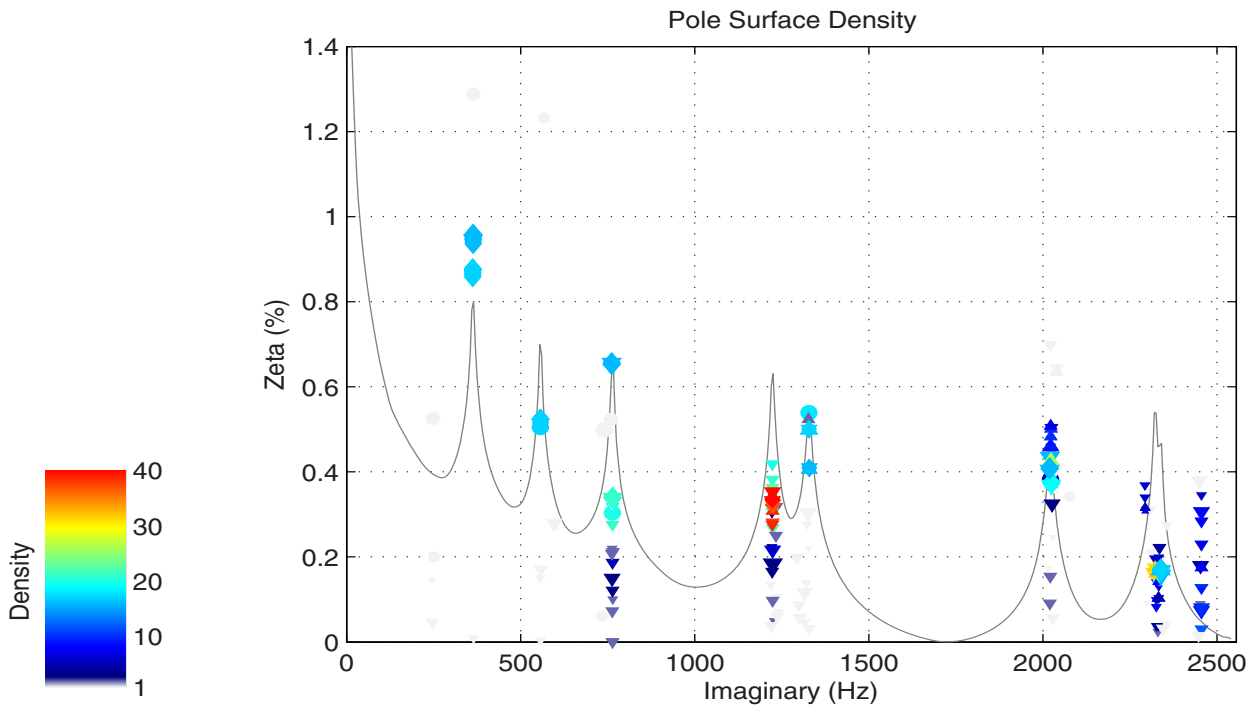


Figure 4. Pole Surface Density Diagram

Figures 3 and 4 presents the same information previously shown in Figures 1 and 2. Note that in all cases, suppressing the obvious spurious computational poles results in a substantially cleaner consistency diagram with clear indications of the pole locations. This translates to the Pole Surface Diagram as well. Note that suppressing spurious modes entails a risk that some

valid modes may be eliminated which may not be attractive behavior once autonomous modal parameter estimation procedures are utilized.

4. Autonomous Modal Parameter Estimation Method

The autonomous modal parameter estimation method developed and presented in the following is a general method that can be used with any algorithm that fits within the UMPA structure. A complete description of the Unified Matrix Polynomial Algorithm (UMPA) thought process can be found in a number of references developed by the authors [4-8, 57]. This means that this method can be applied to both low and high order methods with low or high order base vectors. This also means that most commercial algorithms could take advantage of this procedure. Note that high order matrix coefficient polynomials normally have coefficient matrices of dimension that is based upon the short dimension of the data matrix ($N_S \times N_S$). In these cases, it may be useful to solve for the long dimension modal vectors or to use pole weighted modal vectors. This will extend the temporal-spatial information in the N_S length base vector so that the vector will be more sensitive to change. This characteristic is what gives this autonomous method (CSSAMI) the ability to distinguish between computational and structural modal parameters.

The implementation of the autonomous modal parameter estimation for this method is detailed in the following sections.

4.1 Step 1: Develop a Consistency Diagram

Develop a consistency diagram using any UMPA solution method. Since this autonomous method utilizes a pole surface density plot, having a large number of iterations in the consistency diagram (due to model order, subspace iteration, starting times, equation normalization, etc.) will be potentially advantageous. The possibility of combining solutions from different consistency diagrams originating from different UMPA models is also a natural extension of this autonomous approach.

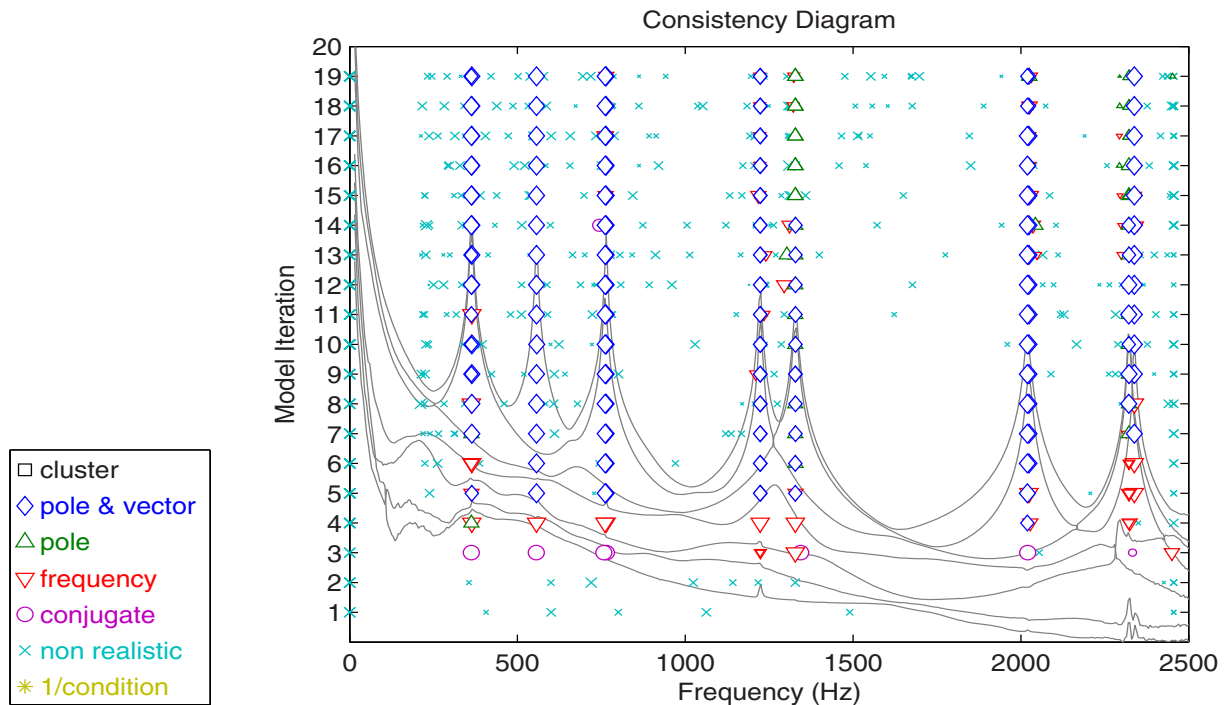


Figure 5. Consistency Diagram Showing All Poles

The larger the number of solutions (represented by symbols) in the consistency diagram, the more computation time and memory will be required. However, restricting the number of solutions using clear stabilization (consistency) methods may be counterproductive [59].

4.2 Step 2: Find Scaled Modal Vectors

If the UMPA method is high order (coefficient matrices of size $N_S \times N_S$), solve for the complete vector (function of N_L for all roots, structural and computational).

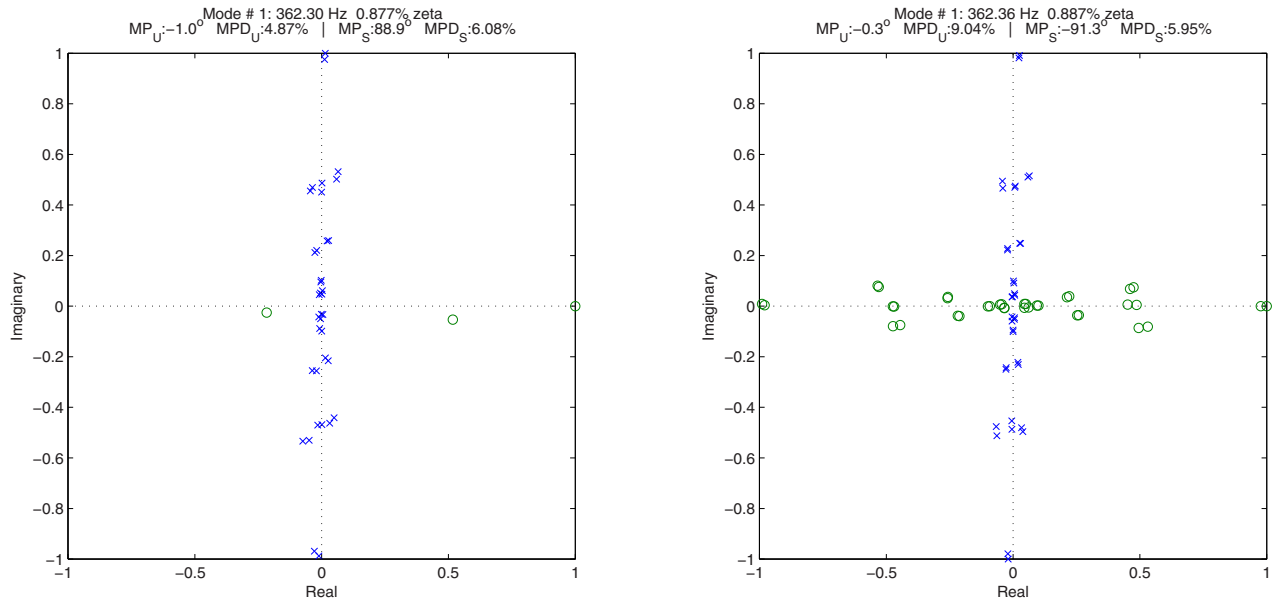


Figure 6. Typical Complex Plot of Unscaled and Scaled Modal Vectors

Figure 6 shows plots of a complex valued modal vector originating from PTD (left) and ERA (right) methods. The green circle symbols represent the normalized modal vector associated with the consistency diagram for one of the poles of one of the high order solutions. The blue x symbols represent the scaled (in terms of residue) full length vectors that can be computed, mode by mode, before continuing. The purpose in calculating the complete, scaled vector is two-fold. The first is the additional discrimination of the algorithm that results from the longer vector length (PTD example on the left). The second is the availability of the modal scaling information, used to calculate Modal A. This scaling information can be useful at the end of the solution process in order to assess the quality of the results (magnitude and phase of Modal A, for example). Even long basis vectors should be scaled so that this assessment information is available for all cases (ERA example on the right).

4.3 Step 3: Determine Pole Surface Density Clusters

Based upon the pole surface density threshold, identify all possible pole densities above some minimum value. This will be a function of the number of possible solutions represented by the consistency diagram. The pole density is defined for each pole as the number other poles within a specified complex tolerance radius. This range can be defined in terms of either absolute or relative frequency. Just as in Step 1, restricting the number of poles reduces both the time and the memory required for solution, but it also reduces the amount of information available to the algorithm. As a result, an overly restrictive threshold may be counterproductive. Figures 7 and 8 show the pole consistency plots (showing pole locations in the second quadrant of the s-plane) that are evaluated in this step.

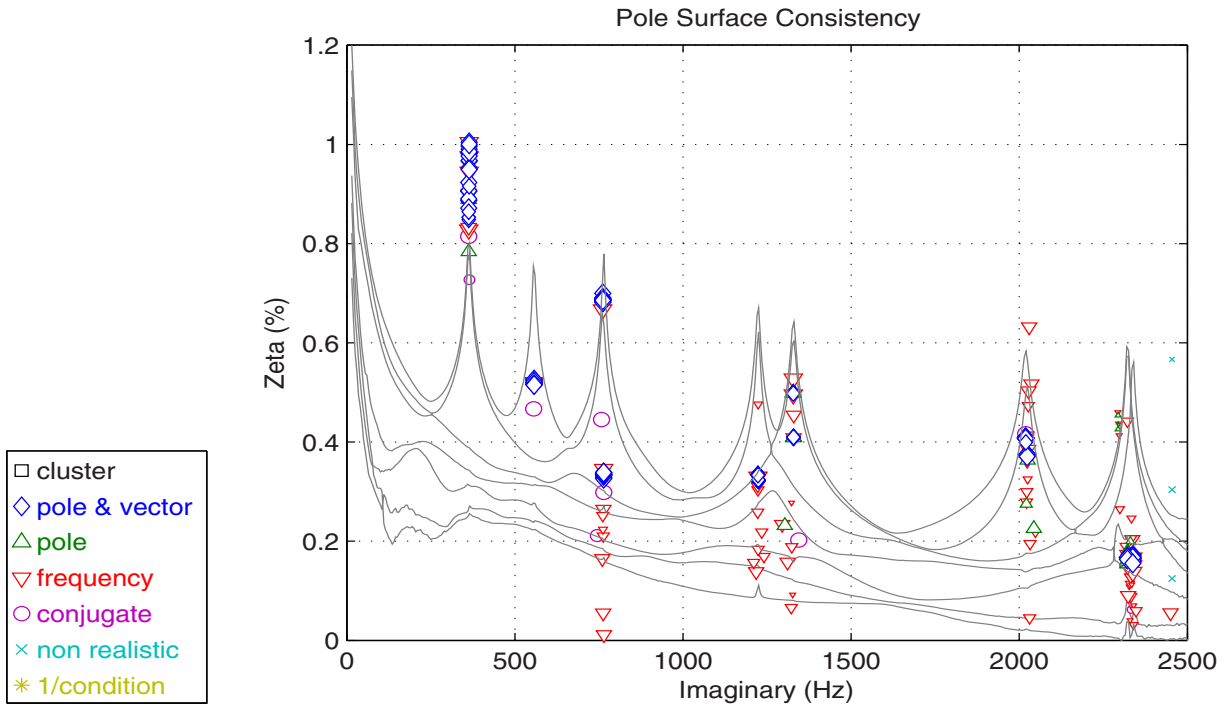


Figure 7. Pole Surface Consistency Showing All Poles

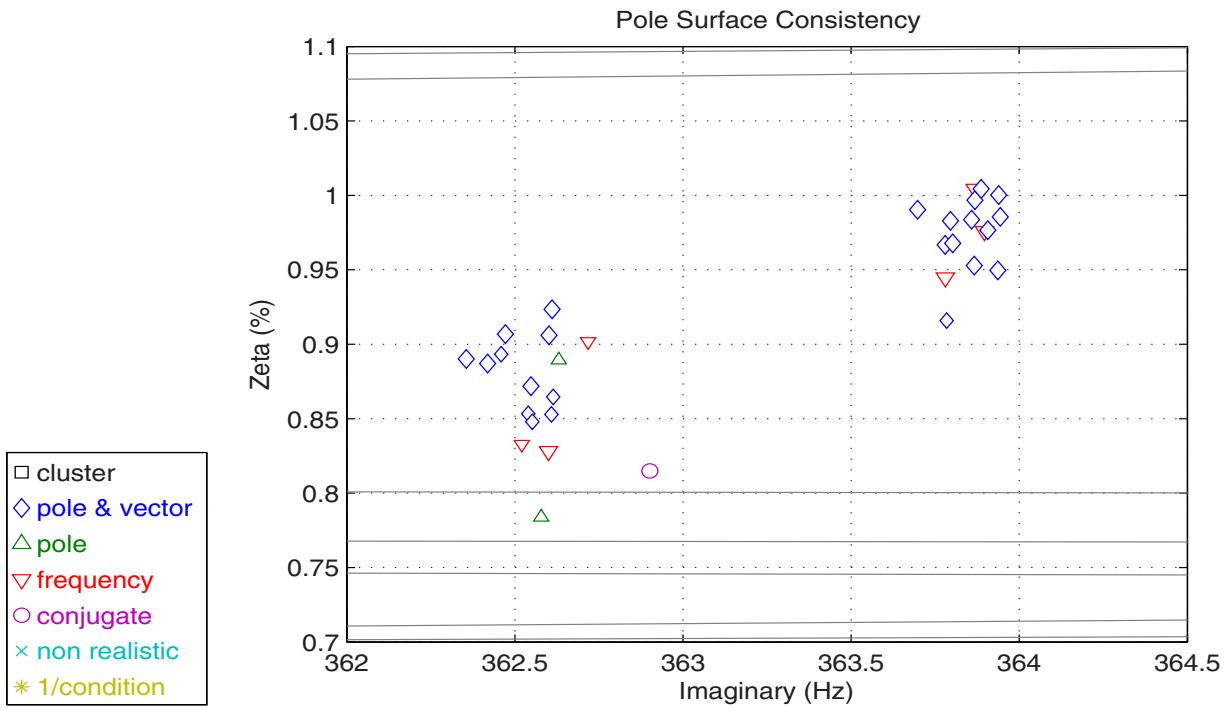


Figure 8. Zoomed Pole Clusters

4.4 Step 4: Construct Normalized Pole Weighted Vectors

Normalize each vector to unity length with dominant real part and then construct a predefined, higher order (typically 10th order), pole weighted vector for each solution ^[47].

$$\{\phi\}_r = \begin{Bmatrix} z_r^v\{\psi\}_r \\ \vdots \\ z_r^2\{\psi\}_r \\ z_r^1\{\psi\}_r \\ z_r^0\{\psi\}_r \end{Bmatrix}$$

4.5 Step 5: Calculate Auto-MAC of Normalized, Pole Weighted Vectors

Sort the normalized pole weighted vectors created in Step 4 into frequency order based upon damped natural frequency (ω_r). Then calculate the Auto-MAC matrix for all pole weighted vectors.

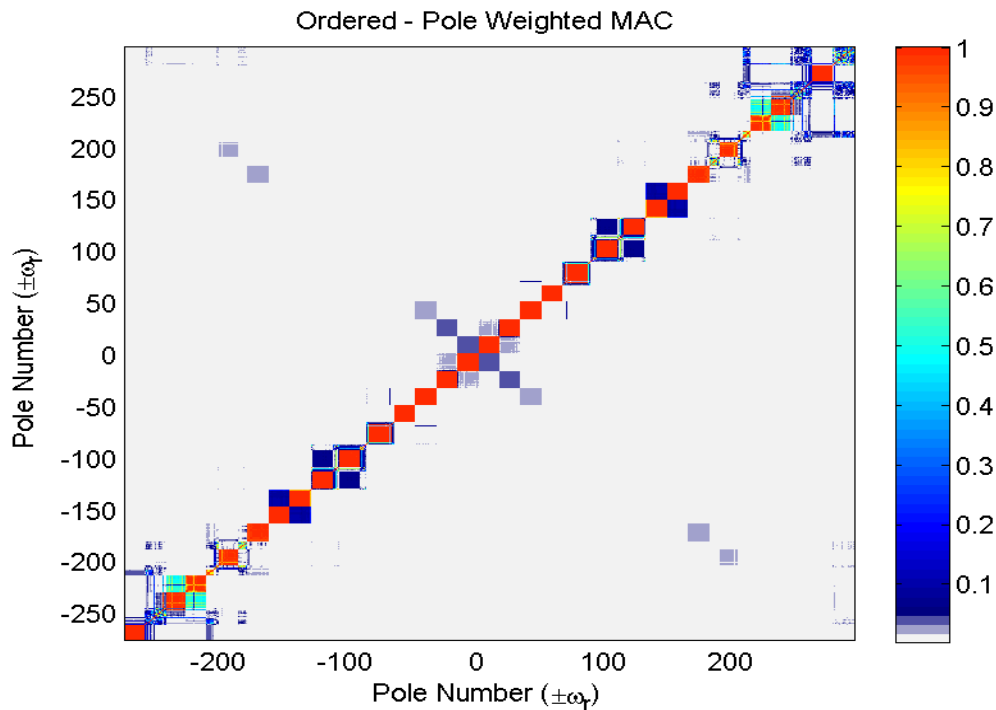


Figure 9. Auto-MAC Color Plot of Tenth Order Pole Weighted Vectors, No Threshold

The size of the red squares in [Figure 9](#) (and in the following [Figure 10](#)) represents the number of vectors in each cluster of poles found anywhere in the consistency diagram.

4.6 Step 6: Remove Pole Weighted Vectors Below Threshold

Retain all Auto-MAC values that have a pole weighted MAC value above a threshold, 0.8 works well for most cases. All values below the threshold are set to 0.0.

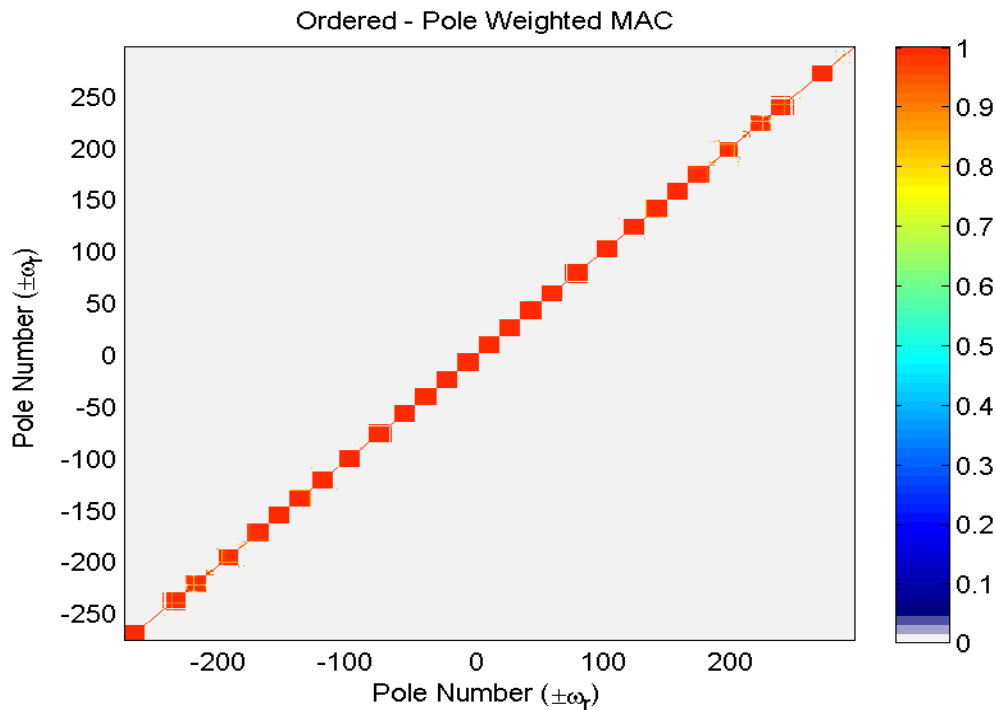


Figure 10. Auto-MAC Color Plot of Tenth Order Pole Weighted Vectors, Above Threshold

4.7 Step 7: Identify and Retain Consistent Pole Weighted Vector Clusters

Identify vector clusters from this pole weighted MAC diagram that represent the same pole weighted vector. This is done by taking the singular value decomposition (SVD) of the pole weighted MAC matrix. The number of significant singular values for this MAC matrix represents the number of significant pole clusters in the pole weighted vector matrix and the value of each significant singular value represents the size of the cluster since the vectors are unitary. Note that the singular value is nominally the square of the number of vectors in the cluster and will likely be different, mode by mode. Recognize also that [Figure 10](#), as a thresholded Auto-MAC plot, will be largely zero and have significant magnitude (above the threshold) only for the pole weighted vectors that represent a cluster.

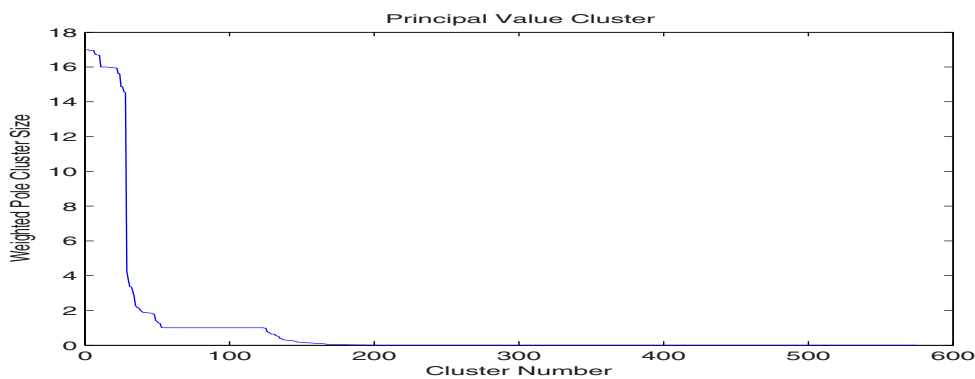


Figure 11. Principal Values of Clusters of Pole Weighted Vectors

[Figure 11](#) then is a plot of the scaled singular values for [Figure 10](#). Each significant singular value as determined by a minimum cluster size threshold (typically 4) represents a cluster of pole weighted vectors with an equivalent spatio-temporal characteristic. The location of the corresponding pole weighted vectors in the pole weighted vector matrix (index) is found

from the associated left singular vector. The singular vector associated with these significant singular values is nominally a logical index vector (when scaled by the square root of the singular value) and is used to determine the location in the original pole weighted vector matrix for those pole weighted vectors that are identified as being in a consistent cluster. This is accomplished by multiplying the left singular vector by the square root of the singular value and retaining all positions (indexes) above a threshold (typically 0.9). The positions of the non-zero elements in this vector are the indexes into the pole weighted vector matrix for all vectors belonging to a single cluster.

4.8 Step 8: Evaluate Pole Cluster

Effectively, Step 7 yields, cluster by cluster, the pole weighted vectors that will be used to identify a single consistent spatio-temporal set of data representing a single complex modal frequency, modal vector, and modal scaling. For each identified pole weighted vector cluster, a singular value decomposition (SVD) is performed on the identified set of pole weighted vectors. Note that the number of pole weighted vectors included in each cluster will in general not be the same. The significant left singular vector is the dominant (average) pole weighted vector. Use the zeroth order portion of this dominant vector to identify the modal vector and the relationship between the zeroth order and the first order portions of the dominant vector to identify the complex modal frequency. Complete the solution for modal scaling by using any MIMO process of your choice. A complete discussion of the choices can be found in the literature ^[48].

4.9 Step 9: Complete Statistical Evaluation for Each Pole Cluster

Since each cluster in Step 8 involves a number of estimates of complex modal frequency, modal vector, and modal scaling, computing statistics on the variation in the cluster is a natural part of this autonomous modal parameter estimation process. Tables 1 to 3 are examples of statistics that can be easily computed based upon these data clusters. Complete details about these statistics, their rationale and how each is computed can be found another paper ^[59].

Naturally, the statistics in these tables give the possibility, with experience, of developing an automatic threshold on any number of physical or statistical values to exclude solutions which are deemed physically unrealistic or statistically unacceptable. At this time, this is left to user interaction at the completion of the CSSAMI processing.

| Index | Sample Size (N) | Frequency (Hz) | Damping (Hz) | Frequency (Hz) (Mean) | Damping (Hz) (Mean) | Std. Dev. (Hz) |
|-------|-----------------|----------------|--------------|--------------------------|------------------------|----------------|
| 8 | 16 | 362.564 | -3.1666 | 362.564 | -3.1670 | 0.1677 |
| 19 | 16 | 363.860 | -3.5650 | 363.860 | -3.5650 | 0.1251 |
| 10 | 16 | 557.055 | -2.8966 | 557.055 | -2.8966 | 0.0795 |
| 12 | 16 | 761.224 | -5.2229 | 761.224 | -5.2229 | 0.1008 |
| 2 | 17 | 764.190 | -2.5371 | 764.190 | -2.5371 | 0.1529 |
| 16 | 16 | 1222.980 | -4.0883 | 1222.980 | -4.0883 | 0.0271 |
| 13 | 16 | 1224.055 | -3.9540 | 1224.055 | -3.9540 | 0.0419 |
| 4 | 17 | 1328.036 | -6.6495 | 1328.036 | -6.6507 | 0.0907 |
| 17 | 16 | 1328.803 | -5.4761 | 1328.803 | -5.4768 | 0.1871 |
| 6 | 17 | 2019.269 | -8.2512 | 2019.271 | -8.2511 | 0.2543 |
| 23 | 15 | 2023.802 | -7.5597 | 2023.801 | -7.5598 | 0.0642 |
| 26 | 10 | 2321.862 | -3.9074 | 2321.860 | -3.9070 | 0.1690 |
| 28 | 8 | 2322.335 | -3.8356 | 2322.335 | -3.8367 | 0.2244 |
| 22 | 15 | 2337.895 | -3.7967 | 2337.895 | -3.7971 | 0.2287 |

TABLE 1. Modal Frequency Statistics

| Index | N | Frequency (Hz) | NMVR ₁ | NMVR ₂ | NSVR ₁ | NSVR ₂ |
|-------|----|----------------|-------------------|-------------------|-------------------|-------------------|
| 8 | 16 | 362.564 | 0.0046 | 0.0730 | 0.0046 | 0.0730 |
| 19 | 16 | 363.860 | 0.0034 | 0.0543 | 0.0034 | 0.0543 |
| 10 | 16 | 557.055 | 0.0001 | 0.0014 | 0.0001 | 0.0014 |
| 12 | 16 | 761.224 | 0.0007 | 0.0092 | 0.0007 | 0.0093 |
| 2 | 17 | 764.190 | 0.0020 | 0.0312 | 0.0020 | 0.0312 |
| 16 | 16 | 1222.980 | 0.0017 | 0.0213 | 0.0017 | 0.0213 |
| 13 | 16 | 1224.055 | 0.0013 | 0.0185 | 0.0013 | 0.0184 |
| 4 | 17 | 1328.036 | 0.0042 | 0.0718 | 0.0042 | 0.0717 |
| 17 | 16 | 1328.803 | 0.0022 | 0.0342 | 0.0022 | 0.0342 |
| 6 | 17 | 2019.269 | 0.0054 | 0.0763 | 0.0054 | 0.0763 |
| 23 | 15 | 2023.802 | 0.0047 | 0.0537 | 0.0047 | 0.0537 |
| 26 | 10 | 2321.862 | 0.0162 | 0.1617 | 0.0162 | 0.1617 |
| 28 | 8 | 2322.335 | 0.0161 | 0.1279 | 0.0161 | 0.1278 |
| 22 | 15 | 2337.895 | 0.0020 | 0.0238 | 0.0020 | 0.0238 |

TABLE 2. Modal Vector Statistics

| Index | N | Frequency (Hz) | ModalA (State Vector) | | | | ModalA (Mean from cluster) | | | | |
|-------|----|----------------|-----------------------|--------------|-------------|--------|----------------------------|--------------|-------------|--------|-------------|
| | | | real | imaginary | magnitude | phase | real | imaginary | magnitude | phase | Std. Dev. |
| 8 | 16 | 362.564 | 3.9663e+002 | -5.7201e+003 | 5.7338e+003 | -86.03 | 3.9574e+002 | -5.7195e+003 | 5.7332e+003 | -86.04 | 1.3866e+002 |
| 19 | 16 | 363.860 | -4.8353e+001 | -4.8716e+003 | 4.8719e+003 | -90.57 | 4.5311e+001 | -4.9271e+003 | 4.9273e+003 | -89.47 | 3.1271e+002 |
| 10 | 16 | 557.055 | 7.3166e+001 | -9.7205e+003 | 9.7207e+003 | -89.57 | 8.4818e+001 | -9.7107e+003 | 9.7111e+003 | -89.50 | 1.2295e+002 |
| 12 | 16 | 761.224 | 9.6911e+001 | -1.8433e+004 | 1.8434e+004 | -89.70 | 9.5750e+001 | -1.8433e+004 | 1.8433e+004 | -89.70 | 2.1414e+002 |
| 2 | 17 | 764.190 | -3.1250e+002 | -7.0511e+003 | 7.0580e+003 | -92.54 | -3.0277e+002 | -7.0524e+003 | 7.0589e+003 | -92.46 | 3.1198e+002 |
| 16 | 16 | 1222.980 | 1.1082e+003 | -1.7259e+004 | 1.7295e+004 | -86.33 | 1.1154e+003 | -1.7253e+004 | 1.7289e+004 | -86.30 | 5.3096e+002 |
| 13 | 16 | 1224.055 | -4.6394e+003 | -3.0840e+004 | 3.1187e+004 | -98.55 | -4.6441e+003 | -3.0074e+004 | 3.0431e+004 | -98.78 | 1.6271e+003 |
| 4 | 17 | 1328.036 | -4.8959e+002 | -1.5810e+004 | 1.5818e+004 | -91.77 | -4.7949e+002 | -1.5803e+004 | 1.5810e+004 | -91.74 | 8.5516e+002 |
| 17 | 16 | 1328.803 | 1.5461e+003 | -1.4661e+004 | 1.4742e+004 | -83.98 | 1.5462e+003 | -1.4659e+004 | 1.4741e+004 | -83.98 | 2.9335e+002 |
| 6 | 17 | 2019.269 | 8.1564e+002 | -1.3301e+004 | 1.3326e+004 | -86.49 | 7.3874e+002 | -1.3345e+004 | 1.3365e+004 | -86.83 | 6.6888e+002 |
| 23 | 15 | 2023.802 | 4.2669e+003 | -6.3248e+004 | 6.3392e+004 | -86.14 | 4.1880e+003 | -6.3244e+004 | 6.3382e+004 | -86.21 | 4.7741e+003 |
| 26 | 10 | 2321.862 | 1.6011e+003 | -2.9188e+004 | 2.9232e+004 | -86.86 | 8.1739e+002 | -3.0454e+004 | 3.0465e+004 | -88.46 | 5.2745e+003 |
| 28 | 8 | 2322.335 | 2.8552e+003 | -3.6135e+004 | 3.6247e+004 | -85.48 | 1.7616e+003 | -3.7289e+004 | 3.7331e+004 | -87.30 | 6.3617e+003 |
| 22 | 15 | 2337.895 | -1.3348e+003 | -5.0815e+004 | 5.0833e+004 | -91.50 | -1.3637e+003 | -5.0848e+004 | 5.0867e+004 | -91.54 | 2.6546e+003 |

TABLE 3. Modal Scaling Statistics

The philosophy involved to this point is to allow all possible poles and vectors that demonstrate some degree of physical and statistical significance, in terms of the pole weighted vector consistency, to be retained by the procedure. The rationale is that it will be easier for a user to interact with this set of final estimates and intelligently remove poor estimates based upon the statistical or other information rather than to have to add estimates to the final identified set of modal parameters. Since each mode cluster provides a set of answers, the statistics that can be computed is one easy way to identify poorly estimated modal parameters. These poor estimates will occur based upon excessive noise in/on the measured data, violation of the assumption of the modal parameter estimation algorithms, or inadequate spatial data in terms of input-output sensor locations. Ultimately, the limitations of information theory will dictate whether a satisfactory set of modal parameters will be obtained.

4.10 Step 10: Assess Quality of Results (User Interaction)

Once the final set of modal parameters, along with their associated statistics, is obtained, quality can be assessed by many methods that are currently available. The most common example is to perform comparisons between the original measurements and measurements synthesized from the modal parameters. Another common example is to look at physical characteristics of the identified parameters such as reasonableness of frequency and damping values, normal mode characteristics in the modal vectors, and appropriate magnitude and phasing in the modal scaling. Other evaluations that may be helpful can be mean phase correlation (MPC) on the vectors, an Auto-MAC looking for agreement between the modal vectors from conjugate poles or any other method available.

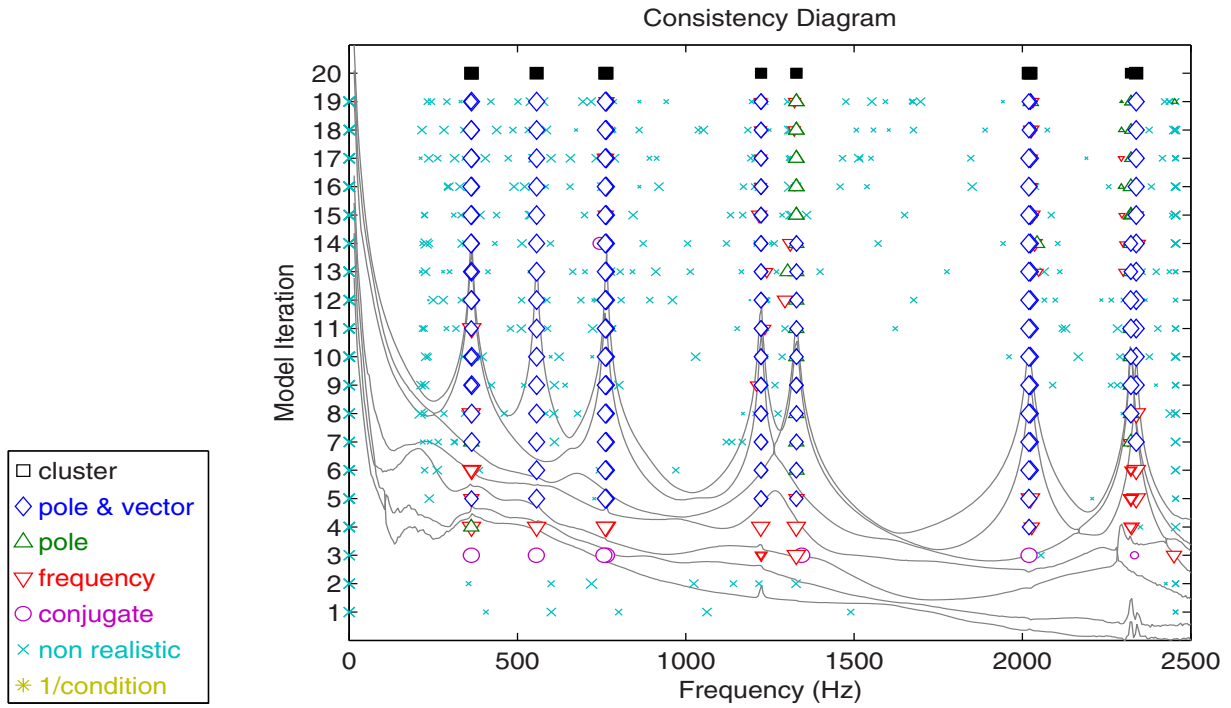


Figure 12. Consistency Diagram with Final Autonomous Estimates

Figure 12 shows the location of the final estimates on a consistency plot and Figure 13 shows their location a pole surface consistency plot. The black squares represent a final solution from the autonomous procedure.

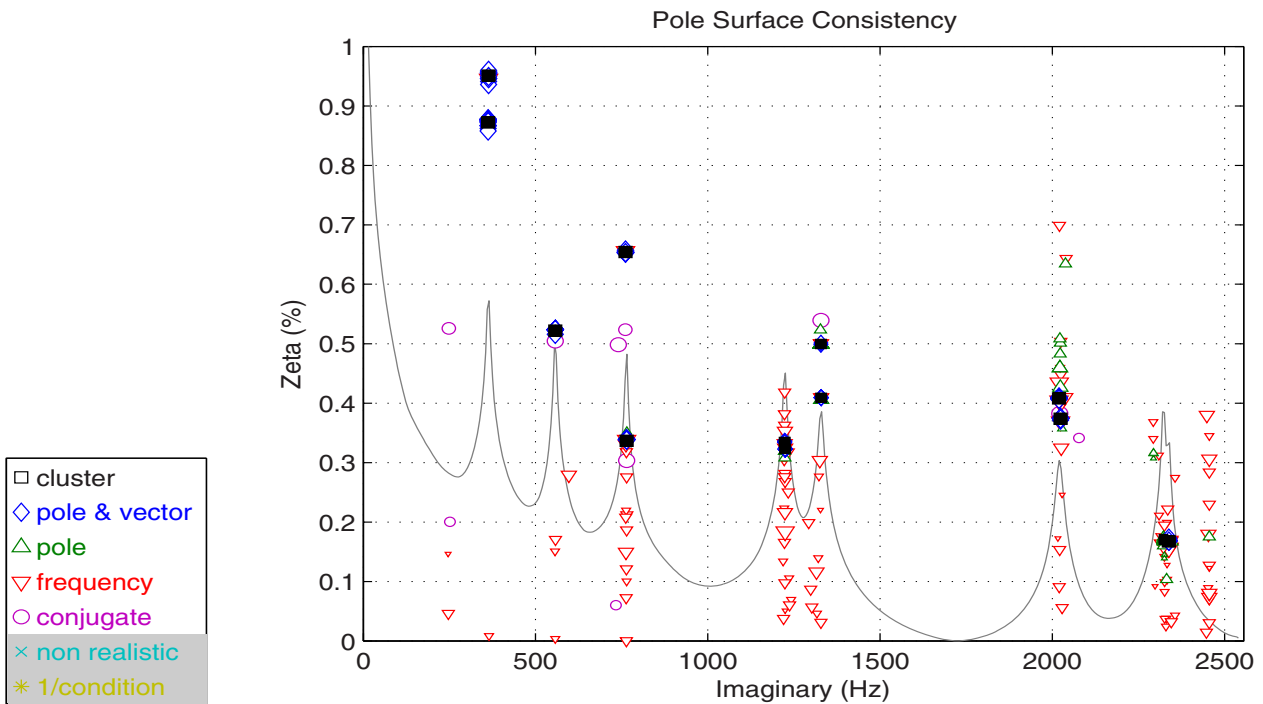


Figure 13. Pole Surface Consistency Clusters with Final Estimates

Figure 14 shows the Auto-MAC comparison of the resulting vectors with their conjugates. The results highlight the quality of the fit.

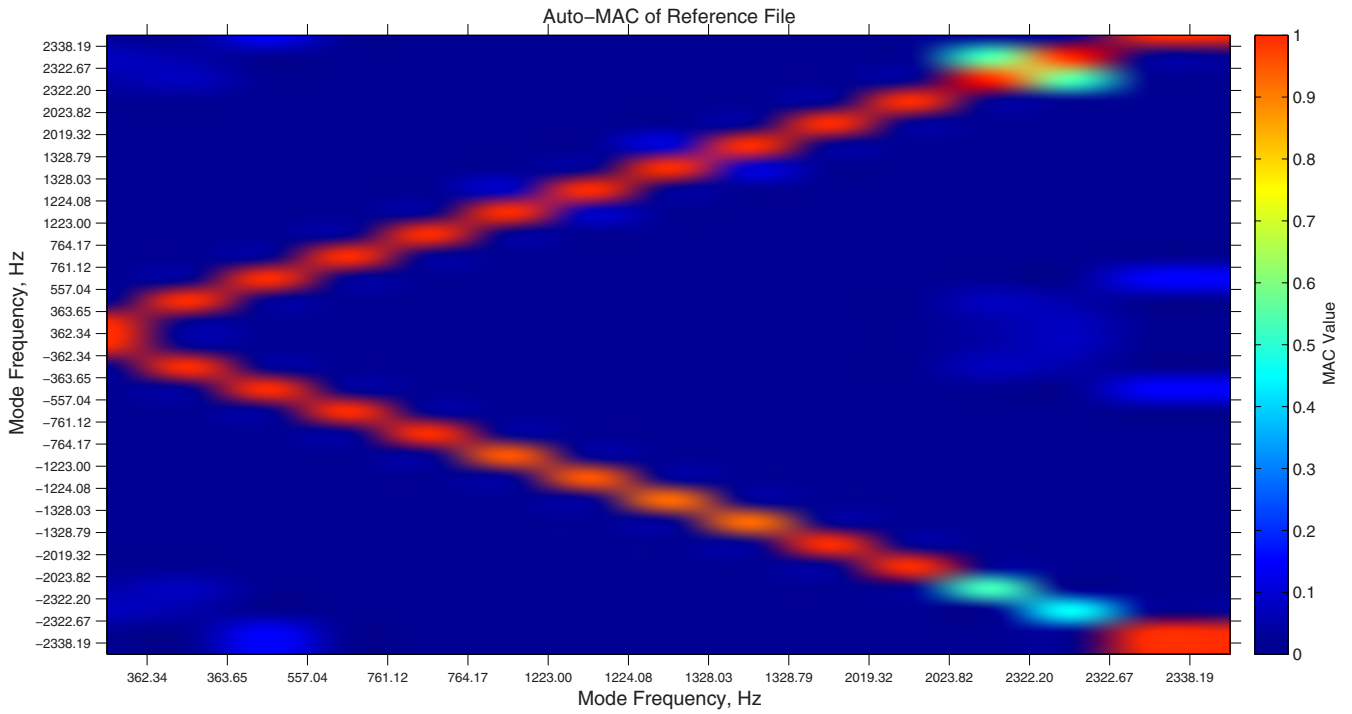


Figure 14. Auto-MAC of Final Autonomous Estimates - Conjugate Poles

5. User Control of Autonomous Process

In the course of this paper, a number of references to the algorithmic control parameters has been made. In this section, a brief discussion of these parameters and their application to the various steps of the procedure is presented. To enhance both visual impression and comprehension, and because the procedure interacts with other display/consistency parameters, some relevant example dialog GUI(s) are shown in [Figures 15](#) and [16](#).

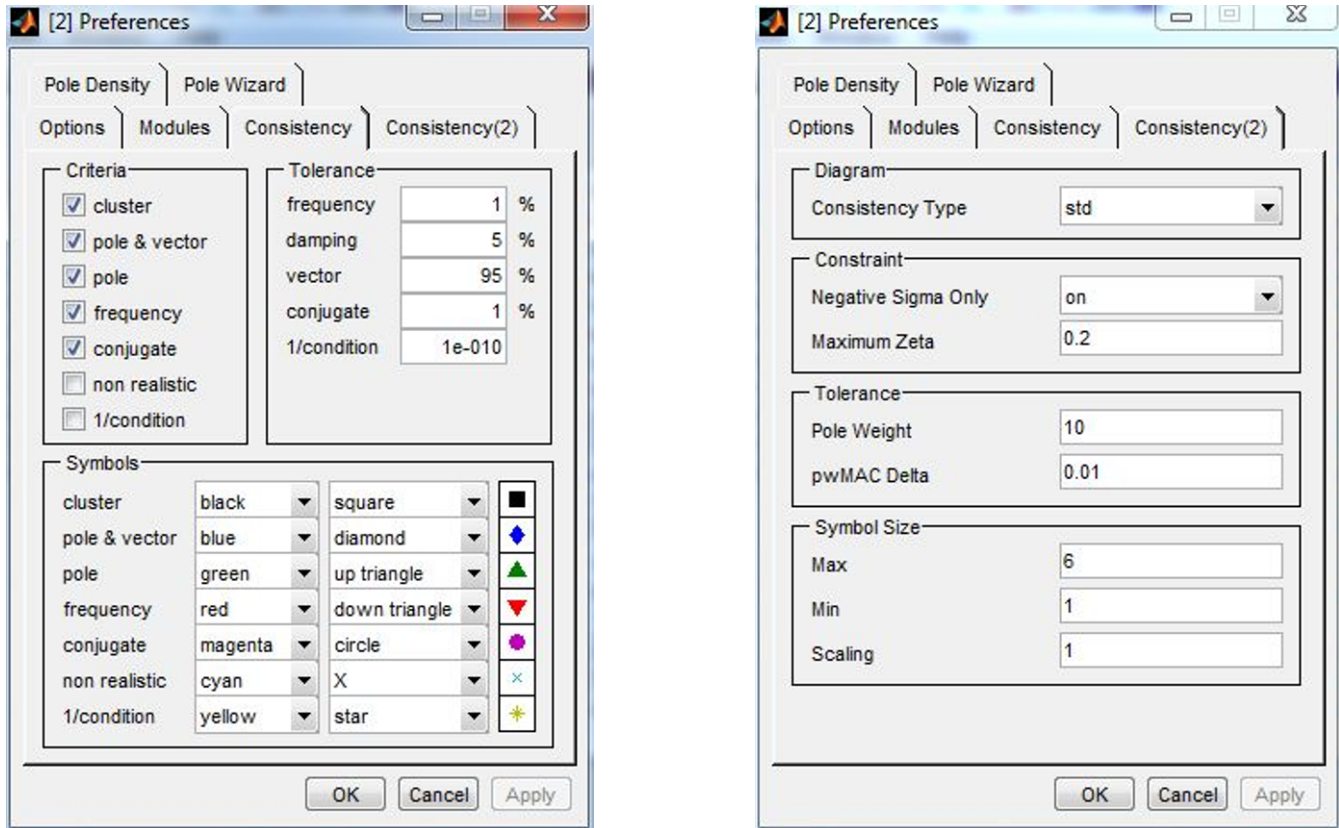


Figure 15. Pole Consistency Preferences GUI

- Consistency: Criteria - This group of parameters determine which set of consistency condition symbols will be displayed on the consistency and pole surface consistency diagrams. This affect procedure Step 1.
- Consistency: Tolerance - This set of parameters determine the criteria for which a pole (and vector) are considered consistent from one model iteration to another. This affects procedure Step 1.
- Consistency(2): Constraint - This pair of parameters is used to define the value of damping (real part of the pole) which is considered realistic. This affects procedure Step 1.
- Consistency(2): Tolerance: Pole Weight - This parameter determines the power of λ or Z used in the evaluation of the pole weighted vector. This affects procedure Step 4.

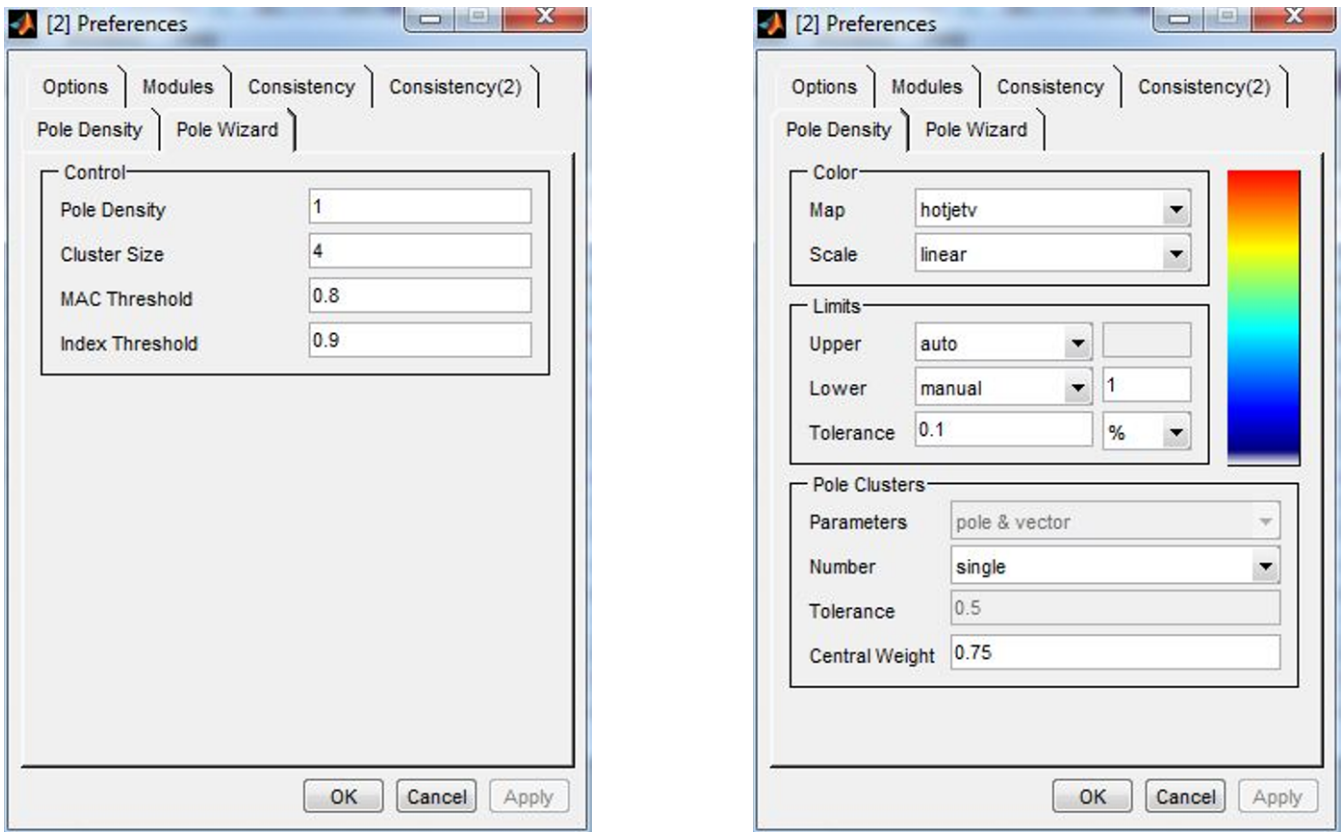


Figure 16. Pole Wizard and Density Preferences GUI

- Pole Wizard: Pole Density - This parameter selects for inclusion in the processing all displayed poles whose density is greater than or equal this value. As shown in the GUI, the value of one uses all displayed poles without limiting the number of poles evaluated. This affects procedure Step 3.
- Pole Wizard: Cluster Size - This parameter determines the minimum number of poles considered to represent an acceptable consistent spatio-temporal cluster. This affects procedure Step 7.
- Pole Wizard: MAC Threshold - This parameter determines the minimum MAC value which is considered significant in the determination of valid vector clusters. This affects procedure Step 6.
- Pole Wizard: Index Threshold - This parameter determines the minimum value of the scaled singular vector at which it is still considered a valid logical index. This affects procedure Step 7.
- Pole Density: Limits: Tolerance - This parameter determines the complex frequency radius around a pole in which any other pole is within this radius is considered to be part its cluster. The pole density is the number of poles located within the circle. This affects procedure Step 3.

6. Summary and Future Work

In this paper, a general autonomous modal parameter identification procedure has been presented along with a review of the history and theory applicable to the development of the autonomous procedures. This autonomous parameter estimation method utilizes the concept of evaluating statistically significant pole weighted vectors among thousands of possible solutions as the primary approach to identifying modal parameters. This involves the correlation of pole weighted vectors from multiple (more than two) sets of solutions involving either long or short basis vectors. This technique has been shown to be general and applicable to most standard commercially available algorithms.

With the advent of more computationally powerful computers and sufficient memory, it has become practical to evaluate sets of solutions involving thousands of modal parameter estimates and to extract the common information from those sets. The

autonomous procedure gives very acceptable results, in some cases superior results, in a fraction of the time required for an experienced user to get the same result.

It is important, however, to reiterate that the use of autonomous procedures or *wizard* tools by users with limited experience is probably not yet appropriate. Such tools are most appropriately used by analysts with the experience to accurately judge the quality of the parameter solutions identified.

Future work on this method planned by the authors include: combining the solutions from different UMPA methods (PTD plus RFP-Z plus ERA, for example), further evaluating the sensitivity of control parameters and thresholds, enhancing the statistical descriptors for each estimated set of modal parameters, and investigating more application cases such as purely academic, theoretical examples as well as difficult sets of measured, real-world data cases, including automotive, flight flutter and operating data applications.

7. References

- [1] Hawkins, F. J., "An Automatic Resonance Testing Technique for Exciting Normal Modes of Vibration of Complex Structures", Symposium IUTAM, "Progres Recents de la Mecanique des Vibrations Lineaires", 1965, pp. 37-41.
- [2] Hawkins, F. J., "GRAMPA - An Automatic Technique for Exciting the Principal Modes of Vibration of Complex Structures", Royal Aircraft Establishment, RAE-TR-67-211, 1967.
- [3] Taylor, G. A., Gaukroger, D. R., Skingle, C. W., "MAMA - A Semi-Automatic Technique for Exciting the Principal Modes of Vibration of Complex Structures", Aeronautical Research Council, ARC-R/M-3590, 1967, 20 pp.
- [4] Allemang, R.J., Phillips, A.W., "The Unified Matrix Polynomial Approach to Understanding Modal Parameter Estimation: An Update", Proceedings, International Conference on Noise and Vibration Engineering (ISMA), 2004.
- [5] Allemang, R.J., Brown, D.L., "A Unified Matrix Polynomial Approach to Modal Identification", ***Journal of Sound and Vibration***, Vol. 211, No. 3, pp. 301-322, April 1998.
- [6] Allemang, R.J., Brown, D.L., "A Unified Matrix Polynomial Approach to Modal Identification", Proceedings, Indo-US Symposium on Emerging Trends in Vibration and Noise Engineering, IIT Dehli, India, Allied Publishers Limited, pp. 379-390, March 1996.
- [7] Allemang, R.J., Brown, D.L., Fladung, W., "Modal Parameter Estimation: A Unified Matrix Polynomial Approach", Proceedings, International Modal Analysis Conference (IMAC), pp. 501-514, 1994.
- [8] Allemang, R.J., Brown, D.L., "Summary of Technical Work", *Experimental Modal Analysis and Dynamic Component Synthesis*, USAF Technical Report, Contract Number F33615-83-C-3218, AFWAL-TR-87-3069, Volume 1, 1987.
- [9] Chauhan, S., Tcherniak, D., "Clustering Approaches to Automatic Modal Parameter Estimation", Proceedings, International Modal Analysis Conference (IMAC), 14 pp., 2008.
- [10] Chhipwadia, K.S., Zimmerman, D.C. and James III, G.H., "Evolving Autonomous Modal Parameter Estimation", Proceedings, International Modal Analysis Conference (IMAC), pp. 819-825, 1999.
- [11] James III, G.H., Zimmerman, D.C., Chhipwadia, K.S., "Application of Autonomous Modal Identification to Traditional and Ambient Data Sets", Proceedings, International Modal Analysis Conference (IMAC), pp. 840-845, 1999.
- [12] Lanslots, J., Rodiers, B., Peeters, B., "Automated Pole-Selection: Proof-of-Concept and Validation", Proceedings, International Conference on Noise and Vibration Engineering (ISMA), 2004.
- [13] Lau, J., Lanslots, J., Peeters, B., Van der Auweraer, "Automatic Modal Analysis: Reality or Myth?", Proceedings, International Modal Analysis Conference (IMAC), 10 pp., 2007.
- [14] Lim, T., Cabell, R. and Silcox, R., "On-line Identification of Modal Parameters Using Artificial Neural Networks", ***Journal of Vibration and Acoustics***, Vol. 118 No. 4, pp. 649-656, 1996.
- [15] Liu, J.M., Ying, H.Q., Shen, S., Dong, S.W., "The Function of Modal Important Index in Autonomous Modal Analysis", Proceedings, International Modal Analysis Conference (IMAC), 6 pp., 2007.

- [16] Mevel, L., Sam, A., Goursat, M., "Blind Modal Identification for Large Aircrafts", Proceedings, International Modal Analysis Conference (IMAC), 8 pp., 2004.
- [17] Mohanty, P., Reynolds, P., Pavic, A., "Automatic Interpretation of Stability Plots for Analysis of a Non-Stationary Structure", Proceedings, International Modal Analysis Conference (IMAC), 7 pp., 2007.
- [18] Pappa, R.S., James, G.H., Zimmerman, D.C., "Autonomous Modal Identification of the Space Shuttle Tail Rudder", ASME-DETC97/VIB-4250, 1997, **Journal of Spacecrafts and Rockets**, Vol. 35 No. 2, pp. 163-169, 1998.
- [19] Pappa, R.S., Woodard, S. E., and Juang, J.-N., "A Benchmark Problem for Development of Autonomous Structural Modal Identification", Proceedings, International Modal Analysis Conference (IMAC), pp 1071-1077, 1997
- [20] Parloo, E., Verboven, P., Guillaume, P., Van Overmeire, M., "Autonomous Structural Health Monitoring - Part II: Vibration-based In-Operation Damage Assessment", **Mechanical Systems and Signal Processing (MSSP)**, Vol. 16 No. 4, pp. 659-675, 2002.
- [21] Poncelet, F., Kerschen, G., Golinval, J.C., "Operational Modal Analysis Using Second-Order Blind Identification", Proceedings, International Modal Analysis Conference (IMAC), 7 pp., 2008.
- [22] Rainieri, C., Fabbrocino, G., Cosenza, E., "Fully Automated OMA: An Opportunity for Smart SHM Systems", Proceedings, International Modal Analysis Conference (IMAC), 9 pp., 2009.
- [23] Takahashi, K., Furusawa, M., "Development of Automatic Modal Analysis", Proceedings, International Modal Analysis Conference (IMAC), pp. 686-692, 1987.
- [24] Vanlanduit, S., Verboven, P., Schoukens, J., Guillaume, P. "An Automatic Frequency Domain Modal Parameter Estimation Algorithm", Proceedings, International Conference on Structural System Identification, Kassel, Germany, pp. 637-646, 2001.
- [25] Vanlanduit, S., Verboven, P., Guillaume, P., Schoukens, J., "An Automatic Frequency Domain Modal Parameter Estimation Algorithm", **Journal of Sound and Vibration**, Vol. 265, pp. 647-661, 2003.
- [26] Verboven, P., Parloo, E., Guillaume, P., Van Overmeire, M., "Autonomous Structural Health Monitoring Part I: Modal Parameter Estimation and Tracking", **Mechanical Systems and Signal Processing**, Vol. 16 No. 4, pp. 637-657, 2002.
- [27] Verboven P., E. Parloo, P. Guillame, and M. V. Overmeire, "Autonomous Modal Parameter Estimation Based On A Statistical Frequency Domain Maximum Likelihood Approach", Proceedings, International Modal Analysis Conference (IMAC), pp. 1511-1517, 2001.
- [28] Yam, Y., Bayard, D.S., Hadaegh, F.Y., Mettler, E., Milman, M.H., Scheid, R.E., "Autonomous Frequency Domain Identification: Theory and Experiment", NASA JPL Report JPL Publication 89-8, 204 pp., 1989.
- [29] Allemang, R.J., Phillips, A.W., "The Impact of Measurement Condensation and Modal Participation Vector Normalization on the Estimation of Modal Vectors and Scaling", Proceedings, International Modal Analysis Conference (IMAC), 12 pp., 2004.
- [30] Basseville, M., Abdelghani, M., Benveniste, A., "Subspace-Based Fault Detection Algorithms for Vibration Monitoring", *Automatica*, Vol. 36, No. 1, pp. 101-109, 2000.
- [31] Brown, D. L., Phillips, A. W., Allemang, R. J., "A First Order, Extended State Vector Expansion Approach to Experimental Modal Parameter Estimation", Proceedings, International Modal Analysis Conference (IMAC), 11 pp., 2005.
- [32] Carden, E.P., Brownjohn, J.M.W., "Fuzzy Clustering of Stability Diagrams for Vibration-Based Structural Health Monitoring", *Computer-Aided Civil and Infrastructure Engineering*, Vol. 23, pp. 360-372, 2008.
- [33] Dippery, K.D., Phillips, A.W., Allemang, R.J., "Condensation of the Spatial Domain in Modal Parameter Estimation", **Modal Analysis: International Journal of Analytical and Experimental Modal Analysis**, Vol. 11, No. 3/4, 6 pp., 1996.
- [34] Dippery, K.D., Phillips, A.W., Allemang, R.J., "Spectral Decimation in Low Order Frequency Domain Modal Parameter Estimation", **Modal Analysis: International Journal of Analytical and Experimental Modal Analysis**, Vol. 11, No. 3/4, 5 pp., 1996.

- [35] Goethals, I., Vanluyten, B., De Moor, B., "Reliable Spurious Mode Rejection using Self Learning Algorithms", Proceedings, International Conference on Noise and Vibration Engineering (ISMA), 2006.
- [36] Goethals, I., De Moor, B., "Model Reduction and Energy Analysis as a Tool to Detect Spurious Modes", Proceedings, International Conference on Noise and Vibration Engineering (ISMA), 2002.
- [37] Goethals, I., De Moor, B., "Subspace Identification Combined With New Mode Selection Techniques For Modal Analysis Of An Airplane", Proc. SYSID-2003, IFAC Symposium on System Identification, pp. 2729, August 2003.
- [38] Guillaume, P., Verboven, P., Vanlanduit, S., "Frequency-Domain Maximum Likelihood Identification Of Modal Parameters With Confidence Intervals", Proceedings, International Conference on Noise and Vibration Engineering (ISMA), 1998.
- [39] Guillaume, P., Verboven, P., Vanlanduit, S., Van der Auweraer, H., Peeters, B., "A Polyreference Implementation of the Least-Squares Complex Frequency Domain Estimator", Proceedings, International Modal Analysis Conference (IMAC), 12 pp., 2003.
- [40] Lanslots, J., Scionti, M., Vecchio, A., "Fuzzy Clustering Techniques To Automatically Assess Stabilization Diagrams", Proceedings, Conference on the Application of Artificial Intelligence to Civil and Structural Eng., Egmond-aan-Zee, The Netherlands, 2003.
- [41] Pappa, R.S., Elliot, K.B., Schenk, K., "Consistent-Mode Indicator for Eigensystem Realization Algorithm", **Journal of Guidance, Control and Dynamics**, Vol. 16 No. 5, pp. 852-858, 1993.
- [42] Phillips, A.W., Allemang, R.J., "Numerical Considerations in Modal Parameter Estimation", Proceedings, International Conference on Noise and Vibration Engineering (ISMA), 10 pp., 1996.
- [43] Phillips, A.W., Allemang, R.J., Pickrel, C.R., "Clustering of Modal Frequency Estimates from Different Solution Sets", Proceedings, International Modal Analysis Conference (IMAC), pp. 1053-1063, 1997.
- [44] Phillips, A.W., Allemang, R.J., Pickrel, C.R., "Estimating Modal Parameters from Different Solution Sets", Proceedings, International Modal Analysis Conference (IMAC), 10 pp., 1998.
- [45] Phillips, A. W., Allemang, R. J., "A Low Order Implementation of the Polyreference Least Squares Complex Frequency (LSCF) Algorithm", Proceedings, International Conference on Noise and Vibration Engineering (ISMA), 2004.
- [46] Phillips, A.W., Allemang, R.J., "Data Presentation Schemes for Selection and Identification of Modal Parameters", Proceedings, International Modal Analysis Conference (IMAC), 10 pp., 2005.
- [47] Phillips, A.W., Allemang, R.J., "Additional Mechanisms for Providing Clear Stabilization (Consistency) Diagrams", Proceedings, International Conference on Noise and Vibration Engineering (ISMA), 15 pp., 2008.
- [48] Phillips, A.W., Allemang, R.J., "Application of Modal Scaling to the Pole Selection Phase of Parameter Estimation", Proceedings, International Modal Analysis Conference (IMAC), 20 pp., 2010.
- [49] Scionti, M., Lanslots, J., "Stabilization Diagrams: Pole Identification Using Fuzzy Clustering Techniques", **Advances in Engineering Software**, Vol. 36, pp. 768-779, 2005.
- [50] Scionti, M., Lanslots, J., Goethals, I., Vecchio, A., Van der Auweraer, H., Peeters, B., De Moor, B., "Tools to Improve Detection of Structural Changes from In-Flight Flutter Data", Proceedings, International Conference on Recent Advances in Structural Dynamics, Southampton, UK, 2003.
- [51] Van Der Auweraer, H., Guillaume, P., Verboven, P., Vanlanduit, S., "Application Of A Fast-Stabilizing Frequency Domain Parameter Estimation Method", **ASME Journal of Dynamic Systems, Measurement, and Control**, Vol. 123 No. 4, pp. 651658, 2001.
- [52] Verboven, P., Cauberghe, B., Guillaume, P., "A Structural Health Monitoring Approach For Flutter Testing" Proceedings, International Conference on Noise and Vibration Engineering (ISMA), pp. 1631-1642, 2002.
- [53] Verboven, P., Guillaume, P., Cauberghe, B., Parloo, E., Vanlanduit, S., "Stabilization Charts and Uncertainty Bounds for Frequency-Domain Linear Least Squares Estimators", Proceedings, International Modal Analysis Conference (IMAC), 10 pp., 2003.

- [54] Verboven, P., Cauberghe, B., Vanlanduit, S., Parloo, E., Guillaume, P., "The Secret Behind Clear Stabilization Diagrams: The Influence of the Parameter Constraint on the Stability of the Poles", Proceedings, Society of Experimental Mechanics (SEM) Annual Conference, 17 pp., 2004.
- [55] Woodard, S.E., Pappa, R.S., "Development of Structural Identification Accuracy Indicators Using Fuzzy Logic", ASME-DETC97/VIB-4258, 1997.
- [56] Allemang, R.J., Brown, D.L., Phillips, A.W., "Survey of Modal Techniques Applicable to Autonomous/Semi-Autonomous Parameter Identification", Proceedings, International Conference on Noise and Vibration Engineering (ISMA), 2010.
- [57] Allemang, R.J., Phillips, A.W., Brown, D.L., "Combined State Order and Model Order Formulations in the Unified Matrix Polynomial Method (UMPA)", Proceedings, International Modal Analysis Conference (IMAC), 25 pp., 2011.
- [58] Brown, D.L., Allemang, R.J., Phillips, A.W., "Autonomous Modal Parameter Estimation: Application Examples", Proceedings, International Modal Analysis Conference (IMAC), 26 pp., 2011.
- [59] Allemang, R.J., Phillips, A.W., Brown, D.L., "Autonomous Modal Parameter Estimation: Statistical Considerations", Proceedings, International Modal Analysis Conference (IMAC), 17 pp., 2011.

Autonomous Modal Parameter Estimation: Statistical Considerations

R.J. Allemang, A.W. Phillips, D.L. Brown
Structural Dynamics Research Laboratory
School of Dynamic Systems
College of Engineering and Applied Science
University of Cincinnati
Cincinnati, OH 45221-0072 USA
Email: Randall.Allemang@UC.EDU

ABSTRACT

Autonomous modal parameter estimations may involve sorting a large number of possible solutions to develop one consistent estimate of the modal parameters (frequency, damping, mode shape, and modal scaling). Once the final, consistent estimate of modal parameters is established, this estimate can be compared to related solutions from the larger set of solutions to develop statistical attributes for the final, consistent set of modal parameters. These attributes will include sample size, standard deviation and other familiar variance estimates. New variance estimates are introduced to categorize the modal vector solution. These modal vector statistics are based upon the residual contributions in a set of correlated modal vectors that are used to estimate a single modal vector. Examples of this statistical information is included for a number of realistic data cases.

Nomenclature

N = Number of vectors in cluster.

σ_r = Singular value r from cluster.

λ_r = S domain polynomial root.

λ_r = Complex modal frequency (rad/sec).

z_r = Z domain polynomial root.

$\{\psi_r\}$ = Base vector (modal vector).

$\{\phi_r\}$ = Pole weighted base vector (state vector).

Std. Dev. = Standard deviation.

NMVR₁ = Normalized modal vector residual 1.

NMVR₂ = Normalized modal vector residual 2.

NSVR₁ = Normalized state vector residual 1.

NSVR₂ = Normalized state vector residual 2.

1. Introduction

The desire to estimate modal parameters automatically, once a set or multiple sets of test data are acquired, has been a subject of great interest for more than 40 years ^[1-24]. In the 1960s, even when modal testing was limited to analog test methods, several researchers were exploring the idea of an automated test procedure for determining modal parameters ^[1-3]. Today, with the increased memory and compute power of current computers used to process test data, an automated or autonomous, modal parameter estimation procedure is entirely possible and is being attempted by numerous researchers.

During the development of a new autonomous modal parameter estimation procedure, it became obvious that, since a large number of possible solutions were being evaluated, that this development was a natural way to introduce statistical evaluations into the modal analysis estimation process. This paper reviews some of the statistical estimates that can aid any user in evaluating possible modal parameter estimation solutions.

The larger question concerning autonomous modal parameter estimation is the intended user. Is the autonomous modal parameter estimation procedure expected to give results sufficiently robust for the novice user? This implies that the user could have no experience with modal analysis and, therefore, have no experiential judgement to use in assessing the quality of the results. The use of the term *wizard* implies that this is the desired situation. In contrast, the user could be very knowledgeable in the theory and experienced. For this case, the autonomous modal parameter estimation procedure is simply an efficient mechanism for sorting a very large number of solutions into a final set of solutions that satisfies a set of criteria

and thresholds that are acceptable to the user. This user is the assumed reader for the purposes of this discussion. The statistical parameters introduced in this paper, however, are designed to give all users additional information that will allow both experienced and novice users to successfully identify the modal parameters, within the limits of the information provided by the measured data.

In order to discuss autonomous modal parameter estimation, some background is needed to clarify terminology and methodology. The reader is directed to a series of companion papers in order to get an overview of the methodology and to view application results for several cases ^[25-26]. The statistics explained in this paper are part of this new general procedure for autonomous modal parameter that is based upon consistent state vectors. This method is referred to as **Common Statistical Subspace Autonomous Mode Identification (CSSAMI)**. Note that much of the background of the CSSAMI method is based upon the Unified Matrix Polynomial Algorithm (UMPA) developed by the authors and described in a number of other papers ^[27-29].

2. Background: Autonomous Modal Parameter Estimation

The interest in automatic modal parameter estimation methods has been documented in the literature since at least the mid 1960s when the primary modal method was the analog, force appropriation method ^[1-3]. Following that early work, there has been a continuing interest in autonomous methods ^[4-24] that, in most cases, have been procedures that are formulated based upon a specific modal parameter estimation algorithm like the Eigensystem Realization Algorithm (ERA), the Polyreference Time Domain (PTD) algorithm or more recently the Polyreference Least Squares Complex Frequency (PLSCF) algorithm or the commercial version of the PLSCF, the PolyMAX [®] method.

Each of these past procedures have shown some promise but have not yet been widely adopted. In many cases, the procedure focussed on a single modal parameter estimation algorithm and did not develop a general procedure. Most of the past procedural methods focussed on pole density but depended on limited modal vector data to identify correlated solutions. Currently, due to increased computational speed and larger availability of memory, procedural methods can be developed that were beyond the computational scope of available hardware only a few years ago. These methods do not require any initial thresholding of the solution sets and rely upon correlation of the vector space of thousands of potential solutions as the primary identification tool. With the addition to any modal parameter estimation algorithm of the concept of pole weighted base vector, the length, and therefore sensitivity, of the extended vectors provides an additional tool that appears to be very useful.

3. Autonomous Modal Parameter Estimation Method

The autonomous modal parameter estimation method developed and presented in the following is a general method that can be used with any algorithm that fits within the UMPA structure. A complete description of the Unified Matrix Polynomial Algorithm (UMPA) thought process can be found in a number of references developed by the authors ^[27-29]. This means that this method can be applied to both low and high order methods with low or high order base vectors. This also means that most commercial algorithms could take advantage of this procedure. Note that high order matrix coefficient polynomials normally have coefficient matrices of dimension that is based upon the short dimension of the data matrix ($N_S \times N_S$). In these cases, it may be useful to solve for the complete modal vector in addition to using the extended base vector as this will extend the temporal-spatial information in the base vector so that the vector will be more sensitive to change. This characteristic is what gives this autonomous method the ability to distinguish between computational and structural modal parameters.

The implementation of the autonomous modal parameter estimation for this method is briefly outlined in the following steps. For complete details, please see the associated papers ^[25-26].

- Develop a consistency diagram using any UMPA solution method. Since this autonomous method utilizes a pole surface density plot, having a large number of iterations in the consistency diagram (due to model order, subspace iteration, starting times, equation normalization, etc.) will be potentially advantageous. However, the larger the number of solutions (represented by symbols) in the consistency diagram, the more computation time and memory will be required. However, restricting the number of solutions using clear stabilization (consistency) methods may be counterproductive.
- If the UMPA method is high order (coefficient matrices of size $N_S \times N_S$), solve for the complete length, scaled vector (function of N_L for all roots, structural and computational).

- Based upon the pole surface density threshold, identify all possible pole densities above some minimum value. This will be a function of the number of possible solutions represented by the consistency diagram.
- Sort the remaining solutions into frequency order based upon damped natural frequency (ω_r).
- Construct the 10th order, pole weighted vector (state vector) for each solution.
- Normalize all pole weighted vectors to unity length with dominant real part.
- Calculate the Auto-MAC matrix for all pole weighted vectors.
- Retain all Auto-MAC values that have a pole weighted MAC value above a threshold, 0.8 works well for most cases. All values below the threshold are set to 0.0.
- Identify vector clusters from this pole weighted MAC diagram that represent the same pole weighted vector. This is done by a singular value decomposition (SVD) of the pole weighted MAC matrix. The number of significant singular values for this MAC matrix represents the number of significant pole clusters in the pole weighted vector matrix and the value of each significant singular value represents the size of the cluster since the vectors are unitary. Note that the singular value is nominally the square of the number of vectors in the cluster and will likely be different, mode by mode.
- For each significant singular value, the location of the corresponding pole weighted vectors in the pole weighted vector matrix (index) is found from the associated left singular vector. This is accomplished by multiplying the left singular vector by the square root of the singular value and retaining all positions (indexes) above a threshold (typically 0.9). The positions of the non-zero elements in this vector are the indexes into the pole weighted vector matrix for all vectors belonging to a single cluster.
- For each identified pole cluster, perform a singular value decomposition (SVD) on the set of pole weighted vectors. The significant left singular vector is the dominant (average) pole weighted vector. Use the zeroth order portion of this dominant vector to identify the modal vector and the relationship between the zeroth order and the first order portions of the dominant vector to identify the modal frequency and modal damping values.
- Estimate appropriate statistics for each mode identified based upon the modes that are grouped in each cluster.
- For the modal parameters identified, complete the solution for modal scaling using any MIMO process of your choice.
- User interaction with the final set of values can exclude poorly identified modes based upon physical or statistical evaluations.

Once the final set of modal parameters, along with their associated statistics, is obtained, quality can be assessed by many methods that are currently available. The most common example is to perform comparisons between the original measurements and measurements synthesized from the modal parameters. Another common example is to look at physical characteristics of the identified parameters such as reasonableness of frequency and damping values, normal mode characteristics in the modal vectors, and appropriate magnitude and phasing in the modal scaling. Other evaluations that may be helpful are mean phase correlation (MPC) on the vectors, an Auto-MAC looking for agreement between the modal vectors from conjugate poles or any other method available.

4. Statistical Evaluation Parameters

Statistical evaluation parameters can be estimated for each common cluster of pole weighted modal vectors on the basis of the complex modal frequency, the modal vector, and the modal scaling. The number of pole weighted vectors will in general be different in each cluster so the statistics will be based upon the number of estimates available (sample size N). Examples of the statistics currently computed for each modal parameter are described in the following sections.

4.1 Modal Frequency Statistics

The weighted modal frequency for the cluster is found by constructing the pole weighted vector (typically 10th order) for each pole retained in a cluster, then taking the SVD of the group of pole weighted vectors and selecting the singular vector associated with the largest singular value. This chosen singular vector contains both the shape and the modal frequency information. The modal frequency is identified by dividing the first order portion by the zeroth order portion of the vector in a least squares sense. (Note that it is also possible to solve the frequency polynomial which would result from using the complete vector.) Also, for numerical reasons, the pole weighted vector is actually computed in the Z -domain.

$$\{\phi\}_r = \begin{Bmatrix} z_r^v\{\psi\}_r \\ \cdot \\ \cdot \\ z_r^2\{\psi\}_r \\ z_r^1\{\psi\}_r \\ z_r^0\{\psi\}_r \end{Bmatrix}_r$$

For comparison purposes, the actual mean value and standard deviation of the poles (as well as, the separate frequency and damping means and standard deviations) which were used in the computation of the weighted solution are computed. Since these results are unweighted by the vector characteristics, they will be somewhat different from the vector weighted solution and provide comparative feedback about the pole.

4.2 Modal Vector Statistics

In order to evaluate the quality of the resulting modal vectors, several different parameters (representing noise to signal ratios) are calculated. These ratios are evaluated for both the original normalized vectors and the pole weighted (state extended) vectors and are computed using the singular value decomposition of each of the set of vectors.

4.2.1 Normalized Modal Vector Residual (NMVR)

The first modal vector parameter is evaluated by taking the total residual magnitude (the Forbenius norm of the residuals) divided by the magnitude of the principal vector magnitude. In other words, the square root of the sum of the squares of the residual singular values divide by the first (largest) singular value. This provides an indication of the consistency of the original contributing vectors. Small values tend to indicate greater consistency. Large values indicate greater variance or the possibility that more than one mode has been included in a cluster.

$$[\sigma] = \text{SVD}\left(\left[\psi_1 \psi_2 \cdots \psi_N\right]\right) \quad (1)$$

$$\text{NMVR}_1 = \frac{\sqrt{\frac{\sum_{k=2}^N \sigma_k^2}{N}}}{\sigma_1} \quad (2)$$

The second modal vector parameter is evaluated by taking the largest residual magnitude divided by the magnitude of the principal vector magnitude. In other words, the second singular value divided by the first singular value. This provides an indication of the consistency of the original contributing vectors. A small value tends to indicate random variance. A large value can indicate a consistent modal contamination of the original vectors, possibly caused by a second mode included in the cluster.

$$\text{NMVR}_2 = \frac{\sigma_2}{\sigma_1} \quad (3)$$

4.2.2 Normalized State Vector Residual (NSVR)

The associated state vector parameters are calculated analogous to the above except that the complete pole weighted (state extended) vector is used.

$$[\sigma] = \text{SVD}\left(\left[\phi_1 \phi_2 \cdots \phi_N\right]\right) \quad (4)$$

$$NSVR_1 = \frac{\sqrt{\frac{\sum_{k=2}^N \sigma_k^2}{N}}}{\sigma_1} \tag{5}$$

$$NSVR_2 = \frac{\sigma_2}{\sigma_1} \tag{6}$$

4.3 Modal Scaling Statistics

If modal scaling (residue) information is available in the original vectors, it can be applied to the principal pole weighted vector such that the consistency of modal scaling (Modal A) can also be evaluated. By scaling the largest driving point response to unity, a uniform, comparable value for Modal A is chosen. Since the modal scaling parameter (Modal A) contains the physical units and hence the relative contribution of each pole/vector combination to the original data set, a means of evaluating the significance and confidence in each estimate is possible. Because the original vectors represent multiple scaled solutions and since Modal A is a single scalar complex value for each pole/vector combination, the statistical distribution of Modal A (mean and standard deviation) of the original cluster can be compared with the scaling estimated from the pole weighted (state extended) vector. The magnitude of Modal A can be used to evaluate the contribution of this vector to the total set of identified vectors. When the user believes that the identified vectors should be normal modes, the phase of the Modal A can be used to evaluate the closeness to a normal mode.

5. Typical Statistics: C-Plate Example

For this example, impact data from a circular plate test article has been used. The FRF data (7x36) was processed using a Rational Fraction Polynomial algorithm with complex z frequency mapping (RFP-Z) with all data between 220 and 2450 Hz included. The model order range used was 2 to 20 with a generalized residual model including all terms from $(j\omega)^{-4}$ to $(j\omega)^2$. Further, low order alpha coefficient normalization has been used and full length phase one residues have been calculated.

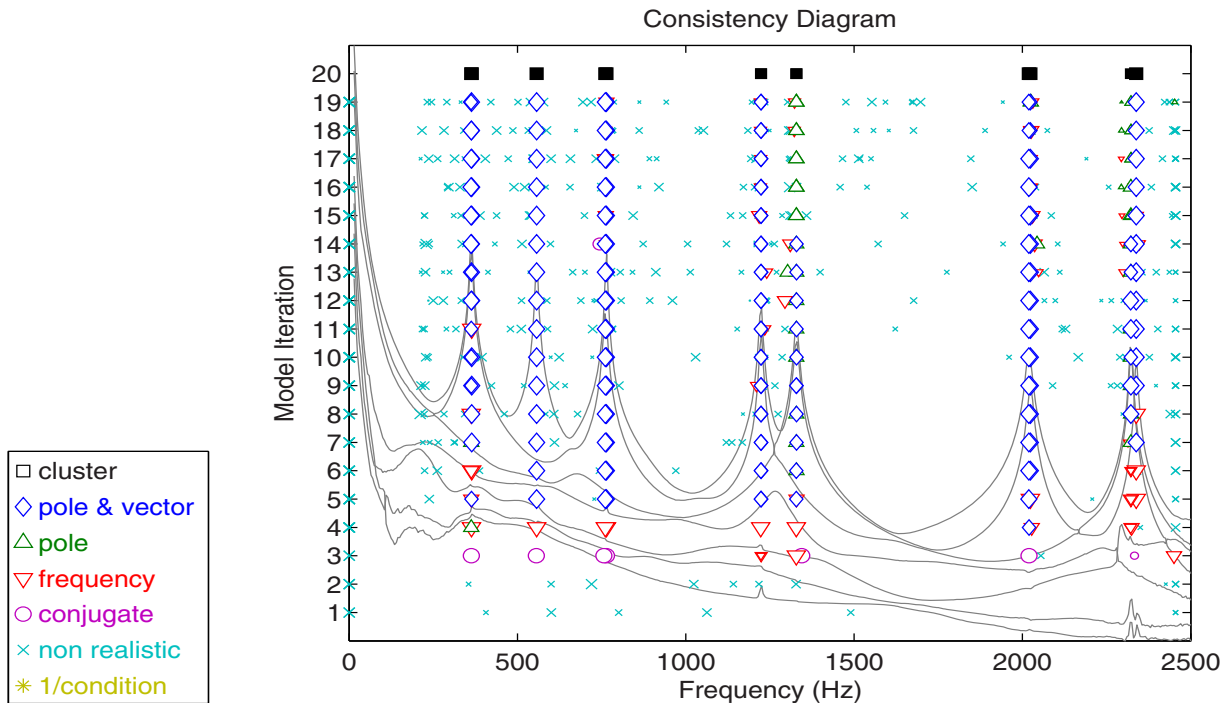


Figure 1. C-Plate Example: Consistency Diagram - All Poles Plotted

For the purposes of demonstration, all calculated poles (both consistent and computational) are included in the plots. As can be observed, though clearly present throughout the frequency range (Figure 1), the non-realistic, computational poles, are not observed in the vicinity of the S-domain computed pole clusters (Figures 2, 3 and 4.)

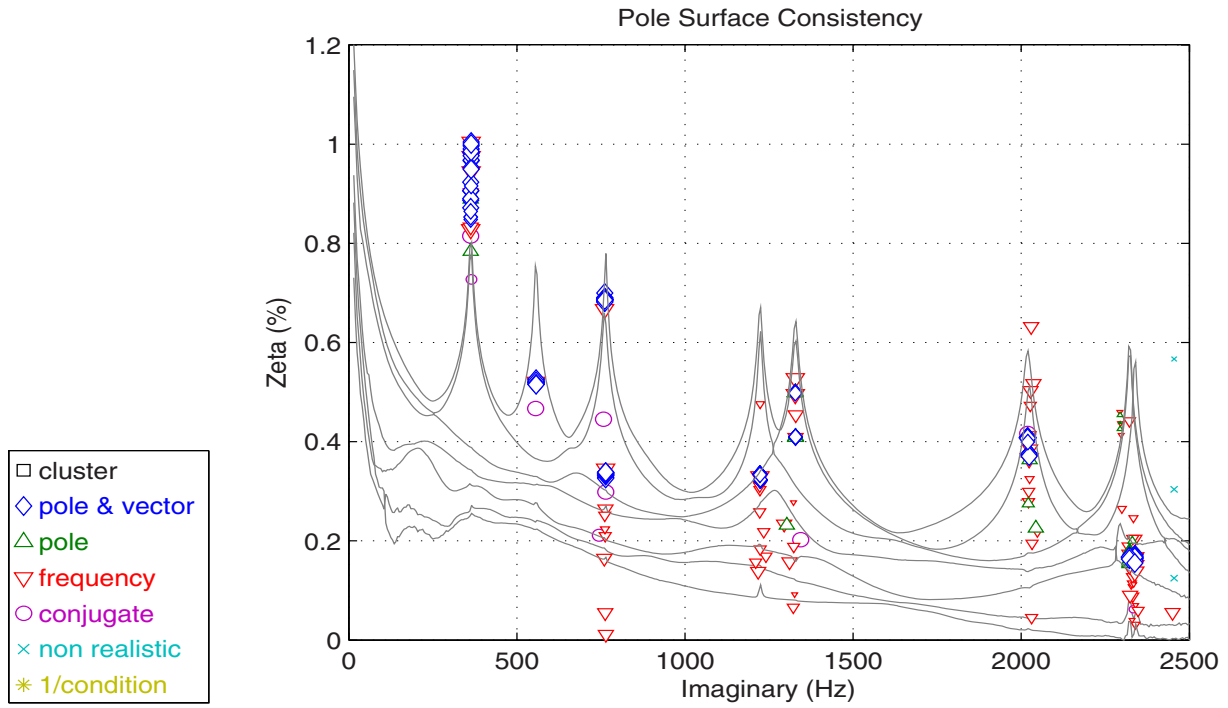


Figure 2. C-Plate Example: Pole Surface Consistency - All Poles Plotted

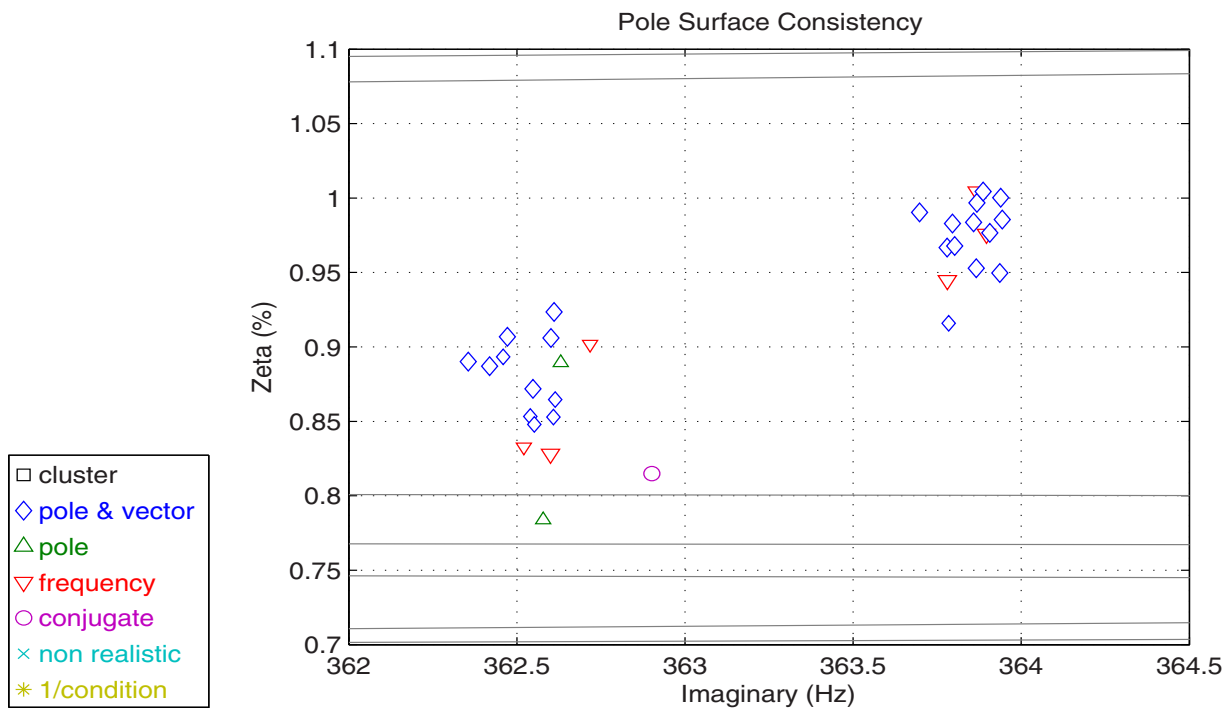


Figure 3. C-Plate Example: Zoomed Pole Clusters - Damping $\% \zeta$

The following plots, [Figures 5](#) and [6](#), are a presentation of the statistical distribution of the pole information for the two clusters (pseudo-repeated root) shown in [Figure 4](#). In [Figures 5](#) and [6](#), the black stars are the original pole estimates and the red star represents the mean pole calculated from this cluster of pole estimates. The large red circle is the one standard deviation radius. The green square is the individual standard deviations for the frequency and the damping. The blue circle is the pole as estimated from the pole weighted (state extended) vector.

Note that the scaling for the two different mode clusters in [Figure 5](#) is consistent so that larger diameter circles will represent more variability.

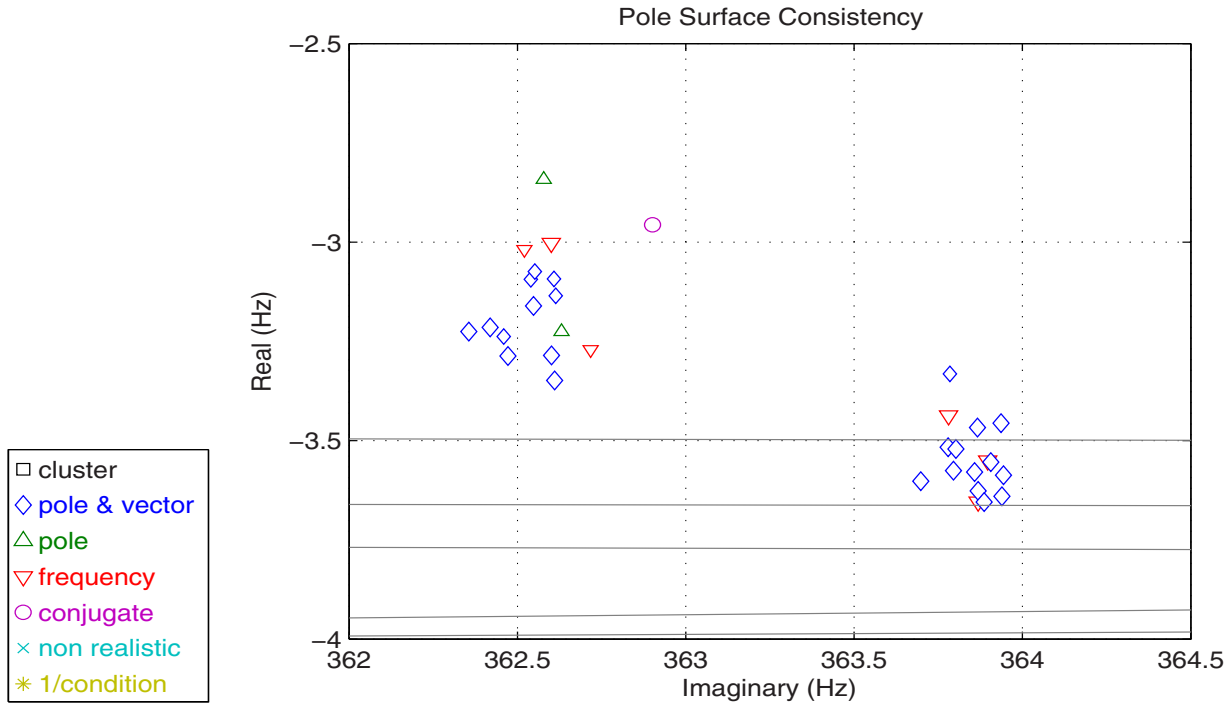


Figure 4. C-Plate Example: Zoomed Pole Clusters - Damping Hz

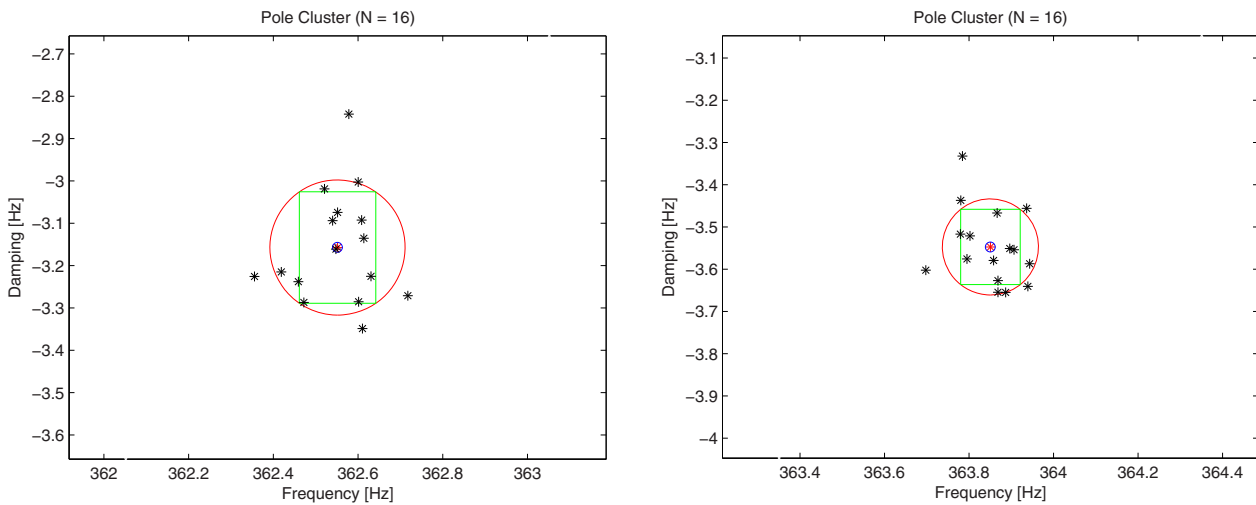


Figure 5. C-Plate Example: 362.6 Hz and 363.9 Hz Pole Clusters - Statistics

The following (Tables 1, 2, and 3) provide a summary of the statistical information evaluated on the C-Plate test structure.

Note that in Table 1 that there is little difference in the complex modal frequency estimated from the most significant pole weighted vector (columns 3 and 4) when compared to the mean values of the complex portions of the modal frequency (columns 5 and 6).

| Index | Sample Size (N) | Frequency (Hz) | Damping (Hz) | Frequency (Hz) (Mean) | Damping (Hz) (Mean) | Std. Dev. (Hz) |
|-------|-----------------|----------------|--------------|--------------------------|------------------------|----------------|
| 8 | 16 | 362.564 | -3.1666 | 362.564 | -3.1670 | 0.1677 |
| 19 | 16 | 363.860 | -3.5650 | 363.860 | -3.5650 | 0.1251 |
| 10 | 16 | 557.055 | -2.8966 | 557.055 | -2.8966 | 0.0795 |
| 12 | 16 | 761.224 | -5.2229 | 761.224 | -5.2229 | 0.1008 |
| 2 | 17 | 764.190 | -2.5371 | 764.190 | -2.5371 | 0.1529 |
| 16 | 16 | 1222.980 | -4.0883 | 1222.980 | -4.0883 | 0.0271 |
| 13 | 16 | 1224.055 | -3.9540 | 1224.055 | -3.9540 | 0.0419 |
| 4 | 17 | 1328.036 | -6.6495 | 1328.036 | -6.6507 | 0.0907 |
| 17 | 16 | 1328.803 | -5.4761 | 1328.803 | -5.4768 | 0.1871 |
| 6 | 17 | 2019.269 | -8.2512 | 2019.271 | -8.2511 | 0.2543 |
| 23 | 15 | 2023.802 | -7.5597 | 2023.801 | -7.5598 | 0.0642 |
| 26 | 10 | 2321.862 | -3.9074 | 2321.860 | -3.9070 | 0.1690 |
| 28 | 8 | 2322.335 | -3.8356 | 2322.335 | -3.8367 | 0.2244 |
| 22 | 15 | 2337.895 | -3.7967 | 2337.895 | -3.7971 | 0.2287 |

TABLE 1. C-Plate Example: Modal Frequency Statistics

In Table 2, note that the fraction of normalized residual (columns 4-7) are all quite small indicated that only one mode has been found in each cluster and that the modal vectors in the cluster were essentially the same modal vector with minimal differences (noise).

| Index | N | Frequency (Hz) | NMVR ₁ | NMVR ₂ | NSVR ₁ | NSVR ₂ |
|-------|----|----------------|-------------------|-------------------|-------------------|-------------------|
| 8 | 16 | 362.564 | 0.0046 | 0.0730 | 0.0046 | 0.0730 |
| 19 | 16 | 363.860 | 0.0034 | 0.0543 | 0.0034 | 0.0543 |
| 10 | 16 | 557.055 | 0.0001 | 0.0014 | 0.0001 | 0.0014 |
| 12 | 16 | 761.224 | 0.0007 | 0.0092 | 0.0007 | 0.0093 |
| 2 | 17 | 764.190 | 0.0020 | 0.0312 | 0.0020 | 0.0312 |
| 16 | 16 | 1222.980 | 0.0017 | 0.0213 | 0.0017 | 0.0213 |
| 13 | 16 | 1224.055 | 0.0013 | 0.0185 | 0.0013 | 0.0184 |
| 4 | 17 | 1328.036 | 0.0042 | 0.0718 | 0.0042 | 0.0717 |
| 17 | 16 | 1328.803 | 0.0022 | 0.0342 | 0.0022 | 0.0342 |
| 6 | 17 | 2019.269 | 0.0054 | 0.0763 | 0.0054 | 0.0763 |
| 23 | 15 | 2023.802 | 0.0047 | 0.0537 | 0.0047 | 0.0537 |
| 26 | 10 | 2321.862 | 0.0162 | 0.1617 | 0.0162 | 0.1617 |
| 28 | 8 | 2322.335 | 0.0161 | 0.1279 | 0.0161 | 0.1278 |
| 22 | 15 | 2337.895 | 0.0020 | 0.0238 | 0.0020 | 0.0238 |

TABLE 2. C-Plate Example: Modal Vector Statistics

In [Table 3](#), note that the method used to compute the modal scaling, Modal A, had little effect on the estimates of Modal A. Also of note in this case, is the phase angle of all Modal A terms is around minus ninety degrees. The sign on the phase angle and the closeness to ninety degrees (rather than zero degrees) is a function of the scaling method chosen for the modal vector.

| Index | N | Frequency (Hz) | ModalA (State Vector) | | | | ModalA (Mean from cluster) | | | | |
|-------|----|----------------|-----------------------|--------------|-------------|--------|----------------------------|--------------|-------------|--------|-------------|
| | | | real | imaginary | magnitude | phase | real | imaginary | magnitude | phase | Std. Dev. |
| 8 | 16 | 362.564 | 3.9663e+002 | -5.7201e+003 | 5.7338e+003 | -86.03 | 3.9574e+002 | -5.7195e+003 | 5.7332e+003 | -86.04 | 1.3866e+002 |
| 19 | 16 | 363.860 | -4.8353e+001 | -4.8716e+003 | 4.8719e+003 | -90.57 | 4.5311e+001 | -4.9271e+003 | 4.9273e+003 | -89.47 | 3.1271e+002 |
| 10 | 16 | 557.055 | 7.3166e+001 | -9.7205e+003 | 9.7207e+003 | -89.57 | 8.4818e+001 | -9.7107e+003 | 9.7111e+003 | -89.50 | 1.2295e+002 |
| 12 | 16 | 761.224 | 9.6911e+001 | -1.8433e+004 | 1.8434e+004 | -89.70 | 9.5750e+001 | -1.8433e+004 | 1.8433e+004 | -89.70 | 2.1414e+002 |
| 2 | 17 | 764.190 | -3.1250e+002 | -7.0511e+003 | 7.0580e+003 | -92.54 | -3.0277e+002 | -7.0524e+003 | 7.0589e+003 | -92.46 | 3.1198e+002 |
| 16 | 16 | 1222.980 | 1.1082e+003 | -1.7259e+004 | 1.7295e+004 | -86.33 | 1.1154e+003 | -1.7253e+004 | 1.7289e+004 | -86.30 | 5.3096e+002 |
| 13 | 16 | 1224.055 | -4.6394e+003 | -3.0840e+004 | 3.1187e+004 | -98.55 | -4.6441e+003 | -3.0074e+004 | 3.0431e+004 | -98.78 | 1.6271e+003 |
| 4 | 17 | 1328.036 | -4.8959e+002 | -1.5810e+004 | 1.5818e+004 | -91.77 | -4.7949e+002 | -1.5803e+004 | 1.5810e+004 | -91.74 | 8.5516e+002 |
| 17 | 16 | 1328.803 | 1.5461e+003 | -1.4661e+004 | 1.4742e+004 | -83.98 | 1.5462e+003 | -1.4659e+004 | 1.4741e+004 | -83.98 | 2.9335e+002 |
| 6 | 17 | 2019.269 | 8.1564e+002 | -1.3301e+004 | 1.3326e+004 | -86.49 | 7.3874e+002 | -1.3345e+004 | 1.3365e+004 | -86.83 | 6.6888e+002 |
| 23 | 15 | 2023.802 | 4.2669e+003 | -6.3248e+004 | 6.3392e+004 | -86.14 | 4.1880e+003 | -6.3244e+004 | 6.3382e+004 | -86.21 | 4.7741e+003 |
| 26 | 10 | 2321.862 | 1.6011e+003 | -2.9188e+004 | 2.9232e+004 | -86.86 | 8.1739e+002 | -3.0454e+004 | 3.0465e+004 | -88.46 | 5.2745e+003 |
| 28 | 8 | 2322.335 | 2.8552e+003 | -3.6135e+004 | 3.6247e+004 | -85.48 | 1.7616e+003 | -3.7289e+004 | 3.7331e+004 | -87.30 | 6.3617e+003 |
| 22 | 15 | 2337.895 | -1.3348e+003 | -5.0815e+004 | 5.0833e+004 | -91.50 | -1.3637e+003 | -5.0848e+004 | 5.0867e+004 | -91.54 | 2.6546e+003 |

TABLE 3. C-Plate Example: Modal Scaling Statistics

6. Typical Statistics: Bridge Example

For this example, impact data from a civil bridge structure test (15x55) has been used. The FRF data was processed using a Z-Domain Rational Fraction Polynomial Algorithm (RFP-Z) with all data between 5 and 30 Hz included. The model order range used was 2 to 20 with a generalized residual model including all terms from $(j\omega)^{-4}$ to $(j\omega)^2$. Further, low order alpha coefficient normalization has been used and full length residues have been calculated to be used in the CSSAMI procedure.

For the purposes of demonstration, all calculated poles (both consistent and computational) are included in the plots. As can be observed, though clearly present throughout the frequency range ([Figures 6, 7 and 8](#)) the non-realistic, computational poles, are not observed in the vicinity of the S-domain computed pole clusters ([Figure 9](#))

The effect of prefiltering (by pole density alone) the information fed into the autonomous parameter estimation algorithm is shown in [Figures 7 and 8](#). A comparison of no filtering ([Figure 7](#)) with prefiltering ([Figure 8](#)) reveals that more potential solutions are identified when the algorithm is allowed to match parameters on the basis of both pole and vector. A review of the results also indicates that the typical procedures for achieving clear consistency diagrams may actually be detrimental to the autonomous procedure because important information which didn't meet some arbitrary criteria was removed from consideration.

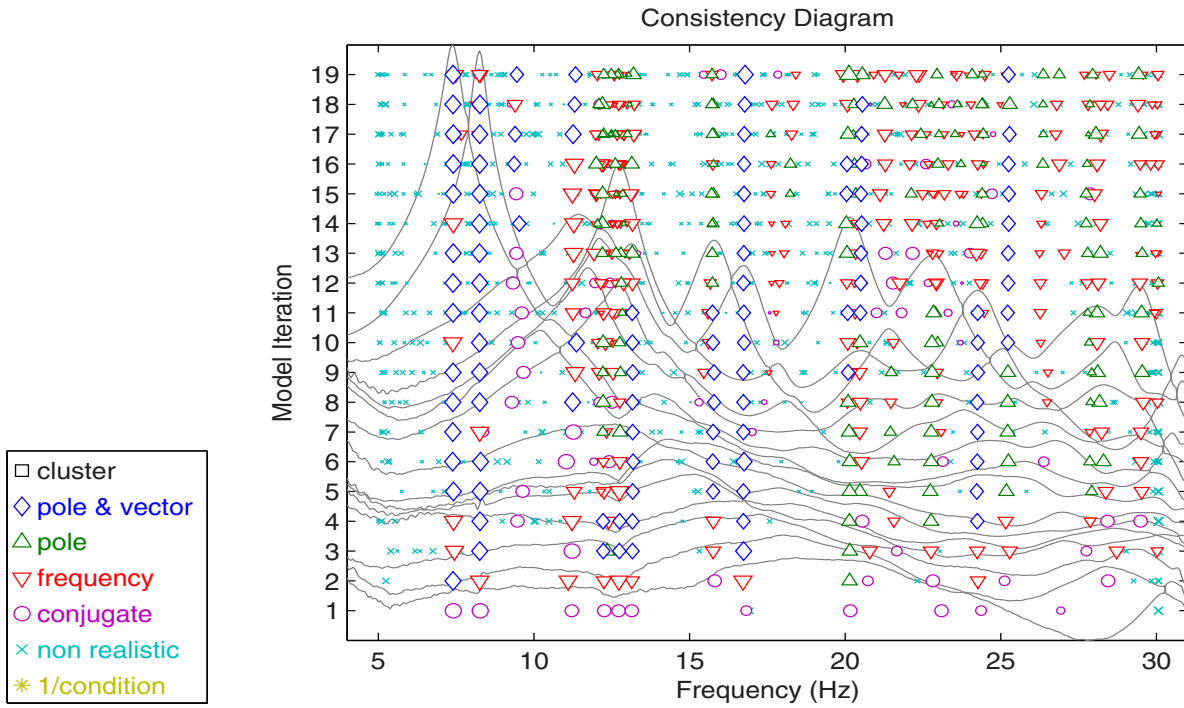


Figure 6. Bridge Example: Consistency Diagram - All Poles

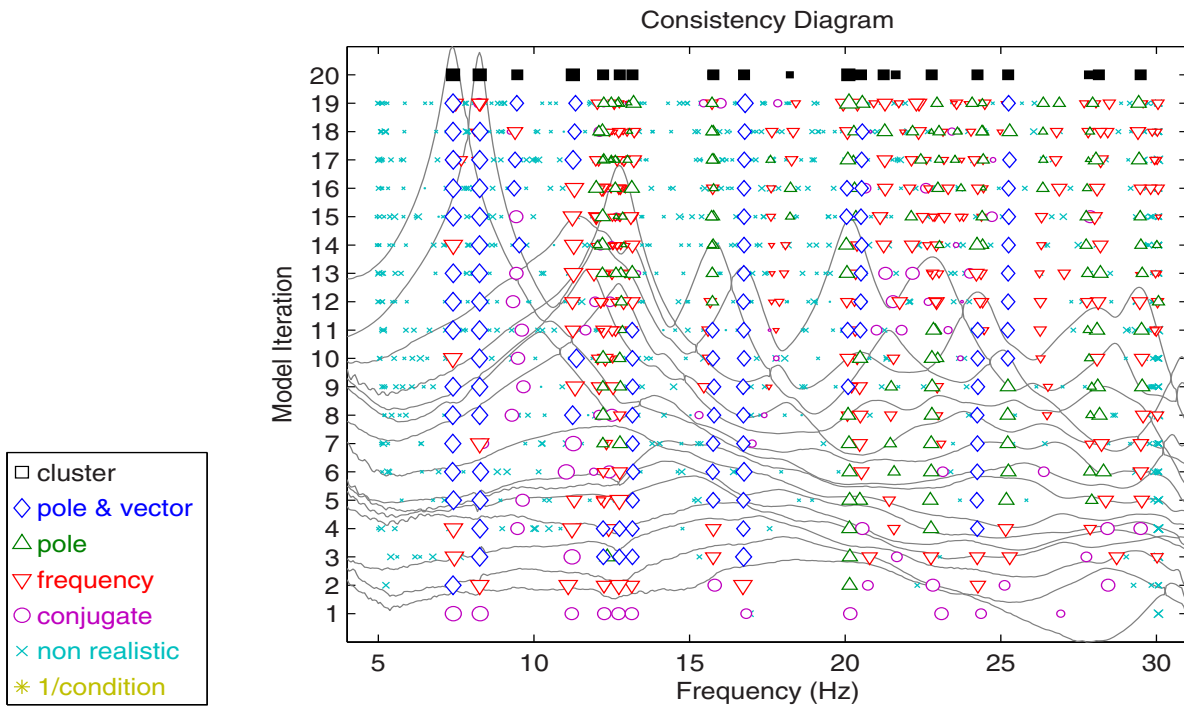


Figure 7. Bridge Example: Consistency Diagram - Pole Density = 1

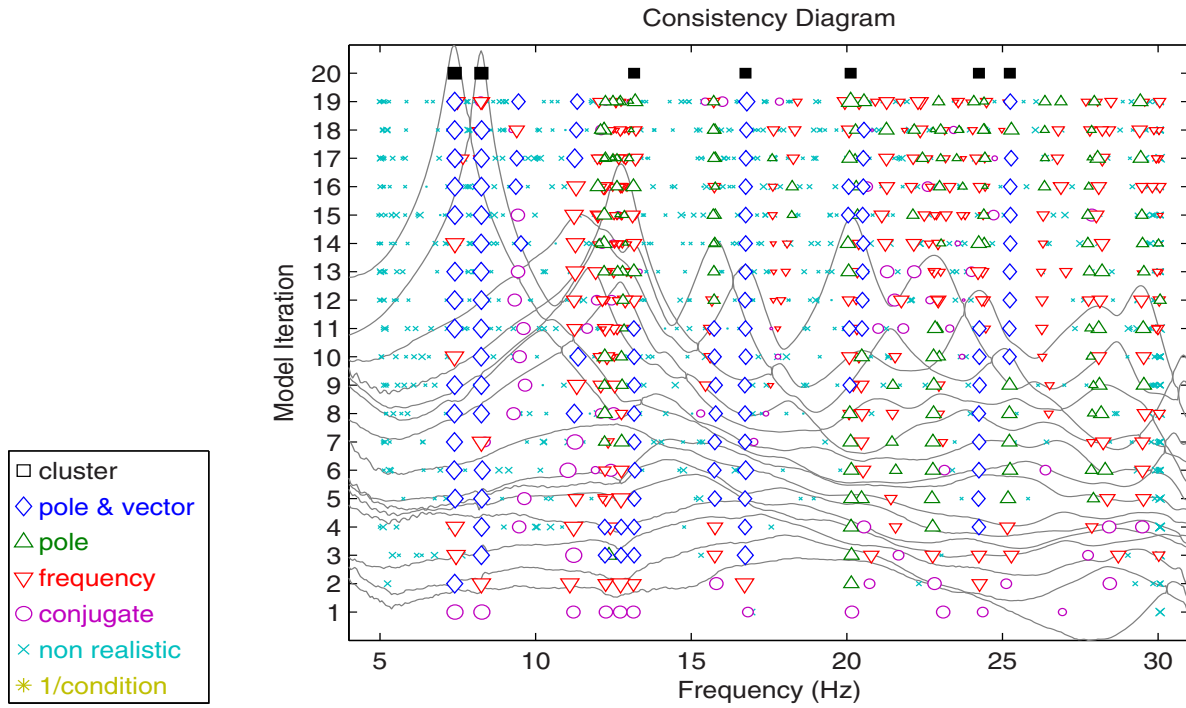


Figure 8. Bridge Example: Consistency Diagram - Pole Density = 4

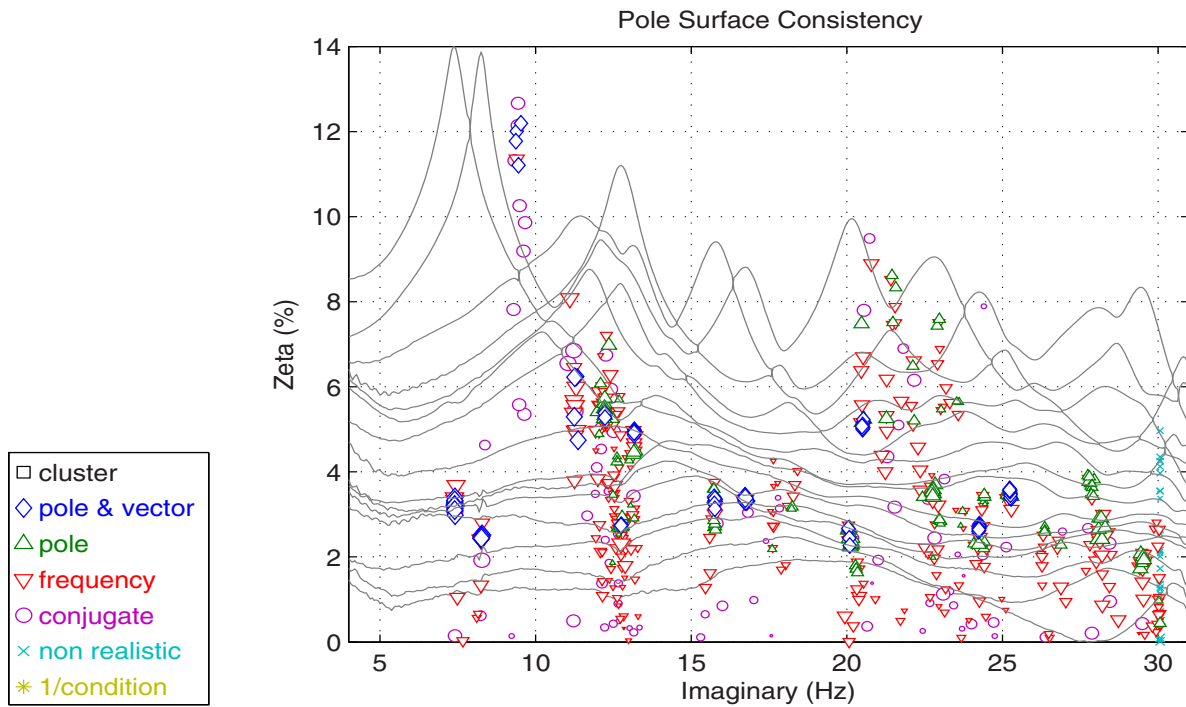


Figure 9. Bridge Example: Pole Surface Consistency - All Poles

The following plots, Figures 10 and 11, are a presentation of the statistical distribution of the pole information for four of the clusters shown in Figure 9. In Figures 10 and 11, the black stars are the original pole estimates and the red star represents the mean pole calculated from the cluster of pole estimates. The large red circle is the one standard deviation radius. The green

square is the individual standard deviations for the frequency and the damping. The blue circle is the pole as estimated from the pole weighted (state extended) vector.

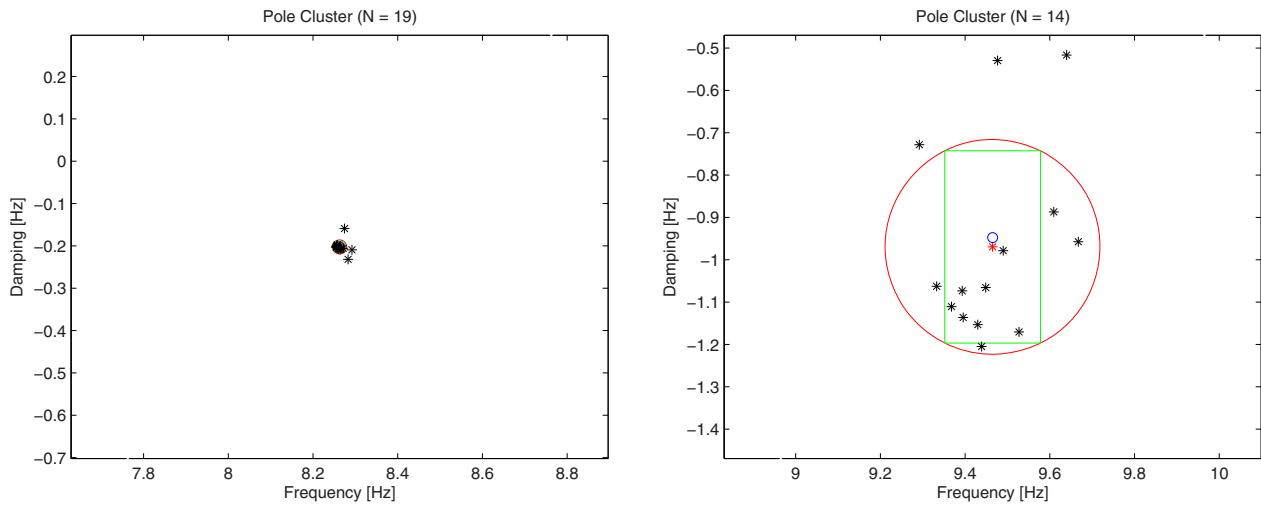


Figure 10. Bridge Example: 8.3 Hz and 9.5 Hz Pole Clusters - Statistics

As in the circular plate example, again note that the scaling in Figures 10 and 11 is consistent so that larger diameter circles will represent more variability.

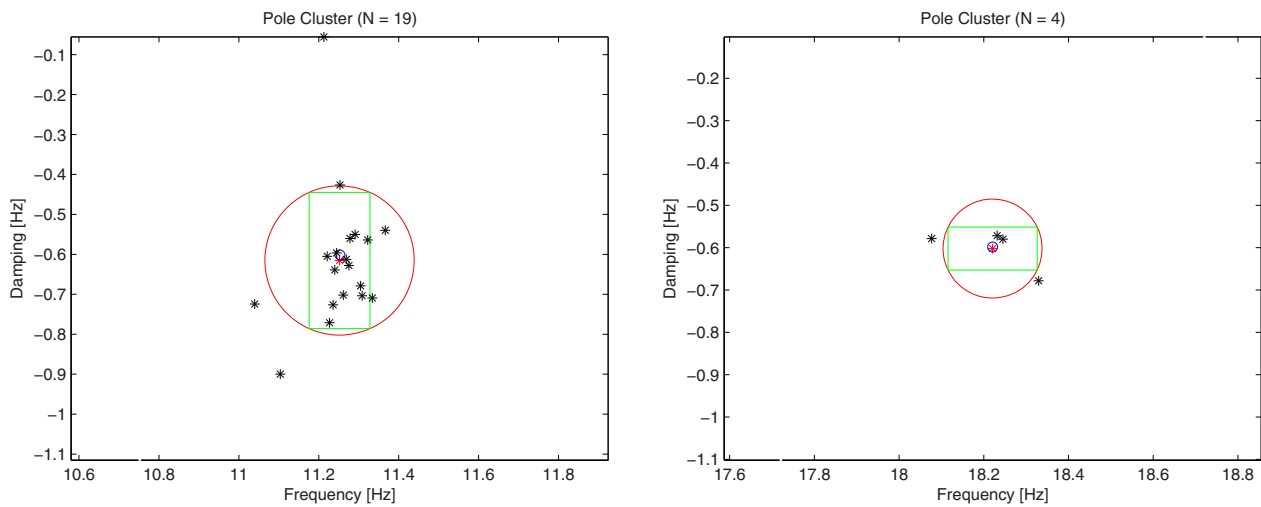


Figure 11. Bridge Example: 11.3 Hz and 18.2 Hz Pole Clusters - Statistics

The following (Tables 4, 5, and 6) provide a summary of the statistical information evaluated on the civil bridge structure.

Note that in Table 4 that there is little difference in the complex modal frequency estimated from the most significant pole weighted vector (columns 3 and 4) when compared to the mean values of the complex portions of the modal frequency (columns 5 and 6).

| Index | Sample Size (N) | Frequency (Hz) | Damping (Hz) | Frequency (Hz) (Mean) | Damping (Hz) (Mean) | Std. Dev. (Hz) |
|-------|-----------------|----------------|--------------|--------------------------|------------------------|----------------|
| 3 | 19 | 7.406 | -0.2404 | 7.406 | -0.2405 | 0.0169 |
| 2 | 19 | 8.263 | -0.2022 | 8.263 | -0.2023 | 0.0165 |
| 21 | 14 | 9.465 | -0.9480 | 9.465 | -0.9698 | 0.2536 |
| 8 | 19 | 11.253 | -0.6015 | 11.252 | -0.6154 | 0.1868 |
| 35 | 6 | 12.224 | -0.6669 | 12.224 | -0.6670 | 0.0182 |
| 32 | 8 | 12.756 | -0.3504 | 12.756 | -0.3508 | 0.0295 |
| 11 | 17 | 13.162 | -0.6187 | 13.162 | -0.6191 | 0.0555 |
| 41 | 6 | 15.729 | -0.5557 | 15.729 | -0.5559 | 0.0294 |
| 30 | 10 | 15.765 | -0.5059 | 15.765 | -0.5065 | 0.0373 |
| 6 | 19 | 16.747 | -0.5606 | 16.748 | -0.5607 | 0.0282 |
| 43 | 4 | 18.221 | -0.5984 | 18.221 | -0.6022 | 0.1169 |
| 16 | 13 | 20.100 | -0.4803 | 20.099 | -0.4817 | 0.0501 |
| 37 | 4 | 20.323 | -0.3610 | 20.323 | -0.3616 | 0.0476 |
| 14 | 16 | 20.507 | -1.1457 | 20.507 | -1.1594 | 0.1925 |
| 39 | 5 | 21.236 | -1.0438 | 21.236 | -1.0540 | 0.1930 |
| 31 | 5 | 21.624 | -1.5834 | 21.623 | -1.5995 | 0.2917 |
| 25 | 10 | 22.778 | -0.7731 | 22.778 | -0.7754 | 0.0856 |
| 28 | 10 | 24.247 | -0.6431 | 24.247 | -0.6433 | 0.0238 |
| 9 | 17 | 25.235 | -0.8774 | 25.235 | -0.8777 | 0.0452 |
| 18 | 14 | 27.824 | -1.0196 | 27.824 | -1.0211 | 0.0749 |
| 23 | 8 | 28.150 | -0.7324 | 28.151 | -0.7365 | 0.1076 |
| 22 | 9 | 29.492 | -0.4523 | 29.492 | -0.4654 | 0.1662 |

TABLE 4. Bridge Example: Modal Frequency Statistics

In [Table 5](#), again note that the fraction of normalized residual (columns 4-7) are all quite small indicated that only one mode has been found in each cluster and that the modal vectors in the cluster were essentially the same modal vector with minimal differences (noise).

| Index | N | Frequency (Hz) | NMVR1 | NMVR2 | NSVR3 | NSVR4 |
|-------|----|----------------|--------|--------|--------|--------|
| 3 | 19 | 7.406 | 0.0008 | 0.0144 | 0.0009 | 0.0144 |
| 2 | 19 | 8.263 | 0.0022 | 0.0383 | 0.0022 | 0.0379 |
| 21 | 14 | 9.465 | 0.0056 | 0.0579 | 0.0079 | 0.0863 |
| 8 | 19 | 11.253 | 0.0053 | 0.0783 | 0.0064 | 0.0914 |
| 35 | 6 | 12.224 | 0.0357 | 0.1690 | 0.0357 | 0.1690 |
| 32 | 8 | 12.756 | 0.0193 | 0.1446 | 0.0194 | 0.1447 |
| 11 | 17 | 13.162 | 0.0087 | 0.0956 | 0.0089 | 0.0966 |
| 41 | 6 | 15.729 | 0.0238 | 0.1146 | 0.0238 | 0.1148 |
| 30 | 10 | 15.765 | 0.0075 | 0.0703 | 0.0076 | 0.0698 |
| 6 | 19 | 16.747 | 0.0039 | 0.0637 | 0.0039 | 0.0649 |
| 43 | 4 | 18.221 | 0.0536 | 0.1532 | 0.0540 | 0.1540 |
| 16 | 13 | 20.100 | 0.0143 | 0.1667 | 0.0143 | 0.1661 |
| 37 | 4 | 20.323 | 0.0408 | 0.1401 | 0.0410 | 0.1402 |
| 14 | 16 | 20.507 | 0.0104 | 0.1236 | 0.0104 | 0.1237 |
| 39 | 5 | 21.236 | 0.0394 | 0.1621 | 0.0406 | 0.1674 |
| 31 | 5 | 21.624 | 0.0385 | 0.1470 | 0.0411 | 0.1553 |
| 25 | 10 | 22.778 | 0.0116 | 0.0884 | 0.0120 | 0.0898 |
| 28 | 10 | 24.247 | 0.0067 | 0.0462 | 0.0068 | 0.0469 |
| 9 | 17 | 25.235 | 0.0072 | 0.0901 | 0.0073 | 0.0916 |
| 18 | 14 | 27.824 | 0.0124 | 0.1356 | 0.0125 | 0.1351 |
| 23 | 8 | 28.150 | 0.0180 | 0.1294 | 0.0183 | 0.1322 |
| 22 | 9 | 29.492 | 0.0238 | 0.1501 | 0.0242 | 0.1549 |

TABLE 5. Bridge Example: Modal Vector Statistics

In Table 6, again note that the method used to compute the modal scaling, Modal A, had little effect on the estimates of Modal A. Also of note in this case, is the phase angle of all Modal A terms is around ninety degrees. The sign on the phase angle and the closeness to ninety degrees (rather than zero degrees) is a function of the scaling method chosen for the modal vector.

| Index | N | Frequency (Hz) | ModalA (State Vector) | | | | ModalA (Mean from cluster) | | | | |
|-------|----|----------------|-----------------------|-------------|-------------|--------|----------------------------|-------------|-------------|--------|-------------|
| | | | real | imaginary | magnitude | phase | real | imaginary | magnitude | phase | Std. Dev. |
| 3 | 19 | 7.406 | -4.0159e+005 | 4.0857e+006 | 4.1054e+006 | 95.61 | -4.0048e+005 | 4.0871e+006 | 4.1067e+006 | 95.60 | 1.3311e+005 |
| 2 | 19 | 8.263 | -4.1063e+005 | 6.0755e+006 | 6.0893e+006 | 93.87 | -3.7199e+005 | 6.0650e+006 | 6.0764e+006 | 93.51 | 7.2975e+005 |
| 21 | 14 | 9.465 | 5.1606e+006 | 1.3773e+007 | 1.4708e+007 | 69.46 | 6.6001e+006 | 1.4598e+007 | 1.6021e+007 | 65.67 | 4.9262e+006 |
| 8 | 19 | 11.253 | -1.0672e+006 | 8.9505e+006 | 9.0139e+006 | 96.80 | -2.6399e+006 | 1.2408e+007 | 1.2686e+007 | 102.01 | 1.5630e+007 |
| 35 | 6 | 12.224 | -2.3579e+006 | 1.3038e+007 | 1.3250e+007 | 100.25 | 1.5347e+006 | 1.1077e+007 | 1.1183e+007 | 82.11 | 4.6407e+006 |
| 32 | 8 | 12.756 | -3.7527e+005 | 8.6561e+006 | 8.6642e+006 | 92.48 | -4.7815e+005 | 8.9063e+006 | 8.9191e+006 | 93.07 | 1.2880e+006 |
| 11 | 17 | 13.162 | 2.9493e+006 | 1.5389e+007 | 1.5669e+007 | 79.15 | 1.6985e+006 | 1.2154e+007 | 1.2272e+007 | 82.04 | 3.9192e+006 |
| 41 | 6 | 15.729 | -1.1722e+006 | 9.6343e+006 | 9.7054e+006 | 96.94 | -1.1850e+006 | 9.6038e+006 | 9.6766e+006 | 97.03 | 1.2406e+006 |
| 30 | 10 | 15.765 | -1.2004e+006 | 1.0006e+007 | 1.0078e+007 | 96.84 | -1.1961e+006 | 1.0022e+007 | 1.0093e+007 | 96.81 | 6.1042e+005 |
| 6 | 19 | 16.747 | -1.5250e+006 | 1.4429e+007 | 1.4510e+007 | 96.03 | -1.5462e+006 | 1.4422e+007 | 1.4504e+007 | 96.12 | 8.2761e+005 |
| 43 | 4 | 18.221 | 6.9955e+007 | 2.0003e+008 | 2.1191e+008 | 70.72 | 7.0403e+007 | 1.9977e+008 | 2.1181e+008 | 70.59 | 1.3292e+007 |
| 16 | 13 | 20.100 | -3.4965e+005 | 1.9290e+007 | 1.9293e+007 | 91.04 | -2.5684e+005 | 1.9387e+007 | 1.9388e+007 | 90.76 | 2.0555e+006 |
| 37 | 4 | 20.323 | -1.6061e+007 | 7.0883e+007 | 7.2680e+007 | 102.77 | -1.7005e+007 | 6.9200e+007 | 7.1258e+007 | 103.81 | 1.5557e+007 |
| 14 | 16 | 20.507 | -3.8264e+005 | 2.2225e+007 | 2.2228e+007 | 90.99 | 4.2840e+006 | 2.3277e+007 | 2.3668e+007 | 79.57 | 9.5171e+006 |
| 39 | 5 | 21.236 | -3.3460e+007 | 2.8599e+007 | 4.4017e+007 | 139.48 | -3.6040e+007 | 2.5029e+007 | 4.3878e+007 | 145.22 | 1.2696e+007 |
| 31 | 5 | 21.624 | 3.4080e+006 | 1.6113e+007 | 1.6469e+007 | 78.06 | 2.4648e+006 | 1.2889e+007 | 1.3122e+007 | 79.17 | 3.3533e+006 |
| 25 | 10 | 22.778 | -1.0823e+006 | 1.0448e+007 | 1.0504e+007 | 95.91 | -1.0941e+006 | 1.0530e+007 | 1.0587e+007 | 95.93 | 1.1060e+006 |
| 28 | 10 | 24.247 | -1.8809e+006 | 1.9384e+007 | 1.9476e+007 | 95.54 | -1.8907e+006 | 1.9378e+007 | 1.9470e+007 | 95.57 | 5.5546e+005 |
| 9 | 17 | 25.235 | -7.2001e+005 | 2.7462e+007 | 2.7471e+007 | 91.50 | -8.3424e+005 | 2.6949e+007 | 2.6962e+007 | 91.77 | 2.2048e+006 |
| 18 | 14 | 27.824 | -2.1672e+006 | 1.3965e+007 | 1.4132e+007 | 98.82 | -2.0185e+006 | 1.4180e+007 | 1.4323e+007 | 98.10 | 3.0505e+006 |
| 23 | 8 | 28.150 | -1.3309e+007 | 2.1013e+007 | 2.4873e+007 | 122.35 | -1.1342e+007 | 2.1981e+007 | 2.4735e+007 | 117.29 | 7.1619e+006 |
| 22 | 9 | 29.492 | -1.0596e+007 | 1.9653e+007 | 2.2327e+007 | 118.33 | -1.2479e+007 | 2.3212e+007 | 2.6353e+007 | 118.26 | 1.5348e+007 |

TABLE 6. Bridge Example: Modal Scaling Statistics

7. Summary and Future Work

This paper has presented the statistics of the estimated modal parameters that are a direct result of a new development in autonomous modal parameter estimation. The proposed method represents an important philosophical and paradigm shift in the process of identifying potentially valid modal parameters. Instead of trying to get only (statistically and numerically) well estimated modes and then adding in the marginally estimated modes from the original estimates from the consistency diagram, the autonomous MPE methodology attempts to estimate all possible modes and use the statistics of the solutions to eliminate the marginal estimates. It has also been observed that, contrary to conventional wisdom, the techniques for producing clear consistency (stabilization) diagrams are at odds with the autonomous procedure. This is in part due to the nature of the consistency diagram where frequency and damping consistency tolerances used in the consistency diagram causes somewhat inconsistent estimates to be eliminated from consideration before the vector consistency can be evaluated. The temporal-spatial nature of the CSSAMI procedure allows these helpful results to be retained by the solution procedure.

One obvious extension of this work is to initiate the autonomous modal parameter estimation process using consistency diagram information from several different methods rather than just one. The inclusion of more estimates from differing algorithms may mean better consistency of estimates for some modes that are poorly estimated from a given algorithm.

8. References

- [1] Hawkins, F. J., "An Automatic Resonance Testing Technique for Exciting Normal Modes of Vibration of Complex Structures", Symposium IUTAM, "Progres Recents de la Mecanique des Vibrations Lineaires", 1965, pp. 37-41.
- [2] Hawkins, F. J., "GRAMPA - An Automatic Technique for Exciting the Principal Modes of Vibration of Complex Structures", Royal Aircraft Establishment, RAE-TR-67-211, 1967.
- [3] Taylor, G. A., Gaukroger, D. R., Skingle, C. W., "MAMA - A Semi-Automatic Technique for Exciting the Principal Modes of Vibration of Complex Structures", Aeronautical Research Council, ARC-R/M-3590, 1967, 20 pp.
- [4] Chauhan, S., Tcherniak, D., "Clustering Approaches to Automatic Modal Parameter Estimation", Proceedings, International Modal Analysis Conference (IMAC), 14 pp., 2008.
- [5] Chhipwadia, K.S., Zimmerman, D.C. and James III, G.H., "Evolving Autonomous Modal Parameter Estimation", Proceedings, International Modal Analysis Conference (IMAC), pp. 819-825, 1999.
- [6] James III, G.H., Zimmerman, D.C., Chhipwadia, K.S., "Application of Autonomous Modal Identification to Traditional and Ambient Data Sets", Proceedings, International Modal Analysis Conference (IMAC), pp. 840-845, 1999.
- [7] Lanslots, J., Rodiers, B., Peeters, B., "Automated Pole-Selection: Proof-of-Concept and Validation", Proceedings, International Conference on Noise and Vibration Engineering (ISMA), 2004.
- [8] Lau, J., Lanslots, J., Peeters, B., Van der Auweraer, "Automatic Modal Analysis: Reality or Myth?", Proceedings, International Modal Analysis Conference (IMAC), 10 pp., 2007.
- [9] Lim, T., Cabell, R. and Silcox, R., "On-line Identification of Modal Parameters Using Artificial Neural Networks", ***Journal of Vibration and Acoustics***, Vol. 118 No. 4, pp. 649-656, 1996.
- [10] Liu, J.M., Ying, H.Q., Shen, S., Dong, S.W., "The Function of Modal Important Index in Autonomous Modal Analysis", Proceedings, International Modal Analysis Conference (IMAC), 6 pp., 2007.
- [11] Mevel, L., Sam, A., Goursat, M., "Blind Modal Identification for Large Aircrafts", Proceedings, International Modal Analysis Conference (IMAC), 8 pp., 2004.
- [12] Mohanty, P., Reynolds, P., Pavic, A., "Automatic Interpretation of Stability Plots for Analysis of a Non-Stationary Structure", Proceedings, International Modal Analysis Conference (IMAC), 7 pp., 2007.
- [13] Pappa, R.S., James, G.H., Zimmerman, D.C., "Autonomous Modal Identification of the Space Shuttle Tail Rudder", ASME-DETC97/VIB-4250, 1997, ***Journal of Spacecrafts and Rockets***, Vol. 35 No. 2, pp. 163-169, 1998.
- [14] Pappa, R.S., Woodard, S. E., and Juang, J.-N., "A Benchmark Problem for Development of Autonomous Structural Modal Identification", Proceedings, International Modal Analysis Conference (IMAC), pp 1071-1077, 1997
- [15] Parloo, E., Verboven, P., Guillaume, P., Van Overmeire, M., "Autonomous Structural Health Monitoring - Part II: Vibration-based In-Operation Damage Assessment", ***Mechanical Systems and Signal Processing (MSSP)***, Vol. 16 No. 4, pp. 659-675, 2002.
- [16] Poncelet, F., Kerschen, G., Golinval, J.C., "Operational Modal Analysis Using Second-Order Blind Identification", Proceedings, International Modal Analysis Conference (IMAC), 7 pp., 2008.
- [17] Rainieri, C., Fabbrocino, G., Cosenza, E., "Fully Automated OMA: An Opportunity for Smart SHM Systems", Proceedings, International Modal Analysis Conference (IMAC), 9 pp., 2009.
- [18] Takahashi, K., Furusawa, M., "Development of Automatic Modal Analysis", Proceedings, International Modal Analysis Conference (IMAC), pp. 686-692, 1987.
- [19] Vanlanduit, S., Verboven, P., Schoukens, J., Guillaume, P. "An Automatic Frequency Domain Modal Parameter Estimation Algorithm", Proceedings, International Conference on Structural System Identification, Kassel, Germany, pp. 637-646, 2001.
- [20] Vanlanduit, S., Verboven, P., Guillaume, P., Schoukens, J., "An Automatic Frequency Domain Modal Parameter Estimation Algorithm", ***Journal of Sound and Vibration***, Vol. 265, pp. 647-661, 2003.

- [21] Verboven, P., Parloo, E., Guillaume, P., Van Overmeire, M., "Autonomous Structural Health Monitoring Part I: Modal Parameter Estimation and Tracking", ***Mechanical Systems and Signal Processing***, Vol. 16 No. 4, pp. 637-657, 2002.
- [22] Verboven P., E. Parloo, P. Guillame, and M. V. Overmeire, "Autonomous Modal Parameter Estimation Based On A Statistical Frequency Domain Maximum Likelihood Approach", Proceedings, International Modal Analysis Conference (IMAC), pp. 15111517, 2001.
- [23] Yam, Y., Bayard, D.S., Hadaegh, F.Y., Mettler, E., Milman, M.H., Scheid, R.E., "Autonomous Frequency Domain Identification: Theory and Experiment", NASA JPL Report JPL Publication 89-8, 204 pp., 1989.
- [24] Allemang, R.J., Brown, D.L., Phillips, A.W., "Survey of Modal Techniques Applicable to Autonomous/Semi-Autonomous Parameter Identification", Proceedings, International Conference on Noise and Vibration Engineering (ISMA), 2010.
- [25] Phillips, A.W., Allemang, R.J., Brown, D.L., "Autonomous Modal Parameter Estimation: Methodology", Proceedings, International Modal Analysis Conference (IMAC), 22 pp., 2011.
- [26] Allemang, R.J., Phillips, A.W., Brown, D.L., "Autonomous Modal Parameter Estimation: Applications", Proceedings, International Modal Analysis Conference (IMAC), 26 pp., 2011.
- [27] Allemang, R.J., Phillips, A.W., "The Unified Matrix Polynomial Approach to Understanding Modal Parameter Estimation: An Update", Proceedings, International Conference on Noise and Vibration Engineering (ISMA), 2004.
- [28] Allemang, R.J., Brown, D.L., "A Unified Matrix Polynomial Approach to Modal Identification", ***Journal of Sound and Vibration***, Vol. 211, No. 3, pp. 301-322, April 1998.
- [29] Allemang, R.J., Phillips, A.W., Brown, D.L., "Combined State Order and Model Order Formulations in the Unified Matrix Polynomial Method (UMPA)", Proceedings, International Modal Analysis Conference (IMAC), 25 pp., 2011.

Autonomous Modal Parameter Estimation: Application Examples

D.L. Brown, R.J. Allemang, A.W. Phillips
Structural Dynamics Research Laboratory
School of Dynamic Systems
College of Engineering and Applied Science
University of Cincinnati
Cincinnati, OH 45221-0072 USA
Email: David.L.Brown@UC.EDU

ABSTRACT

Autonomous modal parameter estimation is an attractive approach when estimating modal parameters (frequency, damping, mode shape, and modal scaling) as long as the results are physically reasonable. Frequently, significant post processing is required to tune the autonomous estimates. A general autonomous method is demonstrated with no post processing of the modal parameters. Example case histories are given for simple measurement cases taken from the laboratory (circular plate) as well as realistic field measurement cases involving significant noise and difficulty (bridge). These application case histories explore the successes and failures of the autonomous modal parameter estimation method and demonstrate the limitations of practical application of automated methods.

Nomenclature

N_i = Number of inputs.

N_o = Number of outputs.

N_S = Short dimension size.

N_L = Long dimension size.

ω_i = Discrete frequency (rad/sec).

s_i = Generalized frequency variable.

$[H(\omega_i)]$ = FRF matrix ($N_o \times N_i$)

$[\alpha]$ = Denominator polynomial matrix coefficient.

$[\beta]$ = Numerator polynomial matrix coefficient.

m = Model order for denominator polynomial.

n = Model order for numerator polynomial.

v = Model order for base vector.

r = Mode number.

UMPA = Unified Matrix Polynomial Algorithm

MAC = Modal Assurance Criterion

1. Introduction

The desire to estimate modal parameters automatically, once a set or multiple sets of test data are acquired, has been a subject of great interest for more than 40 years ^[1-24]. In the 1960s, when modal testing was limited to analog test methods, several researchers were exploring the idea of an automated test procedure for determining modal parameters ^[1-3]. Today, with the increased memory and compute power of current computers used to process test data, an automated or autonomous, modal parameter estimation procedure is entirely possible and is being attempted by numerous researchers.

Before proceeding with a discussion of autonomous modal parameter estimation, some philosophy and definitions regarding what is considered autonomous is required. In general, autonomous modal parameter estimation refers to an automated procedure that is applied to a modal parameter estimation algorithm so that no user interaction is required once the process is initiated. This typically involves setting a number of parameters or thresholds that are used to guide the process in order to exclude solutions that are not acceptable to the user. When the procedure finishes, a set of modal parameters is identified that can then be reduced or expanded if necessary. The goal is that no further reduction, expansion or interaction with the process will be required.

In order to discuss autonomous modal parameter estimation, some background is needed to clarify terminology and

methodology. The reader is directed to a series of companion papers in order to get an overview of the methodology and to view application results for several cases [25-26]. The applications and case histories presented in this paper are part of this new general procedure for autonomous modal parameter that is based upon consistent state vectors. This method is referred to as **Common Statistical Subspace Autonomous Mode Identification (CSSAMI)**. Note that much of the background of the CSSAMI method is based upon the Unified Matrix Polynomial Algorithm (UMPA) developed by the authors and described in a number of other papers [27-29].

2. Background: Autonomous Modal Parameter Estimation

The interest in automatic modal parameter estimation methods has been documented in the literature since at least the mid 1960s when the primary modal method was the analog, force appropriation method [1-3]. Following that early work, there has been a continuing interest in autonomous methods [4-24] that, in most cases, have been procedures that are formulated based upon a specific modal parameter estimation algorithm like the Eigensystem Realization Algorithm (ERA), the Polyreference Time Domain (PTD) algorithm or more recently the Polyreference Least Squares Complex Frequency (PLSCF) algorithm or the commercial version of the PLSCF, the PolyMAX® method.

Each of these past procedures have shown some promise but have not yet been widely adopted. In many cases, the procedure focussed on a single modal parameter estimation algorithm and did not develop a general procedure. Most of the past procedural methods focussed on pole density but depended on limited modal vector data to identify correlated solutions. Currently, due to increased computational speed and larger availability of memory, procedural methods can be developed that were beyond the computational scope of available hardware only a few years ago. These methods do not require any initial thresholding of the solution sets and rely upon correlation of the vector space of thousands of potential solutions as the primary identification tool. With the addition to any modal parameter estimation algorithm of the concept of pole weighted base vector, the length, and therefore sensitivity, of the extended vectors provides an additional tool that appears to be very useful.

3. Autonomous Modal Parameter Estimation Method

The autonomous modal parameter estimation method utilized in the applications and case histories in the following is a general method that can be used with any algorithm that fits within the UMPA structure. A complete description of the Unified Matrix Polynomial Algorithm (UMPA) thought process can be found in a number of references developed by the authors [27-29]. This means that this method can be applied to both low and high order methods with low or high order base vectors. This also means that most commercial algorithms could take advantage of this procedure. Note that high order matrix coefficient polynomials normally have coefficient matrices of dimension that is based upon the short dimension of the data matrix ($N_S \times N_S$). In these cases, it may be useful to solve for the complete modal vector in addition to using the extended base vector as this will extend the temporal-spatial information in the base vector so that the vector will be more sensitive to change. This characteristic is what gives this autonomous method the ability to distinguish between computational and structural modal parameters.

The implementation of the autonomous modal parameter estimation for this method is briefly outlined in the following steps. For complete details, please see the associated papers [25-26].

- Develop a consistency diagram using any UMPA solution method. Since this autonomous method utilizes a pole surface density plot, having a large number of iterations in the consistency diagram (due to model order, subspace iteration, starting times, equation normalization, etc.) will be potentially advantageous. However, the larger the number of solutions (represented by symbols) in the consistency diagram, the more computation time and memory will be required. However, restricting the number of solutions using clear stabilization (consistency) methods may be counterproductive.
- If the UMPA method is high order (coefficient matrices of size $N_S \times N_S$), solve for the complete length, scaled vector (function of N_L for all roots, structural and computational).
- Based upon the pole surface density threshold, identify all possible pole densities above some minimum value. This will be a function of the number of possible solutions represented by the consistency diagram.
- Sort the remaining solutions into frequency order based upon damped natural frequency (ω_r).
- Construct the 10th order, pole weighted vector (state vector) for each solution.

- Normalize all pole weighted vectors to unity length with dominant real part.
- Calculate the Auto-MAC matrix for all pole weighted vectors.
- Retain all Auto-MAC values that have a pole weighted MAC value above a threshold, 0.8 works well for most cases. All values below the threshold are set to 0.0.
- Identify vector clusters from this pole weighted MAC diagram that represent the same pole weighted vector. This is done by a singular value decomposition (SVD) of the pole weighted MAC matrix. The number of significant singular values for this MAC matrix represents the number of significant pole clusters in the pole weighted vector matrix and the value of each significant singular value represents the size of the cluster since the vectors are unitary. Note that the singular value is nominally the square of the number of vectors in the cluster and will likely be different, mode by mode.
- For each significant singular value, the location of the corresponding pole weighted vectors in the pole weighted vector matrix (index) is found from the associated left singular vector. This is accomplished by multiplying the left singular vector by the square root of the singular value and retaining all positions (indexes) above a threshold (typically 0.9). The positions of the non-zero elements in this vector are the indexes into the pole weighted vector matrix for all vectors belonging to a single cluster.
- For each identified pole cluster, perform a singular value decomposition (SVD) on the set of pole weighted vectors. The significant left singular vector is the dominant (average) pole weighted vector. Use the zeroth order portion of this dominant vector to identify the modal vector and the relationship between the zeroth order and the first order portions of the dominant vector to identify the modal frequency and modal damping values.
- Estimate appropriate statistics for each mode identified based upon the modes that are grouped in each cluster.
- For the modal parameters identified, complete the solution for modal scaling using any MIMO process of your choosing.
- User interaction with the final set of values can exclude poorly identified modes based upon physical or statistical evaluations.

Once the final set of modal parameters, along with their associated statistics, is obtained, quality can be assessed by many methods that are currently available. The most common example is to perform comparisons between the original measurements and measurements synthesized from the modal parameters. Another common example is to look at physical characteristics of the identified parameters such as reasonableness of frequency and damping values, normal mode characteristics in the modal vectors, and appropriate magnitude and phasing in the modal scaling. Other evaluations that may be helpful are mean phase correlation (MPC) on the vectors, an Auto-MAC looking for agreement between the modal vectors from conjugate poles, or any other method available.

4. Application Examples

Several case histories involving data from two applications are discussed in the following sections. These two applications were chosen as extremes of data cases, representing a real but very easy modal parameter identification situation (circular plate) and a real but very difficult modal parameter identification situation (civil infrastructure bridge test). The circular plate is lightly damped with many repeated roots but can be readily handled by almost any algorithm within the UMPA framework. The bridge is more moderately damped with significant noise on the data (traffic was maintained on part of the bridge while testing proceeded) and cannot be handled by any of the algorithms within the UMPA framework without significant effort and user interaction. The case histories include cases where the base vector of the algorithm is a function of long and short dimension to demonstrate the sensitivity of the solution to having an adequate spatial basis for determining the consistent vector characteristics. For details concerning the meaning and values of the threshold parameters or a more complete explanation of the CSSAMI procedure, please see the companion papers ^[25-26].

4.1 Application Example: C-Plate Laboratory Test Data

The first example of the CSSAMI procedure is performed on a laboratory test object consisting of a circular plate. This test object is very lightly damped and nearly every peak in the data is associated with a repeated root caused by the symmetry of the test object. This test object has been tested many times and the autonomous UMPA method estimated modal parameters consistent with past analysis. The FRF data in this case has 7 responses and 36 inputs (taken with an impact test method). In this case, a Polyreference Time Domain (PTD) method is used but, for every possible pole estimated over a model order range from 2 to 20, a complete long dimension modal vector was estimated so that sufficient spatial information (base vector

of length 36) is available for sorting out the consistent solutions. For this case, the following thresholds and control parameters were used:

- Lowest order coefficient matrix normalization.
- Pole density threshold (4 and above).
- Pole weighted vector of model order 10.
- Pole weighted MAC threshold (0.8 and above).
- Cluster size threshold (4 and above).
- Cluster identification threshold (0.8 and above).

Figures 1 to 7 represent information used to evaluate the success of the autonomous procedure. These figures are used after the modal parameters have been estimated to assess reasonableness and are not used to guide the procedure. Obviously, when the procedure is complete if modes have been missed or misidentified, adjustments in the control parameters (base vector order and cross MAC thresholds, for example) can be made and the procedure repeated. An experienced user may wish to add or delete modes in a manual interaction as is currently done.

Figure 1 is the complex mode indicator function plot which is used to distinguish close or repeated modes. Figures 2 and 3 show the solutions that are remaining after the initial pole surface density threshold and pole weighted vector correlation threshold have been applied.

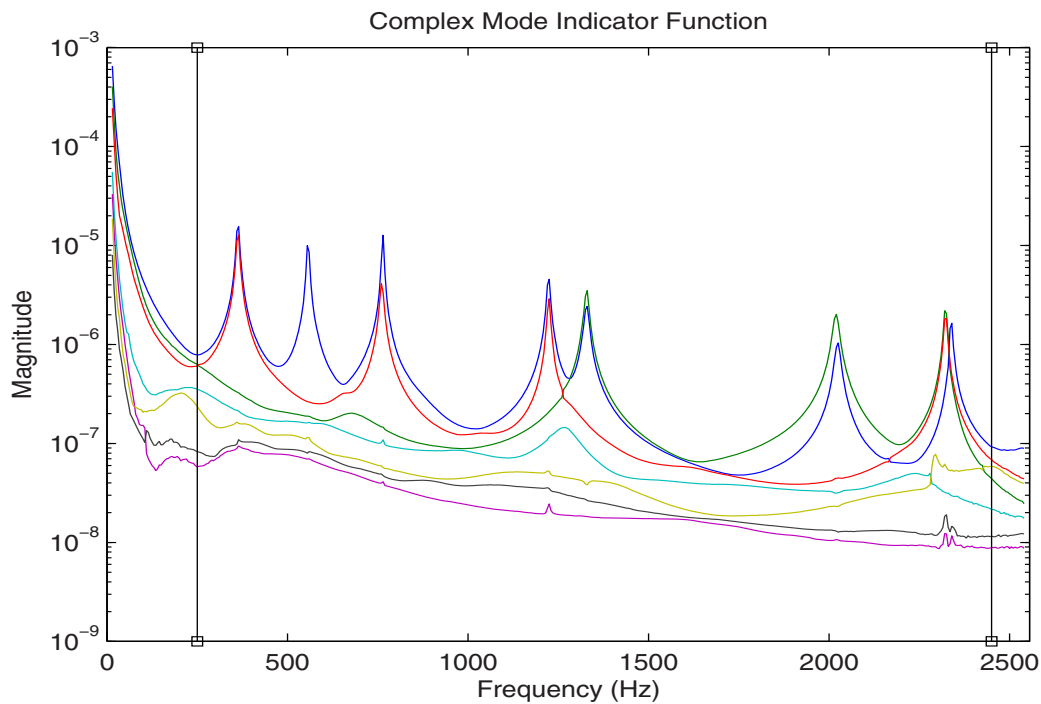


Figure 1. Complex Mode Indicator Function (CMIF)

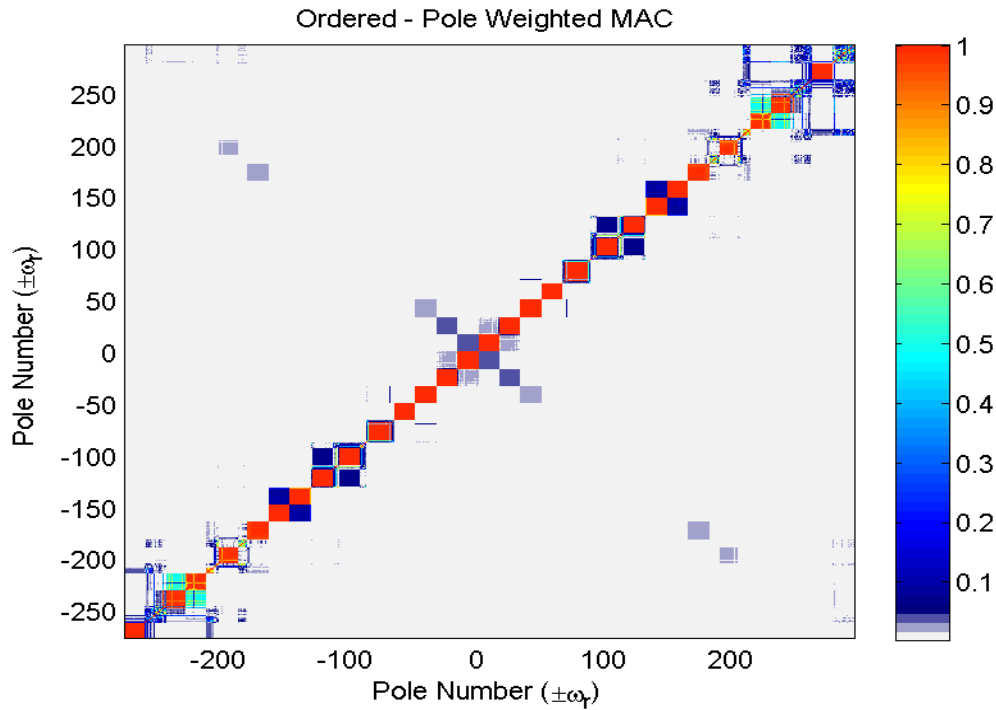


Figure 2. MAC-Tenth Order Pole Weighted Vectors, No Threshold

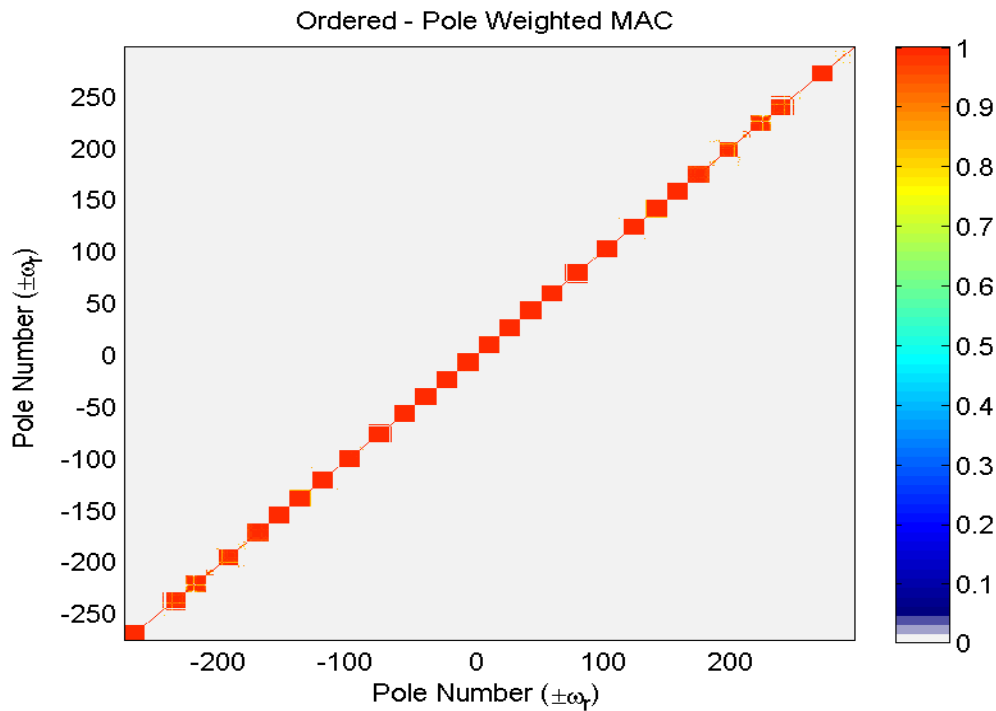


Figure 3. MAC-Tenth Order Pole Weighted Vectors, Above Threshold

The size of the red squares in [Figure 3](#) represents the number of vectors in each cluster of poles found anywhere in the consistency diagram. [Figure 4](#) is a plot of the scaled significant singular values for [Figure 3](#). Only the singular values above the cluster size threshold are retained for the final solution. [Figure 5](#) shows the location of the final estimates on a pole

surface consistency plot. The black squares represent a final solution from the autonomous procedure.

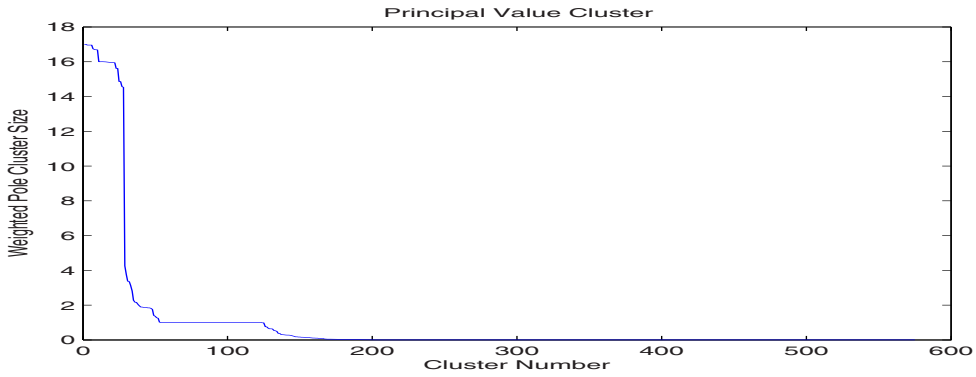


Figure 4. Principal Values of Clusters of Pole Weighted Vectors

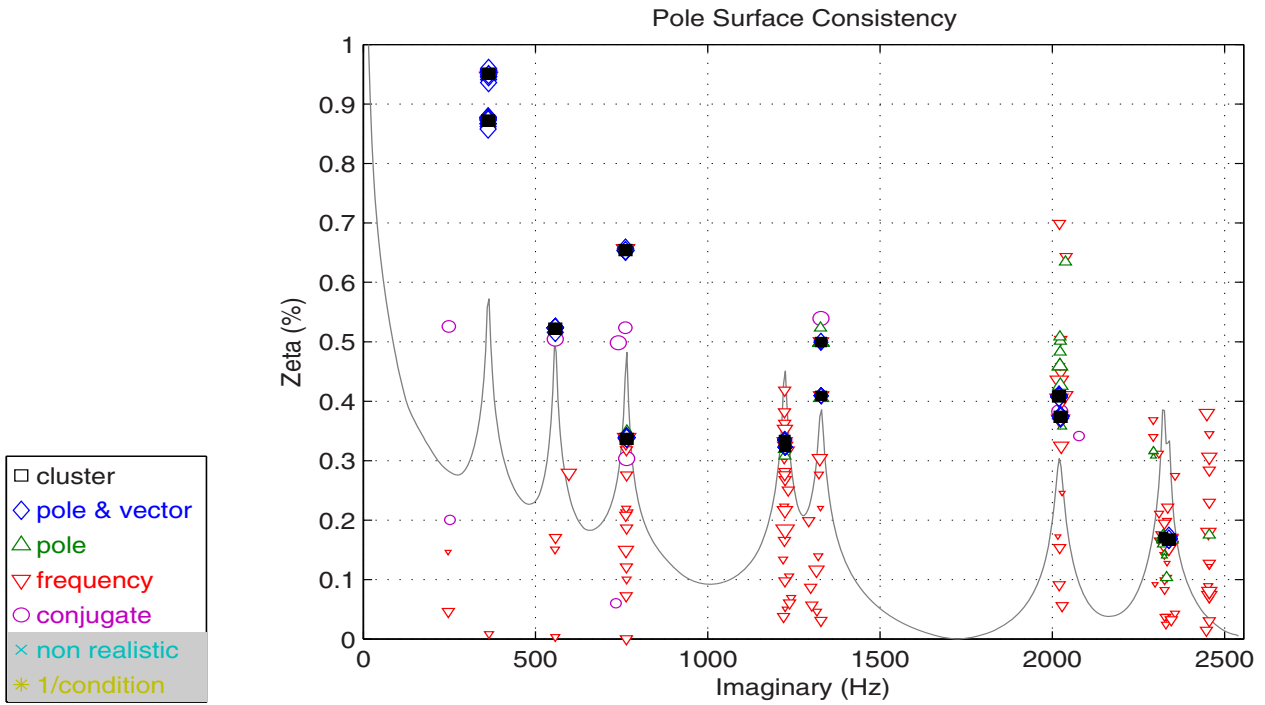


Figure 5. Pole Surface Consistency Clusters with Final Estimates

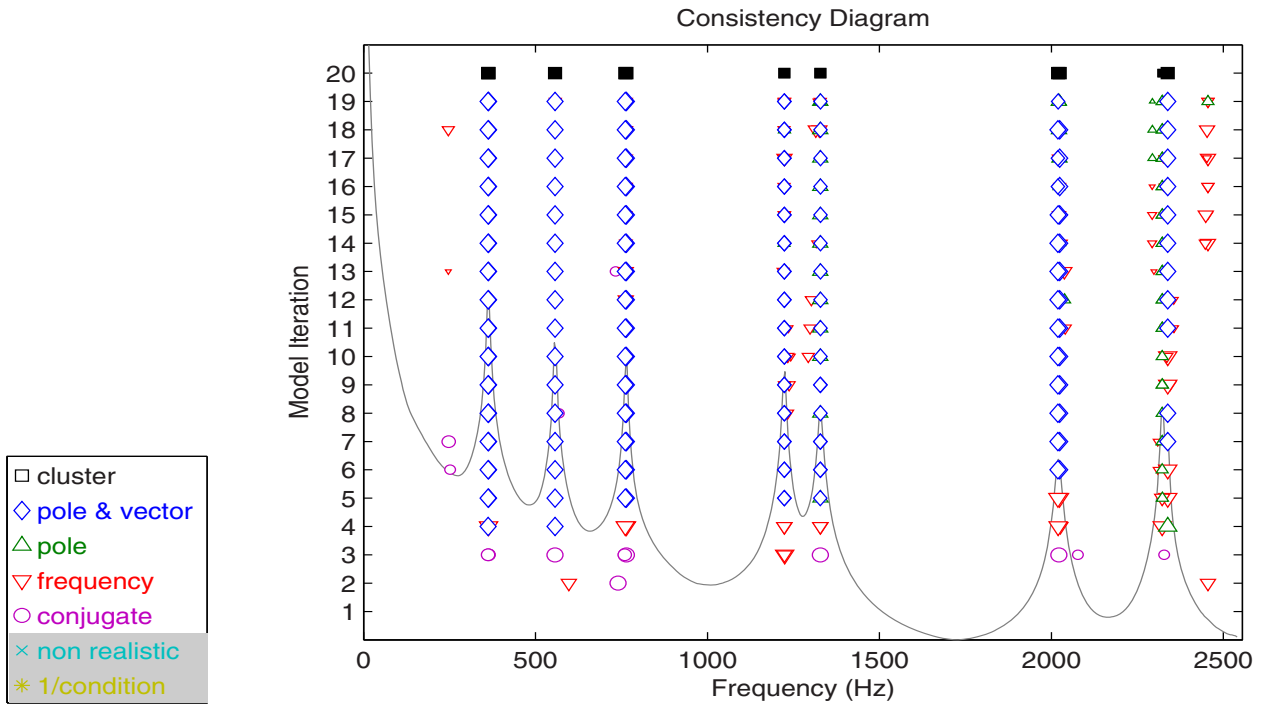


Figure 6. Consistency Diagram with Final Autonomous Estimates

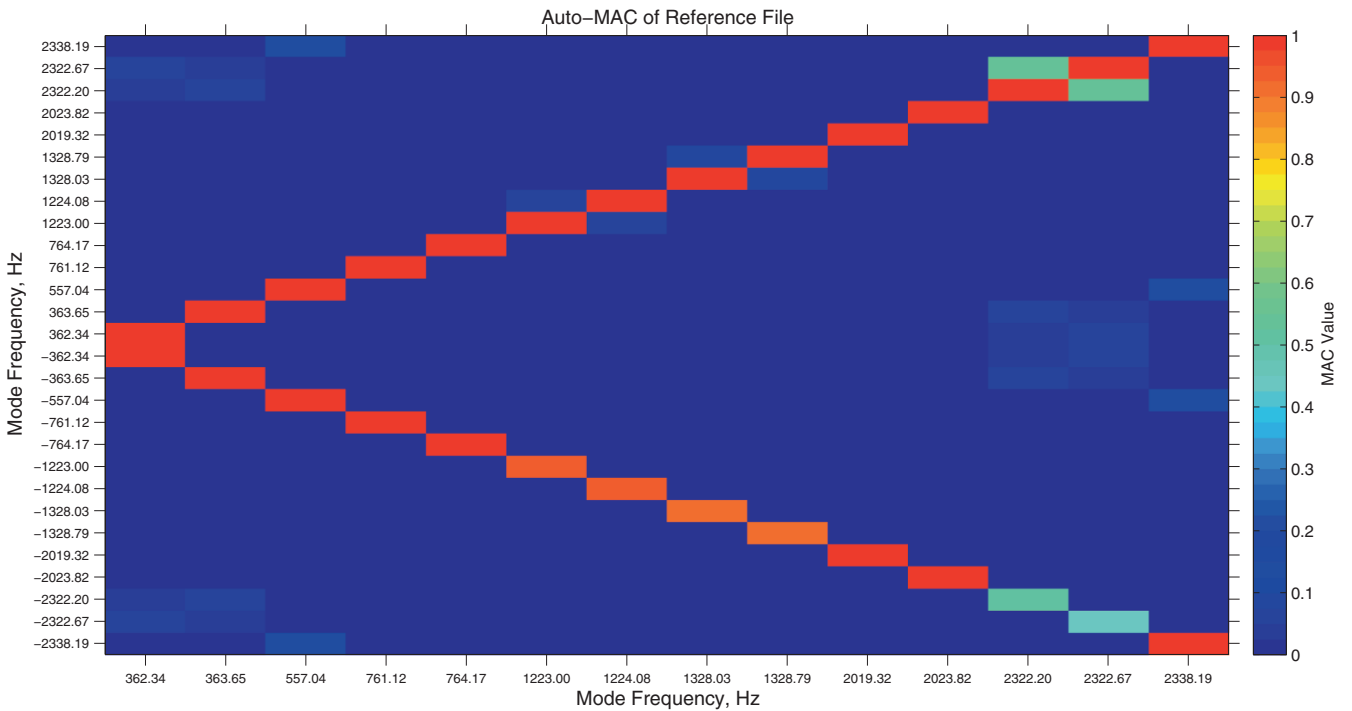


Figure 7. Auto-MAC of Final Autonomous Estimates - Conjugate Poles

Figure 6 has been found to be a useful indicator when estimating modal parameters for a dominantly normal mode system. The Auto-MAC plot of the estimated modal vectors shown in Figure 7 shows a nearly perfect correlation between the vectors associated with the positive frequency and the vectors associated with the estimate of its negative frequency (conjugate pair).

| Index | Sample Size (N) | Frequency (Hz) | Damping (Hz) | Std. Dev. (Hz) |
|-------|-----------------|----------------|--------------|----------------|
| 8 | 16 | 362.552 | -3.1573 | 0.1595 |
| 19 | 16 | 363.851 | -3.5473 | 0.1137 |
| 10 | 16 | 557.053 | -2.8957 | 0.0823 |
| 12 | 16 | 761.222 | -5.2219 | 0.1085 |
| 2 | 17 | 764.187 | -2.5397 | 0.1426 |
| 16 | 16 | 1222.979 | -4.0870 | 0.0314 |
| 13 | 16 | 1224.054 | -3.9543 | 0.0438 |
| 4 | 17 | 1328.036 | -6.6514 | 0.0960 |
| 17 | 16 | 1328.803 | -5.4805 | 0.1976 |
| 6 | 17 | 2019.257 | -8.2429 | 0.2081 |
| 23 | 15 | 2023.803 | -7.5596 | 0.0614 |
| 26 | 11 | 2321.877 | -3.9141 | 0.1761 |
| 28 | 8 | 2322.334 | -3.8351 | 0.2237 |
| 22 | 15 | 2337.894 | -3.7974 | 0.2280 |

TABLE 1. C-Plate Example: Modal Frequency Statistics

Table 1 gives a portion of the results and statistics associated with Figure 7. Since the methods involve a cluster of size N for each mode as part of the solution, statistical information is readily available for all modal parameters. This is discussed and detailed fully in another paper [26] and includes a discussion of the statistics for modal frequencies, modal vectors and modal scaling.

4.2 Application Example: Bridge Field Test Data

The next example of the CSSAMI procedure is performed in the field on a small highway bridge. The FRF data in this case has 55 inputs and 15 responses. This data set has been particularly troublesome when analyzed by any method available and is shown as a significant implementation of the autonomous modal parameter estimation procedure. The autonomous results for this case are as good or better compared to any other solution utilized in the past, as measured by reasonable estimates of frequency and damping and dominantly normal modes.

In this case, a Rational Fraction Polynomial with complex z frequency mapping (RFP-Z) method is used (similar to PLSCF and PolyMAX®) but, for every possible pole estimated over a model order range from 2 to 20, a complete long dimension modal vector was estimated so that sufficient spatial information is available for sorting out the consistent solutions. For this case, the following thresholds and control parameters were used:

- Lowest order coefficient matrix normalization.
- Pole density threshold (4 and above).
- Pole weighted vector of model order 10.
- Pole weighted MAC threshold (0.8 and above).
- Cluster size threshold (3 and above).
- Cluster identification threshold (0.8 and above).

This case demonstrates that, even with clear stabilization diagram techniques, the consistency diagram can get fairly difficult to interpret. Nonetheless, in this application of the autonomous modal parameter estimation procedure, it is possible to identify the modal parameters with little trouble.

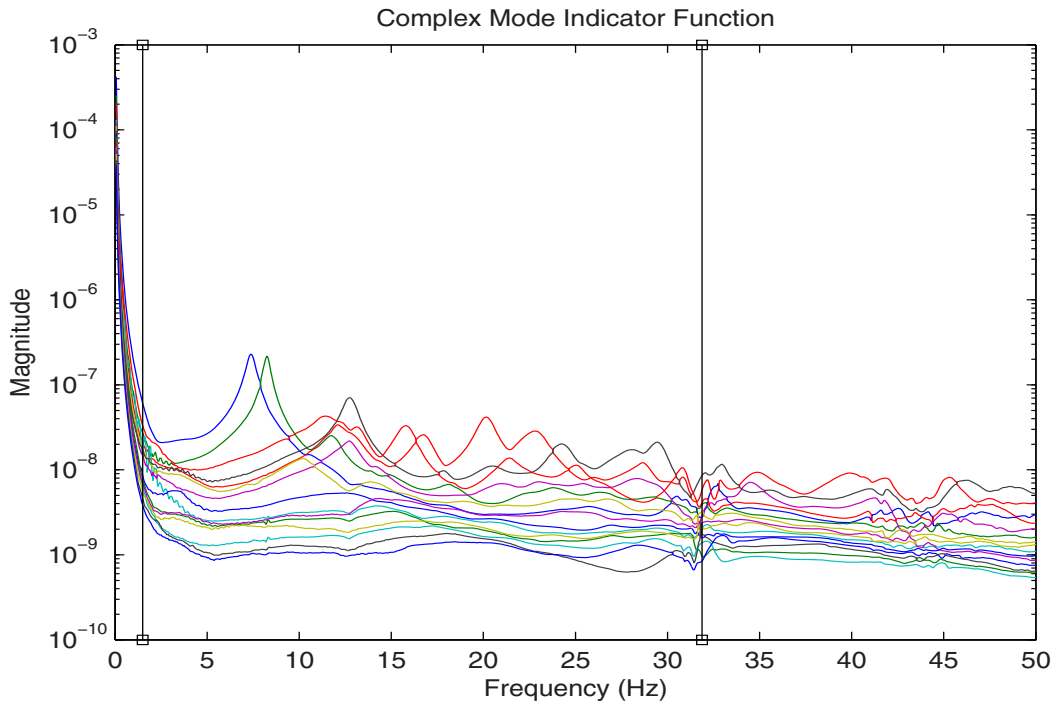


Figure 8. Complex Mode Indicator Function (CMIF)

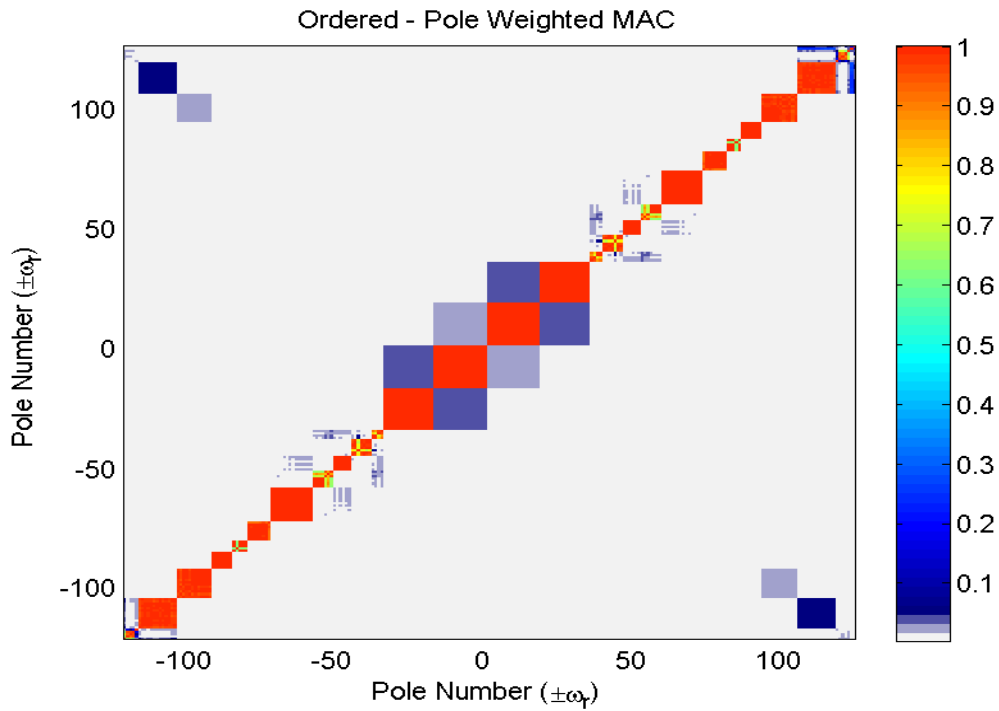


Figure 9. MAC-Tenth Order Pole Weighted Vectors, No Threshold

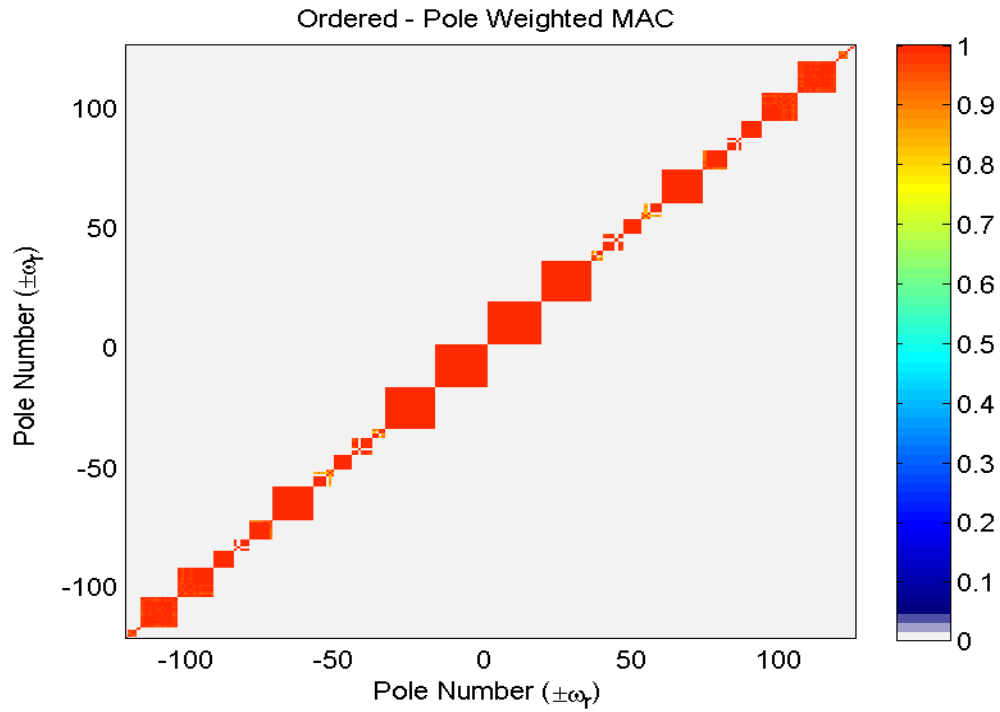


Figure 10. MAC-Tenth Order Pole Weighted Vectors, Above Threshold

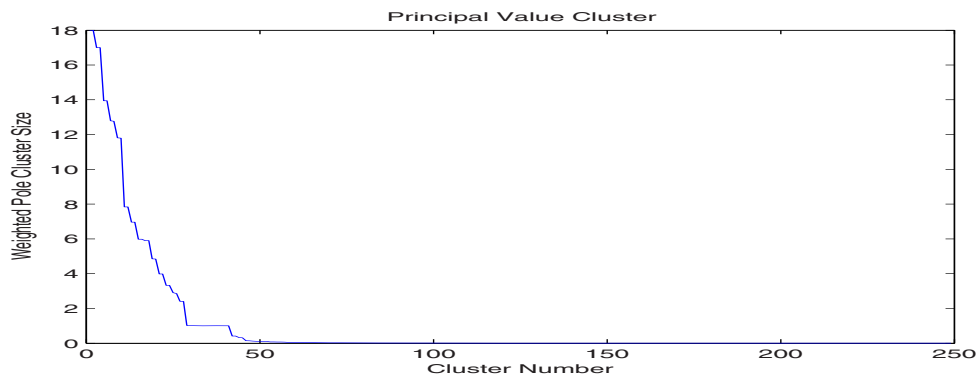


Figure 11. Principal Values of Clusters of Pole Weighted Vectors

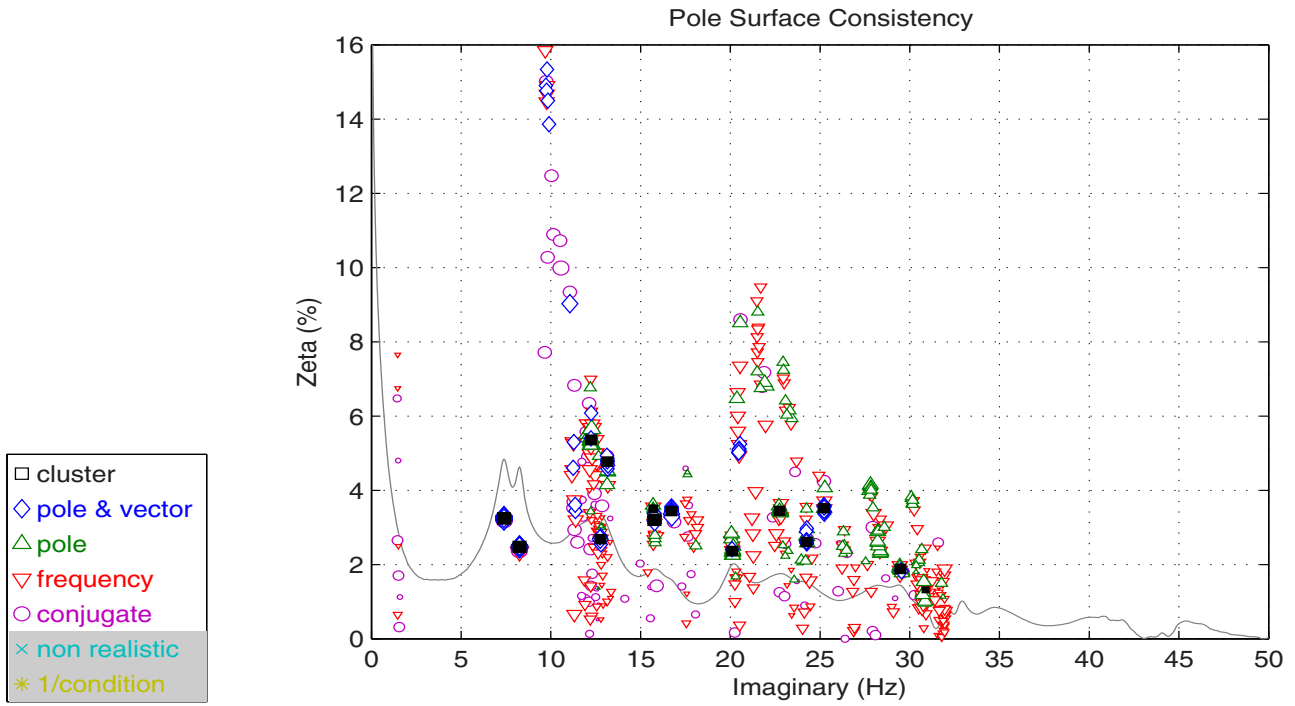


Figure 12. Pole Surface Consistency Clusters with Final Autonomous Estimates

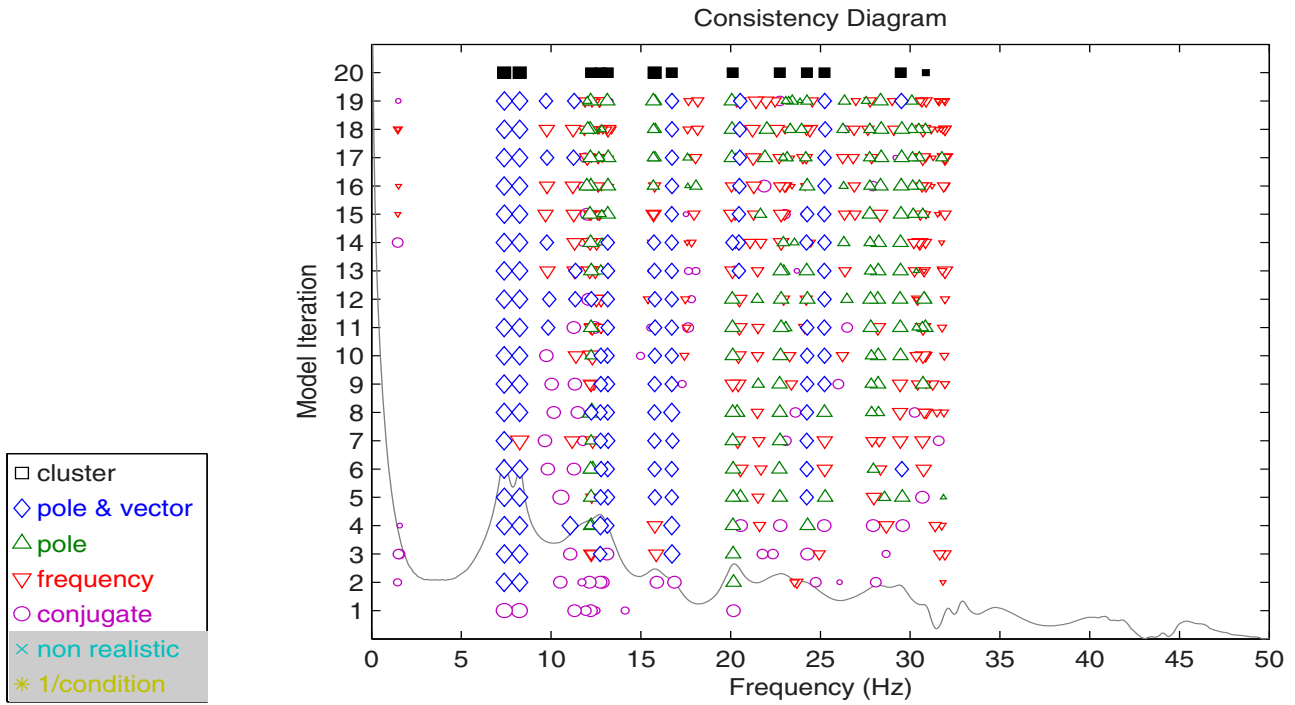


Figure 13. Consistency Diagram with Final Autonomous Estimates

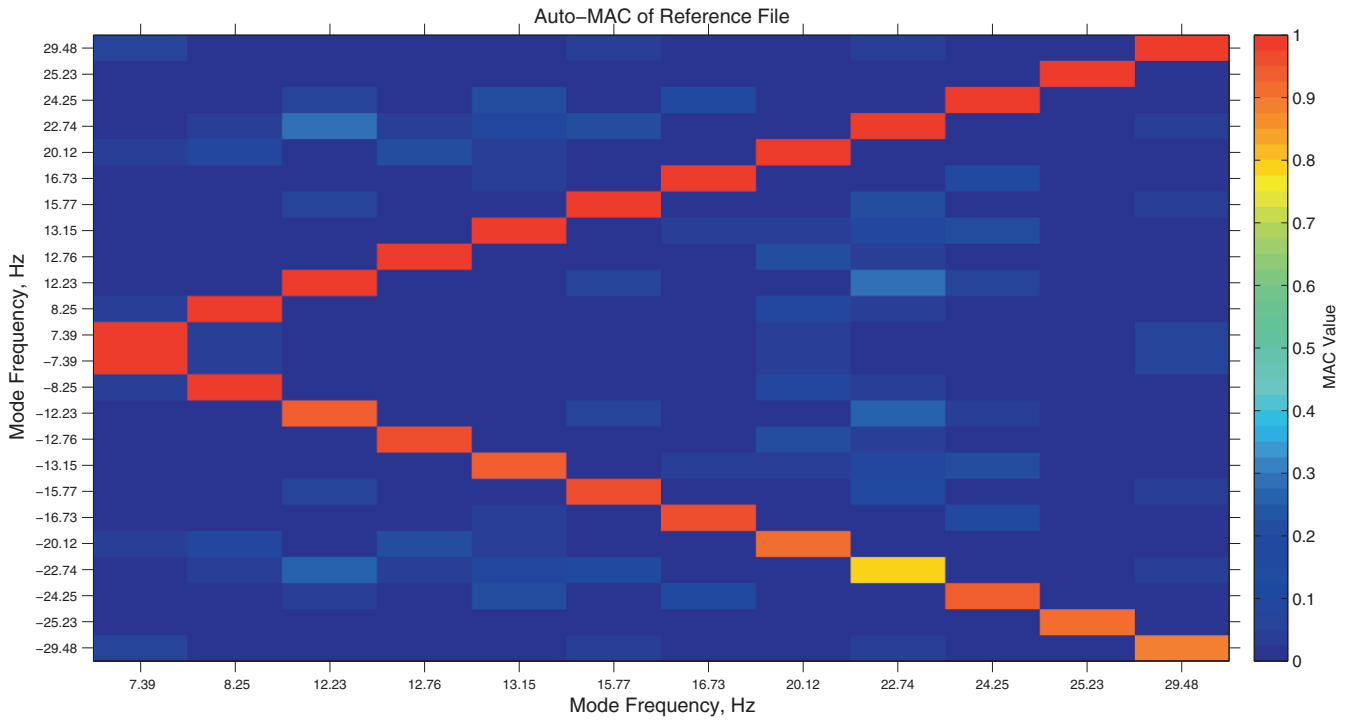


Figure 14. Auto-MAC of Final Autonomous Estimates - Conjugate Poles

Table 2 is a summary of the modal frequency estimates and statistics for this case. Once again, this is discussed and detailed fully in another paper [26] and includes a discussion of the statistics for modal frequencies, modal vectors and modal scaling.

| Index | Sample Size (N) | Frequency (Hz) | Damping (Hz) | Std. Dev. (Hz) |
|-------|-----------------|----------------|--------------|----------------|
| 3 | 19 | 7.406 | -0.2405 | 0.0169 |
| 2 | 19 | 8.263 | -0.2023 | 0.0165 |
| 21 | 14 | 9.465 | -0.9698 | 0.2536 |
| 8 | 19 | 11.252 | -0.6154 | 0.1868 |
| 35 | 6 | 12.224 | -0.6670 | 0.0182 |
| 32 | 8 | 12.756 | -0.3508 | 0.0295 |
| 11 | 17 | 13.162 | -0.6191 | 0.0555 |
| 41 | 6 | 15.729 | -0.5559 | 0.0294 |
| 30 | 10 | 15.765 | -0.5065 | 0.0373 |
| 6 | 19 | 16.748 | -0.5607 | 0.0282 |
| 43 | 4 | 18.221 | -0.6022 | 0.1169 |
| 16 | 13 | 20.099 | -0.4817 | 0.0501 |
| 37 | 4 | 20.323 | -0.3616 | 0.0476 |
| 14 | 16 | 20.507 | -1.1594 | 0.1925 |
| 39 | 5 | 21.236 | -1.0540 | 0.1930 |
| 31 | 5 | 21.623 | -1.5995 | 0.2917 |
| 25 | 10 | 22.778 | -0.7754 | 0.0856 |
| 28 | 10 | 24.247 | -0.6433 | 0.0238 |
| 9 | 17 | 25.235 | -0.8777 | 0.0452 |
| 18 | 14 | 27.824 | -1.0211 | 0.0749 |
| 23 | 8 | 28.151 | -0.7365 | 0.1076 |
| 22 | 9 | 29.492 | -0.4654 | 0.1662 |

TABLE 2. Bridge Example: Modal Frequency Statistics

4.3 Application Example: C-Plate Laboratory Test Data with Short Dimension Base Vector

The next example of the CSSAMI procedure is performed on the same, circular plate laboratory test object. The FRF data is the same as the previous example and the Polyreference Time Domain (PTD) method is used but only the short dimension vectors are used for every possible pole estimated over a model order range from 2 to 20. This means that the spatial information (base vector of length 7) available for sorting out the consistent solutions will be compromised. For this case, the following thresholds and control parameters were used:

- Lowest order coefficient matrix normalization.
- Pole density threshold (4 and above).
- Pole weighted vector of model order 10.
- Pole weighted MAC threshold (0.8 and above).
- Cluster size threshold (4 and above).
- Cluster identification threshold (0.8 and above).

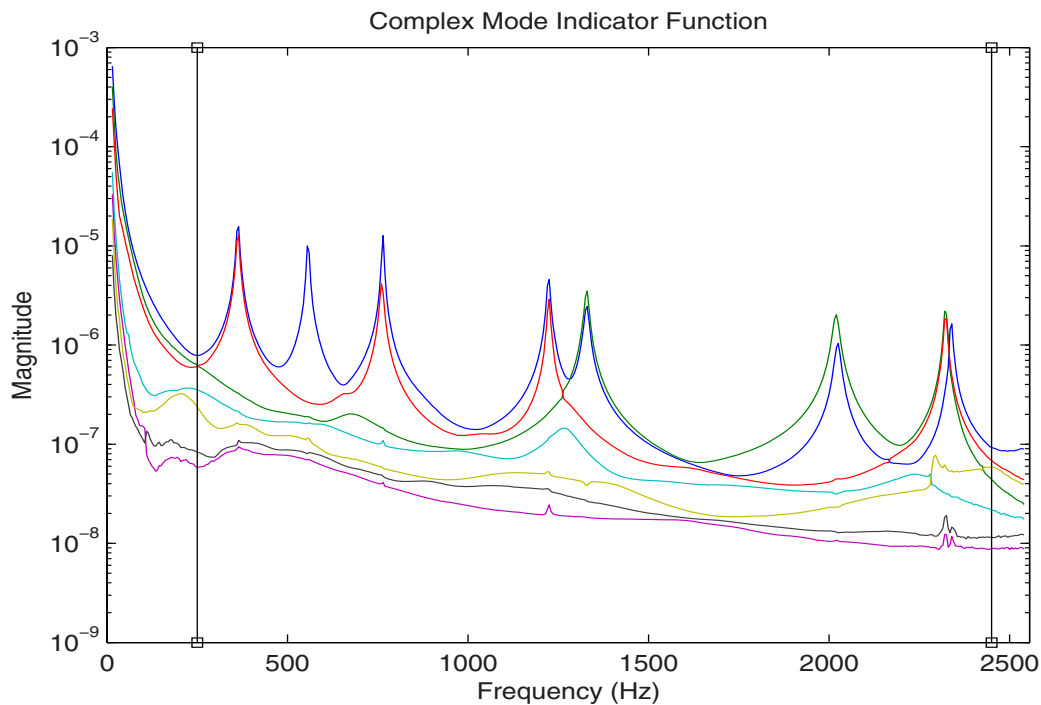


Figure 15. Complex Mode Indicator Function (CMIF)

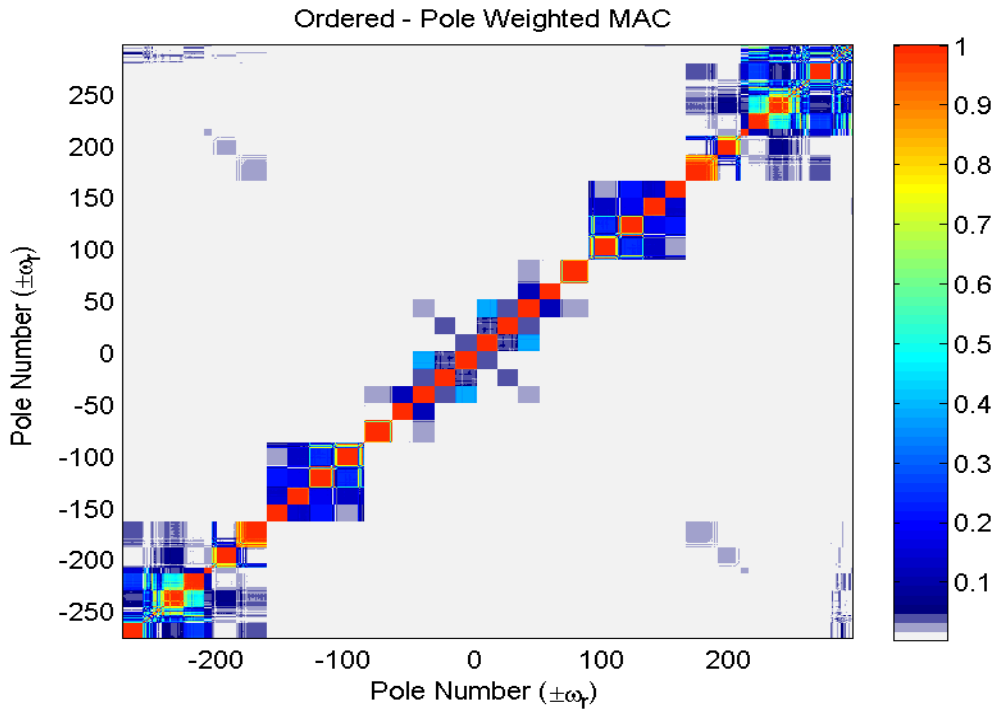


Figure 16. MAC-Tenth Order Pole Weighted Vectors, No Threshold

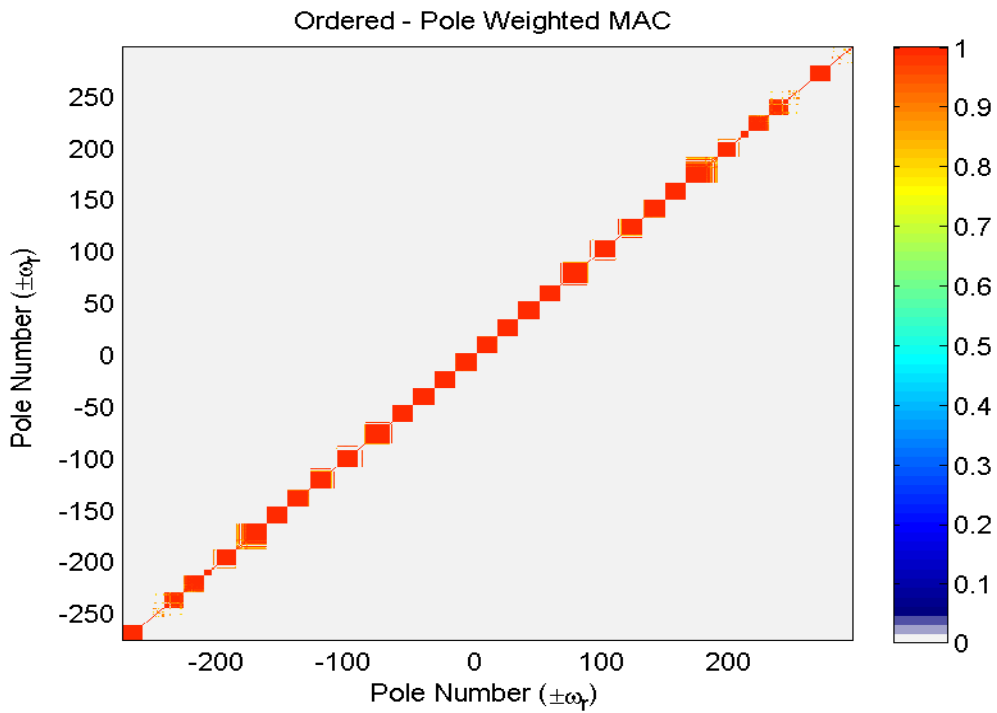


Figure 17. MAC-Tenth Order Pole Weighted Vectors, Above Threshold

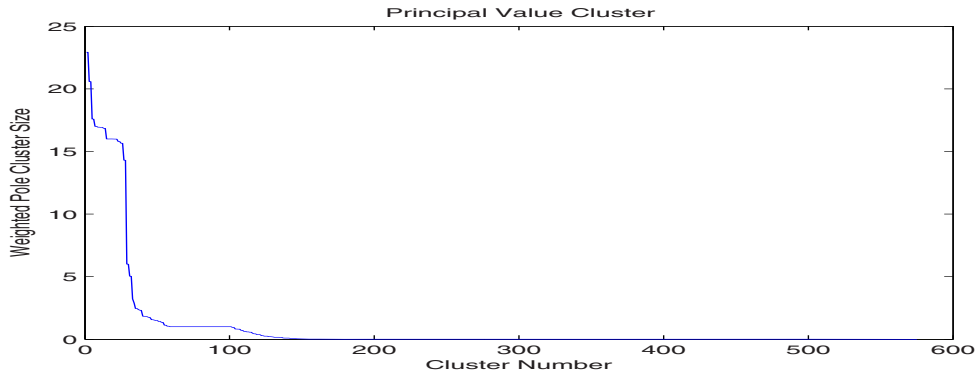


Figure 18. Principal Values of Clusters of Pole Weighted Vectors

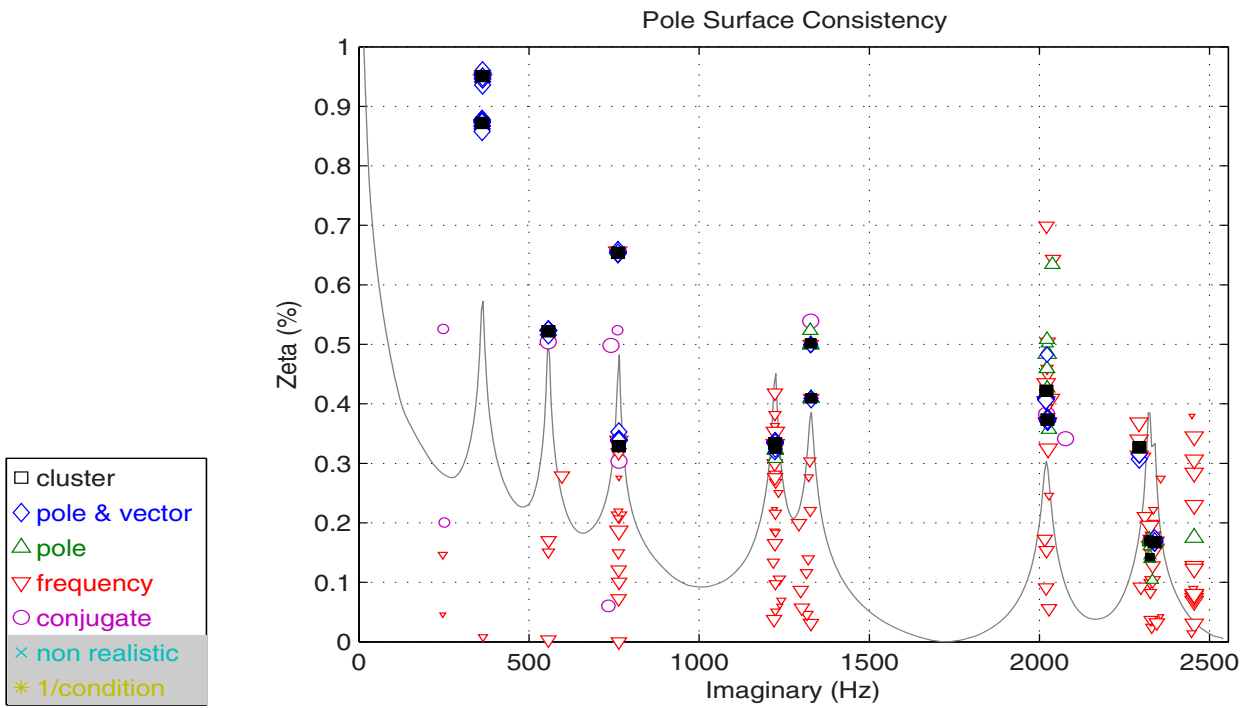


Figure 19. Pole Surface Consistency Clusters with Final Autonomous Estimates

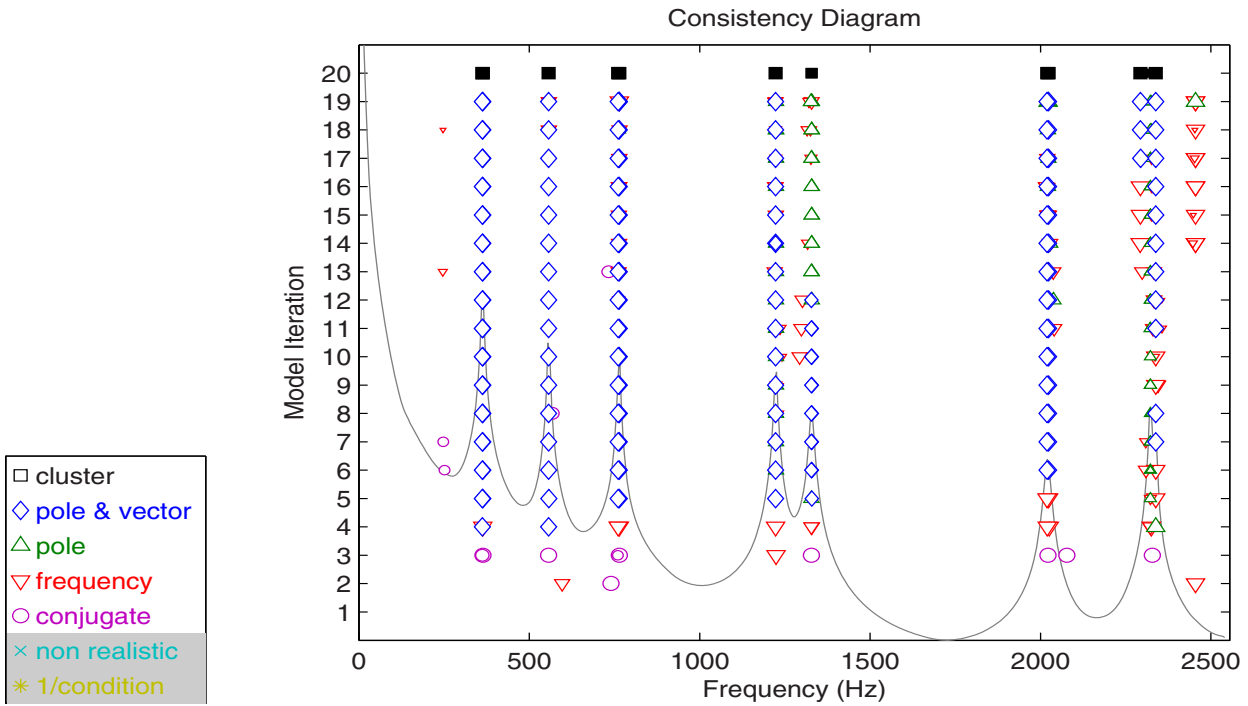


Figure 20. Consistency Diagram with Final Autonomous Estimates

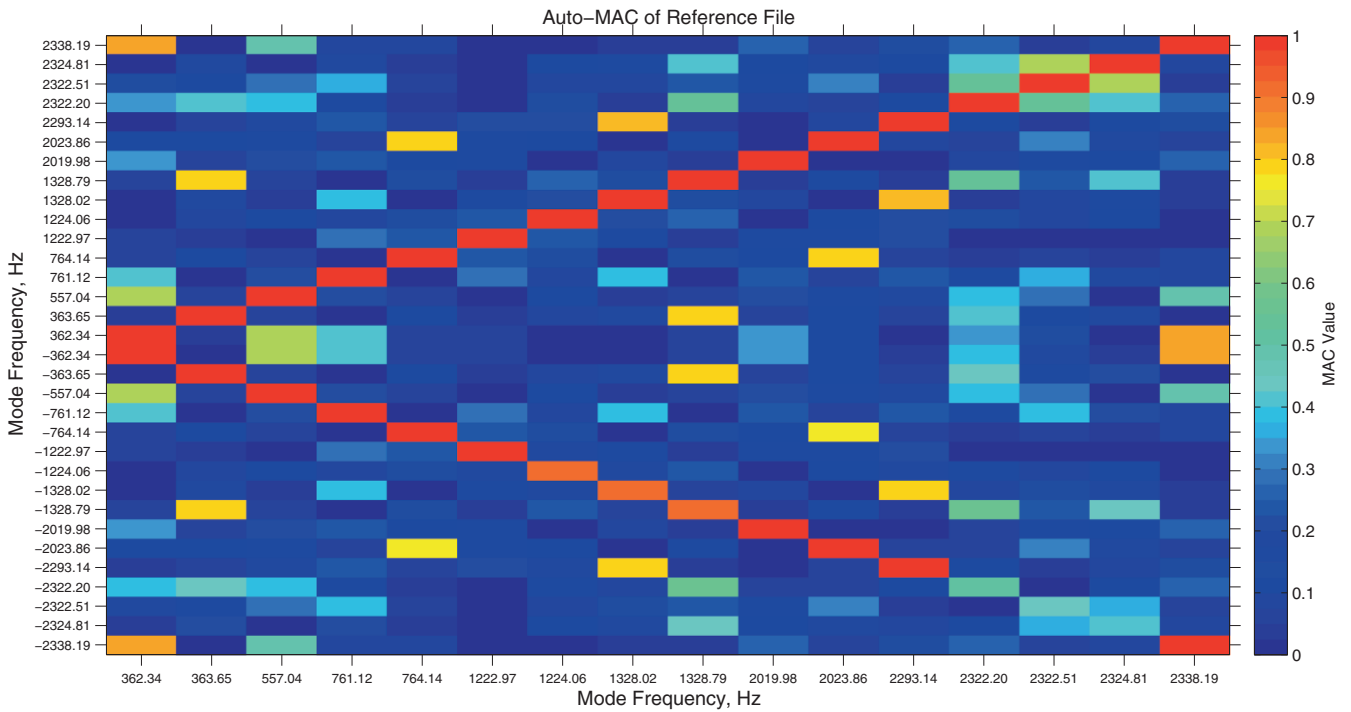


Figure 21. Auto-MAC of Final Autonomous Estimates - Conjugate Poles

While the results are certainly acceptable for this case, the Auto-MAC plot in Figure 21 shows some additional clutter and the conjugate properties of the higher frequency modes do not match as well as in the previous, long dimension base vector example.

4.4 Application Example: C-Plate Laboratory Test Data with Sieved, Short Dimension Base Vector

The next example of the CSSAMI procedure is performed on the same, circular plate laboratory test object. The FRF data is the same as the previous C-Plate examples and the Polyreference Time Domain (PTD) method is used but only the short dimension vectors are used for every possible pole estimated over a model order range from 2 to 20. This short dimension is further sieved to only two references. This means that the spatial information (base vector of length 2) available for sorting out the consistent solutions will be further compromised. For this case, the following thresholds and control parameters were used:

- Lowest order coefficient matrix normalization.
- Pole density threshold (4 and above).
- Pole weighted vector of model order 10.
- Pole weighted MAC threshold (0.8 and above).
- Cluster size threshold (4 and above).
- Cluster identification threshold (0.8 and above).

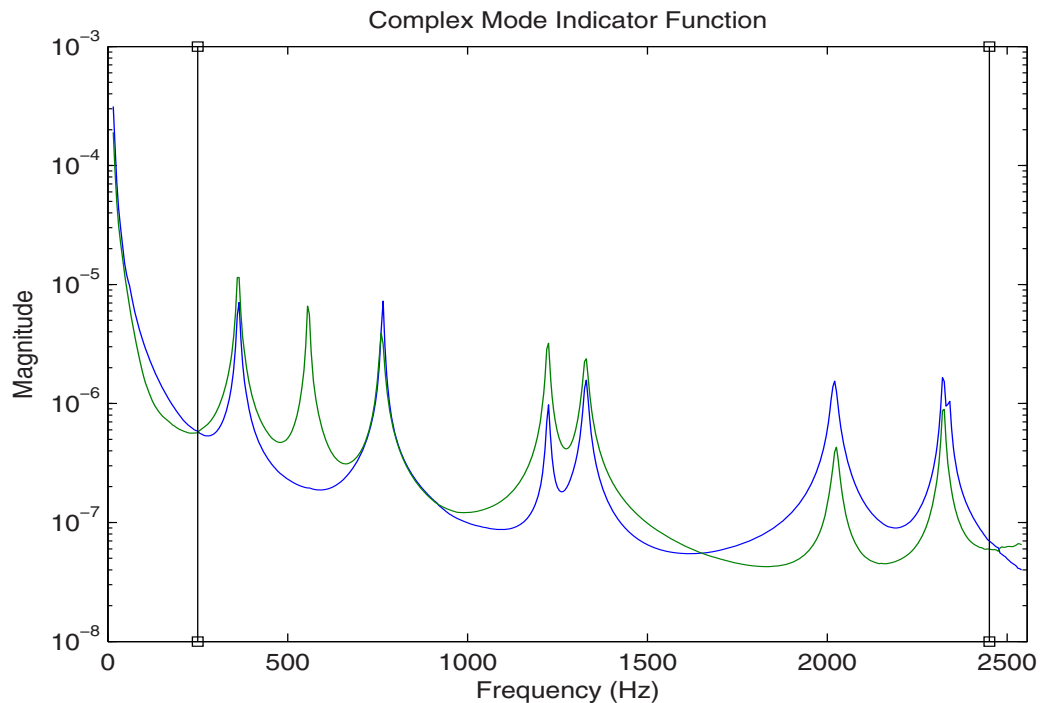


Figure 22. Complex Mode Indicator Function (CMIF)

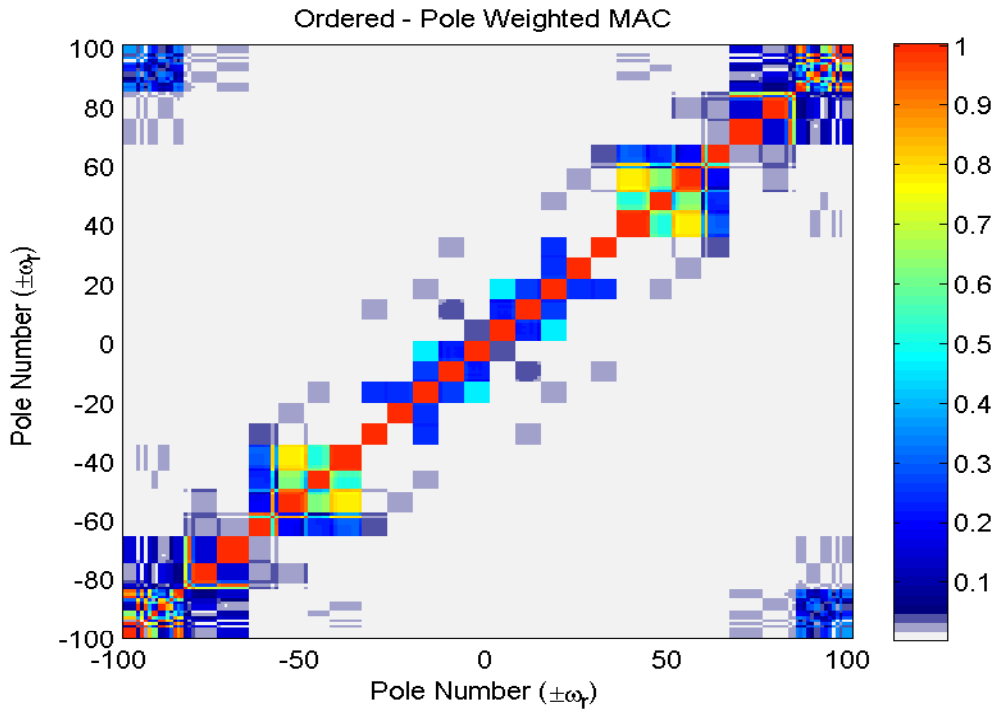


Figure 23. MAC-Tenth Order Pole Weighted Vectors, No Threshold

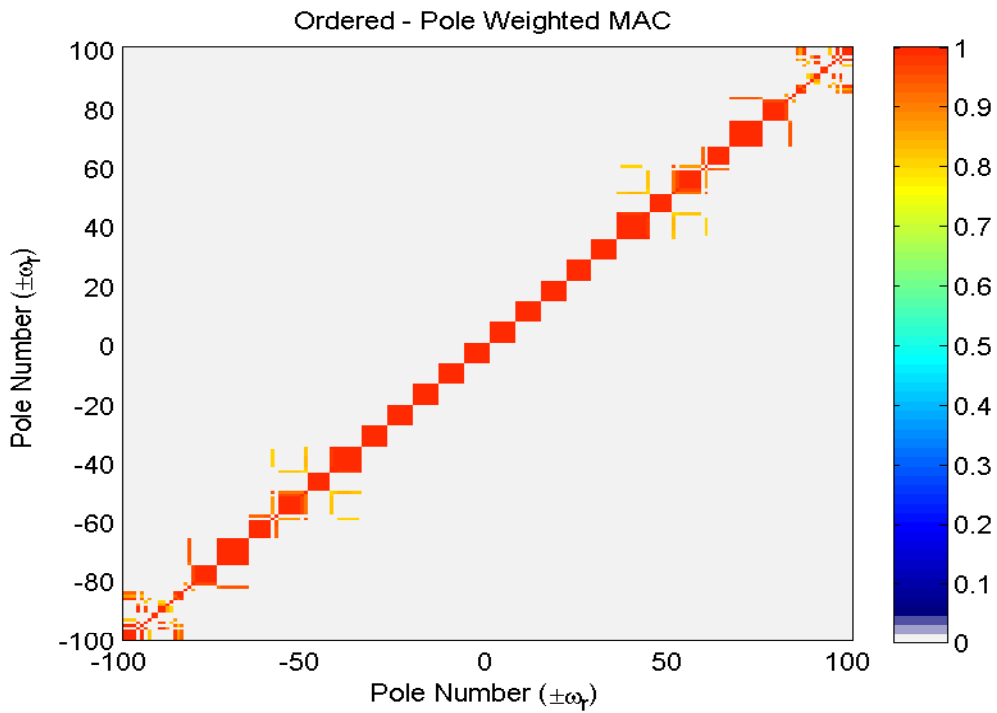


Figure 24. MAC-Tenth Order Pole Weighted Vectors, Above Threshold

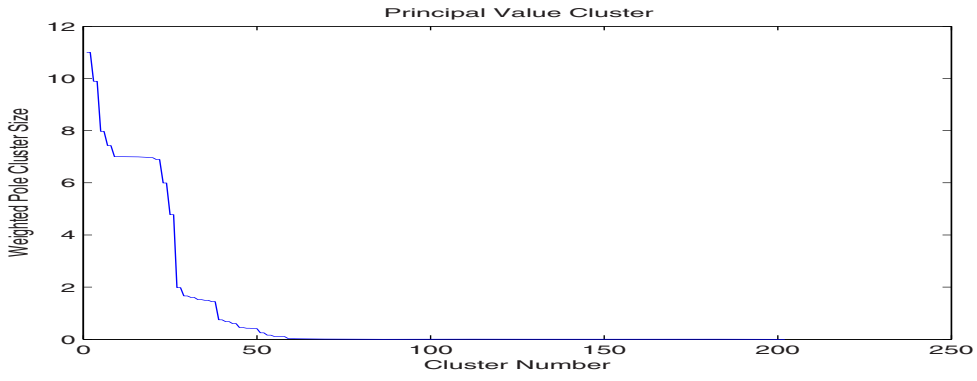


Figure 25. Principal Values of Clusters of Pole Weighted Vectors

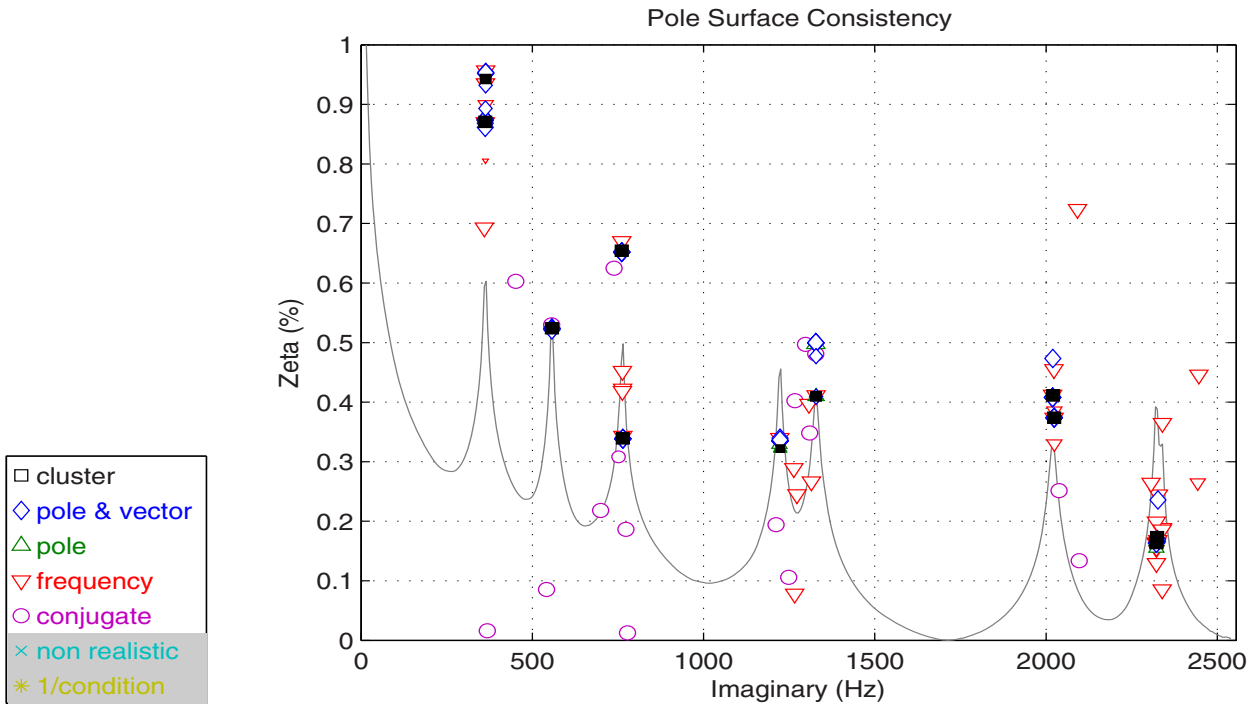


Figure 26. Pole Surface Consistency Clusters with Final Autonomous Estimates

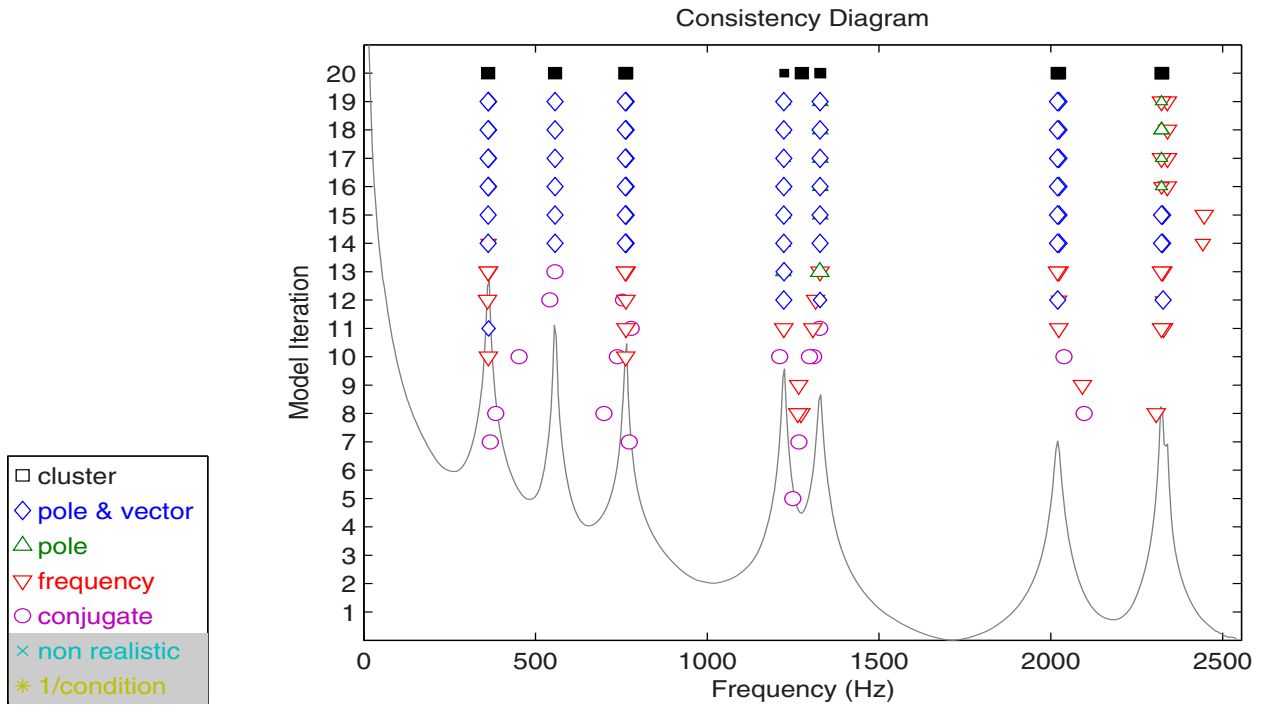


Figure 27. Consistency Diagram with Final Autonomous Estimates

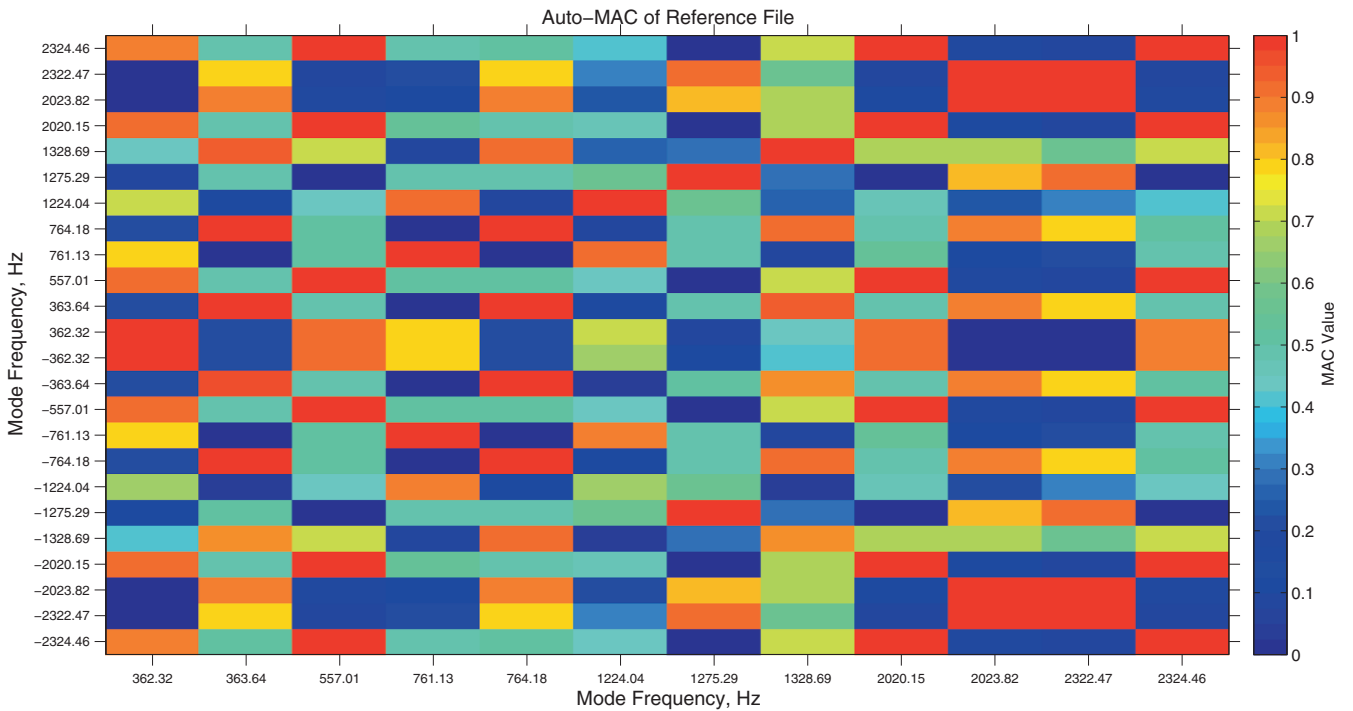


Figure 28. Auto-MAC of Final Autonomous Estimates - Conjugate Poles

The results for this case are further degraded as noted by the Auto-MAC plot in Figure 28 shows some additional clutter and the conjugate properties of the higher frequency modes do not match as well as in the previous, long dimension base vector example.

4.5 Application Example: C-Plate Laboratory Test Data with Sieved, Short Dimension Base Vector

The final example of the CSSAMI procedure is performed on the same, circular plate laboratory test object. The FRF data is the same as the previous C-Plate examples and the Polyreference Time Domain (PTD) method is used but only the short dimension vectors are used for every possible pole estimated over a model order range from 2 to 20. This short dimension is further sieved to only two references. This means that the spatial information (base vector of length 2) available for sorting out the consistent solutions will be compromised. In order to try to compensate for this extremely short base vector, the order of the pole weighted vector is increased to 50. For this case, the following thresholds and control parameters were used:

- Lowest order coefficient matrix normalization.
- Pole density threshold (4 and above).
- Pole weighted vector of model order 50.
- Pole weighted MAC threshold (0.8 and above).
- Cluster size threshold (4 and above).
- Cluster identification threshold (0.8 and above).

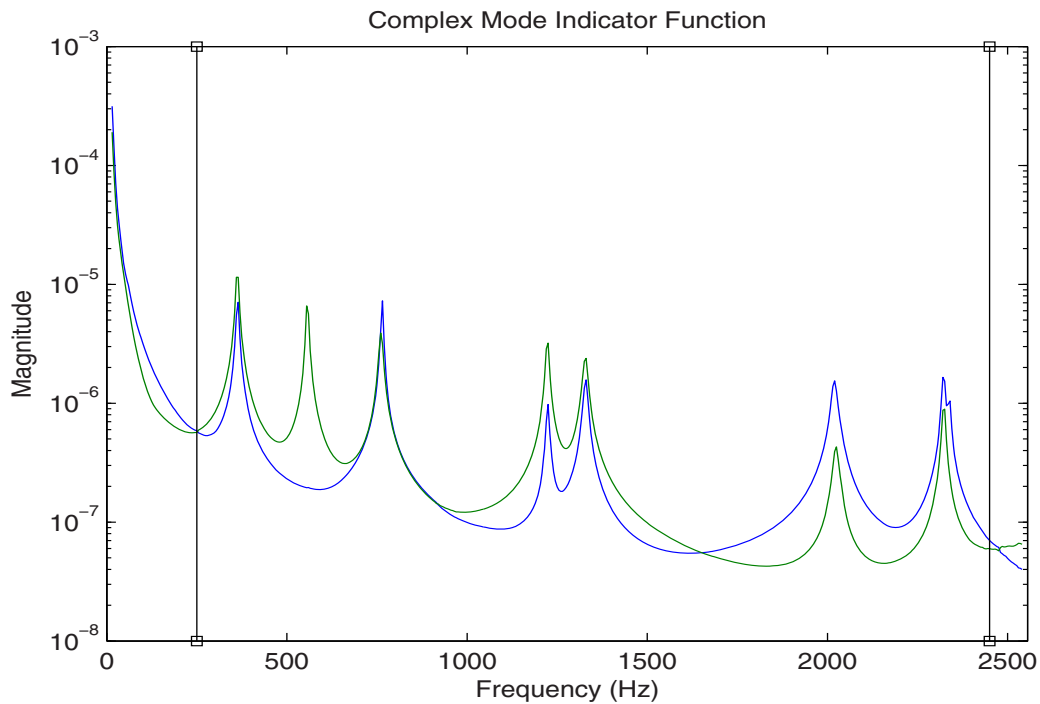


Figure 29. Complex Mode Indicator Function (CMIF)

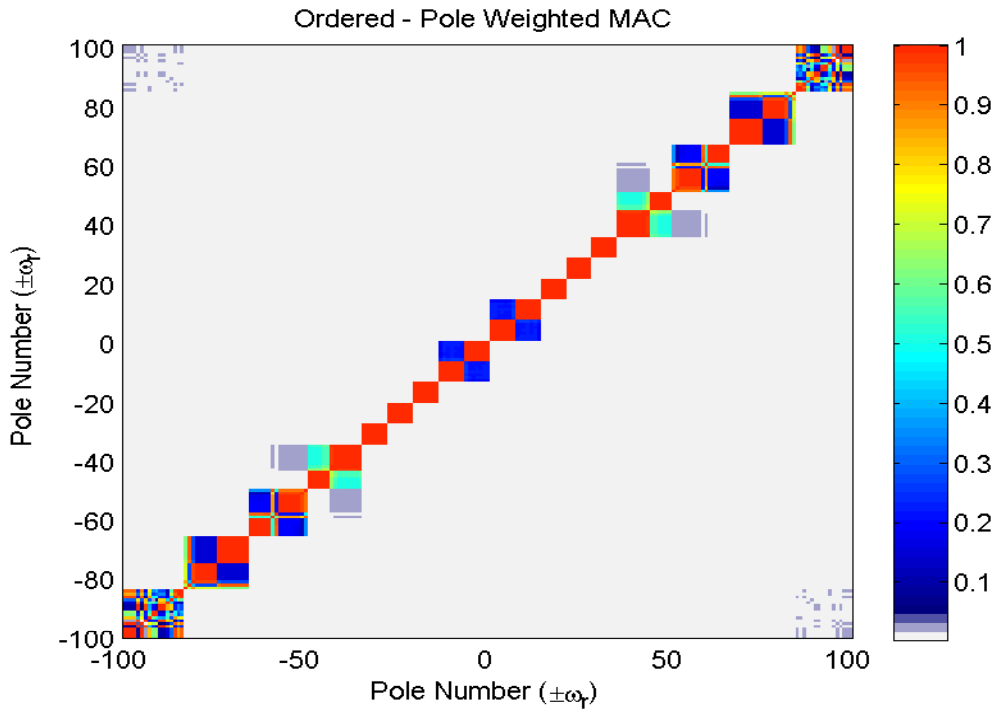


Figure 30. MAC-Fiftieth Order Pole Weighted Vectors, No Threshold

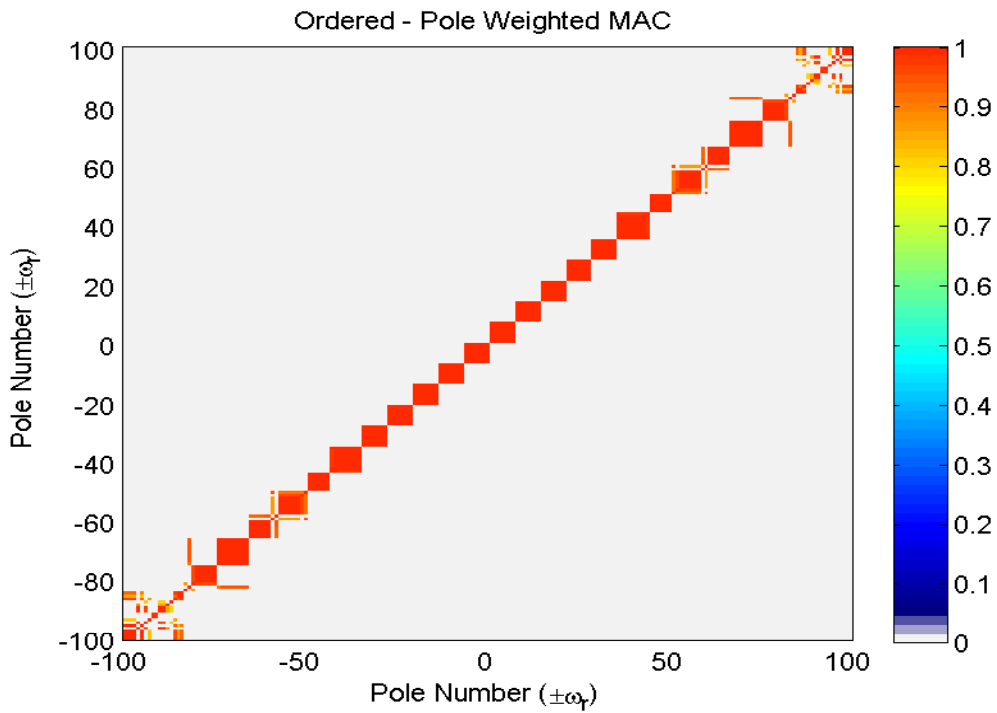


Figure 31. MAC-Fiftieth Order Pole Weighted Vectors, Above Threshold

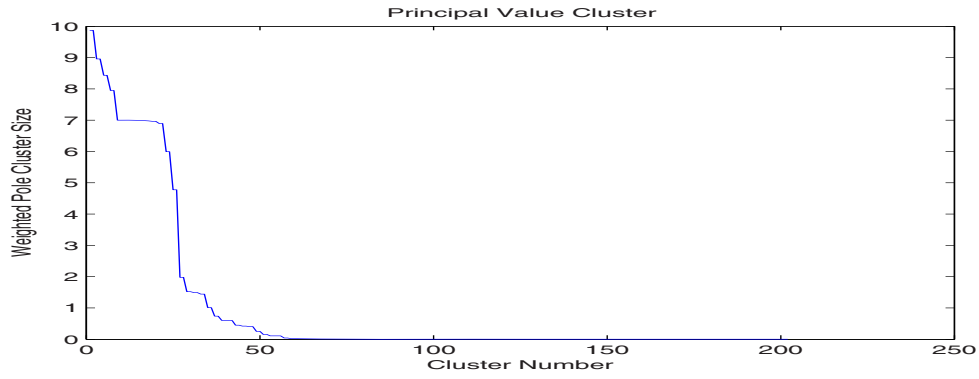


Figure 32. Principal Values of Clusters of Pole Weighted Vectors

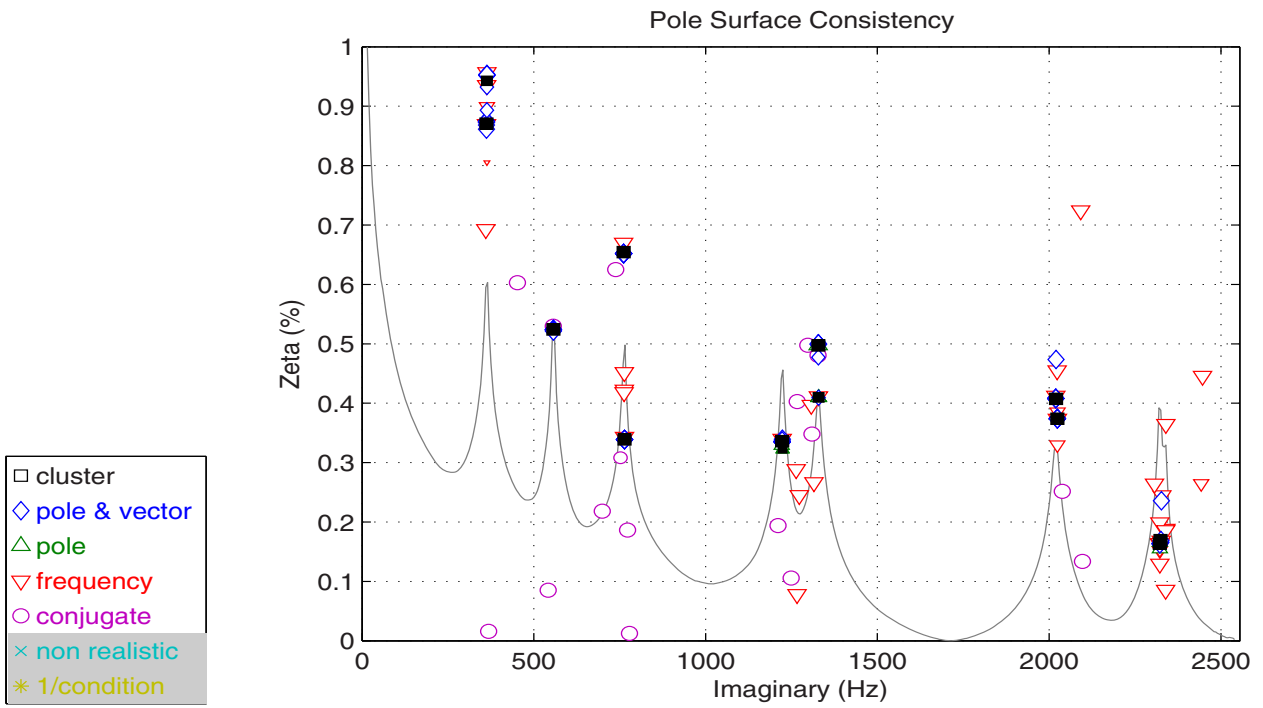


Figure 33. Pole Surface Consistency Clusters with Final Autonomous Estimates

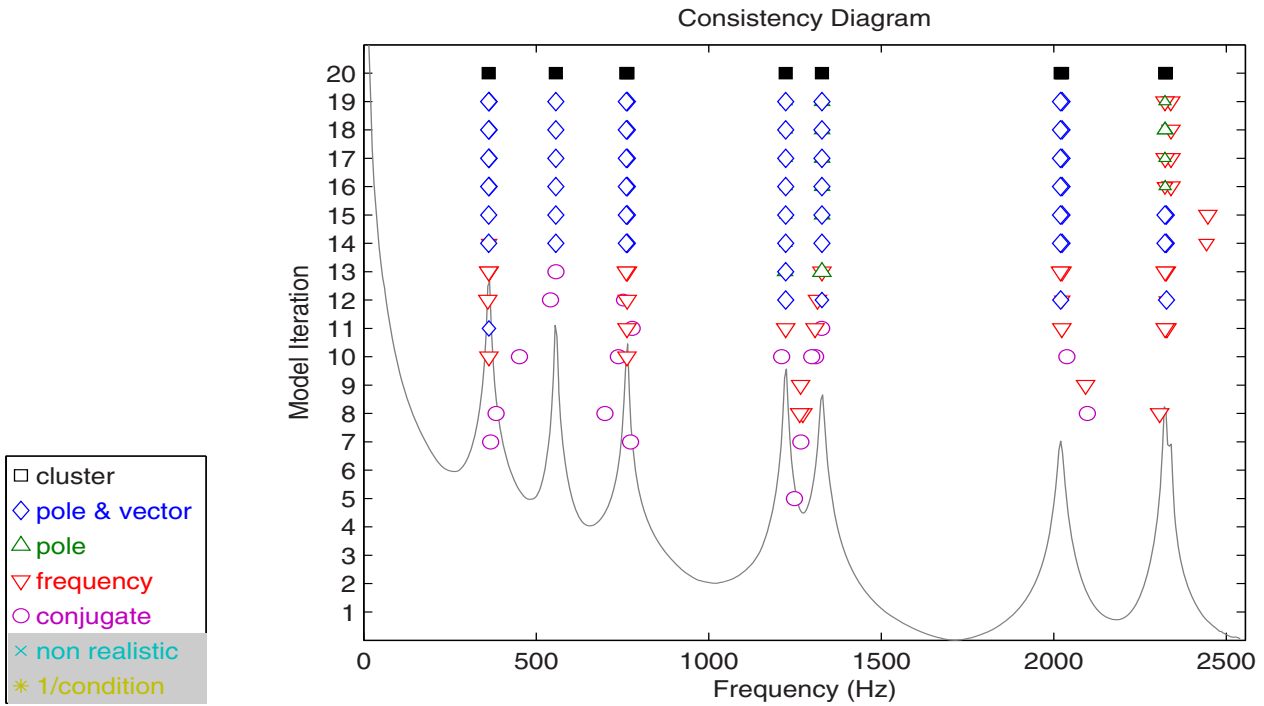


Figure 34. Consistency Diagram with Final Autonomous Estimates

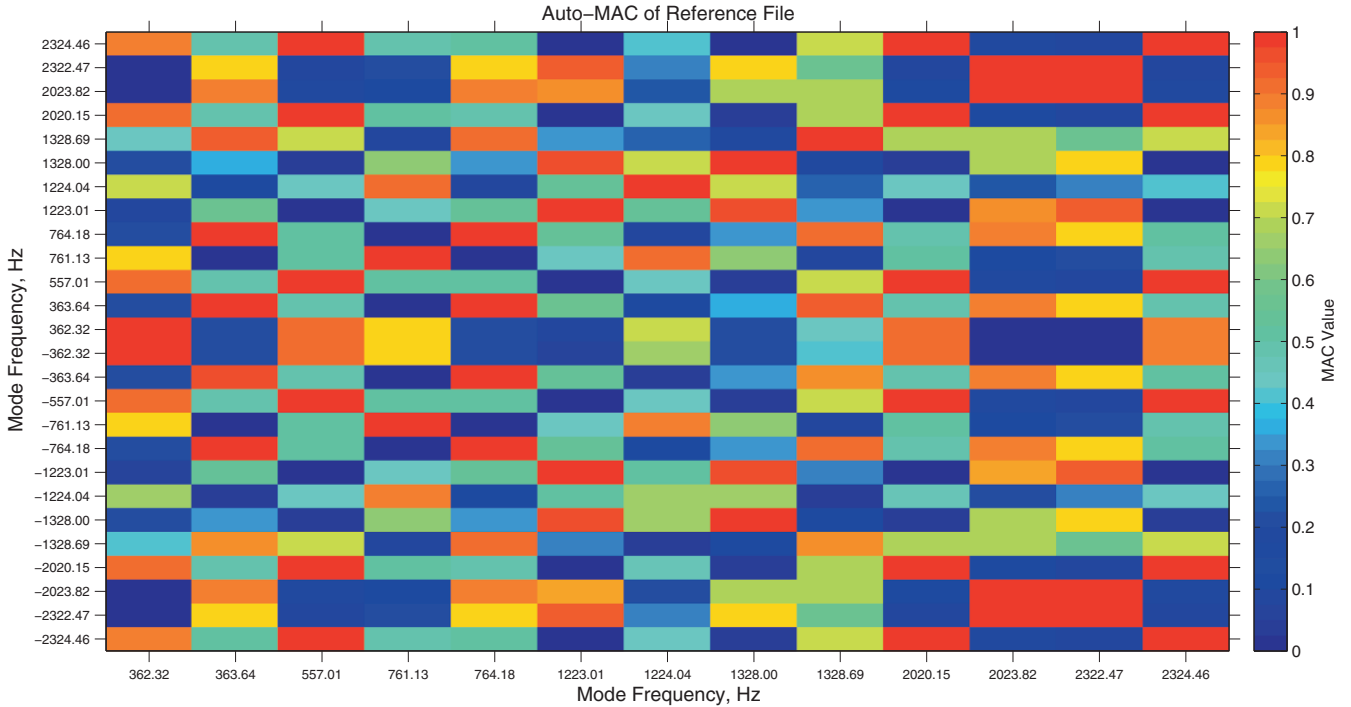


Figure 35. Auto-MAC of Final Autonomous Estimates - Conjugate Poles

The results for this case are very similar to the previous example as noted by the Auto-MAC plot in Figure 35. This Auto-MAC plot shows some additional clutter and the conjugate properties of the higher frequency modes do not match as well as in the previous, long dimension base vector example. The conclusion at this point would be to always utilize the long base

vector in order to get the most reliable result.

5. Summary and Conclusions

In this paper, the application examples for a general autonomous modal parameter identification procedure have been presented along with a brief review of the CSSAMI procedure used to estimate the modal parameters for these cases. This autonomous method utilizes the concept of using correlates results from a cluster of pole weighted modal vectors in order to autonomously identify a set of reasonable modal parameters for the data sets involved. The applications reviewed show that the CSSAMI procedure works best when complete length modal vectors and associated pole weighted modal vectors are available to the procedure. This technique has been shown to be general and applicable to most standard commercially available algorithms. The application of the technique to several case histories has been successfully shown along with the sensitivity to long and short dimension modal vectors.

With the advent of more computationally powerful computers and sufficient memory, it has become practical to evaluate sets of solutions involving thousands of modal parameter estimates and to extract the common information from those sets. The autonomous procedure gives very acceptable results, in some cases superior results, in a fraction of the time required for an experienced user to get the same result.

However, it is important to reiterate that the use of autonomous procedures or *wizard* tools by users with limited experience is probably not yet appropriate. Such tools are most appropriately used by analysts with the experience to accurately judge the quality of the parameter solutions identified. The use of statistical information concerning the results may allow the procedure to be used with success for all levels of users.

6. References

- [1] Hawkins, F. J., "An Automatic Resonance Testing Technique for Exciting Normal Modes of Vibration of Complex Structures", Symposium IUTAM, "Progres Recents de la Mecanique des Vibrations Lineaires", 1965, pp. 37-41.
- [2] Hawkins, F. J., "GRAMPA - An Automatic Technique for Exciting the Principal Modes of Vibration of Complex Structures", Royal Aircraft Establishment, RAE-TR-67-211, 1967.
- [3] Taylor, G. A., Gaukroger, D. R., Skingle, C. W., "MAMA - A Semi-Automatic Technique for Exciting the Principal Modes of Vibration of Complex Structures", Aeronautical Research Council, ARC-R/M-3590, 1967, 20 pp.
- [4] Chauhan, S., Tcherniak, D., "Clustering Approaches to Automatic Modal Parameter Estimation", Proceedings, International Modal Analysis Conference (IMAC), 14 pp., 2008.
- [5] Chhipwadia, K.S., Zimmerman, D.C. and James III, G.H., "Evolving Autonomous Modal Parameter Estimation", Proceedings, International Modal Analysis Conference (IMAC), pp. 819-825, 1999.
- [6] James III, G.H., Zimmerman, D.C., Chhipwadia, K.S., "Application of Autonomous Modal Identification to Traditional and Ambient Data Sets", Proceedings, International Modal Analysis Conference (IMAC), pp. 840-845, 1999.
- [7] Lanslots, J., Rodiers, B., Peeters, B., "Automated Pole-Selection: Proof-of-Concept and Validation", Proceedings, International Conference on Noise and Vibration Engineering (ISMA), 2004.
- [8] Lau, J., Lanslots, J., Peeters, B., Van der Auweraer, "Automatic Modal Analysis: Reality or Myth?", Proceedings, International Modal Analysis Conference (IMAC), 10 pp., 2007.
- [9] Lim, T., Cabell, R. and Silcox, R., "On-line Identification of Modal Parameters Using Artificial Neural Networks", **Journal of Vibration and Acoustics**, Vol. 118 No. 4, pp. 649-656, 1996.
- [10] Liu, J.M., Ying, H.Q., Shen, S., Dong, S.W., "The Function of Modal Important Index in Autonomous Modal Analysis", Proceedings, International Modal Analysis Conference (IMAC), 6 pp., 2007.
- [11] Mevel, L., Sam, A., Goursat, M., "Blind Modal Identification for Large Aircrafts", Proceedings, International Modal Analysis Conference (IMAC), 8 pp., 2004.
- [12] Mohanty, P., Reynolds, P., Pavic, A., "Automatic Interpretation of Stability Plots for Analysis of a Non-Stationary Structure", Proceedings, International Modal Analysis Conference (IMAC), 7 pp., 2007.

- [13] Pappa, R.S., James, G.H., Zimmerman, D.C., "Autonomous Modal Identification of the Space Shuttle Tail Rudder", ASME-DETC97/VIB-4250, 1997, **Journal of Spacecrafts and Rockets**, Vol. 35 No. 2, pp. 163-169, 1998.
- [14] Pappa, R.S., Woodard, S. E., and Juang, J.-N., "A Benchmark Problem for Development of Autonomous Structural Modal Identification", Proceedings, International Modal Analysis Conference (IMAC), pp 1071-1077, 1997
- [15] Parloo, E., Verboven, P., Guillaume, P., Van Overmeire, M., "Autonomous Structural Health Monitoring - Part II: Vibration-based In-Operation Damage Assessment", **Mechanical Systems and Signal Processing (MSSP)**, Vol. 16 No. 4, pp. 659-675, 2002.
- [16] Poncelet, F., Kerschen, G., Golinval, J.C., "Operational Modal Analysis Using Second-Order Blind Identification", Proceedings, International Modal Analysis Conference (IMAC), 7 pp., 2008.
- [17] Rainieri, C., Fabbrocino, G., Cosenza, E., "Fully Automated OMA: An Opportunity for Smart SHM Systems", Proceedings, International Modal Analysis Conference (IMAC), 9 pp., 2009.
- [18] Takahashi, K., Furusawa, M., "Development of Automatic Modal Analysis", Proceedings, International Modal Analysis Conference (IMAC), pp. 686-692, 1987.
- [19] Vanlanduit, S., Verboven, P., Schoukens, J., Guillaume, P. "An Automatic Frequency Domain Modal Parameter Estimation Algorithm", Proceedings, International Conference on Structural System Identification, Kassel, Germany, pp. 637-646, 2001.
- [20] Vanlanduit, S., Verboven, P., Guillaume, P., Schoukens, J., "An Automatic Frequency Domain Modal Parameter Estimation Algorithm", **Journal of Sound and Vibration**, Vol. 265, pp. 647-661, 2003.
- [21] Verboven, P., Parloo, E., Guillaume, P., Van Overmeire, M., "Autonomous Structural Health Monitoring Part I: Modal Parameter Estimation and Tracking", **Mechanical Systems and Signal Processing**, Vol. 16 No. 4, pp. 637-657, 2002.
- [22] Verboven P., E. Parloo, P. Guillame, and M. V. Overmeire, "Autonomous Modal Parameter Estimation Based On A Statistical Frequency Domain Maximum Likelihood Approach", Proceedings, International Modal Analysis Conference (IMAC), pp. 15111517, 2001.
- [23] Yam, Y., Bayard, D.S., Hadaegh, F.Y., Mettler, E., Milman, M.H., Scheid, R.E., "Autonomous Frequency Domain Identification: Theory and Experiment", NASA JPL Report JPL Publication 89-8, 204 pp., 1989.
- [24] Allemang, R.J., Brown, D.L., Phillips, A.W., "Survey of Modal Techniques Applicable to Autonomous/Semi-Autonomous Parameter Identification", Proceedings, International Conference on Noise and Vibration Engineering (ISMA), 2010.
- [25] Phillips, A.W., Allemang, R.J., Brown, D.L., "Autonomous Modal Parameter Estimation: Methodology", Proceedings, International Modal Analysis Conference (IMAC), 25 pp., 2011.
- [26] Allemang, R.J., Phillips, A.W., Brown, D.L., "Autonomous Modal Parameter Estimation: Statistical Considerations", Proceedings, International Modal Analysis Conference (IMAC), 25 pp., 2011.
- [27] Allemang, R.J., Phillips, A.W., "The Unified Matrix Polynomial Approach to Understanding Modal Parameter Estimation: An Update", Proceedings, International Conference on Noise and Vibration Engineering (ISMA), 2004.
- [28] Allemang, R.J., Brown, D.L., "A Unified Matrix Polynomial Approach to Modal Identification", **Journal of Sound and Vibration**, Vol. 211, No. 3, pp. 301-322, April 1998.
- [29] Allemang, R.J., Phillips, A.W., Brown, D.L., "Combined State Order and Model Order Formulations in the Unified Matrix Polynomial Method (UMPA)", Proceedings, International Modal Analysis Conference (IMAC), 25 pp., 2011.

Combined State Order and Model Order Formulations in the Unified Matrix Polynomial Method (UMPA)

R.J. Allemang, A.W. Phillips, D.L. Brown
Structural Dynamics Research Laboratory
School of Dynamic Systems
College of Engineering and Applied Science
University of Cincinnati
Cincinnati, OH 45221-0072 USA
Email: Randall.Allemang@UC.EDU

ABSTRACT

The unified matrix polynomial (coefficient) method (UMPA) has been used by the authors to provide a single, educational framework that encompasses most commercial and research methods used to estimate modal parameters from measured input-output data (normally frequency response functions). In past publications of this methodology, the issue of state order has not clearly been identified in the formulation of the UMPA model. State order refers to the order of the base vector that is an elementary part of the basic UMPA model and has been a part of the modal parameter estimation development since the Ibrahim Time Domain methods in the mid 1970s. The UMPA model is restated to clearly identify the role of base vector order and the relationship between base vector (state) order and polynomial model order. This relationship provides a mechanism for explaining a number of modal parameter estimation methods that have not previously been identified and helps to explain the sensitivity of different modal parameter estimation methods to noise.

Nomenclature

| | |
|--|---|
| N_i = Number of inputs. | t_i = Discrete time (sec). |
| N_o = Number of outputs. | ω_i = Discrete frequency (rad/sec). |
| N_S = Short dimension size. | s_i = Generalized frequency variable. |
| N_L = Long dimension size | $x(t_i)$ = Response function vector ($N_o \times 1$)). |
| N = Number of modal frequencies. | $X(\omega_i)$ = Response function vector ($N_o \times 1$)). |
| λ_r = S domain polynomial root. | $f(t_i)$ = Input function vector ($N_i \times 1$)) |
| λ_r = Complex modal frequency (rad/sec). | $F(\omega_i)$ = Input function vector ($N_i \times 1$)). |
| $\lambda_r = \sigma_r + j \omega_r$ | $[h(t_i)]$ = IRF matrix ($N_o \times N_i$)). |
| σ_r = Modal damping. | $[H(\omega_i)]$ = FRF matrix ($N_o \times N_i$)). |
| ω_r = Damped natural frequency. | $[\alpha]$ = Denominator polynomial matrix coefficient. |
| z_r = Z domain polynomial root. | $[\beta]$ = Numerator polynomial matrix coefficient. |
| $\{\psi_r\}$ = Modal vector. | m = Model order for denominator polynomial. |
| $\{\phi_r\}$ = Pole weighted base vector (state vector). | n = Model order for numerator polynomial. |
| $[A_r]$ = Residue matrix, mode r. | v = Model order for base vector. |
| $[I]$ = Identity matrix. | r = Mode number. |

1. Introduction

During recent research concerning the development of autonomous modal parameter estimation methods, the authors noted that most autonomous methods utilize the concept of correlated complex modal frequency, modal vector and/or modal scaling as mechanisms for sorting out solutions that are physically and statistically relevant. One useful way to combine all of these modal parameters in a single correlation is to synthetically form an extended state vector (high order base vector) for each solution so that these modal parameters are coupled in the correlation procedure. Using higher order, pole weighted modal vectors yields a spatial-temporal vector which is a sensitive correlation vector involving both the complex frequency and the (possibly scaled) modal vector. The use of the extended state vector allows similar modal parameters to be sorted out from a larger set of pole weighted vectors that represent other physical modal vectors or vectors of essentially noise. This extended state vector is the same pole weighted modal vector that has been used successfully in previous work to provide an alternate form of the consistency diagram ^[1-2].

Some existing modal parameter estimation algorithms already involve the state vector in the model. The primary examples of two algorithms that already use an extended base vector are the first order versions of the Eigensystem Realization Algorithm (ERA-1) and the Polyreference Frequency Domain Algorithm (PFD-1). Both of these methods also have alternate forms that utilize the conventional zeroth order base vector (ERA-2 and PFD-2) which appear to give relatively equivalent solutions. For the purpose of sorting correlated solutions in an autonomous modal parameter estimation method, state order above order one is attractive in order to get a longer (spatially) extended state vector which also may have heightened sensitivity to the complex modal frequency differences. Work has already been reported on higher state order methods in the past but this issue has not been discussed ^[5]. When investigating these models further, it is apparent that the Unified Matrix Polynomial Algorithm (UMPA) framework that has been utilized to describe most modal parameter estimation algorithms is not rigorous enough to describe the solutions covered by extended state order formulations without some additional clarification.

2. Background: Modal Parameter Estimation

All modern, commercial algorithms for estimating modal parameters from experimental input-output data can be developed or explained in terms of polynomial based models. For this reason, with minor implementation differences, all of these algorithms can take advantage of the consistency diagram as an aid in identifying the correct modal frequencies from the large number of poles that are found. This section quickly overviews the development of the polynomial models for both the time or frequency domains so that the model order variation options, that are involved in the consistency diagram, can be discussed. This background is detailed more fully in several references ^[6-7]. The algorithms that commonly use an implementation of the consistency diagram for identifying modal parameters are summarized in [Table 1](#).

2.1 Polynomial Modal Identification Models

Rather than using a physically based mathematical model, the common characteristics of different modal parameter estimation algorithms can be more readily identified by using a matrix coefficient polynomial model. One way of understanding the basis of this model can be developed from the polynomial model used historically for the frequency response function. Note the nomenclature in the following equations regarding measured frequency ω_i versus generalized frequency s_i . Measured input and response data are always functions of measured frequency but the generalized frequency variable used in the model may be altered to improve the numerical conditioning as is done with most frequency domain methods (normalized frequency) and specifically with the polyreference least squares complex frequency (PLSCF) method (complex Z transform of frequency). The commercial implementation of the PLSCF

method is known as PolyMAX [®].

Therefore, the multiple input, multiple output (MIMO) FRF model is:

$$\sum_{k=0}^m [\alpha_k] (s_i)^k \left[H(s_i) \right] = \sum_{k=0}^n [\beta_k] (s_i)^k \left[I \right] \quad (1)$$

Equation (1) is evaluated at many frequencies (ω_i) until all data are utilized or a sufficient overdetermination factor is achieved. Note that both positive and negative frequencies are required in order to accurately estimate conjugate modal frequencies. This allows for the coefficients of a matrix coefficient, characteristic polynomial to be identified for a given model order m . The roots of this polynomial can be used to find the modal parameters.

For the general multiple input, multiple output case:

$$\sum_{k=0}^m [\alpha_k] \{x(t_{i+k})\} = \sum_{k=0}^n [\beta_k] \{f(t_{i+k})\} \quad (2)$$

If the discussion is limited to the use of free decay or impulse response function data, the previous time domain equations can be simplified by noting that the forcing function can be assumed to be zero for all time greater than zero. If this is the case, the $[\beta_k]$ coefficients can be eliminated from the equations.

$$\sum_{k=0}^m [\alpha_k] \left[h(t_{i+k}) \right] = 0 \quad (3)$$

Additional equations can be developed by repeating Equation (3) at different time shifts into the data (t_i) until all data are utilized or a sufficient overdetermination factor is achieved. Note that at least one time shift is required in order to accurately estimate conjugate modal frequencies. This allows for the coefficients of the matrix coefficient, characteristic polynomial to be identified for a given model order m . The roots of this polynomial can be used to find the modal parameters.

The models represented by Equation (1) and Equation (3) are referred to as **Unified Matrix Polynomial Approach (UMPA)** models. Both equations yield a matrix coefficient, characteristic polynomial (the $[\alpha]$ polynomial in these models). Equation (3) corresponds to a time domain AutoRegressive-Moving-Average (ARMA(m,n)) model, or more properly an AutoRegressive with eXogenous inputs (ARX(m,n)) model, that is developed from a set of discrete time equations. Since both the frequency and time domain models are based upon functionally similar matrix coefficient, characteristic polynomials, the UMPA(m,n) terminology is used for models in both domains to reflect the order of the denominator polynomial (m) and the order of the numerator polynomial (n). In Section 2.2, this notation will be extended to UMPA(m,n,v) to reflect the order v of the base vector involved in the basic UMPA formulation.

In light of the above discussion, it is now apparent that most of the modal parameter estimation processes available could have been developed by starting from a general matrix polynomial formulation that is justifiable based upon the underlying matrix differential equation. The general matrix polynomial formulation yields essentially the same form of matrix coefficient, characteristic polynomial equation, for both time and frequency domain data.

For the frequency domain data case, this yields:

$$\left| [\alpha_m] s^m + [\alpha_{m-1}] s^{m-1} + [\alpha_{m-2}] s^{m-2} + \dots + [\alpha_0] \right| = 0 \tag{4}$$

where:

$$s_r = \lambda_r \quad \lambda_r = \sigma_r + j \omega_r \tag{5}$$

For the time domain data case, this yields:

$$\left| [\alpha_m] z^m + [\alpha_{m-1}] z^{m-1} + [\alpha_{m-2}] z^{m-2} + \dots + [\alpha_0] \right| = 0 \tag{6}$$

where:

$$z_r = e^{\lambda_r \Delta t} \quad \lambda_r = \sigma_r + j \omega_r \tag{7}$$

$$\sigma_r = \text{Re} \left[\frac{\ln z_r}{\Delta t} \right] \quad \omega_r = \text{Im} \left[\frac{\ln z_r}{\Delta t} \right] \tag{8}$$

Once the matrix coefficients ($[\alpha]$) have been found, the modal frequencies (λ_r or z_r) can be found as the roots of the matrix coefficient polynomial (Equation (4) or (6)) using any one of a number of numerical techniques, normally involving the companion matrix associated with the matrix coefficient polynomial.

Therefore, the roots of the matrix characteristic equation can be found as the eigenvalues of the associated companion matrix. The companion matrix can be formulated in one of several ways. A common formulation is as follows:

$$[C]_{mN_s \times mN_s} = \begin{bmatrix} -[\alpha]_{m-1} & -[\alpha]_{m-2} & \dots & \dots & \dots & -[\alpha]_1 & -[\alpha]_0 \\ [I] & [0] & \dots & \dots & \dots & [0] & [0] \\ [0] & [I] & \dots & \dots & \dots & [0] & [0] \\ [0] & [0] & \dots & \dots & \dots & [0] & [0] \\ \dots & \dots & \dots & \dots & \dots & \dots & \dots \\ \dots & \dots & \dots & \dots & \dots & \dots & \dots \\ \dots & \dots & \dots & \dots & \dots & \dots & \dots \\ [0] & [0] & \dots & \dots & \dots & [0] & [0] \\ [0] & [0] & \dots & \dots & \dots & [0] & [0] \\ [0] & [0] & \dots & \dots & \dots & [I] & [0] \end{bmatrix} \tag{9}$$

Note that the form of the companion matrix shown in Equation (9) is one of four, equivalent forms where the coefficient matrices appear in the first or last rows or columns. The form above will be used as a reference for any further discussion.

The companion matrix is used in the following eigenvalue formulation to determine the modal frequencies for the original matrix coefficient equation:

$$[C]\{X\} = \lambda [I] \{X\} \quad (10)$$

When the modal frequencies are estimated from the eigenvalue-eigenvector problem that is associated with solving this matrix coefficient polynomial equation, a unique estimate of the unscaled modal vector is identified at the same time. The length or dimension of this unscaled modal vector is equal to the dimension of the square alpha coefficients which, in general, is equal to the row dimension of the FRF data matrix in order for the matrix coefficient polynomial equation to be conformal. Normally, this row dimension associated with the FRF or IRF data matrix is assumed to be connected with the number of outputs (N_o) that were measured.

The eigenvector that is found, associated with each eigenvalue, is of length model order m times matrix coefficient size, N_i or N_o . In fact, the unique (meaningful) portion of the eigenvector is of length equal to the size of the coefficient matrices, N_i or N_o , and is repeated in the eigenvector m times.

For each repetition, the unique portion of the eigenvector is repeated, multiplied by a different complex scalar which is a successively larger, integer power of the associated modal frequency. Therefore, the eigenvectors of the companion matrix have the following form:

$$\{\phi\}_r = \left\{ \begin{array}{c} \lambda_r^{m-1} \{\psi\}_r \\ \cdot \\ \cdot \\ \lambda_r^2 \{\psi\}_r \\ \lambda_r^1 \{\psi\}_r \\ \lambda_r^0 \{\psi\}_r \end{array} \right\}_r \quad (11)$$

Since the data matrix (FRF or IRF) is considered to be symmetric or reciprocal, the data matrix can be transposed, switching the effective meaning of the row and column index with respect to the physical inputs and outputs.

$$[H(\omega_i)]_{N_o \times N_i} = [H(\omega_i)]_{N_i \times N_o}^T \quad (12)$$

Since many modal parameter estimation algorithms are developed on the basis of either the number of inputs (N_i) or the number of outputs (N_o), assuming that one or the other is larger based upon test method, some nomenclature conventions are required for ease of further discussion. In terms of the modal parameter estimation algorithms and the ultimate matrix coefficient, characteristic polynomial equation, it is more important to recognize whether the algorithm develops the square matrix coefficient on the basis of the larger (N_L) of N_i or N_o or the smaller (N_S) of N_i or N_o . For this reason, the terminology of *long* (larger of N_i or N_o) dimension or *short* (smaller of N_i or N_o) dimension is easier to understand without confusion. Using this approach, PTD, RFP and PLSCF are all short dimension methods where the vector found as part of the solution for poles is very small while ERA and PFD are long dimension methods where the vector found as part of the solution for poles is of full length, based upon measurement locations.

To eliminate possible confusion, in recent explanations of modal parameter estimation algorithms, the nomenclature of the number of outputs (N_o) and number of inputs (N_i) has been replaced by the length of the long dimension of the data matrix (N_L) and the length of the short dimension (N_S) regardless of

which dimension refers to the physical output or input. This means that the above reciprocity relationship can be restated as:

$$[H(\omega_i)]_{N_L \times N_S} = [H(\omega_i)]_{N_S \times N_L}^T \quad (13)$$

Note that the reciprocity relationships in Equation (12) and (13) are a function of the common degrees of freedom (DOFs) in the short and long dimensions. If there are no common DOFs, there are no reciprocity relationships. Nevertheless, the importance of Equation (12) and (13) comes from the idea that the dimensions of the FRF matrix can be transposed and this affects the size of the square alpha coefficients in the matrix coefficient polynomial equation.

Finally, once the modal frequencies and unscaled modal vectors are estimated via the eigenvalue-eigenvector problem, the residues (numerators) of the partial fraction model of the FRF data matrix are used to estimate the final, scaled modal vectors and modal scaling. Note that the unscaled modal vector found in the eigenvalue-eigenvector problem is available to be used as a weighting vector in the estimation of the residues and, therefore, the final scaled modal vectors and modal scaling. Also note that this weighting vector may be of length equal to the long or short dimension, depending on the modal parameter estimation algorithm being used.

$$[H(\omega_i)]_{N_L \times N_S} = \sum_{r=1}^N \frac{[A_r]_{N_L \times N_S}}{j\omega_i - \lambda_r} + \frac{[A_r^*]_{N_L \times N_S}}{j\omega_i - \lambda_r^*} = \sum_{r=1}^{2N} \frac{[A_r]_{N_L \times N_S}}{j\omega_i - \lambda_r} \quad (14)$$

This process means that most modern modal parameter estimation algorithms are implemented in a two stage procedure that has three steps as follows:

Stage 1, Step 1

- Load Measured Data into Over-Determined Linear Equation Form.
 - Utilize Matrix Coefficient Polynomial Based Model (Equation 1, 2 or 3).
 - Find Scalar or Matrix Coefficients ($[\alpha_k]$ and $[\beta_k]$).
 - Implement for Various Model Orders (Consistency/Stability Diagram).

Stage 1, Step 2

- Solve Matrix Coefficient Polynomial for Modal Frequencies (Equation 4 or 6).
 - Formulate Eigenvalue-Eigenvector Problem.
 - Eigenvalues Determine the Modal Frequencies (λ_r).
 - Eigenvectors Determine the Unscaled Modal Vectors ($\{\psi_r\}$) of dimension N_S or N_L .

Stage 2, Step 3

- Load Measured Data Into Over-Determined Linear Equation Form (Equation 14).
 - Determine Modal Vectors and Modal Scaling from Residues.

The most commonly used modal identification methods can be summarized as shown in [Table 1](#). The

high order model is typically used for those cases where the system is undersampled in the spatial domain. For example, the limiting case is when only one measurement is made on the structure. For this case, the left hand side of the general linear equation corresponds to a scalar polynomial equation with the order equal to or greater than the number of desired modal frequencies. The low order model is used for those cases where the spatial information is complete. In other words, the number of physical coordinates is greater than the number of desired modal frequencies. For this case, the order of the lefthand side of the general linear equation is equal to two. The zero order model corresponds to the case where the temporal information is neglected and only the spatial information is used. These methods directly estimate the eigenvectors as a first step. In general, these methods are programmed to process data at a single temporal condition or variable. In this case, the method is essentially equivalent to the single-degree-of-freedom (SDOF) methods which have been used with frequency response functions. In others words, the zeroth order matrix polynomial model compared to the higher order matrix polynomial models is similar to the comparison between the SDOF and MDOF methods used historically in modal parameter estimation.

| Algorithm | Domain | | Matrix Polynomial Order | | | Coefficients | |
|---|--------|------|-------------------------|-----|------|--------------|------------------|
| | Time | Freq | Zero | Low | High | Scalar | Matrix |
| Complex Exponential Algorithm (CEA) | • | | | | • | • | |
| Least Squares Complex Exponential (LSCE) | • | | | | • | • | |
| Polyreference Time Domain (PTD) | • | | | | • | | $N_S \times N_S$ |
| Ibrahim Time Domain (ITD) | • | | | • | | | $N_L \times N_L$ |
| Multi-Reference Ibrahim Time Domain (MRITD) | • | | | • | | | $N_L \times N_L$ |
| Eigensystem Realization Algorithm (ERA-1, ERA-2) | • | | | • | | | $N_L \times N_L$ |
| Polyreference Frequency Domain (PFD-1, PFD-2) | | • | | • | | | $N_L \times N_L$ |
| Simultaneous Frequency Domain (SFD) | | • | | • | | | $N_L \times N_L$ |
| Multi-Reference Frequency Domain (MRFD) | | • | | • | | | $N_L \times N_L$ |
| Rational Fraction Polynomial (RFP) | | • | | | • | • | $N_S \times N_S$ |
| Orthogonal Polynomial (OP) | | • | | | • | • | $N_S \times N_S$ |
| Polyreference Least Squares Complex Frequency (PLSCF) | | • | | | • | • | $N_S \times N_S$ |
| Rational Fraction Polynomial-Z Domain (RFP-Z) | | • | | | • | • | $N_S \times N_S$ |
| Complex Mode Indication Function (CMIF) | | • | • | | | | $N_L \times N_S$ |

TABLE 1. Summary of Modal Parameter Estimation Algorithms

How the different modal parameter estimation algorithms fit into the UMPA (m,n) model when the extended state order is used requires some clarification. This clarification explains the current state vector methods that utilize a base vector of model order one (ERA-1 and PFD-1) as well as another family of possible modal parameter estimation algorithms that are yet to be formally described. These potential algorithms yield higher order state vectors naturally which would be useful when an autonomous modal parameter estimation procedure is developed. This clarification is discussed in detail in the following section.

3. Clarification: Extended State (Base) Vector Order

When formulating the basic UMPA(m,n) equation for various model orders, the resulting matrix coefficient polynomial involves coefficient matrices which are sized based upon the short or long dimension of the data matrix. Once this matrix coefficient polynomial is chosen, the set of unscaled modal vectors, or base vectors is effectively chosen where the length of each vector matches this dimension.

For model orders (m) equal to one, however, this matrix model will not be able to estimate complex conjugate solutions without at least one time shift (time domain implementation) or one derivative (frequency domain implementation) when the model is formulated. When the solution is formed in this fashion, the base vector is a state vector, or what has alternately been referred to as a pole weighted modal vector, for this system. Instead of the base vector being of zeroth order as for all other UMPA cases, the base vector will be of order one. If successive time shifts or derivatives are included, the base vector can be of higher order. The form of the base vector is as follows where v is the order of the base vector:

$$\{\bar{\psi}\}_r = \begin{Bmatrix} \lambda_r^v \{\psi\}_r \\ \cdot \\ \cdot \\ \lambda_r^2 \{\psi\}_r \\ \lambda_r^1 \{\psi\}_r \\ \lambda_r^0 \{\psi\}_r \end{Bmatrix} \quad (15)$$

This means that the notation for the UMPA(m,n) model does not completely define the UMPA formulation. A more correct formulation would be UMPA(m,n,v). For most commercial algorithms, v is normally zero and the base vector is zeroth order. For the first order version of the Eigensystem Realization Algorithm (ERA-1) and the first order version of the Polyreference Frequency Domain (PFD-1) algorithm, v is one and the base vector is, therefore, first order. While no commercial algorithm utilizes v greater than one, there is no reason to restrict the UMPA(m,n,v) formulation to zeroth and first order base vectors. Allowing the base vector to take on higher orders lengthens the vector while adding a sensitivity to complex modal frequency that will be evaluated for correlation or consistency among all of the possible solutions. This is an extremely useful concept when developing autonomous modal parameter estimation procedures.

3.1 Impact of Base Vector Choice

While the concept of using additional time shifts or derivatives in the formulation of the matrix coefficient polynomial model, the form of the model and of the $[\alpha]$ coefficients changes. As additional time shifts or derivatives are added to the model formulation, much of the solution for the coefficients remains the same but the size of the $[\alpha]$ changes as a function of the UMPA(m,n,v) notation, specifically the v notation. This gives some insight as to what is changing and how it affects the solution from a practical viewpoint.

As an example, let's look at increasingly higher order base vector models of what is essentially an Eigensystem Realization Algorithm (ERA-1) in terms of the $[\alpha]$ coefficients that are found from the measured data. If the long dimension of the measured data space is N_L , the ERA method must involve one time shift at a minimum to achieve a solution. Therefore, the base vector in this case is of length $2 \times N_L$ and the companion matrix, assuming that the leading coefficient matrix is normalized to the identity matrix is as follow:

Case 1:

$$[C] = \begin{bmatrix} -[\alpha]_0 \\ I_{2 \times N_L} \end{bmatrix}_{2 \times N_L \times 2 \times N_L} \quad (16)$$

The above model would be referred to as an UMPA(1,n,1) model using the new notation. The number of unknowns found in the $[\alpha]$ coefficient would be $(2N_L)^2$.

If an additional time shift, involving additional information, is used to form the coefficient matrix, the new form is:

Case 2:

$$[C] = \begin{bmatrix} -[\alpha]_0 \end{bmatrix}_{3*N_L \times 3*N_L} \quad (17)$$

The above model would be referred to as an UMPA(1,n,2) model using the new notation. The number of unknowns found in the $[\alpha]$ coefficient would be $(3N_L)^2$.

With each additional time shift, the square $[\alpha]$ coefficient matrix increases by a factor of N_L in each dimension. The base vector for each case also grows by N_L with additional weighting provided by raising the complex modal frequency (or its Z transform equivalent) to the next successive power.

This approach will yield alternate solution models that have an increasingly larger companion matrix and that also have higher ordered base vectors. The practical cost of these methods is that the memory required to solve for the $[\alpha]$ will be a function of $(v+1) \times N_L$. The solution time for solving the companion matrix will also grow. In light of modern computers, this may not be an issue and large (5th - 10th) state order problems can still be formed and solved in available desktop computing situations.

The alternate, and more natural, approach to involving additional time shifts or derivatives within the UMPA framework would be to leave the base vector at model order zero ($v = 0$) and increase the model order of the $[\alpha]$ matrix coefficient polynomial (m).

With respect to the previous example, the equivalent model to Case 1 would be the equivalent UMPA(2,n,0) model which would have a base vector of length N_L and a companion matrix of the form:

Case 3:

$$[C] = \begin{bmatrix} -[\alpha]_1 & -[\alpha]_0 \\ [I] & [0] \end{bmatrix}_{2*N_L \times 2*N_L} \quad (18)$$

The $[\alpha]$ coefficients in above model would result from exactly the same measured data as used in Case 1. The number of unknowns found in the $[\alpha]$ coefficients would be $2 \times N_L^2$ a much smaller memory footprint than Case 1.

If another time shift is involved in the solution, as in Case 2 in the above example, the UMPA(3,n,0) model would be formed. This model would also have a base vector of length N_L and a companion matrix of the following form:

Case 4:

$$[C] = \begin{bmatrix} -[\alpha]_2 & -[\alpha]_1 & -[\alpha]_0 \\ [I] & [0] & [0] \\ [0] & [I] & [0] \end{bmatrix}_{3*N_L \times 3*N_L} \quad (19)$$

The $[\alpha]$ coefficients in above model would result from exactly the same measured data as used in Case 2. The number of unknowns found in the $[\alpha]$ coefficients would be $3 \times N_L^2$ a much smaller memory footprint than Case 2.

Note that in these two alternate approaches (Case 1-2 versus Case 3-4), while the base vector model order and the polynomial model order are alternatively changed to yield the exact same number of eigenvalues and eigenvectors of the companion matrix (and the same length of eigenvectors), the cost in terms of memory footprint and somewhat in solution times based upon the number of unknowns being found will increase dramatically as base vector model order v is raised compared to the equivalent models formed by raising the order of the $[\alpha]$ polynomial m .

While the the use of higher base vector model orders is possible and theoretically sound, assuming memory and compute time is not a significant issue, the question remains as to whether this approach to model formulation is beneficial in some other way (e.g. numerically). The next section will prove that the apparently different model formulations that involve the same measured data, but different numbers of unknowns, are theoretically no different from one another.

3.2 Base Vector Order v versus $[\alpha]$ Coefficient Order m

The simplest comparison that will demonstrate the relationship between the order of the base vector and the order of the $[\alpha]$ coefficients in the UMPA formulation is to compare the ERA-1 case to the ERA-2 case. The ERA-1 algorithm is an UMPA(1,n,1) model and the ERA-2 is an UMPA(2,n,0) model. Both models generate the same size companion matrix and the same number of eigenvalue-eigenvector solutions. The following equation manipulations will show that the data in each companion matrix must be identical, and therefore yield identical eigenvalue-eigenvector results. This proof is formulated on the basis of normalizing the leading coefficient of the matrix coefficient polynomial to the identity matrix but the result is the same for any other normalization and for any other higher order polynomial algorithm when comparing the same size companion matrices formed by the two alternate approaches.

Basic Equation for ERA-1:

$$\begin{bmatrix} [\bar{\alpha}_0] \end{bmatrix} \begin{bmatrix} [h(t_0)] & [h(t_1)] & [h(t_2)] & \cdots & [h(t_i)] \\ [h(t_1)] & [h(t_2)] & [h(t_3)] & \cdots & [h(t_{i+1})] \end{bmatrix} = - \begin{bmatrix} [h(t_1)] & [h(t_2)] & [h(t_3)] & \cdots & [h(t_{i+1})] \\ [h(t_2)] & [h(t_3)] & [h(t_4)] & \cdots & [h(t_{i+2})] \end{bmatrix} \quad (20)$$

Basic Equation for ERA-2:

$$\begin{bmatrix} [\alpha_0] & [\alpha_1] \end{bmatrix} \begin{bmatrix} [h(t_0)] & [h(t_1)] & [h(t_2)] & \cdots & [h(t_i)] \\ [h(t_1)] & [h(t_2)] & [h(t_3)] & \cdots & [h(t_{i+1})] \end{bmatrix} = - \begin{bmatrix} [h(t_1)] & [h(t_2)] & [h(t_3)] & \cdots & [h(t_{i+1})] \end{bmatrix} \quad (21)$$

In order to simplify the notation of the above two equations, let:

$$\begin{bmatrix} \overline{h(t_0)} \end{bmatrix} = \begin{bmatrix} [h(t_0)] & [h(t_1)] & [h(t_2)] & \cdots & [h(t_i)] \end{bmatrix} \quad (22)$$

$$\begin{bmatrix} \overline{h(t_1)} \end{bmatrix} = \begin{bmatrix} [h(t_1)] & [h(t_2)] & [h(t_3)] & \cdots & [h(t_{i+1})] \end{bmatrix} \quad (23)$$

$$\begin{bmatrix} \overline{h(t_2)} \end{bmatrix} = \begin{bmatrix} [h(t_2)] & [h(t_3)] & [h(t_4)] & \cdots & [h(t_{i+2})] \end{bmatrix} \quad (24)$$

Rewriting Equations (20) and (21),

Basic Equation for ERA-1:

$$\begin{bmatrix} [\bar{\alpha}_0] \end{bmatrix} \begin{bmatrix} [\overline{h(t_0)}] \\ [\overline{h(t_1)}] \end{bmatrix} = - \begin{bmatrix} [\overline{h(t_1)}] \\ [\overline{h(t_2)}] \end{bmatrix} \quad (25)$$

Basic Equation for ERA-2:

$$\begin{bmatrix} [\alpha_0] & [\alpha_1] \end{bmatrix} \begin{bmatrix} [\overline{h(t_0)}] \\ [\overline{h(t_1)}] \end{bmatrix} = - \begin{bmatrix} [\overline{h(t_1)}] \end{bmatrix} \quad (26)$$

Now solve for the $[\alpha]$ coefficient matrices for each case using a psuedo-inverse method.

$[\alpha]$ Coefficient Solution for ERA-1:

$$\begin{bmatrix} [\bar{\alpha}_0] \end{bmatrix} = - \begin{bmatrix} [\overline{h(t_1)}] \\ [\overline{h(t_2)}] \end{bmatrix} \begin{bmatrix} [\overline{h(t_0)}] \\ [\overline{h(t_1)}] \end{bmatrix}^+ \quad (27)$$

$[\alpha]$ Coefficient Solution for ERA-2:

$$\begin{bmatrix} [\alpha_0] & [\alpha_1] \end{bmatrix} = - \begin{bmatrix} [\overline{h(t_1)}] \end{bmatrix} \begin{bmatrix} [\overline{h(t_0)}] \\ [\overline{h(t_1)}] \end{bmatrix}^+ \quad (28)$$

Now note, by definition, the following identity relationships:

$$\begin{bmatrix} [\overline{h(t_0)}] \\ [\overline{h(t_1)}] \end{bmatrix} \begin{bmatrix} [\overline{h(t_0)}] \\ [\overline{h(t_1)}] \end{bmatrix}^+ = [I] = \begin{bmatrix} [I] & [0] \\ [0] & [I] \end{bmatrix} \quad (29)$$

>From the off diagonal terms in Equation (29), the following relationships must be true:

$$\begin{bmatrix} [\overline{h(t_0)}] \end{bmatrix} \begin{bmatrix} [\overline{h(t_1)}] \end{bmatrix}^+ = [0] \quad \begin{bmatrix} [\overline{h(t_1)}] \end{bmatrix} \begin{bmatrix} [\overline{h(t_0)}] \end{bmatrix}^+ = [0] \quad (30)$$

Therefore, the following relationship holds:

$$\begin{bmatrix} [\overline{h(t_0)}] \\ [\overline{h(t_1)}] \end{bmatrix}^+ = \begin{bmatrix} [\overline{h(t_0)}]^+ & [\overline{h(t_1)}]^+ \end{bmatrix} \quad (31)$$

Substituting Equation (31) into Equations (27) and (28), the equivalence between the two approaches can be seen by inspection:

$[\alpha]$ Coefficient Solution for ERA-1:

$$[\alpha_0] = - \begin{bmatrix} [\overline{h(t_1)}] \\ [\overline{h(t_2)}] \end{bmatrix} \begin{bmatrix} [\overline{h(t_0)}] \\ [\overline{h(t_1)}] \end{bmatrix}^+ = - \begin{bmatrix} [\overline{h(t_1)}] \\ [\overline{h(t_2)}] \end{bmatrix} \begin{bmatrix} [\overline{h(t_0)}]^+ & [\overline{h(t_1)}]^+ \end{bmatrix} = - \begin{bmatrix} [\overline{h(t_1)}][\overline{h(t_0)}]^+ & [\overline{h(t_1)}][\overline{h(t_1)}]^+ \\ [\overline{h(t_2)}][\overline{h(t_0)}]^+ & [\overline{h(t_2)}][\overline{h(t_1)}]^+ \end{bmatrix} \quad (32)$$

Simplifying, based upon Equations (30),

$$[\alpha_0] = - \begin{bmatrix} [0] & [I] \\ [\overline{h(t_2)}][\overline{h(t_0)}]^+ & [\overline{h(t_2)}][\overline{h(t_1)}]^+ \end{bmatrix} \quad (33)$$

$[\alpha]$ Coefficient Solution for ERA-2:

$$[\alpha_0] [\alpha_1] = - \begin{bmatrix} [\overline{h(t_1)}] \end{bmatrix} \begin{bmatrix} [\overline{h(t_0)}] \\ [\overline{h(t_1)}] \end{bmatrix}^+ = - \begin{bmatrix} [\overline{h(t_1)}] \end{bmatrix} \begin{bmatrix} [\overline{h(t_0)}]^+ & [\overline{h(t_1)}]^+ \end{bmatrix} = - \begin{bmatrix} [\overline{h(t_2)}][\overline{h(t_0)}]^+ & [\overline{h(t_2)}][\overline{h(t_1)}]^+ \end{bmatrix} \quad (34)$$

Finally,

$$[\alpha_0] [\alpha_1] = - \begin{bmatrix} [\overline{h(t_2)}][\overline{h(t_0)}]^+ & [\overline{h(t_2)}][\overline{h(t_1)}]^+ \end{bmatrix} \quad (35)$$

By comparing Equation (35) with Equation (33), it is clear that the coefficient information in the two companion matrix cases must be exactly the same to within any numerical round-off errors in the zero and identity matrix areas of the companion matrix.

The conclusion, therefore must be that the base vector of order zero in the original UMPA formulation is complete and that no advantage is available when higher order base vectors are used to form alternate models. In fact, models that utilize a base vector model order of zero are better in terms of utilizing a minimal memory footprint and cannot be affected by numerical round-off that occurs in forming the associated companion matrix.

3.2.1 Companion Matrix Structure - Random Data

In order to demonstrate the inherent structure of the companion matrix that results from higher order base vector formulations, a simple numerical example was formed using random data. This random data was purely random data resulting from a random number generator and represents no underlying structural model. The following result was formed by using a first order Rational Fraction Polynomial model with a base vector model order of three. There are block coefficients of size 3×3 reflecting the three references in the artificial data. The model for this case would be an UMPA(1,n,3) model and it would be equivalent to an UMPA(4,n,0) model in terms of companion matrix size.

UMPA(1,n,3) Model:

$$[C] = \begin{bmatrix} -[\alpha]_0 \end{bmatrix}_{12 \times 12} \quad (36)$$

UMPA(4,n,0) Model:

$$[C] = \begin{bmatrix} [0] & [I] & [0] & [0] \\ [0] & [0] & [I] & [0] \\ [0] & [0] & [0] & [I] \\ -[\alpha]_0 & -[\alpha]_1 & -[\alpha]_2 & -[\alpha]_3 \end{bmatrix}_{12 \times 12} \tag{37}$$

$$[C] = \begin{bmatrix} -[\alpha]_3 & -[\alpha]_2 & -[\alpha]_1 & -[\alpha]_0 \\ [I] & [0] & [0] & [0] \\ [0] & [I] & [0] & [0] \\ [0] & [0] & [I] & [0] \end{bmatrix}_{12 \times 12} \tag{38}$$

The following numerical examples parallel the formulations represented by Equations 36-38.

UMPA(1,n,3) Model (Numerical Random Data Case - Equation 36):

| | | | | | | | | | | | |
|-----------|-----------|-----------|-----------|-----------|-----------|-----------|-----------|-----------|-----------|-----------|-----------|
| 6.49e-16 | -8.28e-16 | 1.39e-15 | 1.00e+00 | -4.85e-15 | 9.19e-16 | 2.33e-16 | -4.78e-16 | 2.91e-16 | 7.89e-16 | -1.85e-15 | 5.73e-16 |
| 4.27e-16 | -1.18e-15 | -8.33e-16 | -2.52e-15 | 1.00e+00 | 7.18e-17 | 2.06e-16 | -4.60e-16 | -2.50e-16 | -9.50e-16 | -9.93e-16 | 1.27e-16 |
| -7.52e-16 | -5.59e-16 | -4.57e-16 | -1.74e-15 | 2.61e-15 | 1.00e+00 | -2.24e-16 | 3.64e-17 | -2.66e-16 | -6.39e-16 | 1.00e-15 | -4.67e-16 |
| 1.83e-15 | 6.05e-16 | -3.61e-16 | 1.99e-16 | -7.13e-16 | 2.77e-16 | 1.00e+00 | 1.30e-16 | 0.00e+00 | 3.10e-17 | -8.09e-16 | -5.31e-18 |
| -3.12e-15 | -5.36e-16 | 4.80e-15 | -1.05e-14 | 6.44e-15 | -4.42e-15 | -9.88e-16 | 1.00e+00 | 1.58e-15 | -3.44e-15 | 2.37e-15 | -2.12e-15 |
| 1.78e-15 | -1.48e-15 | 1.78e-15 | 7.52e-15 | 3.00e-15 | -3.11e-15 | 9.16e-16 | -6.38e-16 | 1.00e+00 | 2.81e-15 | 1.55e-15 | -1.19e-15 |
| -2.72e-15 | -6.39e-16 | 1.75e-15 | -4.88e-15 | -9.24e-16 | -3.40e-15 | -1.07e-15 | 1.59e-16 | 1.09e-15 | 1.00e+00 | -6.09e-16 | -1.73e-15 |
| -5.79e-16 | 1.72e-15 | 9.99e-16 | 9.38e-15 | 2.75e-15 | -2.24e-15 | -3.43e-16 | 8.33e-16 | 2.78e-16 | 3.37e-15 | 1.00e+00 | -1.22e-15 |
| 3.27e-15 | 1.79e-15 | -2.10e-15 | 2.67e-15 | -5.80e-15 | -3.03e-15 | 1.03e-15 | 3.68e-16 | -4.23e-16 | 5.43e-16 | -2.26e-15 | 1.00e+00 |
| -2.43e+00 | -1.77e-02 | -9.69e-02 | -1.64e-04 | 6.87e-02 | -1.54e-02 | -3.97e+00 | -2.55e-03 | -6.29e-02 | 4.06e-04 | 2.30e-02 | -1.57e-02 |
| -4.98e-03 | -2.35e+00 | -2.32e-02 | -7.61e-02 | 5.01e-03 | 1.17e-01 | 4.20e-03 | -3.87e+00 | -2.07e-02 | -2.74e-02 | 2.95e-03 | 6.00e-02 |
| -8.98e-02 | -2.93e-02 | -2.34e+00 | 8.26e-03 | -1.31e-01 | -3.24e-03 | -6.10e-02 | -2.56e-02 | -3.89e+00 | 1.18e-02 | -6.83e-02 | -3.35e-03 |

TABLE 2. Companion Matrix Numerical Example - Random Data - UMPA(1,n,3)

UMPA(4,n,0) Model (Numerical Random Data Case - Equation 37):

| | | | | | | | | | | | |
|-----------|-----------|-----------|-----------|-----------|-----------|-----------|-----------|-----------|-----------|-----------|-----------|
| 0.00e+00 | 0.00e+00 | 0.00e+00 | 1.00e+00 | 0.00e+00 | 0.00e+00 | 0.00e+00 | 0.00e+00 | 0.00e+00 | 0.00e+00 | 0.00e+00 | 0.00e+00 |
| 0.00e+00 | 0.00e+00 | 0.00e+00 | 0.00e+00 | 1.00e+00 | 0.00e+00 | 0.00e+00 | 0.00e+00 | 0.00e+00 | 0.00e+00 | 0.00e+00 | 0.00e+00 |
| 0.00e+00 | 0.00e+00 | 0.00e+00 | 0.00e+00 | 0.00e+00 | 1.00e+00 | 0.00e+00 | 0.00e+00 | 0.00e+00 | 0.00e+00 | 0.00e+00 | 0.00e+00 |
| 0.00e+00 | 0.00e+00 | 0.00e+00 | 0.00e+00 | 0.00e+00 | 0.00e+00 | 1.00e+00 | 0.00e+00 | 0.00e+00 | 0.00e+00 | 0.00e+00 | 0.00e+00 |
| 0.00e+00 | 0.00e+00 | 0.00e+00 | 0.00e+00 | 0.00e+00 | 0.00e+00 | 0.00e+00 | 1.00e+00 | 0.00e+00 | 0.00e+00 | 0.00e+00 | 0.00e+00 |
| 0.00e+00 | 0.00e+00 | 0.00e+00 | 0.00e+00 | 0.00e+00 | 0.00e+00 | 0.00e+00 | 0.00e+00 | 1.00e+00 | 0.00e+00 | 0.00e+00 | 0.00e+00 |
| 0.00e+00 | 0.00e+00 | 0.00e+00 | 0.00e+00 | 0.00e+00 | 0.00e+00 | 0.00e+00 | 0.00e+00 | 0.00e+00 | 1.00e+00 | 0.00e+00 | 0.00e+00 |
| 0.00e+00 | 0.00e+00 | 0.00e+00 | 0.00e+00 | 0.00e+00 | 0.00e+00 | 0.00e+00 | 0.00e+00 | 0.00e+00 | 0.00e+00 | 1.00e+00 | 0.00e+00 |
| 0.00e+00 | 0.00e+00 | 0.00e+00 | 0.00e+00 | 0.00e+00 | 0.00e+00 | 0.00e+00 | 0.00e+00 | 0.00e+00 | 0.00e+00 | 0.00e+00 | 1.00e+00 |
| -2.43e+00 | -1.77e-02 | -9.69e-02 | -1.64e-04 | 6.87e-02 | -1.54e-02 | -3.97e+00 | -2.55e-03 | -6.29e-02 | 4.06e-04 | 2.30e-02 | -1.57e-02 |
| -4.98e-03 | -2.35e+00 | -2.32e-02 | -7.61e-02 | 5.01e-03 | 1.17e-01 | 4.20e-03 | -3.87e+00 | -2.07e-02 | -2.74e-02 | 2.95e-03 | 6.00e-02 |
| -8.98e-02 | -2.93e-02 | -2.34e+00 | 8.26e-03 | -1.31e-01 | -3.24e-03 | -6.10e-02 | -2.56e-02 | -3.89e+00 | 1.18e-02 | -6.83e-02 | -3.35e-03 |

TABLE 3. Companion Matrix Numerical Example - Random Data - UMPA(4,n,0)

UMPA(4,n,0) Model (Numerical Random Data Case - Equation 38):

| | | | | | | | | | | | |
|-----------|-----------|-----------|-----------|-----------|-----------|-----------|-----------|-----------|-----------|-----------|-----------|
| 4.06e-04 | 2.30e-02 | -1.57e-02 | -3.97e+00 | -2.55e-03 | -6.29e-02 | -1.64e-04 | 6.87e-02 | -1.54e-02 | -2.43e+00 | -1.77e-02 | -9.69e-02 |
| -2.74e-02 | 2.95e-03 | 6.00e-02 | 4.20e-03 | -3.87e+00 | -2.07e-02 | -7.61e-02 | 5.01e-03 | 1.17e-01 | -4.98e-03 | -2.35e+00 | -2.32e-02 |
| 1.18e-02 | -6.83e-02 | -3.35e-03 | -6.10e-02 | -2.56e-02 | -3.89e+00 | 8.26e-03 | -1.31e-01 | -3.24e-03 | -8.98e-02 | -2.93e-02 | -2.34e+00 |
| 1.00e+00 | 0.00e+00 | 0.00e+00 | 0.00e+00 | 0.00e+00 | 0.00e+00 | 0.00e+00 | 0.00e+00 | 0.00e+00 | 0.00e+00 | 0.00e+00 | 0.00e+00 |
| 0.00e+00 | 1.00e+00 | 0.00e+00 | 0.00e+00 | 0.00e+00 | 0.00e+00 | 0.00e+00 | 0.00e+00 | 0.00e+00 | 0.00e+00 | 0.00e+00 | 0.00e+00 |
| 0.00e+00 | 0.00e+00 | 1.00e+00 | 0.00e+00 | 0.00e+00 | 0.00e+00 | 0.00e+00 | 0.00e+00 | 0.00e+00 | 0.00e+00 | 0.00e+00 | 0.00e+00 |
| 0.00e+00 | 0.00e+00 | 0.00e+00 | 1.00e+00 | 0.00e+00 | 0.00e+00 | 0.00e+00 | 0.00e+00 | 0.00e+00 | 0.00e+00 | 0.00e+00 | 0.00e+00 |
| 0.00e+00 | 0.00e+00 | 0.00e+00 | 0.00e+00 | 1.00e+00 | 0.00e+00 | 0.00e+00 | 0.00e+00 | 0.00e+00 | 0.00e+00 | 0.00e+00 | 0.00e+00 |
| 0.00e+00 | 0.00e+00 | 0.00e+00 | 0.00e+00 | 0.00e+00 | 1.00e+00 | 0.00e+00 | 0.00e+00 | 0.00e+00 | 0.00e+00 | 0.00e+00 | 0.00e+00 |
| 0.00e+00 | 0.00e+00 | 0.00e+00 | 0.00e+00 | 0.00e+00 | 0.00e+00 | 1.00e+00 | 0.00e+00 | 0.00e+00 | 0.00e+00 | 0.00e+00 | 0.00e+00 |
| 0.00e+00 | 0.00e+00 | 0.00e+00 | 0.00e+00 | 0.00e+00 | 0.00e+00 | 0.00e+00 | 1.00e+00 | 0.00e+00 | 0.00e+00 | 0.00e+00 | 0.00e+00 |
| 0.00e+00 | 0.00e+00 | 0.00e+00 | 0.00e+00 | 0.00e+00 | 0.00e+00 | 0.00e+00 | 0.00e+00 | 1.00e+00 | 0.00e+00 | 0.00e+00 | 0.00e+00 |

TABLE 4. Companion Matrix Numerical Example - Random Data - UMPA(4,n,0)

Table 2 shows the numerical round-off error that is slightly contaminating the form of the companion matrix for the higher order base vector methods when compared to Tables 3 and 4. The information in the three matrices is exactly the same otherwise. Note that Equation 38 and Table 4 is presented simply to show the alternate forms of the companion matrix that result from manipulating the solution procedure used to determine the $[\alpha]$ coefficients. If the numerical round-off is sufficiently large enough or similar in magnitude to the data portions of the companion matrix, this could degrade the solution. Since the structure of the companion matrices is based upon forming the solution from time shifts and/or derivatives, allowing this slightly degenerate form is essentially allowing velocity to not be the derivative of displacement.

4. Summary and Future Work

In this paper, the UMPA framework has been extended to encompass the concept of a higher order base vector. Historically, most modal parameter estimation algorithms, except the first order versions of the ERA and PFD algorithms (ERA-1 and PFD-1), have utilized a base vector of zeroth order, that is a structure that corresponds directly to the vector basis of the model (either N_L or N_S .) While developing an automated technique for identifying valid modal parameters, it was observed that having higher order base vectors was advantageous in discriminating between the physical and the computational poles. Several papers were published which discussed this extended basis approach, but only as an extension of the traditional first order methods. As a result, just like ERA-1 and PFD-1, these higher order base vector methods produced a single $[\alpha_0]$ coefficient which was itself the companion matrix.

However, while developing a general autonomous modal parameter estimation methodology, it was recognized that other intermediate formulations were possible. These forms were initially believed to produce a new family of modal parameter estimation algorithms. However, in the course of investigation, the equivalence of the first-order state extended methods and the traditional higher-order methods was demonstrated. Although the thought process used to arrive at these first order methods was different from the higher-order formulation, the final matrix structural form is in fact identical within a computer numerical round-off which has nothing to do with the actual informational content as shown by the identical companion matrix structure resulting from using purely random, unrelated information. This suggests that there is no real advantage in computing these larger, extended basis coefficients. That, at best, doing so simply requires more computer memory and more computational time calculating a-priori known zero and identity quantities. In fact, it appears that if the numerical round-off on these

computed zero and identity terms becomes sufficiently large, the quality of the solution may actually be degraded.

5. References

- [1] Phillips, A.W., Allemang, R.J., "Data Presentation Schemes for Selection and Identification of Modal Parameters", Proceedings, International Modal Analysis Conference (IMAC), 10 pp., 2005.
- [2] Phillips, A.W., Allemang, R.J., "Additional Mechanisms for Providing Clear Stabilization (Consistency) Diagrams", Proceedings, International Conference on Noise and Vibration Engineering (ISMA), 15 pp., 2008.
- [3] Phillips, A.W., Allemang, R.J., Brown, D.L., "Autonomous Modal Parameter Estimation: Methodology", Proceedings, International Modal Analysis Conference (IMAC), 22 pp., 2011.
- [4] Allemang, R.J., Brown, D.L., Phillips, A.W., "Survey of Modal Techniques Applicable to Autonomous/Semi-Autonomous Parameter Identification", Proceedings, International Conference on Noise and Vibration Engineering (ISMA), 2010.
- [5] Brown, D. L., Phillips, A. W., Allemang, R. J., "A First Order, Extended State Vector Expansion Approach to Experimental Modal Parameter Estimation", Proceedings, International Modal Analysis Conference (IMAC), 11 pp., 2005.
- [6] Allemang, R.J., Phillips, A.W., "The Unified Matrix Polynomial Approach to Understanding Modal Parameter Estimation: An Update", Proceedings, International Conference on Noise and Vibration Engineering (ISMA), 2004.
- [7] Allemang, R.J., Brown, D.L., "A Unified Matrix Polynomial Approach to Modal Identification", *Journal of Sound and Vibration*, Vol. 211, No. 3, pp. 301-322, April 1998.

Interaction between Structures and Their Occupants

Lars Pedersen

Aalborg University
Department of Civil Engineering
Sohngaardsholmsvej 57
DK-9000 Aalborg

ABSTRACT

Structures that carry humans are the subject of the studies of this paper. Active humans may cause structural vibrations, which can be problematic, but passive humans (sitting or standing on the structure) are also potentially present on the structure. In predictions of structural vibration performance, the passive humans are often not modelled, but they will interact with the structure. The paper has focus on the effect that the presence of passive humans has on the structural behaviour and modal characteristics of the structure. Based on findings from measurements, the implications of presence of passive humans are discussed.

NOMENCLATURE

| | | | | | |
|-----|------------------|-----------|------------------------|-------------|---------------------|
| e | Response ratio | f_1 | Empty floor frequency | f_2 | Crowd frequency |
| p | Load | ζ_1 | Empty floor damping | ζ_2 | Crowd damping |
| G | Weight of jumper | m_1 | Empty floor modal mass | m_2 | Crowd modal mass |
| k | Spring stiffness | c | Damping coefficient | α_n | Dynamic load factor |
| R | Rms-value | f_i | Jumping frequency | φ_n | Phase |

1. INTRODUCTION

Vibrations in structures may occur as a result of walking, jumping, bouncing or other activities. The humans that perform these activities may be referred to as active humans. Other humans on the structure may be passive, and these humans may be referred to as stationary people. In the paper a group of such people will be referred to as a stationary crowd (even though only very small crowds are considered).

On a variety of different structures it has been verified that stationary humans [1-5] act as attachment systems to the structure which they occupy, and it has been found that a stationary crowd of people with much reasoning can be modelled as a single-degree-of-freedom system (SDOF system) [1-2,5-6]. That a stationary person is dynamic system is known from biomechanics [7], but that a crowd can be modelled as a SDOF system is useful, as it simplifies computations.

This paper assumes a SDOF model for the crowd, and investigates how the presence of this attachment system influences structural response. The response considered is the acceleration response of the structure to the action of a jumping person. It

is a parametric study, in which different modal characteristics for the structural system are assumed, and the size of the stationary crowd of people is also varied so as to investigate its influence on magnitudes of structural response.

The human-structure interaction model assumed for the study is introduced in section 2, and the section also presents the dynamic characteristics assumed for structures and the stationary crowd. The load model and procedures for computing structural response are outlined in section 3. Section 4 presents the results.

2. THE HUMAN-STRUCTURE INTERACTION MODEL

Fig. 1 illustrates the human-structure interaction model assumed for the studies of this paper. The grounded system represents the structural system, which is modelled as SDOF system. The structure carries a stationary crowd of people modelled as a SDOF attached to the structural mass.

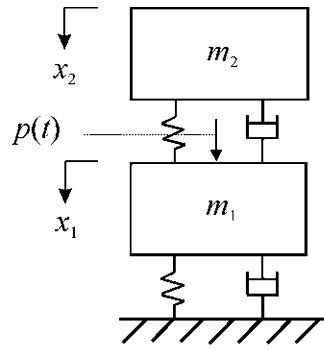


Fig. 1 Human-structure interaction model

It is assumed that the governing mode of the structural system is the first mode of vertical bending. This mode is described by the parameters m_1 , k_1 , and c_1 , representing modal mass, stiffness and damping, respectively. The corresponding parameters for the stationary crowd of people atop the structure are denoted m_2 , k_2 , and c_2 . A load $p(t)$ might be applied to the floor mass bringing the system into vibration.

The following equations are assumed to apply:

$$k_2 = m_2 (2\pi f_2)^2 \quad c_2 = 2\sqrt{m_2 k_2} \zeta_2 \quad (1)$$

$$k_1 = m_1 (2\pi f_1)^2 \quad c_1 = 2\sqrt{m_1 k_1} \zeta_1 \quad (2)$$

where the set (m_1, f_1, ζ_1) represents the dynamic characteristics associated with the first bending mode of the empty structure and the set (m_2, f_2, ζ_2) represents the dynamic characteristics of the crowd.

On these assumptions the governing equation of motion is:

$$\begin{bmatrix} m_1 & 0 \\ 0 & m_2 \end{bmatrix} \begin{bmatrix} \ddot{x}_1 \\ \ddot{x}_2 \end{bmatrix} + \begin{bmatrix} c_1 + c_2 & -c_2 \\ -c_2 & c_2 \end{bmatrix} \begin{bmatrix} \dot{x}_1 \\ \dot{x}_2 \end{bmatrix} + \begin{bmatrix} k_1 + k_2 & -k_2 \\ -k_2 & k_2 \end{bmatrix} \begin{bmatrix} x_1 \\ x_2 \end{bmatrix} = \begin{bmatrix} p(t) \\ 0 \end{bmatrix} \quad (3)$$

For the studies of this paper different structural systems are considered. They are all modelled as SDOF systems and the dynamic characteristics of the individual structures are listed in Table 1.

Table 1 Dynamic characteristics of structures

| Structure | f_1 | m_1 | ζ_1 |
|-----------|--------|----------------------|-----------|
| A1 | 6.0 Hz | $6.82 \cdot 10^3$ kg | 0.5 %cr |
| A2 | 6.0 Hz | $6.82 \cdot 10^3$ kg | 1.0 %cr |
| A3 | 6.0 Hz | $6.82 \cdot 10^3$ kg | 2.0 %cr |
| B1 | 5.0 Hz | $6.82 \cdot 10^3$ kg | 1.0 %cr |
| B2 | 6.0 Hz | $6.82 \cdot 10^3$ kg | 1.0 %cr |
| B3 | 7.0 Hz | $6.82 \cdot 10^3$ kg | 1.0 %cr |

As it appears, the structures are split into two groups (A and B). In each group one of the modal characteristics are varied. For instance in group A, three different damping ratios are considered.

In the studies, the structures will be modelled with and without a stationary crowd of people atop the structure. [Table 2](#) gives the frequency and damping assumed for the crowd.

Table 2 Dynamic characteristics of crowd

| f_1 | ζ_1 |
|--------|-----------|
| 6.0 Hz | 0.35 |

The values are fairly close to those experimentally derived in [5] for a standing crowd of people. The modal mass of the crowd, m_2 , is varied in the studies, so it is not shown in [Table 2](#).

3. LOAD MODEL AND RESPONSE PREDICTION

Below the load assumed acting on the structure is defined. A simplistic model for jumping loads is assumed. The jumping frequency is denoted f_l , and load is modelled as follows:

$$p(t) = G \sum_{n=1}^5 \alpha_n \sin(2n\pi f_l t + \varphi_n) \quad (4)$$

As it appears five harmonics are considered in the Fourier series expansion, where α_n is the dynamic load factor and where φ_n is the phase lag. The factor G represents the weight of the jumper which is assumed to be 750 N, as only a single jumper is assumed. The dynamic load factors are determined from:

$$\alpha_n = \begin{cases} 2 & \text{if } nf_l < 3 \text{ Hz} \\ -0.19nf_l + 2.57 & \text{if } 3 \text{ Hz} \leq nf_l < 13 \text{ Hz} \\ 0.1 & \text{if } nf_l \geq 13 \text{ Hz.} \end{cases} \quad (5)$$

This is a simplistic model for high jumping. For the jumping frequency and array of possibilities are considered namely 2.00 Hz, 2.01 Hz, 2.03 Hz up to 3.00 Hz. These jumping frequencies are quite realistic. For each jumping frequency assumption, the load is computed and so is the rms-value of structural accelerations. The maximum value of the rms-value is identified and is denoted R_e where the subscript 'e' signals that this is the result obtained for the empty structure. Empty here refers to the situation where there are no stationary people on the structure. The only person on the structure is the jumper himself.

However, the exercise of computing rms-values for different jumping frequency assumptions and identifying the maximum value is also carried out for situations where the structure is assumed occupied by a stationary crowd of people of mass m_2 . The maximum rms-value computed for a specific value of m_2 is denoted $R_o(m_2)$, where the subscript 'o' signals that is a result obtained for the structure occupied by a stationary crowd of people.

In presentations of results in terms of structural response, it is considered useful to employ the ratio:

$$e(m_2) = \frac{R_o(m_2)}{R_e} \quad (6)$$

which basically is a normalisation of rms-values obtained for the structure carrying a stationary crowd of people with the result obtained for the empty structure. For values of e smaller than 1, the presence of the stationary crowd has attenuated the structural vibrations.

The load model introduced in this section is a simplification of jumping loads, but it is not all that unreasonable, in that it models the dynamic load factor with a maximum value of 2.0 (for the first dynamic load factor), and superharmonic dynamic load factors are modelled to be lower than this value.

3. RESULTS

The response ratio e was computed for different values of m_2 smaller than 250 kg. Hence quite small stationary crowds of people are considered, as 250 kg might correspond to a group of 3 people.

The response ratio was computed for 3 different assumptions for the damping ratio of the empty structural system (systems A1, A2, A3), and results are shown in Fig. 2.

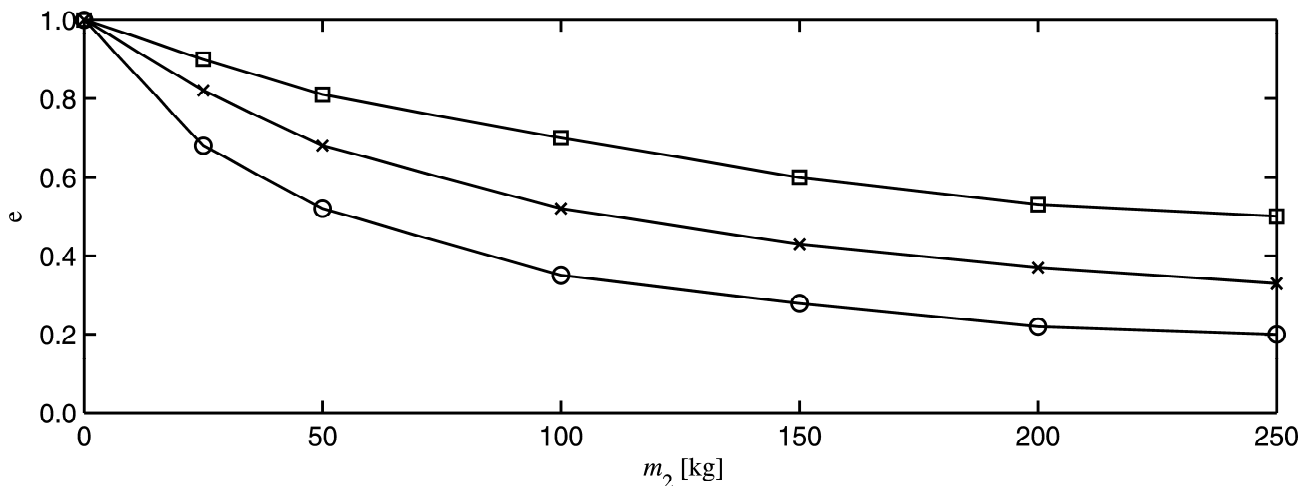


Fig. 2 Response ratio e as function of mass of the stationary crowd of people

$$\zeta_1 = 0.5\% \text{ (o)}, \zeta_1 = 1.0\% \text{ (x)}, \zeta_1 = 2.0\% \text{ (□)}$$

As can be seen, a stationary crowd is found to attenuate the structural response, as all values of e are below 1. There is the tendency that the response reduces as the size of the crowd increases (m_2 increases).

Another item to notice is that as the damping ratio of the empty structure (ζ_1) decreases the attenuating effect of the stationary crowd increases (in that e decreases with decreases in ζ_1 for fixed values of m_2). In fact the results suggest that the attenuating effect of the stationary crowd is quite sensitive the damping ratio of the empty structure.

It is quite obvious that the results shown in Fig. 1 deviate a lot from that would be expected had the stationary crowd been modelled as a mass rigidly attached to the structural mass. It should be noted that realistic values of m_2 might be 75 kg, 150 kg and 225 kg if the group of people (one person, two persons, and three persons, respectively) is located at the point of maximum structural displacement, but if the group of people is located at any other location on the structure these values would reduce.

In terms of the magnitude of the attenuating effect of the stationary crowd, it is noticeable that the calculations predict that a single stationary person ($m_2 = 75$ kg) is capable of reducing structural vibration levels by more than a factor 2 (for $\zeta_1 = 0.5\%$). When mentioning this it should be recalled that the modal mass of the empty structure is assumed to be almost 7000 kg, which is a little less than 100 times the weight of the person.

The response ratio was also computed for different assumptions for the frequency of the empty structure (systems B1, B2, B3), and results are shown in Fig. 3.

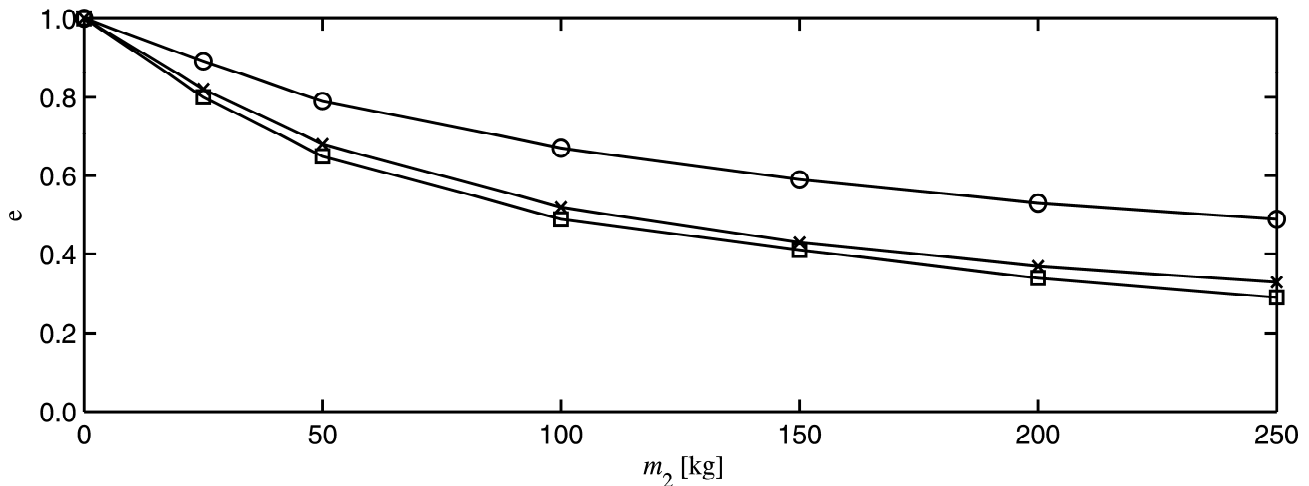


Fig. 3 Response ratio e as function of mass of the stationary crowd of people

$$f_1 = 5 \text{ Hz (o)}, f_1 = 6 \text{ Hz (x)}, f_1 = 7 \text{ Hz (\square)}$$

It appears that the attenuating effect of the stationary crowd of people is also sensitive to the frequency of the empty structure.

6. CONCLUSION AND DISCUSSION

The parametric studies of this paper examined the response of different structural systems to the action of jumping, with and without a stationary crowd present atop the structure.

It was found that even a very small stationary crowd of people can change the response of the structural system quite significantly. Even a single stationary person is predicted to be capable of reducing structural vibration by more than a factor 2 (for one of the structural systems considered for the studies).

It was furthermore found that the vibration attenuating effect of the stationary crowd of people is sensitive to for instance the damping ratio of the empty structure.

REFERENCES

- [1] Sachse, R., Pavic, A., Prichard, S., *The influence of a group of humans on modal properties of a structure*. In: Proceedings of the fifth international conference on structural dynamics, pp 1241-1246, 2002.
- [2] Ellis, B.R., Ji. T., *Human-structure interaction in vertical vibrations*. In: Proceedings of the ICE: Structures and Buildings; Vol. 122, pp. 1-9, 1997
- [3] Brownjohn, J.M.W., *Energy dissipation from vibrating floor slabs due to human-structure interaction*, Shock and Vibration, Vol. 8 (6), pp. 315-323., 2001

- [4] Reynolds, P., Pavic, A., Ibrahim, Z., *Changes of modal properties of a stadium structure occupied by a crowd.* In: Proceedings of the 22nd international modal analysis conference, 2004.
- [5] Pedersen, L., *A contribution to documenting and validating dynamic interaction effects,* In: Proceedings of the 25th international modal analysis conference, Orlando, Florida, 2007.
- [6] Pedersen, L., *Updating of the dynamic model of floors carrying stationary humans.,* In: Proceedings of the 1st international operational modal analysis conference, pp. 421-428., 2005
- [7] Griffin, M.J., *Handbook of human vibration.,* London: Academic Press, 1990.

Evaluation of Site Periods in the Metro Vancouver Region Using Microtremor Testing

¹James Traber, ²Kenny Kutyn, ³Carlos E. Ventura, and ⁴W.D. Liam Finn,

¹jptraber@gmail.com, ²kennykutyn@gmail.com, ³ventura@civil.ubc.ca, ⁴finn@civil.ubc.ca, University of British Columbia, Department of Civil Engineering, Canada

Abstract

Metro Vancouver, located in British Columbia, Canada, comprises the city of Vancouver and twenty more municipalities of its metropolitan area. The Metro Vancouver region has a population of about 2.25 million people and it is located in an area of high seismicity. A future earthquake close to Metro Vancouver would cause tens of billions of dollars damage and would seriously impact the economy of both British Columbia and Canada. Therefore, some of the municipalities in the region have initiated a program to evaluate the level of seismic hazard potential and identify the most vulnerable areas. In this regard, the identification of soil conditions plays a very important role in the evaluation of the seismic hazard potential. A cost effective technique to identify the dynamic characteristics of soil deposits is through microtremor testing.

Between 2009 and 2010 a series of microtremor tests were performed over the region of Metro Vancouver. Data obtained from these tests was analysed using both the horizontal to vertical ratio (H/V) and the frequency domain decomposition techniques of the recorded motions to find the predominant periods of vibration of the ground in the horizontal direction. For each test, in addition to the predominant period, values of peak ground velocity, PGV, root mean square ground velocity (RMS), and amplitude were recorded. Combining the results from a series of tests, maps of site periods were created for the regions investigated. This paper discusses the details of the testing campaign and the site period maps developed for Metro Vancouver.

1.0 Introduction

One of the most important considerations in geotechnical engineering is describing the dynamic characteristics of a soil deposit. These characteristics depend on many factors, including the geometry and mechanical properties of the soil layers and the input motion characteristics [11]. The seismic response of a site is directly related to the dynamic characteristics of that site, and depends upon such variables as period and ground velocity.

Present day in situ testing for determining soil properties consists of destructive sampling methods, including cone penetration tests, standard penetration tests, Becker penetration tests, vane shear tests, and shear wave velocity testing. These different methods of testing require drill rigs which make them expensive and time consuming to perform across a large area [13]. Microtremor testing, conversely, is non-intrusive and allows for a higher rate of testing and lower costs when compared to conventional methods. Additionally, microtremor tests require no external wave source as they rely solely on ambient vibrations caused by wind, traffic, pedestrians, rivers and underground services. Finally, a single tri-axial sensor is the only

required measurement equipment. These testing methods, combined with Nakamura's method and the Frequency Domain Decomposition (FDD) result in a complete testing and analysis procedure that is effective and reliable [1].

This paper presents the results of an NSERC funded study of site response in selected regions of the Metro Vancouver region, in South-western British Columbia. In total, 212 measurements covering almost 400 square kilometers were performed and analysed for fundamental period using Nakamura's method and FDD. In addition, for some of the tests average values of ground velocity were also calculated. As a result of this study, it is possible to know, approximately, the fundamental period anywhere within the study area, specifically the Cities of Richmond and North Vancouver and the Districts of North Vancouver and West Vancouver.

2.0 Description of the Test

2.1 Overview of Study Area

The study area is located within one of the most seismically active regions in Canada. Situated just east of the Cascadia subduction zone, Metro Vancouver is located within only one hundred and fifty of the expected location of a 'mega thrust' earthquake [4]. Other faults in the vicinity of the region have produced crustal and subcrustal earthquakes that, because of the proximity to urban areas, could also generate significant ground shaking that could cause severe damage to the built environment. The entire area of the study is moderately to densely populated and, as a result, the effects of an earthquake are of great interest to municipalities and the provincial government.

The study area can be divided into two regions; the City of Richmond (excluding Sea Island) in the south and three municipalities (City of North Vancouver, District of North Vancouver and District of West Vancouver) which are located north of the City of Vancouver and herein referred to as the North Shore. The study area can be seen in [Figure 1](#).



Fig. 1 Overview of Study Area

The City of Richmond is located on the Fraser River Delta which overlies deltaic sediment deposits up to 300m thick. These sediments are composed primarily of sand and silt and make up the Holocene layer. Beneath the Holocene is a layer of Pleistocene and beneath that, the bedrock [1]. Bedrock varies from 200m to 1000m from the surface with an average of 500m [2]. These soil deposits are prone to amplification, and, as a result of a high ground water table, are also prone to liquefaction [1].

On the North Shore, the sediments are much thinner and overlay the rocks of the coast plutonic complex [2]. The composition of the soil layers varies from till to gravel, sand and small amounts of clay. In some areas, the bedrock is exposed. The bulk of this area is not at high risk of liquefaction [5].

2.2 Measuring Equipment

The equipment used in this study is owned by The University of British Columbia's Earthquake Engineering Research Facility (EERF). The sensors, Pinocchio WL380s, are geophone-based velocity meters capable of taking long measurements (up to 12hrs) at sampling rates of 100sps and can be seen in [Figure 2](#). Each unit has an internal power supply and GPS antenna, increasing the portability and enabling precise location and time synchronization. Two sets of tri-axial geophones make up each Pinocchio, one for each of high and low amplitude motion. The geophones have a natural frequency of 4.5Hz and 56% damping.



Fig. 2 Pinocchio WL380 Sensors in the Field

2.3 Testing Procedure

For each test, the units were programmed using a laptop and Secure Digital card (SD). Tests on the North Shore were 20 minutes in duration and tests in Richmond, 30 minutes. According to Ventura et al [3] and SESAME guidelines [12], longer tests are required to identify longer periods. Previous testing in the City of Richmond confirmed this when it failed to identify the longer periods with 5 minute tests [3]. All tests were performed at 100 samples per second. Once the test was complete, the SD card was removed from the sensor and data saved on the laptop.

Where possible, sensors were placed on concrete or asphalt for the tests as this appeared to give the most precise results. Where concrete was not available, steel plates with four steel spikes were placed into softer ground and the sensor placed on top of the plate. The spikes secured the sensor in place horizontally. The sensors were oriented with the Y axis in the North direction and levelled. On average, moving to the next location, setting up the sensor, programming the test, and running the test took one hour. A total of 212 tests were performed, with a resolution of approximately 500-800m spacing.

3.0 Analysis and Results

Using the commercial software package Matlab [8], data was converted into the ASCII file format which enabled further processing. A baseline correction was also performed on the raw data using a Butterworth high pass filter at 0.1%. After this, data was ready to be processed with Nakamura's technique and The Frequency Domain Decomposition (FDD) method.

3.1 Data Analysed by Nakamura's H/V Technique

Nakamura's method of analysing ambient vibration measurements was first proposed in 1989 by Yutaka Nakamura [6]. Despite several recognized shortcomings of Nakamura's method, such as questionable ability to identify which wave types cause microtremors, recently it has gained popularity as an accurate and cost-effective way of determining the fundamental site period [1].

Nakamura proposes that the soil layer does not amplify the vertical component of ambient noise. Therefore, the period at which a plot of the ratio of horizontal motion to vertical motion (H/V) peaks should correspond directly to the fundamental period of that site [1].

Using the free software package Geopsy [7], time history plots were generated for each test as can be seen in Figure 3. From the time history plot, Geopsy's window selection tool was used to select "windows" of a desired amount of time to be used in further analysis. The goal of window selection was to remove the influence of flawed data in determining the peak in the H/V ratio plot. Any large spikes in time history plot were avoided, as well as segments of the test that were influenced by other noise sources, such as a lawnmowers or traffic in very close proximity. Windows were typically 40 seconds in length, as recommended by SESAME guidelines [12].

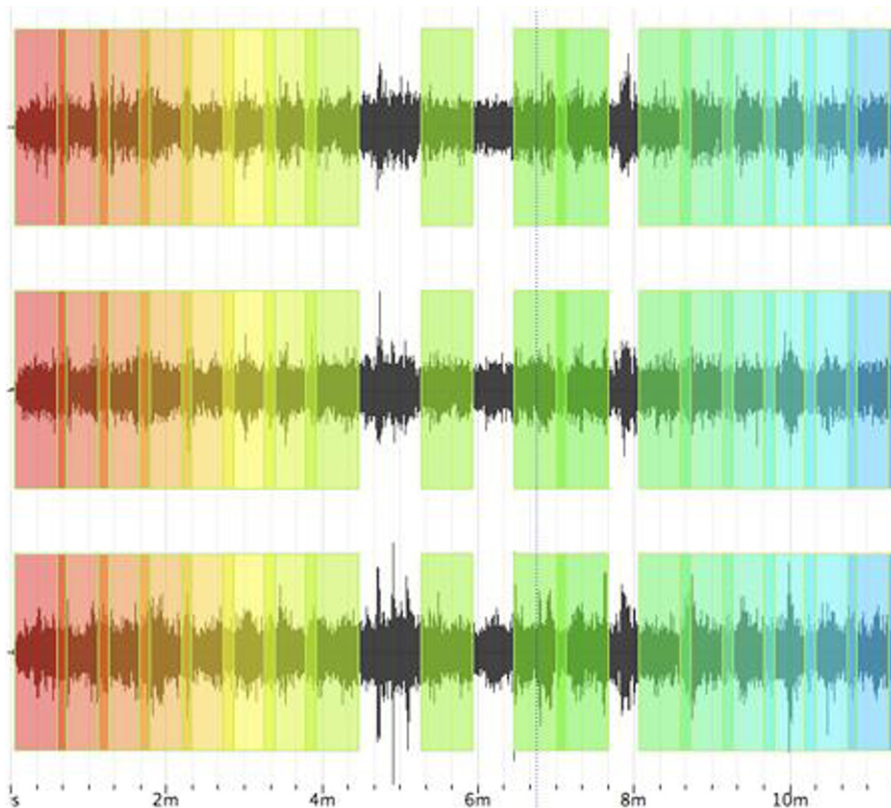


Fig. 3 Time History Plot in Geopsy

Once windows were selected, Geopsy was used to generate an H/V plot for each test, considering only the selected windows. An example plot is displayed in [Figure 4](#). The period at which the plot peaks was taken to be the fundamental period for that site. In some test, peaks were less obvious, or there were multiple possibilities. In these situations, the peak was chosen by comparing the results of the test in question to nearby tests, under the assumption that it is unlikely for the site period to change drastically over only 500 - 800 meters.

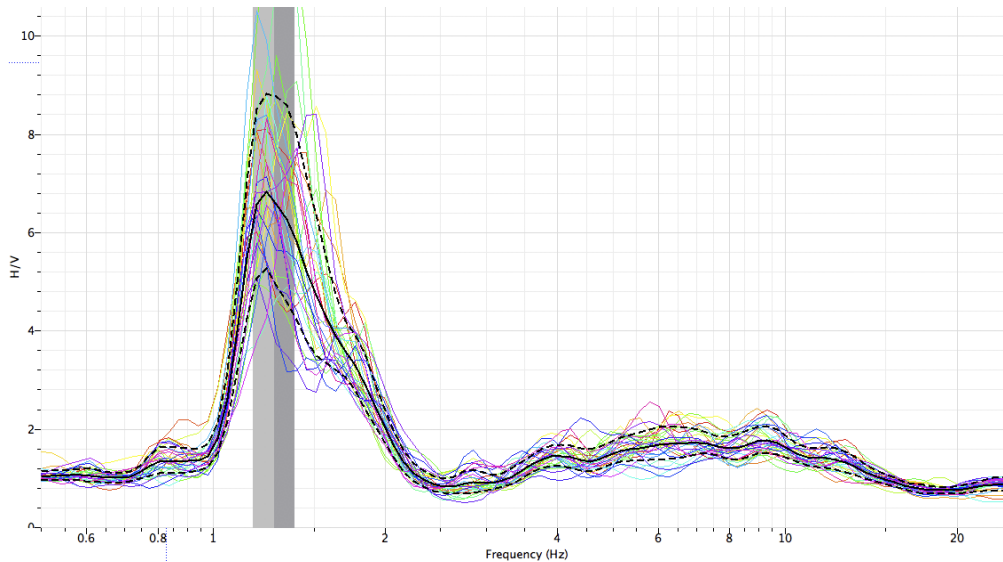


Fig. 4 H/V Ratio Plot in Geopsy

3.2 Data Analysed by the FDD Technique

One shortcoming in the use of Nakamura's method is an inability to determine if peaks in an H/V ratio are associated with horizontal or vertical motion. Assuming microtremor data is treated as output only modal data, it should be possible to apply the Frequency Domain Decomposition (FDD) technique to identify fundamental periods and their associated ground motion principal component [3]. The use of the FDD technique to identify site periods was first proposed by Ventura et. al. in 2004 [3].

Utilizing the commercial software package ARTeMIS Extractor [9], peaks of the FDD plot were chosen, as in [Figure 5](#), and the corresponding dominant motion of each identified. For the purpose of determining site periods, peaks exhibiting horizontal motion were assumed to be representative of the site, while those with vertical motion were discarded.

FDD was used heavily in tests performed on the North Shore as a way of confirming the results achieved through Nakamura's method. In most cases, these two methods agreed upon the dominant period for a site. Testing in Richmond relied almost exclusively upon Nakamura's method to identify the site period as FDD analysis of these tests provided inconsistent results.

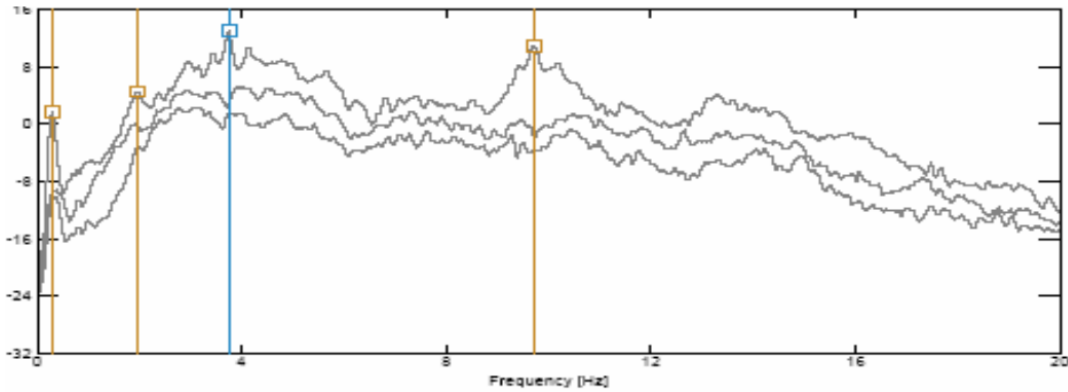


Fig. 5 Example FDD Peak Picking Plot for a Site in Richmond [3]

3.3 Processed Data and Map Generation

Processed data, in the form of a spread sheet containing test name, coordinates and site period, was used to generate iso-period maps of each test region, one for the North Shore and one for Richmond. This mapping was performed with the free software package Google Earth Toolbox [10] and Matlab. Site periods on the North Shore ranged from 0.04 to 1.25 seconds (0.8 to 25 Hz) as can be seen in Figures 6 and 7, and those in Richmond from 0.6 to 5.7 seconds (0.18 to 1.67 Hz) as can be seen in Figures 8 and 9. These results were expected, given the thick sediments of Richmond and the thinner sediments and exposed bedrock of the North Shore.

Although accurate shear wave velocity was not available for this study, the “quarter wavelengths rule,” as seen in Equation 1,

$$P = S_v / 4d \quad (1)$$

(where P is the fundamental site period, S_v is average S wave velocity and d is the depth of the soil layer) can be used as a means of checking results [2]. It can be seen that shorter periods exist on the North Shore directly south of mountain ridges. This is consistent with expectations as the soil layer should be thinner when bedrock is closer to the surface and hence the period is shorter. Likewise, in Richmond longer periods are present where the coastline extends past that of the City of Vancouver’s bedrock. Assuming this peninsula has been built up over time by sediment deposit, it is consistent with expectations that the period of this region would be longer.



Fig. 6 Site Periods (in seconds) on the North Shore



Fig. 7 North Shore Test Locations

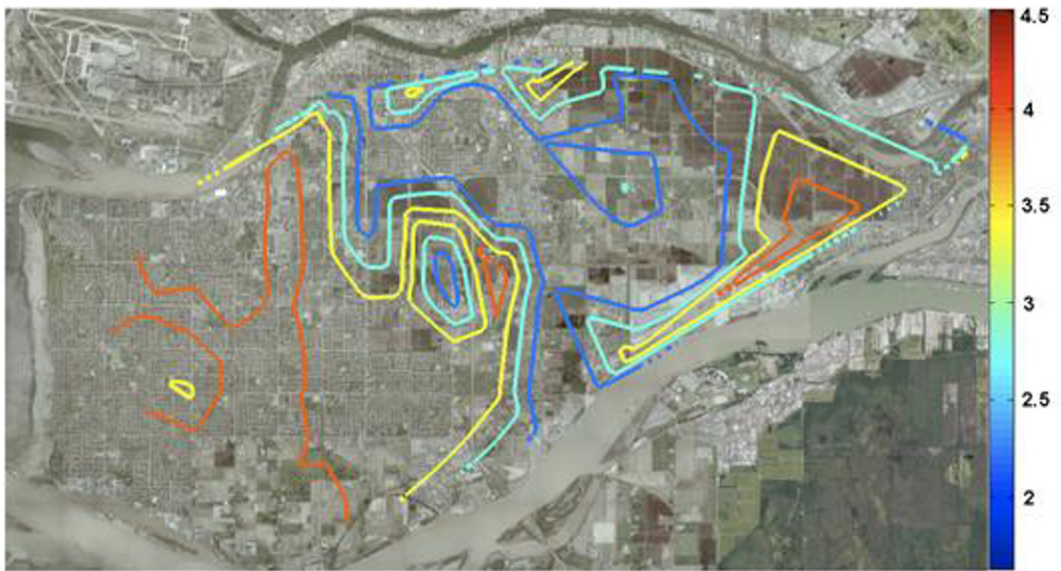


Fig. 8 Site Periods (in seconds) in Richmond

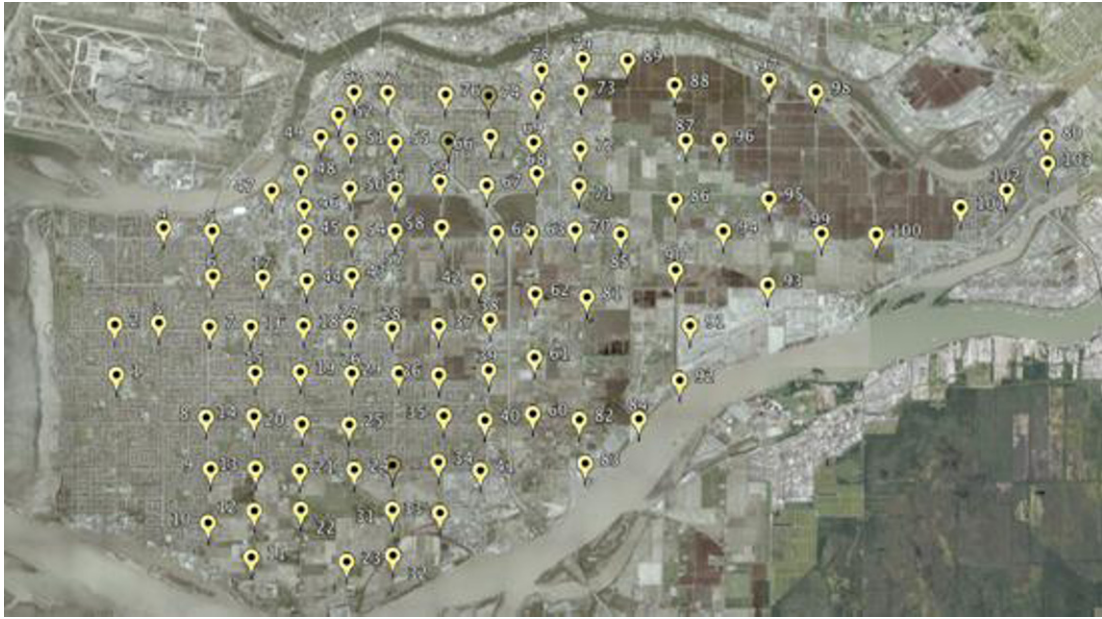


Fig. 9 Richmond Test Locations

4.0 Summary and Conclusions

This paper presented the result of a microtremor testing campaign covering the City of Richmond and the three municipalities north of the City of Vancouver. In total, 212 tests were performed and their data analysed with Nakamura's method to determine the site period for each. In some cases, the Frequency Domain Decomposition technique was used alongside Nakamura's method, with mixed results.

Several iso-period maps were generated from the results of this microtremor testing. These maps could be used as a starting point for determining underlying soil layers and input motion characteristics, estimating the seismic performance of a given area or predicting which magnitude of structures would be at risk as a result of a specific period of ground movement.

The thick sediment layers of the City of Richmond exhibited a site period ranging from 0.6 to 5.7 seconds (0.18 to 1.67 Hz). The North Shore had much shorter periods on average, between 0.04 and 1.25 seconds in length (0.8 to 25 Hz).

It is recommended that this study be expanded to other regions of Metro Vancouver to provide a more comprehensive summary of the region. In addition, further testing should be done to determine the effectiveness of the FDD technique in analysing ambient vibrations.

Acknowledgements

The authors thank Mr. Juan Carlos Carvajal of the University of British Columbia (UBC), Mr. Felix Yao of UBC, and Dr. John Cassidy of the Geological Survey of Canada for their collaboration during testing and analysis. Funding for this project was provided by the Natural Sciences and Engineering Research Council of Canada (NSERC).

References

- [1] Ventura C, Onur T, Hao K. "Site Periods Estimations in the Fraser River Delta Using Microtremor Measurements - Experimental and Analytical Studies." 13th World Conference on Earthquake Engineering, Vancouver, Canada. Paper 1075. 2004
- [2] Cassidy J, Rogers, G. "Seismic Site Response in the Greater Vancouver, British Columbia Area: Spectral Ratios from Moderate Earthquakes." The Canadian Geotechnical Journal. 36: 195-209. 1999
- [3] Ventura C, Thibert K, Onur T. "Site Period Estimations Using Microtremor Measurements - Experimental and Analytical Studies in British Columbia." 2006
- [4] Dragert H, Rogers G. "Geodynamics - Episodic Tremor and Slip (ETS)". Natural Resources Canada. Government of Canada. Web. Oct 2010. http://gsc.nrcan.gc.ca/geodyn/etschatter_e.php
- [5] "Geomap Vancouver - Additional Information". Natural Resources Canada. Government of Canada. Web. Oct 2010. http://gsc.nrcan.gc.ca/urbgeo/geomapvan/geomap2_e.php
- [6] Nakamura Y. "Clear Identification of Fundamental Idea of Nakamura's Technique and Its Applications" 12th World Conference on Earthquake Engineering. Auckland, New Zealand. Paper 2656. 2000.
- [7] Geopsy Software. Network of Research Infrastructures for European Seismology, Institut de Recherche pour le Developpement - Laboratoire de Geophysique Interne et Techtonophysique. 2008. France.
- [8] Matlab Software. The MathWorks, Inc. 1994-2010. USA.
- [9] ARTeMIS Extractor Software. Structural Vibration Solutions Inc. 1999-2003. Denmark.
- [10] Google Earth Toolbox for MATLAB & Octave. 2009. USA.
- [11] Carvajal J, Ventura C. "Identification of Surface Waves in a Stiff Soil Deposit Using a Grid of Microtremor Measurements." International Modal Analysis IMAC XXVII, Orlando, USA. 2009
- [12] Bard P. "Guidelines for the Implementation of the H/V Spectral Ratio Technique on Ambient Vibrations - Measurements, Processing and Interpretation." SESAME European Research Project WP12 - Deliverable D23-12. 2004.
- [13] Budhu M. "Foundations and Earth Retaining Structures." John Wiley and Sons. First Edition: 141-152. 2008

Experimental Study of the Nonlinear Hybrid Energy Harvesting System

M. Amin Karami¹, Paulo S. Varoto² and Daniel J. Inman³

This paper focuses on experimental nonlinear vibration analysis of the proposed hybrid energy harvester. A nonlinear energy harvesting structure is proposed to convert ambient vibrations to the electrical energy using the piezoelectric and electromagnetic mechanisms. A repelling magnetic force is introduced to the system to both reduce the resonant frequency of the system and increase the frequency bandwidth by making the vibrations nonlinear. The paper is the continuation of a previous work by the authors in which the vibrations of the harvester was analytically characterized. Both mono-stable and bi-stable situations are studied. Depending on the level of excitations the bi-stable system can exhibit oscillations about each of its equilibriums, chaotic vibrations or the limit cycle oscillations (LCO) over both of the equilibriums. The proper design of the harvester allows the system to perform Limit Cycle Oscillations in response to moderate base excitations. The paper discusses the experimental results on electro-mechanical vibrations and the energy generation of the nonlinear hybrid harvester at different magnetic force levels, excitation frequencies and excitation levels.

Introduction

Energy harvesting is the act of scavenging small amounts of power from the ambient energy in the environment. This paper focuses on energy harvesting from vibrations. Such ambient energy can come from bridge vibrations, tire motion or the human heart beating. The minute energy can power up sensor nodes and therefore reduce the wiring complications or eliminate the need of changing batteries frequently. For more information on general energy harvesting the reader may refer to [1-6].

During the past two years nonlinear energy harvesting has received substantial attention. The nonlinearity can be natural (for example the nonlinear material properties of the piezoelectric substance [7]) or can be synthetic. If in addition to

¹ ICTAS Doctoral Scholar and PhD candidate, Department of Engineering Science and Mechanics, Virginia Tech, Blacksburg VA, 24061, karami@vt.edu

² Professor on Mechanical Engineering, Universidade de São Paulo, São Paulo, Brazil, varoto@sc.usp.br

³ George R. Goodson Professor, Center for Intelligent Material Systems and Structures, Department of Mechanical Engineering, Virginia Tech, Blacksburg VA, 24061, dinman@vt.edu

the lateral direction the beam is excited longitudinally, the governing equation of the system includes some nonlinear expression in the form of parametric excitation [8]. The most common mechanism of making the beam nonlinear is by placement of permanent magnets [9-17]. After modeling their systems and deriving the nonlinear governing equations most of these researchers have used numerical or experimental methods to solve the governing equations. Among the mentioned literature on magnetically nonlinear harvesters only Ref. [15] uses analytical perturbation methods, but they only solve the mechanical system and ignores the electromechanical coupling.

An electromechanical model was introduced by the first and third author [18] to result the governing equations and predict vibration and power harvesting behavior of the proposed nonlinear hybrid energy harvesting device. Based on the model we designed and fabricate a prototype to show nonlinear vibrations characteristics for low frequency and low amplitude base oscillations. The current paper summarizes the results of experiments performed using the prototype. The paper follows by introducing the hybrid nonlinear harvesting device and driving the governing differential equations. Next we discuss the fabrication of the prototype and the test procedure. The experimental results are presented in three sections. The first two results sections are dedicated to mono-stable harvesting and the third section presents small vibrations, chaotic motion and limit cycle oscillations of the bi-stable harvester.

The nonlinear hybrid energy harvesting device

The hybrid nature of the nonlinear harvesting device proposed here is illustrated in Fig. 1. We use magnetic forces in our system to reduce nonlinear behavior. The magnetic force between the tip and base magnets is repulsive and therefore counteracts the elastic behavior. The existence of nonlinear forces acting on the beam introduces nonlinear hardening terms, which are explained in section 0. The piezoelectric element bounded to the beam harvests energy from beam deflection. As a novel approach we have placed electromagnetic coils in the system. When the beam vibrates the magnetic tip mass passes by the coils and generates electricity. The system is a hybrid energy harvester in the sense that, it uses two different methods (piezoelectric and electromagnetic transduction) for power harvesting.

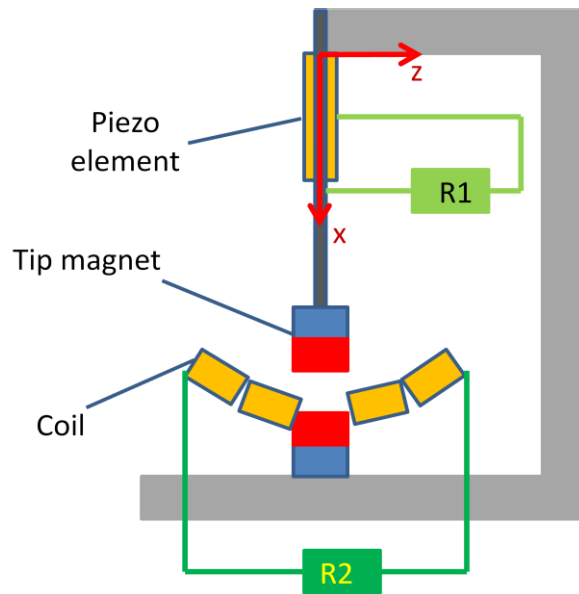


Fig. 1: Schematic View of the harvester

Governing equations and possible scenarios

We use the energy methods to model the dynamics of the system. The harvester is made up of three coupled systems; the cantilever beam which is characterized by the deflection of beam, the circuit connected to the piezoelectric element and the circuit connected to the coils. The electrical circuit for harvesting is simplified to be only a resistor in order to focus on the transduction. The value of the resistive load in the piezoelectric circuit is R_1 and the value of the resistive load in the electromagnetic circuit is R_2 . The energy in various components of the entire electromechanical system is: the elastic and magnetic potential energies stored in the beam and the magnetic field (V), the electrostatic energy stored in the piezoelectric patch (w_e), the kinetic energy stored in the beam and the tip mass (T), the magnetic potential energy between the tip and base magnets (G), the electromagnetic energy stored in the coils (W_m) and the energies dissipated by the resistors and damping of the beam. The displacement of the beam, the flux linkage across the piezoelectric element and the charge through the coils are the coordinates used for identifying the system. Following the guidelines in [19], the Lagrangian of the system is:

$$L_g = T - V + W_e + W_m \quad (1)$$

The dynamic deflection of the beam is simplified by a single mode Galerkin's method. The deflection at each point and at a certain time relative to the base is

$w(x, t) = \phi(x)u(t)$. The approach is a common practice in study of nonlinear vibrations of bi-stable structures [9] and is justified by center manifold reduction[20]. The static deflection shape of the beam under a unit load applied to the tip is used as the shape function.

The following integrals are defined to facilitate abbreviation of formulas:

$$\Phi_{20}^L = \int_0^L \phi(x)^2 dx, \quad \Phi_{20}^{L_1} = \int_0^{L_1} \phi(x)^2 dx, \quad \Phi_{22}^L = \int_0^L \phi''(x)^2 dx, \quad \Phi_{22}^{L_1} = \int_0^{L_1} \phi''(x)^2 dx \quad (2-a)$$

$$\Phi_{10}^L = \int_0^L \phi(x) dx, \quad \Phi_{10}^{L_1} = \int_0^{L_1} \phi(x) dx, \quad \Phi_{12}^{L_1} = \int_0^{L_1} \phi''(x) dx \quad (2-b)$$

Each of the terms in Lagrangian are related to the states as follows:

$$W_e - V = \iiint_{\text{vol}} \left(-\frac{1}{2} c_{ij} S_i S_j + e_{ij} E_i S_j + \frac{1}{2} \epsilon_{ij} E_i E_j \right) - G(w_{\text{end}}(t)) \quad (3)$$

where c_{ij} are the stiffness coefficients, e_{ij} are the piezoelectric constants [21], E_i are the electric field components and $G(w_{\text{end}}(t))$ is the magnetic force potential. The Magnetic force is experimentally measured and is characterized as $f = -a w_{\text{end}} + b w_{\text{end}}^3$. The magnetic force potential is therefore: $G(w_{\text{end}}) = -\frac{a}{2} w_{\text{end}}^2 + \frac{b}{4} w_{\text{end}}^4$. We let Y_s denote the Young's modulus of the steel substrate, Y_p the Young's modulus of the piezoelectric patch, I_s the area moment of inertia of the steel beam about its geometric center and I_p stand for the area moment of inertial of the cross section of each piezoelectric patch about the center line of the steel substructure. Eq. (3) is simplified to:

$$W_e - V = -\frac{b\phi(L)^4}{4} u(t)^4 - \left\{ -\frac{a\phi(L)^2}{2} + \frac{1}{2} Y_s I_s \Phi_{22}^L + Y_p I_p \Phi_{22}^{L_1} \right\} u(t)^2 + \frac{2A_p \bar{z}_p \Phi_{22}^{L_1} e_{13}}{h_p} \dot{\lambda}_1(t) u(t) + \frac{\epsilon_{33} A_p L_1}{h_p^2} \dot{\lambda}_1(t)^2 \quad (4)$$

In Eq. (4), $\lambda_1(t)$ is the flux linkage across the piezoelectric patch, A_p is the cross-sectional area and \bar{z}_p is the z -coordinate of the centroid of the patch. The z and x -coordinates have been defined in Fig. 1. The base motion, characterized by $r(t)$, should be taken into account when calculating the kinetic energy. The kinetic energy is evaluated as

$$T = \left[\frac{1}{2} \rho_s A_s \Phi_{20}^L + \rho_p A_p \Phi_{20}^{L_1} + \frac{1}{2} M_{\text{tip}} \phi(L)^2 \right] \dot{u}(t)^2 + \left[\rho_s A_s \Phi_{10}^L + 2\rho_p A_p \Phi_{10}^{L_1} + M_{\text{tip}} \phi(L) \right] \dot{u}(t) \dot{r}(t) + \frac{1}{2} \left[M_{\text{tip}} + M_s + 2M_p \right] \dot{r}(t)^2 \quad (5)$$

The densities of the steel substrate and the piezoelectric patch are ρ_s and ρ_p respectively. The total mass of the substrate and each of the piezoelectric patches are M_s and M_p . The cross sectional area of the substrate is ρ_s and M_{tip} stands for the

mass of the tip magnet. When the tip magnet passes by the coils some electromagnetic energy conversion occurs. The electromagnetic coupling can be characterized by the coupling coefficient, T_m .

When the tip magnet passes by the coils with the velocity \dot{w}_{end} , a force of magnitude $T_m \dot{i}_2$ impedes the motion of tip magnet. The current in the coils is i_2 . At the same time a potential difference is generated across the coil which equals $T_m \dot{w}_{\text{end}}$. The charge passing through the coils is noted by q_2 and the overall inductance of the coils is l . The following two terms in the Lagrangian represent the electromechanical energy in the coils:

$$W_m^* - V = \frac{1}{2} l \dot{q}_2^2 + T_m \dot{q}_2 \phi(L) u \quad (6)$$

The Euler-Lagrange equations for our three degrees of freedom system is:

$$\begin{cases} \frac{d}{dt} \left(\frac{\partial L_g}{\partial \dot{u}} \right) - \frac{\partial L_g}{\partial u} = -c_f \dot{u} \\ \frac{d}{dt} \left(\frac{\partial L_g}{\partial \dot{\lambda}_1} \right) - \frac{\partial L_g}{\partial \lambda_1} = -\frac{\lambda_1}{R_1} \\ \frac{d}{dt} \left(\frac{\partial L_g}{\partial \dot{q}_2} \right) - \frac{\partial L_g}{\partial q_2} = -R_2 \dot{q}_2 \end{cases} \quad (7)$$

The damping coefficient of the mechanical spring is denoted by c_f . Performing the derivations in Eq. (7), dividing by the modal mass and grouping the terms results:

$$\begin{cases} \ddot{u} + ku + \tilde{b}u^3 = -d\dot{u} - \tilde{\psi}_1 V_1 + \tilde{\gamma} \dot{q}_2 - \tilde{m} \ddot{r}(t) \\ \dot{V}_1 + \frac{V_1}{R_1 C_0} = \frac{\tilde{\psi}_2}{C_0} \dot{u} \\ \frac{di_2}{dt} + \frac{R_2}{l} i_2 = -\tilde{\gamma} \dot{u} \end{cases} \quad (8)$$

The coefficients in Eq. (8) are:

$$\begin{aligned} \tilde{m} &= \rho_s A_s \Phi_{20}^L + 2\rho_p A_p \Phi_{20}^{L_1} + M_{\text{tip}} \phi(L)^2, \quad \hat{m} = \frac{\rho_s A_s \Phi_{10}^L + 2\rho_p A_p \Phi_{10}^{L_1} + M_{\text{tip}} \phi(L)}{\tilde{m}}, \\ k &= \frac{-a\phi(L)^2 + Y_s I_s \Phi_{22}^L + 2Y_p I_p \Phi_{22}^{L_1}}{\tilde{m}}, \quad \tilde{b} = \frac{b\phi(L)^4}{\tilde{m}}, \quad d = \frac{c_f}{\tilde{m}}, \quad \tilde{\psi}_1 = -\frac{2A_p \bar{z}_p \Phi_{12}^{L_1} e_{13}}{\tilde{m} h_p}, \quad \tilde{\psi}_2 = \tilde{m} \tilde{\psi}_1, \\ C_0 &= \frac{2\epsilon_{33} A_p L_1}{h_p^2}, \quad \tilde{\gamma} = T_m \phi(L) \end{aligned} \quad (9)$$

The second and third terms on the right hand side of Eq. (8-a) represent the ‘‘drag’’ terms introduced by the piezoelectric patch and the electromagnetic coils. The energy transferred to the electric circuits reduces the mechanical energy of the beam and therefore slightly suppresses its oscillations.

The sign of the linear restoring coefficient, k , can be positive or negative. The familiar positive coefficient corresponds to low magnetic forces. In this situation

the zero deflection equilibrium is stable and the system is a “nonlinear mono-stable oscillator” coupled to the piezoelectric and electromagnetic circuits.

If the tip magnet is close to the base the repelling force between the magnets, which forces the tip away from the zero deflection, becomes significant. The $u = 0$ equilibrium will be unstable but there will be two stable equilibriums on the left and right side of zero deflection ($u = \pm u^*$). In this situation the system is “nonlinear bi-stable oscillator” coupled to the piezoelectric and electromagnetic circuits. The nonlinear vibrations of the nonlinear bi-stable oscillator is discussed in section 0.

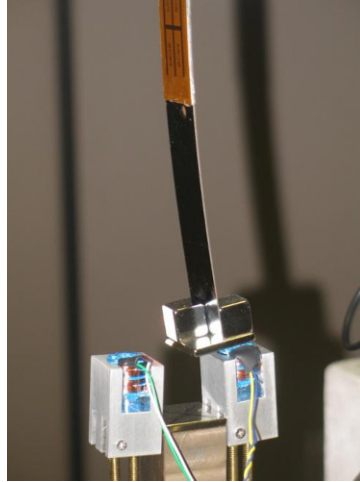


Fig. 2: The transduction element

Fabrication and testing procedure

The beam element in the hybrid harvester is a bimorph where the substrate is a 152.4 X 25.4 X 0.635 mm spring steel beam. There are two QP10n Mide’ Quick-Packs placed on the sides of the beam. For proper clamping of the beam part of the piezoelectric patches and the substrate are clamped. The effective length of the substrate outside the clamp is 127 mm. The first 38.1 mm of the beam is covered on both sides by the Quickpacks. The blue electromagnetic coils illustrated in Fig. 2 are modified small transformers. The ferroelectric coil of the transformer has been removed to prevent sudden interference with the motion of the tip magnet. Only one of the coils of the transformer (the top coils) are wired to the electromagnetic load. The coils are placed in carefully machined aluminum supports. The aluminum support can be elevated and oriented using the two brass vertical screws. This allows optimal placement of the electromagnetic coils along the course of motion of the tip magnet.

The tip magnet is composed of three rare earth magnets the two 12.7 X 12.7 X 12.7 mm cubic magnets are stabilized on the sides of the ferroelectric spring steel

by being placed on top of a 25.4 X 25.4 X 3.17 mm magnet. All the magnets are positioned to have their south poles pointed downwards. The base magnet is a 25.4 X 25.4 X 3.17 mm rare earth magnet with its south pole oriented upwards to repel the tip magnets. The strong magnetic force attaches the base magnet to a steel block, used to position the base magnet. A rail mechanism allows positioning of the base magnet and the two electromagnetic coils on its sides. The height of the vertical support connected to the column of the energy harvester can be adjusted. By adjusting the elevation of the beam we can vary the distance between the tip and base magnets and achieve different vibration scenarios.

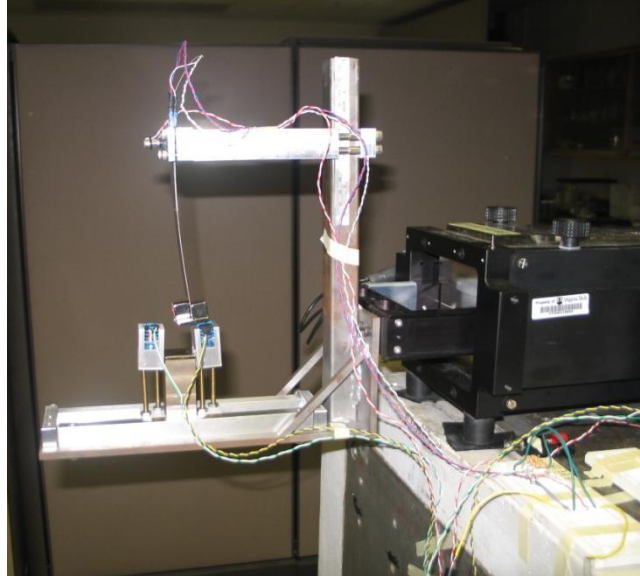


Fig. 3: Connection of the hybrid harvester to the shaker

The velocity of the tip magnet is measured using a Polytec OFV 303 laser vibrometer. The base acceleration (the acceleration of the frame of the harvester) is measured by a tear drop accelerometer. The voltage across the resistive load connected to the piezoelectric patches, and the voltage across the electromagnetic load are also measured. Siglab data acquisition interface from Spectral Dynamics is used for data collection.

Mono-stable piezoelectric harvester

The mono-stable nonlinear vibrations occur when the distance between the base and the tip magnets is larger than a certain threshold. In that working condition the passive magnetic forces reduce the natural frequency of the harvester and also make it nonlinear. The zero deflection equilibrium however remains stable. The following tests examine the vibration characteristics and the power harvesting

trend of the hybrid energy harvester as a function of the distance between the magnets, the base excitation level, the excitation frequency and the load. The Virtual Sine Sweep (VSS) feature of Siglab has been used to collect the data presented in this section. The VSS software only records the ratio between input to its 2nd-4th channel and the voltage reading at its first channel. We therefore have measured the transfer function corresponding to tip velocity, piezoelectric voltage and the electromagnetic voltage divided by the base accelerations. As the first step we only implement the piezoelectric harvesting and do not install the electromagnetic coils.

Magnet spacing

The distance between the magnets changes the magnetic force and thus changes both the natural frequency and the nonlinearities. The smaller the distance between the magnets, the smaller the natural frequency and the more significant the nonlinear effect. It can be seen from Fig. 4 that smaller magnet gap also corresponds to larger damping. Clearly the peaks of tip velocity FRF at small magnet gaps are shorter and wider compared to the corresponding peaks when the magnets are far from each other. One reason for this phenomenon is the eddy currents generated in the steel block, which hold the base magnet in place. When the tip and base magnets are close to each other the magnetic field fluctuations due to the motion of the tip magnet are significant. This field fluctuation induces eddy currents in the structure and dissipates some energy.

The nonlinearity is hardening nonlinearity and becomes more visible when the amplitude of the tip deflection is large. For large tip deflections the peaks of FRF curve bends to the right, but at the same time shortens. This increases the bandwidth of the harvester but reduces the power generation.

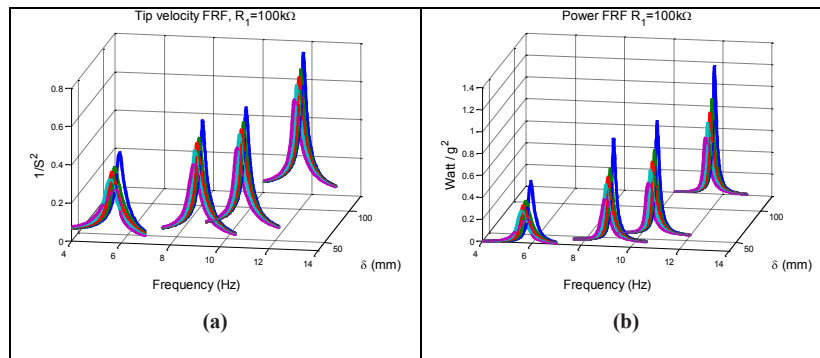


Fig. 4: Relation between the magnet spacing and a) Tip velocity/base acceleration frequency response function and b) harvested power/ base acceleration² frequency response function. The colors represent different base acceleration: blue: 0.15, green 0.3, red 0.74, cyan 1.5, magenta 3 m.s⁻².

Resistive load

There is an optimal value for the resistive load in terms of the power production. At this optimal value however the velocity will be minimal. Since the nonlinearity is more significant when the amplitude of motion is large, at optimal resistance where the amplitude of motion is minimal, the nonlinear effects become less dominant. This phenomenon is illustrated in Fig. 5.

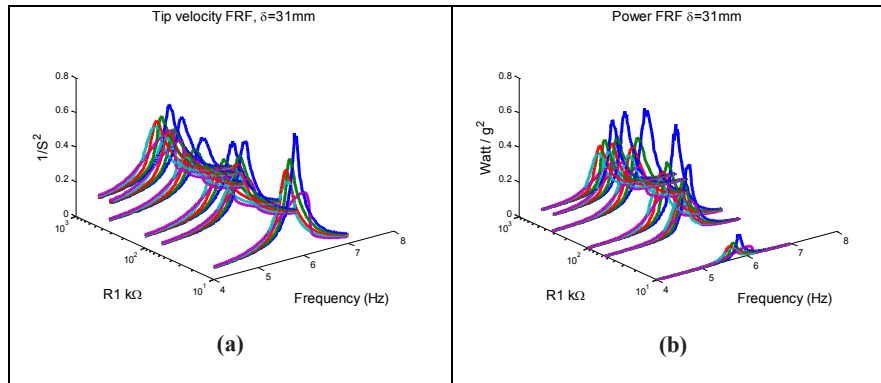


Fig. 5: Relation between the resistive load across the piezoelectric patch and a) Tip velocity/base acceleration frequency response function and b) harvested power/ base acceleration² frequency response function. The colors represent different base acceleration: blue: 0.15, green 0.3, red 0.74, cyan 1.5, magenta 3 m.s⁻².

Mono-stable Hybrid Harvester

This section explores the behavior of hybrid mono-stable nonlinear harvester. The main difference between this section and previous section is the inclusion of the electromagnetic harvesting in experimental study.

magnet distance

Fig. 6 illustrates that the natural frequency of the harvester increases with magnet distance. The hardening nonlinearity however decreases with the magnet gap. The damping in the structure decreases with the magnet distance due to presence of eddy currents. Decreasing the distance therefore increases the bandwidth at the cost of reduction in motion amplitude. The decrease in the velocity magnifies in piezoelectric and electromagnetic power curves. The electromagnetic power is more sensitive to amplitude of oscillation than the piezoelectric power. As illustrated in Fig. 2 the coils are on the sides of the tip magnet. If the range of motion of the tip mass is below a certain limit, the magnet would not pass over the coils and therefore there would be a significant loss in electromagnetic power generation.

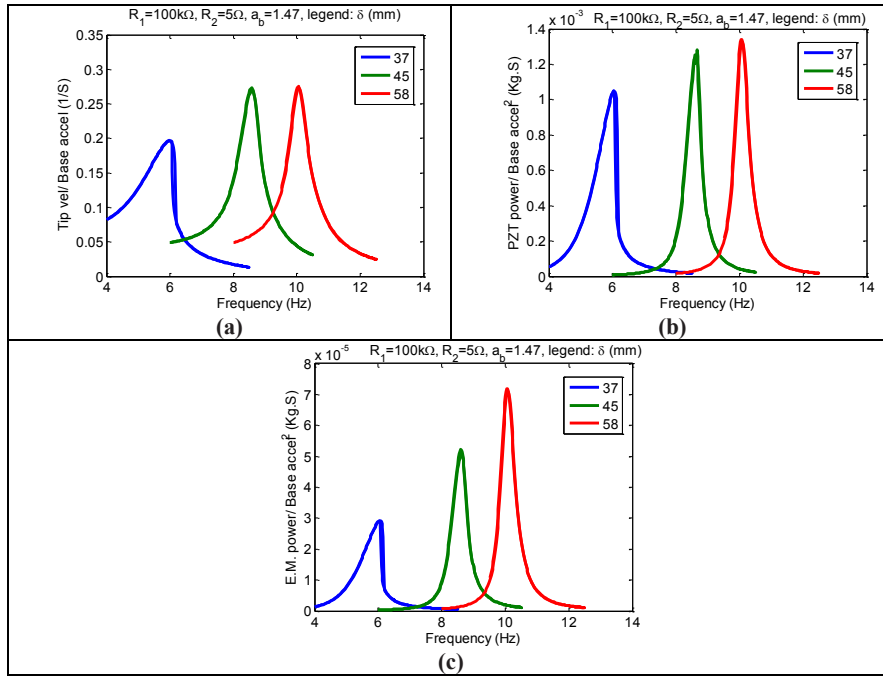
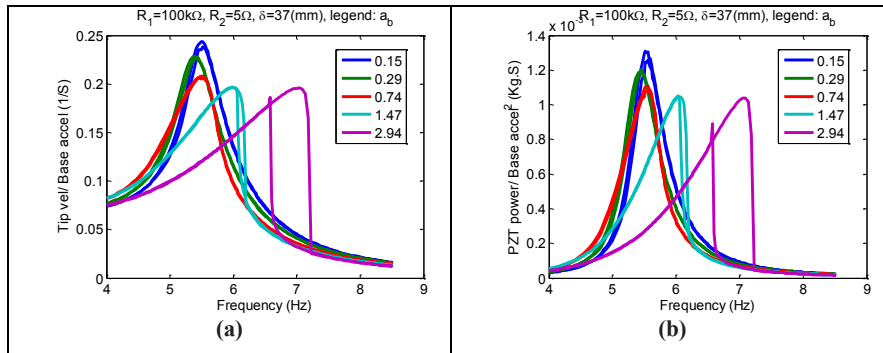


Fig. 6: Relation between the magnet distance and a) tip velocity transfer function, b) piezoelectric power transfer function, c) electromagnetic power transfer function.

Base acceleration

As illustrated in Fig. 7 the nonlinear behavior intensifies with the base acceleration. Since the type of nonlinearity is hardening this results in some decrease in the amplitude of motion and correspondingly the harvested power. The power drop in electromagnetic harvesting is more visible for the reasons discussed in previous sections.



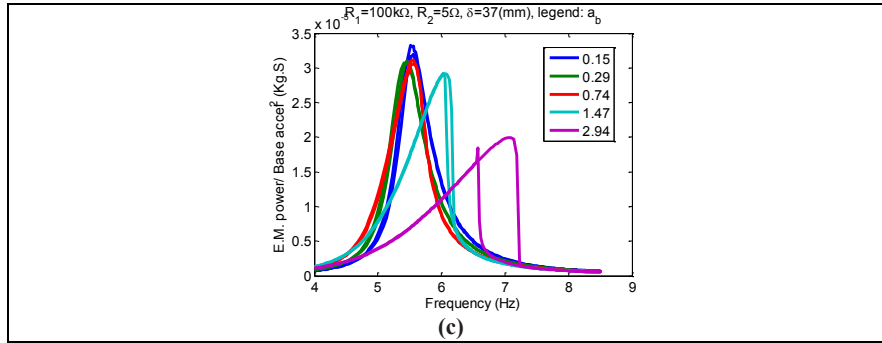


Fig. 7: Relation between the base acceleration and a) tip velocity transfer function, b) piezoelectric power transfer function, c) electromagnetic power transfer function.

The piezoelectric load

The variations in the piezoelectric shunt resistance results in effects similar to changes in resonant frequency and damping. Fig. 8 illustrates that the optimal resistance for Piezoelectric harvesting is 100 kΩ. The optimal piezoelectric load however results in the minimum tip velocity and correspondingly minimum electromagnetic power generation.

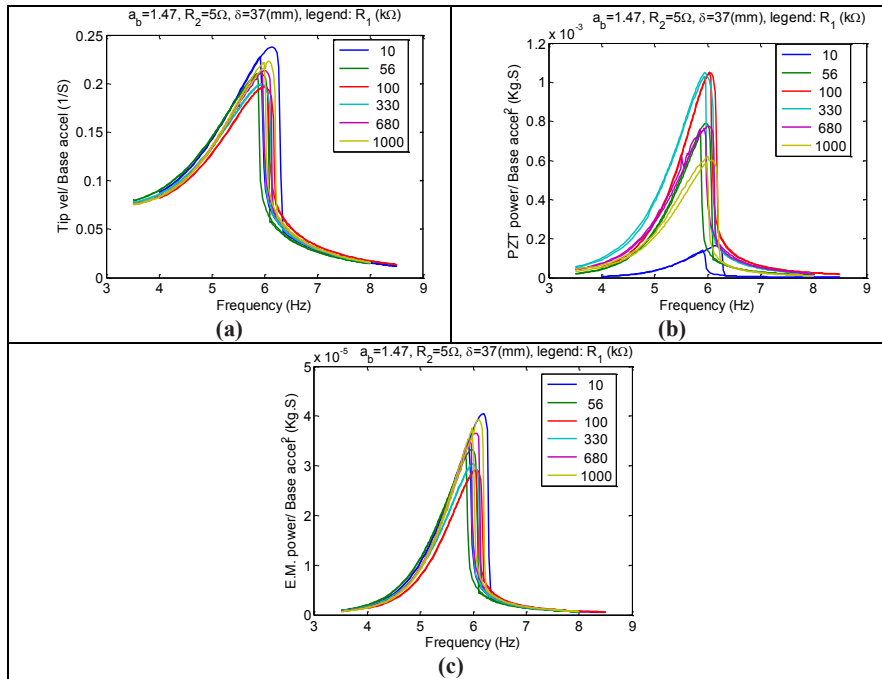


Fig. 8: Relation between the piezoelectric load and a) tip velocity transfer function, b) piezoelectric power transfer function, c) electromagnetic power transfer function.

The electromagnetic load

In principle, the electromagnetic load affects the power harvesting similar to the piezoelectric load. However the optimal electromagnetic load is in order of Ohms and for the examined device is less than the resistance of the wires. As illustrated in Fig. 9, the optimal electromagnetic load is less than the smallest shunt resistance and the power decreases with the electromagnetic resistance. The tip velocity and the piezoelectric power are almost insensitive to the electromagnetic shunt resistance. The situation has been predicated by modeling performed in [18].

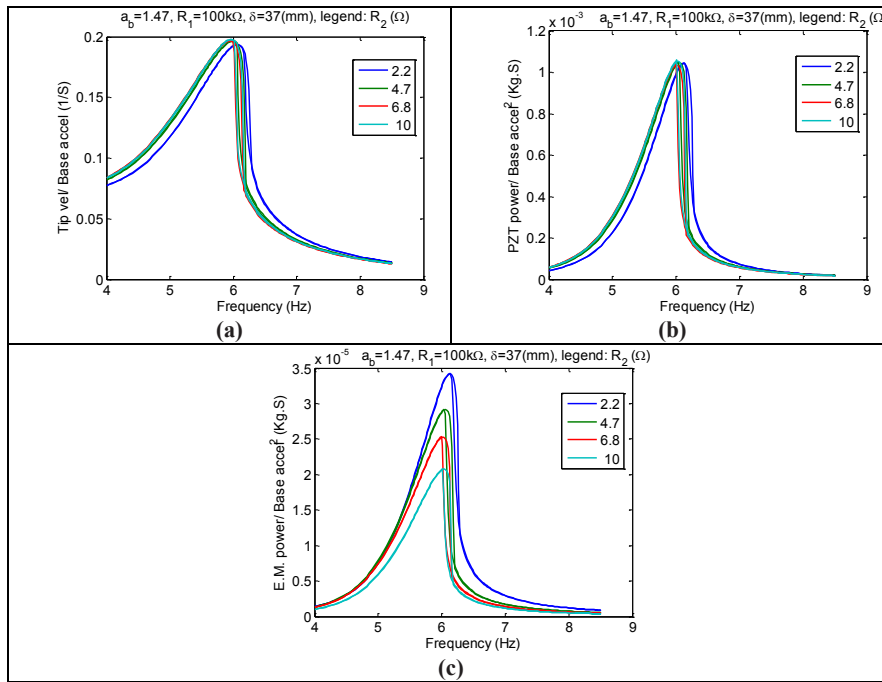


Fig. 9: Relation between the electromagnetic load and a) tip velocity transfer function, b) piezoelectric power transfer function, c) electromagnetic power transfer function.

Bi-stable Harvester

When the distance between the base and the tip magnets is less than 27mm the zero deflection equilibrium of the beam is not stable. There are two equilibriums on the sides which are stable. The motion of the harvester can be one of three forms: small oscillations about any of the stable equilibriums, chaotic motion, or large limit cycle oscillations circling both stable equilibriums. In the following we experimentally examine the conditions that give rise to any of the possible motion patterns.

Base acceleration

The experimental results for the case where the magnet distances is 27 mm has been illustrated in Fig. 10. When the base excitations are smaller than 3 m.s^{-2} the beam oscillates about either of the stable equilibriums. The motion is referred to as small amplitude oscillations. For larger base excitations the motion can be chaotic or limit cycle oscillations. The amount of harvested power from limit cycle oscillations is an order of magnitude larger than power from chaotic motion which in turn is an order of magnitude larger than small oscillations' power.

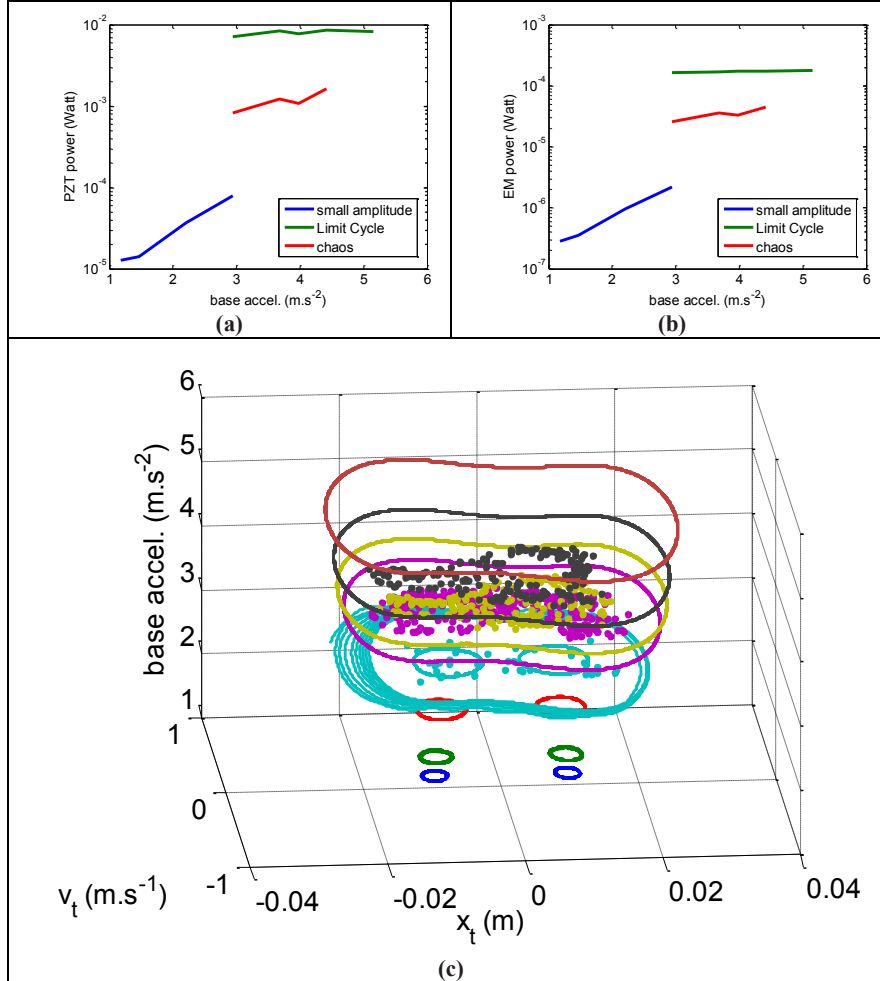


Fig. 10: Relation between the base acceleration and a) power from piezoelectric patched, b) power from electromagnetic coils, c) phase portrait and Poincaré map.

Excitation frequency

In the following we examine the variations of mechanical motion and harvested power with the base excitation frequency. The effects are different depending on the level of base accelerations. We therefore conduct three series of tests and illustrate the results in Fig. 11, Fig. 12 and Fig. 13.

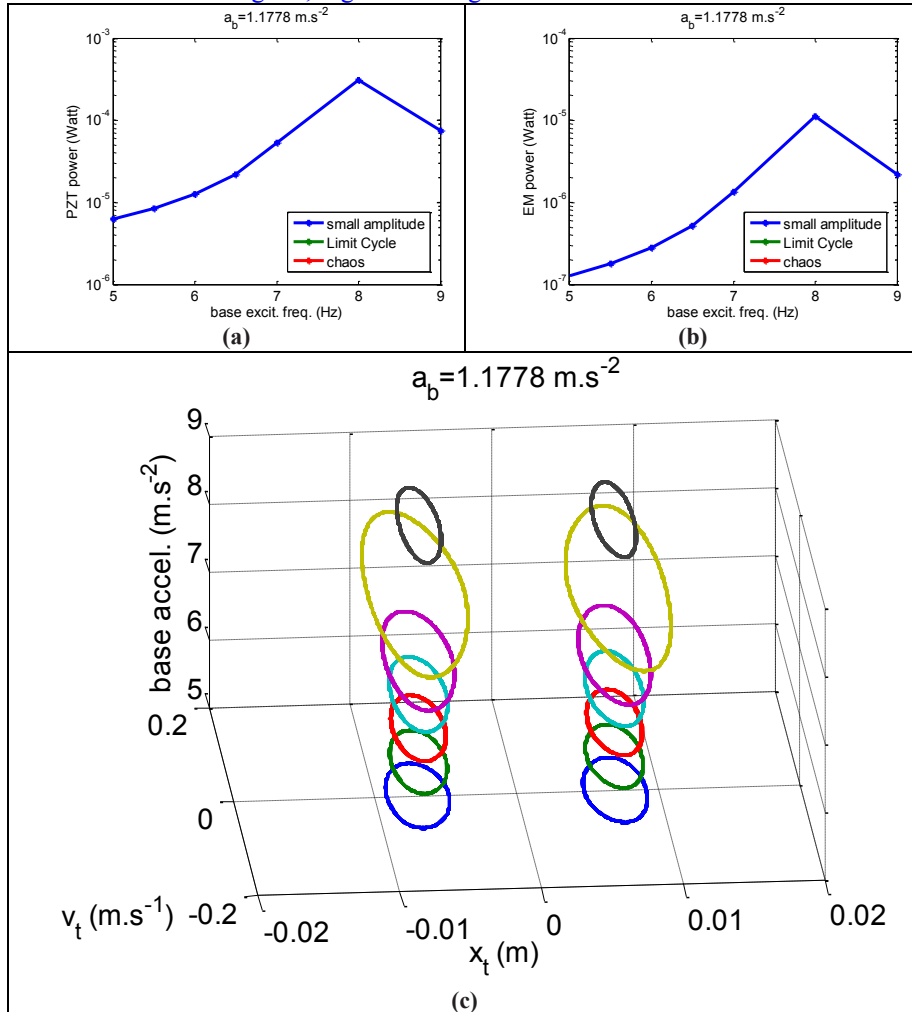


Fig. 11: Relation between the frequency of the 1.18 m.s^{-2} base excitation and a) power from piezoelectric patched, b) power from electromagnetic coils, c) phase portrait.

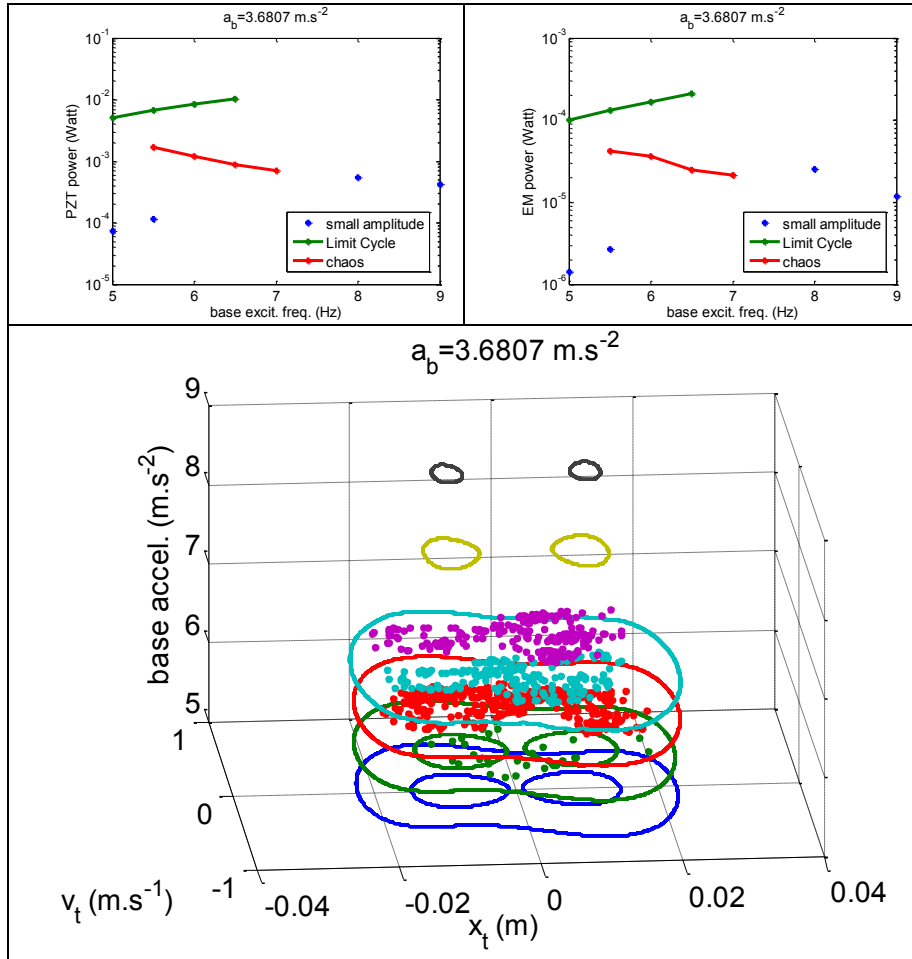
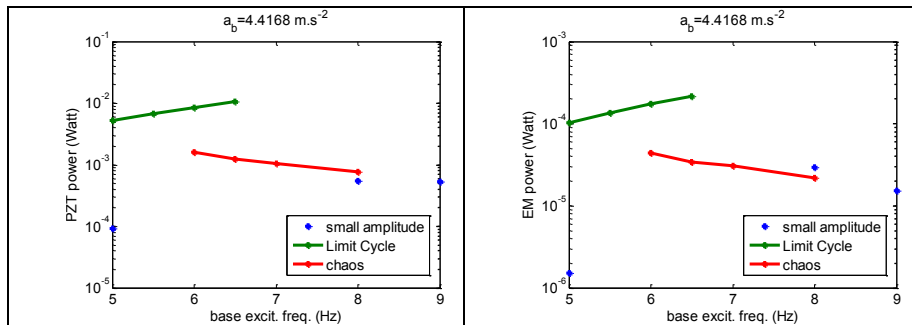


Fig. 12: Relation between the frequency of the 3.68 m.s^{-2} base excitation and a) power from piezoelectric patched, b) power from electromagnetic coils, c) phase portrait.



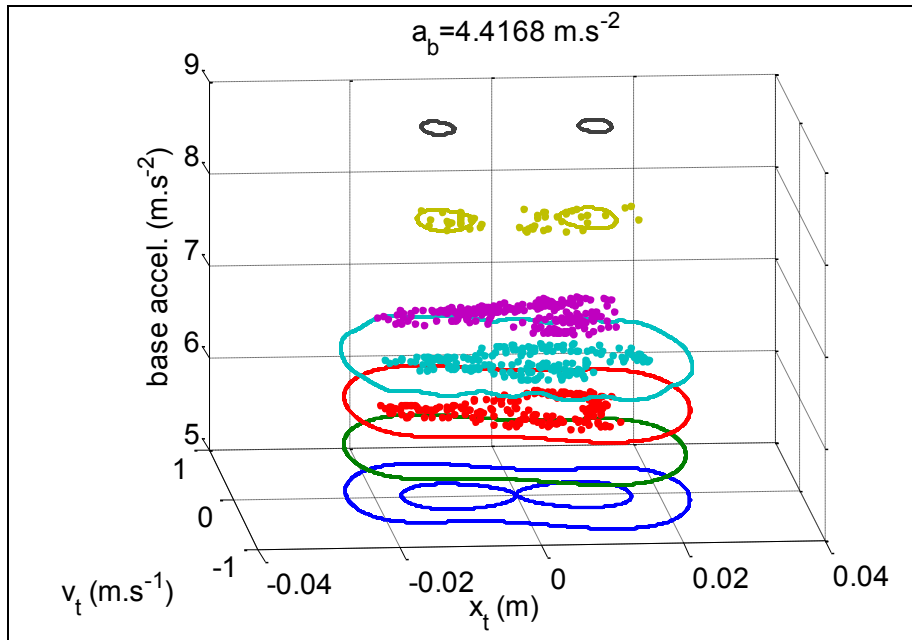


Fig. 13: Relation between the frequency of the 4.42 m.s^{-2} base excitation and a) power from piezoelectric patched, b) power from electromagnetic coils, c) phase portrait.

Conclusions

A comprehensive experimental investigation was conducted on the vibrations characteristics and power generation of the novel hybrid nonlinear energy harvester. The harvester utilizes passive magnetic forces to both reduce the natural frequency and introduce useful nonlinearities to the harvesting system. The device has been modeled using energy methods. The first set of experiments is for the softly nonlinear system where only piezoelectric transduction is implemented. The second case study considers the softly nonlinear system where both piezoelectric and electromagnetic transductions harvest energy. The final set of tests is dedicated to bi-stable situation and the small amplitude oscillation, chaotic motion and limit cycle oscillations are all investigated.

References

- [1] S. P. Beeby, M. J. Tudor, and N. M. White, "Energy harvesting vibration sources for microsystems applications," *Measurement science and technology*, vol. 17, p. 175, 2006.

- [2] S. Anton and H. Sodano, "A review of power harvesting using piezoelectric materials (2003-2006)," *Smart Materials and Structures*, vol. 16, p. 1, 2007.
- [3] D. Arnold, "Review of microscale magnetic power generation," *IEEE Transactions on Magnetics*, vol. 43, pp. 3940-3951, 2007.
- [4] K. Cook-Chennault, N. Thambi, and A. Sastry, "Powering MEMS portable devices—a review of non-regenerative and regenerative power supply systems with special emphasis on piezoelectric energy harvesting systems," *Smart Materials and Structures*, vol. 17, p. 043001, 2008.
- [5] S. Priya, "Advances in energy harvesting using low profile piezoelectric transducers," *Journal of Electroceramics*, vol. 19, pp. 167-184, 2007.
- [6] S. Priya and D. Inman, *Energy Harvesting Technologies*: Springer, 2008.
- [7] A. Triplett and D. Quinn, "The Effect of Non-linear Piezoelectric Coupling on Vibration-based Energy Harvesting," *Journal of Intelligent Material Systems and Structures*, vol. 20, p. 1959, 2009.
- [8] M. Daqaq, C. Stabler, Y. Qaroush, and T. Seuaciuc-Osorio, "Investigation of Power Harvesting via Parametric Excitations," *Journal of Intelligent Material Systems and Structures*, vol. 20, p. 545, 2009.
- [9] S. Stanton, C. McGehee, and B. Mann, "Nonlinear dynamics for broadband energy harvesting: Investigation of a bistable piezoelectric inertial generator," *Physica D: Nonlinear Phenomena*, 2010.
- [10] F. Cottone, H. Vocca, and L. Gammaitoni, "Nonlinear energy harvesting," *Physical Review Letters*, vol. 102, p. 80601, 2009.
- [11] S. Shahruz, "Increasing the Efficiency of Energy Scavengers by Magnets," *Journal of Computational and Nonlinear Dynamics*, vol. 3, p. 041001, 2008.
- [12] A. Erturk, J. Hoffmann, and D. Inman, "A piezomagnetoelastic structure for broadband vibration energy harvesting," *Applied Physics Letters*, vol. 94, p. 254102, 2009.
- [13] B. Mann, "Energy criterion for potential well escapes in a bistable magnetic pendulum," *Journal of Sound and Vibration*, vol. 323, pp. 864-876, 2009.
- [14] B. Mann and B. Owens, "Investigations of a nonlinear energy harvester with a bistable potential well," *Journal of Sound and Vibration*, 2009.
- [15] B. Mann and N. Sims, "Energy harvesting from the nonlinear oscillations of magnetic levitation," *Journal of Sound and Vibration*, vol. 319, pp. 515-530, 2009.
- [16] S. Stanton, C. McGehee, and B. Mann, "Reversible hysteresis for broadband magnetopiezoelectric energy harvesting," *Applied Physics Letters*, vol. 95, p. 174103, 2009.
- [17] D. A. W. Barton, S. G. Burrow, and L. R. Clare, "Energy harvesting from vibrations with a nonlinear oscillator," in *ASME-IDETC*, San Diego CA, 2009.

- [18] M. A. Karami and D. J. Inman, "Nonlinear Hybrid Energy Harvesting utilizing a Piezo-magneto-elastic spring," presented at the 17th SPIE Annual International Symposium on Smart Structures and Materials & Nondestructive Evaluation and Health Monitoring, San Diego, CA, 2010.
- [19] A. Preumont, *Mechatronics: dynamics of electromechanical and piezoelectric systems*: Kluwer Academic Pub, 2006.
- [20] F. Moon and P. Holmes, "A magnetoelastic strange attractor," *Journal of Sound Vibration*, vol. 65, pp. 275-296, 1979.
- [21] D. J. Leo, *Engineering Analysis of Smart Material Systems*: Wiley 2007.

Using Transmissibility measurements for Nonlinear Identification

A Carrella¹, DJ Ewins¹, L Harper²

¹ University of Bristol, Faculty of Engineering, Bristol, BS8 1TR,
² AgustaWestland UK, Yeovil, BA20 2YB

Abstract

In order to improve the predictive capability of the mathematical or numerical models of engineering structures, there is a need to capture their physical behaviour based on experimental measurements. In dynamics, this is accomplished with specific vibration tests, such as the Ground Vibration Test (GVT) used in aerospace applications. Currently, it seems that the engineering community lacks appropriate tools for the detection and quantification of dynamic nonlinearities during vibration tests. Of the nonlinear identification methods developed during the past 30 years, only a few are suitable for application on practical engineering structures. One of these has the particular advantage of requiring standard measurement techniques and sensors and is based on the analysis of Frequency Response Function (FRF) data. However, in many practical applications, structures are required to be tested by excitation of the base, so that transmissibilities are measured in place of FRFs. In this paper an existing identification method based on FRF data is shown to be applicable also when transmissibility is measured. Numerical simulations are used to demonstrate the applicability of the method.

INTRODUCTION

In many engineering applications, numerical analysis based on mathematical models is becoming a major feature of the design stage. The main purpose of the model, most commonly a Finite Element (FE) model, is to enable the designers to predict a system's dynamic under different structural and loading conditions. It can be argued that in order to increase the accuracy and the prediction capability of the numerical models, nonlinear effects cannot be neglected. The *validation* process aims at ameliorating the quality of the model by comparing the numerical analysis results with experimental data and applying the necessary changes to the model in order to minimise the difference between simulations and experiments. For a more reliable and accurate model, there is thus a need for being able to extract nonlinear parameters from measured data. The modal parameters (natural frequencies, modal damping and mode shapes) extracted using standard - and nowadays very advanced - techniques, are in many cases accurate enough for structural dynamic design purposes. However, there are instances in which the nonlinear effects cannot be ignored. A nonlinear behaviour can result in drastic changes of natural frequency or damping. Furthermore, these modal quantities can be dependent on several variables, i.e. the nature of the nonlinearities is due, for example, to amplitude of vibration, frequency of excitation, temperature, etc. There is a need for a structured procedure, or Non Linear Modal Testing (NLMT), which allow engineers and dynamicists to identify and quantify the structural nonlinearities in standard testing environment.

The reference textbook, and arguably the only book on the subject, on identification and quantification of nonlinearities in structural dynamics was published in 2001 by Worden and Tomlinson [1]. Some years later, Kershen *et al* [2] have contributed to the subject by publishing a review paper in which 446 references were cited. As these authors stated, their review has inevitably missed some works on the subject. Probably for reasons of commercial interest, there is a scarcity of works published on NLMT that refers to industrial research and/or practice. Some methods that the authors of this paper deem of practical applicability are the *Restoring Force Surface (RFS)*, [3], the *Inverse Method* [4] and the *Linearity Plots*,

[5]. Link *at al* [6] have also presented a practical method for nonlinear identification: the paper is of particular interest for two main reasons: (1) because it presents a practical method for nonlinear identification; and (2) the modal parameters are extracted from the transmissibility function, as opposed to the standard Frequency Response Function (FRF).

A method for the identification and quantification of nonlinearities, based on the analysis of measured FRF data, coded as CONCERTO, was recently published by the authors [7]. However, in many practical cases test-pieces are subject to base excitation and therefore only transmissibility data are available. In this paper it is shown that the application of CONCERTO to simulated FRF and transmissibility functions yield the same results. Nonetheless, the method presents some shortfalls which need to be addressed in the future.

NONLINEAR IDENTIFICATION METHOD USING FRF DATA

As a comprehensive study of the method is presented in [7], only a brief summary is given here. Consider a nonlinear single-degree-of-freedom (SDOF) system of a mass m , with amplitude-dependent damping and/or stiffness - which are the most common classes of nonlinearity in engineering structures - excited by a harmonic force, as depicted in Fig. 1(a). The equation of motion is

$$m\ddot{x} + c(X)\dot{x} + k(X) = F \sin(\omega t) \quad (1)$$

where X is the amplitude of the response (assumed to be harmonic), $c(X)$ and $k(X)$ are the damping and stiffness functions respectively, F_0 is the amplitude of the excitation force and ω is the excitation frequency. Note that a linear system is a special case of Eqn.(1) in which the functions $c(X)$ and $k(X)$ are constants. The identification method discussed in this paper is based on a stepped-sine excitation. Assuming that the system responds at the same frequency as the excitation, the receptance FRF is measured as the ratio between the displacement and the force at steady-state. It is sometimes preferred (but is not strictly necessary) to maintain a constant force level throughout the test, primarily in order to minimise the effect of the force-drop-out near resonance. However, at any given response amplitude, X , the functions $c(X)$ and $k(X)$ in Eqn.(1) are in effect constants. In other words, it is possible to linearise the system at that specific response amplitude so that the system's receptance is given by

$$H(X, \omega) = \frac{X(\omega)}{F(\omega)} = \frac{1}{\omega_0^2(X) - \omega^2 + \omega_0^2(X)\eta(X)} \quad (2)$$

where $\omega_0(X)$ and $\eta(X)$ are the natural frequency and the modal loss factor at that given amplitude. It is important to note that the linearisation must refer to a given value of the amplitude of displacement response and *not* receptance amplitude.

The functions $\omega_0(X)$ and $\eta(X)$ can be extracted from the measured real and imaginary part of the receptance as

$$\omega_0^2(X) = \frac{(R_2 - R_1)(R_2 \omega_2^2 - R_1 \omega_1^2) + (I_2 - I_1)(I_2 \omega_2^2 - I_1 \omega_1^2)}{(R_2 - R_1)^2 + (I_2 - I_1)^2} \quad (3)$$

$$\eta(X) = \left| \frac{(I_2 - I_1)(R_2 \omega_2^2 - R_1 \omega_1^2) + (R_2 - R_1)(I_2 \omega_2^2 - I_1 \omega_1^2)}{\omega_r^2 [(R_2 - R_1)^2 + (I_2 - I_1)^2]} \right| \quad (4)$$

where R_1 and R_2 (I_1 and I_2) are the real (imaginary) part of the receptance at the amplitude X which have been measured at the frequencies ω_1 and ω_2 (before and after the resonance peak).

The theory presented above is implemented in the COde for Nonlinear identiFication from mEasured Response To vibratiOn (CONCERTO) which is used for the analysis of both numerical and experimental data [7].

NONLINEAR IDENTIFICATION METHOD USING TRANSMISSIBILITY DATA

Consider the Single-Degree-Of-Freedom (SDOF) system depicted in Fig.1. A mass m , suspended on a spring with amplitude dependent complex stiffness $k(Z)(1 + j\eta(Z))$, where η is the system's loss factor. It is important to notice that in case of base excitation the characteristics of the support, or mount, are dependent on its effective displacement (or deformation) which is the relative displacement between the mass the base, $z = x - y$.

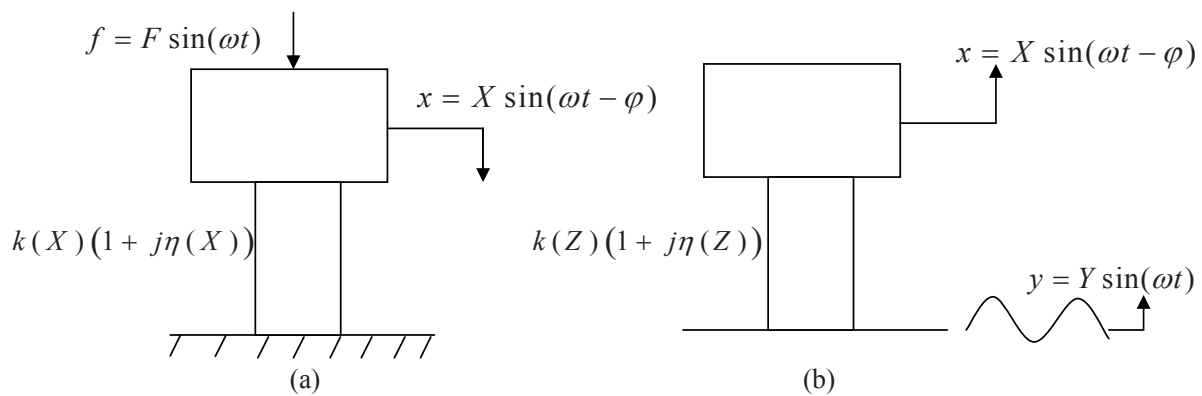


Fig.1: Schematic representations of a SDOF system of a mass suspended on a nonlinear mount with complex stiffness: (a) force excitation, (b) base excitation

The steady-state response under harmonic excitation of the system depicted in Fig.1(b) is

$$\left[-\omega^2 m + k(1 + j\eta) \right] X = \left[k(1 + j\eta) \right] Y \quad (5)$$

or

$$\left[-m\omega^2 + k(1 + j\eta) \right] Z = m\omega^2 Y \quad (6)$$

where $z = x - y$ is the relative displacement (and Z its amplitude) between the mass and the base, that is the deformation of the mount and ω the excitation frequency. Note that the dependency of the stiffness and damping from the amplitude Z has been omitted for clarity.

The transmissibility is defined as the nondimensional quantity that at each frequency quantify how much disturbance has passed from the source to the receiver through the transmission path. Two types of transmissibility can be defined. The absolute transmissibility is

$$|T| = \left| \frac{X}{Y} \right| = \left| \frac{k(1+j\eta)}{k(1+j\eta) - m\omega^2} \right| \quad (7)$$

which can be expressed in terms of modal quantities as

$$|T| = \left| \frac{\omega_0^2 + j\omega_0^2\eta}{\omega_0^2 - \omega^2 + j\omega_0^2\eta} \right| = |R + jI| \quad (8)$$

On the other hand, the relative transmissibility is

$$|T_r| = \left| \frac{Z}{Y} \right| = \left| \frac{X - Y}{Y} \right| = |T - 1| = \left| \frac{m\omega^2}{k(1+j\eta) - m\omega^2} \right| \quad (9)$$

or

$$|T_r| = \left| \frac{\omega^2}{\omega_0^2 - \omega^2 + j\eta\omega_0^2} \right| \quad (10)$$

The relative transmissibility is important because (i) it is related to the actual deformation of the mount and (ii) the direct numerical integration of the equation of motion using the Runge-Kutta 4th order expansion it is implemented to yield the relative displacement z from which the mass displacement x can be calculated and finally the absolute transmissibility computed. However, of greatest value is the absolute transmissibility because this is directly measurable (as the ratio between output and input). Also, the nonlinear identification algorithm needs to be applied to the (measured) absolute transmissibility. In Eqn.(8) or Eqn.(10) the two unknowns are the natural frequency, ω_0 , and the loss factor, η , which can be both amplitude-dependent, while the frequency of excitation, ω , the real (R) and the imaginary (I) parts of the response are all measurable quantities.

It is noticeable that the expressions of the FRF and of the absolute transmissibility, Eqns. (2) and (8) are very similar as their denominator is equal and their numerator is independent of the excitation frequency. This is not the case for the relative transmissibility, Eqn.(10), whose numerator contains the excitation frequency ω .

It is possible to use Eqn.(8) in the same way as the FRF has been used to extract the modal parameters as function of the amplitude of the displacement response and computing the modal quantities Eqns.(3,4). Repeating the calculations for different response levels enable one to obtain the required natural frequency and damping as functions of the displacement amplitude of the mass (or absolute response). It is crucial that the CONCERTO identification method is applied to the absolute transmissibility data, and attention is paid in relating the amplitude dependency to the actual deformation of the mount which is the relative displacement.

NUMERICAL SIMULATIONS OF FRF AND TRANSMISSIBILITY DATA FOR NL SYSTEMS

A comprehensive analysis of the method implemented in CONCERTO based on Frequency Response Functions data is given in reference [7]. In the present paper, in order to verify the extension of the method to transmissibility data, a comparison is performed between the

nonlinear identification method on simulated FRF and Transmissibility data. Numerical values are taken from reference [7] for consistency. The equation of motion of the force-excited system (FRF) is

$$m\ddot{x} + c\dot{x} + f_c(\dot{X}) + kx + f_k(X) = F_0 \sin(\omega t) \quad (11)$$

where the parameters are described in Tab.1. Eqn.(8) has been solved by direct integration using the built-in Matlab solver ODE45 for each case at different frequencies of excitation (separated by a step of 0.005Hz). The FRF has then been computed by simulating the operation of a Frequency Response Analyser (FRA) that is by computing the ratio between the Fourier coefficients of the response and the force at the excitation frequency. In addition, several levels of excitation force have been used.

Similarly, the transmissibility (base-excitation) simulations derive from the integration of the equation of motion

$$m\ddot{z} + c\dot{z} + f_c(\dot{Z}) + kz + f_k(Z) = \omega^2 mY \sin(\omega t) \quad (12)$$

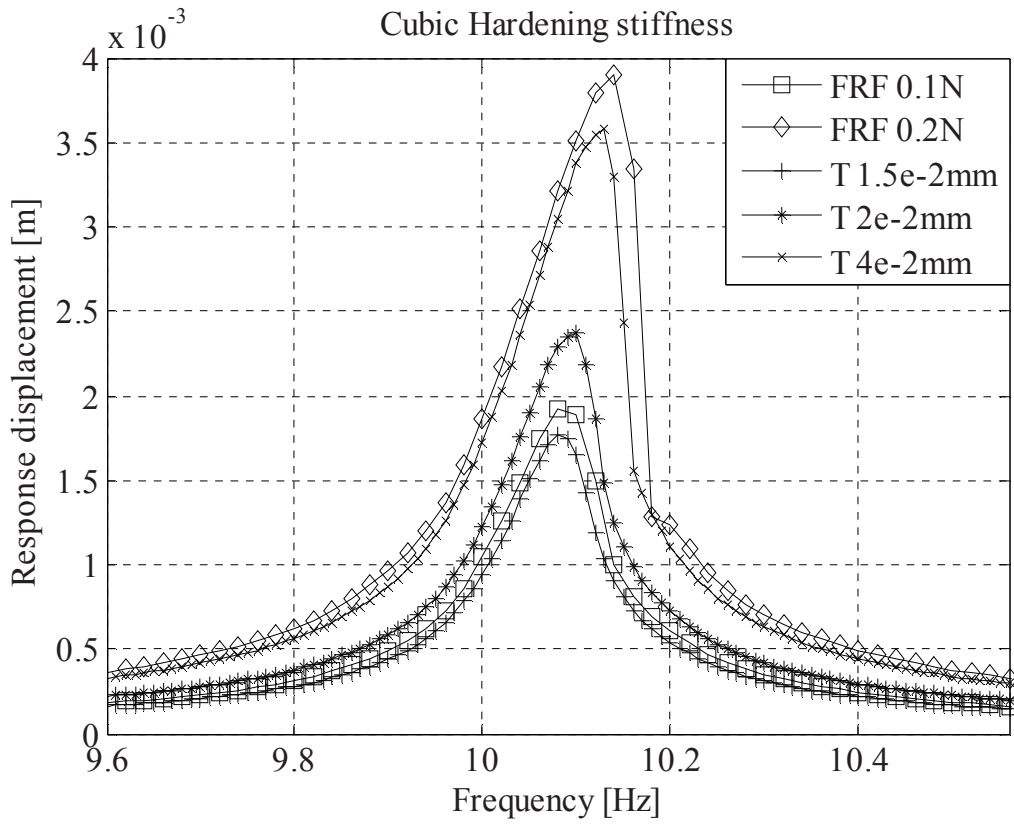
where $z = x - y$ is the relative displacement between the mass and the base and Y is the amplitude of the base displacement. After the integration the absolute displacement has been computed before calculating the absolute transmissibility which is needed to perform the nonlinear identification with CONCERTO.

| Mass $m = 1.5$ kg Damping Coefficient $c = 0.8$ Ns/m Stiffness $k = 6000$ N/m | | | |
|---|----------------------------------|-------------------|--|
| Nonlinearity | Damping f_c | Stiffness f_k | Values |
| Cubic stiffness (hardening) | 0 | $f_k = k_{nl}x^3$ | $k_{nl} = 7e^6 \text{ Nm}^{-3}$ |
| Quadratic Damping | $f_c = c_{nl}\dot{x} \dot{x} $ | 0 | $c_{nl} = 8 \text{ N s}^2\text{m}^{-2}$ |
| Coulomb Damping | $f_c = F_f \text{sign}(\dot{x})$ | 0 | $F_f = 0.85$ |
| Quadratic Damping + Cubic stiffness | $f_c = c_{nl}\dot{x} \dot{x} $ | $f_k = k_{nl}x^3$ | $k_{nl} = 7e^6 \text{ Nm}^{-3}$ $c_{nl} = 8 \text{ N s}^2\text{m}^{-2}$ |

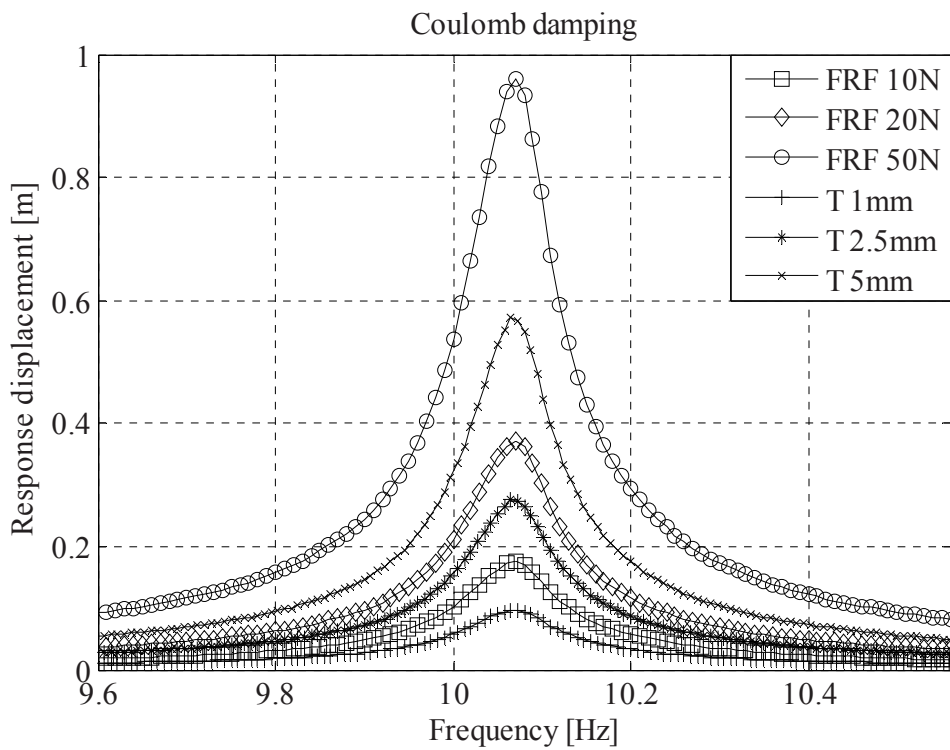
Table 1: Type and values of nonlinearities used for the numerical simulations. For the base-excitation simulations the stiffness and damping are functions of the relative displacement z

As an example of the numerical simulation, Fig.2 (a,b) shows the FRF and transmissibility functions for the SDOF system with a combined hardening cubic stiffness and Coulomb damping.

It should be pointed out that in Table 1 only the mass displacement x has been used. This is correct in the case of force excitation (FRF) but for the case of base-excitation the mount's properties are function of the effective amplitude of deformation which is the relative displacement z .



(a)



(b)

Fig.2: Simulated FRF and Transmissibility of a SDOF nonlinear system with different levels of force and base-displacement excitation: (a) hardening cubic stiffness, (b) Coulomb damping.

In Fig.3 there is a snapshot of CONCERTO's output to the analysis of simulated transmissibility of a system with combined nonlinearities (quadratic damping + cubic stiffness) excited by a harmonic base oscillation with amplitude $Y = 0.5\text{mm}$. In the top-left corner, there are the measured points, displayed as response (displacement) spectrum. The transmissibility is also displayed as a Nyquist plot (top-right). The information on the nonlinearities of the system are contained in the two plots in the lower-left corner: one depicts the extracted natural frequency, Eqn.(3), and the other the loss factor, Eqn.(4), (displayed as damping ratio using the approximation $\eta \approx 2\zeta$) as function of the amplitude of vibration displacement response of the mass.

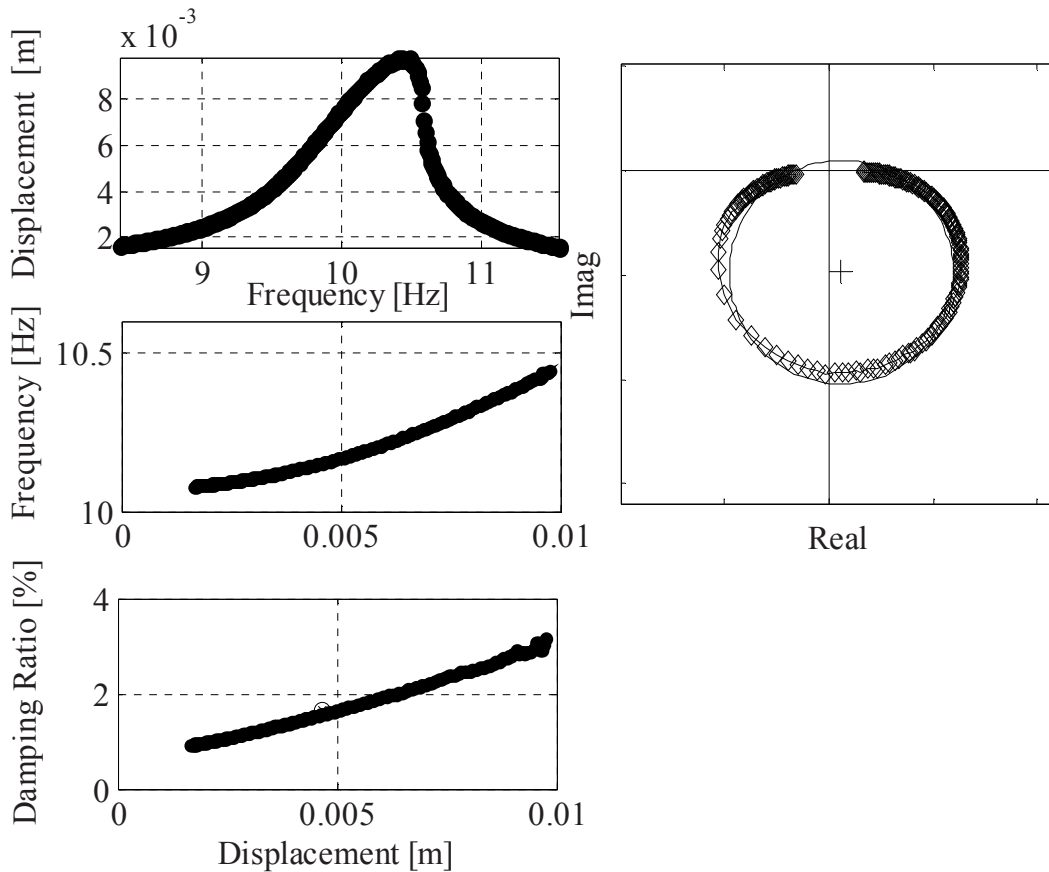


Fig.3: Example of CONCERTO output for the analysis of a nonlinear system with combined cubic stiffness and quadratic damping

From the frequency and damping plots (against the displacement), it is possible to identify rather clearly the stiffening effects and the linear increase of damping with displacement (an indication of a quadratic function of the velocity).

In order to assess the quality of the results obtained with CONCERTO when applied to transmissibility data, these are compared with those obtained using the identification method on FRF data and which have been published in reference [7].

The results obtained with the identification algorithm CONCERTO are shown in Fig.4-6.

Fig. 4 (a) shows the results obtained by analysing a system with cubic hardening spring: it can be seen that by increasing the level of excitation, and thus the amplitude of response, there is a

consistent increase in natural frequency (due to the hardening stiffness). On the other hand, the damping is rather linear.

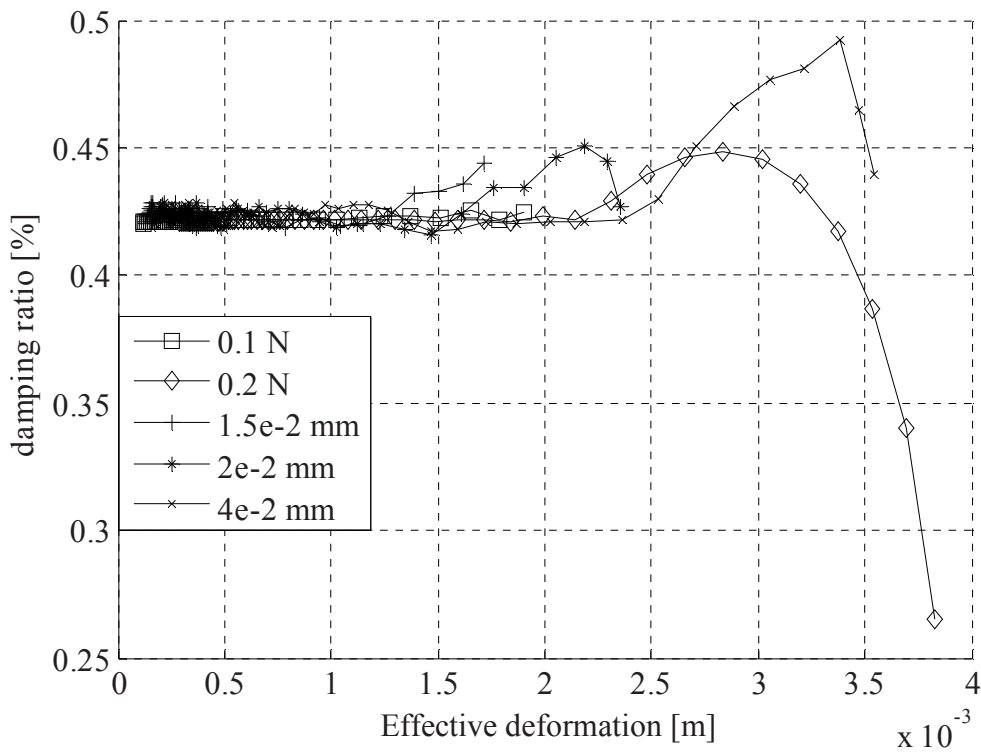
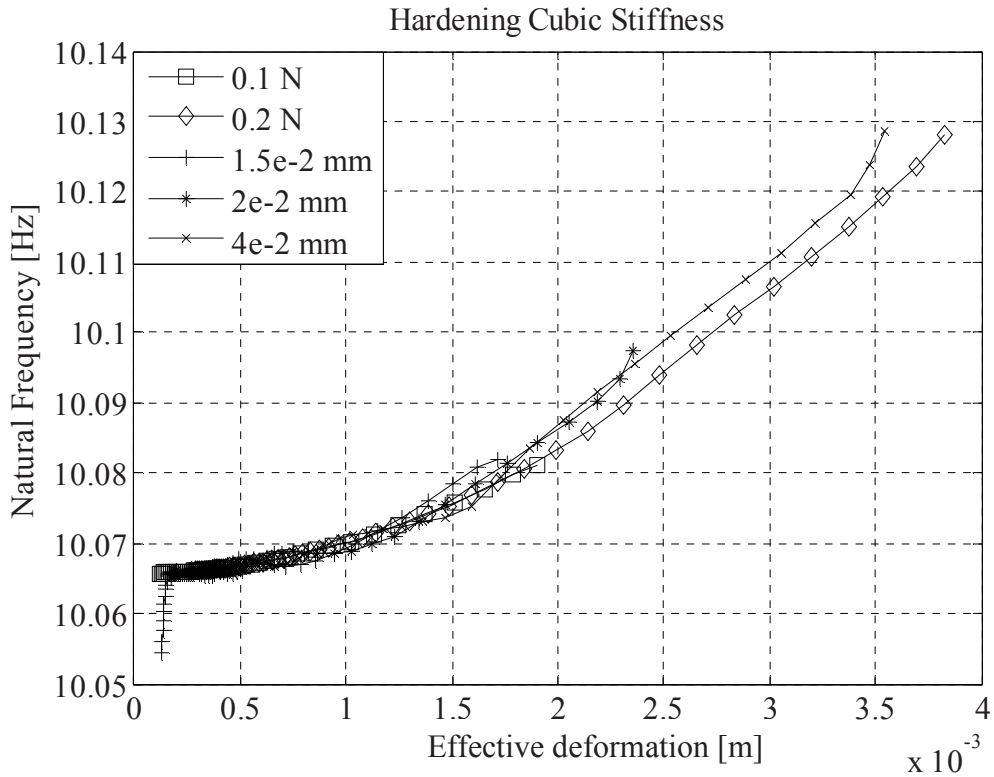
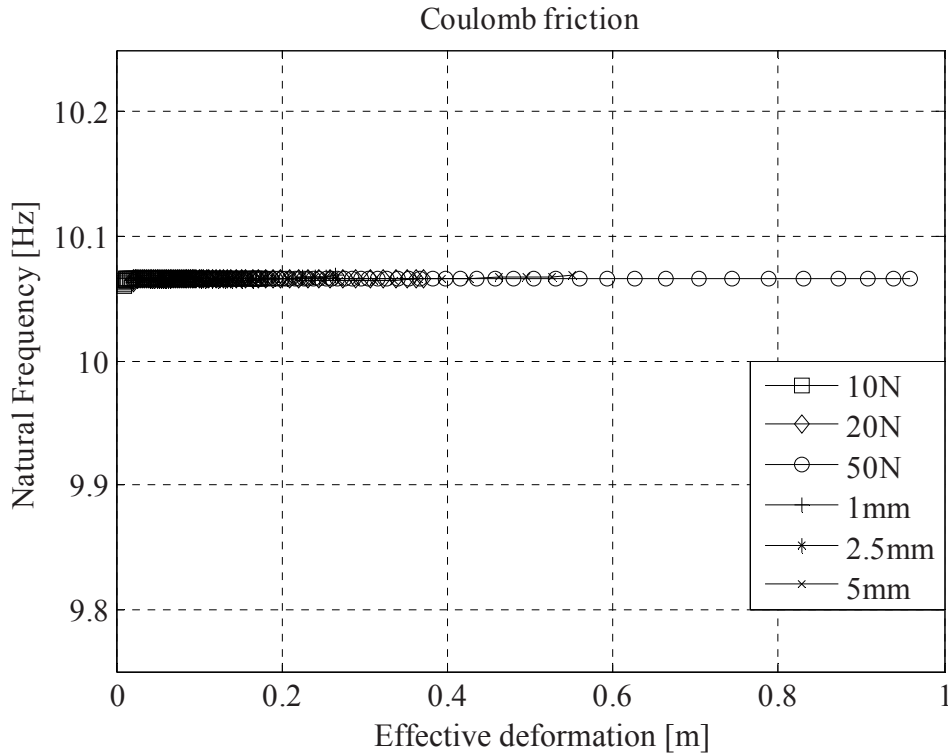
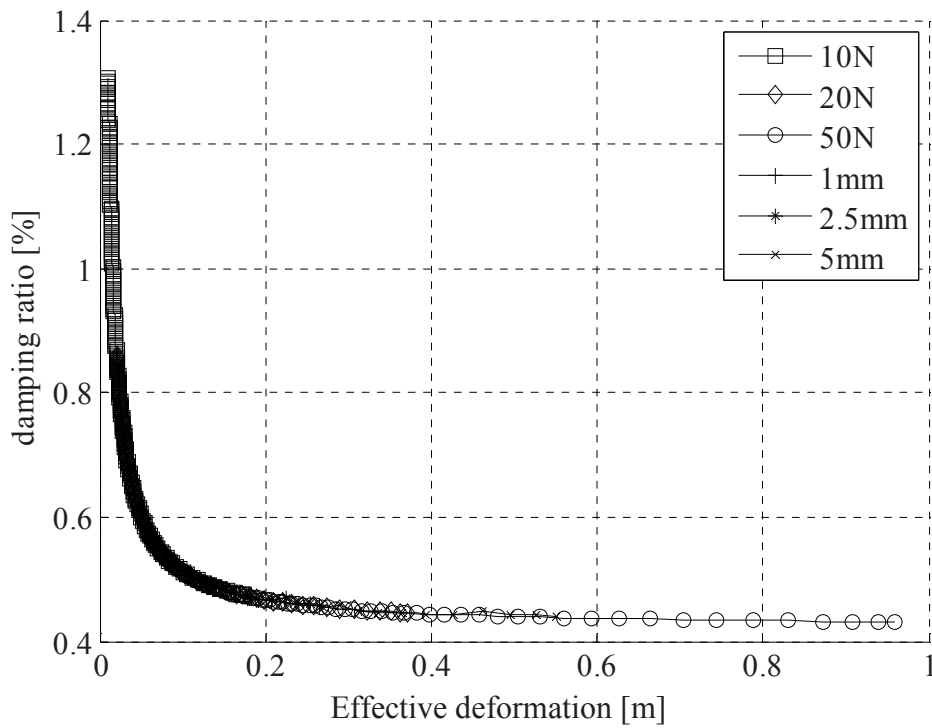


Fig.4: CONCERTO's analysis of both FRF and transmissibility of a system with linear damping and hardening cubic spring: (a) natural frequency and (b) damping as functions of the mount displacement amplitude

The plots in Fig. 5(a,b) are the results of the analysis of the FRF and transmissibility properties of a system with Coulomb damping. The constant natural frequency, Fig. 5 (a), is indicative of a linear stiffness element, whilst the decrease in damping with amplitude with hyperbolic trend is typical of Coulomb damping.



(a)



(b)

Fig. 5: CONCERTO's analysis of both FRF and transmissibility of a system with Coulomb damping : (a) natural frequency and (b) damping as functions of the response displacement amplitude

Finally, the natural frequency and damping ratio as function of the mount displacement amplitude of a system with combined nonlinearities (cubic stiffness + quadratic damping) are shown in Fig.6

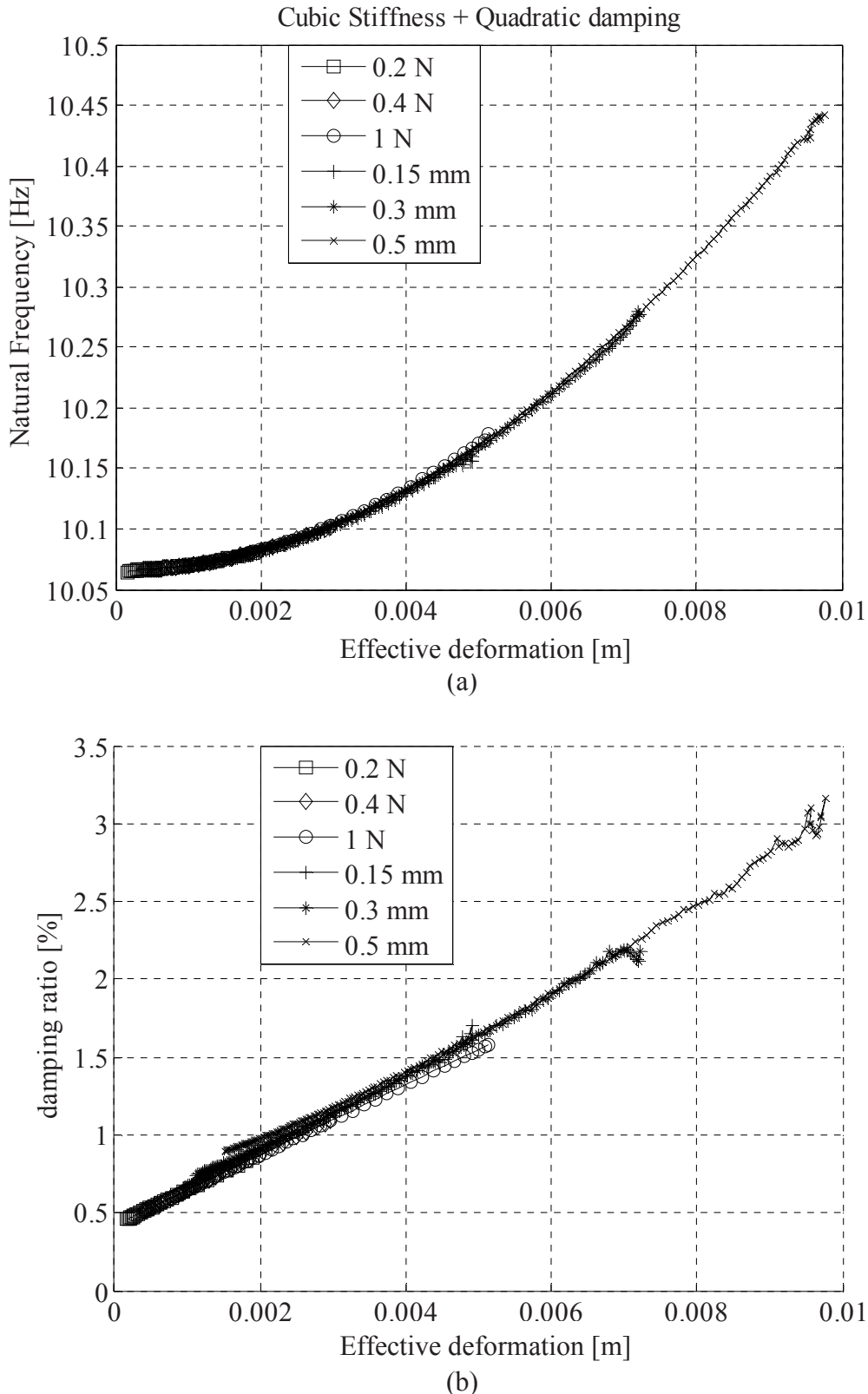


Fig.6: CONCERTO's analysis of both FRF and transmissibility of a system with a combination of nonlinearities (hardening cubic spring + quadratic damping): (a) natural frequency and (b) damping as functions of the response displacement amplitude

Figures 4-6 show that there is no difference between the natural frequency and damping ratio identified with CONCERTO when this is applied to FRF or transmissibility data.

CONCLUSION

Identification of structural nonlinearities in dynamics is becoming a pressing issue. The reliability of models and their accuracy can only improve if nonlinearities are accounted for. Different methods which aim at extracting the nonlinear stiffness and damping have been proposed which rely on the Frequency Response Function of the system. However, there are practical cases in which the FRF cannot be measured and instead a base-excitation test needs to be conducted (e.g. airworthiness certification of some aerospace items). It remains the question if an established FRF method, implemented in CONCERTO, can be extended and used for transmissibility measurements.

The numerical study conducted in this paper shows that the algorithm produces the same results whether it is fed with absolute transmissibility or FRF data. It is important to highlight that for a better physical interpretation of the results, these needs to be plotted as function of the effective displacement of the spring/damper (i.e. the elements supporting the mass or the mount): this displacement is the absolute displacement of the mass in case of force excitation and the relative displacement between the mass and the base when the system is excited at the base.

Albeit of important practical value, more work is needed to improve the identification method. Firstly, there is need to assess the validity of the SDOF assumption upon which is based. A different shortfall to tackle is the assumption of amplitude-dependent nonlinearities. Most notably, transmissibility tests are required for vibration isolation devices such as rubber mounts: these present not only amplitude-dependent stiffness but also a marked frequency-dependency which need to be extracted.

ACKNOWLEDGMENT

This research was conducted at the AgustaWestland Bristol University Technology Centre (AWB-UTC) under the programme “Nonlinear Modal Testing” funded by AgustaWestland Helicopters Company. Also, the authors thank Trevor Walton, AgustaWestland, for his support and fruitful discussions on the topic.

REFERENCES

1. Worden, K. and G.R. Tomlison, *Nonlinearity in Structural Dynamics*. 2001: Institute of Physics.
2. Kerschen, G., et al., *Past, present and future of nonlinear system identification in structural dynamics*. *Mechanical Systems And Signal Processing*, 2006. **20**(3): p. 505-592.
3. Masri, S.F. and T.K. Caughey, *Nonparametric Identification Technique For Non-Linear Dynamic Problems*. *Journal Of Applied Mechanics-Transactions Of The Asme*, 1979. **46**(2): p. 433--447.
4. He, J. and D.J. Ewins. *A Simple Method of Interpretation for the Modal Analysis of Nonlinear Structures*. in *IMAC V*. 1987. London.
5. Goge, D., et al., *Detection and description of non-linear phenomena in experimental modal analysis via linearity plots*. *International Journal Of Non-Linear Mechanics*, 2005. **40**(1): p. 27--48.
6. Link, M., et al., *An Approach to Non-linear Experimental Modal Analysis*, Proceeding of IMAC XXVIII, Jacksonville, FL, 2010
7. Carrella, A and Ewins DJ, *Identifying and quantifying structural nonlinearities in engineering applications from measured frequency response functions*, *Mechanical Systems and Signal Processing*, article in press

Steer Control of Motorcycle by Power Steering

Takayuki Koizumi, Nobutaka Tsujichi, Tetsuaki Takemura
Department of Engineering, Doshisha University,
1-3, Tataramiyakodani, Kyotanabe-city, Kyoto, 610-0321, Japan

ABSTRACT

The introduction of the power steering will be thought also the motorcycle in the future. It is because of an increase of a large-scale motorcycle in recent years and the possibility for rider's supplementary role by an electric motor. In this research, the authors do the experiment that uses the motorcycle, and examine the steering wheel torque characteristic when the corner running for the electric power steering system. Finally, experimental results indicated that steering torques from the rider are similar at the low speed. It means there are possibility to construct the power steering system for the motorcycles at low speed.

Introduction

Recently, the motorcycle has enlarged because of the exhaust emissions regulations and the performance. The number of riders in his/her teens decreases, and the number of riders in his/her fifties has increased. The average age of the rider is as a whole 42.7 years old in Japan. The change is seen in maker's lineup as the rider ages, and the motorcycle also has the possibility that the steering wheel assistance function is introduced in the future.

As for the steering wheel system of the four-wheeled vehicle, a steer-by-wire system is adopted now[1]. This system controls the angle of the tire with the motor and the steering wheel and the tire are not mechanically connected. However, in case of the motorcycle, from the problem of weight, the possibility that an electric power steering by an electric motor is introduced is high. Therefore, we construct the power steering system equipped with the DC motor in an ordinary steering wheel in the present study.

In this study, the authors examined the steering torque at the only low speed, because of the occasion of the experimental location and safety.

1. Composition of power steering

Figure 1 shows the composition of the power steering. At first, when the rider turns the steering wheel to changes the traveling direction, the torque sensor and the rotary encoder detect the torque that the rider gave and the direction of the rotation and the rotational speed of the steering wheel. And the speed sensor installed in the body detects the vehicle speed. These values are sent to the controller, and the control signal is sent from the controller to the motor driver. Afterwards, the DC motor is rotated by a specified rotational speed, and the tire is steered through the gear. In this study, we use the warp gauge installed in the steering wheel as a torque sensor.

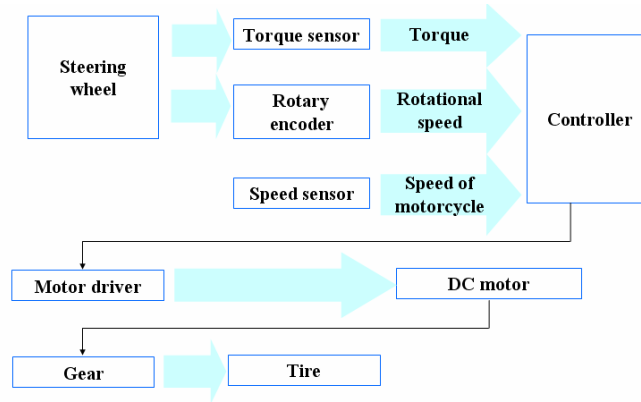


Fig. 1 Composition of power steering

2. Steering wheel characteristic for vehicle speed

There is a necessity that the assistance torque that assists in the steering wheel torque is adjusted according to the vehicle speed because of safety and the steer feeling improvement. The adjustment of this assistance torque is especially important for the motorcycle. A big assistance torque is necessary when vehicle speed is high, and small assistance is necessary when it is low as shown in [Figure 2](#). Therefore, there is necessity to investigate the relation between a speed of the vehicle and a necessary assistance torque by the experiment.

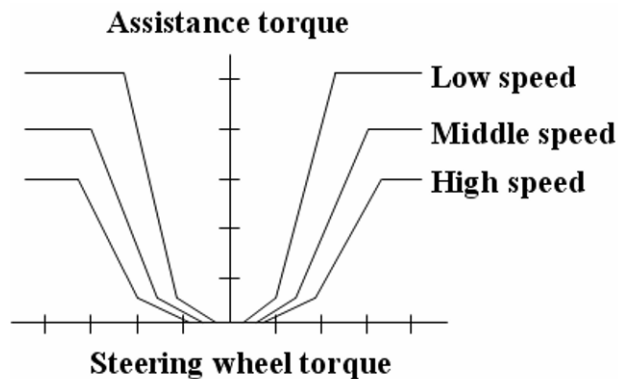


Fig. 2 Assistance torque and Steering wheel torque

3. Experimental equipment

We experiments with the experiment machine. [Figure 3](#) shows Kawasaki ZRX400. This experimental vehicle is the most general size in the two-wheeled motor vehicle in Japan now. [Table 1](#) shows details of the experimental vehicle. The steering wheel torque is measured by using Kyowa Electronic Instruments KFG-3-120-D16-11L3M2S that shows in [Figure 4](#). The measurement place of the swerve is a part in a parallel direction and the vertical direction against the steering wheel axis near the handlebar. It is shown in [Figure 4](#). Because the gauge picks up an extra transformation when

loads other than the direction of steer to the handlebar, the measurement with high accuracy cannot be done. Then, the gauge is pasted to four places of the direction where the steering wheel is rotated the steer, and four active gauge method is used as a connection method to the bridged circuit. The steering torque is recorded by TEAC es8 at 100Hz sampling frequency. The bend can be output by the twice while deleting compression, hitching and twist by using this connection method. When the relation between these measured swerve and steering wheel torque is proofread, it comes to be able to specify the steering wheel torque only by measuring the swerve. The steering wheel torque can be requested as follows.

$$T_S = (F_{SL} + F_{SR}) \times L$$

T_S : Steering wheel torque F_{SL} : Load to handlebar of steering wheel axis with left hand F_{SR} : Load to handlebar of steering wheel axis with right hand L : Length from steer axis to action point of handlebar load



Fig. 3 Kawasaki ZRX400

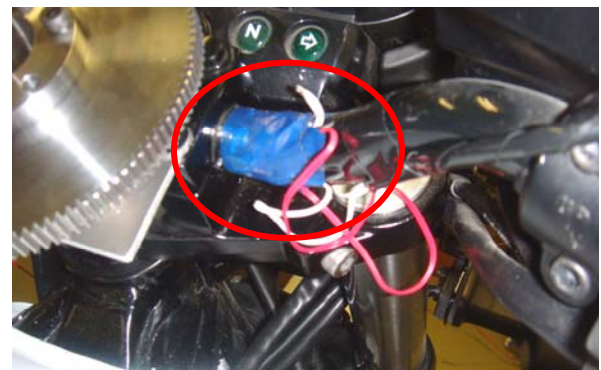


Fig. 4 KYOWA KFG-3-120-D16-11L3M2S

Table 1 Specification of experimental motorcycle

| Detail | ZRX400 (Kawasaki) |
|--------------------------|-------------------|
| Overall length | 2100 [mm] |
| Overall width | 755 [mm] |
| Overall height | 1095 [mm] |
| Wheelbase | 1440 [mm] |
| Minimum ground clearance | 120 [mm] |
| Total weight | 198 [kg] |

4. Experimental method

To examine the relation between the corner radius and the steering torque, we measured the steering torque when running the corner of 5m in the radius and 10m. The motorcycle speed was assumed to be 15km/h when 5m in radius, 20km/h when 10m in radius. These are the speeds that can start most smoothly in each corner. Figure 6 illustrates the experimental method. The motorcycle accelerated enough in the straight-line before it entered the corner and the speed did not fall when the corner running.

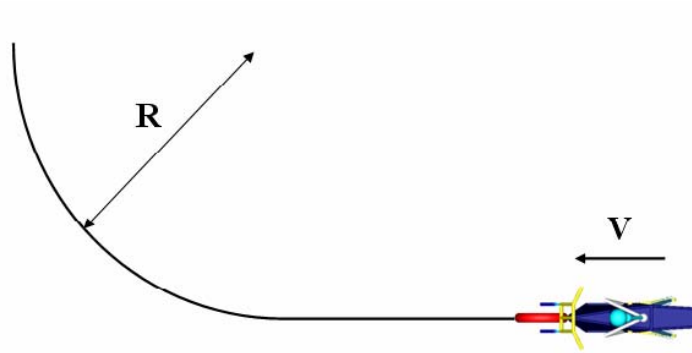


Fig. 5 Corner radius and running route

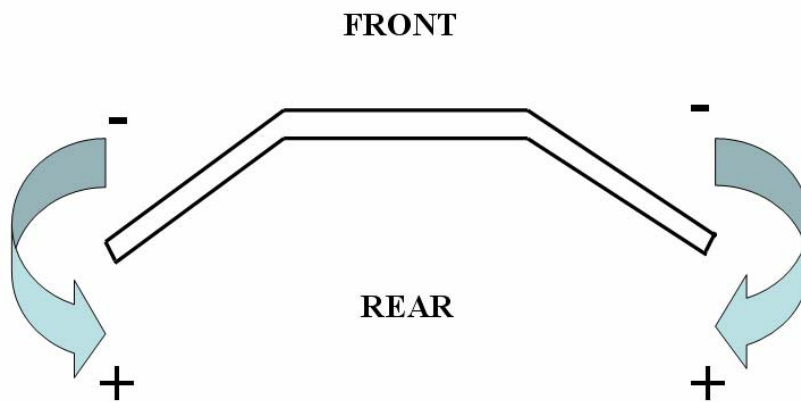


Fig. 6 The direction of steering torque

5.Experimental result

Figure 8 shows the steering torque when running 15 km/h in the corner of 5m in radius. And Figure 9 shows the steering torque when running 20 km/h in the corner of 10m in radius. These two experimental results show that the change is not seen so much in the input of the steering torque though change the corner radius when it is low-speed. It was clarified to the steering wheel torque input to tend to have looked like well though it ran in the corner where the radius was different.

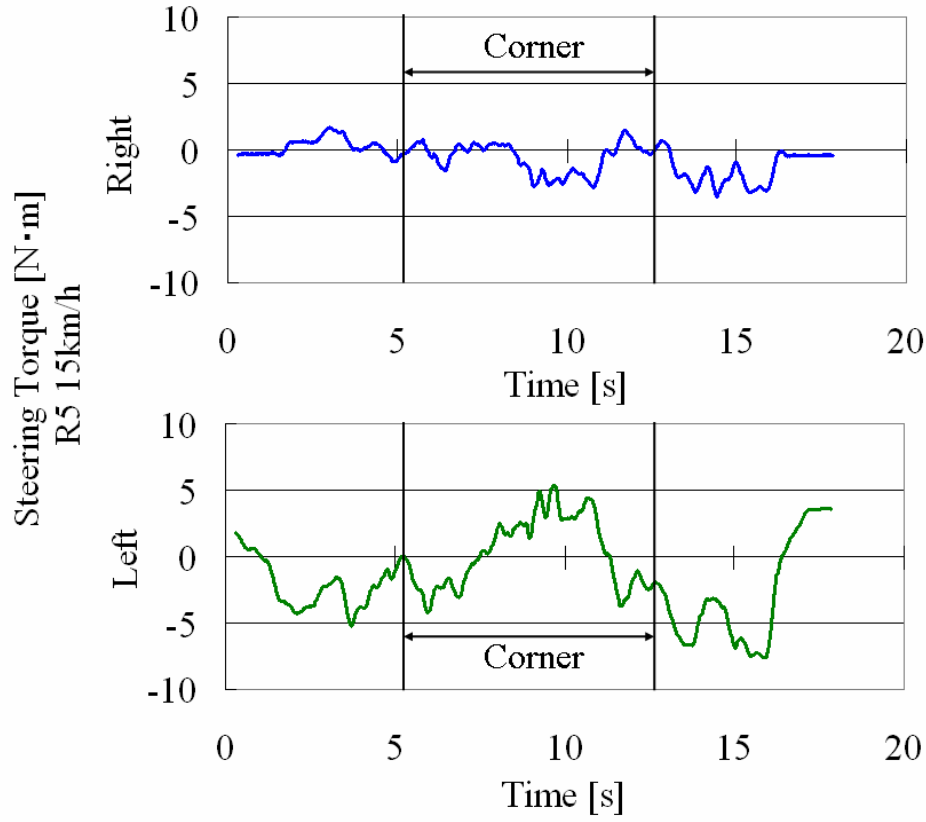


Fig. 7 Steering torque <R5 15km/h>

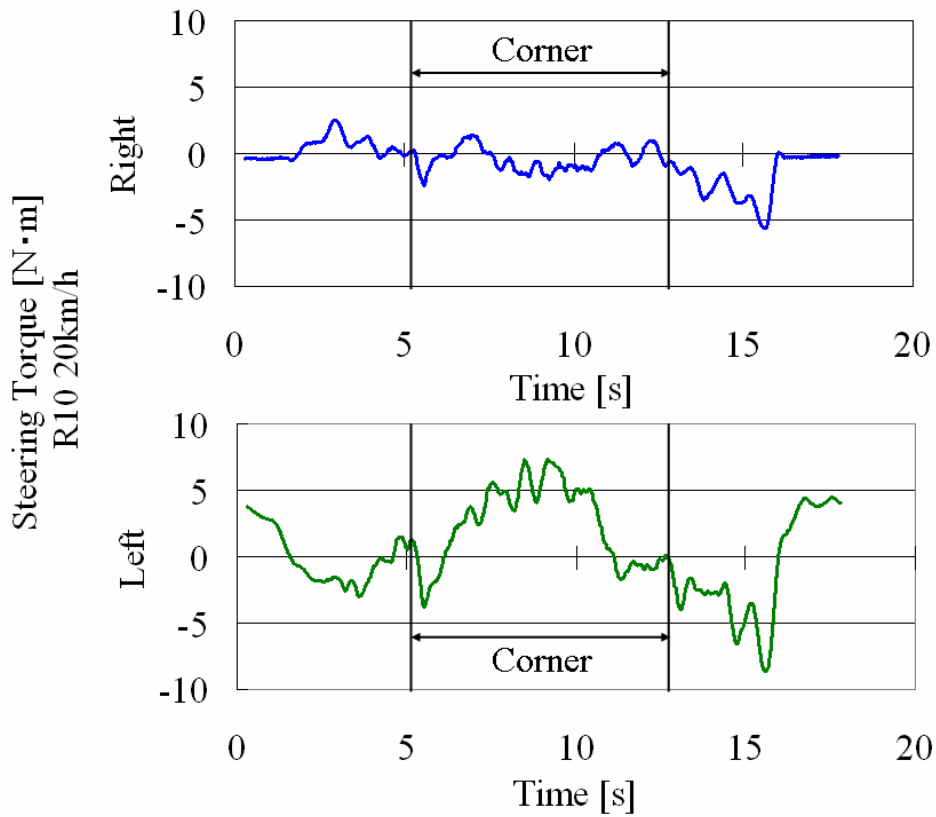


Fig.8 Steering torque <R10 20km/h>

CONCLUSIONS

As for the steering torque, the change is not so seen even if the corner radius changes when it is low-speed. Moreover, a lot of similar points are seen in the steering wheel torque even if the corner radius is changed. And it was clarified to the steering wheel torque input to tend to have looked like well even if running in the corner where the radius was different, and showed the possibility of the power steering in the motorcycle.

REFERENCE

- [1] Ryokan Takebayashi, Kochi University of Technology graduate school,,Development of a small-sized electric vehicle with driving control mechanism by steer-by-wire 17-18
- [2] Zhao Xue-Ping, Li Xin, Chen Jie, Men Jin Lai School of Mechanical Engineering, Shanghai Jiaotong University, No.800 Dong Chuan Road, Shanghai, China Parameter design and application of steering characteristic curve in control for electric power steering
- [3] Ji-Hoon kim, Jae-Bok Song Department of Mechanical Engineering, Korea University, 5 Anam-dong, Sungbuk-gu, Seoul 136-701, South Korea Control logic for an electric power steering system using assist motor
- [4] Takayuki Koizumi, Nobutaka Tsuziuchi, Yuya Ezaki, Department of Mechanical Engineering, Doshisha University, Tatara 1-3, Kyotanabe, Kyoto, Japan Disturbance Rejection Control in Motorcycle
- [5] Nozomi Katagiri, Yoshitaka Marumo, Hitoshi Tsunashima College of Industrial Technology, Nihon University, 1-2-1 Izumi-cho, Narashino, Chiba, 275-8575 Japan Improved Handling and Stability of Two-Wheeled Vehicles Using Steer-By-Wire Technology
- [6] Yuuya Aikawa, Ichiro Kageyama, Yukiyo Kuriyagawa, College of Industrial Technology, Nihon University, 1-2-1 Izumi-cho, Narashino, Chiba, 275-8575 Japan Study on Motorcycle Dynamics and Tire Characteristics

Estimating Low-Bias Frequency Response Using Random Decrement

Rune Brincker

Aarhus School of Engineering, Aarhus University,
Ny Munkegade 120, Building 1521, DK-8000 Aarhus C, Denmark

Anders Brandt

Department of Industrial and Civil Engineering, University of Southern Denmark,
Niels Bohrs Allé 1, DK-5230 Odense M, Denmark

NOMENCLATURE

| | |
|--|-------------------------------------|
| t, t_k : | Continuous, discrete time |
| $x(t), y(t)$: | Signals, stochastic processes |
| $h(t)$: | Impulse response function |
| ω : | Angular frequency |
| $X(\omega), Y(\omega)$: | Signal Fourier transforms |
| $\hat{G}_{XX}(\omega), \hat{G}_{YY}(\omega)$: | Spectral densities |
| $H_1(\omega), H_2(\omega)$: | Frequency response functions |
| $\gamma(\omega)$: | Coherence |
| $D_{XX}(\tau), D_{XY}(\tau)$: | Random decrement functions |
| $\hat{D}_{XX}(\tau), \hat{D}_{XY}(\tau)$: | Random decrement function estimates |

ABSTRACT

It is well known that in order to minimize the influence of leakage bias in frequency response function (FRF) estimates, smooth windows should be applied in the FFT processing. It is also normal practice to use self windowing excitation signals whenever possible. However, in many cases FRFs have to be estimated on systems where the excitation signal cannot be altered. Since random data can be compressed in a random decrement function, and since this procedure introduces a natural window, using this technique significantly reduces the influence of leakage bias, and thus, can be used as an alternative to Welch based estimates in cases where the signals involved are random. This means that almost bias-free FRF estimates can be obtained from stationary random excitation. In the paper it is shown how the random decrement technique can be applied to process the time series, and the level of bias on the FRF is estimated and compared to normal Welch based FRF estimates.

INTRODUCTION

The way most vibration data acquisition systems are designed is based on the premises in the 1970's when the first FFT analyzers became available. One restriction in those days was the price of memory, and thus the way the data processing was implemented was to reduce data as soon as possible after acquisition. The result became the frequency block averaging that is commonly used today, usually referred to as Welch averaging after [1]. This procedure is well investigated and a current discussion of its use can be found in [2].

It is well known that Welch's method includes bias and random errors and that these errors are contradictory. A trade-off between bias and random errors thus has to be made, given that a certain amount of data is available. Recently [5] investigated this thoroughly, and the main outcome of their paper, of interest in the present paper, is that the minimum errors (bias and random) using Welch's method are obtained by using a half-sine window and 67% overlap processing instead of the more traditionally advocated Hanning window with 50% overlap.

Alternative techniques for computing FRFs such as Danielle's method, or "smoothed periodogram method", and the original Blackman-Tukey method, where correlation functions are computed followed by applying FFT, are also well known and described in for example [3]. However, since using Welch's method is an established "de facto standard" in commercial analysis systems, we will focus on this method for estimating FRFs in the comparisons below.

In [4] it was shown that the random decrements (RD) technique can be used to compute frequency responses from impact testing. The RD technique offers an alternative to the above mentioned techniques for FRF estimation where the basic idea is in line with the Blackman-Tukey method, but where the estimation procedure is buffer oriented like Welch. In the following, a method using RD on systems excited by random forces is introduced and compared with the traditional technique using Welch's method.

WELCH'S METHOD

We will assume that the signals exciting a linear system are random. Welch's method is based on dividing the total data into a number of overlapping segments, applying a time window to each segment, and then computing the DFT of each windowed segment. When these steps have been taken, the spectral densities are estimated by

$$\begin{aligned}\hat{G}_{XX}(\omega) &= \frac{1}{K} \sum_{k=1}^K X_k^*(\omega) X_k(\omega) \\ \hat{G}_{XY}(\omega) &= \frac{1}{K} \sum_{k=1}^K X_k^*(\omega) Y_k(\omega) \\ \hat{G}_{YX}(\omega) &= \frac{1}{K} \sum_{k=1}^K Y_k^*(\omega) X_k(\omega) \\ \hat{G}_{YY}(\omega) &= \frac{1}{K} \sum_{k=1}^K Y_k^*(\omega) Y_k(\omega)\end{aligned}\tag{1}$$

where $X_k(\omega)$ is the DFT result of the k-th time windowed segment $x_k(t)$. Frequency Response Function (FRF) estimates $\hat{H}_1(\omega)$ and $\hat{H}_2(\omega)$ are estimated from

$$\begin{aligned}\hat{H}_1(\omega) &= \frac{\hat{G}_{XY}(\omega)}{\hat{G}_{XX}(\omega)} \\ \hat{H}_2(\omega) &= \frac{\hat{G}_{YX}(\omega)}{\hat{G}_{YY}(\omega)}\end{aligned}\tag{2}$$

As mentioned in the introduction, estimates in Eq. (2) are affected by bias as well as random errors. For analysis around a resonance of a mechanical system, the bias error is in principle dependent on the ratio of the resonance bandwidth and the frequency increment [3, 2], $B_r / \Delta f$, where $B_r \approx 2\zeta_r f_r$, and it is highest at the frequency line closest to the resonance frequency. The normalized random error is more complicated. In the case used in the present paper with no contaminating noise, however, as shown in [5], the random error is minimized by using the half-sine window with 67% overlap processing.

A good alternative to the above mentioned solutions to the bias problem is to use random signals and then reducing the bias by estimating RD functions and afterwards estimating the Frequency Response Functions (FRFs) from the RD functions. In

the following a short introduction to RD functions is given. It is shown how FRFs can be estimated from the RD functions, and finally the bias reduction is illustrated on a simulated case with two degrees-of-freedom.

THE RANDOM DECREMENT ALGORITHM

Some initial considerations about using the RD technique for modal data processing have been given in [6] and [7]. An introduction to the general RD technique is given in [8]. The Random decrement function is defined as the conditional expectation of a stochastic Process $x(t)$

$$D_{XX}(\tau) = E[x(t_k + \tau)|T(x(t_k))] \quad (3)$$

and from a time series the corresponding estimate is found as the conditional mean

$$\hat{D}_{XX}(\tau) = \frac{1}{N} \sum_{k=1}^N x(t_k + \tau)|T(x(t_k)) \quad (4)$$

where the triggering condition $T(x(t_k))$ is given by for instance

$$\begin{aligned} T(x(t_k)): \quad x(t_k) &= a \\ T(x(t_k)): \quad x(t_k) &> a \end{aligned} \quad (5)$$

This defines an auto RD function where the averaging and the triggering are performed on the same time series. Corresponding cross RD functions can be defined and estimated as

$$\begin{aligned} D_{YX}(\tau) &= E[y(t_k + \tau)|T(x(t_k))] & \hat{D}_{YX}(\tau) &= \frac{1}{N} \sum_{k=1}^N y(t_k + \tau)|T(x(t_k)) \\ D_{XY}(\tau) &= E[x(t_k + \tau)|T(y(t_k))] & \hat{D}_{XY}(\tau) &= \frac{1}{N} \sum_{k=1}^N x(t_k + \tau)|T(y(t_k)) \end{aligned} \quad (6)$$

ESTIMATING FRF's FROM RANDOM DECREMENT FUNCTIONS

If we assume the classical linear input-output relation between $x(t)$ and $y(t)$

$$y(t) = \int_{-\infty}^t h(t - \eta)x(\eta)d\eta \quad (7)$$

then it is easy to show that the following relations exist between the RD functions

$$\begin{aligned} D_{YX}(\tau) &= \int_{-\infty}^{\tau} h(t - \eta)D_{XX}(\eta)d\eta \\ D_{YY}(\tau) &= \int_{-\infty}^{\tau} h(t - \eta)D_{XY}(\eta)d\eta \end{aligned} \quad (8)$$

Now taking the Fourier transform of the RD functions defines the Fourier transform pairs

$$\begin{aligned}
D_{XX}(\tau) &\leftrightarrow Z_{XX}(\omega) \\
D_{XY}(\tau) &\leftrightarrow Z_{XY}(\omega) \\
D_{YX}(\tau) &\leftrightarrow Z_{YX}(\omega) \\
D_{YY}(\tau) &\leftrightarrow Z_{YY}(\omega)
\end{aligned} \tag{9}$$

and the Fourier transform of Eq. (9) defines the corresponding FRF estimates

$$\begin{aligned}
\hat{H}_1(\omega) &= \frac{\hat{Z}_{XY}(\omega)}{\hat{Z}_{XX}(\omega)} \\
\hat{H}_2(\omega) &= \frac{\hat{Z}_{YY}(\omega)}{\hat{Z}_{YX}(\omega)}
\end{aligned} \tag{10}$$

COMPARING RD WITH TRADITIONAL FRF ESTIMATES

In the following a 2 degree-of-freedom system is loaded by Gaussian white noise, the response is simulated using the theoretical FRF matrix and FFT, and finally the FRF's are estimated by the traditional technique (in the following denoted "Welch") and by RD functions. All simulations were made using 1,048,576 data points, and the damping, ζ , and the data segment length, N , were varied.

The data segment length is also used as the total size of the buffer window used for estimation of RD functions. An example of RD functions is shown in [Figure 1](#). As it appears, the window buffer is not defined to be symmetrical around the triggering point (where the spike is located in $D_{XX}(\tau)$). The reason is that the buffering window should be defined in order to include maximum information, and since the function $D_{YX}(\tau)$ only has system information for negative times, the buffer is defined in order to include the RD functions for negative time lags.

The corresponding FRF's, estimated as $\hat{H}_1(\omega)$ according to Eqs. (2) and (10) for both techniques, are shown in [Figure 2](#). It can be seen that at the resonance peak, the bias error in the RD estimate is significantly smaller than the bias error in the Welch estimate. The full band errors ε_0 are quantified by calculating the RMS value of the difference $|H(\omega) - \hat{H}_1(\omega)|$, i.e. this error measure is the sum of the bias and random error. The narrow band error ε_1 is calculated as the maximum difference value, at the peak. Typical errors are shown in [Tables 1](#) and [2](#).

It appears that the random error of the estimates based on the RD technique is larger than for Welch estimates, which can be seen in larger full band errors in [Table 1](#). The bias errors at the resonance peak are however considerably smaller in the RD estimates than in the Welch estimates. This is to be expected, as the trade-off between bias and random error is applicable also to RD functions. The noise properties of RD functions are, however, different from the noise properties of the more well-known correlation functions, and this will be further analyzed in future work.

Table 1. Full band error, ε_0

| N | $\zeta = 0.2\%$ | | | | | $\zeta = 1\%$ | | | | |
|-------|-----------------|------|------|------|------|---------------|------|------|------|------|
| | 256 | 512 | 1024 | 2048 | 4096 | 256 | 512 | 1024 | 2048 | 4096 |
| Welch | 0,60 | 0,57 | 0,50 | 0,23 | 0,09 | 0,18 | 0,08 | 0,02 | 0,01 | 0,02 |
| RD | 0,85 | 1,06 | 1,76 | 1,77 | 1,82 | 0,77 | 0,81 | 0,82 | 0,81 | 0,82 |

Table 2. Maximum error, ε_1

| N | $\zeta = 0.2\%$ | | | | | $\zeta = 1\%$ | | | | |
|-------|-----------------|------|------|------|------|---------------|------|------|------|------|
| | 256 | 512 | 1024 | 2048 | 4096 | 256 | 512 | 1024 | 2048 | 4096 |
| Welch | 3,35 | 4,15 | 8,59 | 3,47 | 3,32 | 1,28 | 0,74 | 0,38 | 0,18 | 0,14 |
| RD | 1,95 | 2,78 | 0,40 | 0,24 | 0,35 | 0,09 | 0,01 | 0,07 | 0,13 | 0,30 |

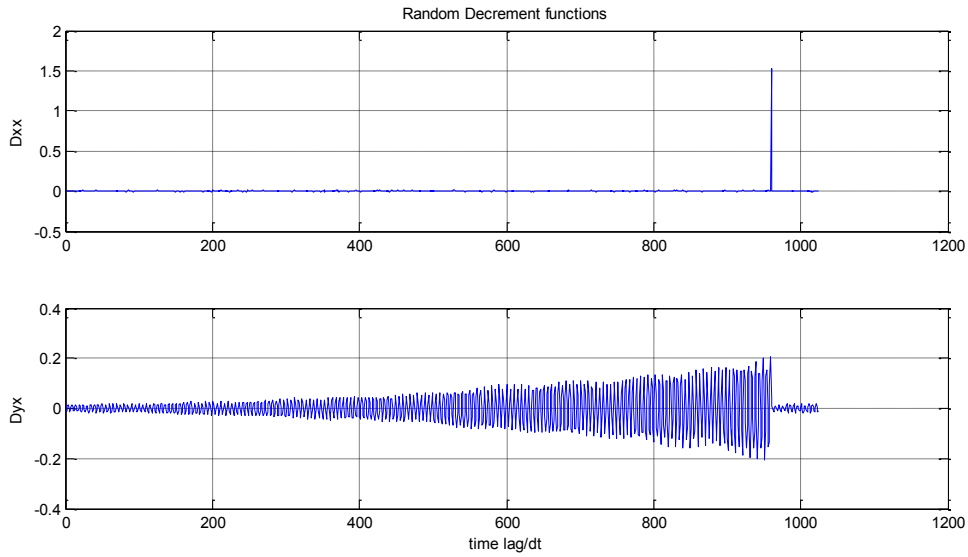


Figure 1. Example of RD functions $D_{XX}(\tau)$ and $D_{YX}(\tau)$, in this case the damping $\zeta = 0.2\%$ and $N = 1024$.

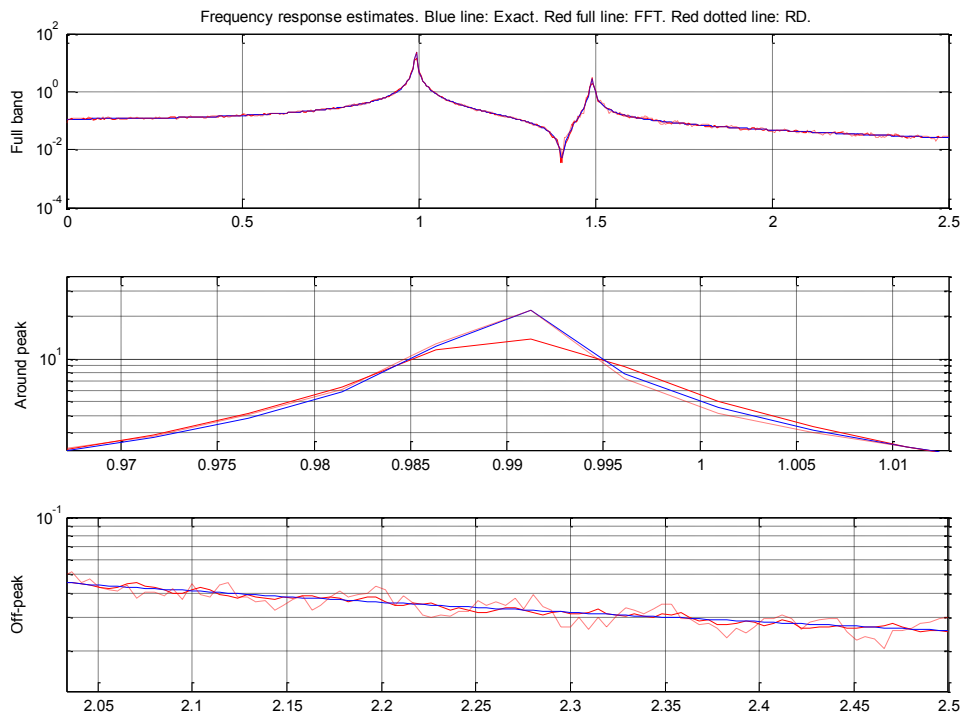


Figure 2. Example of estimation of FRF's, in this case the damping $\zeta = 0.2\%$ and FFT block size $N = 1024$.

CONCLUSIONS

The RD technique has been introduced and used on simulated modal data in order to compare the bias on the FRF estimates estimated from RD functions with the bias from the traditional Welch based FRF estimates. The RD based technique is buffer oriented like Welch, but is based on the same idea as Blackman-Tukey, i.e. the FRF is estimated by taking a Fourier transform of the bias-free time domain function. Therefore, as expected, the RD based FRF estimation shows a significantly lower bias for the same buffer size (data segment size) than the Welch based FRF estimation. On the other hand, the RD based FRF estimates has larger random errors. These random errors can be reduced by introducing a window on the time domain function; this is to be investigated further in future investigations. Further, RD-based FRF estimates might have a special value in cases where effects of small non-linearities are to be studied.

REFERENCES

- [1] Welch, P.: *The Use of Fast Fourier Transform for the Estimation of Power Spectra: A Method Based on Time Averaging Over Short, Modified Periodograms*, IEEE Trans. On Audio and Electroacoustics, 1967, AU-15, pp. 70-73.
- [2] Brandt, A.: *Noise and Vibration analysis – Signal Analysis and Measurement Procedures*, Wiley, 2011.
- [3] Bendat, J. & Piersol, A. G.: *Random Data: Analysis and Measurement Procedures*, 4th Ed., Wiley Interscience, 2010.
- [4] Brincker, R. and Brandt, A.: *Random Decrement Signal Processing of Modal Impact Test Data*, Proc 28th International Modal analysis Conference, Jacksonville, Florida, USA, Feb. 1-4, 2010.
- [5] Antoni, J. & Schoukens, J.: *Optimal Settings for Measuring Frequency Response Functions with Weighted Overlapped Segment Averaging*, IEEE Transactions On Instrumentation and Measurement, 2009, 58, pp. 3276-3287.
- [6] Rasmussen, J.C. and Brincker, R.: *Estimation of Frequency Response Functions by Random Decrement*. Proc 14th International Modal analysis Conference, Dearborn, Michigan, USA, Feb. 12-15, 1996, pp. 246-252.
- [7] Brincker, R. and Rasmussen, J.C.: *Random Decrement Based FRF Estimation*. Proc 15th International Modal analysis Conference, Orlando, Florida, USA, Feb. 3-6, 1997, pp. 1571-1576.
- [8] Rasmussen, J.C. *Modal Analysis Based on the Random Decrement Technique*. Ph.D. Thesis, Aalborg University, Department of Building Technology and Structural Engineering, 1997.

A study of mechanical impedance in mechanical test rigs performing endurance testing using electromagnetic shakers

D. Di Maio, D. J. Ewins

Dario Di Maio, Post-Doctoral researcher, University of Bristol (UK)

Prof. David Ewins, Director of Blade, University of Bristol (UK)

ABSTRACT

Aircraft engine components, such as bladed discs, are subjected to high levels of vibration due to their service conditions and vibratory stresses can reduce the expected operational life. High Cycle Fatigue (HCF) is the most common cause of component failure in gas turbine engines. Laboratory testing is important for understanding the fatigue properties of materials and for producing a database eventually used during the design of new components. HCF test can be performed in the laboratory using a test rig on which is installed a test structure, connected to an electromagnetic shaker supplying the excitation. A simple test rig can be made comprising a holding block connected by push rod to the armature of a shaker so as to produce a base excitation. Such a test rig can be specifically designed to increase the test piece vibration levels by tuning it to one resonance of the structure. However, in doing so, a test rig of this type can present an impedance which is mismatched with the shaker, thereby causing dissipation of the excitation force. Any power loss can be a problem, exacerbated by components presenting high levels of structural damping, because of the higher force levels required to achieve high levels of vibration. Hence, any HCF test can be ineffective because of the diversion of shaker power from the test component to other parts of the test setup. The aim of this paper is to study the impedance mismatch between test rig and shaker by modelling a simple test rig, using a lumped-parameter model, for designing and measuring vibrations of the test rig to identify its weakness for HCF.

NOMENCLATURE

| | | | |
|----------|--------------------------|-----------|---------------------------|
| M_{TS} | Mass test structure | K_{Rod} | Stiffness rod |
| K_{TS} | Stiffness test structure | M_{SA} | Mass shaker armature |
| C_{TS} | Damping test structure | K_{SA} | Stiffness shaker armature |

| | | | |
|-----------|--------------------|----------|-------------------------|
| M_{HB} | Mass holding block | C_{SA} | Damping shaker armature |
| C_{Rod} | Damping rod | | |

1 Introduction

High Cycle Fatigue (HCF) [1] is one of the commonest causes of component failure in gas turbine engines and there are many sources of HCF damage such as: (i) aerodynamic excitation, (ii) mechanical vibrations and (iii) airfoil flutter. Although new engine designs have reduced problems caused by vibratory stress, HCF is still one of the main concerns of turbo machineries. The standard practice for HCF risk assessment, for example of a blade, can be summarized briefly as follows. There are two important steps during the Finite Element (FE) model analysis: (i) stress analysis and (ii) structural dynamics analysis. One is to determine the mean stresses and the other is to determine resonant frequencies, mode shapes and dynamic stresses. Predicted resonant frequencies are compared with integral order engine excitation data on a Campbell diagram in which the crossing of natural frequencies of the blades and the engine excitation can be determined. This process is crucial to predict the strength of the excitation driver which is associated to dynamic stress. When this process is completed positively, a component can be manufactured and, subsequently, tested both in the laboratory and in engine verification testing. Technology for HCF testing of metallic components became more established during the past decades by using either, for example, electromagnetic (EM) shakers or an air jet or a pulsed air jet. These could produce levels of force sufficient for exciting up to large vibration test structures. Hence, a consistent database of fatigue test data could be produced and used for: (i) the design of metallic components and (ii) the stress analysis prediction. The introduction of new materials, such as carbon fibre based composites, in the design process required the production of a new database of fatigue or “endurance” data set, because of the mechanical failure of composite materials being very different from the metallic ones. The same technology used for running HCF on metallic component was so used for the composite components. This paper presents some experimental results, obtained during the course of several months, of HCF testing performed on composite components using an electromagnetic shaker. A mechanical test rig was designed and built to be tuned with one resonance of the component to be test for HCF. This was capable of exciting a specimen to high levels of vibration but driving the shaker to work out of specification. Impedance mismatched between the shaker and the test rig is the cause of the underperforming shaker and measurements are provided to support this study.

2 Problem background

Carbon fibre materials, as already introduced, are increasingly used for manufacturing engine components such as fan blades, vanes or casings. Stress limits of composite are studied both statically and dynamically by performing several tests in the laboratory. The amount of data generated is then used to characterize the material properties which are used to produce more reliable FE models. Modal parameter estimation can be performed by modal analysis using different test approaches such as impact testing or phase resonance testing. The vibratory stress level of a component can be determined using either air jet or electromagnetic shaker excitation. Air jet excitation methods, such as constant or pulsed flow, present some limitations when compared with the EM

shaker. In fact, the excitation can be produced: (i) by flutter, as happens in the constant flow air jet, or (ii) by periodically impacting the structure with pulsed air jets. The first method can usually be performed on first-order modes- for example, 1F, 2F and 1T, all of which can be “easily” excited by flutter whereas it is more difficult to excite high order modes with this method. A pulsed air jet offers a better control of the excitation because it is produced by a perforated rotating disc whose rotational speed governs the excitation frequency of the tested component. This machine can produce excitation in a frequency bandwidth which depends on the max rotational speed and the number of holes of the sampling disc. The excitation force is applied to the component through a nozzle and its level depends on the pressure of the air impacting the component. The larger the impacting area, the larger is the force applied for a given constant pressure. However, a larger impacting area could produce a smaller response when higher order modes are excited because of nodal lines close to the excitation position. An EM shaker is a versatile exciter which can control the excitation frequency more precisely and for a wider frequency bandwidth as compared with previous exciters. Force transducers can be installed for measuring the force input into the structure allowing the measurements of a Frequency Response Functions (FRF). This cannot be done using the other two exciters because in there the force level can be only estimated.

Generally, when an HCF test is performed using an EM shaker, the test component is installed in a test rig. The simplest rig set up would be to connect a holding block to a shaker using a push rod to perform a base excitation. A component can be so constrained to the holding block which transfers the excitation force. Such a test rig configuration can be very sensitive to energy dissipation because of the many components connected. However a solution for enhancing its capability is to design a test rig to be tuneable to one resonance of a test piece.

3 Model of test rig configuration

A simple lumped parameter spring-mass model, representing a test rig and specimen, was used to simulate forced response so as to calculate some design parameters of the rig. **Figure 1** presents a simple model of the test rig in which the dashed boxes represent the test structure and the shaker armature, (a) and (b) respectively. This system provides three variables which can be used for designing and tuning the test rig, and these are: (i) the mass of the holding block (\mathbf{M}_{HB}), (ii) the stiffness of the rod (\mathbf{K}_{Rod}) and (iii) the mass of the armature (\mathbf{M}_{SA}). A first run of simulations was produced for designing the rod dimensions, diameter and length, and other simulations were performed for sensitivity analysis. The latter was needed to identify the parameters which could be easily modifiable for fine tuning of the rig. Results of the simulations showed that the mass of the holding block was quite insensitive for tuning whereas the rod dimensions and the mass of the shaker armature demonstrated to be very sensitive. A modal test of the test structure, constrained in the holding block, was produced so to identify a mode shape and its natural frequency. Using the measured natural frequency the analytical model calculated a set of dimensions for the push rod. **Table 1** reports the modes, natural frequencies and loss factors, and it is interesting to note that the composite material used here shows higher values of damping than a metallic equivalent one. We can say that, for a given excitation force, the levels of vibration achievable with metal components can be higher than the one achievable with composite ones. Hence, a shaker needs to work harder to excite a composite specimen to equivalent vibration level. The component was constrained with good accuracy by gluing two

polished metal plates on both sides and, then, clamped the assembly in the holding block. This approach was chosen so as to minimise power loss because of the friction in the clamped areas specifically at high level of vibrations. The mode chosen for the HCF study was mode-5 at 339.15Hz. Hence, **Table 2** reports the parameters used for designing the rod.

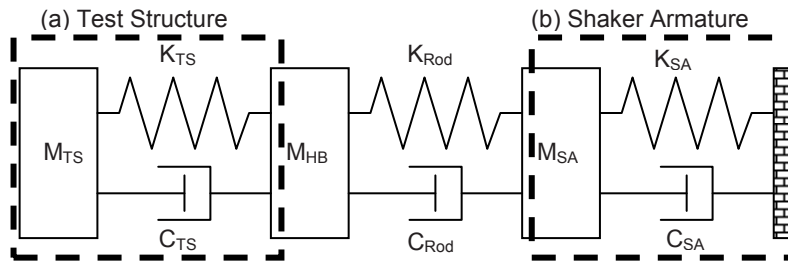


Figure 1 Simplified model of test rig for HCF testing

| | Mode-1 | Mode-2 | Mode-3 | Mode-4 | Mode-5 | Mode-6 | Mode-7 |
|-----------------|--------|--------|--------|--------|--------|--------|--------|
| Frequency [Hz] | 83.29 | 217.03 | 339.15 | 249.05 | 634.16 | 712.68 | 945.4 |
| Loss factor [%] | 0.7 | 0.5 | 0.4 | 0.4 | 0.4 | 0.4 | 0.5 |

Table 1 Modal properties of test structure

| Armature mass | Young's modulus | Holding block mass | Sample modal mass | Sample resonance frequency |
|---------------|-----------------|--------------------|-------------------|----------------------------|
| 11.25kg | 210E9 | 86kg | 0.2kg | 339.15Hz |

Table 2 Values used for running the parametric model

Figure 2 presents the driving rod designed for tuning the rig at the frequency of interest. The rod was manufactured to have a right hand thread at the holding block and a left hand one at the shaker armature so to tighten them together by rotating the rod. The holding block was supported on a three rollers to allow free movements along the direction of the push rod and this set up was decided to minimize possible buckling of the rod, already calculated during the design process. It is important to avoid buckling during the HCF test because of unwanted vibrations occurring on the sample. **Figure 3** shows the assembled test rig.

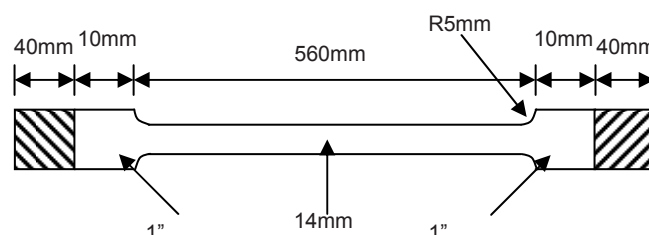


Figure 2 Dimensions of the designed push rod

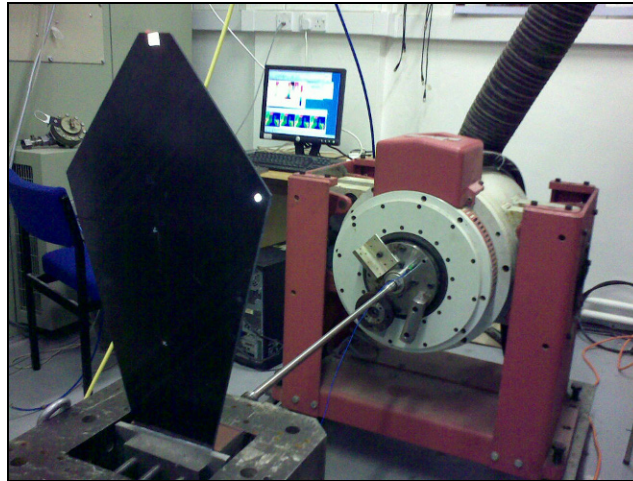


Figure 3 Test rig with the sample mounted in the holding block

4 Tuning of test rig

The method for tuning the rig, introduced earlier, is to design a push rod of correct dimensions which connects the shaker armature and the holding block. The armature of the shaker combined with the push rod should resonate at the same frequency as the target mode of the tested structure. Although the simplified parametric model helped to calculate the correct dimensions, the test rig required an additional fine-tuning to match the rig and specimen resonances precisely. A technique for tuning the rig can be to increase the mass of the shaker armature. This fine tuning can also be done by fine adjustment of the rod dimensions but this approach can be very time-consuming because of repeated dismantling of rig. Resonances were measured using impact testing, as shown in [Figure 4a](#) and [4b](#). The frequency distance between the specimen and the rig were measured at every modification applied. The tuning technique considered for this work consisted in adding small weights on the armature and measuring the resonant frequencies until the correct weight was found as shown by plots depicted in [Figure 4c](#). [Figure 5](#) shows the shaker armature with the additional tuning weights and the position of the impact, indicated by a black mark.

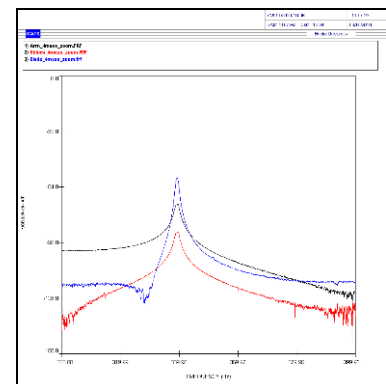
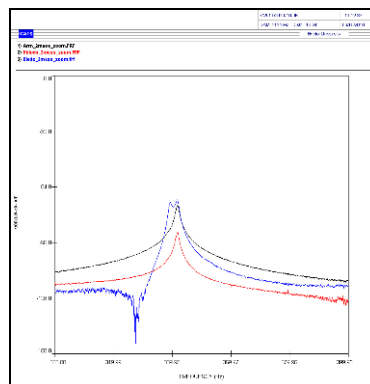
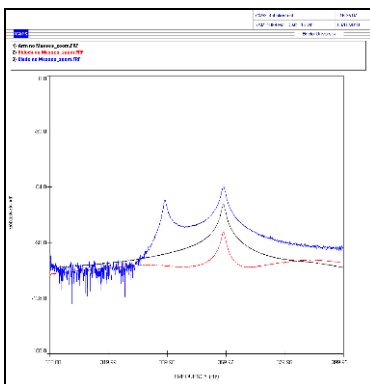


Figure 4a Tuning of rig

Figure 4b Tuning of rig

Figure 4c Rig tuned

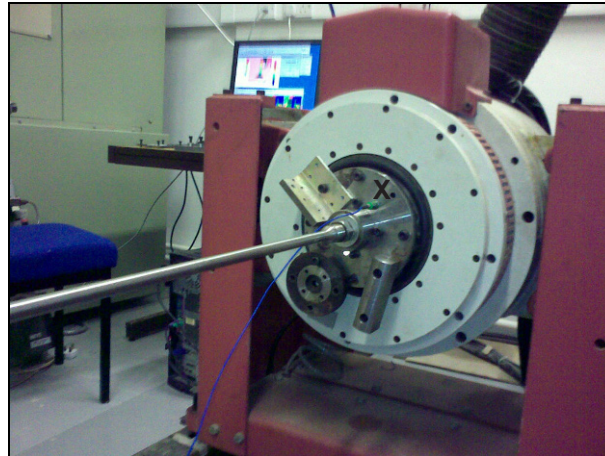


Figure 5 Tuning weights installed on the shaker armature and the impact position

It was found on the tuned test rig that the amplitude of the resonance of the specimen, as shown in **Figure 6** was (black curve), 77% higher than the one measured when the rig is not tuned, as shown in **Figure 6** (red curve). The excitation was produced using an impact hammer and the shaker armature was not active as the shaker amplifier was turned off during the measurement.

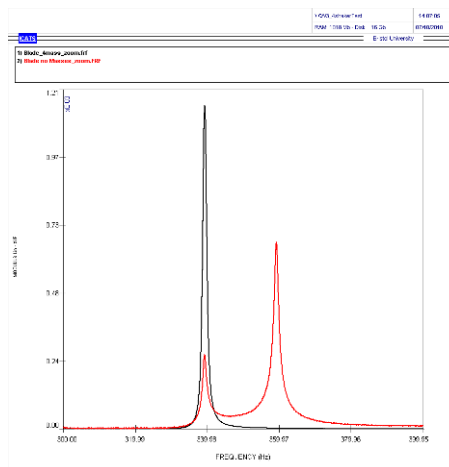


Figure 6 Increase of the response level of mode-5 before (red) and after (black) the tuning of the test rig

The experiment of tuning the rig was also performed by stepped sine test around the resonance of the rig and adding weights until the frequency match was found. **Figure 7a** shows the responses measured at the armature and at the sample during the tuning process. **Figure 7b** shows the response measured at the specimen only. It is interesting to notice that when the shaker is armed the response measured at the armature seems more heavily damped than when the shaker is not armed. This can be explained by the change of the dynamics of the armature because of the electromagnetic field produced. Measuring the responses before and after the tuning the level of amplitude at the sample increased by only 33%.

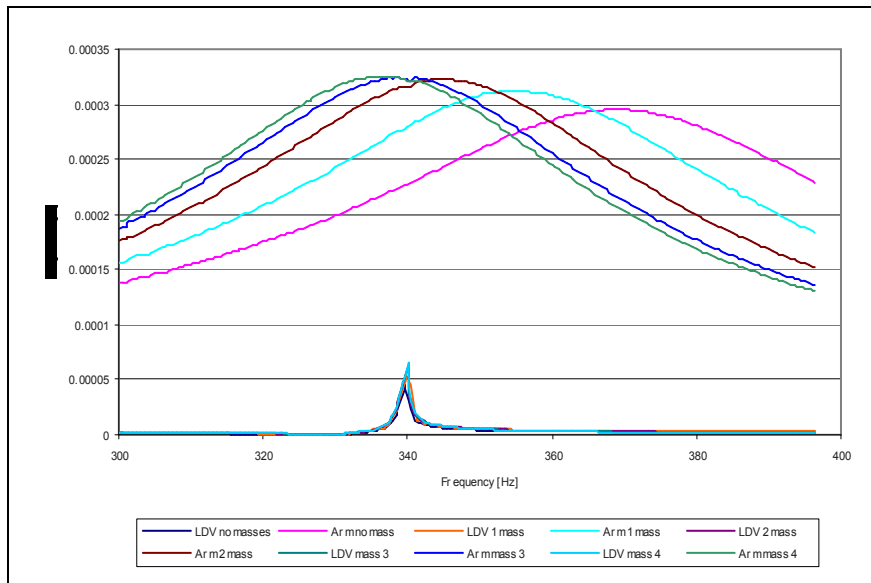


Figure 7a Tuning of the rig using, armature and specimen response

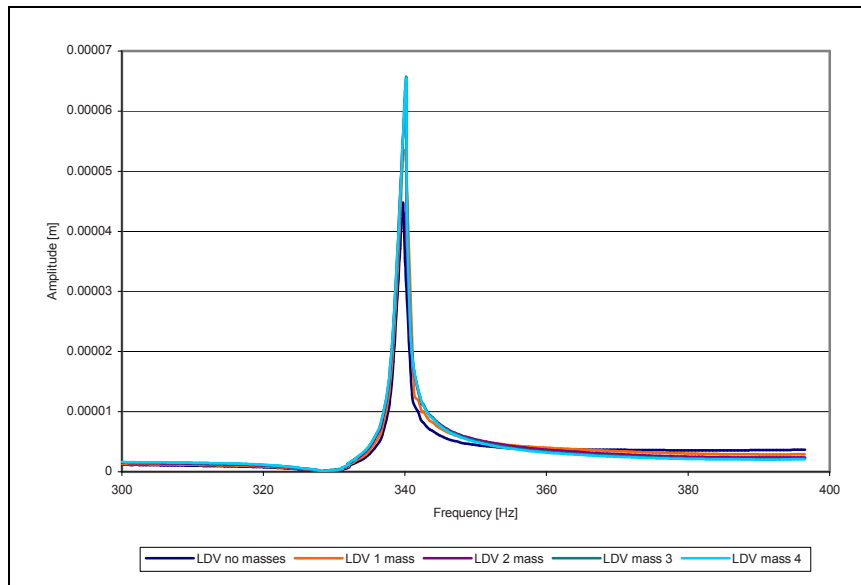


Figure 7b Tuning of the rig using, specimen response

5 Performance of the tuned test rig

The previous section presented two methods for tuning the designed test rig so that it could be capable of amplifying the response of the tested structure. This section will present an additional experiment to assess if the test rig is capable of performing efficiently the excitation when the level of the output force is increased. In fact, it was suspected that the test rig would present an impedance mismatch to the shaker. A sine-step around the resonance of mode 5 was performed for 7 levels of gain generated by an electronic output card, the gain of the amplifier was kept constant during all the experiments. **Figure 8a** presents the acceleration measured at the armature for the highest level of force at the resonance of mode5 while **Figure 8b** shows the logarithm of the frequency spectrum of the response. Before commenting these plots, it is important to say that the shaker used

for this experiment is capable of outputting a maximum acceleration of 95g. We can see from **Figure 8a** that a sinusoidal excitation waveform is amplified incorrectly by the amplifier, in fact, the signals measured from the accelerometer exhibit an increasing level of non linearity with many high harmonics observed in the signal.

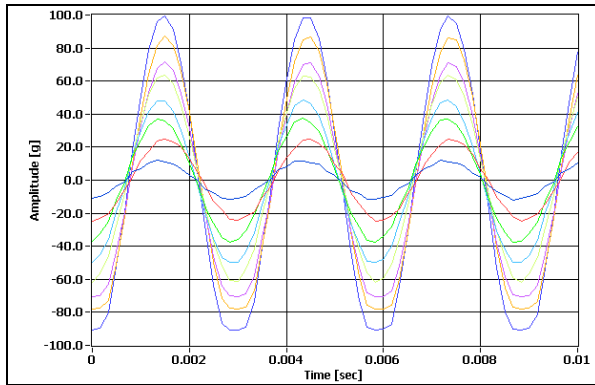


Figure 7a Response measured at the armature for 7 levels of gain

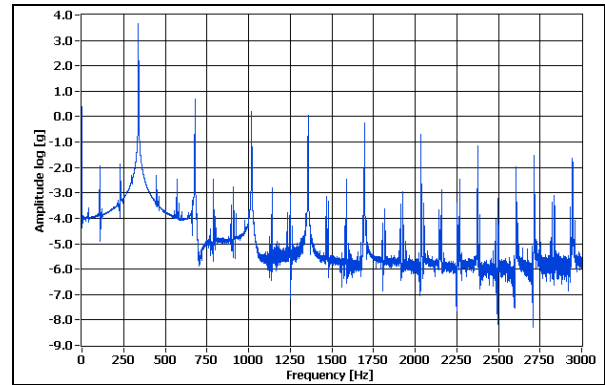


Figure 7b Frequency spectrum of the response measured for the highest gain

The maximum capability of the shaker, provided by its specification data, is claimed to be at a level of 95g, 30A and 70V and so the max output power is 2.1kW. A quick experiment for measuring the output power was run to measure the actual power produced for the highest level of gain possible on the amplifier. It was noted that the output levels of the amplifier were 2A and 70V producing an output power of 140W, at the frequency the test rig was tuned for. Such a low output power suggests that the shaker armature was vibrating excessively without producing very much force to the test structure

6 Discussions and improvements

We concluded in the previous section that the shaker amplifier was underperforming by outputting a level of power much lower than the maximum achievable. It was understood that poor performance can be caused because of the test rig design, in which the armature resonates at high vibration amplitudes. This mechanical system is capable of producing high responses on the test structure but not using most of the power available. The concept of tuning a test rig proved to be correct but the implementation of it, by using the armature mass as a tuner, proved to be not optimal. Specifically, for testing composite structures which require more power from the shaker because of higher levels of damping as already introduced.

The presented mechanical test rig can be used for amplifying the response of the tested component but, in order to do that, the armature of the shaker should vibrate up to the allowable acceleration and in out of phase with the connected rig so as to generate the maximum force. **Figure 8** indicates the test rig must be connected to the shaker by a mechanism presenting very high impedance. Another important parameter to take into account during the design of a tuneable rig, is the consequential shift of the resonance of the test structure in the rig. In fact, high-level vibration produced on the specimen can enhance phenomena of non linearity. When this happens, the resonance of the sample can move to a frequency which is different to the one used for tuning the test rig. Hence,

it would be important to perform some linearity checks on the sample to predict where the resonant frequency might move to during the HCF test. **Figure 9** presents an FRF of a similar sample to the one shown earlier, whose frequency of interest was around 560Hz. This example aims to explain more clearly the reason for tuning a test rig to a frequency matching the one run during the HCF. In fact, the rig was tuned to a frequency of 560Hz which, with the increase of the excitation force, did not match the sample resonance anymore thereby reducing the amplification effect of the mechanical test rig.

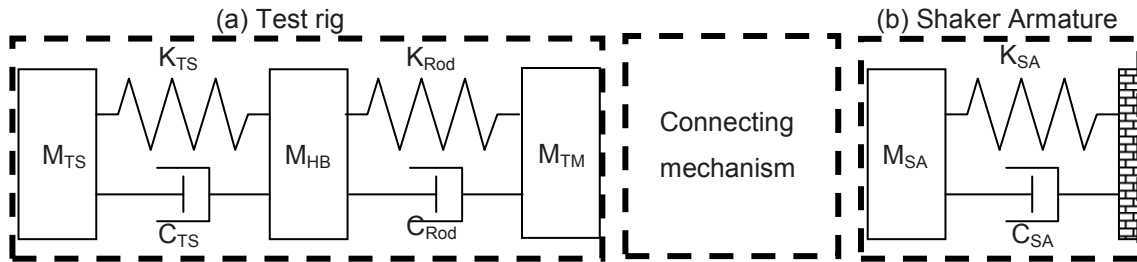


Figure 9 Test rig (a), connecting mechanism and shaker armature (b)

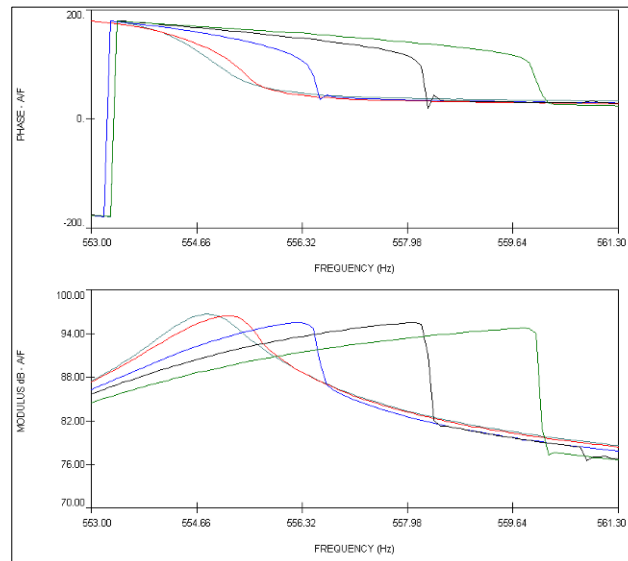


Figure 10 Non linear responses of a specimen

7 Conclusions

This work has presented a simple but practical study of the effect of impedance mismatch between an electromagnetic shaker and a test rig used for performing HCF measurements. The endurance measurement is becoming increasingly important for building data sets of fatigue properties of new composite materials. The

current technology developed using a test rig such as the one introduced, proved to be correct when used for testing lightly damped materials, which require relatively small excitation forces. When the damping is higher, as for composite materials, the excitation force must be increased. A tuneable test rig is an excellent mechanical amplifier of vibrations but, when wrongly implemented, it can result shaker underperforming or performing outside its specifications. A mechanical amplifier should be connected to a shaker using a mechanism with high impedance so that the armature

REFERENCES

[1] B A Cowles, High cycle fatigue in aircraft gas turbines- an industry perspective. *International Journal of Fracture* 80:147-163, 1996

A Global-local Approach to Nonlinear System Identification

Young S. Lee⁽¹⁾, Alexander Vakakis⁽²⁾, D. Michael McFarland⁽³⁾, Lawrence Bergman⁽³⁾

⁽¹⁾ Department of Mechanical and Aerospace Engineering, New Mexico State University, 1040 S. Horseshoe St., Las Cruces, NM 88003, U.S.A.; younglee@nmsu.edu

⁽²⁾ Department of Mechanical Science and Engineering, University of Illinois at Urbana-Champaign, 1206 W. Green St., Urbana, IL 61801, U.S.A.; avakakis@illinois.edu

⁽³⁾ Department of Aerospace Engineering, University of Illinois at Urbana-Champaign, 104 S. Wright St., Urbana, IL 61801, U.S.A.; [dmmcf](mailto:dmmcf@illinois.edu), lbergman@illinois.edu

ABSTRACT

We present the basic components of a time-domain nonlinear system identification (NSI) method with promise of applicability to a broad class of smooth and non-smooth dynamical systems. The proposed NSI method is based on the close correspondence between analytical and empirical slow-flow dynamics, and relies on direct analysis of measured time series without any a priori assumptions on the system dynamics. The central assumption is that the measured time series can be decomposed in terms of a finite number of oscillating components that are in the form of fast monochromatic oscillations modulated by slow amplitudes. The empirical slow-flow model of the dynamics is obtained from empirical mode decomposition, and its correspondence to the analytical slow-flow model establishes a local nonlinear interaction model (NIM). A NIM consists of a set of intrinsic modal oscillators (IMOs) that can reproduce the measured time series over different time scales and can account for (even strongly) nonlinear modal interactions. Hence, it represents a local model of the dynamics, identifying specific nonlinear transitions. By collecting energy-dependent frequency behaviors from all identified IMOs, a frequency-energy plot (in the modal space) can be constructed, which depicts global features of the dynamical system.

1. INTRODUCTION

The need for system identification and reduced-order modeling in dynamical systems arises from the fact that, presented with sensor data, the analyst is often unaware of details of the underlying system from which they originated. The straightforward approach to this dilemma is to assume that the dynamical system is linear and that the measured responses are stationary in time. This facilitates the use, for example, of the numerical Fourier transform (FT) followed by experimental modal analysis (EMA [1]) to extract natural frequencies, mode shapes and modal damping ratios, from which the parameters of the assumed linear model can be determined if the mass distribution is known. This approach, which is fully nonparametric, has served the dynamics and controls community well, even in the presence of weakly nonlinear system behavior. Clearly, though, as systems become more complex, incorporating not only electrical and mechanical components but also biological and biomimetic elements, the likelihood exists that the observed data will reflect strong nonlinearity and nonstationarity. Such behaviors can result from, for example, local buckling, clearance and backlash, friction, hysteresis, local damage, large displacements and/or strains, and so forth (see, for example, [2]). And as we think more in terms of multi-physics problems, one must also include nonlinearities due to interfacial effects such as shear lag between actuator and structure, fluid-structure interactions, sensor-tissue interactions, and others. Thus, a physically-based parametric model of the system will not, in general, be known *a priori*.

However, given a sufficiently dense set of sensors, measured time series recorded throughout the system will contain all of the information reflecting both nonlinearity and nonstationarity. Methods based upon the FT are not able to properly isolate and extract this information and, in fact, may lead the less experienced analyst to mistake phenomena such as internal and combination resonances for natural frequencies [3], to mistake time dependence for damping, and to fail to

account for sensitivities of the response to force and voltage magnitudes and to initial conditions, all of which can lead to large changes in response over short time. One cannot overestimate the importance of the need for an effective, straightforward, system identification and reduced-order modeling method for characterizing strongly nonlinear and nonstationary, complex, multi-component systems. However, the difficulty in developing a method of broad applicability is the well-recognized, highly individualistic nature of nonlinear systems which restricts the unifying dynamical features that are amenable to system identification.

Reviews of nonlinear system identification (NSI) and reduced-order methods are presented in Kerschen *et al.* [4,5]. Moon [6] notes suitable methods for diagnosing chaotic motion which are also useful for determining when observed responses result from strongly nonlinear systems. These include analysis of time series of the response, interpretation of phase space trajectories and Poincaré maps, examination of power spectra of the response, and observation of system response when individual parameters are varied. Nichols and Virgin [7] presented a method for estimating damping in a system by chaotic interrogation, and Feeny *et al.* [8] performed NSI of a magneto-elastic two-well chaotic system. Typical nonparametric NSI methods include proper orthogonal decomposition, Volterra theory, and pattern recognition based on artificial neural networks. For example, Silva [9] performed NSI using Volterra theory on aeroelastic systems, developed computationally-efficient reduced-order models (ROMs) employing an Euler/Navier-Stokes fluid solver, and finally derived analytically Volterra kernels for nonlinear aeroelastic systems from data of flight flutter tests of an active aeroelastic wing aircraft.

There are alternative well-established methods for nonlinear parameter estimation, such as the restoring force surface method [10], NARMAX (Nonlinear Auto-Regressive Moving Average models with eXogenous inputs) methods [11,12], methods based on Hilbert transforms [13,14], and others. Thothadri *et al.* [15] performed NSI of multi-degree-of-freedom (MDOF) fluid-structure interaction systems using the principle of harmonic balance (HB). The main advantage of the HB technique is its usefulness to predict bifurcation behavior of a nonlinear system, for which nonparametric methods are not usually well suited. This is performed by exploiting the periodicity in the response of an experimental system, when parametric time-domain methods such as the NARMAX fail. A multi-staged approach for fitting the excitation of a nonlinear system in nonparametric form was developed in Masri *et al.* [16,17]. Also, a general data-based approach for developing ROMs for nonlinear MDOF systems was proposed assuming no information about the system mass [18]. reduced-order modeling based on nonlinear normal modes [19] has been discussed in Touzé *et al.* [20-22]. However, these techniques are only applicable to specific classes of dynamical systems; in addition, some type of functional form is assumed for modeling the system nonlinearity, and the main task becomes the determination of the corresponding coefficients. The key to a successful NSI method is the recognition that a single parametric model derived from data at a specific operating point in the frequency-energy space will not be globally descriptive. Rather, the method should non-parametrically provide a global picture of system behavior leading naturally to local parametric models capable of reproducing the strongly nonlinear phenomena at the operating points.

With this idea in mind, we recently proposed a time-domain (nonparametric) NSI method based on equivalence or correspondence between analytical and empirical slow flows of a dynamical system [23,24], and studied its application to targeted energy transfers in 2-degree-of-freedom dynamical system, aeroelastic instability suppression [25], and a rod with an essentially nonlinear end attachment [26]. The proposed NSI method is feasible for broad classes of applications involving time-variant/time-invariant, linear/nonlinear, and smooth/non-smooth dynamical systems. Furthermore, it requires no *a priori* system information but only measured (or simulated) time series; *i.e.*, it is purely an output-based approach. Empirical mode decomposition (EMD [27]) is employed to yield intrinsic mode functions (IMFs) of the measured time series as empirical slow flows, and its correspondence to the analytical slow-flow dynamics enables us to establish a nonlinear interaction model (NIM). The NIM consists of a set of intrinsic modal oscillators (IMO), an equivalent linear oscillator that can produce a given time series over different time scales and keeps any existing nonlinear modal interactions in its time-varying forcing term. An IMO, the solution of which reproduces the corresponding IMF, represents dynamical characteristics of the system under certain initial or parameter conditions (*i.e.*, local aspects). By extracting energy-dependent frequency behavior from identified IMOs, a frequency-energy plot (in the modal space) can be constructed as global features of the dynamical system.

2. REDUCED SLOW-FLOW DYNAMICS AND EMD

Slow-flow reduction of the dynamics is a useful tool for understanding the major features of a dynamical system. The reduced slow-flow model of a dynamical process is derived by introducing a slow/fast partition of the dynamics whereby the (non-essential) fast dynamics is averaged out to reveal the (essential) slow-flow modulations of appropriately defined amplitudes and phases. Perturbation tools have been developed to perform this task; e.g., the Linstedt-Poincaré method

of direct series expansions, singular perturbation methods [28], the method of multiple scales and the harmonic balance method [3], the method of averaging [29], *etc.* The complexification-averaging (CX-A) technique [30] has received much recent attention due to its capacity to provide slow-flow models even for strongly nonlinear transient dynamical interactions; e.g., resonance capture phenomena in coupled oscillators with essential nonlinearities [31]. Focusing on the CX-A method, we demonstrate the extraction of the slow-flow dynamics of a general n -degree-of-freedom (DOF), nonlinear dynamical system of the form

$$\dot{\mathbf{X}} = \mathbf{f}(\mathbf{X}, t), \mathbf{X} = \{\mathbf{x}^T \dot{\mathbf{x}}^T\}^T \in \mathbb{R}^{2n}, t \in \mathbb{R} \quad (1)$$

where \mathbf{x} is an n -response vector and \mathbf{f} is an n -vector function. Assume that the dynamics possesses N distinct components at frequencies $\omega_1, \omega_2, \dots, \omega_N$, so the response of each DOF of the system can be expressed as a summation of N independent components,

$$x_k(t) = x_k^{(1)}(t) + \dots + x_k^{(m)}(t) + \dots + x_k^{(N)}(t), k = 1, \dots, n \quad (2)$$

where $x_k^{(m)}(t)$ indicates the response of the k -th coordinate of (1), associated with the basic frequency ω_m with the ordering $\omega_1 < \omega_2 < \dots < \omega_N$. We assume at this point that all the basic frequencies in the response are well separated. It turns out that even strongly nonlinear dynamical processes can be analyzed by CX-A, first introduced by Manevitch [30] (for an extensive discussion of this technique and numerous applications refer to Vakakis *et al.* [31]). In particular, for each component in (2) we assign a new complex variable defined by

$$\psi_k^{(m)}(t) = \dot{x}_k^{(m)}(t) + j\omega_m x_k^{(m)}(t) \equiv \varphi_k^{(m)}(t) e^{j\omega_m t} \quad (3)$$

where a slow/fast partition of the dynamics in terms of the ‘slow’ (complex) amplitude $\varphi_k^{(m)}(t)$ and the ‘fast’ oscillation $e^{j\omega_m t}$ is assumed. Substituting (2) and (3) into (1) and performing multi-phase averaging [32] for each of the fast frequencies we obtain the slow flow of (1):

$$\dot{\phi}_k = F_k(\varphi_1, \varphi_2, \dots, \varphi_n) \in \mathbb{C}^N \quad (4)$$

where $\varphi_k = \{\varphi_k^{(1)}, \varphi_k^{(2)}, \dots, \varphi_k^{(N)}\}^T, k = 1, \dots, n$. The number of fast frequencies (N) determines the dimensionality of the slow flow (4).

As an example we consider a weakly damped linear oscillator (LO) coupled to a light attachment by means of essential stiffness nonlinearity of the third degree. In previous work the nonlinear oscillator was termed a ‘nonlinear energy sink’ (NES) due to its capacity to passively absorb and dissipate energy from the LO over broad frequency ranges [31]:

$$\ddot{y} + \omega_0^2 y + \epsilon \lambda_1 \dot{y} + \epsilon \lambda_2 (\dot{y} - \dot{v}) + C(y - v)^3 = 0, \quad \epsilon \ddot{v} + \epsilon \lambda_2 (\dot{v} - \dot{y}) + C(v - y)^3 = 0 \quad (5)$$

where y and v are the displacements of the LO and NES, respectively; ω_0 is the linearized natural frequency of the LO; ϵ the mass ratio of the NES to the LO; C the essentially nonlinear stiffness coefficient; and $\lambda_{1,2}$ the damping coefficients. We assign $\omega_0 = 1, C = 1, \epsilon = 0.05$, and $\lambda_{1,2} = 0.03$ and the initial conditions $y(0) = v(0) = 0$ and $\dot{y}(0) = -0.059443193, \dot{v}(0) = 0.014995493$. Then, a 1:3 transient resonance capture (TRC [33]) takes place during which the NES engages in transient resonance with the LO, and strong energy exchanges between the two oscillators occur [34]. [Figure 1](#) depicts the responses of the two oscillators in time and frequency (wavelet transform spectra). There exist two dominant fast frequencies in the dynamics, at $\omega_2 = \omega_0$ (high-frequency - HF) and at $\omega_1 = \omega_0 / 3$ (low-frequency - LF), respectively.

Given that there are only two fast frequencies in the transient responses we express the responses as $x_1(t) \triangleq y(t) = y^{(1)}(t) + y^{(2)}(t), x_2(t) \triangleq v(t) = v^{(1)}(t) + v^{(2)}(t)$, and the slow/fast partitions as,

$$\psi_1^{(m)}(t) = \dot{y}^{(m)}(t) + j\omega_m y^{(m)}(t) \equiv \varphi_1^{(m)}(t) e^{j\omega_m t}, \quad \psi_2^{(m)}(t) = \dot{v}^{(m)}(t) + j\omega_m v^{(m)}(t) \equiv \varphi_2^{(m)}(t) e^{j\omega_m t} \quad (6)$$

where $m = 1, 2$. When substituted in (5) and averaged with respect to ω_1 and ω_2 , the complexification (6) leads to the slow-flow equations

$$\dot{\phi}_1 = F_1(\varphi_1, \varphi_2), \quad \dot{\phi}_2 = F_2(\varphi_1, \varphi_2) \quad (7)$$

where $\varphi_1 = \{\varphi_1^{(1)}, \varphi_1^{(2)}\}^T$ and $\varphi_2 = \{\varphi_2^{(1)}, \varphi_2^{(2)}\}^T$. The details of the functions F_1 and F_2 can be found in Kerschen *et al.* [34]. In the left of [Fig. 2](#) we present the slow flow approximation of the LO and NES responses, demonstrating that the slow flow accurately approximates the strongly nonlinear transient response.

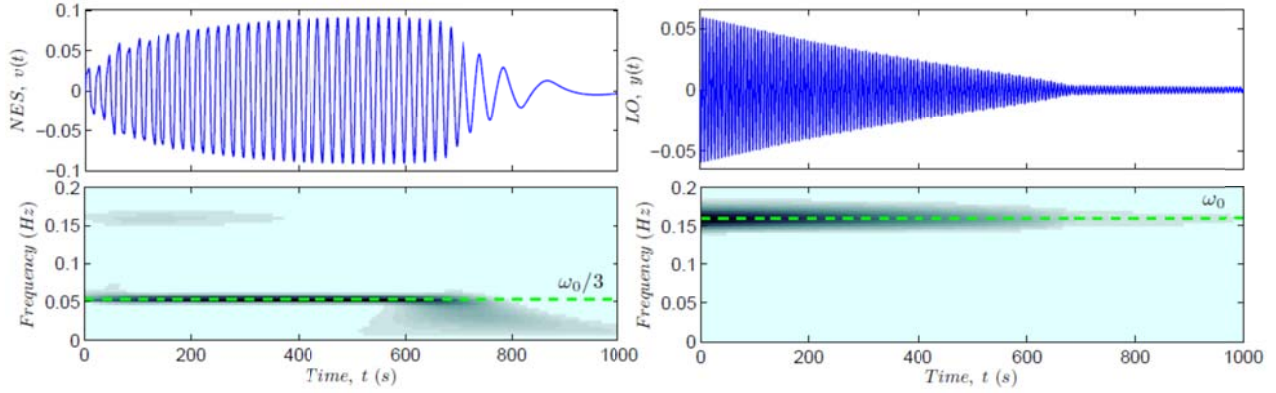


Fig. 1 Responses of NES (left) and LO during (right) 1:3 TRC

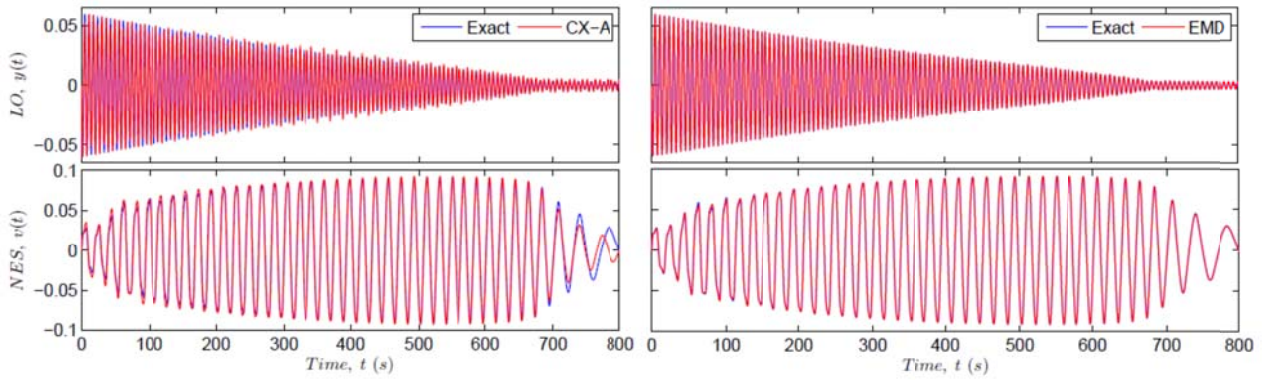


Fig. 2 Reconstruction of the LO and NES displacements: CX-A (left) and EMD (right)

The slow-flow model (4) provides an important theoretical foundation for performing nonlinear system identification (NSI). To show this we first review the basic elements of empirical mode decomposition (EMD), conceived as a numerical post-processing technique for analyzing nonstationary and nonlinear time series. Since EMD combined with Hilbert spectral analysis was introduced in Huang *et al.* [27,35-37], numerous applications to system identification [38-40], nonlinear dynamics [41-44] and damage detection [45,46] have appeared. This decomposition method, based on identifying the characteristic time scales in measured time series, is adaptive, highly efficient, and suitable for nonlinear and nonstationary processes. In particular, EMD yields a complete and nearly (but not completely) orthogonal basis of intrinsic mode functions (IMFs); these are oscillatory modes embedded in the time series, each with its own characteristic time scale, whose linear superposition reconstructs the measured time series. In other words EMD is a multi-scale decomposition of a measured time series in terms of embedded oscillatory modes at different time scales. Some recent EMD developments can be found in references [37,47-50].

As a result of EMD analysis, we write the *ad hoc* numerical decomposition of the dynamics of the general system (1) as

$$x_k(t) \approx c_1^{(k)}(t) + \dots + c_m^{(k)}(t) + \dots + c_N^{(k)}(t), \quad k = 1, \dots, n \quad (8)$$

where $c_m^{(k)}(t)$ is the m -th dominant IMF of the response $x_k(t)$, associated with the fast frequency ω_m , with $\omega_1 < \omega_2 < \dots < \omega_N$. By this construction process the superposition of the N leading IMFs reconstruct approximately the measured time series; however, due to the *ad hoc* nature of the sifting algorithm only a subset of these IMFs are physically meaningful with the rest being of spurious nature. As discussed in previous work [41,42,44], the dominant (and physically meaningful) IMFs can be identified by comparing their instantaneous frequencies to the wavelet transform (WT) spectra of the original time series: the instantaneous frequencies of the dominant IMFs coincide with the dominant harmonics of the wavelet spectra. This process also identifies the dominant time scales (or frequencies) of the dynamics in the time series. On the right of Fig. 2 we reconstruct the responses of system (5) using two dominant IMFs for each subsystem, namely $c_1^{(1)}(t)$ (LF LO component at ω_1 - it turns out that this is negligible) and $c_2^{(1)}(t)$ (HF LO component at ω_2) for the LO, and two dominant IMFs $c_1^{(2)}(t)$ (LF NES component) and $c_2^{(2)}(t)$ (HF NES component)

for the NES. By comparing with the exact numerical time series we establish the completeness of the decomposition; i.e., $x_1(t) \triangleq y(t) = c_1^{(1)}(t) + c_2^{(1)}(t)$, $x_2(t) \triangleq v(t) = c_1^{(2)}(t) + c_2^{(2)}(t)$.

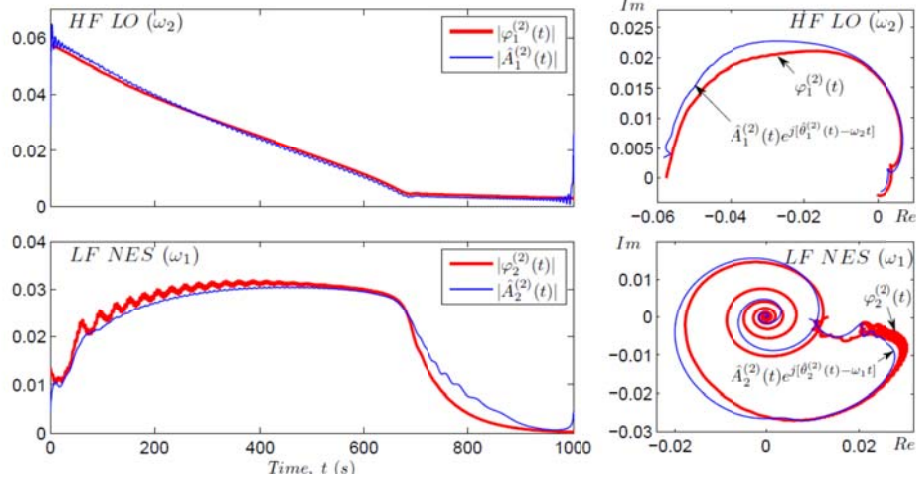


Fig. 3 Correspondence between theory (slow flow dynamics) and numerics (EMD results) for the system (5): HF response of LO (first row) and LF response of the NES (second row)

Comparing the EMD result (8) with the slow/fast decomposition (3) we clearly establish the possibility of relating the two expansions thus providing a theoretical basis for EMD in terms of the underlying slow flow dynamics. This important result was established in Lee *et al.* [23] and will form the basis of the NSI method. Motivated by the mathematical fact that a complex function whose imaginary part is the Hilbert transform of the real part is analytic, we complexify the m -th IMF $c_m^{(k)}(t)$ of the time series $x_k(t)$ in (8) by defining the analytic complex function

$$\hat{\psi}_k^{(m)}(t) = c_m^{(k)}(t) + j\mathcal{H}[c_m^{(k)}(t)] \equiv \hat{A}_m^{(k)}(t)e^{j[\hat{\theta}_m^{(k)}(t) - \omega_m^{(k)}t]} e^{j\omega_m^{(k)}t} \quad (9)$$

where $\mathcal{H}[\cdot]$ denotes Hilbert transformation, and $\hat{A}_m^{(k)}(t)$ and $\hat{\theta}_m^{(k)}(t)$ are the instantaneous envelope and phase of $c_m^{(k)}(t)$ such that

$$\hat{A}_m^{(k)}(t) = \sqrt{c_m^{(k)}(t)^2 + \mathcal{H}[c_m^{(k)}(t)]^2}, \hat{\theta}_m^{(k)}(t) = \tan^{-1} \left[\mathcal{H}[c_m^{(k)}(t)] / c_m^{(k)}(t) \right] \quad (10)$$

We note that by complexifying the identified IMFs in (9) we have a direct way to relate them to the governing slow flow dynamics (e.g., the complex amplitudes $\psi_k^{(m)}(t)$ in the expression (3)). This will provide a way to physically interpret the (until now *ad hoc*) dominant IMFs in terms of the slow-flow dynamics. Given, however, that the time series is decomposed in terms of dominant IMFs, it follows that $\omega_m^{(k)} \approx \omega_m$ for $m = 1, \dots, N$, where N is the number of dominant harmonic components in the slow-flow decomposition of the dynamics (*i.e.*, the dimensionality, or the number of significant frequency-time scales in the dynamics). It follows that the above partitions can be related since they represent identical theoretical (*i.e.*, $x_k^{(m)}(t)$) and numerical (*i.e.*, $c_m^{(k)}(t)$) multi-scale slow-fast decompositions of the measured time series. Hence, we make the association

$$\psi_k^{(m)}(t) \rightarrow \hat{\psi}_k^{(m)}(t) \Rightarrow \varphi_k^{(m)} \rightarrow \hat{A}_m^{(k)}(t)e^{j[\hat{\theta}_m^{(k)}(t) - \omega_m^{(k)}t]} \quad (11)$$

where the second half addresses the equivalence of 'slow' complex amplitudes. These relations provide a physics-based theoretical foundation for EMD, whereby the dominant IMFs represent the underlying slow flow and, hence, capture all the important (multi-scale) dynamics. This important result derived by Lee *et al.* [23] provides the foundation for the development of the NSI methodology of broad applicability (cf. Section 3.2). We note that no assumptions have been made regarding the type or dimensionality of system and the type and strength of the nonlinearity. It follows that the slow-fast partitions discussed above and the physical interpretation of the results of EMD should hold for a broad class of dynamical systems. In fact, EMD can provide us with the added benefit of separating the smooth from non-smooth dynamics by localizing all non-smooth effects (e.g., due to clearances) in the leading order IMFs. Hence, the NSI methodology can be extended also to non-smooth dynamical systems.

An example of this correspondence is now given in terms of the previous strongly nonlinear example (5). In the left column of Fig. 3 we depict a comparison between the magnitudes of the slowly varying amplitudes of the low- and high-

frequency (LF and HF) components of the LO and the NES derived by slow flow analysis and EMD; in the right column, we present the corresponding slow components in the complex plane (which incorporates phase information). There is good correspondence between the analytical and numerical results for these two dominant components (cf. Fig. 1) confirming the previous theoretical arguments (for additional applications we refer to Lee *et al.* [25] and Tsakirtzis *et al.* [26]).

3. NONLINEAR SYSTEM IDENTIFICATION

3.1 Global and Local Issues

Compared to linear modal analysis, NSI of dynamical systems is far more complex. Nonlinear systems are energy- and initial conditions-dependent, so that even the simple task of identifying a set of (linearized) modal matrices modified ('perturbed') by nonlinear corrections might be an oversimplification of the problem. Using as an example the 1:3 transient resonance capture of the strongly nonlinear system (5) we should recognize that a change in initial conditions can result in drastically different transient dynamics. To illustrate this point we introduce in our discussion the concept of frequency-energy plot (FEP [31]), which provides a global picture of the dynamics.

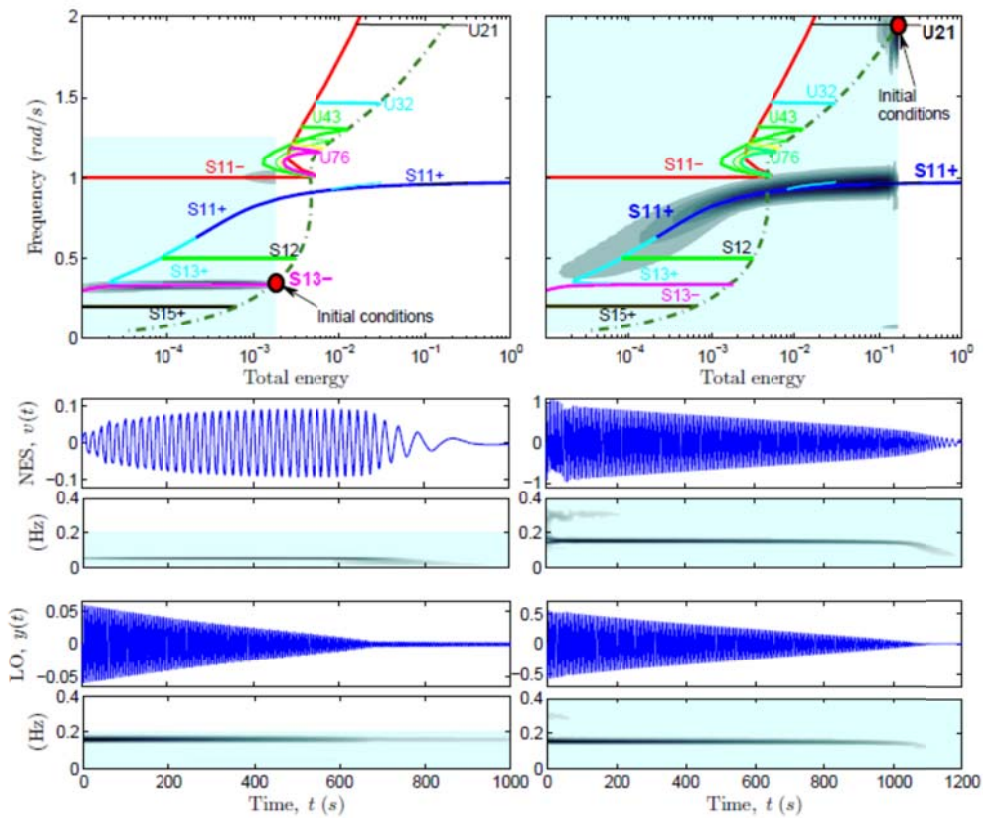


Fig. 4 Two different damped nonlinear transitions of system (5) depicted in the FEP: (left) 1:3 transient resonance capture; (right) transition with zero initial conditions but $y(0) = -0.579$

To construct the Hamiltonian FEP for system (5) we set $\lambda_1 = \lambda_2 = 0$ and compute its periodic orbits [51]. The resulting FEP is in the background in the first row of Fig. 4, where a frequency index (FI) of a periodic orbit is depicted against its (conserved) energy. Symmetric periodic orbits $Snm \pm$ correspond to curves in the configuration plane (y, v) , with $m:n$, indicating the internal resonance (e.g., a 1:1 internal resonance is realized on $S11 \pm$, with both the LO and the NES oscillating with identical dominant frequencies). The (\pm) signs indicate in-phase or out-of-phase motions of the LO and the NES. Unsymmetric periodic orbits $Upq \pm$ are Lissajous curves in the configuration plane. Then, the FI of a periodic orbit on branches $Snm \pm$ and $Unm \pm$ is given by $FI = no_0 / m$. The (seemingly simple) system (5) possesses a countable infinity of periodic orbits. Near-horizontal branches are linearized or weakly nonlinear motions (weak frequency-energy dependence), whereas curved branches imply strongly nonlinear responses (the corresponding linear 2-DOF system would possess a FEP with just two horizontal lines corresponding to its natural frequencies).

A very useful feature of the Hamiltonian FEP is its relation to the transient dynamics of the corresponding weakly damped system. As discussed in Vakakis *et al.* [31] the dynamics of the weakly damped system can be closely related to the underlying Hamiltonian dynamics: indeed, for weak damping the transient dynamics tracks specific branches of periodic orbits in the FEP. As energy decreases due to damping dissipation sudden transitions may occur as the damped response jumps from the neighborhood of one branch of periodic solutions to another. The sequence of branches of periodic orbits tracked by the damped dynamics in the FEP is ultimately dictated by the initial conditions and the level of damping in the system. Using as an example system (5), the close correspondence between the weakly damped and Hamiltonian dynamics can best be demonstrated by superimposing on the Hamiltonian FEP the wavelet spectra of the time series corresponding to the difference $y(t) - v(t)$. This is done in the left column of Fig. 4 for the 1:3 transient resonance capture depicted of Fig. 1. In the same figure we depict the transient responses $v(t)$ and $y(t)$ together with their wavelet spectra. We see that during 1:3 transient resonance capture the dynamics tracks closely the 1:3 subharmonic ‘tongue’ $S13 - [31]$, so a relatively simple topological picture of the transition emerges. Using, however, a different set of initial conditions we get drastically different dynamics as evidenced by the high-frequency transition depicted in the right column of Fig. 4. In this case the dynamics is initiated on the higher energy superharmonic tongue $U21$ so the damped dynamics tracks a completely different set of branches in the FEP. This results in a complicated multi-frequency nonlinear transition which, however, can be analyzed through theoretical and numerical slow-fast partitioning of the dynamics. It is evident though that performing NSI based only on either one of the measured time series we would miss a component of the dynamics. Moreover, even if both transitions are analyzed, NSI would still be incomplete as there would still exist dynamics not captured by the transitions of Fig. 4.

The previous example highlights the important challenges that the analyst is faced with when performing NSI. The first challenge is to address the (generic) feature of nonlinear systems to exhibit qualitatively different responses with varying energy and/or initial conditions. To address this challenge one needs to adopt a global approach for identifying the basic (essential) dynamical features of a system over broad frequency and energy ranges. The second challenge is to be able to identify complex multi-frequency transitions (such as the ones depicted in Fig. 4) for fixed sets of initial conditions (or energy). This dictates a local approach to NSI whereby a specific nonlinear transition is considered and the task is to identify the nonlinear modal interactions that govern this transition. The NSI methodology presented in this paper addresses both of the above challenges by proposing a combined global/local approach to NSI: *global features of the dynamics are identified in the frequency-energy domain by constructing FEPs, whereas local transitions (such as the ones depicted in Fig. 4) are identified by constructing appropriate slow-flow models.* In this way we ensure that both the global and local requirements of NSI are addressed. The added benefit of this approach is that it is based on direct analysis of measured time series which contain complete information of the nonlinear dynamics to be identified.

3.2 Methodology

Based on the previous discussion we summarize the methodology for NSI of dynamical systems. The methodology has global and local components and relies on direct processing of measured time series. The central assumption of the method is that the measured dynamics can be decomposed in terms of slowly modulated fast oscillations, which is a reasonable assumption for non-chaotic measured data. The basic elements of the method are outlined below:

- (i) Measure time series from a number of sensors throughout the system under transient excitation, and perform empirical mode decomposition (EMD) of the measured time series. Extract the intrinsic mode functions (IMFs) at each sensing location. Hilbert-transform the computed IMFs to extract their instantaneous frequencies and compare them to wavelet transform (WT) spectra of the corresponding time series; thus, determine the dominant IMFs and the corresponding fast frequencies in the dynamics at each sensing location. This will identify the basic time scales and the dimensionality of the dynamics.
- (ii) Based on the correspondence between the measured dominant IMFs and the underlying slow-flow dynamics of the system (*cf.* Section 2), relate the slow components of the dominant IMFs to the slow flow dynamics. Using the dominant IMFs reconstruct the time series and depict it in a frequency-energy plot; under the assumption of weak dissipation this will reconstruct a portion of the FEP of the dynamics of the system under investigation; no *a priori* model is assumed for this reconstruction (nonparametric global component of NSI).
- (iii) For a given nonlinear transition in the FEP define a parametric reduced-order slow-flow model of the system with the dimensionality of the dynamics, and identify its parameters; thus construct a local slow-flow model of the dynamics (parametric local aspect of NSI).
- (iv) By varying the excitation and/or the initial conditions, consider different nonlinear transitions of the system over different frequency and energy ranges, and construct the corresponding portions of the FEP of the system together with the associated local slow-flow models.

- (v) The final outcomes of the NSI are: (a) a frequency-energy plot of the global dynamics depicting the possible coexisting families of solutions and their bifurcations over the frequency and energy ranges of interest (global result); and (b) the corresponding local slow flow models of the dynamics describing nonlinear transitions on the FEP (local results).

The approach summarized above addresses in a systematic way a fundamental limitation of current nonlinear system identification methods: their inability to allow that the responses of nonlinear systems may depend crucially on initial conditions and/or the applied excitations. Instead, the NSI methodology takes into account that nonlinear systems may change their dynamics with energy and possibly possess numerous co-existing solutions (attractors). The added flexibility of ‘probing’ the dynamics over different frequency and energy ranges in order to extract different local models is important when identifying systems capable of strongly nonlinear dynamical behavior. The global aspect of our method, namely FEP construction, can be applied to both discrete and continuous nonlinear dynamical systems irrespective of dimensionality. By constructing FEPs we can identify global features of the dynamics, e.g., ranges of frequencies and energies where the system possesses linearized responses (corresponding to nearly horizontal branches of solutions in the FEP), coexisting branches of strongly nonlinear solutions, bifurcation points signifying the limits of response branches, *etc.* In addition, it is well established that forced resonances of nonlinear systems occur in neighborhoods of free periodic solutions (or nonlinear normal modes); hence, by identifying the FEPs we gain understanding of the structure of nonlinear (fundamental or subharmonic) resonances in the forced dynamics.

Finally, we point out the added benefit of considering transient instead of steady-state responses in our NSI method. Indeed, analyzing transient responses is an efficient way of probing the dynamics (as the damped transitions in the FEP plots of Fig. 4 demonstrate; *i.e.*, steady-state motions would appear merely as isolated dots in these plots as they would correspond to fixed frequencies and energies). Performing transient tests allows us to effectively probe the dynamics of a system and to depict these results in compact form in an FEP.

4. APPLICATIONS

4.1 Global Aspect of NSI: FEP Construction

The instantaneous frequency of an identified dominant IMF, $c_m^{(k)}(t)$, can be computed directly from expression (10) as, $\hat{\omega}_m^{(k)}(t) = \hat{\theta}_m^{(k)}(t)$. The corresponding instantaneous energy of the IMF can be expressed as a sum of kinetic and potential energies as $E_m^{(k)}(t) = [\hat{c}_m^{(k)}(t)^2 + \omega_m^2 c_m^{(k)}(t)^2] / 2$. If the mass distribution for the system is known then the instantaneous mechanical energy of the system can be estimated as a summation of the energies of the IMFs multiplied by appropriate mass factors,

$$E_{tot}(t) = \eta \sum_{k=1}^n \sum_{m=1}^N m_k E_m^{(k)}(t) \quad (12)$$

where $m_k, k=1, \dots, n$ corresponds to the mass distribution of the system among components (and can be deduced from the physical configuration of the system), and η is a factor used to match the exact initial conditions of the damped transition with the approximate initial conditions satisfied by the IMFs (this can be directly deduced from the measured time series). If the system is linear then $\eta = 1$, so $\eta > 1$ accounts for the energy of the nonlinear terms. Using these expressions a partial construction of the frequency-energy plot (FEP) can be made (corresponding to the studied transition) and a global picture of the dynamics deduced. By considering different nonlinear transitions we may construct different regions of the FEP and perform global identification of the dynamics over broad frequency and energy ranges.

As a demonstration of global nonlinear identification, in Fig. 5 we provide a partial reconstruction of the FEP for the strongly nonlinear system of coupled oscillators (5), and compare it to the exact result. The reconstructions were performed for the two damped transitions depicted in Fig. 4. In this case, the mass distribution of the system is $m_1 = 1$ (LO) and $m_2 = \epsilon = 0.05$ (NES), and the correction factor is computed as $\eta = 1.5$. In the left of Fig. 5 the FEP reconstructions are performed using the instantaneous frequency and energy estimates derived above, whereas the right is based on direct wavelet transform spectra of the identified dominant IMFs. In both cases we demonstrate the efficacy of performing global nonlinear system identification based on the identified dominant IMFs of the responses.

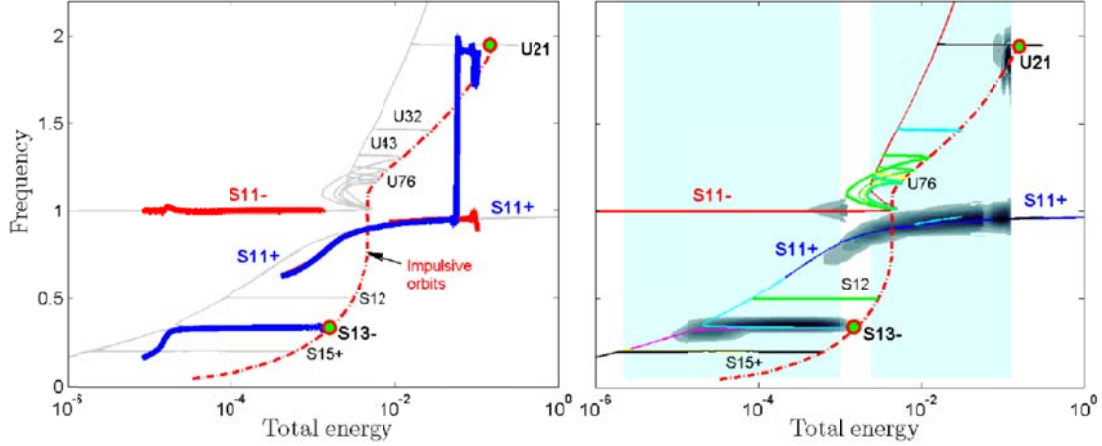


Fig. 5 Global identification on the FEP of system (5): reconstructions based on frequency and energy estimates of the IMFs (left), and direct wavelet transform spectra of the IMFs (right)

4.2 Local Aspect of NSI: Slow-Flow Models

To each transition in the FEP there corresponds a local model of the dynamics which we now proceed to construct. As discussed previously *nonlinear systems may possess multiple co-existing solutions, so when performing NSI we must account for this eventuality*; i.e., the possibility that depending on the initial conditions the system may possess different co-existing local models in the same energy range. The global transitions in the FEP discussed in the previous section can help us clarify this issue. The construction of the local model for a given transition in the FEP will be based on the correspondence between the theoretical and empirical slow-flows discussed in Section 2. This allows us to interpret the slow components of the identified IMFs of the nonlinear systems as the underlying slow-flow responses of the system. Hence, we define the local model as a set of *intrinsic modal oscillators (IMOs) that reproduce the measured time series; moreover, each IMO should approximately reproduce one of the identified dominant IMFs*. As an example, we consider again the nonlinear system of coupled oscillators (5) and develop a local model for the damped transition depicted in Fig. 4 (case of 1:3 transient resonance capture). The dimensionality of the local model depends on the number of dominant IMFs in the corresponding damped dynamics. In this case there exist three dominant IMFs: an IMF for the linear oscillator (LO) at frequency $\omega_2 = 1$ (HF LO), and two IMFs for the nonlinear oscillator (the NES) at frequencies $\omega_1 = 1/3$ (HF NES) and $\omega_2 = 1$ (LF NES), respectively. It follows that the local model should be 3-DOF, and each IMO should reproduce the response of an identified dominant IMF. Hence, we express the local model in the following form,

$$\begin{aligned}
 \text{HF LO} : \ddot{c}_2^{(1)}(t) + 2\zeta_1^{(2)}\omega_2\dot{c}_2^{(1)}(t) + \omega_2^2c_2^{(1)}(t) &\approx \text{Re}[\Lambda_1^{(2)}(t)e^{j\omega_2 t}] \\
 \text{LF NES} : \ddot{c}_1^{(2)}(t) + 2\zeta_2^{(1)}\omega_1\dot{c}_1^{(2)}(t) + \omega_1^2c_1^{(2)}(t) &\approx \text{Re}[\Lambda_2^{(1)}(t)e^{j\omega_1 t}] \\
 \text{HF NES} : \ddot{c}_2^{(2)}(t) + 2\zeta_2^{(2)}\omega_2\dot{c}_2^{(2)}(t) + \omega_2^2c_2^{(2)}(t) &\approx \text{Re}[\Lambda_2^{(2)}(t)e^{j\omega_2 t}]
 \end{aligned} \tag{13}$$

where we keep the notations for the IMFs introduced in Section 2 (cf. Fig. 3), and we omitted the contribution of the low-frequency IMF $c_1^{(1)}(t)$ of the LO as insignificant. The rationale for expressing the local model in the form (13) is that during 1:3 TRC the fast frequencies of the IMFs lock in 1:3 ratio and remain approximately constant; in cases where the fast frequencies vary slowly with time, or we have closely spaced fast frequencies the slow model would need to be modified accordingly (see discussion in Lee *et al.* [24]). The forcing terms in (13) are in the form of fast oscillating terms $e^{j\omega_m t}$, $m = 1, 2$ modulated by slowly-varying complex amplitudes. This particular form of excitation is chosen since otherwise it would be off-resonance and its effect on the dynamics negligible [52]. *In essence, the forcing terms in (13) represent the transient nonlinear modal interactions between the LO and the NES at the dominant fast frequencies of the dynamics.*

The construction of the local model describing the damped transition is facilitated by decomposing the IMOs (13) in terms of slow and fast components, and focusing exclusively on the slow dynamics (as mentioned previously they represent the important underlying dynamics of the transition). This can be achieved by applying complexification-averaging in (13) and introducing the new complex variables, $\dot{c}_m^{(k)}(t) + j\omega_m c_m^{(k)}(t) \equiv \hat{\phi}_k^{(m)}(t)e^{j\omega_m t}$ (LO- $k = 1, m = 1$; NES- $k = 2, m = 1, 2$). Then, we obtain the following slow flow model for the IMOs,

$$\Lambda_k^{(m)}(t) \approx 2 \left[\dot{\hat{\phi}}_k^{(m)}(t) + \zeta_k^{(m)} \omega_m \hat{\phi}_k^{(m)}(t) \right] \quad (14)$$

where the forcing terms on the right-hand-sides are the slow components of the nonlinear modal interactions in (13). The slow complex amplitudes $\hat{\phi}_k^{(m)}(t)$ in (14) can be extracted directly from the identified dominant IMFs $c_m^{(k)}(t)$, so that the slow components of the nonlinear modal interactions, $\Lambda_k^{(m)}(t)$, can be computed once the damping coefficients are estimated. This estimation is performed using an optimization process by imposing the requirement that each of the equations in (13) reproduces the corresponding slow component of the IMF. Further details are provided in Lee *et al.* [24]. It follows that we can directly compute the nonlinear modal interactions (i.e., the forcing terms) in (14) and computationally reconstruct the slow-flow dynamics for this transition. Additional applications of the outlined NSI methodology were performed in identifying and reduced-order modeling of the strongly nonlinear interactions that trigger aeroelastic instability (flutter) of an in-flow wing [25]; in identifying the nonlinear interactions governing passive flutter suppression of a wing with an attached nonlinear energy sink [24]; and in the study of nonlinear interactions of a flexible component with an attached essentially nonlinear substructure [26]. Current work focuses in extending the methodology to dynamical systems with closely spaced modes and in systems with non-smooth nonlinearities. This second aspect is discussed below.

5. CONCLUDING REMARKS

We presented the basic elements of a time-domain nonlinear system identification (NSI) method based on the close correspondence between analytical and empirical slow-flow dynamics, and modeling the local and global nonlinear dynamics of both smooth and non-smooth dynamical systems. Since the NSI method requires no *a priori* system information but instead relies only on direct analysis of measured time series (i.e., it is a purely output-based approach), it holds promise of broad applicability to a general class of nonlinear systems. The derived nonlinear interaction models (NIMs) are sets of intrinsic modal oscillators (IMOs) that result from direct empirical slow-flow analysis of the time series. Finally, the instantaneous frequencies and total energies in the modal space are calculated with the help of the established NIMs. The resulting frequency-energy plots (FEPs) provide a global model of the nonlinear dynamics. We provided two examples that demonstrate that the branches obtained from the NSI method can approximate those calculated from the corresponding mathematical model with reasonable accuracy.

ACKNOWLEDGMENTS

This material is based upon work supported by the National Science Foundation under Grant Nos. CMMI-0927995 and CMMI-0928062.

REFERENCES

- [1] Ewins DJ. *Modal Testing: Theory and Practice*. Research Studies Press, UK, 1990.
- [2] Brandon JA. Some insights into the dynamics of defective structures. *Proceedings of the Institution of Mechanical Engineers, Part C: Journal of Mechanical Engineering Science* 1998; 212(6): 441-454.
- [3] Nayfeh AH, Mook D. *Nonlinear Oscillations*. Wiley Interscience: New York, 1985.
- [4] Kerschen G, Golinval J-C, Vakakis AF, Bergman LA. The method of proper orthogonal decomposition for order reduction of mechanical systems: An overview. *Nonlinear Dynamics* 2005; 41(1-3): 147-170.
- [5] Kerschen G, Worden K, Vakakis AF, Golinval J-C. Past, present and future of nonlinear system identification in structural dynamics. *Mechanical Systems and Signal Processing* 2005; 20(3): 505-592.
- [6] Moon FC. *Chaotic Vibrations: An Introduction for Applied Scientists and Engineers*. Wiley Interscience: New York, 2004.
- [7] Nichols JM, Virgin LN. System identification through chaotic interrogation. *Journal of Sound and Vibration* 2003; 17(4): 871-881.
- [8] Feeny BF, Yuan C-M, Cusumano JP. Parametric identification of an experimental magneto-elastic oscillator. *Journal of Sound and Vibration* 2001; 247(5): 785-806.
- [9] Silva W. Identification of nonlinear aeroelastic systems based on the Volterra theory: Progress and opportunities. *Nonlinear Dynamics* 2005; 39: 25-62.
- [10] Masri S, Caughey T. A nonparametric identification technique for nonlinear dynamic systems. *Transactions of the ASME, Journal of Applied Mechanics* 1979; 46: 433-441.
- [11] Leontaritis IJ, Billings SA. Input-output parametric models for nonlinear systems. Part I. Deterministic nonlinear systems. *International Journal of Control* 1985; 41: 303-328.
- [12] Leontaritis IJ, Billings SA. Input-output parametric models for nonlinear systems. Part II. Stochastic nonlinear systems. *International Journal of Control* 1985; 41: 329-344.

- [13] Feldman M. Non-linear system vibration analysis using Hilbert transform-I. Free vibration analysis method 'FREEVIB'. *Mechanical Systems and Signal Processing* 1994; 8(2): 119-127.
- [14] Feldman M. Non-linear system vibration analysis using Hilbert transform-II. Forced vibration analysis method 'FORCEVIB'. *Mechanical Systems and Signal Processing* 1994; 8(3): 309-318.
- [15] Thothadri M, Casas RA, Moon FC, D'Andrea R, Johnson CR. Nonlinear system identification of multi-degree-of-freedom systems. *Nonlinear Dynamics* 2003; 32: 307-322.
- [16] Masri S, Miller R, Saud A, Caughey T. Identification of nonlinear vibrating structures. I. Formulation. *Transactions of the ASME, Journal of Applied Mechanics* 1987; 54(4): 918-922.
- [17] Masri S, Miller R, Saud A, Caughey T. Identification of nonlinear vibrating structures. II. Applications. *Transactions of the ASME, Journal of Applied Mechanics* 1987; 54(4): 923-950.
- [18] Masri SF, Caffrey JP, Caughey TK, Smyth AW, Chassiakos AG. A general data-based approach for developing reduced-order models of nonlinear MDOF systems. *Nonlinear Dynamics* 2005; 39(1): 95-112.
- [19] Vakakis AF, Manevitch L, Mikhlin Y, Pilipchuk V, Zevin A. *Normal Modes and Localization in Nonlinear Systems*. Wiley Interscience: New York, 1996.
- [20] Amabili M, Touzé C. Reduced-order models for nonlinear vibrations of circular cylindrical shells: Comparison of POD and asymptotic nonlinear normal modes methods. *Journal of Fluids and Structures* 2007; 23(6): 885-903.
- [21] Touzé C, Thomas O, Chaigne A. Hardening/softening behaviour in nonlinear oscillations of structural systems using nonlinear normal modes. *Journal of Sound and Vibration* 2004; 273: 77-101.
- [22] Touzé C, Amabili M. Nonlinear normal modes for damped geometrically nonlinear systems: Application to reduced-order modeling of harmonically forced structures. *Journal of Sound and Vibration* 2006; 298: 958-981.
- [23] Lee YS, Tsakirtzis S, Vakakis AF, Bergman LA, McFarland DM. Physics-based foundation for empirical mode decomposition: Correspondence between intrinsic mode functions and slow flows. *AIAA Journal* 2009; 47(12): 2938-2963.
- [24] Lee YS, Tsakirtzis S, Vakakis AF, McFarland DM, Bergman LA. A time-domain nonlinear system identification method based on multiscale dynamic partitions. *Meccanica*, in press.
- [25] Lee YS, Vakakis AF, McFarland DM, Bergman LA. Time-domain nonlinear system identification of the dynamics of aeroelastic instability suppression based on targeted energy transfers. *The Aeronautical Journal* 2010; 114(1151).
- [26] Tsakirtzis S, Lee YS, Vakakis AF, Bergman LA, McFarland DM. Modeling of nonlinear modal interactions in the transient dynamics of an elastic rod with an essentially nonlinear attachment. *Communications in Nonlinear Science and Numerical Simulations* 2010; 15 (9): 2617-2633.
- [27] Huang N, Shen Z, Long S, Wu M, Shih H, Zheng Q, Yen N-C, Tung C, Liu H. The empirical mode decomposition and the Hilbert spectrum for nonlinear and non-stationary time series analysis. *Proceedings of the Royal Society of London, Series A. Mathematical and Physical Sciences* 1998; 454: 903-995.
- [28] Manevitch L. The description of localized normal modes in a chain of nonlinear coupled oscillators using complex variables. *Nonlinear Dynamics* 2001; 25: 95-109.
- [29] Verhulst F. Singular perturbation methods for slow-fast dynamics. *Nonlinear Dynamics* 2007; 50: 747-753.
- [30] Verhulst F. *Nonlinear Differential Equations and Dynamical Systems*. Springer-Verlag: New York, Inc., 2nd ed., 1995.
- [31] Vakakis AF, Gendelman O, Bergman LA, McFarland DM, Kerschen G, Lee YS. *Passive Nonlinear Targeted Energy Transfer in Mechanical and Structural Systems: I and II*. Springer-Verlag: Berlin and New York, 2008.
- [32] Lochak P, Meunier C. *Multiphase Averaging for Classical Systems: With Applications to Adiabatic Theorems*. Springer-Verlag, 1988.
- [33] Arnold VI. *Dynamical Systems III, Encyclopedia of Mathematical Sciences Vol. 3*. Springer Verlag: Berlin and New York, 1988.
- [34] Kerschen G, Lee YS, Vakakis AF, McFarland DM, Bergman LA. Irreversible passive energy transfer in coupled oscillators with essential nonlinearity. *SIAM Journal on Applied Mathematics* 2006; 66(2): 648-679.
- [35] Huang N, Shen Z, Long S. A new view of nonlinear water waves: The Hilbert spectrum. *Annual Review of Fluid Mechanics* 1999; 31: 417-457.
- [36] Huang N, Wu M-L, Long SR, Shen S, Qu W, Gloersen P, Fan K. A confidence limit for the empirical mode decomposition and Hilbert spectral analysis. *Proceedings of the Royal Society of London, Series A. Mathematical and Physical Sciences* 2003; 459: 2317-2345.
- [37] Wu Z, Huang NE. Ensemble empirical mode decomposition: A noise-assisted data analysis method. *Advances in Adaptive Data Analysis* 2009; 1: 1-41.
- [38] Yang JN, Lei Y, Pan S, Huang N. System identification of linear structures based on Hilbert-Huang spectral analysis. Part 1: Normal modes. *Earthquake Engineering & Structural Dynamics* 2003; 32: 1443-1467.
- [39] Yang JN, Lei Y, Pan S, Huang N. System identification of linear structures based on Hilbert-Huang spectral analysis. Part 2: Complex modes. *Earthquake Engineering & Structural Dynamics* 2003; 32: 1533-1554.
- [40] Pai PF. Nonlinear vibration characterization by signal decomposition. *Journal of Sound and Vibration* 2007; 307: 527-544.

- [41] Tsakirtzis S. *Passive targeted energy transfers from elastic continua to essentially nonlinear attachments for suppressing dynamical disturbances*. PhD Thesis, Department of Applied Mathematical and Physical Sciences, National Technical University of Athens, Athens, Greece, 2006.
- [42] Georgiades F. *Nonlinear localization and targeted energy transfer phenomena in vibrating systems with smooth and non-smooth stiffness nonlinearities*. PhD Thesis, Department of Applied Mathematical and Physical Sciences, National Technical University of Athens, Athens, Greece, 2006.
- [43] Panagopoulos PN, Georgiades F, Tsakirtzis S, Vakakis AF, Bergman LA. Multi-scaled analysis of the damped dynamics of an elastic continuum with an essentially nonlinear end attachment. *International Journal of Solids and Structures* 2007; 44: 6256-6278.
- [44] Georgiades F, Vakakis AF, Kerschen G. Broadband passive targeted energy transfer from a linear dispersive rod to a lightweight essentially nonlinear end attachment. *International Journal of Non-Linear Mechanics* 2007; 42: 773-788.
- [45] Yu D, Cheng J, Yang Y. Application of EMD method and Hilbert spectrum to the fault diagnosis of roller bearings. *Mechanical Systems and Signal Processing* 2005; 19: 259-270.
- [46] Junsheng C, Dejie Y, Yu Y. The application of energy operator demodulation approach based on EMD in machinery fault diagnosis. *Mechanical Systems and Signal Processing* 2007; 21: 668-677.
- [47] Rilling G, Flandrin P, Gonçalves P. On empirical modedecomposition and its algorithms. *IEEE-Eurasip Workshop on Nonlinear Signal and Image Processing*, Grado, Italy, June 2003.
- [48] Flandrin P, Rilling G, Gonçalves P. Empirical mode decomposition as a filter bank; *IEEE Signal Processing Letters* 2004; 11(2): 112-114.
- [49] Feldman M. Time-varying vibration decomposition and analysis based on the Hilbert transform. *Journal of Sound and Vibration* 2006; 295(3-5): 518-530.
- [50] Rilling G, Flandrin P. One or two frequencies? The empirical mode decomposition answers. *IEEE Transactions on Signal Processing* 2008; 56(1): 85-95.
- [51] Lee YS, Kerschen G, Vakakis AF, Panagopoulos P, Bergman LA, McFarland DM. Complicated dynamics of a linear oscillator with a light, essentially nonlinear attachment. *Physica D* 2005; 204(1-2): 41-69.
- [52] Harvey TJ. Natural forcing functions in nonlinear systems. *AMSE Journal of Applied Mechanics* 1958; 25: 352-356.

Characterization of Rotating Structures in Coast-down by means of Continuous Tracking Laser Doppler Vibrometer

M. Martarelli¹, C. Santolini², P. Castellini²

¹Università degli Studi e-Campus - Via Isimbardi 10 - 22060 Novedrate (CO), Italy

²Università Politecnica delle Marche, via Brecce Bianche, 60131 Ancona, Italy

ABSTRACT

In rotating machinery variations of modal parameters with rotation speed may be extremely important in particular if very light and undamped structures are taken into account, like helicopters rotors or wind turbines.

The relation between natural frequencies and rotation speed is expressed in the form of Campbell diagrams. However it could be required to know also the deviation of operational or mode shapes.

In several cases it is not possible to fully control the rotating speed of the machine and only coast-down tests can be performed. Such kind of tests is often fast due to the reduced inertia of rotors: for this reason, an experimental technique able to determine Operational Deflection Shapes (ODSs) in short time and with sufficient accuracy, appears very promising. Moreover coast-down processes are very difficult to be controlled, they causing unsteady vibrations.

The need to obtain ODSs from coast-down experiments requires the measurement over a large number of points and therefore a very efficient approach for the rotation control and synchronous acquisition must be developed.

In this paper a continuous scanning system operating on rotating structures has been developed, that allows to measure ODS and natural frequencies excited in rotating conditions at different rotation speed during a coast down. This techniques has been tested on a laboratory test bench and compared with traditional Experimental Modal Analysis (EMA) results obtained in non-rotating conditions and with data from Tracking Laser Doppler Vibrometry (TLDV) operating in coast down and at consecutive constant rotation speeds (i.e. each measurement was performed in steady conditions). EMA and TLDV have been performed over a grid of points in order to have ODSs with adequate spatial resolution, it requiring long measurement time. However these data has been used as reference to validate the continuous scanning approach.

1. Introduction

The dynamic characterization of rotating structures is an important task for understanding their structural behavior in operating conditions and in relation to the operation speed. The theory behind the variation of the modal parameters with the rotation speed has been deeply studied, see [1], [2] and [3]. This theory has been applied in the past to rotating machinery, in particular, turbine engines, turbofan and helicopter rotors. Nowadays the topic becomes very interesting for the understating of wind turbines dynamics and the work carried out in this paper can be applied in this context. Typical excitations of wind turbines, inducing vibrations, are: (i) aerodynamic, (ii) mass (tuned at the engine orders), (iii) gyroscopic and friction (acting at the rolling surfaces) forces, (iv) oscillating torque of the motor.

It is well known that the natural frequencies of rotating structures increases depending to the speed because rotation introduces a gyroscopic force acting as tensile axial load inducing stiffness raising. The relation between natural frequencies of a uniform rectangular plate (as it can be seen a single blade of the rotating structure studied in this paper, see Fig. 2), subject to normal in-plane load ($f_{Li,j}$) and the natural frequencies of the unloaded plate ($f_{i,j}$) is given by the following equation [4]:

$$f_{Li,j} = \sqrt{f_{i,j} + \frac{hF_g}{4Xm}} = \sqrt{f_{i,j} + \frac{hF_g}{4Xm} m\omega^2 Y} \quad (1)$$

where F_g is the normal load, X , Y and m the plate dimensions and mass, see scheme in Fig. 1, and h a tabulated coefficient depending on mode shapes and boundary conditions (clamped-free in this case). The normal load is the centrifugal force, $m\omega^2 Y$, ω being the rotational speed.

The trend of the first fourth theoretical natural frequencies, calculated from the static ones (measured as shown in Section 3), are reported in Fig. 1 (right). It can be noticed that the parabolic trend, as expected from eq. 1, is more marked for the first and third mode. This is explained by the fact that these modes have horizontal Nodal Lines (NL) and therefore they are more influenced by the gyroscopic force, acting to the NL perpendicular direction, unlike it happens for the modes with vertical NL.

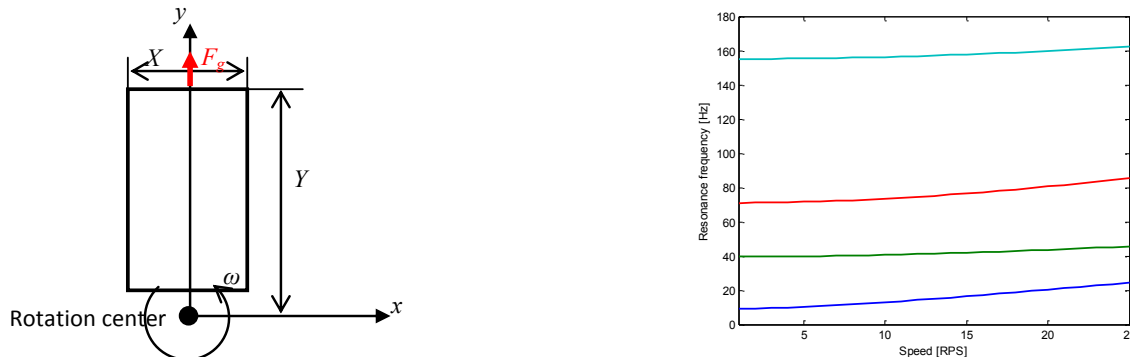


Fig. 1 Blade layout (left) and theoretical dependence of the natural frequencies on the rotation speed (right)

It has been demonstrated in [5] that the in-plane (tensile or compression) load acting on a beam has no significant effect on the mode shapes and this stands also for isotropic and orthotropic plates.

On the other hands, if the structure is made of composite material, this assessment does not go anymore [6]. In this case the possibility of measuring and monitoring the ODSs of the blade during different rotation speeds is an important issue.

In this paper the blade under test has been characterized, first, in static condition using modal analysis of impact test data and, secondly, in rotation by measuring on a grid of points over its surface with LDV synchronous with the rotation, i.e. TLDV, [7], [8] and [9]. This technique is based on the use of the Scanning Laser Doppler Vibrometer (SLDV) for Lagrangian measurements. The goal is to lock the laser beam to a single point as that point moves and vibrates with the structure. This enables structural vibrations to be measured in operating conditions. The TLDV [10] is basically a SLDV system modified into a controlled tracking system for rotational motions by driving the two moving mirrors via clock signals generated by an angular position transducer (encoder) linked to the shaft of the rotating device. This strategy has been applied in several kinds of rotating machinery, as helicopter rotors [11] and fans [12].

Therefore, an optimized methodology to recover the ODSs of rotating structures has been applied to the blade during constant regime and also coast-down. The method is based on Continuous Scanning Laser Doppler Vibrometry (CSLDV) synchronous with the structure rotation, i.e. operating in tracking fashion and hence called Tracking CSLDV (TCSLDV). Laser Doppler Vibrometry (LDV) is a non contact techniques allowing to perform remote measurements of structural vibration velocities that is a prerequisite in rotating machinery tests [13], [14]. Based on LDV, the CSLDV is able to reconstruct ODSs with a single shot measurement, because the LDV output is modulated by the ODS itself, the laser beam being scanning over the whole surface of the structure, [15]. This technique has been usually applied in controlled excitation conditions and mostly in resonance lock-in, this allowing a higher Signal to Noise Ratio (SNR) and a better reconstruction of the ODS by demodulation. For structures with well separated mode shapes it has been also used in impact testing [16]. For rotating structures, as bladed discs, the CSLDV has been applied in the asynchronous fashion in [17] and synchronously with rotation in [18], but it has never been applied in coast-down. In the case of rotating structure characterization, the CSLDV has been always employed with controlled excitation. In rotating conditions the coupling of the excitation source and the moving structure is a challenging task since the contact techniques must be obviously avoided. Typical exciters used in the state of the art are electromagnetic or pulsed laser. This latter has been deeply studied in [19], where the force induced by the laser pulse has been simulated via FEM and quantified in [20].

In this work, instead, the excitation is due uniquely by the forces acting in operating conditions (engine order, friction, aerodynamic loads, motor torque oscillation). For this reason together with the well-known CSLDV drawback, i.e. the speckle noise, an optimization between laser beam scanning frequencies in dependence to the actual excitation must be performed as suggested in [21].

2. Method and instrumentation

2.1 Test bench

The experimental item is a two blade rotating structure built-up with the aim to fine-tune the TCSLDV methodology to be applied in operating excitation conditions. Each blade is made of aluminum and has dimensions of $0.270 \times 0.180 \times 0.025$ m. The motor drive of the fan is clamped to a rigid and massive concrete block, see Fig. 2. The fan is put into rotation by an in-

verter. In order to improve the quality of the LDV data the blades have been covered with retro-reflective tape allowing to increase the scattering of the laser light backwards to the photodetector. This tape allowed also a significant increase of structural damping of the blades.



Fig. 2 Two blade fan

2.2 Measurement techniques

The complete set of testing strategies (SLDV, TLDV, CSLDV and TCSLDV) employed, as basic component, a single point Polytec vibrometer, specifically the OFV-505 with VD-01 velocity decoder. The laser beam was moved point by point, for SLDV purpose, and continuously, for TLDV and CSLDV purpose, via a couple of galvanometric mirrors driven by a thermally controlled PID board. The mirror driving signals have been generated by a NI-PXI-6733 board (16 bit resolution). During the measurement in rotating conditions the laser beam had to move synchronously with the blade. Therefore the generation of the mirrors feeding signals was triggered with a clock provided by the output of an incremental encoder installed on the propeller shaft.

A NI-PXI-4472 board has been used to acquire simultaneously sampled analog inputs with 24-bit resolution. The acquired data were:

- Actual position of the horizontal mirror,
- Actual position of the vertical mirror,
- LDV optical signal level
- LDV velocity signal.

3. Non-rotating characterization

The blade characterization has been performed in static conditions by forcing it into vibration via an impact hammer and measuring its dynamic behavior with a scanning LDV. Modal analysis has been carried out in the measurement data in order to extract modal parameters (frequency, damping and modal vectors). The impulse imposed by the hammer allowed to excite almost all the natural modes of the structure up to 2kHz.

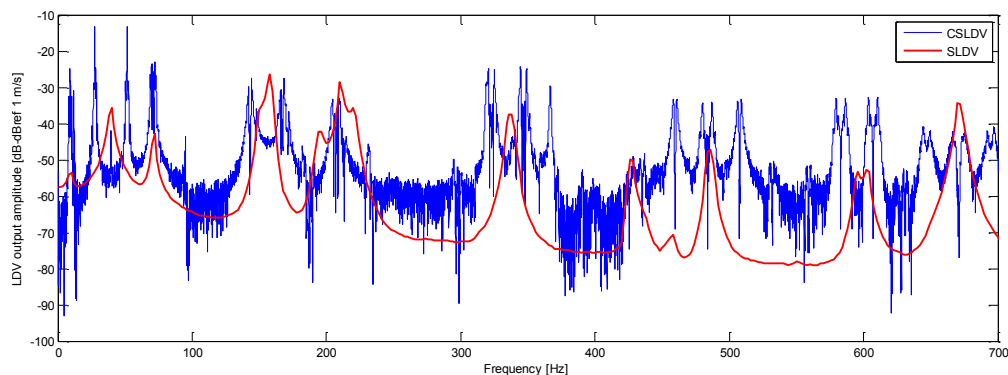


Fig. 3 Scaled FRF sum from the SLDV test (red) and CSLDV output spectrum (blue)

This configuration has been chosen in order to have a range of excitation wider enough to evidence the structural response of the blade to the operating excitation, which can be split in two categories of different nature:

- Engine order excitation depending on unbalancing and mistuning whose energy is inversely proportional to the frequency but increases with RPM,

- Broadband excitation due to the aerodynamic forces and the friction ones acting at the surfaces of the rolling elements and randomly distributed in time. This kind of excitation has increasing amplitude with higher RPM, as well.

The static characterization of the blade has been firstly performed by carrying out a modal analysis of it from the SLDV output data measured over a grid of 7x10 points on each blade excited via impact hammer. The sum of the measured FRFs, appropriately scaled, is reported in Fig. 3.

Then a CSLDV test has been performed on the steady blade excited via impact hammer. In order to cover the whole surface of the blade the mirrors have been fed by sinewaves at the frequencies of 1.1 and 12 Hz (non integer multiple frequencies to achieve a Lissajous picture and sweep different positions over subsequent cycles). The operational deflection shapes of the structure have been recovered from a single shot measurement. Modal analysis could be performed on the unique FRF given by the ratio of the output vibration velocity and the input force (measured by the CSLDV and the hammer). In fact this FRF contains both the time and spatial information needed for the ODS reconstruction. However the modal analysis is not presented in this paper.

The LDV output spectrum measured in CSLDV mode is reported in Fig. 3, superimposed to the EMA FRFs sum. The typical sideband structure is evident from the spectrum. The modal parameters extracted from the SLDV test are reported in Table 1 together with the ODS recovered with CSLDV. A zoom of the spectrum over the natural frequency position is reported in Table 1 for each ODS.

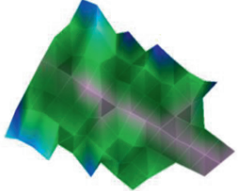
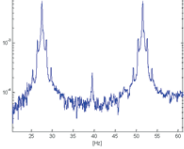
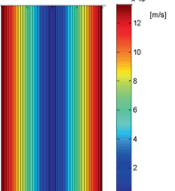
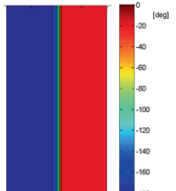
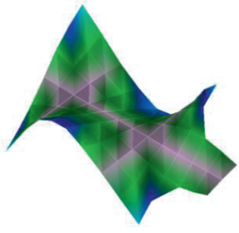
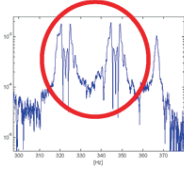
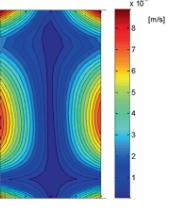
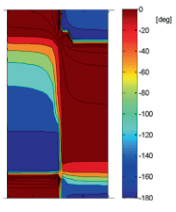
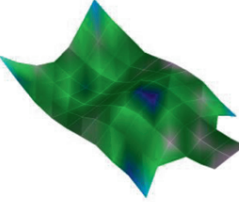
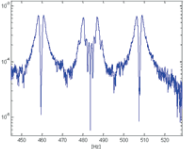
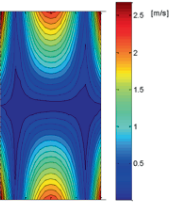
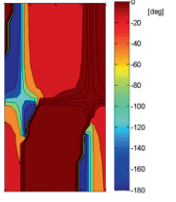
| Mode identification | EMA | | | CSLDV | | |
|---------------------|----------------|-------------|---|--|---|---|
| | Frequency [Hz] | Damping (%) | Mode shape | Frequency and sideband spectrum | Amplitude [m/s] | Phase [deg] |
| 01 | 39.6 | 0.11 |  | 39.6 Hz  |  |  |
| 21 | 334.8 | 0.08 |  | 334.8 Hz  |  |  |
| 12 | 483.6 | 0.13 |  | 483.6 Hz  |  |  |

Table 1 Blade modal parameters and CSLDV ODSs

The sideband spectrum characteristic of each ODS is visible, except for the modes that are not sufficiently excited, i.e. 431 Hz, or for close modes, i.e. the ones in the region for 340 Hz.

4. Rotating characterization

The dynamic characterization of the blade in rotating conditions has been performed by means of the TLDV method, in which it is possible to change the position of the measurement point in the rotating coordinate system by varying the amplitude and phase of the signals that drives the mirrors. This allows to track a single point or to measure sequentially on a grid of points in order to have the spatial information related to the structure ODSs.

The blade has then been tested in TCSLDV fashion when rotating at different RPM steps. By synchronizing the continuous scan with the blade rotation, the Lissajous figure covered by the laser beam is illustrated in Fig. 4.

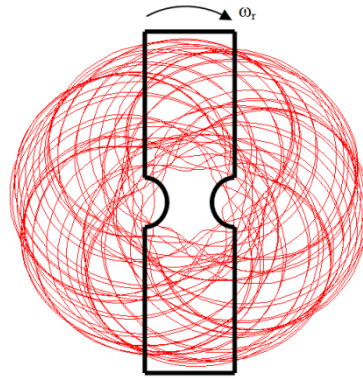


Fig. 4 Laser path synchronized with the blade rotating at ω_r

The blade dynamics has been characterized in rotating conditions at different speeds, from about 2 up to 25 rotation per second [RPS]. The measurement has been performed with TLDV with the laser beam pointed to the tip right corner. By observing the built-up spectrogram, Fig. 5, it can be noticed the second order (parabolic) dependence of the resonance frequencies on the speed, caused by the gyroscopic force. This gyroscopic effect is more marked for resonance frequencies corresponding to natural modes with 10 NL (red lines) rather than modes with 01 NL (black lines), as it has been previously pointed out.

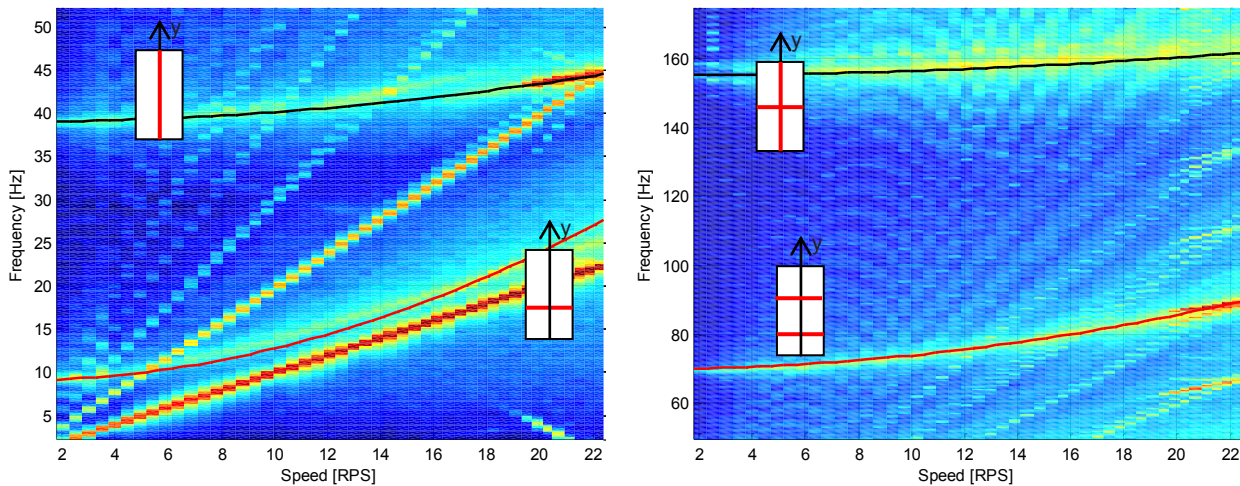


Fig. 5 Stepped run-up spectrogram zoomed around the first and second natural frequencies (left) and around the third and fourth ones (right)

The same has been done by using TCSLDV. The built-up spectrogram is shown in Fig. 6 together with a zoom around the third and fourth resonances. In the last plot the characteristic sidebands are evident: notice that the scanning frequency in y-direction is varying, between 3 and 14 Hz, with the rotation speed in order to optimize the CSLDV output. Therefore the y-sideband spacing (see mode at 155 Hz, black line in Fig. 6) changes. Another parameter that has been varied at the different speed was the LDV sensitivity that was of 25 mm/s/V below 11 RPS, 125 mm/s/V between 12 and 21 RPS and 1000 mm/s/V at 14 and 22 RPS. The reason of the need to set the sensitivity at the lowest value at 14 RPS was related to the presence of a resonance of the rotor support that accidentally correspond to the II mode of the blade, see Fig. 6, left.

To complete the characterization of the blade behavior in rotating conditions the ODSs have been extracted from the CSLDV data. Moreover it has been performed a TLDV test at each rotation speed over a grid of 7x10 points on the blade. The fourth ODS recovered from TLDV and CSLDV data measured at the speeds of 5, 10 and 20 RPS is reported in Table 2. ODSs recovered from TLDV data are given only in terms of amplitude because during the scanning it has not been used a phase reference.

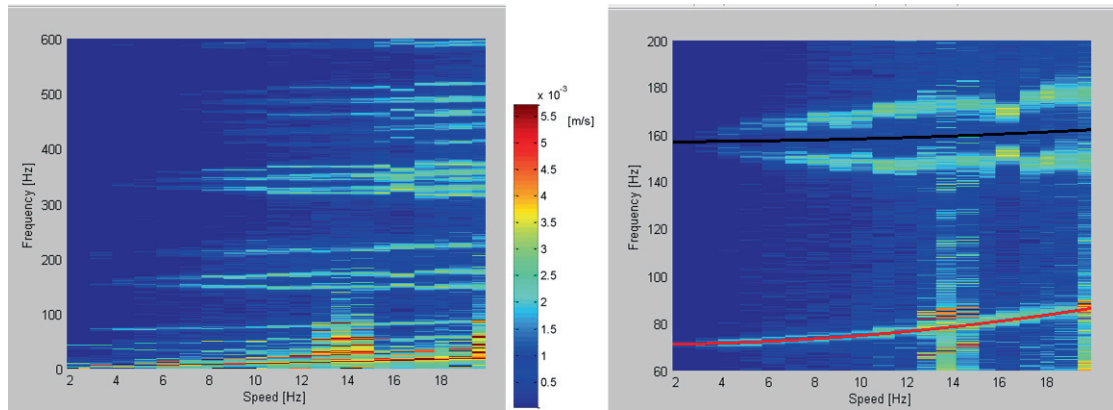


Fig. 6 Stepped CSLDV run-up spectrogram (left) and its zoom around the III and IV blade resonances

| | CSLDV | | TLDV |
|--------|-----------|-------|-----------|
| | Amplitude | Phase | Amplitude |
| 5 RPS | | | |
| 10 RPS | | | |
| 20 RPS | | | |

Table 2 Blade 4th ODS (158 Hz at 0 RPS) obtained via CSLDV and TLDV at different RPS

5. Coast-down characterization

The TLDV and TCSLDV have been finally applied during the rotor coast-down starting from a rotation of 25 RPS. The experimental implementation required an accurate synchronization between the RPM reading, the generation of the waveforms feeding the mirrors and the TCSLDV output acquisition.

The spectrograms relative to TLDV and TCSLDV are shown in Fig. 7 and Fig. 8. In the first one the second order dependence of the blade natural frequencies on the rotational speed is evident. The black lines superimposed to the spectrogram confirm this fact. The spectrogram relative to the TCSLDV agrees with the TLDV one although it is more complex to read because of the sidebands nature of the spectrum around each resonance. Hence Fig. 8 reports only two zooms of the spectrogram in the region of the I, II and III modes (left spectrogram) and of the VI, VII and VIII modes (right spectrogram). The parabolic lines superimposed to the spectrograms are given also for the sidebands of the natural frequencies. The VII mode ones are colored in black to be distinguished from the ones relative to the VI mode, they being overlapping, at least for high rotation speed. The smaller dependence on the gyroscopic effect of the $0i$ NL modes (parabolic lines with less marked curvature) is confirmed.

Table 3 shows the ODSs recovered at two different sections of the coast-down spectrogram, i.e. at average speed of 20.64 and 9.10 RPS respectively. The shapes are almost identical to the ones measured at the corresponding speed given in the previous section. The differences (e.g. deformation of the nodal lines) can be attributed to the lower quality of the LDV signal (lower SNR) due to two facts:

- laser beam scanning frequencies not optimized for the different speeds, but kept constant (e.g. 1.1 Hz and 12 Hz in the x- and y-directions respectively),
- LDV sensitivity maintained fixed to the lowest value (1000 mm/s/V).

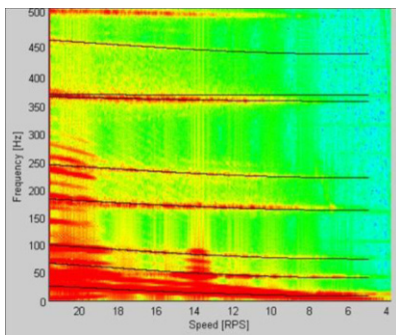


Fig. 7 Coast down spectrogram with natural frequencies parabolic trend

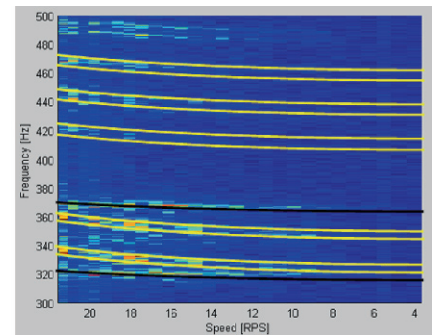
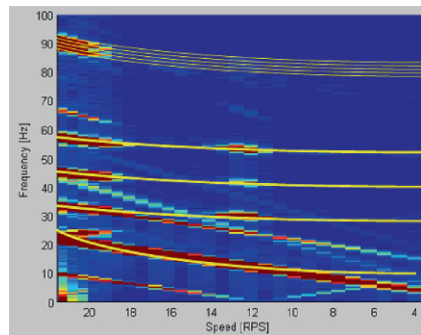


Fig. 8 Coast down spectrogram with superimposed natural frequencies and sidebands parabolic trend

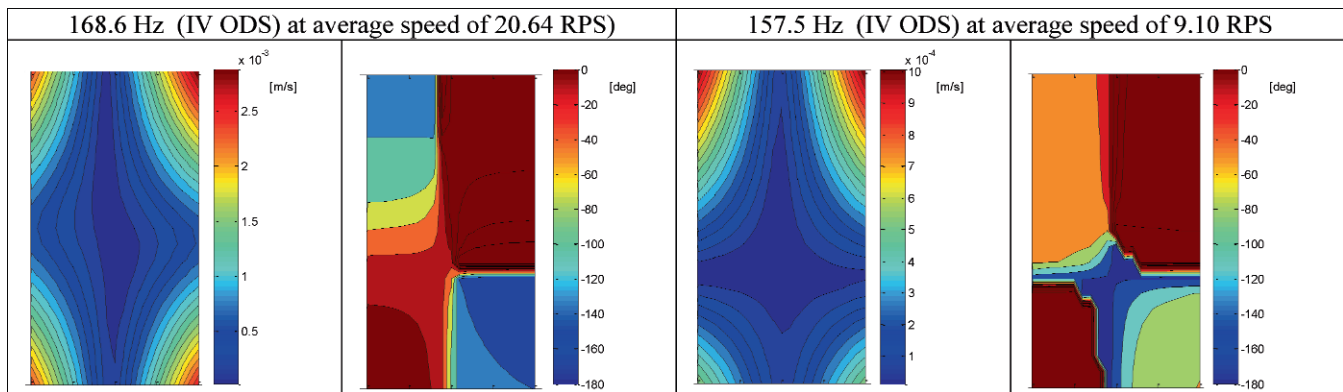


Table 3 Blade ODSs obtained via CSLDV in coast-down (section at average speed of 9.10 RPS and 20.64 RPS)

6. Conclusions

This paper explores the problem of the analysis of vibrational behavior of rotors at different rotational speeds, observing not only the variations of resonant frequencies, but also of the mode shapes. Considering that potential applications of major interest (like wind turbines and helicopter rotors) cannot easily be controlled in the rotating speed, experimental technique must operate in coast-down (or run-up) conditions.

This paper describes the development and testing of a continuous scanning system operating on rotating structures in such a way to measure ODS and natural frequencies excited in rotating conditions at different rotation speed during the coast down. The results obtained on a laboratory bench were compared with theoretical predictions, traditional EMA in non-rotating conditions and with TLDV (both single point and over a grid of points) operating both in coast down and in step-RPM mode (measurement in steady conditions at different rotating speed).

7. Acknowledgements

The activity is partially funded by National Ministry of University with the project PRIN 2008 “Diagnostics methodologies for wind power systems”, prot. 2008AFZKX5.

Authors would like to acknowledge Francesca Sopranzetti and Lorenzo Egidi for the precious support in the experimental campaign.

8. References

- 1 Ewins D. J., (2000). Modal testing. Research studies press LTD.
- 2 Genta G., (2004). Dynamics of Rotating Systems. Mechanical Engineering Series
- 3 Campbell W., (1924). Protection of Steam Turbine Disk Wheels from Axial Vibration. Transactions of the ASME: 31–160.
- 4 Blewins, R. D., (1984). Formulas for natural frequency and mode shape. R.E. Krieger publishing CO., INC.
- 5 McConnell, K. G., (1995). Vibration Testing, Theory and Practice. JOHN WILEY & SONS, INC.
- 6 Sung Kyun Kim, Hong Hee Yoo Vibration Analysis of Rotating Composite Cantilever Plates, *KSME International Journal*. Vol. 16 No.3. pp. 320-326, 2002
- 7 P.Castellini, C.Santolini, “Vibration measurements on blades of naval propeller rotating in water”, in: Proceedings of the Second International Conference of Vibration Measurement by Laser Techniques, SPIE 2368, Ancona, Italy, 1996, pp. 186–194.
- 8 A. Fioretti, D. Di Maio, D. J. Ewins, P. Castellini, E.P.Tomasini, Deflection shape reconstructions of a rotating five-blade helicopter rotor from SLDV measurements, 9th International Conference on Vibration Measurements by Laser and Noncontact Techniques & Short Course, Ancona, 22-25 June 2010.
- 9 S. Di Battista, D. Di Maio, D. J. Ewins, P. Castellini, E.P. Tomasini, Development of a Comprehensive Mathematical Model for Simulating the Effects of Misalignments in Vibration Measurements using Scanning LDV Measurement Systems, 9th International Conference on Vibration Measurements by Laser and Noncontact Techniques & Short Course, Ancona, 22-25 June 2010.
- 10 P.Castellini, N.Paone, “Development of the tracking laser vibrometer: performance and uncertainty analysis”, *Review of Scientific Instruments* 71 (12) (2000) 4639–4647.
- 11 A. Colombo, Applications of Laser Vibrometry to Rotorcraft Development: on-going projects at AgustaWestland in collaboration with Università Politecnica delle Marche, Oral presentation only, 8th International Conference on Vibration Measurements by Laser Techniques & Short Course, Ancona, 17- 20 June 2008
- 12 A.Gasparoni, M. S. Allen, S. Yang, M. W. Sracic, P. Castellini, E.P. Tomasini, Experimental Modal Analysis on a Rotating Fan Using Tracking-CSLDV", 9th International Conference on Vibration Measurements by Laser and Noncontact Techniques & Short Course, Ancona, 22-25 June 2010.
- 13 P.Castellini, G. M.Revel, and E. P. Tomasini, “Laser Doppler Vibrometry: A Review of Advances and Applications”, in *The Shock and vibration digest; a publication of the Shock and Vibration, Information Center, Naval Research Laboratory*, vol. 30, 1998.
- 14 P.Castellini, M. Martarelli, E.P. Tomasini, “Laser Doppler Vibrometry: Development of advanced solutions answering to technology’s needs” in *Mechanical Systems and Signal Processing* 20 (2006) 1265–1285.
- 15 Martarelli M., (2001). M. Martarelli, Exploiting the Laser Scanning Facility for Vibration Measurements. vol. Doctor of Philosophy London: Imperial College of Science, Technology & Medicine University of London.
- 16 A. B. Stanbridge, M. Martarelli, and D. J. Ewins, "Scanning laser Doppler vibrometer applied to impact modal testing," in 17th International Modal Analysis Conference - IMAC XVII. vol. 1 Kissimmee, FL, USA: SEM, Bethel, CT, USA, 1999, pp. 986-991.
- 17 Stanbridge, A. B., Martarelli, M., Ewins, D. J., (2001). Rotating disc vibration analysis with a circular-scanning LDV. In *Proceedings of IMAC XIX*, Kissimmee.
- 18 D. Di Maio, D.J. Ewins, Applications of continuous tracking SLDV measurement methods to axially symmetric rotating structures using different excitation methods, *Mechanical Systems and Signal Processing*, 24, 3013–3036, 2010
- 19 P.Castellini, G.M.Revel, L.Scalise, R.M.De Andrade, “Experimental and numerical investigation on structural effects of laser pulses for modal parameter measurement”, *Optics and Laser in Engineering*, vol.32, pp.565-581, 2000, ed. Elsevier Science Ltd., Northern Ireland, ISSN 0143-8166
- 20 P.Castellini, G.M.Revel, Laser vibration measurements and data processing for structural diagnostic on composite material, *Review of Scientific Instruments*, Volume 71, Issue 1, January 2000, 207-215
- 21 Martarelli M., Ewins D. J., Continuous scanning Laser Doppler Vibrometry and speckle noise occurrence, *Mechanical Systems and Signal Processing*, 20, 8, 2006, pp. 2277-2289, ISSN 0888-3270.

Pyroshock Loaded MISO Response

Janet C. Wolfson* and Jason R. Foley

Air Force Research Laboratory

* AFRL/RWMF; 306 W. Eglin Blvd., Bldg. 432; Eglin AFB, FL 32542-5430, janet.wolfson@eglin.af.mil

Alain L. Beliveau

Applied Research Associates, Inc.

Greg Falbo and Jeff Van Karsen

LMS Americas

ABSTRACT

The Air Force Research Laboratory has developed a new testing method that utilizes pyroshock loading to excite a structure simultaneously over multiple axes. One of the areas of investigation in developing this test capability is the effects of multiple pyroshock loading on the output response of the test structure. A series of Single Input-Single Output (SISO) and Multiple Input-Single Output (MISO) tests have been performed using a combination of single and multiple impact hammers in different geometric configurations. The impacts were applied both simultaneously and individually. The response of the structure was analyzed evaluating the acceleration time history, Frequency Response Functions, and Shock Response Spectra. This analysis was used to determine optimum placement of the multiple input locations and desired output response for the future field tests.

INTRODUCTION

The Air Force Research Lab (AFRL) conducts research in a wide variety of energy regimes. This research is designed to evaluate aspects of a test article over a variety of scales from components to systems and sub-scale to full-scale. One aspect of these endeavors is the multi-axial excitation of a system over the entire frequency spectrum from low (10 Hz) to high (10 kHz) as well as different amplitudes (i.e. – accelerations). A new test article was proposed and an the initial computational study was performed. The analytical results were then compared to a similar near-field pyroshock test. [1] This analysis led to the development of the Multi-Axial Pyroshock Plate (MAPP) test set-up. Initial pyroshock tests were performed on the MAPP test set-up where acceleration time histories were captured and Shock Response Spectra (SRS) were calculated. The success of the tests was determined by comparing the SRS from the tests with a desired SRS band. These initial tests show that the technology could simulate aspects of the SRS, however, the application of the pyroshock needs further refinement. In order to determine the optimum placement of pyroshock inputs a study utilizing the Multiple Input-Single Output (MISO) methodology was performed. A series of laboratory tests were completed on a small aluminum plate. The initial tests focused on a Single Input-Multiple Output (SIMO) analysis at thirty-two different input locations and four output locations. Acceleration time-histories were captured at each location. From that data the Frequency Response Functions (FRF) and Shock Response Spectra (SRS) are calculated. The second series of laboratory tests involved performing a series of Multiple Input-Single Output (MISO) tests. The same analysis was performed on these tests and a comparison was made between the FRF's and SRS's of the single and multiple inputs. Based on the data analyzed from the laboratory tests initial locations of small pyroshock inputs were determined and a test plan was developed for future field tests to determine the feasibility of this approach for larger input forces.

This paper will provide a brief overview of the initial MAPP field tests and discuss the results from that analysis. It will then provide a detailed discussion of the sub-scale laboratory tests and the SIMO and MISO studies that were performed. It will show the benefits of utilizing the MISO methodology over the SIMO tests in achieving a higher magnitude of response depicted in a FRF and SRS. The paper will conclude with a brief discussion of the field tests that will be performed to verify this methodology before it is expanded to include the MAPP test set-up.

MULTI-AXIAL PYROSHOCK PLATE (MAPP) SET-UP

The initial study of the Multi-Axis Pyroshock Plate (MAPP) test set-up occurred in April 2010. The test article consists of a 4' x 8' x 1" thick T6061 aluminum plate that is hung from an aluminum tube by turn buckles. They suspend the plate in simulated Free-Free boundary conditions. The aluminum tube that supports the MAPP test system spans 22' and is connected to concrete blast walls through the use of 3/8" expansion anchors. A "bookshelf" has been welded to the front of the plate, it is 6" long and is constructed out of T6061 Aluminum tube stock. The nominal dimensions on the tube stock are 6" x 6" x 1/2". Figure 1(a) depicts the entire plate with the bookshelf. Figure 1(b) shows a closer view of the bookshelf and a steel plate that is attached to it. In order to allow for the connection of the steel plate, or any other test article, to the bookshelf a series of 8 - 0.32" diameter thru holes were drilled into the bookshelf.

A standard x-, y-, z, coordinate system is assumed for this test article. The x-axis runs along the long side of the plate [along the bottom edge of the plate shown in Figure 1(a)] while the y-axis is located parallel to the short side of the plate [along the left hand side of the plate in Figure 1(a)]. The origin of the coordinate system is located at the lower left hand corner of the plate in the photo below. The z-axis comes out of the plate and runs along the 6" length of the bookshelf. This coordinate system will be used in the discussion of the results for both the field and laboratory tests.



a) Overall MAPP Test Set-up

b) view of "bookshelf" and steel plate

Figure 1 MAPP test article

A series of four tests were performed using small amount of explosive near the center of the plate. Two of the tests utilized a custom AFRL tri-axial mount that housed three shock accelerometers placed in the center of the steel plate attached to the bookshelf. The other two tests utilized a component centered on the bookshelf with the same AFRL tri-axial mount and accelerometers placed within it. The component was attached to the bookshelf through a series of bolts.

INITIAL TEST RESULTS

In the complex environment that AFRL is interested in there is an accepted methodology of developing test requirements using a Shock Response Spectrum (SRS), which was used as our initial figure of merit. The SRS has been proposed as a tool for evaluating the damage potential in a given acceleration time history. The SRS is defined using an array of 1-D spring-mass systems, each with a spring constant tuned to a different resonant frequency ($\omega = \sqrt{k/m}$). The maximum acceleration by an oscillator when coupled to a rigid base moving with the specified acceleration time history defines the "positive" or "negative" SRS depending on the direction of the shock. Further details on the SRS can be found in comprehensive reviews, e.g., Irvine [2]; other spectral

analyses can be found in Scavuzzo and Pusey [3]. The SRS shown in Figure 2 were calculated using the improved filter bank method developed by Smallwood [4, 5]. The positive and negative maximum SRS gives the maximum acceleration of the 1-D spring mass in the respective directions due to the acceleration time history. The SRS provides a measure of the effect of the pyroshock on a simple mechanical model with a single degree of freedom. Generally, a measured acceleration time-history is applied to the model and the maximum acceleration response is calculated. An ensemble of maximum absolute-value accelerations responses is calculated for various natural frequencies of the model.

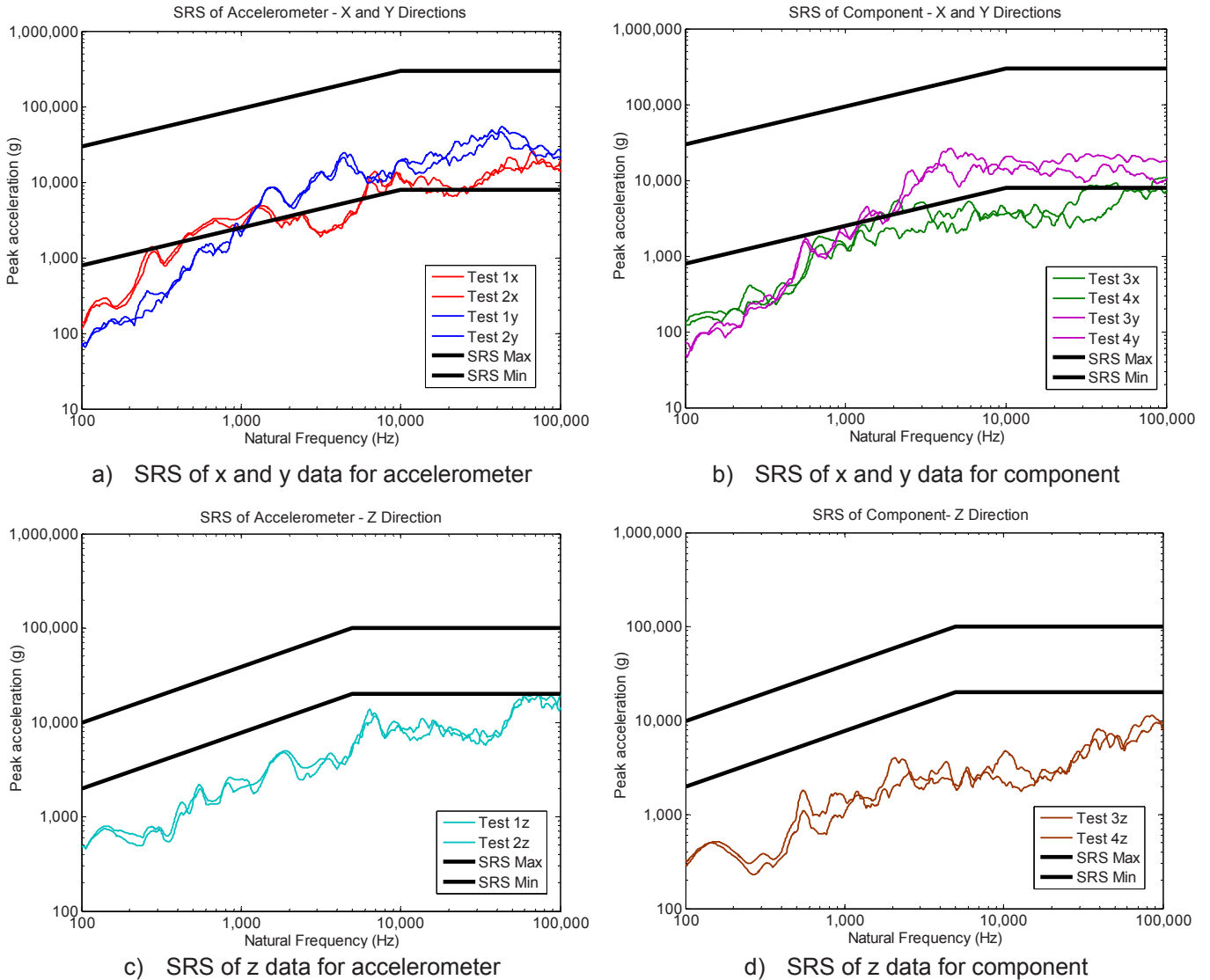


Figure 2 Initial Shock Response Spectra Data

The maximum positive SRS for each test and each axis of the tri-axial accelerometer were calculated and are shown in Figure 2(a) and (c). Figure 2(b) and (d) depict the maximum positive SRS of the tri-axial accelerometer in the component. Figure 2(a) and (b) compares the response of the x- and y-axis for the accelerometer and tri-axial accelerometer in the component, respectively. While, similarly, Figure 2(c) and (d) depict the response of the z-axis for the accelerometer and tri-axial accelerometer in the component. These figures show a variety of interesting phenomena, specifically the consistency in SRS behavior between tests. While this is expected when applying a mechanical shock, it is not as expected when using live explosives to apply energy to the system. It verifies that our test apparatus stays in the elastic regime and is not damaged, or altered, between tests. Additionally, the plots show that in the x- and y-directions the tests were generally successful in achieving the

minimum SRS band above 1,000 Hz. However, it was not able to achieve the desired SRS response in the z-direction for either test article.

SUB-SCALE LABORATORY STUDY

The next phase of this research effort focused on developing a methodology that would allow the engineer, or designer, to pre-determine a specific output response (i.e. – time history, frequency response function, or shock response spectra) and determine the appropriate input. This input could be from an array of mechanical, or pyrotechnic, inputs with three distinct variables: magnitude of input, location of input, and time delay between inputs. In order to develop this methodology an initial laboratory study was performed on an aluminum plate. It focused on developing an array of Frequency Response Functions (FRF) and Shock Response Spectra (SRS) on thirty-two single axis input locations and four tri-axial output locations. The individual input locations were located on a grid placed on a 4' x 2' Aluminum plate. [Figure 3](#) depicts the aluminum plate supported along the long edge of the plate from bungee cords and hung from an A-Frame in simulated the Free-Free boundary conditions (similar to the MAPP test set-up). The FRF study was completed in two roves where the accelerometers are moved from one location to another. On the back side of the plate four tri-axial accelerometers were placed to aid in the determination for the optimum output location. The initial study of the plate involved a Single Input-Multiple Output (SIMO) methodology. The single input from an impact hammer occurred at an accelerometer and the output was measured at every other input and output location. This allowed for the calculation of all of the Autopower Spectra, Cross Power Spectra, and SRS at each of the locations through two roves of accelerometers. The second study involved a Multiple Input-Single Output (MISO) methodology. For these tests two impact hammers were used at to simulate the multiple inputs. The impacts were as simultaneous as possible, but were not exact. The same analysis was performed on the outputs from this test as the SIMO tests.

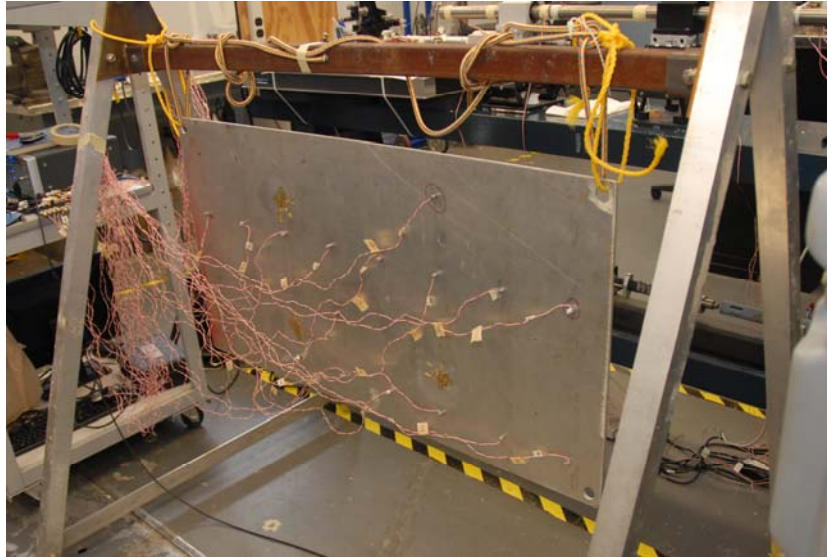


Figure 3 Test Set-up for Laboratory MISO Study

The impacts were as simultaneous as possible, but were not exact. The same analysis was performed on the outputs from this test as the SIMO tests.

ANALYSIS AND DISCUSSION

The results from the laboratory tests show that multiple inputs can significantly affect the desired outputs. An example that compares the results from individual inputs at Point 1 and Point 2 with the results from the simultaneous inputs at Point 1 and 2 are discussed below. Other locations were examined, however, this example depicts the overall trends. [Figure 4](#) shows the acceleration time histories for the z-axis output (orthogonal with the plate) for Point 1 [[Figure 4\(a\)](#)], Point 2 [[Figure 4\(b\)](#)], and the simultaneous impacts at Points 1 and 2, or Combined Points [[Figure 4\(c\)](#)]. It can be seen that the individual impacts have a maximum force of less than 40 g 's, however, if they are combined their overall force magnitude is higher at over 60 g 's. This point is further illustrated in the Frequency Response Functions (FRF's) shown in [Figure 5\(a\)](#). In this plot, similar to [Figure 4](#), the red line represents the FRF at the output location from an input at Point 1. Similarly, the green line represents an input at Point 2, and the blue line is the combined input at Point 1 and 2. [Figure 5\(a\)](#) shows that there are some different principal modes in the two individual inputs, but there are many frequencies where they do have similar responses. When the inputs are combined the magnitude of the response at specific frequencies are generally increased, however, in some instances the overall behavior is reduced at that frequency. The final comparison chart, and the one that shows the most significance, is in [Figure 5\(b\)](#). It shows the comparison of SRS from the individual and combined inputs. The SRS plots shown in [Figure 5\(b\)](#) were calculated using LMS Test.Lab. Unlike the previous SRS plots ([Figure 2](#)), that were calculated in Matlab, this plot has a linear distribution of the frequency and logarithmic distribution of the peak acceleration. The SRS is still valid, and it does not affect the results, it is just another way at looking at the same data. This comparison shows a significant

increase in the damage potential at the output point due to the simultaneous impacts. Above 1000 Hz, there appears to be an order of magnitude increase in the SRS. This initial study has shown the effect that simultaneous impacts can have on the FRF's and the SRS's for the aluminum plate.

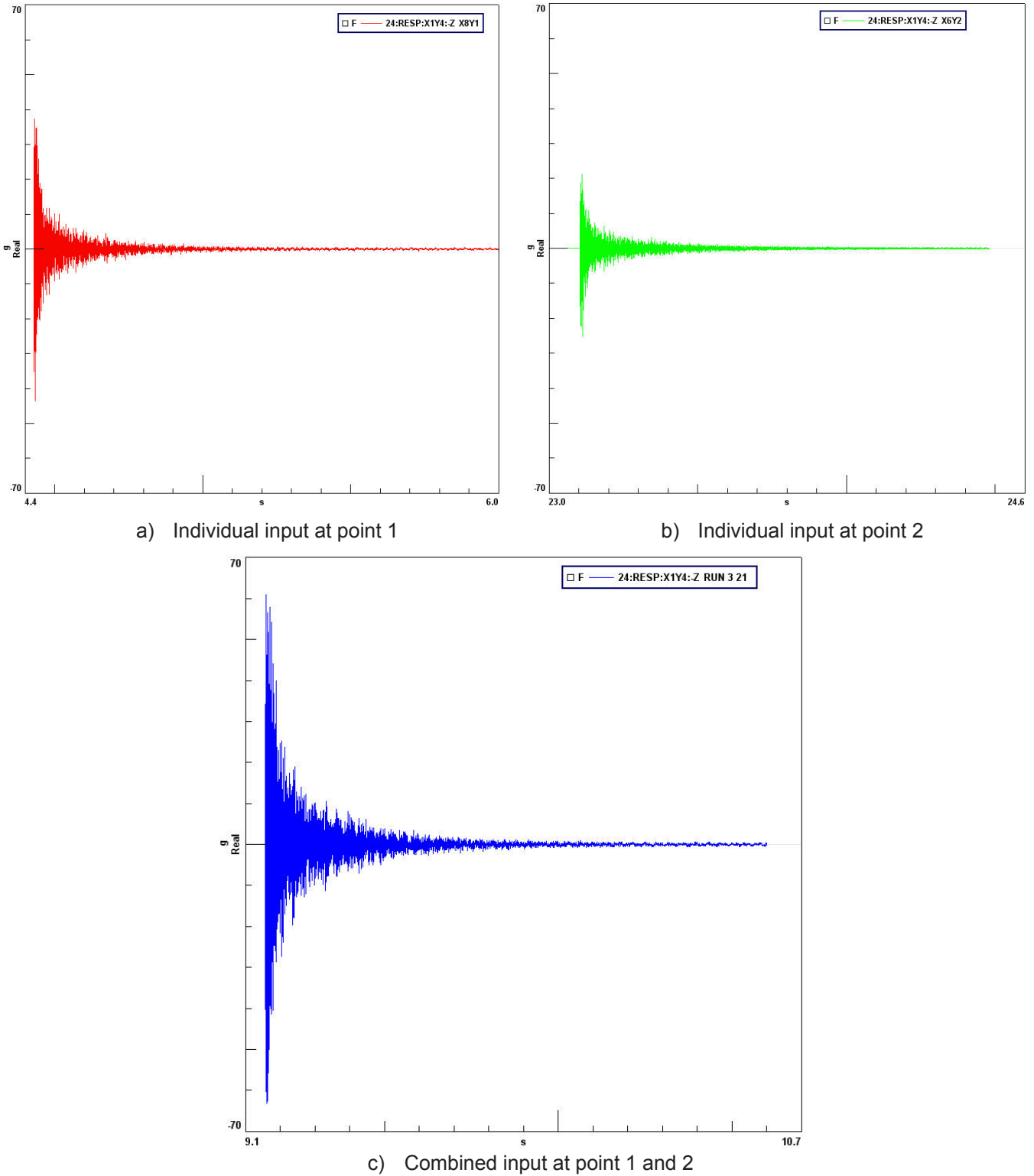


Figure 4 Time History of Individual and Combined Inputs

FUTURE MISO FIELD TESTS

The next step in this research endeavor is to apply this same concept to the aluminum plate tested in the laboratory using pyrotechnic input excitation, as opposed to mechanical input. This test series will evaluate the effects of three detonators applied directly to the aluminum plate and measure the output response at another location. Three input points will be chosen and marked on the plate at the locations shown in Figure 6. For the first series of tests each of the input locations will be evaluated independently. A RP83 detonator will be placed on the back side of the plate shown in Figure 6 at location 1, an ENDEVCO 7570 shock accelerometer will be placed on the front side of the plate at the same location. A tri-axial accelerometer will be placed on the front side of the plate at location 4 that will measure the output. This test will allow for the creation of a FRF between the input and output location based on the acceleration-time histories. Upon completion of the tests and the analysis of the results the FRF's from the pyroshock tests can be compared to similar FRF's of the acceleration time-history captured in the laboratory. For statistical consideration the initial test of one detonator at location1 will be performed a total of six times. The same tests will be performed at input location 2 and 3; however, these tests will only be performed once. Once that initial study is completed the second portion of this test series will be evaluated. It will consist of utilizing all three input locations and simultaneously initiate the detonators. Similar to the previous tests, accelerometers will capture the initial input from each of the RP83 detonators and a tri-axial accelerometer will measure the output. This test will also be performed a total of six times, and are scheduled to be completed at the end of October 2010.

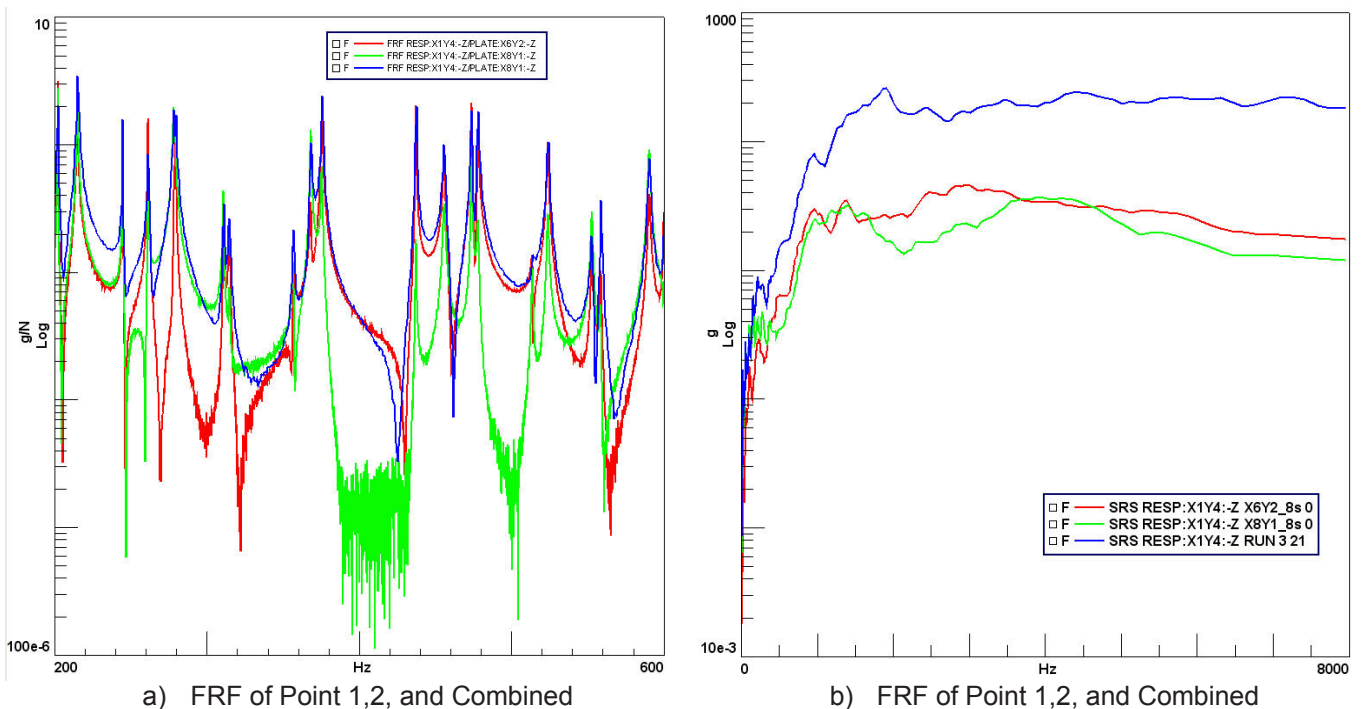


Figure 5 Frequency Response Function and Shock Response Spectra of Points 1 and 2 and Combined

SUMMARY

A new test apparatus to impart a specific shock level (amplitude, frequency, and direction) that has been exhibited under impact tests, called the Multi-Axial Pyroshock Plate test set-up, has been developed. Initial tests showed that using a small amount of explosives near the center of the plate can excite an accelerometer and a component such that it crosses the minimum Shock Response Spectra line at frequencies over 1000 Hz. Based on the initial test series a further study of Single Input-Multiple Output (SIMO) and Multiple Input-Single Output (MISO) laboratory tests were performed on an aluminum plate. They showed that by providing multiple impacts on a plate, at specific locations, the additional input can generally increase the magnitude of the Frequency Response Functions. Additionally, when looking at the Shock Response Spectra there is a significant increase in the damage potential at the output point due to the simultaneous impacts. Initial results show an order of magnitude increase in the Shock Response Spectra at natural frequencies above 1000 Hz. Based on this initial laboratory study a field experiment has been proposed that will evaluate the same types of inputs developed in

the laboratory. Three distinct locations will be excited both individually and simultaneously by a small explosive. An analysis will be performed on the data recovered from these tests and compare the Frequency Response Functions and the Shock Response Spectra of the individual inputs and the multiple inputs to determine the effects of the differences in Single Input-Single Output and Multiple Input-Single Output responses.

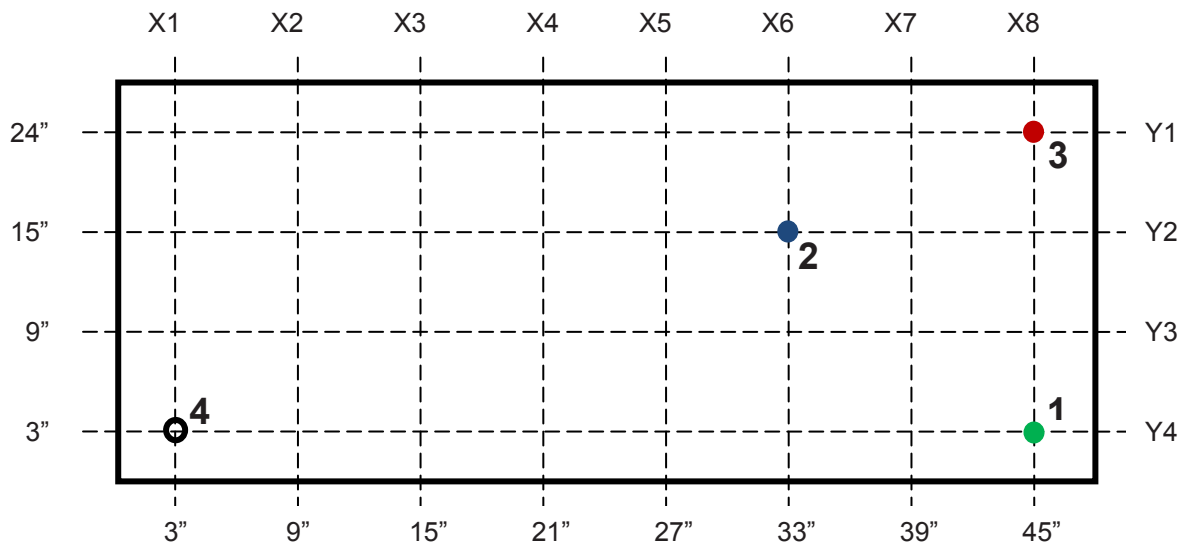


Figure 6 Input and Output Locations for Future MISO Tests

ACKNOWLEDGEMENTS

Janet Wolfson would like to acknowledge research funding from Mr. Danny Hayles and the Defense Threat Reduction Agency.

REFERENCES

1. Wolfson, J., et al., *Modal Testing of Complex Hardened Structures*, in *IMAC XXVIII A Conference and Exposition on Structural Dynamics*. 2010: Jacksonville, FL.
2. Irvine, T., *An Introduction to the Shock Response Spectrum*. 2002.
3. Scavuzzo, R.J. and H.C. Pusey, *Principles and Techniques of Shock Data Analysis*. 2nd Edition ed. 1995, Arlington, VA: SAVIAC.
4. Smallwood, D.O., *The Shock Spectrum at Low Frequencies*. *Shock and Vibration Bulletin*, 1986. **56**(No. 1, Appendix A): p. 9.
5. Smallwood, D.O. *Improved recursive formula for calculating shock response spectra*. in *Proceedings of 51st Symposium on Shock and Vibration*. 1981. San Diego, CA: SAVIAC.
6. Harris, C.M. and A.G. Piersol, eds. *Harris' Shock and Vibration Handbook*. Fifth ed. 2002, McGraw-Hill.
7. Foley, J.R., et al. *Wideband Characterization of the Shock and Vibration Response of Impact-Loaded Structures*. in *SEM IMAC XXVII*. 2009. Orlando, FL: SEM.

Development of a Long Term Viable Dynamic Data Archive Format

Allyn W. Phillips, PhD, Research Associate Professor
Randall J. Allemang, PhD, Professor
School of Dynamic Systems, College of Engineering and Applied Sciences
PO Box 210072, University of Cincinnati, Cincinnati, OH 45221-0072 USA

ABSTRACT

For nearly forty years, the Universal File Format has served as a de facto standard for cross platform data interchange and archiving. However, as technology has progressed, the aging nature of this eighty character ASCII FORTRAN card image based format has become problematic. As a result, with the ever increasing legal requirements of long term record keeping, a flexible, open definition file format suitable for viable long term archiving of data and results, which is not dependent upon any particular hardware or operating system environment has become necessary. This paper focuses upon the various (sometimes conflicting) issues involved in the decision process and the resulting principal identified features necessary for realistic, long term reliable recovery of information and successful community adoption.

1. Introduction

1.1 DSA Objective

Within the vibration technical community, there is a need for a long term viable, open definition file format for the archiving of dynamic signal data and results. This flexible archive format, independent of any particular hardware or operating system environment and distinct from any particular database management structure, is needed in order to satisfy the increasing legal requirements of long term record keeping. For many years, the Universal File Format has been the de facto standard in this area. However, as technology has progressed, the aging nature of this eighty character line oriented, ASCII, FORTRAN card image based format has become problematic. Following a brief discussion of some of the strengths and weaknesses of existing data formats, this document focuses upon the identified feature set needed for realistic, long term reliable recovery of information and successful future community adoption.

Additionally, as a direct outgrowth of the long term archive integrity objective and the ever increasing capacity of data storage media, the opportunity for an important paradigm shift from the traditional storage of reduced frequency data to the storage of complete raw time series becomes viable. The long term preservation of the underlying original data sources provides the capability to reanalyze the acquired test data at some unknown future date. Such unforeseen analyses and data mining exercises are anticipated in the event of unexplained system behavior and/or as more sophisticated data reduction algorithms are developed.

DISCLAIMER

This work of authorship and those incorporated herein were prepared by Contractor as accounts of work sponsored by an agency of the United States Government. Neither the United States Government nor any agency thereof, nor Contractor, nor any of their employees, makes any warranty, express or implied, or assumes any legal liability or responsibility for the accuracy, completeness, use made, or usefulness of any information, apparatus, product, or process disclosed, or represents that its use would not infringe privately owned rights. Reference herein to any specific commercial product, process, or service by trade name, trademark, manufacturer, or otherwise, does not necessarily constitute or imply its endorsement, recommendation, or favoring by the United States Government or any agency or Contractor thereof. The views and opinions of authors expressed herein do not necessarily state or reflect those of the United States Government or any agency or Contractor thereof.

COPYRIGHT NOTICE

This document has been authored by a subcontractor of the U.S. Government under contract DE-AC05-00OR-22800. Accordingly, the U.S. Government retains a paid-up, nonexclusive, irrevocable, worldwide license to publish or reproduce the published form of this contribution, prepare derivative works, distribute copies to the public, and perform publicly and display publicly, or allow others to do so, for U. S. Government purposes.

1.2 Guiding Principals

It should be noted that, for the purposes of discussion, the existing Universal File Format (UFF) has been taken as the initial starting reference point. Various other formats were reviewed and considered for content and applicability; however, in order to facilitate technical community adoption, the final resulting format has been specified to be open, extensible, and non-proprietary. In addition, the principle of 'keeping it simple' has been followed in order to facilitate both industry acceptance and long term comprehension. The recognition is that if it gets too complicated, no one will use, support, or adopt it. For this reason, the final resulting format will probably not be perfect for everyone but it should be sufficient for everyone's needs, in other words, a 95% solution. This decision is consistent with the consensus of opinion expressed at a meeting of users and vendors held at IMAC in 1998. The focus of that meeting was to determine the interest level and collect ideas for extending the UFF to address some of its basic deficiencies. In many respects, this project has benefited from and is somewhat of an outgrowth of that activity.

Before discussing the new format, it is important to avoid initial misconceptions by discussing briefly what the new format is not. The new format is focused upon long term archival of dynamic data; as such, issues like the data storage media (hardware) and the vendor specific internal database structures are not being addressed. There is no intention or desire to force any particular hardware or internal database structure upon individual vendors or users. The only goal is to produce a long term, viable, cross platform, open architecture, dynamic data storage format. In practical terms, this format should allow users to export data into a data archival structure that is independent of computer operating system and/or the original application program that generated the data and ultimately retrieve the data into other operating systems and other application programs at some later date (up to 50-75 years later, if necessary). The realistic need to move the data archive from one form of data storage media to another over this extended period of time is not a concern of this effort.

It is also important to recognize that since the content focus is dynamic data, other data content types, such as CAD/CAE, video, pictures, etc., will not be specifically included in the format. It should be noted, however, that although such data will not be specifically identified and targeted for support, nothing in the definition will prevent referencing such information via the metadata records or including it within the data archive container.

One overarching principal however is recoverability! As a long term archive format, any feature or suggestion which jeopardizes recoverability must be subservient. One example of this is the decision to abandon strict backward compatibility with the existing UFF definition; instead, to handle UFF as well as other data formats via an importer/convertor.

1.3 Long Term Goals

The UFF was developed in the late 1960's by the Structural Dynamics Research Corporation (SDRC). The original intent was as a cross platform (software) interchange format. It functioned well in that capacity and because of its success it became the default archive format.

The advantage is that the UFF has been relatively stable and effective for around 40 years. While nobody particularly likes it, nonetheless, as a least common denominator, it has in the past basically gotten the job done. What is needed is to address the core UFF weaknesses that have developed over the years as technology has advanced. The DSA format is intended to fundamentally extend and/or replace the UFF; hence it might be thought of as roughly 'UFF2ish', a sort of second generation UFF.

Again, another important point of clarity should be noted: the purpose of the format is primarily archival, not an active database. As a result, the focus of the definition is upon an archive (streamed) format, NOT upon any particular programming language implementation or representation. Retrieval performance of the data is also NOT a primary concern. (Although as computers get faster, discs get bigger, and memory gets cheaper, the issue of adequate performance should be moot.) As an archival format, there is no particular emphasis upon any particular performance in random access (read) or upon necessarily even supporting random access (write) capability.

The long term goal is to encourage adoption by the dynamics community (both vendor and user) as an export and import format by having a set of libraries in both source and executable format on the University of Cincinnati - Structural Dynamics Research Laboratory (UC-SDRL) web site for use by the community. The UC-SDRL web site will provide a clearing house for enhancements and bug fixes which can be submitted back to UC-SDRL for

incorporation into the reference implementations. Currently, the UC-SDRL web site provides documentation for the existing UFF data structures.

Finally, it is the intention that long term there will be a set of software test suites to facilitate compliance and validation checking of implementations. There is no intention to require the community (and vendors in particular) to use the reference implementations in order to achieve compliance. Anyone may develop an optimized version from the specification and validate against the compliance test suite.

1.4 Historical Weaknesses & Abuses of the UFF

One of the primary UFF weaknesses is in the area of metadata where there is no well-understood mechanism for users to attach arbitrary, test relevant condition information or other pertinent comments to UFF data records in a portable manner. The desired format must include a naturally extensible metadata capability by providing mechanisms for easy, natural extension as new needs develop, while providing backward compatibility, as much as practical. Another known weakness is the aging, eighty ASCII character, FORTRAN card image format. Still another weakness is the serial stream dependency in the UFF definition. This is most serious in the area of units handling, where a loss or error can cause all succeeding records to be misinterpreted.

Over the years, because of misunderstanding of the Universal File Format definition and because of the uncertainty about handling various data types, there has arisen several frequent and yet understandable abuses of the UFF which cause the files to be less portable than they might otherwise be and effectively non-transportable between different hardware and software systems or even unreadable and unrecoverable. Some of the most notable problems have been:

- Storing critical, non-documentary information in textual ID lines
- Exceeding the 80 character line length limit
- Inconsistent, order dependent units issues (default SI units definition)
- Misunderstanding the format definition
- Invalid field data values and formats (frequently arising from programming language behavior differences [e.g. C vs. FORTRAN])
- White space errors (spaces vs. tabs)
- No clear procedure for format error handling
- Lack of user definable fields resulting in storing critical, non-documentary information in textual fields

In each of these situations, the result was a format that became less portable (at times even non-transportable) and potentially unreadable or unrecoverable.

2. History of the Project

2.1 First Year Activity

Over the course of the project, a number of different data storage formats were considered and investigated. Most of the formats, besides not meeting all the goals of the project, could not be seriously considered due to legal usage restrictions. At the end of the first phase, three potentially viable foundational solution options (or directions) which required further investigation had been identified.

The first was a DOE sponsored effort, the HDF (Hierarchical Data Format). While not specifically targeted at long-term, dynamic data archiving, it appeared to support all (or most) of the necessary features needed for such applications. The second was to use a specific vendor proprietary format as a basis of development. The third was to develop a new format from scratch based upon the needs of B&W/Y12/DOE and the aggregated vendor/user feedback.

Clearly, there was significant advantage to leveraging the work of an existing format and tailoring it to this specific application and so at that time the first option was preferred. Even so, the process of identifying and evaluating other existing data formats continued.

- Neutral Files - the Neutral File format focuses upon CAD/CAE and does not support dynamic data.
- ASAM/ODS - the thrust of ASAM/ODS is the definition of the interface into an ORACLE database.
- XML - a structured, textual information format. While not a dynamic data format, its structured organization is interesting for the metadata. (NOTE: Can contain "arbitrary binary" information through textual encoding. Typically increases file size by about 1/3.)

- Institute of Environmental Sciences and Technology (IEST): WG-DTE042: Vibration/Shock Data Storage - the WG was to focus on “establishing a standard for the storage of large binary files used mainly in vibration and acoustic testing.”

Although they couldn't be considered for the basis of the format specification, several commercial databases were reviewed for content to determine the key features which needed to be supported in order to achieve acceptance among vendors.

Following the conclusion of the first phase effort and prior to the resumption in the second, a limited review of formats identified and evaluation of the feedback received continued.

2.2 Second Year Activity

Overall, the project is focused upon the long term archival of dynamic measurements and associated metadata. Performance and size of the archival are not the primary objectives; data integrity and recoverability are the prime objectives. The project is limited to the detection of inadvertent data corruption and extraction of remaining valid data. The problems associated with malicious damage are specifically outside the scope. The issue of refreshing the data, as media storage technology changes, will be required but is also not the concern of this project.

One of the challenges to this project has been that there are very few data formats that are open and usable without restriction. As the project resumed, three primary candidates which had been identified in the interim for consideration as the format basis were HDF, ASAM-ODS ATF-XML, and a custom developed XML format.

Unfortunately, each had a significant weakness.

- The weakness of the HDF format is that it is essentially a binary file system embedded in a file. Long term damaged data recovery could be problematic. Also, since the two most recent versions of the format specification, HDF4 and HDF5, are incompatible, there is the additional concern that long term file compatibility could also be at risk.
- The thrust of ASAM/ODS is the definition of the interface into an ORACLE database. One of its weaknesses is that the format prefers external binary files for large data components. Using direct file references for these parts makes long term data integrity problematic. The common actions of moving or renaming files, potentially places the entire dataset at risk of complete loss.
- The weakness of a straight XML implementation is that the XML standard requires that any conforming parser must stop processing upon encountering any error. Further, extraction of any data information requires effectively reading the entire file.

Because the only historically successful, long term archival format is the traditional book, there was a focus upon ASCII/textual data type formats.

The process of reviewing the three primary archival format candidates noted above proceeded, in part, by reviewing existing available data format options with a specific focus upon applicable features for incorporation into the resultant archival format. Since most data formats are targeted at either data transport or active database manipulation, some of their design decisions are at odds with the long term archival goal of the project; nonetheless, many of their specific data features are still relevant. Some of the positive and negative aspects of these different formats were considered in light of these specific features and how long term implementation might be affected. Consideration was also given to the feature characteristics needed for long term read/recovery viability and industry acceptance. In particular, these two elements favor a format that is principally textual (ASCII) encoded data, which is nominally familiar, is simple to implement and can be mapped relatively straightforward to existing proprietary databases.

Although proprietary data formats exist which are fundamentally ASCII/binary data interleaved, such formats could not be considered because of their proprietary nature. However, one format specification standard, developed in the area of textual document interchange, appeared to have significant application to this project. It is the 'Office Open XML Format, ECMA-376, Second Edition, Dec. 2008.'

The textual document attributes of headers, footers, cross references, body text, etc. share many conceptual features common to the archiving of dynamic data, that is, data headers, metadata, cross channel references, etc. Hence, the packaging of such data can conceptually be considered a type of dynamic document. The Office Open XML Format and in particular the portion referred to as 'Open Packaging Conventions', includes many of the characteristics of the desired archive data definition. While the specification was primarily developed to support textual documents, the actual specification is general and not specific to such documents. Effectively the definition is a random access

container holding primarily textual data. By being based upon familiar industry standards (some being de facto definitions), the format has the potential for easier industry acceptance.

Thus for the second phase, the operating plan for the primary data container was to use the ECMA-376 ‘Open Container’ (or close equivalent.) It is essentially a restricted format, industry standard ZIP file. The contents, of which, were envisioned primarily as sets of XML data streams. The strength of this container is that it can hold structurally organized data and retain the structure. It can also contain and store non-format defined (vendor specific, informational data, pictures, movies, etc.) data.

The data recovery features of the potential format are not focused upon deliberate malicious data manipulation, but upon inadvertent corruption. Depending upon the type and degree of corruption, through the use of appropriately tagged prefix metadata (linkage, checksum, et al.; effectively providing redundant container information), the valid uncorrupted data could still be extracted from a damaged archive. Thus, potentially all or most of an archive could be reconstructed in the event of container information corruption.

2.3 Third Year Activity

While there were several minor suggestions made during the third phase, only two design significant requests were received – (1) support a native file system usage/layout capability to enable convenient use of the archive format as a program or application specific native database and (2) support user specified units’ features to allow arbitrary explicit units definition. The primary feedback from discussions and presentations was a reiteration of the need for an intrinsically, user extensible metadata capability to accommodate unforeseen future informational storage needs.

Overall, the third phase of the project focused primarily upon reducing the many feature suggestions and the observed archive needs to a viable format requirement specification and identifying the minimum required feature set for successful deployment. Most of the rest of the feature requests will be adopted as optional archive extensions.

3. Current Requirements for Specification

This section presents the overarching picture of the format requirement specification as it currently stands and represents the starting point for a potential two or three phase implementation and validation effort.

3.1 Design Challenge: Simplicity vs. Complexity

It is important at this point to recognize the fact that despite the apparent complexity of the proposed solution, the basic simplicity of the UFF structure has been preserved. The apparent complexity of some of the features like the matrix definition, specifically the sub-matrix partitioning scheme, are included to support the needs of certain vendor/user communities. It must be emphasized, however, that it is not necessary to utilize all the features in order to write a compliant archive.

As examples of these differing user community needs, consider the widely variant requirements of the following user scenarios and note the challenge for how the specification addresses each of their unique data archival needs. There are those users with minimal, basic needs (e.g. 4 channel trouble shooting); those with large channel count FRF needs (e.g. 3 in x 250 out); those with high-speed, long record time capture involving multiple test conditions (e.g. jet engine testing); and those acquiring specialized information who require secure, multi-path delivery (military); et al.

The following sections expand upon the various feature suggestions and start to clarify and distinguish between the minimum necessary information and the recommended, but optional, documentary information, thus illustrating the underlying simplicity of the fundamental solution.

3.2 Archive Feature Specifications

During the various formal and informal discussions with users and vendors that have occurred during this project, many suggestions for desirable features were offered which, while perhaps not immediately applicable to the project effort then underway, were worth noting for consideration during future work. Many of the suggestions do not affect the principal data per se, but rather focus on the retention of historical metadata information and the like. Examples of these suggestions and concerns are:

- It should be possible to write verbose output (i.e. redundant info) with equivalence constraint testing capability (e.g. writing multiple measurement vectors from measurement matrix and checking measurement characteristics or constraints. [fmin, deltaf, testid, block length, etc.]
- When preserving data it should be possible to write a verbose output with some form of back trace to the original database fields. (e.g. perhaps writing `<meas vendorSource="hatchTest[1]">... data ...</meas>` where "hatchTest[1]" may be the original vendor data ID.)
- It might be advantageous to reserve all 'vendorXXX' attribute fields for vendor use.
- It might also be advantageous to reserve all 'userXXX' attribute fields for end-user use.
- In developing the XML data specification, attributes should not provide any data information, but only metadata information about the data.
- It should be possible to tag or log any hardware or software that has touched/modified the data (i.e. retain the data history path.)
- It should be possible to document vendor specific or proprietary information within the container using human readable ASCII/XML - *NOT* PDF/DOC/etc.
- The 'Open Container' should allow inclusion of other non-format defined information types. (e.g. images, sounds, etc.)
- The format should have clearly defined behavior as well as content. (i.e. specified error handling in the presence of malformed data.)
- Inline data should be written in decimal: floating point or bytes. Complex data should be specified as successive pairs of real values.

Although additional feedback was (and is) expected as the project continues to progress, these types of comments favor the development of an 'XMLized' UFF-like format definition. Additionally, many of these suggestions are inherently supported by the working concept through the synergy of the ECMA 'Open Container' (or a close equivalent) coupled with a predominantly XML data definition. Further, an 'XMLized' UFF has the strength of familiarity, thus facilitating community acceptance.

The review of the ECMA 'Open Container' contributed much to the conceptual design of the format, even though strictly the specification will not be used as the primary data container. Strict conformance to the 'Open Packaging' specification has been abandoned due to the risk of single point concentration failure of the record association hash table, as well as, the documented ability to silently replace records. (While the ability may be advantageous for replacing logos and other local document customizations in the field of desktop publishing, the feature represents a significant inadvertent corruption risk.) Since the protection against this (and other) failure requires that complete association information to be stored integrally with each record, there remains no advantage to maintaining this redundancy. (Although performance was not a primary concern for this project, limited testing has indicated that write performance degradation grows with increasing number of archive elements potentially making the archive non-manipulative when size exceeds in memory capacity.) The advantages obtained by abandoning strict conformance also include the ability to support a native file system container basis and the potential to support other (current and future) file container archive formats.

3.3 Feature Elements Driven by Recoverability

Since the overarching principal is long-term recoverability, many of the archive feature characteristics chosen have been governed by that objective. As mentioned before, the only historically successful, long term archival format has been printed matter. Books, papyri, engravings, etc. all yield valuable (and recoverable) information, even when significantly damaged. The following discussion presents the design impact of recoverability upon some of the archive features.

All data shall be written in UTF-8 encoding to facilitate recovery. Because UTF-8 encoding is backward compatible with ASCII, it guarantees that no low order (0x00-0x7F) ASCII characters occur in any multi-byte encoding, thus the data stream is also self-synchronizing. This behavior, coupled with additional constraints, such as requiring all UFR format master control field names to be strict ASCII UPPERCASE (e.g. DRT, VER, LREF, XREF, etc.) and requiring all record specific informational field names to be ASCII MixedCase. (e.g. DataType, TemperatureOffset, Length, etc.), enables more robust data recovery in the event of inadvertent archive corruption.

To facilitate recovery, large data records should be broken into smaller, more manageable pieces (e.g. segments of 50-100 kb.) The various pieces shall be associated using connection references and segment variable features (such

as Fmin or Tmin) shall be adjusted to be correct for each segment. For example, the format (structural arrangement) of time series (function) data must have ability to be partitioned throughout the data stream as needed for best resilience against data corruption. The series shall be broken into a set of manageable pieces, each with individual checksum coding. The checksum encoding must be distinct from the validation code stored in the ZIP container element header. The series pieces can be organized by any of the following from single complete channel record to multiple channels interleaved (with a granularity [blocksize] from complete record down to single point). In order to support this capability properly, it requires that the functional information must intrinsically support multidimensional data.

The archive must contain redundant structural (data organizational) information (preserved with each data record element) in an extractable ASCII readable form. The archive must support redundant (duplicate) data records for key informational content. Also as part of the semantic (informational) structure, each data matrix should receive a unique identification (UID/name) thus also helping to support multiple sets of similar information within the archive and allowing more convenient mapping of vendor database structures.

All field definition (content) strings should be trimmed of leading and trailing white-space. This helps address the issue of the user adding white-space for visual and/or readability purposes, but which is not relevant (or influential) to the information being stored. Thus the ability of the software to read and interpret the informational field correctly is not compromised by a user preference or idiosyncrasy.

Other feature concepts which support recoverability include:

- Each container (ZIP) file entry contains a single archive data record.
- Binary data must NOT be mixed (interspersed) with ASCII (textual) data.
- All basic record field names shall be defined using mixed-case English.
- All archive entry names must be archive root relative.
- All external names must be either archive root relative or file system absolute.
- Each EXT (extension) reference, regardless of being internal or external, must consist of the Path, Name, UID, and Type.

Many of these features have been so chosen in order to facilitate the development and utility of recovery codes capable of scanning a damaged archive and then extracting and reconstructing as much as practical of the original information.

3.4 Format Design Principles

3.4.1 Error Detection / Correction

Because of the block oriented nature of most data storage devices (disks, CDs, DVDs, flash memory, etc.) bit stream encoding errors are unlikely. Generally, the failure will be entire blocks of lost information. Also, since the fundamental block size of the different devices vary (historically discs were 512 bytes, more recent formats are 4096; CD/DVDs are 2048, etc.) and these devices typically use some form of block based bit stream encoding for error recovery purposes anyway, block oriented schemes which preserve the data information more naturally coupled with simpler limited sized (~100k) record based checksums should be preferable.

Therefore, since the process of error detection is focused upon the identification of inadvertent data corruption, not deliberate manipulation, and the proposed record granularity is recommended to be 50-100k, simpler error detection schemes should be adequate. Since an additional goal is to be able to extract readable information from potentially corrupted archives, simpler hashing/message digest type schemes (CRC32, MD5, et al.) should be preferable to encoding schemes (RS, et al.) because the data remains ASCII. For error detection purposes, each field may have an individual hash coding (CRC, et al.) attribute representing the field informational content and shall be processed based upon the native UTF-8 encoding prior to the encoding of any forbidden XML character sequences. (e.g. <GenericInfoField CRC32="A23CDE87">Potentially meaningful informational content</GenericInfoField>)

Just as error correction is outside the scope of this project and should be handled external to the format definition by the media storage system, the security measure of data encryption is also beyond the scope of this project. Technology is expected to continue to grow over the life of the archive and more sophisticated means develop.

Furthermore, by its design, encryption is intended to make extraction of information inherently difficult and is therefore at odds with the goal of long term viability and recoverability.

3.4.2 Data Homogeneity

All data records shall represent conceptually homogeneous information. For example, heterogeneous array information shall be partitioned into homogeneous informational sections and these sections written out individually. As another example, the heterogeneous DSP parameters describing a multi-rate acquisition shall be written as separated DSP records for each rate condition.

3.4.3 Matrix Data Storage Organization

The format of time series and other functional data shall have ability to be partitioned throughout the data stream as needed for best resilience against data corruption. The series shall be broken into a set of manageable pieces, each with individual checksum coding. The encoding shall be distinct from the validation code stored in the ZIP container element header. The series pieces will be arranged by any of the following: single complete channel record, multiple channels interleaved (granularity [blocksize] from complete record down to single point). The pieces should be associated using connection references and variable features (e.g. Fmin) shall be adjusted to be correct for each segment.

Every non-scalar informational element shall be defined as a matrix. This generalized vector/matrix/array data layout shall intrinsically support multidimensional data, as well as, sparse data. The resulting matrix type shall handle the sequencing, sparseness, interleave, storage characteristics, as well as, the data type (integer/float, ASCII/binary) characteristics. The partitioning aspect of the data stream means that sparse data (at least on the macro scale) becomes intrinsically supported.

Thus, write out all matrices (arrays) as inherently sparse. Prefix (attribute) each partition/segment with the starting position, dimensional strides, and dimensional run lengths. Each segment shall contain only a single data type (e.g. real, float, integer, complex, string, etc.) For matrices with heterogeneous elements, write out each distinct type as a separate partition/segment. (e.g. given [1 2 X ; 3 4 Y ; 5 6 Z] – write out as [1 2 ; 3 4 ; 5 6] & [X ; Y ; Z]) For encoding purposes, all format based subscripts are (1-based) natural numbers (1, 2, 3, etc.) Also, identify indexing permutations (e.g. [1 2 3], [2 3 1], etc.), as well as, stride/blocking/run length structure (e.g. [1:10 2:15 3:1024], dim:len) for partitioned storage. With the chunk size limited to about 100k, a coarser explicitly defined blocking scheme is probably unwarranted as the pieces can be scattered purposefully about the archive to achieve the same result.

When writing out any generalized matrix, the values of the dimensional axes (e.g. frequency, temperature, DOF, etc.) shall be recorded for each partition. By doing so, each partition segment is individually structurally complete. When writing out any generalized (multi-dimensional) matrix, extra-dimensional information may be written either explicitly as additional dimensions or implicitly as coordinated metadata. For example, a single channel waterfall plot of response amplitude vs. both frequency and speed could be written explicitly as a 2D matrix with dimensional axes of frequency (Hz) and speed (RPM). Alternatively, it could be written as a series of 1D matrices with a dimensional axis of frequency (Hz) and a coordinated metadata entry of speed (RPM). This facility for writing matrix information using explicit or implicit axis information shall be fully scalable to any number of dimensions; the limiting (and perhaps absurd) case being the writing of a single scalar value and all dimensional axis information in metadata form.

For measurement data (time/frequency/etc. or FRF/COH/et al.), the matrix coordinate encoding and dimensionality can include: channels (input, output), temporal (time, frequency), auxiliary axis (temperature, speed, altitude) although generally this axis (if scalar) should be stored as metadata. In general, the dimensionality could then be encoded in a natural form, that is, an FRF could be written as 3D even when input-output dimensions are singleton DOFs (and by analogy, MCOH as 2D, etc.).

3.4.4 Information Encoding

Because of the overarching issue of recoverability, the importance of the numeric, vector/matrix data representation cannot be overstressed. Specifically, representing data as ASCII numeric should be the primary practice for long term archiving, since the primary objective is long term recoverability. However, for short term storage and transport, binary encoding (for size) may be more appropriate. Finally, for temporary or transient intermediate

usage, a strict native binary representation may be most appropriate. The key decision point is the cost of error recovery (e.g. re-write the file, re-take the test, degrade the analysis, irreplaceable or total loss, etc.) In many respects this also affects the issues of redundancy. Hence the need for redundant (backup) records for key failure point records (e.g. units)

All record entries shall use verbose textual field enumerations instead of numerical coding. Although verbose field identifiers and content admit the possibility of spelling errors that do not occur with numeric field enumerations (e.g. 1=FRF, 2=COH, etc.) the advantages outweigh the potential inconveniences, since misspelled words are often easy to correlate with their properly spelled counterpart, recovery from such errors is more easily accomplished. Recovery in the case of actual miscoding is more challenging as there is no redundant information. Of course, true coding errors such as labeling an FRF as a COH is not addressed by either scheme and such detection involves more sophisticated data analysis and is always problematic.

To prevent an artificial inflation of apparent informational precision, there should be a mechanism for indicating the numerical data precision, particularly of floating point data, both for the original information and for the information as encoded in the archive.

3.4.5 Informational Disambiguation

To support the long term viability goal, each data record shall contain a record versioning string (e.g. X.Y.Z, where X = Major Revision - Addition of new fields; Y = Minor Revision - Addition of new field values; Z = Patch - Correction of spelling or clarification of decoding) defining either the minimum specification under which the record can be decoded or the current record specification at the time of writing.

To help support multiple sets of similar information within the archive each data matrix shall receive a unique identification (UID/name).

When redundant records are used one record shall be designated as the master record and all other redundant records as slaves. However, in the event of corruption of the master record, the first valid redundant reference shall become master.

Because of the potential for misinterpretation for a 'successive pairs of real values' encoding of complex data, particularly in the event of data recovery, the information should be disambiguated by requiring an explicit complex format (e.g. 1.2+3.4i, 5.6e+7-8.9e0j, -1.4-j6.2, etc.)

To reduce the potential for misinterpretation, an explicit units suffix capability has been suggested (e.g. <Frequency>1.35 Hz<Frequency/>, where 'Hz' is defined in a units system suffix table.)

Within the dynamics test community, there are numerous nomenclature terminologies which can often refer to the same or similar informational content. For example:

- Ensembles, Scans, Traces, Functions, Maps, Blocks, ...
- BlockSize, Span, Number of Spectral Lines, ...
- Projects, Groups, Sessions, ...
- Elements, Records, DataSets, ...

Such common cross terminology usages shall be footnoted for each record or informational field type.

All field definition (content) strings shall be trimmed of leading and trailing white-space. This helps address the issue of the user adding white-space for visual and/or readability purposes, but which is not relevant (or influential) to the information being stored. Thus the ability of the software to read and interpret the informational field correctly is not compromised by a user preference or idiosyncrasy.

3.4.6 Record/Field Detail Notes

The field names and types are designed to map naturally to various programming language integral types like structures, cell arrays, and/or name value pairs.

All UFR format master control fields shall be strict ASCII UPPERCASE. (e.g. DRT, VER, LREF, XREF, etc.)

All record specific informational fields shall be ASCII MixedCase. (e.g. DataType, TemperatureOffset, Length, etc.)

An empty field (e.g. <EmptyFieldName/>) shall be considered a null value for numeric fields and an empty string for character values.

Each time an archive is touched (modified), a comment record should be added to the MASTER header (EXT). Each EXT reference, regardless of being internal or external, shall consist of the target name, UID, Version, and Type.

Where data fields contain coordinated data, it is the responsibility of the generating code to maintain consistency and it is the responsibility of the consuming code to detect inconsistency.

All data shall be written in UTF-8 encoding to facilitate recovery and must include the XML prologue material - <?xml version="1.0" encoding="UTF-8" ?>

4. Summary / Conclusions

This paper documents the first three years of effort and leaves the design in a form that can be resumed in any potential follow on phase of work.

Over the course of the project, numerous formal and informal discussions were held. These discussions were intended to represent a cross-cutting industry comment solicitation activity of users, vendors, and government installations. Overwhelmingly, those contacted expressed support for the project and many times the responses could be summarized as ‘sounds good’, ‘this is needed’, or ‘let us know when it’s ready’. All significant design comments and suggestions have been evaluated and integrated as appropriate and even those comments which were not specifically immediate design relevant were preserved against potential relevance in future phases.

The result has been that most of the requirements for that absolute minimum set of features which a vendor/user must use in a compliant archive have been identified. Additional features that a vendor has the option to use have also been identified. Some features, however, only make sense to completely define during an implementation stage as they can affect recoverability and/or performance.

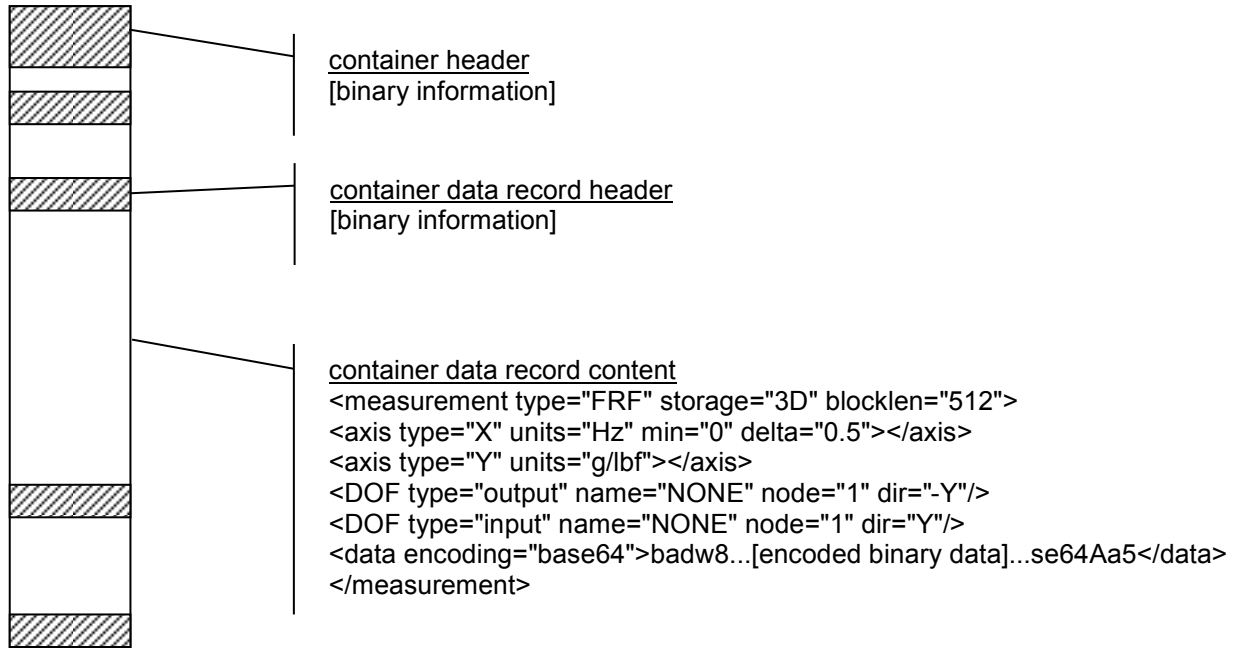
Bibliography

- Phillips, A.W., Allemang, R.J., “Requirements for a Long-term Viable, Archive Data Format”, IMAC, 2010, 5 pp.
- Phillips, A.W., Allemang, R.J., “Archive Format Requirements for Long Term Storage of Dynamic Signal Data”, ISMA, 2010, 8 pp.

Appendix A

A.1 Pictorial Concept Example

The following example is presented for conceptual discussion purposes, giving only an impression of the style of data storage. It is not intended to be complete or to represent any particular likely final implementation.



Note that, in support of the different envisioned operational usage paradigms, additional data encoding/representations are planned, specifically an ASCII decimal and a referenced native binary.

Appendix B

The following example data records are not intended to represent a complete definition. Instead, they are presented in order to provide a sense of the initial expected representation for a few of the principal required data records. Numerous other key records, not listed here, are also in draft form.

B.1 Master Data Record

| Field Name | Count | Content | Comments |
|------------|-------|--------------|---|
| DRT | 1 | String | Data record type or kind |
| VER | 1 | String | Record format revision |
| UID | 1 | String | Unique record identification string |
| SELF | 1 | String | Self-referential archive root relative path |
| EXT | 0-1 | String Array | List of extension record references |

Table 1: Prototypical Master Field Definition – Information common to all records

Record Notes:

- Whitespace encoding needs to differentiate between format-free and user-defined whitespace information. ‘blanks’, ‘tabs’, ‘newlines’, ‘carriage returns’, ‘line feeds’, etc. are considered format-free, that is, they can be changed, replaced, or expanded at will or need without regard to usage. Such whitespace is useful for field value separation and delimiting.
- If user-defined whitespace is to be preserved without modification, it shall be explicitly encoded (%20, %09, %0A, etc.) within the record.
- For error detection code (CRC32, et al.) purposes, all contiguous format-free whitespace shall be treated as a single ASCII blank character (0x20).

B.2 Reference Record

| Field Name | Count | Content | Comments |
|------------|-------|---------|--------------------------|
| Target | 1 | String | Target record - pathname |
| TargetUID | 1 | String | Target record UID |
| TargetVER | 1 | String | Target record VER |
| TargetDRT | 1 | String | Target record DRT |

Table 2: Prototypical Master Reference Definition

Record Notes:

- The self/cross reference record structure capability and behavior. In particular how external archive references should be able to tunnel into other archives. The potential usages of this feature include: scrubbed data reassembly (i.e. from delivery via different paths), correlated test info, etc. While such a feature would be a poor choice to use for long term storage, it may be imperative for secure delivery or transport. (And hence impact certain industry acceptance.)
- Particularly for the support of “external/scrubbed” data content, the concept possibility implementing inline references through attributes (e.g. <DataContent Target="/Measurement/Units/UnitSet1.DSR" TargetUID="Units-1a" TargetVER="1.0.0" TargetDRT="Units" />) should be evaluated. This could also become the mechanism basis for referencing native binary content (e.g. either by referencing the binary record or direct reference coding.)

Concept of References - local (within archive), external (to file system or other archive)

aref - absolute reference
 lref - local reference
 rref - relative reference
 xref - cross reference (or maybe back/return reference)

Example: Generic data driven reference record

```
<REF>
<Target> /Measurement/Units/UnitSet1.DSR </Target>
<TargetUID> Units-1a </TargetUID>
<TargetVER> 1.0.0 </TargetVER>
<TargetDRT> Units </TargetDRT>
</REF>
```

Example: Generic attribute driven reference record

```
<REF Target="/Measurement/Units/UnitSet1.DSR" TargetUID="Units-1a" TargetVER="1.0.0"
TargetDRT="Units" />
```

The final decision on whether or not REF(erences) should be “data” driven or “attribute” driven, along with the relative advantages and disadvantages of each approach, will be resolved during the initial reference implementation phase.

B.3 File Header Record

| Field Name | Count | Content | Comments |
|-----------------|-------|--------------|---|
| DRT | 1 | String | Data record type or kind |
| VER | 1 | String | Record format revision |
| UID | 1 | String | Unique record identification string |
| SELF | 1 | String | Self-referential archive root relative path |
| EXT | 0-1 | String Array | List of extension record references |
| FileStamp | 1 | String | |
| DateStamp | 1 | Date String | |
| TimeStamp | 1 | Time String | |
| CreationDate | 1 | Date String | |
| CreationTime | 1 | Time String | |
| DatabaseVersion | 1 | String | |

Table 3: File Header Definition

File Header Example

```

<UFR>
<DRT>FileHeader</DRT><VER>1.0.0</VER><UID>FileHeader-1a</UID>
<SELF>/FileHeader1.DSR</SELF><EXT/>
<FileStamp> C:\Projects\PlateTest\Test1.DSA </FileStamp>
<DateStamp> 14-July-2010</DateStamp><TimeStamp> 14:23:05 </TimeStamp>
</UFR>

```

B.4 Comment Record

| Field Name | Count | Content | Comments |
|-------------|-------|--------------|---|
| DRT | 1 | String | Data record type or kind |
| VER | 1 | String | Record format revision |
| UID | 1 | String | Unique record identification string |
| SELF | 1 | String | Self-referential archive root relative path |
| EXT | 0-1 | String Array | List of extension record references |
| Description | 1 | String | User meaningful description |
| CommentLog | 0+ | String | Sets of user comments/logs |

Table 4: Comment Record Definition

Comment Example

```

<UFR>
<DRT>Comment</DRT><VER>1.0.0</VER><UID>Comment-1a</UID>
<SELF>/CommentRecord1.DSR</SELF><EXT/>
<Description>First principal c-plate test.</Description>
<CommentLog>3-August-2010 16:06 - Initial dispersion failed. Will reattempt using second generation mark 2!</CommentLog>
<CommentLog>5-August-2010 08:43 – Test cancelled. Second delivery aborted.</CommentLog>
</UFR>

```

B.5 Units Record

The Units Record shall be used to define the system of units employed, not the specific units of any particular data element.

| Field Name | Count | Content | Comments |
|-------------------|-------|--------------|---|
| DRT | 1 | String | Data record type or kind |
| VER | 1 | String | Record format revision |
| UID | 1 | String | Unique record identification string |
| SELF | 1 | String | Self-referential archive root relative path |
| EXT | 0-1 | String Array | List of extension record references |
| System | 1 | String | Canonical units system name |
| Length | 1 | Scalar Float | Conversion factor to SI unit (meter) |
| Force | 1 | Scalar Float | Conversion factor to SI unit (Newton) |
| Temperature | 1 | Scalar Float | Conversion factor to SI unit (K) |
| TemperatureOffset | 1 | Scalar Float | Temperature base reference |
| TemperatureMode | 1 | String | Temperature measurement mode (abs/rel) |
| Time | 1 | Scalar Float | Conversion factor to SI unit (sec) |
| | | | |
| Current | 1 | Scalar Float | |
| LuminalIntensity | 1 | Scalar Float | |
| Ohms | 1 | Scalar Float | |
| Mole | 1 | Scalar Float | |
| PlaneAngle | 1 | Scalar Float | |

Table 5: Units Record Definition

Record Notes:

- The Units Record descriptor will need to expand to accommodate the suggested ‘UnitSuffixTable’ descriptor.
- When using the ‘UnitSuffixTable’, all unit encodings should utilize as near as possible to the standard units names or abbreviations. For example, ‘Hz’ shall refer to a frequency unit of ‘1/sec’.
- The use of the ‘UnitSuffixTable’ for informational obfuscation should be limited to specialized security needs.

Units Example

```
<UFR>
<DRT>Units</DRT><VER>1.0.0</VER><UID>Units-1a</UID>
<SELF>/Measurement/Units/UnitSet1.DSR</SELF><EXT/><System>SI</System>
<Length>1.0</Length><Force>1.0</Force><Temperature>1.0</Temperature>
<TemperatureOffset>273.15</TemperatureOffset><TemperatureMode>absolute</TemperatureMode>
</UFR>
```

Appendix C

C.1 Other Content Information

The definition and development of results records refers primarily to retained computational results. In one sense, this is an almost unending task; however, initially this should be limited to the most common dynamics measurement processed results (e.g. modal parameters [UF55] & general matrices [mass/stiffness/damping/etc.]). Note that this would not be computed measured results like FRF, COH, and the like, which are already included in the dynamic data measurement record.

While not truly dynamic information, but for completeness and successful community adoption, a set of geometric information records corresponding roughly to the UFF records nodal coordinates (UF15), components, coordinate systems (UF18), trace lines (UF82), etc. needs to be developed.

C.2 User Extensibility

Follow on implementation efforts need to include the development of sets of convenient, extensible metadata record definitions for non-critical common data documentary information which include the metadata record name, user defined name-value pair information, and value data type definition (char, string, numeric, integer, floating point, complex, vector, matrix, etc.)

Finally, the implementation of user records needs to clearly define the process of creating user/custom data records which should include the potential for embedded syntactic/semantic user documentation. The primary point of this is to allow user developed records to be self-documenting.

Data Analysis Strategies for Characterizing Helmet-Head Performance

Tyler Robbins Graduate Researcher, Dr. Douglas Adams Professor, Purdue Center for Systems Integrity, Purdue University, 1500 Kepner Rd, Lafayette, IN 47905
Dr. Shawn Walsh, Army Research Laboratory, Aberdeen Proving Ground

Abstract

Soldiers sometimes experience traumatic brain injury (TBI) during combat. Helmet design research is being conducted to reduce injuries; however, most research is centered on crash worthiness or ballistic impact. The objective of this work is to characterize the dynamic response of helmets to broadband loading for helmets of various materials and designs while the helmet is coupled to a head-neck system. The experimental setup consists of a Denton Hybrid III 50th percentile crash test head and neck attached to an optical isolation table to simulate the human torso. Initial experiments included standard modal impact tests with sensors on the helmet, neck, table, and head to measure the dynamic helmet-head coupling. Impact test results were used to extract the Complex Mode Indicator Function for two helmets. The CMIF results indicated that the first helmet absorbed more energy from a blunt impact than the second helmet resulting in less transfer of energy to the head and neck. Transmissibility function analysis was conducted to confirm this finding that the first helmet attenuated the transmitted force relative to the second helmet. The boundary conditions of the helmet on the head including the chin strap and padding are believed to be the source of these significant differences in dynamic performance of the two helmets.

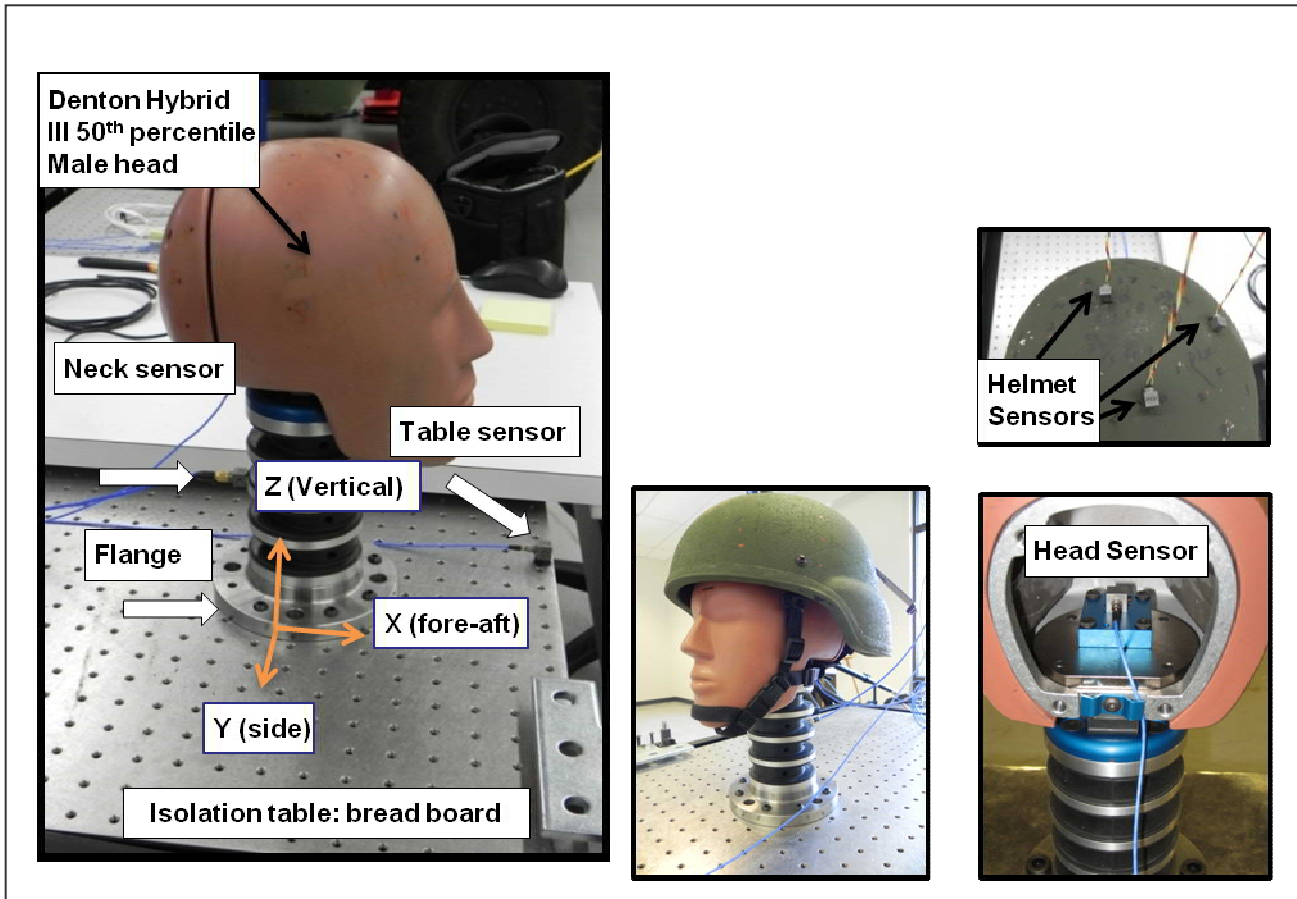
Motivation

It was estimated that 380,000 service member experienced traumatic brain injury (TBI) in 2008. The effects of TBI are wide-ranging and vary person to person. TBI can cause reduction in cognitive ability, behavioral problems, and physical problems such as loss of sight. The Army Research Laboratory is conducting research that aims to improve helmet designs in an effort to reduce TBI in service members [1].

The presence of TBI is not always physically apparent in that the head and helmet may show little visible signs of damage. Therefore, a method to compare the performance of various helmets that does not damage the helmets is needed. To develop a method for comparing two helmets, this research has investigated the structural dynamic response of each helmet. The dynamic response in the form of vibrations determines how forces are transmitted from the helmet to the head. In addition, the vibrational characteristics of the helmet are dependent on material properties of the helmet as well as the boundary conditions. In addition, the vibrational response is sensitive to changes in the interface between the helmet and the head, such as helmet size, chin and rear strap tautness, and padding material and layout.

Model

To enable comparisons of the dynamic performance of one helmet relative to another helmet, a test fixture was developed using a Denton Hybrid III 50th male (crash test) head-neck assembly and an isolation table (Fig 1a). This test fixture enabled repeatable experiments to be conducted using the same boundary conditions and input and output degrees of freedom. The crash test head has a representative shape and dynamic properties including the moment of inertia and mass. The neck allows the head to undergo the same range of motion as an actual human head. The stiffness of the neck is a function of radial position; therefore, the neck is stiffer when bending forward than when bending backwards or to either side. Data from the Hybrid III test fixture for each helmet is analyzed in terms of the vibrational dynamics (nondestructive), rather than damage to the helmet (destructive) or physiological symptoms. An isolation table was used to reduce the effects of noise and provide a realistic boundary condition that mimics the inertial reaction provided by the human torso. In academic terms, the head-neck-table system simulates a free-free boundary condition. Because the human body is rarely fixed to a single point, any impacts to the head will cause the body to absorb momentum. Sensors were placed on the table, neck, and inside the head (Fig 1c) and three sensors were placed on each helmet (Fig 1c).



Analysis

Impact tests were initially conducted on the test fixture with no helmet on the head. A medium size modally tuned hammer (PCB 086D05) with a rubber tip was used. The head was impacted nine times at 42 different locations. A modified exponential window was applied to the time data to compensate for weakly damped low frequency responses due to the isolation table. The time history data was used to estimate the frequency response function in two ways providing H_1 and H_2 . Both frequency response estimates are a function of the auto-power G_{xx} (Equation 1) and cross-power G_{xy} (Equation 2), which are calculated using N_{avg} averages of the digitally sampled input (impulse hammer), X_i , and output (accelerometer response), Y_i , frequency spectra measurements. The frequency response estimate H_1 (Equation 3) is more accurate when there is little noise on the input, whereas H_2 (Equation 4) is more accurate when there is little noise on the output.

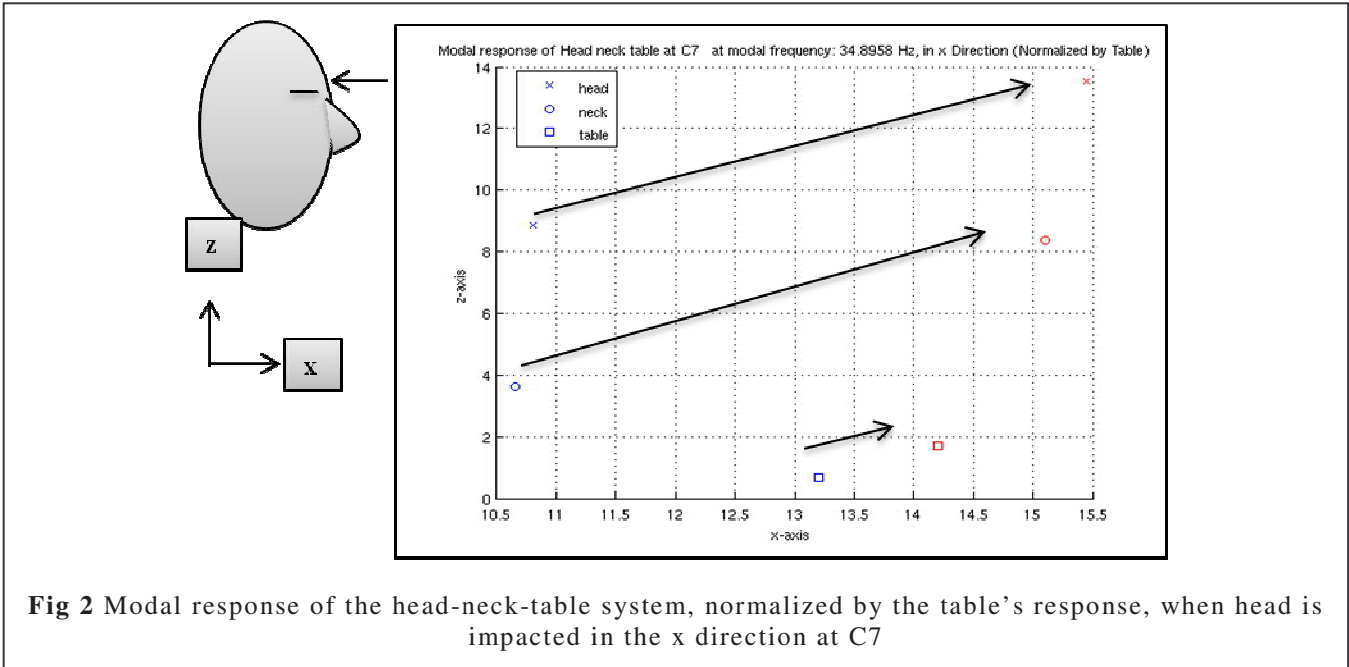
$$G_{xx}(\omega) = \sum_{i=1}^{N_{avg}} X_i(\omega) X_i^*(\omega) \quad (1)$$

$$G_{xy}(\omega) = \sum_{i=1}^{N_{avg}} X_i(\omega) Y_i^*(\omega) \quad (2)$$

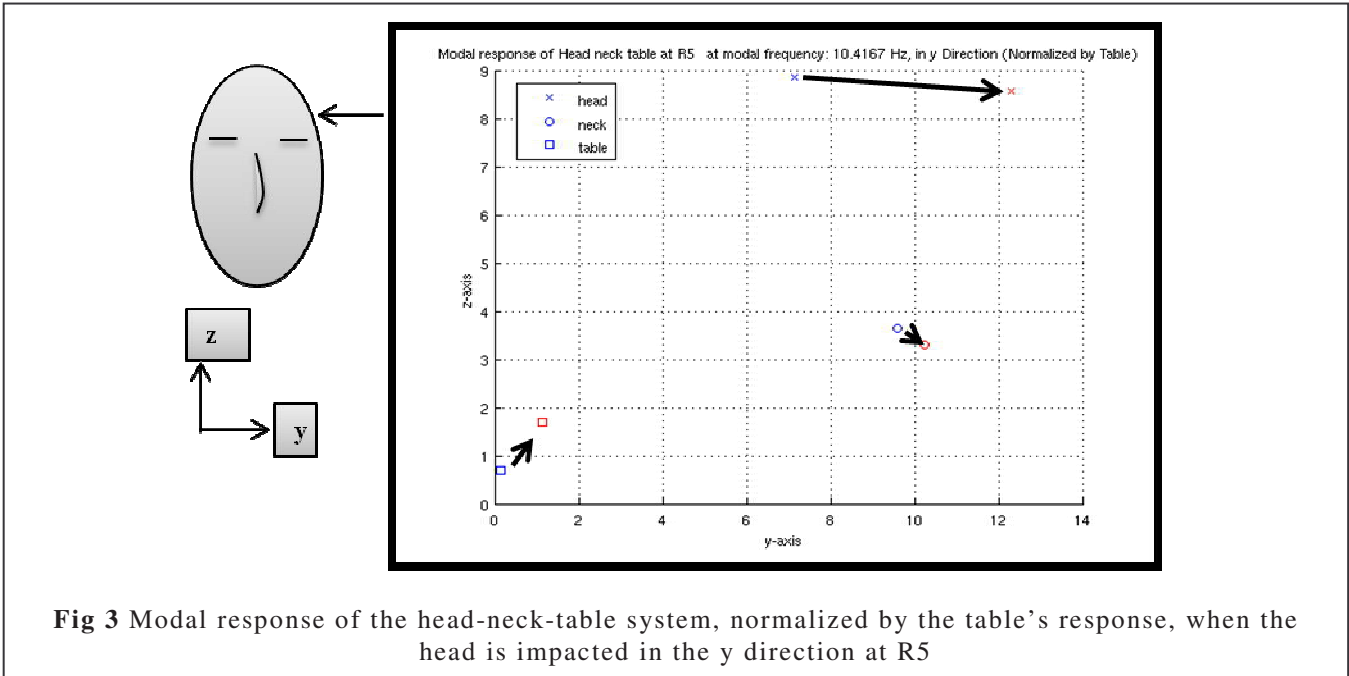
$$H_1(\omega) = \frac{G_{xy}(\omega)}{G_{xx}(\omega)} \quad (3)$$

$$H_2(\omega) = \frac{G_{yy}(\omega)}{G_{xy}(\omega)} \quad (4)$$

For the purposes of analysis and further data processing, the H_1 estimator was the only estimator considered in this paper. The modal hammers used for the impact tests were tuned and were assumed to introduce less noise into the measurements than the noise observed in the output signal supplied by the accelerometers.



The frequency response, H_f , was used to conduct modal analysis to determine the estimated mode shapes of the system. It is believed that mode shapes would be an effective means of understanding the differences in performance of one helmet relative to another helmet. Frequency responses are dependent on impact location and direction, e.g., the frequency response in the x direction is not the same as in the y or z direction due to the stiffnesses of the neck in these directions. As a result, each impact location may result in different modal frequencies and mode shapes dominating the dynamic response. For example, if the head is struck at location C7, which is largely in the x direction (Fig 2), the dominant modal frequency is



34.9 Hz. The modal shape corresponding with the placement of the three sensors (Fig 2) indicates that all three sensors move in the same direction. The head and neck deflect more than the table. In addition, the deflection of the head and neck are mostly in phase with the table, and only slightly out of phase with each other. In comparison, if the head is struck at R5, which is largely in the y direction (Fig 3), the dominant modal frequency is 10.4 Hz. The mode shape (Fig 3) is different than the one corresponding to the dominant modal frequency for an impact at C7. In addition, the head and neck are 180 degrees

out of phase with the table. This indicates that the table (or the body) would deflect in one direction while the head and neck deflect in the opposite direction.

The response for every dominant frequency for each impact location was not analyzed because this would not be an effective way to compare the dynamic performance of two helmets. Instead, an overall (aggregate) response of the head-neck system was analyzed that consisted of the Complex Mode Indicator Function (CMIF). The CMIF estimates the eigenvalues and eigenvectors of the frequency response function matrix using the Singular Value Decomposition (SVD) in Equation (5). In this set of measurements, the frequency response matrix consists of the frequency response, H_j , of each sensor (x, y, z) for all impacts. The [S] matrix consists of the singular values of [H]. The [U] and [V] matrices are the left and right singular value vectors, respectively. These matrices contain phase information and are orthogonal matrices with unity length. The CMIF can be used to estimate the global resonant frequencies as well as the global deflection vectors:

$$[H(\omega_i)]_{(N_0 \times N_i)} = [U]_{(N_0 \times N_i)} [S]_{(N_i \times N_i)} [V]^{-1}_{(N_0 \times N_i)} \quad (5)$$

The dominant modes for the head, neck, and table obtained from using the CMIF (Fig 4) indicate several strong modes of vibration for each component. In addition, the CMIF indicates common (heavily coupled) modes (20~30 Hz) as well as frequency ranges where the responses of the components are relatively decoupled (~ 10 Hz).

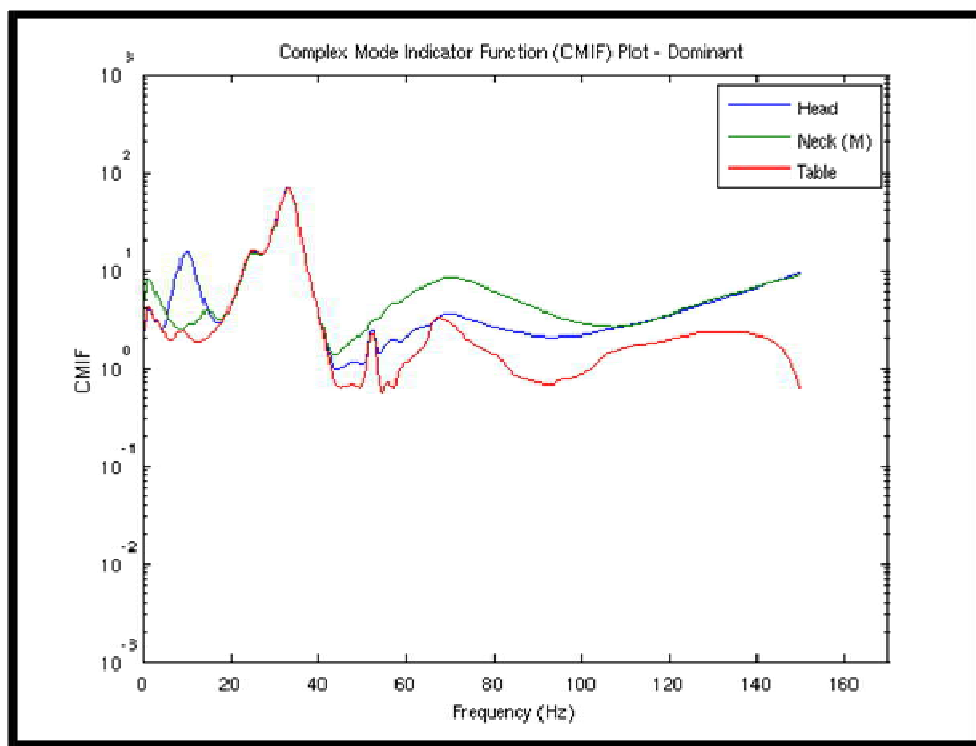


Fig 4 Dominant CMIF Modes for the head, neck, and table based on impact tests without a helmet

The modal impact tests that were conducted on the system with the helmet strapped to the head were similar to the modal tests on the head-neck system. The main difference in these two tests is that two rounds of tests were conducted with the helmet using two different modal impact hammers: small and large hammers. The small impact hammer (PCB 086D05) excites a large frequency range (0-2,500 Hz) with a sharp impulse; the large impact hammer (PCB 086C01) excites a smaller frequency range (0-250 Hz) with a wider broadband loading. All future

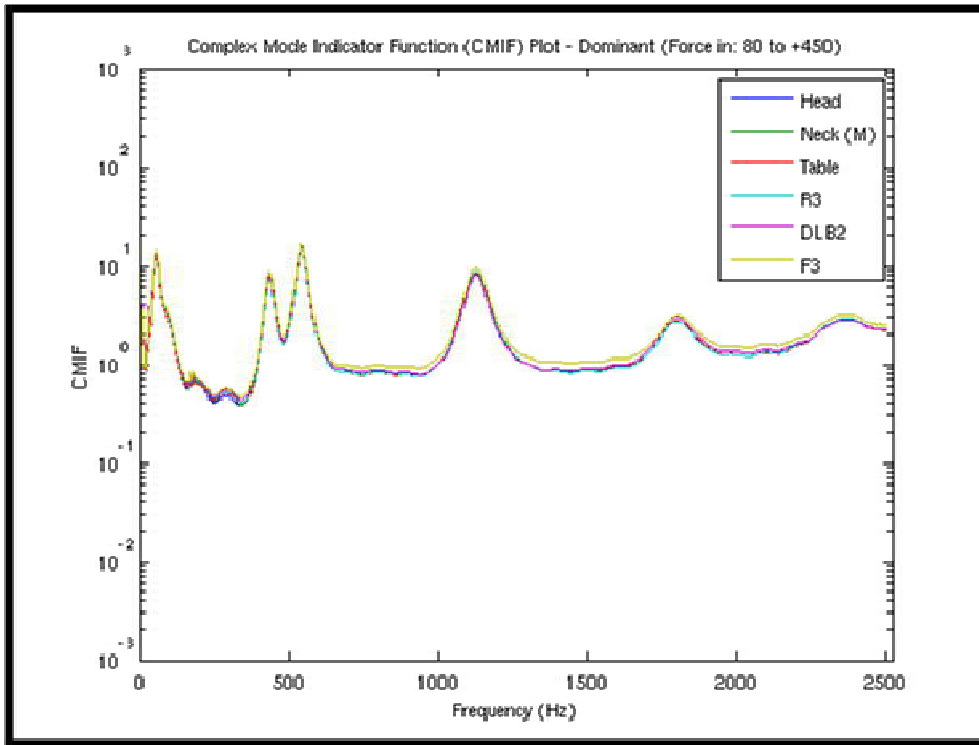


Fig 5 Dominant CMIF Modes for the Helmet ARL1, head, neck, and table

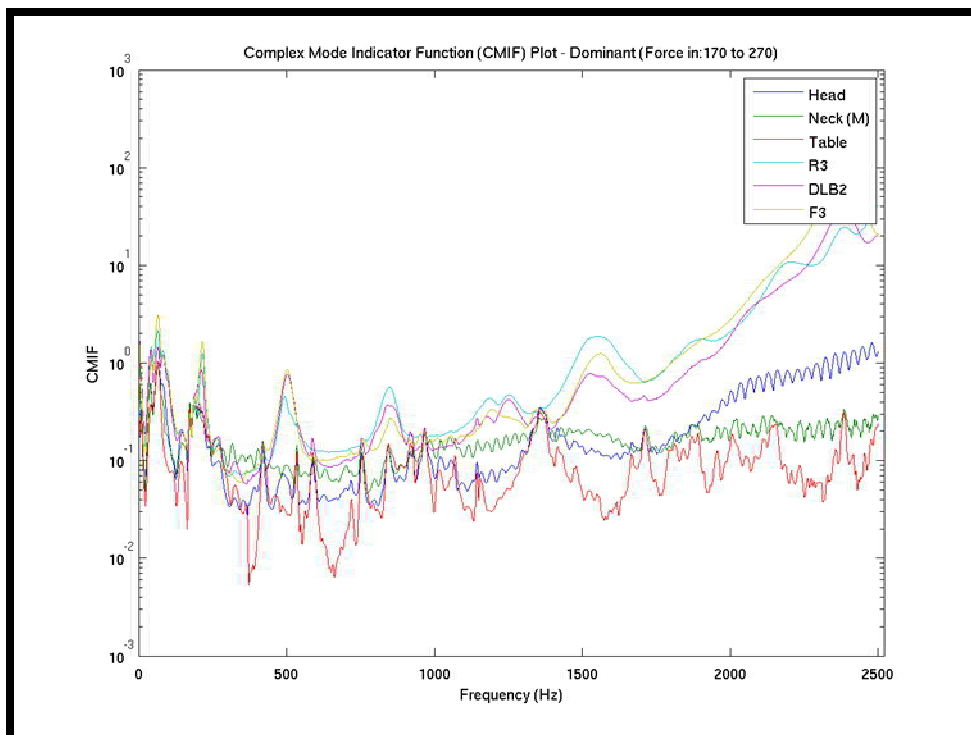


Fig 6 Dominant CMIF Modes for the Helmet ARL3, head, neck, and table

analysis and responses considered here were obtained using the small modal impact hammer. The size and shape of the helmets allowed for more impact points to be applied. Both helmets were impacted at approximately 100 impact locations with five impacts per impact point ($N_{avg}=5$).

The modal analysis conducted on the head was also conducted on the helmets. The dominant modes of the CMIF for each helmet can be compared. The dominant CMIF modes of the first helmet tested (ARL1) are similar for all sensor degrees of freedom (Fig 5). The three helmet sensors and the head, neck, and table sensor degrees of freedom all exhibit similar responses. The dominant CMIF modes of ARL1 suggest the helmet, head, neck, and table are strongly coupled. In addition, all sensors appear to have approximately the same amount of spectral energy (area under the CMIF spectrum). In comparison, the dominant CMIF modes of the second helmet tested (ARL3) are different for the sensor degrees of freedom (Fig 6). The responses of the helmet sensors are slightly similar; however, they are significantly different than the head, neck, and table sensors. As in the case of the ARL1 helmet, ARL3 exhibits coupling between the head, neck, and table. However, ARL3 is only coupled at particular frequency ranges where the dominant modes are closely spaced. Conversely, the frequency ranges where the modes are clearly separated correspond with uncoupled modes of vibration. In addition, the response magnitudes of the head, neck, and table are less, if not an order of magnitude less, than the helmet sensors. The lower response magnitude indicates less force and energy are experienced by the head, neck, and table. The CMIF suggests that ARL3 is a more effective helmet from a standpoint of low energy dynamic absorption compared with ARL1, because the ARL3 absorbs more energy than ARL1.

Another method to determine the effectiveness of a helmet is to calculate the transmissibility of the helmet (as observed by the sensors placed on the helmet) to the head. The transmissibility (force, displacement, velocity, acceleration) is a function of the frequency response for the output and input degrees of freedom (Equation 6). For example, the transmissibility of the helmet to the head is a function of the output (the frequency response of the head) and the input (the frequency response of the helmet). Since the transmissibility is a ratio, if the transmissibility is greater than one, the output experiences more dynamic force than the input: the force is amplified. Conversely, if it is less than one the output experiences less dynamic force than the input: the force is attenuated.

$$Tr = \frac{H_{1_{out}}}{H_{2_{in}}} \quad (6)$$

For every pair of frequency response functions, there is a corresponding transmissibility function. Therefore, two aggregate methods were developed to compare helmet transmissibilities: aggregate mean (AM) transmissibility and impact location average (ILA) transmissibility. The AM transmissibility is determined by calculating the mean cross-power and auto-power and using the results to calculate the mean frequency responses. The AM transmissibility provides a transmissibility function dependent on frequency. Therefore, plots can be created for each direction of each helmet sensor over the frequency range of interest. It is useful to focus on specific frequency ranges where the helmet amplifies or absorbs the force to the head. The AM transmissibility of ARL1 (Fig 7) confirms the analysis of the dominant CMIF modes of ARL1: the helmet does not significantly amplify or absorb force applied to the helmet. The AM transmissibility remains relatively close to one, neither significantly absorbing nor amplifying the force applied to the helmet. In comparison, the AM transmissibility of ARL3 (Fig 8) drops significantly less than one; this indicates the helmet absorbs force. However, the AM transmissibility in the y direction has several frequency ranges where the transmissibility is significantly greater than one. This indicates force applied to the helmet is amplified to the head for those specific frequency ranges. The amplification caused by ARL3 is significantly greater than any amplification caused by ARL1.

The ILA transmissibility aggregate tool provides similar insight but from a different approach. The ILA transmissibility is calculated by normalizing the integral of the transmissibility function by the frequency range. Essentially the ILA transmissibility is the average transmissibility. Therefore, the ILA transmissibility is calculated for each impact location and sensor direction. The ILA transmissibility aggregate tool is an array of single values; if a value is greater than one, then on average force is amplified – if it is less than one, force is absorbed. The ILA transmissibility of ARL1 (Fig 9) indicates, on average, force is amplified from the helmet to the head, particularly in the x and y directions. In comparison, the ILA transmissibility of ARL3 (Fig 10) indicates, on average, force is absorbed by the helmet. It is interesting to note the ILA for both helmets indicates force in the z direction is always absorbed. This is most likely caused by the boundary conditions. In particular, the neck, as well as the isolation table, is stiffer in the z direction than the x or y direction.

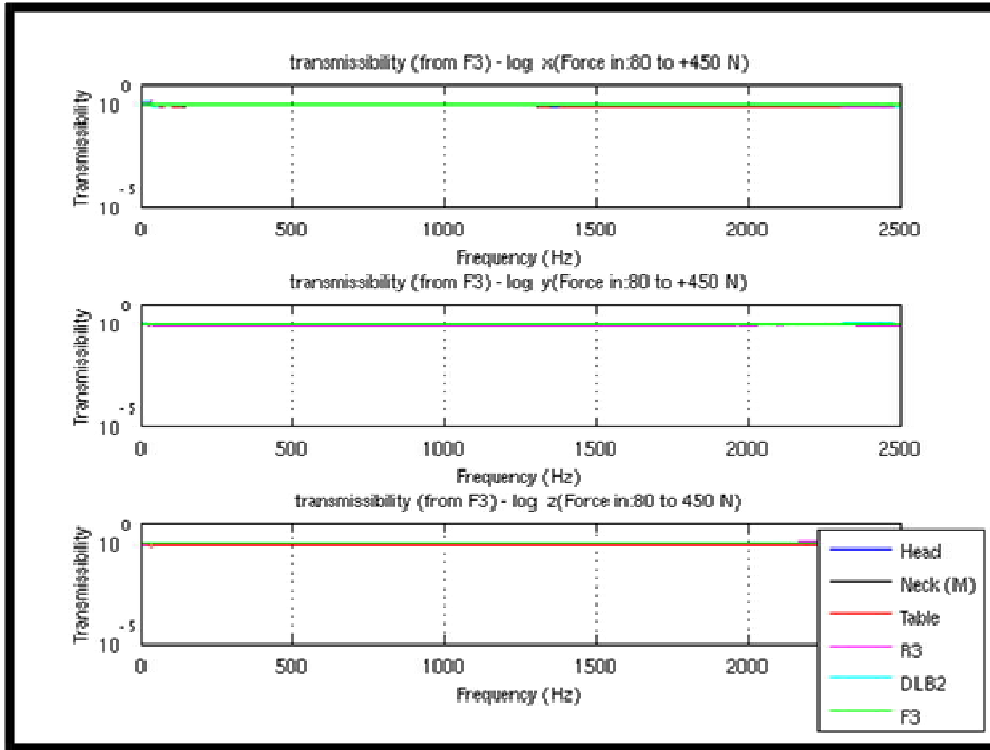


Fig 7 Helmet ARL1: Aggregate mean transmissibility for each axial direction based on sensor located at F2

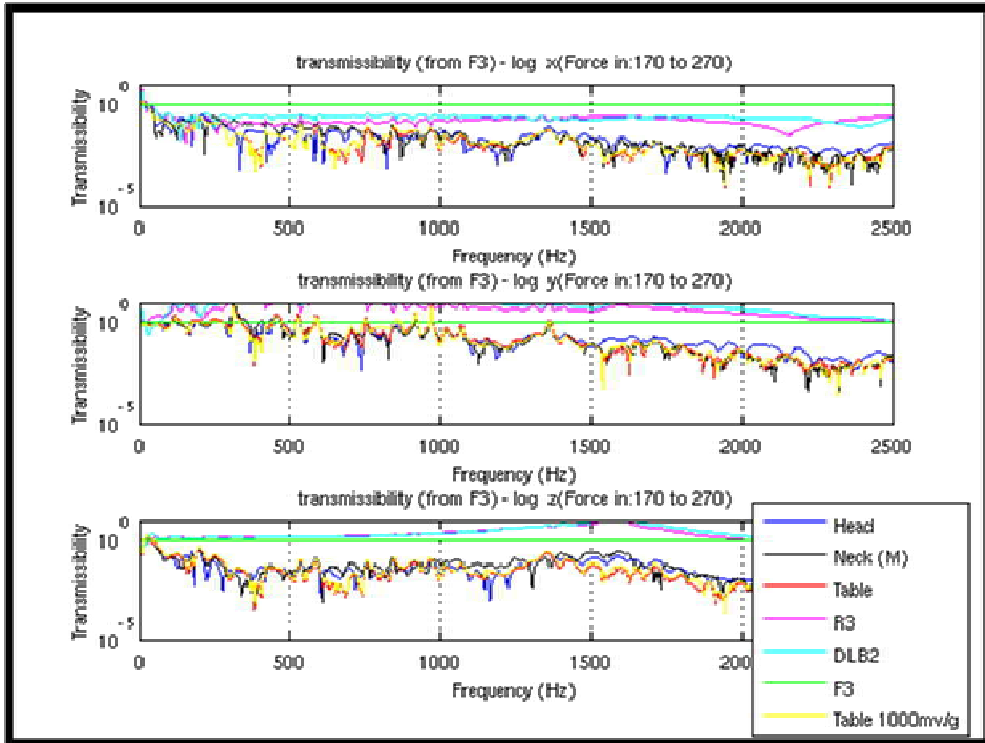


Fig8 Helmet ARL3: Aggregate mean transmissibility for each axial direction based on sensor located at F3

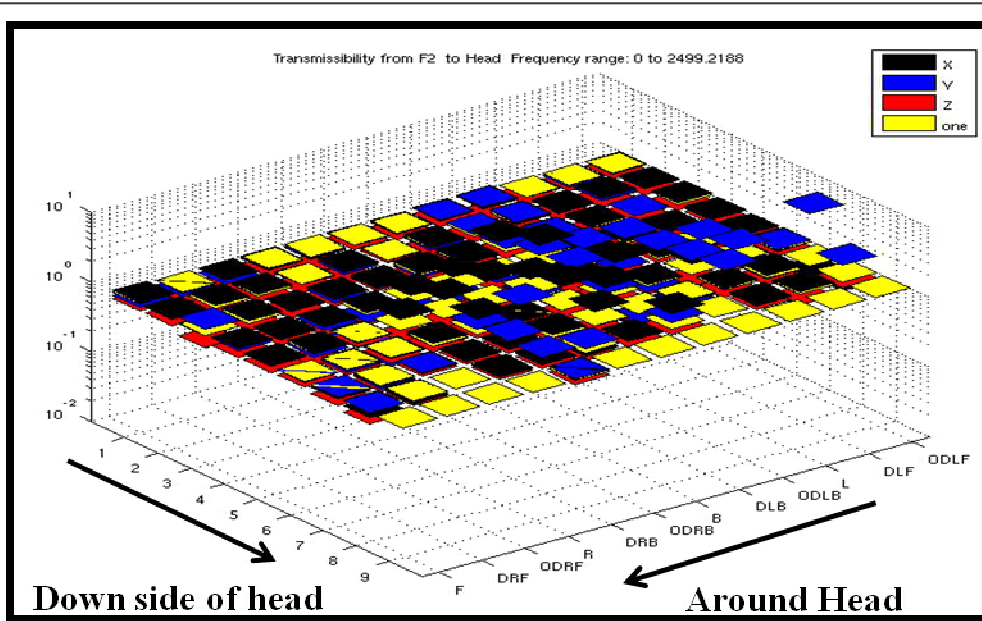


Fig 9 Helmet ARL1: Impulse location average transmissibility for all three axes, based on sensor located at F2

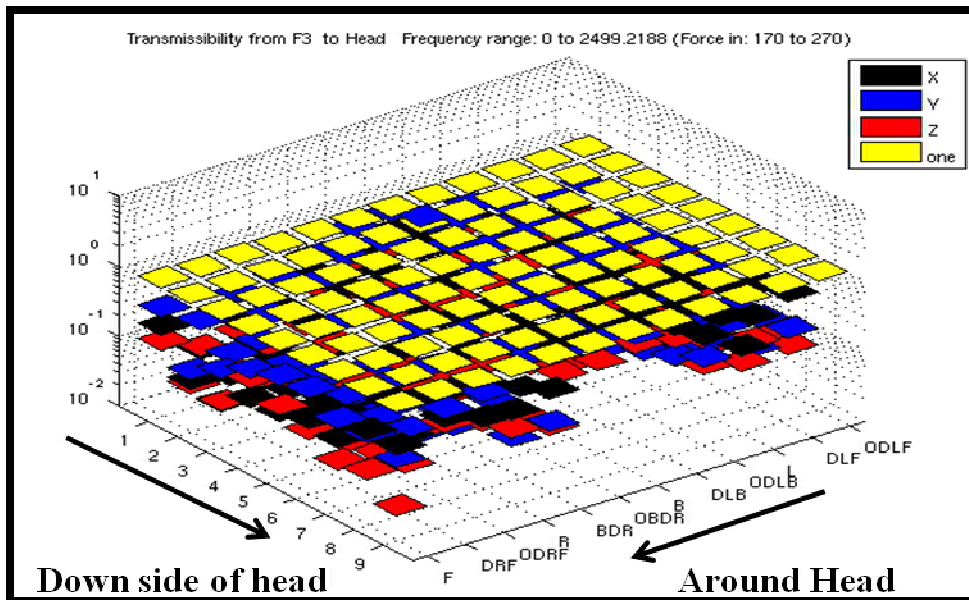


Fig 10 Helmet ARL3: Impulse location average transmissibility for all three axes, based on sensor located at F3

Conclusion

The study is not complete with one additional helmet to test and is a single blind study. Therefore, the material properties of ARL1 and ARL3 are not yet known to the experimentalist. However, both helmets appear similar in design. One difference that is apparent is that ARL1 appears to be larger than ARL3. ARL3 appears to fit the crash test head better than ARL1. The pads in ARL1 are not preloaded to the same level as ARL3 even though the chin straps are tightened to the same degree. This could explain differences in dynamic effectiveness. ARL3 is the more effective helmet from a standpoint of dynamic absorption over the frequency range considered. The response of ARL1 is strongly coupled to the head, neck and table. In essence, the head appears to be directly excited by impacts on ARL1 whereas ARL3 absorbs more force and transfers less force to the head.

References

1. Davenport, Christian. "Traumatic Brain Injury Leaves an Often-invisible, Life-altering Wound." *Washington Post - Politics, National, World & D.C. Area News and Headlines - Washingtonpost.com*. 3 Oct. 2010. Web. 19 Oct. 2010. <<http://www.washingtonpost.com/>>.

Understanding the Effect of Preload on the Measurement of Forces Transmitted Across a Bolted Interface

Charles Butner¹
Research Assistant

Douglas Adams¹
Professor

Jason Foley²
Research Engineer

¹Purdue University, Center for Systems Integrity, 1500 Kepner Drive, Lafayette, IN 47905

²Air Force Research Laboratory Munitions Directorate, Fuzes Branch, Eglin Air Force Base

ABSTRACT

Often in the study of bodies that undergo shock loading, it is desirable to measure the response of such bodies with an instrumentation package. This instrumentation can be separated from the external housing by several preloaded interfaces. To better understand the effects of preload on the nonlinear dynamics introduced into the measurement, a simple preloaded interface has been fabricated that consists of an upper smaller mass body bolted at three locations to a lower, larger mass body. A finite element model of the fixture was used to study the modal characteristics of the individual components and the coupled bodies. A series of modal impact tests were used to analyze the effects of a varying preload between the bodies on the linear and nonlinear features observed in the dynamic response of the coupled bodies. High amplitude shock loading was also used to understand if the laboratory results would be indicative of a more realistic loading scenario. The results of these measurements lead to the determination that a simple two degree of freedom model could be used to explain some aspects of the system.

INTRODUCTION AND BACKGROUND

A common problem in vibrations testing is to identify and manage uncertainties associated with the mounting condition of the sensor. In a particular representative problem currently being studied, a tri-axial sensor mount is bolted to a larger body. The goal of the sensor is to measure the response of the body to which it is attached, but the bolted interface between two such bodies introduces both linear and nonlinear features in the sensor data, and leads to errors in the measured response of the body of interest. To study this particular interaction, a test fixture was designed and built to simulate the interface. The fixture design is illustrated in Fig. 1.

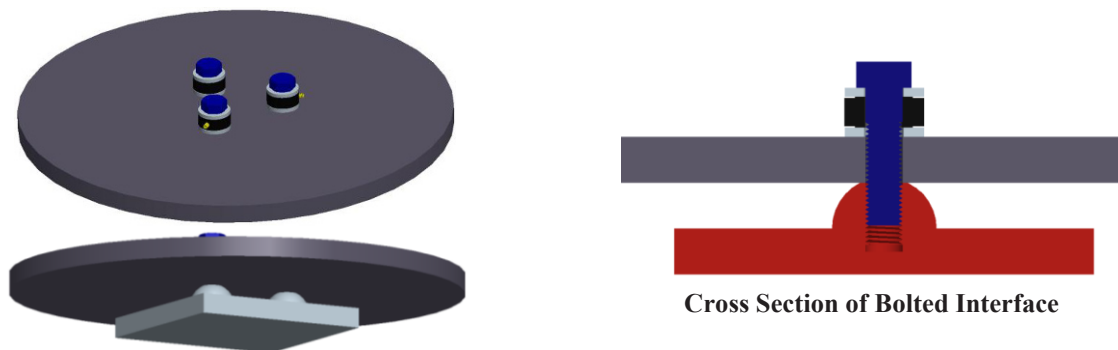


Fig. 1 Bolted Interface Test Fixture Used for Experiment

The first component of the fixture is a large circular plate with a diameter of 460mm, and a thickness of 20mm. The second component of the fixture is a smaller square plate with a 180mm height and width and a 20mm thickness. The square plate also contains three spherical standoffs of 20mm height that localize the contact area between the two plates. Both plates were machined from 4140 Alloy Steel. The fixture is assembled by bolting the two components together with M-16 bolts and load washers to measure the static and dynamic preload in the bolts.

The fixture was used to study the behavior of the bolted joint due to impulsive loading. In the problem being simulated by the fixture, the load path passes through the circular plate and into the square plate. The primary goal of the experiments that were conducted was to determine how preload in the bolts affects the force transmission across the interface. First, modal analysis was conducted on the test fixture for various preload levels and impact amplitudes, and then high amplitude impacts were applied to the test fixture with a Hopkinson bar in order to approach a more realistic loading scenario. The results of the modal impact tests were used to demonstrate the effect of bolt preload on the linear response, while the results of the high amplitude impact testing were used to demonstrate that the force amplification characteristics across the boundary can be explained with a lumped parameter two degree of freedom dynamic model.

According to work by Peairs, Park, and Inman (2001), bolt preload level is important in a bolted interface because “varying the preload tension in a bolt changes the integrity of the particular joint and also changes the structure's global dynamic properties.” It was expected that these changes would be reflected in the mode shapes, and that the experiments performed could quantify the particular properties of the test fixture that are most affected by changes in preload. Change in modal frequencies due to varying bolt preload is also examined in literature as described in the work by Chang, Erickson, Lee, and Todd (2004), where an experiment was presented as part of a damage detection study that studied the percentage change of natural frequencies for five modes of vibration as a function of bolt preload level. The experimental setup consisted of two thin (¼ inch thick) metal beams affixed with a single bolt. The result of this study showed that, although the change in frequency was different for each mode, there was certainly an upward shift in natural frequency that occurred as a result of increasing the preload of the bolt. It was determined that “higher frequencies are [sic] generally a better indicator of damage because the change in frequency at low frequency ranges is very small, even though the percentage change may be slightly larger.” The nonlinear effects of bolted joints were also studied by Ibrahim and Pettit (2005), where the filtering properties of threaded interfaces are characterized by the use of transmissibility functions. Finally, in a paper from IMAC XXVIII, Adams et. al. (2010), also used transmissibility functions to investigate the effect of threaded joint preload on structural response for a particular cylindrical structure that can undergo shock loading. The substructure being studied in this paper is a component from the structure studied in Adams et. al. (2010).

EXPERIMENTAL APPROACH

The modal impact testing of the bolted interface between the square and circular plate was carried out based on the results of a finite element analysis of the system that produced the estimated real normal mode shapes and undamped natural frequencies. The analysis showed that a total of 46 impact testing points would be sufficient to observe modes of vibration up to 6 kHz. The 46 points were distributed with 9 points on the square plate, 31 points on the circular plate, and 6 points near the accelerometers for driving point measurements. The modal grid that was used is shown in Fig. 2. The equipment that was used for the test consisted of six PCB 356A32 100 mV/g tri-axial accelerometers rigidly attached with superglue, three RS Technologies Bolt Load Force Transducers (Model 054216) connected to PCB Strain Gauge Signal Conditioners with digital display units (PCB Series 8159), two PCB modal impact hammers (Model 086C03 and Model 086C01), and a VXI Mainframe rack unit (Agilent E8408A) with three 4-16 channel 51.2 KSa/s A/D+DSP circuit cards (Agilent E8491B, E1432A, and HP E1432A). The accelerometers were placed at each end of the three bolts in the joint. The test setup is shown in Fig. 3.



Fig. 2 Modal Grid

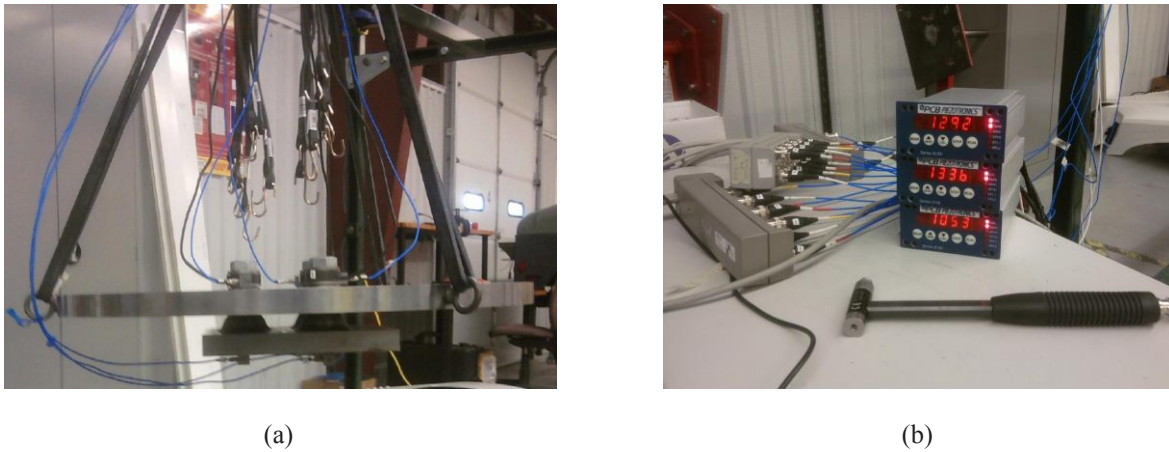


Fig. 3 (a) Instrumented Test Fixture and (b) Impact Hammer with Load Washer Signal Conditioners

Four complete modal impact tests were conducted on the fixture using this test setup. Two variables were adjusted between the tests. The modal impact tests were conducted with the static preload in the bolts tuned at levels between 1kN and 20kN, and the amplitude range of the impacts were held between 10lbf and 20lbf in one set of tests or between 200lbf and 300lbf for a second set of tests. The goal of the test was to characterize the nonlinear response characteristics due to impact amplitude as the preload in the bolts was adjusted. Three impacts were applied at each point on the modal grid where it was determined that the coherence was acceptable.

A second experiment was conducted using a Hopkinson Bar to impact the test fixture. The Hopkinson bar applies an impact through a transfer bar. This method was chosen because a one inch diameter aluminum transfer bar could be used in order to prevent deformation at the impact location on the much harder steel test fixture. These tests were conducted by suspending the test fixture vertically from an engine hoist and preloading a transfer bar against the test fixture. The bolts were tightened to a pre-defined torque with a torque wrench, and each load cell's static value was recorded. The transfer bar was then impacted by a projectile that was fired by a gas gun. The impact force was stepped up by monitoring the air pressure that was used to launch the projectile. For this experiment, six PCB 350C02 shock accelerometers were used to measure acceleration at both ends of each of the three bolts. For each test, the six acceleration measurements were acquired as was the velocity at the center of the square plate using a laser velocimeter. The load cell dynamic data was also recorded. During this round of testing, preload levels of hand tight, 50ft-lb, and fully tight, 100ft-lb, were tested with impacts at 5psi, 10psi, 15psi, and 20psi. The aim of this experiment was to achieve an excitation that better reflected the realistic loading scenario that was expected. The setup for these tests is shown in Fig. 4.

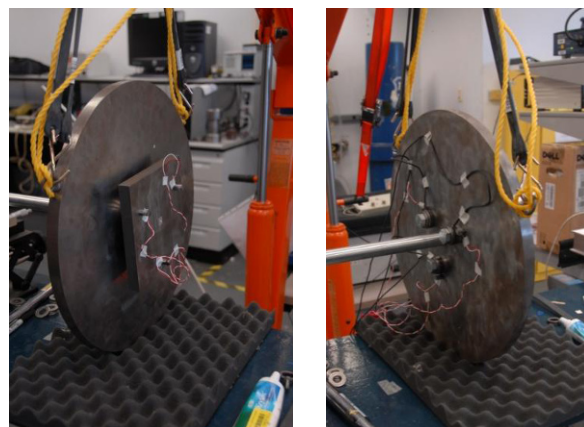


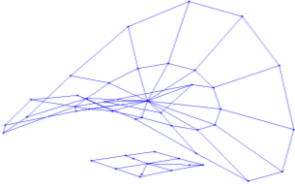
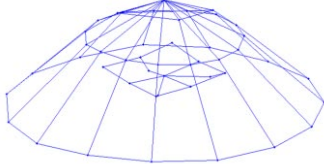
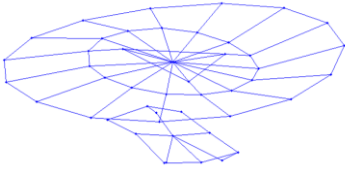
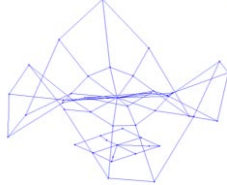
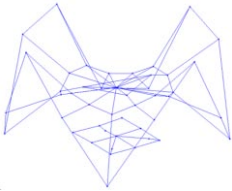
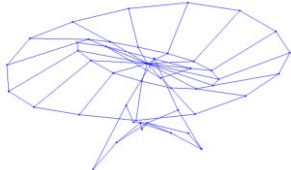
Fig. 4 Hopkinson Bar Test Setup

KEY RESULTS AND DISCUSSION

As mentioned in the previous section, the planning of the first experiment began with the creation of a finite element model. Before performing any experiments, this model was created because it provided a means to predict the experimental results given a certain set of measurement degrees of freedom. By knowing what outcome to expect, the experiment was designed to meet the expectations of algorithms that were planned in areas like impact force identification. For this particular experiment, a finite element model was used to predict the undamped natural frequencies and real normal mode shapes. By knowing the modal frequencies and mode shapes, an appropriate measurement frequency range and spatial modal test grid was chosen.

The finite element model was created using Abaqus. Properties were determined for the material that comprised the fixture: 4140 alloy steel. In order to account for the likelihood of relative motion across the bolted interface, a thin layer of lower stiffness material was inserted between the two components of the fixture in the model. The intermediate layer had properties similar to those of aluminum. It was understood that this approach was an approximation for modeling the bolted interface. The results could then be compared between the model and the experiment to determine the validity of the method. **Table 1** contains pictures and descriptions of the six mode shapes that were estimated experimentally and were the focus of this analysis. Note that all of the shapes except Mode B had repeated roots present in the experimental data. **Table 2** contains a comparison of the average frequency at which each of the six modes occurred in the tests alongside the predicted frequency from the finite element model. Differences in modal frequency from test to test are discussed later in this section. The largest percent difference in natural frequency of 5.88% was for Mode D. Considering the difficulty of modeling the bolted interface, the model was considered to be reasonable for predicting the modal properties of the test fixture. The mode shapes predicted by the model were also very close to what was observed experimentally. Once the model was determined to be adequate, the effects of nonlinearity due to preload level in the bolts was analyzed in the test data.

Table 1 Mode Shapes Found in Experiment with Descriptions

| | |
|--|--|
|  |  |
| <p><u>Mode A:</u> Saddle Shape in Circular plate with little motion in square plate. This corresponds to the first mode of the circular plate.*</p> | <p><u>Mode B:</u> Bowl shape of the circular plate, while square plate moves rigidly with circular plate. This corresponds to the second mode of the circular plate.</p> |
|  |  |
| <p><u>Mode C:</u> Rigid tilting of the square plate with undulations at attachment points, resembling second bending across the diameter of plate.*</p> | <p><u>Mode D:</u> Six point sine wave around edge of circular plate, with little motion in square plate. This corresponds to the third mode of the circular plate.*</p> |
|  |  |
| <p><u>Mode E:</u> Eight point sine wave around edge of circular plate, with little motion in square plate. This corresponds to the fourth mode of the circular plate.*</p> | <p><u>Mode F:</u> First bending along the diagonal of the square plate with undulations at attachment points, resembling second bending across the diameter of plate.*</p> |

*Repeated Root Exists for this Shape

Table 2 Comparison of Predicted and Measured Modal Frequencies

| Mode Shape | Modal Frequency (Hz) | | Percent Difference |
|------------|----------------------|----------------------|--------------------|
| | FEA Model | Experimental Average | |
| A | 483 | 504.5 | 4.35 |
| B | 652 | 666.25 | 2.16 |
| C | 1138 | 1109.5 | 2.54 |
| D | 1082 | 1147.5 | 5.88 |
| E | 1875 | 1973.5 | 5.12 |
| F | 2303 | 2230 | 3.22 |

In order to determine the modal frequencies and shapes that are summarized in [Table 1](#) and [Table 2](#), the Complex Mode Indicator Function (CMIF) method was used to analyze the data. This method utilized all six of the vertical sensor reference channels to analyze the data, and also made it possible to identify repeated roots in the data. Other common methods for modal parameter estimation, such as peak-pick, do not allow for the detection of repeated roots. The CMIF method uses the Singular Value Decomposition (SVD) of the frequency response function matrix to identify peak frequencies (natural frequencies) in the singular value matrix and their corresponding modal vectors. This method was utilized for all four modal tests to determine and animate the mode shapes.

It was predicted that an increase in bolt preload level should result in some increase in each of the system's modal frequencies. This hypothesis was investigated by comparing the frequencies at which each of the fixture's first six modes (named A through F) occurred for each bolt preload level and impact amplitude. In a linear system, modal properties should not depend on impact amplitude, but at low preloads it was expected that the assumption of linearity would be poorer than at high preloads. The modal frequencies of the first six modes for the system for each of the four tests are listed in [Table 3](#).

Table 3 Modal Frequencies as a Function of Bolt Preload and Impact Amplitude

| Mode Shape | Modal Frequencies (Hz) | | | | Predicted |
|------------|------------------------|----------------|---------------------|----------------|-----------|
| | 1000N Bolt Preload | | 20000N Bolt Preload | | |
| | Low Amplitude | High Amplitude | Low Amplitude | High Amplitude | |
| A | 498 | 498 | 511 | 511 | 483 |
| B | 655 | 654 | 678 | 678 | 652 |
| C | 1036 | 1013 | 1195 | 1194 | 1138 |
| D | 1147 | 1146 | 1149 | 1148 | 1082 |
| E | 1973 | 1973 | 1975 | 1973 | 1875 |
| F | 2193 | 2152 | 2289 | 2286 | 2303 |

As expected, there is an increase in modal frequency for each mode when the bolt preload is increased, although this increase is nearly negligible for modes C and D. This result is most likely due to the fact that little motion along the axis of the bolts is present in these modes. The large jump in frequency for mode C when the preload is increased is particularly interesting. This mode is the third mode of vibration for the low preload value tests, but this mode becomes the fourth mode of vibration for the tests with the high preload value. This switch is due to geometric stiffening in the bolts as the preload is increased. Mode C exhibits the most motion along the bolt axis, and is, therefore, the most affected mode due to the effects of bolt stiffening.

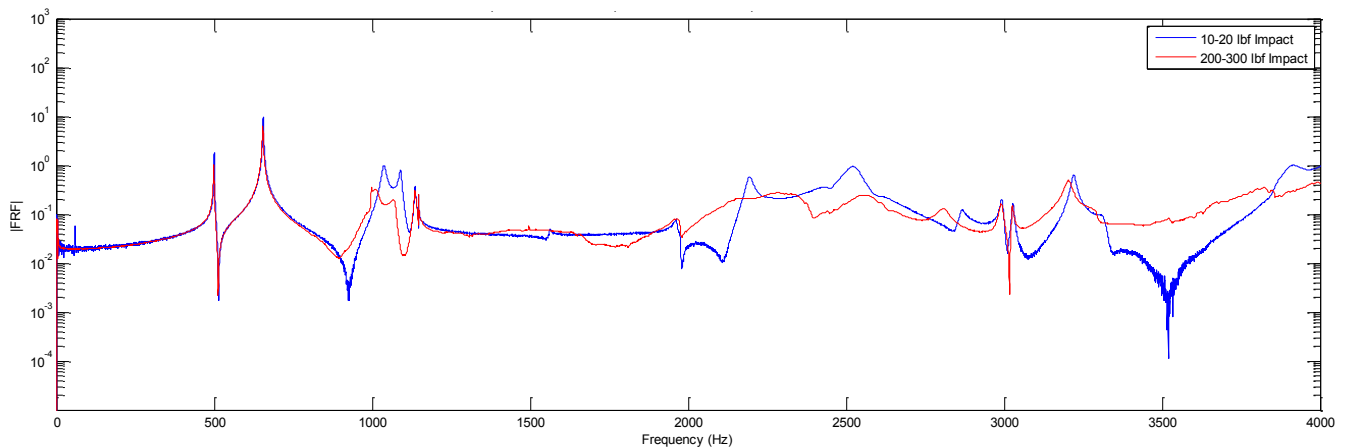
It was initially believed that the nonlinearity due to impact amplitude could be observed by examining modal frequencies. It was expected that the nonlinearities would be larger for the low preload value than the high preload value because the higher preload level increases coupling thereby allowing less relative motion. A comparison of modal frequencies from impacts of different amplitudes is shown in [Table 4](#). Although the changes in modal frequency for the low preload level were greater, the difference between the two preload levels is nearly negligible. This does not indicate that the two cases have the same amount of nonlinearity. As discussed earlier, the literature suggests that the largest changes in modal frequency due to nonlinearity normally occur at higher frequency modes. Another method for characterizing nonlinearity was needed based on these results.

Table 4 Percent Differences of Modal Frequencies for Varying Impact Amplitudes

| Modal Frequency: 1,000N Bolt Preload Level | | | |
|--|---------------|----------------|--------------|
| Mode Shape | Low Amplitude | High Amplitude | % Difference |
| A | 498 | 498 | 0.00 |
| B | 655 | 654 | 0.15 |
| C | 1036 | 1013 | 2.24 |
| D | 1147 | 1146 | 0.09 |
| E | 1973 | 1973 | 0.00 |
| F | 2193 | 2152 | 1.89 |

| Modal Frequency: 20,000N Bolt Preload Level | | | |
|---|---------------|----------------|--------------|
| Mode Shape | Low Amplitude | High Amplitude | % Difference |
| A | 511 | 511 | 0.00 |
| B | 678 | 678 | 0.00 |
| C | 1195 | 1194 | 0.08 |
| D | 1149 | 1148 | 0.09 |
| E | 1975 | 1973 | 0.10 |
| F | 2289 | 2286 | 0.13 |

Since the modal frequencies were a poor indicator of nonlinearity in this frequency range, another analysis method was needed to quantify a change in nonlinearity. In this case, a simple comparison of frequency response functions was the clearest indicator of nonlinearity. In the problem being modeled, the load path enters through the rim of the circular plate and moves through the bolts into the square plate. To simulate this transmission of force, frequency response functions were measured between an impact point near the outer edge of the circular plate and the acceleration response on the square plate for both preload levels and both impact amplitude levels. These frequency response functions for both impact levels and the 1000N preload level are shown in Fig. 5. The same data for the 20000N preload level is shown in Fig. 6. The two responses vary substantially for impacts of different amplitude when the preload is low. This difference indicates significant system nonlinearity due to impact amplitude. The two responses are nearly identical, however, for the case where the preload is high. This result indicates that the nonlinearity due to impact amplitude decreases for higher preloads. This result was expected since the system behaves more as a single body, with little relative motion between the two plates. This decrease in nonlinearity will lead to an improved ability to estimate forces from a response measured across the boundary.

**Fig. 5** Frequency Response Functions for 1000N Preload Level

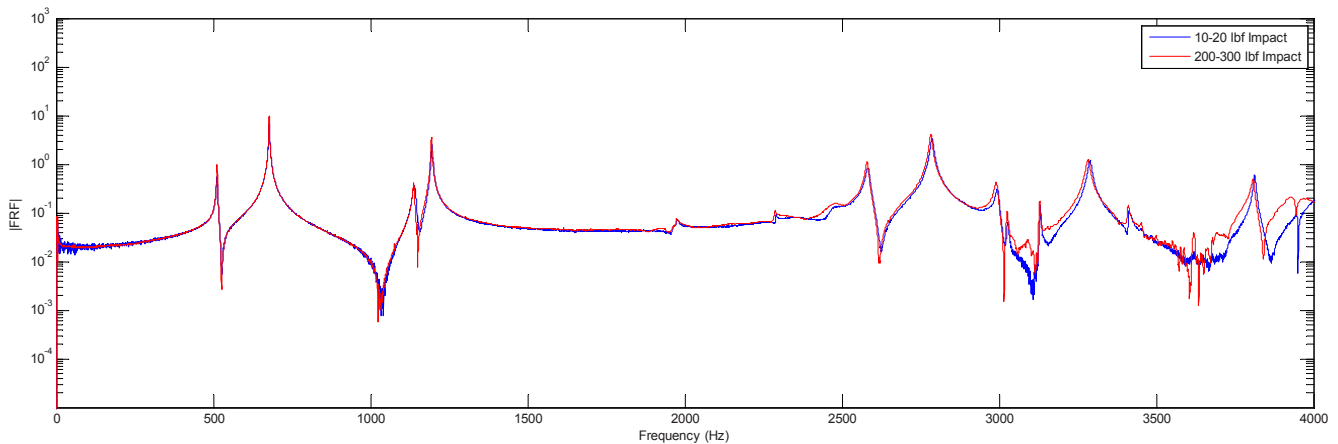


Fig. 6 Frequency Response Functions for 20000N Preload Level

A second experiment was conducted with a Hopkinson bar as discussed previously. The primary purpose of this experiment was to impact the fixture with much higher-level impacts and investigate the system behavior. Since the forces used to impact the fixture were only characterized by the pressure used to launch the striking projectile, the actual impact force is unknown. Analysis is underway to predict these forces using a model that was created with a modal impact hammer after testing was completed. The hammer was used to strike the end of the transfer bar where the load would normally initiate. This procedure allowed for the measurement of frequency response functions. These functions will eventually be used to generate force estimates for the Hopkinson bar tests, but issues with the boundary conditions and system nonlinearities have complicated the process. Early estimates predict that the largest impacts generated in this test were on the order of 8000lbf, which is more than twenty times larger than previously generated forces. Because these forces are not completely known at this time, the analysis of the data has focused for now on the acceleration response measured on the plates.

The most notable result for these large level impacts is the effect of preload on the amplification or attenuation of forces across the interface. While the impact was always applied to the center of the circular plate in order to avoid effects due to asymmetrical loading, the acceleration response was sometimes larger on the smaller, square plate. The acceleration response near the end of the measurement window for a 20 psi impact and a hand tight preload condition is shown in Fig. 7. The responses for the 50ft-lb and 100ft-lb preload level are shown in Fig. 8 and Fig. 9, respectively. Each plot shows the acceleration response for accelerometers located directly across from one another, with one on each plate. These accelerometers were located at either end of the bolted joint. For the hand tight preload level, the bolts were tightened to a snug level with no tools. This procedure resulted in low coupling between the two plates and a large amount of relative motion. In this case, the acceleration response on the circular plate was larger. When the bolts were tightened to 50ft-lb, the response changed drastically. The responses were noticeably more synchronous as the coupling in the system was increased. For this case, the smaller square plate actually responded at a higher level than the larger plate, where the impact occurred. The results for the 100ft-lb preload followed the same trend, with even a greater amplification of force across the interface. This result was significant since the square plate is an analog for a sensor mount. This acceleration amplification effect could result in damage to the sensors that are used in the application of interest.

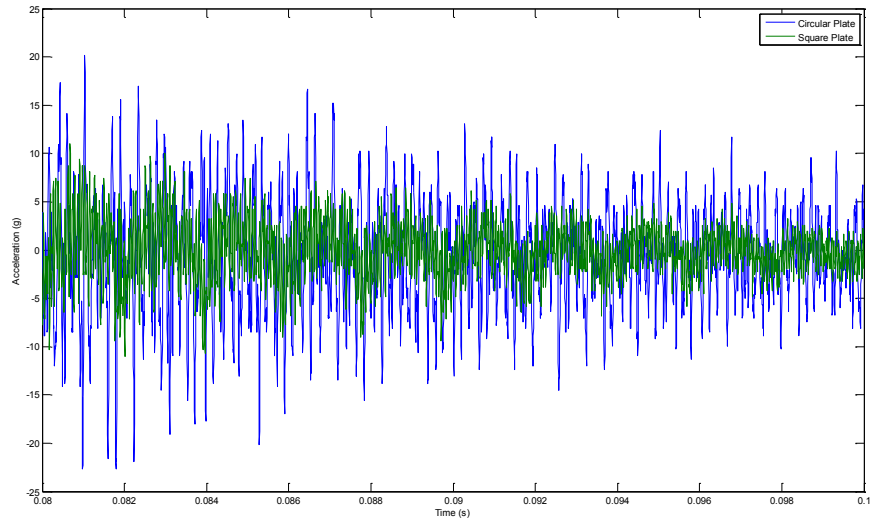


Fig. 7 Acceleration Response for 20psi Impact and Hand Tight Preload Level

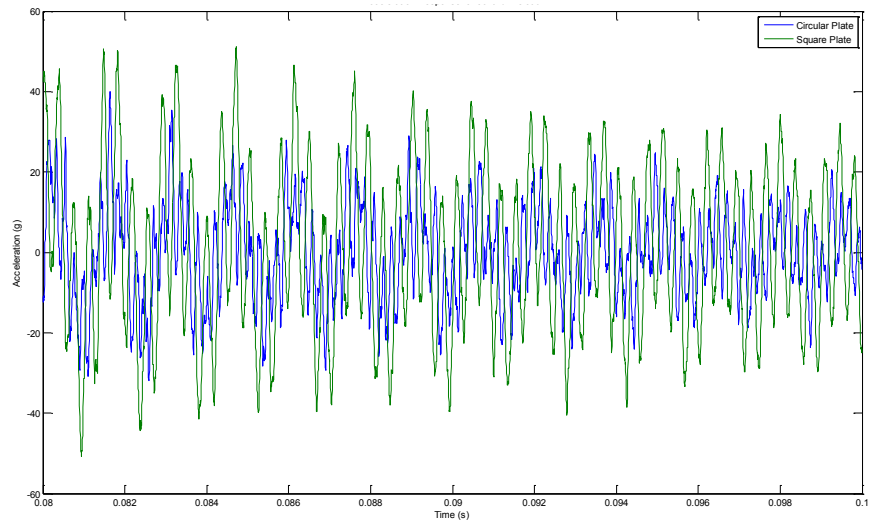


Fig. 8 Acceleration Response for 20psi Impact and 50ft-lb Preload Level

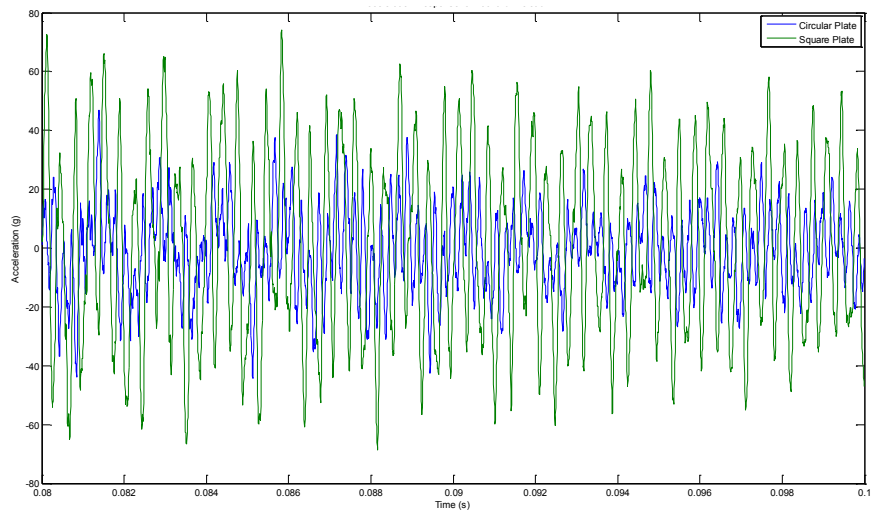


Fig. 9 Acceleration Response for 20psi Impact and 100ft-lb Preload Level

To explain why an amplification effect is seen for the higher preload levels, the system was approximated by the simple lumped parameter two degree of freedom system shown in Fig. 10. The larger mass, M_1 , represents the circular plate while the smaller mass, M_2 , represents the square plate. The bolts are represented by a piecewise linear spring and damper. The impact force is applied to the center of M_1 , as in the real system. The position of the large mass is denoted as x , while the position of the smaller mass is denoted as y . For this simple model, the values for M_1 and M_2 were chosen to be 4kg and 1kg, respectively. The value of C was chosen based on a proportional damping estimate and is always one thousandth of the value of K . The values of K were varied in order to simulate stiffening in the bolts. The system has a free-free boundary condition. The frequency response functions between the input force and the two plates' responses were calculated and plotted. The frequency response of the system for $K=0.5\text{N/m}$ is shown in Fig. 11. The result when the value of K is raised to 10N/m is shown in Fig. 12. The result for $K=30\text{N/m}$ is shown in Fig. 13. For all three responses, two modes of vibration can be observed. At DC, the rigid body mode occurs. The response of both bodies overlaps for a region, and then as the larger body M_1 begins to enter an anti-resonance, the motion is larger on the smaller body M_2 . In the anti-resonance region, the motion of the larger body goes to nearly zero and only the smaller body responds. In this vibration phenomenon, one body is excited, yet the largest motion occurs in the other body. After this region, the second mode of vibration, which consists of asynchronous motion between the bodies, can be observed. Shortly after this peak, the motion of the larger body begins to dominate. In the region around the anti-resonance, the smaller body acts as a tuned mass vibration absorber. The three plots show that the frequency bounds for each of these regions are highly dependent on the value of K , and, subsequently, the preload in the bolts. For the lowest stiffness, which simulates very low preload, the region in which motion is amplified on the smaller plate is almost completely below 1 rad/s . When the stiffness is raised to 10N/m , the region stretches from less than 1 rad/s to nearly 4.5 rad/s . For the highest preload value of 30N/m , the region lasts from less than 1 rad/s to nearly 8 rad/s . It should also be noted that the width of the anti-resonance in the response of the large plate, where the amplification of motion is the greatest, grows with the stiffness value. In general, as preload increases, the range where the motion of the smaller plate is greater than that of the larger plate increases as well. This result qualitatively agrees with the amplification of motion across the interface for higher preload values that was observed in the experimental data.

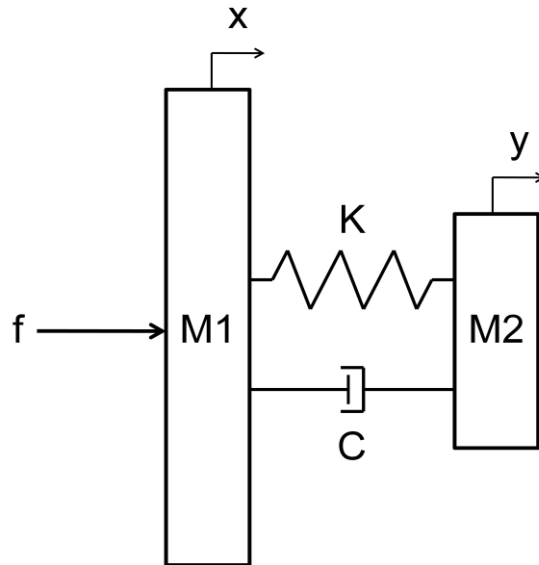


Fig. 10 Lumped Parameter Two Degree of Freedom System Model

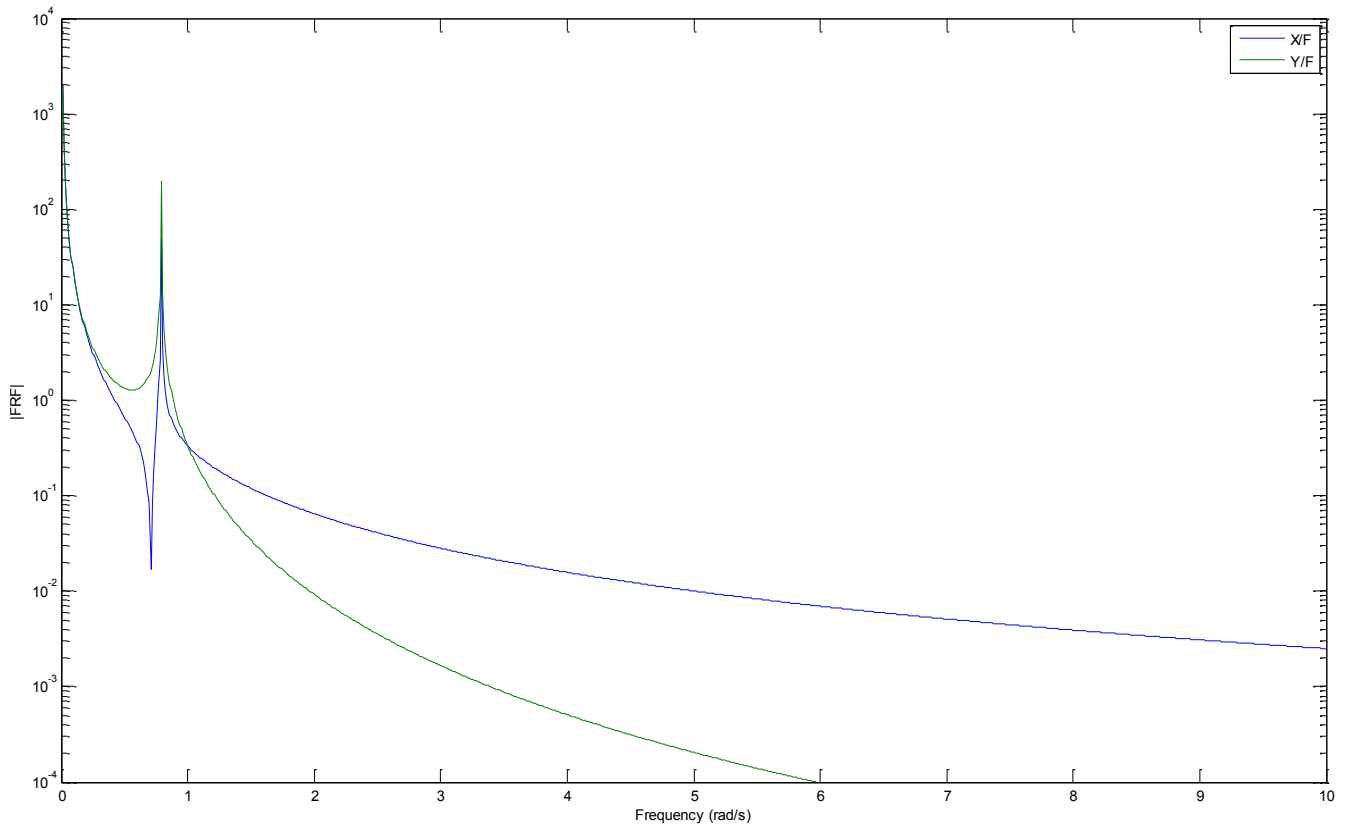


Fig. 11 Frequency Response Functions for System Model with $K=0.5\text{N/m}$

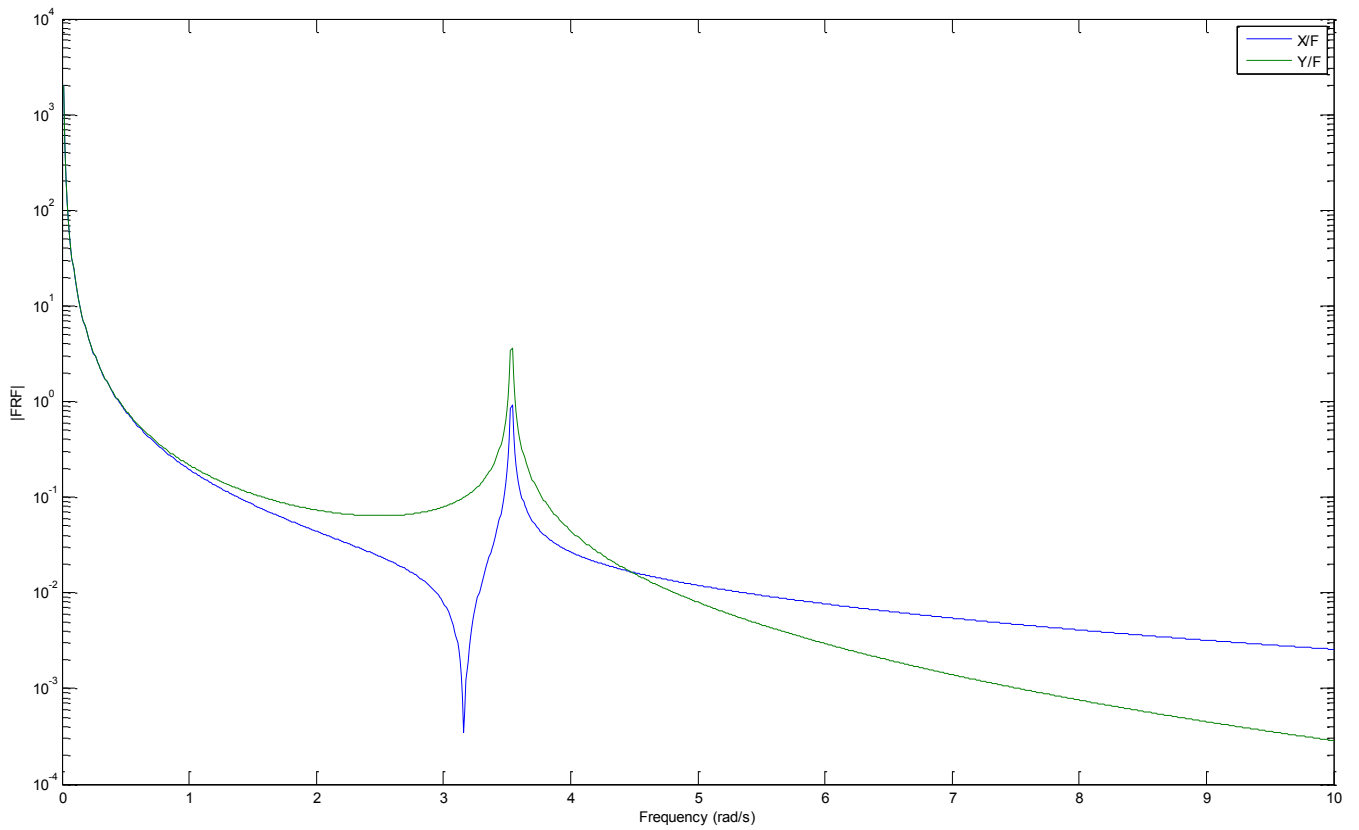


Fig. 12 Frequency Response Functions for System Model with $K=10\text{N/m}$

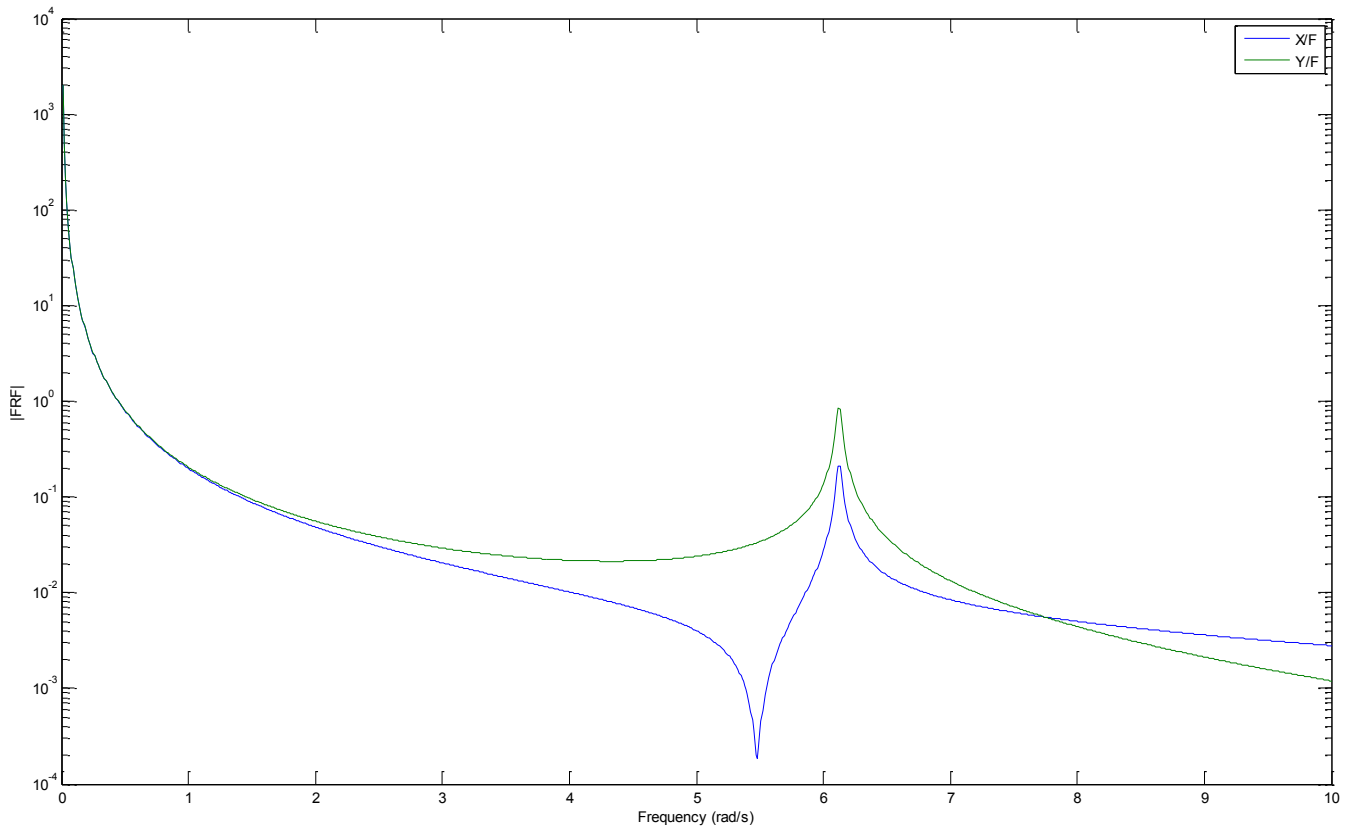


Fig. 13 Frequency Response Functions for System Model with $K=30\text{N/m}$

During this experiment, the static preload levels in the bolts before and after impact events were recorded using the load washers. While there was no definitive trend for different initial preload levels and impact amplitudes, it was noted that the static preload in the bolts was always lower after an impact than before. This preload relaxation actually causes the system dynamics to change during an impact event. Several examples of the drastic effects of changing preload have been presented in this paper, and the fact that preload is changing as a result of the force that is being measured could lead to many issues in the effort to accurately measure the impact forces because the system frequency response function is time-varying due to these time-varying preload levels.

CONCLUSIONS

A test fixture was constructed to simulate a preloaded sensor mount interface from a physical system being studied. This test fixture was analyzed using modal impact testing and acceleration response measurements in order to characterize the behavior of the system as the preload level in the bolted interface is changed. It was shown through modal impact testing that the modes of vibration that most excited deformation along the axis of the bolts were the most affected by changes in preload. It was also shown that the lower frequency modes were not subject to shifts in modal frequency due to impact amplitude, despite the nonlinearity observed in the system. Frequency response functions measured across the interface of the fixture were used to demonstrate the drastic decrease in nonlinearity in the system due to increases in preload. While it was shown that high preload values result in a much more linear system response, it was also shown that the system has the tendency to amplify motion across the interface when preload levels are raised. This could lead to the damage of instrumentation in the system being modeled. This amplification of motion was explained using a simple two degree of freedom model to demonstrate how the width and location of the circular plate's anti-resonance changes as a function of bolt stiffness. Finally, it was explained that the static preload in the bolts routinely decreased as the result of an impact event, which could lead to many complications in the effort to accurately measure forces across the interface.

REFERENCES

- [1] Peairs, D. M., Park, G., and Inman, D. J., 2001, "Investigation of Self-Monitoring and Self-Healing Bolted Joints", *Proc. 3rd Intl. Workshop on Structural Health Monitoring*, Stanford, California, USA, pp 430-439.
- [2] Chang, L.Y., Erickson, K.A., Lee, K.G., and Todd, M. D., 2004, "Structural Damage Detection using Chaotic Time Series Excitation", *Proc. 22nd Intl. Model Analysis Conference*, Dearborn, Michigan, USA, paper no. 221.
- [3] Ibrahim, R. A., and Pettit, C. L., 2005, "Uncertainties and Dynamic Problems of Bolted Joints and other Fasteners", *Journal of Sound and Vibration* 279 (3-5), pp. 857-936.
- [4] Adams, D. E., Yoder, N., Butner, C. M., Bono, R., Foley, J., and Wolfson, J., 2010, "Transmissibility Analysis for State Awareness in High Bandwidth Structures Under Broadband Loading Conditions" , *Proc. IMAC XXVII*, Jacksonville, FL, USA